











Distribution of Chromium Species and Physico-Chemical Analysis of Various Industrial Effluents in Hyderabad and Jamshoro, Pakistan

Muhammad Kashif Channa¹ , Jameel Ahmed Baig¹ , Khalil Akhtar^{1*} , Mirza Junaid²,
Tasneem Gul Kazi¹ , Hassan Imran Afridi¹ , Shakoor Ahmed Solangi¹ ,
Saima Perveen¹ , and Bibi Sara¹ 

¹Centre of Excellence in Analytical Chemistry, University of Sindh, Jamshoro 76080, Sindh., Pakistan.

²Department of Pediatrics, Peoples University of Medical and Health Science for Women, Shaheed Banazirabad 67480, Pakistan.

Abstract: This research aimed to quantify the speciation of chromium in different industrial effluent samples of Hyderabad and Jamshoro, Pakistan. The hexavalent chromium (Cr(VI)) was determined by microsample injection system flame atomic absorption spectroscopy (MIS-FAAS). The total chromium was measured by MIS-FAAS after the oxidation of trivalent chromium (Cr(III)) to hexavalent chromium (Cr(VI)) by $\text{Ce}(\text{SO}_4)_2$ in an acidic medium (0.07 M H_2SO_4). The content of Cr(III) was measured by the difference method (total chromium – hexavalent chromium). In the effluent samples of textile and fabrics industries, the total Cr was observed 400 to 1600 times higher than the US-EPA and WHO regulatory limit (0.10 mg/L) in the industrial discharge. In the effluent of food and plastic industries, the Cr(VI) was found to be high as compared to the Cr(III), and the Cr(III) was observed high in the effluent samples of chemical as well as textile and fabrics industries. The Cr(VI) was higher than the US-EPA and WHO regulatory limit (0.05 mg/L) in the effluent samples of all selected industries, but the Cr(III) was within the US-EPA and WHO regulatory limit (170 mg/L) in the industrial discharges.

Keywords: Chromium; Solid phase extraction; Micro sample injection system; Flame atomic absorption; Industrial effluent.

Submitted: May 10, 2022. **Accepted:** October 11, 2022.

Cite this: Channa MK, Baig JA, Akhtar K, Junaid M, Kazi TG, Afridi HI, et al. Distribution of Chromium Species and Physico-Chemical Analysis of Various Industrial Effluents in Hyderabad and Jamshoro, Pakistan. JOTCSA. 2023;10(1):1-10.

DOI: <https://doi.org/10.18596/jotcsa.1107392>.

***Corresponding author. E-mail:** khalilakhtre789@gmail.com.

1. INTRODUCTION

Industrial effluent is one of the main direct and often continuous input sources of pollutants into aquatic systems. These pollutants have long-term impacts on natural ecosystems, including changes in food availability and a grave threat to the ability of the biosphere to self-regulate. The industrial discharges or wastes have heavy metals, polychlorinated biphenyls (PCBs), pesticides, dioxins, polycyclic hydrocarbons (PAHs), phenolic compounds, and petrochemicals and microorganisms. All the industrial effluents are usually discharged into the natural water resources such as rivers and lakes, and cumulative hazardous

consequences on the ecosystem have received a lot of attention. Untreated municipal and industrial wastewater has posed serious environmental risks to humanity. Industrial effluent discharge is a potential source of environmental pollution throughout the world. In Pakistan, the untreated effluents are either released to the agricultural land for irrigation purposes or disposed of in the nearby water bodies due to a lack of sewage treatment plants. Thus, the contaminants are either accumulated in soil or may enter through the food chain to generate several occupational health consequences. The pollution of heavy metals from industrial effluent has become a major public and scientific problem because of their hazardous

effects on humans and other biological pathways. The increasing influx of heavy metals can be dispersed by water and wind, which make them accessible to animals and plants. Therefore, the information on toxic metals, especially chromium (Cr), and its different forms found in industrial effluents. It is important because of their relative toxicity, which may depend on their chemical properties and bioavailability.

The significance of chromium (Cr) speciation is associated with its toxic effects on different oxidation states. The Cr(III) and Cr(VI) are two stable chromium species found in the environment. Cr(III) is a relatively non-toxic and essential nutrient for humans, especially mammals, for their appropriate carbohydrate tolerance factor, protein, and lipid metabolism. The toxic effects of Cr(VI) are common due to its higher oxidation state and relatively smaller in size, allowing it to pass through the cell membranes and cause serious damage to proteins, DNA, and other macromolecules. The Cr(VI) suppresses the cell's enzymatic sulfur uptake and affects the lungs, kidneys, and liver. The major toxic effects of Cr(VI) include dermatitis, chronic ulcers, the corrosive reaction of the nasal septum, and lung infections. However, the determination of chromium is crucial with appropriate accuracy and sensitivity. The Cr species are usually discharged into the natural water resources due to different industrial activities, such as leather tanning, electroplating, steel works, pigments, refractories, oxidative dyeing, and lumber processing. In the water bodies, the Cr species usually exist in the form of chromate and hydroxo-complexes. Several strategies like coprecipitation, solvent extraction, electrochemical methods, solid phase extraction (SPE), ion-exchange separation, capillary electrophoresis, and ion chromatography have been developed for the determination of Cr species in different oxidation states (Cr(III), and Cr(VI)). SPE has some advantages over the techniques mentioned earlier in the speciation analysis of Cr because of its safety, flexibility, environment-friendly, selectivity, absence of emulsion, ease of automation, and simplicity. Amberlite XAD resins have been extensively used in SPE for various metals because of their cross-linked polymeric nature, which enhances their adsorptive properties due to their macro reticular type structure and greater active surface area. This macro reticular structure exhibits excellent chemical, mechanical, and thermal stability, making it an excellent candidate for the adsorption of various metal ions. In the ground waterway, Cr pollution has been reported as a result of the environmental effects of industrial wastewater drainage by the tanning industry. It may alter the pH, and enhances the biochemical oxygen demand (BOD), total dissolved solids (TDS), and electric conductivity (EC), which may give intense colourations to rivers. Therefore, the ecology is highly affected by microbial populations, which could be poisonous, mutagenic,

or carcinogenic for aquatic animals. Based on these facts, the gradual monitoring and assessment of Cr and its different forms in industrial effluents are very important. Moreover, the effect of different quality parameters of industrial effluents on the mobility of Cr species is the need of hours.

The total Cr and its species in Hyderabad and Jamshoro district industrial effluents were investigated. The Cr(VI) was determined by a solid phase extraction procedure using Amberlite XAD-4 resin. At the same time, Cr(III) was calculated by subtracting Cr(VI) concentration from total Cr in the studied industrial effluent samples. The variation of physical quality parameters like pH, BOD, TDS, and EC in different industries has been quantified.

2. MATERIAL AND METHOD

2.1. Reagents and Glassware

The analytical grade nitric acid ($\text{HNO}_3 \geq 65\%$ with Sp.gr: 1.41) and hydrogen peroxide ($\text{H}_2\text{O}_2 \geq 30\%$ with Sp.gr: 1.11) were purchased from Merck (Germany). A certified standard solution of Cr (1000 mg/L, Fluka Kamica, Switzerland) was used to calibrate the quantitative determination of total Cr. For Cr(VI), the calibration curve was drawn using a standard solution of $\text{K}_2\text{Cr}_2\text{O}_7$ (dissolving 0.372 g of $\text{K}_2\text{Cr}_2\text{O}_7$ in 1.0 L deionized water), and 1.0 M HNO_3 was used to prepare appropriate dilute solutions. Deionized water (electrical conductivity 0.050 $\mu\text{S}/\text{cm}$) was prepared by the water purification system of ELGA laboratory (Bucks, UK). The adsorbent, Amberlite XAD-4, with surface area and pore diameter of 735 m^2/g and 20–50 μm , respectively, were used. Before use, all glassware (pyrex) and plastic (polyethylene) bottles were carefully washed. The glasswares were soaked in 5.0 M HNO_3 for 24 hours, then rinsed with deionized water.

2.2. Instrumentation

The concentration of Cr was determined using a flame atomic absorption spectrometer (Hitachi model 180-50; Tokyo, Japan) equipped with Cr hollow cathode lamp (HCL), and a flame atomizer (air-acetylene). The wavelength, spectral bandwidths, and lamp current were used as 358.0 nm, 0.70 nm, and 25.0 mA, respectively.

2.3. Preparation of Column

The preconcentration of Cr was achieved using a 15.0 cm long, 1.2 cm diameter glass column. The column was packed up to the height of 4.0 cm with a slurry of 1.2 g Amberlite XAD-4 resin in 25.0 mL deionized water. The adsorbent material was properly settled by using glass wool at the top and bottom of the column then 0.1 M H_2SO_4 was used to activate the column.

2.4. Sample Collection

Random samples of industrial effluents were collected from twenty industrial effluents of Hyderabad and Jamshoro, Pakistan, located at different places. These industries were divided into four categories based on their natural food industry (FI), plastic industry (PI), chemical industry (CI), and textile and fabrics industry (TFI). For sampling, ten samples were randomly collected from two to three industries for each category of industry ($n = 40$). Microbiological examination vials of 500.0 mL capacity were used to collect the industrial effluent samples, and the physicochemical parameters such as biological oxygen demand (BOD), total dissolved solids (TDS), pH, and electric conductivity (EC) of each sample were analyzed by the method described by AOAC .

2.5. Determination of Hexavalent Chromium

The Cr(VI) content was determined by solid phase extraction (SPE), as reported by Rajesh et al. 2008 . For SPE, a 1.0 mL of 10.0 mg/L solution of Cr(VI) was added to a 100 mL volumetric flask along with 3.0 mL of 0.5 M H₂SO₄, followed by the addition of 3.0 mL of 0.25 % diphenylcarbazide and the solution mixture was diluted up to the mark with deionized water. The sample solution was loaded onto the column containing Amberlite XAD-4 resin, maintaining a flow rate of 2.0 mL/min. The Cr-diphenylcarbazide complex (reddish violet colored) was adsorbed onto the column, which was evident from the absorbance of the resulting solution. The adsorbed complex was then eluted using 15.0 mL of 2.5 M H₂SO₄ in acetone. The solution was placed on the hot plate to evaporate the acetone and added 5.0 mL of 0.2 N HNO₃ solutions in the residue. The solution was filtered with filter paper, and the concentration of Cr(VI) was determined by micro-sample injection system flame atomic absorption spectrophotometry (MIS-FAAS) as reported by Baig et al. 2012 .

2.6. Determination of Total Chromium

The total Cr was also determined by SPE MIS-FAAS after the oxidation of Cr(III) to Cr(VI) by using Ce(SO₄)₂, as reported by Baig et al. 2012 . The Ce(IV) in acidic media (0.07 mol/L, H₂SO₄) is used to

oxidize Cr(III) to Cr(VI), and the resulted solution was treated as mentioned in the section on the determination of Cr(VI).

2.7. Calculation of Trivalent Chromium

The contents of Cr(III) could not be determined directly by the above analytical procedure, but their concentrations were given by the difference between the total Cr and Cr(VI) .

2.8. Analytical Figure of Merits

The analytical characteristics of the developed approach for determining Cr were calculated using optimized instrumental conditions. The standard addition method was used to draw the calibration curve for the determination Cr(VI) by SPE MIS-FAAS . The limit of detection and quantification (LOD and LOQ) of the developed method were calculated as $3 \times S/m$ and $10 \times S/m$, respectively. Where S is the standard deviation (std.) of blank signals ($n = 10$) and m is the slope of the linear calibration graph . The LOD and LOQ of the developed approach for determining Cr(VI) were found to be 0.037 and 0.124 mg/L, respectively. The calibration curve of Cr(VI) for this interval was determined by the regression equation $A = 1.47 \times 10^{-2} [\text{Cr(VI)}] + 3.00 \times 10^{-5}$. Where, A is the analytical signal (absorbance in nm) and $[\text{Cr(VI)}]$ is the concentration of analyte (Cr(VI)) in the sample solution (mg/L). The calculated coefficient of determination (R^2) for Cr(VI) was about 0.996.

The precision of the developed analytical approach was evaluated by percent relative standard deviation (%RSD) for each analyzed concentration, and %RSD was calculated as $(\text{Std./X})100$, where Std stands for a standard deviation for seven measurements and X is the mean value of these measurements. The %RSD of method was found to be $< 1.50\%$ ($n = 6$). The reliability of the developed method for determining Cr(VI) by SPE MIS-FAAS in the aqueous medium was evaluated by spiking the three known concentrations of Cr(VI) in the concentration range of 10.0 - 30.0 mg/L, and percentage recoveries were found to be $> 99.0\%$ (Table 1).

Table 1: The results for the test of standard addition/recovery for Cr(VI) by solid phase extraction in industrial effluent samples ($n = 6$).

	Amount added (mg/L)	Found values Mean \pm Std. (mg/L)	%Recovery ^a	%RSD
	---	14.72 \pm 0.18	--	0.37
Cr(VI)	10.00	24.64 \pm 0.13	99.20	1.09
	20.00	34.82 \pm 0.23	100.5	0.75
	30.00	45.32 \pm 0.11	102.0	0.91

$$\% \text{Recovery}_a = \frac{C_{\text{after spiked}} - C_{\text{initial}}}{C_{\text{spiked}}} \times 100$$

2.9. Statistical Evaluation

Excel 2003 (Microsoft Office ®) and STATISTICA 6 (StatSoft, Inc.®) were used to perform all mathematical and statistical calculations. Means \pm SD, and Student's t-test were used to express the distributed data to evaluate linear associations between physical quality measures and total Cr, and Pearson correlation coefficients were determined. All of the tests were two-sided with a 0.05 p-value significant.

3. RESULT AND DISCUSSION

In all the analyzed effluent samples, the temperature had a distinct annual cycle, in which the summer season showed higher values and the winter season showed lower values. The results of physicochemical parameters (pH, EC, TDS, and BOD) of industrial effluent samples (collected from four different industries) are shown in Table 2. The pH values of effluent samples of FI, PI, CI, and TFI were 7.00 – 8.60, 6.60 – 6.80, 6.70 – 7.90, and 6.10 – 6.6 respectively (Table 2). PI and TFI are slightly acidic because of various chemicals in these sectors' cleaning, washing, and polymerization/dyeing processes. The effluents had a slightly acidic pH (5.96 ± 0.09) and the exposure pH should be higher (7.16 ± 0.02). The basic pH of the natural water may cause damage to the fish's outer surfaces, such as the skin, eyes, and gills, and render them unable to dispose of metabolic wastes.

However, the highly acidic industrial effluents may enhance the toxicity of the organic compounds. The TDS were found at 951-1820, 1348-1382, 1348-1382, and 450-1322 mg/L in FI, PI, CI, and TFI industrial effluents samples.

The EC of industrial effluents (FI, PI, CI, and TFI) were found in the range of 0.87-4.01, 3.00-3.60, 2.88-3.72, 0.40-5.30 mS/cm, respectively. The EC of all the analyzed industrial effluents was greater than US-EPA allowed limits (1.00 mS/cm) for industrial effluents. The higher concentration of EC may be due to the dissociation of the dissolved substances present in the samples, concentration of ions, degree of dissociation, and temperature. The EC values of the effluent samples collected from FI were found to be higher than the other three industrial effluents ($p < 0.05$). The highest values of EC were found in TFI effluent samples. These may result from the released oil, grease, ammonia, sulfide, and dyes alongside the wastage effluents of TFI, which may also contaminate drinking water. These industries may be released a large quantity of residual chemicals and biological material waste into natural water sources such as rivers and canals without proper treatment, which may cause several health issues. The level of BOD was found at 475 ± 61.4 , 575 ± 7.10 , 565 ± 7.10 , and 580 ± 20.0 mg/L in the analyzed effluent samples of FI, PI, CI and TFI, respectively as shown in Table 2.

Table 2: Physico-chemical characteristics of industrial effluents of Hyderabad and Jamshoro-Pakistan.

		pH	TDS (mg/L)	EC (mS/cm)	BOD (mg/L)
FI (n = 30)	Mean \pm Std.	7.60 \pm 0.80	1403 \pm 435.00	2.33 \pm 1.57	47.5 \pm 6.10
	Range	7.00-8.60	951-1820	0.87-4.01	40.5-52.0
PI (n = 30)	Mean \pm Std.	6.70 \pm 0.10	1365 \pm 20.01	3.30 \pm 0.30	57.5 \pm 5.10
	Range	6.60-6.80	1348-1382	3.00-3.60	57.0-58.0
CI (n = 30)	Mean \pm Std.	7.20 \pm 0.50	1365 \pm 24.04	3.30 \pm 0.42	56.5 \pm 7.06
	Range	6.70-7.70	1348-1382	2.88-3.72	55.8-57.5
TFI (n = 30)	Mean \pm Std.	6.30 \pm 0.20	951 \pm 491.01	2.83 \pm 2.45	58.0 \pm 2.00
	Range	6.10-6.60	450-1322	0.40-5.30	56.0-60.0

Std. = Standard Deviation

The BOD levels in all the analyzed effluent samples were observed at 8.0 to 12.0 times higher than the US EPA's recommended tolerance limit (50 mg/L) for industrial effluent discharge into rivers. The high level of BOD in effluent samples of all the industrial sectors might be attributed to the elevated concentration of organic matter produced by several chemicals utilized in the various industrial processes. However, a high level of BOD was observed in TFI effluent samples compared to other industrial effluents. It might be due to different chemicals used in textile industries for mercerizing,

bleaching/scouring, and yawing, which include sodium chloride, sodium sulfite, NaCl, sodium bisulfate, sodium bicarbonate, formic acid, H₂SO₄, vegetable tannins, resins, sodium formate, polyurethane, fat emulsions, dyes, binders, waxes, pigments, lacquers/formaldehyde, NaOH, sodium phosphate, sodium hypochlorite, acids, H₂O₂, surfactants, Cl₂, and NaSiO₃. The findings of the current work showed that the difference among industries was statistically significantly different from each other ($P < 0.05$). Moreover, it was observed that the effluents from the studied

industries remained continuously discharged into the nearby natural waterbodies during the sampling period.

The total Cr contents in effluents of FI, PI, CI and TFI varied between 30.0-38.0, 23.0-27.0, 35.0-95.0, and 40.0-180 mg/L respectively (Table 3). However, the total Cr concentration in the selected four industries increased as $PI < FI < CI < TFI$, with TFI showing the highest Cr concentration. The total Cr levels in the effluent samples analyzed from all the industrial sectors were higher than the US EPA standard for total Cr (0.10 mg/L). The possible sources of Cr in these industrial effluents are the Cr compounds employed for various industrial applications like catalysts, dyers, and modifiers among others. The total Cr contents showed significantly positive correlation with pH, TDS and EC in effluent samples of FI ($r > 0.60$; $p < 0.001$), while strongly negative correlation was observed between total Cr and BOD ($r = -0.821$; $p < 0.001$). The total Cr contents in effluent samples of PI were reversely correlated with pH and TDS ($r > -0.90$; $p < 0.0001$), whereas, it has significantly correlation with EC and BOD ($r > 0.80$; $p < 0.0001$). On the other hand, the total Cr contents of effluent samples of CI have no significant correlation with the four studied physical parameters ($P > 0.140$). It might be due to the low variation in the contents of total Cr in different effluent samples of CI of the Jamshoro district. However, total Cr levels have positive correlation with pH and TDS ($r > 0.60$; $p < 0.001$) and negative correlation with EC and BOD ($r > -0.60$; $p < 0.001$) (Table 4).

The Chromium speciation in industrial effluent is very important in determining the level of contamination and toxicity. Chromium speciation in industrial effluent samples of FI, PI, CI and TFI are important in determining mobilization and toxicity. The contents of Cr(VI) and Cr(III) in effluent samples of FI, PI, CI and TFI varied in the ranges [23.0 - 36.0, 2.00 - 7.00], [19.0 - 20.0, 4.00 - 7.00], [9.00 to 23.0, 26.0 - 72.0] and [16.0 - 48.0, 24.0 - 132 mg/L] respectively. The cluster analysis was employed on industrial effluent samples to distribute Cr contamination. A cluster graph is used to detect spatial resemblance in different groups of industrial effluents (spatial variability). The obtained dendrogram categorized all the four sampling industrial effluents into three major clusters, as effluents of PI and FI have lower mutual dissimilarities than industrial effluents of CI and TFI (Figure 1). The comparatively high contents of Cr(VI) were found in effluent samples of FI and PI, because of the large application of dichromate/chromate in these industries. The contents of Cr(VI) in effluent samples of four industries were found to be higher than the U.S. EPA regulatory limit for Cr(VI) (0.05 mg/L). The high levels of Cr(VI) may cause disorders of the skin, gastrointestinal tract, kidney, liver, circulatory, and nerve tissues, as well as lung carcinoma among others. The level of Cr(III) was found to be higher in effluent samples of CI and TFI than FI and PI ($p < 0.05$). The concentration of Cr(III) contents in the industrial effluent samples were within the recommended level of Cr(III) (170 mg/L) in industrial discharges of FI and PI were significantly lower than the level of Cr(VI) may be due to the large application of dichromate/chromate.

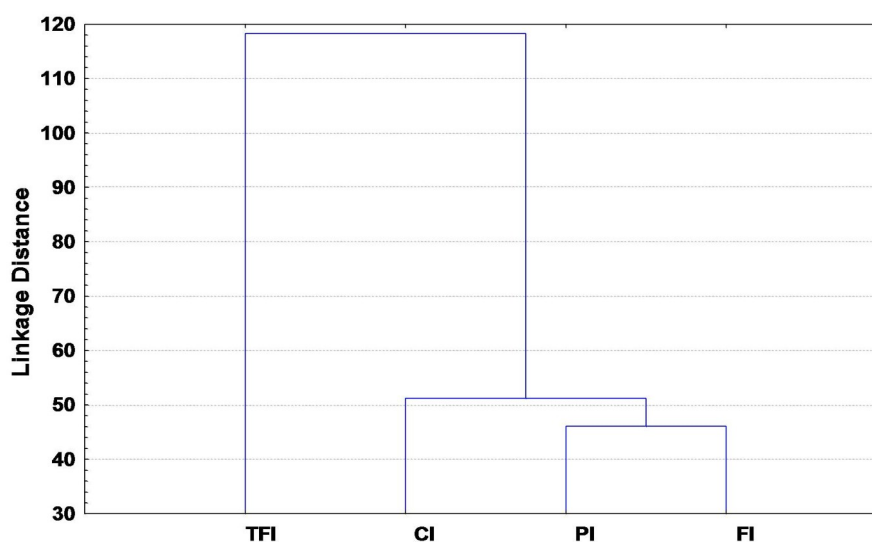


Figure 1: Dendrogram showing clustering of different origins of industrial effluents according to distribution of Cr species.

Table 3: Analytical results of chromium speciation (mg/L) in industrial effluents of different industries of Hyderabad and Jamshoro, Pakistan.

		Total Cr	Cr(VI)	Cr(III)
FI (n = 30)	Mean ± Std.	34.0±4.00	29.5±6.50	4.50±2.50
	Range	30.0-38.0	23.0-36.0	2.0-7.0
PI (n = 30)	Mean ± Std.	25.0±2.00	19.5±0.50	5.5±1.50
	Range	23.0-27.0	19.0-20.0	4.0-7.0
CI (n = 30)	Mean ± Std.	65.0±30.00	16.0±7.00	49.0±23.00
	Range	35.0-95.0	9.0-23.0	26.0-72.0
TFI (n = 30)	Mean ± Std.	110±70.00	32.0±16.01	78.0±54.00
	Range	40.0-180	16.0-48.0	24.0-132.0

Std. = Standard Deviation

Table 4: Correlation of total Cr with the physicochemical characteristics of industrial effluents.

		pH	TDS	EC	BOD
FI	r -value	0.697	0.874	0.600	-0.821
	p-value	0.00001	< 0.00001	0.0004	< 0.00001
PI	r - value	-0.923	-0.970	0.844	0.881
	p - value	< 0.00001	< 0.00001	< 0.00001	< 0.00001
CI	r - value	0.197	0.124	0.169	0.074
	p - value	0.149	0.514	0.372	0.699
TFI	r - value	0.721	0.653	-0.721	-0.626
	p - value	< 0.00001	< 0.00001	<0.00001	0.0002

The Cr(III) level in the effluent samples of CI and TFI was two to three-fold higher than the Cr(VI) level. It might be due to the large application of Cr(III) salts (nitrate or sulfate) in studied CI and TFI for different industrial processes. The level of Cr(III) in the effluent samples may not have significant toxic effects. Based on the elevated Cr(VI) level in the industrial effluent samples, it is suggested that the effluent of studied industries cannot be used directly for agricultural or other commercial applications. Thus, the level of Cr(III) may be increased due to the conversion of high contents of Cr(VI) discharged from industries into natural water bodies, which may convert into Cr(III) either by the increase in pH up to 7.0 or the dilution by the river or canal water. It is recommended that contaminated industrial effluent could not be discharged into streams of rivers or canals.

The results of total Cr concentration in industrial effluent samples were compared with other previous studies in different countries (Table 5). The total Cr content in industrial effluents samples from district Jamshoro, Pakistan, was found much higher than the reported results in other countries including Pakistan.

The contents of Cr(VI) in industrial effluent samples of the study area were lower than Hyderabad, India and Jeddah, Saudi Arabia and other previous studies from various Scholars . The contents of Cr(III) in industrial effluents of Hyderabad- India, Tabriz-Iran and Jeddah-Saudi Arabia were two to four-fold higher than the contents of Cr(III) in industrial effluents of the study areas .

Table 5: Comparison of previously reported research on total Cr and its species (mg/L) in industrial effluents with this study.

Region	Cr(III)	Cr(VI)	Total Cr	References
Bahia, Brazil	2.63±0.07	--	2.80±0.12	(6)
Denizli, Turkey	16.8±9.6	23.3±5.3	40.1±8.0	(3)
Gaborone, Botswana	--	20.7 ± 0.9	30.7 ± 1.2	(31)
Hyderabad, India	95 ± 2	98.0 ± 2.0	--	(7)
Lucknow, India	--	1.64±0.002	45.1±0.03	(35)
Kasur, Pakistan	--	--	2.10±0.08	(34)
Karachi, Pakistan	--	--	15.2-185	(33)
Tabriz, Iran	46.3 ± 0.8	12.3 ± 0.4	--	(36)
Jeddah, Saudi Arabia	99.0 ± 2.0	99.9 ± 4.0	--	(29)
Jeddah, Saudi Arabia	10.0	--	13.1±0.2	(9)
Jeddah, Saudi Arabia	10.4 ± 0.12	2.4 ± 0.11	12.9 ± 0.1	(32)
Hyderabad and Jamshoro, Pakistan	28.5 ±19.5	74.5±58.0	102±78.0	Current study

These industrial sectors may discharge the untreated effluents into natural water resources through open or closed pathways, which is hazardous to local inhabitants and wildlife. Almost all industries in Hyderabad and Jamshoro either disregarded or partly obeyed international industrial discharge rules. However, some enterprises have established the effluents treatment facility, but this is only a show for the pleasure of national and international organizations.

4. CONCLUSION

The contents of EC, TDS, and BOD in effluent samples of four industries were significantly high than the legal threshold levels set by the US Environmental Protection Agency. Total Cr concentration in textile and fabric industry effluent samples was 400-1800 times greater than the maximum concentration allowed by the US Environmental Protection Agency (EPA). The Cr(VI) was the dominant species in the effluent of FI and PI, but the Cr(III) level is relatively high in the effluent samples of CI and TFI ($p < 0.05$). Cr(VI) levels in effluent samples of four studied industries were higher but below regulatory limits set by the US EPA and WHO. The correlation study indicated that total Cr in effluents of different industries showed a different behaviour with quality parameters depending on the nature of effluent chemical residues. Thus, a continuous assessment and monitoring of the industrial activities is recommended for developing a greener Pakistan. Meanwhile, there is a need for university-industry collaboration to develop industrial eco-friendly and cost-effective solutions.

5. ACKNOWLEDGMENTS

This work was partially supported by The World Academy of Science (TWAS), Italy (Grant No.: 13-346 G/MSN/AS_C_UNESCO FR: 3240279204). We are grateful to Dr. Akhtar Mahmoud Baig, president of Young Welfare Society (YWS) Sindh, for assistance in sampling.

6. REFERENCES

1. Nwosu UL, Ajiwe VIE, Okoye PAC. Assessment of Heavy Metal Pollution of Effluents from three (3) Food Industries in Nnewi/Ogidi areas of Anambra State, Nigeria. IOSRJESTFT. 2014;8(11):13-21. [<URL>](#).
2. Baig JA, Kazi TG, Shah AQ, Kandhro GA, Afridi HI, Khan S, et al. Arsenic speciation and other parameters of surface and ground water samples of Jamshoro, Pakistan. International Journal of Environmental Analytical Chemistry. 2012 Jan 15;92(1):28-42. [<URL>](#).
3. Baig JA, Hol A, Akdogan A, Kartal AA, Divrikli U, Kazi TG, et al. A novel strategy for chromium speciation at ultra-trace level by microsample injection flame atomic absorption spectrophotometry. J Anal At Spectrom. 2012;27(9):1509. [<URL>](#).
4. Pavesi T, Moreira JC. Mechanisms and individuality in chromium toxicity in humans. J Appl Toxicol. 2020 Sep;40(9):1183-97. [<URL>](#).
5. DesMarias TL, Costa M. Mechanisms of chromium-induced toxicity. Current Opinion in Toxicology. 2019 Apr;14:1-7. [<URL>](#).

6. Matos GD, dos Reis EB, Costa ACS, Ferreira SLC. Speciation of chromium in river water samples contaminated with leather effluents by flame atomic absorption spectrometry after separation/preconcentration by cloud point extraction. *Microchemical Journal*. 2009 Jul;92(2):135-9. [<URL>](#).
7. Gopi Krishna P, Mary Gladis J, Rambabu U, Prasada Rao T, Naidu GRK. Preconcentrative separation of chromium(VI) species from chromium(III) by coprecipitation of its ethyl xanthate complex onto naphthalene. *Talanta*. 2004 Jun;63(3):541-6. [<URL>](#).
8. Alamri S, Ali HM, Khan MIR, Singh VP, Siddiqui MH. Exogenous nitric oxide requires endogenous hydrogen sulfide to induce the resilience through sulfur assimilation in tomato seedlings under hexavalent chromium toxicity. *Plant Physiology and Biochemistry*. 2020 Oct;155:20-34. [<URL>](#).
9. El-Shahawi MS, Hassan SSM, Othman AM, El-Sonbati MA. Retention profile and subsequent chemical speciation of chromium (III) and (VI) in industrial wastewater samples employing some onium cations loaded polyurethane foams. *Microchemical Journal*. 2008 Jun;89(1):13-9. [<URL>](#).
10. Pakade VE, Tavengwa NT, Madikizela LM. Recent advances in hexavalent chromium removal from aqueous solutions by adsorptive methods. *RSC Adv*. 2019;9(45):26142-64. [<URL>](#).
11. Pradhan D, Sukla LB, Sawyer M, Rahman PKSM. Recent bioreduction of hexavalent chromium in wastewater treatment: A review. *Journal of Industrial and Engineering Chemistry*. 2017 Nov;55:1-20. [<URL>](#).
12. Zhou L, Li R, Zhang G, Wang D, Cai D, Wu Z. Zero-valent iron nanoparticles supported by functionalized waste rock wool for efficient removal of hexavalent chromium. *Chemical Engineering Journal*. 2018 May;339:85-96. [<URL>](#).
13. Matsuoka S, Nakatsu Y, Takehara K, Saputro S, Yoshimura K. On-line Electrochemical Oxidation of Cr(III) for the Determination of Total Cr by Flow Injection-Solid Phase Spectrophotometry. *ANAL SCI*. 2006 Dec;22(12):1519-24. [<URL>](#).
14. Wolf RE, Morrison JM, Goldhaber MB. Simultaneous determination of Cr(III) and Cr(VI) using reversed-phased ion-pairing liquid chromatography with dynamic reaction cell inductively coupled plasma mass spectrometry. *J Anal At Spectrom*. 2007;22(9):1051. [<URL>](#).
15. Rodrigues E, Almeida O, Brasil H, Moraes D, dos Reis MAL. Adsorption of chromium (VI) on hydrotalcite-hydroxyapatite material doped with carbon nanotubes: Equilibrium, kinetic and thermodynamic study. *Applied Clay Science*. 2019 May;172:57-64. [<URL>](#).
16. Rajesh N, Jalan RK, Hotwany P. Solid phase extraction of chromium(VI) from aqueous solutions by adsorption of its diphenylcarbazide complex on an Amberlite XAD-4 resin column. *Journal of Hazardous Materials*. 2008 Feb;150(3):723-7. [<URL>](#).
17. Hasan SMdM, Akber MdA, Bahar MdM, Islam MdA, Akbor MdA, Siddique MdAB, et al. Chromium Contamination from Tanning Industries and Phytoremediation Potential of Native Plants: A Study of Savar Tannery Industrial Estate in Dhaka, Bangladesh. *Bull Environ Contam Toxicol*. 2021 Jun;106(6):1024-32. [<URL>](#).
18. Asad S, Amoozegar MA, Pourbabae AA, Sarbolouki MN, Dastgheib SMM. Decolorization of textile azo dyes by newly isolated halophilic and halotolerant bacteria. *Bioresource Technology*. 2007 Aug;98(11):2082-8. [<URL>](#).
19. Godoy V, Blázquez G, Calero M, Quesada L, Martín-Lara MA. The potential of microplastics as carriers of metals. *Environmental Pollution*. 2019 Dec;255:113363. [<URL>](#).
20. Kazemi A, Esmaeilbeigi M, Sahebi Z, Ansari A. Health risk assessment of total chromium in the ganat as historical drinking water supplying system. *Science of The Total Environment*. 2022 Feb;807:150795. [<URL>](#).
21. Granato ET, Meiller-Legrand TA, Foster KR. The Evolution and Ecology of Bacterial Warfare. *Current Biology*. 2019 Jun;29(11):R521-37. [<URL>](#).
22. Channa GM, Baig J, Kazi T, Afridi H. Quantitative Assessment of Some Toxic Elements and Physicochemical Parameters in Wastewater of Dyeing Industry: A Case Study. *Pak J Anal Environ Chem*. 2020 Jun 30;21(1):132-9. [<URL>](#).
23. Baig JA, Kazi TG, Elci L, Afridi HI, Khan MI, Naseer HM. Ultratrace Determination of Cr(VI) and Pb(II) by Microsample Injection System Flame Atomic Spectroscopy in Drinking Water and Treated and Untreated Industrial Effluents. *Journal of Analytical Methods in Chemistry*. 2013;2013:1-8. [<URL>](#).
24. Arain SA, Kazi TG, Afridi HI, Arain MS, Panhwar AH, Khan N, et al. A new dispersive liquid-liquid microextraction using ionic liquid based microemulsion coupled with cloud point extraction for determination of copper in serum and water samples. *Ecotoxicology and Environmental Safety*. 2016 Apr;126:186-92. [<URL>](#).
25. Akhtar K, Ahmed Baig J, Gul Kazi T, Sirajuddin, Imran Afridi H, Naz Talpur F, et al. Novel fluoride

- selective voltammetric sensing method by amino phenylboronic acid-zirconium oxide nanoparticles modified gold electrode. *Microchemical Journal*. 2022 Mar;174:107073. [<URL>](#).
26. Ghaly A, Mahmoud N, Ibrahim M, Mostafa E, Abdelrahman E, Emam R, et al. Water use, wastewater characteristics, best management practices and reclaimed water criteria in the carwash industry: a review. *International Journal of Bioprocess & Biotechnological Advancements*. 2021;7(1):240-61.
27. Azeem H. Analysis of industrial waste water from Kot Lakhpat area (Lahore, Pakistan) by atomic absorption spectrometer. *Biologia (Pakistan)*. 2009;55(1 & 2):35-41.
28. Akan JC, Ogugbuaja VO, Abdulrahman FI, Ayodele JT. Pollutant levels in effluent samples from tanneries and textiles of Kano industrial areas, Nigeria. *Glo Jnl Pure Appl Sci [Internet]*. 2009 Dec 3 [cited 2022 Oct 26];15(3-4). Available from: [<URL>](#).
29. Mahmoud ME, Yakout AA, Ahmed SB, Osman MM. Speciation, selective extraction and preconcentration of chromium ions via alumina-functionalized-isatin-thiosemicarbazone. *Journal of Hazardous Materials*. 2008 Oct 30;158(2-3):541-8. [<URL>](#).
30. Treviño P, Ibáñez Cornejo JG, Vázquez Medrano RC. Chromium (VI) reduction kinetics by zero-valent aluminum. *Int J Electrochem Sci*. 2014;9:2556-64.
31. Kiptoo J. Speciation studies of nickel and chromium in wastewater from an electroplating plant. *Talanta*. 2004 Sep;64(1):54-9. [<URL>](#).
32. El-Shahawi MS, Bashammakh AS, Abdelmageed M. Chemical Speciation of Chromium(III) and (VI) Using Phosphonium Cation Impregnated Polyurethane Foams Prior to Their Spectrometric Determination. *Anal Sci*. 2011 Jul;27(7):757-63. [<URL>](#).
33. Parveen R, Ashfaq M, Qureshi J, Ali SMM, Qadri M. Estimation of Chromium in Effluents from Tanneries of Korangi Industrial Area. *Pak J Chem*. 2013 Mar 30;3(1):29-33. [<URL>](#).
34. Rehman A, Shakoori FR, Shakoori AR. Heavy metals resistant rotifers from a chromium contaminated wastewater can help in environmental clean-up. *Pakistan J Zool*. 2008;40(5):309-16.
35. Shukla O, Rai U, Dubey S. Involvement and interaction of microbial communities in the transformation and stabilization of chromium during the composting of tannery effluent treated biomass of *Vallisneria spiralis* L. *Bioresource Technology*. 2009 Apr;100(7):2198-203. [<URL>](#).
36. Abdolmohammad-Zadeh H, Sadeghi GH. A nano-structured material for reliable speciation of chromium and manganese in drinking waters, surface waters and industrial wastewater effluents. *Talanta*. 2012 May;94:201-8. [<URL>](#).



A Short Review on Structural Concepts of Metal Complexes of Proton Transfer Salts of Pyridine-2-Carboxylic Acid

Nurgün Büyükkıdan^{1*} 

¹Kütahya Dumlupınar University, Department of Chemistry, Kütahya, Türkiye

Abstract: In this study, a brief review of the proton transfer salts synthesized from the reaction of piperazine with pyridine-2-carboxylic acid and their metal complexes since 2009 was made. The metals in the studied compounds are mostly d-block metals. In complexes, the anionic component of the salt is coordinated to the metal, while the cationic component is present only as a complementary ion in a complex.

Keywords: Pyridine, piperazine, acid, base, salt.

Submitted: June 24, 2022. **Accepted:** October 14, 2022.

Cite this: Büyükkıdan N. A Short Review on Structural Concepts of Metal Complexes of Proton Transfer Salts of Pyridine-2-Carboxylic Acid. JOTCSA. 2023;10(1):11-20.

DOI: <https://doi.org/10.18596/jotcsa.1135570>.

***Corresponding author. E-mail:** nurgun.buyukkidan@dpu.edu.tr.

1. INTRODUCTION

Pyridine carboxylates containing two functional groups are among the most versatile ligands that can coordinate with metal (1). Studies with such molecules have mainly focused on the development of metal-based compounds containing pyridine-2-carboxylic acid (2-picolinic acid) for dietary supplementation and numerous articles and reviews have been conducted (2). Later, such ligands were used for coordination to different transition metals. These compounds usually form five-membered rings by bonding to the metal *via* carboxylate-O and pyridine-N donor atoms (3, 4) (Figure 1).

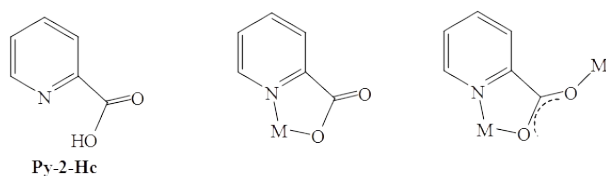


Figure 1: Coordination modes of Py-2-Hc.

As a terminal tryptophan metabolite, 2-picolinic acid is an important structural motif of enzymes and is the active component of many drugs (5, 6). An increase in the number of anticancer agents has been observed with the synthesis of pyridine-2-carboxylic acid type ligands with anti-cancer

properties and complexes of different transition metals (7, 8). The complexes with metal ions have been studied as models for broad biological activity spectra such as enzyme activity and DNA (9-11). Proton transfer salts, which consist of a good proton donor-acceptor systems, and their reactions with metals can form supramolecular compounds called Metal-organic frameworks (MOF) (12). It is very important to prepare an effective ion pair that forms the components of the proton transfer salt and accelerates the formation of the metal complexes. Among the proton donor and proton acceptor groups, which are components of the proton transfer salt, carboxylic acids and amines are a good pair. In recent years, the development of new pharmaceutical components with proton transfer reactions has accelerated (13-16). For the synthesis of complexes to be successful, care must be taken to select polydentate ligands and components capable of intermolecular H bonding (17, 18). Piperazines, which are cyclic amines, have many biological activities such as anti-depressant (19), anti-fungal (20), anti-tumor, (21, 22), anti-inflammatory (23), anti-migraine (24) and anti-malarial (25). In this work, an investigation of the transition metal complexes of compounds containing 2-picolinic acid and piperazine as structural units of proton transfer salt was carried out.

2. SYNTHESIS

2.1. Proton Transfer Reaction

The reaction or reaction mechanism in which a proton (H^+) is separated from one species such as an acid and accepted by another species such as a base is called a proton transfer reaction. The product of the proton transfer reaction between donors and acceptors is named differently as the proton transfer salt (26-29) the H-bonded complex (30-33) and the charge transfer complex (34-37).

In this study, proton transfer salts of pyridine-2-carboxylic as a proton donor and piperazine as proton acceptor and metal complexes of these salts were investigated.

2.1.1. Proton transfer salt, $(H_2Ppz)(Py-2-c)_2$ (**1**)

A mixture of pyridine-2-carboxylic acid (Py-2-Hc) in H_2O and piperazine (Ppz) in THF gave colorless crystals on slow evaporation after one week (**38**) (Figure 2).

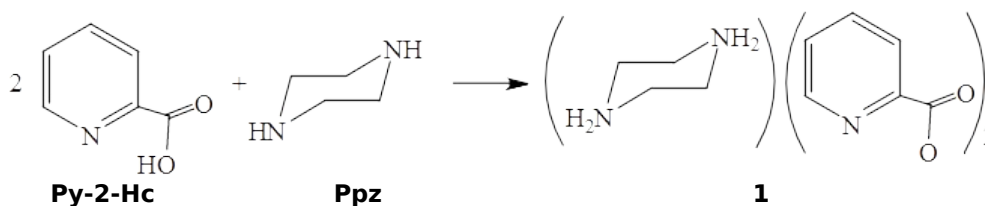


Figure 2: Synthesis of $(H_2Ppz)(Py-2-c)_2$ (**1**).

2.1.2. Mg(II) (**2**), Zn(II) (**3**) and Cd(II) (**4**) metal complexes of **1**

The complexes, $[Mg(Py-2-c)_2(H_2O)_2] \cdot H_2O$ (**2**),

$[Zn(Py-2-c)_2(H_2O)_2] \cdot H_2O$ (**3**) and $(H_2Ppz)[Cd(Py-2-c)_3] \cdot 3H_2O$ (**4**), of proton transfer salt **1** were synthesized (**38**) (Figure 3).

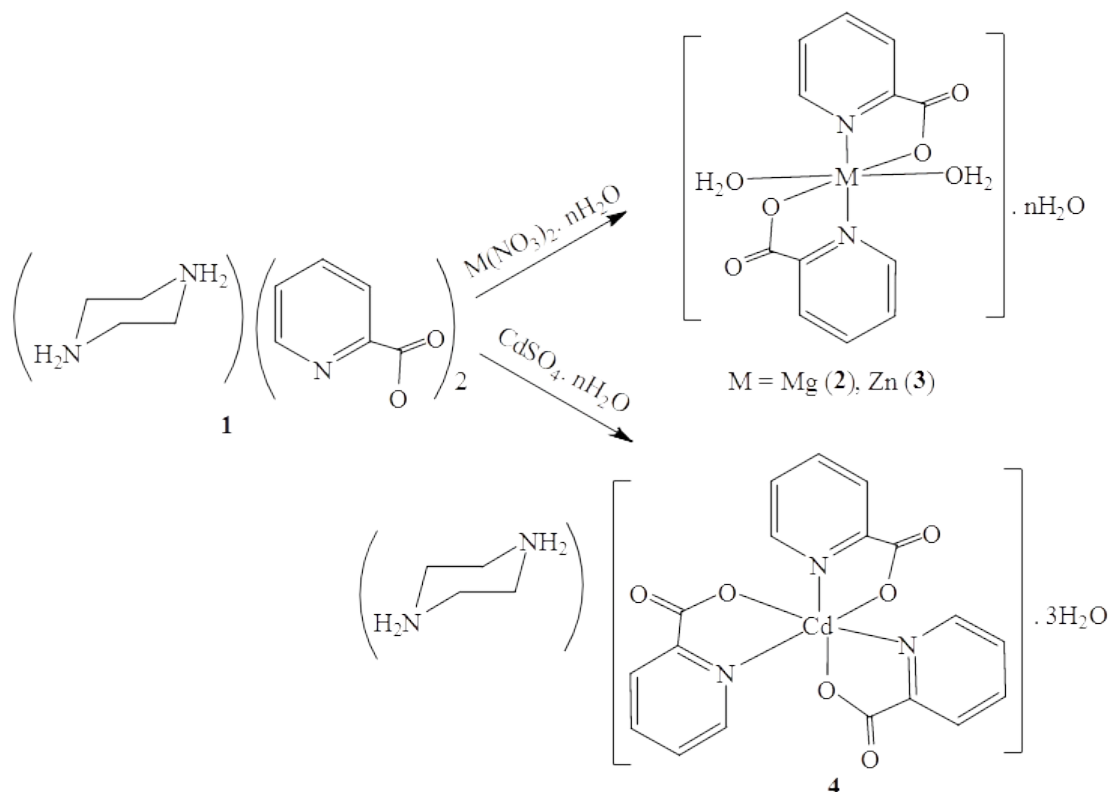


Figure 3: Synthesis of complexes **2-4**.

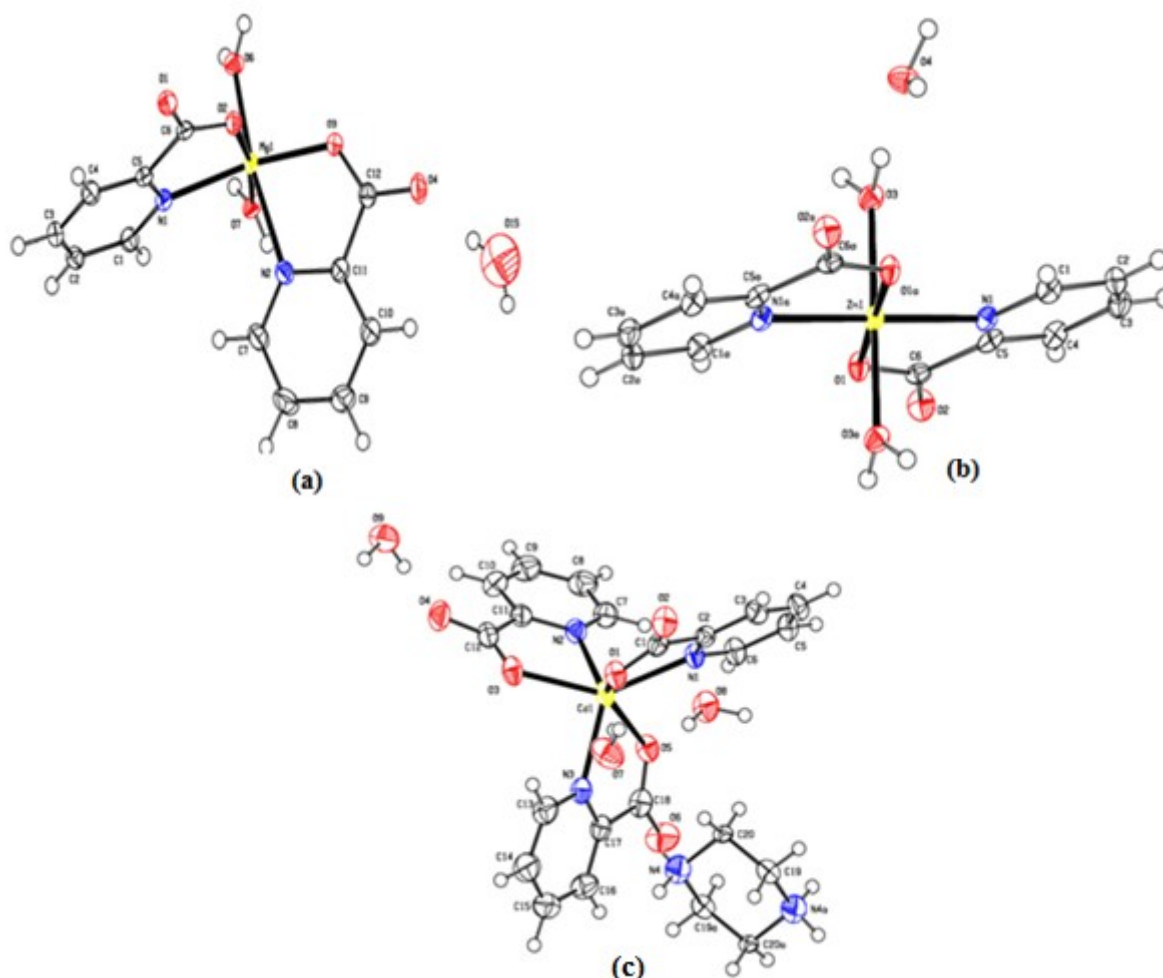
The analyses, crystal systems and space groups of the compounds (**1-4**) reported in the literature are given in Table 1.

Table 1: Proton transfer salt, (H₂Ppz)(Py-2-c)₂, and its Mg(II) (**2**), Zn(II) (**3**) and Cd(II) (**4**) complexes.

Ref. No	Analyses	Proton Transfer Salt and Complexes	Space Group	Crystal system
(38)	IR and NMR	(H ₂ Ppz)(Py-2-c) ₂ (1)	-	-
(38)	IR and X-ray	[Mg(Py-2-c) ₂ (H ₂ O) ₂].H ₂ O (2)	<i>P2₁/n</i>	Monoclinic
(38)	IR and X-ray	[Zn(Py-2-c) ₂ (H ₂ O) ₂].H ₂ O (3)	<i>P2₁/n</i>	Monoclinic
(38)	IR and X-ray	(H ₂ Ppz)[Cd(Py-2-c) ₃].3H ₂ O (4)	<i>P2₁/n</i>	Monoclinic

In compound **2**, the Mg²⁺ coordinates to two oxygen (O2 and O3) and two nitrogen atoms (N1a and N2) of the two Py-2-c⁻ ligands, and two oxygen atoms (O6 and O7) of the two H₂O molecules, forming the distorted octahedral geometry. The torsion angles

of N2-Mg1-N1-C1 and N2-Mg1-N1-C5 are -84.43(11) and 96.05(8) Å, respectively, indicating that the planes of the two ligands are coplanar (38) (Figure 4a).

**Figure 4:** Crystal structures (a) for **2**, (b) for **3** and (c) for **4**.

In [Zn(Py-2-c)₂(H₂O)₂].H₂O (**3**) complex, the N1-Zn1-N1a, O1-Zn1-O1a and O3-Zn1-O3a angles around the Zn²⁺ ion are equivalent to 180.00°, indicating that the geometry is a normal octahedral (Figure 4b). In the Zn(II) (**3**) complex, there are many O-H...O H-bonds between the metal and the coordinated and uncoordinated H₂O molecule (38).

In asymmetric unit of Cd(II) (**4**) compound contains two ionic moieties [Cd(Py-2-c)₃]²⁻ anion and (pipH₂)²⁺ cation and three lattice water molecules. The Cd(II) ion, which has six coordination numbers

in the complex, is attached to the three oxygen and three nitrogen atoms of the three Py-2-c⁻ rings (Figure 4c). The extensive hydrogen bond interactions between cationic, anionic moieties, and uncoordinated H₂O molecules along the lattice of the (H₂Ppz)[Cd(Py-2-c)₃].3H₂O (**4**) complex are of great importance in stabilizing the crystal (38).

2.2. The proton transfer compound, (H₂Ppz)(Py-2-c)₂.H₂O (**5**)

Proton transfer compound, (H₂Ppz)(Py-2-c)₂.H₂O (**5**), was prepared (39, 40) from the reaction of Py-2-Hc

and Ppz (Figure 5).

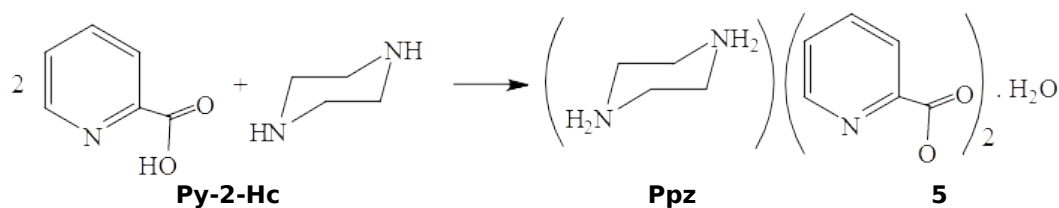


Figure 5: Synthesis of $(\text{H}_2\text{Ppz})(\text{Py-2-c})_2 \cdot \text{H}_2\text{O}$ (**5**).

The NMR (^1H and ^{13}C) spectrum data confirmed the formation of the proton transfer salt **5**. ^1H NMR spectrum of $(\text{H}_2\text{Ppz})(\text{Py-2-c})_2 \cdot \text{H}_2\text{O}$ (**5**) exhibited signals at 7.0, 8.0 and 8.1 ppm in the aromatic region for Py-2-c⁻ ring protons and signals at 3.41 ppm for $\text{H}_2\text{Ppz}^{2+}$ protons. The carbonyl group carbon atom was observed in down field at 169.25 ppm. Five signals in the aromatic region were attributed to the Py-2-c⁻ ring carbons (124.12,

127.51, 143.14, 148.45, 149.15 ppm). The piperazine ring carbons resonated in the high field at 40.49 ppm. From the intensities of the peaks of ^1H NMR spectrum of $(\text{H}_2\text{Ppz})(\text{Py-2-c})_2 \cdot \text{H}_2\text{O}$, the $\text{H}_2\text{Ppz}^{2+}$ to Py-2-c⁻ molar ratio was found to be 1:2. The proton transfer salt (**5**) contains in its asymmetric unit a $\text{H}_2\text{Ppz}^{2+}$ cation, two Py-2-c⁻ anions and a H_2O molecule (39) (Figure 6).

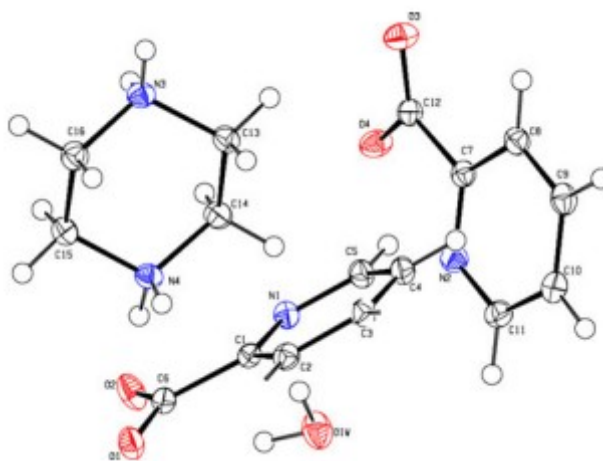


Figure 6: Molecular structure of $(\text{H}_2\text{Ppz})(\text{Py-2-c})_2 \cdot \text{H}_2\text{O}$ (**5**).

This salt is formed through electrostatic attraction between ions $(\text{Py-2-c})^-$ and $(\text{H}_2\text{Ppz})^{2+}$, different H-bonds ($\text{O-H}\cdots\text{O}$, $\text{O-H}\cdots\text{N}$, $\text{N-H}\cdots\text{O}$, $\text{N-H}\cdots\text{N}$, $\text{C-H}\cdots\text{O}$), and stacking interactions of $\text{C-H}\cdots\pi$ groups. The

crystal structure of **5** exhibits the strongest $\text{C-H}\cdots\pi$ interactions between C5-H5A and N2 , the C7-C11 ring and the C11-H11A and N1 , C1-C5 ring, with distances of 2.608 Å and 2.627 Å, respectively (39) (Figure 7).

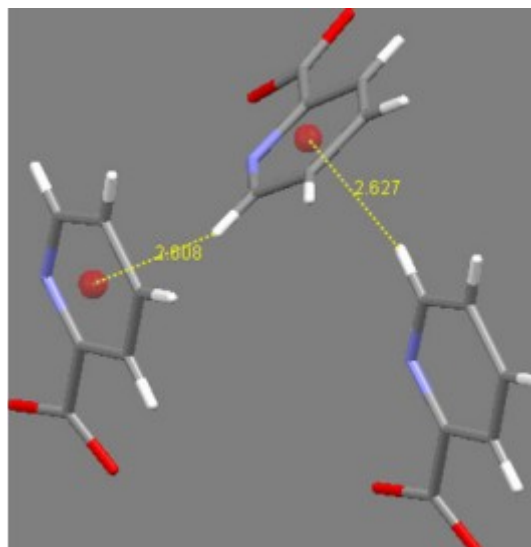


Figure 7: The C-H... π stacking interactions in **5**.

Mn(II) (**6**), *Ni(II)* (**7**) and *Cu(II)* (**8**) complexes of **5**
Complexes of proton transfer salt **5** $[\text{Mn}(\text{Py-2-c})_2(\text{H}_2\text{O})_2]_2 \cdot 2\text{H}_2\text{O}$ (**6**), $[\text{Ni}(\text{Py-2-c})_2(\text{H}_2\text{O})_2] \cdot \text{H}_2\text{O}$ (**7**) and $[\text{Cu}(\text{Py-2-c})_2\text{H}_2\text{O}]_n$ (**8**) were prepared (39) (Figure 8).

The analyzes, crystal systems and space groups of the compounds **5-8** reported in the literature are given in Table 2.

Table 2: Proton transfer salt, $(\text{H}_2\text{Ppz})(\text{Py-2-c})_2 \cdot \text{H}_2\text{O}$ (**5**), and its *Mn(II)* (**6**), *Ni(II)* (**7**) and *Cu(II)* (**8**) compounds.

Ref. No	Analyses	Proton Transfer Salt and Complexes	Space Group	Crystal system
(39)	NMR, IR, X-ray and elemental analysis	$(\text{H}_2\text{Ppz})(\text{Py-2-c})_2 \cdot \text{H}_2\text{O}$ (5)	$P2_1/c$	Monoclinic
(39)	NMR, IR, X-ray and elemental analysis	$[\text{Mn}(\text{Py-2-c})_2(\text{H}_2\text{O})_2]_2 \cdot 2\text{H}_2\text{O}$ (6)	$P1$	Triclinic
(39)	NMR, IR, X-ray and elemental analysis	$[\text{Ni}(\text{Py-2-c})_2(\text{H}_2\text{O})_2] \cdot \text{H}_2\text{O}$ (7)	$P2_1/n$	Monoclinic
(39)	NMR, IR, X-ray and elemental analysis	$[\text{Cu}(\text{Py-2-c})_2\text{H}_2\text{O}]_n$ (8)	$P1$	Triclinic

$[\text{Mn}(\text{Py-2-c})_2(\text{H}_2\text{O})_2]_2 \cdot 2\text{H}_2\text{O}$ (**6**), $[\text{Ni}(\text{Py-2-c})_2(\text{H}_2\text{O})_2] \cdot \text{H}_2\text{O}$ (**7**) and $[\text{Cu}(\text{Py-2-c})_2\text{H}_2\text{O}]_n$ (**8**) complexes contain Py-2-c⁻ ring and water molecule of proton transfer salt (**5**) components. In the molecular structures of the complexes (Figures 9 for **6**, 10a for **7** and 11 for **8**), it was observed that

pyridine-2-carboxylate was coordinated to each M(II) ion as a bidentate ligand. In these complexes extensive H-bonds such as O-H...O, O-H...N, N-H...O, N-H...N, C-H...O and C-H... π and C-O... π interactions provides to form a 3-D structure (39).

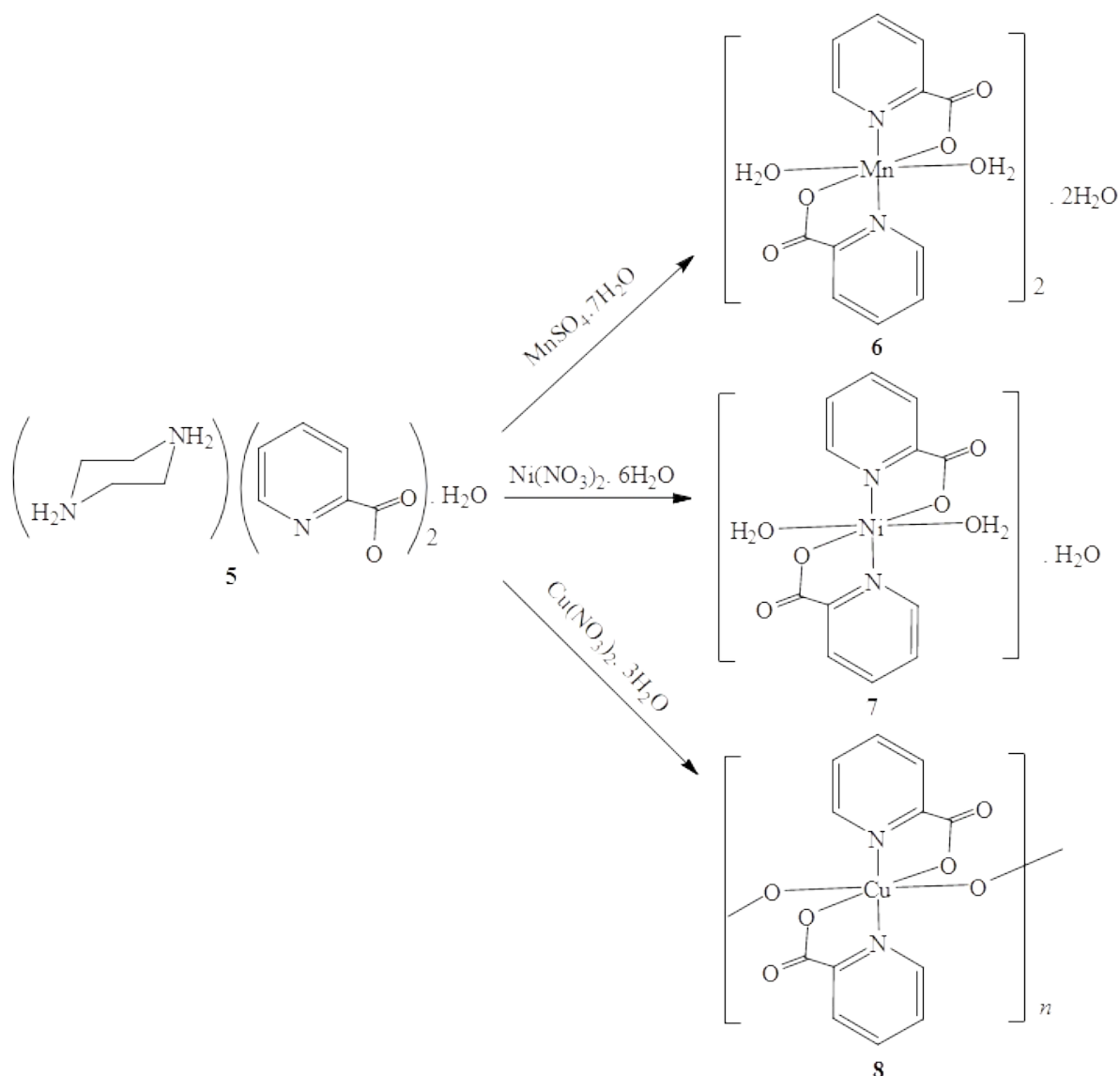


Figure 8: Synthesis of complexes 6-8.

The asymmetric unit of $[\text{Mn}(\text{Py-2-c})_2(\text{H}_2\text{O})_2]_2 \cdot 2\text{H}_2\text{O}$ (**6**) complex consists of two neutral Mn(II) molecules and H_2O molecules (Figure 9). The two complexes differ slightly in terms of bond angles and bond lengths. Each Mn(II) ion in the complex binds to the nitrogen and oxygen atoms of two Py-2-c-rings, as well as to the oxygens of two H_2O molecules, forming a six-coordinated distorted

octahedral geometry. In Mn(II) complex (**6**), it was observed that the O3-Mn1-O5 ($164.19(17)^\circ$) and O9-Mn2-O11 ($167.77(17)^\circ$) angles deviated from linearity around Mn^{2+} ions (Mn1 and Mn2). The total bond angles around Mn1 and Mn2 are equal to 362.4° . This means that the atoms form a flattened tetrahedral around the central atom and the Mn^{2+} ion is out of plane (39).

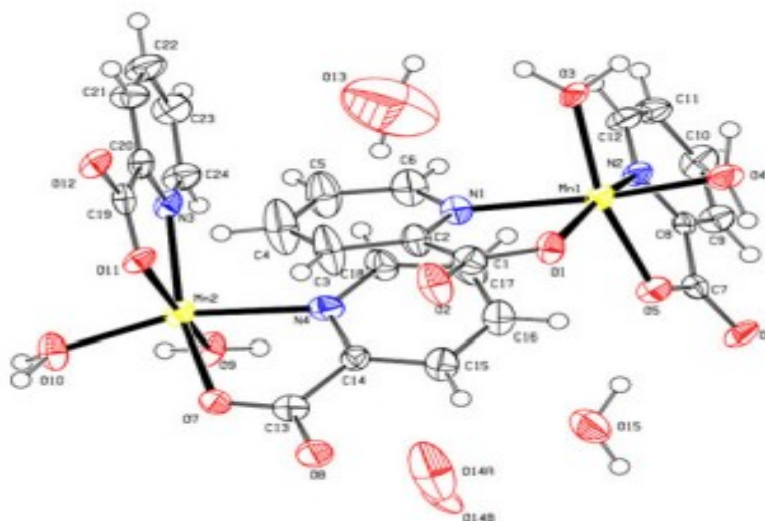


Figure 9: Molecular structure of **6**.

In the $[\text{Ni}(\text{Py-2-c})_2(\text{H}_2\text{O})_2]\cdot\text{H}_2\text{O}$ (**7**) complex, the Ni(II) ion is coordinated by the two nitrogen and two oxygen atoms of the two Py-2-c⁻ rings and the oxygens of the two H₂O molecules and has a distorted octahedral geometry. The oxygen atoms (O3 and O3a) of the coordinated H₂O molecules are in the axial position, while the two oxygen and two

nitrogen atoms (O2, O2a, N1 and N1a) of the Py-2-c⁻ anion are in the equatorial position. The bond angles around Ni(II) (N-Ni-N and O-Ni-O) are 180°, indicating that the coordination around Ni²⁺ is octahedral (Figure 10a). The cavity between the layers of the $[\text{Ni}(\text{Py-2-c})_2(\text{H}_2\text{O})_2]$ (**7**) part is filled by the H₂O molecules (39) (Figure 10b).

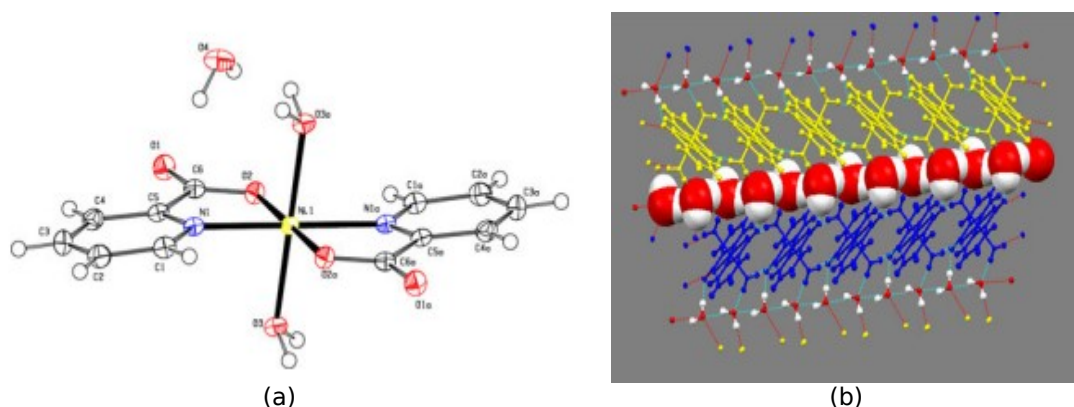


Figure 10: (a) Molecular structure and (b) A layered packing of $[\text{Ni}(\text{Py-2-c})_2(\text{H}_2\text{O})_2]\cdot\text{H}_2\text{O}$ (**7**).

In the $[\text{Cu}(\text{Py-2-c})_2(\text{H}_2\text{O})_n]$ (**8**) complex, Cu(II) atoms have six coordination environments, with the two nitrogen and two oxygen atoms of the two

carboxylate ligands and the two oxygen atoms of the two pyridine 2-carboxylate ions acting as bridges between the two Cu(II) ions.

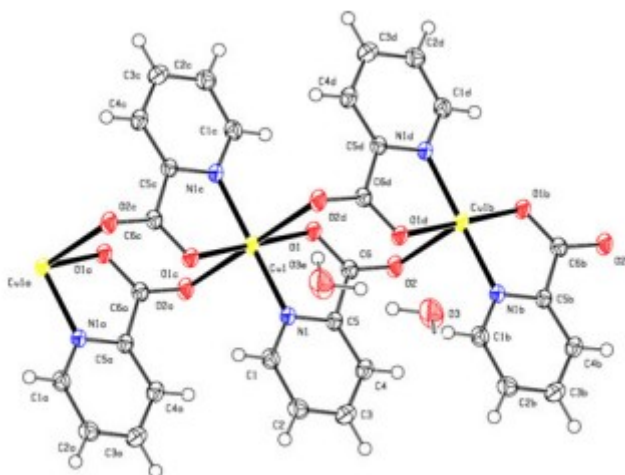


Figure 11: Molecular structure of $[\text{Cu}(\text{Py-2-c})_2\text{H}_2\text{O}]_n$ (**8**).

$[\text{Cu}(\text{Py-2-c})_2\text{H}_2\text{O}]_n$ (**8**) includes neutral polymeric compound and lattice H_2O molecule (Figure 11). Cu^{2+} ion is coordinated to oxygen [Cu1-O1 1.930(2) Å] and nitrogen Cu1-N1 1.959(2) Å atoms of two Py-2-c⁻ anions and two bridging oxygen atoms of the other carboxylate groups. Intramolecular O-H...O and C-H...O H-bonds with D...A ranging from 2.826(4) to 3.202(3) Å stabilize the molecular structure (39).

3. CONCLUSION

In this study, proton transfer salts synthesized from piperazine and pyridine-2-carboxylic acid and their metal complexes from 2009 to the present are presented. It was observed that pyridine-2-carboxylate was coordinated to metal ions but not piperazine in all complexes containing mostly d-block metals. Only one of the studied complexes contains piperazine as a complementary ion.

4. CONFLICT OF INTEREST

The authors declare no conflicts of interest.

5. REFERENCES

- Celestine MJ, Bullock JL, Boodram S, Rambaran VH, Holder AA. Interesting properties of p-, d-, and f-block elements when coordinated with dipicolinic acid and its derivatives as ligands: their use as inorganic pharmaceuticals. *Reviews in Inorganic Chemistry*. 2015 Jun 1;35(2):57-67. [<URL>](#).
- Mihajlović-Lalić LE, Poljarević J, Grgurić-Šipka S. Metal complexes with α -picolinic acid frameworks and their antitumor activity. *Inorganica Chimica Acta*. 2021 Nov;527:120582. [<URL>](#).
- Soares-Santos PCR, Paz FAA, Ferreira RAS, Klinowski J, Carlos LD, Trindade T, et al. Coordination modes of pyridine-carboxylic acid derivatives in samarium (III) complexes. *Polyhedron*. 2006 Aug;25(12):2471-82. [<URL>](#).
- Moore JW, Glick MD, Baker WA. Crystal structures of hydrated lanthanide(III) nicotinate, $\text{La}_2(\text{C}_5\text{H}_4\text{NCO}_2)_6(\text{H}_2\text{O})_4$ and $\text{Sm}_2(\text{C}_5\text{H}_4\text{NCO}_2)_6(\text{H}_2\text{O})_4$. *Journal of the American Chemical Society*. 1972 Mar;94(6):1858-65. [<URL>](#).
- Mahler HR, Cordes EH. In: *Biological Chemistry*. 2nd edition. New York: Harper and Row Publishers; 1971. p. 801-3.
- Ogata S, Takeuchi M, Okumura K, Taguchi H. Apoptosis Induced by Niacin-related Compounds in HL-60 Cells. *Bioscience, Biotechnology, and Biochemistry*. 1998 Jan;62(12):2351-6. [<URL>](#).
- Berner TO, Murphy MM, Slesinski R. Determining the safety of chromium tripicolinate for addition to foods as a nutrient supplement. *Food and Chemical Toxicology*. 2004 Jun;42(6):1029-42. [<URL>](#).
- Maret W. Chromium supplementation in human health, metabolic syndrome, and diabetes. *Metal Ions in Life Sciences*. 2019;19:231-51.
- Avcı D, Altürk S, Sönmez F, Tamer Ö, Başoğlu A, Atalay Y, et al. Three novel Cu(II), Cd(II) and Cr(III) complexes of 6-Methylpyridine-2-carboxylic acid with thiocyanate: Synthesis, crystal structures, DFT calculations, molecular docking and α -Glucosidase inhibition studies. *Tetrahedron*. 2018 Dec;74(50):7198-208. [<URL>](#).
- Avcı D, Altürk S, Sönmez F, Tamer Ö, Başoğlu A, Atalay Y, et al. A novel series of mixed-ligand M(II) complexes containing 2,2'-bipyridyl as potent α -glucosidase inhibitor: synthesis, crystal structure, DFT calculations, and molecular docking. *Journal of Biological Inorganic Chemistry*. 2019 Aug 1;24(5):747-64. [<URL>](#).
- Avcı D, Altürk S, Sönmez F, Tamer Ö, Başoğlu A, Atalay Y, et al. Novel Cu(II), Co(II) and Zn(II) metal complexes with mixed-ligand: Synthesis, crystal structure, α -glucosidase inhibition, DFT calculations, and molecular docking. *Journal of Molecular Structure*. 2019 Dec;1197:645-55. [<URL>](#).
- Zhang M, Chen C, Wang Q, Fu W, Huang K, Zhou W. A metal-organic framework functionalized with piperazine exhibiting enhanced CH₄ storage. *Journal of Materials Chemistry A*. 2017;5(1):349-54. [<URL>](#).
- Reddy JS, Ganesh SV, Nagalapalli R, Dandela R, Solomon KA, Kumar KA, et al. Fluoroquinolone salts with carboxylic acids. *Journal of Pharmaceutical Sciences*. 2011 Aug;100(8):3160-76. [<URL>](#).

14. Stepanovs D, Jure M, Mishnev A. Preparation and crystal structure of sildenafil salicylate. *Mendeleev Communications*. 2015 Jan;25(1):49-50. [<URL>](#).
15. Vepuri SB, Devarajegowda HC, Soliman ME. Synthesis, characterization and molecular modelling of a novel dipyridamole supramolecule - X-ray structure, quantum mechanics and molecular dynamics study to comprehend the hydrogen bond structure-activity relationship. *Journal of Molecular Structure*. 2016 Feb;1105:194-204. [<URL>](#).
16. Satyanarayana Reddy J, Ravikumar N, Gaddamanugu G, Naresh KN, Rajan SS, Anand Solomon K. Synthesis, crystal structure, spectral characterization and fluorescence studies of salts of α -mangostin with APIs. *Journal of Molecular Structure*. 2013 May;1039:137-43. [<URL>](#).
17. Aghabozorg H, Manteghi F, Sheshmani S. A brief review on structural concepts of novel supramolecular proton transfer compounds and their metal complexes. *Journal of the Iranian Chemical Society*. 2008 Jun;5(2):184-227. [<URL>](#).
18. Moghimi A, Moosavi SM, Kordestani D, Maddah B, Shamsipur M, Aghabozorg H, et al. Pyridine-2,6-bis(monothiocarboxylic) acid and 2-aminopyridine as building blocks of a novel proton transfer compound: Solution and X-ray crystal structural studies. *Journal of Molecular Structure*. 2007 Feb;828(1-3):38-45. [<URL>](#).
19. Pytka K, Rapacz A, Zygmunt M, Olczyk A, Waszkielewicz A, Sapa J, et al. Antidepressant-like activity of a new piperazine derivative of xanthone in the forced swim test in mice: The involvement of serotonergic system. *Pharmacological Reports*. 2015 Feb;67(1):160-5. [<URL>](#).
20. Thamban Chandrika N, Shrestha SK, Ngo HX, Tsodikov OV, Howard KC, Garneau-Tsodikova S. Alkylated Piperazines and Piperazine-Azole Hybrids as Antifungal Agents. *Journal of Medicinal Chemistry*. 2018 Jan 11;61(1):158-73. [<URL>](#).
21. McNair TJ, Wubin FA, Hoppe ET, Schmidt JL, dePeyster FA. Antitumor action of several new piperazine derivatives compared to certain standard anticancer agents. *Journal of Surgical Research*. 1963 May;3(3):130-6. [<URL>](#).
22. Ananda Kumar CS, Nanjunda Swamy S, Thimmegowda NR, Benaka Prasad SB, Yip GW, Rangappa KS. Synthesis and evaluation of 1-benzhydryl-sulfonyl-piperazine derivatives as inhibitors of MDA-MB-231 human breast cancer cell proliferation. *Medicinal Chemistry Research*. 2007 Sep;16(4):179-87. [<URL>](#).
23. Ahmadi A, Khalili M, Nafarie A, Yazdani A, Nahri-Niknafs B. Synthesis and anti-inflammatory effects of new piperazine and ethanolamine derivatives of H1-antihistaminic drugs. *Mini-Reviews in Medicinal Chemistry*. 2012 Sep 1;12(12):1282-92. [<URL>](#).
24. Brown AM, Patch TL, Kaumann AJ. The antimigraine drugs ergotamine and dihydroergotamine are potent 5-HT_{1C} receptor agonists in piglet choroid plexus. *British Journal of Pharmacology*. 1991 Sep;104(1):45-8. [<URL>](#).
25. Kumar Parai M, Panda G, Srivastava K, Kumar Puri S. Design, synthesis and antimalarial activity of benzene and isoquinoline sulfonamide derivatives. *Bioorganic & Medicinal Chemistry Letters*. 2008 Jan;18(2):776-81. [<URL>](#).
26. Fazil S, Ravindran R, Sarau Devi A, Bijili BK. Structural studies of 1-phenyl-2,3-dimethyl-5-oxo-1,2-dihydro-1H-pyrazol-4-ammonium 2[(2-carboxyphenyl)disulfanyl]benzoate. *Journal of Molecular Structure*. 2012 Aug;1021:147-52. [<URL>](#).
27. Ghasemi K, Ghasemi F, Rezvani AR, Shokrollahi A, Refahi M, García-Granda S, et al. Mn(II) and Zn(II) ions catalytic oxidation of o-phenylenediamine and characterization, X-ray crystal structure and solution study of the final products DAPH+Cl⁻·3H₂O and [DAPH][Zn(dipicH)(dipic)]·4H₂O. *Polyhedron*. 2016 May;110:55-62. [<URL>](#).
28. Majerz I, Olovsson I. Influence of proton transfer on the geometry of the donor and acceptor in NHN+ hydrogen bonds. *Journal of Molecular Structure*. 2010 Jul;976(1-3):11-8. [<URL>](#).
29. Özdemir N. Structural and spectroscopic characterization of 2-mesityl-1H-benzo[d]imidazol-3-ium chloride: A combined experimental and theoretical analysis. *Spectrochimica Acta Part A: Molecular and Biomolecular Spectroscopy*. 2012 Jun;91:51-60. [<URL>](#).
30. Ghasemi K, Rezvani AR, Shokrollahi A, Zarghampour F, Moghimi A, García-Granda S, et al. Synthesis, characterization, crystal structure and solution studies of a novel proton transfer (charge transfer) complex of 2,2'-dipyridylamine with 2,6-pyridine dicarboxylic acid. *Journal of Molecular Structure*. 2015 Jun;1089:184-90. [<URL>](#).
31. Takaiwa T, Koyama A, Nagaishi Y, Nakajima K, Sumimoto M, Hori K, et al. Structural characterization of 2,3,5,6-tetramethyl-p-phenylenediamine radical cation and its dimer in molecular crystals. *Journal of Molecular Structure*. 2015 Mar;1083:260-7. [<URL>](#).
32. Ghasemi K, Rezvani AR, Habibi-Khorassani SM, Shahraiki M, Shokrollahi A, Moghimi A, et al. An experimental and theoretical study of a hydrogen-bonded complex: O-phenylenediamine with 2,6-pyridinedicarboxylic acid. *Journal of Molecular Structure*. 2015 Nov;1100:597-604. [<URL>](#).
33. Gopi R, Ramanathan N, Sundararajan K. Hydrogen-bonded complexes of acetylene and acetonitrile: A matrix isolation infrared and computational study. *Journal of Molecular Structure*. 2015 Mar;1083:364-73. [<URL>](#).
34. Shehab OR, Mansour AM. Sparfloxacin charge transfer complexes with 2,3-dichloro-5,6-dicyano-1,4-benzoquinone and tetracyanoquinodimethane: Molecular structures, spectral, and DFT studies. *Journal of Molecular Structure*. 2015 Aug;1093:186-94. [<URL>](#).
35. Rzokey AA, Ahmad A. Synthesis, spectroscopic studies and thermal analysis of charge-transfer complex of 2,2'-bipyridine with 4-hydroxybenzoic acid in different polar solvents. *Journal of Molecular Structure*. 2014 Nov;1076:453-60. [<URL>](#).
36. Refat MS, Adam AMA, Saad HA. Utility of charge-transfer complexation for the assessment of macrocyclic polyethers: Spectroscopic, thermal and surface morphology characteristics of two highly crown ethers complexed with acido acceptors. *Journal of Molecular Structure*. 2015 Apr;1085:178-90. [<URL>](#).
37. Singh N, Ahmad A. Synthesis and spectrophotometric studies of charge transfer complexes of p-nitroaniline with benzoic acid in different polar solvents. *Journal of Molecular Structure*. 2014 Sep;1074:408-15. [<URL>](#).

38. Ghadermazi M, Soleimannejad J, Sheshmani S, Shamsipur M, Ghanbari M, Eslami MR. Characterization, crystal structures and solution studies of Zn(II), Cd(II) and Mg(II) complexes obtained from a proton transfer compound including pyridine-2-carboxylic acid and piperazine. Journal of the Iranian Chemical Society. 2012 Aug;9(4):579-89. [<URL>](#).

39. Sheshmani S, Soleimannejad J, Ghadermazi M, Shamsipur M, Ghanbari M, Motieian E, et al. Comparative study on MnII, NiII and CuII supramolecular complexes

obtained from a proton transfer methodology: solid- and solution-state studies. Journal of the Iranian Chemical Society. 2013 Aug;10(4):817-29. [<URL>](#).

40. Rekha P, Chakkaravarthi G, Mohan Kumar R, Vinitha G, Kanagadurai R. Growth, structural and optical limiting property of a new third order nonlinear optical material: piperazinium bis (2-carboxypyridine) monohydrate. Journal of Materials Science: Materials in Electronics. 2019 May;30(10):9471-88. [<URL>](#).



Acetylcholinesterase Inhibition Properties and Docking Studies of Compounds Based on 6-Hydrazinyl-1,3,4-Trimethyl-1H-Pyrazolo[3,4-b]Pyridine

Seyit Ali GÜNGÖR^{1*} 

¹ Kahramanmaraş Sutcu Imam University, Department of Chemistry, Faculty of Science, Kahramanmaraş, 46050, Turkey

Abstract: New compounds based on 6-hydrazinyl-1,3,4-trimethyl-1H-pyrazolo[3,4-b]pyridine (**3a** and **3b**) were synthesized and characterized by FTIR and ¹H/¹³C NMR spectroscopic methods and their *in vitro* acetylcholinesterase (AChE) inhibition studies were evaluated. Compound **3b** (IC₅₀ value 104.4 μM) exhibited stronger AChE inhibitory activity than the reference galantamine compound (IC₅₀ value 139.4 μM). Molecular docking studies were performed to determine the key interactions and possible binding modes between AChE of compounds. The most active one, **3b**, showed a binding affinity of -10.28 kcal/mol.

Keywords: Synthesis, AChE inhibition, Docking.

Submitted: May 16, 2022. **Accepted:** October 11, 2022.

Cite this: Güngör SA. Acetylcholinesterase Inhibition Properties and Docking Studies of Compounds Based on 6-Hydrazinyl-1,3,4-Trimethyl-1H-Pyrazolo[3,4-b]Pyridine. JOTCSA. 2023;10(1):21-30.

DOI: <https://doi.org/10.18596/jotcsa.1117324>.

***Corresponding author. E-mail:** sagungor@ksu.edu.tr

1. INTRODUCTION

Alzheimer's disease (AD) set off 60-70% of dementia cases worldwide with an approximated global incidence of 24.3 million cases. AD is a chronic syndrome that disrupts the central nervous system (CNS). The mechanism of action for AChE inhibitors is the compensation for the loss of central cholinergic neurons in AD (and thus loss of the neurotransmitter acetylcholine (ACh)) through decreased breakdown of ACh. AChE inhibitors are actively used for the effective treatment of Alzheimer's disease. AD causes deficiencies in important features of the brain such as language, learning, orientation, memory, and decision making (1). Old age comes first among the most important risk factors for AD (2). However, the exercises that can be done can cause a slight decrease in AD (3).

Among the most important therapeutic targets for AD are cholinesterases (4,5). The most important reason for the increase in cognitive disorders in AD

patients is the deterioration and neurodegeneration of cholinergic neurons in the brain. The cholinergic hypothesis postulates that Alzheimer's results from a reduced ability to synthesize (ACh) in an individual, leading to progressive neurodegeneration. For this reason, AChE inhibitors have been used to reduce the degradation rate of ACh. AChE inhibitors increase the amount of ACh by preventing degradation and may increase the function of neural cells. The differential distribution of AChE and BuChE within the brain suggests that both of these enzymes may play important biological roles in their interaction. Although animal models are not transferable to human subjects due to different species-dependent systemic effects both models have proven to have a positive effect on cognitive abilities in the absence of BChE. Therefore, it has been suggested that BChE can be considered as a clinical target in the AD process, as it can take over the function of AChE in the regulation of cholinergic signalling.

There are several drugs used as cholinesterase inhibitors in the treatment of the disease. Donepezil, galantamine and rivastigmine (Figure 1) are the most widely used and have received regulatory approval for the treatment of people with mild to moderate Alzheimer's disease in all jurisdictions (6).

There is also evidence to suggest that donepezil can improve the cognitive, functional and neuropsychiatric status of patients with more advanced Alzheimer's disease (7-9). However, the high side effects of these drugs prompted researchers to find new cholinesterase inhibitors.

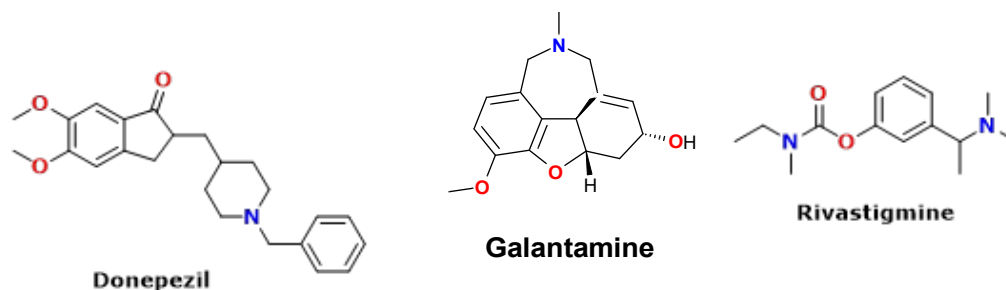


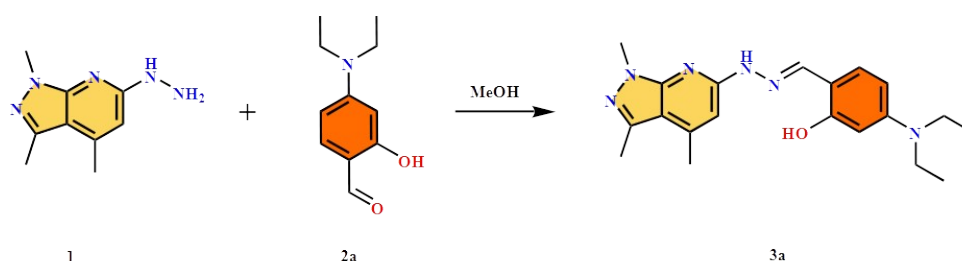
Figure 1: Drugs used for Alzheimer's.

In this study, two new compounds based on 6-hydrazinyl-1,3,4-trimethyl-1H-pyrazolo[3,4-*b*]pyridine were synthesized and their inhibitory effects on (AChE) activity were evaluated. Docking studies were performed to identify possible binding modes of compounds with residues in the AChE active site.

2. EXPERIMENTAL

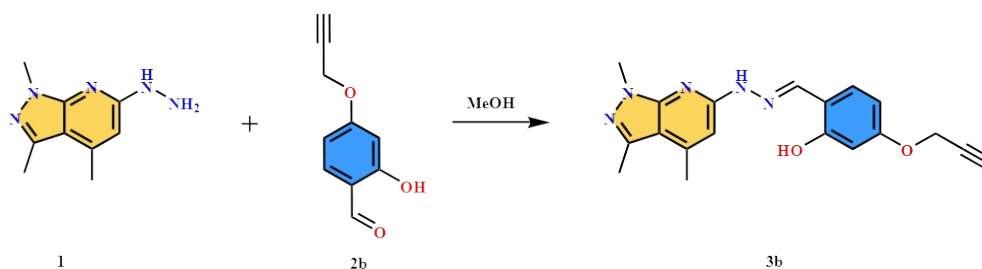
2.1. Synthesis of Compounds 3a and 3b

6-hydrazinyl-1,3,4-trimethyl-1H-pyrazolo[3,4-*b*]pyridine (0.65 mmol, 0.125 g) was dissolved in MeOH. Compound **2b** was synthesized according to the literature (10,11). Then compound **2a** (0.65 mmol, 0.126 g) or compound **2b** (0.65 mmol, 0.114 g) added by dissolving with MeOH (15 mL). The reaction mixture was left to reflux overnight. It was then allowed to cool to room temperature and the solvent was removed with evaporator and obtain solid.



(*E*)-5-(diethylamino)-2-((2-(1,3,4-trimethyl-1H-pyrazolo[3,4-*b*]pyridin-6-yl)hydrazinylidene)methyl)phenol (**3a**): $C_{20}H_{26}N_6O$. Yield: 93%, Color: Light Yellow. 1H NMR (d_6 -DMSO, δ) 11.03 (s, 1H), 10.89 (s, 1H), 8.12 (s, 1H), 7.22 (d, $J = 8.5$ Hz, 1H), 6.48 (s, 1H), 6.24 (d, $J = 8.5$ Hz, 1H), 6.14 (s, 1H), 3.78 (s, 3H), 3.34 (d, $J = 6.9$

Hz, 4H), 2.55 (s, 3H), 2.48 (s, 3H), 1.11 (t, $J = 6.7$ Hz, 6H). ^{13}C NMR (d_6 -DMSO, δ) 158.85, 155.84, 151.30, 149.59, 144.09, 142.81, 140.24, 130.33, 109.00, 108.16, 104.00, 102.55, 98.13, 44.24, 33.17, 19.43, 14.95, 13.00. FTIR (ν , cm^{-1}): 2969, 1631 (-C=N-), 1588, 1387, 1351, 1247, 1218, 1190, 1126, 1091, 1070, 819.



(*E*)-5-(prop-2-yn-1-yloxy)-2-((2-(1,3,4-trimethyl-1H-pyrazolo[3,4-*b*]pyridin-6-yl)hydrazinylidene)methyl)phenol (**3b**): C₁₉H₁₉N₅O₂. Yield: 90%, Color: Light Yellow. ¹H NMR (d₆-DMSO, δ) 11.11 (s, 2H), 8.22 (s, 1H), 7.62 – 7.37 (m, 1H), 6.60 (s, 1H), 6.57 – 6.44 (m, 1H), 4.81 (d, J = 2.1 Hz, 1H), 3.79 (s, 2H), 3.63 (s, 1H), 2.57 (s, 2H), 2.49 (s, 2H). ¹³C NMR (d₆-DMSO, δ) 159.23, 158.18, 155.86, 151.17, 144.35, 140.30, 129.41, 114.41, 109.30, 107.15, 102.74, 102.58, 79.57, 78.89, 55.94, 33.23, 19.42, 14.96. FTIR (ν, cm⁻¹): 2923, 2109 (-C≡CH), 1626 (-C=N-), 1593, 1497, 1386, 1242, 1160, 1028.

2.2. AChE Inhibitors' Activities

Inhibitory activities of compounds based on 6-hydrazinyl-1,3,4-trimethyl-1H-pyrazolo[3,4-*b*]pyridine (**3a** and **3b**) on acetylcholinesterase enzyme (AChE) were determined using the Ellman's method (12,13). *Electrophorus electricus* (electric eel AChE) is well known that the fish enzyme from was used due to lower price, availability, and high compatible to human AChE. The enzyme solution was prepared as 0.22 units/mL. Compounds **3a** and **3b** were the dissolved in water (1×10⁻⁴–1×10⁻⁷ M). 100 μL of phosphate buffer (pH: 6.7) was added to each well of 96 well-plates. Afterwards, different concentrations of the tested compounds (20 μL) and AChE (20 μL/well) were added and incubated at 25 °C for 10 min. Chromatographic reagent 5,5-dithio-bis(2-nitrobenzoic acid) (DTNB) (3 mM, 50 μL/well) and substrates acetylthiocholine iodine (ATCI) (3 mM, 50 μL/well) was added to the enzyme-inhibitor mixture. Yellow anion (2-nitro-5-thiobenzoic acid) formation was recorded at 412 nm for 10 min. It was determined by preparing an identical solution of the enzyme in the absence of tested compounds (as a control). Control and inhibitor readings were corrected with a blank read. All operations were repeated three times. Concentrations of samples that inhibit degradation of substrate (acetylcholine) by 50% (IC₅₀) were determined by linear regression analysis between percent inhibition and sample concentration using Excel program. Galantamine was used as a standard and results were compared.

2.3. Docking Studies

The binding modes and interactions of **3a** and **3b** compounds, whose ACh inhibitory effects of examined by in vitro method were investigated molecular docking studies using AutoDock 4.2 software (14). For this purpose, crystal structure of acetylcholinesterase (AChE) (pdb code: 4EY6) were downloaded from the RCSB Protein Data Bank. Then using AutoDock Tools version 1.5.6 ligands, anions and water molecules were removed from the enzymes and polar hydrogen atoms, Kollman and Gasteiger charges were added to amino acid residues in the protein structure (15). The number

of points in the x, y and z dimensions was 60 × 60 × 60. The root mean squared deviation (RMSD) of the atomic position between the original orientation of the co-crystal ligand and the re-docked ligand is computed. If the RMSD value is less than or equal to 2.0 Å is acceptable. To visualize molecular docking results of conformations with the lowest binding energy, Discovery Studio 2021 (16) and PyMOL (17) were used.

3. RESULTS AND DISCUSSION

3.1. FTIR Analyses of Compounds 3a and 3b

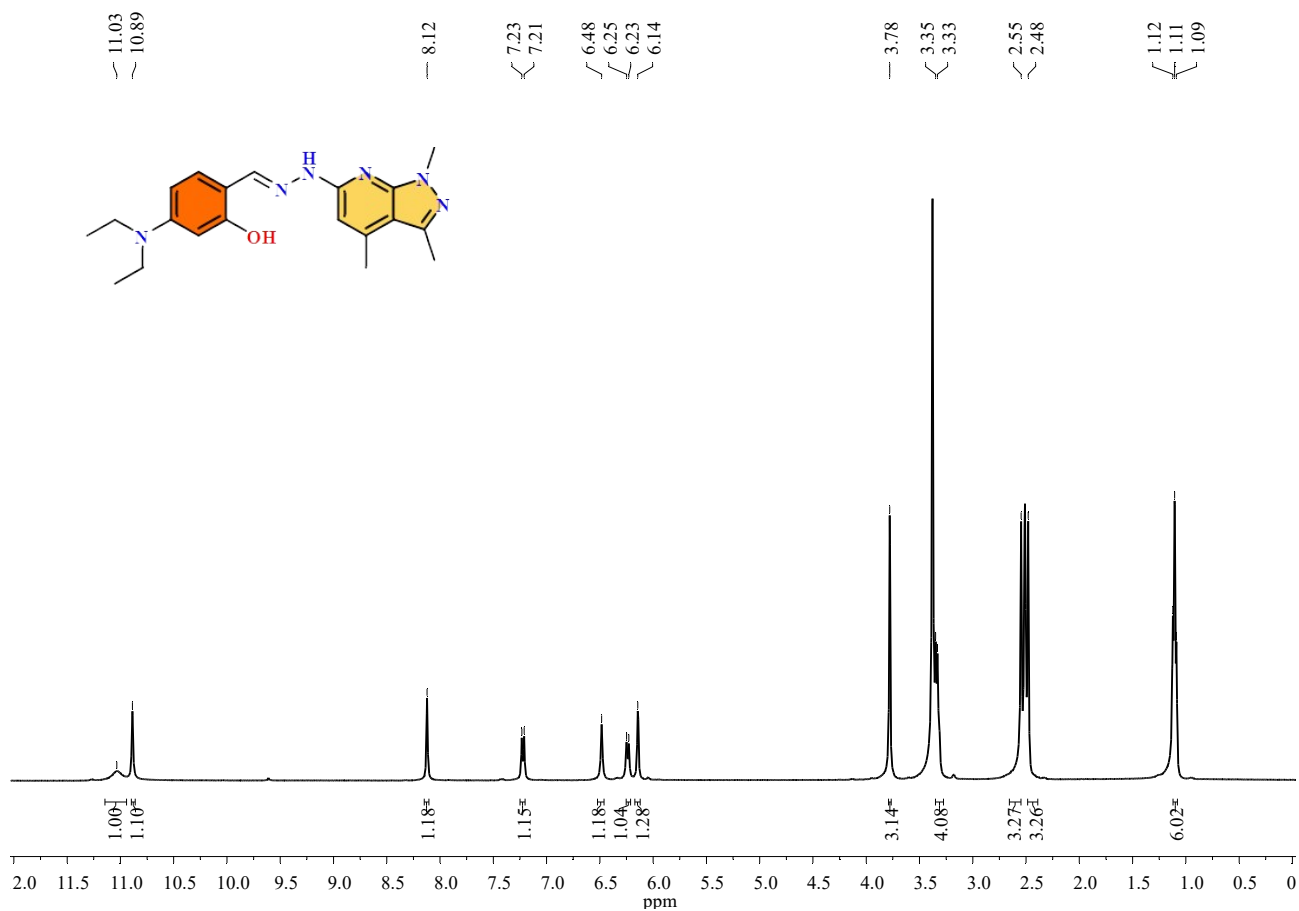
FT-IR analysis with ATR was performed to investigate the characteristic vibrational bands of compounds **3a** and **3b**. In the FT-IR spectra of the compounds, the carbonyl (C=O) group peaks of the starting compounds did not appear and the vibration bands of the imine (C=N) group were 1631 cm⁻¹ for **3a** and 1626 cm⁻¹ for **3b** was observed. In addition, vibrational band of the characteristic propargyl (C≡C) group of **3b** was observed at 2109 cm⁻¹.

3.2. NMR Analyses of Compounds 3a and 3b

¹H/¹³C NMR spectra of compounds **3a** and **3b** were recorded in d₆-DMSO and data are presented in the experimental part. ¹H/¹³C NMR spectra of the compounds are given in Figures 1 and 2. When the ¹H-NMR spectra of **3a** and **3b** are examined, the methyl group protons on the pyrazole and pyridine rings can be attributed to peaks at 2.48 ppm, 2.55 ppm and 3.78 ppm (NCH₃), respectively. The observed peaks in the range of 6.14-7.53 ppm belong to the aromatic ring protons. Imine group (HC=N) protons were observed at 8.12 and 8.22 ppm, respectively. The hydroxyl group (OH) protons of **3a** were observed at 11.03 ppm and the NH protons at 10.89 ppm, while the hydroxyl and NH protons of **3b** overlapped at 11.11 ppm. The methyl (CH₃) protons of the *N,N*-diethyl group of **3a** were detected at 1.09-1.12 ppm and the protons of the NCH₂ group at 3.33-3.35 ppm. In the ¹H-NMR spectrum of **3b**, the peak at 3.63 ppm the propargyl group proton and the peaks observed at 4.80-4.81 ppm to the OCH₂ protons are attributed. When the ¹³C-NMR spectra of **3a** and **3b** were examined, the imine group carbon atom signals were observed at 158.85 ppm and 159.23 ppm, respectively. Proton signals of aromatic ring carbon atoms were observed in the range of 98.13-158.18 ppm. The methyl group carbon atoms on the pyrazole and pyridine rings are attributed to signals observed around 14.95 ppm, 19.42 ppm and 33.17 ppm, respectively. The methyl (CH₃) and NCH₂ group carbon atom signals of the *N,N*-diethyl group of **3a** were observed at 13.00 ppm and 44.24 ppm, respectively. The propargyl group carbon atom signals of **3b** were observed at 78.89-79.57 ppm and the OCH₂ carbon atom signal was at 55.94 ppm.



Figure 2: FTIR spectra of compounds 3a and 3b.



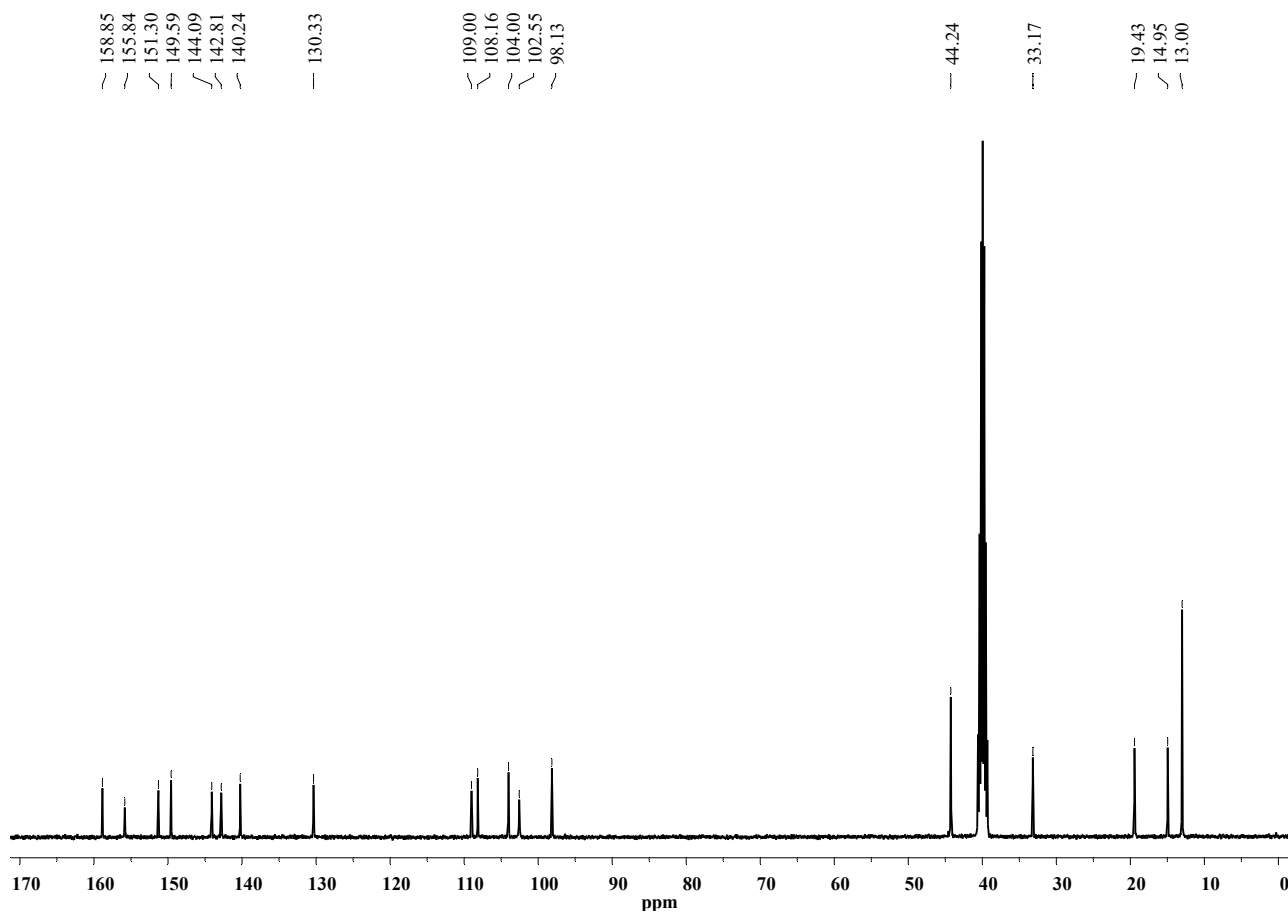
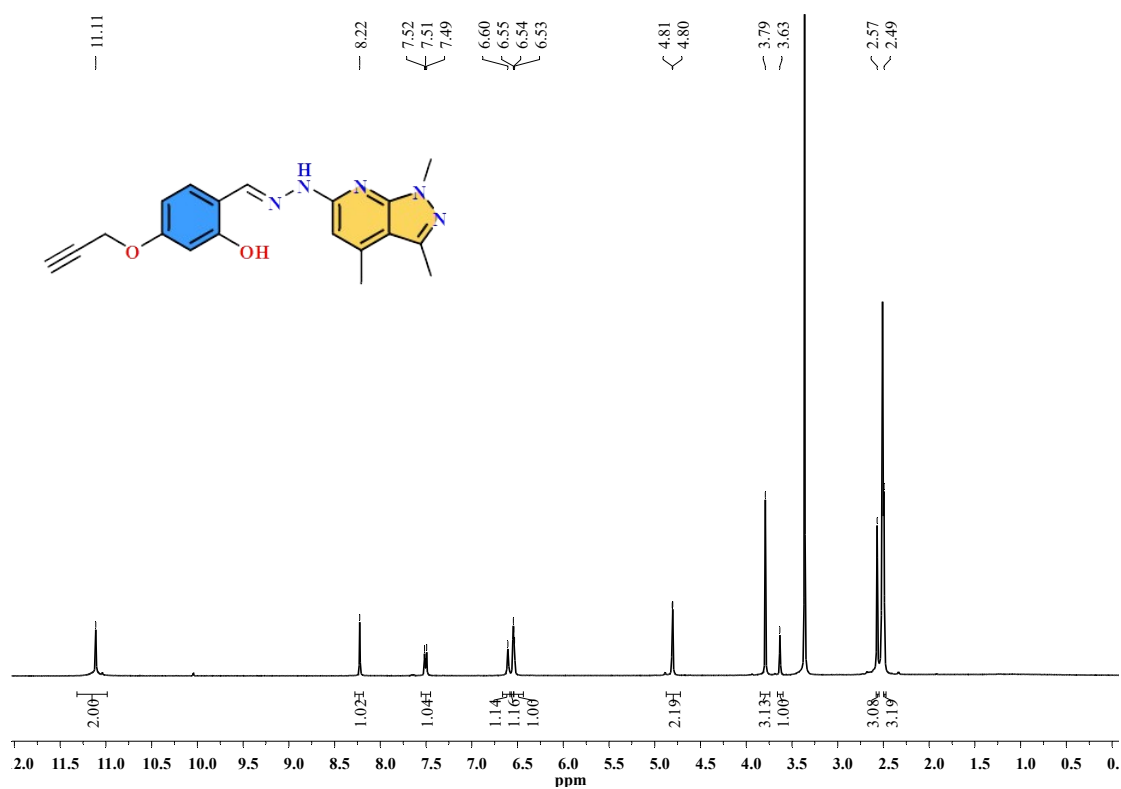


Figure 3: ^1H (^{13}C) NMR spectra of compound 3a.



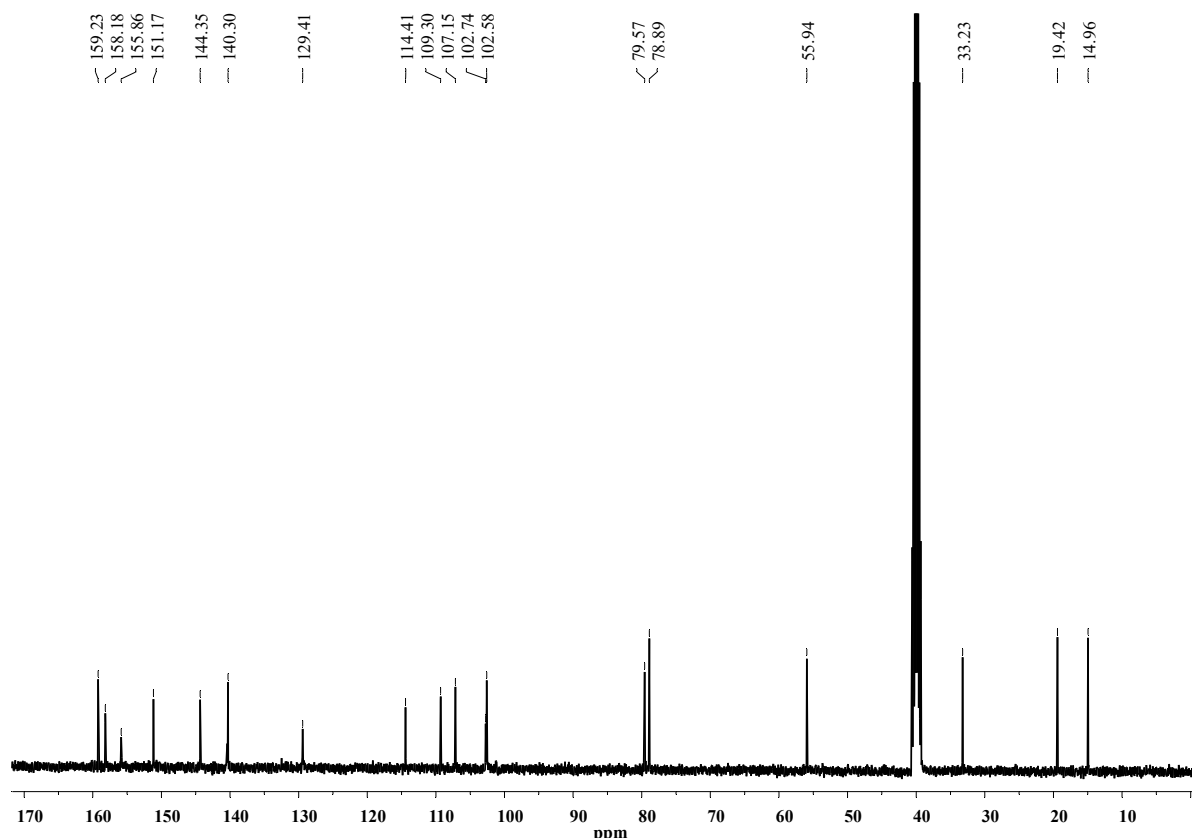


Figure 4: $^1\text{H}(^{13}\text{C})$ NMR spectra of compound **3b**.

3.3. Inhibitory Activity against AChE

The *in vitro* activities of compounds **3a** and **3b** were investigated against acetylcholinesterase (AChE), one of the main enzymes of Alzheimer's disease. Galantamine was used as a positive control. The inhibitory effects of compounds **3a** and **3b** on AChE (IC_{50} values of 282.37 μM and 104.4 μM , respectively) were evaluated and found to be the most active compound **3b**. Active compound **3b** also showed stronger inhibition than control galantamine (IC_{50} value 139.42 μM). *N,N*-diethyl ($\text{N}(\text{C}_2\text{H}_5)_2$) and propargyl ($\text{OCH}_2\text{C}\equiv\text{CH}$) groups were effective in determining the strength of the inhibitory effect of compounds **3a** and **3b** against AChE. The propargyl group end proton of the compound **3b** the hydrophilic interaction with the residues in the active site of enzyme may have been effective increase the inhibitory property. Molecular docking was performed to identify possible modes of binding between AChE and inhibitors.

3.4. Molecular Docking Studies of Compounds **3a** and **3b**

AChE inhibition effects of compounds based on 6-hydrazinyl-1,3,4-trimethyl-1H-pyrazolo[3,4-b]pyridine (**3a** and **3b**) were investigated by *in vitro* method. Molecular docking study was performed to determine the possible binding poses, interactions, affinities and complex structures of these compounds with AChE. Autodock 4.2 software program was used to determine the active site of AChE. First, the GNT compound co-crystallized with the enzyme was redocking to the active site of the enzyme by the docking procedure. In consequence of placing on the AChE active site, the best binding affinity of GNT was determined as -9.39 kcal/mol.

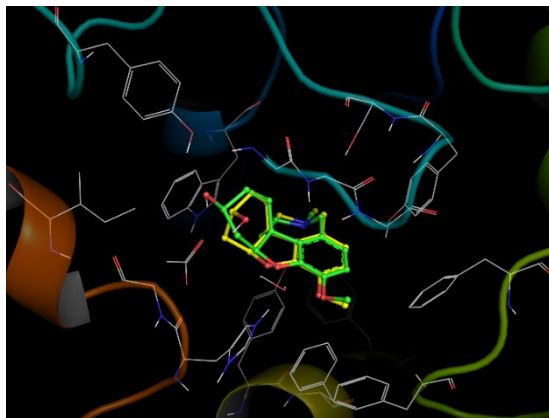


Figure 5: Docking verification. The carbon atoms of the co-crystallized ligand are represented by the ball and stick modeling in yellow, while the carbon atoms of the inserted ligand are represented by the ball and stick modeling in green.

Molecular docking studies of compounds against AChE have been performed. According to the docking results, compound **3b** showed the strongest inhibitory property with -10.28 kcal/mol the lowest binding affinity. Compound **3b** hydrogen bonded with residues Arg296 (2.2 Å), Phe295 (2.1 Å), Tyr337 (2.0 Å and 2.5 Å), Tyr124 (1.9 Å, 2.6 Å and 2.9 Å) and Ser125 (2.7 Å and 2.9 Å) in the active site of the enzyme. Compound **3b** made π - π interactions with amino acids Tyr341 (4.33 Å), Phe297 (5.91 Å), and Trp86 (4.98 Å, 5.53 Å and 5.89 Å). In addition, compound **3b** formed numerous hydrophobic interactions with residues in the active site of AChE. Residues Tyr124 and Tyr341 in the peripheral anionic region (PAS), Phe295 and Phe297 in the acyl binding pocket and Trp86 is located in the active site. Compound **3b** interacts with Trp286 π -alkyl interaction and Asp74 attractive charge. Compound **3a** formed the most stable complex with a binding affinity of -10.05 kcal/mol as a result of docking at the active site of AChE. Compound **3a** interacted with similar residues as compound **3b** in the active site. Compound **3b**

involved in more hydrogen bonds and π - π interactions than that of compound **3a**.

4. CONCLUSION

Two different compounds based on 6-hydrazinyl-1,3,4-trimethyl-1H-pyrazolo[3,4-b]pyridine (**3a** and **3b**) designed and synthesized and their structures were determined by FTIR and $^1\text{H}/^{13}\text{C}$ NMR spectroscopic methods. *In vitro* inhibitory effects of compounds **3a** and **3b** against AChE were evaluated. Compound **3b** exhibited stronger inhibitory activity than both the reference drug galantamine and compound **3a**. Docking studies were performed to identify possible binding modes of the compounds. In consequence of docking, Compound **3b** was found to have the highest activity with the lowest binding affinity. The pyrazole, pyridine, and hydrazine units were found to make hydrophobic and hydrophilic interactions with the residues in the active site of the enzyme. In addition, the propargyl group was thought to be responsible in the strong inhibitory activity of compound **3b**.

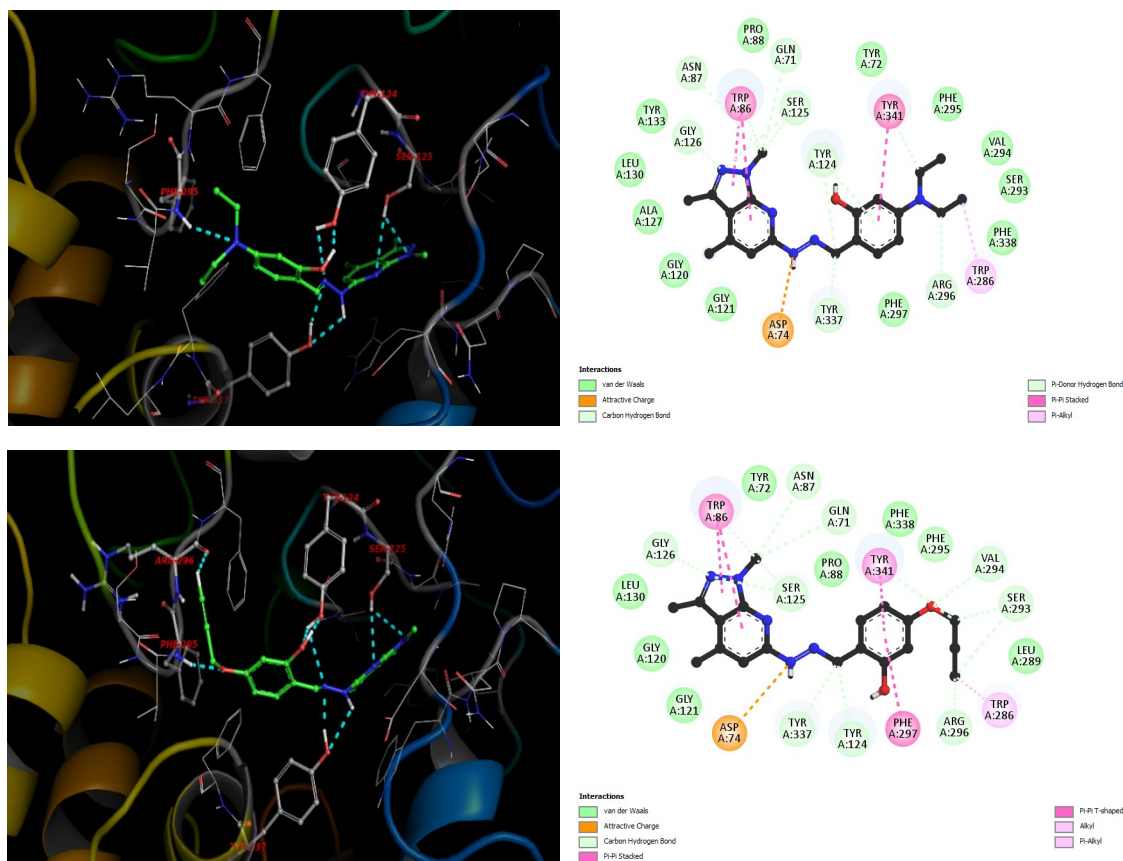


Figure 6: 2D Hydrophobic interaction profile with AChE of compounds **3a** (upper right) and **3b** (lower right). 3D bonding mode of the lowest energy conformation with AChE of compounds **3a** (upper left) and **3b** (lower left). The carbon atoms green color of compounds **3a** and **3b** and the carbon atoms gray color of amino acids are shown as ball and stick model. The hydrogen bond interaction between ligands and residues is shown by turquoise dashed lines.

5. REFERENCES

1. Khachaturian ZS. Conference R Diagnosis of Alzheimer's Disease. Arizona Heal Sci Libr User. 1985;42:1097-105. Available from: <DOI>
2. Sharma K. Cholinesterase inhibitors as Alzheimer's therapeutics (Review). Mol Med Rep. 2019;20(2):1479-87. Available from: <DOI>
3. Cheng ST. Cognitive Reserve and the Prevention of Dementia: the Role of Physical and Cognitive Activities. Curr Psychiatry Rep. 2016;18(9). Available from: <DOI>
4. Maxwell CJ, Vu M, Hogan DB, Patten SB, Jantzi M, Kergoat MJ, et al. Patterns and determinants of dementia pharmacotherapy in a population-based cohort of home care clients. Drugs and Aging. 2013;30(7):569-85. Available from: <DOI>
5. Silman I, Sussman JL. Acetylcholinesterase: "Classical" and "non-classical" functions and pharmacology. Curr Opin Pharmacol. 2005;5(3 SPEC. ISS.):293-302. Available from: <DOI>
6. Birks JS. Cholinesterase inhibitors (ChEIs), donepezil, galantamine and rivastigmine are efficacious for mild to moderate Alzheimer's disease. 2012;(5). Available from: <DOI>
7. Tschanz JT, Corcoran CD, Schwartz S, Treiber K, Green RC, Norton MC, et al. Progression of cognitive, functional, and neuropsychiatric symptom domains in a population cohort with alzheimer dementia: The cache county dementia progression study. Am J Geriatr Psychiatry. 2011;19(6):532-42. Available from: <DOI>
8. Parsons C, Lim WY, Loy C, McGuinness B, Passmore P, Ward SA, et al. Withdrawal or continuation of cholinesterase inhibitors or memantine or both, in people with dementia. Cochrane Database Syst Rev. 2021;2021(1). Available from: <DOI>
9. Feldman H, Gauthier S, Hecker J, Vellas B, Subbiah P, Whalen E. A 24-week, randomized, double-blind study of donepezil in moderate to severe Alzheimer's disease. Neurology. 2001;57(4):613-20. Available from: <DOI>
10. Selvarani V, Annaraj B, Neelakantan MA, Sundaramoorthy S, Velmurugan D. Synthesis and crystal structure of hydroxyacetophenone Schiff bases containing propargyl moiety: Solvent effects on UV-visible spectra. Spectrochim Acta - Part A Mol Biomol Spectrosc. 2012;91:329-37. Available from: <DOI>

11. Güngör SA, Tümer M, Köse M, Erkan S. Benzaldehyde derivatives with functional propargyl groups as α -glucosidase inhibitors. J Mol Struct. 2020;1206. Available from: [<DOI>](#)
12. Ellman GL, Courtney KD, Andres V, Featherstone RM. A new and rapid colorimetric determination of acetylcholinesterase activity. Biochem Pharmacol. 1961;7(2):88–95. Available from: [<DOI>](#)
13. Güngör Ö, Köse M. Design, synthesis and biological evaluation of biguanids and biguanid-sulfonamides as cholinesterase inhibitors. J Mol Struct. 2022;1260. Available from: [<DOI>](#)
14. Allouche A. Software News and Updates Gabedit – A Graphical User Interface for Computational Chemistry Softwares. J Comput Chem. 2012;32:174–82.
15. Şahin İ, Bingöl Z, Onur S, Güngör SA, Köse M, Gülçin İ, et al. Enzyme Inhibition Properties and Molecular Docking Studies of 4-Sulfonate Containing Aryl α -Hydroxyphosphonates Based Hybrid Molecules. Chem Biodivers. 2022; Available from: [<DOI>](#)
16. BIOVIA DS. Discovery studio visualizer. In San Diego, CA, USA; 2017. p. 298.
17. Lill MA, Danielson ML. Computer-aided drug design platform using PyMOL. J Comput Aided Mol Des. 2011;25(1):13–9. Available from: [<DOI>](#)



Physical and Spectroscopic Characterization of the Microcrystalline Cellulose Derivatives from Corn Cob and *Daniella Oliveri* Wastes

Mariam Temitope Baker*¹ , Olubunmi Stephen Oguntoye¹ 

¹University of Ilorin, Department of Chemistry, Ilorin, P.M.B. 1515, Nigeria.

Abstract: Cellulose was extracted from wood dust waste samples of *Daniella oliveri* and corn cobs by acetic acid and alkaline pretreatment methods, while microcrystalline cellulose (MCC) derivative was produced by acid hydrolysis in 2 M HCl. The samples were tested for pH, moisture content, swelling capacities and ash contents. The data obtained were compared with those of commercial MCCs found in the literature. The functional groups in the microcrystalline cellulose derivatives was confirmed by the Fourier transform infrared (FTIR) spectroscopic method with characteristic absorption bands of; -OH stretching at 3416 cm^{-1} ; C-H stretching at 2918 cm^{-1} ; -OH bending at 1377 cm^{-1} ; 1159 cm^{-1} ; and C-O-C pyranose ring skeletal vibrations at 1026-1033 cm^{-1} . The crystallinity absorption bands appeared at 1436 and 850 cm^{-1} . The characteristic morphological features were established by scanning electron microscopy (SEM). Furthermore, the crystallinity of the microcrystalline cellulose was further confirmed using the X-ray powder diffraction (X-RD) technique, which showed three main reflections at $2\theta=14.70^\circ$, 22.09° , and 34.24° . These results supported that microcrystalline cellulose derivative as cellulose I type and the acid pretreatment did not affect the structure of the MCC. The crystallinity indices were 69.3 and 73.2%, respectively. *Daniella Oliveri* and corn cob microcrystalline cellulose are, therefore, potential materials for further processing.

Keywords: Microcrystalline cellulose derivative, *Daniella oliveri*, corn cobs, wood dust waste, FTIR, XRD, TGA/DTA, SEM, physical characteristics, potential applications

Submitted: April 23, 2022. **Accepted:** October 22, 2022.

Cite this: Baker MT, Oguntoye OS. Physical and Spectroscopic Characterization of Corn Cob and *Daniella Oliveri* Wastes Microcrystalline Cellulose Derivatives. JOTCSA. 2023; 10(1):31-8.

DOI: <https://doi.org/10.18596/jotcsa.1107627>.

***Corresponding author. E-mail:** temitopemariam11@yahoo.com, arowona.mt@unilorin.edu.ng.

1. INTRODUCTION

Pollution is a pronounced concern in our community/environment as a result of poor waste management and disposal. The majority of these wastes are either piled up as an eyesore or left to fester, putting human and animal life at risk. It is worth noting that the majority of these wastes are cellulose-rich agricultural byproducts, including maize cobs, rice husks, and wood dust, from a variety of tree species. The production of agricultural byproducts is projected to be approximately 12 million tons per year, with the majority of them not being converted into other materials for future use (1). Cellulose is a polymer of D-glucose linked by the -1,4-D-glucopyranose

ring (2). It is made up of hundreds to thousands of monomers of glucose that are linked together. An anhydroglucose unit of cellulose consists of two glucose units linked together by a -1,4-glycosidic bond and weighs 162.1 gmol^{-1} (3). Cellulose and its derivatives have important applications in a variety of fields, including pharmaceuticals, biomedical, paint industries, water purification, and cosmetics (1,4-6). Microcrystalline cellulose (MCC) is a partially depolymerized cellulose in which the amorphous region of cellulose is hydrolyzed to produce crystalline cellulose with a larger surface area for better application (7-9). MCCs, like cellulose, are white, colourless, and odourless but have a larger surface area and a more ordered crystalline structure.

Corn is cultivated all over the world and consumed daily by man and animal in different forms. Knoema estimated the global corn cultivation to be 3.13 million thousand tonnes in 1971 alone, with an annual 3.06% increase, the production rise to 1.162 billion tonnes in 2020 (10). It is estimated that the ratio of corn grains to corncob is 100:18 (11). From the figures quoted earlier, this implies annual corn cob generation of corncob in 2020 alone is approximately 210 million tonnes. Corncobs find application in their uses as poultry feed formulation, polisher, bio-oil and biochar. The efficacy of corncob as alternative source of microcrystalline cellulose in pharmaceutical formulation has also been investigated (12,13). Apart from the applications stated above, several reports are available on the use of corncob as a very good source of compounds such as furfural, ethanol, xylitol, succinic and propionic acid, phenolic compounds, bio-adsorbent, biobased rigid polyurethane foam, hollow spherical carbon, and p-hydroxycinnamic esters (1,14,15).

Daniellia oliveri (DAN) is a soft wood deciduous mostly cultivated in the tropical region of Africa (16). This plant is basically cultivated for medicinal and economic benefits; the young leaves of this plants are cooked and consumed (17), the matured are used for the treatment of stomach troubles, diabetes, dysmenorrhoea, haemorrhoids due to their abortifacient, aphrodisiac, astringent, diuretic, emmenagogue and stomachic properties (18). The seeds are eaten (19), decoction from the roots are used in the treatment of gonorrhoea and skin diseases (20). The gum-resin from the stem-bark and wood is used in the treatment of gonorrhoea and laxative and also used for the manufacture of wood polish, perfumes and varnishes (21). The gum-resin obtained from the wood of this plant has also been used as binder in pharmaceutical formulation (22). An aqueous extract of the powdered bark has been shown to have effective pain-reduction properties and also to be antioxidant. The trunk are sold as timber for furniture and manufacture of equipment (23).

Characterization and use of the cellulosic content of the DAN. plant have not been widely studied in literature, to the best of the author's knowledge. Cellulose however, can be obtained from different part of the plant: For example, the wood dusts which is a waste or by product of milling the timber obtained from the DAN. for production of furniture and other tools are good source of cellulose for extraction and characterization. Some of the physical and spectroscopic characteristics of corncob MCC in comparison to that obtained from DAN, another plant specie is not widely investigated for its cellulosic content. This research therefore, reports some of the physical and spectroscopic properties of MCCs produced from *Daniellia oliveri*'s cellulosic waste and corncobs. This broadens the

horizon of cellulose sources and applications because, it is expected to replace toxic and non-biodegradable raw materials in the near future.

2. MATERIALS AND METHODS

2.1. Sample Collection and Preparation

Corncob (C.C) wastes lying fallow in the environment were randomly picked in the north-central part of Nigeria during the maize harvest season. This was to help clean up the litters from the environment. Wood dust of DAN tree species was obtained from a local wood milling factory environment in Kwara state, north-central, Nigeria. The local name for the *Daniella oliveri* sample was identified at the point of collection by its local name, while the botanical name was obtained through herbarium of University of Ilorin. Both samples (corn cob and *Daniella oliveri* wood dust) were sun dried to remove excess water for easy grinding and further processing.

2.2. Extraction of Cellulose

Cellulose I was extracted by the chemical pretreatment method, while Cellulose II was obtained by acid hydrolysis in 2 M HCl. The method of cellulose extraction used in our previous publication (24), we employed a slight modification. 500 g of DA or Corn cob was weighed into a quick fit flask, and 10% sodium hydroxide was added. It was then refluxed for four hours. The mixture was left to cool. It was then filtered and washed with water until neutral, washed with ethanol and dried. The dried residue was poured into a beaker, 10% acetic acid was added, and the beaker was heated for three hours. It was then filtered and washed with water and ethanol and dried. Hydrogen peroxide was added to the sample, and it was refluxed for three hours to further delignify. It was filtered and washed with water and ethanol. Hypochlorite was added and refluxed for three hours (until it turned white/off-white). The sample was thereafter washed with water and ethanol, dried, and blended into finer particles and stored for further use.

2.3. Preparation of MCC

MCC was prepared by acid hydrolysis of the cellulose samples obtained above in 2 M HCl under reflux in a 500 mL quick-fit flask. The reaction was carried out at 80 °C for 4 h with a continuous stirring speed of 700 rpm. The reaction mixture was cooled to room temperature and filtered, and the residue was repeatedly washed with distilled water until it was free from acid residue by testing the pH of the solution with a digital pH meter. The obtained MCC was dried in a hot air oven at 80 °C until a constant weight was achieved. Using the dry blender compartment, the dried MCC lumped together was ground into a fine powder.

2.4. Percentage Yield

The percentage yield of cellulose was calculated by dividing the final weight of cellulose obtained by the initial weight of the cellulosic sample. The percentage yield of both cellulose and MCC was obtained using the expression below;

$$Y_{cell} = \frac{Fw_{cell}}{Cw_{cell} * 100} \quad (1)$$

$$Y_{mcc} = \frac{Wh}{Fw_{cell} * 100} \quad (2)$$

Y_{cell} = Percentage Yield of cellulose;
Fw_{cell} = Weight of cellulose extracted;
Cw_{cell} = Weight of crude cellulose
Y_{mcc} = Percentage Yield of MCC;
Wh = Weight of Hydrolyzed cellulose;

2.5. Starch Test

The presence of starch in the sample was investigated by adding approximately 3 mL of iodine solution to 0.1 g MCC samples in a beaker. For comparison, the same amount of iodine solution (3 mL) was added to 0.1 g of reference standard starch in another beaker. Blue-black colouration indicates the presence of starch, while no change in colour indicates the absence of starch in the cellulose backbone. The absence of blue black colouration was taken as an indication of a positive result for cellulose.

2.6. Ash Content

Each of the prepared MCCs (2 g) was placed in a furnace at 600 °C for 6 h. The ash content was determined using the following equation:

$$\left[\left(\frac{W_i - W_f}{W_i} \right) \times 100 \right] - 100 \quad (3)$$

where W_i = initial weight of the sample W_f = final weight of the sample (i.e weight of ash)

2.7. Moisture Content

Each of the samples (1 g) was placed independently in a white porcelain crucible with a cover. The samples were dried in an oven for 3 h at 105 °C. During drying, the weight of the samples was taken at 30 min intervals until a constant weight was obtained. The moisture content was calculated using the equation below. (25)

$$\left(\frac{A - B}{A} \right) * 100 \quad (4)$$

A = initial weight of MCC
B = final weight of MCC after drying

2.8. pH Measurement

Each of the samples (1 g) was placed in a 10 ml clean measuring cylinder, a few milliliters of distilled water was added to the samples and shaken together, and the volume of the sample and water was brought to 10 mL. The mixture was left to settle, and the pH of the supernatant liquid was measured with a digital pH meter.

2.9. Water Uptake Capacity

Distilled water (4 mL) was poured into a 10 mL beaker containing MCC samples whose bulk and tapped volume had been obtained. The mixture was agitated, and the volume of the mixture reached 10 mL. The mixtures were left to stand for 72 hrs, the swelling volume V_s was obtained, and the water uptake capacity was calculated using the equation:

$$WUC(\%) = \frac{V_s - V_t}{V_t} \times 100 \quad (5)$$

WUC (%) = Percent Water uptake capacity
V_s = volume of sample after swelling
V_t = Tapped volume of the sample

2.10. Fourier Transform Infrared Spectroscopy (FTIR)

The chemical composition of each sample was determined by determining the functional groups using FTIR spectroscopy. A few milligrammes (mg) of dried cellulose and MCC derivatives were mixed with potassium bromide (1:90) and compacted into transparent tablets using a hydraulic press (M-15, Technosearch). An FTIR spectrometer (ALPHA-II, Bruker, Germany) was utilized to investigate the transparent tablets in the range of 4000–400 cm⁻¹.

2.11. X-Ray Powder Diffraction Spectroscopy (XRD)

The degree of crystallinity of the MCC derivatives was determined using an X-ray diffractometer machine (PANalytical, Model: X'pert PRO) powered by a 40 kilovolt X-ray generator at an input of 30 Ma with Cu K alpha radiation. The crystallinity indices of the samples were calculated from the spectrum obtained using the origin software by determining the area of the crystalline region and the area of the crystallinity as well as the amorphous region and then using the equation below to determine the crystallinity index of each sample.

$$C.I = \left(\frac{I_c}{I_a + I_c} \right) \times 100 \quad (6)$$

C. I = Crystallinity index; I_c = Area of Crystalline peaks, I_a + I_c = Area of Amorphous and Crystalline peaks.

2.12. Scanning Electron Microscopy (SEM)

The degree of crystallinity of the MCC derivatives was evaluated using X-ray diffractometer equipment (PANalytical, Model: X'pert PRO) using Cu K alpha radiation and a 40 kilovolt X-ray generator at an input of 30 Ma.

2.13. Thermogravimetric and Differential Thermal Analysis (TG/DTA)

Thermogravimetric analysis (TGA) was performed on the derivatives to track the thermal degradation trend, whereas DTA was used to determine how much weight was lost at a given temperature. TGA measurements were carried out with an STA449 (F3, Netzsch, Germany) under a nitrogen atmosphere (40 mL/min), and the derivatives were heated at a rate of 10 °C/min from 50 °C to 850 °C. The remaining weight loss was determined by measuring it at 850 °C.

3. RESULTS AND DISCUSSION

3.1. Appearance

The cellulose revealed white to off-white with a rough to smooth appearance due to the presence of both crystalline and amorphous regions of the cellulose molecule. On the other hand, the MCCs prepared from the initial cellulose appeared smooth with white to off-white in colour. The smooth appearance of the MCCs is related to the breakdown of the amorphous part of the cellulose compound leaving behind the powdery crystalline region.

3.2. Percentage Yield

The percentage yields of the cellulose was calculated by dividing the weight of the cellulosic biomass before extraction by the weight of the

cellulose obtained after extraction. The percent yield of the MCCs was obtained by dividing the mass of the cellulose obtained before hydrolysis by the mass of the product obtained after hydrolysis. The percentage yields of cellulose samples were 60% for C.C and 55% for DAN. The MCC yields were 80 and 75% for C.C and DAN samples, respectively. This showed that the method of preparation of the cellulose compound gave cellulose with a good degree of crystallinity, hence leaving behind a larger amount of the crystalline region than the amorphous region after extraction. This claim was proven by the small difference in the crystallinity indices of the cellulose and MCC derivatives, which was supported in the XRD analysis. The percentage yield of the cellulose is as presented in the table 1 below:



Figure 1: Cellulose extracted (left) and prepared microcrystalline cellulose (right).

Table 1: Percent Yield of Cellulose and Microcrystalline cellulose.

No.	Sample	Cellulose(%)	MCC(%)
1.	CORN COB	60.0±0.5	80.0±0.5
2.	DANIELLA OLIVERI	56.5±0.29	75.0±1.0

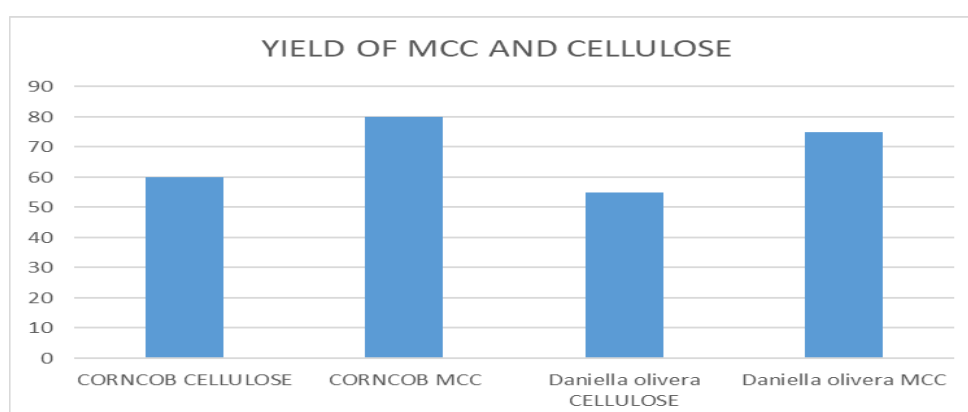


Figure 2: Bar chart representation of yields.

3.3. Starch Test

A starch test was conducted on the MCC derivatives to ascertain the absence of other carbohydrate such as starch, in the cellulose molecule. The MCC derivatives gave no colour change upon the addition of Iodine, as the reddish brown iodine remained, while starch gave blue-black colouration. The blue-black colouration of the starch was persistent, while the reddish brown colour of the iodine sublimed from the MCC solution after being kept at room temperature for 2 h. This is because, starch being a branched α -polymer of glucose, forms helical secondary structures which can hold iodine, which leads to a reaction and consequent colour change. But cellulose a linear β -polymer of glucose, does not contain helices, and so cannot hold iodine which prevents interaction, hence, no color change.

3.4. Ash Content

The percentage ash content values obtained are shown in the table 2 below, which was taken as evidence that the MCCs derivatives had very little non-cellulosic residues (25). The results were corroborated with those in the literature, with a percentage ash concentration of 1.95 for Avicel-102, a commercial excipient. This finding demonstrated that MCCs derivatives derived from these two agricultural wastes samples can compete rather well with commercially available MCCs (26,27).

Table 2: Percent Ash content of MCCs.

No.	Samples	%Ash content (%)
1.	Corn Cob	0.80±0.10
2.	<i>Daniella oliveri</i>	1.30±0.05

3.5. Moisture Content

The moisture content of MCCs reveals how much water they can absorb from the environment. The lower the moisture content of the material, the better it can be utilized as a material for direct compression excipient in pharmaceutical application while the higher the moisture content (28), the better is it to be used in other applications such as hydrogel for water storage for plant (29). According to the results from this study, the values obtained are within the usual range of less than 7% reported in the literature (27). The results of this study are presented in the table 3 below:

Table 3: Percent Moisture content of the MCCs.

No.	Samples	Moisture Content (%)
1.	Corn cob	1.80±0.12
2.	<i>Daniella oliveri</i>	10.10±1.0

3.6. pH Determination

The pH of the derivatives was found to be neutral, falling within the standard acceptable limit values

for neutral MCCs of pH 6-7.5 (30). Table 4 below summarizes the findings:

Table 4: pH Values of the MCCs.

No.	Samples	pH
1.	Corn Cob	6.56±0.02
2.	<i>Daniella oliveri</i>	6.3±0.01

3.7. Water Uptake Capacity

The increase in the volume of water taken up by the MCC derivatives following absorption was measured by the water uptake capacity, which measures the ability of the sample to swell. The derivatives have a moderate to high swelling ability, according to the results. The values for the swelling ability of the MCC derivatives are shown in the table 6 below, and these values favourably agreed with those reported in the literature (26). The values obtained for the two samples showed the corn has a better ability to take up more water into its cellulosic backbone than the *DAN samples* but the moisture contents value suggests the DAN sample takes up moisture easily from the atmosphere than the corncob. This phenomenon might be due to difference in their cellulosic origin which might make cellulosic sample to absorb moisture easily but releases it easily as well due smaller surface area. This can be explained by the SEM appearance of the MCC samples showing *DAN* with longer strands than the C.C with shorter agglomerates due to larger surface area and higher crystallinity as evidenced in the crystallinity indices values of the materials.

Table 5: Water uptake Capacity of the MCCs.

No.	Samples	WUC (%)
1.	Corn Cob	115.00±0.58
2.	<i>Daniella oliveri</i>	78.60±2.00

3.8. Fourier Transform Infrared Spectroscopy (FTIR)

The FTIR spectra of cellulose and MCC derivatives are presented in the figure 3. Native cellulose affords absorption bands at approximately 3300, 2900, 1430, 1374, 1100, 1050, and 890 cm^{-1} Liu, 2007. Absorbance peaks in the regions of 3450–3300 cm^{-1} and 2900–2800 cm^{-1} are caused by stretching of O-H groups and saturated aliphatic C-H, respectively. The skeletal vibrations of the C-O-C pyranose ring are responsible for the peaks that occurred at approximately 1050 cm^{-1} (8,31,32). The C-O asymmetric bridge stretching was caused by absorption bands at approximately 1374 cm^{-1} . Furthermore, the absorption peak at 1429 cm^{-1} , due to a symmetric CH_2 bending vibration and referred to as the "crystallinity band," due to a symmetric CH_2 bending vibration (33). Because of the hydrophilic nature of cellulosic material, the absorption peak at 1624 cm^{-1} is responsible for water absorption (34). The absence of peaks at

1512 cm^{-1} and 1735 cm^{-1} , which correspond to the C-C aromatic bending and aromatic C-O stretching in hemicelluloses and lignin, respectively, indicated that the pretreatment procedure effectively removed noncellulosic components of the raw materials (35–38).

3.9. X-Ray Powder Diffraction (XRD)

The crystallinity indices of the derivatives indicated that the amorphous cellulose region was broken down, leaving the crystalline cellulose material behind, generating microcrystalline cellulose. *DAN*. and C.C had crystallinity index values of 69.3 and 73.2% respectively, which is a good value for microcrystalline cellulose. The increase in value for the MCCs over the cellulose samples indicated that the amorphous region of the cellulose samples was broken down during hydrolysis. The samples' XRD Spectra are shown below. The diffraction patterns of all the MCC samples showed sharp peaks at 2 angles of approximately 14.5°, 17°, 22.7°, and 35.5° for all the compounds, which were assigned to the usual cellulose I reflection planes. The results were identical to those found in the literature for carbon nanocellulose and microcrystalline cellulose (39–42).

3.10. Scanning Electron Microscopy (SEM)

From the overall view, the SEM micrographs of the cellulose samples showed the fibre strands with long and short tubes connected to one another, and the presence of both long and short tubes was due to the amorphous and crystalline structure in the cellulose backbone. The microcrystalline cellulose derivatives showed non-uniformly distributed and shorter microcrystalline particles, creating microcrystals due to hydrolysis and displaying a large sample surface area. This was caused by the amorphous region breaking down during hydrolysis, resulting in a microcrystalline structure with a huge surface area. The surface area patterns from the analyzed varieties were similar but those of corncobs formed agglomerates better than those of the *DAN sample* which makes it (C.C MCC) more crystalline as evident in the crystallinity indices of the materials calculated from the XRD results. Overall, the microcrystalline cellulose from each of these samples may be used as raw starting materials for further processing either as direct compression excipient in pharmaceutical drug formulation, biomedical and paint industry due to their crystallinity and appearance. Their water holding capacities suggests the samples as good candidates in hydrogel formation for water storage agent for plants' roots..

3.11. Energy Dispersive X-Ray Spectroscopic (EDS) Analysis

The EDS analysis of the samples showed the presence of Carbon (C) and oxygen (O) as the predominant element, which revealed materials prepared are purely cellulose. As expected for pure

cellulose products, elements like sodium (Na) and sulfur (S), which might be present as contaminants during pretreatment and Microcrystalline cellulose preparation, were absent. Conclusively, good grade cellulose successfully, were prepared. It is worthy of note that the presence of Au and Nb elements is due to gold element used in coating the samples before analysis.

3.12. Thermogravimetric/Differential Thermal Analysis (TGA/DTA)

The thermogravimetric curve demonstrated that the microcrystalline cellulose derivatives degraded in a single step from 400 to 500 °C. The first degradation step is as a result of loss of water or moisture due to the hydrophilic nature of the samples while the other step involves the breakdown of the microcrystalline cellulose derivatives into ashes. From the thermogram, C.C MCC had better thermal stability than *DAN* MCC at a degradation temperature of 500 °C, which could be due to its high swelling capacity. Overall, the samples' thermal breakdown patterns verified the absence of hemicelluloses, lignin, and little or no residues of contaminants in their core structure. As a result, the MCCs are thermally stable. Similar results are widely reported in literature for microcrystalline cellulose derivatives from other plant species such as date seeds, tea wastes, rice husk, pomelo peels, wheat straw and cotton. (2,8,24,28,34,43) The T_{max} (temperature at which maximum weight loss occurs) for the samples was 450 °C. These samples, which are thermally stable, serve as raw materials for future material functionalization and applications.

4. CONCLUSION

Microcrystalline cellulose compounds were prepared and characterized from cellulose isolated through alkaline hydrolysis of cellulosic wastes. This work serve as a workable model to clean up the environment by removing some of the cellulosic wastes from the environment, therefore reducing possible environmental pollution by their presence. On the other hand, the wastes were converted into good-grade microcrystalline cellulose that will be useful in various areas such as in direct compression excipient in pharmaceutical formulation or agriculture as water storage excipient. From the properties displayed by these two MCCs, the C.C sample gave cellulose with better yield and physical as well as spectroscopic properties. Due to their (C.C) high water uptake ability, they can be employed in agriculture as water retaining hydrogels that can be prepared by grafting the MCC compounds onto other natural or synthetic polymers. This is owing to their high water uptake ability. The derivatives from *Daniella oliveri*, an underutilized plant in the area of cellulosic application on the other hand, might serve as a good or even better candidate in the

pharmaceutical, biomedical or paint industry than the corncob derivatives. Overall, good grade MCCs were prepared from wastes obtained from nature. The wastes were processed into useful raw materials that will now be sent back to nature in a useful form as raw materials for several applications.

5. ACKNOWLEDGMENTS

The authors would like to thank CSIR-IMMT, Bhubaneswar, Odisha, India for assistance in providing access to the analytical equipment free of cost. Special 'thank you' to Dr. R. Boopathy of the Environment and Sustainability Department of the Institute for providing needed guidance in the course of the research.

6. REFERENCES

- Bian B, Hu X, Zhang S, Lv C, Yang Z, Yang W, et al. Pilot-scale composting of typical multiple agricultural wastes: Parameter optimization and mechanisms. *Bioresour Technol* [Internet]. 2019 Sep 1 [cited 2021 Apr 9];287. Available from: [<URL>](#).
- Abu-Thabit NY, Judeh AA, Hakeem AS, Ul-Hamid A, Umar Y, Ahmad A. Isolation and characterization of microcrystalline cellulose from date seeds (*Phoenix dactylifera* L.). *Int J Biol Macromol* [Internet]. 2020;155:730–9. Available from: [<URL>](#).
- Granström M. *Cellulose Derivatives: Synthesis, Properties and Applications*. 2009. ISBN: 978-952-10-5485-3.
- Kumar V, Pathak P, Bhardwaj NK. Waste paper: An underutilized but promising source for nanocellulose mining. *Waste Manag* [Internet]. 2020;102:281–303. Available from: [<URL>](#).
- Czaja W, Krystynowicz A, Bielecki S, Brown RM. Microbial cellulose - The natural power to heal wounds. *Biomaterials*. 2006;27(2):145–51. Available from: [<URL>](#).
- Kostag M, Jedvert K, Ahtel C, Heinze T, El Seoud OA. Recent advances in solvents for the dissolution, shaping and derivatization of cellulose: Quaternary ammonium electrolytes and their solutions in water and molecular solvents. *Molecules*. 2018;23(3). Available from: [<URL>](#).
- Kunusa WR, Isa I, Laliyo LAR, Iyabu H. FTIR, XRD and SEM Analysis of Microcrystalline Cellulose (MCC) Fibers from Corncorbs in Alkaline Treatment. *J Phys Conf Ser*. 2018;1028(1). Available from: [<URL>](#).
- Zhao T, Chen Z, Lin X, Ren Z, Li B, Zhang Y. Preparation and characterization of microcrystalline cellulose (MCC) from tea waste. *Carbohydr Polym*. 2018 Mar 15;184:164–70. Available from: [<URL>](#).
- Garba ZN, Lawan I, Zhou W, Zhang M, Wang L, Yuan Z. Microcrystalline cellulose (MCC) based materials as emerging adsorbents for the removal of dyes and heavy metals – A review. *Sci Total Environ* [Internet]. 2020;717(Mcc):135070. Available from: [<URL>](#).
- Knoema. Search, Discover, Catalog and Access Your Data Seamlessly. October 29, 2022 ([<URL>](#). Opens in new tab).
- Cao Q, Xie KC, Bao WR, Shen SG. Pyrolytic behavior of waste corn cob. *Bioresour Technol*. 2004;94(1):83–9. [<URL>](#).
- Ravikumar C, Senthil Kumar P, Subhashni SK, Tejaswini P V., Varshini V. Microwave assisted fast pyrolysis of corn cob, corn stover, saw dust and rice straw: Experimental investigation on bio-oil yield and high heating values. *Sustain Mater Technol* [Internet]. 2017;11:19–27. Available from: [<URL>](#).
- Zhang Q, Zhang D, Xu H, Lu W, Ren X, Cai H, et al. Biochar filled high-density polyethylene composites with excellent properties: Towards maximizing the utilization of agricultural wastes [Internet]. 2020 [cited 2021 Apr 9]. Available from: [<URL>](#).
- Wang S, Gao W, Li H, Xiao LP, Sun RC, Song G. Selective fragmentation of biorefinery corncob lignin into p-hydroxycinnamic esters with a supported zinc molybdate catalyst. *ChemSusChem*. 2018;11(13):2114–23. Available from: [<URL>](#).
- Duan C, Meng X, Liu C, Lu W, Liu J, Dai L, et al. Carbohydrates-rich corncobs supported metal-organic frameworks as versatile biosorbents for dye removal and microbial inactivation. *Carbohydr Polym* [Internet]. 2019;222:115042. Available from: [<URL>](#).
- agritrop-eprint-317983. *Useful Tropical Plants*. July 20, 2022 ([<URL>](#). opens in new tab).
- Shackleton CM, Pasquini MW, Drescher AW. African indigenous vegetables in urban agriculture. *African Indigenous Vegetables in Urban Agriculture*. 2009. 1–298 p. ISBN: 9781136574993 .
- Ahmadu AA, Zezi AU, Yaro AH. Anti-diarrheal activity of the leaf extracts of *Daniellia Oliveri* hutch and Dalz (Fabaceae) and *ficus sycomorus* Miq (Moraceae). *African J Tradit Complement Altern Med*. 2007;4(4):524–8. Available from: [<URL>](#).
- Burkill HM. *The useful plants of west tropical Africa, Vols. 1-3*. 1995;(2. ed.), ISBN: 094764301x. [<URL>](#).
- Dinku W, Isaksson J, Rylandsholm FG, Bouř P, Brichtová E, Choi SU, et al. Anti-proliferative activity of a novel tricyclic triterpenoid acid from *Commiphora africana* resin against four human cancer cell lines. *Appl Biol Chem* [Internet]. 2020;63(1). Available from: [<URL>](#).
- Alagbe, J.O., Sharma, R., Eunice AbidemiOjo., Shittu, M.D and Bello KA. Proximate , Mineral and Phytochemical Analysis of *Piliostigma Thonningii* Stem Bark and Roots. *Int J Biol , Phys Chem Stud (JBPCS)*. 2020;(c):1–7. Available from: [<URL>](#).
- Adeyanju O, Olatoyinbo FA. Toxicological Studies and Utilization of DAN. Gum as Binder in Drug Formulation. *J Pharm Appl Chem*. 2018;4(3):169–74. Available from: [<URL>](#).
- Ajala, O. O., Awotedu, O.O. and Ogunbamowo PO. Comparative assessment of briquette produced from

- selected wood species. *J Sustain Environ Manag* [Internet]. 2016;8(ISSN: 2141-0267):1-12. Available from: [<URL>](#).
24. Arowona MT, Olatunji GA, Saliu OD, Adeniyi OR, Atolani O, Adisa MJ. Thermally stable rice husk microcrystalline cellulose as adsorbent in PTLC plates. *J Turkish Chem Soc Sect A Chem*. 2018;5(3):1177-84. [<URL>](#).
25. Kharismi RRAY, Sutriyo, Suryadi H. Preparation and characterization of microcrystalline cellulose produced from betung bamboo (*dendrocalamus asper*) through acid hydrolysis. *J Young Pharm*. 2018;1 (2):s79--s83. [<URL>](#).
26. Nwachukwu N, Ofoefule SI. Effect of drying methods on the powder and compaction properties of microcrystalline cellulose derived from gossypium herbaceum. *Brazilian J Pharm Sci*. 2020;56:1-17. [<URL>](#).
27. Kharismi RRAY, Sutriyo, Suryadi H. Preparation and characterization of microcrystalline cellulose produced from betung bamboo (*dendrocalamus asper*) through acid hydrolysis. *J Young Pharm*. 2018;10(2):s79-83. [<URL>](#).
28. Krivokapić J, Ivanović J, Djuriš J, Medarević D, Potpara Z, Maksimović Z, et al. Tableting properties of microcrystalline cellulose obtained from wheat straw measured with a single punch bench top tablet press. *Saudi Pharm J*. 2020;28(6):710-8. [<URL>](#).
29. Geng H. A one-step approach to make cellulose-based hydrogels of various transparency and swelling degrees. *Carbohydr Polym* [Internet]. 2018;186:208-16. Available from: [<URL>](#).
30. Viera-Herrera C, Santamaría-Aguirre J, Vizuete K, Debut A, Whitehead DC, Alexis F. Microcrystalline cellulose extracted from native plants as an excipient for solid dosage formulations in drug delivery. *Nanomaterials*. 2020;10(5):1-12. Available from: [<URL>](#).
31. Liu C-F, Sun R-C, Zhang A-P, Qin M-H, Ren J-L, Wang X-A. Preparation and Characterization of Phthalated Cellulose Derivatives in Room-Temperature Ionic Liquid without Catalysts. 2007; Available from: [<URL>](#).
32. Beroual M, Boumaza L, Mehelli O, Trache D, Tarchoun AF, Khimeche K. Physicochemical Properties and Thermal Stability of Microcrystalline Cellulose Isolated from Esparto Grass Using Different Delignification Approaches. *J Polym Environ* [Internet]. 2021;29(1):130-42. Available from: [<URL>](#).
33. Szymanska-Chargot M, Chylinska M, Gdula K, Koziol A, Zdunek A. Isolation and characterization of cellulose from different fruit and vegetable pomaces. *Polymers (Basel)* [Internet]. 2017;9(10). Available from: [<URL>](#).
34. Hachaichi A, Kouini B, Kian LK, Asim M, Jawaid M. Extraction and Characterization of Microcrystalline Cellulose from Date Palm Fibers using Successive Chemical Treatments. *J Polym Environ* [Internet]. 2021; (0123456789). Available from: [<URL>](#).
35. Usmani Z, Sharma M, Gupta P, Karpichev Y, Gathergood N, Liang James Hawkins Michael E Ries Peter J Hine YE, et al. A study on the microstructural development of gel polymer electrolytes and different imidazolium-based ionic liquids for dye-sensitized solar cells. *Carbohydr Polym* [Internet]. 1st ed. 2017 Mar 15 [cited 2021 Mar 29];10(1):1-12. Available from: [<URL>](#).
36. Hina S, Zhang Y, Wang H. Role of ionic liquids in dissolution and regeneration of cellulose. *Rev Adv Mater Sci*. 2015;40(3):215-26. Available from: [<URL>](#).
37. Cheng W, He J, Wu Y, Song C, Xie S, Huang Y, et al. Preparation and characterization of oxidized regenerated cellulose film for hemostasis and the effect of blood on its surface. *Cellulose*. 2013;20(5):2547-58. [<URL>](#).
38. Nascimento DM d., Almeida JS, Vale M do S, Leitão RC, Muniz CR, Figueirêdo MCB d., et al. A comprehensive approach for obtaining cellulose nanocrystal from coconut fiber. Part I: Proposition of technological pathways. *Ind Crops Prod* [Internet]. 2016;93:66-75. Available from: [<URL>](#).
39. Rahman MS, H. Mondal MI, Yeasmin MS, Sayeed MA, Hossain MA, Ahmed MB. Conversion of Lignocellulosic Corn Agro-Waste into Cellulose Derivative and Its Potential Application as Pharmaceutical Excipient. *Processes* [Internet]. 2020 Jun 19 [cited 2021 Apr 9];8(6):711. Available from: [<URL>](#).
40. Hu F, Lin N, Chang PR, Huang J. Reinforcement and nucleation of acetylated cellulose nanocrystals in foamed polyester composites. *Carbohydr Polym* [Internet]. 2015;129:208-15. Available from: [<URL>](#).
41. Mahmoudian S, Wahit MU, Ismail AF, Balakrishnan H, Imran M. Bionanocomposite fibers based on cellulose and montmorillonite using ionic liquid 1-ethyl-3-methylimidazolium acetate. *J Mater Sci*. 2015;50(3):1228-36. [<URL>](#).
42. W. R. Kunusa*, I. Isa LAL& HI. FTIR, XRD and SEM Analysis of Microcrystalline Cellulose (MCC) Fibers from Corncorbs in Alkaline Treatment. *J Phys Conf Ser* 1028. 2018 Mar 15;1(1):258-66. [<URL>](#).
43. Liu Y, Liu A, Ibrahim SA, Yang H, Huang W. Isolation and characterization of microcrystalline cellulose from pomelo peel. *Int J Biol Macromol* [Internet]. 2018;111:717-21. Available from: [<URL>](#).



The Analytical Survey of Mercury Content in Whitening Cream Sold in Banjarnegara Regency's Traditional Market

Sabtanti Harimurti^{1*} , Angelina Mawarni¹ , Ika Sevi Deriyanti¹ , Hari Widada¹ ,
Dyani Primasari Sukamdi¹ 

¹Universitas Muhammadiyah Yogyakarta, School of Pharmacy, Faculty of Medicine and Health Sciences #1, JL. Brawijaya, Tamantirto, Kasihan, Bantul, Yogyakarta 55183, Indonesia

Abstract: Whitening cream is a mixture of active substances and the other additives that can be used to brighten the skin. Mercury is one of the whitening ingredients of the creams that can cause health problems when it is absorbed into the tissue. This study aims to identify whether there is a mercury content and how much mercury is contained in the whitening cream, which does not have a BPOM RI registration number (National Agency of Food and Drug Control, Republic of Indonesia) circulating in the market in Banjarnegara regency, Central Java, Indonesia. This research was conducted with purposive sampling, and 20 samples were obtained from the traditional market in Banjarnegara regency. The qualitative analysis method used the Potassium Iodide (KI) color reaction test and amalgam formation with copper rods, while the quantitative analysis used the Cold Vapor Mercury Analyzer at a wavelength of 253.7 nm. The results showed the presence of three positive samples containing mercury at average levels of 0.04217 mg / kg (ppm), 0.01814 mg / kg, and 0.91000 mg / kg. These findings suggest that mercury was added at the whitening cream and distributed in the market. Customers should be more careful when choosing a whitening cream to prevent health problems.

Keywords: Amalgam test and mercury analyzer-CV, KI test, mercury, whitening cream.

Submitted: July 30, 2022. **Accepted:** November 07, 2022.

Cite this: Harimurti S, Mawarni A, Deriyanti IS, Widada H, Sukamdi DP. The Analytical Survey of Mercury Content in Whitening Cream Sold in Banjarnegara Regency's Traditional Market. JOTCSA. 2023;10(1):39-46. **DOI:** <https://doi.org/10.18596/jotcsa.1151307>.

*Corresponding author. E-mail: sabtanti@umy.ac.id

1. INTRODUCTION

Cosmetics are pharmaceutical preparations widely used to support a person's daily appearance. Cosmetics can also help to improve the dry, dull, or blemished skin (1,2). They have both positive and negative impacts on public health (3). Whitening cream is one type of cosmetic that is most widely used to improve the facial skin, such as by making it brighter and whiter. One of the ingredients that can be used as lightning or bleaching is mercury (4).

Indonesia has issued regulations to control what ingredients are safe and can be used to a certain extent through the BPOM (Indonesian national agency of drug and food control (Badan Pengawas Obat dan Makanan) RI. It has been confirmed that many cosmetic products contain heavy metals such as mercury, arsenic, and hydroquinone that exceed

the specified limits regulated by 21CFR700.13 FDA and BPOM RI (2,5). This issue, therefore, causes BPOM RI to issue a *public warning* number B-IN.05.03.1.43.12.17.5965 on December 11, 2017, concerning cosmetics that contain harmful ingredients so that they are withdrawn and are discovered to contain dangerous metals (6). During 2017, BPOM RI has also found 26 types of cosmetics containing hazardous materials. In the use of cosmetics, they must be adjusted to the rules of their use (7).

In 2018, there was a whitening cream that was positively found to contain mercury. It was found in the preliminary research of several researchers, such as Walangitan *et al.* (2018) and Mona *et al.* (2018). The mercury concentration of three samples from seven samples circulated in the Manado district, which were measured by using the Atomic

Absorption Spectrophotometry (AAS) method, was 0.1299 mg/kg, 0.1822 mg/kg, and 0.0566 mg/kg, respectively (8,9). Furthermore, mercury concentrations in two samples of six taken from the Manado region, measured by using the Mercury Analyzer method, were 229.38 ppm and 101.17 ppm (9).

According to BPOM RI in 2019, heavy metal mercury (Hg) should be not found inside cosmetics (2). Besides, the World Health Organization states that each country has its own policy regarding the amounts of mercury that can be used in cosmetic products (10).

According to Tranggono et al. (2014), mercury is proposed to be a skin whitening ingredient as it has the potential to be a reducing agent of skin color with a very strong whitening power (11). Mercury ions are considered to inhibit melanin synthesis of skin pigment in melanocyte cells (12,13). Melanin in people with dark skin is more abundant than in people with brownish yellow skin. It can be said that the function of melanin in the skin is to give the skin a brown color (14). When this process is inhibited, melanin will not be formed. This is the basis for the mechanism of various bleaching active ingredients to reduce the melanocyte cells that produce melanin. In the initial use of mercury, it can irritate and cause dependence. When the use is stopped, it will cause an itchy and uncomfortable feeling on the facial skin (15,16). Furthermore, mercury can also cause skin cancer with long-term use (17).

Since there are a lot of reports stating that there are harmful effects of mercury on the use of bleaching creams by women in Indonesia and the survey results in the Traditional Market of Banjarnegara showed there were a lot of circulating cream products that were sold without BPOM RI registration numbers. Therefore, 20 samples of whitening cream without BPOM RI registration number that are circulated in the traditional market of Banjarnegara district were collected and then analyzed. This paper deals with the explanation of qualitative and quantitative analysis of mercury in the samples.

2. EXPERIMENTAL SECTION

2.1. Research Tools

Copper rods, sandpaper, filter paper, tongs, dropper pipettes, burners, tube racks, electric stoves (Maspion ®), beaker glass (Pyrex ®), 100 mL Erlenmeyer (Pyrex ®), volumetric flask 25 mL; 100 mL (Pyrex ®), volumetric pipette 1mL; 5mL; 10 mL; 25 mL (Pyrex ®), measuring pipette 5mL; 50 mL; 100 mL (Pyrex ®), test tubes (Pyrex ®), digital scales (Mettler Toledo AL 204), Mercury analyzer (AULA 254 ®) were used in the present study.

2.2. Research Materials

The materials used in this study were 20 types of facial whitening cream samples collected from traditional market of Banjarnegara Regency. The

concentrated HNO₃ solution, concentrated HCl solution, and distilled water were purchased from Bratachem. The 0.5 N KI solution, KMnO₄, hydroxylamine hydrochloride, and SnCl₂. 2H₂O were obtained from Merck. The standard mercury solution was purchased from Sigma-Aldrich.

2.3. Procedures

2.3.1. Qualitative sample test

Sample preparation: Two (2) grams of sample were weighed using a digital scale, added to 25 mL of distilled water, and then went through wet destruction with 10 mL of aqua regia solution (the combination of concentrated HCl and concentrated HNO₃ at a ratio of 1:3). The wet destruction was done for 15 minutes, until the sample almost dried. The heating was conducted during the destruction using a hot plate. The end of destruction was then added 10 mL of distilled water. Furthermore, it was boiled briefly for 5 minutes, cooled, and filtered (15).

2.3.2. Mercury identification test

Color reaction test by using KI: The color test was done in the test tube (Pyrex ®). Two (2) drops of 0.5 N KI was added to one (1) mL of filtered sample in the test tube. The addition was done slowly through the wall of the test tube. The orange solid will appear if it is positively identified to contain mercury (8,18).

2.3.3. Amalgam test

Three (3) mL of filtered sample solution was added into the test tube, and then the copper rod was sanded until it was glossy. It was then dipped for some time into the test tube containing the tested solution. The copper rod will be coated with glossy grey patches if it is positively identified to contain mercury. The grey color will disappear if it is heated on a flame (18-20).

2.4. Quantitative Analysis of Samples Using a Mercury Analyzer

2.4.1. Sample preparation

Samples were weighed and placed in a 100 mL Erlenmeyer flask, followed by 10 mL of HNO₃ and HClO₄ with a ratio of 1:1. The mixture was then heated on a hot plate until it turned clear and a white smoke appeared. Afterward, the samples were filtered, and 50 mL were taken by using a volumetric flask (21).

2.4.2. Measuring mercury concentration using a Mercury analyzer (AULA 254®)

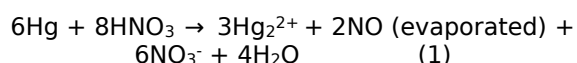
A 10-mL volumetric pipette was used to collect samples, which were then placed in a test tube. 0.1 mL of KMnO₄ (0.1%), 0.1 mL of hydroxylamine hydrochloride, and 0.5 mL of SnCl₂.2H₂O were added. It was also measured with a Mercury analyzer at a wavelength of 253.7 nm (1,21,22).

3. RESULTS AND DISCUSSION

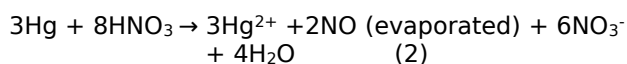
The qualitative analysis of mercury in the whitening cream samples from the traditional market of Banjarnegara Regency was done by using the KI color

reaction and Amalgam formation (18-20). The wet destruction was conducted before the test. The heating of organic samples in the presence of strong oxidizing agents such as single or combinations of mineral acids is known as wet digestion or destruction. The sample is completely oxidized to form an inorganic compound suitable for analysis if it is heated at a suitable temperature continuously for a sufficiently long time. Generally, HNO_3 is used for wet destruction as it cannot react with a saline solution such as HCl or H_2SO_4 (23). The wet destruction of this research used aqua regia solution, which is a mixture of HCl and HNO_3 with a ratio of 1:3 (24). HCl and HNO_3 were used because they are strong acids and oxidizing agents to break the bond of organic metals (Hg-organic) so that inorganic metals (Hg^{2+}) were formed.

Mercurium (I) is produced by combining cold concentrated and moderately concentrated nitric acid (HNO_3) with excessive mercurium, which is the reaction that occurs between a mercury metal and concentrated HNO_3 . The resulting reaction is depicted in Equation 1.

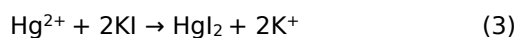


By using excessively concentrated heated nitric acid (HNO_3), mercurium (II) ions are formed with the following Equation 2.



Mercury (Hg) is very distinct from the reagents used in the systematic qualitative analysis, and it is therefore included in two different analytic classes. Mercury ions (I) belong to the first cation group, while mercury ions (II) belong to the second cation group (18).

The analysis was carried out using potassium iodide. The reaction that occurs between mercury and potassium iodide is given by Equation 3 (25).

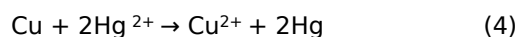


The reaction produced an orange-red solid of HgI_2 (19), as shown in Figure 1.



Figure 1: KI test of whitening cream.

Amalgam reaction formation is carried out by using Cu or a sanded copper rod. Amalgam is a metal solution from mercury produced by copper rods that can be dissolved by mercury. If it is positively identified to contain mercury, there will appear a layer containing grey glossy spots on the surface of the copper rod, which indicates a form of metal mercury (18,19,26,27). It happens from the results of the reaction (18,27), as in Equation 4.



Based on that reaction, 2Hg solid produced the layer with glossy grey patches.



Figure 2: Amalgam test of whitening cream.

The result obtained was negative amalgam with no glossy grey patches on the surface of the copper rod. It is because the sample contained less mercury that made it hardly detected. The KI color test and amalgam qualitative analysis are summarized in Table 1.

Table 1: The Result of the Qualitative Analysis Using a Color Test (Potassium Iodide Test) and the Formation of Amalgam.

Sample Code	Replication	KI Color Test	Amalgam Formation Test	Information (+/-)
1	1	Clear	No glossy grey color change	-
	1.1	Clear	No glossy grey color change	-
2	2	Clear	No glossy grey color change	-
	2.1	Clear	No glossy grey color change	-
3	3	Clear	No glossy grey color change	-
	3.1	Clear	No glossy grey color change	-
4	4	Clear	No glossy grey color change	-
	4.1	Clear	No glossy grey color change	-
5	5	Clear	No glossy grey color change	-
	5.1	Clear	No glossy grey color change	-
6	6	Clear	No glossy grey color change	-
	6.1	Clear	No glossy grey color change	-
7	7	Clear	No glossy grey color change	-
	7.1	Clear	No glossy grey color change	-
8	8	Clear	No glossy grey color change	-
	8.1	Clear	No glossy grey color change	-
9	9	Clear	No glossy grey color change	-
	9.1	Clear	No glossy grey color change	-
10	10	Clear	No glossy grey color change	-
	10.1	Clear	No glossy grey color change	-
11	11	Clear	No glossy grey color change	-
	11.1	Clear	No glossy grey color change	-
12	12	Red and orange solid	No glossy grey color change	+
	12.1	Red and orange solid	No glossy grey color change	+
13	13	Clear	No glossy grey color change	-
	13.1	Clear	No glossy grey color change	-
14	14	Clear	No glossy grey color change	-
	14.1	Clear	No glossy grey color change	-
15	15	Colored and red solid	No glossy grey color	+

Sample Code	Replication	KI Color Test	Amalgam Formation Test	Information (+/-)
	15.1	Colored and red solid	No glossy grey color change	+
16	16	Clear	No glossy grey color change	-
	16.1	Clear	No glossy grey color change	-
17	17	Red colored and orange red solid	No glossy grey color change	+
	R17	Red colored and orange solid	No glossy grey color change	+
18	18	Clear	No glossy grey color change	-
	18.1	Clear	No glossy grey color change	-
19	19	Clear	No glossy grey color change	-
	19.1	Clear	No glossy grey color change	-
20	20	Clear	No glossy grey color change	-
	20.1	Clear	No glossy grey color change	-

Based on the results, there are three positive samples containing mercury, namely sample numbers 12, 15, and 17, as there is a permanent change in the orange color and a red solid using KI color test. This result is in accordance with the previous identification of mercury in the whitening cream sold in Manado, Banjarmasin, and Palu, Indonesia (8,25,26), even in Shijiazhuang, China (13). To ascertain the result and find out how much mercury is contained in the sample, a quantitative analysis was carried out on the three samples by using a mercury analyzer.

Mercury analyzer includes in the spectrophotometric analysis technique of atomic absorption the administration of cold vapor samples. Mercury has the unique characteristic of having a high vapor pressure at room temperature (0.16 Pa at 293 K).

The vapor produced is stable and monatomic, so that the atomic composition of the mercury vapor can be read, without the use of a flame or other atomizing techniques with a wavelength of 253.7 nm (28). The first thing to be prepared was the standard curve. A mercury concentration in the sample preparation was then measured by using a mercury analyzer at a wavelength of 253.7 nm. The wavelength was selected as it indicated the best sensitivity and did not indicate an interaction with other metals in the samples. In the atomization process, it used SnCl₂, which was an olive reducing agent. The reaction occurred as described in equation 5 and the concentrations of mercury in the three (3) samples of whitening cream are represented in Table 2.

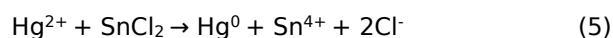


Table 2: The result of the quantitative analysis using mercury analyzer.

Sample Code	Sample weight (g)	Results (ppm)
12	1.0346	0.04217
15	1.0086	0.01814
17	1.0872	0.91000

Based on Table 2, upon conducting a quantitative test by using Mercury Analyzer with a wavelength of 253.7 nm, three samples were found to contain mercury, namely samples 12, 15, and 17, with an average level of 0.04217 ppm, 0.01814 ppm, and 0.91000 ppm, respectively. The concentration of the mercury was similar to the previous research that reported on mercury analysis in the whitening cream sold in Palu, Indonesia (25). Moreover, based on WHO 2011, the policy to limit the use of

mercury depends on each country (10). It is necessary to conduct a routine check on whitening cream products sold in the market to minimize the spread of harmful cosmetics. It is also expected that the public will be more careful in selecting whitening cosmetics to use.

4. CONCLUSION

Based on the analysis of whitening creams sold in Banjarnegara Regency using KI color test, it was found that three (3) whitening creams contained mercury out of the 20 collected samples. The concentrations of the mercury in the three whitening creams were between 0.01814 -0.91000 ppm based on mercury analyzer. According to the results, the consumer must be more careful when choosing a whitening cream to prevent the negative effects of its use.

5. CONFLICT OF INTEREST

There is no conflict of interest for this publication.

6. ACKNOWLEDGMENTS

The authors are grateful for the facilities provided by Universitas Muhammadiyah Yogyakarta.

7. REFERENCES

1. Juliana Anggraeni V, Yuliantini A, Rahmawati F, Studi PS, Farmakokimia R, Tinggi Farmasi Bandung Jalan Soekarno Hatta no S. Analisis cemaran logam berat merkuri dalam krim pemutih wajah yang beredar dipasar tradisional dengan metode spektrofotometri serapanatom. *J Pharmacopolium* [Internet]. 2018 Sep 3 [cited 2022 Jul 28];1(1):44-50. Available from: [<URL>](#).
2. BPOMRI. Peraturan Badan Pengawas Obat dan Makanan Tentang Persyaratan Teknis Bahan Kosmetika. 2019.
3. Pangaribuan L. Efek samping kosmetik dan penanganannya bagi kaum perempuan. *J Kel SEHAT Sejah* [Internet]. 2018 Jan 3 [cited 2022 Jul 28];15(2):20-8. Available from: [<URL>](#).
4. Parengkuan K, Fatimawali F, Citraningtyas G. Analisis kandungan merkuri pada krim pemutih yang beredar di kota manado. *Pharmacon* [Internet]. 2013 Feb 1 [cited 2022 Jul 28];2(1). Available from: [<URL>](#).
5. USFDA. Food and Drug Administration Department of Health and Human Services. 2011. Part 700-General. Subpart B-Requirements for specific cosmetic products. 700.13 Use of mercury compounds in cosmetics including use as skin bleaching agents in cosmetic preparatio. 2011.
6. BPOMRI. Public Warning nomor B-IN.05.03.1.43.12.17.5965 tanggal 11 Desember 2017 tentang Kosmetika mengandung bahan berbahaya. Keputusan kepala badan pengawas obat dan makanan Republik Indonesia. Jakarta; 2017.
7. Wurdianto G. Merkuri, bahayanya dan pengukurannya. 2007.
8. Mona RK. Analisis kandungan merkuri (hg) pada beberapa krim pemutih wajah tanpa ijin bpom yang beredar di pasar 45 manado. *Pharmacon* [internet]. 2018 Jul 1 [cited 2022 Jul 29];7(3). Available from: [<URL>](#).
9. Walangitan VM, Rorong JA, Sudewi S. Analisis merkuri (Hg) pada krim pemutih wajah yang beredar di kota manado. *Pharmacon* [Internet]. 2018 Jul 1 [cited 2022 Jul 29];7(3). Available from: [<URL>](#).
10. WHO. Mercury in Skin Lightening Products. Geneva: Public Health and Environment; 2011.
11. Tranggono, R.I.; Latifah F. Buku Pegangan Dasar Kosmetologi. Jakarta: Sagung Seto; 2014.
12. Sembel D. Toksikologi Lingkungan. Yogyakarta: Penerbit Andi; 2015.
13. Wang L, Zhang H. Mercury content in marketed cosmetics: analytical survey in Shijiazhuang, China. [Internet]. 2015 Oct 2 [cited 2022 Jul 29];34(4):322-6. Available from: [<URL>](#).
14. Mayaserli DP, Sasmita W. Pemeriksaan kadar merkuri dan keluhan kesehatan dalam darah wanita pemakai krim pemutih dengan metoda inductively coupled plasma. *Sainstek J Sains dan Teknol* [Internet]. 2017 Mar 15 [cited 2022 Jul 29];8(2):159-65. Available from: [<URL>](#).
15. Sari AK, Saputera MMA, Ayuhecacia N, Pratiwi ME. Analisis kualitatif merkuri pada lotion pemutih yang dijual di online shop daerah kota banjarmasin. *J Ilm Ibnu Sina* [Internet]. 2017 Apr 11 [cited 2022 Jul 29];2(1):13-9. Available from: [<URL>](#).
16. Erasiska, Bali S, Hanifah TA. Analisis Kandungan Logam Timbal, Kadmium dan Merkuri dalam Produk Krim Pemutih Wajah. *J Online Mhs Fak Mat dan Ilmu Pengetah Alam Univ Riau*. 2015;2(1).
17. Sun GF, Hu WT, Yuan ZH, Zhang BA, Lu H. Characteristics of mercury intoxication induced by skin-lightening products. *Chin Med J (Engl)* [Internet]. 2017 Dec 20 [cited 2022 Oct 7];130(24):3003-4. Available from: www.cmj.org.
18. Svehla G. Vogel Bagian I. Buku teks Analisis Anorganik Kualitatif Makro dan Semimikro. Jakarta; 1990.
19. Madania M, Martani MM. Analisis Logam Merkuri (Hg) Pada Krim Pemutih Wajah Merek X Dengan Metode Spektrofotometri Serapan Atom (SSA). *Al-Kimia*. 2014;2(2).
20. Kala'lembang C, Pinontoan OR, Ratag BT. Kandungan merkuri pada losion pemutih tangan dan badan yang digunakan oleh masyarakat di kelurahan tataaran patar kecamatan tondano selatan kabupaten minahasa. *Pharmacon*. 2016;5(2).
21. LPPTUGM. Metode Uji Mercury Analyzerl Dokumen RDP/5.10.2/LPPT Rev 1. Yogyakarta: Universitas Gadjah Mada; 2019.
22. Male YT, Nanlohy AC, Asriningsih. Introduction analysis of several levels of the mercury (hg) in shells. *Ind J Chem Res* . 2014;2:136-41.
23. Keccakus B. Sample Preparation Techniques in Analytical Chemistry. Mitra S, editor. New York: Interscience Then John Wiley; 2003. 227-270 p.
24. Ariska Trisnawati F, Herlina Yulianti C, Gusti Ebtavanny T, Program Studi III Farmasi MD, Farmasi Surabaya A, Ilmu Kimia B, et al. Identifikasi Kandungan Merkuri pada Beberapa Krim Pemutih yang Beredar di Pasaran (Studi dilakukan di Pasar DTC Wonokromo Surabaya). *J Pharmasci (Journal Pharm Sci* [Internet]. 2017 Jul 7 [cited 2022 Jul 30];2(2):35-40. Available from: [<URL>](#).
25. Rohaya U, Ibrahim N, Jurusan J, Fakultas F.

Analisis Kandungan Merkuri (Hg) Pada Krim Pemutih Wajah Tidak Terdaftar Yang Beredar Di Pasar Inpres Kota Palu: J Farm Galen (Galenika J Pharmacy) [Internet]. 2017 Mar 1 [cited 2022 Jul 30];3(1):77-83. Available from: [<URL>](#).

26. Rakhmina D, Joko Kartiko Jurusan Analis Kesehatan Poltekkes Kemenkes Banjarmasin Jl Mistar Cokrokusumo J. Logam Merkuri pada Masker Pemutih Wajah di Pasar Martapura. Med Lab Technol J [Internet]. 2017 Dec 29 [cited 2022 Jul 30];3(2):53-7. Available from: [<URL>](#).

27. Rasyid R, Susanti E, Azhar R. Pemeriksaan Kualitatif Hidrokuinon dan Merkuri dalam Krim Pemutih. J Farm Higea [Internet]. 2017 Feb 22 [cited 2022 Jul 30];7(1):63-73. Available from: [<URL>](#) .

28. Lajunen L. Spectrochemical analysis by atomic absorption and emission. London: Royal Society of Chemistry; 2007.



Theoretical Investigation of the Structures and Energetics of (MX)-Ethanol Complexes in the Gas Phase

Ahmed M. SADOON^{1*} 

¹University of Mosul, College of Education for Pure Science, Department of Chemistry, Mosul, Iraq.

Abstract: The structures and energy of alkali halide salt (MX) complexes with ethanol have been investigated in this work. The core of this study is to explore the effect of ion size on the interactions between solvent and solute. LiF and KBr as monovalent salts with different sizes of inion and cation have been chosen to explore this difference in addition to various physical properties. Three complexes of each LiF and KBr with ethanol taking the formula $\text{MX}(\text{CH}_3\text{CH}_2\text{OH})_n$ ($n=1-3$), were studied. *Ab-initio* calculations have been performed to optimize the chemical structures of these complexes and explore the possible structures, isomers, and their corresponding IR spectra using Density functional theory (DFT/ B3LYP). 6-311G** were chosen as basis sets for these calculations. The geometry evaluations, energy searches, vibrational frequency calculations, and each complex's binding energy were also theoretically extracted in this study. The minimum energy structures were calculated, and different isomers were found. The presence of Ionic hydrogen bonds (IHBs) was observed and proposed to be the main binding between the MX salt and ethanol. Also, the infrared vibrational bands in the OH stretching region were recorded for the minimum structures, and the determined red-shift was at about 400 cm^{-1} . In addition, the binding energy calculations found a gradual rise in the BE value with every additional ethanol molecule added to MX salt.

Keywords: Infrared Spectroscopy, DFT, Alkaline metal, Ethanol.

Submitted: July 20, 2022. **Accepted:** November 02, 2022.

Cite this: Sadoon AM. Theoretical Investigation of the Structures and Energetics of (MX)-Ethanol Complexes in the Gas Phase. JOTCSA. 2023;10(1):47-54.

DOI: <https://doi.org/10.18596/jotcsa.1146250>.

***Corresponding author. E-mail:** ams95@uomosul.edu.iq

1. INTRODUCTION

The interaction between the salt and solute in polar solutions has been in the spotlight of many studies to understand the behavior of anions and cations in this medium due to their essential role in chemical reactions. In addition to many applications of union and cation behavior in specific fields such as electrochemistry and environmental chemistry (1-3).

The interaction between the salt and polar solvent is usually expressed as *kosmotropic* or *chaotropic*. *Kosmotropic* are called (order-makers), which increase the stability of the hydrogen bonding network, while chaotropic ions (disorder-makers) reduce the stability of the hydrogen bonding grid

and thus reduce the stability of the salt-solvent structures (4, 5).

It is well known that alkaline halides behave as monovalent salts. These salts are dissolved in polar solvents (water, ethanol, etc.) to form separated ions in dilute solutions. The size and charge density of the cation and anion plays a critical role in giving the ability of a single alkaline halide molecule to dissolve in a numerical number of solvent molecules. LiF and KBr were chosen for this study as an example of salt with different sizes and charges of cation and anion.

Lithium fluoride is widely used in industry as an ingredient in lithium-ion battery electrolytes (6). Also, LiF is used as specialized optics for the vacuum ultraviolet spectrum (7) and in light-

emitting diodes production (LED) as a coupling layer to enhance electron injection (8). In addition to many applications in manufacturing nuclear reactors and radiation detectors (9).

Potassium bromide is most commonly used in medical drugs as an anticonvulsant drug to phenobarbital and as an antiepileptic medication for dogs(10), in addition to many other medical and veterinary applications. For industrial applications, KBr plays a significant role in Optics as infrared optical windows and is used widely in components for general spectroscopy (11) and photography as a restrainer by improving differentiation between exposed and unexposed crystals of silver halide to reduce fog(12).

Early studies concentrated on the structure of Alkaline halide (MX) complexes with water (13-16). These studies focused on MX-water complexes geometry structures, infrared (IR), and Mass spectrum using Helium nanodroplet apparatus. The outcome data show the critical role of ionic hydrogen bonds (IHBs) between MX salt and water.

No research has studied the structure of LiF and KBr- ethanol clusters. Only a few studies focused on studying LiF and ethanol's structure separately in the gas phase. LiF as a salt vapor was studied theoretically to investigate the landscape of a numerical number of (LiF)_n (n=1-8) (17). Ethanol clusters have also been investigated using ab-initio calculations (18), and the thermodynamic properties were recorded in this study.

The theoretical calculation of chemical reactions was widely used in many recent studies, (19-23) due to the unique environment and the ability to study the reactions that cannot be easily prepared in standard lab conditions. The formation of MX-solvent complexes is usually prepared and studied in bulk solutions (19, 20). Even in the diluted solutions, separating MX-(solvent)_n complexes, where n has a numerical value, is difficult because of the strong ionic hydrogen network (21). Unfortunately, an accurate simulation of the properties is still difficult to record, even in simple electrolytic solutions (22). Considering this limited experimental evidence, the ab-initio calculations study of these complexes looks useful and provides a unique tool to explore the chemistry of these complexes. So, this study will concentrate on studying the interaction of Alkaline halides (MX) with ethanol in gas phase theoretically using ab-initio calculations.

2. EXPERIMENTAL

2.1. MX(CH₃OH)_n formation

LiF and KBr complexes with ethanol (CH₃OH)_n, (n=1-3) were shaped using the Chemcraft software package (23). The premier structures were created with different positions and randomly rotated for MX and ethanol molecules to examine a wide range of potential geometries and isomers of MX(CH₃OH)_n complexes. The structure geometries were then optimized to find the minimum structures of each complex using ab-initio calculations.

2.1.1. Ab-initio calculations

Ab-initio calculations were applied using Density functional theory (DFT) with Becke three-parameter exchange and Lee-Yang-Parr correlation (B3LYP) within the Gaussian 03 software package (24). The basis set (6-311G**) obtained from the EMSL basis set exchange library (25) was then used to optimize the formatted structures. Each complex's minimum energy isomer structure was used to extract the data of geometry, energy, and infrared (IR) spectra (vibrational frequency values). In order to reduce the calculation time, the Hartree-Fock (HF) level of theory was first used with (6-311G**) bases set to evaluate the optimized structures. The optimized structures at the HF level were then re-optimized using the DFT(b3lyp) level of theory at the same basis set. A scaling factor of 0.967 was used to correct the values of vibrational frequencies of the final optimized structures. This factor is advised by the National Institute of Standards and Technology (NIST) for the DFT/B3LYP level of theory (26).

2.1.2. Geometry and structure

The final optimized structures of each complex were utilized to extract the information on the minimum energy of isomers, frequencies in the region of OH stretching bands, bond length, angles, dihedral angle, and the Binding Energy (BE). These results were obtained using Chemcraft software.

3. RESULTS AND DISCUSSION

3.1. MX(CH₃CH₂OH)_n structures

3.1.1. LiF(CH₃CH₂OH)_n structures

Several isomers were applied in DFT calculations for LiF(CH₃CH₂OH)_n complexes. For LiF(CH₃CH₂OH) complex, two optimized structures were found for this complex among many tested isomers, see Figure 1. The global minimum structure shows that the LiF salt takes the position so that the hydrogen ion of the hydroxyl group can form IHB with the fluoride atom. The higher energy structure shows that the methyl group in ethanol forms an IHB with a fluoride atom. The length of IHB in the minimum structure is about 1.68 Å while 2.203 Å in the higher energy isomer. Additional stabilization comes from the Li⁺ ion to the O⁻ atom.

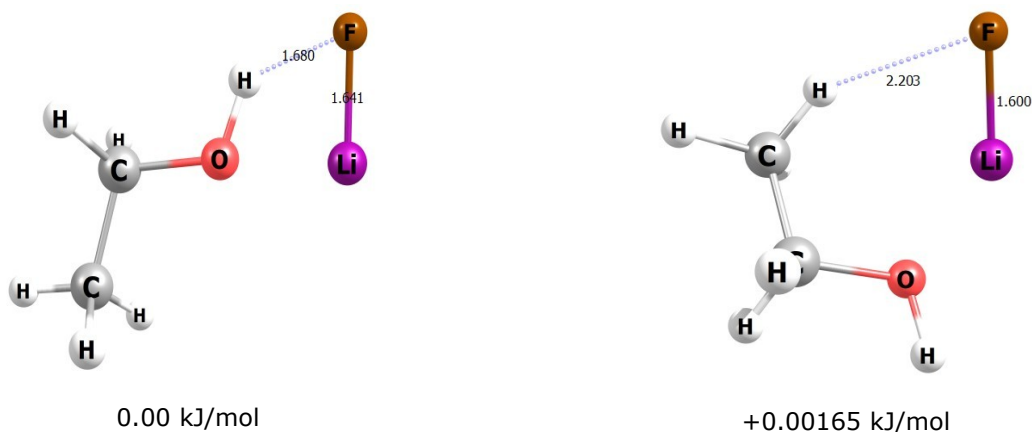


Figure 1: The minima structures for $\text{LiF}(\text{CH}_3\text{CH}_2\text{OH})$ with their energies in kJ/mol using DFT/B3LYP level of theory and 6-311G** as basis set

Three minima structures were recorded for $\text{LiF}(\text{CH}_3\text{CH}_2\text{OH})_2$, as can be seen in Figure 2. The global minimum structure is similar to the $n = 1$ complex but now has two IHBs bonding the fluoride ion and the H atoms of the hydroxyl group. The following minimum structure has an energy of 23.31 kJ/mol, higher than the global minimum structure energy, and also has two IHBs between the hydrogen of each ethanol methyl group and fluoride ion. The bond length of these two structures were 1.744 and 1.654 Å, respectively. The last structure

had energy above the global minimum structure at about 38.33 kJ/mol. Two ethanol molecules of this structure interacted with each other via one IHB. Another IHB seen in this structure bonded the hydrogen atom of the ethanol methyl group with the fluoride ion. The significant point seen in this complex, compared with $\text{LiF}(\text{CH}_3\text{CH}_2\text{OH})$ complex, is the difference in LiF bond length in the minimum structures that increased from 1.641 Å to 1.744 Å. This difference may be related to the reduction of fluoride ion charge bonded to a couple of IHBs.

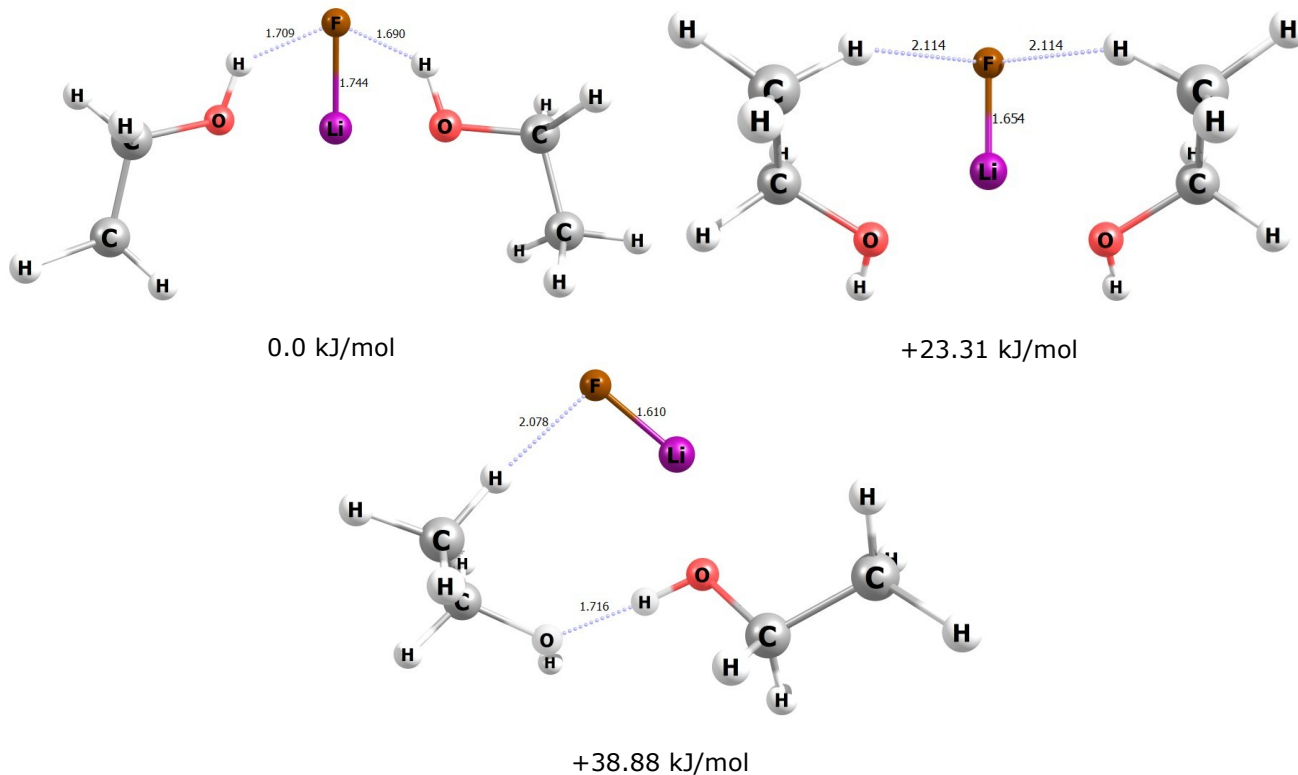


Figure 2: The minima structures for $\text{LiF}(\text{CH}_3\text{CH}_2\text{OH})_2$ with their energies in kJ/mol using DFT/B3LYP level of theory and 6-311G** as basis set

For $n = 3$, Three minima structures were found; see Figure 3. The global minimum for $\text{LiF}(\text{CH}_3\text{CH}_2\text{OH})_3$ is similar to those found for $\text{LiF}(\text{CH}_3\text{CH}_2\text{OH})$ and $\text{LiF}(\text{CH}_3\text{CH}_2\text{OH})_2$. Three ethanol molecules were bonded to fluoride ion by 3 IHBs between the F atom and the hydrogen of the hydroxyl group. The other isomer has higher energy from the global

minimum structure of about 9.74 kJ/mol. This isomer takes the formula where three ethanol bonded together via two IHBs and with one IHB with fluoride ion. The last isomer bonded to LiF salt via three IHBs similar to $\text{LiF}(\text{CH}_3\text{CH}_2\text{OH})_2$. LiF bonds in the three structures were about 1.91, 1.644, and 1.695 Å, respectively.

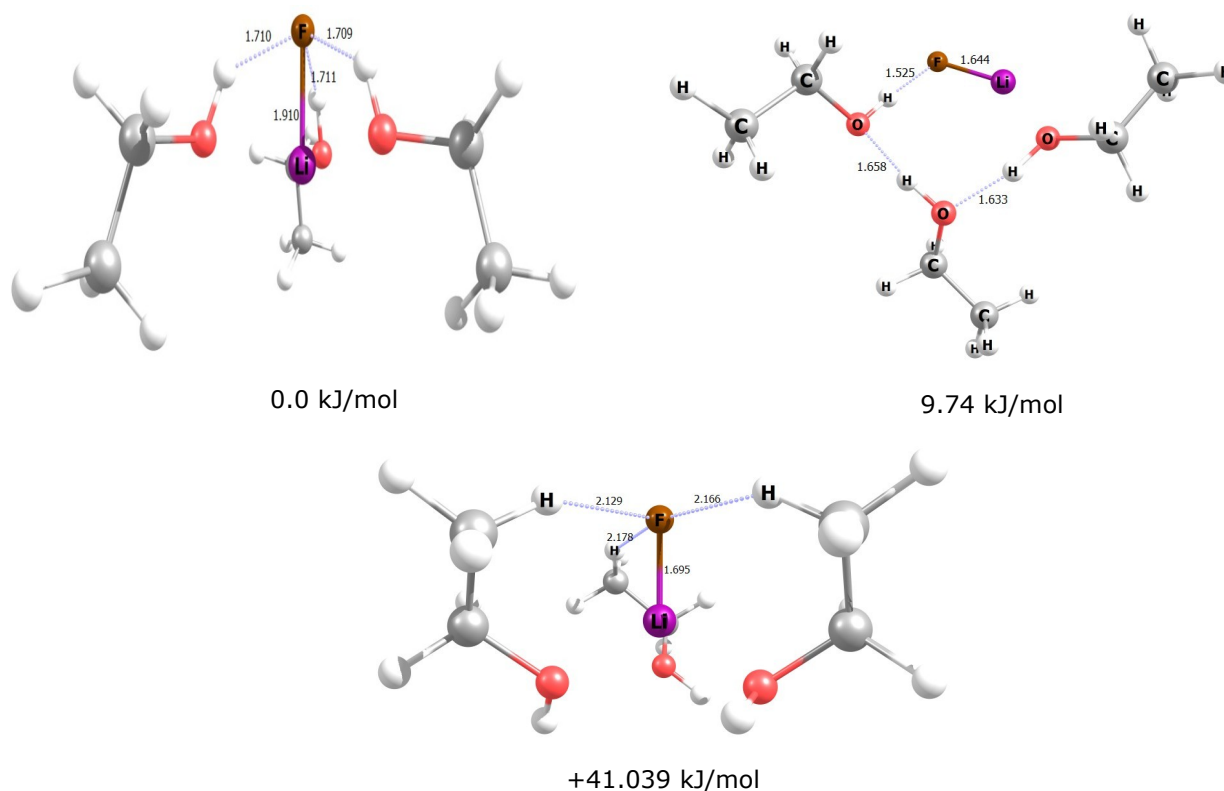


Figure 3: The minima structures for $\text{LiF}(\text{CH}_3\text{CH}_2\text{OH})_3$ with their energies in kJ/mol using DFT/B3LYP level of theory and 6-311G** as basis set.

3.1.2. $\text{KBr}(\text{CH}_3\text{CH}_2\text{OH})_n$ structures

The *ab-initio* calculations for $\text{KBr}(\text{CH}_3\text{CH}_2\text{OH})_n$ ($n=1-3$) were found and seen in Figures 4,5, and 6, respectively. No significant changes were observed in these structures for these complexes compared with $\text{LiF}(\text{CH}_3\text{CH}_2\text{OH})_n$ calculations. A significant difference in $\text{KBr}(\text{CH}_3\text{CH}_2\text{OH})_n$ complexes was seen

in the IHBs, which were longer than the IHBs in the $\text{LiF}(\text{CH}_3\text{CH}_2\text{OH})_n$ structures, due to the low electronegativity of Br atom compared with Li atom electronegativity. For KBr bond length, it increased gradually with every additional ethanol molecule and gave 2.95, 3.09, and 3.29 Å, respectively, for the $\text{KBr}(\text{CH}_3\text{CH}_2\text{OH})_n$ ($n=1-3$) minimum structures.

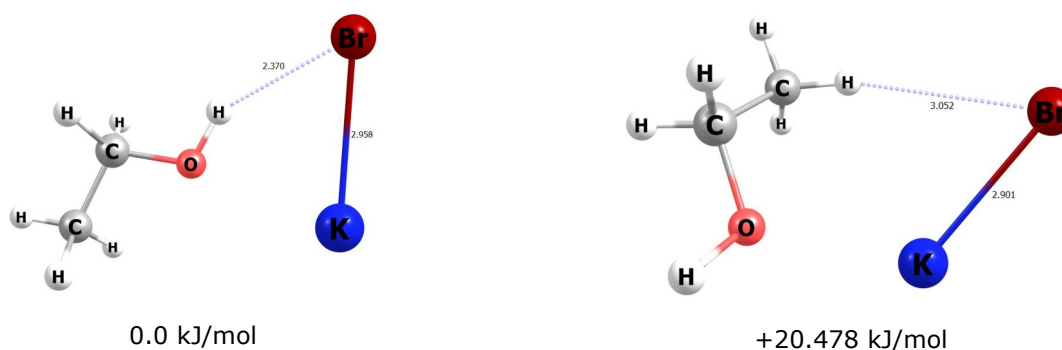


Figure 4: The calculated structures for $\text{MgCl}_2(\text{H}_2\text{O})$ with their energies in kJ/mol using DFT/B3LYP level of theory and 6-311G** as basis set.

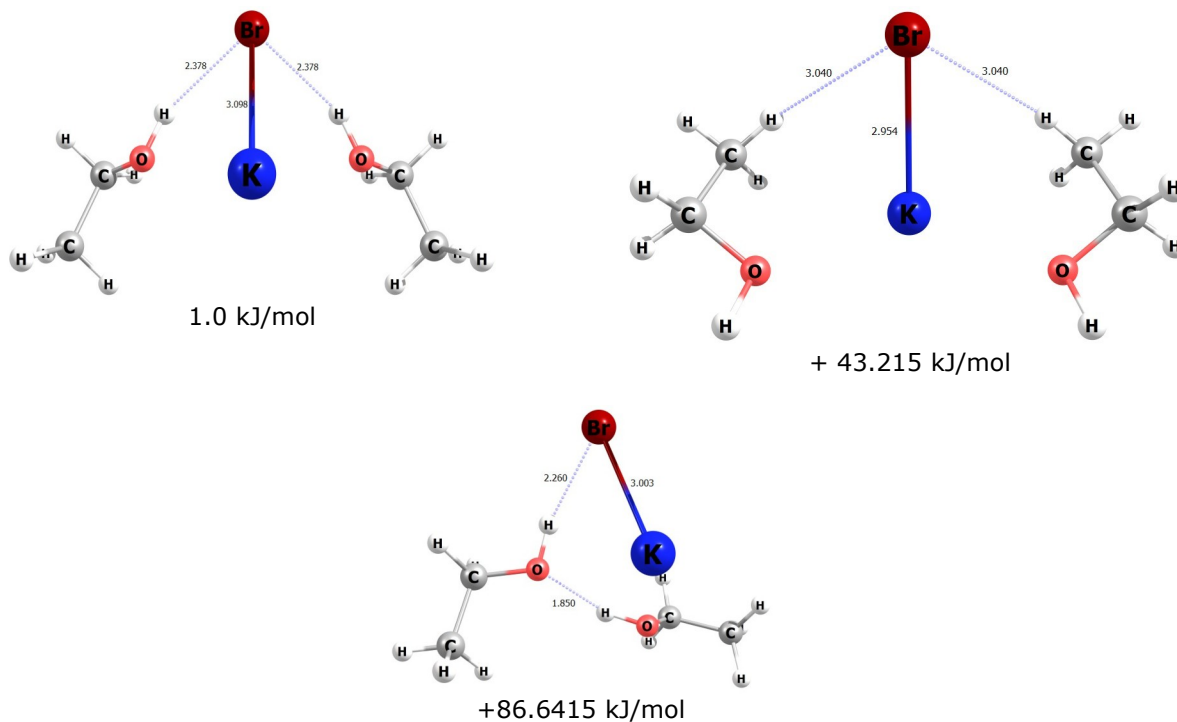


Figure 5: The calculated structures for $MgCl_2(H_2O)_2$ with their energies in kJ/mol using DFT/B3LYP level of theory and 6-311G** as basis set.

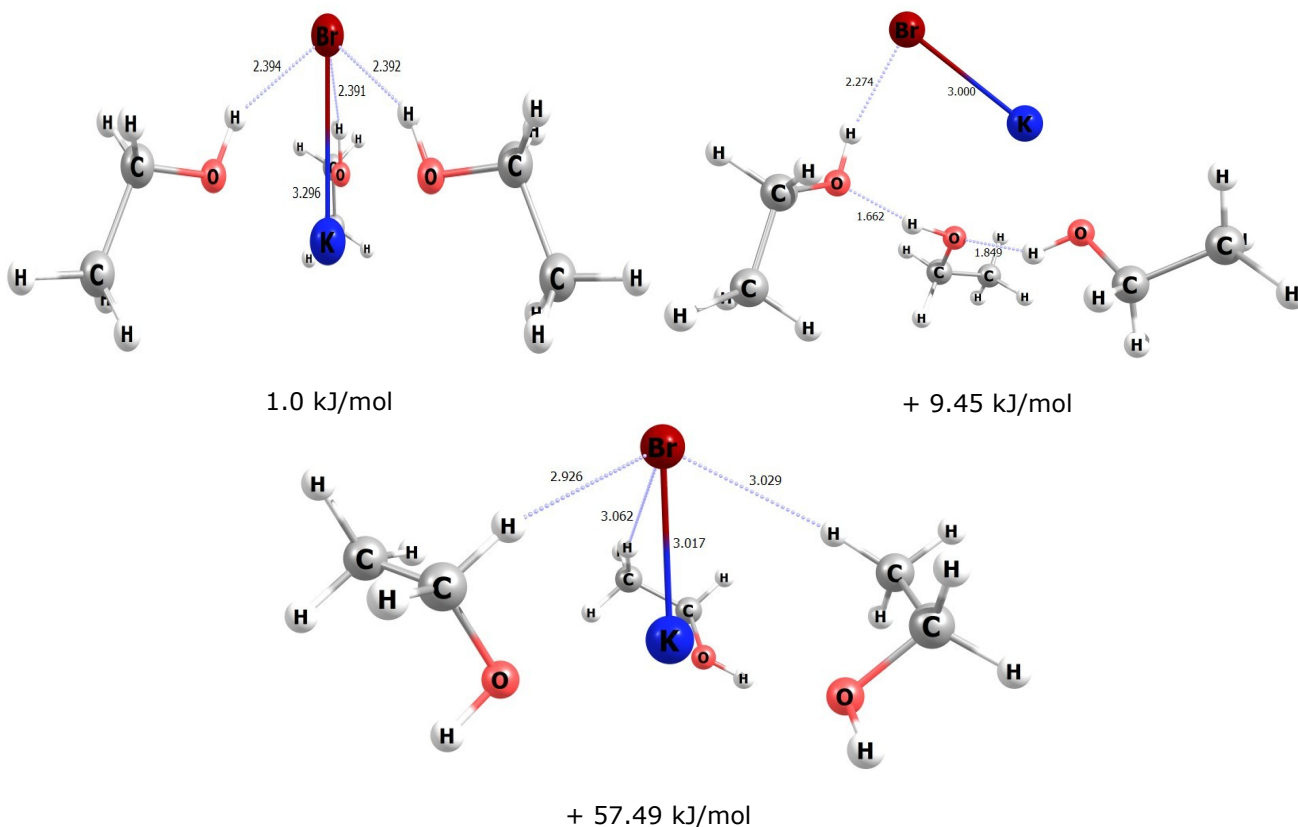


Figure 6: The calculated structures for $MgCl_2(H_2O)_3$ with their energies in kJ/mol using DFT/B3LYP level of theory and 6-311G** as basis set.

3.2. Infrared Spectra of $\text{MX}(\text{CH}_3\text{CH}_2\text{OH})_n$ Complexes

Infrared spectra of $\text{LiF}(\text{CH}_3\text{CH}_2\text{OH})_n$, $n=1-3$, were assigned theoretically using the DFT/B3LYP level of theory on the OH stretching region to evaluate the effect of IHBs on the OH symmetric stretching band. The stretching frequency values were corrected using a scaling factor of 0.967. Only global minimum structures were chosen for IR analysis.

The prediction of DFT calculations at the OH symmetric stretching frequencies is summarized in Table 1. In general, the absorption of OH bands of $\text{LiF}(\text{CH}_3\text{CH}_2\text{OH})_n$ complexes are red-shifted from the OH stretching band of the free ethanol molecule that is seen at 3721 cm^{-1} . This trend of OH stretching red-shift has been recorded previously in several studies(13, 27, 28). The OH band frequency of the $\text{LiF}(\text{CH}_3\text{CH}_2\text{OH})$ complex was found in 3149 cm^{-1} and then raised to 3208 cm^{-1} for $\text{LiF}(\text{CH}_3\text{CH}_2\text{OH})_2$ and 3263 cm^{-1} for $\text{LiF}(\text{CH}_3\text{CH}_2\text{OH})_3$. This red shift can be attributed to the OH band,

which bonded to the fluoride ion via an ionic hydrogen bond (IHB). This behavior of OH frequency fluctuation can be assigned to the high electronegativity of the Fluoride atom in the $n=1$ complex. This electronegativity has decreased gradually with every additional ethanol molecule. Therefore, OH frequency has increased again in $n=2$ and 3 complexes.

The same trend of OH stretching frequency behavior in $\text{LiF}(\text{CH}_3\text{CH}_2\text{OH})_n$ complexes was seen for the minimum structures of $\text{KBr}(\text{CH}_3\text{CH}_2\text{OH})_n$, $n=1-3$, complexes. Red shifts of OH stretching bands were recorded in these complexes due to IHBs effect on bromide electronegativity reduced more with every additional ethanol molecule. The *ab-initio* calculations recorded the OH symmetric stretching frequency of $\text{KBr}(\text{CH}_3\text{CH}_2\text{OH})$ at 3318 cm^{-1} . For $\text{KBr}(\text{CH}_3\text{CH}_2\text{OH})_n$ where $n=2$ and 3, the OH symmetric stretching band was observed at 3346 cm^{-1} and 3382 cm^{-1} , respectively; see Table 2.

Table 1: Infrared spectra for the minimum structures of $\text{LiF}(\text{CH}_3\text{CH}_2\text{OH})_n$ ($n=1-3$) complexes for the OH stretching region using DFT/B3LYP level of theory.

OH frequency band/ cm^{-1}	Vibration frequency assignment	Complex
3149	symmetric stretching	$\text{LiF}(\text{CH}_3\text{CH}_2\text{OH})$
3208	symmetric stretching	$\text{LiF}(\text{CH}_3\text{CH}_2\text{OH})_2$
3266	asymmetric stretching	
3263	symmetric stretching	$\text{LiF}(\text{CH}_3\text{CH}_2\text{OH})_3$
3265	asymmetric stretching	
3336	asymmetric stretching	

Table 2: Infrared spectra for the minimum structures of $\text{KBr}(\text{CH}_3\text{CH}_2\text{OH})_n$ ($n=1-3$) complexes for the OH stretching region using DFT/B3LYP level of theory.

OH frequency band/ cm^{-1}	Vibration frequency assignment	Complex
3318	symmetric stretching	$\text{KBr}(\text{CH}_3\text{CH}_2\text{OH})$
3346	symmetric stretching	$\text{KBr}(\text{CH}_3\text{CH}_2\text{OH})_2$
3370	asymmetric stretching	
3382	symmetric stretching	$\text{KBr}(\text{CH}_3\text{CH}_2\text{OH})_3$
3384	asymmetric stretching	
3414	asymmetric stretching	

3.3. Binding energy calculations for $\text{MX}(\text{CH}_3\text{CH}_2\text{OH})_n$ ($n = 1-3$) complexes

The Binding energy (BE) of the global minimum structure of $\text{MX}(\text{CH}_3\text{CH}_2\text{OH})_n$ complexes was calculated from the DFT/B3LYP calculations and summarized in Table 3 for $\text{LiF}(\text{CH}_3\text{CH}_2\text{OH})_n$ and in Table 4 for $\text{KBr}(\text{CH}_3\text{CH}_2\text{OH})_n$ complexes. The BE was calculated using the following equation:

$$\text{BE} = \Delta E = E(\text{MX}(\text{CH}_3\text{CH}_2\text{OH})_n) - (E(\text{MX}) + E(\text{CH}_3\text{CH}_2\text{OH})_n)$$

In general, a gradual increase in the values of BE was seen in both $\text{MX}(\text{CH}_3\text{CH}_2\text{OH})_n$ complexes, where ($n=1-3$), with increasing n value of ethanol. Also, the BE of $\text{LiF}(\text{CH}_3\text{CH}_2\text{OH})_n$ complexes were higher than the BE of $\text{KBr}(\text{CH}_3\text{CH}_2\text{OH})_3$ complexes. This difference may relate to the high

electronegativity of F⁻ ion in contrast with Br⁻ ion electronegativity. The BE of LiF(CH₃CH₂OH)_n and KBr(CH₃CH₂OH)_n complexes can be seen in Tables 3 and 4, respectively.

The BE of the minimum structures of LiF(CH₃CH₂OH)_n, n=1-3, were (102, 197, and 282)

kJ/mol respectively. On the other hand, The BE of the minimum structure of KBr(CH₃CH₂OH)_n, n=1-3, complexes were (75, 146, and 212) kJ/mol, respectively. This increase may come from the additional IHBs and the proximity of M⁺ ion to O atom of the hydroxyl group that increased with every additional ethanol molecule.

Table 3: The binding energy of LiF(CH₃CH₂OH)_n (n = 1–3) complexes using DFT/B3LYP level of theory.

Binding Energy kJ/mol	Complex
102.37	LiF(CH ₃ CH ₂ OH)
197.90	LiF(CH ₃ CH ₂ OH) ₂
282.24	LiF(CH ₃ CH ₂ OH) ₃

Table 4: The binding energy of KBr(CH₃CH₂OH)_n (n = 1–3) complexes using DFT/B3LYP level of theory.

Binding Energy kJ/mol	Complex
75.04	KBr(CH ₃ CH ₂ OH)
146.23	KBr(CH ₃ CH ₂ OH) ₂
212.82	KBr(CH ₃ CH ₂ OH) ₃

4. CONCLUSION

Structure parameters, Infrared spectra (IR), and the Binding Energy of MX(CH₃CH₂OH)_n complexes, where n = 1–3 and MX =LiF and KBr, have been performed in this work using *Ab-initio* calculations. Several isomers of these complexes have been recorded. A significant observation was seen for MX(CH₃CH₂OH)_n complexes that show a significant increase in the M-X bond length. This increment comes from the effect of the ethanol hydroxyl group that inserts between M and X ions and reduces their interaction by forming IHBs. The global minimum structures of complexes were then used to extract the information on the Vibrational frequency bands in OH stretching regions and the binding energy. The formation of IHBs was observed between the hydrogen of the ethanol hydroxyl group. For IR spectra, a Red-shift in the positions of the OH stretching bands was seen, which is consistent with the presence of the IHBs. Also, a significant increase in the Binding energy (BE) was seen with the increasing n value of ethanol. This increase indicated that the IHB and the proximity of the M⁺ ion to the O atom play a critical role in MX(CH₃CH₂OH)_n complexes.

5. ACKNOWLEDGMENTS

The author is grateful to the University of Mosul and the Chemistry department at the College of Education for pure sciences for their support and funding of this work.

6. REFERENCES

- Satchell DPN. Ions in solution: Basic principles of chemical interactions. Endeavour [Internet]. 1988 Jan [cited 2022 Nov 27];12(4):195. Available from: <URL>
- Marcus Y. Ions in Solution and their Solvation: Marcus/Ions in Solution and their Solvation [Internet]. Hoboken, NJ: John Wiley & Sons, Inc; 2015 [cited 2022 Nov 27]. Available from: <URL>
- Friedman HaroldL. Ionic hydration in chemistry and biophysics. Journal of Electroanalytical Chemistry and Interfacial Electrochemistry [Internet]. 1982 Jan [cited 2022 Nov 27];131:407–8. Available from: <URL>
- Marcus Y. Effect of ions on the structure of water. Pure and Applied Chemistry [Internet]. 2010 Jun 19 [cited 2022 Nov 27];82(10):1889–99. Available from: <URL>
- Moelbert S, Normand B, De Los Rios P. Kosmotropes and chaotropes: modelling preferential exclusion, binding and aggregate stability. Biophysical Chemistry [Internet]. 2004 Dec [cited 2022 Nov 27];112(1):45–57. Available from: <URL>
- Aigueperse J, Mollard P, Devilliers D, Chemla M, Faron R, Romano R, et al. Fluorine Compounds, Inorganic. In: Wiley-VCH Verlag GmbH & Co. KGaA, editor. Ullmann's Encyclopedia of Industrial Chemistry [Internet]. Weinheim, Germany: Wiley-VCH Verlag GmbH & Co. KGaA; 2000 [cited 2022 Nov 27]. p. a11_307. Available from: <URL>
- Zheng Y, Song W, Mo W ting, Zhou L, Liu JW. Lithium fluoride recovery from cathode material of spent lithium-ion battery. RSC Adv [Internet]. 2018 [cited 2022 Nov 27];8(16):8990–8. Available from: <URL>

8. Andeen C, Fontanella J, Schuele D. Low-Frequency Dielectric Constant of LiF, NaF, NaCl, NaBr, KCl, and KBr by the Method of Substitution. *Phys Rev B* [Internet]. 1970 Dec 15 [cited 2022 Nov 27];2(12):5068–73. Available from: [<URL>](#)
9. McGregor DS, Bellinger SL, Shultis JK. Present status of microstructured semiconductor neutron detectors. *Journal of Crystal Growth* [Internet]. 2013 Sep [cited 2022 Nov 27];379:99–110. Available from: [<URL>](#)
10. De Lahunta A, Glass E, Kent M. *Veterinary Neuroanatomy and Clinical Neurology* [Internet]. Elsevier; 2009 [cited 2022 Nov 27]. Available from: [<URL>](#)
11. Alpert NL, Keiser WE., Szymanski HA. *IR: Theory and Practice of Infrared Spectroscopy*. Cham: Springer International Publishing; 2012. 381 p.
12. Anchell S. *The Film Developing Cookbook* [Internet]. 1st ed. Routledge; 1998 [cited 2022 Nov 27]. Available from: [<URL>](#)
13. Tandy J, Feng C, Boatwright A, Sarma G, Sadoon AM, Shirley A, et al. Communication: Infrared spectroscopy of salt-water complexes. *The Journal of Chemical Physics* [Internet]. 2016 Mar 28 [cited 2022 Nov 27];144(12):121103. Available from: [<URL>](#)
14. Sadoon AM, Sarma G, Cunningham EM, Tandy J, Hanson-Heine MWD, Besley NA, et al. Infrared Spectroscopy of NaCl(CH₃OH)_n Complexes in Helium Nanodroplets. *J Phys Chem A* [Internet]. 2016 Oct 20 [cited 2022 Nov 27];120(41):8085–92. Available from: [<URL>](#)
15. Li RZ, Liu CW, Gao YQ, Jiang H, Xu HG, Zheng WJ. Microsolvation of LiI and CsI in Water: Anion Photoelectron Spectroscopy and ab initio Calculations. *J Am Chem Soc* [Internet]. 2013 Apr 3 [cited 2022 Nov 27];135(13):5190–9. Available from: [<URL>](#)
16. Mizoguchi A, Ohshima Y, Endo Y. The study for the incipient solvation process of NaCl in water: The observation of the NaCl-(H₂O)_n (n = 1, 2, and 3) complexes using Fourier-transform microwave spectroscopy. *The Journal of Chemical Physics* [Internet]. 2011 Aug 14 [cited 2022 Nov 27];135(6):064307. Available from: [<URL>](#)
17. Doll K, Schön JC, Jansen M. Ab initio energy landscape of LiF clusters. *The Journal of Chemical Physics* [Internet]. 2010 Jul 14 [cited 2022 Nov 27];133(2):024107. Available from: [<URL>](#)
18. Umer M, Kopp WA, Leonhard K. Efficient yet accurate approximations for ab initio calculations of alcohol cluster thermochemistry. *The Journal of Chemical Physics* [Internet]. 2015 Dec 7 [cited 2022 Nov 27];143(21):214306. Available from: [<URL>](#)
19. Sangoro J, Cosby T, Kremer F. Rotational and Translational Diffusion in Ionic Liquids. In: Paluch M, editor. *Dielectric Properties of Ionic Liquids* [Internet]. Cham: Springer International Publishing; 2016 [cited 2022 Nov 27]. p. 29–51. (Advances in Dielectrics). Available from: [<URL>](#)
20. Nancollas GH. The thermodynamics of metal-complex and ion-pair formation. *Coordination Chemistry Reviews* [Internet]. 1970 Dec [cited 2022 Nov 27];5(4):379–415. Available from: [<URL>](#)
21. Meot-Ner (Mautner) M. Update 1 of: Strong Ionic Hydrogen Bonds. *Chem Rev* [Internet]. 2012 Oct 10 [cited 2022 Nov 27];112(10):PR22–103. Available from: [<URL>](#)
22. Eisenberg B. Ionic Interactions Are Everywhere. *Physiology* [Internet]. 2013 Jan [cited 2022 Nov 27];28(1):28–38. Available from: [<URL>](#)
23. Zhurko G, Zhurko D. Chemcraft-graphical software for visualization of quantum chemistry computations [Internet]. 2016. Available from: [<URL>](#)
24. Frisch MJ, Trucks GW, Schlegel HB, Scuseria GE, Robb MA, Cheeseman JR, et al. *Gaussian 03, Revision C.02* [Internet]. Gaussian, Inc.; 2004. Available from: [<URL>](#)
25. Schuchardt KL, Didier BT, Elsethagen T, Sun L, Gurumoorthi V, Chase J, et al. Basis Set Exchange: A Community Database for Computational Sciences. *J Chem Inf Model* [Internet]. 2007 May 1 [cited 2022 Nov 27];47(3):1045–52. Available from: [<URL>](#)
26. Johnson R. Computational Chemistry Comparison and Benchmark Database, NIST Standard Reference Database 101 [Internet]. National Institute of Standards and Technology; 2002 [cited 2022 Nov 27]. Available from: [<URL>](#)
27. Cabarcos OM, Weinheimer CJ, Martínez TJ, Lisy JM. The solvation of chloride by methanol—surface versus interior cluster ion states. *The Journal of Chemical Physics* [Internet]. 1999 May 15 [cited 2022 Nov 27];110(19):9516–26. Available from: [<URL>](#)
28. Beck JP, Lisy JM. Cooperatively Enhanced Ionic Hydrogen Bonds in Cl – (CH₃OH)_{1–3} Ar Clusters. *J Phys Chem A* [Internet]. 2010 Sep 23 [cited 2022 Nov 27];114(37):10011–5. Available from: [<URL>](#)



Spectral Investigation of Yb³⁺/Ho³⁺/Tm³⁺:Y₂Si₂O₇ Upconverting Nanophosphors for the Usage of Temperature Sensing

Murat Erdem^{1*} , Kadir Esmer¹ , and Gonul Eryurek² 

¹Marmara University, Physics Department, Istanbul, 34722, Turkey

²Istanbul Technical University, Physics Engineering Department, Istanbul, 34722, Turkey

Abstract: Rare earth (Yb³⁺, Ho³⁺, Tm³⁺) yttrium disilicate phosphors were produced by sol-gel technique and heated at 1050 °C temperature. The sizes of the phosphors vary between 20-30 nm according to the images obtained from the Transmission Electron Microscope. The up-conversion (UC) emissions of the nanopowders were measured in the range of 500–900 nm wavelength under 950 nm laser excitation. A linear increase with power was observed in the emission intensity ratio depending on the laser excitation power. Using the FIR technique, the phosphor's temperature was determined by the heating effect caused by the laser pump power. Due to the change in intensity ratio versus temperature, the temperature sensitivity at 428 K was calculated as 0.781x10⁻²K⁻¹ and it was suggested that it can be used as a promising temperature sensor probe in photonic devices.

Keywords: Nanophosphors; Sol-gel; Up-conversion; Temperature sensing.

Submitted: August 08, 2022. **Accepted:** November 07, 2022.

Cite this: Erdem M, Esmer K, Eryurek G. Spectral investigation of Yb³⁺/Ho³⁺/Tm³⁺:Y₂Si₂O₇ upconverting nanophosphors for the usage of temperature sensing. Journal of the Turkish Chemical Society, Section A: Chemistry. 2023;10(1):55–62.

DOI: <https://doi.org/10.18596/jotcsa.1159026>.

***Corresponding author. E-mail:** merdem@marmara.edu.tr.

1. INTRODUCTION

The optical temperature sensing of luminescent materials, which detects temperature changes precisely at small spatial resolution in inaccessible environments, has attracted great interest recently, especially concerning their high-temperature sensitivity (1-6). Luminescent thermography-based temperature sensing is an alternative method, which stands out with its non-contact measurements in many areas that traditional thermometers cannot reach, such as high-voltage power plants, microfluidics, bio-objects, and small-sized circuits below 10 μm (7,8).

The laser excitation power induces heat, which increases the temperature of the rare earth (RE) doped phosphors. Therefore, the emission intensities of RE³⁺ ions become sensitive to temperature change. Consequently, the sensitive effect of excitation power on emission intensity can

lead to the calculation of the temperature of phosphors using the Boltzmann electron distribution between the nearest neighbor energy levels (9). As the difference in nearest energy levels of some RE³⁺ ions varies between about 200 cm⁻¹ and 2000 cm⁻¹ (10), this benefits the development of temperature-sensitive phosphors for optical thermometers.

The optical thermometer properties of RE³⁺: Yb³⁺/Ho³⁺ doped phosphors are limited to a few studies. For example, the sensor sensitivities are 0.0053 K⁻¹ at 93 K for Yb³⁺/Ho³⁺:BaCaTiO₃, 0.0077 K⁻¹ at 366 K for Yb³⁺/Ho³⁺: Pb(MgNb)O₃PbTiO₃, and 0.005 K⁻¹ at 923 K for Yb³⁺/Ho³⁺: CaWO₄, respectively (11-13). The primary goal in the field of optical thermometry is to manufacture the sensor with the highest sensitivity. Therefore, the selection of suitable host materials for the high solubility of RE ions may provide a significant advantage in luminescence properties for the development of optical temperature sensing. Among the many main

lattices, yttrium disilicate ($Y_2Si_2O_7$) activated by RE^{3+} ions, either by the upconversion or by direct excitation, has attracted attention due to white light generation in practical uses for LED applications (14-19). Unlike these studies, it has been proposed to use $Y_2Si_2O_7$ nano phosphors doped with $Yb^{3+}/Ho^{3+}/Tm^{3+}$ ions as temperature sensing probes from the up-conversion spectral intensity ratios depending on the laser excitation power.

2. MATERIALS AND METHODS

The chemicals with a purity of 99.9%, which were bought from Sigma-Aldrich used to synthesize nanocrystalline α - $Y_2Si_2O_7$ doped with RE^{3+} . To obtain desired phosphor powders tetraethyl orthosilicate, yttrium(III) hexahydrate nitrate, ytterbium(III) nitrate pentahydrate, holmium(III) nitrate pentahydrate, thulium(III) nitrate were employed as precursors with a proper stoichiometry by sol-gel technique. Preparation method of RE^{3+} doped $Y_2Si_2O_7$ as detailed in our previous work (20).

In the set of YSYHT compositions, Yb^{3+} and Tm^{3+} molar ratios were kept at 2.0 and 0.5 respectively. Ho^{3+} molar percentage ratios were also increased from 0.5 to 1.5 with the step of 0.5. Thus, three different compositions of YSYHT were obtained and labeled as YSYHT1, YSYHT2, and YSYHT3. All prepared compounds were heated at 1050 °C for 12 h.

The structural and morphological properties of the powders were investigated by Bruker D2 Phaser model X-ray diffractometer, JEOL-JEM-2100 model High resolution-Transmission Emission Microscope,

and FEI Inc. Inspect S50 model Scanning Electron Microscope. Energy dispersive X-ray measurements were taken using an EDAX Inc.-Octane Prime spectrometer to analyze the elements in the compound. The selected field diffraction (SAED) pattern was also taken to evaluate the crystallinity of the sample.

A UV-Vis spectrophotometer (Perkin-Elmer Lambda 35) was used to reveal absorption lines from diffuse reflectance spectra of RE^{3+} ions in the spectral wavelength range between 400 and 1050 nm at room temperature. A laser diode source with a 950 nm wavelength (Laser Drive Inc. LDI-820) was utilized to investigate the UC photoluminescence of the phosphors. The McPearson Inc. Model 2051 Monochromator with a PMT (Hamamatsu R1387) detector was used to measure the spectral outputs of the phosphors. To prevent light scattered from the material in different directions from entering the monochromator, a short-wavelength filter (850 nm) was placed prior to the monochromator. The measured data were processed by an EG&G Model 5210 lock-in amplifier and saved to the computer using the Labview program.

3. RESULTS AND DISCUSSION

3.1. Structural Studies

Figure 1 demonstrates the XRD patterns of YSYHT nanopowders. The figures show that most of the diffraction peak locations for three powders show good agreement with the JCPDS: 38-0223 card data of α - $Y_2Si_2O_7$. In addition, no other phase was detected apart from the α - $Y_2Si_2O_7$ phase seen in XRD measurements of all powders.

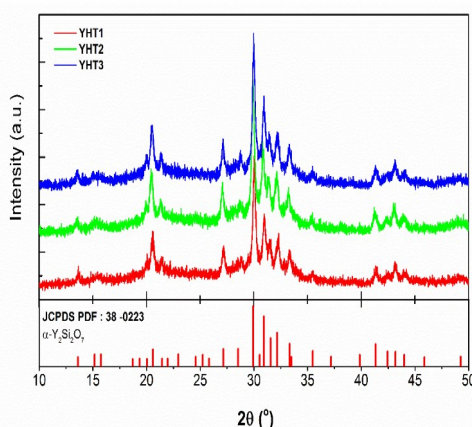


Figure 1: XRD graphs of Yb^{3+} , Ho^{3+} , and Tm^{3+} doped $Y_2Si_2O_7$ samples annealed at 1050 °C.

The electron microscope images, elemental analysis (EDAX), and selected area diffraction pattern (SAED) of YSHYT nanopowders are presented in Figure 2. As seen in SEM and TEM images of the triple rare-earth-doped α - $Y_2Si_2O_7$ nanoparticles, the

samples consist of nearly spherical nanoparticles ranging in size from about 20 to 40 nm. In addition, the peaks obtained from the EDAX spectrum of the nanoparticles given in Figure 2 show the elemental presence of Y, Si, O₂, Yb, Ho, and Tm in the phosphorus material.

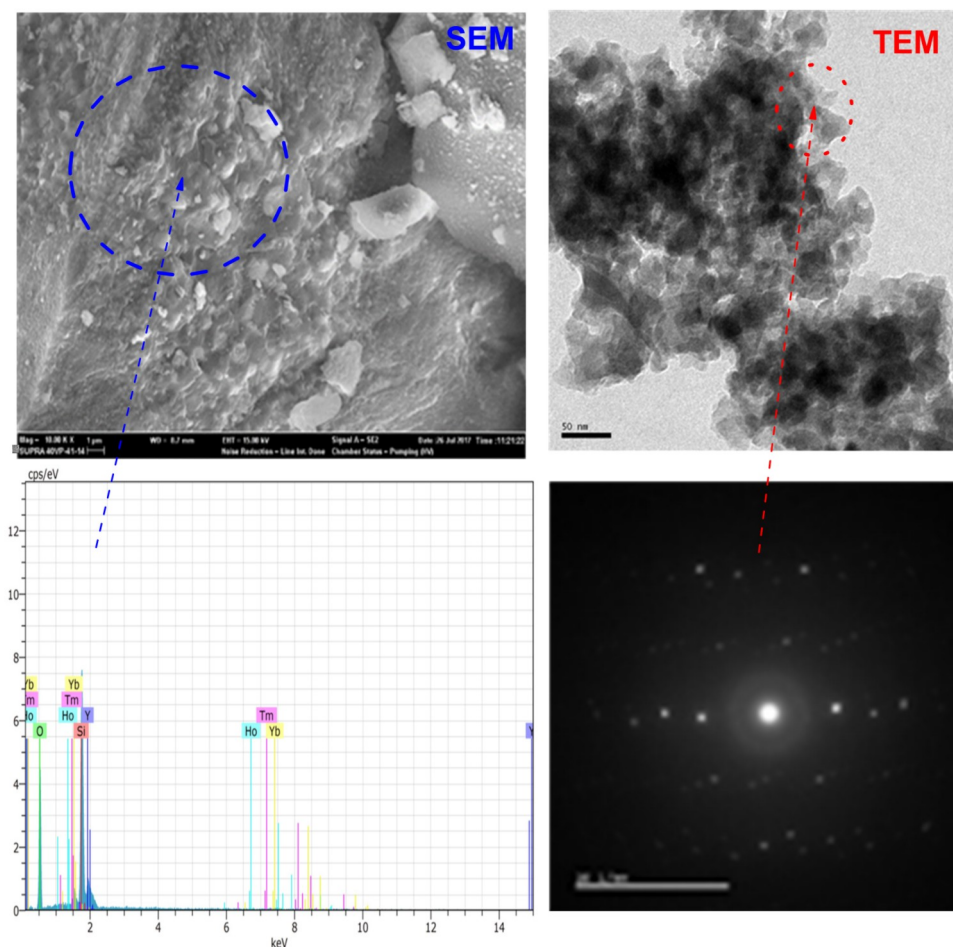


Figure 2: Electron microscope images, EDAX spectrum, and SAED pattern of $\text{Yb}^{3+}/\text{Ho}^{3+} / \text{Tm}^{3+}$ doped $\alpha\text{-Y}_2\text{Si}_2\text{O}_7$ (YSYHT2).

3.2. Spectral Studies

3.2.1. Diffuse Reflectance Spectra

Figure 1 shows the diffuse reflection spectra of the $\text{Yb}:\text{Ho}:\text{Tm}$ doped $\alpha\text{-Y}_2\text{Si}_2\text{O}_7$ samples in the 400 – 1050 nm range. Of the eleven absorption bands that appear, six absorption bands correspond to different excited states of Ho^{3+} ions from the $^5\text{I}_8$ ground state. Three absorption bands are corresponding to the different excited states of Tm^{3+} ions from the $^4\text{I}_{15/2}$ ground state transitions. In addition, only one Yb^{3+} absorption corresponds to the $^2\text{F}_{7/2} \rightarrow ^2\text{F}_{5/2}$ transition.

3.2.2. Upconversion luminescence of the samples

Figure 4 demonstrates the UC emission spectra of the elements in the range of 500-850 nm under 950 nm excitation. The green emissions around 525 and 547 nm were ascribed to the $^5\text{F}_4 \rightarrow ^5\text{I}_8$ and $^5\text{S}_2 \rightarrow ^5\text{I}_8$

transitions of the Ho^{3+} ions, respectively. The red emission around 660 nm was attributed to the $^5\text{F}_5 \rightarrow ^5\text{I}_8$ transition of Ho^{3+} ions and $^3\text{F}_{2,3} \rightarrow ^3\text{H}_6$ transition of Tm^{3+} ions. The turquoise blue (492 nm) and infrared emission (790 nm) were also attributed to the $^1\text{G}_4 \rightarrow ^3\text{H}_6$ (Tm^{3+}) and $^3\text{H}_4 \rightarrow ^3\text{H}_6$ (Tm^{3+}) transitions, respectively.

Figure 5 indicates the UC emission spectra depending on the laser pump power. The calculated slope values of triple doped $\alpha\text{-Y}_2\text{Si}_2\text{O}_7$ nanoparticles were found to be 1.4, 2.2, and 3.1 for red, green, and blue emissions, respectively. According to slope values, while the red (660 nm) and green (525 nm) emissions are taking place via a two-photon absorption process, the turquoise blue emission (492 nm) is based on three-photon absorption.

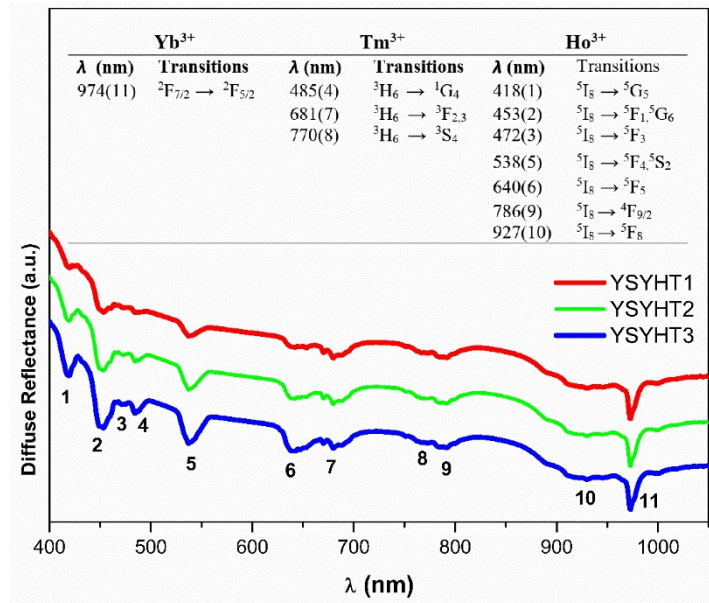


Figure 3: Diffuse Reflectance spectra of YSYHT samples.

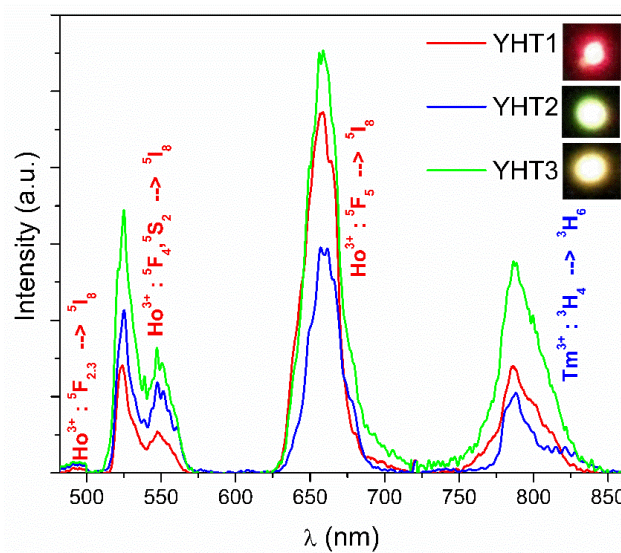


Figure 4: UC luminescence spectra of YSYHT samples.

The energy transfer from the Yb³⁺ ions to the Ho³⁺ and Tm³⁺ ions can efficiently occur to populate the high excited levels of those due to energy match among those. As indicated in Figure 6, the following points can be made (21-24):

- i. The energy transfer from the Yb³⁺ ions to the Ho³⁺ ions occurs by the process of ⁵I₈ (Ho³⁺) + ²F_{5/2} (Yb³⁺) → ⁵I₆ (Ho³⁺) + ²F_{7/2} (Yb³⁺). And it may be responsible for the increase of the population of ⁵I₆ (Ho³⁺) level.
- ii. The ⁵I₆ level of Ho³⁺ is populated with the probable ways as follows: ⁵I₆ (Ho³⁺) + ²F_{5/2} (Yb³⁺) → ⁵F_{4,5}S₂ (Ho³⁺) + ²F_{7/2} energy transfer or ⁵I₆ (Ho³⁺) + a photon (950nm) → ⁵F_{4,5}S₂ (Ho³⁺). These processes fill the ⁵F_{4/5}S₂ level of Ho³⁺, and then the ⁵F_{4/5}S₂ level relaxes to the ⁵I₈ (Ho³⁺) level. Consequently, these processes cause the green emission at 525 and 547 nm corresponding to ⁵F₄→⁵I₈, and ⁵S₂→⁵I₈ transitions, respectively.
- iii. In the red emission process, with the help of non-radiative transitions, both the transitions from the ⁵F_{4/5}S₂ levels populate the ⁵F₅ level, and the transitions from the ⁵I₆ level to the ⁵I₇ take place. Then the ⁵F₅ level can be populated through the ⁵I₇ → ⁵F₅ transition via the energy transfer process from ⁵I₇ (Ho³⁺) + ²F_{5/2} (Yb³⁺) → ⁵F₅ (Ho³⁺) + ⁵F_{7/2} (Yb³⁺) transition. Finally, the red emission at 660 nm comes true via ⁵F₅ → ⁵I₈ transition.

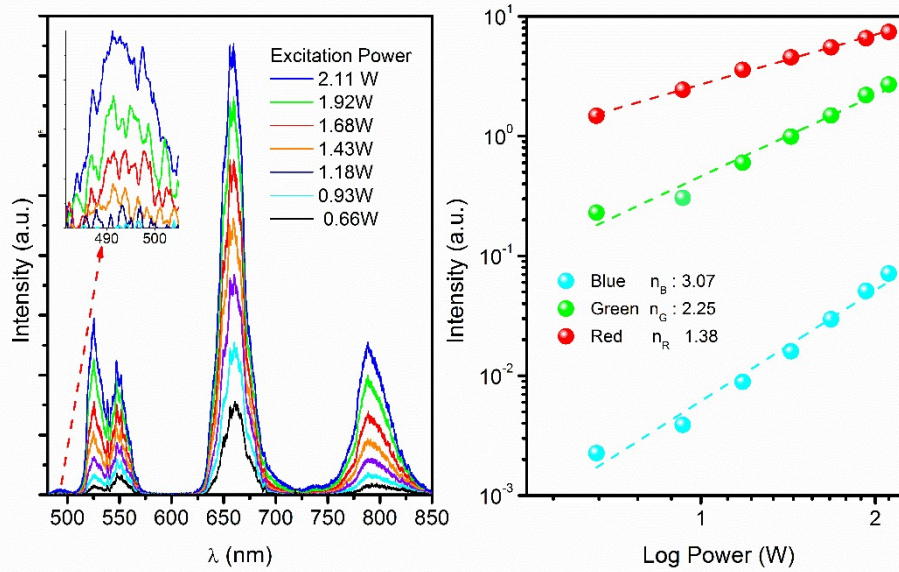


Figure 5: UC luminescence intensity vs. Excitation power for the YSYHT2 sample.

iv. In the blue emission (492 nm) process, the ${}^5F_{2,3}$ excited energy level of the Ho^{3+} ion can be populated by the energy transfer from the Yb^{3+} ions in the ground state via three-photon processes. This process is as follows: ${}^5I_5 (\text{Ho}^{3+}) + {}^2F_{5/2} (\text{Yb}^{3+}) \rightarrow {}^5F_{2,3} (\text{Ho}^{3+}) + {}^5F_{7/2} (\text{Yb}^{3+})$ energy transfer.

v. Consequently, Tm^{3+} ions at level 3H_6 can fill the 1G_4 level via energy transfer from Yb^{3+} to the Tm^{3+} ions. Then the ${}^1G_4 (\text{Tm}^{3+}) \rightarrow {}^3F_4 (\text{Tm}^{3+})$ transition cause the red emission (651 nm). In addition, the ${}^3F_{2,3} \rightarrow {}^3H_4$ transition occurs thanks to non-radiative processes. Thus, the transition from the 3H_4 level to the ${}^3H_6 (\text{Tm}^{3+})$ level produces infrared emission at 790 nm.

The UC spectral profiles of YSYHT phosphors at different power values of 950 nm excitation are additionally shown in Figure 7a. The UC emission intensity ratio is found from the intensity ratio of the ${}^5F_4 \rightarrow {}^5I_8$ (525 nm) and ${}^5S_2 \rightarrow {}^5I_8$ (547 nm) transitions of the Ho^{3+} ion.

The energy difference (ΔE_s) provided by these two transitions in the spectra was calculated to be 766.03 cm^{-1} . As seen from Figure 7a, the UC emission intensity ratio of these two close levels indicates a linear change with increasing the pump power. Therefore, the fluorescence intensity ratio (FIR) (9,25,26), on which the Boltzmann distribution of electrons is based, is used to determine the temperature-sensitive effect on the emission intensity.

The intensity ratio (I_R) and sensitivity are functions of temperature and are given by the following equations:

$$I_R = \frac{I_2}{I_1} = A \exp\left(\frac{-\Delta E}{k_B T}\right) \quad (1)$$

$$\text{Sensitivity} = \frac{dI_R}{dT} = A \exp\left(\frac{-\Delta E}{k_B T}\right) \times \left(\frac{\Delta E}{k_B T^2}\right) \quad (2)$$

where, A is a constant that includes the frequencies of emissions, degeneration factors, and cross-sections of the emissions. ΔE is the energy difference among the nearest two levels, and k_B is the Boltzmann's constant.

In the FIR technique, each FIR value is represented by a specific temperature (27-29). The increase in host temperature occurs with the increase of heat-inducing laser pump power. Therefore, the intensities of RE^{3+} ions' emissions become sensitive to temperature change. Now, let's consider this at low pump power (0.66 W) at room temperature. And if the spectral energy difference (ΔE_s) was used instead of the energy difference expressed in Equation (1), the calculated value of constant A is found as 17.615. Then the temperature of powders correlating with different intensity ratio values of the ${}^5F_4 \rightarrow {}^5I_8$ and ${}^5S_2 \rightarrow {}^5I_8$ transitions at different pump powers can easily be calculated using Eq. (3) which is provided in Eq. (1).

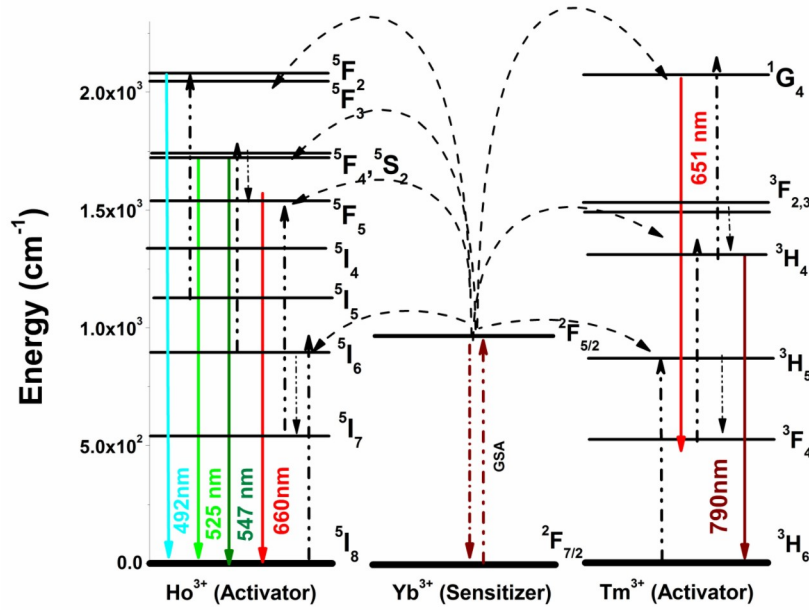


Figure 6: Possible energy transitions for Yb³⁺, Ho³⁺, and Tm³⁺ ions in YSYHT powders.

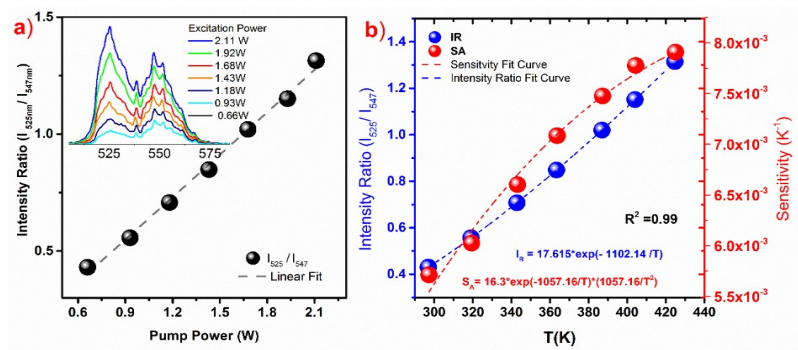


Figure 7: a) Intensity ratio of emission peaks due to laser pump power. b) Temperature sensing in terms of power heating relationship.

$$T = \left[\frac{1}{\ln A - \ln(I_R)} \right] \frac{\Delta E}{k} \quad (3)$$

Thus, the temperatures corresponding to the different intensity ratios and the sensitivity calculated using Eq. (2) are shown in Figure 7b. The maximum sensitivity with a value of $0.781 \times 10^{-2} \text{ K}^{-1}$ at 428 K was calculated from the fitting sensitivity curve's maximum value. When compared with the literature, this sensitivity value was found to be compatible with the sensitivity values of some RE³⁺ doped phosphorus materials given in Table 1. Consequently, as YSYHT phosphors can convert laser excitation power into heat, these phosphors can be used in promising applications as temperature sensor probes.

4. CONCLUSION

Sol-gel synthesized Yb³⁺:Ho³⁺:Tm³⁺ doped α -Y₂Si₂O₇ nano-powders indicated that most of the peaks matched well with the standard JCPDS:38-0223 card data of α -Y₂Si₂O₇. Morphology investigations with TEM microscopy showed that triple rare earth combinations mixed with α -Y₂Si₂O₇ presented nearly spherical nanoparticles in size varying from 20 to 30 nm for the powders.

The diffuse reflection spectra of the powders presented reflection data matching the absorption transitions of Yb³⁺, Ho³⁺ and Tm³⁺ ions in the α -Y₂Si₂O₇ samples in the 400 – 1050 nm. Up-converted blue, green, and red emissions were obtained in the visible region from Yb³⁺:Ho³⁺:Tm³⁺ doped α -Y₂Si₂O₇ nano-powders at 950 nm laser excitation. The slope values of laser power intensity revealed that the up-conversion mechanism comes true via two and three-photon absorption processes.

The UC emission intensity ratio of the ${}^5F_4 \rightarrow {}^5I_8$ and ${}^5S_2 \rightarrow {}^5I_8$ transitions corresponding to the Ho^{3+} ion depends on the pump power. Depending on the variation of the laser excitation power with the emission intensity ratio, the temperature range of 297-425 K corresponding to the laser excitation

power range of 0.66 – 2.11 W was calculated by the FIR technique. The maximum sensitivity value of $7.81 \times 10^{-3} \text{ K}^{-1}$ at 428 K was determined from the fitting sensitivity curve's maximum value. Consequently, $\text{Yb}^{3+}:\text{Ho}^{3+}:\text{Tm}^{3+}$ doped $\alpha\text{-Y}_2\text{Si}_2\text{O}_7$ nano-phosphors can be used as promising temperature sensor probes in photonic devices.

Table1: Sensitivity values of some RE^{3+} doped phosphorus materials.

Materials	Temperature Range [K]	Intensity Ratio	Sensitivity [K^{-1}]	Ref.
$\text{Yb}^{3+}/\text{Ho}^{3+}/\text{Tm}^{3+}:\text{Y}_2\text{Si}_2\text{O}_7$	290-440	I_{525}/I_{547}	0.0078 @ 428 K	Present work
$\text{Yb}^{3+}/\text{Ho}^{3+}:\text{Ba}_{0.77}\text{Ca}_{0.23}\text{TiO}_3$	93-300	I_{525}/I_{547}	0.0053 @ 93 K	(11)
$\text{Yb}^{3+}/\text{Ho}^{3+}:\text{CaWO}_4$	298-553	I_{460}/I_{487}	0.005 @ 923 K	(13)
$\text{Yb}^{3+}/\text{Ho}^{3+}:\text{TeO}_2\text{-ZnO-BaO}$	303-503	I_{660}/I_{547}	0.0073 @ 503 K	(22)
$\text{Yb}^{3+}/\text{Ho}^{3+}:\text{PSN-PMN-PT}$	173-493	I_{665}/I_{554}	0.0022 @ 93 K	(30)
$\text{Yb}^{3+}/\text{Ho}^{3+}:\text{KLa}(\text{MoO}_4)_2$	293-473	I_{651}/I_{546}	0.0356 @ 503 K	(31)
$\text{Yb}^{3+}/\text{Ho}^{3+}:(\text{Y}_{0.88},\text{La}_{0.09},\text{Zr}_{0.03})_2\text{O}_3$	293-563	I_{667}/I_{549}	0.0071 @ 563K	(32)

5. CONFLICT OF INTEREST

There are no conflicts that need to be reported.

6. ACKNOWLEDGMENTS

The study was carried out with the support of the Marmara University Scientific Research Projects Unit, project number FEN-B-150513-0170. We thank Prof. Dr. Baldassare Di Bartolo for the photoluminescent measurements performed in the Spectroscopy Laboratory at Boston College.

7. REFERENCES

- Marciniak L, Waszniewska K, Bednarkiewicz A, Hreniak D, Strek W. Sensitivity of a Nanocrystalline Luminescent Thermometer in High and Low Excitation Density Regimes. *J Phys Chem C* [Internet]. 2016 Apr 28 [cited 2022 Nov 27];120(16):8877–82. Available from: [<URL>](#)
- Marciniak L, Bednarkiewicz A, Kowalska D, Strek W. A new generation of highly sensitive luminescent thermometers operating in the optical window of biological tissues. *J Mater Chem C* [Internet]. 2016 [cited 2022 Nov 27];4(24):5559–63. Available from: [<URL>](#)
- Balabhadra S, Debasu ML, Brites CDS, Nunes LAO, Malta OL, Rocha J, et al. Boosting the sensitivity of Nd³⁺-based luminescent nanothermometers. *Nanoscale* [Internet]. 2015 [cited 2022 Nov 27];7(41):17261–7. Available from: [<URL>](#)
- Du P, Tang J, Li W, Luo L. Exploiting the diverse photoluminescence behaviors of $\text{NaLuF}_4:\text{xEu}^{3+}$ nanoparticles and g-C₃N₄ to realize versatile applications in white light-emitting diode and optical thermometer. *Chem Eng J* [Internet]. 2021 Feb [cited 2022 Nov 27];406:127165. Available from: [<URL>](#)
- Doğan A, Erdem M. Investigation of the optical temperature sensing properties of up-converting $\text{TeO}_2\text{-ZnO-BaO}$ activated with $\text{Yb}^{3+}/\text{Tm}^{3+}$ glasses. *Sens Actuat A: Phys* [Internet]. 2021 May [cited 2022 Nov 27];322:112645. Available from: [<URL>](#)
- Doğan A, Yıldırım SM, Erdem M, Esmer K, Eryürek G. Investigation of spectral output of Er^{3+} and $\text{Yb}^{3+}/\text{Er}^{3+}$ doped $\text{TeO}_2\text{-ZnO-BaO}$ glasses for photonic applications. *New J Chem* [Internet]. 2021 [cited 2022 Nov 27];45(8):3790–9. Available from: [<URL>](#)
- Liu X, Chen Y, Shang F, Chen G, Xu J. Wide-range thermometry and up-conversion luminescence of $\text{Ca}_5(\text{PO}_4)_3\text{F}:\text{Yb}^{3+}/\text{Er}^{3+}$ transparent glass ceramics. *J Mater Sci: Mater Electron* [Internet]. 2019 Mar [cited 2022 Nov 27];30(6):5718–25. Available from: [<URL>](#)
- Fischer LH, Harms GS, Wolfbeis OS. Upconverting Nanoparticles for Nanoscale Thermometry. *Angew Chem Int Ed* [Internet]. 2011 May 9 [cited 2022 Nov 27];50(20):4546–51. Available from: [<URL>](#)
- Wade SA, Collins SF, Baxter GW. Fluorescence intensity ratio technique for optical fiber point temperature sensing. *J Appl Phys* [Internet]. 2003 [cited 2022 Nov 27];94(8):4743. Available from: [<URL>](#)
- Lei R, Luo X, Yuan Z, Wang H, Huang F, Deng D, et al. Ultrahigh-sensitive optical temperature sensing in $\text{Pr}^{3+}:\text{Y}_2\text{Ti}_2\text{O}_7$ based on diverse thermal response from trap emission and Pr^{3+} red luminescence. *J Lumin* [Internet]. 2019 Jan [cited 2022 Nov 27];205:440–5. Available from: [<URL>](#)
- Du P, Luo L, Yu JS. Low-temperature thermometry based on upconversion emission of Ho/Yb -codoped $\text{Ba}_{0.77}\text{Ca}_{0.23}\text{TiO}_3$ ceramics. *J Alloy Comp* [Internet]. 2015 May [cited 2022 Nov 27];632:73–7. Available from: [<URL>](#)

12. Liu Z, Jiang G, Wang R, Chai C, Zheng L, Zhang Z, et al. Temperature and concentration effects on upconversion photoluminescence properties of Ho^{3+} and Yb^{3+} codoped $0.67\text{Pb}(\text{Mg}_{1/3}\text{Nb}_{2/3})\text{O}_3-0.33\text{PbTiO}_3$ multifunctional ceramics. *Ceram Int* [Internet]. 2016 Jul [cited 2022 Nov 27];42(9):11309–13. Available from: [<URL>](#)
13. Xu W, Zhao H, Li Y, Zheng L, Zhang Z, Cao W. Optical temperature sensing through the upconversion luminescence from $\text{Ho}^{3+}/\text{Yb}^{3+}$ codoped CaWO_4 . *Sens Actuat B: Chem* [Internet]. 2013 Nov [cited 2022 Nov 27];188:1096–100. Available from: [<URL>](#)
14. Marciniak L, Hreniak D, Streck W, Piccinelli F, Spgehini A, Bettinelli M, et al. Spectroscopic and structural properties of polycrystalline $\text{Y}_2\text{Si}_2\text{O}_7$ doped with Er^{3+} . *J Lumin* [Internet]. 2016 Feb [cited 2022 Nov 27];170:614–8. Available from: [<URL>](#)
15. Sokolnicki J. Rare earths (Ce, Eu, Tb) doped $\text{Y}_2\text{Si}_2\text{O}_7$ phosphors for white LED. *J Lumin* [Internet]. 2013 Feb [cited 2022 Nov 27];134:600–6. Available from: [<URL>](#)
16. Erdem M, Sitt B. Up conversion based white light emission from sol-gel derived $\alpha\text{-Y}_2\text{Si}_2\text{O}_7$ nanoparticles activated with Yb^{3+} , Er^{3+} ions. *Optical Materials* [Internet]. 2015 Aug [cited 2022 Nov 27];46:260–4. Available from: [<URL>](#)
17. Erdem M, Tabanlı S, Eryurek G, Samur R, Di Bartolo B. Crystalline phase effect on the up-conversion processes and white emission of $\text{Yb}^{3+}/\text{Er}^{3+}/\text{Tm}^{3+}:\text{Y}_2\text{Si}_2\text{O}_7$ nanocrystals. *Dalton Trans* [Internet]. 2019 [cited 2022 Nov 27];48(19):6464–72. Available from: [<URL>](#)
18. Tomala R, Hreniak D, Streck W. Laser induced broadband white emission of $\text{Y}_2\text{Si}_2\text{O}_7$ nanocrystals. *J Rare Earths* [Internet]. 2019 Nov [cited 2022 Nov 27];37(11):1196–9. Available from: [<URL>](#)
19. Rakov N. $\text{Tm}^{3+}, \text{Yb}^{3+}:\text{Y}_2\text{SiO}_5$ up-conversion phosphors: Exploration of temperature sensing performance by monitoring the luminescence emission. *Physica B: Cond Mat* [Internet]. 2022 Mar [cited 2022 Nov 27];628:413572. Available from: [<URL>](#)
20. Erdem M, Özen G, Tav C. Crystallization behaviour of neodymium doped yttrium silicate nanophosphors. *Journal of the Eur Ceram Soc* [Internet]. 2011 Nov [cited 2022 Nov 27];31(14):2629–31. Available from: [<URL>](#)
21. Jiang C, Xu W. Theoretical Model of $\text{Yb}^{3+}/\text{Er}^{3+}/\text{Tm}^{3+}$ -Codoped System for White Light Generation. *J Display Technol* [Internet]. 2009 Aug [cited 2022 Nov 27];5(8):312–8. Available from: [<URL>](#)
22. Doğan A, Erdem M, Esmer K, Eryürek G. Upconversion luminescence and temperature sensing characteristics of $\text{Ho}^{3+}/\text{Yb}^{3+}$ co-doped tellurite glasses. *J Non-Cryst Sol* [Internet]. 2021 Nov [cited 2022 Nov 27];571:121055. Available from: [<URL>](#)
23. Tavares MCP, da Costa EB, Bueno LA, Gouveia-Neto AS. White phosphor using Yb^{3+} -sensitized Er^{3+} - and Tm^{3+} -doped sol-gel derived lead-fluorosilicate transparent glass ceramic excited at 980 nm. *Opt Mater* [Internet]. 2018 Jan [cited 2022 Nov 27];75:733–8. Available from: [<URL>](#)
24. Pandey A, Rai VK. Colour emission tunability in $\text{Ho}^{3+}-\text{Tm}^{3+}-\text{Yb}^{3+}$ co-doped Y_2O_3 upconverted phosphor. *Appl Phys B* [Internet]. 2012 Dec [cited 2022 Nov 27];109(4):611–6. Available from: [<URL>](#)
25. Wade SA. Temperature measurement using rare earth doped fibre fluorescence [Internet] [PhD Thesis]. [Australia]: Victoria University; 1999. Available from: [<URL>](#)
26. Wang X, Liu Q, Bu Y, Liu CS, Liu T, Yan X. Optical temperature sensing of rare-earth ion doped phosphors. *RSC Adv* [Internet]. 2015 [cited 2022 Nov 27];5(105):86219–36. Available from: [<URL>](#)
27. Tang J, Du P, Li W, Luo L. Boosted thermometric performance in $\text{NaGdF}_4:\text{Er}^{3+}/\text{Yb}^{3+}$ upconverting nanorods by Fe^{3+} ions doping for contactless nanothermometer based on thermally and non-thermally coupled levels. *J Lumin* [Internet]. 2020 Aug [cited 2022 Nov 27];224:117296. Available from: [<URL>](#)
28. Du P, Luo L, Park HK, Yu JS. Citric-assisted sol-gel based $\text{Er}^{3+}/\text{Yb}^{3+}$ -codoped $\text{Na}_{0.5}\text{Gd}_{0.5}\text{MoO}_4$: A novel highly-efficient infrared-to-visible upconversion material for optical temperature sensors and optical heaters. *Chem Eng J* [Internet]. 2016 Dec [cited 2022 Nov 27];306:840–8. Available from: [<URL>](#)
29. Jacinto C, Vermelho MVD, Gouveia EA, de Araujo MT, Udo PT, Astrath NGC, et al. Pump-power-controlled luminescence switching in $\text{Yb}^{3+}/\text{Tm}^{3+}$ codoped water-free low silica calcium aluminosilicate glasses. *Appl Phys Lett* [Internet]. 2007 Aug 13 [cited 2022 Nov 27];91(7):071102. Available from: [<URL>](#)
30. He A, Xi Z, Li X, Long W, Fang P, Zhang J. Temperature dependence of upconversion luminescence and sensing sensitivity of $\text{Ho}^{3+}/\text{Yb}^{3+}$ modified PSN-PMN-PT crystals. *J Alloy Comp* [Internet]. 2019 Sep [cited 2022 Nov 27];803:450–5. Available from: [<URL>](#)
31. Zhang Y, Wang T, Liu H, Liu D, Liu Y, Fu Z. Optical temperature sensing behavior for $\text{KLa}(\text{MoO}_4)_2:\text{Ho}^{3+}/\text{Yb}^{3+}$ phosphors based on fluorescence intensity ratios. *Optik* [Internet]. 2020 Feb [cited 2022 Nov 27];204:164100. Available from: [<URL>](#)
32. Zhou J, Chen Y, Lei R, Wang H, Zhu Q, Wang X, et al. Excellent photoluminescence and temperature sensing properties in $\text{Ho}^{3+}/\text{Yb}^{3+}$ codoped $(\text{Y}_{0.88}\text{La}_{0.09}\text{Zr}_{0.03})_2\text{O}_3$ transparent ceramics. *Ceramics International* [Internet]. 2019 Apr [cited 2022 Nov 27];45(6):7696–702. Available from: [<URL>](#)



Study on Recycling of Waste Glass Fiber Reinforced Polypropylene Composites: Examination of Mechanical and Thermal Properties

Ezgi Sözen^{1,2} , Aref Cevahir² , Sennur Deniz^{1*} 

^{1*}Yıldız Technical University, Faculty of Chemical and Metallurgical Engineering, Department of Chemical Engineering, 34210, Istanbul, Türkiye.

²Şişecam Science and Technology Center, Atmospheric Coating Management, 41400, Gebze, Türkiye.

Abstract: This study presents the preparation of short glass fiber reinforced polypropylene (PP/FG) composites using with waste (post-consumer) polypropylene composite containing long glass fiber (PP/LFG) obtained from the recycling of battery covers of trucks. Waste PP/LFG composite parts were mechanically grinded before adding to PP/FG composites. An injection molding machine was used to produce the PP/FG composite test samples loading with recycled waste PP/LFG composite in the range of 1-20% by weight. Effects of recycled waste PP/LFG content on the mechanical, thermal, and morphological properties of the PP/FG composites were investigated. The following three different tests, at various waste PP/LFG ratios, were conducted: Izod/Charpy Impact test, bending test, and tensile test. Mechanical test results showed that mechanical strength of prepared PP/FG composites were not influenced by content of waste PP/LFG material up to 10 wt.%. Differential scanning calorimetry (DSC) was used for the evaluation of thermal parameters such as melting point and crystallization temperature of the polymer matrix in the composites studied. Furthermore, by analyzing the values of thermal effects determined using the DSC method, it was possible to determine the degree of crystallinity. The DSC results showed that crystallinity %, melting, and crystallization temperatures of PP/FG composites were not influenced to adding waste PP/LFG at different ratios. The morphology of composite materials was investigated by SEM analysis. Good fiber dispersion was observed in the PP matrix for PP/FG composites containing short glass fiber prepared with all ratios of recycled waste PP/LFG material containing long glass fiber.

Keywords: Glass fiber, Polypropylene, Polymer composite, Recycled materials, Mechanical properties.

Submitted: September 21, 2022. **Accepted:** January 11, 2023.

Cite this: Sözen E, Cevahir A, Deniz S. Study on Recycling of Waste Glass Fiber Reinforced Polypropylene Composites: Examination of Mechanical and Thermal Properties. JOTCSA. 2023;10(1):63-76.

DOI: <https://doi.org/10.18596/jotcsa.1178019>.

***Corresponding author. E-mail:** deniz@yildiz.edu.tr.

1. INTRODUCTION

As examined on the properties of materials (concrete, glass, metal alloys, wood materials, carbon, plastic and etc.) used for general needs in the early days, it is understood that new materials with light, superior and specific properties are needed. Composite materials with desired properties cannot be produced at the expected level due to the high production cost. Despite all these, their usage is rapidly becoming widespread and is expected to increase further. In the 21st century, the demand for thermoplastic polymer composites is increasing, which is due to their superior physical and mechanical strengths. High strength, high rigidity, long fatigue

life, low density, and adaptability to the desired properties are the advantages of polymer composite materials over single phase products. Corrosion resistance, appearance, temperature dependent behavior, thermal insulation, thermal conductivity and acoustic insulation can also be significant characteristics arising from their high specific strength and rigidity (1-5).

In terms of mechanical properties, three regions consisting of reinforcement, matrix, and interface are effective in the structure of polymer composite defined as 'material formed by combination of two or more different components along the interface in the macro dimension'. The tasks of these regions

are, respectively; to carry the load on the structure, to keep the composite structure together and distribute the loads homogeneously, and to bond the matrix with reinforcement zones. The factors determining the mechanical properties of composite can be listed as the matrix type, the type, and form of reinforcement material. In addition, the compatibility of the reinforcement and the matrix is a requirement for the production of composite with good mechanical strength. Tensile and bending properties decrease when the cavity content of composite materials is above 3-6%. The weakening of the interface bond at high temperatures is one of the main reasons for the production efficiency to be locked. To achieve the good interface interaction, it is reported in the literature that the use of compatibilizers improved the interface adhesion between matrix and reinforcement materials (for example; the use of maleic anhydride modified (grafted) polypropylene for PP composites). Beside this, it is also known that the use of compatibilizers contributes to thermal and mechanical properties of composites (6-8).

Polypropylene (PP) is one of the most widely used thermoplastic polyolefinic material that is most commonly utilized in plastic and automotive industries. PP is determined by its versatile characteristics, chemical resistance, low density, excellent barrier properties, ease of formulation, and good flexibility (9, 10). In contrast, there is a need to cope with some limitations of PP, such as low stiffness and low strength, susceptibility to oxidation (11). Fabrication of PP composites with reinforcing materials is a method of improving their mechanical properties, so the application areas of PP can be expanded through the blending process with the incorporation of various materials. Different reinforcement materials, some mostly preferred inorganic fillers, such as glass fiber (FG), carbon nanotubes, and clays are employed to enhance the properties of the PP polymer. To obtain a high-performance dielectric PP composite, it is reported that an increase in energy storage values is obtained using a blend of maleic anhydride grafted polypropylene (MAPP) and graphene oxide (12). After the increase in use of nanomaterials in the literature, the enhancement of mechanical properties was achieved using PP and 10% nano silica (13). For the fiber addition, a hybrid system was created using basalt fiber on behalf of the environmental approach and therefore an increase in tensile strength was obtained (14). Of these PP composites, glass fiber reinforced PP/FG composites prepared with different types of glass fibers (E-type, S-type so on) are very attractive materials with their ease of fabrication, superior mechanical properties (high specific modulus and strength), and low manufacturing cost (15). PP/FG composites are mostly favored in the developing automotive industry due to the need for lightweight and high mechanical strength. E-type glass fibers are used in a wide range of development studies of PP composites (16-21). In glass fiber reinforced PP/FG composites, the process generally uses E-type glass fibers, long and short fibers in shape depend-

ing on their mechanical expectations. In addition, using a MAPP results in a structure with higher mechanical strength in PP composites (17). PP/FG composites are developed as an alternative and stronger structure for bone fracture fixation plates (21).

In the PP/FG composites, it is also important that the polymer matrix has good wetting ability and no chemical bonding on the fiber surface, and the fiber also has surface properties suitable for interaction with the polymer. The low wetting ability of the polymer leads to the formation of voids on the contact surface of the fiber which negatively affects the mechanical properties of the composite structure (22). E-type glass fiber is often preferred for PP/FG composites, taking advantage of its adequate electrical properties compared to other types of glass fibers. In terms of engineering properties, fiber length, and diameter, fiber orientation, and volume ratio are important parameters in the PP/FG composite materials. Among of long (continuous) or short (discontinuous) fibers in length, long fibers are difficult to handle, whereas short fibers are easy to manipulate and process. Also, high elastic modulus and strength are expected properties for fibers. The use of glass fiber increases the mechanical properties of the polymer composite by 2-3 times. Continuous fiber reinforced composites are used for higher values of strength and stiffness, while discontinuous fiber reinforced products are preferred in areas where cost is important (6). In composite preparation with the intended properties, fiber type selection should be made by evaluating the desired properties and cost (23). Continuous fibers are the most durable reinforcing product and increases tensile modulus, dimensional stability, hydraulic stability, and fatigue and impact behavior of composites. The PP/LFG composites used in luggage and load carrier parts of cars have been developed with long fibers with a length of 10 mm instead of short fibers with a length of 0.7-1.5 mm. Recycling of glass fiber reinforced PP composites is an option considering the cost of using it in pure form (3, 24).

Plastic wastes emerge as both daily use and process waste. The recycling of these products is valuable in terms of preventing environmental pollution, saving energy from scratch, reducing the use of pure raw materials. Recycling is a remarkable process in terms of cost and storage. However, considering of only one quarter of the waste is recycled, these products can be used in residential and construction areas. Because of softening and melting properties of thermoplastics, it is possible to produce reusable products from them. Since the recycling of thermoplastics reduces mechanical and other properties, the supplement of recycled waste products should be approximately 10 to 15% on the basis of pure material. In the plastic industry, usually 20% of waste and 80% of thermoplastic polymers are mixed and new plastic batches are formed. The properties of the matrix, fiber, and interface change in each step of composite fabrication, and at this point, the aspect ratio (L/D) of fiber length (L) and fiber diame-

ter (D)) are important parameters for the interface bonding and transferring load. Fracture stress limit is one of the factors which determining the amount of recycling. Thermoplastic products can be recycled by resin dissolving process. Glass fibers separated by dissolution have the same tensile strength as pure glass fibers, but they have 12% less hardness than pure glass fibers. Although there are difficulties for recycled glass fiber reinforced thermoplastic materials obtained by pyrolysis process, researches and calculations are made considering the increasing needs and economic conditions (24-28).

The main objective of this study is to prepare the PP/FG composites with short glass fiber using with waste PP/LFG composites containing with long glass fibers and to recycle the waste PP/LFG composite. For this purpose, PP/LFG composite parts obtained from waste battery covers of trucks was shredded by using mechanical grinder for recycling. Before adding to PP/FG composite, the fiber content and diameter in the waste grinded PP/LFG composites were characterized with burning tests and dimension measurements, respectively. The results of me-

chanical and thermal tests of PP/FG composites prepared with the adding of waste PP/LFG were compared and evaluated, and determined to the highest amount of recycled waste composite. As a result of the tests, it has been observed that the certain contribution rates of waste PP/LFG composite to produced PP/FG composite structure can be recycled.

2. EXPERIMENTAL

2.1. Material

The raw materials used in this study are glass fiber, polypropylene, and binder material. Table 1 lists the materials' compositions with weight ratios of the constituents and also the symbols which were used in this study. Polypropylene, which is a semi-crystalline polymer and used as a polymer matrix, was purchased from PETKİM in granular form (density: 0.902-0.910 g/cm³; melting point: 164 °C). As a thermoplastic engineering polymer, PP has superior mechanical properties such as good resistance to stress, low specific gravity, and good impact strength (25, 26).

Table 1: Designation and composition of composites.

Sample	Ratio (wt.%)	Notes
FG	100	Chopped Short Glass Fiber
PP	100	PP granules
PP/LFG (waste composite)	70/30	Waste battery covers of trucks
PP/FG/LFG-X (composite)	70/30/X	Combination of PP, FG, and waste PP/LFG (LFG-X; wt% of waste PP/LFG)

Glass fiber (FG), which is used as a reinforcement material, was purchased from Şişecam Elyaf Sanayii AŞ., in chopped short glass fiber (E-type) form. The length and diameter of the chopped glass fibers is 4.5 mm and at least 14 µm, respectively. The glass fiber diameter distribution (using the Cottonscope

device) of the chopped product of short glass fiber is given in Figure 1. Glass fiber consists of silicone, calcium, boron, sodium, iron, and aluminum elements is amorphous and of isotropic material form (27, 31).

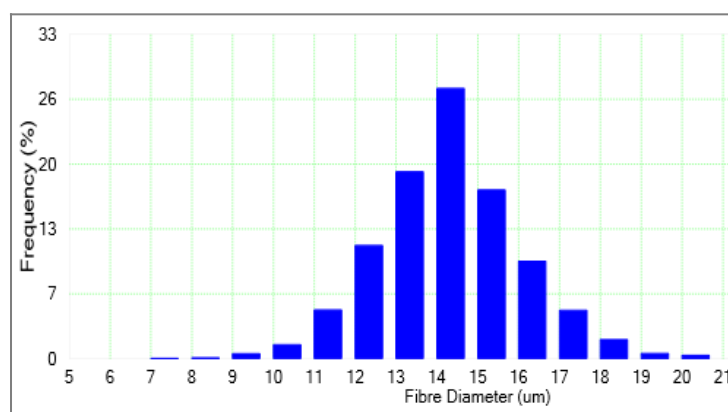


Figure 1: Fiber diameter distribution of the chopped short glass fiber.

Polybond® 3200, a maleic anhydride modified polypropylene, ($\rho = 0.91$ g/mL, acid value = 6.1 mg/KOH g, MA content = 1.0 wt.%) was purchased from CHEMTURA, USA. It was used as a chemical

coupling agent for glass fiber reinforced PP. Polybond® 3200 is used to improve the adhesion strength between glass fiber and PP, and to enhance physical and thermal properties.

The waste PP/LFG material to be recycled is the battery cover for trucks, and this composite material weighs 2500 grams. The fiber diameter distribution

of the recycling material is given in Figure 2. The PP/LFG ratio of waste material was found to be 70/30 by burning test.

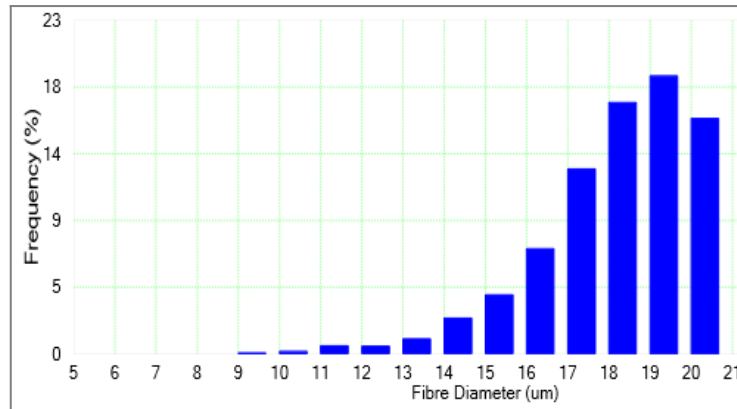


Figure 2: Fiber diameter distribution of the recycling waste PP/LFG composite.

2.2. Preparation, Characterizing and Tests

2.2.1. Sizing of PP/LFG waste composite

Shredding: The waste material for recycling is 60 cm x 40 cm. First, 15-20 large pieces were obtained and then cut to get 2 cm x 2 cm pieces with saw. These parts were transferred to the grinding step.

Grinding: Grinding was performed on IKA WERKE, MF 10 Basic Microfine Grinder Drive. The screen size of the grinder is 0.25 - 0.5 - 1 - 2 mm. 2 mm sieve type was chosen due to the biggest dimensions suitable for in this study. The grinding speed was selected as the maximum level of 6500 min⁻¹. In addition, external cooling was performed with vortex tube in order to prevent heating of the device during the process.

Dimension measurement: The length of the glass fiber was measured using optical microscope and accordingly 135 data were collected from the remaining burnt composite waste. In this study, several composite samples were produced with and without waste material. There was no difference in fiber diameter in PP/FG/LFG-0 samples, is 200 data were taken. For the other sample sets, 100 data were obtained with the fiber diameter being thin and thick. The surface area information of the milled grains obtained from the waste sample was measured as 0.4 mm² by optical microscope.

2.3. Preparation of PP/FG/LFG Composites

In the preparation of PP/FG/LFG composites, the waste PP/LFG (LFG-X, wt.%) content was determined as 1, 5, 7, 10, 15 and 20% by weight. The total weight of each blend containing polypropylene, glass fiber, waste PP/LFG, and Polybond® 3200 is 1500 grams. The combination of all samples were

determined according to the combustion test which is based on TS 1177 EN ISO 1172 standard. Firstly, the waste material was directly incinerated at 610 °C. As a result of the combustion, the polymer fraction was burned and leaving only glass fibers. Glass fiber ratios of waste composite were calculated by taking the weight difference before and after combustion. According to this calculation, the glass fiber content of composite composition by weight was 30%. By knowing the content of the waste product, combinations were formed with final glass ratio of 30%. The combination of PP/FG/LFG composites are given in Table 2.

2.4. Extrusion and Injection of PP/FG/LFG Composites

The temperature ranges of extrusion process were set to 240-230-230-230 °C for PP. The processing temperature for PP and glass fiber reinforced PP composites was determined as 230-240 °C, according to the literature (35, 36). The prepared batch sets were fed to COMAC Plast single screw extruder machine (screw speed: 6-6.6 rpm). The molten blend was cooled with cold water and dried with cold air. The dried long yarn-shaped material was passed through the cutting machine for the granular form.

The obtained granules were kept in the oven at 80 °C for 24 hours to remove moisture. The temperature ranges of injection molding were set to 230-230-230-230 °C for four zones, respectively. The granules were fed to the ENGEL injection molding machine. After the heat and pressure treatment molten PP pressed into the mold suitable for mechanical tests.

Table 2: The combination of PP/FG/LFG composites prepared with waste PP/LFG.

Blend Samples	Pure PP (g)	Pure Glass Fiber (FG) (g)	Binder (Polybond®) (g)	Waste PP/LFG (g)	Waste Glass Fiber (g)
PP/FG/LFG-0	1029.0	450.0	21.0	-	-
PP/FG/LFG-1	1018.5	445.5	21.0	10.5	4.5
PP/FG/LFG-5	976.5	427.5	21.0	52.5	22.5
PP/FG/LFG-7	955.5	418.5	21.0	73.5	31.5
PP/FG/LFG-10	924.0	405.0	21.0	105.0	45.0
PP/FG/LFG-15	871.5	382.5	21.0	157.5	67.5
PP/FG/LFG-20	819.0	360.0	21.0	210.0	90.0

2.5. Characterization

2.5.1. Mechanical tests

Mechanical tests are applied to four different types molded products. The main tests are basically divided into three subjects; impact, bending, and tensile. Impact tests are classified according to their vertical-horizontal and notched-unnotched form.

Izod: Samples (80*4*10 mm in size) are used for vertically applied impact test. One of the two test specimens in the mold sample was mechanically tested on the Zwick universal test machine, one notched and the other unnotched. MF 10 Basic-IKA WERKE notching device was used for notching. Five samples were tested for each composite and the average values were reported. Izod impact tests were done according to TS EN ISO 180 standard test method.

Charpy: This horizontal impact is applied to five of the samples of the same length and the same procedures as for the Izod impact test. Izod impact tests were done according to the EN ISO 179-2 standard test method for the Charpy impact test.

Bending: Three-point bending tests were done according to TS EN ISO 178 standard test method. The dimensions of the bending samples are 60*4*10 mm. As a result of this test, F-max flexural strength and F-max deformation data are examined.

Tensile: Tensile tests were done according to TS EN ISO 527-1 standard test method. In accordance with the standard, a dog bone sample of 4*10 mm was used. As a result of this test, F-max tensile strength and F-max elongation at break are examined.

2.5.2. DSC Analyses

Differential Scanning Calorimetry (DSC) test was performed on the sample taken from four different parts of the waste battery cover. Analysis was performed on the samples taken, polypropylene, and Polybond® 3200 raw materials.

2.5.3. SEM Analyses

To perform the SEM analyses of PP/FG composites, the surface of each samples was coated with Au/Pd. SEM Images were taken from the fracture surfaces of Izod impact samples in each set. The fracture surfaces of PP/FG composite samples and the bonding between the glass fiber and polypropylene matrix were investigated from the SEM images.

3. RESULTS AND DISCUSSION

3.1. Mechanical Properties

In this study, the PP/FG composites with short glass fiber using with the waste PP/LFG composites containing with long glass fibers are prepared with the different ratios of recycled waste PP/LFG composite. The diameters of the long fibers from the waste composite are larger than that of the short fibers using in the prepared PP/FG composite, and are 18.61 and 14.05 μm , respectively. As a result of the mechanical tests, it is seen that increasing the fiber diameter with the adding of waste PP/LFG in composite structure decreases the strength of PP/FG/LFG composites. The effect of the addition of waste composite with long fiber on the mechanical strength values of PP/FG/LFG composites can be evaluated with the data given in Table 3.

As the flexural strength of prepared composites is examined, a significant decrease is observed above the 10% of waste PP/LFG ratio added to the PP/FG composite. The flexural strength and modulus are similar to the reference PP/FG composite value prepared without any waste material, up to the PP/FG/LFG-10 composite with the 10% of waste material and then starts dropping, due to the addition of long fiber in higher weight fraction. On the other hand, the tensile strength values of composites decreases linearly with increasing waste amounts in prepared PP/FG/LFG composite. For the amount of waste composite above the 1%, more than 3% decrease is observed in the breaking strengths of composites prepared with all other waste additives, but the addition of waste material in the ratios of 5, 7 and 10% gives similar values,

are of 88.1, 87.8, and 87.1, respectively. In this case, as in the results of flexural strength, it is appropriate to add the waste composite up to 10%. It was observed that in all the specimen under with the 20% of waste additive, the flexural and tensile properties were close to those of reference PP/FG composite without waste additive. Mechanical properties of a composite mainly depend on the fiber ratio, individual properties of fiber and polymer matrix and interfacial bonding of them (17, 18). Besides that, it can be said that the aspect ratio of fibers is the major factor in deciding and affecting the mechanical properties of the composites.

Histogram of fracture energy (kJ/m^2) at F_{\max} against PP/LFG content (wt.%) for the same specimen sizes of composites at 25 °C are depicted in Figure 5. From the histogram, it can be observed that, generally, the tensile strength and fracture energy values decrease with respect to increasing the waste PP/LFG content with long fiber for tensile and impact specimens, respectively.

For tensile specimens, this trend is expected as the presence of fibers tends to reduce resistance to

crack initiation, therefore increasing the material brittleness, while at the same time reducing crack propagation through the matrix by forcing crack lines around the fiber ends. However, for unnotched Charpy impact specimen, there is no sharp decrease in fracture energy (8%) with the incorporation of up to 15% of waste PP/LFG loading compared with neat PP/FG composite (54.8 mJ).

For unnotched Izod impact specimens, this trend is similarly observed that the fracture energy (7.5%) decrease with up to 15% of waste PP/LFG content in composite accordance with neat PP/FG composite (55.2 mJ). For the results of notched Izod and Charpy impact tests, no significant variation for fracture energy is observed with increase in waste PP/LFG content of composites. It is observing to note that further addition of up to 20% of waste PP/LFG does not produce any significant effect on fracture energy values of prepared composites. Meanwhile, in order of increasing the waste loading to 15%, identical trends in notched Izod and Charpy impact values are observed as resulted in 10.5 kJ/m^2 .

Table 3: Mechanical test results of PP/FG/LFG composites.

Samples	PP/FG /LFG-0	PP/FG /LFG-1	PP/FG /LFG-5	PP/FG /LFG-7	PP/FG /LFG-10	PP/FG /LFG-15	PP/FG /LFG-20
Flexural Strength (MPa)	141.1±1.4	142.4±1.8	139.0±2.3	138.6±1.6	139.3±1.2	128.9±0.6	127.8±0.1
Flexural Modulus (GPa)	6.7	7.0	6.9	6.9	7.0	6.1	6.1
Tensile Strength (MPa)	92.4±1.0	91.3±0.8	88.1±0.1	87.8±0.3	87.1±1.3	85.9±0.6	84.3±0.5
Tensile Modulus (GPa)	5.8	4.7	5.3	5.1	5.5	5.9	5.9
Unnotched Izod Impact (kJ/m^2)	59.7±3.3	60.2±5.4	56.5±4.5	55.7±3.2	55.4±2.5	55.2±2.1	54.0±3.0
Unnotched Charpy Impact (kJ/m^2)	54.8±4.4	56.2±1.6	51.2±2.8	51.9±2.2	50.9±2.7	50.4±2.7	47.6±2.5
Notched Izod Impact (kJ/m^2)	11.7±0.7	11.8±0.3	10.5±0.3	10.7±0.5	10.4±0.3	10.5±0.4	9.9±0.3
Notched Charpy Impact (kJ/m^2)	10.8±0.2	11.2±0.3	10.6±0.5	10.4±0.5	10.7±0.4	10.5±0.6	9.6±0.2

Figure 3 shows the relationship by the way the flexural strength and strain data for the bending test. In Figure 3 (a) (red line), and (b) (green line) refer to the neat PP/FG/LFG-0 composite and the PP/FG/LFG-7 with 7% of waste material, respectively. As can be seen from this graph, the flexural force values are close to each other and the resistance

value decreases slightly with the addition of recycled waste. In Figure 4, the tensile strength of PP/FG/LFG-10 composite is given by the graphs obtained from repeat tests of 5 samples. For the tensile strength of the composite loaded with 10% of recycled waste, the repeatable values appear to be obtained in close agreement.

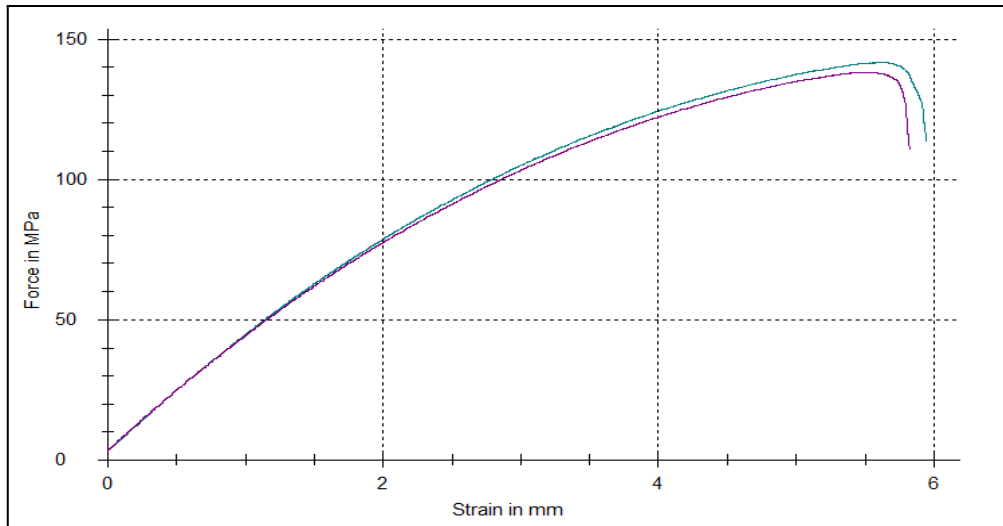


Figure 3: Graphs for the flexural strength: (a) PP/FG/LFG-0 (green line; top) and (b) PP/FG/LFG-7 (red line; bottom).

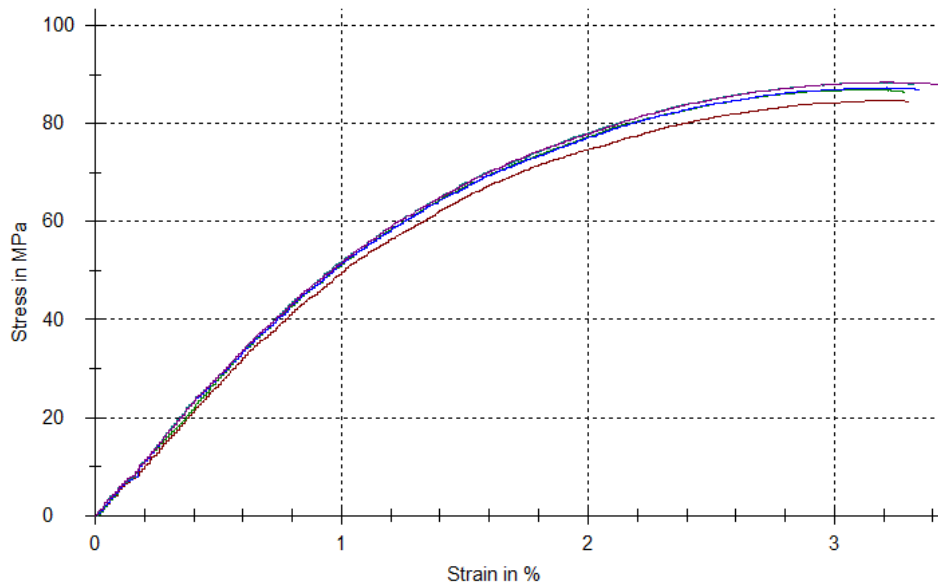


Figure 4: Graphs for tensile strength of PP/FG/LFG-10.

As a result of the strength values of PP/FG/LFG composites, it is found that the optimum ratio of recycled waste is 10% and above this ratio, it affects the mechanical strength of composites negatively. While the flexural strength is not significantly altered with an increase in recycled waste loading,

the tensile strength values decreases to a certain extent. It is observed that the impact strength is reduced with incorporation of recycled waste in the composites. The data on mechanical strength properties are given in Figure 5.

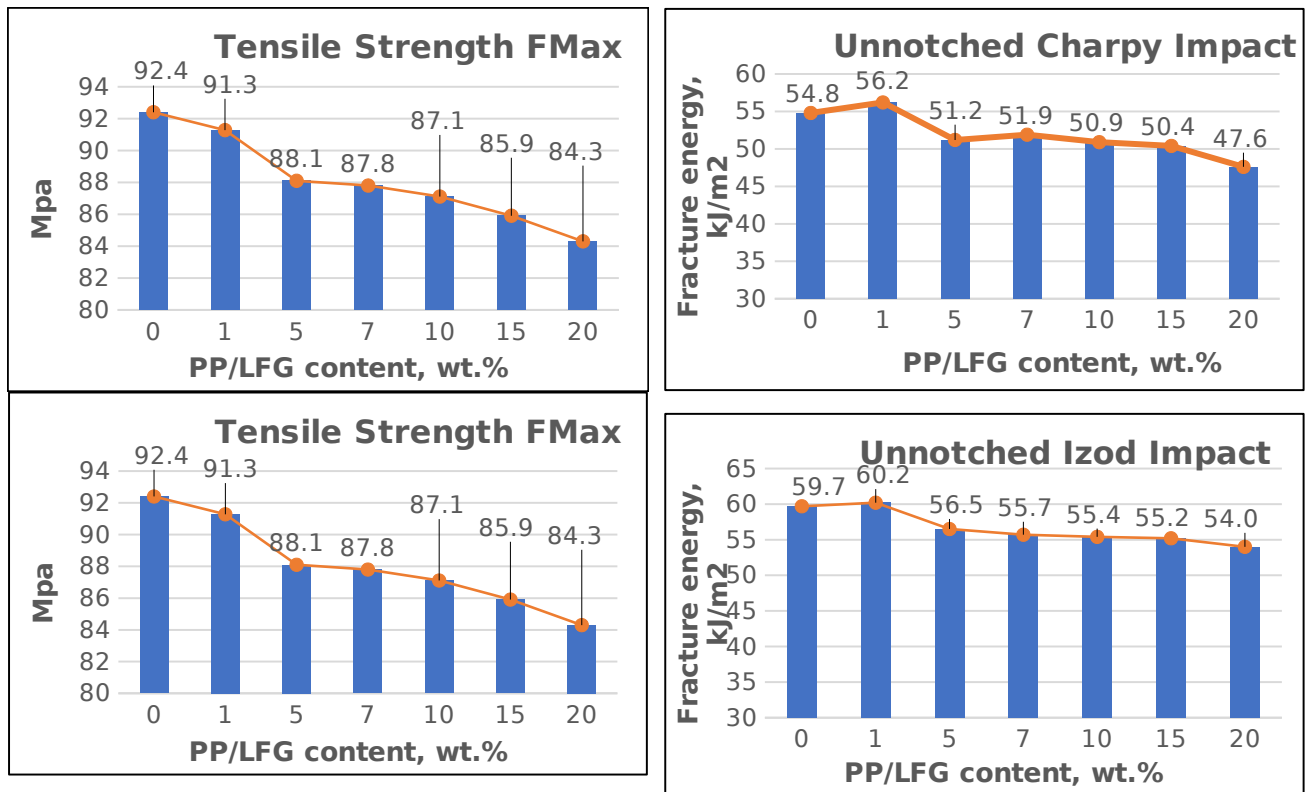


Figure 5: Mechanical strength properties for PP/FG/LFG composites.

In a previous study, it was reported that the recycled glass fiber reinforced composites showed lower tensile strength (-30%) compared to the untreated glass fiber composite (32). The loss in mechanical performance can be explained by the fact that the recycled glass fiber filled composite is subject to fiber breakage and is unable to regenerate the fibers during the injection molding process.

3.2. Thermal Properties

As seen in Figure 6, DSC thermograms show that the neat PP/FG/LFG-0 composite, which is the reference sample, and recycled waste containing samples exhibit similar behavior. Temperature range from -40 °C to 200 °C, suitable for PP. All measurements were taken under nitrogen atmosphere at the same heating and cooling rates of 10 °C/min. The process, which starts and ends at room temperature, is carried out with cooling and then heating.

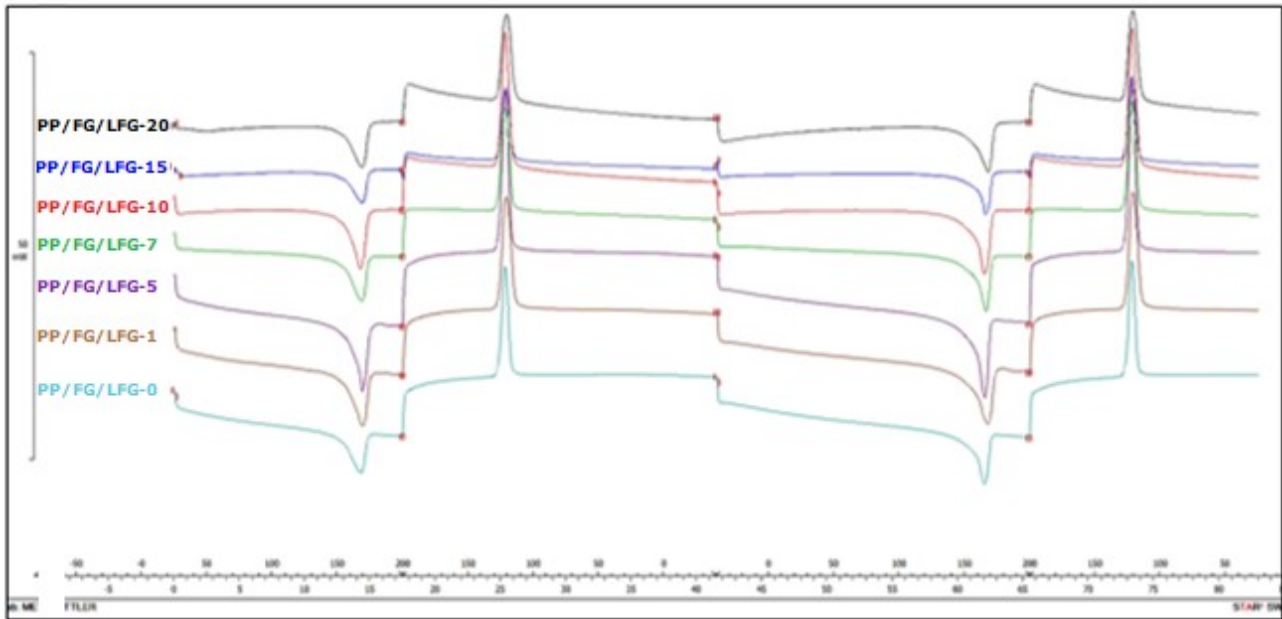


Figure 6: DSC thermograms of PP/FG/LFG composites.

During this process, the first peak gives melting temperatures, and the second peak refers to the crystallization temperature. Applying DSC analysis to all samples gives close melting and crystallization temperatures. Therefore, it is understood that the contributions of thermally converted wastes are at a standard level. These results are consistent with the literature. Lee et al. showed that crystallinity of the PP decreases with wood flour whereas it increases with clay and MAPP (33).

The percentage of crystallinity (X_c %) of a sample was calculated as follows Equation 1:

$$X_c (\%) = \left[\frac{\Delta H_f}{\Delta H_0} \right] \times 100 \quad (\text{Eq. 1})$$

where ΔH_f is the heat of fusion of PP/FG/LFG in a composite determined from the DSC thermogram, ΔH_0 is the heat of fusion of 100% crystalline PP/FG/LFG-X which equals 183.1 J/g, and $W\%$ is the weight percentage of PP/FG/LFG-X in the composite (34).

The melting temperature (T_m), crystallization temperature (T_c) and percentage of crystallinity (X_c %) of these recycled materials are listed in Table 4.

Table 4: Melting temperature, crystallization temperature and crystallinity of PP/FG/LFG composites.

Samples	T_m (°C)	T_c (°C)	X_c (%)
PP/FG/LFG-0	155.26	129.00	28.265
PP/FG/LFG-1	158.36	129.03	28.829
PP/FG/LFG-5	156.48	128.17	28.487
PP/FG/LFG-7	157.79	128.71	28.725
PP/FG/LFG-10	157.89	128.63	28.743
PP/FG/LFG-15	159.01	128.25	28.947
PP/FG/LFG-20	156.05	128.18	28.408

3.3. The Morphology of PP/FG/LFG Composites

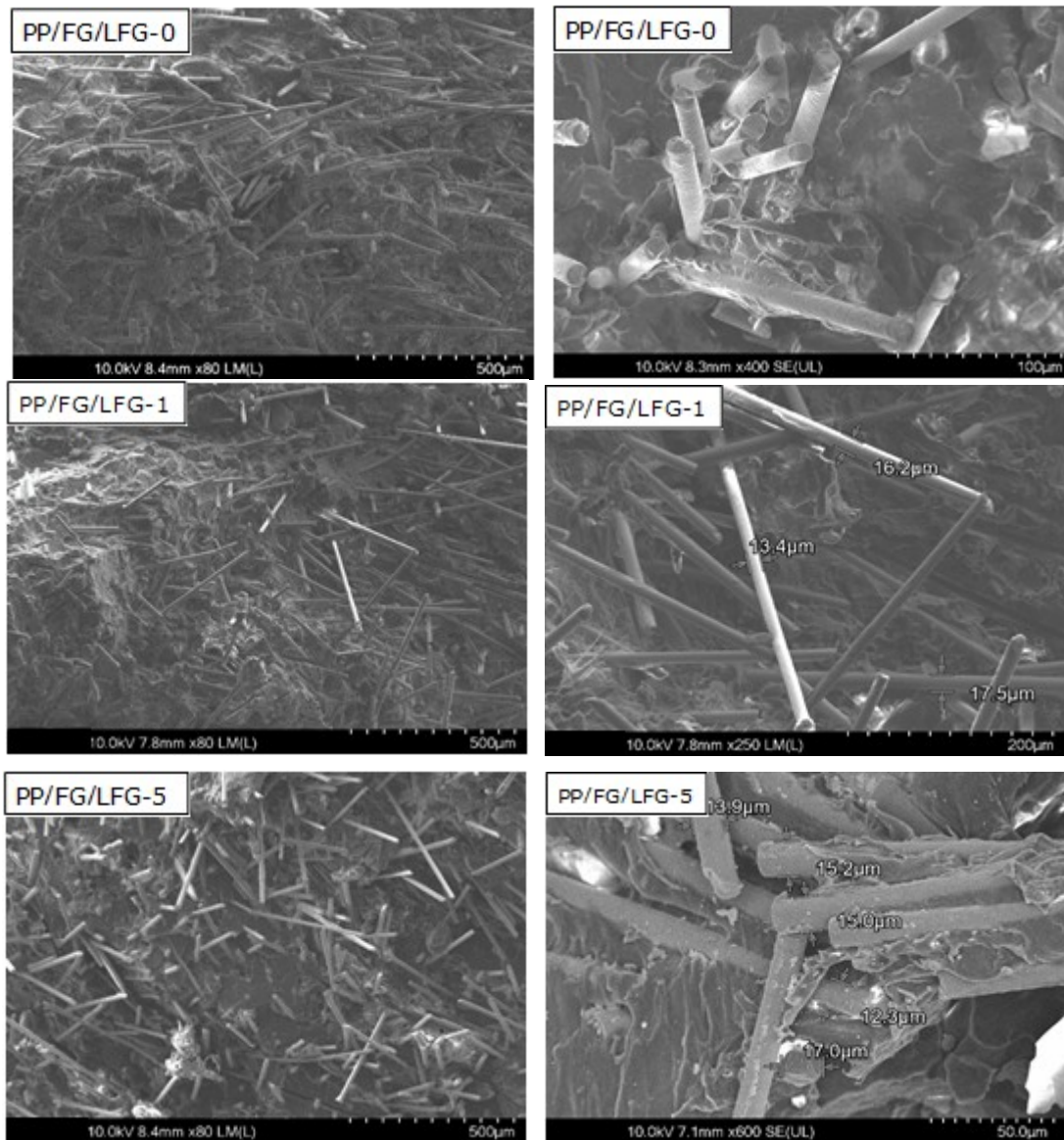
Figure 7 shows the SEM micrographs of all sets and these images were taken from the samples subjected to Izod impact test. The SEM images show the properties of adhesion, orientation, and separation after impact. Good fiber dispersion is observed for all compounds. The images in the left column show the remote views of the samples. In

the right column, the images were taken closer and the fiber diameters were measured in order to reveal the diameter difference.

For the PP/FG/LFG-0 sample, no diameter difference was observed because there was no long fiber coming from the waste composite additive. The presence of long fibers in the PP/FG/LFG-1 sample is

seen by the measuring fiber diameter. As can be seen from SEM images, both short fibers with a diameter of 13.5 μm and long fibers with a diameter of 18.2 μm are found in PP/FG/LFG composite structures. In the PP/FG/LFG-5 sample, it is understood that the matrix and the supplements adhere well. In the PP/FG/LFG-7 sample, it is observed that the orientation of the glass fibers varies. It was determined that PP/FG/LFG-10 had good adhesion with the matrix on long fibers as seen in the close image. The PP/FG/LFG-20 sample

has proven to be capable of separating the fiber from the matrix by impact. With the SEM analysis, the increase in the amount of waste and the increase in the amount of long fibers are proved by observing the fiber diameter data. With this analysis, it is seen that the part which is mechanically recycled in adhesion also adheres like pure products. It is observed that after the rupture process the fibers can break or come out at the break points.



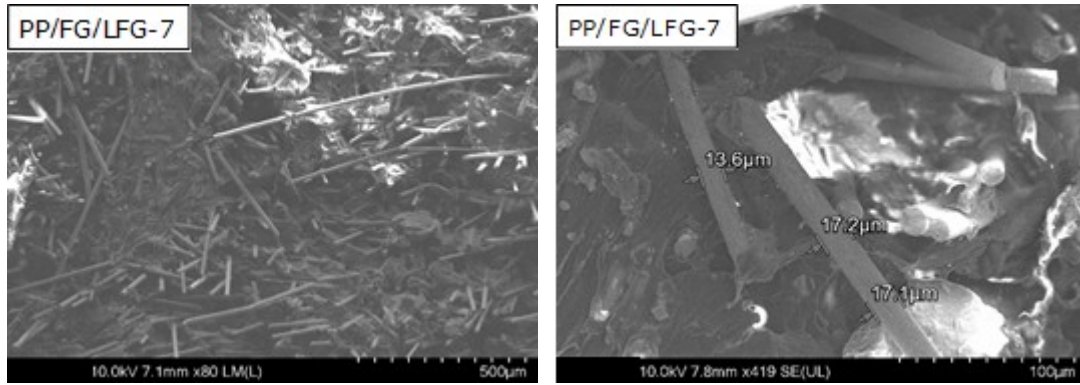


Figure 7: SEM micrographs of fracture surface of PP/FG/LFG composites.

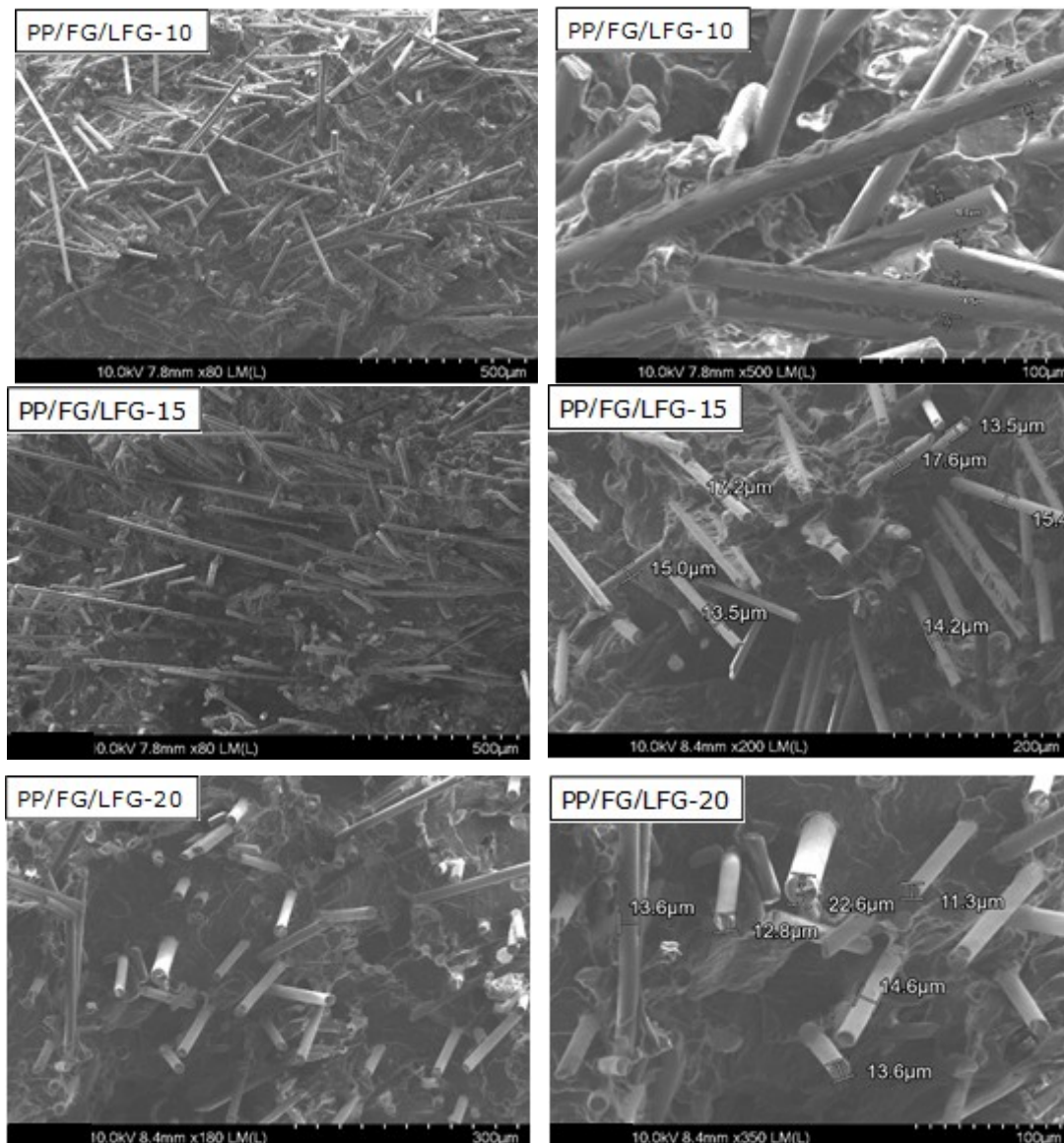


Figure 7 (contd): SEM micrographs of fracture surface of PP/FG/LFG composites.

As a result of the mechanical test results and SEM images, it can be said that the tensile behavior of PP

composites prepared with discontinuous glass fiber depends on the fiber length and the fiber orientation

according to the loaded direction by looking at the distribution of the fibers in the composite material.

4. CONCLUSION

In this study, it is aimed that recycling of waste polypropylene composites with long fibers obtained from battery covers of trucks. Since long fiber products are new and superior technology, long fiber reinforced waste PP/LFG composite recycled with mechanically is added to short fiber reinforced PP/FG composite in this work. The thermal, mechanical and morphological properties of composites were presented and discussed. As a result of the characterization tests performed on the PP/FG/LFG composites prepared with recycled waste PP/LFG, it was reasoned that the waste PP composite contribution to PP/FG composite structure could be optimum amount of 10%. Also, the SEM micrographs revealed that the adhesion and bonding limits between the fibers and the matrix were exceeded as fiber pull out and interfacial delamination were observed. As a result of mechanical tests, it can be said that the increasing in the fiber diameter decreases the strength values of prepared PP/FG/LFG composite with more than 10% of waste PP with long fibers. As for the thermal properties, for the all contents of the recycled waste PP/LFG composite, the short and long glass fibers in PP composite structures had no effect on the crystallinity of PP matrix. Based on the experimental results, it can be concluded that recycled long fiber reinforced PP composites have great potential to replace traditional PP composite used in various applications.

5. ACKNOWLEDGMENTS

The authors would like to thank Şişecam Inc. who supported the work reported in this paper and İsmail Oral, laboratory technician, for support and assistance in technical applications.

6. REFERENCES

- Günaydın E. Polimer matriksli karbon nanotüp-cam elyaf takviyeli kompozitlerde çarpma sonrası basma özelliklerinin incelenmesi [MSc Thesis]. [Samsun]: Ondokuz Mayıs University; 2018. [<URL>](#)
- Gügül H. Karbon Nanotüp Ve Cam Elyaf Takviyeli Yüksek Yoğunluklu Polietilen Hibrit Kompozit Malzemelerin Mekanik Özelliklerinin İncelenmesi [MSc Thesis]. [İskenderun]: İskenderun Technical University; 2018. [<URL>](#)
- Sabancı Ş. Fiber Takviyeli Polimer Matriksli Kompozitlerin Enjeksiyon Yöntemi İle Üretimi [MSc Thesis]. [İstanbul]: Yıldız Technical University; 2005. [<URL>](#)
- Moritzer E., Heiderich G. Mechanical recycling of continuous fiber-reinforced thermoplastic sheets. Proceedings of PPS-31. AIP Conf. Proc. 2016 Mar; 1713(1):120013-1-5. [<DOI>](#)
- Ünal E. Cam Elyafli Kompozit Malzemelerin Atmosferik Ortamda Ve Deniz Ortamında Yorulma Simülasyonu [MSc Thesis]. [İzmir]: Ege University; 2006. [<URL>](#)
- Kandaş H. Farklı Ön Gerilme Yüklerinde Cam Elyaf Takviyeli Polipropilen Kompozitlerin Düşük Hızlı Darbe Davranışı [MSc Thesis]. [İzmir]: Dokuz Eylül University; 2018. [<URL>](#)
- Liu D, Ding J, Fan X, Lin X, Zhu Y. Non-isothermal forming of glass fiber/polypropylene commingled yarn fabric composites. Materials and Design. 2014 Jan; 57:608-15. [<DOI>](#)
- Kim HS, Lee BH, Choi SW, Kim S, Kim HJ. The effect of types of maleic anhydride-grafted polypropylene (MAPP) on the interfacial adhesion properties of bio-flour-filled polypropylene composites. Composites: Part A. 2007 Jan; 38(6):1473-82. [<DOI>](#)
- Gill, R. M. Carbon fibres in composite materials. London: Iliffe Books for the Plastics Institute. 1972. ISBN 13: 978-0-5920-0069-5.
- Hassan, A., Rahman, N. A., & Yahya, R. Extrusion and injection-molding of glass fiber/MAPP/polypropylene: effect of coupling agent on DSC, DMA and mechanical properties. Journal of Reinforced Plastics and Composites, 2011 Sep; 30(14):1223-1232. [<DOI>](#)
- Fu, S. Y., Feng, X. Q., Lauke, B., & Mai, Y. W. Effects of particle size, particle/matrix interface adhesion and particle loading on mechanical properties of particulate-polymer composites. Composites. Part B, Engineering. 2008 Sep; 39(6):933-961. [<DOI>](#)
- Han, L., Wang, H., Lang, X., Wang, X., Zong, Y., Zong, C. Preparation of graphene/ polypropylene composite with high dielectric constant and low dielectric loss via constructing a segregated graphene network. Royal Society of Chemistry. 2021 Nov; 11:38264-38272. [<DOI>](#)
- Awad, S.A., Khalaf, E.M. Investigation of improvement of properties of polypropylene modified by nano silica composites. Composites Communications. 2019 Apr; 12:59-63. [<DOI>](#)
- Kufel, A., Para, S., Kuciel, S. Basalt/Glass fiber polypropylene hybrid composites: mechanical properties at different temperatures and under cyclic loading and micromechanical modelling. Materials. 2021 Sep; 14:5574-5591. [<DOI>](#)
- Schwartz, M. Composite materials handbook. 2nd ed. New York: McGraw-Hill; 1992. ISBN-13: 978-0-0705-5743-7.

16. Shinzawa, H., Itasaka, H. Glass fiber (GF)/polypropylene (PP) composite studied by Raman disrelation mapping. *Spectrochimica Acta Part A: Molecular and Biomolecular Spectroscopy*. 2022 May; 273:121056. [<DOI>](#).
17. Watanabe, R., Sugahara, A., Hagihara, H., Mizukado, J., Shinzawa, H. Insight into interfacial compatibilization of glass-fiber-reinforced polypropylene (PP) using maleic-anhydride modified PP employing infrared spectroscopic imaging. *Composites Science and Technology*. 2020 July; 199:108379. [<DOI>](#).
18. Liu, W., Zhu, Y., Qian, C., Dai, H., Fu, Y., Dong, Y. Interfacial modification between glass fiber and polypropylene using a novel waterborne amphiphilic sizing agent. *Composites Part B*. 2022 July; 241:110029. [<DOI>](#).
19. Zhou, P., Li, C., Bai, Y., Dong, S., Xian, G., Vedernikov, A., Akhatov, I., Safonov, A., Yue, Q. Durability study on the interlaminar shear behavior of glass-fibre reinforced polypropylene (GFRPP) bars for marine applications. *Construction and Building Materials*. 2022 Sep; 349:128694. [<DOI>](#).
20. Dong, S., Zhou, P., Guo, R., Li, C., Xian, G. Durability study of glass fiber reinforced polypropylene sheet under simulated seawater sea sand concrete environment. *Journal of Materials Research and Technology*. 2022 Sep; 20:1079-1092. [<DOI>](#).
21. Kabiri, A., Liaghat, G., Alavi, F. Biomechanical evaluation of glass fiber/polypropylene composite bone fracture fixation plates: Experimental and numerical analysis. *Computers in Biology and Medicine*. 2021 May; 132:104303. [<DOI>](#).
22. Şahin S. Sürekli Cam Elyaf Takviyeli Polipropilen Levhaların Şekillendirilmesi Ve Karakterizasyonu [MSc Thesis]. [İstanbul]: Marmara University; 2015. [<URL>](#).
23. Baydar DG, Bekem A, Doğu M, Gemici Z, Ünal A. Sürekli Cam Fiber Takviyeli Polipropilen Kompozitlerin Üretimi Ve Karakterizasyonu. *Sigma Journal of Engineering and Natural Sciences*. 2011 Dec; 30:120-132. [<URL>](#).
24. Naqvia SR, Prabhakaraa HM, Bramera EA, Dierkesa W, Akkerman R, Brema G. A critical review on recycling of end-of-life carbon fibre/glass fibre reinforced composites waste using pyrolysis towards a circular economy. *Resources, Conservation & Recycling*. 2018 Apr; 136:118-129. [<DOI>](#).
25. Medar MM. Geri Dönüştürülmüş Cam Elyaf Katkılı ve Katkısız Polipropilen-Polietilen Malzemelerin Mekanik ve Kimyasal Özelliklerinin İncelenmesi [MSc Thesis]. [Kocaeli]: Gebze Technical University; 2013. [<URL>](#).
26. Bajracharya RM, Manalo AC, Karunasena W, Lau K. An overview of mechanical properties and durability of glass-fibre reinforced recycled mixed plastic waste composites. *Materials and Design*. 2014 Oct; 62:98-112. [<DOI>](#).
27. Şentürk O. Kısa Cam Elyaf Ve Kalsit Dolgulu Polipropilen Hibrit Kompozitlerin Fiziksel Ve Mekanik Özelliklerinin İncelenmesi [MSc Thesis]. [İstanbul]: Istanbul Technical University; 2014. [<URL>](#).
28. Lila MK, Singhal A, Banwait SS, Singh I. A recyclability study of bagasse fiber reinforced polypropylene composites. *Polymer Degradation and Stability*. 2018 June; 152:272-79. [<DOI>](#).
29. Feih S, Mouritz AP, Case SW. Determining the mechanism controlling glass fibre strength loss during thermal recycling of waste composites. *Composites Part A: Applied Science and Manufacturing*. 2015 Sep; 76:255-61. [<DOI>](#).
30. Cousins DS, Suzuki Y, Murray RE, Samaniuk JR. Recycling glass fiber thermoplastic composites from wind turbine blades. *Journal of Cleaner Production*. 2019 Feb; 209:1252-63. [<DOI>](#).
31. Vaidya UK, Chawla KK. Processing of fibre reinforced thermoplastic composites. *International Materials Reviews*. 2013 Jul; 185-218. [<DOI>](#).
32. Chen, T., Mansfield, C.D., Ju, L., Baird, D.G. The influence of mechanical recycling on the properties of thermotropic liquid crystalline polymer and long glass fiber reinforced polypropylene. *Composite Part B*. 2020 Nov; 200: 108316. [<DOI>](#).
33. Lee SY, Kang IA, Doh GH, Kim WJ, Kim JS, Yoon HG, Wu QH. Thermal, mechanical and morphological properties of polypropylene/clay/wood flour nano composites. *Express Polymer Letters*. 2008 Mar; 2(2):894-9. [<DOI>](#).
34. Al-Maadeed MA, Shabana YM, Khanam PN. Processing, characterization and modeling of recycled polypropylene/glass fibre/wood flour composites. *Materials and Design*. 2014 June; 58:374-380. [<DOI>](#).
35. Choi, E.Y., Kim, C.K., Park, C.B. Fabrication of MA-EPDM grafted MWCNTs by reactive extrusion for enhanced interfacial adhesion and mechanical properties of PP/ MA-EPDM composite. *Composites Part B*. 2022 Aug; 242:110043. [<DOI>](#).
36. Pourali, M., Peterson, A.M. The effects of toolpath and glass fiber reinforcement on bond strength and dimensional accuracy in material extrusion of a hot melt adhesive. *Additive Manufacturing*. 202258 Oct; 58:103056. [<DOI>](#).



Effect of Nd³⁺ Doping on Structural, Near-Infrared, and Cathodoluminescent Properties for Cadmium Tantalate Phosphors

Lütfiye Feray Gülyüz* 

*Department of Mechanical Engineering, Ege University, Bornova, 35040, İzmir, Turkey

Abstract: Cd_{1-x}Ta₂O₆:xNd³⁺ (x=0.5, 1.5, 3, 5, 7, and 10 mol%) phosphor series were fabricated by conventional solid state method at 1100 °C for 17 hours. The samples of cadmium tantalate were investigated by structural (XRD, SEM) and spectroscopic (CL, PL) analyses. In XRD results, the symmetry of CdTa₂O₆ phase with orthorhombic columbite structure was confirmed between 0.5 and 10 mol% Nd³⁺ doping concentrations. SEM analysis of the grains revealed round and shapeless morphology while grain sizes ranged from submicron to several microns. The emission spectra of Cd_{1-x}Ta₂O₆:xNd³⁺ (x=0.5, 1.5, 3, 5, 7 and 10 mol%) phosphor series recorded with the transitions of ⁴F_{3/2}→⁴I_{9/2} and ⁴F_{3/2}→⁴I_{11/2}. Among these transitions, the transition ⁴F_{3/2}→⁴I_{9/2} (at 889 nm) has a high near-infrared emission intensity, which can be attributed to the laser potential of the phosphor. The NIR emission of the phosphor increased with increasing concentration of Nd³⁺ up to 5 mol% and then declined because of concentration quenching phenomenon. The CL emission peak at about 450 nm found in all samples is related to the intrinsic emission of the cadmium tantalate host. In addition, Nd³⁺ doped phosphors exhibited the ⁴F_{3/2}→⁴I_{9/2} transition of Nd³⁺ and defect-related CL emissions at 670 nm. Decreasing crystallinity with increasing Nd³⁺ concentration caused a decrease in host emission intensity at 450 nm.

Keywords: CdTa₂O₆; Cathodoluminescence; Nd³⁺; Near infrared luminescence.

Submitted: November 10, 2022. Accepted: December 29, 2022.

Cite this: Gülyüz LF. Effect of Nd³⁺ Doping on Structural, Near-Infrared, and Cathodoluminescent Properties for Cadmium Tantalate Phosphors. JOTCSA. 2023;10(1):77-88.

DOI: <https://doi.org/10.18596/jotcsa.1202284>.

*Corresponding author. E-mail: ferayguleryuz@hotmail.com

INTRODUCTION

The phosphors, which are doped with the rare-earth (RE) ions, have some convenient features such as remarkable efficiency, long lifetime, energy saving, enhanced physical robustness, kindly to environment properties, smaller size and faster switching (1-22). Among RE³⁺ (trivalent) ions, Nd (neodymium) is one of the earliest RE³⁺ ions used in solid-state lasers. Therefore, Nd³⁺ activated materials are well-known as solid-state phosphors due to their laser emissions at beneficial wavelengths such

as ⁴F_{3/2}→⁴I_{9/2} transition and also the other possible transitions ⁴F_{3/2}→⁴I_{15/2}, ⁴F_{3/2}→⁴I_{13/2} and ⁴F_{3/2}→⁴I_{11/2} (15-22). Among the ⁴F_{3/2}→⁴I_j transitions of Nd³⁺ ion, the ⁴F_{3/2}→⁴I_{9/2} transition at 880 nm finds application as a powerful diode laser transition. The ⁴F_{3/2}→⁴I_{11/2} transition stands out due to its ability to be easily operated at room temperature and pumped efficiently by flash lamp. The lasing transition at 1350 nm (⁴F_{3/2}→⁴I_{13/2}) is finding application as telecommunication transition window (22). The cathodoluminescence (CL) produced in the UV-visible-NIR system of the electromagnetic

spectrum is due to the interaction of the material with the electron beam, where optical characterization is performed by means of the cathode rays (fast electrons) provided by an electron gun and the luminescence (light emission) formed. The CL analysis can be interpreted via spectral lines that are similar to those from other luminescence techniques, and characteristically dominate the spectrum with bound excitonic states and changes from emission lines, donor-acceptor double bands, and defect-related properties (23-27).

The ternary oxides of general formula AB_2O_6 ($A=M^{2+}$, $B=Nb^{5+}$, Ta^{5+}) crystallize in the columbite structure. The cations of A and B are located in the center of the octahedra surrounded by six oxygen atoms while the AO_6 and BO_6 octahedra share the edges, forming independent zigzag chains. This sequential situation repeats as ABBABB octahedral layers as the chains are connected by sharing corners in order to the AO_6 chain- BO_6 chain- BO_6 chain (5-11). $CdTa_2O_6$, as an AB_2O_6 oxide structure, has been studied in the literature in terms of its luminescence and thermodynamic properties. The white-light properties of Dy^{3+} doped $CdTa_2O_6$, and the PL-RL properties of Eu^{3+} doped $CdTa_2O_6$ have been reported by (7) and, (8) respectively. The molar heat capacity of $CdTa_2O_6$ has been reported as $179.65 \text{ J mol}^{-1} \text{ K}^{-1}$, at ambient temperature (28). In addition, cadmium-containing phosphor materials are attracting attention in the field of optics as a new material class due to their broad potential applications such as solar cells, biosensors, biomedical scanning, and light-emitting diodes (LEDs) (29-33). The inherent toxicity of cadmium limits its applications, especially in the industrial and biomedical fields, so the genotoxicity and cytotoxicity of $CdSe/ZnS$ (cadmium selenide/Zinc sulfide) core/shell QDs for applications in cancer therapy have been discussed (34). However, cadmium-based phosphors provide a high level of brightness, leading to a reduction in the need for high levels of X-ray doses, which can minimize the risk of health problems (29,35).

In the study, NIR photoluminescence and cathodoluminescence of $Cd_{1-x}Ta_2O_6:xNd^{3+}$ ($x=0.5, 1.5, 3, 5, 7, 10 \text{ mol}\%$) phosphors were studied. The spectroscopic and structural characterizations of the samples were carried out by XRD, SEM-EDS, FTIR, PL, and CL analyses.

EXPERIMENTAL SECTION

Undoped and $Cd_{1-x}Ta_2O_6:xNd^{3+}$ ($0.005 \leq x \leq 0.1$ or $0.5 \leq x \leq 10 \text{ mol}\%$) materials were fabricated using solid state reaction. Nd_2O_3 (Alfa Aesar, 99.9%) was used as a dopant. $Cd(NO_3)_2 \cdot 4H_2O$ (Sigma-Aldrich, 99%) and Ta_2O_5 (Alfa Aesar, 99.9%) powders were used as starting materials. The powders of $Cd(NO_3)_2 \cdot 4H_2O$, Ta_2O_5 and Nd_2O_3 were prepared and homogenized in agate mortar according to stoichiometry of $Cd_{1-x}Ta_2O_6:xNd^{3+}$ where $CdTa_2O_6$ ($x=0$), $Cd_{0.995}Nd_{0.005}Ta_2O_6$ ($x=0.005$), $Cd_{0.985}Nd_{0.015}Ta_2O_6$ ($x=0.015$), $Cd_{0.97}Nd_{0.03}Ta_2O_6$ ($x=0.03$), $Cd_{0.95}Nd_{0.05}Ta_2O_6$ ($x=0.05$), $Cd_{0.93}Nd_{0.07}Ta_2O_6$ ($x=0.07$), $Cd_{0.90}Nd_{0.10}Ta_2O_6$ ($x=0.1$), respectively. Prepared powders were sintered at $1100 \text{ }^\circ\text{C}$ for 17 hours in an electric furnace under air atmosphere after pelleting.

The phase structure of the ceramics were performed by X-ray diffraction (D-MAX 2200, Rigaku Corp., Japan) using $Cu-K_\alpha$ radiation, Ni filter, scan rate = $2 \text{ }^\circ/\text{min}$, and $2\theta=20-65^\circ$. The grain morphology and elemental identification of the ceramic samples were carried out by SEM (JSM-5910LV, JEOL Ltd., Japan) equipped with EDS (INCAx-Sight 7274, Oxford Industries, UK) after Au/Pd (gold/palladium) coating. FTIR (fourier transform infrared spectrometer) spectra were taken by Perkin-Elmer ATR-FTIR. Near emission spectra of powders were measured in the range of 850-1450 nm using a diode laser of 800 nm excitation at 300 K. Cathodoluminescence (CL) spectra were performed with a monochromatic spectrometer (DATAN-Mono CL4) attached to an electron microscope (NOVA-NANOSEM 650) with an emission gun (working distance 6.6 mm, voltage 15 kV, spot size 3.5) in high vacuum. Besides CL imaging, the spectrometer allows acquisition of CL spectra at highly localized points of a sample.

RESULTS AND DISCUSSION

Structural and Morphological Characterization

Figure 1 shows the XRD results of undoped sample and $Cd_{1-x}Ta_2O_6:xNd^{3+}$ ($x=0.5, 1.5, 3, 5, 7$ and $10 \text{ mol}\%$) samples. The XRD patterns of the samples (JCPDS card No.39-1431) can be indexed space group *Pbcn*. As seen in the XRD patterns of all the samples, there are no different minor phases in the range of two theta degree (for 20° and 65°). The cell parameters of $CdTa_2O_6$ structure are $a=5.8510 \text{ \AA}$, $b=14.7847 \text{ \AA}$, $c=5.1462 \text{ \AA}$, and $V=445.17 \text{ \AA}^3$ (36). The orthorhombic structure of $CdTa_2O_6$ along the c-

axis has been illustrated in Figure 2. Octahedra with the same central cation share edges forming zigzag chains along the c-axis while TaO₆ octahedra of adjacent chains share corners to form double layers, parallel to the bc-plane, which are connected via CdO₆ octahedra through common corners (37). On the basis of the ion radius and coordination number (CN), the formation of the single-phase can be attributed to the substitution of Nd³⁺ ions with ionic radius 0.983 Å (for 6 C.N) by Cd²⁺ ions ($r=0.95$ Å, for C.N. 6). Figure 3 shows the XRD peaks of the (131) reflection. As seen in the XRD peaks, there was a slight shift towards smaller two theta angles due to the increase in Nd³⁺ concentration. This may be attributed to the expansion of the lattice volume due to the slightly large ionic radius of the Nd³⁺ ion, where the Nd³⁺ substitution instead of Cd²⁺ is also likely to affect the charge balance and form

some stress in the structure, albeit limited. However, despite some expansion in the lattice volume, the existence of the single-phase structure was preserved up to 10 mol% concentration, indicating that the dopant ion has located into the structure successfully.

SEM micrographs at 10.000x magnification of undoped and 0.5, 3, and 10 mol% Nd³⁺ doped samples are shown in Figure 4(a-d). The grain shapes of Nd³⁺ doped samples have elliptical shapes and a shapeless morphology, while the grain sizes varied from 0.5 to 3.5 μm. Figure 5 shows the EDS spectra and elemental compositions of (weight%, atomic%) and theoretical atomic (%) values for Cd_{1-x}Ta₂O₆:Nd³⁺ grains were detected by EDS at 20 kV of SEM acceleration voltage, where atomic (%) compositions are compatible with theoretical atomic (%) values.

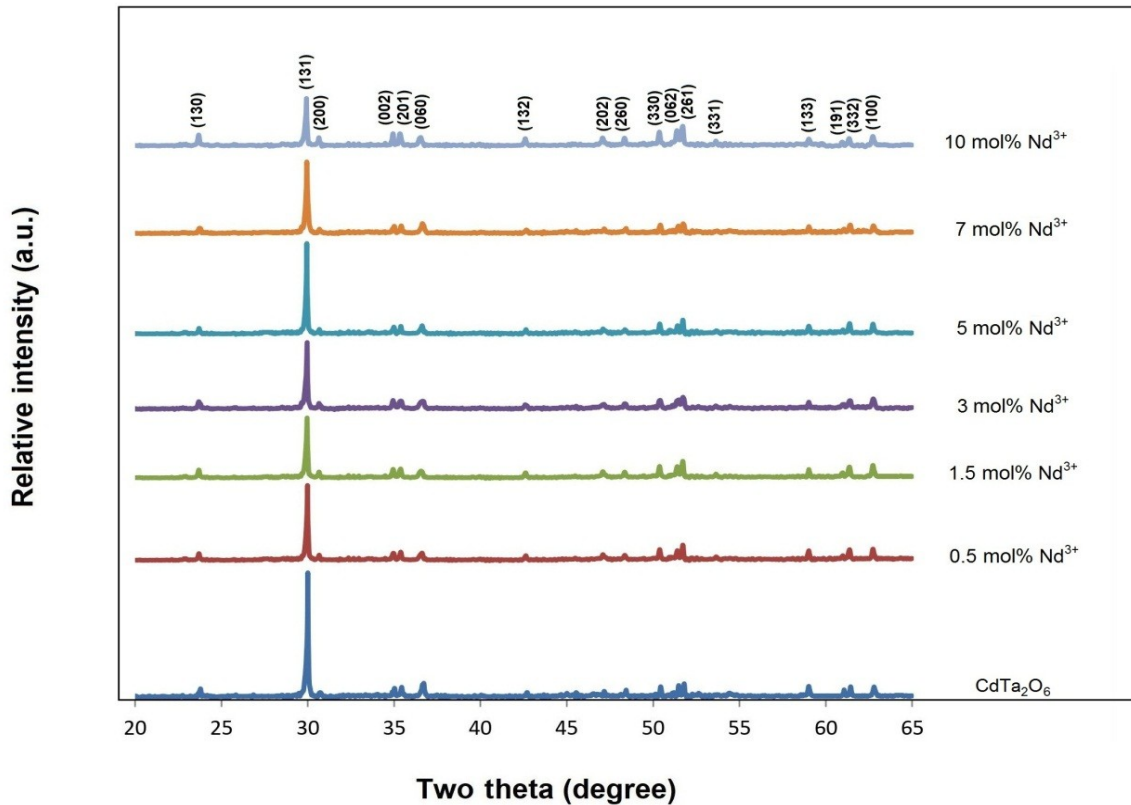


Figure 1: XRD results of undoped and Cd_{1-x}Ta₂O₆:xNd³⁺ (x=0.5, 1.5, 3, 5, 7, and 10 mol%) samples.

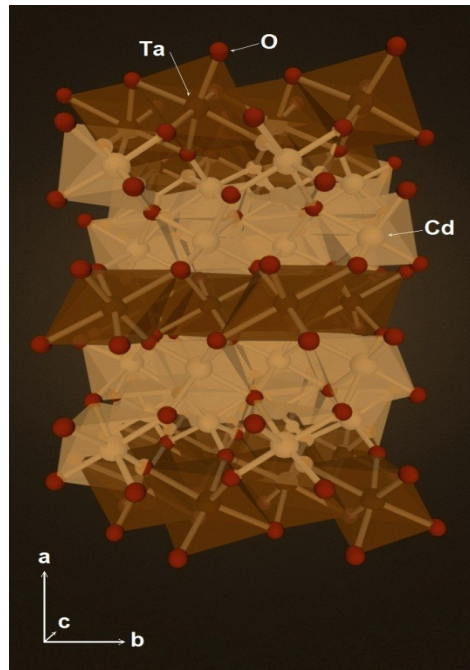


Figure 2: Schematic illustration of the CdTa_2O_6 crystal in the direction of the c axis.

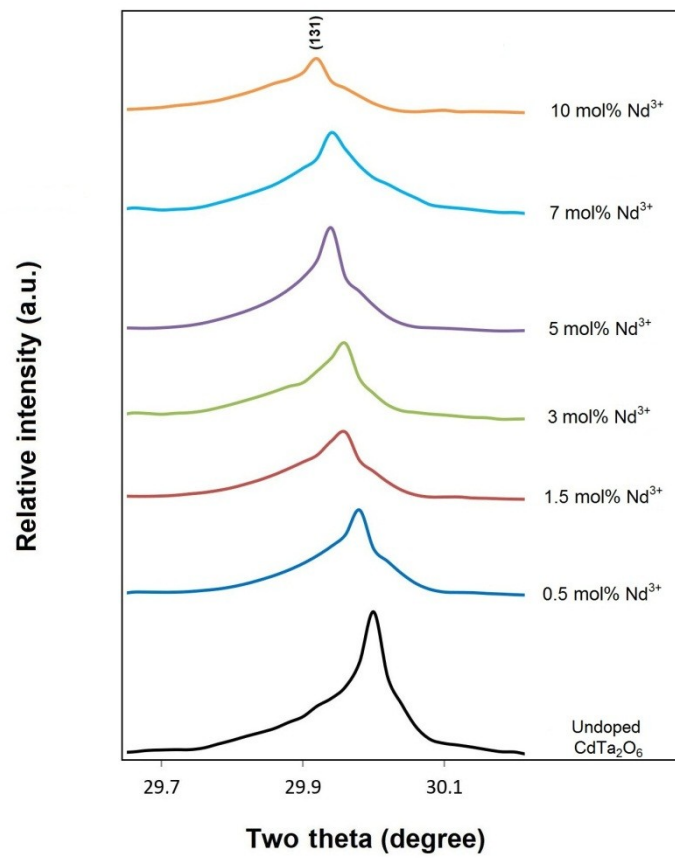


Figure 3: XRD two theta angles (131) shifted to lower angles with Nd^{3+} concentration.

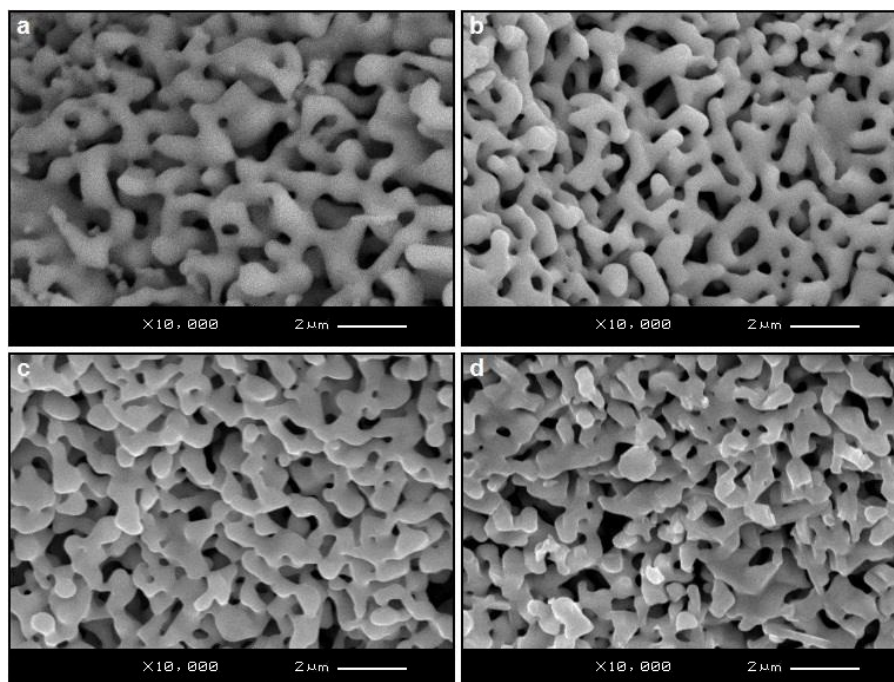


Figure 4: SEM micrographs of (a) undoped and (b) 0.5, (c) 3, (d) 10 mol% Nd³⁺ doped samples at 20 kV acceleration voltage, and 10.000× magnification.

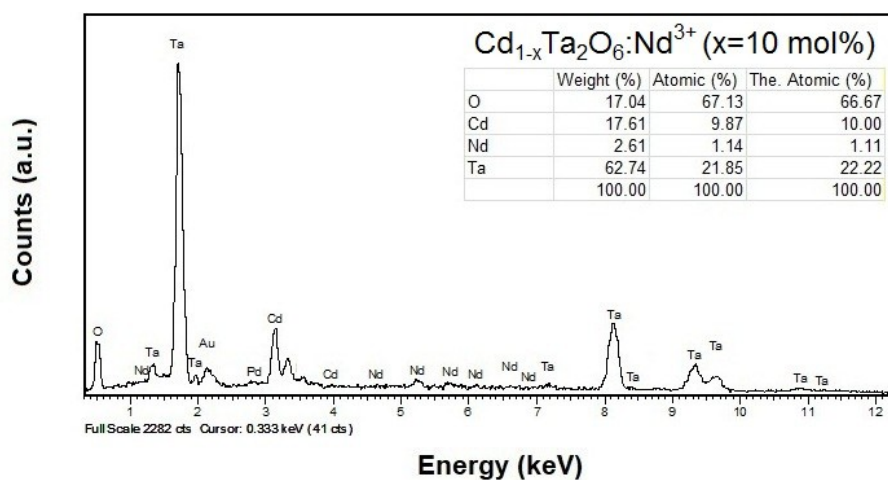


Figure 5: EDS spectrum and compositions (wt%, at%) and theoretical at% values for 10 mol% Nd³⁺ doped sample.

FTIR Analysis

FTIR spectra of undoped sample and Cd_{1-x}Ta₂O₆:xNd³⁺ (x=1.5, 5 and 10 mol%) samples in the range of 500–4000 cm⁻¹ are presented in Figure 6. The molecular structure of the metal oxides with IR spectroscopy can be detected from M=O vibrations in the 500–1000 cm⁻¹ while

the peaks of 2800–4000 cm⁻¹ shows the fundamental stretching of OH groups (38). FTIR peaks of 800–1000 cm⁻¹ can be associated with the Ta–O bond vibrations while the small peaks in between 1000–1500 cm⁻¹ are due to Cd–O–Ta vibrations.

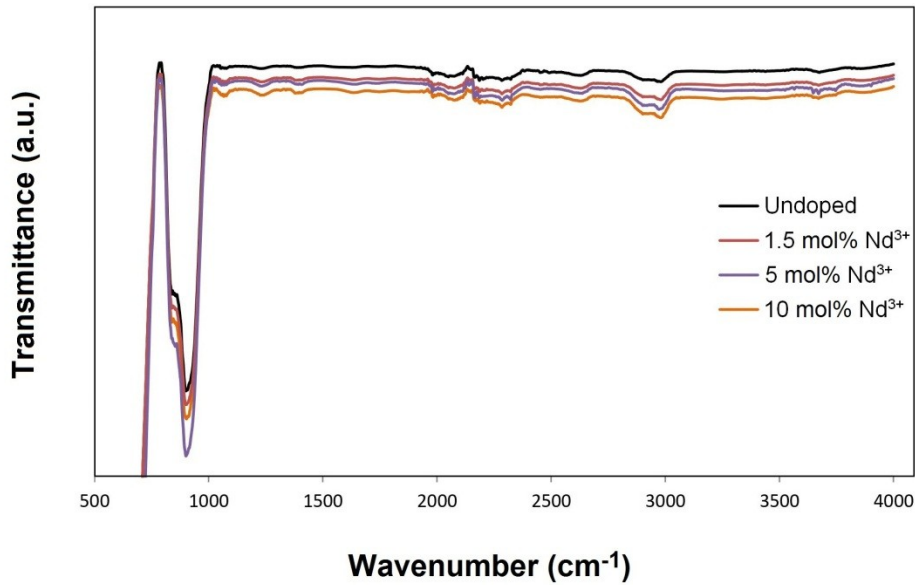


Figure 6: FTIR spectra of undoped and $\text{Cd}_{1-x}\text{Ta}_2\text{O}_6:\text{xNd}^{3+}$ ($x=1.5, 5, 10$ mol%) samples.

NIR luminescence of $\text{Cd}_{1-x}\text{Ta}_2\text{O}_6:\text{xNd}^{3+}$ ($x=0.5, 1.5, 3, 5, 7$ and 10 mol%) phosphors

Figure 7 shows the NIR emission spectra of $\text{Cd}_{1-x}\text{Ta}_2\text{O}_6:\text{xNd}^{3+}$ ($x=0.5, 1.5, 3, 5, 7, 10$ mol%) phosphors were used a laser diode with excitation source 800 nm. The emissions of the phosphors were monitored corresponding to the ${}^4\text{F}_{3/2}\rightarrow{}^4\text{I}_{9/2}$ and ${}^4\text{F}_{3/2}\rightarrow{}^4\text{I}_{11/2}$ transitions at 889 and 1073, respectively. The ${}^4\text{F}_{3/2}\rightarrow{}^4\text{I}_{9/2}$ transition (at 889 nm) is a potential laser transition that appears to be more intense than the ${}^4\text{F}_{3/2}\rightarrow{}^4\text{I}_{11/2}$. Although the overall energy level of the 4f electrons of the Nd^{3+} ion protected by the outer shell $5s^2$ and $5p^6$ electrons does not vary greatly in different hosts, the energy level surrounding the Nd^{3+} ions can be subdivided into $2J+1$ sublevels by the local crystal field (39). As seen in Figure 7, there are many splits resulting from the ${}^4\text{F}_{3/2}\rightarrow{}^4\text{I}_{9/2}$ transition with the highest emission peak in the 860–940 nm range, while the ${}^4\text{F}_{3/2}\rightarrow{}^4\text{I}_{11/2}$ transition exhibits emission around 1070 nm. The Stark components of both transitions of Nd^{3+} ions are similar, which can be associated with the similarity of local symmetry of ligand ions surrounding the Nd^{3+} ion (19–21). The near infrared emission of the phosphor rose up to 5 mol%, and emission declined at 7 and 10 mol% concentrations. The decrease in PL density may be associated with higher Nd^{3+} concentrations (or beyond 5% mol), which promotes the migration of excitation energy between active ions (22,40). As Nd^{3+} concentration continues to increase, cross-

relaxation mechanism between Nd^{3+} - Nd^{3+} ions becomes more and more important, and therefore non-radiation transitions will be more likely to occur due to the nearness between the Nd^{3+} ions (17).

Cathodoluminescence of undoped and $\text{Cd}_{1-x}\text{Ta}_2\text{O}_6:\text{xNd}^{3+}$ ($x=1.5, 5, \text{ and } 10$ mol %) phosphors

Figure 8 shows the cathodoluminescence spectra of undoped sample and $\text{Cd}_{1-x}\text{Ta}_2\text{O}_6:\text{xNd}^{3+}$ ($x=1.5, 5, \text{ and } 10$ mol%) phosphors. In CL emissions, the peak at about 450 nm is related to the intrinsic emission of the polycrystal host, and is present in all samples (41,42). For the similar compound, orthorhombic columbite CdNb_2O_6 , the host emission has been reported as 460 nm (43,44). Accordingly, the CL host emission of CdTa_2O_6 observed at 450 nm is consistent with the PL host emission of CdNb_2O_6 . On the other hand, the undoped sample has the highest host emission intensity, while the intrinsic emission intensity of Nd^{3+} doped samples at 450 nm decreases with increasing concentration. This is due to the inclusion of Nd^{3+} ion in the lattice affected the crystallinity (45). As seen from the CL spectra, 10 mol% Nd^{3+} doped phosphor has lowest intrinsic emission intensity, which can be attributed to the fact that Nd^{3+} doping causes the most distortion (or the highest effect on crystallization) at this concentration. The emission peak of Nd^{3+} doped phosphors at about 670 nm (red emission) show a red

emission which is associated with the defect related to deep emission (45,46), the recombination of electrons in the non-bridging oxygen band-gap state with holes in the valence band edge (47,48). The final luminescence peak of 900 nm indicates neodymium emission from the 4f shell transition of Nd^{3+} ions corresponding to the ground state ($4I_{9/2}$) from the excited state ($4F_{3/2}$) in the host lattice (49).

CL micrographs of undoped sample and $\text{Cd}_{1-x}\text{Ta}_2\text{O}_6:\text{xNd}^{3+}$ ($x=1.5, 5, 10$ mol%) phosphors are shown in Figure 9(a-d). In CL micrographs, the undoped sample has a blue emission appearance due to the 450 nm peak (as mentioned earlier), while the doped samples show blue-red-blue emissions due to the 450 and 670 nm peaks.

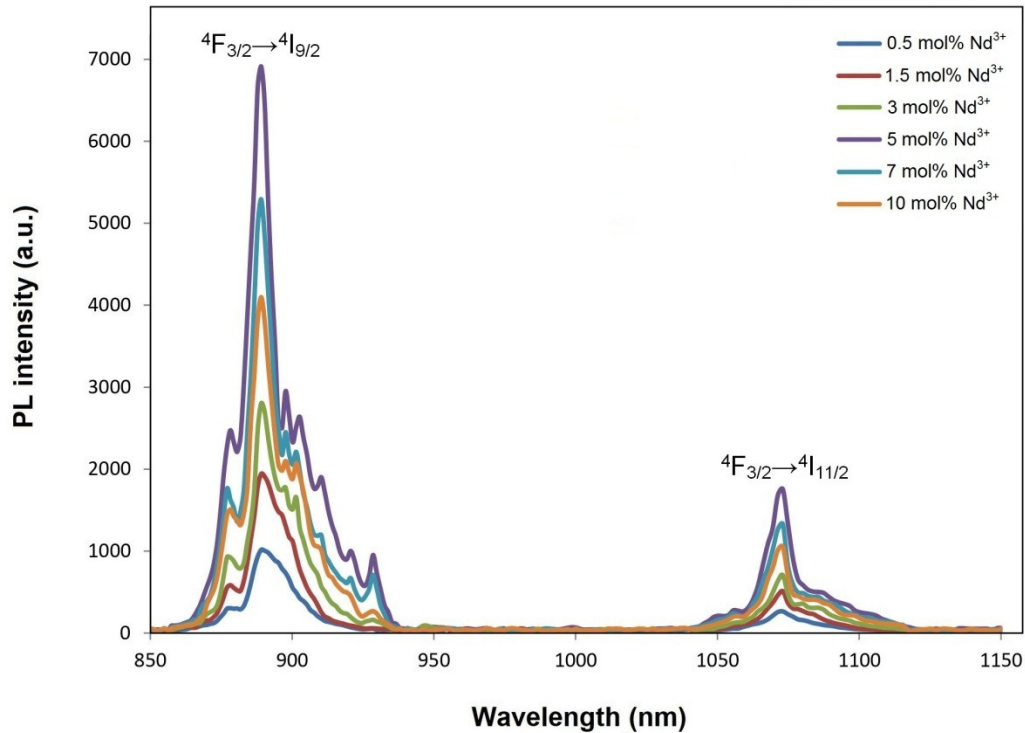


Figure 7: Near-infrared emission spectra of $\text{Cd}_{1-x}\text{Ta}_2\text{O}_6:\text{xNd}^{3+}$ ($x=0.5, 1.5, 3, 5, 7,$ and 10 mol%) phosphors by diode laser under 800 nm excitation.

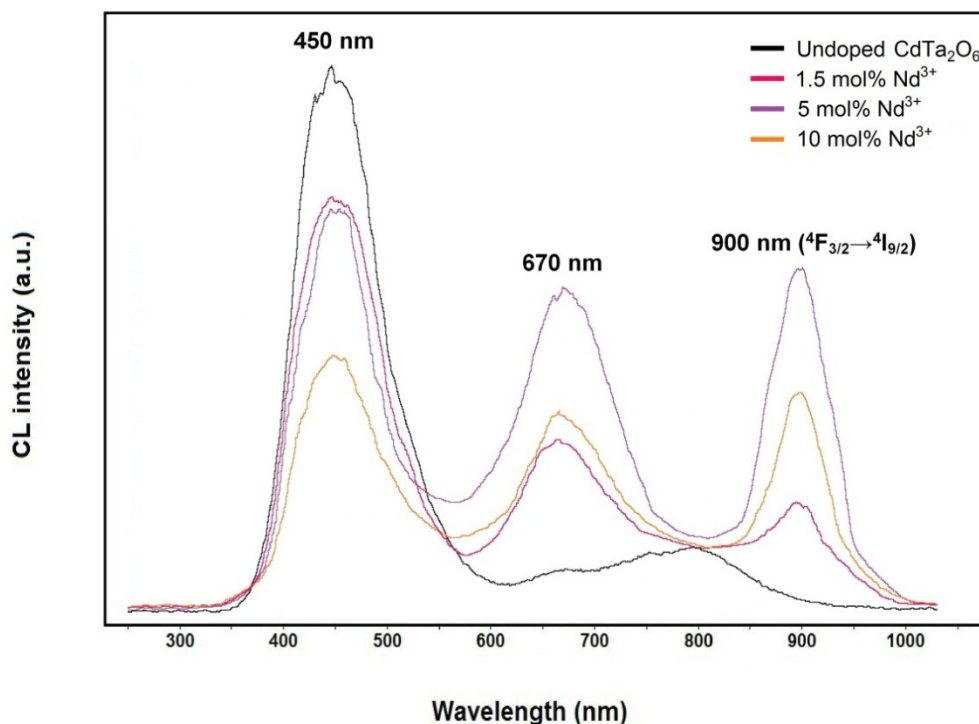


Figure 8: CL emission spectra of undoped CdTa_2O_6 , and $\text{Cd}_{1-x}\text{Ta}_2\text{O}_6:x\text{Nd}^{3+}$ ($x=1.5, 5,$ and 10 mol%) phosphors.

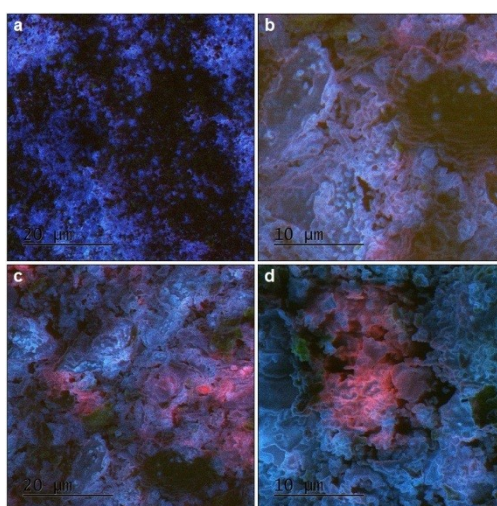


Figure 9: CL micrographs for (a) undoped sample, and (b) 1.5, (c) 5, (d) 10 mol% Nd^{3+} doped cadmium tantalate phosphors.

CONCLUSION

$\text{Cd}_{1-x}\text{Ta}_2\text{O}_6:x\text{Nd}^{3+}$ ($x=0.5, 1.5, 3, 5, 7$ and 10 mol %) phosphors were fabricated by solid state method. XRD results indicated the presence of

the single phase Nd^{3+} concentrations from 0.5 to 10 mol%. SEM examinations revealed the shapeless/rounded grain morphology with the sizes of 0.5 - 3.5 micron while EDS identified elemental compositions of the grains. The NIR

emissions of the phosphors monitored with the transitions of ${}^4F_{3/2} \rightarrow {}^4I_{9/2}$ (889 nm) and ${}^4F_{3/2} \rightarrow {}^4I_{11/2}$ (1073 nm), where the ${}^4F_{3/2} \rightarrow {}^4I_{9/2}$ transition is a potential laser transition that appears to be more intense than the ${}^4F_{3/2} \rightarrow {}^4I_{11/2}$. The CL emission of undoped sample was observed with the peak of 450 nm, in which the decreased CL intensity of the phosphors is related to the effect of crystallinity. Nd^{3+} -doped phosphors exhibited the 900 nm peak due to the ${}^4F_{3/2} \rightarrow {}^4I_{9/2}$ transition, as well as the 450 and 670 nm peaks of structural origin. Based on the observed results, it could be concluded that the $\text{Cd}_{1-x}\text{Ta}_2\text{O}_6:\text{Nd}^{3+}$ phosphor with the strong transition of ${}^4F_{3/2} \rightarrow {}^4I_{9/2}$ has potential for diode lasing applications.

CONFLICT OF INTEREST

There is no conflict of interest.

REFERENCES

- Ekmekçi MK. Influence of europium doping on the crystallization, morphology, and cathodoluminescent properties of $\text{PbNb}_2\text{O}_6:\text{Eu}^{3+}$ phosphors. *JOTCSA*. 2022;1129-1140. <URL>.
- Nagaraj R, Rajagopal V, Raja A, Ranjith S. Influence of Dy^{3+} ion concentration on photoluminescence and energy transfer mechanism of promising $\text{KBaScSi}_3\text{O}_9$ phosphors for warm white LEDs. *Spectrochim. Acta A Mol. Biomol. Spectrosc.* 2022;264:120212. <URL>.
- İlhan M, Katı Mİ, Keskin İÇ, Güteryüz LF. Evaluation of structural and spectroscopic results of tetragonal tungsten bronze $\text{MTa}_2\text{O}_6:\text{Eu}^{3+}$ (M = Sr, Ba, Pb) phosphors and comparison on the basis of Judd-Ofelt parameters. *J. Alloy. Comp.* 2022;901:163626. <URL>.
- Yao S, Lv S, Feng Z. Synthesis and photoluminescent properties of $\text{Dy}^{3+}:\text{CaYAlO}_4$ phosphors. *Appl. Phys. A* 2021;127:773. <URL>.
- Ekmekçi MK, İlhan M, Güteryüz LF, Mergen A. Study on molten salt synthesis, microstructural determination and white light emitting properties of $\text{CoNb}_2\text{O}_6:\text{Dy}^{3+}$ phosphor. *Optik*. 2017 Oct;128:26-33. <URL>.
- İlhan M, Ekmekçi MK, Keskin İÇ. Judd-Ofelt parameters and X-ray irradiation results of $\text{MNb}_2\text{O}_6:\text{Eu}^{3+}$ (M = Sr, Cd, Ni) phosphors synthesized via a molten salt method. *RSC Adv.* 2021 Feb;11:10451. <URL>.
- İlhan M, Ekmekçi MK. Synthesis and photoluminescence properties of Dy^{3+} doped white light emitting CdTa_2O_6 phosphors. *J. Solid State Chem.* 2015;226:243-249. <URL>.
- İlhan M, Keskin İÇ. Photoluminescence, radioluminescence and thermoluminescence properties of Eu^{3+} doped cadmium tantalate phosphor. *Dalton Trans.* 2018;47:13939-13948. <URL>.
- Erdem R, İlhan M, Ekmekçi MK, Erdem Ö. Electrospinning, preparation and photoluminescence properties of $\text{CoNb}_2\text{O}_6:\text{Dy}^{3+}$ incorporated polyamide 6 composite fibers. *Appl. Surf. Sci.* 2017;421:240-246. <URL>.
- Başak AS, Ekmekçi MK, Erdem M, İlhan M, Mergen A. Investigation of boron-doping effect on photoluminescence properties of $\text{CdNb}_2\text{O}_6:\text{Eu}^{3+}$ phosphors. *J. Fluoresc* 2016;26:719-724. <URL>.
- İlhan M, Keskin İÇ. Analysis of Judd-Ofelt parameters and radioluminescence results of $\text{SrNb}_2\text{O}_6:\text{Dy}^{3+}$ phosphors synthesized via molten salt method. *Phys. Chem. Chem. Phys.* 2020;2:19769. <URL>.
- He X, Fang B, Zhang S, Lu X, Ding J. Preparation and properties of Nd-doped BCTH lead-free ceramics by solid-phase twin crystal method. *Curr. Appl. Phys.* 2022;38:30-39. <URL>.
- İlhan M, Güteryüz LF, Keskin İÇ, Katı Mİ. A comparison of spectroscopic properties of Dy^{3+} -doped tetragonal tungsten bronze MTa_2O_6 (M = Sr, Ba, Pb) phosphors based on Judd-Ofelt parameters. *Mater. Sci: Mater. Electron* 2022;33:16606-16620. <URL>.
- İlhan M, Keskin İÇ. Evaluation of structural behaviour, radioluminescence, Judd-Ofelt analysis and thermoluminescence kinetic parameters of Eu^{3+} doped TTB-type lead metaniobate phosphor. *Phys. B: Condens. Matter* 2020;585:412106. <URL>.
- He X, Fang B, Zhang S, Lu X, Ding J. Preparation of nanoscale $[(\text{Ba}_{0.85}\text{Ca}_{0.15})_{0.995}\text{Nd}_{0.005}](\text{Ti}_{0.9}\text{Hf}_{0.1})\text{O}_3$ ceramics via hydrothermal method and effect of grain size on multifunctional performance. *J. Alloys Compd.* 2022;925:166249. <URL>.
- İlhan M, Keskin İÇ, Çatalgöl Z, Samur R. NIR photoluminescence and radioluminescence characteristics of Nd^{3+} doped BaTa_2O_6 phosphor. *Int. J. Appl. Ceram. Technol.* 2018;15: 1594-1601. <URL>.
- Wang X, Zhao H, Li A, Tian K, Brambilla G, Wang P. Near-infrared luminescence and single-mode laser emission from Nd^{3+} doped compound glass and glass microsphere. *Front. Mater. Sci.* 2019;6:237. <URL>.
- Prasad RNA, Vijaya N, Babu P, Mohan NK, Praveena R. Optical absorption and NIR photoluminescence of Nd^{3+} -activated strontium phosphate glasses. *J. Electron. Mater.* 2020;49:6358-6368. <URL>.
- İlhan M, Ekmekçi MK, Oraltay RG, Başak AS. Structural and near-infrared properties of Nd^{3+} activated Lu_3NbO_7 Phosphor. *J. Fluoresc.* 2017;27:199-203. <URL>.
- Ekmekçi MK, İlhan M, Ege A, Ayvacıklı M. Microstructural and radioluminescence characteristics

- of Nd³⁺ doped columbite-type SrNb₂O₆ phosphor. *J. Fluoresc.* 2017;27:973-979. <URL>.
21. Ekmekçi MK, Erdem M, Başak AS, İlhan M, Mergen A. Molten salt synthesis and optical properties of Eu³⁺, Dy³⁺ or Nd³⁺ doped NiNb₂O₆ columbite-type phosphors. *Ceram. Int.* 2015;41:9680-9685. <URL>.
22. Mahamuda Sk, Swapna K, Rao AS, Jayasimhadri M, Sasikala T, Pavani K, Moorthy LR. Spectroscopic properties and luminescence behavior of Nd³⁺ doped zinc alumino bismuth borate glasses. *J. Phys. Chem.* 2013;74:1308-1315. <URL>.
23. Edwards PR, Martin RW. Cathodoluminescence nano-characterization of semiconductors. *Semicond. Sci. Technol.* 2011;26:064005. <URL>.
24. Ma DDD, Lee ST, Mueller P, Alvarado SF. Scanning tunneling microscope excited cathodoluminescence from ZnS nanowires. *Nano Lett.* 2006;6:926. <URL>.
25. Dierre B, Yuan XL, Sekiguchi T. Sci. Low-energy cathodoluminescence microscopy for the characterization of nanostructures. *Technol. Adv. Mater.* 2010;11:043001. <URL>.
26. İlhan M, Güteryüz LF. Cathodoluminescence and photoluminescence of BaTa₂O₆:Sm³⁺ phosphor depending on the sintering temperature. *Chem. Pap.* 2022;76:6963-6974. <URL>.
27. Mitsui T, Yamamoto N, Tadokoro T, Ohta S. Cathodoluminescence image of defects and luminescence centers in ZnS/GaAs(100). *J. Appl. Phys.* 1996;80:6972. <URL>.
28. İlhan M. Heat capacities and thermodynamic functions of CdNb₂O₆ and CdTa₂O₆. *J. Therm. Anal. Calorim.* 2022;147:12383-12389. <URL>.
29. European Coordination Committee of the Radiological, Electromedical and Healthcare IT Industry, COCIR application for new exemption Page 1-12, Blvd A. Reyers 80 1020 Brussels, 2011.
30. Colvin VL, Schlamp MC, Alivisatos AP. Light-emitting diodes made from cadmium selenide nanocrystals and a semiconducting polymer. *Nature* 1994;370:354-357. <URL>.
31. Chaar LE, Lamont LA, Zein NE. Review of photovoltaic technologies. *Renewable Sustainable Energy Rev.* 2011;15:2165-75. <URL>.
32. Iorgu AI, Berger D, Alexandrescu L, Vasile BS, Matei C. Synthesis of photoluminescent pure and doped cadmium sulfide by reverse microemulsion method. *Chalcogenide Lett.* 2013;10:525-531.
33. Willner I, Baron R, Willner B. Integrated nanoparticle-biomolecule systems for biosensing and bioelectronics. *Biosens. Bioelectron.* 2007;22:1841. <URL>.
34. Choi YJ, Kim YJ, Lee JW, Lee Y, Lim YB, Chung HW. Cyto/genotoxic effect of CdSe/ZnS quantum dots in human lung adenocarcinoma cells for potential photodynamic UV therapy applications. *J. Nanosci. Nanotechnol.* 2012;12:2160-2168. <URL>.
35. Su Y, He Y, Lu H, Sai L, Li Q, Li W, Wang L, Shen P, Huang Q, Fan C. The cytotoxicity of cadmium based, aqueous phase - Synthesized, quantum dots and its modulation by surface coating. *Biomaterials* 2009;30:19-25. <URL>.
36. Wong-Ng W, McMurdie HF, Paretzkin B, Kuchinski MA, Dragoo AL. Standard X-Ray Diffraction Powder Patterns of Fourteen Ceramic Phases. *Powder Diffr.* 1988;3:246-254.
37. Tealdi C, Mozzati MC, Malavasi L, Ciabatonni T, Amantea R, Azzoni CB. Columbite-type Fe_xMn_{1-x}Nb₂O₆ solid solution: structural and magnetic characterization. *Phys. Chem. Chem. Phys.* 2004;6:4056-4061. <URL>.
38. Wachs IE. Infrared spectroscopy of supported metal oxide catalysts. *Colloid Surface A.* 1995;105:143-149.
39. Ayvacikli M, Kotan Z, Ekdal E, Karabulut Y, Canimoglu A, Guinea JG, Khatab A, Henini M, Can N. Solid state synthesis of SrAl₂O₄:Mn²⁺ co-doped with Nd³⁺ phosphor and its optical properties. *J. Lumin.* 2013;144:128-132. <URL>.
40. Sontakke AD, Biswas K, Mandal AK, Annapurna K. Concentration quenched luminescence and energy transfer analysis of Nd³⁺ ion doped Ba-Al-metaphosphate laser glasses. *Appl. Phys. B* 2010;101:235-244. <URL>.
41. MacRae CM, Wilson NC, Torpy A, Davidson CJ. Hyperspectral cathodoluminescence imaging and analysis extending from ultraviolet to near infrared. *Microsc. Microanal.* 2012;18:1239-1245. <URL>.
42. Lamrani MA, Addou M, Sofiani Z, Sahraoui B, Ebothe J, El Hichou A, Fellahi N, Bernede JC, Dounia R. Cathodoluminescent and nonlinear optical properties of undoped and erbium doped nanostructured ZnO films deposited by spray pyrolysis. *Opt. Commun.* 2007;277:196-201. <URL>.
43. Hsiao YJ, Fang TH, Ji LW, Chi SS. Surface and photoluminescence characteristics of CdNb₂O₆ Nanocrystals. *Open Surf. Sci. J.* 2009;1:30-33. <URL>.
44. Hsiao YJ, Chang YS, Chen GJ, Chang YH. Synthesis and the luminescent properties of CdNb₂O₆ oxides by sol-gel process. *J. Alloys Compd.* 2009;471:259-262. <URL>.
45. Cherrad H, Addou M, Hssein M, Bahedi K, Jbilou M, Mrigal A, Salmani E, Rouchdi M, Mezred A, Ftouhi H, Diani M, Jouad ME. Theoretical and experimental investigation of structural, electronic and optical properties of neodymium doped ZnO. *MATEC Web of Conferences* 2020;307:01018. <URL>.

46. El Hichou A, Addou M, Ebothé J, Troyon M. Influence of deposition temperature (Ts), air flow rate (f) and precursors on cathodoluminescence properties of ZnO thin films prepared by spray pyrolysis]. *Lumin.* 2005;113:183-190. [<URL>](#).









47. Sittner J, Götze J. Cathodoluminescence (CL) characteristics of quartz from different metamorphic rocks within the Kaoko Belt (Namibia). *Minerals* 2018;8;190. [<URL>](#).

48. Siegel GH, Marrone MJ. Photoluminescence in as-drawn and irradiated silica optical fibers: an assessment of the role of non-bridging oxygen defect centers. *J. Non Cryst. Solids* 1981;45:235-247. [<URL>](#).

49. Karl A, Gschneidner Jr, LeRoy E. *Handbook on the Physics and Chemistry of Rare Earths* volume 4 Non-Metallic Compounds - II. 293, 1979.



Distribution of Chromium Species and Physico-Chemical Analysis of Various Industrial Effluents in Hyderabad and Jamshoro, Pakistan

Muhammad Kashif Channa¹ , Jameel Ahmed Baig¹ , Khalil Akhtar^{1*} , Mirza Junaid²,
Tasneem Gul Kazi¹ , Hassan Imran Afridi¹ , Shakoor Ahmed Solangi¹ ,
Saima Perveen¹ , and Bibi Sara¹ 

¹Centre of Excellence in Analytical Chemistry, University of Sindh, Jamshoro 76080, Sindh., Pakistan.

²Department of Pediatrics, Peoples University of Medical and Health Science for Women, Shaheed Banazirabad 67480, Pakistan.

Abstract: This research aimed to quantify the speciation of chromium in different industrial effluent samples of Hyderabad and Jamshoro, Pakistan. The hexavalent chromium (Cr(VI)) was determined by microsample injection system flame atomic absorption spectroscopy (MIS-FAAS). The total chromium was measured by MIS-FAAS after the oxidation of trivalent chromium (Cr(III)) to hexavalent chromium (Cr(VI)) by $\text{Ce}(\text{SO}_4)_2$ in an acidic medium (0.07 M H_2SO_4). The content of Cr(III) was measured by the difference method (total chromium – hexavalent chromium). In the effluent samples of textile and fabrics industries, the total Cr was observed 400 to 1600 times higher than the US-EPA and WHO regulatory limit (0.10 mg/L) in the industrial discharge. In the effluent of food and plastic industries, the Cr(VI) was found to be high as compared to the Cr(III), and the Cr(III) was observed high in the effluent samples of chemical as well as textile and fabrics industries. The Cr(VI) was higher than the US-EPA and WHO regulatory limit (0.05 mg/L) in the effluent samples of all selected industries, but the Cr(III) was within the US-EPA and WHO regulatory limit (170 mg/L) in the industrial discharges.

Keywords: Chromium; Solid phase extraction; Micro sample injection system; Flame atomic absorption; Industrial effluent.

Submitted: May 10, 2022. **Accepted:** October 11, 2022.

Cite this: Channa MK, Baig JA, Akhtar K, Junaid M, Kazi TG, Afridi HI, et al. Distribution of Chromium Species and Physico-Chemical Analysis of Various Industrial Effluents in Hyderabad and Jamshoro, Pakistan. JOTCSA. 2023;10(1):1-10.

DOI: <https://doi.org/10.18596/jotcsa.1107392>.

***Corresponding author. E-mail:** khalilakhtre789@gmail.com.

1. INTRODUCTION

Industrial effluent is one of the main direct and often continuous input sources of pollutants into aquatic systems. These pollutants have long-term impacts on natural ecosystems, including changes in food availability and a grave threat to the ability of the biosphere to self-regulate. The industrial discharges or wastes have heavy metals, polychlorinated biphenyls (PCBs), pesticides, dioxins, polycyclic hydrocarbons (PAHs), phenolic compounds, and petrochemicals and microorganisms. All the industrial effluents are usually discharged into the natural water resources such as rivers and lakes, and cumulative hazardous

consequences on the ecosystem have received a lot of attention. Untreated municipal and industrial wastewater has posed serious environmental risks to humanity. Industrial effluent discharge is a potential source of environmental pollution throughout the world. In Pakistan, the untreated effluents are either released to the agricultural land for irrigation purposes or disposed of in the nearby water bodies due to a lack of sewage treatment plants. Thus, the contaminants are either accumulated in soil or may enter through the food chain to generate several occupational health consequences. The pollution of heavy metals from industrial effluent has become a major public and scientific problem because of their hazardous

effects on humans and other biological pathways. The increasing influx of heavy metals can be dispersed by water and wind, which make them accessible to animals and plants. Therefore, the information on toxic metals, especially chromium (Cr), and its different forms found in industrial effluents. It is important because of their relative toxicity, which may depend on their chemical properties and bioavailability.

The significance of chromium (Cr) speciation is associated with its toxic effects on different oxidation states. The Cr(III) and Cr(VI) are two stable chromium species found in the environment. Cr(III) is a relatively non-toxic and essential nutrient for humans, especially mammals, for their appropriate carbohydrate tolerance factor, protein, and lipid metabolism. The toxic effects of Cr(VI) are common due to its higher oxidation state and relatively smaller in size, allowing it to pass through the cell membranes and cause serious damage to proteins, DNA, and other macromolecules. The Cr(VI) suppresses the cell's enzymatic sulfur uptake and affects the lungs, kidneys, and liver. The major toxic effects of Cr(VI) include dermatitis, chronic ulcers, the corrosive reaction of the nasal septum, and lung infections. However, the determination of chromium is crucial with appropriate accuracy and sensitivity. The Cr species are usually discharged into the natural water resources due to different industrial activities, such as leather tanning, electroplating, steel works, pigments, refractories, oxidative dyeing, and lumber processing. In the water bodies, the Cr species usually exist in the form of chromate and hydroxo-complexes. Several strategies like coprecipitation, solvent extraction, electrochemical methods, solid phase extraction (SPE), ion-exchange separation, capillary electrophoresis, and ion chromatography have been developed for the determination of Cr species in different oxidation states (Cr(III), and Cr(VI)). SPE has some advantages over the techniques mentioned earlier in the speciation analysis of Cr because of its safety, flexibility, environment-friendly, selectivity, absence of emulsion, ease of automation, and simplicity. Amberlite XAD resins have been extensively used in SPE for various metals because of their cross-linked polymeric nature, which enhances their adsorptive properties due to their macro reticular type structure and greater active surface area. This macro reticular structure exhibits excellent chemical, mechanical, and thermal stability, making it an excellent candidate for the adsorption of various metal ions. In the ground waterway, Cr pollution has been reported as a result of the environmental effects of industrial wastewater drainage by the tanning industry. It may alter the pH, and enhances the biochemical oxygen demand (BOD), total dissolved solids (TDS), and electric conductivity (EC), which may give intense colourations to rivers. Therefore, the ecology is highly affected by microbial populations, which could be poisonous, mutagenic,

or carcinogenic for aquatic animals. Based on these facts, the gradual monitoring and assessment of Cr and its different forms in industrial effluents are very important. Moreover, the effect of different quality parameters of industrial effluents on the mobility of Cr species is the need of hours.

The total Cr and its species in Hyderabad and Jamshoro district industrial effluents were investigated. The Cr(VI) was determined by a solid phase extraction procedure using Amberlite XAD-4 resin. At the same time, Cr(III) was calculated by subtracting Cr(VI) concentration from total Cr in the studied industrial effluent samples. The variation of physical quality parameters like pH, BOD, TDS, and EC in different industries has been quantified.

2. MATERIAL AND METHOD

2.1. Reagents and Glassware

The analytical grade nitric acid ($\text{HNO}_3 \geq 65\%$ with Sp.gr: 1.41) and hydrogen peroxide ($\text{H}_2\text{O}_2 \geq 30\%$ with Sp.gr: 1.11) were purchased from Merck (Germany). A certified standard solution of Cr (1000 mg/L, Fluka Kamica, Switzerland) was used to calibrate the quantitative determination of total Cr. For Cr(VI), the calibration curve was drawn using a standard solution of $\text{K}_2\text{Cr}_2\text{O}_7$ (dissolving 0.372 g of $\text{K}_2\text{Cr}_2\text{O}_7$ in 1.0 L deionized water), and 1.0 M HNO_3 was used to prepare appropriate dilute solutions. Deionized water (electrical conductivity 0.050 $\mu\text{S}/\text{cm}$) was prepared by the water purification system of ELGA laboratory (Bucks, UK). The adsorbent, Amberlite XAD-4, with surface area and pore diameter of 735 m^2/g and 20–50 μm , respectively, were used. Before use, all glassware (pyrex) and plastic (polyethylene) bottles were carefully washed. The glasswares were soaked in 5.0 M HNO_3 for 24 hours, then rinsed with deionized water.

2.2. Instrumentation

The concentration of Cr was determined using a flame atomic absorption spectrometer (Hitachi model 180-50; Tokyo, Japan) equipped with Cr hollow cathode lamp (HCL), and a flame atomizer (air-acetylene). The wavelength, spectral bandwidths, and lamp current were used as 358.0 nm, 0.70 nm, and 25.0 mA, respectively.

2.3. Preparation of Column

The preconcentration of Cr was achieved using a 15.0 cm long, 1.2 cm diameter glass column. The column was packed up to the height of 4.0 cm with a slurry of 1.2 g Amberlite XAD-4 resin in 25.0 mL deionized water. The adsorbent material was properly settled by using glass wool at the top and bottom of the column then 0.1 M H_2SO_4 was used to activate the column.

2.4. Sample Collection

Random samples of industrial effluents were collected from twenty industrial effluents of Hyderabad and Jamshoro, Pakistan, located at different places. These industries were divided into four categories based on their natural food industry (FI), plastic industry (PI), chemical industry (CI), and textile and fabrics industry (TFI). For sampling, ten samples were randomly collected from two to three industries for each category of industry ($n = 40$). Microbiological examination vials of 500.0 mL capacity were used to collect the industrial effluent samples, and the physicochemical parameters such as biological oxygen demand (BOD), total dissolved solids (TDS), pH, and electric conductivity (EC) of each sample were analyzed by the method described by AOAC .

2.5. Determination of Hexavalent Chromium

The Cr(VI) content was determined by solid phase extraction (SPE), as reported by Rajesh et al. 2008 . For SPE, a 1.0 mL of 10.0 mg/L solution of Cr(VI) was added to a 100 mL volumetric flask along with 3.0 mL of 0.5 M H₂SO₄, followed by the addition of 3.0 mL of 0.25 % diphenylcarbazide and the solution mixture was diluted up to the mark with deionized water. The sample solution was loaded onto the column containing Amberlite XAD-4 resin, maintaining a flow rate of 2.0 mL/min. The Cr-diphenylcarbazide complex (reddish violet colored) was adsorbed onto the column, which was evident from the absorbance of the resulting solution. The adsorbed complex was then eluted using 15.0 mL of 2.5 M H₂SO₄ in acetone. The solution was placed on the hot plate to evaporate the acetone and added 5.0 mL of 0.2 N HNO₃ solutions in the residue. The solution was filtered with filter paper, and the concentration of Cr(VI) was determined by micro-sample injection system flame atomic absorption spectrophotometry (MIS-FAAS) as reported by Baig et al. 2012 .

2.6. Determination of Total Chromium

The total Cr was also determined by SPE MIS-FAAS after the oxidation of Cr(III) to Cr(VI) by using Ce(SO₄)₂, as reported by Baig et al. 2012 . The Ce(IV) in acidic media (0.07 mol/L, H₂SO₄) is used to

oxidize Cr(III) to Cr(VI), and the resulted solution was treated as mentioned in the section on the determination of Cr(VI).

2.7. Calculation of Trivalent Chromium

The contents of Cr(III) could not be determined directly by the above analytical procedure, but their concentrations were given by the difference between the total Cr and Cr(VI) .

2.8. Analytical Figure of Merits

The analytical characteristics of the developed approach for determining Cr were calculated using optimized instrumental conditions. The standard addition method was used to draw the calibration curve for the determination Cr(VI) by SPE MIS-FAAS . The limit of detection and quantification (LOD and LOQ) of the developed method were calculated as $3 \times S/m$ and $10 \times S/m$, respectively. Where S is the standard deviation (std.) of blank signals ($n = 10$) and m is the slope of the linear calibration graph . The LOD and LOQ of the developed approach for determining Cr(VI) were found to be 0.037 and 0.124 mg/L, respectively. The calibration curve of Cr(VI) for this interval was determined by the regression equation $A = 1.47 \times 10^{-2} [\text{Cr(VI)}] + 3.00 \times 10^{-5}$. Where, A is the analytical signal (absorbance in nm) and $[\text{Cr(VI)}]$ is the concentration of analyte (Cr(VI)) in the sample solution (mg/L). The calculated coefficient of determination (R^2) for Cr(VI) was about 0.996.

The precision of the developed analytical approach was evaluated by percent relative standard deviation (%RSD) for each analyzed concentration, and %RSD was calculated as $(\text{Std.}/X)100$, where Std stands for a standard deviation for seven measurements and X is the mean value of these measurements. The %RSD of method was found to be $< 1.50\%$ ($n = 6$). The reliability of the developed method for determining Cr(VI) by SPE MIS-FAAS in the aqueous medium was evaluated by spiking the three known concentrations of Cr(VI) in the concentration range of 10.0 - 30.0 mg/L, and percentage recoveries were found to be $> 99.0\%$ (Table 1).

Table 1: The results for the test of standard addition/recovery for Cr(VI) by solid phase extraction in industrial effluent samples ($n = 6$).

	Amount added (mg/L)	Found values Mean \pm Std. (mg/L)	%Recovery ^a	%RSD
	---	14.72 \pm 0.18	--	0.37
Cr(VI)	10.00	24.64 \pm 0.13	99.20	1.09
	20.00	34.82 \pm 0.23	100.5	0.75
	30.00	45.32 \pm 0.11	102.0	0.91

$$\% \text{Recovery}_a = \frac{C_{\text{after spiked}} - C_{\text{initial}}}{C_{\text{spiked}}} \times 100$$

2.9. Statistical Evaluation

Excel 2003 (Microsoft Office ®) and STATISTICA 6 (StatSoft, Inc.®) were used to perform all mathematical and statistical calculations. Means \pm SD, and Student's t-test were used to express the distributed data to evaluate linear associations between physical quality measures and total Cr, and Pearson correlation coefficients were determined. All of the tests were two-sided with a 0.05 p-value significant.

3. RESULT AND DISCUSSION

In all the analyzed effluent samples, the temperature had a distinct annual cycle, in which the summer season showed higher values and the winter season showed lower values. The results of physicochemical parameters (pH, EC, TDS, and BOD) of industrial effluent samples (collected from four different industries) are shown in Table 2. The pH values of effluent samples of FI, PI, CI, and TFI were 7.00 – 8.60, 6.60 – 6.80, 6.70 – 7.90, and 6.10 – 6.6 respectively (Table 2). PI and TFI are slightly acidic because of various chemicals in these sectors' cleaning, washing, and polymerization/dyeing processes. The effluents had a slightly acidic pH (5.96 ± 0.09) and the exposure pH should be higher (7.16 ± 0.02). The basic pH of the natural water may cause damage to the fish's outer surfaces, such as the skin, eyes, and gills, and render them unable to dispose of metabolic wastes.

However, the highly acidic industrial effluents may enhance the toxicity of the organic compounds. The TDS were found at 951-1820, 1348-1382, 1348-1382, and 450-1322 mg/L in FI, PI, CI, and TFI industrial effluents samples.

The EC of industrial effluents (FI, PI, CI, and TFI) were found in the range of 0.87-4.01, 3.00-3.60, 2.88-3.72, 0.40-5.30 mS/cm, respectively. The EC of all the analyzed industrial effluents was greater than US-EPA allowed limits (1.00 mS/cm) for industrial effluents. The higher concentration of EC may be due to the dissociation of the dissolved substances present in the samples, concentration of ions, degree of dissociation, and temperature. The EC values of the effluent samples collected from FI were found to be higher than the other three industrial effluents ($p < 0.05$). The highest values of EC were found in TFI effluent samples. These may result from the released oil, grease, ammonia, sulfide, and dyes alongside the wastage effluents of TFI, which may also contaminate drinking water. These industries may be released a large quantity of residual chemicals and biological material waste into natural water sources such as rivers and canals without proper treatment, which may cause several health issues. The level of BOD was found at 475 ± 61.4 , 575 ± 7.10 , 565 ± 7.10 , and 580 ± 20.0 mg/L in the analyzed effluent samples of FI, PI, CI and TFI, respectively as shown in Table 2.

Table 2: Physico-chemical characteristics of industrial effluents of Hyderabad and Jamshoro-Pakistan.

		pH	TDS (mg/L)	EC (mS/cm)	BOD (mg/L)
FI (n = 30)	Mean \pm Std.	7.60 \pm 0.80	1403 \pm 435.00	2.33 \pm 1.57	47.5 \pm 6.10
	Range	7.00-8.60	951-1820	0.87-4.01	40.5-52.0
PI (n = 30)	Mean \pm Std.	6.70 \pm 0.10	1365 \pm 20.01	3.30 \pm 0.30	57.5 \pm 5.10
	Range	6.60-6.80	1348-1382	3.00-3.60	57.0-58.0
CI (n = 30)	Mean \pm Std.	7.20 \pm 0.50	1365 \pm 24.04	3.30 \pm 0.42	56.5 \pm 7.06
	Range	6.70-7.70	1348-1382	2.88-3.72	55.8-57.5
TFI (n = 30)	Mean \pm Std.	6.30 \pm 0.20	951 \pm 491.01	2.83 \pm 2.45	58.0 \pm 2.00
	Range	6.10-6.60	450-1322	0.40-5.30	56.0-60.0

Std. = Standard Deviation

The BOD levels in all the analyzed effluent samples were observed at 8.0 to 12.0 times higher than the US EPA's recommended tolerance limit (50 mg/L) for industrial effluent discharge into rivers. The high level of BOD in effluent samples of all the industrial sectors might be attributed to the elevated concentration of organic matter produced by several chemicals utilized in the various industrial processes. However, a high level of BOD was observed in TFI effluent samples compared to other industrial effluents. It might be due to different chemicals used in textile industries for mercerizing,

bleaching/scouring, and yawing, which include sodium chloride, sodium sulfite, NaCl, sodium bisulfate, sodium bicarbonate, formic acid, H₂SO₄, vegetable tannins, resins, sodium formate, polyurethane, fat emulsions, dyes, binders, waxes, pigments, lacquers/formaldehyde, NaOH, sodium phosphate, sodium hypochlorite, acids, H₂O₂, surfactants, Cl₂, and NaSiO₃. The findings of the current work showed that the difference among industries was statistically significantly different from each other ($P < 0.05$). Moreover, it was observed that the effluents from the studied

industries remained continuously discharged into the nearby natural waterbodies during the sampling period.

The total Cr contents in effluents of FI, PI, CI and TFI varied between 30.0-38.0, 23.0-27.0, 35.0-95.0, and 40.0-180 mg/L respectively (Table 3). However, the total Cr concentration in the selected four industries increased as $PI < FI < CI < TFI$, with TFI showing the highest Cr concentration. The total Cr levels in the effluent samples analyzed from all the industrial sectors were higher than the US EPA standard for total Cr (0.10 mg/L). The possible sources of Cr in these industrial effluents are the Cr compounds employed for various industrial applications like catalysts, dyers, and modifiers among others. The total Cr contents showed significantly positive correlation with pH, TDS and EC in effluent samples of FI ($r > 0.60$; $p < 0.001$), while strongly negative correlation was observed between total Cr and BOD ($r = -0.821$; $p < 0.001$). The total Cr contents in effluent samples of PI were reversely correlated with pH and TDS ($r > -0.90$; $p < 0.0001$), whereas, it has significantly correlation with EC and BOD ($r > 0.80$; $p < 0.0001$). On the other hand, the total Cr contents of effluent samples of CI have no significant correlation with the four studied physical parameters ($P > 0.140$). It might be due to the low variation in the contents of total Cr in different effluent samples of CI of the Jamshoro district. However, total Cr levels have positive correlation with pH and TDS ($r > 0.60$; $p < 0.001$) and negative correlation with EC and BOD ($r > -0.60$; $p < 0.001$) (Table 4).

The Chromium speciation in industrial effluent is very important in determining the level of contamination and toxicity. Chromium speciation in industrial effluent samples of FI, PI, CI and TFI are important in determining mobilization and toxicity. The contents of Cr(VI) and Cr(III) in effluent samples of FI, PI, CI and TFI varied in the ranges [23.0 - 36.0, 2.00 - 7.00], [19.0 - 20.0, 4.00 - 7.00], [9.00 to 23.0, 26.0 - 72.0] and [16.0 - 48.0, 24.0 - 132 mg/L] respectively. The cluster analysis was employed on industrial effluent samples to distribute Cr contamination. A cluster graph is used to detect spatial resemblance in different groups of industrial effluents (spatial variability). The obtained dendrogram categorized all the four sampling industrial effluents into three major clusters, as effluents of PI and FI have lower mutual dissimilarities than industrial effluents of CI and TFI (Figure 1). The comparatively high contents of Cr(VI) were found in effluent samples of FI and PI, because of the large application of dichromate/chromate in these industries. The contents of Cr(VI) in effluent samples of four industries were found to be higher than the U.S. EPA regulatory limit for Cr(VI) (0.05 mg/L). The high levels of Cr(VI) may cause disorders of the skin, gastrointestinal tract, kidney, liver, circulatory, and nerve tissues, as well as lung carcinoma among others. The level of Cr(III) was found to be higher in effluent samples of CI and TFI than FI and PI ($p < 0.05$). The concentration of Cr(III) contents in the industrial effluent samples were within the recommended level of Cr(III) (170 mg/L) in industrial discharges of FI and PI were significantly lower than the level of Cr(VI) may be due to the large application of dichromate/chromate.

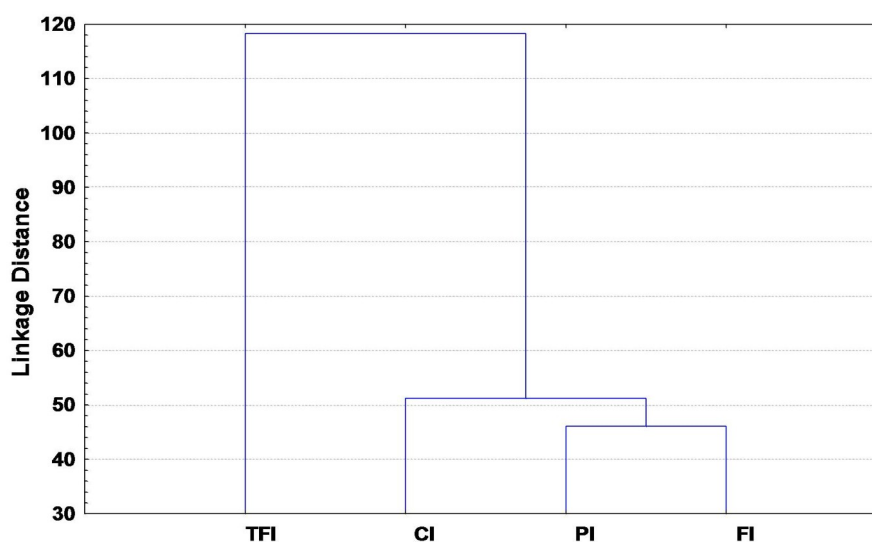


Figure 1: Dendrogram showing clustering of different origins of industrial effluents according to distribution of Cr species.

Table 3: Analytical results of chromium speciation (mg/L) in industrial effluents of different industries of Hyderabad and Jamshoro, Pakistan.

		Total Cr	Cr(VI)	Cr(III)
FI (n = 30)	Mean ± Std.	34.0±4.00	29.5±6.50	4.50±2.50
	Range	30.0-38.0	23.0-36.0	2.0-7.0
PI (n = 30)	Mean ± Std.	25.0±2.00	19.5±0.50	5.5±1.50
	Range	23.0-27.0	19.0-20.0	4.0-7.0
CI (n = 30)	Mean ± Std.	65.0±30.00	16.0±7.00	49.0±23.00
	Range	35.0-95.0	9.0-23.0	26.0-72.0
TFI (n = 30)	Mean ± Std.	110±70.00	32.0±16.01	78.0±54.00
	Range	40.0-180	16.0-48.0	24.0-132.0

Std. = Standard Deviation

Table 4: Correlation of total Cr with the physicochemical characteristics of industrial effluents.

		pH	TDS	EC	BOD
FI	r -value	0.697	0.874	0.600	-0.821
	p-value	0.00001	< 0.00001	0.0004	< 0.00001
PI	r - value	-0.923	-0.970	0.844	0.881
	p - value	< 0.00001	< 0.00001	< 0.00001	< 0.00001
CI	r - value	0.197	0.124	0.169	0.074
	p - value	0.149	0.514	0.372	0.699
TFI	r - value	0.721	0.653	-0.721	-0.626
	p - value	< 0.00001	< 0.00001	<0.00001	0.0002

The Cr(III) level in the effluent samples of CI and TFI was two to three-fold higher than the Cr(VI) level. It might be due to the large application of Cr(III) salts (nitrate or sulfate) in studied CI and TFI for different industrial processes. The level of Cr(III) in the effluent samples may not have significant toxic effects. Based on the elevated Cr(VI) level in the industrial effluent samples, it is suggested that the effluent of studied industries cannot be used directly for agricultural or other commercial applications. Thus, the level of Cr(III) may be increased due to the conversion of high contents of Cr(VI) discharged from industries into natural water bodies, which may convert into Cr(III) either by the increase in pH up to 7.0 or the dilution by the river or canal water. It is recommended that contaminated industrial effluent could not be discharged into streams of rivers or canals.

The results of total Cr concentration in industrial effluent samples were compared with other previous studies in different countries (Table 5). The total Cr content in industrial effluents samples from district Jamshoro, Pakistan, was found much higher than the reported results in other countries including Pakistan.

The contents of Cr(VI) in industrial effluent samples of the study area were lower than Hyderabad, India and Jeddah, Saudi Arabia and other previous studies from various Scholars . The contents of Cr(III) in industrial effluents of Hyderabad- India, Tabriz-Iran and Jeddah-Saudi Arabia were two to four-fold higher than the contents of Cr(III) in industrial effluents of the study areas .

Table 5: Comparison of previously reported research on total Cr and its species (mg/L) in industrial effluents with this study.

Region	Cr(III)	Cr(VI)	Total Cr	References
Bahia, Brazil	2.63±0.07	--	2.80±0.12	(6)
Denizli, Turkey	16.8±9.6	23.3±5.3	40.1±8.0	(3)
Gaborone, Botswana	--	20.7 ± 0.9	30.7 ± 1.2	(31)
Hyderabad, India	95 ± 2	98.0 ± 2.0	--	(7)
Lucknow, India	--	1.64±0.002	45.1±0.03	(35)
Kasur, Pakistan	--	--	2.10±0.08	(34)
Karachi, Pakistan	--	--	15.2-185	(33)
Tabriz, Iran	46.3 ± 0.8	12.3 ± 0.4	--	(36)
Jeddah, Saudi Arabia	99.0 ± 2.0	99.9 ± 4.0	--	(29)
Jeddah, Saudi Arabia	10.0	--	13.1±0.2	(9)
Jeddah, Saudi Arabia	10.4 ± 0.12	2.4 ± 0.11	12.9 ± 0.1	(32)
Hyderabad and Jamshoro, Pakistan	28.5 ±19.5	74.5±58.0	102±78.0	Current study

These industrial sectors may discharge the untreated effluents into natural water resources through open or closed pathways, which is hazardous to local inhabitants and wildlife. Almost all industries in Hyderabad and Jamshoro either disregarded or partly obeyed international industrial discharge rules. However, some enterprises have established the effluents treatment facility, but this is only a show for the pleasure of national and international organizations.

4. CONCLUSION

The contents of EC, TDS, and BOD in effluent samples of four industries were significantly high than the legal threshold levels set by the US Environmental Protection Agency. Total Cr concentration in textile and fabric industry effluent samples was 400-1800 times greater than the maximum concentration allowed by the US Environmental Protection Agency (EPA). The Cr(VI) was the dominant species in the effluent of FI and PI, but the Cr(III) level is relatively high in the effluent samples of CI and TFI ($p < 0.05$). Cr(VI) levels in effluent samples of four studied industries were higher but below regulatory limits set by the US EPA and WHO. The correlation study indicated that total Cr in effluents of different industries showed a different behaviour with quality parameters depending on the nature of effluent chemical residues. Thus, a continuous assessment and monitoring of the industrial activities is recommended for developing a greener Pakistan. Meanwhile, there is a need for university-industry collaboration to develop industrial eco-friendly and cost-effective solutions.

5. ACKNOWLEDGMENTS

This work was partially supported by The World Academy of Science (TWAS), Italy (Grant No.: 13-346 G/MSN/AS_C_UNESCO FR: 3240279204). We are grateful to Dr. Akhtar Mahmoud Baig, president of Young Welfare Society (YWS) Sindh, for assistance in sampling.

6. REFERENCES

1. Nwosu UL, Ajiwe VIE, Okoye PAC. Assessment of Heavy Metal Pollution of Effluents from three (3) Food Industries in Nnewi/Ogidi areas of Anambra State, Nigeria. IOSRJESTFT. 2014;8(11):13-21. [<URL>](#).
2. Baig JA, Kazi TG, Shah AQ, Kandhro GA, Afridi HI, Khan S, et al. Arsenic speciation and other parameters of surface and ground water samples of Jamshoro, Pakistan. International Journal of Environmental Analytical Chemistry. 2012 Jan 15;92(1):28-42. [<URL>](#).
3. Baig JA, Hol A, Akdogan A, Kartal AA, Divrikli U, Kazi TG, et al. A novel strategy for chromium speciation at ultra-trace level by microsample injection flame atomic absorption spectrophotometry. J Anal At Spectrom. 2012;27(9):1509. [<URL>](#).
4. Pavesi T, Moreira JC. Mechanisms and individuality in chromium toxicity in humans. J Appl Toxicol. 2020 Sep;40(9):1183-97. [<URL>](#).
5. DesMarias TL, Costa M. Mechanisms of chromium-induced toxicity. Current Opinion in Toxicology. 2019 Apr;14:1-7. [<URL>](#).

6. Matos GD, dos Reis EB, Costa ACS, Ferreira SLC. Speciation of chromium in river water samples contaminated with leather effluents by flame atomic absorption spectrometry after separation/preconcentration by cloud point extraction. *Microchemical Journal*. 2009 Jul;92(2):135-9. [<URL>](#).
7. Gopi Krishna P, Mary Gladis J, Rambabu U, Prasada Rao T, Naidu GRK. Preconcentrative separation of chromium(VI) species from chromium(III) by coprecipitation of its ethyl xanthate complex onto naphthalene. *Talanta*. 2004 Jun;63(3):541-6. [<URL>](#).
8. Alamri S, Ali HM, Khan MIR, Singh VP, Siddiqui MH. Exogenous nitric oxide requires endogenous hydrogen sulfide to induce the resilience through sulfur assimilation in tomato seedlings under hexavalent chromium toxicity. *Plant Physiology and Biochemistry*. 2020 Oct;155:20-34. [<URL>](#).
9. El-Shahawi MS, Hassan SSM, Othman AM, El-Sonbati MA. Retention profile and subsequent chemical speciation of chromium (III) and (VI) in industrial wastewater samples employing some onium cations loaded polyurethane foams. *Microchemical Journal*. 2008 Jun;89(1):13-9. [<URL>](#).
10. Pakade VE, Tavengwa NT, Madikizela LM. Recent advances in hexavalent chromium removal from aqueous solutions by adsorptive methods. *RSC Adv*. 2019;9(45):26142-64. [<URL>](#).
11. Pradhan D, Sukla LB, Sawyer M, Rahman PKSM. Recent bioreduction of hexavalent chromium in wastewater treatment: A review. *Journal of Industrial and Engineering Chemistry*. 2017 Nov;55:1-20. [<URL>](#).
12. Zhou L, Li R, Zhang G, Wang D, Cai D, Wu Z. Zero-valent iron nanoparticles supported by functionalized waste rock wool for efficient removal of hexavalent chromium. *Chemical Engineering Journal*. 2018 May;339:85-96. [<URL>](#).
13. Matsuoka S, Nakatsu Y, Takehara K, Saputro S, Yoshimura K. On-line Electrochemical Oxidation of Cr(III) for the Determination of Total Cr by Flow Injection-Solid Phase Spectrophotometry. *ANAL SCI*. 2006 Dec;22(12):1519-24. [<URL>](#).
14. Wolf RE, Morrison JM, Goldhaber MB. Simultaneous determination of Cr(III) and Cr(VI) using reversed-phased ion-pairing liquid chromatography with dynamic reaction cell inductively coupled plasma mass spectrometry. *J Anal At Spectrom*. 2007;22(9):1051. [<URL>](#).
15. Rodrigues E, Almeida O, Brasil H, Moraes D, dos Reis MAL. Adsorption of chromium (VI) on hydrotalcite-hydroxyapatite material doped with carbon nanotubes: Equilibrium, kinetic and thermodynamic study. *Applied Clay Science*. 2019 May;172:57-64. [<URL>](#).
16. Rajesh N, Jalan RK, Hotwany P. Solid phase extraction of chromium(VI) from aqueous solutions by adsorption of its diphenylcarbazide complex on an Amberlite XAD-4 resin column. *Journal of Hazardous Materials*. 2008 Feb;150(3):723-7. [<URL>](#).
17. Hasan SMdM, Akber MdA, Bahar MdM, Islam MdA, Akbor MdA, Siddique MdAB, et al. Chromium Contamination from Tanning Industries and Phytoremediation Potential of Native Plants: A Study of Savar Tannery Industrial Estate in Dhaka, Bangladesh. *Bull Environ Contam Toxicol*. 2021 Jun;106(6):1024-32. [<URL>](#).
18. Asad S, Amoozegar MA, Pourbabae AA, Sarbolouki MN, Dastgheib SMM. Decolorization of textile azo dyes by newly isolated halophilic and halotolerant bacteria. *Bioresource Technology*. 2007 Aug;98(11):2082-8. [<URL>](#).
19. Godoy V, Blázquez G, Calero M, Quesada L, Martín-Lara MA. The potential of microplastics as carriers of metals. *Environmental Pollution*. 2019 Dec;255:113363. [<URL>](#).
20. Kazemi A, Esmaeilbeigi M, Sahebi Z, Ansari A. Health risk assessment of total chromium in the ganat as historical drinking water supplying system. *Science of The Total Environment*. 2022 Feb;807:150795. [<URL>](#).
21. Granato ET, Meiller-Legrand TA, Foster KR. The Evolution and Ecology of Bacterial Warfare. *Current Biology*. 2019 Jun;29(11):R521-37. [<URL>](#).
22. Channa GM, Baig J, Kazi T, Afridi H. Quantitative Assessment of Some Toxic Elements and Physicochemical Parameters in Wastewater of Dyeing Industry: A Case Study. *Pak J Anal Environ Chem*. 2020 Jun 30;21(1):132-9. [<URL>](#).
23. Baig JA, Kazi TG, Elci L, Afridi HI, Khan MI, Naseer HM. Ultratrace Determination of Cr(VI) and Pb(II) by Microsample Injection System Flame Atomic Spectroscopy in Drinking Water and Treated and Untreated Industrial Effluents. *Journal of Analytical Methods in Chemistry*. 2013;2013:1-8. [<URL>](#).
24. Arain SA, Kazi TG, Afridi HI, Arain MS, Panhwar AH, Khan N, et al. A new dispersive liquid-liquid microextraction using ionic liquid based microemulsion coupled with cloud point extraction for determination of copper in serum and water samples. *Ecotoxicology and Environmental Safety*. 2016 Apr;126:186-92. [<URL>](#).
25. Akhtar K, Ahmed Baig J, Gul Kazi T, Sirajuddin, Imran Afridi H, Naz Talpur F, et al. Novel fluoride

- selective voltammetric sensing method by amino phenylboronic acid-zirconium oxide nanoparticles modified gold electrode. *Microchemical Journal*. 2022 Mar;174:107073. [<URL>](#).
26. Ghaly A, Mahmoud N, Ibrahim M, Mostafa E, Abdelrahman E, Emam R, et al. Water use, wastewater characteristics, best management practices and reclaimed water criteria in the carwash industry: a review. *International Journal of Bioprocess & Biotechnological Advancements*. 2021;7(1):240-61.
27. Azeem H. Analysis of industrial waste water from Kot Lakhpat area (Lahore, Pakistan) by atomic absorption spectrometer. *Biologia (Pakistan)*. 2009;55(1 & 2):35-41.
28. Akan JC, Ogugbuaja VO, Abdulrahman FI, Ayodele JT. Pollutant levels in effluent samples from tanneries and textiles of Kano industrial areas, Nigeria. *Glo Jnl Pure Appl Sci [Internet]*. 2009 Dec 3 [cited 2022 Oct 26];15(3-4). Available from: [<URL>](#).
29. Mahmoud ME, Yakout AA, Ahmed SB, Osman MM. Speciation, selective extraction and preconcentration of chromium ions via alumina-functionalized-isatin-thiosemicarbazone. *Journal of Hazardous Materials*. 2008 Oct 30;158(2-3):541-8. [<URL>](#).
30. Treviño P, Ibáñez Cornejo JG, Vázquez Medrano RC. Chromium (VI) reduction kinetics by zero-valent aluminum. *Int J Electrochem Sci*. 2014;9:2556-64.
31. Kiptoo J. Speciation studies of nickel and chromium in wastewater from an electroplating plant. *Talanta*. 2004 Sep;64(1):54-9. [<URL>](#).
32. El-Shahawi MS, Bashammakh AS, Abdelmageed M. Chemical Speciation of Chromium(III) and (VI) Using Phosphonium Cation Impregnated Polyurethane Foams Prior to Their Spectrometric Determination. *Anal Sci*. 2011 Jul;27(7):757-63. [<URL>](#).
33. Parveen R, Ashfaq M, Qureshi J, Ali SMM, Qadri M. Estimation of Chromium in Effluents from Tanneries of Korangi Industrial Area. *Pak J Chem*. 2013 Mar 30;3(1):29-33. [<URL>](#).
34. Rehman A, Shakoori FR, Shakoori AR. Heavy metals resistant rotifers from a chromium contaminated wastewater can help in environmental clean-up. *Pakistan J Zool*. 2008;40(5):309-16.
35. Shukla O, Rai U, Dubey S. Involvement and interaction of microbial communities in the transformation and stabilization of chromium during the composting of tannery effluent treated biomass of *Vallisneria spiralis* L. *Bioresource Technology*. 2009 Apr;100(7):2198-203. [<URL>](#).
36. Abdolmohammad-Zadeh H, Sadeghi GH. A nano-structured material for reliable speciation of chromium and manganese in drinking waters, surface waters and industrial wastewater effluents. *Talanta*. 2012 May;94:201-8. [<URL>](#).



A Short Review on Structural Concepts of Metal Complexes of Proton Transfer Salts of Pyridine-2-Carboxylic Acid

Nurgün Büyükkıdan^{1*} 

¹Kütahya Dumlupınar University, Department of Chemistry, Kütahya, Türkiye

Abstract: In this study, a brief review of the proton transfer salts synthesized from the reaction of piperazine with pyridine-2-carboxylic acid and their metal complexes since 2009 was made. The metals in the studied compounds are mostly d-block metals. In complexes, the anionic component of the salt is coordinated to the metal, while the cationic component is present only as a complementary ion in a complex.

Keywords: Pyridine, piperazine, acid, base, salt.

Submitted: June 24, 2022. **Accepted:** October 14, 2022.

Cite this: Büyükkıdan N. A Short Review on Structural Concepts of Metal Complexes of Proton Transfer Salts of Pyridine-2-Carboxylic Acid. JOTCSA. 2023;10(1):11-20.

DOI: <https://doi.org/10.18596/jotcsa.1135570>.

***Corresponding author. E-mail:** nurgun.buyukkidan@dpu.edu.tr.

1. INTRODUCTION

Pyridine carboxylates containing two functional groups are among the most versatile ligands that can coordinate with metal (1). Studies with such molecules have mainly focused on the development of metal-based compounds containing pyridine-2-carboxylic acid (2-picolinic acid) for dietary supplementation and numerous articles and reviews have been conducted (2). Later, such ligands were used for coordination to different transition metals. These compounds usually form five-membered rings by bonding to the metal *via* carboxylate-O and pyridine-N donor atoms (3, 4) (Figure 1).

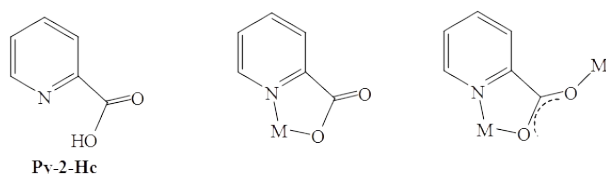


Figure 1: Coordination modes of Py-2-Hc.

As a terminal tryptophan metabolite, 2-picolinic acid is an important structural motif of enzymes and is the active component of many drugs (5, 6). An increase in the number of anticancer agents has been observed with the synthesis of pyridine-2-carboxylic acid type ligands with anti-cancer

properties and complexes of different transition metals (7, 8). The complexes with metal ions have been studied as models for broad biological activity spectra such as enzyme activity and DNA (9-11). Proton transfer salts, which consist of a good proton donor-acceptor systems, and their reactions with metals can form supramolecular compounds called Metal-organic frameworks (MOF) (12). It is very important to prepare an effective ion pair that forms the components of the proton transfer salt and accelerates the formation of the metal complexes. Among the proton donor and proton acceptor groups, which are components of the proton transfer salt, carboxylic acids and amines are a good pair. In recent years, the development of new pharmaceutical components with proton transfer reactions has accelerated (13-16). For the synthesis of complexes to be successful, care must be taken to select polydentate ligands and components capable of intermolecular H bonding (17, 18). Piperazines, which are cyclic amines, have many biological activities such as anti-depressant (19), anti-fungal (20), anti-tumor, (21, 22), anti-inflammatory (23), anti-migraine (24) and anti-malarial (25). In this work, an investigation of the transition metal complexes of compounds containing 2-picolinic acid and piperazine as structural units of proton transfer salt was carried out.

2. SYNTHESIS

2.1. Proton Transfer Reaction

The reaction or reaction mechanism in which a proton (H^+) is separated from one species such as an acid and accepted by another species such as a base is called a proton transfer reaction. The product of the proton transfer reaction between donors and acceptors is named differently as the proton transfer salt (26-29) the H-bonded complex (30-33) and the charge transfer complex (34-37).

In this study, proton transfer salts of pyridine-2-carboxylic as a proton donor and piperazine as proton acceptor and metal complexes of these salts were investigated.

2.1.1. Proton transfer salt, $(H_2Ppz)(Py-2-c)_2$ (**1**)

A mixture of pyridine-2-carboxylic acid (Py-2-Hc) in H_2O and piperazine (Ppz) in THF gave colorless crystals on slow evaporation after one week (**38**) (Figure 2).

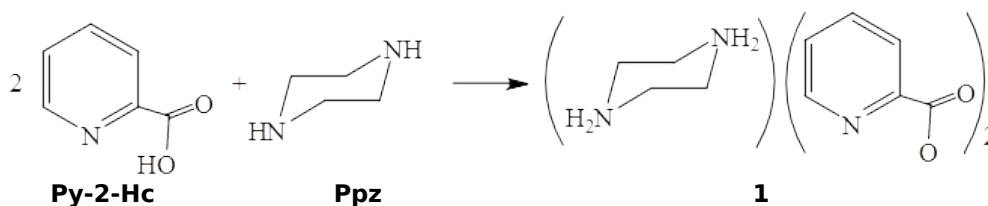


Figure 2: Synthesis of $(H_2Ppz)(Py-2-c)_2$ (**1**).

2.1.2. Mg(II) (**2**), Zn(II) (**3**) and Cd(II) (**4**) metal complexes of **1**

The complexes, $[Mg(Py-2-c)_2(H_2O)_2] \cdot H_2O$ (**2**),

$[Zn(Py-2-c)_2(H_2O)_2] \cdot H_2O$ (**3**) and $(H_2Ppz)[Cd(Py-2-c)_3] \cdot 3H_2O$ (**4**), of proton transfer salt **1** were synthesized (**38**) (Figure 3).

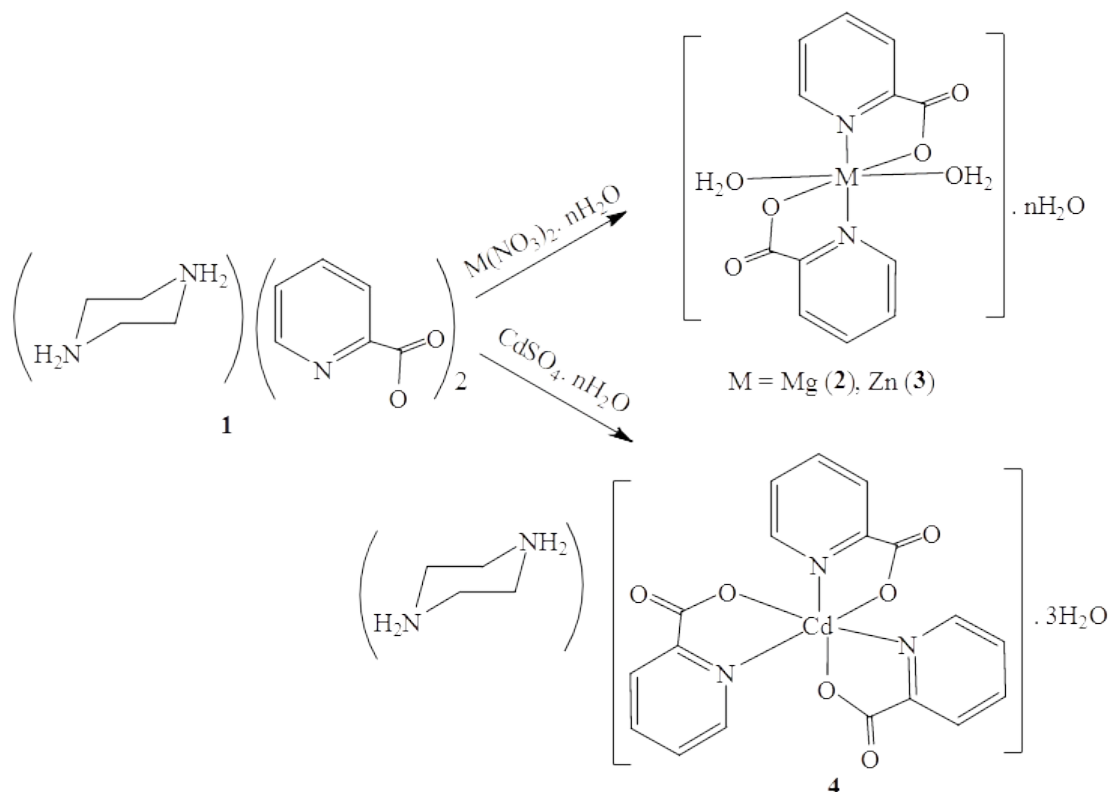


Figure 3: Synthesis of complexes **2-4**.

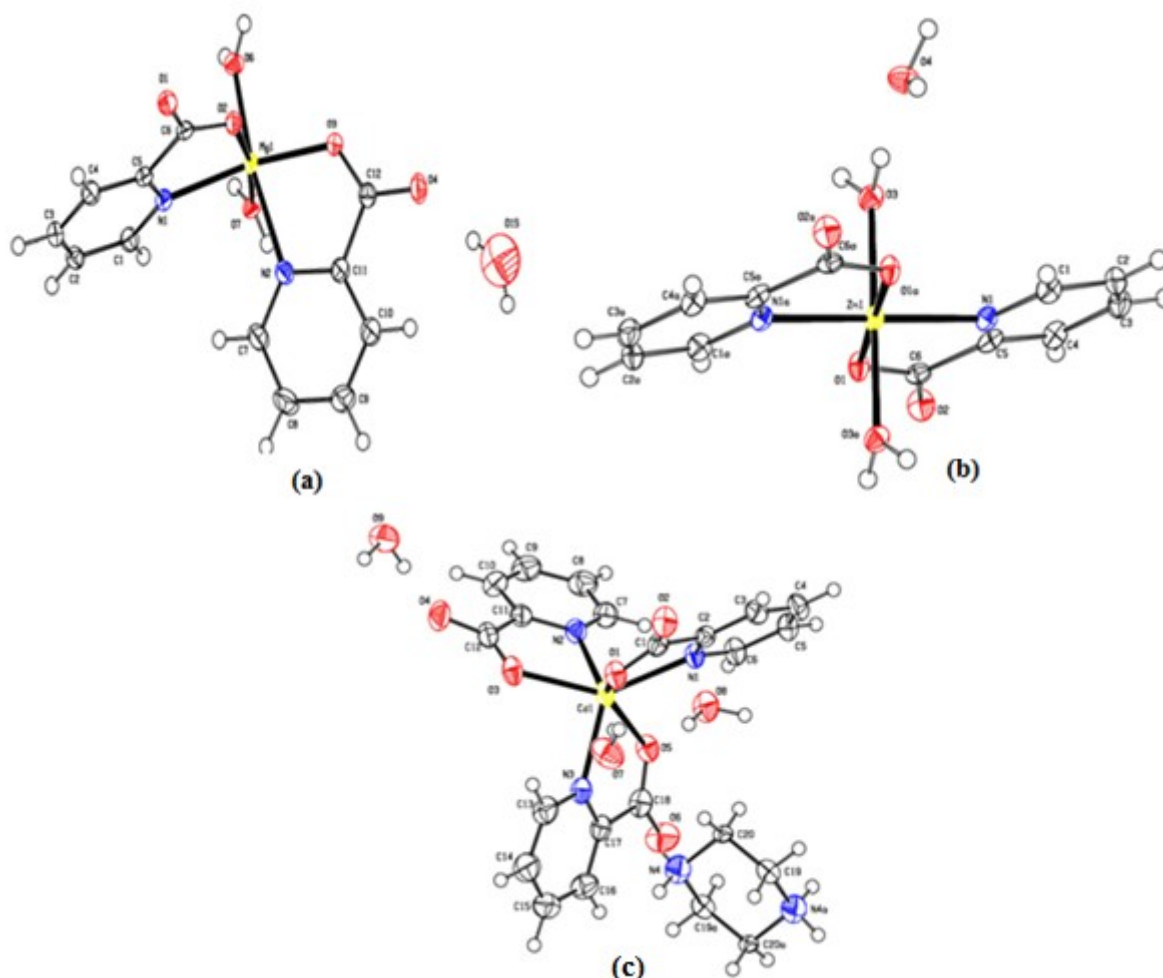
The analyses, crystal systems and space groups of the compounds (**1-4**) reported in the literature are given in Table 1.

Table 1: Proton transfer salt, $(\text{H}_2\text{Ppz})(\text{Py-2-c})_2$, and its Mg(II) (**2**), Zn(II) (**3**) and Cd(II) (**4**) complexes.

Ref. No	Analyses	Proton Transfer Salt and Complexes	Space Group	Crystal system
(38)	IR and NMR	$(\text{H}_2\text{Ppz})(\text{Py-2-c})_2$ (1)	-	-
(38)	IR and X-ray	$[\text{Mg}(\text{Py-2-c})_2(\text{H}_2\text{O})_2]\cdot\text{H}_2\text{O}$ (2)	$P2_1/n$	Monoclinic
(38)	IR and X-ray	$[\text{Zn}(\text{Py-2-c})_2(\text{H}_2\text{O})_2]\cdot\text{H}_2\text{O}$ (3)	$P2_1/n$	Monoclinic
(38)	IR and X-ray	$(\text{H}_2\text{Ppz})[\text{Cd}(\text{Py-2-c})_3]\cdot 3\text{H}_2\text{O}$ (4)	$P2_1/n$	Monoclinic

In compound **2**, the Mg^{2+} coordinates to two oxygen (O2 and O3) and two nitrogen atoms (N1a and N2) of the two Py-2-c⁻ ligands, and two oxygen atoms (O6 and O7) of the two H₂O molecules, forming the distorted octahedral geometry. The torsion angles

of N2-Mg1-N1-C1 and N2-Mg1-N1-C5 are -84.43(11) and 96.05(8) Å, respectively, indicating that the planes of the two ligands are coplanar (38) (Figure 4a).

**Figure 4:** Crystal structures (a) for **2**, (b) for **3** and (c) for **4**.

In $[\text{Zn}(\text{Py-2-c})_2(\text{H}_2\text{O})_2]\cdot\text{H}_2\text{O}$ (**3**) complex, the N1-Zn1-N1a, O1-Zn1-O1a and O3-Zn1-O3a angles around the Zn^{2+} ion are equivalent to 180.00°, indicating that the geometry is a normal octahedral (Figure 4b). In the Zn(II) (**3**) complex, there are many O-H...O H-bonds between the metal and the coordinated and uncoordinated H₂O molecule (38).

In asymmetric unit of Cd(II) (**4**) compound contains two ionic moieties $[\text{Cd}(\text{Py-2-c})_3]^{2-}$ anion and $(\text{pipH}_2)^{2+}$ cation and three lattice water molecules. The Cd(II) ion, which has six coordination numbers

in the complex, is attached to the three oxygen and three nitrogen atoms of the three Py-2-c⁻ rings (Figure 4c). The extensive hydrogen bond interactions between cationic, anionic moieties, and uncoordinated H₂O molecules along the lattice of the $(\text{H}_2\text{Ppz})[\text{Cd}(\text{Py-2-c})_3]\cdot 3\text{H}_2\text{O}$ (**4**) complex are of great importance in stabilizing the crystal (38).

2.2. The proton transfer compound, $(\text{H}_2\text{Ppz})(\text{Py-2-c})_2\cdot\text{H}_2\text{O}$ (**5**)

Proton transfer compound, $(\text{H}_2\text{Ppz})(\text{Py-2-c})_2\cdot\text{H}_2\text{O}$ (**5**), was prepared (39, 40) from the reaction of Py-2-Hc

and Ppz (Figure 5).

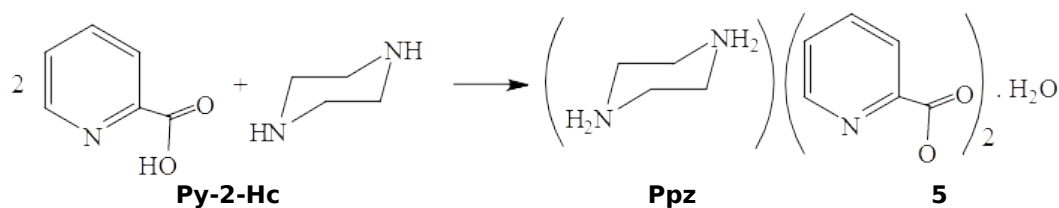


Figure 5: Synthesis of $(\text{H}_2\text{Ppz})(\text{Py-2-c})_2 \cdot \text{H}_2\text{O}$ (**5**).

The NMR (^1H and ^{13}C) spectrum data confirmed the formation of the proton transfer salt **5**. ^1H NMR spectrum of $(\text{H}_2\text{Ppz})(\text{Py-2-c})_2 \cdot \text{H}_2\text{O}$ (**5**) exhibited signals at 7.0, 8.0 and 8.1 ppm in the aromatic region for Py-2-c $^-$ ring protons and signals at 3.41 ppm for $\text{H}_2\text{Ppz}^{2+}$ protons. The carbonyl group carbon atom was observed in down field at 169.25 ppm. Five signals in the aromatic region were attributed to the Py-2-c $^-$ ring carbons (124.12,

127.51, 143.14, 148.45, 149.15 ppm). The piperazine ring carbons resonated in the high field at 40.49 ppm. From the intensities of the peaks of ^1H NMR spectrum of $(\text{H}_2\text{Ppz})(\text{Py-2-c})_2 \cdot \text{H}_2\text{O}$, the $\text{H}_2\text{Ppz}^{2+}$ to Py-2-c $^-$ molar ratio was found to be 1:2. The proton transfer salt (**5**) contains in its asymmetric unit a $\text{H}_2\text{Ppz}^{2+}$ cation, two Py-2-c $^-$ anions and a H_2O molecule (39) (Figure 6).

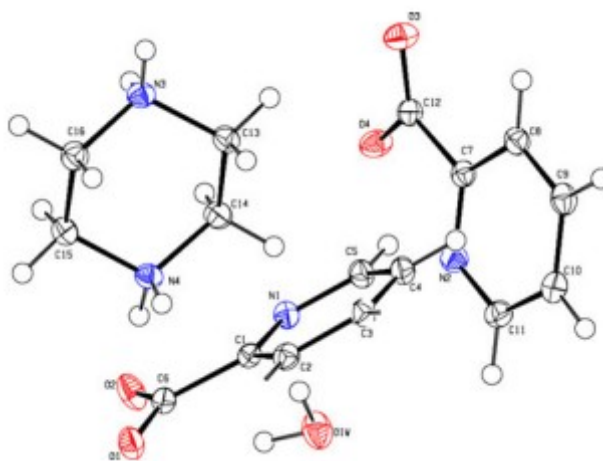


Figure 6: Molecular structure of $(\text{H}_2\text{Ppz})(\text{Py-2-c})_2 \cdot \text{H}_2\text{O}$ (**5**).

This salt is formed through electrostatic attraction between ions $(\text{Py-2-c})^-$ and $(\text{H}_2\text{Ppz})^{2+}$, different H-bonds ($\text{O-H}\cdots\text{O}$, $\text{O-H}\cdots\text{N}$, $\text{N-H}\cdots\text{O}$, $\text{N-H}\cdots\text{N}$, $\text{C-H}\cdots\text{O}$), and stacking interactions of $\text{C-H}\cdots\pi$ groups. The

crystal structure of **5** exhibits the strongest $\text{C-H}\cdots\pi$ interactions between C5-H5A and N2 , the C7-C11 ring and the C11-H11A and N1 , C1-C5 ring, with distances of 2.608 Å and 2.627 Å, respectively (39) (Figure 7).

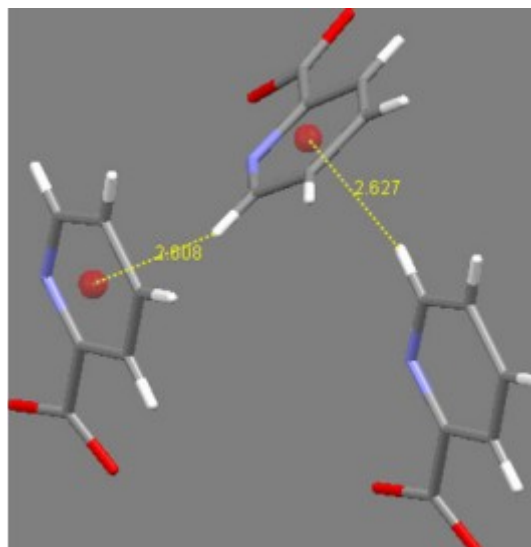


Figure 7: The C-H... π stacking interactions in **5**.

Mn(II) (**6**), *Ni(II)* (**7**) and *Cu(II)* (**8**) complexes of **5**
Complexes of proton transfer salt **5** $[\text{Mn}(\text{Py-2-c})_2(\text{H}_2\text{O})_2]_2 \cdot 2\text{H}_2\text{O}$ (**6**), $[\text{Ni}(\text{Py-2-c})_2(\text{H}_2\text{O})_2] \cdot \text{H}_2\text{O}$ (**7**) and $[\text{Cu}(\text{Py-2-c})_2\text{H}_2\text{O}]_n$ (**8**) were prepared (39) (Figure 8).

The analyzes, crystal systems and space groups of the compounds **5-8** reported in the literature are given in Table 2.

Table 2: Proton transfer salt, $(\text{H}_2\text{Ppz})(\text{Py-2-c})_2 \cdot \text{H}_2\text{O}$ (**5**), and its *Mn(II)* (**6**), *Ni(II)* (**7**) and *Cu(II)* (**8**) compounds.

Ref. No	Analyses	Proton Transfer Salt and Complexes	Space Group	Crystal system
(39)	NMR, IR, X-ray and elemental analysis	$(\text{H}_2\text{Ppz})(\text{Py-2-c})_2 \cdot \text{H}_2\text{O}$ (5)	$P2_1/c$	Monoclinic
(39)	NMR, IR, X-ray and elemental analysis	$[\text{Mn}(\text{Py-2-c})_2(\text{H}_2\text{O})_2]_2 \cdot 2\text{H}_2\text{O}$ (6)	$P1$	Triclinic
(39)	NMR, IR, X-ray and elemental analysis	$[\text{Ni}(\text{Py-2-c})_2(\text{H}_2\text{O})_2] \cdot \text{H}_2\text{O}$ (7)	$P2_1/n$	Monoclinic
(39)	NMR, IR, X-ray and elemental analysis	$[\text{Cu}(\text{Py-2-c})_2\text{H}_2\text{O}]_n$ (8)	$P1$	Triclinic

$[\text{Mn}(\text{Py-2-c})_2(\text{H}_2\text{O})_2]_2 \cdot 2\text{H}_2\text{O}$ (**6**), $[\text{Ni}(\text{Py-2-c})_2(\text{H}_2\text{O})_2] \cdot \text{H}_2\text{O}$ (**7**) and $[\text{Cu}(\text{Py-2-c})_2\text{H}_2\text{O}]_n$ (**8**) complexes contain Py-2-c⁻ ring and water molecule of proton transfer salt (**5**) components. In the molecular structures of the complexes (Figures 9 for **6**, 10a for **7** and 11 for **8**), it was observed that

pyridine-2-carboxylate was coordinated to each M(II) ion as a bidentate ligand. In these complexes extensive H-bonds such as O-H...O, O-H...N, N-H...O, N-H...N, C-H...O and C-H... π and C-O... π interactions provides to form a 3-D structure (39).

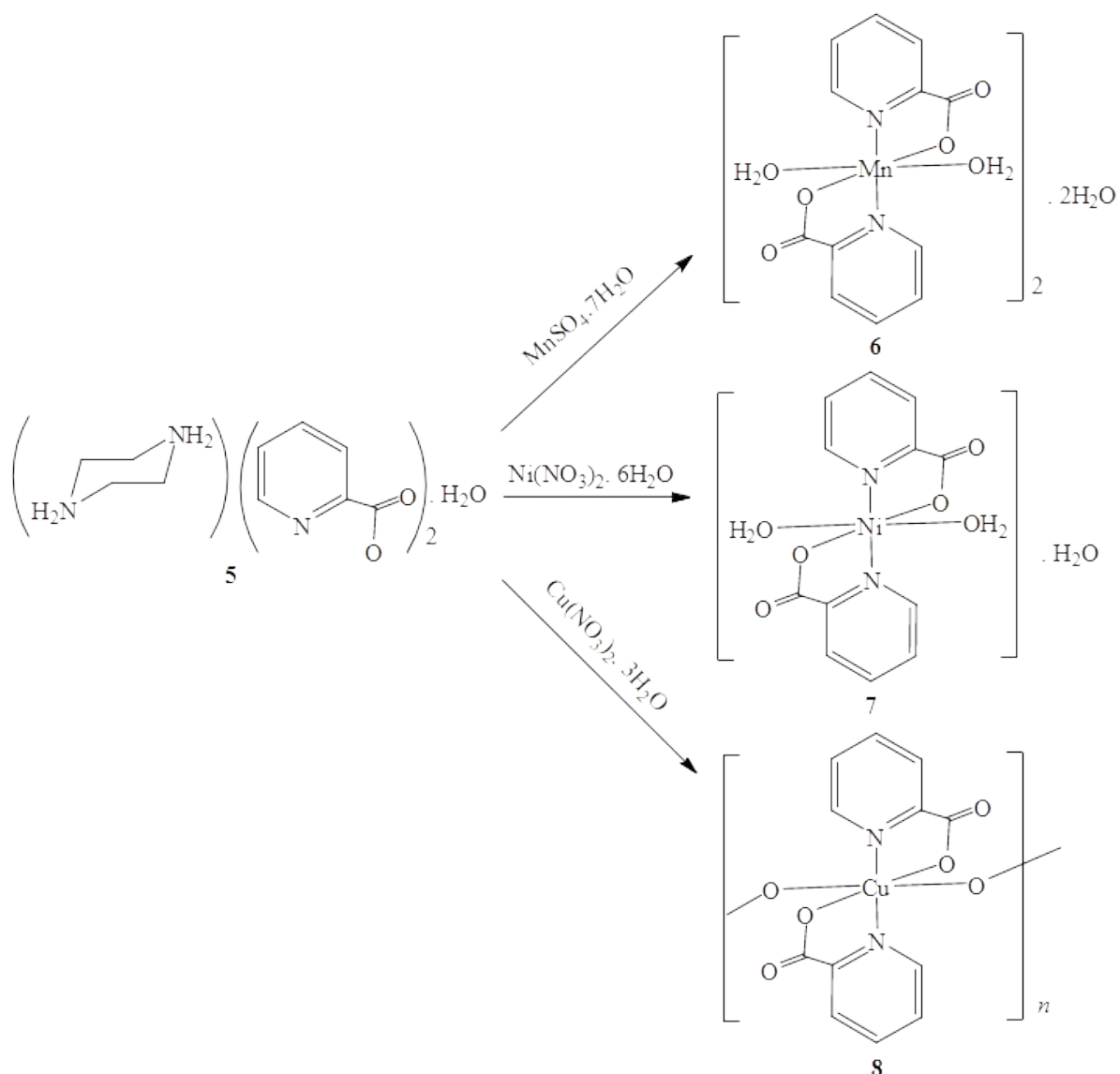


Figure 8: Synthesis of complexes 6-8.

The asymmetric unit of $[\text{Mn}(\text{Py-2-c})_2(\text{H}_2\text{O})_2]_2 \cdot 2\text{H}_2\text{O}$ (**6**) complex consists of two neutral Mn(II) molecules and H_2O molecules (Figure 9). The two complexes differ slightly in terms of bond angles and bond lengths. Each Mn(II) ion in the complex binds to the nitrogen and oxygen atoms of two Py-2-c-rings, as well as to the oxygens of two H_2O molecules, forming a six-coordinated distorted

octahedral geometry. In Mn(II) complex (**6**), it was observed that the O3-Mn1-O5 ($164.19(17)^\circ$) and O9-Mn2-O11 ($167.77(17)^\circ$) angles deviated from linearity around Mn^{2+} ions (Mn1 and Mn2). The total bond angles around Mn1 and Mn2 are equal to 362.4° . This means that the atoms form a flattened tetrahedral around the central atom and the Mn^{2+} ion is out of plane (39).

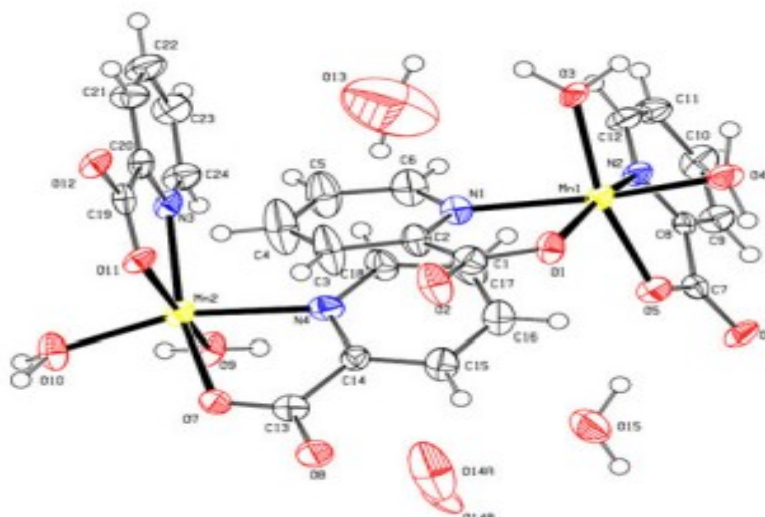


Figure 9: Molecular structure of **6**.

In the $[\text{Ni}(\text{Py-2-c})_2(\text{H}_2\text{O})_2]\cdot\text{H}_2\text{O}$ (**7**) complex, the Ni(II) ion is coordinated by the two nitrogen and two oxygen atoms of the two Py-2-c⁻ rings and the oxygens of the two H₂O molecules and has a distorted octahedral geometry. The oxygen atoms (O3 and O3a) of the coordinated H₂O molecules are in the axial position, while the two oxygen and two

nitrogen atoms (O2, O2a, N1 and N1a) of the Py-2-c⁻ anion are in the equatorial position. The bond angles around Ni(II) (N-Ni-N and O-Ni-O) are 180°, indicating that the coordination around Ni²⁺ is octahedral (Figure 10a). The cavity between the layers of the $[\text{Ni}(\text{Py-2-c})_2(\text{H}_2\text{O})_2]$ (**7**) part is filled by the H₂O molecules (39) (Figure 10b).

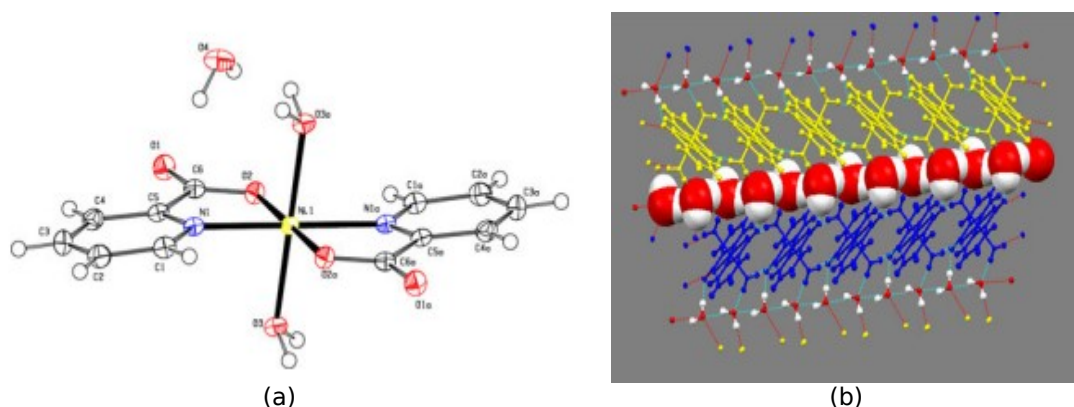


Figure 10: (a) Molecular structure and (b) A layered packing of $[\text{Ni}(\text{Py-2-c})_2(\text{H}_2\text{O})_2]\cdot\text{H}_2\text{O}$ (**7**).

In the $[\text{Cu}(\text{Py-2-c})_2(\text{H}_2\text{O})_n]$ (**8**) complex, Cu(II) atoms have six coordination environments, with the two nitrogen and two oxygen atoms of the two

carboxylate ligands and the two oxygen atoms of the two pyridine 2-carboxylate ions acting as bridges between the two Cu(II) ions.

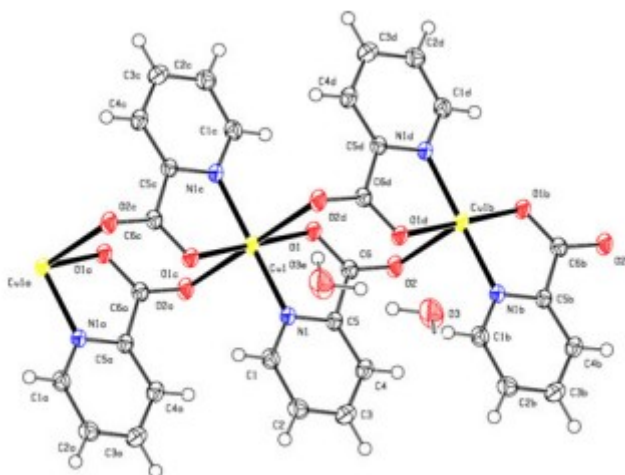


Figure 11: Molecular structure of $[\text{Cu}(\text{Py-2-c})_2\text{H}_2\text{O}]_n$ (**8**).

$[\text{Cu}(\text{Py-2-c})_2\text{H}_2\text{O}]_n$ (**8**) includes neutral polymeric compound and lattice H_2O molecule (Figure 11). Cu^{2+} ion is coordinated to oxygen [Cu1-O1 1.930(2) Å] and nitrogen Cu1-N1 1.959(2) Å atoms of two Py-2-c⁻ anions and two bridging oxygen atoms of the other carboxylate groups. Intramolecular O-H...O and C-H...O H-bonds with D...A ranging from 2.826(4) to 3.202(3) Å stabilize the molecular structure (39).

3. CONCLUSION

In this study, proton transfer salts synthesized from piperazine and pyridine-2-carboxylic acid and their metal complexes from 2009 to the present are presented. It was observed that pyridine-2-carboxylate was coordinated to metal ions but not piperazine in all complexes containing mostly d-block metals. Only one of the studied complexes contains piperazine as a complementary ion.

4. CONFLICT OF INTEREST

The authors declare no conflicts of interest.

5. REFERENCES

- Celestine MJ, Bullock JL, Boodram S, Rambaran VH, Holder AA. Interesting properties of p-, d-, and f-block elements when coordinated with dipicolinic acid and its derivatives as ligands: their use as inorganic pharmaceuticals. *Reviews in Inorganic Chemistry*. 2015 Jun 1;35(2):57-67. [<URL>](#).
- Mihajlović-Lalić LE, Poljarević J, Grgurić-Šipka S. Metal complexes with α -picolinic acid frameworks and their antitumor activity. *Inorganica Chimica Acta*. 2021 Nov;527:120582. [<URL>](#).
- Soares-Santos PCR, Paz FAA, Ferreira RAS, Klinowski J, Carlos LD, Trindade T, et al. Coordination modes of pyridine-carboxylic acid derivatives in samarium (III) complexes. *Polyhedron*. 2006 Aug;25(12):2471-82. [<URL>](#).
- Moore JW, Glick MD, Baker WA. Crystal structures of hydrated lanthanide(III) nicotinate, $\text{La}_2(\text{C}_5\text{H}_4\text{NCO}_2)_6(\text{H}_2\text{O})_4$ and $\text{Sm}_2(\text{C}_5\text{H}_4\text{NCO}_2)_6(\text{H}_2\text{O})_4$. *Journal of the American Chemical Society*. 1972 Mar;94(6):1858-65. [<URL>](#).
- Mahler HR, Cordes EH. In: *Biological Chemistry*. 2nd edition. New York: Harper and Row Publishers; 1971. p. 801-3.
- Ogata S, Takeuchi M, Okumura K, Taguchi H. Apoptosis Induced by Niacin-related Compounds in HL-60 Cells. *Bioscience, Biotechnology, and Biochemistry*. 1998 Jan;62(12):2351-6. [<URL>](#).
- Berner TO, Murphy MM, Slesinski R. Determining the safety of chromium tripicolinate for addition to foods as a nutrient supplement. *Food and Chemical Toxicology*. 2004 Jun;42(6):1029-42. [<URL>](#).
- Maret W. Chromium supplementation in human health, metabolic syndrome, and diabetes. *Metal Ions in Life Sciences*. 2019;19:231-51.
- Avcı D, Altürk S, Sönmez F, Tamer Ö, Başoğlu A, Atalay Y, et al. Three novel Cu(II), Cd(II) and Cr(III) complexes of 6-Methylpyridine-2-carboxylic acid with thiocyanate: Synthesis, crystal structures, DFT calculations, molecular docking and α -Glucosidase inhibition studies. *Tetrahedron*. 2018 Dec;74(50):7198-208. [<URL>](#).
- Avcı D, Altürk S, Sönmez F, Tamer Ö, Başoğlu A, Atalay Y, et al. A novel series of mixed-ligand M(II) complexes containing 2,2'-bipyridyl as potent α -glucosidase inhibitor: synthesis, crystal structure, DFT calculations, and molecular docking. *Journal of Biological Inorganic Chemistry*. 2019 Aug 1;24(5):747-64. [<URL>](#).
- Avcı D, Altürk S, Sönmez F, Tamer Ö, Başoğlu A, Atalay Y, et al. Novel Cu(II), Co(II) and Zn(II) metal complexes with mixed-ligand: Synthesis, crystal structure, α -glucosidase inhibition, DFT calculations, and molecular docking. *Journal of Molecular Structure*. 2019 Dec;1197:645-55. [<URL>](#).
- Zhang M, Chen C, Wang Q, Fu W, Huang K, Zhou W. A metal-organic framework functionalized with piperazine exhibiting enhanced CH₄ storage. *Journal of Materials Chemistry A*. 2017;5(1):349-54. [<URL>](#).
- Reddy JS, Ganesh SV, Nagalapalli R, Dandela R, Solomon KA, Kumar KA, et al. Fluoroquinolone salts with carboxylic acids. *Journal of Pharmaceutical Sciences*. 2011 Aug;100(8):3160-76. [<URL>](#).

14. Stepanovs D, Jure M, Mishnev A. Preparation and crystal structure of sildenafil salicylate. *Mendeleev Communications*. 2015 Jan;25(1):49-50. [<URL>](#).
15. Vepuri SB, Devarajegowda HC, Soliman ME. Synthesis, characterization and molecular modelling of a novel dipyridamole supramolecule - X-ray structure, quantum mechanics and molecular dynamics study to comprehend the hydrogen bond structure-activity relationship. *Journal of Molecular Structure*. 2016 Feb;1105:194-204. [<URL>](#).
16. Satyanarayana Reddy J, Ravikumar N, Gaddamanugu G, Naresh KN, Rajan SS, Anand Solomon K. Synthesis, crystal structure, spectral characterization and fluorescence studies of salts of α -mangostin with APIs. *Journal of Molecular Structure*. 2013 May;1039:137-43. [<URL>](#).
17. Aghabozorg H, Manteghi F, Sheshmani S. A brief review on structural concepts of novel supramolecular proton transfer compounds and their metal complexes. *Journal of the Iranian Chemical Society*. 2008 Jun;5(2):184-227. [<URL>](#).
18. Moghimi A, Moosavi SM, Kordestani D, Maddah B, Shamsipur M, Aghabozorg H, et al. Pyridine-2,6-bis(monothiocarboxylic) acid and 2-aminopyridine as building blocks of a novel proton transfer compound: Solution and X-ray crystal structural studies. *Journal of Molecular Structure*. 2007 Feb;828(1-3):38-45. [<URL>](#).
19. Pytka K, Rapacz A, Zygmunt M, Olczyk A, Waszkielewicz A, Sapa J, et al. Antidepressant-like activity of a new piperazine derivative of xanthone in the forced swim test in mice: The involvement of serotonergic system. *Pharmacological Reports*. 2015 Feb;67(1):160-5. [<URL>](#).
20. Thamban Chandrika N, Shrestha SK, Ngo HX, Tsodikov OV, Howard KC, Garneau-Tsodikova S. Alkylated Piperazines and Piperazine-Azole Hybrids as Antifungal Agents. *Journal of Medicinal Chemistry*. 2018 Jan 11;61(1):158-73. [<URL>](#).
21. McNair TJ, Wubin FA, Hoppe ET, Schmidt JL, dePeyster FA. Antitumor action of several new piperazine derivatives compared to certain standard anticancer agents. *Journal of Surgical Research*. 1963 May;3(3):130-6. [<URL>](#).
22. Ananda Kumar CS, Nanjunda Swamy S, Thimmegowda NR, Benaka Prasad SB, Yip GW, Rangappa KS. Synthesis and evaluation of 1-benzhydryl-sulfonyl-piperazine derivatives as inhibitors of MDA-MB-231 human breast cancer cell proliferation. *Medicinal Chemistry Research*. 2007 Sep;16(4):179-87. [<URL>](#).
23. Ahmadi A, Khalili M, Nafarie A, Yazdani A, Nahri-Niknafs B. Synthesis and anti-inflammatory effects of new piperazine and ethanolamine derivatives of H1-antihistaminic drugs. *Mini-Reviews in Medicinal Chemistry*. 2012 Sep 1;12(12):1282-92. [<URL>](#).
24. Brown AM, Patch TL, Kaumann AJ. The antimigraine drugs ergotamine and dihydroergotamine are potent 5-HT_{1C} receptor agonists in piglet choroid plexus. *British Journal of Pharmacology*. 1991 Sep;104(1):45-8. [<URL>](#).
25. Kumar Parai M, Panda G, Srivastava K, Kumar Puri S. Design, synthesis and antimalarial activity of benzene and isoquinoline sulfonamide derivatives. *Bioorganic & Medicinal Chemistry Letters*. 2008 Jan;18(2):776-81. [<URL>](#).
26. Fazil S, Ravindran R, Sarau Devi A, Bijili BK. Structural studies of 1-phenyl-2,3-dimethyl-5-oxo-1,2-dihydro-1H-pyrazol-4-ammonium 2[(2-carboxyphenyl)disulfanyl]benzoate. *Journal of Molecular Structure*. 2012 Aug;1021:147-52. [<URL>](#).
27. Ghasemi K, Ghasemi F, Rezvani AR, Shokrollahi A, Refahi M, García-Granda S, et al. Mn(II) and Zn(II) ions catalytic oxidation of o-phenylenediamine and characterization, X-ray crystal structure and solution study of the final products DAPH+Cl⁻·3H₂O and [DAPH][Zn(dipicH)(dipic)]·4H₂O. *Polyhedron*. 2016 May;110:55-62. [<URL>](#).
28. Majerz I, Olovsson I. Influence of proton transfer on the geometry of the donor and acceptor in NHN+ hydrogen bonds. *Journal of Molecular Structure*. 2010 Jul;976(1-3):11-8. [<URL>](#).
29. Özdemir N. Structural and spectroscopic characterization of 2-mesityl-1H-benzo[d]imidazol-3-ium chloride: A combined experimental and theoretical analysis. *Spectrochimica Acta Part A: Molecular and Biomolecular Spectroscopy*. 2012 Jun;91:51-60. [<URL>](#).
30. Ghasemi K, Rezvani AR, Shokrollahi A, Zarghampour F, Moghimi A, García-Granda S, et al. Synthesis, characterization, crystal structure and solution studies of a novel proton transfer (charge transfer) complex of 2,2'-dipyridylamine with 2,6-pyridine dicarboxylic acid. *Journal of Molecular Structure*. 2015 Jun;1089:184-90. [<URL>](#).
31. Takaiwa T, Koyama A, Nagaishi Y, Nakajima K, Sumimoto M, Hori K, et al. Structural characterization of 2,3,5,6-tetramethyl-p-phenylenediamine radical cation and its dimer in molecular crystals. *Journal of Molecular Structure*. 2015 Mar;1083:260-7. [<URL>](#).
32. Ghasemi K, Rezvani AR, Habibi-Khorassani SM, Shahraiki M, Shokrollahi A, Moghimi A, et al. An experimental and theoretical study of a hydrogen-bonded complex: O-phenylenediamine with 2,6-pyridinedicarboxylic acid. *Journal of Molecular Structure*. 2015 Nov;1100:597-604. [<URL>](#).
33. Gopi R, Ramanathan N, Sundararajan K. Hydrogen-bonded complexes of acetylene and acetonitrile: A matrix isolation infrared and computational study. *Journal of Molecular Structure*. 2015 Mar;1083:364-73. [<URL>](#).
34. Shehab OR, Mansour AM. Sparfloxacin charge transfer complexes with 2,3-dichloro-5,6-dicyano-1,4-benzoquinone and tetracyanoquinodimethane: Molecular structures, spectral, and DFT studies. *Journal of Molecular Structure*. 2015 Aug;1093:186-94. [<URL>](#).
35. Rzokey AA, Ahmad A. Synthesis, spectroscopic studies and thermal analysis of charge-transfer complex of 2,2'-bipyridine with 4-hydroxybenzoic acid in different polar solvents. *Journal of Molecular Structure*. 2014 Nov;1076:453-60. [<URL>](#).
36. Refat MS, Adam AMA, Saad HA. Utility of charge-transfer complexation for the assessment of macrocyclic polyethers: Spectroscopic, thermal and surface morphology characteristics of two highly crown ethers complexed with acido acceptors. *Journal of Molecular Structure*. 2015 Apr;1085:178-90. [<URL>](#).
37. Singh N, Ahmad A. Synthesis and spectrophotometric studies of charge transfer complexes of p-nitroaniline with benzoic acid in different polar solvents. *Journal of Molecular Structure*. 2014 Sep;1074:408-15. [<URL>](#).

38. Ghadermazi M, Soleimannejad J, Sheshmani S, Shamsipur M, Ghanbari M, Eslami MR. Characterization, crystal structures and solution studies of Zn(II), Cd(II) and Mg(II) complexes obtained from a proton transfer compound including pyridine-2-carboxylic acid and piperazine. Journal of the Iranian Chemical Society. 2012 Aug;9(4):579-89. [<URL>](#).

39. Sheshmani S, Soleimannejad J, Ghadermazi M, Shamsipur M, Ghanbari M, Motieian E, et al. Comparative study on MnII, NiII and CuII supramolecular complexes

obtained from a proton transfer methodology: solid- and solution-state studies. Journal of the Iranian Chemical Society. 2013 Aug;10(4):817-29. [<URL>](#).

40. Rekha P, Chakkaravarthi G, Mohan Kumar R, Vinitha G, Kanagadurai R. Growth, structural and optical limiting property of a new third order nonlinear optical material: piperazinium bis (2-carboxypyridine) monohydrate. Journal of Materials Science: Materials in Electronics. 2019 May;30(10):9471-88. [<URL>](#).



Acetylcholinesterase Inhibition Properties and Docking Studies of Compounds Based on 6-Hydrazinyl-1,3,4-Trimethyl-1H-Pyrazolo[3,4-b]Pyridine

Seyit Ali GÜNGÖR^{1*} 

¹ Kahramanmaraş Sutcu Imam University, Department of Chemistry, Faculty of Science, Kahramanmaraş, 46050, Turkey

Abstract: New compounds based on 6-hydrazinyl-1,3,4-trimethyl-1h-pyrazolo[3,4-b]pyridine (3a and 3b) were synthesized and characterized by FTIR and ¹H/¹³C NMR spectroscopic methods and their *in vitro* acetylcholinesterase (AChE) inhibition studies were evaluated. Compound 3b (IC₅₀ value 104.4 μM) exhibited stronger AChE inhibitory activity than the reference galantamine compound (IC₅₀ value 139.4 μM). Molecular docking studies were performed to determine the key interactions and possible binding modes between AChE of compounds. The most active 3b the binding affinity is -10.28 kcal/mol.

Keywords: Synthesis, AChE inhibition, Docking.

Submitted: May 16, 2022. **Accepted:** October 11, 2022.

Cite this: Güngör SA. Acetylcholinesterase Inhibition Properties and Docking Studies of Compounds Based on 6-Hydrazinyl-1,3,4-Trimethyl-1H-Pyrazolo[3,4-b]Pyridine. JOTCSA. 2023;10(1):21–30.

DOI: <https://doi.org/10.18596/jotcsa.1117324>.

***Corresponding author. E-mail:** sagungor@ksu.edu.tr

1. INTRODUCTION

Alzheimer's disease (AD) set off 60-70% of dementia cases worldwide with an approximated global incidence of 24.3 million cases. AD is a chronic syndrome that disrupts the central nervous system (CNS). The mechanism of action for AChE inhibitors is the compensation for the loss of central cholinergic neurons in AD (and thus loss of the neurotransmitter acetylcholine (ACh)) through decreased breakdown of ACh. (AChE) inhibitors are actively used for the effective treatment of Alzheimer's disease. AD causes deficiencies in important features of the brain such as language, learning, orientation, memory and decision making (1). Old age comes first among the most important risk factors for AD (2). However, the exercises that can be done can cause a slight decrease in AD (3).

Among the most important therapeutic targets for AD are cholinesterase's (4,5). The most important reason for the increase in cognitive disorders in AD patients is the deterioration and neurodegeneration of cholinergic neurons in the brain. The cholinergic hypothesis postulates that Alzheimer's results from a reduced ability to synthesize (ACh) in an

individual, leading to progressive neurodegeneration. For this reason, AChE inhibitors have been used to reduce the degradation rate of ACh. AChE inhibitors increase the amount of ACh by preventing degradation and may increase the function of nerve cells. The differential distribution of AChE and BuChE within the brain suggests that both of these enzymes may play important biological roles in their interaction. Although animal models are not transferrable to human subjects due to different species-dependent systemic effects both models have proven to have a positive effect on cognitive abilities in the absence of BChE. Therefore, it has been suggested that BChE can be considered as a clinical target in the AD process, as it can take over the function of AChE in the regulation of cholinergic signalling.

There are several drugs used as cholinesterase inhibitors in the treatment of the disease. Donepezil, galantamine and rivastigmine (Figure 1) are the most widely used and have received regulatory approval for the treatment of people with mild to moderate Alzheimer's disease in all jurisdictions (6). There is also evidence to suggest that donepezil can improve the cognitive, functional and

neuropsychiatric status of patients with more advanced Alzheimer's disease (7-9). However, the high side effects of these drugs prompted researchers to find new cholinesterase inhibitors.

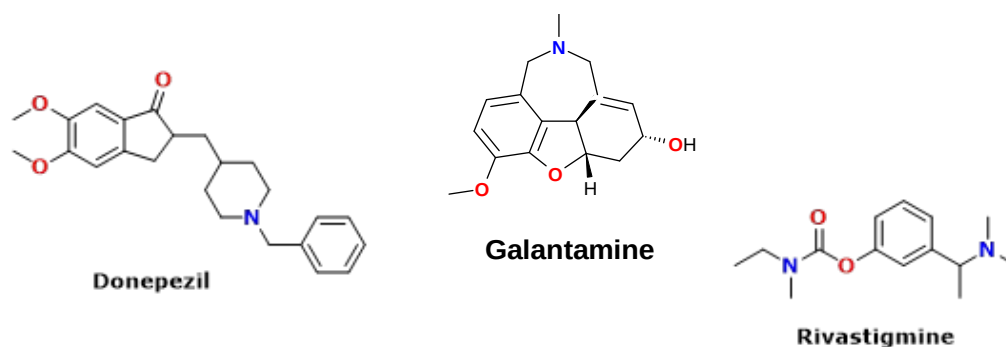


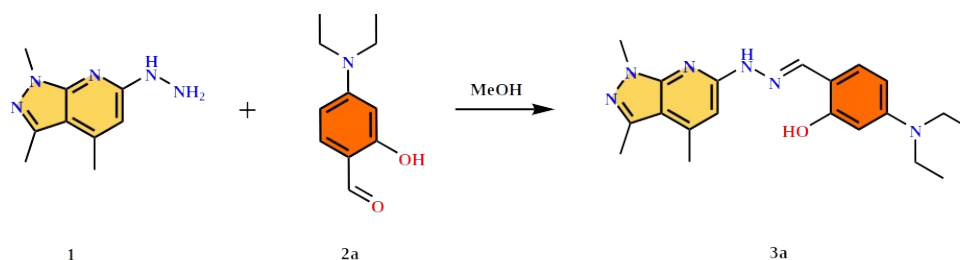
Figure 1: Drugs used for Alzheimer's.

In this study, two new compounds based on 6-hydrazinyl-1,3,4-trimethyl-1H-pyrazolo[3,4-*b*]pyridine were synthesized and their inhibitory effects on (AChE) activity were evaluated. Docking studies were performed to identify possible binding modes of compounds with residues in the AChE active site.

2. EXPERIMENTAL

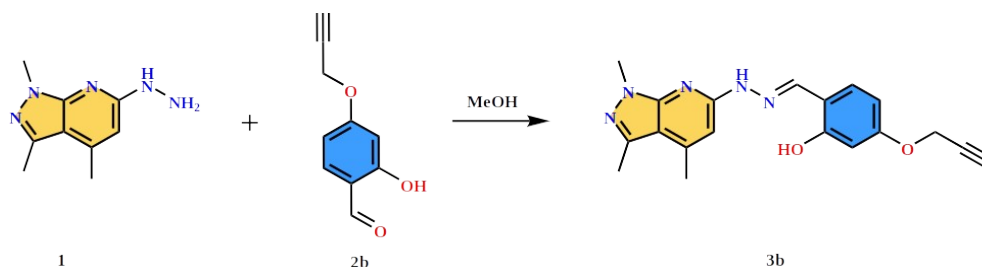
2.1. Synthesis of Compounds 3a and 3b

6-hydrazinyl-1,3,4-trimethyl-1H-pyrazolo[3,4-*b*]pyridine (0.65 mmol, 0.125 g) was dissolved in MeOH. Compound 2b was synthesized according to the literature (10,11). Then compound 2a (0.65 mmol, 0.126 g) or compound 2b (0.65 mmol, 0.114 g) added by dissolving with MeOH (15 mL). The reaction mixture was left to reflux overnight. It was then allowed to cool to room temperature and the solvent was removed with evaporator and obtain solid.



(*E*)-5-(diethylamino)-2-((2-(1,3,4-trimethyl-1H-pyrazolo[3,4-*b*]pyridin-6-yl)hydrazinylidene)methyl)phenol (**3a**): C₂₀H₂₆N₆O. **Yield:** 93%, **Color:** Light Yellow. **¹H NMR** (d₆-DMSO, δ) 11.03 (s, 1H), 10.89 (s, 1H), 8.12 (s, 1H), 7.22 (d, J = 8.5 Hz, 1H), 6.48 (s, 1H), 6.24 (d, J = 8.5 Hz, 1H), 6.14 (s, 1H), 3.78 (s, 3H), 3.34 (d, J = 6.9 Hz, 4H),

2.55 (s, 3H), 2.48 (s, 3H), 1.11 (t, J = 6.7 Hz, 6H). **¹³C NMR** (d₆-DMSO, δ) 158.85, 155.84, 151.30, 149.59, 144.09, 142.81, 140.24, 130.33, 109.00, 108.16, 104.00, 102.55, 98.13, 44.24, 33.17, 19.43, 14.95, 13.00. **FTIR** (ν, cm⁻¹): 2969, 1631 (-C=N-), 1588, 1387, 1351, 1247, 1218, 1190, 1126, 1091, 1070, 819.



(*E*)-5-(prop-2-yn-1-yloxy)-2-((2-(1,3,4-trimethyl-1H-pyrazolo[3,4-*b*]pyridin-6-yl)hydrazinylidene)methyl)phenol (**3b**): C₁₉H₁₉N₅O₂ **Yield:** 90%, **Color:** Light Yellow. **¹H NMR** (d₆-DMSO, δ) 11.11 (s, 2H), 8.22 (s, 1H), 7.62 - 7.37 (m, 1H), 6.60 (s, 1H), 6.57 - 6.44 (m, 1H), 4.81 (d, J

= 2.1 Hz, 1H), 3.79 (s, 2H), 3.63 (s, 1H), 2.57 (s, 2H), 2.49 (s, 2H). **¹³C NMR** (d₆-DMSO, δ) 159.23, 158.18, 155.86, 151.17, 144.35, 140.30, 129.41, 114.41, 109.30, 107.15, 102.74, 102.58, 79.57, 78.89, 55.94, 33.23, 19.42, 14.96. **FTIR** (ν, cm⁻¹): 2923,

2109 (-C≡CH), 1626 (-C=N-), 1593, 1497, 1386, 1242, 1160, 1028.

2.2. AChE inhibitors activities

Inhibitory activities of compounds based on 6-hydrazinyl-1,3,4-trimethyl-1h-pyrazolo[3,4-*b*]pyridine (3a and 3b) on acetylcholinesterase enzyme (AChE) were determined using the Ellman's method (12,13). Electrophorus electricus (electric eel AChE) is well known that the fish enzyme from was used due to lower price, availability, and high compatible to human AChE. The enzyme solution was prepared as 0.22 units/mL. Compounds 3a and 3b were dissolved in water (1×10^{-4} - 1×10^{-7} M). 100 μ L of phosphate buffer (pH: 6.7) was added to each well of 96 well-plates. Afterwards, different concentrations of the tested compounds (20 μ L) and AChE (20 μ L/well) were added and incubated at 25 °C for 10 min. Chromatographic reagent 5,5-dithio-bis(2-nitrobenzoic acid) (DTNB) (3 mM, 50 μ L/well) and substrates acetylthiocholine iodine (ATCI) (3 mM, 50 μ L/well) was added to the enzyme-inhibitor mixture. Yellow anion (2-Nitro-5-thiobenzoic acid) formation was recorded at 412 nm for 10 min. It was determined by preparing an identical solution of the enzyme in the absence of tested compounds (as a control). Control and inhibitor readings were corrected with a blank read. All operations were repeated three times. Concentrations of samples that inhibit degradation of substrate (acetylcholine) by 50% (IC₅₀) were determined by linear regression analysis between percent inhibition and sample concentration using Excel program. Galantamine was used as a standard and results were compared.

2.3. Docking Studies

The binding modes and interactions of 3a and 3b compounds, whose ACh inhibitory effects of examined by in vitro method were investigated molecular docking studies using AutoDock 4.2 software (14). For this purpose, crystal structure of acetylcholinesterase (AChE) (pdb code: 4EY6) were downloaded from the RCSB Protein Data Bank. Then using AutoDock Tools version 1.5.6 ligands, anions and water molecules were removed from the enzymes and polar hydrogen atoms, Kollman and Gasteiger charges were added to amino acid residues in the protein structure (15). The number of points in the x, y and z dimensions was 60 × 60 × 60. The root mean squared deviation (RMSD) of the atomic position between the original orientation of the co-crystal ligand and the re-docked ligand is computed. If the RMSD value is less than or equal to 2.0 Å is acceptable. To visualize molecular docking

results of conformations with the lowest binding energy Discovery Studio 2021 (16) and PyMOL (17) were used.

3. RESULTS AND DISCUSSION

3.1. FTIR analyses of compounds 3a and 3b

FT-IR analysis with ATR was performed to investigate the characteristic vibrational bands of compounds 3a and 3b. In the FT-IR spectra of the compounds, the carbonyl (C=O) group peaks of the starting compounds did not appear and the vibration bands of the imine (C=N) group were 1631 cm⁻¹ for 3a and 1626 cm⁻¹ for 3b was observed. In addition, vibrational band of the characteristic propargyl (C≡C) group of 3b was observed in 2109 cm⁻¹.

3.2. NMR analyses of compounds 3a and 3b

¹H/¹³C NMR spectra of compounds 3a and 3b were recorded in d₆-DMSO and data are presented in the experimental part. ¹H/¹³C NMR spectra of the compounds are given in figures 1 and 2. When the ¹H-NMR spectra of 3a and 3b are examined, the methyl group protons on the pyrazole and pyridine rings can be attribute to peaks around 2.48 ppm, 2.55 ppm and 3.78 ppm (NCH₃), respectively. The observed peaks in the range of 6.14-7.53 ppm belong to the aromatic ring protons. Imine group (HC=N) protons were observed at 8.12 and 8.22 ppm, respectively. The hydroxyl group (OH) protons of 3a were observed at 11.03 ppm and the NH protons at 10.89 ppm, while the hydroxyl and NH protons of 3b overlapped at 11.11 ppm. The methyl (CH₃) protons of the *N,N*-diethyl group of 3a were detected at 1.09-1.12 ppm and the protons of the NCH₂ group at 3.33-3.35 ppm. In the ¹H-NMR spectrum of 3b, the peak at 3.63 ppm the propargyl group proton and the peaks observed at 4.80-4.81 ppm to the OCH₂ protons are attributed. When the ¹³C-NMR spectra of 3a and 3b were examined, the imine group carbon atom signals were observed at 158.85 ppm and 159.23 ppm, respectively. Proton signals of aromatic ring carbon atoms were observed in the range of 98.13-158.18 ppm. The methyl group carbon atoms on the pyrazole and pyridine rings are attributed to signals observed around 14.95 ppm, 19.42 ppm and 33.17 ppm, respectively. The methyl (CH₃) and NCH₂ group carbon atom signals of the *N,N*-diethyl group of 3a were observed at 13.00 ppm and 44.24 ppm, respectively. The propargyl group carbon atom signals of 3b were observed at 78.89-79.57 ppm and the OCH₂ carbon atom signal was at 55.94 ppm.

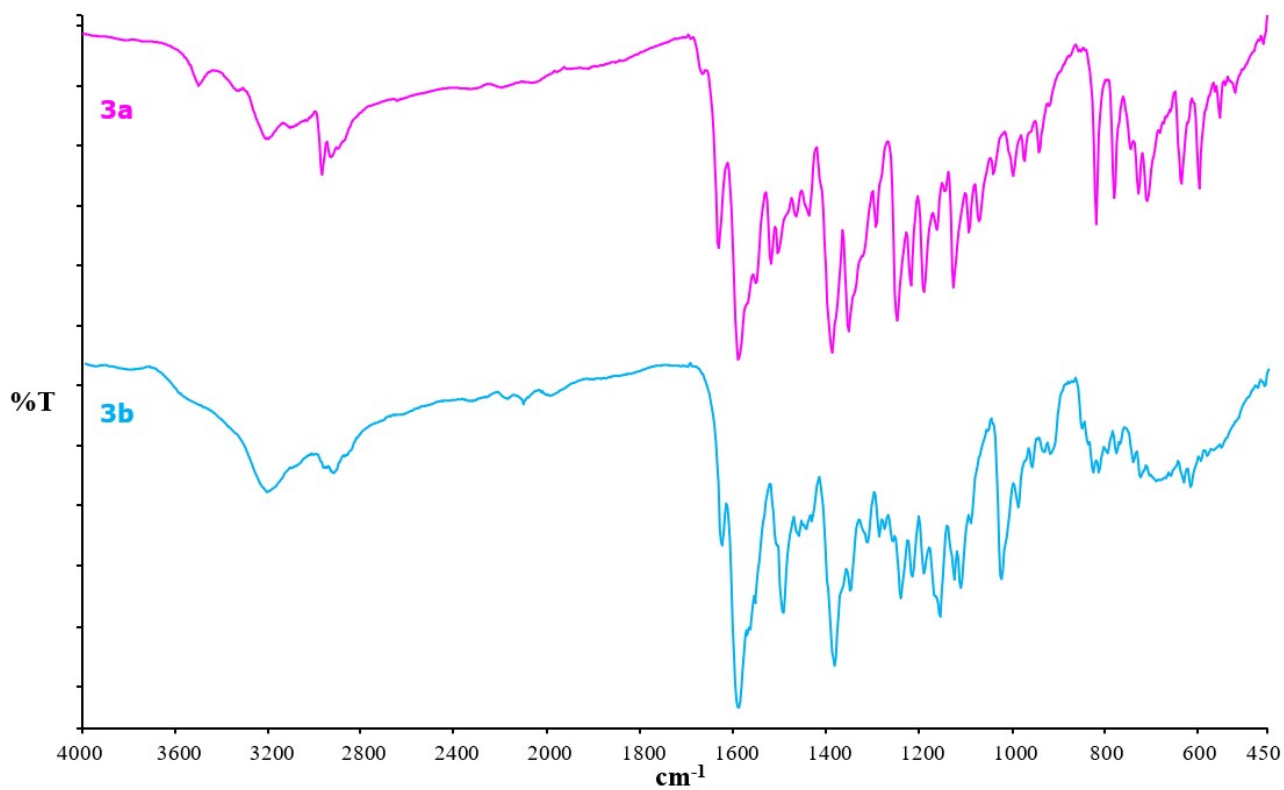
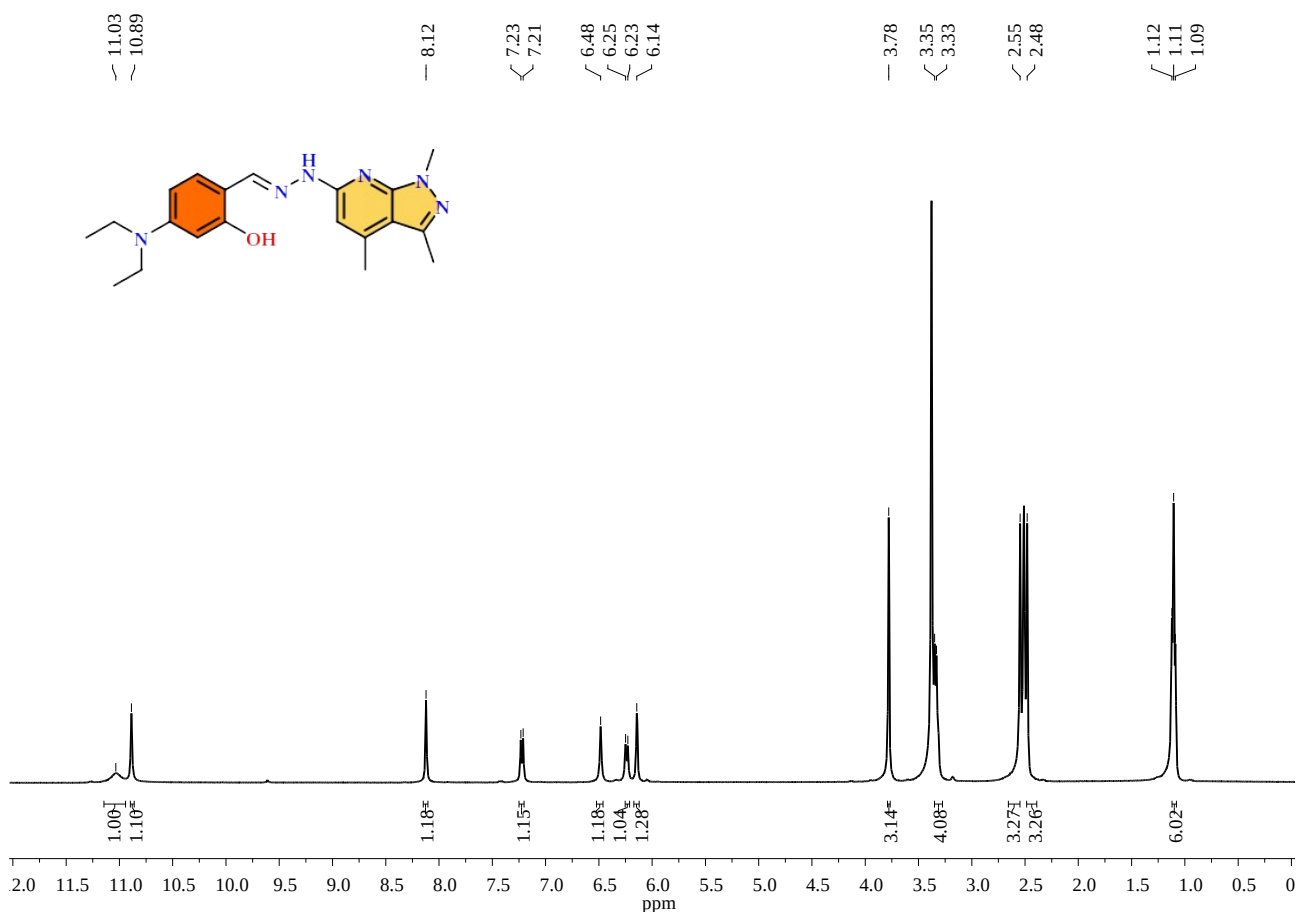


Figure 2: FTIR spectra of compounds 3a and 3b.



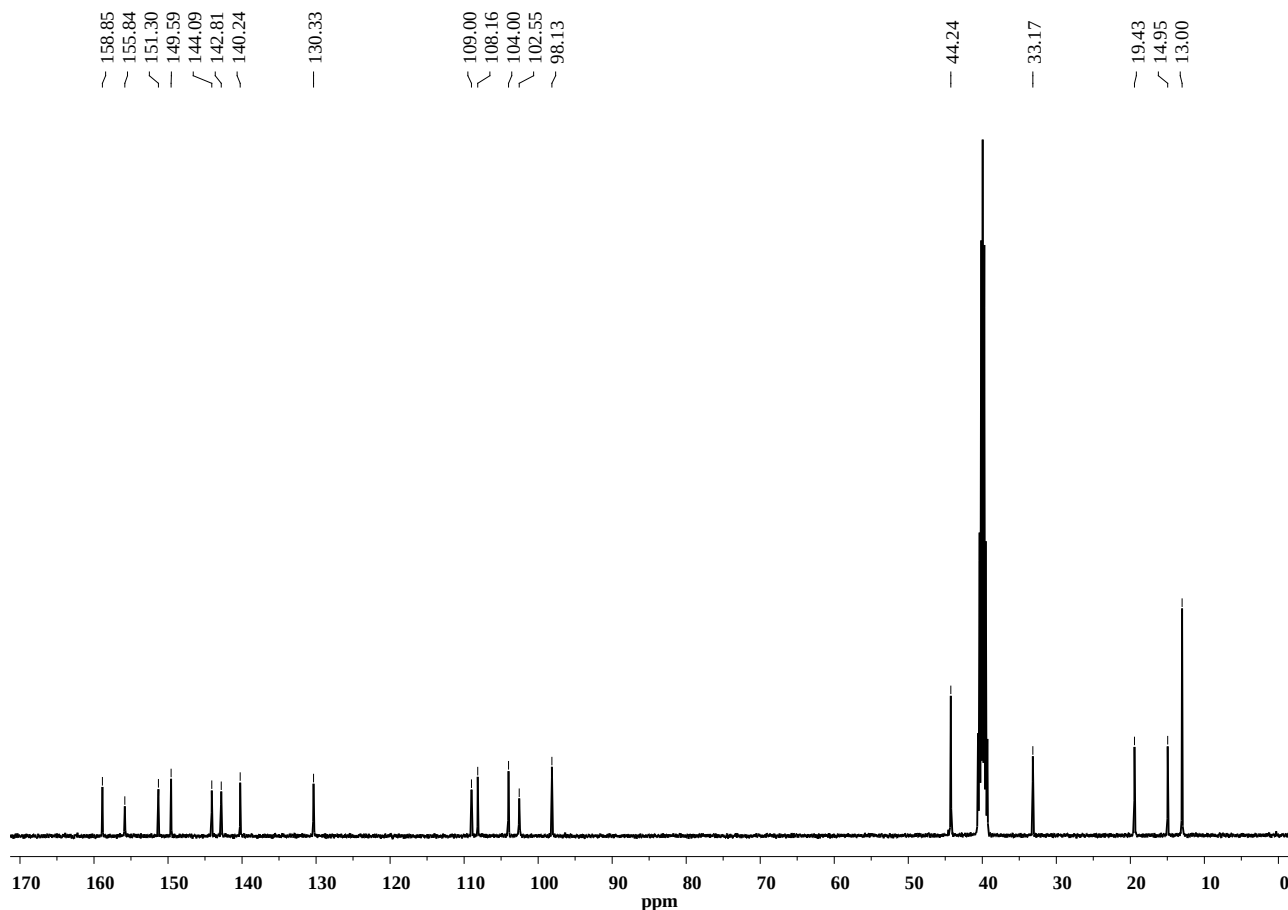
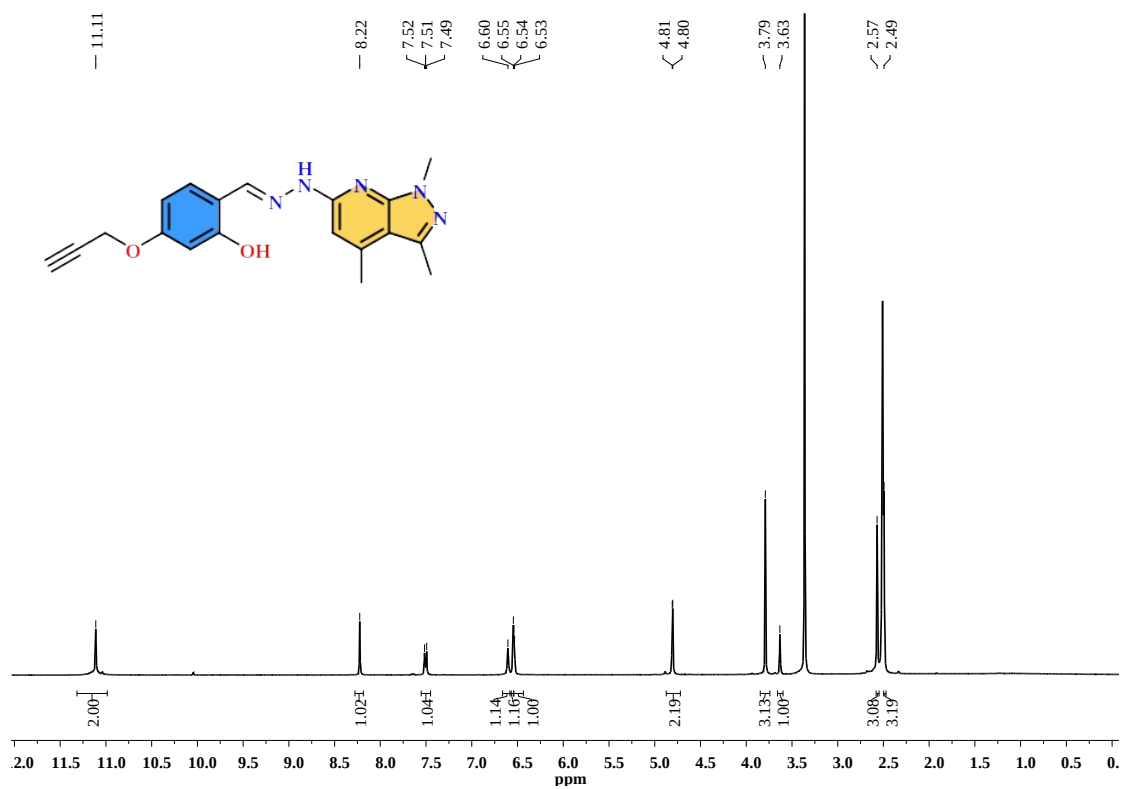


Figure 3: ^1H (^{13}C) NMR spectra of compound 3a



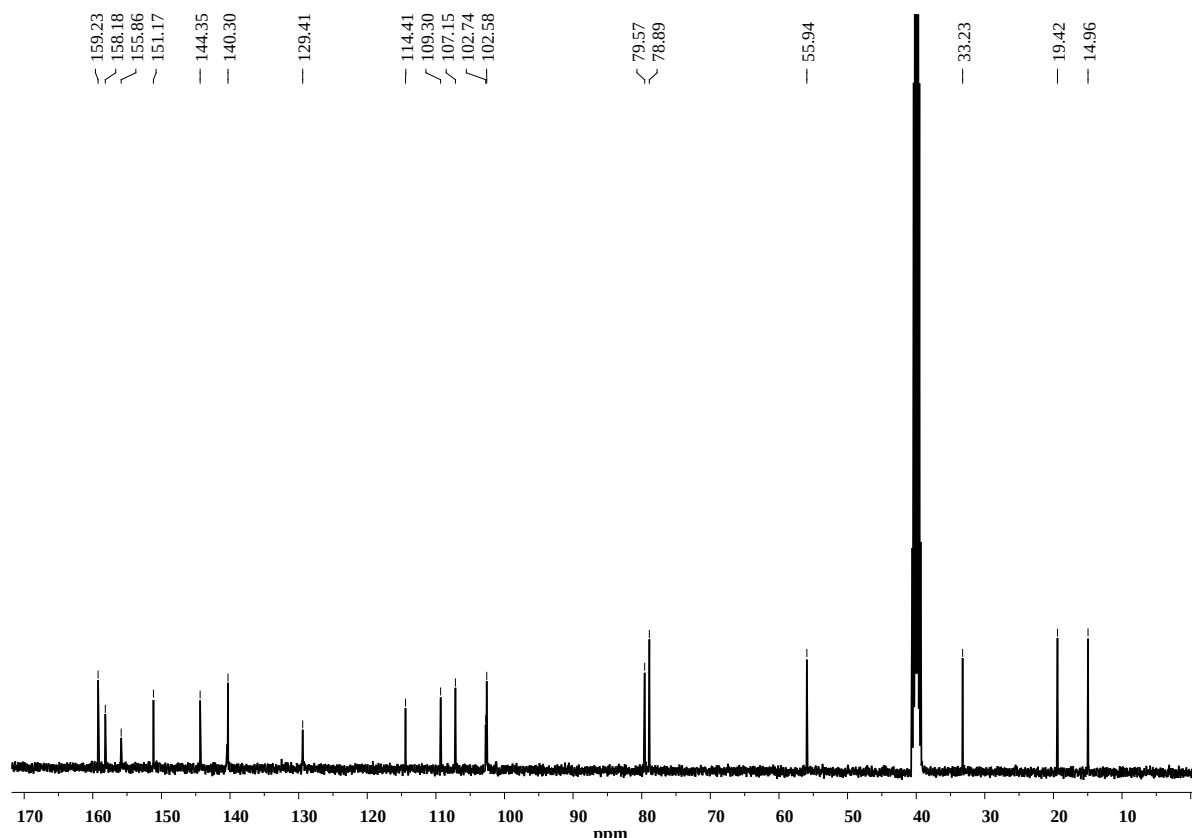


Figure 4: $^1\text{H}(^{13}\text{C})$ NMR spectra of compound 3b.

3.3. Inhibitory activity against AChE

The *in vitro* activities of compounds 3a and 3b were investigated against acetylcholinesterase (AChE) that one of the main enzymes of Alzheimer's disease. Galantamine was used as a positive control. The inhibitory effects of compounds 3a and 3b on AChE (IC_{50} values of 282.37 μM and 104.4 μM , respectively) were evaluated and found to be the most active compound 3b. Active compound 3b also showed stronger inhibition than control galantamine (IC_{50} value 139.42 μM). *N,N*-diethyl ($\text{N}(\text{C}_2\text{H}_5)_2$) and propargyl ($\text{OCH}_2\text{C}\equiv\text{CH}$) groups were effective in determining the strength of the inhibitory effect of compounds 3a and 3b against AChE. The propargyl group end proton of the compound 3b the hydrophilic interaction with the residues in the active site of enzyme may have been effective increase the inhibitory property. Molecular docking was performed to identify possible modes of binding between AChE and inhibitors.

3.4. Molecular docking studies of compounds 3a and 3b

AChE inhibition effects of compounds based on 6-hydrazinyl-1,3,4-trimethyl-1h-pyrazolo[3,4-b]pyridine (3a and 3b) were investigated by *in vitro* method. Molecular docking study was performed to determine the possible binding poses, interactions, affinities and complex structures of these compounds with AChE. Autodock 4.2 software program was used to determine the active site of AChE. First, the GNT compound co-crystallized with the enzyme was redocking to the active site of the enzyme by the docking procedure. In consequence of placing on the AChE active site, the best binding affinity of GNT was determined as -9.39 kcal/mol.

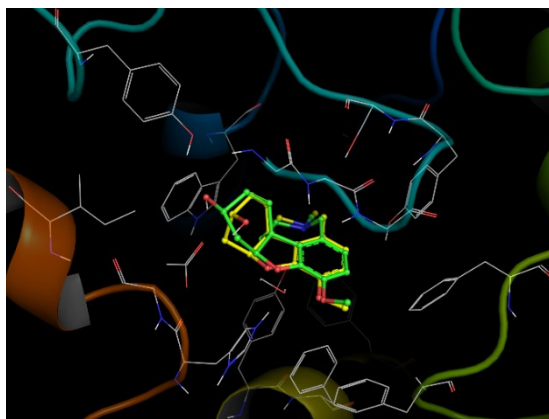


Figure 5: Docking verification. The carbon atoms of the co-crystallized ligand are represented by the ball and stick modeling in yellow, while the carbon atoms of the inserted ligand are represented by the ball and stick modeling in green.

Molecular docking studies of compounds against AChE have been performed. According to the docking results, compound 3b showed the strongest inhibitory property with -10.28 kcal/mol the lowest binding affinity. Compound 3b hydrogen bonded with residues Arg296 (2.2 Å), Phe295 (2.1 Å), Tyr337 (2.0 Å and 2.5 Å), Tyr124 (1.9 Å, 2.6 Å and 2.9 Å) and Ser125 (2.7 Å and 2.9 Å) in the active site of the enzyme. Compound 3b made π - π interactions with amino acids Tyr341 (4.33 Å), Phe297 (5.91 Å), and Trp86 (4.98 Å, 5.53 Å and 5.89 Å). In addition, compound 3b formed numerous hydrophobic interactions with residues in the active site of AChE. Residues Tyr124 and Tyr341 in the peripheral anionic region (PAS), Phe295 and Phe297 in the acyl binding pocket and Trp86 is located in the active site. Compound 3b interacts with Trp286 π -alkyl interaction and Asp74 attractive charge. Compound 3a formed the most stable complex with a binding affinity of -10.05 kcal/mol as a result of docking at the active site of AChE. Compound 3a interacted with similar residues as compound 3b in the active

site. Compound 3b involved in more hydrogen bonds and π - π interactions than that of compound 3a.

4. CONCLUSION

Two different compounds based on 6-hydrazinyl-1,3,4-trimethyl-1h-pyrazolo[3,4-b]pyridine (3a and 3b) designed and synthesized and their structures were determined by FTIR and $^1\text{H}/^{13}\text{C}$ NMR spectroscopic methods. *In vitro* inhibitory effects of compounds 3a and 3b against AChE were evaluated. Compound 3b exhibited stronger inhibitory activity than both the reference drug galantamine and compound 3a. Docking studies were performed to identify possible binding modes of the compounds. In consequence of docking, Compound 3b was found to have the highest activity with the lowest binding affinity. The pyrazole, pyridine and hydrazine units were found to make hydrophobic and hydrophilic interactions with the residues in the active site of the enzyme. In addition, the propargyl group was thought to be responsible in the strong inhibitory activity of compound 3b.

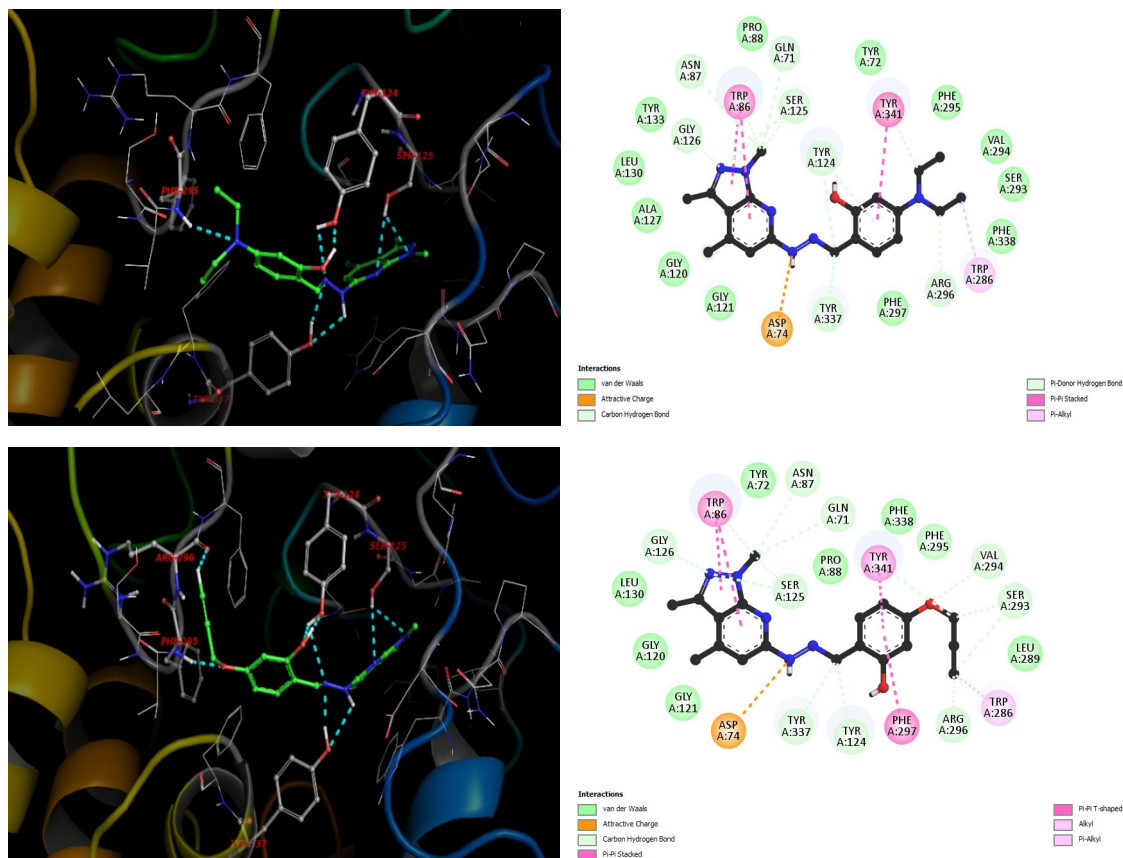


Figure 6: 2D Hydrophobic interaction profile with AChE of compounds 3a (upper right) and 3b (lower right). 3D bonding mode of the lowest energy conformation with AChE of compounds 3a (upper left) and 3b (lower left). The carbon atoms green colour of compounds 3a and 3b and the carbon atoms gray colour of amino acids are shown as ball and stick model. The hydrogen bond interaction between ligands and residues is shown by turquoise dashed lines.

5. REFERENCES

1. Khachaturian ZS. Conference R Diagnosis of Alzheimer's Disease. Arizona Heal Sci Libr User. 1985;42:1097-105. Available from: <DOI>
2. Sharma K. Cholinesterase inhibitors as Alzheimer's therapeutics (Review). Mol Med Rep. 2019;20(2):1479-87. Available from: <DOI>
3. Cheng ST. Cognitive Reserve and the Prevention of Dementia: the Role of Physical and Cognitive Activities. Curr Psychiatry Rep. 2016;18(9). Available from: <DOI>
4. Maxwell CJ, Vu M, Hogan DB, Patten SB, Jantzi M, Kergoat MJ, et al. Patterns and determinants of dementia pharmacotherapy in a population-based cohort of home care clients. Drugs and Aging. 2013;30(7):569-85. Available from: <DOI>
5. Silman I, Sussman JL. Acetylcholinesterase: "Classical" and "non-classical" functions and pharmacology. Curr Opin Pharmacol. 2005;5(3 SPEC. ISS.):293-302. Available from: <DOI>
6. Birks JS. Cholinesterase inhibitors (ChEIs), donepezil, galantamine and rivastigmine are efficacious for mild to moderate Alzheimer's disease. 2012;(5). Available from: <DOI>
7. Tschanz JT, Corcoran CD, Schwartz S, Treiber K, Green RC, Norton MC, et al. Progression of cognitive, functional, and neuropsychiatric symptom domains in a population cohort with alzheimer dementia: The cache county dementia progression study. Am J Geriatr Psychiatry. 2011;19(6):532-42. Available from: <DOI>
8. Parsons C, Lim WY, Loy C, McGuinness B, Passmore P, Ward SA, et al. Withdrawal or continuation of cholinesterase inhibitors or memantine or both, in people with dementia. Cochrane Database Syst Rev. 2021;2021(1). Available from: <DOI>
9. Feldman H, Gauthier S, Hecker J, Vellas B, Subbiah P, Whalen E. A 24-week, randomized, double-blind study of donepezil in moderate to severe Alzheimer's disease. Neurology. 2001;57(4):613-20. Available from: <DOI>
10. Selvarani V, Annaraj B, Neelakantan MA, Sundaramoorthy S, Velmurugan D. Synthesis and crystal structure of hydroxyacetophenone Schiff bases containing propargyl moiety: Solvent effects on UV-visible spectra. Spectrochim Acta - Part A Mol Biomol Spectrosc. 2012;91:329-37. Available from: <DOI>
11. Güngör SA, Tümer M, Köse M, Erkan S. Benzaldehyde derivatives with functional propargyl groups as α -glucosidase inhibitors. J Mol Struct. 2020;1206. Available from: <DOI>

12. Ellman GL, Courtney KD, Andres V, Featherstone RM. A new and rapid colorimetric determination of acetylcholinesterase activity. *Biochem Pharmacol.* 1961;7(2):88-95. Available from: [<DOI>](#)
13. Güngör Ö, Köse M. Design, synthesis and biological evaluation of biguanids and biguanid-sulfonamides as cholinesterase inhibitors. *J Mol Struct.* 2022;1260. Available from: [<DOI>](#)
14. Allouche A. Software News and Updates Gabedit — A Graphical User Interface for Computational Chemistry Softwares. *J Comput Chem.* 2012;32:174-82.
15. Şahin İ, Bingöl Z, Onur S, Güngör SA, Köse M, Gülçin İ, et al. Enzyme Inhibition Properties and Molecular Docking Studies of 4-Sulfonate Containing Aryl α -Hydroxyphosphonates Based Hybrid Molecules. *Chem Biodivers.* 2022; Available from: [<DOI>](#)
16. BIOVIA DS. Discovery studio visualizer. In San Diego, CA, USA; 2017. p. 298.
17. Lill MA, Danielson ML. Computer-aided drug design platform using PyMOL. *J Comput Aided Mol Des.* 2011;25(1):13-9. Available from: [<DOI>](#)



Physical and Spectroscopic Characterization of the Microcrystalline Cellulose Derivatives from Corn Cob and *Daniella Oliveri* Wastes

Mariam Temitope Baker*¹ , Olubunmi Stephen Oguntoye¹ 

¹University of Ilorin, Department of Chemistry, Ilorin, P.M.B. 1515, Nigeria.

Abstract: Cellulose was extracted from wood dust waste samples of *Daniella oliveri* and corn cobs by acetic acid and alkaline pretreatment methods, while microcrystalline cellulose (MCC) derivative was produced by acid hydrolysis in 2 M HCl. The samples were tested for pH, moisture content, swelling capacities and ash contents. The data obtained were compared with those of commercial MCCs found in the literature. The functional groups in the microcrystalline cellulose derivatives was confirmed by the Fourier transform infrared (FTIR) spectroscopic method with characteristic absorption bands of; -OH stretching at 3416 cm⁻¹; C-H stretching at 2918 cm⁻¹; -OH bending at 1377 cm⁻¹; 1159 cm⁻¹; and C-O-C pyranose ring skeletal vibrations at 1026-1033 cm⁻¹. The crystallinity absorption bands appeared at 1436 and 850 cm⁻¹. The characteristic morphological features were established by scanning electron microscopy (SEM). Furthermore, the crystallinity of the microcrystalline cellulose was further confirmed using the X-ray powder diffraction (X-RD) technique, which showed three main reflections at 2θ=14.70°, 22.09°, and 34.24°. These results supported that microcrystalline cellulose derivative as cellulose I type and the acid pretreatment did not affect the structure of the MCC. The crystallinity indices were 69.3 and 73.2%, respectively. *Daniella Oliveri* and corn cob microcrystalline cellulose are, therefore, potential materials for further processing.

Keywords: Microcrystalline cellulose derivative, *Daniella oliveri*, corn cobs, wood dust waste, FTIR, XRD, TGA/DTA, SEM, physical characteristics, potential applications

Submitted: April 23, 2022. **Accepted:** October 22, 2022.

Cite this: Baker MT, Oguntoye OS. Physical and Spectroscopic Characterization of Corn Cob and *Daniella Oliveri* Wastes Microcrystalline Cellulose Derivatives. JOTCSA. 2023; 10(1):31-8.

DOI: <https://doi.org/10.18596/jotcsa.1107627>.

***Corresponding author. E-mail:** temitopemariam11@yahoo.com, arowona.mt@unilorin.edu.ng.

1. INTRODUCTION

Pollution is a pronounced concern in our community/environment as a result of poor waste management and disposal. The majority of these wastes are either piled up as an eyesore or left to fester, putting human and animal life at risk. It is worth noting that the majority of these wastes are cellulose-rich agricultural byproducts, including maize cobs, rice husks, and wood dust, from a variety of tree species. The production of agricultural byproducts is projected to be approximately 12 million tons per year, with the majority of them not being converted into other materials for future use (1). Cellulose is a polymer of D-glucose linked by the -1,4-D-glucopyranose

ring (2). It is made up of hundreds to thousands of monomers of glucose that are linked together. An anhydroglucose unit of cellulose consists of two glucose units linked together by a -1,4-glycosidic bond and weighs 162.1 gmol⁻¹ (3). Cellulose and its derivatives have important applications in a variety of fields, including pharmaceuticals, biomedical, paint industries, water purification, and cosmetics (1,4-6). Microcrystalline cellulose (MCC) is a partially depolymerized cellulose in which the amorphous region of cellulose is hydrolyzed to produce crystalline cellulose with a larger surface area for better application (7-9). MCCs, like cellulose, are white, colourless, and odourless but have a larger surface area and a more ordered crystalline structure.

Corn is cultivated all over the world and consumed daily by man and animal in different forms. Knoema estimated the global corn cultivation to be 3.13 million thousand tonnes in 1971 alone, with an annual 3.06% increase, the production rise to 1.162 billion tonnes in 2020 (10). It is estimated that the ratio of corn grains to corncob is 100:18 (11). From the figures quoted earlier, this implies annual corn cob generation of corncob in 2020 alone is approximately 210 million tonnes. Corncobs find application in their uses as poultry feed formulation, polisher, bio-oil and biochar. The efficacy of corncob as alternative source of microcrystalline cellulose in pharmaceutical formulation has also been investigated (12,13). Apart from the applications stated above, several reports are available on the use of corncob as a very good source of compounds such as furfural, ethanol, xylitol, succinic and propionic acid, phenolic compounds, bio-adsorbent, biobased rigid polyurethane foam, hollow spherical carbon, and p-hydroxycinnamic esters (1,14,15).

Daniellia oliveri (DAN) is a soft wood deciduous mostly cultivated in the tropical region of Africa (16). This plant is basically cultivated for medicinal and economic benefits; the young leaves of this plants are cooked and consumed (17), the matured are used for the treatment of stomach troubles, diabetes, dysmenorrhoea, haemorrhoids due to their abortifacient, aphrodisiac, astringent, diuretic, emmenagogue and stomachic properties (18). The seeds are eaten (19), decoction from the roots are used in the treatment of gonorrhoea and skin diseases (20). The gum-resin from the stem-bark and wood is used in the treatment of gonorrhoea and laxative and also used for the manufacture of wood polish, perfumes and varnishes (21). The gum-resin obtained from the wood of this plant has also been used as binder in pharmaceutical formulation (22). An aqueous extract of the powdered bark has been shown to have effective pain-reduction properties and also to be antioxidant. The trunk are sold as timber for furniture and manufacture of equipment (23).

Characterization and use of the cellulosic content of the DAN. plant have not been widely studied in literature, to the best of the author's knowledge. Cellulose however, can be obtained from different part of the plant: For example, the wood dusts which is a waste or by product of milling the timber obtained from the DAN. for production of furniture and other tools are good source of cellulose for extraction and characterization. Some of the physical and spectroscopic characteristics of corncob MCC in comparison to that obtained from DAN, another plant specie is not widely investigated for its cellulosic content. This research therefore, reports some of the physical and spectroscopic properties of MCCs produced from *Daniellia oliveri's* cellulosic waste and corncobs. This broadens the

horizon of cellulose sources and applications because, it is expected to replace toxic and non-biodegradable raw materials in the near future.

2. MATERIALS AND METHODS

2.1. Sample Collection and Preparation

Corncob (C.C) wastes lying fallow in the environment were randomly picked in the north-central part of Nigeria during the maize harvest season. This was to help clean up the litters from the environment. Wood dust of DAN tree species was obtained from a local wood milling factory environment in Kwara state, north-central, Nigeria. The local name for the *Daniella oliveri* sample was identified at the point of collection by its local name, while the botanical name was obtained through herbarium of University of Ilorin. Both samples (corn cob and *Daniella oliveri* wood dust) were sun dried to remove excess water for easy grinding and further processing.

2.2. Extraction of Cellulose

Cellulose I was extracted by the chemical pretreatment method, while Cellulose II was obtained by acid hydrolysis in 2 M HCl. The method of cellulose extraction used in our previous publication (24), we employed a slight modification. 500 g of DA or Corn cob was weighed into a quick fit flask, and 10% sodium hydroxide was added. It was then refluxed for four hours. The mixture was left to cool. It was then filtered and washed with water until neutral, washed with ethanol and dried. The dried residue was poured into a beaker, 10% acetic acid was added, and the beaker was heated for three hours. It was then filtered and washed with water and ethanol and dried. Hydrogen peroxide was added to the sample, and it was refluxed for three hours to further delignify. It was filtered and washed with water and ethanol. Hypochlorite was added and refluxed for three hours (until it turned white/off-white). The sample was thereafter washed with water and ethanol, dried, and blended into finer particles and stored for further use.

2.3. Preparation of MCC

MCC was prepared by acid hydrolysis of the cellulose samples obtained above in 2 M HCl under reflux in a 500 mL quick-fit flask. The reaction was carried out at 80 °C for 4 h with a continuous stirring speed of 700 rpm. The reaction mixture was cooled to room temperature and filtered, and the residue was repeatedly washed with distilled water until it was free from acid residue by testing the pH of the solution with a digital pH meter. The obtained MCC was dried in a hot air oven at 80 °C until a constant weight was achieved. Using the dry blender compartment, the dried MCC lumped together was ground into a fine powder.

2.4. Percentage Yield

The percentage yield of cellulose was calculated by dividing the final weight of cellulose obtained by the initial weight of the cellulosic sample. The percentage yield of both cellulose and MCC was obtained using the expression below;

$$Y_{cell} = \frac{Fw_{cell}}{Cw_{cell} * 100} \quad (1)$$

$$Y_{mcc} = \frac{Wh}{Fw_{cell} * 100} \quad (2)$$

Y_{cell} = Percentage Yield of cellulose;
Fw_{cell} = Weight of cellulose extracted;
Cw_{cell} = Weight of crude cellulose
Y_{mcc} = Percentage Yield of MCC;
Wh = Weight of Hydrolyzed cellulose;

2.5. Starch Test

The presence of starch in the sample was investigated by adding approximately 3 mL of iodine solution to 0.1 g MCC samples in a beaker. For comparison, the same amount of iodine solution (3 mL) was added to 0.1 g of reference standard starch in another beaker. Blue-black colouration indicates the presence of starch, while no change in colour indicates the absence of starch in the cellulose backbone. The absence of blue black colouration was taken as an indication of a positive result for cellulose.

2.6. Ash Content

Each of the prepared MCCs (2 g) was placed in a furnace at 600 °C for 6 h. The ash content was determined using the following equation:

$$\left[\left(\frac{W_i - W_f}{W_i} \right) \times 100 \right] - 100 \quad (3)$$

where W_i = initial weight of the sample W_f = final weight of the sample (i.e weight of ash)

2.7. Moisture Content

Each of the samples (1 g) was placed independently in a white porcelain crucible with a cover. The samples were dried in an oven for 3 h at 105 °C. During drying, the weight of the samples was taken at 30 min intervals until a constant weight was obtained. The moisture content was calculated using the equation below. (25)

$$\left(\frac{A - B}{A} \right) * 100 \quad (4)$$

A = initial weight of MCC
B = final weight of MCC after drying

2.8. pH Measurement

Each of the samples (1 g) was placed in a 10 ml clean measuring cylinder, a few milliliters of distilled water was added to the samples and shaken together, and the volume of the sample and water was brought to 10 mL. The mixture was left to settle, and the pH of the supernatant liquid was measured with a digital pH meter.

2.9. Water Uptake Capacity

Distilled water (4 mL) was poured into a 10 mL beaker containing MCC samples whose bulk and tapped volume had been obtained. The mixture was agitated, and the volume of the mixture reached 10 mL. The mixtures were left to stand for 72 hrs, the swelling volume V_s was obtained, and the water uptake capacity was calculated using the equation:

$$WUC(\%) = \frac{V_s - V_t}{V_t} \times 100 \quad (5)$$

WUC (%) = Percent Water uptake capacity
V_s = volume of sample after swelling
V_t = Tapped volume of the sample

2.10. Fourier Transform Infrared Spectroscopy (FTIR)

The chemical composition of each sample was determined by determining the functional groups using FTIR spectroscopy. A few milligrammes (mg) of dried cellulose and MCC derivatives were mixed with potassium bromide (1:90) and compacted into transparent tablets using a hydraulic press (M-15, Technosearch). An FTIR spectrometer (ALPHA-II, Bruker, Germany) was utilized to investigate the transparent tablets in the range of 4000–400 cm⁻¹.

2.11. X-Ray Powder Diffraction Spectroscopy (XRD)

The degree of crystallinity of the MCC derivatives was determined using an X-ray diffractometer machine (PANalytical, Model: X'pert PRO) powered by a 40 kilovolt X-ray generator at an input of 30 Ma with Cu K alpha radiation. The crystallinity indices of the samples were calculated from the spectrum obtained using the origin software by determining the area of the crystalline region and the area of the crystallinity as well as the amorphous region and then using the equation below to determine the crystallinity index of each sample.

$$C.I = \left(\frac{I_c}{I_a + I_c} \right) \times 100 \quad (6)$$

C. I = Crystallinity index; I_c = Area of Crystalline peaks, I_a + I_c = Area of Amorphous and Crystalline peaks.

2.12. Scanning Electron Microscopy (SEM)

The degree of crystallinity of the MCC derivatives was evaluated using X-ray diffractometer equipment (PANalytical, Model: X'pert PRO) using Cu K alpha radiation and a 40 kilovolt X-ray generator at an input of 30 Ma.

2.13. Thermogravimetric and Differential Thermal Analysis (TG/DTA)

Thermogravimetric analysis (TGA) was performed on the derivatives to track the thermal degradation trend, whereas DTA was used to determine how much weight was lost at a given temperature. TGA measurements were carried out with an STA449 (F3, Netzsch, Germany) under a nitrogen atmosphere (40 mL/min), and the derivatives were heated at a rate of 10 °C/min from 50 °C to 850 °C. The remaining weight loss was determined by measuring it at 850 °C.

3. RESULTS AND DISCUSSION

3.1. Appearance

The cellulose revealed white to off-white with a rough to smooth appearance due to the presence of both crystalline and amorphous regions of the cellulose molecule. On the other hand, the MCCs prepared from the initial cellulose appeared smooth with white to off-white in colour. The smooth appearance of the MCCs is related to the breakdown of the amorphous part of the cellulose compound leaving behind the powdery crystalline region.

3.2. Percentage Yield

The percentage yields of the cellulose was calculated by dividing the weight of the cellulosic biomass before extraction by the weight of the

cellulose obtained after extraction. The percent yield of the MCCs was obtained by dividing the mass of the cellulose obtained before hydrolysis by the mass of the product obtained after hydrolysis. The percentage yields of cellulose samples were 60% for C.C and 55% for DAN. The MCC yields were 80 and 75% for C.C and DAN samples, respectively. This showed that the method of preparation of the cellulose compound gave cellulose with a good degree of crystallinity, hence leaving behind a larger amount of the crystalline region than the amorphous region after extraction. This claim was proven by the small difference in the crystallinity indices of the cellulose and MCC derivatives, which was supported in the XRD analysis. The percentage yield of the cellulose is as presented in the table 1 below:



Figure 1: Cellulose extracted (left) and prepared microcrystalline cellulose (right).

Table 1: Percent Yield of Cellulose and Microcrystalline cellulose.

No.	Sample	Cellulose(%)	MCC(%)
1.	CORN COB	60.0±0.5	80.0±0.5
2.	DANIELLA OLIVERI	56.5±0.29	75.0±1.0

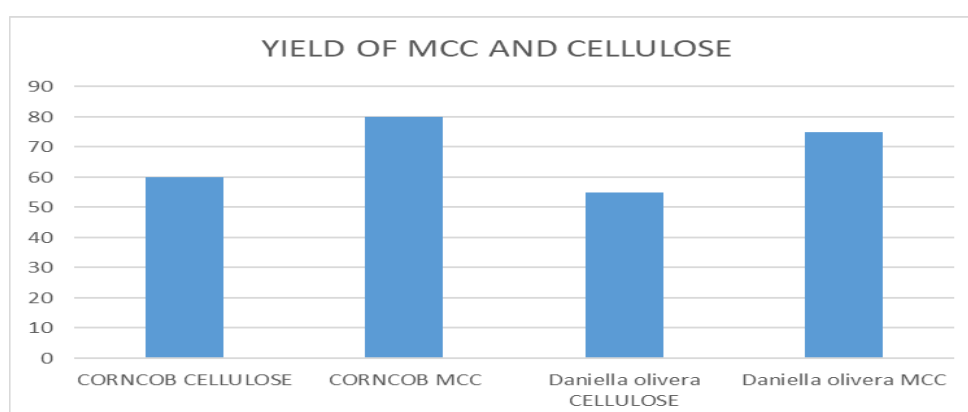


Figure 2: Bar chart representation of yields.

3.3. Starch Test

A starch test was conducted on the MCC derivatives to ascertain the absence of other carbohydrate such as starch, in the cellulose molecule. The MCC derivatives gave no colour change upon the addition of Iodine, as the reddish brown iodine remained, while starch gave blue-black colouration. The blue-black colouration of the starch was persistent, while the reddish brown colour of the iodine sublimed from the MCC solution after being kept at room temperature for 2 h. This is because, starch being a branched α -polymer of glucose, forms helical secondary structures which can hold iodine, which leads to a reaction and consequent colour change. But cellulose a linear β -polymer of glucose, does not contain helices, and so cannot hold iodine which prevents interaction, hence, no color change.

3.4. Ash Content

The percentage ash content values obtained are shown in the table 2 below, which was taken as evidence that the MCCs derivatives had very little non-cellulosic residues (25). The results were corroborated with those in the literature, with a percentage ash concentration of 1.95 for Avicel-102, a commercial excipient. This finding demonstrated that MCCs derivatives derived from these two agricultural wastes samples can compete rather well with commercially available MCCs (26,27).

Table 2: Percent Ash content of MCCs.

No.	Samples	%Ash content (%)
1.	Corn Cob	0.80±0.10
2.	<i>Daniella oliveri</i>	1.30±0.05

3.5. Moisture Content

The moisture content of MCCs reveals how much water they can absorb from the environment. The lower the moisture content of the material, the better it can be utilized as a material for direct compression excipient in pharmaceutical application while the higher the moisture content (28), the better is it to be used in other applications such as hydrogel for water storage for plant (29). According to the results from this study, the values obtained are within the usual range of less than 7% reported in the literature (27). The results of this study are presented in the table 3 below:

Table 3: Percent Moisture content of the MCCs.

No.	Samples	Moisture Content (%)
1.	Corn cob	1.80±0.12
2.	<i>Daniella oliveri</i>	10.10±1.0

3.6. pH Determination

The pH of the derivatives was found to be neutral, falling within the standard acceptable limit values

for neutral MCCs of pH 6-7.5 (30). Table 4 below summarizes the findings:

Table 4: pH Values of the MCCs.

No.	Samples	pH
1.	Corn Cob	6.56±0.02
2.	<i>Daniella oliveri</i>	6.3±0.01

3.7. Water Uptake Capacity

The increase in the volume of water taken up by the MCC derivatives following absorption was measured by the water uptake capacity, which measures the ability of the sample to swell. The derivatives have a moderate to high swelling ability, according to the results. The values for the swelling ability of the MCC derivatives are shown in the table 6 below, and these values favourably agreed with those reported in the literature (26). The values obtained for the two samples showed the corn has a better ability to take up more water into its cellulosic backbone than the *DAN samples* but the moisture contents value suggests the DAN sample takes up moisture easily from the atmosphere than the corncob. This phenomenon might be due to difference in their cellulosic origin which might make cellulosic sample to absorb moisture easily but releases it easily as well due smaller surface area. This can be explained by the SEM appearance of the MCC samples showing *DAN* with longer strands than the C.C with shorter agglomerates due to larger surface area and higher crystallinity as evidenced in the crystallinity indices values of the materials.

Table 5: Water uptake Capacity of the MCCs.

No.	Samples	WUC (%)
1.	Corn Cob	115.00±0.58
2.	<i>Daniella oliveri</i>	78.60±2.00

3.8. Fourier Transform Infrared Spectroscopy (FTIR)

The FTIR spectra of cellulose and MCC derivatives are presented in the figure 3. Native cellulose affords absorption bands at approximately 3300, 2900, 1430, 1374, 1100, 1050, and 890 cm^{-1} Liu, 2007. Absorbance peaks in the regions of 3450–3300 cm^{-1} and 2900–2800 cm^{-1} are caused by stretching of O-H groups and saturated aliphatic C-H, respectively. The skeletal vibrations of the C-O-C pyranose ring are responsible for the peaks that occurred at approximately 1050 cm^{-1} (8,31,32). The C-O asymmetric bridge stretching was caused by absorption bands at approximately 1374 cm^{-1} . Furthermore, the absorption peak at 1429 cm^{-1} , due to a symmetric CH_2 bending vibration and referred to as the "crystallinity band," due to a symmetric CH_2 bending vibration (33). Because of the hydrophilic nature of cellulosic material, the absorption peak at 1624 cm^{-1} is responsible for water absorption (34). The absence of peaks at

1512 cm^{-1} and 1735 cm^{-1} , which correspond to the C-C aromatic bending and aromatic C-O stretching in hemicelluloses and lignin, respectively, indicated that the pretreatment procedure effectively removed noncellulosic components of the raw materials (35–38).

3.9. X-Ray Powder Diffraction (XRD)

The crystallinity indices of the derivatives indicated that the amorphous cellulose region was broken down, leaving the crystalline cellulose material behind, generating microcrystalline cellulose. *DAN*. and C.C had crystallinity index values of 69.3 and 73.2% respectively, which is a good value for microcrystalline cellulose. The increase in value for the MCCs over the cellulose samples indicated that the amorphous region of the cellulose samples was broken down during hydrolysis. The samples' XRD Spectra are shown below. The diffraction patterns of all the MCC samples showed sharp peaks at 2 angles of approximately 14.5°, 17°, 22.7°, and 35.5° for all the compounds, which were assigned to the usual cellulose I reflection planes. The results were identical to those found in the literature for carbon nanocellulose and microcrystalline cellulose (39–42).

3.10. Scanning Electron Microscopy (SEM)

From the overall view, the SEM micrographs of the cellulose samples showed the fibre strands with long and short tubes connected to one another, and the presence of both long and short tubes was due to the amorphous and crystalline structure in the cellulose backbone. The microcrystalline cellulose derivatives showed non-uniformly distributed and shorter microcrystalline particles, creating microcrystals due to hydrolysis and displaying a large sample surface area. This was caused by the amorphous region breaking down during hydrolysis, resulting in a microcrystalline structure with a huge surface area. The surface area patterns from the analyzed varieties were similar but those of corncobs formed agglomerates better than those of the *DAN sample* which makes it (C.C MCC) more crystalline as evident in the crystallinity indices of the materials calculated from the XRD results. Overall, the microcrystalline cellulose from each of these samples may be used as raw starting materials for further processing either as direct compression excipient in pharmaceutical drug formulation, biomedical and paint industry due to their crystallinity and appearance. Their water holding capacities suggests the samples as good candidates in hydrogel formation for water storage agent for plants' roots..

3.11. Energy Dispersive X-Ray Spectroscopic (EDS) Analysis

The EDS analysis of the samples showed the presence of Carbon (C) and oxygen (O) as the predominant element, which revealed materials prepared are purely cellulose. As expected for pure

cellulose products, elements like sodium (Na) and sulfur (S), which might be present as contaminants during pretreatment and Microcrystalline cellulose preparation, were absent. Conclusively, good grade cellulose successfully, were prepared. It is worthy of note that the presence of Au and Nb elements is due to gold element used in coating the samples before analysis.

3.12. Thermogravimetric/Differential Thermal Analysis (TGA/DTA)

The thermogravimetric curve demonstrated that the microcrystalline cellulose derivatives degraded in a single step from 400 to 500 °C. The first degradation step is as a result of loss of water or moisture due to the hydrophilic nature of the samples while the other step involves the breakdown of the microcrystalline cellulose derivatives into ashes. From the thermogram, C.C MCC had better thermal stability than *DAN* MCC at a degradation temperature of 500 °C, which could be due to its high swelling capacity. Overall, the samples' thermal breakdown patterns verified the absence of hemicelluloses, lignin, and little or no residues of contaminants in their core structure. As a result, the MCCs are thermally stable. Similar results are widely reported in literature for microcrystalline cellulose derivatives from other plant species such as date seeds, tea wastes, rice husk, pomelo peels, wheat straw and cotton. (2,8,24,28,34,43) The T_{max} (temperature at which maximum weight loss occurs) for the samples was 450 °C. These samples, which are thermally stable, serve as raw materials for future material functionalization and applications.

4. CONCLUSION

Microcrystalline cellulose compounds were prepared and characterized from cellulose isolated through alkaline hydrolysis of cellulosic wastes. This work serve as a workable model to clean up the environment by removing some of the cellulosic wastes from the environment, therefore reducing possible environmental pollution by their presence. On the other hand, the wastes were converted into good-grade microcrystalline cellulose that will be useful in various areas such as in direct compression excipient in pharmaceutical formulation or agriculture as water storage excipient. From the properties displayed by these two MCCs, the C.C sample gave cellulose with better yield and physical as well as spectroscopic properties. Due to their (C.C) high water uptake ability, they can be employed in agriculture as water retaining hydrogels that can be prepared by grafting the MCC compounds onto other natural or synthetic polymers. This is owing to their high water uptake ability. The derivatives from *Daniella oliveri*, an underutilized plant in the area of cellulosic application on the other hand, might serve as a good or even better candidate in the

pharmaceutical, biomedical or paint industry than the corncob derivatives. Overall, good grade MCCs were prepared from wastes obtained from nature. The wastes were processed into useful raw materials that will now be sent back to nature in a useful form as raw materials for several applications.

5. ACKNOWLEDGMENTS

The authors would like to thank CSIR-IMMT, Bhubaneswar, Odisha, India for assistance in providing access to the analytical equipment free of cost. Special 'thank you' to Dr. R. Boopathy of the Environment and Sustainability Department of the Institute for providing needed guidance in the course of the research.

6. REFERENCES

- Bian B, Hu X, Zhang S, Lv C, Yang Z, Yang W, et al. Pilot-scale composting of typical multiple agricultural wastes: Parameter optimization and mechanisms. *Bioresour Technol* [Internet]. 2019 Sep 1 [cited 2021 Apr 9];287. Available from: [<URL>](#).
- Abu-Thabit NY, Judeh AA, Hakeem AS, Ul-Hamid A, Umar Y, Ahmad A. Isolation and characterization of microcrystalline cellulose from date seeds (*Phoenix dactylifera* L.). *Int J Biol Macromol* [Internet]. 2020;155:730–9. Available from: [<URL>](#).
- Granström M. *Cellulose Derivatives: Synthesis, Properties and Applications*. 2009. ISBN: 978-952-10-5485-3.
- Kumar V, Pathak P, Bhardwaj NK. Waste paper: An underutilized but promising source for nanocellulose mining. *Waste Manag* [Internet]. 2020;102:281–303. Available from: [<URL>](#).
- Czaja W, Krystynowicz A, Bielecki S, Brown RM. Microbial cellulose - The natural power to heal wounds. *Biomaterials*. 2006;27(2):145–51. Available from: [<URL>](#).
- Kostag M, Jedvert K, Ahtel C, Heinze T, El Seoud OA. Recent advances in solvents for the dissolution, shaping and derivatization of cellulose: Quaternary ammonium electrolytes and their solutions in water and molecular solvents. *Molecules*. 2018;23(3). Available from: [<URL>](#).
- Kunusa WR, Isa I, Laliyo LAR, Iyabu H. FTIR, XRD and SEM Analysis of Microcrystalline Cellulose (MCC) Fibers from Corncorbs in Alkaline Treatment. *J Phys Conf Ser*. 2018;1028(1). Available from: [<URL>](#).
- Zhao T, Chen Z, Lin X, Ren Z, Li B, Zhang Y. Preparation and characterization of microcrystalline cellulose (MCC) from tea waste. *Carbohydr Polym*. 2018 Mar 15;184:164–70. Available from: [<URL>](#).
- Garba ZN, Lawan I, Zhou W, Zhang M, Wang L, Yuan Z. Microcrystalline cellulose (MCC) based materials as emerging adsorbents for the removal of dyes and heavy metals – A review. *Sci Total Environ* [Internet]. 2020;717(Mcc):135070. Available from: [<URL>](#).
- Knoema. Search, Discover, Catalog and Access Your Data Seamlessly. October 29, 2022 ([<URL>](#). Opens in new tab).
- Cao Q, Xie KC, Bao WR, Shen SG. Pyrolytic behavior of waste corn cob. *Bioresour Technol*. 2004;94(1):83–9. [<URL>](#).
- Ravikumar C, Senthil Kumar P, Subhashni SK, Tejaswini P V., Varshini V. Microwave assisted fast pyrolysis of corn cob, corn stover, saw dust and rice straw: Experimental investigation on bio-oil yield and high heating values. *Sustain Mater Technol* [Internet]. 2017;11:19–27. Available from: [<URL>](#).
- Zhang Q, Zhang D, Xu H, Lu W, Ren X, Cai H, et al. Biochar filled high-density polyethylene composites with excellent properties: Towards maximizing the utilization of agricultural wastes [Internet]. 2020 [cited 2021 Apr 9]. Available from: [<URL>](#).
- Wang S, Gao W, Li H, Xiao LP, Sun RC, Song G. Selective fragmentation of biorefinery corncob lignin into p-hydroxycinnamic esters with a supported zinc molybdate catalyst. *ChemSusChem*. 2018;11(13):2114–23. Available from: [<URL>](#).
- Duan C, Meng X, Liu C, Lu W, Liu J, Dai L, et al. Carbohydrates-rich corncobs supported metal-organic frameworks as versatile biosorbents for dye removal and microbial inactivation. *Carbohydr Polym* [Internet]. 2019;222:115042. Available from: [<URL>](#).
- agritrop-eprint-317983. *Useful Tropical Plants*. July 20, 2022 ([<URL>](#). opens in new tab).
- Shackleton CM, Pasquini MW, Drescher AW. African indigenous vegetables in urban agriculture. *African Indigenous Vegetables in Urban Agriculture*. 2009. 1–298 p. ISBN: 9781136574993 .
- Ahmadu AA, Zezi AU, Yaro AH. Anti-diarrheal activity of the leaf extracts of *Daniellia Oliveri* hutch and Dalz (Fabaceae) and *ficus sycomorus* Miq (Moraceae). *African J Tradit Complement Altern Med*. 2007;4(4):524–8. Available from: [<URL>](#).
- Burkill HM. *The useful plants of west tropical Africa, Vols. 1-3*. 1995;(2. ed.), ISBN: 094764301x. [<URL>](#).
- Dinku W, Isaksson J, Rylandsholm FG, Bouř P, Brichtová E, Choi SU, et al. Anti-proliferative activity of a novel tricyclic triterpenoid acid from *Commiphora africana* resin against four human cancer cell lines. *Appl Biol Chem* [Internet]. 2020;63(1). Available from: [<URL>](#).
- Alagbe, J.O., Sharma, R., Eunice AbidemiOjo., Shittu, M.D and Bello KA. Proximate , Mineral and Phytochemical Analysis of *Piliostigma Thonningii* Stem Bark and Roots. *Int J Biol , Phys Chem Stud (JBPCS)*. 2020;(c):1–7. Available from: [<URL>](#).
- Adeyanju O, Olatoyinbo FA. Toxicological Studies and Utilization of DAN. Gum as Binder in Drug Formulation. *J Pharm Appl Chem*. 2018;4(3):169–74. Available from: [<URL>](#).
- Ajala, O. O., Awotedu, O.O. and Ogunbamowo PO. Comparative assessment of briquette produced from

- selected wood species. *J Sustain Environ Manag* [Internet]. 2016;8(ISSN: 2141-0267):1-12. Available from: [<URL>](#).
24. Arowona MT, Olatunji GA, Saliu OD, Adeniyi OR, Atolani O, Adisa MJ. Thermally stable rice husk microcrystalline cellulose as adsorbent in PTLC plates. *J Turkish Chem Soc Sect A Chem*. 2018;5(3):1177-84. [<URL>](#).
25. Kharismi RRAY, Sutriyo, Suryadi H. Preparation and characterization of microcrystalline cellulose produced from betung bamboo (*dendrocalamus asper*) through acid hydrolysis. *J Young Pharm*. 2018;1 (2):s79--s83. [<URL>](#).
26. Nwachukwu N, Ofoefule SI. Effect of drying methods on the powder and compaction properties of microcrystalline cellulose derived from gossypium herbaceum. *Brazilian J Pharm Sci*. 2020;56:1-17. [<URL>](#).
27. Kharismi RRAY, Sutriyo, Suryadi H. Preparation and characterization of microcrystalline cellulose produced from betung bamboo (*dendrocalamus asper*) through acid hydrolysis. *J Young Pharm*. 2018;10(2):s79-83. [<URL>](#).
28. Krivokapić J, Ivanović J, Djuriš J, Medarević D, Potpara Z, Maksimović Z, et al. Tableting properties of microcrystalline cellulose obtained from wheat straw measured with a single punch bench top tablet press. *Saudi Pharm J*. 2020;28(6):710-8. [<URL>](#).
29. Geng H. A one-step approach to make cellulose-based hydrogels of various transparency and swelling degrees. *Carbohydr Polym* [Internet]. 2018;186:208-16. Available from: [<URL>](#).
30. Viera-Herrera C, Santamaría-Aguirre J, Vizuete K, Debut A, Whitehead DC, Alexis F. Microcrystalline cellulose extracted from native plants as an excipient for solid dosage formulations in drug delivery. *Nanomaterials*. 2020;10(5):1-12. Available from: [<URL>](#).
31. Liu C-F, Sun R-C, Zhang A-P, Qin M-H, Ren J-L, Wang X-A. Preparation and Characterization of Phthalated Cellulose Derivatives in Room-Temperature Ionic Liquid without Catalysts. 2007; Available from: [<URL>](#).
32. Beroual M, Boumaza L, Mehelli O, Trache D, Tarchoun AF, Khimeche K. Physicochemical Properties and Thermal Stability of Microcrystalline Cellulose Isolated from Esparto Grass Using Different Delignification Approaches. *J Polym Environ* [Internet]. 2021;29(1):130-42. Available from: [<URL>](#).
33. Szymanska-Chargot M, Chylinska M, Gdula K, Koziol A, Zdunek A. Isolation and characterization of cellulose from different fruit and vegetable pomaces. *Polymers (Basel)* [Internet]. 2017;9(10). Available from: [<URL>](#).
34. Hachaichi A, Kouini B, Kian LK, Asim M, Jawaid M. Extraction and Characterization of Microcrystalline Cellulose from Date Palm Fibers using Successive Chemical Treatments. *J Polym Environ* [Internet]. 2021; (0123456789). Available from: [<URL>](#).
35. Usmani Z, Sharma M, Gupta P, Karpichev Y, Gathergood N, Liang James Hawkins Michael E Ries Peter J Hine YE, et al. A study on the microstructural development of gel polymer electrolytes and different imidazolium-based ionic liquids for dye-sensitized solar cells. *Carbohydr Polym* [Internet]. 1st ed. 2017 Mar 15 [cited 2021 Mar 29];10(1):1-12. Available from: [<URL>](#).
36. Hina S, Zhang Y, Wang H. Role of ionic liquids in dissolution and regeneration of cellulose. *Rev Adv Mater Sci*. 2015;40(3):215-26. Available from: [<URL>](#).
37. Cheng W, He J, Wu Y, Song C, Xie S, Huang Y, et al. Preparation and characterization of oxidized regenerated cellulose film for hemostasis and the effect of blood on its surface. *Cellulose*. 2013;20(5):2547-58. [<URL>](#).
38. Nascimento DM d., Almeida JS, Vale M do S, Leitão RC, Muniz CR, Figueirêdo MCB d., et al. A comprehensive approach for obtaining cellulose nanocrystal from coconut fiber. Part I: Proposition of technological pathways. *Ind Crops Prod* [Internet]. 2016;93:66-75. Available from: [<URL>](#).
39. Rahman MS, H. Mondal MI, Yeasmin MS, Sayeed MA, Hossain MA, Ahmed MB. Conversion of Lignocellulosic Corn Agro-Waste into Cellulose Derivative and Its Potential Application as Pharmaceutical Excipient. *Processes* [Internet]. 2020 Jun 19 [cited 2021 Apr 9];8(6):711. Available from: [<URL>](#).
40. Hu F, Lin N, Chang PR, Huang J. Reinforcement and nucleation of acetylated cellulose nanocrystals in foamed polyester composites. *Carbohydr Polym* [Internet]. 2015;129:208-15. Available from: [<URL>](#).
41. Mahmoudian S, Wahit MU, Ismail AF, Balakrishnan H, Imran M. Bionanocomposite fibers based on cellulose and montmorillonite using ionic liquid 1-ethyl-3-methylimidazolium acetate. *J Mater Sci*. 2015;50(3):1228-36. [<URL>](#).
42. W. R. Kunusa*, I. Isa LAL& HI. FTIR, XRD and SEM Analysis of Microcrystalline Cellulose (MCC) Fibers from Corncorbs in Alkaline Treatment. *J Phys Conf Ser* 1028. 2018 Mar 15;1(1):258-66. [<URL>](#).
43. Liu Y, Liu A, Ibrahim SA, Yang H, Huang W. Isolation and characterization of microcrystalline cellulose from pomelo peel. *Int J Biol Macromol* [Internet]. 2018;111:717-21. Available from: [<URL>](#).



The Analytical Survey of Mercury Content in Whitening Cream Sold in Banjarnegara Regency's Traditional Market

Sabtanti Harimurti^{1*} , Angelina Mawarni¹ , Ika Sevi Deriyanti¹ , Hari Widada¹ ,
Dyani Primasari Sukamdi¹ 

¹Universitas Muhammadiyah Yogyakarta, School of Pharmacy, Faculty of Medicine and Health Sciences #1, JL. Brawijaya, Tamantirto, Kasihan, Bantul, Yogyakarta 55183, Indonesia

Abstract: Whitening cream is a mixture of active substances and the other additives that can be used to brighten the skin. Mercury is one of the whitening ingredients of the creams that can cause health problems when it is absorbed into the tissue. This study aims to identify whether there is a mercury content and how much mercury is contained in the whitening cream, which does not have a BPOM RI registration number (National Agency of Food and Drug Control, Republic of Indonesia) circulating in the market in Banjarnegara regency, Central Java, Indonesia. This research was conducted with purposive sampling, and 20 samples were obtained from the traditional market in Banjarnegara regency. The qualitative analysis method used the Potassium Iodide (KI) color reaction test and amalgam formation with copper rods, while the quantitative analysis used the Cold Vapor Mercury Analyzer at a wavelength of 253.7 nm. The results showed the presence of three positive samples containing mercury at average levels of 0.04217 mg / kg (ppm), 0.01814 mg / kg, and 0.91000 mg / kg. These findings suggest that mercury was added at the whitening cream and distributed in the market. Customers should be more careful when choosing a whitening cream to prevent health problems.

Keywords: Amalgam test and mercury analyzer-CV, KI test, mercury, whitening cream.

Submitted: July 30, 2022. **Accepted:** November 07, 2022.

Cite this: Harimurti S, Mawarni A, Deriyanti IS, Widada H, Sukamdi DP. The Analytical Survey of Mercury Content in Whitening Cream Sold in Banjarnegara Regency's Traditional Market. JOTCSA. 2023;10(1):39-46. **DOI:** <https://doi.org/10.18596/jotcsa.1151307>.

*Corresponding author. E-mail: sabtanti@umy.ac.id

1. INTRODUCTION

Cosmetics are pharmaceutical preparations widely used to support a person's daily appearance. Cosmetics can also help to improve the dry, dull, or blemished skin (1,2). They have both positive and negative impacts on public health (3). Whitening cream is one type of cosmetic that is most widely used to improve the facial skin, such as by making it brighter and whiter. One of the ingredients that can be used as lightning or bleaching is mercury (4).

Indonesia has issued regulations to control what ingredients are safe and can be used to a certain extent through the BPOM (Indonesian national agency of drug and food control (Badan Pengawas Obat dan Makanan) RI. It has been confirmed that many cosmetic products contain heavy metals such as mercury, arsenic, and hydroquinone that exceed

the specified limits regulated by 21CFR700.13 FDA and BPOM RI (2,5). This issue, therefore, causes BPOM RI to issue a *public warning* number B-IN.05.03.1.43.12.17.5965 on December 11, 2017, concerning cosmetics that contain harmful ingredients so that they are withdrawn and are discovered to contain dangerous metals (6). During 2017, BPOM RI has also found 26 types of cosmetics containing hazardous materials. In the use of cosmetics, they must be adjusted to the rules of their use (7).

In 2018, there was a whitening cream that was positively found to contain mercury. It was found in the preliminary research of several researchers, such as Walangitan *et al.* (2018) and Mona *et al.* (2018). The mercury concentration of three samples from seven samples circulated in the Manado district, which were measured by using the Atomic

Absorption Spectrophotometry (AAS) method, was 0.1299 mg/kg, 0.1822 mg/kg, and 0.0566 mg/kg, respectively (8,9). Furthermore, mercury concentrations in two samples of six taken from the Manado region, measured by using the Mercury Analyzer method, were 229.38 ppm and 101.17 ppm (9).

According to BPOM RI in 2019, heavy metal mercury (Hg) should be not found inside cosmetics (2). Besides, the World Health Organization states that each country has its own policy regarding the amounts of mercury that can be used in cosmetic products (10).

According to Tranggono et al. (2014), mercury is proposed to be a skin whitening ingredient as it has the potential to be a reducing agent of skin color with a very strong whitening power (11). Mercury ions are considered to inhibit melanin synthesis of skin pigment in melanocyte cells (12,13). Melanin in people with dark skin is more abundant than in people with brownish yellow skin. It can be said that the function of melanin in the skin is to give the skin a brown color (14). When this process is inhibited, melanin will not be formed. This is the basis for the mechanism of various bleaching active ingredients to reduce the melanocyte cells that produce melanin. In the initial use of mercury, it can irritate and cause dependence. When the use is stopped, it will cause an itchy and uncomfortable feeling on the facial skin (15,16). Furthermore, mercury can also cause skin cancer with long-term use (17).

Since there are a lot of reports stating that there are harmful effects of mercury on the use of bleaching creams by women in Indonesia and the survey results in the Traditional Market of Banjarnegara showed there were a lot of circulating cream products that were sold without BPOM RI registration numbers. Therefore, 20 samples of whitening cream without BPOM RI registration number that are circulated in the traditional market of Banjarnegara district were collected and then analyzed. This paper deals with the explanation of qualitative and quantitative analysis of mercury in the samples.

2. EXPERIMENTAL SECTION

2.1. Research Tools

Copper rods, sandpaper, filter paper, tongs, dropper pipettes, burners, tube racks, electric stoves (Maspion ®), beaker glass (Pyrex ®), 100 mL Erlenmeyer (Pyrex ®), volumetric flask 25 mL; 100 mL (Pyrex ®), volumetric pipette 1mL; 5mL; 10 mL; 25 mL (Pyrex ®), measuring pipette 5mL; 50 mL; 100 mL (Pyrex ®), test tubes (Pyrex ®), digital scales (Mettler Toledo AL 204), Mercury analyzer (AULA 254 ®) were used in the present study.

2.2. Research Materials

The materials used in this study were 20 types of facial whitening cream samples collected from traditional market of Banjarnegara Regency. The

concentrated HNO₃ solution, concentrated HCl solution, and distilled water were purchased from Bratachem. The 0.5 N KI solution, KMnO₄, hydroxylamine hydrochloride, and SnCl₂. 2H₂O were obtained from Merck. The standard mercury solution was purchased from Sigma-Aldrich.

2.3. Procedures

2.3.1. Qualitative sample test

Sample preparation: Two (2) grams of sample were weighed using a digital scale, added to 25 mL of distilled water, and then went through wet destruction with 10 mL of aqua regia solution (the combination of concentrated HCl and concentrated HNO₃ at a ratio of 1:3). The wet destruction was done for 15 minutes, until the sample almost dried. The heating was conducted during the destruction using a hot plate. The end of destruction was then added 10 mL of distilled water. Furthermore, it was boiled briefly for 5 minutes, cooled, and filtered (15).

2.3.2. Mercury identification test

Color reaction test by using KI: The color test was done in the test tube (Pyrex ®). Two (2) drops of 0.5 N KI was added to one (1) mL of filtered sample in the test tube. The addition was done slowly through the wall of the test tube. The orange solid will appear if it is positively identified to contain mercury (8,18).

2.3.3. Amalgam test

Three (3) mL of filtered sample solution was added into the test tube, and then the copper rod was sanded until it was glossy. It was then dipped for some time into the test tube containing the tested solution. The copper rod will be coated with glossy grey patches if it is positively identified to contain mercury. The grey color will disappear if it is heated on a flame (18-20).

2.4. Quantitative Analysis of Samples Using a Mercury Analyzer

2.4.1. Sample preparation

Samples were weighed and placed in a 100 mL Erlenmeyer flask, followed by 10 mL of HNO₃ and HClO₄ with a ratio of 1:1. The mixture was then heated on a hot plate until it turned clear and a white smoke appeared. Afterward, the samples were filtered, and 50 mL were taken by using a volumetric flask (21).

2.4.2. Measuring mercury concentration using a Mercury analyzer (AULA 254®)

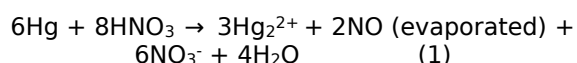
A 10-mL volumetric pipette was used to collect samples, which were then placed in a test tube. 0.1 mL of KMnO₄ (0.1%), 0.1 mL of hydroxylamine hydrochloride, and 0.5 mL of SnCl₂.2H₂O were added. It was also measured with a Mercury analyzer at a wavelength of 253.7 nm (1,21,22).

3. RESULTS AND DISCUSSION

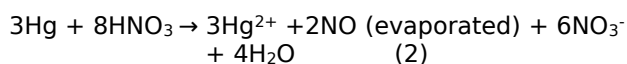
The qualitative analysis of mercury in the whitening cream samples from the traditional market of Banjarnegara Regency was done by using the KI color

reaction and Amalgam formation (18-20). The wet destruction was conducted before the test. The heating of organic samples in the presence of strong oxidizing agents such as single or combinations of mineral acids is known as wet digestion or destruction. The sample is completely oxidized to form an inorganic compound suitable for analysis if it is heated at a suitable temperature continuously for a sufficiently long time. Generally, HNO_3 is used for wet destruction as it cannot react with a saline solution such as HCl or H_2SO_4 (23). The wet destruction of this research used aqua regia solution, which is a mixture of HCl and HNO_3 with a ratio of 1:3 (24). HCl and HNO_3 were used because they are strong acids and oxidizing agents to break the bond of organic metals (Hg-organic) so that inorganic metals (Hg^{2+}) were formed.

Mercurium (I) is produced by combining cold concentrated and moderately concentrated nitric acid (HNO_3) with excessive mercurium, which is the reaction that occurs between a mercury metal and concentrated HNO_3 . The resulting reaction is depicted in Equation 1.

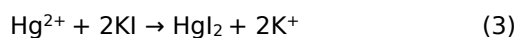


By using excessively concentrated heated nitric acid (HNO_3), mercurium (II) ions are formed with the following Equation 2.



Mercury (Hg) is very distinct from the reagents used in the systematic qualitative analysis, and it is therefore included in two different analytic classes. Mercury ions (I) belong to the first cation group, while mercury ions (II) belong to the second cation group (18).

The analysis was carried out using potassium iodide. The reaction that occurs between mercury and potassium iodide is given by Equation 3 (25).

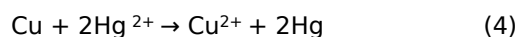


The reaction produced an orange-red solid of HgI_2 (19), as shown in Figure 1.



Figure 1: KI test of whitening cream.

Amalgam reaction formation is carried out by using Cu or a sanded copper rod. Amalgam is a metal solution from mercury produced by copper rods that can be dissolved by mercury. If it is positively identified to contain mercury, there will appear a layer containing grey glossy spots on the surface of the copper rod, which indicates a form of metal mercury (18,19,26,27). It happens from the results of the reaction (18,27), as in Equation 4.



Based on that reaction, 2Hg solid produced the layer with glossy grey patches.



Figure 2: Amalgam test of whitening cream.

The result obtained was negative amalgam with no glossy grey patches on the surface of the copper rod. It is because the sample contained less mercury that made it hardly detected. The KI color test and amalgam qualitative analysis are summarized in Table 1.

Table 1: The Result of the Qualitative Analysis Using a Color Test (Potassium Iodide Test) and the Formation of Amalgam.

Sample Code	Replication	KI Color Test	Amalgam Formation Test	Information (+/-)
1	1	Clear	No glossy grey color change	-
	1.1	Clear	No glossy grey color change	-
2	2	Clear	No glossy grey color change	-
	2.1	Clear	No glossy grey color change	-
3	3	Clear	No glossy grey color change	-
	3.1	Clear	No glossy grey color change	-
4	4	Clear	No glossy grey color change	-
	4.1	Clear	No glossy grey color change	-
5	5	Clear	No glossy grey color change	-
	5.1	Clear	No glossy grey color change	-
6	6	Clear	No glossy grey color change	-
	6.1	Clear	No glossy grey color change	-
7	7	Clear	No glossy grey color change	-
	7.1	Clear	No glossy grey color change	-
8	8	Clear	No glossy grey color change	-
	8.1	Clear	No glossy grey color change	-
9	9	Clear	No glossy grey color change	-
	9.1	Clear	No glossy grey color change	-
10	10	Clear	No glossy grey color change	-
	10.1	Clear	No glossy grey color change	-
11	11	Clear	No glossy grey color change	-
	11.1	Clear	No glossy grey color change	-
12	12	Red and orange solid	No glossy grey color change	+
	12.1	Red and orange solid	No glossy grey color change	+
13	13	Clear	No glossy grey color change	-
	13.1	Clear	No glossy grey color change	-
14	14	Clear	No glossy grey color change	-
	14.1	Clear	No glossy grey color change	-
15	15	Colored and red solid	No glossy grey color	+

Sample Code	Replication	KI Color Test	Amalgam Formation Test	Information (+/-)
	15.1	Colored and red solid	No glossy grey color change	+
16	16	Clear	No glossy grey color change	-
	16.1	Clear	No glossy grey color change	-
17	17	Red colored and orange red solid	No glossy grey color change	+
	R17	Red colored and orange solid	No glossy grey color change	+
18	18	Clear	No glossy grey color change	-
	18.1	Clear	No glossy grey color change	-
19	19	Clear	No glossy grey color change	-
	19.1	Clear	No glossy grey color change	-
20	20	Clear	No glossy grey color change	-
	20.1	Clear	No glossy grey color change	-

Based on the results, there are three positive samples containing mercury, namely sample numbers 12, 15, and 17, as there is a permanent change in the orange color and a red solid using KI color test. This result is in accordance with the previous identification of mercury in the whitening cream sold in Manado, Banjarmasin, and Palu, Indonesia (8,25,26), even in Shijiazhuang, China (13). To ascertain the result and find out how much mercury is contained in the sample, a quantitative analysis was carried out on the three samples by using a mercury analyzer.

Mercury analyzer includes in the spectrophotometric analysis technique of atomic absorption the administration of cold vapor samples. Mercury has the unique characteristic of having a high vapor pressure at room temperature (0.16 Pa at 293 K).

The vapor produced is stable and monatomic, so that the atomic composition of the mercury vapor can be read, without the use of a flame or other atomizing techniques with a wavelength of 253.7 nm (28). The first thing to be prepared was the standard curve. A mercury concentration in the sample preparation was then measured by using a mercury analyzer at a wavelength of 253.7 nm. The wavelength was selected as it indicated the best sensitivity and did not indicate an interaction with other metals in the samples. In the atomization process, it used SnCl₂, which was an olive reducing agent. The reaction occurred as described in equation 5 and the concentrations of mercury in the three (3) samples of whitening cream are represented in Table 2.

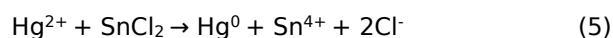


Table 2: The result of the quantitative analysis using mercury analyzer.

Sample Code	Sample weight (g)	Results (ppm)
12	1.0346	0.04217
15	1.0086	0.01814
17	1.0872	0.91000

Based on Table 2, upon conducting a quantitative test by using Mercury Analyzer with a wavelength of 253.7 nm, three samples were found to contain mercury, namely samples 12, 15, and 17, with an average level of 0.04217 ppm, 0.01814 ppm, and 0.91000 ppm, respectively. The concentration of the mercury was similar to the previous research that reported on mercury analysis in the whitening cream sold in Palu, Indonesia (25). Moreover, based on WHO 2011, the policy to limit the use of

mercury depends on each country (10). It is necessary to conduct a routine check on whitening cream products sold in the market to minimize the spread of harmful cosmetics. It is also expected that the public will be more careful in selecting whitening cosmetics to use.

4. CONCLUSION

Based on the analysis of whitening creams sold in Banjarnegara Regency using KI color test, it was found that three (3) whitening creams contained mercury out of the 20 collected samples. The concentrations of the mercury in the three whitening creams were between 0.01814 -0.91000 ppm based on mercury analyzer. According to the results, the consumer must be more careful when choosing a whitening cream to prevent the negative effects of its use.

5. CONFLICT OF INTEREST

There is no conflict of interest for this publication.

6. ACKNOWLEDGMENTS

The authors are grateful for the facilities provided by Universitas Muhammadiyah Yogyakarta.

7. REFERENCES

- Juliana Anggraeni V, Yuliantini A, Rahmawati F, Studi PS, Farmakokimia R, Tinggi Farmasi Bandung Jalan Soekarno Hatta no S. Analisis cemaran logam berat merkuri dalam krim pemutih wajah yang beredar dipasar tradisional dengan metode spektrofotometri serapanatom. *J Pharmacopolium* [Internet]. 2018 Sep 3 [cited 2022 Jul 28];1(1):44-50. Available from: [<URL>](#).
- B POMRI. Peraturan Badan Pengawas Obat dan Makanan Tentang Persyaratan Teknis Bahan Kosmetika. 2019.
- Pangaribuan L. Efek samping kosmetik dan penanganannya bagi kaum perempuan. *J Kel SEHAT Sejah* [Internet]. 2018 Jan 3 [cited 2022 Jul 28];15(2):20-8. Available from: [<URL>](#).
- Parengkuan K, Fatimawali F, Citraningtyas G. Analisis kandungan merkuri pada krim pemutih yang beredar di kota manado. *Pharmacon* [Internet]. 2013 Feb 1 [cited 2022 Jul 28];2(1). Available from: [<URL>](#).
- USFDA. Food and Drug Administration Department of Health and Human Services. 2011. Part 700-General. Subpart B-Requirements for specific cosmetic products. 700.13 Use of mercury compounds in cosmetics including use as skin bleaching agents in cosmetic preparatio. 2011.
- B POMRI. Public Warning nomor B-IN.05.03.1.43.12.17.5965 tanggal 11 Desember 2017 tentang Kosmetika mengandung bahan berbahaya. Keputusan kepala badan pengawas obat dan makanan Republik Indonesia. Jakarta; 2017.
- Wurdiyanto G. Merkuri, bahayanya dan pengukurannya. 2007.
- Mona RK. Analisis kandungan merkuri (hg) pada beberapa krim pemutih wajah tanpa ijin bpom yang beredar di pasar 45 manado. *Pharmacon* [internet]. 2018 Jul 1 [cited 2022 Jul 29];7(3). Available from: [<URL>](#).
- Walangitan VM, Rorong JA, Sudewi S. Analisis merkuri (Hg) pada krim pemutih wajah yang beredar di kota manado. *Pharmacon* [Internet]. 2018 Jul 1 [cited 2022 Jul 29];7(3). Available from: [<URL>](#).
- WHO. Mercury in Skin Lightening Products. Geneva: Public Health and Environment; 2011.
- Tranggono, R.I.; Latifah F. Buku Pegangan Dasar Kosmetologi. Jakarta: Sagung Seto; 2014.
- Sembel D. Toksikologi Lingkungan. Yogyakarta: Penerbit Andi; 2015.
- Wang L, Zhang H. Mercury content in marketed cosmetics: analytical survey in Shijiazhuang, China. [Internet]. 2015 Oct 2 [cited 2022 Jul 29];34(4):322-6. Available from: [<URL>](#).
- Mayaserli DP, Sasmita W. Pemeriksaan kadar merkuri dan keluhan kesehatan dalam darah wanita pemakai krim pemutih dengan metoda inductively coupled plasma. *Sainstek J Sains dan Teknol* [Internet]. 2017 Mar 15 [cited 2022 Jul 29];8(2):159-65. Available from: [<URL>](#).
- Sari AK, Saputera MMA, Ayuhecacia N, Pratiwi ME. Analisis kualitatif merkuri pada lotion pemutih yang dijual di online shop daerah kota banjarmasin. *J Ilm Ibnu Sina* [Internet]. 2017 Apr 11 [cited 2022 Jul 29];2(1):13-9. Available from: [<URL>](#).
- Erasiska, Bali S, Hanifah TA. Analisis Kandungan Logam Timbal, Kadmium dan Merkuri dalam Produk Krim Pemutih Wajah. *J Online Mhs Fak Mat dan Ilmu Pengetah Alam Univ Riau*. 2015;2(1).
- Sun GF, Hu WT, Yuan ZH, Zhang BA, Lu H. Characteristics of mercury intoxication induced by skin-lightening products. *Chin Med J (Engl)* [Internet]. 2017 Dec 20 [cited 2022 Oct 7];130(24):3003-4. Available from: www.cmj.org.
- Svehla G. Vogel Bagian I. Buku teks Analisis Anorganik Kualitatif Makro dan Semimikro. Jakarta; 1990.
- Madania M, Martani MM. Analisis Logam Merkuri (Hg) Pada Krim Pemutih Wajah Merek X Dengan Metode Spektrofotometri Serapan Atom (SSA). *Al-Kimia*. 2014;2(2).
- Kala'lembang C, Pinontoan OR, Ratag BT. Kandungan merkuri pada losion pemutih tangan dan badan yang digunakan oleh masyarakat di kelurahan tataaran patar kecamatan tondano selatan kabupaten minahasa. *Pharmacon*. 2016;5(2).
- LPPTUGM. Metode Uji Mercury Analyzerl Dokumen RDP/5.10.2/LPPT Rev 1. Yogyakarta: Universitas Gadjah Mada; 2019.
- Male YT, Nanlohy AC, Asriningsih. Introduction analysis of several levels of the mercury (hg) in shells. *Ind J Chem Res* . 2014;2:136-41.
- Kebbekus B. Sample Preparation Techniques in Analytical Chemistry. Mitra S, editor. New York: Interscience Then John Wiley; 2003. 227-270 p.
- Ariska Trisnawati F, Herlina Yulianti C, Gusti Ebtavanny T, Program Studi III Farmasi MD, Farmasi Surabaya A, Ilmu Kimia B, et al. Identifikasi Kandungan Merkuri pada Beberapa Krim Pemutih yang Beredar di Pasaran (Studi dilakukan di Pasar DTC Wonokromo Surabaya). *J Pharmasci (Journal Pharm Sci* [Internet]. 2017 Jul 7 [cited 2022 Jul 30];2(2):35-40. Available from: [<URL>](#).
- Rohaya U, Ibrahim N, Jurusan J, Fakultas F.

Analisis Kandungan Merkuri (Hg) Pada Krim Pemutih Wajah Tidak Terdaftar Yang Beredar Di Pasar Inpres Kota Palu: J Farm Galen (Galenika J Pharmacy) [Internet]. 2017 Mar 1 [cited 2022 Jul 30];3(1):77-83. Available from: [<URL>](#).

26. Rakhmina D, Joko Kartiko Jurusan Analis Kesehatan Poltekkes Kemenkes Banjarmasin Jl Mistar Cokrokusumo J. Logam Merkuri pada Masker Pemutih Wajah di Pasar Martapura. Med Lab Technol J [Internet]. 2017 Dec 29 [cited 2022 Jul 30];3(2):53-7. Available from: [<URL>](#).

27. Rasyid R, Susanti E, Azhar R. Pemeriksaan Kualitatif Hidrokuinon dan Merkuri dalam Krim Pemutih. J Farm Higea [Internet]. 2017 Feb 22 [cited 2022 Jul 30];7(1):63-73. Available from: [<URL>](#) .

28. Lajunen L. Spectrochemical analysis by atomic absorption and emission. London: Royal Society of Chemistry; 2007.



Theoretical Investigation of the Structures and Energetics of (MX)-Ethanol Complexes in the Gas Phase

Ahmed M. SADOON^{1*} 

¹University of Mosul, College of Education for Pure Science, Department of Chemistry, Mosul, Iraq.

Abstract: The structures and energy of alkali halide salt (MX) complexes with ethanol have been investigated in this work. The core of this study is to explore the effect of ion size on the interactions between solvent and solute. LiF and KBr as monovalent salts with different sizes of inion and cation have been chosen to explore this difference in addition to various physical properties. Three complexes of each LiF and KBr with ethanol taking the formula $\text{MX}(\text{CH}_3\text{CH}_2\text{OH})_n$ ($n=1-3$), were studied. *Ab-initio* calculations have been performed to optimize the chemical structures of these complexes and explore the possible structures, isomers, and their corresponding IR spectra using Density functional theory (DFT/ B3LYP). 6-311G** were chosen as basis sets for these calculations. The geometry evaluations, energy searches, vibrational frequency calculations, and each complex's binding energy were also theoretically extracted in this study. The minimum energy structures were calculated, and different isomers were found. The presence of Ionic hydrogen bonds (IHBs) was observed and proposed to be the main binding between the MX salt and ethanol. Also, the infrared vibrational bands in the OH stretching region were recorded for the minimum structures, and the determined red-shift was at about 400 cm^{-1} . In addition, the binding energy calculations found a gradual rise in the BE value with every additional ethanol molecule added to MX salt.

Keywords: Infrared Spectroscopy, DFT, Alkaline metal, Ethanol.

Submitted: July 20, 2022. **Accepted:** November 02, 2022.

Cite this: Sadoon AM. Theoretical Investigation of the Structures and Energetics of (MX)-Ethanol Complexes in the Gas Phase. JOTCSA. 2023;10(1):47-54.

DOI: <https://doi.org/10.18596/jotcsa.1146250>.

***Corresponding author. E-mail:** ams95@uomosul.edu.iq

1. INTRODUCTION

The interaction between the salt and solute in polar solutions has been in the spotlight of many studies to understand the behavior of anions and cations in this medium due to their essential role in chemical reactions. In addition to many applications of union and cation behavior in specific fields such as electrochemistry and environmental chemistry (1-3).

The interaction between the salt and polar solvent is usually expressed as *kosmotropic* or *chaotropic*. *Kosmotropic* are called (order-makers), which increase the stability of the hydrogen bonding network, while chaotropic ions (disorder-makers) reduce the stability of the hydrogen bonding grid

and thus reduce the stability of the salt-solvent structures (4, 5).

It is well known that alkaline halides behave as monovalent salts. These salts are dissolved in polar solvents (water, ethanol, etc.) to form separated ions in dilute solutions. The size and charge density of the cation and anion plays a critical role in giving the ability of a single alkaline halide molecule to dissolve in a numerical number of solvent molecules. LiF and KBr were chosen for this study as an example of salt with different sizes and charges of cation and anion.

Lithium fluoride is widely used in industry as an ingredient in lithium-ion battery electrolytes (6). Also, LiF is used as specialized optics for the vacuum ultraviolet spectrum (7) and in light-

emitting diodes production (LED) as a coupling layer to enhance electron injection (8). In addition to many applications in manufacturing nuclear reactors and radiation detectors (9).

Potassium bromide is most commonly used in medical drugs as an anticonvulsant drug to phenobarbital and as an antiepileptic medication for dogs(10), in addition to many other medical and veterinary applications. For industrial applications, KBr plays a significant role in Optics as infrared optical windows and is used widely in components for general spectroscopy (11) and photography as a restrainer by improving differentiation between exposed and unexposed crystals of silver halide to reduce fog(12).

Early studies concentrated on the structure of Alkaline halide (MX) complexes with water (13-16). These studies focused on MX-water complexes geometry structures, infrared (IR), and Mass spectrum using Helium nanodroplet apparatus. The outcome data show the critical role of ionic hydrogen bonds (IHBs) between MX salt and water.

No research has studied the structure of LiF and KBr- ethanol clusters. Only a few studies focused on studying LiF and ethanol's structure separately in the gas phase. LiF as a salt vapor was studied theoretically to investigate the landscape of a numerical number of (LiF)_n (n=1-8) (17). Ethanol clusters have also been investigated using ab-initio calculations (18), and the thermodynamic properties were recorded in this study.

The theoretical calculation of chemical reactions was widely used in many recent studies, (19-23) due to the unique environment and the ability to study the reactions that cannot be easily prepared in standard lab conditions. The formation of MX-solvent complexes is usually prepared and studied in bulk solutions (19, 20). Even in the diluted solutions, separating MX-(solvent)_n complexes, where n has a numerical value, is difficult because of the strong ionic hydrogen network (21). Unfortunately, an accurate simulation of the properties is still difficult to record, even in simple electrolytic solutions (22). Considering this limited experimental evidence, the ab-initio calculations study of these complexes looks useful and provides a unique tool to explore the chemistry of these complexes. So, this study will concentrate on studying the interaction of Alkaline halides (MX) with ethanol in gas phase theoretically using ab-initio calculations.

2. EXPERIMENTAL

2.1. MX(CH₃OH)_n formation

LiF and KBr complexes with ethanol (CH₃OH)_n, (n=1-3) were shaped using the Chemcraft software package (23). The premier structures were created with different positions and randomly rotated for MX and ethanol molecules to examine a wide range of potential geometries and isomers of MX(CH₃OH)_n complexes. The structure geometries were then optimized to find the minimum structures of each complex using ab-initio calculations.

2.1.1. Ab-initio calculations

Ab-initio calculations were applied using Density functional theory (DFT) with Becke three-parameter exchange and Lee-Yang-Parr correlation (B3LYP) within the Gaussian 03 software package (24). The basis set (6-311G**) obtained from the EMSL basis set exchange library (25) was then used to optimize the formatted structures. Each complex's minimum energy isomer structure was used to extract the data of geometry, energy, and infrared (IR) spectra (vibrational frequency values). In order to reduce the calculation time, the Hartree-Fock (HF) level of theory was first used with (6-311G**) bases set to evaluate the optimized structures. The optimized structures at the HF level were then re-optimized using the DFT(b3lyp) level of theory at the same basis set. A scaling factor of 0.967 was used to correct the values of vibrational frequencies of the final optimized structures. This factor is advised by the National Institute of Standards and Technology (NIST) for the DFT/B3LYP level of theory (26).

2.1.2. Geometry and structure

The final optimized structures of each complex were utilized to extract the information on the minimum energy of isomers, frequencies in the region of OH stretching bands, bond length, angles, dihedral angle, and the Binding Energy (BE). These results were obtained using Chemcraft software.

3. RESULTS AND DISCUSSION

3.1. MX(CH₃CH₂OH)_n structures

3.1.1. LiF(CH₃CH₂OH)_n structures

Several isomers were applied in DFT calculations for LiF(CH₃CH₂OH)_n complexes. For LiF(CH₃CH₂OH) complex, two optimized structures were found for this complex among many tested isomers, see Figure 1. The global minimum structure shows that the LiF salt takes the position so that the hydrogen ion of the hydroxyl group can form IHB with the fluoride atom. The higher energy structure shows that the methyl group in ethanol forms an IHB with a fluoride atom. The length of IHB in the minimum structure is about 1.68 Å while 2.203 Å in the higher energy isomer. Additional stabilization comes from the Li⁺ ion to the O⁻ atom.

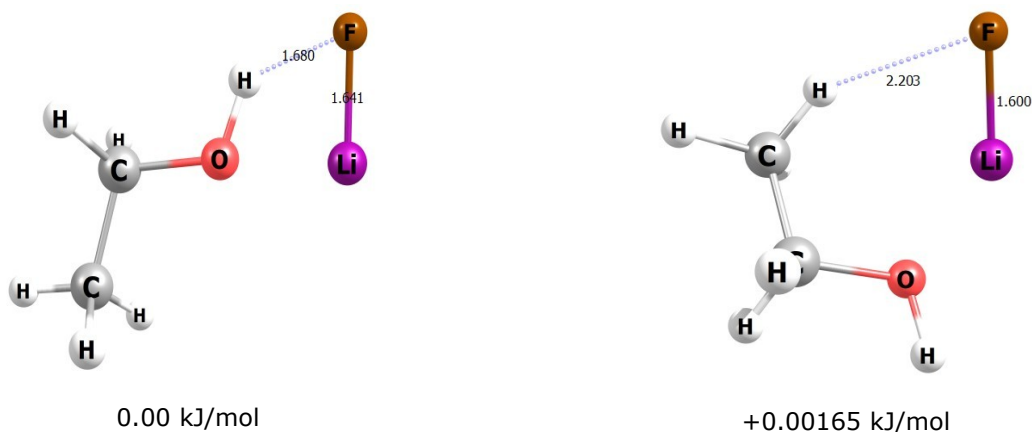


Figure 1: The minima structures for $\text{LiF}(\text{CH}_3\text{CH}_2\text{OH})$ with their energies in kJ/mol using DFT/B3LYP level of theory and 6-311G** as basis set

Three minima structures were recorded for $\text{LiF}(\text{CH}_3\text{CH}_2\text{OH})_2$, as can be seen in Figure 2. The global minimum structure is similar to the $n = 1$ complex but now has two IHBs bonding the fluoride ion and the H atoms of the hydroxyl group. The following minimum structure has an energy of 23.31 kJ/mol, higher than the global minimum structure energy, and also has two IHBs between the hydrogen of each ethanol methyl group and fluoride ion. The bond length of these two structures were 1.744 and 1.654 Å, respectively. The last structure

had energy above the global minimum structure at about 38.33 kJ/mol. Two ethanol molecules of this structure interacted with each other via one IHB. Another IHB seen in this structure bonded the hydrogen atom of the ethanol methyl group with the fluoride ion. The significant point seen in this complex, compared with $\text{LiF}(\text{CH}_3\text{CH}_2\text{OH})$ complex, is the difference in LiF bond length in the minimum structures that increased from 1.641 Å to 1.744 Å. This difference may be related to the reduction of fluoride ion charge bonded to a couple of IHBs.

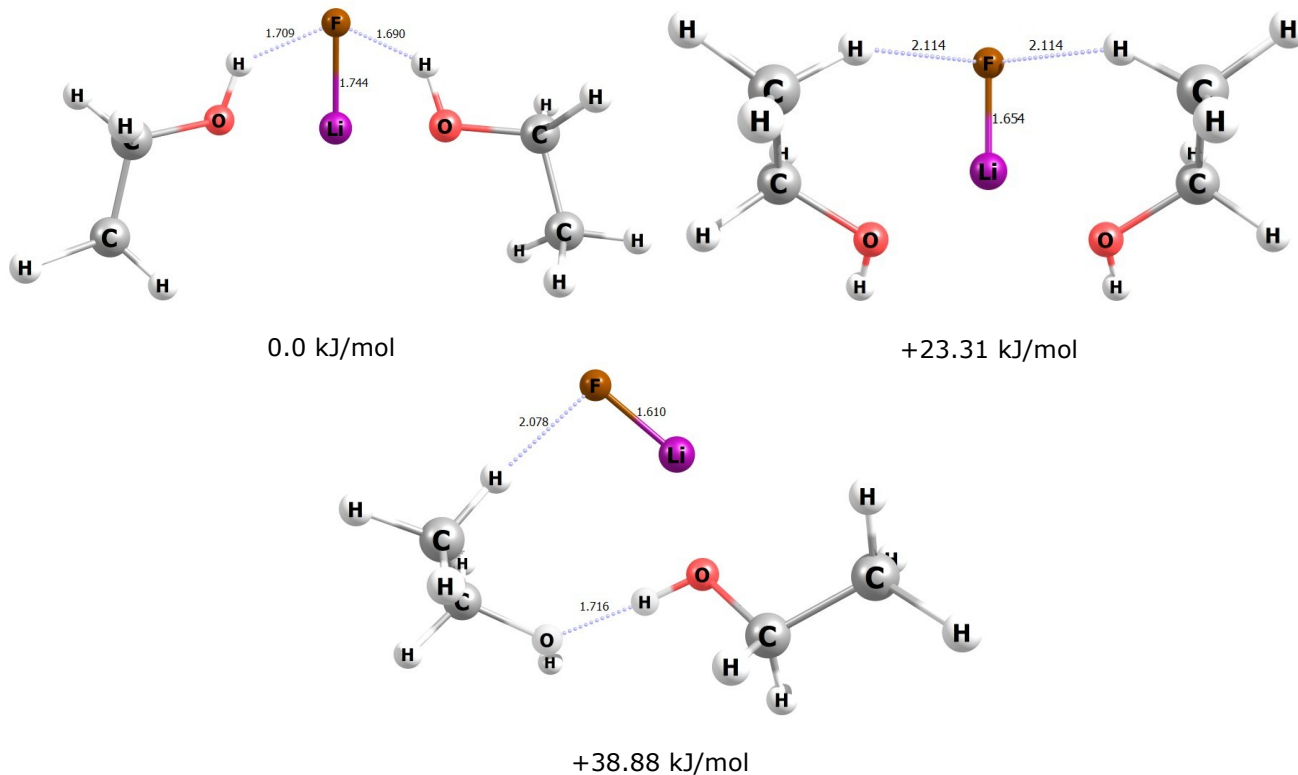


Figure 2: The minima structures for $\text{LiF}(\text{CH}_3\text{CH}_2\text{OH})_2$ with their energies in kJ/mol using DFT/B3LYP level of theory and 6-311G** as basis set

For $n = 3$, Three minima structures were found; see Figure 3. The global minimum for $\text{LiF}(\text{CH}_3\text{CH}_2\text{OH})_3$ is similar to those found for $\text{LiF}(\text{CH}_3\text{CH}_2\text{OH})$ and $\text{LiF}(\text{CH}_3\text{CH}_2\text{OH})_2$. Three ethanol molecules were bonded to fluoride ion by 3 IHBs between the F atom and the hydrogen of the hydroxyl group. The other isomer has higher energy from the global

minimum structure of about 9.74 kJ/mol. This isomer takes the formula where three ethanol bonded together via two IHBs and with one IHB with fluoride ion. The last isomer bonded to LiF salt via three IHBs similar to $\text{LiF}(\text{CH}_3\text{CH}_2\text{OH})_2$. LiF bonds in the three structures were about 1.91, 1.644, and 1.695 Å, respectively.

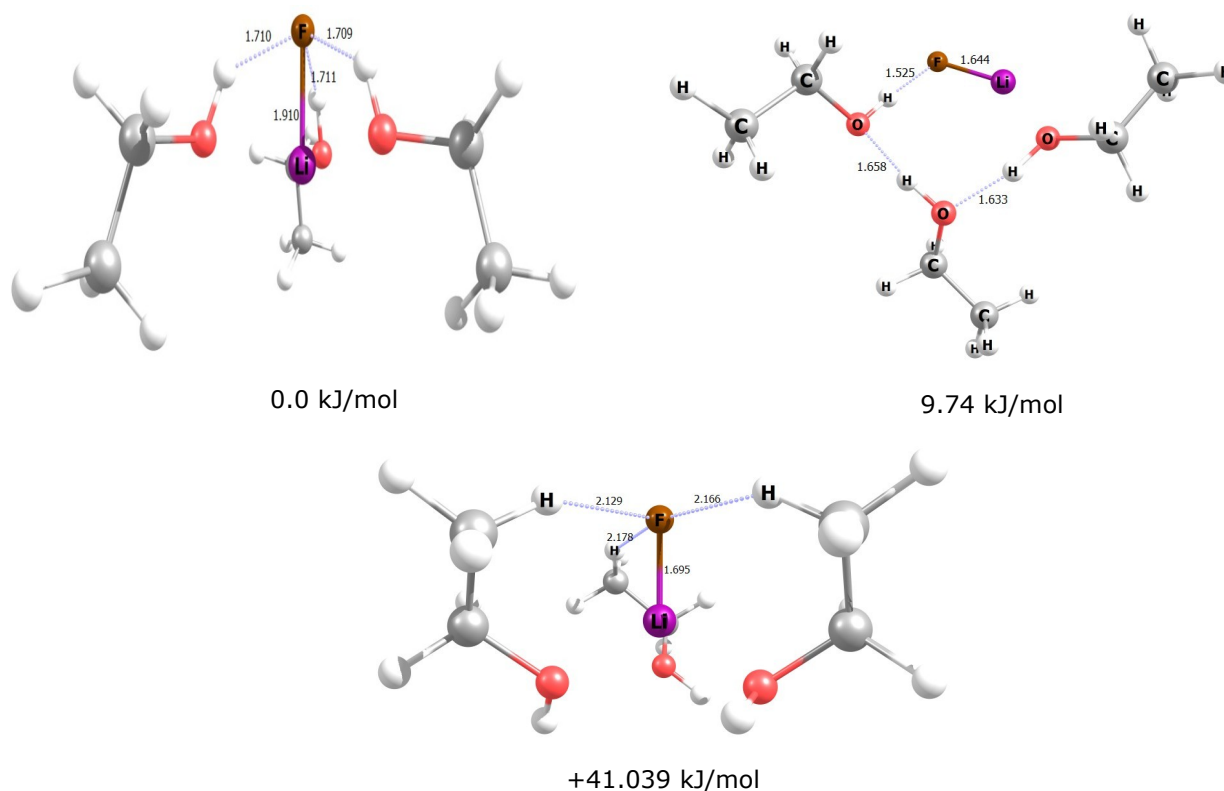


Figure 3: The minima structures for $\text{LiF}(\text{CH}_3\text{CH}_2\text{OH})_3$ with their energies in kJ/mol using DFT/B3LYP level of theory and 6-311G** as basis set.

3.1.2. $\text{KBr}(\text{CH}_3\text{CH}_2\text{OH})_n$ structures

The *ab-initio* calculations for $\text{KBr}(\text{CH}_3\text{CH}_2\text{OH})_n$ ($n=1-3$) were found and seen in Figures 4, 5, and 6, respectively. No significant changes were observed in these structures for these complexes compared with $\text{LiF}(\text{CH}_3\text{CH}_2\text{OH})_n$ calculations. A significant difference in $\text{KBr}(\text{CH}_3\text{CH}_2\text{OH})_n$ complexes was seen

in the IHBs, which were longer than the IHBs in the $\text{LiF}(\text{CH}_3\text{CH}_2\text{OH})_n$ structures, due to the low electronegativity of Br atom compared with Li atom electronegativity. For KBr bond length, it increased gradually with every additional ethanol molecule and gave 2.95, 3.09, and 3.29 Å, respectively, for the $\text{KBr}(\text{CH}_3\text{CH}_2\text{OH})_n$ ($n=1-3$) minimum structures.

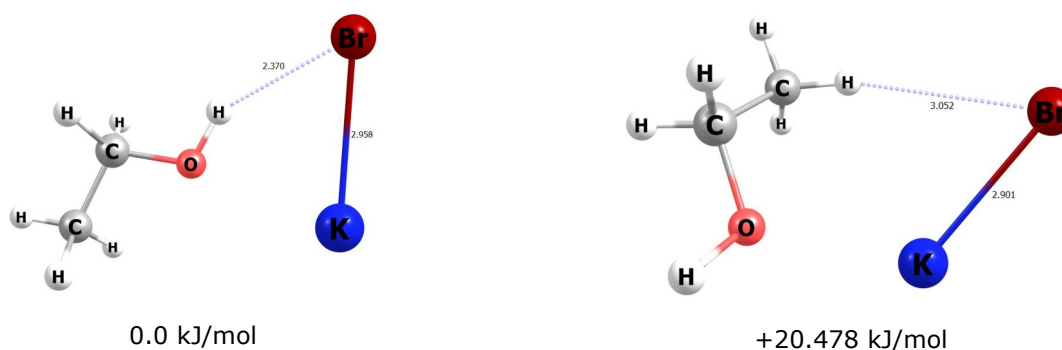


Figure 4: The calculated structures for $\text{MgCl}_2(\text{H}_2\text{O})$ with their energies in kJ/mol using DFT/B3LYP level of theory and 6-311G** as basis set.

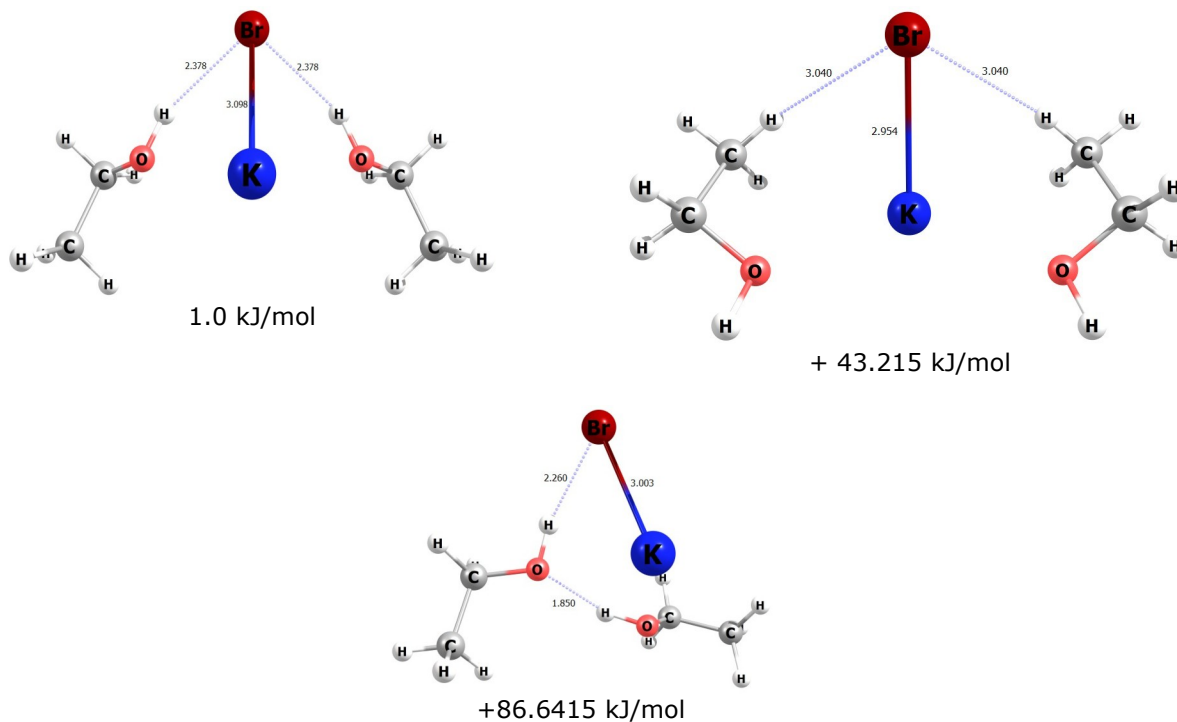


Figure 5: The calculated structures for $MgCl_2(H_2O)_2$ with their energies in kJ/mol using DFT/B3LYP level of theory and 6-311G** as basis set.

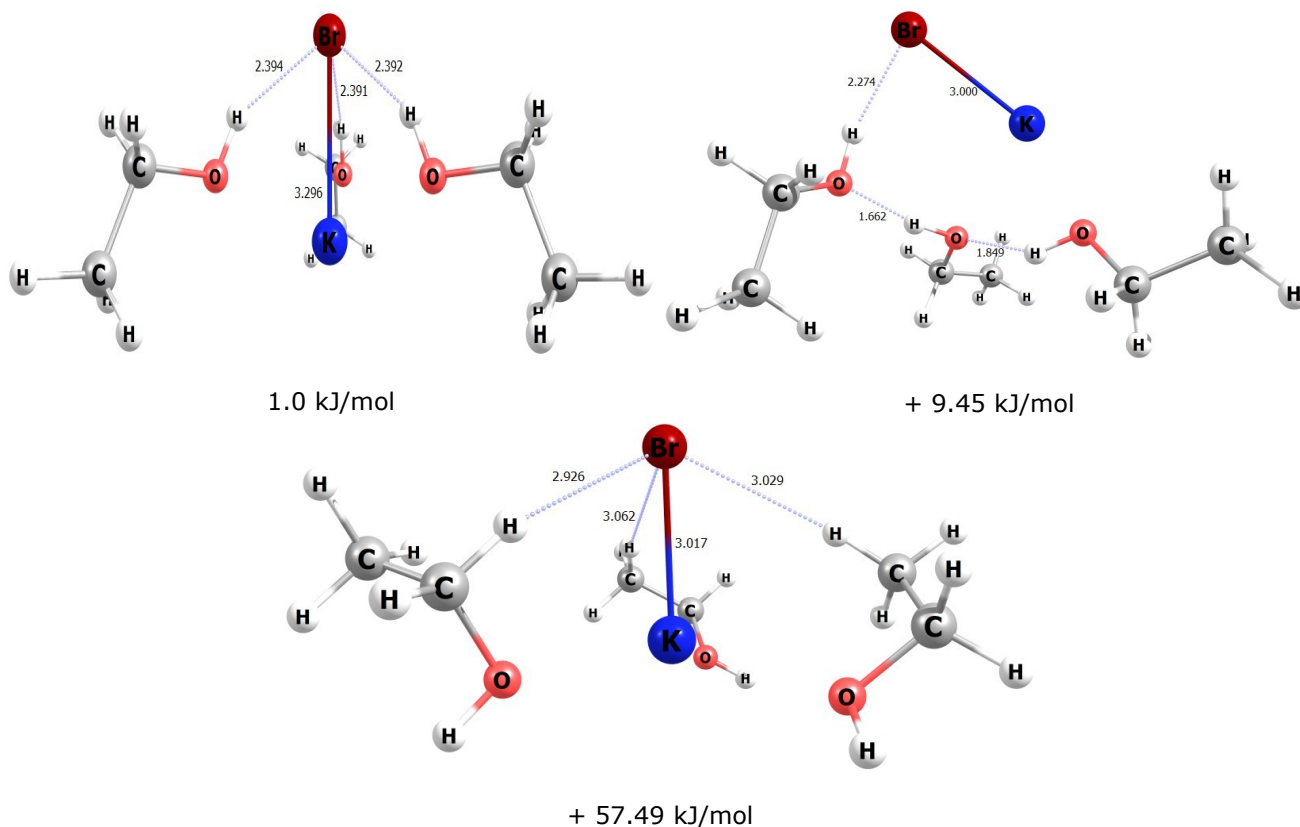


Figure 6: The calculated structures for $MgCl_2(H_2O)_3$ with their energies in kJ/mol using DFT/B3LYP level of theory and 6-311G** as basis set.

3.2. Infrared Spectra of $\text{MX}(\text{CH}_3\text{CH}_2\text{OH})_n$ Complexes

Infrared spectra of $\text{LiF}(\text{CH}_3\text{CH}_2\text{OH})_n$, $n=1-3$, were assigned theoretically using the DFT/B3LYP level of theory on the OH stretching region to evaluate the effect of IHBs on the OH symmetric stretching band. The stretching frequency values were corrected using a scaling factor of 0.967. Only global minimum structures were chosen for IR analysis.

The prediction of DFT calculations at the OH symmetric stretching frequencies is summarized in Table 1. In general, the absorption of OH bands of $\text{LiF}(\text{CH}_3\text{CH}_2\text{OH})_n$ complexes are red-shifted from the OH stretching band of the free ethanol molecule that is seen at 3721 cm^{-1} . This trend of OH stretching red-shift has been recorded previously in several studies (13, 27, 28). The OH band frequency of the $\text{LiF}(\text{CH}_3\text{CH}_2\text{OH})$ complex was found in 3149 cm^{-1} and then raised to 3208 cm^{-1} for $\text{LiF}(\text{CH}_3\text{CH}_2\text{OH})_2$ and 3263 cm^{-1} for $\text{LiF}(\text{CH}_3\text{CH}_2\text{OH})_3$. This red shift can be attributed to the OH band,

which bonded to the fluoride ion via an ionic hydrogen bond (IHB). This behavior of OH frequency fluctuation can be assigned to the high electronegativity of the Fluoride atom in the $n=1$ complex. This electronegativity has decreased gradually with every additional ethanol molecule. Therefore, OH frequency has increased again in $n=2$ and 3 complexes.

The same trend of OH stretching frequency behavior in $\text{LiF}(\text{CH}_3\text{CH}_2\text{OH})_n$ complexes was seen for the minimum structures of $\text{KBr}(\text{CH}_3\text{CH}_2\text{OH})_n$, $n=1-3$, complexes. Red shifts of OH stretching bands were recorded in these complexes due to IHBs effect on bromide electronegativity reduced more with every additional ethanol molecule. The *ab-initio* calculations recorded the OH symmetric stretching frequency of $\text{KBr}(\text{CH}_3\text{CH}_2\text{OH})$ at 3318 cm^{-1} . For $\text{KBr}(\text{CH}_3\text{CH}_2\text{OH})_n$ where $n=2$ and 3, the OH symmetric stretching band was observed at 3346 cm^{-1} and 3382 cm^{-1} , respectively; see Table 2.

Table 1: Infrared spectra for the minimum structures of $\text{LiF}(\text{CH}_3\text{CH}_2\text{OH})_n$ ($n=1-3$) complexes for the OH stretching region using DFT/B3LYP level of theory.

OH frequency band/ cm^{-1}	Vibration frequency assignment	Complex
3149	symmetric stretching	$\text{LiF}(\text{CH}_3\text{CH}_2\text{OH})$
3208	symmetric stretching	$\text{LiF}(\text{CH}_3\text{CH}_2\text{OH})_2$
3266	asymmetric stretching	
3263	symmetric stretching	$\text{LiF}(\text{CH}_3\text{CH}_2\text{OH})_3$
3265	asymmetric stretching	
3336	asymmetric stretching	

Table 2: Infrared spectra for the minimum structures of $\text{KBr}(\text{CH}_3\text{CH}_2\text{OH})_n$ ($n=1-3$) complexes for the OH stretching region using DFT/B3LYP level of theory.

OH frequency band/ cm^{-1}	Vibration frequency assignment	Complex
3318	symmetric stretching	$\text{KBr}(\text{CH}_3\text{CH}_2\text{OH})$
3346	symmetric stretching	$\text{KBr}(\text{CH}_3\text{CH}_2\text{OH})_2$
3370	asymmetric stretching	
3382	symmetric stretching	$\text{KBr}(\text{CH}_3\text{CH}_2\text{OH})_3$
3384	asymmetric stretching	
3414	asymmetric stretching	

3.3. Binding energy calculations for $\text{MX}(\text{CH}_3\text{CH}_2\text{OH})_n$ ($n = 1-3$) complexes

The Binding energy (BE) of the global minimum structure of $\text{MX}(\text{CH}_3\text{CH}_2\text{OH})_n$ complexes was calculated from the DFT/B3LYP calculations and summarized in Table 3 for $\text{LiF}(\text{CH}_3\text{CH}_2\text{OH})_n$ and in Table 4 for $\text{KBr}(\text{CH}_3\text{CH}_2\text{OH})_n$ complexes. The BE was calculated using the following equation:

$$\text{BE} = \Delta E = E(\text{MX}(\text{CH}_3\text{CH}_2\text{OH})_n) - (E(\text{MX}) + E(\text{CH}_3\text{CH}_2\text{OH})_n)$$

In general, a gradual increase in the values of BE was seen in both $\text{MX}(\text{CH}_3\text{CH}_2\text{OH})_n$ complexes, where ($n=1-3$), with increasing n value of ethanol. Also, the BE of $\text{LiF}(\text{CH}_3\text{CH}_2\text{OH})_n$ complexes were higher than the BE of $\text{KBr}(\text{CH}_3\text{CH}_2\text{OH})_3$ complexes. This difference may relate to the high

electronegativity of F⁻ ion in contrast with Br⁻ ion electronegativity. The BE of LiF(CH₃CH₂OH)_n and KBr(CH₃CH₂OH)_n complexes can be seen in Tables 3 and 4, respectively.

The BE of the minimum structures of LiF(CH₃CH₂OH)_n, n=1-3, were (102, 197, and 282)

kJ/mol respectively. On the other hand, The BE of the minimum structure of KBr(CH₃CH₂OH)_n, n=1-3, complexes were (75, 146, and 212) kJ/mol, respectively. This increase may come from the additional IHBs and the proximity of M⁺ ion to O atom of the hydroxyl group that increased with every additional ethanol molecule.

Table 3: The binding energy of LiF(CH₃CH₂OH)_n (n = 1–3) complexes using DFT/B3LYP level of theory.

Binding Energy kJ/mol	Complex
102.37	LiF(CH ₃ CH ₂ OH)
197.90	LiF(CH ₃ CH ₂ OH) ₂
282.24	LiF(CH ₃ CH ₂ OH) ₃

Table 4: The binding energy of KBr(CH₃CH₂OH)_n (n = 1–3) complexes using DFT/B3LYP level of theory.

Binding Energy kJ/mol	Complex
75.04	KBr(CH ₃ CH ₂ OH)
146.23	KBr(CH ₃ CH ₂ OH) ₂
212.82	KBr(CH ₃ CH ₂ OH) ₃

4. CONCLUSION

Structure parameters, Infrared spectra (IR), and the Binding Energy of MX(CH₃CH₂OH)_n complexes, where n = 1–3 and MX =LiF and KBr, have been performed in this work using *Ab-initio* calculations. Several isomers of these complexes have been recorded. A significant observation was seen for MX(CH₃CH₂OH)_n complexes that show a significant increase in the M-X bond length. This increment comes from the effect of the ethanol hydroxyl group that inserts between M and X ions and reduces their interaction by forming IHBs. The global minimum structures of complexes were then used to extract the information on the Vibrational frequency bands in OH stretching regions and the binding energy. The formation of IHBs was observed between the hydrogen of the ethanol hydroxyl group. For IR spectra, a Red-shift in the positions of the OH stretching bands was seen, which is consistent with the presence of the IHBs. Also, a significant increase in the Binding energy (BE) was seen with the increasing n value of ethanol. This increase indicated that the IHB and the proximity of the M⁺ ion to the O atom play a critical role in MX(CH₃CH₂OH)_n complexes.

5. ACKNOWLEDGMENTS

The author is grateful to the University of Mosul and the Chemistry department at the College of Education for pure sciences for their support and funding of this work.

6. REFERENCES

- Satchell DPN. Ions in solution: Basic principles of chemical interactions. Endeavour [Internet]. 1988 Jan [cited 2022 Nov 27];12(4):195. Available from: <URL>
- Marcus Y. Ions in Solution and their Solvation: Marcus/Ions in Solution and their Solvation [Internet]. Hoboken, NJ: John Wiley & Sons, Inc; 2015 [cited 2022 Nov 27]. Available from: <URL>
- Friedman HaroldL. Ionic hydration in chemistry and biophysics. Journal of Electroanalytical Chemistry and Interfacial Electrochemistry [Internet]. 1982 Jan [cited 2022 Nov 27];131:407–8. Available from: <URL>
- Marcus Y. Effect of ions on the structure of water. Pure and Applied Chemistry [Internet]. 2010 Jun 19 [cited 2022 Nov 27];82(10):1889–99. Available from: <URL>
- Moelbert S, Normand B, De Los Rios P. Kosmotropes and chaotropes: modelling preferential exclusion, binding and aggregate stability. Biophysical Chemistry [Internet]. 2004 Dec [cited 2022 Nov 27];112(1):45–57. Available from: <URL>
- Aigueperse J, Mollard P, Devilliers D, Chemla M, Faron R, Romano R, et al. Fluorine Compounds, Inorganic. In: Wiley-VCH Verlag GmbH & Co. KGaA, editor. Ullmann's Encyclopedia of Industrial Chemistry [Internet]. Weinheim, Germany: Wiley-VCH Verlag GmbH & Co. KGaA; 2000 [cited 2022 Nov 27]. p. a11_307. Available from: <URL>
- Zheng Y, Song W, Mo W ting, Zhou L, Liu JW. Lithium fluoride recovery from cathode material of spent lithium-ion battery. RSC Adv [Internet]. 2018 [cited 2022 Nov 27];8(16):8990–8. Available from: <URL>

8. Andeen C, Fontanella J, Schuele D. Low-Frequency Dielectric Constant of LiF, NaF, NaCl, NaBr, KCl, and KBr by the Method of Substitution. *Phys Rev B* [Internet]. 1970 Dec 15 [cited 2022 Nov 27];2(12):5068–73. Available from: [<URL>](#)
9. McGregor DS, Bellinger SL, Shultis JK. Present status of microstructured semiconductor neutron detectors. *Journal of Crystal Growth* [Internet]. 2013 Sep [cited 2022 Nov 27];379:99–110. Available from: [<URL>](#)
10. De Lahunta A, Glass E, Kent M. *Veterinary Neuroanatomy and Clinical Neurology* [Internet]. Elsevier; 2009 [cited 2022 Nov 27]. Available from: [<URL>](#)
11. Alpert NL, Keiser WE., Szymanski HA. *IR: Theory and Practice of Infrared Spectroscopy*. Cham: Springer International Publishing; 2012. 381 p.
12. Anchell S. *The Film Developing Cookbook* [Internet]. 1st ed. Routledge; 1998 [cited 2022 Nov 27]. Available from: [<URL>](#)
13. Tandy J, Feng C, Boatwright A, Sarma G, Sadoon AM, Shirley A, et al. Communication: Infrared spectroscopy of salt-water complexes. *The Journal of Chemical Physics* [Internet]. 2016 Mar 28 [cited 2022 Nov 27];144(12):121103. Available from: [<URL>](#)
14. Sadoon AM, Sarma G, Cunningham EM, Tandy J, Hanson-Heine MWD, Besley NA, et al. Infrared Spectroscopy of NaCl(CH₃OH)_n Complexes in Helium Nanodroplets. *J Phys Chem A* [Internet]. 2016 Oct 20 [cited 2022 Nov 27];120(41):8085–92. Available from: [<URL>](#)
15. Li RZ, Liu CW, Gao YQ, Jiang H, Xu HG, Zheng WJ. Microsolvation of LiI and CsI in Water: Anion Photoelectron Spectroscopy and ab initio Calculations. *J Am Chem Soc* [Internet]. 2013 Apr 3 [cited 2022 Nov 27];135(13):5190–9. Available from: [<URL>](#)
16. Mizoguchi A, Ohshima Y, Endo Y. The study for the incipient solvation process of NaCl in water: The observation of the NaCl-(H₂O)_n (n = 1, 2, and 3) complexes using Fourier-transform microwave spectroscopy. *The Journal of Chemical Physics* [Internet]. 2011 Aug 14 [cited 2022 Nov 27];135(6):064307. Available from: [<URL>](#)
17. Doll K, Schön JC, Jansen M. Ab initio energy landscape of LiF clusters. *The Journal of Chemical Physics* [Internet]. 2010 Jul 14 [cited 2022 Nov 27];133(2):024107. Available from: [<URL>](#)
18. Umer M, Kopp WA, Leonhard K. Efficient yet accurate approximations for ab initio calculations of alcohol cluster thermochemistry. *The Journal of Chemical Physics* [Internet]. 2015 Dec 7 [cited 2022 Nov 27];143(21):214306. Available from: [<URL>](#)
19. Sangoro J, Cosby T, Kremer F. Rotational and Translational Diffusion in Ionic Liquids. In: Paluch M, editor. *Dielectric Properties of Ionic Liquids* [Internet]. Cham: Springer International Publishing; 2016 [cited 2022 Nov 27]. p. 29–51. (Advances in Dielectrics). Available from: [<URL>](#)
20. Nancollas GH. The thermodynamics of metal-complex and ion-pair formation. *Coordination Chemistry Reviews* [Internet]. 1970 Dec [cited 2022 Nov 27];5(4):379–415. Available from: [<URL>](#)
21. Meot-Ner (Mautner) M. Update 1 of: Strong Ionic Hydrogen Bonds. *Chem Rev* [Internet]. 2012 Oct 10 [cited 2022 Nov 27];112(10):PR22–103. Available from: [<URL>](#)
22. Eisenberg B. Ionic Interactions Are Everywhere. *Physiology* [Internet]. 2013 Jan [cited 2022 Nov 27];28(1):28–38. Available from: [<URL>](#)
23. Zhurko G, Zhurko D. Chemcraft-graphical software for visualization of quantum chemistry computations [Internet]. 2016. Available from: [<URL>](#)
24. Frisch MJ, Trucks GW, Schlegel HB, Scuseria GE, Robb MA, Cheeseman JR, et al. *Gaussian 03, Revision C.02* [Internet]. Gaussian, Inc.; 2004. Available from: [<URL>](#)
25. Schuchardt KL, Didier BT, Elsethagen T, Sun L, Gurumoorthi V, Chase J, et al. Basis Set Exchange: A Community Database for Computational Sciences. *J Chem Inf Model* [Internet]. 2007 May 1 [cited 2022 Nov 27];47(3):1045–52. Available from: [<URL>](#)
26. Johnson R. Computational Chemistry Comparison and Benchmark Database, NIST Standard Reference Database 101 [Internet]. National Institute of Standards and Technology; 2002 [cited 2022 Nov 27]. Available from: [<URL>](#)
27. Cabarcos OM, Weinheimer CJ, Martínez TJ, Lisy JM. The solvation of chloride by methanol—surface versus interior cluster ion states. *The Journal of Chemical Physics* [Internet]. 1999 May 15 [cited 2022 Nov 27];110(19):9516–26. Available from: [<URL>](#)
28. Beck JP, Lisy JM. Cooperatively Enhanced Ionic Hydrogen Bonds in Cl – (CH₃OH)_{1–3} Ar Clusters. *J Phys Chem A* [Internet]. 2010 Sep 23 [cited 2022 Nov 27];114(37):10011–5. Available from: [<URL>](#)



Spectral Investigation of Yb³⁺/Ho³⁺/Tm³⁺:Y₂Si₂O₇ Upconverting Nanophosphors for the Usage of Temperature Sensing

Murat Erdem^{1*} , Kadir Esmer¹ , and Gonul Eryurek² 

¹Marmara University, Physics Department, Istanbul, 34722, Turkey

²Istanbul Technical University, Physics Engineering Department, Istanbul, 34722, Turkey

Abstract: Rare earth (Yb³⁺, Ho³⁺, Tm³⁺) yttrium disilicate phosphors were produced by sol-gel technique and heated at 1050 °C temperature. The sizes of the phosphors vary between 20-30 nm according to the images obtained from the Transmission Electron Microscope. The up-conversion (UC) emissions of the nanopowders were measured in the range of 500–900 nm wavelength under 950 nm laser excitation. A linear increase with power was observed in the emission intensity ratio depending on the laser excitation power. Using the FIR technique, the phosphor's temperature was determined by the heating effect caused by the laser pump power. Due to the change in intensity ratio versus temperature, the temperature sensitivity at 428 K was calculated as 0.781x10⁻²K⁻¹ and it was suggested that it can be used as a promising temperature sensor probe in photonic devices.

Keywords: Nanophosphors; Sol-gel; Up-conversion; Temperature sensing.

Submitted: August 08, 2022. **Accepted:** November 07, 2022.

Cite this: Erdem M, Esmer K, Eryurek G. Spectral investigation of Yb³⁺/Ho³⁺/Tm³⁺:Y₂Si₂O₇ upconverting nanophosphors for the usage of temperature sensing. Journal of the Turkish Chemical Society, Section A: Chemistry. 2023;10(1):55–62.

DOI: <https://doi.org/10.18596/jotcsa.1159026>.

***Corresponding author. E-mail:** merdem@marmara.edu.tr.

1. INTRODUCTION

The optical temperature sensing of luminescent materials, which detects temperature changes precisely at small spatial resolution in inaccessible environments, has attracted great interest recently, especially concerning their high-temperature sensitivity (1-6). Luminescent thermography-based temperature sensing is an alternative method, which stands out with its non-contact measurements in many areas that traditional thermometers cannot reach, such as high-voltage power plants, microfluidics, bio-objects, and small-sized circuits below 10 μm (7,8).

The laser excitation power induces heat, which increases the temperature of the rare earth (RE) doped phosphors. Therefore, the emission intensities of RE³⁺ ions become sensitive to temperature change. Consequently, the sensitive effect of excitation power on emission intensity can

lead to the calculation of the temperature of phosphors using the Boltzmann electron distribution between the nearest neighbor energy levels (9). As the difference in nearest energy levels of some RE³⁺ ions varies between about 200 cm⁻¹ and 2000 cm⁻¹ (10), this benefits the development of temperature-sensitive phosphors for optical thermometers.

The optical thermometer properties of RE³⁺: Yb³⁺/Ho³⁺ doped phosphors are limited to a few studies. For example, the sensor sensitivities are 0.0053 K⁻¹ at 93 K for Yb³⁺/Ho³⁺:BaCaTiO₃, 0.0077 K⁻¹ at 366 K for Yb³⁺/Ho³⁺: Pb(MgNb)O₃PbTiO₃, and 0.005 K⁻¹ at 923 K for Yb³⁺/Ho³⁺: CaWO₄, respectively (11-13). The primary goal in the field of optical thermometry is to manufacture the sensor with the highest sensitivity. Therefore, the selection of suitable host materials for the high solubility of RE ions may provide a significant advantage in luminescence properties for the development of optical temperature sensing. Among the many main

lattices, yttrium disilicate ($Y_2Si_2O_7$) activated by RE^{3+} ions, either by the upconversion or by direct excitation, has attracted attention due to white light generation in practical uses for LED applications (14-19). Unlike these studies, it has been proposed to use $Y_2Si_2O_7$ nano phosphors doped with $Yb^{3+}/Ho^{3+}/Tm^{3+}$ ions as temperature sensing probes from the up-conversion spectral intensity ratios depending on the laser excitation power.

2. MATERIALS AND METHODS

The chemicals with a purity of 99.9%, which were bought from Sigma-Aldrich used to synthesize nanocrystalline α - $Y_2Si_2O_7$ doped with RE^{3+} . To obtain desired phosphor powders tetraethyl orthosilicate, yttrium(III) hexahydrate nitrate, ytterbium(III) nitrate pentahydrate, holmium(III) nitrate pentahydrate, thulium(III) nitrate were employed as precursors with a proper stoichiometry by sol-gel technique. Preparation method of RE^{3+} doped $Y_2Si_2O_7$ as detailed in our previous work (20).

In the set of YSYHT compositions, Yb^{3+} and Tm^{3+} molar ratios were kept at 2.0 and 0.5 respectively. Ho^{3+} molar percentage ratios were also increased from 0.5 to 1.5 with the step of 0.5. Thus, three different compositions of YSYHT were obtained and labeled as YSYHT1, YSYHT2, and YSYHT3. All prepared compounds were heated at 1050 °C for 12 h.

The structural and morphological properties of the powders were investigated by Bruker D2 Phaser model X-ray diffractometer, JEOL-JEM-2100 model High resolution-Transmission Emission Microscope,

and FEI Inc. Inspect S50 model Scanning Electron Microscope. Energy dispersive X-ray measurements were taken using an EDAX Inc.-Octane Prime spectrometer to analyze the elements in the compound. The selected field diffraction (SAED) pattern was also taken to evaluate the crystallinity of the sample.

A UV-Vis spectrophotometer (Perkin-Elmer Lambda 35) was used to reveal absorption lines from diffuse reflectance spectra of RE^{3+} ions in the spectral wavelength range between 400 and 1050 nm at room temperature. A laser diode source with a 950 nm wavelength (Laser Drive Inc. LDI-820) was utilized to investigate the UC photoluminescence of the phosphors. The McPearson Inc. Model 2051 Monochromator with a PMT (Hamamatsu R1387) detector was used to measure the spectral outputs of the phosphors. To prevent light scattered from the material in different directions from entering the monochromator, a short-wavelength filter (850 nm) was placed prior to the monochromator. The measured data were processed by an EG&G Model 5210 lock-in amplifier and saved to the computer using the Labview program.

3. RESULTS AND DISCUSSION

3.1. Structural Studies

Figure 1 demonstrates the XRD patterns of YSYHT nanopowders. The figures show that most of the diffraction peak locations for three powders show good agreement with the JCPDS: 38-0223 card data of α - $Y_2Si_2O_7$. In addition, no other phase was detected apart from the α - $Y_2Si_2O_7$ phase seen in XRD measurements of all powders.

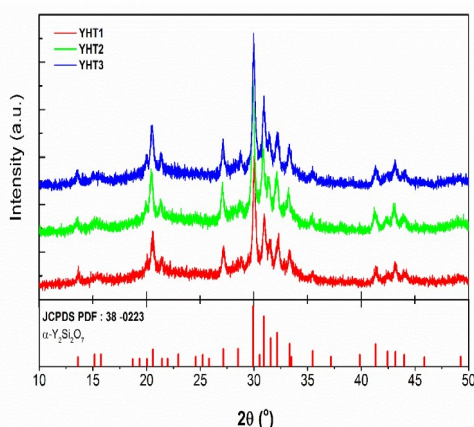


Figure 1: XRD graphs of Yb^{3+} , Ho^{3+} , and Tm^{3+} doped $Y_2Si_2O_7$ samples annealed at 1050 °C.

The electron microscope images, elemental analysis (EDAX), and selected area diffraction pattern (SAED) of YSHYT nanopowders are presented in Figure 2. As seen in SEM and TEM images of the triple rare-earth-doped α - $Y_2Si_2O_7$ nanoparticles, the

samples consist of nearly spherical nanoparticles ranging in size from about 20 to 40 nm. In addition, the peaks obtained from the EDAX spectrum of the nanoparticles given in Figure 2 show the elemental presence of Y, Si, O₂, Yb, Ho, and Tm in the phosphorus material.

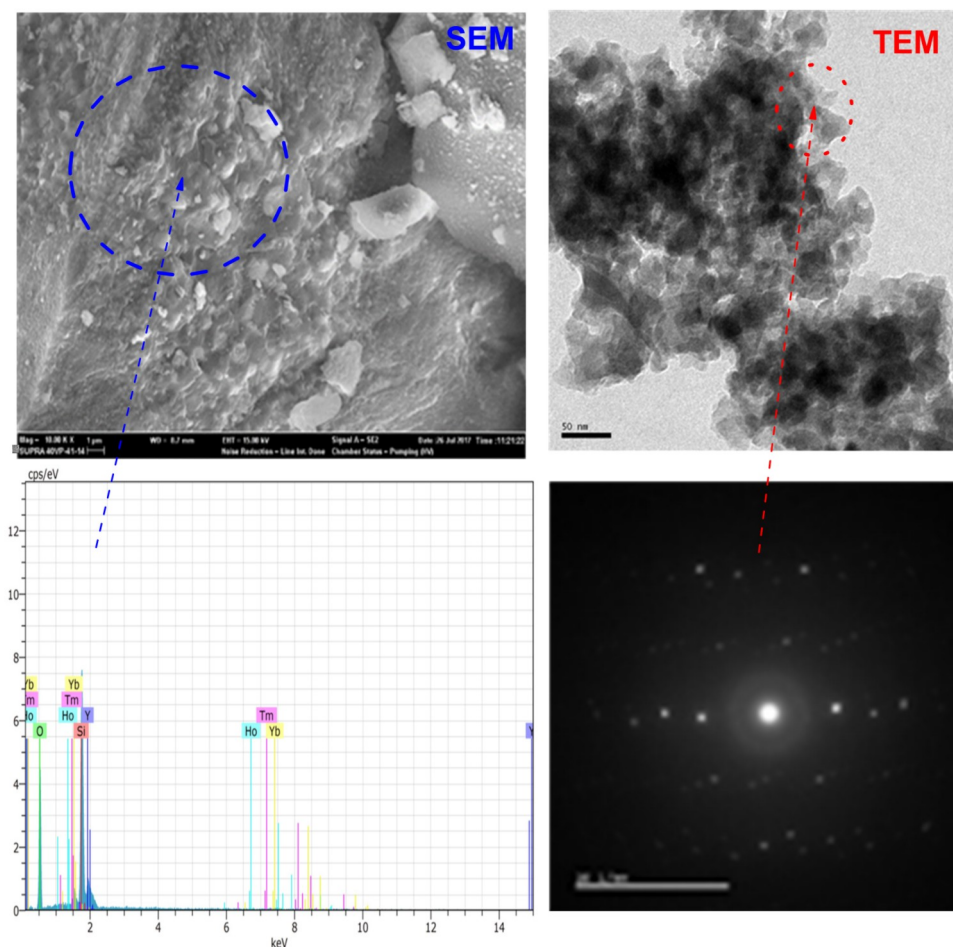


Figure 2: Electron microscope images, EDAX spectrum, and SAED pattern of $\text{Yb}^{3+}/\text{Ho}^{3+} / \text{Tm}^{3+}$ doped $\alpha\text{-Y}_2\text{Si}_2\text{O}_7$ (YSYHT2).

3.2. Spectral Studies

3.2.1. Diffuse Reflectance Spectra

Figure 1 shows the diffuse reflection spectra of the $\text{Yb}:\text{Ho}:\text{Tm}$ doped $\alpha\text{-Y}_2\text{Si}_2\text{O}_7$ samples in the 400 – 1050 nm range. Of the eleven absorption bands that appear, six absorption bands correspond to different excited states of Ho^{3+} ions from the $^5\text{I}_8$ ground state. Three absorption bands are corresponding to the different excited states of Tm^{3+} ions from the $^4\text{I}_{15/2}$ ground state transitions. In addition, only one Yb^{3+} absorption corresponds to the $^2\text{F}_{7/2} \rightarrow ^2\text{F}_{5/2}$ transition.

3.2.2. Upconversion luminescence of the samples

Figure 4 demonstrates the UC emission spectra of the elements in the range of 500-850 nm under 950 nm excitation. The green emissions around 525 and 547 nm were ascribed to the $^5\text{F}_4 \rightarrow ^5\text{I}_8$ and $^5\text{S}_2 \rightarrow ^5\text{I}_8$

transitions of the Ho^{3+} ions, respectively. The red emission around 660 nm was attributed to the $^5\text{F}_5 \rightarrow ^5\text{I}_8$ transition of Ho^{3+} ions and $^3\text{F}_{2,3} \rightarrow ^3\text{H}_6$ transition of Tm^{3+} ions. The turquoise blue (492 nm) and infrared emission (790 nm) were also attributed to the $^1\text{G}_4 \rightarrow ^3\text{H}_6$ (Tm^{3+}) and $^3\text{H}_4 \rightarrow ^3\text{H}_6$ (Tm^{3+}) transitions, respectively.

Figure 5 indicates the UC emission spectra depending on the laser pump power. The calculated slope values of triple doped $\alpha\text{-Y}_2\text{Si}_2\text{O}_7$ nanoparticles were found to be 1.4, 2.2, and 3.1 for red, green, and blue emissions, respectively. According to slope values, while the red (660 nm) and green (525 nm) emissions are taking place via a two-photon absorption process, the turquoise blue emission (492 nm) is based on three-photon absorption.

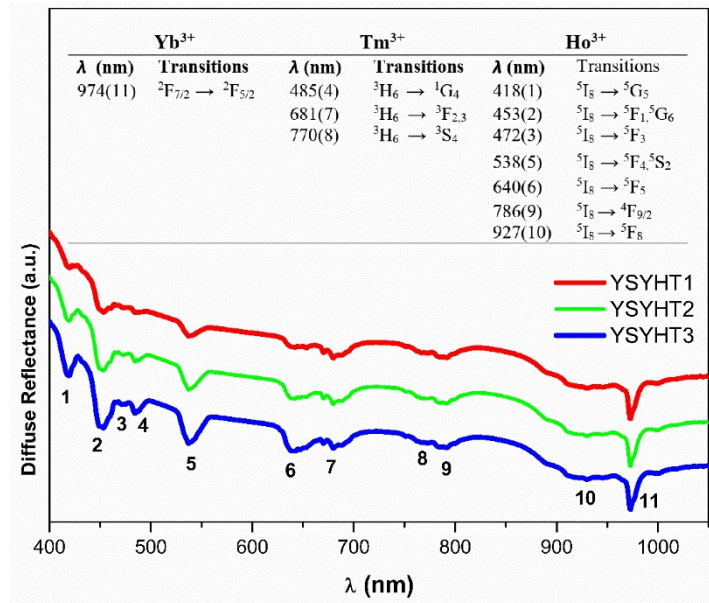


Figure 3: Diffuse Reflectance spectra of YSYHT samples.

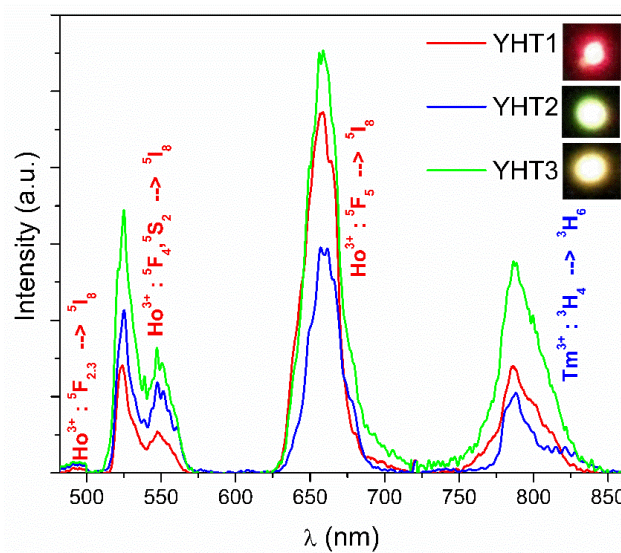


Figure 4: UC luminescence spectra of YSYHT samples.

The energy transfer from the Yb³⁺ ions to the Ho³⁺ and Tm³⁺ ions can efficiently occur to populate the high excited levels of those due to energy match among those. As indicated in Figure 6, the following points can be made (21-24):

- i. The energy transfer from the Yb³⁺ ions to the Ho³⁺ ions occurs by the process of ⁵I₈ (Ho³⁺) + ²F_{5/2} (Yb³⁺) → ⁵I₆ (Ho³⁺) + ²F_{7/2} (Yb³⁺). And it may be responsible for the increase of the population of ⁵I₆ (Ho³⁺) level.
- ii. The ⁵I₆ level of Ho³⁺ is populated with the probable ways as follows: ⁵I₆ (Ho³⁺) + ²F_{5/2} (Yb³⁺) → ⁵F_{4,5}S₂ (Ho³⁺) + ²F_{7/2} energy transfer or ⁵I₆ (Ho³⁺) + a photon (950nm) → ⁵F_{4,5}S₂ (Ho³⁺). These processes fill the ⁵F_{4/5}S₂ level of Ho³⁺, and then the ⁵F_{4/5}S₂ level relaxes to the ⁵I₈ (Ho³⁺) level. Consequently, these processes cause the green emission at 525 and 547 nm corresponding to ⁵F₄→⁵I₈, and ⁵S₂→⁵I₈ transitions, respectively.
- iii. In the red emission process, with the help of non-radiative transitions, both the transitions from the ⁵F_{4/5}S₂ levels populate the ⁵F₅ level, and the transitions from the ⁵I₆ level to the ⁵I₇ take place. Then the ⁵F₅ level can be populated through the ⁵I₇ → ⁵F₅ transition via the energy transfer process from ⁵I₇ (Ho³⁺) + ²F_{5/2} (Yb³⁺) → ⁵F₅ (Ho³⁺) + ⁵F_{7/2} (Yb³⁺) transition. Finally, the red emission at 660 nm comes true via ⁵F₅ → ⁵I₈ transition.

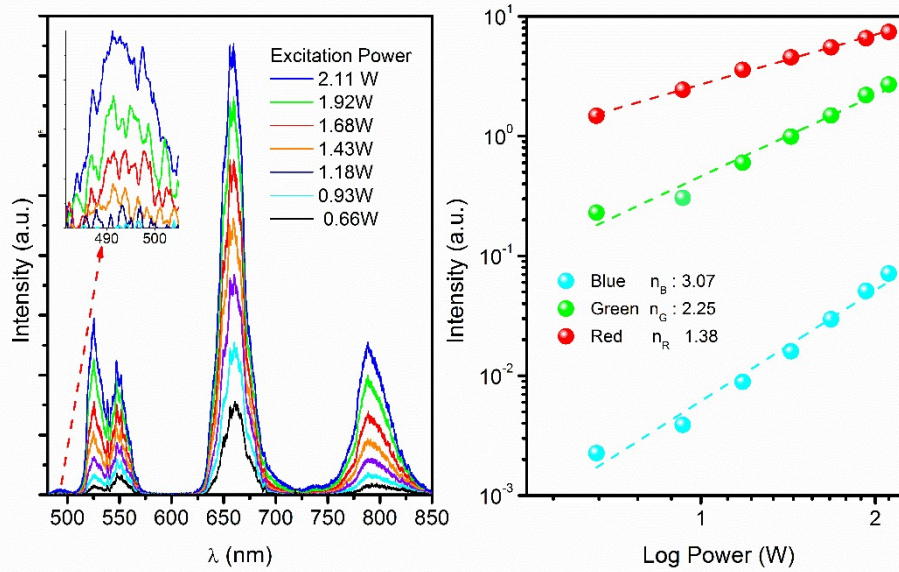


Figure 5: UC luminescence intensity vs. Excitation power for the YSYHT2 sample.

iv. In the blue emission (492 nm) process, the ${}^5F_{2,3}$ excited energy level of the Ho^{3+} ion can be populated by the energy transfer from the Yb^{3+} ions in the ground state via three-photon processes. This process is as follows: ${}^5I_5 (\text{Ho}^{3+}) + {}^2F_{5/2} (\text{Yb}^{3+}) \rightarrow {}^5F_{2,3} (\text{Ho}^{3+}) + {}^5F_{7/2} (\text{Yb}^{3+})$ energy transfer.

v. Consequently, Tm^{3+} ions at level 3H_6 can fill the 1G_4 level via energy transfer from Yb^{3+} to the Tm^{3+} ions. Then the ${}^1G_4 (\text{Tm}^{3+}) \rightarrow {}^3F_4 (\text{Tm}^{3+})$ transition cause the red emission (651 nm). In addition, the ${}^3F_{2,3} \rightarrow {}^3H_4$ transition occurs thanks to non-radiative processes. Thus, the transition from the 3H_4 level to the ${}^3H_6 (\text{Tm}^{3+})$ level produces infrared emission at 790 nm.

The UC spectral profiles of YSYHT phosphors at different power values of 950 nm excitation are additionally shown in Figure 7a. The UC emission intensity ratio is found from the intensity ratio of the ${}^5F_4 \rightarrow {}^5I_8$ (525 nm) and ${}^5S_2 \rightarrow {}^5I_8$ (547 nm) transitions of the Ho^{3+} ion.

The energy difference (ΔE_s) provided by these two transitions in the spectra was calculated to be 766.03 cm^{-1} . As seen from Figure 7a, the UC emission intensity ratio of these two close levels indicates a linear change with increasing the pump power. Therefore, the fluorescence intensity ratio (FIR) (9,25,26), on which the Boltzmann distribution of electrons is based, is used to determine the temperature-sensitive effect on the emission intensity.

The intensity ratio (I_R) and sensitivity are functions of temperature and are given by the following equations:

$$I_R = \frac{I_2}{I_1} = A \exp\left(\frac{-\Delta E}{k_B T}\right) \quad (1)$$

$$\text{Sensitivity} = \frac{dI_R}{dT} = A \exp\left(\frac{-\Delta E}{k_B T}\right) \times \left(\frac{\Delta E}{k_B T^2}\right) \quad (2)$$

where, A is a constant that includes the frequencies of emissions, degeneration factors, and cross-sections of the emissions. ΔE is the energy difference among the nearest two levels, and k_B is the Boltzmann's constant.

In the FIR technique, each FIR value is represented by a specific temperature (27-29). The increase in host temperature occurs with the increase of heat-inducing laser pump power. Therefore, the intensities of RE^{3+} ions' emissions become sensitive to temperature change. Now, let's consider this at low pump power (0.66 W) at room temperature. And if the spectral energy difference (ΔE_s) was used instead of the energy difference expressed in Equation (1), the calculated value of constant A is found as 17.615. Then the temperature of powders correlating with different intensity ratio values of the ${}^5F_4 \rightarrow {}^5I_8$ and ${}^5S_2 \rightarrow {}^5I_8$ transitions at different pump powers can easily be calculated using Eq. (3) which is provided in Eq. (1).

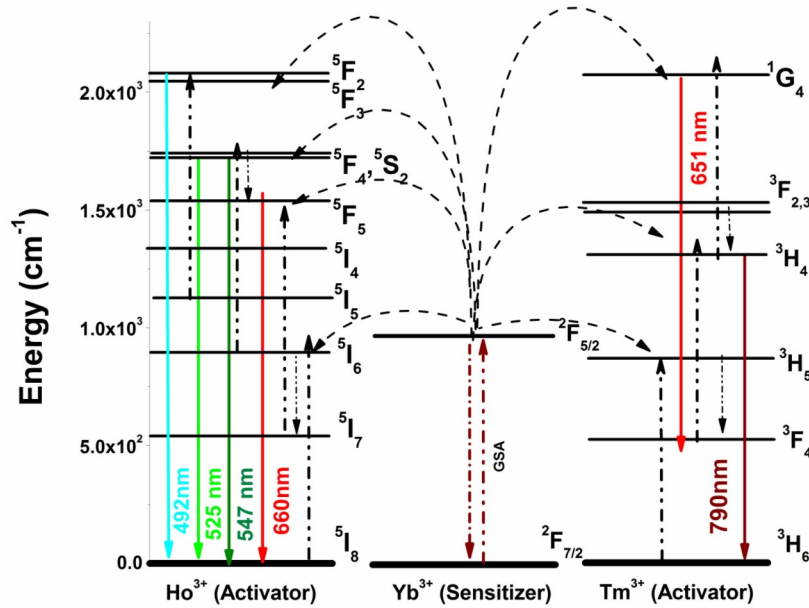


Figure 6: Possible energy transitions for Yb³⁺, Ho³⁺, and Tm³⁺ ions in YSYHT powders.

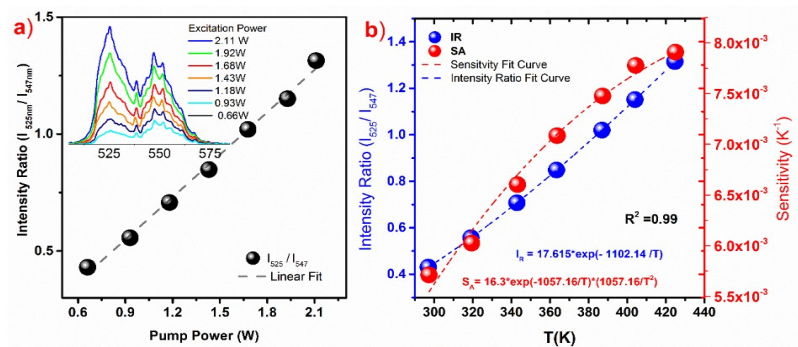


Figure 7: a) Intensity ratio of emission peaks due to laser pump power. b) Temperature sensing in terms of power heating relationship.

$$T = \left[\frac{1}{\ln A - \ln(I_R)} \right] \frac{\Delta E}{k} \quad (3)$$

Thus, the temperatures corresponding to the different intensity ratios and the sensitivity calculated using Eq. (2) are shown in Figure 7b. The maximum sensitivity with a value of $0.781 \times 10^{-2} \text{ K}^{-1}$ at 428 K was calculated from the fitting sensitivity curve's maximum value. When compared with the literature, this sensitivity value was found to be compatible with the sensitivity values of some RE³⁺ doped phosphorus materials given in Table 1. Consequently, as YSYHT phosphors can convert laser excitation power into heat, these phosphors can be used in promising applications as temperature sensor probes.

4. CONCLUSION

Sol-gel synthesized Yb³⁺:Ho³⁺:Tm³⁺ doped α -Y₂Si₂O₇ nano-powders indicated that most of the peaks matched well with the standard JCPDS:38-0223 card data of α -Y₂Si₂O₇. Morphology investigations with TEM microscopy showed that triple rare earth combinations mixed with α -Y₂Si₂O₇ presented nearly spherical nanoparticles in size varying from 20 to 30 nm for the powders.

The diffuse reflection spectra of the powders presented reflection data matching the absorption transitions of Yb³⁺, Ho³⁺ and Tm³⁺ ions in the α -Y₂Si₂O₇ samples in the 400 – 1050 nm. Up-converted blue, green, and red emissions were obtained in the visible region from Yb³⁺:Ho³⁺:Tm³⁺ doped α -Y₂Si₂O₇ nano-powders at 950 nm laser excitation. The slope values of laser power intensity revealed that the up-conversion mechanism comes true via two and three-photon absorption processes.

The UC emission intensity ratio of the ${}^5F_4 \rightarrow {}^5I_8$ and ${}^5S_2 \rightarrow {}^5I_8$ transitions corresponding to the Ho^{3+} ion depends on the pump power. Depending on the variation of the laser excitation power with the emission intensity ratio, the temperature range of 297-425 K corresponding to the laser excitation

power range of 0.66 – 2.11 W was calculated by the FIR technique. The maximum sensitivity value of $7.81 \times 10^{-3} \text{ K}^{-1}$ at 428 K was determined from the fitting sensitivity curve's maximum value. Consequently, $\text{Yb}^{3+}:\text{Ho}^{3+}:\text{Tm}^{3+}$ doped $\alpha\text{-Y}_2\text{Si}_2\text{O}_7$ nano-phosphors can be used as promising temperature sensor probes in photonic devices.

Table1: Sensitivity values of some RE^{3+} doped phosphorus materials.

Materials	Temperature Range [K]	Intensity Ratio	Sensitivity [K^{-1}]	Ref.
$\text{Yb}^{3+}/\text{Ho}^{3+}/\text{Tm}^{3+}:\text{Y}_2\text{Si}_2\text{O}_7$	290-440	I_{525}/I_{547}	0.0078 @ 428 K	Present work
$\text{Yb}^{3+}/\text{Ho}^{3+}:\text{Ba}_{0.77}\text{Ca}_{0.23}\text{TiO}_3$	93-300	I_{525}/I_{547}	0.0053 @ 93 K	(11)
$\text{Yb}^{3+}/\text{Ho}^{3+}:\text{CaWO}_4$	298-553	I_{460}/I_{487}	0.005 @ 923 K	(13)
$\text{Yb}^{3+}/\text{Ho}^{3+}:\text{TeO}_2\text{-ZnO-BaO}$	303-503	I_{660}/I_{547}	0.0073 @ 503 K	(22)
$\text{Yb}^{3+}/\text{Ho}^{3+}:\text{PSN-PMN-PT}$	173-493	I_{665}/I_{554}	0.0022 @ 93 K	(30)
$\text{Yb}^{3+}/\text{Ho}^{3+}:\text{KLa}(\text{MoO}_4)_2$	293-473	I_{651}/I_{546}	0.0356 @ 503 K	(31)
$\text{Yb}^{3+}/\text{Ho}^{3+}:(\text{Y}_{0.88},\text{La}_{0.09},\text{Zr}_{0.03})_2\text{O}_3$	293-563	I_{667}/I_{549}	0.0071 @ 563K	(32)

5. CONFLICT OF INTEREST

There are no conflicts that need to be reported.

6. ACKNOWLEDGMENTS

The study was carried out with the support of the Marmara University Scientific Research Projects Unit, project number FEN-B-150513-0170. We thank Prof. Dr. Baldassare Di Bartolo for the photoluminescent measurements performed in the Spectroscopy Laboratory at Boston College.

7. REFERENCES

- Marciniak L, Waszniewska K, Bednarkiewicz A, Hreniak D, Strek W. Sensitivity of a Nanocrystalline Luminescent Thermometer in High and Low Excitation Density Regimes. *J Phys Chem C* [Internet]. 2016 Apr 28 [cited 2022 Nov 27];120(16):8877–82. Available from: [<URL>](#)
- Marciniak L, Bednarkiewicz A, Kowalska D, Strek W. A new generation of highly sensitive luminescent thermometers operating in the optical window of biological tissues. *J Mater Chem C* [Internet]. 2016 [cited 2022 Nov 27];4(24):5559–63. Available from: [<URL>](#)
- Balabhadra S, Debasu ML, Brites CDS, Nunes LAO, Malta OL, Rocha J, et al. Boosting the sensitivity of Nd³⁺-based luminescent nanothermometers. *Nanoscale* [Internet]. 2015 [cited 2022 Nov 27];7(41):17261–7. Available from: [<URL>](#)
- Du P, Tang J, Li W, Luo L. Exploiting the diverse photoluminescence behaviors of $\text{NaLuF}_4:\text{xEu}^{3+}$ nanoparticles and g-C₃N₄ to realize versatile applications in white light-emitting diode and optical thermometer. *Chem Eng J* [Internet]. 2021 Feb [cited 2022 Nov 27];406:127165. Available from: [<URL>](#)
- Doğan A, Erdem M. Investigation of the optical temperature sensing properties of up-converting TeO₂-ZnO-BaO activated with $\text{Yb}^{3+}/\text{Tm}^{3+}$ glasses. *Sens Actuat A: Phys* [Internet]. 2021 May [cited 2022 Nov 27];322:112645. Available from: [<URL>](#)
- Doğan A, Yıldırım SM, Erdem M, Esmer K, Eryürek G. Investigation of spectral output of Er^{3+} and $\text{Yb}^{3+}/\text{Er}^{3+}$ doped TeO₂-ZnO-BaO glasses for photonic applications. *New J Chem* [Internet]. 2021 [cited 2022 Nov 27];45(8):3790–9. Available from: [<URL>](#)
- Liu X, Chen Y, Shang F, Chen G, Xu J. Wide-range thermometry and up-conversion luminescence of $\text{Ca}_5(\text{PO}_4)_3\text{F}:\text{Yb}^{3+}/\text{Er}^{3+}$ transparent glass ceramics. *J Mater Sci: Mater Electron* [Internet]. 2019 Mar [cited 2022 Nov 27];30(6):5718–25. Available from: [<URL>](#)
- Fischer LH, Harms GS, Wolfbeis OS. Upconverting Nanoparticles for Nanoscale Thermometry. *Angew Chem Int Ed* [Internet]. 2011 May 9 [cited 2022 Nov 27];50(20):4546–51. Available from: [<URL>](#)
- Wade SA, Collins SF, Baxter GW. Fluorescence intensity ratio technique for optical fiber point temperature sensing. *J Appl Phys* [Internet]. 2003 [cited 2022 Nov 27];94(8):4743. Available from: [<URL>](#)
- Lei R, Luo X, Yuan Z, Wang H, Huang F, Deng D, et al. Ultrahigh-sensitive optical temperature sensing in $\text{Pr}^{3+}:\text{Y}_2\text{Ti}_2\text{O}_7$ based on diverse thermal response from trap emission and Pr^{3+} red luminescence. *J Lumin* [Internet]. 2019 Jan [cited 2022 Nov 27];205:440–5. Available from: [<URL>](#)
- Du P, Luo L, Yu JS. Low-temperature thermometry based on upconversion emission of Ho/Yb-codoped $\text{Ba}_{0.77}\text{Ca}_{0.23}\text{TiO}_3$ ceramics. *J Alloy Comp* [Internet]. 2015 May [cited 2022 Nov 27];632:73–7. Available from: [<URL>](#)

12. Liu Z, Jiang G, Wang R, Chai C, Zheng L, Zhang Z, et al. Temperature and concentration effects on upconversion photoluminescence properties of Ho^{3+} and Yb^{3+} codoped $0.67\text{Pb}(\text{Mg}_{1/3}\text{Nb}_{2/3})\text{O}_3-0.33\text{PbTiO}_3$ multifunctional ceramics. *Ceram Int* [Internet]. 2016 Jul [cited 2022 Nov 27];42(9):11309–13. Available from: [<URL>](#)
13. Xu W, Zhao H, Li Y, Zheng L, Zhang Z, Cao W. Optical temperature sensing through the upconversion luminescence from $\text{Ho}^{3+}/\text{Yb}^{3+}$ codoped CaWO_4 . *Sens Actuat B: Chem* [Internet]. 2013 Nov [cited 2022 Nov 27];188:1096–100. Available from: [<URL>](#)
14. Marciniak L, Hreniak D, Streck W, Piccinelli F, Speghini A, Bettinelli M, et al. Spectroscopic and structural properties of polycrystalline $\text{Y}_2\text{Si}_2\text{O}_7$ doped with Er^{3+} . *J Lumin* [Internet]. 2016 Feb [cited 2022 Nov 27];170:614–8. Available from: [<URL>](#)
15. Sokolnicki J. Rare earths (Ce, Eu, Tb) doped $\text{Y}_2\text{Si}_2\text{O}_7$ phosphors for white LED. *J Lumin* [Internet]. 2013 Feb [cited 2022 Nov 27];134:600–6. Available from: [<URL>](#)
16. Erdem M, Sitt B. Up conversion based white light emission from sol-gel derived $\alpha\text{-Y}_2\text{Si}_2\text{O}_7$ nanoparticles activated with Yb^{3+} , Er^{3+} ions. *Optical Materials* [Internet]. 2015 Aug [cited 2022 Nov 27];46:260–4. Available from: [<URL>](#)
17. Erdem M, Tabanlı S, Eryurek G, Samur R, Di Bartolo B. Crystalline phase effect on the up-conversion processes and white emission of $\text{Yb}^{3+}/\text{Er}^{3+}/\text{Tm}^{3+}:\text{Y}_2\text{Si}_2\text{O}_7$ nanocrystals. *Dalton Trans* [Internet]. 2019 [cited 2022 Nov 27];48(19):6464–72. Available from: [<URL>](#)
18. Tomala R, Hreniak D, Streck W. Laser induced broadband white emission of $\text{Y}_2\text{Si}_2\text{O}_7$ nanocrystals. *J Rare Earths* [Internet]. 2019 Nov [cited 2022 Nov 27];37(11):1196–9. Available from: [<URL>](#)
19. Rakov N. $\text{Tm}^{3+}, \text{Yb}^{3+}:\text{Y}_2\text{SiO}_5$ up-conversion phosphors: Exploration of temperature sensing performance by monitoring the luminescence emission. *Physica B: Cond Mat* [Internet]. 2022 Mar [cited 2022 Nov 27];628:413572. Available from: [<URL>](#)
20. Erdem M, Özen G, Tav C. Crystallization behaviour of neodymium doped yttrium silicate nanophosphors. *Journal of the Eur Ceram Soc* [Internet]. 2011 Nov [cited 2022 Nov 27];31(14):2629–31. Available from: [<URL>](#)
21. Jiang C, Xu W. Theoretical Model of $\text{Yb}^{3+}/\text{Er}^{3+}/\text{Tm}^{3+}$ -Codoped System for White Light Generation. *J Display Technol* [Internet]. 2009 Aug [cited 2022 Nov 27];5(8):312–8. Available from: [<URL>](#)
22. Doğan A, Erdem M, Esmer K, Eryürek G. Upconversion luminescence and temperature sensing characteristics of $\text{Ho}^{3+}/\text{Yb}^{3+}$ co-doped tellurite glasses. *J Non-Cryst Sol* [Internet]. 2021 Nov [cited 2022 Nov 27];571:121055. Available from: [<URL>](#)
23. Tavares MCP, da Costa EB, Bueno LA, Gouveia-Neto AS. White phosphor using Yb^{3+} -sensitized Er^{3+} - and Tm^{3+} -doped sol-gel derived lead-fluorosilicate transparent glass ceramic excited at 980 nm. *Opt Mater* [Internet]. 2018 Jan [cited 2022 Nov 27];75:733–8. Available from: [<URL>](#)
24. Pandey A, Rai VK. Colour emission tunability in $\text{Ho}^{3+}-\text{Tm}^{3+}-\text{Yb}^{3+}$ co-doped Y_2O_3 upconverted phosphor. *Appl Phys B* [Internet]. 2012 Dec [cited 2022 Nov 27];109(4):611–6. Available from: [<URL>](#)
25. Wade SA. Temperature measurement using rare earth doped fibre fluorescence [Internet] [PhD Thesis]. [Australia]: Victoria University; 1999. Available from: [<URL>](#)
26. Wang X, Liu Q, Bu Y, Liu CS, Liu T, Yan X. Optical temperature sensing of rare-earth ion doped phosphors. *RSC Adv* [Internet]. 2015 [cited 2022 Nov 27];5(105):86219–36. Available from: [<URL>](#)
27. Tang J, Du P, Li W, Luo L. Boosted thermometric performance in $\text{NaGdF}_4:\text{Er}^{3+}/\text{Yb}^{3+}$ upconverting nanorods by Fe^{3+} ions doping for contactless nanothermometer based on thermally and non-thermally coupled levels. *J Lumin* [Internet]. 2020 Aug [cited 2022 Nov 27];224:117296. Available from: [<URL>](#)
28. Du P, Luo L, Park HK, Yu JS. Citric-assisted sol-gel based $\text{Er}^{3+}/\text{Yb}^{3+}$ -codoped $\text{Na}_{0.5}\text{Gd}_{0.5}\text{MoO}_4$: A novel highly-efficient infrared-to-visible upconversion material for optical temperature sensors and optical heaters. *Chem Eng J* [Internet]. 2016 Dec [cited 2022 Nov 27];306:840–8. Available from: [<URL>](#)
29. Jacinto C, Vermelho MVD, Gouveia EA, de Araujo MT, Udo PT, Astrath NGC, et al. Pump-power-controlled luminescence switching in $\text{Yb}^{3+}/\text{Tm}^{3+}$ codoped water-free low silica calcium aluminosilicate glasses. *Appl Phys Lett* [Internet]. 2007 Aug 13 [cited 2022 Nov 27];91(7):071102. Available from: [<URL>](#)
30. He A, Xi Z, Li X, Long W, Fang P, Zhang J. Temperature dependence of upconversion luminescence and sensing sensitivity of $\text{Ho}^{3+}/\text{Yb}^{3+}$ modified PSN-PMN-PT crystals. *J Alloy Comp* [Internet]. 2019 Sep [cited 2022 Nov 27];803:450–5. Available from: [<URL>](#)
31. Zhang Y, Wang T, Liu H, Liu D, Liu Y, Fu Z. Optical temperature sensing behavior for $\text{KLa}(\text{MoO}_4)_2:\text{Ho}^{3+}/\text{Yb}^{3+}$ phosphors based on fluorescence intensity ratios. *Optik* [Internet]. 2020 Feb [cited 2022 Nov 27];204:164100. Available from: [<URL>](#)
32. Zhou J, Chen Y, Lei R, Wang H, Zhu Q, Wang X, et al. Excellent photoluminescence and temperature sensing properties in $\text{Ho}^{3+}/\text{Yb}^{3+}$ codoped $(\text{Y}_{0.88}\text{La}_{0.09}\text{Zr}_{0.03})_2\text{O}_3$ transparent ceramics. *Ceramics International* [Internet]. 2019 Apr [cited 2022 Nov 27];45(6):7696–702. Available from: [<URL>](#)



Study on Recycling of Waste Glass Fiber Reinforced Polypropylene Composites: Examination of Mechanical and Thermal Properties

Ezgi Sözen^{1,2} , Aref Cevahir² , Sennur Deniz^{1*} 

^{1*}Yıldız Technical University, Faculty of Chemical and Metallurgical Engineering, Department of Chemical Engineering, 34210, Istanbul, Türkiye.

²Şişecam Science and Technology Center, Atmospheric Coating Management, 41400, Gebze, Türkiye.

Abstract: This study presents the preparation of short glass fiber reinforced polypropylene (PP/FG) composites using with waste (post-consumer) polypropylene composite containing long glass fiber (PP/LFG) obtained from the recycling of battery covers of trucks. Waste PP/LFG composite parts were mechanically grinded before adding to PP/FG composites. An injection molding machine was used to produce the PP/FG composite test samples loading with recycled waste PP/LFG composite in the range of 1-20% by weight. Effects of recycled waste PP/LFG content on the mechanical, thermal, and morphological properties of the PP/FG composites were investigated. The following three different tests, at various waste PP/LFG ratios, were conducted: Izod/Charpy Impact test, bending test, and tensile test. Mechanical test results showed that mechanical strength of prepared PP/FG composites were not influenced by content of waste PP/LFG material up to 10 wt.%. Differential scanning calorimetry (DSC) was used for the evaluation of thermal parameters such as melting point and crystallization temperature of the polymer matrix in the composites studied. Furthermore, by analyzing the values of thermal effects determined using the DSC method, it was possible to determine the degree of crystallinity. The DSC results showed that crystallinity %, melting, and crystallization temperatures of PP/FG composites were not influenced to adding waste PP/LFG at different ratios. The morphology of composite materials was investigated by SEM analysis. Good fiber dispersion was observed in the PP matrix for PP/FG composites containing short glass fiber prepared with all ratios of recycled waste PP/LFG material containing long glass fiber.

Keywords: Glass fiber, Polypropylene, Polymer composite, Recycled materials, Mechanical properties.

Submitted: September 21, 2022. **Accepted:** January 11, 2023.

Cite this: Sözen E, Cevahir A, Deniz S. Study on Recycling of Waste Glass Fiber Reinforced Polypropylene Composites: Examination of Mechanical and Thermal Properties. JOTCSA. 2023;10(1):63-76.

DOI: <https://doi.org/10.18596/jotcsa.1178019>.

***Corresponding author. E-mail:** deniz@yildiz.edu.tr.

1. INTRODUCTION

As examined on the properties of materials (concrete, glass, metal alloys, wood materials, carbon, plastic and etc.) used for general needs in the early days, it is understood that new materials with light, superior and specific properties are needed. Composite materials with desired properties cannot be produced at the expected level due to the high production cost. Despite all these, their usage is rapidly becoming widespread and is expected to increase further. In the 21st century, the demand for thermoplastic polymer composites is increasing, which is due to their superior physical and mechanical strengths. High strength, high rigidity, long fatigue

life, low density, and adaptability to the desired properties are the advantages of polymer composite materials over single phase products. Corrosion resistance, appearance, temperature dependent behavior, thermal insulation, thermal conductivity and acoustic insulation can also be significant characteristics arising from their high specific strength and rigidity (1-5).

In terms of mechanical properties, three regions consisting of reinforcement, matrix, and interface are effective in the structure of polymer composite defined as 'material formed by combination of two or more different components along the interface in the macro dimension'. The tasks of these regions

are, respectively; to carry the load on the structure, to keep the composite structure together and distribute the loads homogeneously, and to bond the matrix with reinforcement zones. The factors determining the mechanical properties of composite can be listed as the matrix type, the type, and form of reinforcement material. In addition, the compatibility of the reinforcement and the matrix is a requirement for the production of composite with good mechanical strength. Tensile and bending properties decrease when the cavity content of composite materials is above 3-6%. The weakening of the interface bond at high temperatures is one of the main reasons for the production efficiency to be locked. To achieve the good interface interaction, it is reported in the literature that the use of compatibilizers improved the interface adhesion between matrix and reinforcement materials (for example; the use of maleic anhydride modified (grafted) polypropylene for PP composites). Beside this, it is also known that the use of compatibilizers contributes to thermal and mechanical properties of composites (6-8).

Polypropylene (PP) is one of the most widely used thermoplastic polyolefinic material that is most commonly utilized in plastic and automotive industries. PP is determined by its versatile characteristics, chemical resistance, low density, excellent barrier properties, ease of formulation, and good flexibility (9, 10). In contrast, there is a need to cope with some limitations of PP, such as low stiffness and low strength, susceptibility to oxidation (11). Fabrication of PP composites with reinforcing materials is a method of improving their mechanical properties, so the application areas of PP can be expanded through the blending process with the incorporation of various materials. Different reinforcement materials, some mostly preferred inorganic fillers, such as glass fiber (FG), carbon nanotubes, and clays are employed to enhance the properties of the PP polymer. To obtain a high-performance dielectric PP composite, it is reported that an increase in energy storage values is obtained using a blend of maleic anhydride grafted polypropylene (MAPP) and graphene oxide (12). After the increase in use of nanomaterials in the literature, the enhancement of mechanical properties was achieved using PP and 10% nano silica (13). For the fiber addition, a hybrid system was created using basalt fiber on behalf of the environmental approach and therefore an increase in tensile strength was obtained (14). Of these PP composites, glass fiber reinforced PP/FG composites prepared with different types of glass fibers (E-type, S-type so on) are very attractive materials with their ease of fabrication, superior mechanical properties (high specific modulus and strength), and low manufacturing cost (15). PP/FG composites are mostly favored in the developing automotive industry due to the need for lightweight and high mechanical strength. E-type glass fibers are used in a wide range of development studies of PP composites (16-21). In glass fiber reinforced PP/FG composites, the process generally uses E-type glass fibers, long and short fibers in shape depend-

ing on their mechanical expectations. In addition, using a MAPP results in a structure with higher mechanical strength in PP composites (17). PP/FG composites are developed as an alternative and stronger structure for bone fracture fixation plates (21).

In the PP/FG composites, it is also important that the polymer matrix has good wetting ability and no chemical bonding on the fiber surface, and the fiber also has surface properties suitable for interaction with the polymer. The low wetting ability of the polymer leads to the formation of voids on the contact surface of the fiber which negatively affects the mechanical properties of the composite structure (22). E-type glass fiber is often preferred for PP/FG composites, taking advantage of its adequate electrical properties compared to other types of glass fibers. In terms of engineering properties, fiber length, and diameter, fiber orientation, and volume ratio are important parameters in the PP/FG composite materials. Among of long (continuous) or short (discontinuous) fibers in length, long fibers are difficult to handle, whereas short fibers are easy to manipulate and process. Also, high elastic modulus and strength are expected properties for fibers. The use of glass fiber increases the mechanical properties of the polymer composite by 2-3 times. Continuous fiber reinforced composites are used for higher values of strength and stiffness, while discontinuous fiber reinforced products are preferred in areas where cost is important (6). In composite preparation with the intended properties, fiber type selection should be made by evaluating the desired properties and cost (23). Continuous fibers are the most durable reinforcing product and increases tensile modulus, dimensional stability, hydraulic stability, and fatigue and impact behavior of composites. The PP/LFG composites used in luggage and load carrier parts of cars have been developed with long fibers with a length of 10 mm instead of short fibers with a length of 0.7-1.5 mm. Recycling of glass fiber reinforced PP composites is an option considering the cost of using it in pure form (3, 24).

Plastic wastes emerge as both daily use and process waste. The recycling of these products is valuable in terms of preventing environmental pollution, saving energy from scratch, reducing the use of pure raw materials. Recycling is a remarkable process in terms of cost and storage. However, considering of only one quarter of the waste is recycled, these products can be used in residential and construction areas. Because of softening and melting properties of thermoplastics, it is possible to produce reusable products from them. Since the recycling of thermoplastics reduces mechanical and other properties, the supplement of recycled waste products should be approximately 10 to 15% on the basis of pure material. In the plastic industry, usually 20% of waste and 80% of thermoplastic polymers are mixed and new plastic batches are formed. The properties of the matrix, fiber, and interface change in each step of composite fabrication, and at this point, the aspect ratio (L/D) of fiber length (L) and fiber diame-

ter (D)) are important parameters for the interface bonding and transferring load. Fracture stress limit is one of the factors which determining the amount of recycling. Thermoplastic products can be recycled by resin dissolving process. Glass fibers separated by dissolution have the same tensile strength as pure glass fibers, but they have 12% less hardness than pure glass fibers. Although there are difficulties for recycled glass fiber reinforced thermoplastic materials obtained by pyrolysis process, researches and calculations are made considering the increasing needs and economic conditions (24-28).

The main objective of this study is to prepare the PP/FG composites with short glass fiber using with waste PP/LFG composites containing with long glass fibers and to recycle the waste PP/LFG composite. For this purpose, PP/LFG composite parts obtained from waste battery covers of trucks was shredded by using mechanical grinder for recycling. Before adding to PP/FG composite, the fiber content and diameter in the waste grinded PP/LFG composites were characterized with burning tests and dimension measurements, respectively. The results of me-

chanical and thermal tests of PP/FG composites prepared with the adding of waste PP/LFG were compared and evaluated, and determined to the highest amount of recycled waste composite. As a result of the tests, it has been observed that the certain contribution rates of waste PP/LFG composite to produced PP/FG composite structure can be recycled.

2. EXPERIMENTAL

2.1. Material

The raw materials used in this study are glass fiber, polypropylene, and binder material. Table 1 lists the materials' compositions with weight ratios of the constituents and also the symbols which were used in this study. Polypropylene, which is a semi-crystalline polymer and used as a polymer matrix, was purchased from PETKİM in granular form (density: 0.902-0.910 g/cm³; melting point: 164 °C). As a thermoplastic engineering polymer, PP has superior mechanical properties such as good resistance to stress, low specific gravity, and good impact strength (25, 26).

Table 1: Designation and composition of composites.

Sample	Ratio (wt.%)	Notes
FG	100	Chopped Short Glass Fiber
PP	100	PP granules
PP/LFG (waste composite)	70/30	Waste battery covers of trucks
PP/FG/LFG-X (composite)	70/30/X	Combination of PP, FG, and waste PP/LFG (LFG-X; wt% of waste PP/LFG)

Glass fiber (FG), which is used as a reinforcement material, was purchased from Şişecam Elyaf Sanayii AŞ., in chopped short glass fiber (E-type) form. The length and diameter of the chopped glass fibers is 4.5 mm and at least 14 µm, respectively. The glass fiber diameter distribution (using the Cottonscope

device) of the chopped product of short glass fiber is given in Figure 1. Glass fiber consists of silicone, calcium, boron, sodium, iron, and aluminum elements is amorphous and of isotropic material form (27, 31).

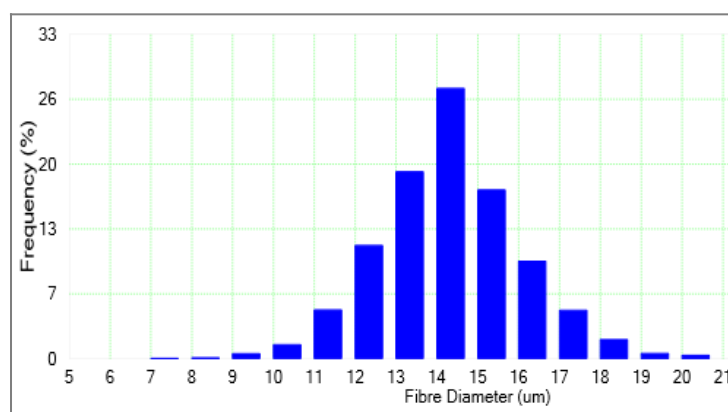


Figure 1: Fiber diameter distribution of the chopped short glass fiber.

Polybond® 3200, a maleic anhydride modified polypropylene, ($\rho = 0.91$ g/mL, acid value = 6.1 mg/KOH g, MA content = 1.0 wt.%) was purchased from CHEMTURA, USA. It was used as a chemical

coupling agent for glass fiber reinforced PP. Polybond® 3200 is used to improve the adhesion strength between glass fiber and PP, and to enhance physical and thermal properties.

The waste PP/LFG material to be recycled is the battery cover for trucks, and this composite material weighs 2500 grams. The fiber diameter distribution

of the recycling material is given in Figure 2. The PP/LFG ratio of waste material was found to be 70/30 by burning test.

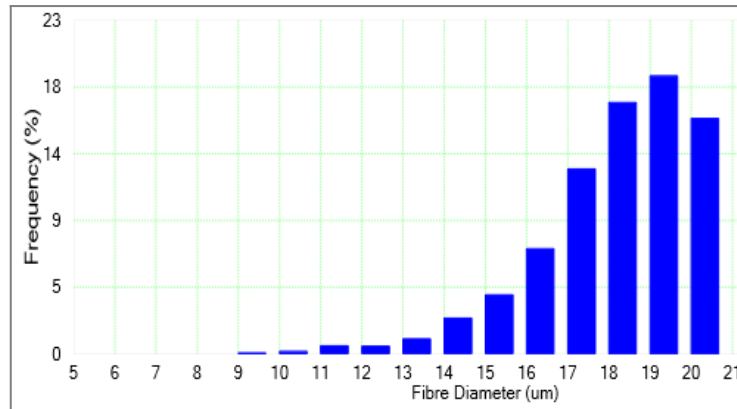


Figure 2: Fiber diameter distribution of the recycling waste PP/LFG composite.

2.2. Preparation, Characterizing and Tests

2.2.1. Sizing of PP/LFG waste composite

Shredding: The waste material for recycling is 60 cm x 40 cm. First, 15-20 large pieces were obtained and then cut to get 2 cm x 2 cm pieces with saw. These parts were transferred to the grinding step.

Grinding: Grinding was performed on IKA WERKE, MF 10 Basic Microfine Grinder Drive. The screen size of the grinder is 0.25 - 0.5 - 1 - 2 mm. 2 mm sieve type was chosen due to the biggest dimensions suitable for in this study. The grinding speed was selected as the maximum level of 6500 min⁻¹. In addition, external cooling was performed with vortex tube in order to prevent heating of the device during the process.

Dimension measurement: The length of the glass fiber was measured using optical microscope and accordingly 135 data were collected from the remaining burnt composite waste. In this study, several composite samples were produced with and without waste material. There was no difference in fiber diameter in PP/FG/LFG-0 samples, is 200 data were taken. For the other sample sets, 100 data were obtained with the fiber diameter being thin and thick. The surface area information of the milled grains obtained from the waste sample was measured as 0.4 mm² by optical microscope.

2.3. Preparation of PP/FG/LFG Composites

In the preparation of PP/FG/LFG composites, the waste PP/LFG (LFG-X, wt.%) content was determined as 1, 5, 7, 10, 15 and 20% by weight. The total weight of each blend containing polypropylene, glass fiber, waste PP/LFG, and Polybond® 3200 is 1500 grams. The combination of all samples were

determined according to the combustion test which is based on TS 1177 EN ISO 1172 standard. Firstly, the waste material was directly incinerated at 610 °C. As a result of the combustion, the polymer fraction was burned and leaving only glass fibers. Glass fiber ratios of waste composite were calculated by taking the weight difference before and after combustion. According to this calculation, the glass fiber content of composite composition by weight was 30%. By knowing the content of the waste product, combinations were formed with final glass ratio of 30%. The combination of PP/FG/LFG composites are given in Table 2.

2.4. Extrusion and Injection of PP/FG/LFG Composites

The temperature ranges of extrusion process were set to 240-230-230-230 °C for PP. The processing temperature for PP and glass fiber reinforced PP composites was determined as 230-240 °C, according to the literature (35, 36). The prepared batch sets were fed to COMAC Plast single screw extruder machine (screw speed: 6-6.6 rpm). The molten blend was cooled with cold water and dried with cold air. The dried long yarn-shaped material was passed through the cutting machine for the granular form.

The obtained granules were kept in the oven at 80 °C for 24 hours to remove moisture. The temperature ranges of injection molding were set to 230-230-230-230 °C for four zones, respectively. The granules were fed to the ENGEL injection molding machine. After the heat and pressure treatment molten PP pressed into the mold suitable for mechanical tests.

Table 2: The combination of PP/FG/LFG composites prepared with waste PP/LFG.

Blend Samples	Pure PP (g)	Pure Glass Fiber (FG) (g)	Binder (Polybond®) (g)	Waste PP/LFG (g)	Waste Glass Fiber (g)
PP/FG/LFG-0	1029.0	450.0	21.0	-	-
PP/FG/LFG-1	1018.5	445.5	21.0	10.5	4.5
PP/FG/LFG-5	976.5	427.5	21.0	52.5	22.5
PP/FG/LFG-7	955.5	418.5	21.0	73.5	31.5
PP/FG/LFG-10	924.0	405.0	21.0	105.0	45.0
PP/FG/LFG-15	871.5	382.5	21.0	157.5	67.5
PP/FG/LFG-20	819.0	360.0	21.0	210.0	90.0

2.5. Characterization

2.5.1. Mechanical tests

Mechanical tests are applied to four different types molded products. The main tests are basically divided into three subjects; impact, bending, and tensile. Impact tests are classified according to their vertical-horizontal and notched-unnotched form.

Izod: Samples (80*4*10 mm in size) are used for vertically applied impact test. One of the two test specimens in the mold sample was mechanically tested on the Zwick universal test machine, one notched and the other unnotched. MF 10 Basic-IKA WERKE notching device was used for notching. Five samples were tested for each composite and the average values were reported. Izod impact tests were done according to TS EN ISO 180 standard test method.

Charpy: This horizontal impact is applied to five of the samples of the same length and the same procedures as for the Izod impact test. Izod impact tests were done according to the EN ISO 179-2 standard test method for the Charpy impact test.

Bending: Three-point bending tests were done according to TS EN ISO 178 standard test method. The dimensions of the bending samples are 60*4*10 mm. As a result of this test, F-max flexural strength and F-max deformation data are examined.

Tensile: Tensile tests were done according to TS EN ISO 527-1 standard test method. In accordance with the standard, a dog bone sample of 4*10 mm was used. As a result of this test, F-max tensile strength and F-max elongation at break are examined.

2.5.2. DSC Analyses

Differential Scanning Calorimetry (DSC) test was performed on the sample taken from four different parts of the waste battery cover. Analysis was performed on the samples taken, polypropylene, and Polybond® 3200 raw materials.

2.5.3. SEM Analyses

To perform the SEM analyses of PP/FG composites, the surface of each samples was coated with Au/Pd. SEM Images were taken from the fracture surfaces of Izod impact samples in each set. The fracture surfaces of PP/FG composite samples and the bonding between the glass fiber and polypropylene matrix were investigated from the SEM images.

3. RESULTS AND DISCUSSION

3.1. Mechanical Properties

In this study, the PP/FG composites with short glass fiber using with the waste PP/LFG composites containing with long glass fibers are prepared with the different ratios of recycled waste PP/LFG composite. The diameters of the long fibers from the waste composite are larger than that of the short fibers using in the prepared PP/FG composite, and are 18.61 and 14.05 μm , respectively. As a result of the mechanical tests, it is seen that increasing the fiber diameter with the adding of waste PP/LFG in composite structure decreases the strength of PP/FG/LFG composites. The effect of the addition of waste composite with long fiber on the mechanical strength values of PP/FG/LFG composites can be evaluated with the data given in Table 3.

As the flexural strength of prepared composites is examined, a significant decrease is observed above the 10% of waste PP/LFG ratio added to the PP/FG composite. The flexural strength and modulus are similar to the reference PP/FG composite value prepared without any waste material, up to the PP/FG/LFG-10 composite with the 10% of waste material and then starts dropping, due to the addition of long fiber in higher weight fraction. On the other hand, the tensile strength values of composites decreases linearly with increasing waste amounts in prepared PP/FG/LFG composite. For the amount of waste composite above the 1%, more than 3% decrease is observed in the breaking strengths of composites prepared with all other waste additives, but the addition of waste material in the ratios of 5, 7 and 10% gives similar values,

are of 88.1, 87.8, and 87.1, respectively. In this case, as in the results of flexural strength, it is appropriate to add the waste composite up to 10%. It was observed that in all the specimen under with the 20% of waste additive, the flexural and tensile properties were close to those of reference PP/FG composite without waste additive. Mechanical properties of a composite mainly depend on the fiber ratio, individual properties of fiber and polymer matrix and interfacial bonding of them (17, 18). Besides that, it can be said that the aspect ratio of fibers is the major factor in deciding and affecting the mechanical properties of the composites.

Histogram of fracture energy (kJ/m^2) at F_{\max} against PP/LFG content (wt.%) for the same specimen sizes of composites at 25 °C are depicted in Figure 5. From the histogram, it can be observed that, generally, the tensile strength and fracture energy values decrease with respect to increasing the waste PP/LFG content with long fiber for tensile and impact specimens, respectively.

For tensile specimens, this trend is expected as the presence of fibers tends to reduce resistance to

crack initiation, therefore increasing the material brittleness, while at the same time reducing crack propagation through the matrix by forcing crack lines around the fiber ends. However, for unnotched Charpy impact specimen, there is no sharp decrease in fracture energy (8%) with the incorporation of up to 15% of waste PP/LFG loading compared with neat PP/FG composite (54.8 mJ).

For unnotched Izod impact specimens, this trend is similarly observed that the fracture energy (7.5%) decrease with up to 15% of waste PP/LFG content in composite accordance with neat PP/FG composite (55.2 mJ). For the results of notched Izod and Charpy impact tests, no significant variation for fracture energy is observed with increase in waste PP/LFG content of composites. It is observing to note that further addition of up to 20% of waste PP/LFG does not produce any significant effect on fracture energy values of prepared composites. Meanwhile, in order of increasing the waste loading to 15%, identical trends in notched Izod and Charpy impact values are observed as resulted in 10.5 kJ/m^2 .

Table 3: Mechanical test results of PP/FG/LFG composites.

Samples	PP/FG /LFG-0	PP/FG /LFG-1	PP/FG /LFG-5	PP/FG /LFG-7	PP/FG /LFG-10	PP/FG /LFG-15	PP/FG /LFG-20
Flexural Strength (MPa)	141.1±1.4	142.4±1.8	139.0±2.3	138.6±1.6	139.3±1.2	128.9±0.6	127.8±0.1
Flexural Modulus (GPa)	6.7	7.0	6.9	6.9	7.0	6.1	6.1
Tensile Strength (MPa)	92.4±1.0	91.3±0.8	88.1±0.1	87.8±0.3	87.1±1.3	85.9±0.6	84.3±0.5
Tensile Modulus (GPa)	5.8	4.7	5.3	5.1	5.5	5.9	5.9
Unnotched Izod Impact (kJ/m^2)	59.7±3.3	60.2±5.4	56.5±4.5	55.7±3.2	55.4±2.5	55.2±2.1	54.0±3.0
Unnotched Charpy Impact (kJ/m^2)	54.8±4.4	56.2±1.6	51.2±2.8	51.9±2.2	50.9±2.7	50.4±2.7	47.6±2.5
Notched Izod Impact (kJ/m^2)	11.7±0.7	11.8±0.3	10.5±0.3	10.7±0.5	10.4±0.3	10.5±0.4	9.9±0.3
Notched Charpy Impact (kJ/m^2)	10.8±0.2	11.2±0.3	10.6±0.5	10.4±0.5	10.7±0.4	10.5±0.6	9.6±0.2

Figure 3 shows the relationship by the way the flexural strength and strain data for the bending test. In Figure 3 (a) (red line), and (b) (green line) refer to the neat PP/FG/LFG-0 composite and the PP/FG/LFG-7 with 7% of waste material, respectively. As can be seen from this graph, the flexural force values are close to each other and the resistance

value decreases slightly with the addition of recycled waste. In Figure 4, the tensile strength of PP/FG/LFG-10 composite is given by the graphs obtained from repeat tests of 5 samples. For the tensile strength of the composite loaded with 10% of recycled waste, the repeatable values appear to be obtained in close agreement.

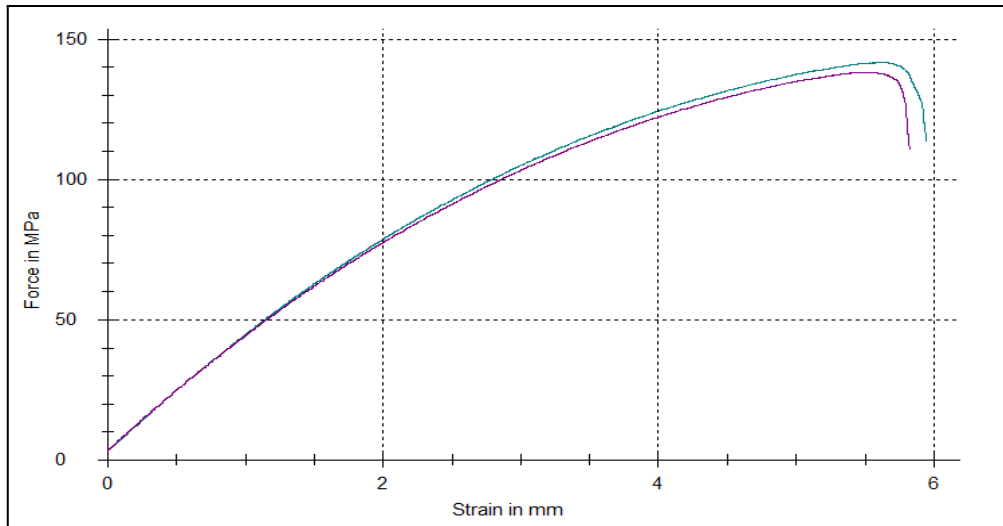


Figure 3: Graphs for the flexural strength: (a) PP/FG/LFG-0 (green line; top) and (b) PP/FG/LFG-7 (red line; bottom).

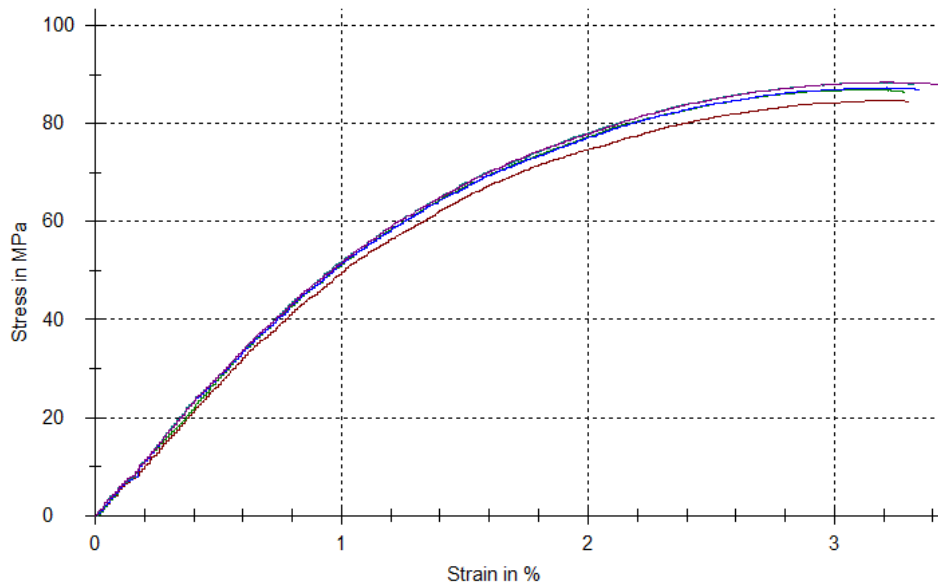


Figure 4: Graphs for tensile strength of PP/FG/LFG-10.

As a result of the strength values of PP/FG/LFG composites, it is found that the optimum ratio of recycled waste is 10% and above this ratio, it affects the mechanical strength of composites negatively. While the flexural strength is not significantly altered with an increase in recycled waste loading,

the tensile strength values decreases to a certain extent. It is observed that the impact strength is reduced with incorporation of recycled waste in the composites. The data on mechanical strength properties are given in Figure 5.

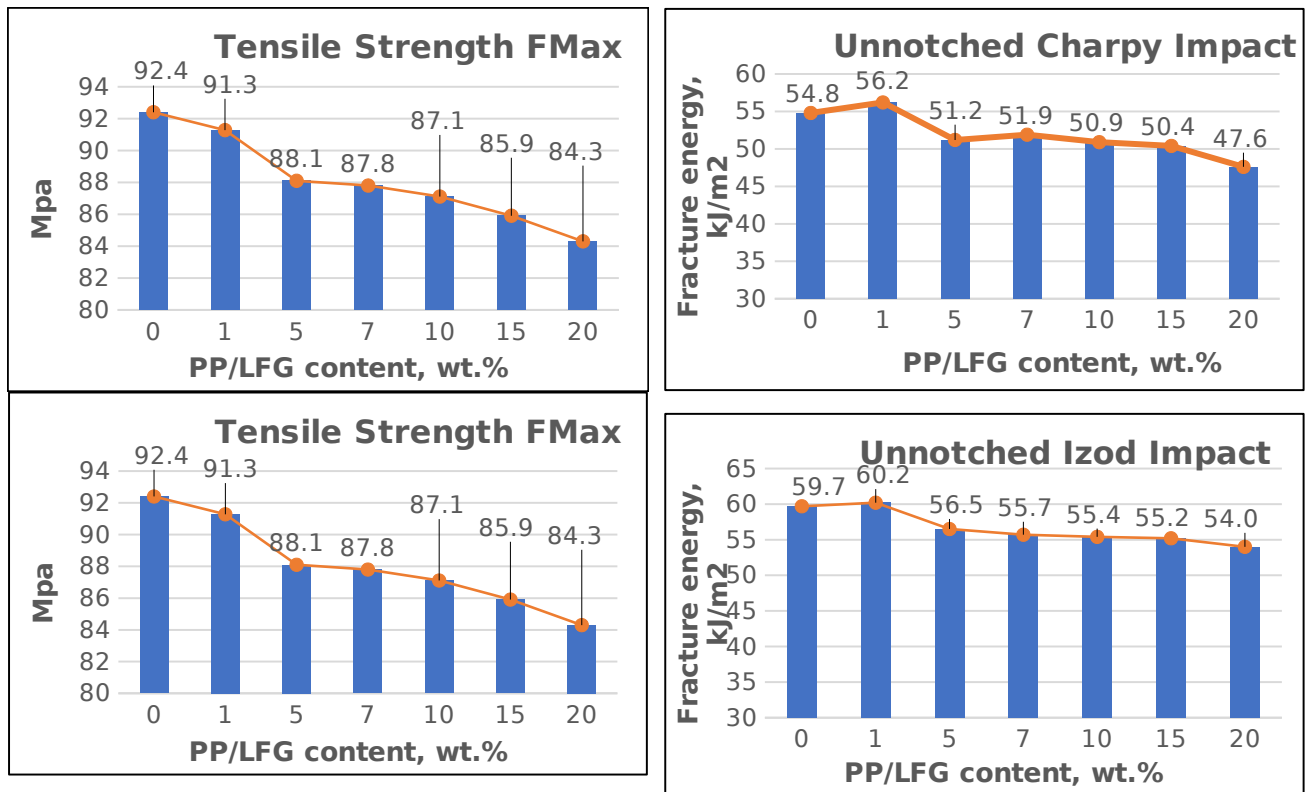


Figure 5: Mechanical strength properties for PP/FG/LFG composites.

In a previous study, it was reported that the recycled glass fiber reinforced composites showed lower tensile strength (-30%) compared to the untreated glass fiber composite (32). The loss in mechanical performance can be explained by the fact that the recycled glass fiber filled composite is subject to fiber breakage and is unable to regenerate the fibers during the injection molding process.

3.2. Thermal Properties

As seen in Figure 6, DSC thermograms show that the neat PP/FG/LFG-0 composite, which is the reference sample, and recycled waste containing samples exhibit similar behavior. Temperature range from -40 °C to 200 °C, suitable for PP. All measurements were taken under nitrogen atmosphere at the same heating and cooling rates of 10 °C /min. The process, which starts and ends at room temperature, is carried out with cooling and then heating.

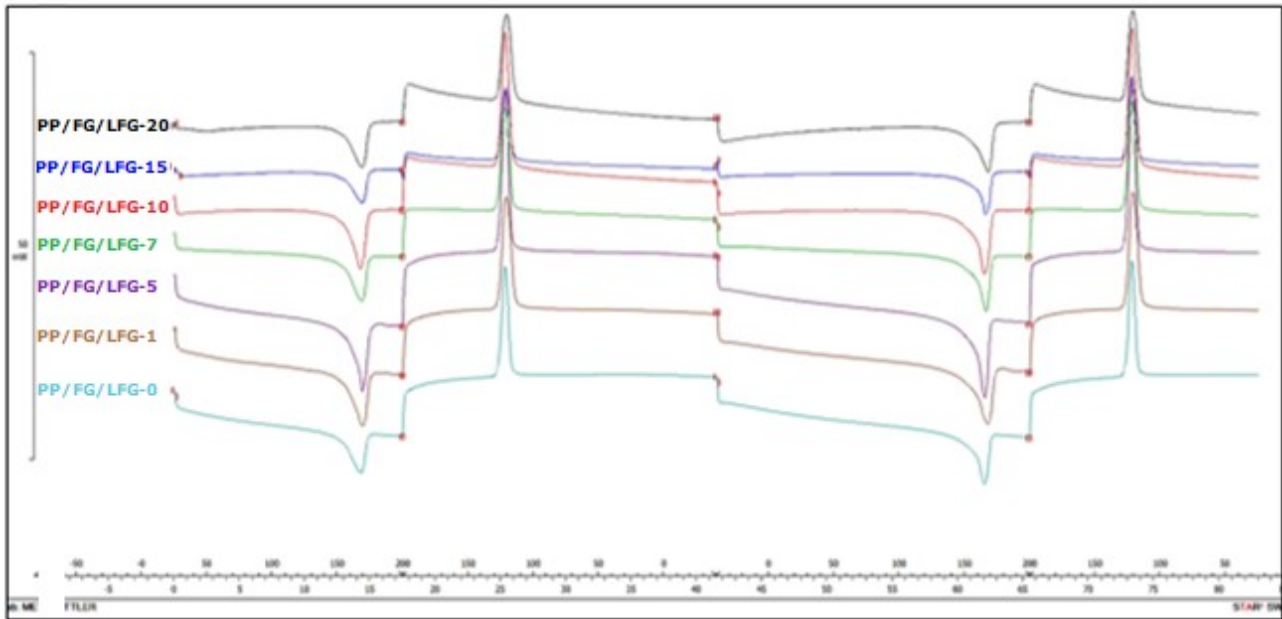


Figure 6: DSC thermograms of PP/FG/LFG composites.

During this process, the first peak gives melting temperatures, and the second peak refers to the crystallization temperature. Applying DSC analysis to all samples gives close melting and crystallization temperatures. Therefore, it is understood that the contributions of thermally converted wastes are at a standard level. These results are consistent with the literature. Lee et al. showed that crystallinity of the PP decreases with wood flour whereas it increases with clay and MAPP (33).

The percentage of crystallinity (X_c %) of a sample was calculated as follows Equation 1:

$$X_c (\%) = \left[\frac{\Delta H_f}{\Delta H_0} \right] \times 100 \quad (\text{Eq. 1})$$

where ΔH_f is the heat of fusion of PP/FG/LFG in a composite determined from the DSC thermogram, ΔH_0 is the heat of fusion of 100% crystalline PP/FG/LFG-X which equals 183.1 J/g, and $W\%$ is the weight percentage of PP/FG/LFG-X in the composite (34).

The melting temperature (T_m), crystallization temperature (T_c) and percentage of crystallinity (X_c %) of these recycled materials are listed in Table 4.

Table 4: Melting temperature, crystallization temperature and crystallinity of PP/FG/LFG composites.

Samples	T_m (°C)	T_c (°C)	X_c (%)
PP/FG/LFG-0	155.26	129.00	28.265
PP/FG/LFG-1	158.36	129.03	28.829
PP/FG/LFG-5	156.48	128.17	28.487
PP/FG/LFG-7	157.79	128.71	28.725
PP/FG/LFG-10	157.89	128.63	28.743
PP/FG/LFG-15	159.01	128.25	28.947
PP/FG/LFG-20	156.05	128.18	28.408

3.3. The Morphology of PP/FG/LFG Composites

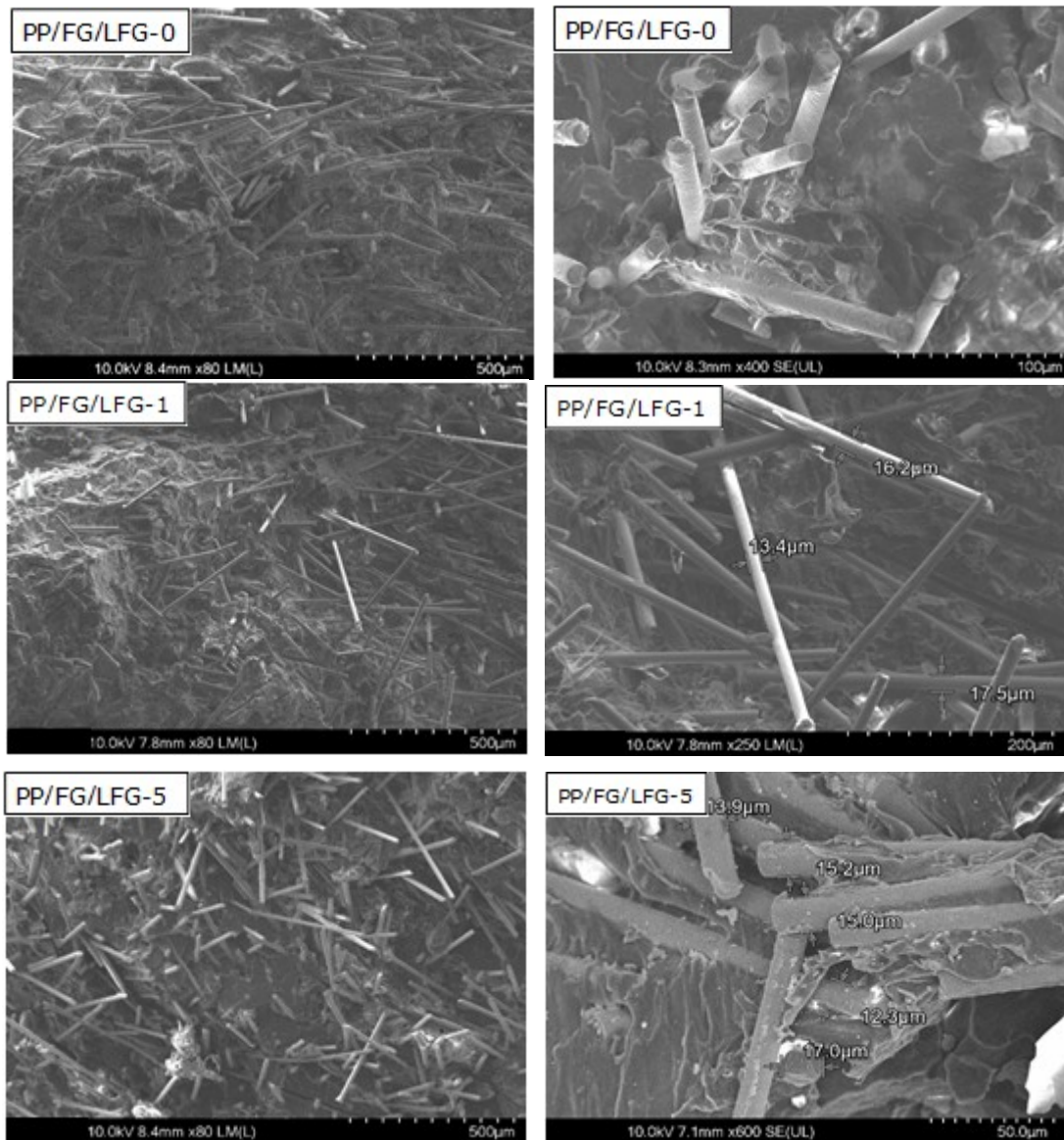
Figure 7 shows the SEM micrographs of all sets and these images were taken from the samples subjected to Izod impact test. The SEM images show the properties of adhesion, orientation, and separation after impact. Good fiber dispersion is observed for all compounds. The images in the left column show the remote views of the samples. In

the right column, the images were taken closer and the fiber diameters were measured in order to reveal the diameter difference.

For the PP/FG/LFG-0 sample, no diameter difference was observed because there was no long fiber coming from the waste composite additive. The presence of long fibers in the PP/FG/LFG-1 sample is

seen by the measuring fiber diameter. As can be seen from SEM images, both short fibers with a diameter of $13.5\ \mu\text{m}$ and long fibers with a diameter of $18.2\ \mu\text{m}$ are found in PP/FG/LFG composite structures. In the PP/FG/LFG-5 sample, it is understood that the matrix and the supplements adhere well. In the PP/FG/LFG-7 sample, it is observed that the orientation of the glass fibers varies. It was determined that PP/FG/LFG-10 had good adhesion with the matrix on long fibers as seen in the close image. The PP/FG/LFG-20 sample

has proven to be capable of separating the fiber from the matrix by impact. With the SEM analysis, the increase in the amount of waste and the increase in the amount of long fibers are proved by observing the fiber diameter data. With this analysis, it is seen that the part which is mechanically recycled in adhesion also adheres like pure products. It is observed that after the rupture process the fibers can break or come out at the break points.



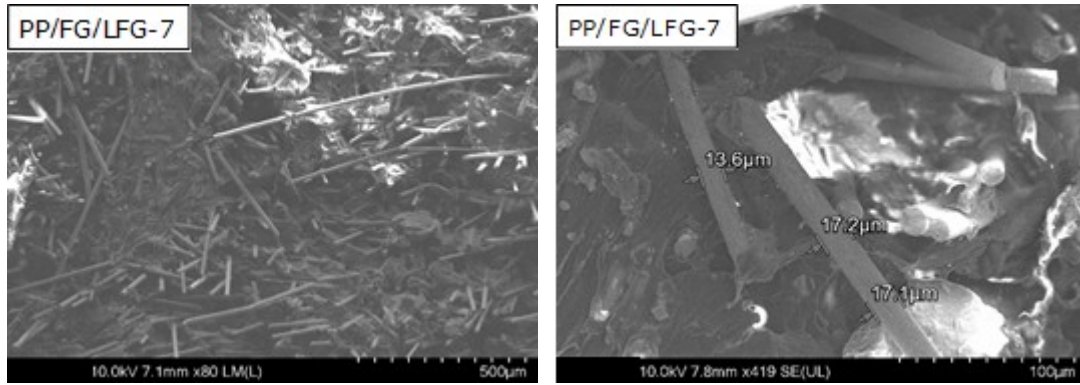


Figure 7: SEM micrographs of fracture surface of PP/FG/LFG composites.

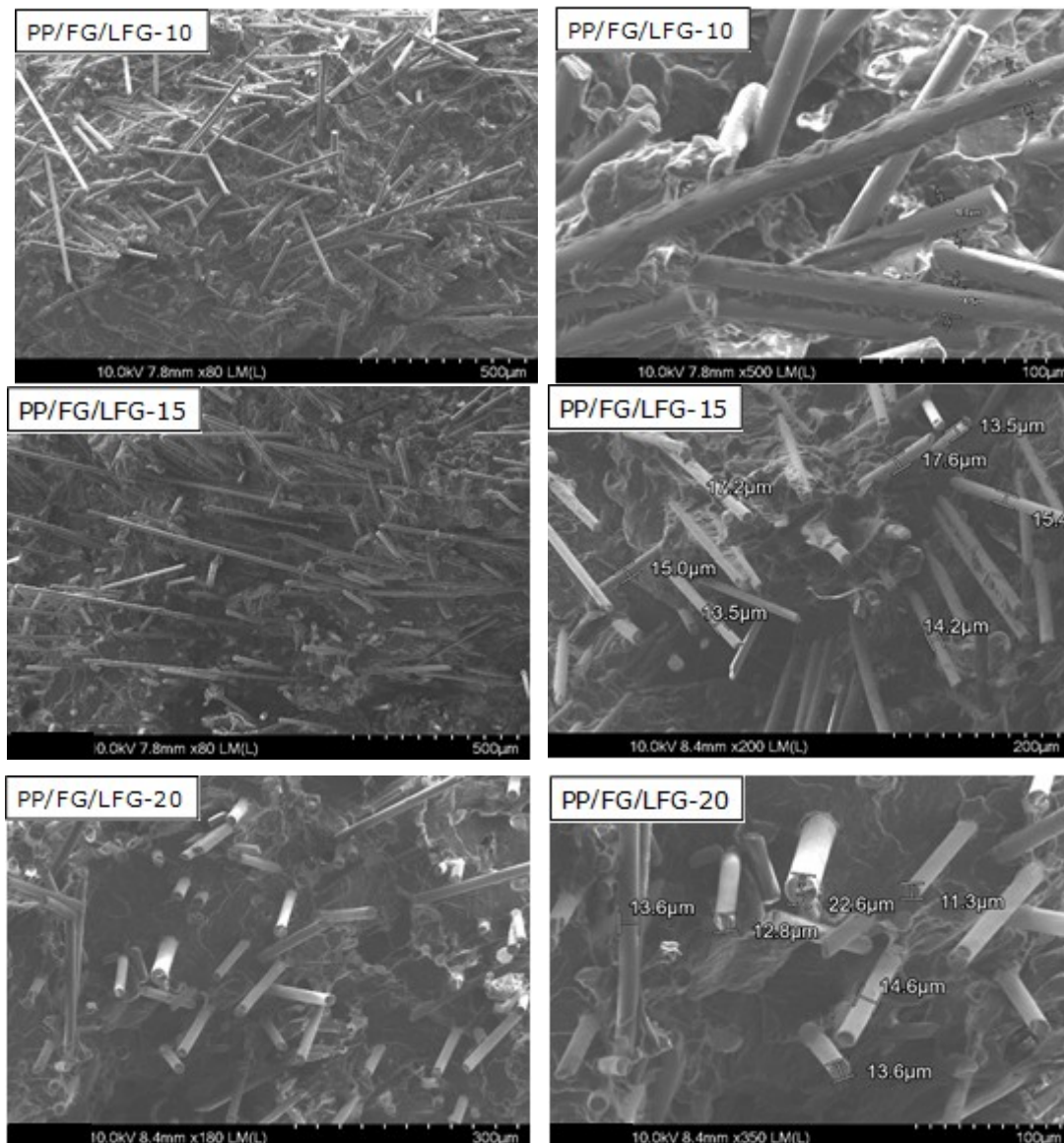


Figure 7 (contd): SEM micrographs of fracture surface of PP/FG/LFG composites.

As a result of the mechanical test results and SEM images, it can be said that the tensile behavior of PP

composites prepared with discontinuous glass fiber depends on the fiber length and the fiber orientation

according to the loaded direction by looking at the distribution of the fibers in the composite material.

4. CONCLUSION

In this study, it is aimed that recycling of waste polypropylene composites with long fibers obtained from battery covers of trucks. Since long fiber products are new and superior technology, long fiber reinforced waste PP/LFG composite recycled with mechanically is added to short fiber reinforced PP/FG composite in this work. The thermal, mechanical and morphological properties of composites were presented and discussed. As a result of the characterization tests performed on the PP/FG/LFG composites prepared with recycled waste PP/LFG, it was reasoned that the waste PP composite contribution to PP/FG composite structure could be optimum amount of 10%. Also, the SEM micrographs revealed that the adhesion and bonding limits between the fibers and the matrix were exceeded as fiber pull out and interfacial delamination were observed. As a result of mechanical tests, it can be said that the increasing in the fiber diameter decreases the strength values of prepared PP/FG/LFG composite with more than 10% of waste PP with long fibers. As for the thermal properties, for the all contents of the recycled waste PP/LFG composite, the short and long glass fibers in PP composite structures had no effect on the crystallinity of PP matrix. Based on the experimental results, it can be concluded that recycled long fiber reinforced PP composites have great potential to replace traditional PP composite used in various applications.

5. ACKNOWLEDGMENTS

The authors would like to thank Şişecam Inc. who supported the work reported in this paper and İsmail Oral, laboratory technician, for support and assistance in technical applications.

6. REFERENCES

- Günaydın E. Polimer matriksli karbon nanotüp-cam elyaf takviyeli kompozitlerde çarpma sonrası basma özelliklerinin incelenmesi [MSc Thesis]. [Samsun]: Ondokuz Mayıs University; 2018. [<URL>](#)
- Gügül H. Karbon Nanotüp Ve Cam Elyaf Takviyeli Yüksek Yoğunluklu Polietilen Hibrit Kompozit Malzemelerin Mekanik Özelliklerinin İncelenmesi [MSc Thesis]. [İskenderun]: İskenderun Technical University; 2018. [<URL>](#)
- Sabancı Ş. Fiber Takviyeli Polimer Matriksli Kompozitlerin Enjeksiyon Yöntemi İle Üretimi [MSc Thesis]. [İstanbul]: Yıldız Technical University; 2005. [<URL>](#)
- Moritzer E., Heiderich G. Mechanical recycling of continuous fiber-reinforced thermoplastic sheets. Proceedings of PPS-31. AIP Conf. Proc. 2016 Mar; 1713(1):120013-1-5. [<DOI>](#)
- Ünal E. Cam Elyafli Kompozit Malzemelerin Atmosferik Ortamda Ve Deniz Ortamında Yorulma Simülasyonu [MSc Thesis]. [İzmir]: Ege University; 2006. [<URL>](#)
- Kandaş H. Farklı Ön Gerilme Yüklerinde Cam Elyaf Takviyeli Polipropilen Kompozitlerin Düşük Hızlı Darbe Davranışı [MSc Thesis]. [İzmir]: Dokuz Eylül University; 2018. [<URL>](#)
- Liu D, Ding J, Fan X, Lin X, Zhu Y. Non-isothermal forming of glass fiber/polypropylene commingled yarn fabric composites. Materials and Design. 2014 Jan; 57:608-15. [<DOI>](#)
- Kim HS, Lee BH, Choi SW, Kim S, Kim HJ. The effect of types of maleic anhydride-grafted polypropylene (MAPP) on the interfacial adhesion properties of bio-flour-filled polypropylene composites. Composites: Part A. 2007 Jan; 38(6):1473-82. [<DOI>](#)
- Gill, R. M. Carbon fibres in composite materials. London: Iliffe Books for the Plastics Institute. 1972. ISBN 13: 978-0-5920-0069-5.
- Hassan, A., Rahman, N. A., & Yahya, R. Extrusion and injection-molding of glass fiber/MAPP/polypropylene: effect of coupling agent on DSC, DMA and mechanical properties. Journal of Reinforced Plastics and Composites, 2011 Sep; 30(14):1223-1232. [<DOI>](#)
- Fu, S. Y., Feng, X. Q., Lauke, B., & Mai, Y. W. Effects of particle size, particle/matrix interface adhesion and particle loading on mechanical properties of particulate-polymer composites. Composites. Part B, Engineering. 2008 Sep; 39(6):933-961. [<DOI>](#)
- Han, L., Wang, H., Lang, X., Wang, X., Zong, Y., Zong, C. Preparation of graphene/ polypropylene composite with high dielectric constant and low dielectric loss via constructing a segregated graphene network. Royal Society of Chemistry. 2021 Nov; 11:38264-38272. [<DOI>](#)
- Awad, S.A., Khalaf, E.M. Investigation of improvement of properties of polypropylene modified by nano silica composites. Composites Communications. 2019 Apr; 12:59-63. [<DOI>](#)
- Kufel, A., Para, S., Kuciel, S. Basalt/Glass fiber polypropylene hybrid composites: mechanical properties at different temperatures and under cyclic loading and micromechanical modelling. Materials. 2021 Sep; 14:5574-5591. [<DOI>](#)
- Schwartz, M. Composite materials handbook. 2nd ed. New York: McGraw-Hill; 1992. ISBN-13: 978-0-0705-5743-7.

16. Shinzawa, H., Itasaka, H. Glass fiber (GF)/polypropylene (PP) composite studied by Raman disrelation mapping. *Spectrochimica Acta Part A: Molecular and Biomolecular Spectroscopy*. 2022 May; 273:121056. [<DOI>](#).
17. Watanabe, R., Sugahara, A., Hagihara, H., Mizukado, J., Shinzawa, H. Insight into interfacial compatibilization of glass-fiber-reinforced polypropylene (PP) using maleic-anhydride modified PP employing infrared spectroscopic imaging. *Composites Science and Technology*. 2020 July; 199:108379. [<DOI>](#).
18. Liu, W., Zhu, Y., Qian, C., Dai, H., Fu, Y., Dong, Y. Interfacial modification between glass fiber and polypropylene using a novel waterborne amphiphilic sizing agent. *Composites Part B*. 2022 July; 241:110029. [<DOI>](#).
19. Zhou, P., Li, C., Bai, Y., Dong, S., Xian, G., Vedernikov, A., Akhatov, I., Safonov, A., Yue, Q. Durability study on the interlaminar shear behavior of glass-fibre reinforced polypropylene (GFRPP) bars for marine applications. *Construction and Building Materials*. 2022 Sep; 349:128694. [<DOI>](#).
20. Dong, S., Zhou, P., Guo, R., Li, C., Xian, G. Durability study of glass fiber reinforced polypropylene sheet under simulated seawater sea sand concrete environment. *Journal of Materials Research and Technology*. 2022 Sep; 20:1079-1092. [<DOI>](#).
21. Kabiri, A., Liaghat, G., Alavi, F. Biomechanical evaluation of glass fiber/polypropylene composite bone fracture fixation plates: Experimental and numerical analysis. *Computers in Biology and Medicine*. 2021 May; 132:104303. [<DOI>](#).
22. Şahin S. Sürekli Cam Elyaf Takviyeli Polipropilen Levhaların Şekillendirilmesi Ve Karakterizasyonu [MSc Thesis]. [İstanbul]: Marmara University; 2015. [<URL>](#).
23. Baydar DG, Bekem A, Doğu M, Gemici Z, Ünal A. Sürekli Cam Fiber Takviyeli Polipropilen Kompozitlerin Üretimi Ve Karakterizasyonu. *Sigma Journal of Engineering and Natural Sciences*. 2011 Dec; 30:120-132. [<URL>](#).
24. Naqvia SR, Prabhakaraa HM, Bramera EA, Dierkesa W, Akkerman R, Brema G. A critical review on recycling of end-of-life carbon fibre/glass fibre reinforced composites waste using pyrolysis towards a circular economy. *Resources, Conservation & Recycling*. 2018 Apr; 136:118-129. [<DOI>](#).
25. Medar MM. Geri Dönüştürülmüş Cam Elyaf Katkılı ve Katkısız Polipropilen-Polietilen Malzemelerin Mekanik ve Kimyasal Özelliklerinin İncelenmesi [MSc Thesis]. [Kocaeli]: Gebze Technical University; 2013. [<URL>](#).
26. Bajracharya RM, Manalo AC, Karunasena W, Lau K. An overview of mechanical properties and durability of glass-fibre reinforced recycled mixed plastic waste composites. *Materials and Design*. 2014 Oct; 62:98-112. [<DOI>](#).
27. Şentürk O. Kısa Cam Elyaf Ve Kalsit Dolgulu Polipropilen Hibrit Kompozitlerin Fiziksel Ve Mekanik Özelliklerinin İncelenmesi [MSc Thesis]. [İstanbul]: Istanbul Technical University; 2014. [<URL>](#).
28. Lila MK, Singhal A, Banwait SS, Singh I. A recyclability study of bagasse fiber reinforced polypropylene composites. *Polymer Degradation and Stability*. 2018 June; 152:272-79. [<DOI>](#).
29. Feih S, Mouritz AP, Case SW. Determining the mechanism controlling glass fibre strength loss during thermal recycling of waste composites. *Composites Part A: Applied Science and Manufacturing*. 2015 Sep; 76:255-61. [<DOI>](#).
30. Cousins DS, Suzuki Y, Murray RE, Samaniuk JR. Recycling glass fiber thermoplastic composites from wind turbine blades. *Journal of Cleaner Production*. 2019 Feb; 209:1252-63. [<DOI>](#).
31. Vaidya UK, Chawla KK. Processing of fibre reinforced thermoplastic composites. *International Materials Reviews*. 2013 Jul; 185-218. [<DOI>](#).
32. Chen, T., Mansfield, C.D., Ju, L., Baird, D.G. The influence of mechanical recycling on the properties of thermotropic liquid crystalline polymer and long glass fiber reinforced polypropylene. *Composite Part B*. 2020 Nov; 200: 108316. [<DOI>](#).
33. Lee SY, Kang IA, Doh GH, Kim WJ, Kim JS, Yoon HG, Wu QH. Thermal, mechanical and morphological properties of polypropylene/clay/wood flour nano composites. *Express Polymer Letters*. 2008 Mar; 2(2):894-9. [<DOI>](#).
34. Al-Maadeed MA, Shabana YM, Khanam PN. Processing, characterization and modeling of recycled polypropylene/glass fibre/wood flour composites. *Materials and Design*. 2014 June; 58:374-380. [<DOI>](#).
35. Choi, E.Y., Kim, C.K., Park, C.B. Fabrication of MA-EPDM grafted MWCNTs by reactive extrusion for enhanced interfacial adhesion and mechanical properties of PP/ MA-EPDM composite. *Composites Part B*. 2022 Aug; 242:110043. [<DOI>](#).
36. Pourali, M., Peterson, A.M. The effects of toolpath and glass fiber reinforcement on bond strength and dimensional accuracy in material extrusion of a hot melt adhesive. *Additive Manufacturing*. 202258 Oct; 58:103056. [<DOI>](#).



Effect of Nd³⁺ Doping on Structural, Near-Infrared, and Cathodoluminescent Properties for Cadmium Tantalate Phosphors

Lütfiye Feray Gülyüz* 

*Department of Mechanical Engineering, Ege University, Bornova, 35040, İzmir, Turkey

Abstract: Cd_{1-x}Ta₂O₆:xNd³⁺ (x=0.5, 1.5, 3, 5, 7, and 10 mol%) phosphor series were fabricated by conventional solid state method at 1100 °C for 17 hours. The samples of cadmium tantalate were investigated by structural (XRD, SEM) and spectroscopic (CL, PL) analyses. In XRD results, the symmetry of CdTa₂O₆ phase with orthorhombic columbite structure was confirmed between 0.5 and 10 mol% Nd³⁺ doping concentrations. SEM analysis of the grains revealed round and shapeless morphology while grain sizes ranged from submicron to several microns. The emission spectra of Cd_{1-x}Ta₂O₆:xNd³⁺ (x=0.5, 1.5, 3, 5, 7 and 10 mol%) phosphor series recorded with the transitions of ⁴F_{3/2}→⁴I_{9/2} and ⁴F_{3/2}→⁴I_{11/2}. Among these transitions, the transition ⁴F_{3/2}→⁴I_{9/2} (at 889 nm) has a high near-infrared emission intensity, which can be attributed to the laser potential of the phosphor. The NIR emission of the phosphor increased with increasing concentration of Nd³⁺ up to 5 mol% and then declined because of concentration quenching phenomenon. The CL emission peak at about 450 nm found in all samples is related to the intrinsic emission of the cadmium tantalate host. In addition, Nd³⁺ doped phosphors exhibited the ⁴F_{3/2}→⁴I_{9/2} transition of Nd³⁺ and defect-related CL emissions at 670 nm. Decreasing crystallinity with increasing Nd³⁺ concentration caused a decrease in host emission intensity at 450 nm.

Keywords: CdTa₂O₆; Cathodoluminescence; Nd³⁺; Near infrared luminescence.

Submitted: November 10, 2022. Accepted: December 29, 2022.

Cite this: Gülyüz LF. Effect of Nd³⁺ Doping on Structural, Near-Infrared, and Cathodoluminescent Properties for Cadmium Tantalate Phosphors. JOTCSA. 2023;10(1):77-88.

DOI: <https://doi.org/10.18596/jotcsa.1202284>.

*Corresponding author. E-mail: ferayguleryuz@hotmail.com

INTRODUCTION

The phosphors, which are doped with the rare-earth (RE) ions, have some convenient features such as remarkable efficiency, long lifetime, energy saving, enhanced physical robustness, kindly to environment properties, smaller size and faster switching (1-22). Among RE³⁺ (trivalent) ions, Nd (neodymium) is one of the earliest RE³⁺ ions used in solid-state lasers. Therefore, Nd³⁺ activated materials are well-known as solid-state phosphors due to their laser emissions at beneficial wavelengths such

as ⁴F_{3/2}→⁴I_{9/2} transition and also the other possible transitions ⁴F_{3/2}→⁴I_{15/2}, ⁴F_{3/2}→⁴I_{13/2} and ⁴F_{3/2}→⁴I_{11/2} (15-22). Among the ⁴F_{3/2}→⁴I_j transitions of Nd³⁺ ion, the ⁴F_{3/2}→⁴I_{9/2} transition at 880 nm finds application as a powerful diode laser transition. The ⁴F_{3/2}→⁴I_{11/2} transition stands out due to its ability to be easily operated at room temperature and pumped efficiently by flash lamp. The lasing transition at 1350 nm (⁴F_{3/2}→⁴I_{13/2}) is finding application as telecommunication transition window (22). The cathodoluminescence (CL) produced in the UV-visible-NIR system of the electromagnetic

spectrum is due to the interaction of the material with the electron beam, where optical characterization is performed by means of the cathode rays (fast electrons) provided by an electron gun and the luminescence (light emission) formed. The CL analysis can be interpreted via spectral lines that are similar to those from other luminescence techniques, and characteristically dominate the spectrum with bound excitonic states and changes from emission lines, donor-acceptor double bands, and defect-related properties (23-27).

The ternary oxides of general formula AB_2O_6 ($A=M^{2+}$, $B=Nb^{5+}$, Ta^{5+}) crystallize in the columbite structure. The cations of A and B are located in the center of the octahedra surrounded by six oxygen atoms while the AO_6 and BO_6 octahedra share the edges, forming independent zigzag chains. This sequential situation repeats as ABBABB octahedral layers as the chains are connected by sharing corners in order to the AO_6 chain- BO_6 chain- BO_6 chain (5-11). $CdTa_2O_6$, as an AB_2O_6 oxide structure, has been studied in the literature in terms of its luminescence and thermodynamic properties. The white-light properties of Dy^{3+} doped $CdTa_2O_6$, and the PL-RL properties of Eu^{3+} doped $CdTa_2O_6$ have been reported by (7) and, (8) respectively. The molar heat capacity of $CdTa_2O_6$ has been reported as $179.65 \text{ J mol}^{-1} \text{ K}^{-1}$, at ambient temperature (28). In addition, cadmium-containing phosphor materials are attracting attention in the field of optics as a new material class due to their broad potential applications such as solar cells, biosensors, biomedical scanning, and light-emitting diodes (LEDs) (29-33). The inherent toxicity of cadmium limits its applications, especially in the industrial and biomedical fields, so the genotoxicity and cytotoxicity of $CdSe/ZnS$ (cadmium selenide/Zinc sulfide) core/shell QDs for applications in cancer therapy have been discussed (34). However, cadmium-based phosphors provide a high level of brightness, leading to a reduction in the need for high levels of X-ray doses, which can minimize the risk of health problems (29,35).

In the study, NIR photoluminescence and cathodoluminescence of $Cd_{1-x}Ta_2O_6:xNd^{3+}$ ($x=0.5, 1.5, 3, 5, 7, 10 \text{ mol}\%$) phosphors were studied. The spectroscopic and structural characterizations of the samples were carried out by XRD, SEM-EDS, FTIR, PL, and CL analyses.

EXPERIMENTAL SECTION

Undoped and $Cd_{1-x}Ta_2O_6:xNd^{3+}$ ($0.005 \leq x \leq 0.1$ or $0.5 \leq x \leq 10 \text{ mol}\%$) materials were fabricated using solid state reaction. Nd_2O_3 (Alfa Aesar, 99.9%) was used as a dopant. $Cd(NO_3)_2 \cdot 4H_2O$ (Sigma-Aldrich, 99%) and Ta_2O_5 (Alfa Aesar, 99.9%) powders were used as starting materials. The powders of $Cd(NO_3)_2 \cdot 4H_2O$, Ta_2O_5 and Nd_2O_3 were prepared and homogenized in agate mortar according to stoichiometry of $Cd_{1-x}Ta_2O_6:xNd^{3+}$ where $CdTa_2O_6$ ($x=0$), $Cd_{0.995}Nd_{0.005}Ta_2O_6$ ($x=0.005$), $Cd_{0.985}Nd_{0.015}Ta_2O_6$ ($x=0.015$), $Cd_{0.97}Nd_{0.03}Ta_2O_6$ ($x=0.03$), $Cd_{0.95}Nd_{0.05}Ta_2O_6$ ($x=0.05$), $Cd_{0.93}Nd_{0.07}Ta_2O_6$ ($x=0.07$), $Cd_{0.90}Nd_{0.10}Ta_2O_6$ ($x=0.1$), respectively. Prepared powders were sintered at $1100 \text{ }^\circ\text{C}$ for 17 hours in an electric furnace under air atmosphere after pelleting.

The phase structure of the ceramics were performed by X-ray diffraction (D-MAX 2200, Rigaku Corp., Japan) using $Cu-K_\alpha$ radiation, Ni filter, scan rate = $2 \text{ }^\circ/\text{min}$, and $2\theta=20-65^\circ$. The grain morphology and elemental identification of the ceramic samples were carried out by SEM (JSM-5910LV, JEOL Ltd., Japan) equipped with EDS (INCAx-Sight 7274, Oxford Industries, UK) after Au/Pd (gold/palladium) coating. FTIR (fourier transform infrared spectrometer) spectra were taken by Perkin-Elmer ATR-FTIR. Near emission spectra of powders were measured in the range of 850-1450 nm using a diode laser of 800 nm excitation at 300 K. Cathodoluminescence (CL) spectra were performed with a monochromatic spectrometer (DATAN-Mono CL4) attached to an electron microscope (NOVA-NANOSEM 650) with an emission gun (working distance 6.6 mm, voltage 15 kV, spot size 3.5) in high vacuum. Besides CL imaging, the spectrometer allows acquisition of CL spectra at highly localized points of a sample.

RESULTS AND DISCUSSION

Structural and Morphological Characterization

Figure 1 shows the XRD results of undoped sample and $Cd_{1-x}Ta_2O_6:xNd^{3+}$ ($x=0.5, 1.5, 3, 5, 7$ and $10 \text{ mol}\%$) samples. The XRD patterns of the samples (JCPDS card No.39-1431) can be indexed space group *Pbcn*. As seen in the XRD patterns of all the samples, there are no different minor phases in the range of two theta degree (for 20° and 65°). The cell parameters of $CdTa_2O_6$ structure are $a=5.8510 \text{ \AA}$, $b=14.7847 \text{ \AA}$, $c=5.1462 \text{ \AA}$, and $V=445.17 \text{ \AA}^3$ (36). The orthorhombic structure of $CdTa_2O_6$ along the c-

axis has been illustrated in Figure 2. Octahedra with the same central cation share edges forming zigzag chains along the c-axis while TaO₆ octahedra of adjacent chains share corners to form double layers, parallel to the bc-plane, which are connected via CdO₆ octahedra through common corners (37). On the basis of the ion radius and coordination number (CN), the formation of the single-phase can be attributed to the substitution of Nd³⁺ ions with ionic radius 0.983 Å (for 6 C.N) by Cd²⁺ ions ($r=0.95$ Å, for C.N. 6). Figure 3 shows the XRD peaks of the (131) reflection. As seen in the XRD peaks, there was a slight shift towards smaller two theta angles due to the increase in Nd³⁺ concentration. This may be attributed to the expansion of the lattice volume due to the slightly large ionic radius of the Nd³⁺ ion, where the Nd³⁺ substitution instead of Cd²⁺ is also likely to affect the charge balance and form

some stress in the structure, albeit limited. However, despite some expansion in the lattice volume, the existence of the single-phase structure was preserved up to 10 mol% concentration, indicating that the dopant ion has located into the structure successfully.

SEM micrographs at 10.000x magnification of undoped and 0.5, 3, and 10 mol% Nd³⁺ doped samples are shown in Figure 4(a-d). The grain shapes of Nd³⁺ doped samples have elliptical shapes and a shapeless morphology, while the grain sizes varied from 0.5 to 3.5 μm. Figure 5 shows the EDS spectra and elemental compositions of (weight%, atomic%) and theoretical atomic (%) values for Cd_{1-x}Ta₂O₆:Nd³⁺ grains were detected by EDS at 20 kV of SEM acceleration voltage, where atomic (%) compositions are compatible with theoretical atomic (%) values.

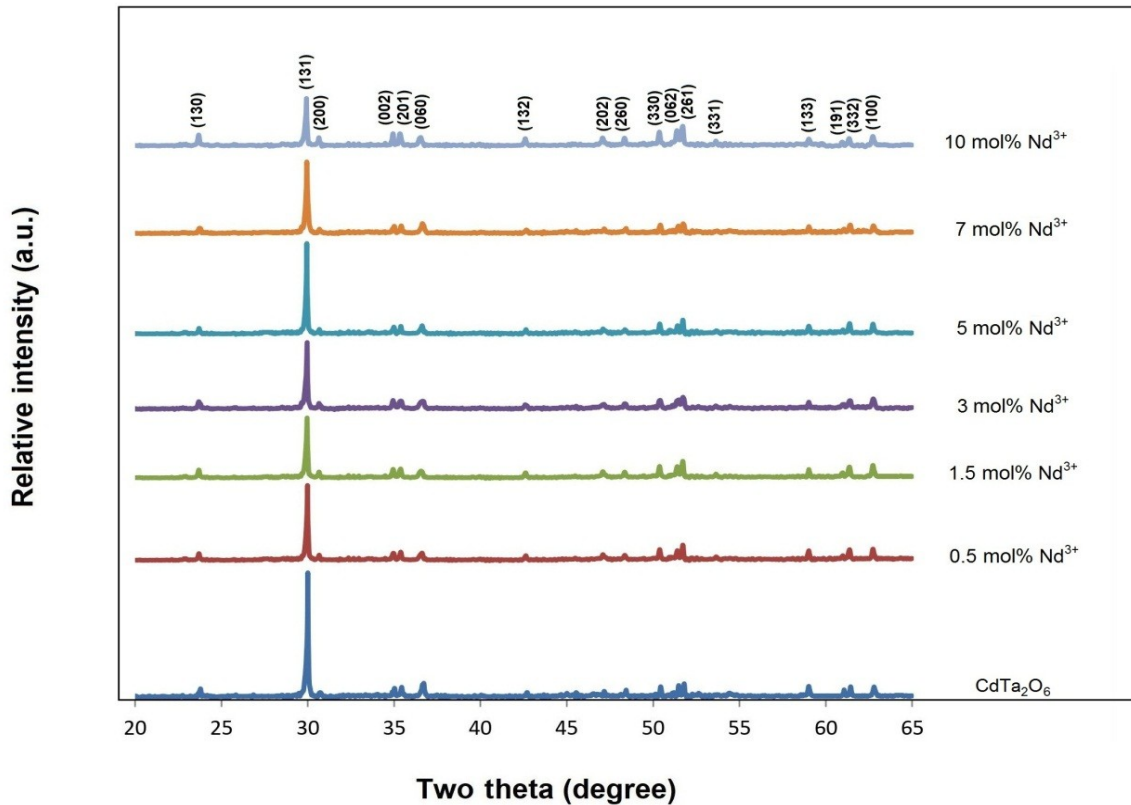


Figure 1: XRD results of undoped and Cd_{1-x}Ta₂O₆:xNd³⁺ (x=0.5, 1.5, 3, 5, 7, and 10 mol%) samples.

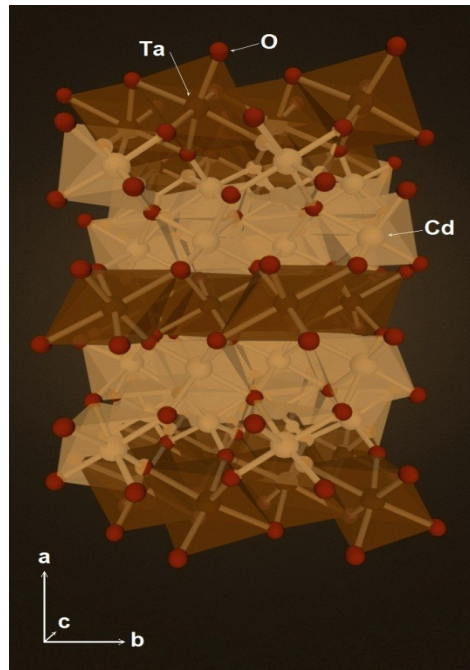


Figure 2: Schematic illustration of the CdTa₂O₆ crystal in the direction of the c axis.

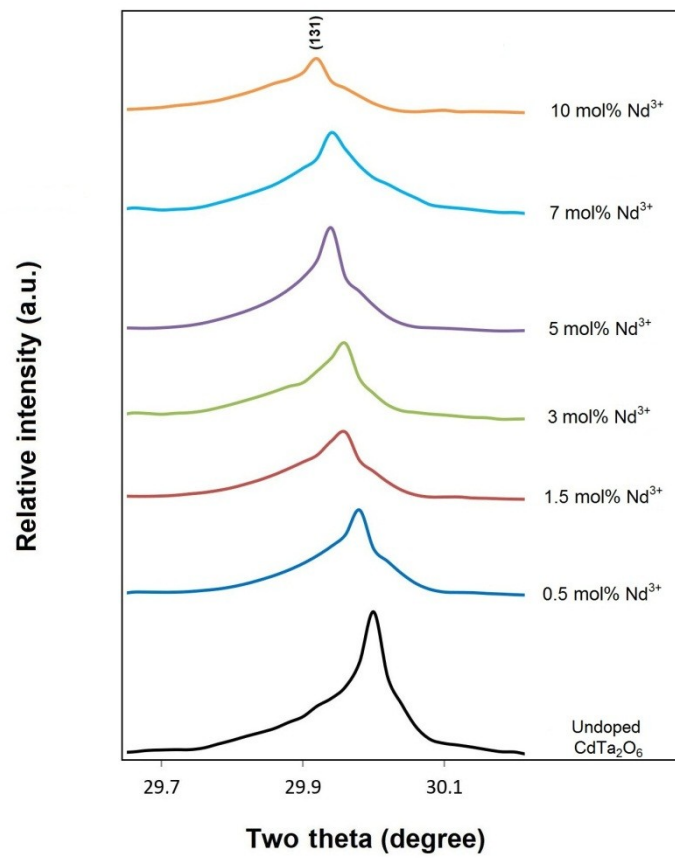


Figure 3: XRD two theta angles (131) shifted to lower angles with Nd³⁺ concentration.

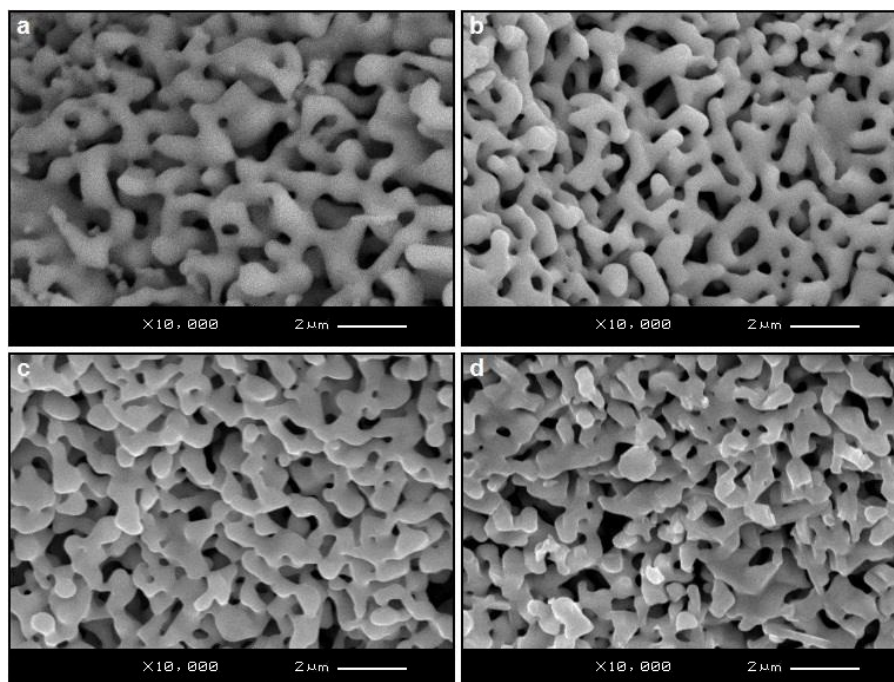


Figure 4: SEM micrographs of (a) undoped and (b) 0.5, (c) 3, (d) 10 mol% Nd^{3+} doped samples at 20 kV acceleration voltage, and 10.000× magnification.

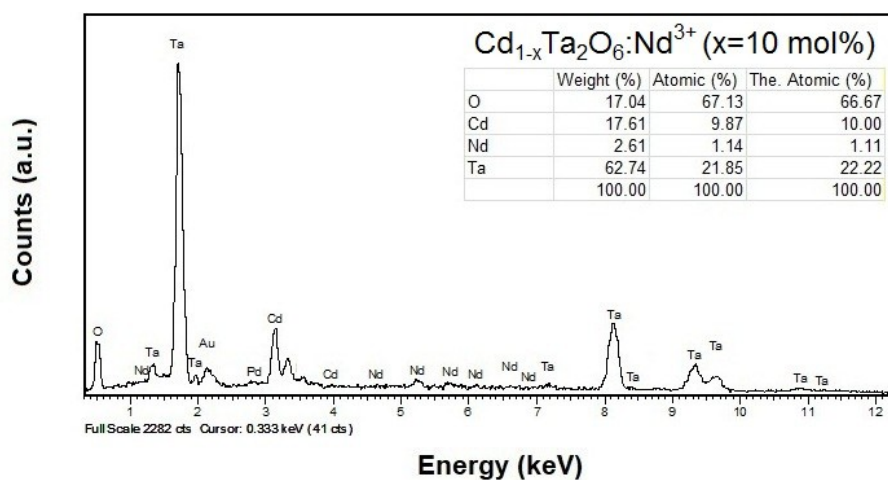


Figure 5: EDS spectrum and compositions (wt%, at%) and theoretical at% values for 10 mol% Nd^{3+} doped sample.

FTIR Analysis

FTIR spectra of undoped sample and $\text{Cd}_{1-x}\text{Ta}_2\text{O}_6:\text{xNd}^{3+}$ ($x=1.5, 5$ and 10 mol%) samples in the range of 500–4000 cm^{-1} are presented in Figure 6. The molecular structure of the metal oxides with IR spectroscopy can be detected from $\text{M}=\text{O}$ vibrations in the 500–1000 cm^{-1} while

the peaks of 2800–4000 cm^{-1} shows the fundamental stretching of OH groups (38). FTIR peaks of 800–1000 cm^{-1} can be associated with the Ta–O bond vibrations while the small peaks in between 1000–1500 cm^{-1} are due to Cd–O–Ta vibrations.

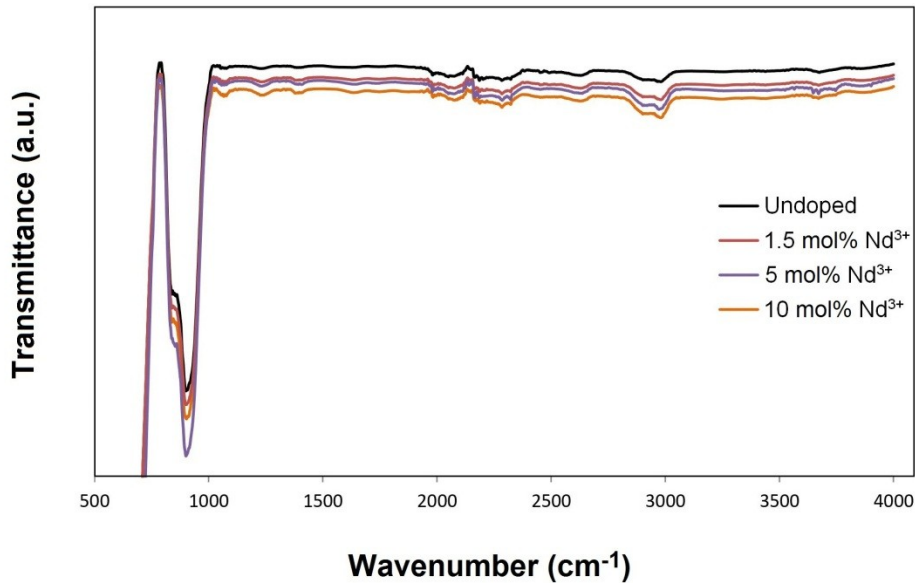


Figure 6: FTIR spectra of undoped and $\text{Cd}_{1-x}\text{Ta}_2\text{O}_6:\text{xNd}^{3+}$ ($x=1.5, 5, 10$ mol%) samples.

NIR luminescence of $\text{Cd}_{1-x}\text{Ta}_2\text{O}_6:\text{xNd}^{3+}$ ($x=0.5, 1.5, 3, 5, 7$ and 10 mol%) phosphors

Figure 7 shows the NIR emission spectra of $\text{Cd}_{1-x}\text{Ta}_2\text{O}_6:\text{xNd}^{3+}$ ($x=0.5, 1.5, 3, 5, 7, 10$ mol%) phosphors were used a laser diode with excitation source 800 nm. The emissions of the phosphors were monitored corresponding to the ${}^4\text{F}_{3/2} \rightarrow {}^4\text{I}_{9/2}$ and ${}^4\text{F}_{3/2} \rightarrow {}^4\text{I}_{11/2}$ transitions at 889 and 1073, respectively. The ${}^4\text{F}_{3/2} \rightarrow {}^4\text{I}_{9/2}$ transition (at 889 nm) is a potential laser transition that appears to be more intense than the ${}^4\text{F}_{3/2} \rightarrow {}^4\text{I}_{11/2}$. Although the overall energy level of the 4f electrons of the Nd^{3+} ion protected by the outer shell $5s^2$ and $5p^6$ electrons does not vary greatly in different hosts, the energy level surrounding the Nd^{3+} ions can be subdivided into $2J+1$ sublevels by the local crystal field (39). As seen in Figure 7, there are many splits resulting from the ${}^4\text{F}_{3/2} \rightarrow {}^4\text{I}_{9/2}$ transition with the highest emission peak in the 860–940 nm range, while the ${}^4\text{F}_{3/2} \rightarrow {}^4\text{I}_{11/2}$ transition exhibits emission around 1070 nm. The Stark components of both transitions of Nd^{3+} ions are similar, which can be associated with the similarity of local symmetry of ligand ions surrounding the Nd^{3+} ion (19-21). The near infrared emission of the phosphor rose up to 5 mol%, and emission declined at 7 and 10 mol% concentrations. The decrease in PL density may be associated with higher Nd^{3+} concentrations (or beyond 5% mol), which promotes the migration of excitation energy between active ions (22,40). As Nd^{3+} concentration continues to increase, cross-

relaxation mechanism between Nd^{3+} - Nd^{3+} ions becomes more and more important, and therefore non-radiation transitions will be more likely to occur due to the nearness between the Nd^{3+} ions (17).

Cathodoluminescence of undoped and $\text{Cd}_{1-x}\text{Ta}_2\text{O}_6:\text{xNd}^{3+}$ ($x=1.5, 5,$ and 10 mol %) phosphors

Figure 8 shows the cathodoluminescence spectra of undoped sample and $\text{Cd}_{1-x}\text{Ta}_2\text{O}_6:\text{xNd}^{3+}$ ($x=1.5, 5,$ and 10 mol%) phosphors. In CL emissions, the peak at about 450 nm is related to the intrinsic emission of the polycrystal host, and is present in all samples (41,42). For the similar compound, orthorhombic columbite CdNb_2O_6 , the host emission has been reported as 460 nm (43,44). Accordingly, the CL host emission of CdTa_2O_6 observed at 450 nm is consistent with the PL host emission of CdNb_2O_6 . On the other hand, the undoped sample has the highest host emission intensity, while the intrinsic emission intensity of Nd^{3+} doped samples at 450 nm decreases with increasing concentration. This is due to the inclusion of Nd^{3+} ion in the lattice affected the crystallinity (45). As seen from the CL spectra, 10 mol% Nd^{3+} doped phosphor has lowest intrinsic emission intensity, which can be attributed to the fact that Nd^{3+} doping causes the most distortion (or the highest effect on crystallization) at this concentration. The emission peak of Nd^{3+} doped phosphors at about 670 nm (red emission) show a red

emission which is associated with the defect related to deep emission (45,46), the recombination of electrons in the non-bridging oxygen band-gap state with holes in the valence band edge (47,48). The final luminescence peak of 900 nm indicates neodymium emission from the 4f shell transition of Nd^{3+} ions corresponding to the ground state ($4I_{9/2}$) from the excited state ($4F_{3/2}$) in the host lattice (49).

CL micrographs of undoped sample and $\text{Cd}_{1-x}\text{Ta}_2\text{O}_6:\text{xNd}^{3+}$ ($x=1.5, 5, 10$ mol%) phosphors are shown in Figure 9(a-d). In CL micrographs, the undoped sample has a blue emission appearance due to the 450 nm peak (as mentioned earlier), while the doped samples show blue-red-blue emissions due to the 450 and 670 nm peaks.

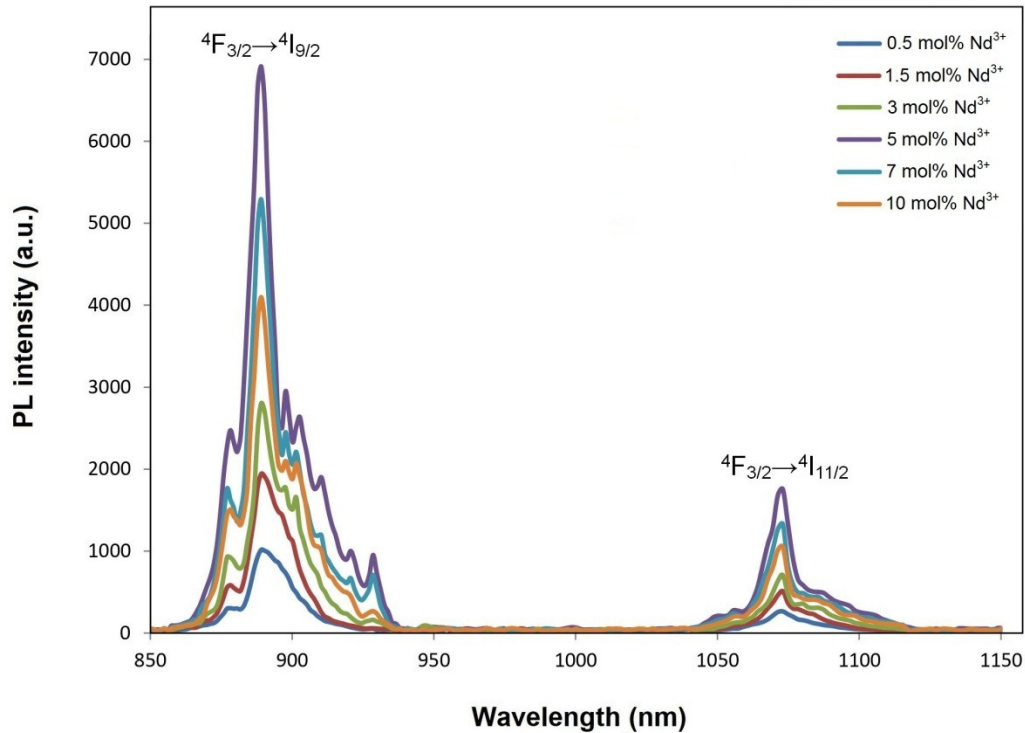


Figure 7: Near-infrared emission spectra of $\text{Cd}_{1-x}\text{Ta}_2\text{O}_6:\text{xNd}^{3+}$ ($x=0.5, 1.5, 3, 5, 7,$ and 10 mol%) phosphors by diode laser under 800 nm excitation.

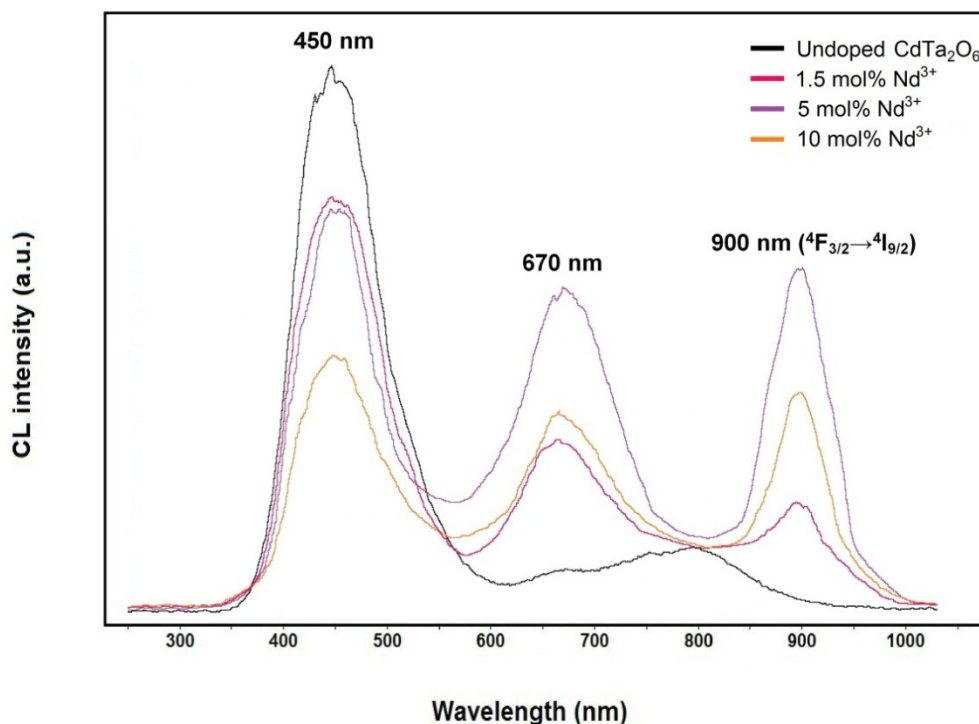


Figure 8: CL emission spectra of undoped CdTa_2O_6 , and $\text{Cd}_{1-x}\text{Ta}_2\text{O}_6:x\text{Nd}^{3+}$ ($x=1.5, 5,$ and 10 mol%) phosphors.

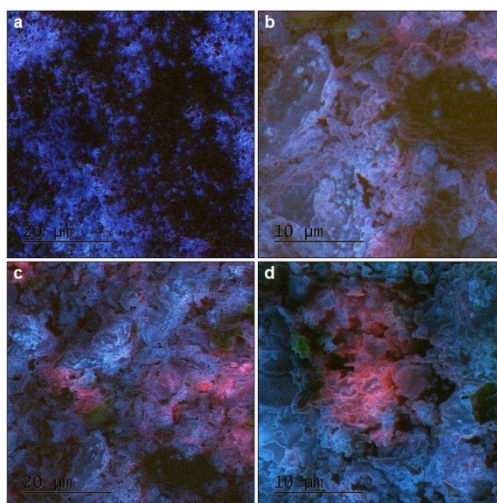


Figure 9: CL micrographs for (a) undoped sample, and (b) 1.5, (c) 5, (d) 10 mol% Nd^{3+} doped cadmium tantalate phosphors.

CONCLUSION

$\text{Cd}_{1-x}\text{Ta}_2\text{O}_6:x\text{Nd}^{3+}$ ($x=0.5, 1.5, 3, 5, 7$ and 10 mol %) phosphors were fabricated by solid state method. XRD results indicated the presence of

the single phase Nd^{3+} concentrations from 0.5 to 10 mol%. SEM examinations revealed the shapeless/rounded grain morphology with the sizes of 0.5 - 3.5 micron while EDS identified elemental compositions of the grains. The NIR

emissions of the phosphors monitored with the transitions of ${}^4F_{3/2} \rightarrow {}^4I_{9/2}$ (889 nm) and ${}^4F_{3/2} \rightarrow {}^4I_{11/2}$ (1073 nm), where the ${}^4F_{3/2} \rightarrow {}^4I_{9/2}$ transition is a potential laser transition that appears to be more intense than the ${}^4F_{3/2} \rightarrow {}^4I_{11/2}$. The CL emission of undoped sample was observed with the peak of 450 nm, in which the decreased CL intensity of the phosphors is related to the effect of crystallinity. Nd^{3+} -doped phosphors exhibited the 900 nm peak due to the ${}^4F_{3/2} \rightarrow {}^4I_{9/2}$ transition, as well as the 450 and 670 nm peaks of structural origin. Based on the observed results, it could be concluded that the $\text{Cd}_{1-x}\text{Ta}_2\text{O}_6:\text{Nd}^{3+}$ phosphor with the strong transition of ${}^4F_{3/2} \rightarrow {}^4I_{9/2}$ has potential for diode lasing applications.

CONFLICT OF INTEREST

There is no conflict of interest.

REFERENCES

- Ekmekçi MK. Influence of europium doping on the crystallization, morphology, and cathodoluminescent properties of $\text{PbNb}_2\text{O}_6:\text{Eu}^{3+}$ phosphors. JOTCSA. 2022;1129-1140. <URL>.
- Nagaraj R, Rajagopal V, Raja A, Ranjith S. Influence of Dy^{3+} ion concentration on photoluminescence and energy transfer mechanism of promising $\text{KBaScSi}_3\text{O}_9$ phosphors for warm white LEDs. Spectrochim. Acta A Mol. Biomol. Spectrosc. 2022;264:120212. <URL>.
- İlhan M, Katı Mİ, Keskin İÇ, Güteryüz LF. Evaluation of structural and spectroscopic results of tetragonal tungsten bronze $\text{MTa}_2\text{O}_6:\text{Eu}^{3+}$ (M = Sr, Ba, Pb) phosphors and comparison on the basis of Judd-Ofelt parameters. J. Alloy. Comp. 2022;901:163626. <URL>.
- Yao S, Lv S, Feng Z. Synthesis and photoluminescent properties of $\text{Dy}^{3+}:\text{CaYAlO}_4$ phosphors. Appl. Phys. A 2021;127:773. <URL>.
- Ekmekçi MK, İlhan M, Güteryüz LF, Mergen A. Study on molten salt synthesis, microstructural determination and white light emitting properties of $\text{CoNb}_2\text{O}_6:\text{Dy}^{3+}$ phosphor. Optik. 2017 Oct;128:26-33. <URL>.
- İlhan M, Ekmekçi MK, Keskin İÇ. Judd-Ofelt parameters and X-ray irradiation results of $\text{MNb}_2\text{O}_6:\text{Eu}^{3+}$ (M = Sr, Cd, Ni) phosphors synthesized via a molten salt method. RSC Adv. 2021 Feb;11:10451. <URL>.
- İlhan M, Ekmekçi MK. Synthesis and photoluminescence properties of Dy^{3+} doped white light emitting CdTa_2O_6 phosphors. J. Solid State Chem. 2015;226:243-249. <URL>.
- İlhan M, Keskin İÇ. Photoluminescence, radioluminescence and thermoluminescence properties of Eu^{3+} doped cadmium tantalate phosphor. Dalton Trans. 2018;47:13939-13948. <URL>.
- Erdem R, İlhan M, Ekmekçi MK, Erdem Ö. Electrospinning, preparation and photoluminescence properties of $\text{CoNb}_2\text{O}_6:\text{Dy}^{3+}$ incorporated polyamide 6 composite fibers. Appl. Surf. Sci. 2017;421:240-246. <URL>.
- Başak AS, Ekmekçi MK, Erdem M, İlhan M, Mergen A. Investigation of boron-doping effect on photoluminescence properties of $\text{CdNb}_2\text{O}_6:\text{Eu}^{3+}$ phosphors. J. Fluoresc 2016;26:719-724. <URL>.
- İlhan M, Keskin İÇ. Analysis of Judd-Ofelt parameters and radioluminescence results of $\text{SrNb}_2\text{O}_6:\text{Dy}^{3+}$ phosphors synthesized via molten salt method. Phys. Chem. Chem. Phys. 2020;2:19769. <URL>.
- He X, Fang B, Zhang S, Lu X, Ding J. Preparation and properties of Nd-doped BCTH lead-free ceramics by solid-phase twin crystal method. Curr. Appl. Phys. 2022;38:30-39. <URL>.
- İlhan M, Güteryüz LF, Keskin İÇ, Katı Mİ. A comparison of spectroscopic properties of Dy^{3+} -doped tetragonal tungsten bronze MTa_2O_6 (M = Sr, Ba, Pb) phosphors based on Judd-Ofelt parameters. Mater. Sci: Mater. Electron 2022;33:16606-16620. <URL>.
- İlhan M, Keskin İÇ. Evaluation of structural behaviour, radioluminescence, Judd-Ofelt analysis and thermoluminescence kinetic parameters of Eu^{3+} doped TTB-type lead metaniobate phosphor. Phys. B: Condens. Matter 2020;585:412106. <URL>.
- He X, Fang B, Zhang S, Lu X, Ding J. Preparation of nanoscale $[(\text{Ba}_{0.85}\text{Ca}_{0.15})_{0.995}\text{Nd}_{0.005}](\text{Ti}_{0.9}\text{Hf}_{0.1})\text{O}_3$ ceramics via hydrothermal method and effect of grain size on multifunctional performance. J. Alloys Compd. 2022;925:166249. <URL>.
- İlhan M, Keskin İÇ, Çatalgöl Z, Samur R. NIR photoluminescence and radioluminescence characteristics of Nd^{3+} doped BaTa_2O_6 phosphor. Int. J. Appl. Ceram. Technol. 2018;15: 1594-1601. <URL>.
- Wang X, Zhao H, Li A, Tian K, Brambilla G, Wang P. Near-infrared luminescence and single-mode laser emission from Nd^{3+} doped compound glass and glass microsphere. Front. Mater. Sci. 2019;6:237. <URL>.
- Prasad RNA, Vijaya N, Babu P, Mohan NK, Praveena R. Optical absorption and NIR photoluminescence of Nd^{3+} -activated strontium phosphate glasses. J. Electron. Mater. 2020;49:6358-6368. <URL>.
- İlhan M, Ekmekçi MK, Oraltay RG, Başak AS. Structural and near-infrared properties of Nd^{3+} activated Lu_3NbO_7 Phosphor. J. Fluoresc. 2017;27:199-203. <URL>.
- Ekmekçi MK, İlhan M, Ege A, Ayvacıklı M. Microstructural and radioluminescence characteristics

- of Nd³⁺ doped columbite-type SrNb₂O₆ phosphor. *J. Fluoresc.* 2017;27:973-979. <URL>.
21. Ekmekçi MK, Erdem M, Başak AS, İlhan M, Mergen A. Molten salt synthesis and optical properties of Eu³⁺, Dy³⁺ or Nd³⁺ doped NiNb₂O₆ columbite-type phosphors. *Ceram. Int.* 2015;41:9680-9685. <URL>.
22. Mahamuda Sk, Swapna K, Rao AS, Jayasimhadri M, Sasikala T, Pavani K, Moorthy LR. Spectroscopic properties and luminescence behavior of Nd³⁺ doped zinc alumino bismuth borate glasses. *J. Phys. Chem.* 2013;74:1308-1315. <URL>.
23. Edwards PR, Martin RW. Cathodoluminescence nano-characterization of semiconductors. *Semicond. Sci. Technol.* 2011;26:064005. <URL>.
24. Ma DDD, Lee ST, Mueller P, Alvarado SF. Scanning tunneling microscope excited cathodoluminescence from ZnS nanowires. *Nano Lett.* 2006;6:926. <URL>.
25. Dierre B, Yuan XL, Sekiguchi T. Sci. Low-energy cathodoluminescence microscopy for the characterization of nanostructures. *Technol. Adv. Mater.* 2010;11:043001. <URL>.
26. İlhan M, Güteryüz LF. Cathodoluminescence and photoluminescence of BaTa₂O₆:Sm³⁺ phosphor depending on the sintering temperature. *Chem. Pap.* 2022;76:6963-6974. <URL>.
27. Mitsui T, Yamamoto N, Tadokoro T, Ohta S. Cathodoluminescence image of defects and luminescence centers in ZnS/GaAs(100). *J. Appl. Phys.* 1996;80:6972. <URL>.
28. İlhan M. Heat capacities and thermodynamic functions of CdNb₂O₆ and CdTa₂O₆. *J. Therm. Anal. Calorim.* 2022;147:12383-12389. <URL>.
29. European Coordination Committee of the Radiological, Electromedical and Healthcare IT Industry, COCIR application for new exemption Page 1-12, Blvd A. Reyers 80 1020 Brussels, 2011.
30. Colvin VL, Schlamp MC, Alivisatos AP. Light-emitting diodes made from cadmium selenide nanocrystals and a semiconducting polymer. *Nature* 1994;370:354-357. <URL>.
31. Chaar LE, Lamont LA, Zein NE. Review of photovoltaic technologies. *Renewable Sustainable Energy Rev.* 2011;15:2165-75. <URL>.
32. Iorgu AI, Berger D, Alexandrescu L, Vasile BS, Matei C. Synthesis of photoluminescent pure and doped cadmium sulfide by reverse microemulsion method. *Chalcogenide Lett.* 2013;10:525-531.
33. Willner I, Baron R, Willner B. Integrated nanoparticle-biomolecule systems for biosensing and bioelectronics. *Biosens. Bioelectron.* 2007;22:1841. <URL>.
34. Choi YJ, Kim YJ, Lee JW, Lee Y, Lim YB, Chung HW. Cyto-/genotoxic effect of CdSe/ZnS quantum dots in human lung adenocarcinoma cells for potential photodynamic UV therapy applications. *J. Nanosci. Nanotechnol.* 2012;12:2160-2168. <URL>.
35. Su Y, He Y, Lu H, Sai L, Li Q, Li W, Wang L, Shen P, Huang Q, Fan C. The cytotoxicity of cadmium based, aqueous phase - Synthesized, quantum dots and its modulation by surface coating. *Biomaterials* 2009;30:19-25. <URL>.
36. Wong-Ng W, McMurdie HF, Paretzkin B, Kuchinski MA, Dragoo AL. Standard X-Ray Diffraction Powder Patterns of Fourteen Ceramic Phases. *Powder Diffr.* 1988;3:246-254.
37. Tealdi C, Mozzati MC, Malavasi L, Ciabattoni T, Amantea R, Azzoni CB. Columbite-type Fe_xMn_{1-x}Nb₂O₆ solid solution: structural and magnetic characterization. *Phys. Chem. Chem. Phys.* 2004;6:4056-4061. <URL>.
38. Wachs IE. Infrared spectroscopy of supported metal oxide catalysts. *Colloid Surface A.* 1995;105:143-149.
39. Ayvacikli M, Kotan Z, Ekdal E, Karabulut Y, Canimoglu A, Guinea JG, Khatab A, Henini M, Can N. Solid state synthesis of SrAl₂O₄:Mn²⁺ co-doped with Nd³⁺ phosphor and its optical properties. *J. Lumin.* 2013;144:128-132. <URL>.
40. Sontakke AD, Biswas K, Mandal AK, Annapurna K. Concentration quenched luminescence and energy transfer analysis of Nd³⁺ ion doped Ba-Al-metaphosphate laser glasses. *Appl. Phys. B* 2010;101:235-244. <URL>.
41. MacRae CM, Wilson NC, Torpy A, Davidson CJ. Hyperspectral cathodoluminescence imaging and analysis extending from ultraviolet to near infrared. *Microsc. Microanal.* 2012;18:1239-1245. <URL>.
42. Lamrani MA, Addou M, Sofiani Z, Sahraoui B, Ebothe J, El Hichou A, Fellahi N, Bernede JC, Dounia R. Cathodoluminescent and nonlinear optical properties of undoped and erbium doped nanostructured ZnO films deposited by spray pyrolysis. *Opt. Commun.* 2007;277:196-201. <URL>.
43. Hsiao YJ, Fang TH, Ji LW, Chi SS. Surface and photoluminescence characteristics of CdNb₂O₆ Nanocrystals. *Open Surf. Sci. J.* 2009;1:30-33. <URL>.
44. Hsiao YJ, Chang YS, Chen GJ, Chang YH. Synthesis and the luminescent properties of CdNb₂O₆ oxides by sol-gel process. *J. Alloys Compd.* 2009;471:259-262. <URL>.
45. Cherrad H, Addou M, Hssein M, Bahedi K, Jbilou M, Mrigal A, Salmani E, Rouchdi M, Mezred A, Ftouhi H, Diani M, Jouad ME. Theoretical and experimental investigation of structural, electronic and optical properties of neodymium doped ZnO. *MATEC Web of Conferences* 2020;307:01018. <URL>.

46. El Hichou A, Addou M, Ebothé J, Troyon M. Influence of deposition temperature (Ts), air flow rate (f) and precursors on cathodoluminescence properties of ZnO thin films prepared by spray pyrolysis]. *Lumin.* 2005;113:183-190. [<URL>](#).

47. Sittner J, Götze J. Cathodoluminescence (CL) characteristics of quartz from different metamorphic rocks within the Kaoko Belt (Namibia). *Minerals* 2018;8;190. [<URL>](#).

48. Siegel GH, Marrone MJ. Photoluminescence in as-drawn and irradiated silica optical fibers: an assessment of the role of non-bridging oxygen defect centers. *J. Non Cryst. Solids* 1981;45:235-247. [<URL>](#).

49. Karl A, Gschneidner Jr, LeRoy E. *Handbook on the Physics and Chemistry of Rare Earths* volume 4 Non-Metallic Compounds - II. 293, 1979.



A Simultaneous Determination Method for the Analysis of Chloride and Nitrate Ions in Air Samples by PLS1

Çiğdem Kuş¹ , Havva Bekiroğlu Ataş^{1,2} , Adnan Kenar¹ , Mustafa Taştekin^{1*} 

¹Department of Chemistry, Faculty of Science, Ankara University, 06100, Ankara, Turkey

²General Directorate of Public Health /Department of Consumer Safety and Public Health Laboratories, National Public Health Reference Laboratory, 06100, Ankara, Turkey

Abstract: This study describes a multi-ion-selective electrode system for the simultaneous determination of nitrate and chloride ions in air samples by using multivariate calibration methods. The measurement system was constituted of two ion-selective electrodes, an Ag/AgCl double-junction reference electrode and a multi-potentiometer. The measurements were performed at pH 5.0 acetic acid/sodium acetate buffer. The obtained data were evaluated by using Partial Least Squares (PLS1). The system was used to analyze the synthetic samples and fume-hood samples in terms of the amount of chloride and nitrate. The percentage recovery values obtained from fume-hood samples were $93.8\% \pm 3.8$ and $102.4\% \pm 2.5$ for chloride and nitrate, respectively. The presented system could be an easy-to-use approach for monitoring the amount of chloride and nitrate species in the scope of occupational health and safety analysis.

Keywords: Multiple ion-selective electrode array, nitrate analysis, chloride analysis, multivariate calibration techniques, chemometrics, air samples.

Submitted: June 01, 2022. **Accepted:** January 04, 2023.

Cite this: Kuş Ç, Bekiroğlu Ataş H, Kenar A, Taştekin M. A Simultaneous Determination Method for the Analysis of Chloride and Nitrate Ions in Air Samples by PLS1. JOTCSA. 2023;10(1):89-96.

DOI: <https://doi.org/10.18596/jotcsa.1124772>.

***Corresponding author. E-mail:** mustafa.tastekin@science.ankara.edu.tr.

INTRODUCTION

Chloride and nitrate ions are frequently encountered in environmental samples such as water, soil and air, and these components affect human health. These ions are also found in the structure of strong acids such as hydrochloric acid and nitric acid.

Nitric acid is used in explosives and ammonium nitrate production for fertilization. In addition, it is used in organic synthesis, metallurgy, ore flotation (separation of free ore grains in liquid by flotation method, etc.), and reprocessing of spent nuclear fuels. Nitric acid is highly corrosive to most metals. Reactions between nitric acid and various organic metals are often highly exothermic and explosive. In addition, toxic gases are released when nitric acid reacts with metals.

The chloride ion is often used to purify drinking water and wastewater treatment. On the other

hand, hydrochloric acid is used as an industrial acidifier. It is also used for refining tantalum and tin ores, converting corn starch to syrup, removing stones formed in heat exchangers and boilers in the industry.

The analysis of these and similar ions has always attracted attention. For example, ion chromatography is one of the most used methods (1). In addition, there are other studies conducted by capillary electrophoresis (2) and voltammetric (3) or potentiometric ion-selective electrodes (4, 5) in order to do anion analysis.

Nowadays, special attention is paid to occupational health and safety issues, and some sanctions are applied when necessary. For example, in the industry, the employer has to make some analyses done in the work environment to save the employees' health. According to the Occupational Safety and Health Administration (OSHA), about 32 million workers work with and are potentially

exposed to one or more chemical hazards (6). It is also known that chemical exposure may cause or contribute to many serious health effects such as heart ailments, kidney and lung damage, cancer, burns, and rashes.

Chemicals have exposure limits in the scope of occupational health and safety. For example, the legal airborne permissible exposure limit (PEL) for hydrochloric acid is 5 ppm and can not be exceeded at any time (7). On the other hand, the PEL value is lower for nitric acid, and it is 2 ppm averaged over an 8-hour work shift (8). In such cases, the sampling for air should be done from the environment near the employee's breathing zone, where the ions are most intense.

Analyses can be conducted when a lot of types of components are together in the matrix. The analyses may result in errors due to the species that cause interference. To prevent this, the species that have an interfering effect should be removed from the matrix or masked. After these sample preparations, analysis is carried out by single-variate calibration techniques. However, this situation leads to loss of time and extra cost, and as the number of processes increases, systematic error possibility rises. In order to prevent these adverse effects, multivariate calibration methods can be an alternative (9).

Multivariate calibration methods have been preferred several times by the researchers that carry out spectroscopic studies (10-13). In addition, the use of these techniques with electrochemical studies such as anodic or cathodic differential pulse voltammetry have been reported before (14, 15). Many of these methods, especially spectroscopic ones, have advantages such as repeatability and sensitivity. On the other hand, the main handicaps of spectroscopic techniques are being overpriced, having complex procedures, and being more suitable for benchtop analysis. Potentiometry has become a good alternative for multivariate calibration studies since it has a small and uncomplicated design that allows field measurements. Moreover, compared to the other methods, it is relatively cheap and can be applied easily (16).

The technology, which is created by using multi-ion selective electrode arrays and multivariate calibration methods together, calls "electronic tongue" (17). Electronic tongues benefit the cross sensitivities of different ion-selective electrodes involving a sensor array and evaluate the results by a chemometric database. Although the use of multi-ISE arrays and chemometrics for the qualitative and quantitative analysis of different cations have been reported frequently (18-25), there are limited studies about the anion analyses by using the multi-ISE arrays (26-31). Some of these reported studies are only for anion analysis, while others are based on the analysis of both anions and cations. Also, in some cases, while the

study was designed for the simultaneous determination of more than one anion, researchers could not get that point by virtue of the interfering effect of analytes on each other (32).

Different multivariate calibration methods can be used during the electronic tongue studies, such as Classical Least Squares (CLS), Principal Component Regression (PCR) and Partial Least Squares (PLS1). Among all these methods, PLS1 is one of the most preferred multivariate calibration methods for the simultaneous determination of interfering species. It has also been previously reported that, in many different respects, PLS can be considered as a first-stop convenience method because it is well known and used (33).

In the study described here, a multi-ion-selective electrode array (multi-ISE array) was designed for the simultaneous determination of chloride and nitrate anions in the air samples. The system was used for analyzing the fume-hood samples, and the obtained results were evaluated by PLS1. While there are previously reported studies with the application in various samples such as water, beverages, honey, etc., to the best of our knowledge, this is the first study in which simultaneous determination of chloride and nitrate ions has been conducted in air samples by using a multi-ISE array and multi-variable calibration methods.

EXPERIMENTAL SECTION

Reagents and Solutions

Acetic acid, ammonium acetate, disodium hydrogen phosphate (Na_2HPO_4), potassium dihydrogen phosphate (KH_2PO_4), hydrochloric acid, nitric acid, sodium acetate, sodium chloride, sodium hydroxide, and sodium nitrate were purchased from Merck. Deionized water (Mes Mp Minupure Basic pure) was used to prepare stock solutions, buffer solutions, and synthetic samples.

Equipment

The potential measurements were conducted by a Lawson EMF-16 multiplexer, and the obtained data was recorded in a computer via EMF program. During the measurements, a double junction Ag/AgCl electrode (Thermo Orion) was used as a reference electrode. A Sentek P11 pH electrode was used for pH measurements. The chloride-selective electrode (Sentek) and the nitrate-selective electrode (Sentek) used in the study were commercially available. The fume-hood samples were prepared by using an air sampling pump (GirlAir-PLUS).

Preparation of the training set solutions

Chloride and nitrate stock solutions were prepared from sodium salts. A two-factor/five-level experimental design was used to prepare the training set solutions, and the five-level experimental design was simplified to 25 calibration solutions as described in the literature

(34). The level and concentration values of training set solutions are given in Table 1. 5 mL of chloride and nitrate stock solutions (ten times concentrated according to the concentrations stated in Table 1)

and 5 mL of pH=5.0 acetic acid/sodium acetate buffer were placed into a volumetric flask, and the final volume was completed to 50 mL with deionized water.

Table 1: Level and concentration values for the calibration solutions.

Level Values	Cl ⁻ (mol/L)	NO ₃ ⁻ (mol/L)
-2	0.0001	0.0001
-1	0.0003	0.0003
0	0.0010	0.0010
1	0.0030	0.0030
2	0.0100	0.0100

Preparation of synthetic samples

Both synthetic chloride and nitrate samples were prepared with a concentration of 0.002 mol/L. 5 mL synthetic sample stock solution (ten times concentrated stock solutions) and 5 mL pH=5.0 acetic acid/sodium acetate buffer were mixed in a volumetric flask, and the final volume was completed to 50 mL with deionized water.

hood and kept at the specified time. Hydrochloric acid and nitric acid solutions were placed in a glass beaker and heated by a heater to evaporate more quickly. The air sampling pump, which was adjusted to 3000 mL per minute, was attached to the washing flask. The air sample was collected in the washing flask for three hours and thirty minutes.

Preparation of fume-hood samples

The air sample collection mechanism used during the study is shown in Figure 1. 0.001 mol/L 200 mL NaOH solution was put into the washing flask of the mechanism. The mechanism was placed in a fume-

5 mL of air sample collected in NaOH solution and 5 mL of buffer solution were mixed in a volumetric flask, and the final volume was adjusted to 50 mL with deionized water.



Figure 1: The air sample collection mechanism.

Potentiometric measurements

The multi-ISE array consists of a chloride-selective commercial electrode, a nitrate-selective commercial electrode and a double junction

Ag/AgCl reference electrode. Potentiometric measurements were conducted in the presence of acetic acid/ sodium acetate buffer solution (pH=5.0). The EMF measurement of the multi-ISE

array was compared against the reference electrode. The changes in the EMF were measured twice consecutively with the Lawson L-EMF DAQ 3.0 software of the multiplexer, and these changes were recorded on a computer.

Data Processing

The acquired data were evaluated by using PLS1. A training set and a potential matrix with basic codes written in the laboratory in Octave 5.1.0 free licensed software compatible MATLAB were used in order to perform the multivariate calibration techniques (9, 34). The EMF values of the training set, synthetic samples, and the fume-hood samples were recorded in the computer. The predicted values were calculated, and the differences between the known and the predicted concentrations were used to evaluate the EMF values.

First, a cross-validation process was performed with the results of training set solutions. After that, the number of principal components was found by plotting the predicted residual error of sum of squares (PRESS) values against the factor numbers. Chloride and nitrate concentrations were estimated in the training, synthetic and fume-hood sample sets with PLS1 by applying a cross-validation process again with the number of principal components obtained by the graphical results.

Analysis of the synthetic and fume-hood samples

The synthetic samples and the fume-hood samples were analyzed with the prepared multi-electrode array. In order to calculate the recovery values, the standard addition method was used. Chloride and nitrate standard solutions (1 mol/L) were spiked to both synthetic and fume-hood samples after the calibration with the training set. Standard additions were conducted by using 50 μL , 100 μL , 100 μL , 100 μL volumes respectively. Percentage recoveries of both chloride and nitrate anions were obtained using the difference between the anion concentrations calculated at the end of the standard addition and the initially calculated anion concentrations.

RESULTS AND DISCUSSION

Performance characteristics of the ion-selective electrodes

In nitrate and chloride calibration solutions, the slopes, correlation coefficients (R^2), and linear working ranges of each ion-selective electrode composing a multi-ISE array were determined separately. Calibration solutions were prepared in the range of $1,0 \times 10^{-1}$ mol/L - $1,0 \times 10^{-6}$ mol/L. Also, the selectivity coefficients of electrodes against other analyte ions were determined by using the IUPAC recommended separate solution method (35). The selectivity coefficients and the performance characteristics calculated from calibrations are given in Table 2.

Table 2: Performance characteristics of the ion-selective electrodes.

Ion-selective electrode	Slope (mV per decade)	R^2	Working Range (mol/L)	$\log K_{A,B}^*$
Chloride	51.48	0.9999	1×10^{-1} - 1×10^{-3}	0.205
Nitrate	51.15	0.9964	1×10^{-1} - 1×10^{-4}	1.054

$$*E_2 - E_1 / \pm s = \log K_{A,B}$$

The effect of pH on the performance of ion-selective electrodes

To determine the effect of pH on the performance of the ion-selective electrodes, the measurements were carried out in the solutions that contained no buffer, pH=7.0 buffer (ammonium acetate),

pH=6.8 ($\text{KH}_2\text{PO}_4/\text{Na}_2\text{HPO}_4$) buffer and pH=5.0 (acetic acid/sodium acetate) buffer. When the obtained data were evaluated, it was observed that the best slope, intercept and R^2 values were gained at pH=5.0. The results are detailed in Table 3.

Table 3: The effect of pH on the performance of the multi-ISE array.

Buffer Solution	Ion	Slope	R^2	Intercept
No Buffer	NO_3^-	0.9929	0.9862	0.0003
	Cl^-	0.9847	0.9725	0.0005
pH=7.0 Buffer	NO_3^-	0.9829	0.9973	0.0002
	Cl^-	0.7864	0.8647	0.0004
pH=6.8 Buffer	NO_3^-	0.9903	0.9942	0.0003
	Cl^-	0.9739	0.9741	0.0008
pH=5.0 Buffer	NO_3^-	0.9962	0.9987	0.00008
	Cl^-	0.9972	0.9938	0.00007

Data Processing

Cross-Validation: To perform the cross-validation of the method "leave-one-out" technique was used. In accordance with this purpose, one of the 25 training set solutions was accepted as a sample, and the remaining 24 training set solutions were used in calibration. In the calibration made with 24 training solutions, the content of the 25th solution was determined. The same procedure was repeated for each solution.

PRESS values and the factor numbers were plotted by using distinctions between known and predicted concentrations in each solution. The principal

component numbers were appointed from the minimum points of these graphs. The obtained graphs are given in Figure 2. The principal component numbers were six for both chloride and nitrate by PLS1.

The concentrations of the analytes in synthetic samples were estimated via PLS1 by applying a cross-validation process with the principal component numbers. The percentage recovery values calculated according to described in Experimental Section were found $103.8\% \pm 3.5$ and $103.1\% \pm 1.6$ for chloride and nitrate, respectively.

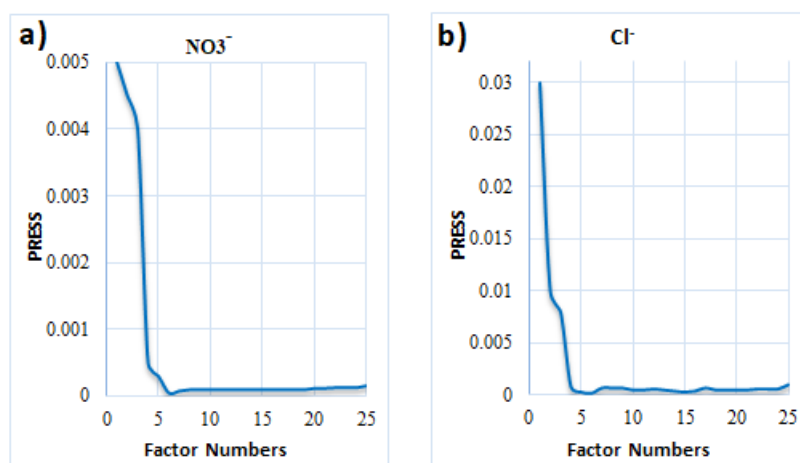


Figure 2: The number of factors according to PRESS values for PLS1 method.

Analytical application of the multi-ISE array to the fume-hood samples

The $C_{\text{known}} - C_{\text{predicted}}$ graphs obtained by PLS1 are given in Figure 3. Measurements were taken with multi-ISE in six different fume cupboard samples prepared according to described in Experimental

Section. The chloride and nitrate concentrations were calculated by PLS1, and according to these calculations, 0.63 m³ of air was drawn from the fume-hood and 41.87 mg chloride ions and 77.46 mg nitrate ions were found in 1 m³ air.

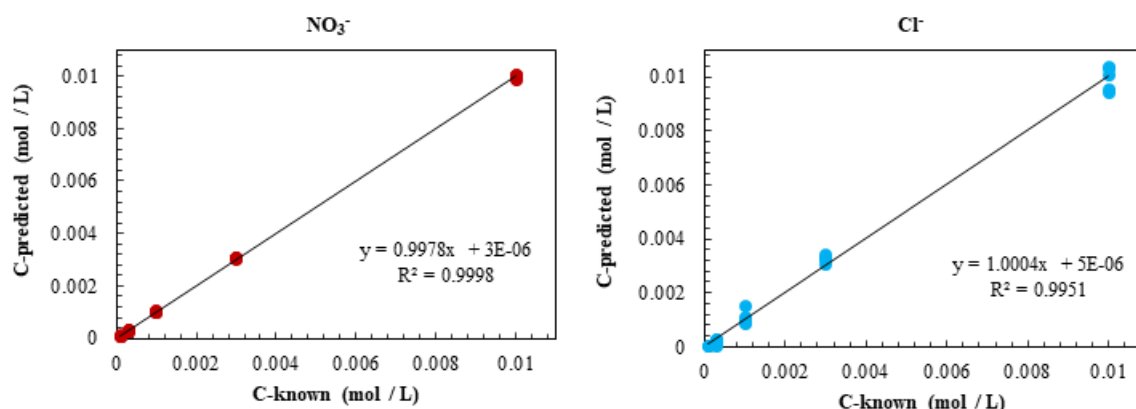


Figure 3: The concentration values calculated by PLS1 against the known concentrations.

When the percentage recovery values calculated from the standard addition were evaluated, it was observed that these values were $93.8\% \pm 3.8$ and $102.4\% \pm 2.5$ for chloride and nitrate, respectively. In addition, the percentage recovery results were

checked for systematic errors using the *t*-test and it was determined that there was no systematic error at 99% confidence level (degree of freedom (DF):3) in the results obtained from the multi-ISE array (Table 4). According to these results, it can

be concluded that the use of multi-variable calibration methods with the multi-ISE array is could be a good alternative for the anion analysis

because it is not only easy and cheap but also gives good recovery values.

Table 4: Statistical comparison of the nitrate and chloride concentrations in fume-hood samples.

	Analyte	Recovery%	t_e	t_c	$t_c > t_e$
$t_e = \frac{\mu - \bar{x}}{\frac{s}{\sqrt{n}}}$	NO ₃ ⁻	102.4 ± 2.5	1.92	5.84	5.84 > 1.92
	Cl ⁻	93.8 ± 3.8	3.26	5.84	5.84 > 3.26

There are many commercially available anion and cation-selective electrodes on the market. The costs of these electrodes are quite affordable compared to more complex analytical devices, which are suitable for benchtop analysis. In fact, the proposed system can be used in different sample matrices for different anions/cations with the help of a chemometric approach and different ion-selective electrodes. On the other hand, in the light of this study, laboratories can also develop similar systems with ion-selective electrodes, which they designed.

Results obtained from single ion-selective electrodes

Both nitrate and chloride concentrations in the fume-hood samples were determined using single ion-selective electrodes. To that end, potential readings were acquired in the calibration solutions of the analytes to each ion-selective electrode sensitive, and concentration values were obtained by using the created calibration curves and the Nernst equation. As indicated in Table 5, there is a significant difference between the results obtained from single ion-selective electrodes and multi-ISE array, especially for nitrate concentrations.

Table 5: The percentage recoveries of Cl⁻ and NO₃⁻ in fume hood samples by using single ISEs.

	ISE	Analyte	Recovery%	t_e	t_c	$t_c > t_e$
$t_e = \frac{\mu - \bar{x}}{s/\sqrt{n}}$	Nitrate ISE	NO ₃ ⁻	60.3 ± 3.1	25.61	5.84	5.84 < 25.61
	DF : 3	Chloride ISE	Cl ⁻	104.1 ± 5.3	1.55	5.84

According to these results, it can be concluded that the use of a multi-ISE array in the analysis could be more advantageous. Also, more accurate results can be gained compared to a single electrode.

CONCLUSION

In this study, we proposed a multi-ISE array for the simultaneous determination of chloride and nitrate anions in air samples. The system was used to analyze the synthetic samples and fume-hood samples in terms of the amount of chloride and nitrate anions. The measurement system was consisted of two ion-selective electrodes, an Ag/AgCl double-junction reference electrode, and a multi-potentiometer. The obtained data were evaluated by using PLS1. The application of the multi-ISE array was demonstrated by the simultaneous determination of nitrate and chloride ions in air samples obtained from a fume-hood with good recoveries. The presented sensor could be an easy to use approach for monitoring the amount of chloride and nitrate in the scope of occupational health and safety analysis.

While it is possible to analyze samples taken from air samples by chromatography systems combined with thermal desorption, it is possible to conduct the analysis more straightforward and cheaper

with the system proposed in the study. To the best of our knowledge, this is the first study in which simultaneous determination of chloride and nitrate ions has been carried out in air samples by a multi-ISE array and multi-variable calibration methods. Considering the benefits of the proposed system, such as reducing costs and minimizing the need for extensive facilities and number of personnel, we believe that this study will elucidate future studies and will be of interest to most laboratories that carry out similar analyses.

CONFLICT OF INTEREST

The authors declare that they have no conflict of interest.

ACKNOWLEDGMENTS

The authors gratefully acknowledge the financial support of Ankara University Research Fund (BAP No. 12B4240008).

REFERENCES

- Gómez-Ordóñez E, Alonso E, Rupérez P. A simple ion chromatography method for inorganic anion analysis in edible seaweeds. *Talanta*. 2010;82(4):1313-1317. <DOI>.

2. Baryla NE, Lucy C. A. Semi-permanent surfactant coatings for inorganic anion analysis in capillary electrophoresis. *J. Chromatogr. A.* 2002;956(1-2):271-277. [<DOI>](#).
3. Zhang J, Harris A R, Cattrall RW, Bond AM. Voltammetric ion-selective electrodes for the selective determination of cations and anions. *Anal. Chem.* 2010;82(5):1624-1633. [<DOI>](#).
4. Dalkıran B, Ertürün HEK, Özel AD, Canel E, Özkınalı S, Kılıç E. Chromate-selective electrodes prepared by using calix [4] arenes for the speciation of Cr (VI) and Cr (III). *Ionics.* 2017;23(9):2509-2519. [<DOI>](#).
5. Suman S, Singh R. Anion selective electrodes: A brief compilation. *Microchem. J.* 2019;(149):104045. [<DOI>](#).
6. OSHA 3084, (1998). Chemical Hazard Communication U.S. Department of Labor Occupational Safety and Health Administration. June 01, 2022 [<URL>](#).
7. Hazardous Substance Fact Sheet, Hydrogen Chloride (2016). June 01, 2022. [<URL>](#).
8. Hazardous Substance Fact Sheet, Nitric Acid (2016). June 01, 2022. [<URL>](#).
9. Gemperline P. Practical Guide to Chemometrics. 2nd ed. Boca Raton: CRC Press; 2006. [<DOI>](#).
10. Moreno-Martin G, León-González ME, Madrid Y. Simultaneous determination of the size and concentration of AgNPs in water samples by UV-vis spectrophotometry and chemometrics tools. *Talanta.* 2018;(188):393-403. [<DOI>](#).
11. Altunay N, Katin KP, Gürsoy N, Elik A, Şimşek S, Kaya S. Spectrophotometric determination of aflatoxin B1 in food sample: Chemometric optimization and theoretical supports for reaction mechanisms and binding regions. *J. Food Compos. Anal.* 2020;(94):103646. [<DOI>](#).
12. Elmas ŞNK, Arslan FN, Akin G, Kenar A, Janssen HG, Yılmaz I. Synchronous fluorescence spectroscopy combined with chemometrics for rapid assessment of cold-pressed grape seed oil adulteration: Qualitative and quantitative study. *Talanta.* 2019;(196):22-31. [<DOI>](#).
13. Ata Ş, Akyüz M, Dinç E. Chemometric approach to the optimisation of LC-FL and GC-MS methods for the determination of nitrite and nitrate in some biological, food and environmental samples. *Int. J. Environ. Anal. Chem.* 2016;96(7):636-652. [<DOI>](#).
14. Gardiner J, Stiff MJ. The determination of cadmium, lead, copper and zinc in ground water, estuarine water, sewage and sewage effluent by anodic stripping voltammetry. *Water Res.* 1975;9(5-6):517-523. [<DOI>](#).
15. Locatelli C, Torsi G. Determination of Se, As, Cu, Pb, Cd, Zn and Mn by anodic and cathodic stripping voltammetry in marine environmental matrices in the presence of reciprocal interference. Proposal of a new analytical procedure. *Microchem. J.* 2000;65(3):293-303. [<DOI>](#).
16. Ergün EGC, Kenar A. Simultaneous determination of copper (II) and zinc (II) via simple acid-base titrimetry using glass pH electrode. *Turk. J. Chem.* 2018;42(2):257-263. [<DOI>](#).
17. Del Valle M. Sensor arrays and electronic tongue systems. *Int. J. Electrochem.* 2012;212:986025. [<DOI>](#).
18. Ataş HB, Kenar A, Taştekin M. An electronic tongue for simultaneous determination of Ca²⁺, Mg²⁺, K⁺ and NH₄⁺ in water samples by multivariate calibration methods. *Talanta.* 2020;(217):121110. [<DOI>](#).
19. Eylem CC, Taştekin M, Kenar A. Simultaneous determination of copper and zinc in brass samples by PCR and PLS1 methods using a multiple ion-selective electrode array. *Talanta.* 2018;(183):184-191. [<DOI>](#).
20. Saurina J, López-Aviles E, Moal A, Hernández-Cassou S. Determination of calcium and total hardness in natural waters using a potentiometric sensor array. *Anal. Chim. Acta.* 2002;464(1):89-98. [<DOI>](#).
21. Gallardo J, Alegret S, Muñoz R, De-Román M, Leija L, Hernandez PR, Del Valle M. An electronic tongue using potentiometric all-solid-state PVC-membrane sensors for the simultaneous quantification of ammonium and potassium ions in water. *Anal. Bioanal. Chem.* 2003;377(2):248-256. [<DOI>](#).
22. Calvo D, Bartrolí J, Del Valle M. Multicomponent Titration of Calcium+ Magnesium Mixtures Employing a Potentiometric Electronic-Tongue. *Anal. Lett.* 2007;40(8):1579-1595. [<DOI>](#).
23. Wilson D, Del Valle M, Alegret S, Valderrama C, Florido A. Potentiometric electronic tongue-flow injection analysis system for the monitoring of heavy metal biosorption processes. *Talanta.* 2012;93:285-292. [<DOI>](#).
24. Calvo D, del Valle M. Simultaneous titration of ternary alkaline-earth mixtures employing a potentiometric electronic tongue. *Microchem. J.* 2007;87(1):27-34. [<DOI>](#).
25. Nery EW, Kubota LT. Integrated, paper-based potentiometric electronic tongue for the analysis of beer and wine. *Anal. Chim. Acta.* 2016;918:60-68. [<DOI>](#).
26. Cortina M, Duran A, Alegret S, Del Valle M. A sequential injection electronic tongue employing the transient response from potentiometric sensors for anion multidetermination. *Anal. Bioanal. Chem.* 2006;385(7):1186-1194. [<DOI>](#).
27. Cuartero M, García MS, Ortuño JA. Differential dynamic potentiometric responses obtained with ion-selective electrodes for perchlorate, thiocyanate, iodide, nitrate, sulfate, picrate and bis (trifluoromethylsulfonyl) imide. *Electrochim. Acta.* 2013;(93):272-278. [<DOI>](#).
28. Wilson D, Abbas MN, Radwan ALA, Del Valle M. Potentiometric electronic tongue to resolve mixtures of sulfide and perchlorate anions. *Sensors.* 2011;11(3):3214-3226. [<DOI>](#).
29. Gil L, García-Breijo E, Ibañez J, Labrador RH, Llobet E, Martínez-Máñez R, Soto J. Electronic tongue for qualitative analysis of aqueous solutions of salts using thick-film technology and metal electrodes. *Sensors.* 2006;6(9):1128-1138. [<DOI>](#).
30. Shirmardi A, Shamsipur M, Akhond M, Monjezi J. Electronic tongue for simultaneous determination of cyanide, thiocyanate and iodide. *Measurement.* 2016;88:27-33. [<DOI>](#).
31. Nuñez L, Cetó X, Pividori MI, Zanon MVB, Del Valle M. Development and application of an electronic tongue for detection and monitoring of nitrate, nitrite and ammonium levels in waters. *Microchem. J.* 2013;110:273-279. [<DOI>](#).

32. Gutiérrez M, Alegret S, Caceres R, Casadesús J, Marfa O, Del Valle M. Application of a potentiometric electronic tongue to fertigation strategy in greenhouse cultivation. *Comput. Electron. Agr.* 2007;57(1):12-22. [<DOI>](#).

33. Ni Y, Kokot S. Does chemometrics enhance the performance of electroanalysis?. *Anal. Chim. Acta.* 2008;626(2):130-146. [<DOI>](#)







34. Brereton RG. Multilevel Multifactor Designs for Multivariate Calibration. *Analyst.* 1997;122(12):1521-1529. [<DOI>](#).

35. Brereton RG. *Chemometrics*. Chichester, UK: John Wiley & Sons; 2003. ISBN: 978-0-470-84574-5.

36. Umezawa Y, Umezawa K, Sato H. Selectivity coefficients for ion-selective electrodes: recommended methods for reporting K_A , B_{pot} values (Technical Report). *Pure Appl. Chem.* 1995;67(3):507-518. [<DOI>](#).



Comparative Studies of some Chemical and Micronutrient Contents in three Sprouted Samples of Bambaranut (*Vigna subterranean* [I] verdc.) Landraces

Tasiu Mikail^{1,2} , Muhammad Sani Sule² , Adamu Jubril Alhassan² ,
Abdullahi Abdulkadir Imam² , Yusuf Yunusa Muhammad² , Sagir Ismail¹ ,
Kamaluddeen Babagana² , Abdulmumin Yunusa¹ 

¹Kano University of Science and Technology, Department of Biochemistry, Wudil, Nigeria

²Bayero University, Department of Biochemistry, Kano, Nigeria

³Bayero University, Department of Animal Science, Kano, Nigeria

Abstract: The research was carried out to evaluate the effect of sprouting on chemical and micronutrient contents of Bambaranut (*Vigna subterranea* [I] verdc.) grown in Kano, Nigeria. Three landraces of Bambaranut (cream, black and zebra) were used for the study. The proximate and mineral contents were analyzed in accordance with the standard methods of analysis. The result of the proximate analysis showed that the moisture and carbohydrate contents reduced significantly ($P < 0.05$) after sprouting while ash, crude protein, crude fat, and crude fiber significantly increased, there was no significant ($P < 0.05$) difference in moisture, crude fiber, and carbohydrate contents between the landraces. The landraces differ in crude protein and fat contents. The results of minerals analysis shows that the landraces differ significantly in Na, Fe, Ca, K, Mg, and Se. However, the amount of Zn, Mn did not significantly differ between the landraces irrespective of sprouting or not. All the three landraces did not differ ($P < 0.05$) in Cu contents. Sprouting leads to decrease in Na, Fe, K, Zn, Mg and Se and increase in Ca and Mn. This study showed that sprouting improves the nutritional quality of Bambaranut irrespective of the landrace.

Keywords: Sprouting, Chemical, Micronutrients, Bambaranut

Submitted: August 27, 2022. **Accepted:** January 14, 2023.

Cite this: Mikail T, Sule MS, Alhassan AJ, Imam AA, Muhammad YY, Sagir I, et al. Comparative Studies of some Chemical and Micronutrient Contents in three Sprouted Samples of Bambaranut (*Vigna subterranea* [I] verdc.). JOTCSA. 2023;10(1):97-108.

DOI: <https://doi.org/10.18596/jotcsa.1167021>.

***Corresponding author. E-mail:** tasiuikail@kustwudil.edu.ng.

1. INTRODUCTION

Bambaranut (*Vigna subterranea* (L.) Verdc) is the third most important grain legume in semi-arid Africa. Resistant to high temperature, drought, insect and weevil attack, bambaranut is suitable for poor soils and has high nutritive value (1). Bambaranut (*Vigna subterranea* (L.) Verdc) has a large number of landraces throughout Africa where small-scale farmers have preserved its genetic diversity on-farm (2). Bambara groundnut is an excellent source macro and micronutrients and has

nutritional potentials that can mitigate malnutrition when properly explored. Therefore, Bambaranut is very important food for poor people especially in Africa who cannot have access to the expensive animal protein. The seed of Bambaranut (Figure 1) is rich in essential amino acids including isoleucine, leucine, lysine, methionine, phenylalanine, threonine, and valine but has not been considered as staple food as cereals such as wheat, maize, and rice (3). Bambara groundnut oil could have medicinal and nutritional benefits, it contains saturated fatty acids that help in lowering the

levels of LDL cholesterol in while increasing HDL cholesterol in blood, this can in turn lower the risk of developing cardiovascular diseases, while providing nutrients, such as vitamin E.

Sprouting is a period characterized by intense metabolic activity in the plant and represents a re-emerging trend in healthy foods and has positive impact on the enhancement of the nutritional properties (4) and taste (5). Germination was reported to increase the nutritional value of cereals and legumes through activation of endogenous enzymes (6). According to the European Sprouted Seeds Association (ESSA) (7) sprouts are the product that results from the germination of seeds and their growth in water or another medium, harvested prior to the development of true leaves and which is set to be eaten whole, including the seed. Consumption of sprouted grains is said to be useful for human health. Positive consumer perceptions about sprouted cereals have resulted in new food and beverage product launches (8). Under ambient conditions, when grains and seeds are soaked and sprouted, endogenous and newly synthesized enzymes begin to alter the seed constituents. Thus, complex macromolecules are broken down into lower molecular weight molecules which are more digestible and more readily absorbed by the body (9). In this work, we determine the effect of sprouting on proximate and mineral composition of three landraces of bambaranut grown in Kano, Nigeria.



Figure 1: Bambaranut seeds.

2. MATERIALS AND METHODS

2.1. Sample Collection and Preparation

Three Bambaranut landraces samples (cream, black, and zebra) were obtained from four areas of Kano state. The sample was sorted, cleaned, washed, and soaked in water overnight. The water was changed at intervals of 3 hours to avoid fermentation (10). The cream and zebra colored samples were soaked for 15 hours overnight whereas the black colored was soaked for 24 hours. The soaked samples were placed in petri dishes for germination period of 5 days. The dishes were covered with cotton to create enabling environment for sprouting to occur. After a period of 5 days, the samples developed shoots (sprouts)

(see Figure 3A, B and C). After sprouting, the sprouted samples were dried and milled. The resulting powdered samples were used for proximate and mineral analysis. The graphical sketch of sprouting are presented in Figure 2.

3. METHODS

3.1. Determination of the Proximate Composition

The proximate composition (moisture, ash, crude protein, crude fat, fiber, and carbohydrate) of Bambaranut was determined in accordance with standard methods of AOAC (11) as follows.

3.2. Determination of Moisture Content

A clean petri dish was weighed (W_1) and 5 g of the powdered sample was placed in the dish and then weighed (W_2). The content was placed in an oven at 120 °C for 3 hours. The dish was removed and cooled in desiccators for 30 minutes and finally weighed (W_3) (14). The moisture content was calculated using the equation below.

$$\%Moisture = \frac{W_2 - W_3}{W_2 - W_1} \times 100$$

3.3. Determination of Ash Content

A clean crucible was weighed (W_1) and 5 g of dried powdered sample was measured in to the crucible and weighed (W_2). The crucible was transferred in to muffle furnace at 550 °C for ashing. After ashing, the furnace was turned off and allowed to cool. The samples were carefully removed from the furnace to avoid losing ash that may be fluffy. The crucibles were transferred to desiccator and allowed to cool for 30 minutes and then weighed (W_3) (13). The ash content was calculated using the following equation

$$\%Ash = \frac{W_3 - W_1}{W_2 - W_1} \times 100$$

3.4. Determination of Crude Protein Content

The crude protein was determined by Kjeldahl distillation as described by (13). Based on the Kjeldahl procedure, proteins and other organic food constituents in a sample are digested using sulfuric acid and with catalysts. The total organic nitrogen is transformed to ammonium sulfate and the digest is neutralized using alkali and distilled into a boric acid solution. The resulting borate anions are titrated using standardized acid, which is converted to nitrogen in the sample. The result of the analysis represents the crude protein content of the food because nitrogen also comes from non-protein components.

3.5. General Procedures and Reactions

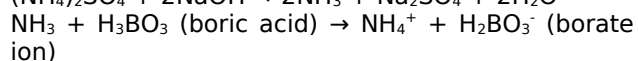
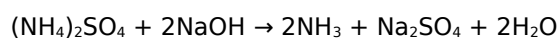
3.5.1. Digestion

The samples were placed in Kjeldahl flask. Acid and catalyst were added to the flask, the mixtures were

allowed to digest formation of clear mixture indicates a complete breakdown of all organic matter in the samples. Non volatile ammonium sulfate was formed in the reaction of nitrogen and sulfuric acid. in the course of digestion, protein nitrogen was liberated leading to the formation of ammonium ions, sulfuric acid oxidizes organic matter and reacts with ammonium that was formed, carbon and hydrogen are converted to carbon dioxide and water.

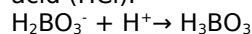
3.5.2. Neutralization and distillation

The digest was diluted using water. Alkali containing sodium thiosulfate was added so that the sulfuric acid is neutralized. The resulting ammonia was distilled into a boric acid solution containing the indicators methylene blue and methyl red.



3.5.3. Titration

Borate ion (proportional to the amount of nitrogen) is titrated with standardized 0.02 M Hydrochloric acid (HCl).



The amount of nitrogen was calculated using the following formula

Moles of HCl = Moles of NH_3 = Moles of N in the sample

A reagent blank is run and reagent nitrogen was subtracted from the sample nitrogen.

$$\%N = \frac{NH_4Cl \times \text{corrected acid volume}}{\text{weight of sample in g}} \times \frac{14 \text{ g of N}}{1 \text{ mole of N}} \times 100$$

Where NH_4Cl = Normality of HCl in moles/1000 mL
Corrected acid volume = (mL of std. acid for sample) - (mL of std. acid for blank)

14 = atomic weight of nitrogen

A factor is used to convert percent N to percent crude protein. Most proteins contain 16 percent N, so the conversion factor is 6.25 (100/16 = 6.25).

$\% N \times 6.25 = \% \text{ protein}$

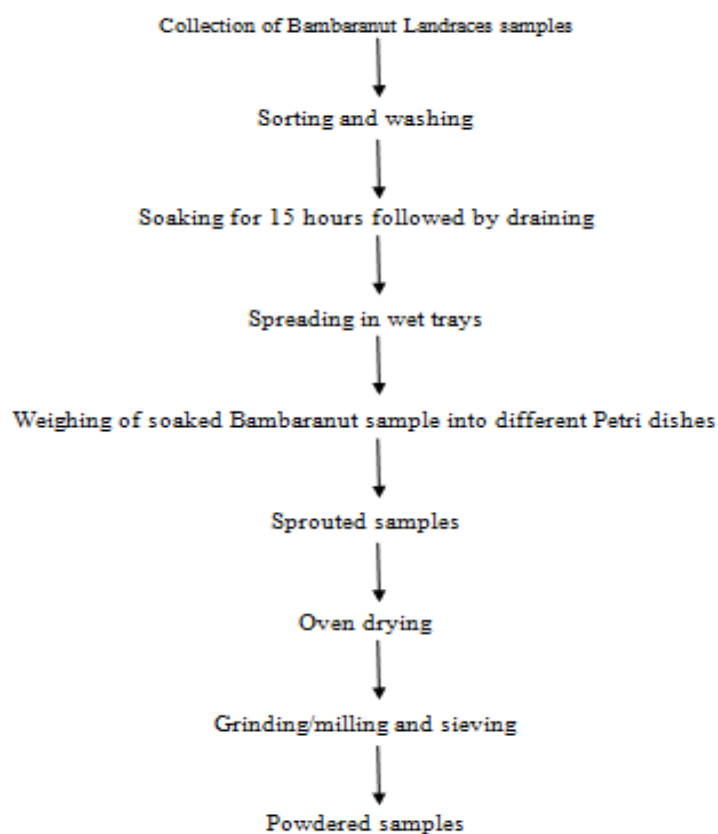


Figure 2: Schematic presentation of sprouting.

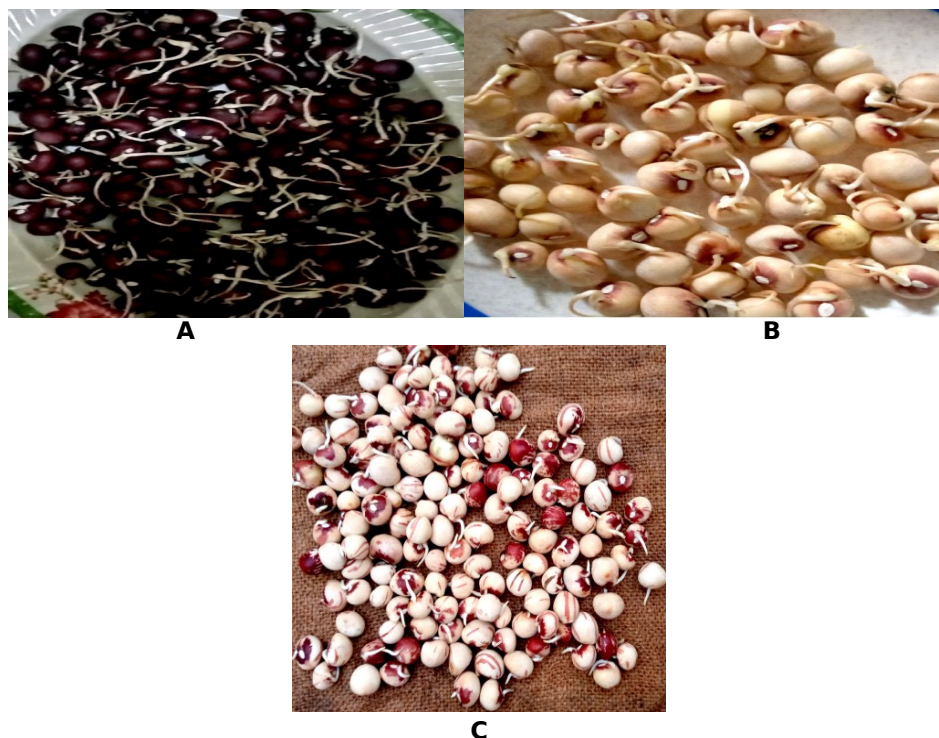


Figure 3: Sprouted Bambaranut (A) Black landrace, (B) Cream landrace (C) Zebra landrace.

3.6. Determination of Crude Fat

3.6.1. Principle

Organic solvents, such as petroleum ether, have the ability to dissolve fat in a given sample. It has a low boiling point (40-80 °C). Therefore when in Soxhlet assembly connected to a reflux condenser, it dissolves the fat in the sample and washes it down in to the flask, and the ether can easily be evaporated and recollected afterwards. The difference in weight between the empty flask before extraction and the weight of flask after extraction gives the weight of lipid being extracted (13).

3.6.2. Procedure

A quantity (3 g) of the sample was carefully weighed (W_1) in to a folded filter paper and small cotton wool placed on top. The content was accurately tied by a thread at both ends of the filter paper and weighed. The content was positioned in the extraction thimble and little cotton wool positioned on top. The whole apparatus was subsequently connected following the addition of 300 milliliters of petroleum ether in to the extraction flask and weighed (W_2). The extraction was maintained for 3 hours by means of the heating mantle and making sure of the incessant flow of water in the condenser. The sample was then removed, air-dried and then positioned in an oven at 80 °C until a constant weight was determined. The extraction flask was transferred to an oven so that the solvent (petroleum ether) can easily be evaporated leaving behind the extract. After evaporation the flask was weighed (W_3). The crude fat in the sample was

calculated using the following equation;

$$\% \text{ crude fat in the sample} = \frac{W_3 - W_2}{W_1} \times 100$$

3.7. Determination of Crude Fiber

Crude fiber is the insoluble and combustible organic residue which remains after the sample has been treated under prescribed conditions of consecutive treatments with light petroleum ether, boiling in dilute sulfuric acid and sodium hydroxide, and washing with boiling water, alcohol and petroleum ether (13).

3.7.1. Procedure

In to the extraction apparatus, 3 g of the sample was weighed and extracted three times using light petroleum ether by stirring, settling followed by decantation. The extracted air dried sample was placed in to a dried 100-milliliter conical flask, 200 mL of 0.127 sulfuric acid was added in to the flask, the sample was dispersed by some of the solution. The content was boiled for 30 minutes, at the same time a stable volume was maintained. The flask was made to rotate every few minutes so as to mix up the contents and get rid of particles from the side. The Buchner funnel was prepared while waiting for the mixture to boil. The Buchner funnel was preset to a perforated plate and linked with the funnel, the filter paper was as well preset to envelop the openings in the plate. The boiled water was added in to the funnel and was allowed to wait until the funnel was hot and afterwards drained by suction. At the end of 30 minutes of the boiling

period, the mixture was allowed to stand for a minute and then poured immediately in to shallow layer of hot water under gentle suction in to the funnel. The insoluble matter was washed with boiled water for several times until the washing was free from acid, then it was washed back in to the original flask by means of a wash bottle containing 200 mL of 0.313 M sodium hydroxide solution. The mixture was boiled for 30 minutes with the same precautions as those used in the earlier boiling with acid. After 30 minutes of boiling, it was made to stand for a minute and subsequently filtered without delay. The insoluble material was placed in to the filter paper using boiling water, after that it was washed using 1% hydrochloric acid, it was finally washed with boiling water making it free from acid. This was subsequently washed two times using alcohol and three times using petroleum ether. The insoluble material was then placed in to a dried weighed crucible and dried at 100 °C to constant weight. The crucible with its contents was transferred to a heating mantle in a fume cupboard to remove the organic matter. Subsequently, the crucible was transferred to a muffle furnace at 550°C for 3 hours. The ash content was then obtained by weighing. The crude fiber was calculated using the following equation;

$$\%Crude\ Fiber = \frac{weight\ of\ ash}{weight\ of\ sample} \times 100$$

3.8. Determination of Carbohydrate by Difference

Carbohydrate content was determined by difference as follows;

$$\%Carbohydrate = 100 - (Moisture + Ash) \\ (+ Protein + Lipid + Crude Fiber)$$

3.9. Determination of Mineral Elements Atomic Absorption Spectroscopy (AAS)

Principle

Atomic Absorption Spectrophotometer is an analytical instrument that is based on the principle of atomic absorption spectroscopy. This involves the aspiration of sample solution into the flame and the sample element is changed to atomic vapor. The flame therefore contains atoms of that

element. Some are thermally energized by the flame, but the majority stayed in the ground state. These ground state atoms subsequently absorb radiation of particular wavelengths that is formed by a special source prepared from that element. The absorption follows Beer's Law, that the absorbance is directly proportional to the concentration of the atomic vapor in the flame. That is the concentration of atomic vapor is directly proportional to the concentration of the element in solution being aspirated (16).

3.9.1. Procedure for AAS

The minerals (Ca, Cu, Fe, K, Mg, Mn, Na, Zn, and Se) were determined by Atomic Absorption Spectrophotometer as described by (15). A hollow cathode lamp was selected for the analysis, the lamp was made to warm up for 15 minutes. For the duration of the 15 minutes period, the instrument was aligned by positioning the monochromator at the right wavelength. The monochromator slit width was chosen. The hollow cathode current was as well adjusted in line with the manufacturer's reference. Afterward, the flame was lit and the flow of fuel and oxidant were regulated. The burner and nebulizer flow rate for maximum percent absorption and stability were adjusted after which the photometer was balanced. The samples were aspirated and the concentrations were obtained using calibration curve. A series of standards of the elements in question were run and a calibration curve was constructed by plotting the concentrations of the standards against the absorbance.

3.10. Statistical analysis

Results were analyzed by two-way analysis of variance (Post hoc) using SPSS software. Difference of mean were determined at P<0.05 level of significance.

4. RESULTS

4.1. Proximate Composition

Table 1 presents the effect of sprouting on the proximate contents of three landraces of Bambaranut grown in Kano. The result indicates significant increase in ash, crude protein, crude fat, and crude fiber and decrease in moisture and carbohydrate contents after sprouting.

Table 1: Effect of sprouting on the proximate contents of three landraces of Bambaranut.

Parameter (%)	Sprouted			Unsprouted		
	Black	Cream	Zebra	Black	Cream	Zebra
Moisture	7.10 ± 0.50 ^a	7.42 ± 0.06 ^a	6.81 ± 0.16 ^a	11.99 ± 1.03 ^b	12.01 ± 0.22 ^b	12.09 ± 0.04 ^b
Ash	4.68 ± 0.29 ^a	4.28 ± 0.05 ^b	4.30 ± 0.02 ^a	2.09 ± 0.05 ^c	3.84 ± 0.25 ^d	2.25 ± 0.08 ^c
Crude Protein	17.45 ± 0.56 ^a	19.93 ± 0.13 ^b	15.65 ± 0.37 ^c	4.63 ± 0.07 ^d	10.05 ± 0.08 ^e	6.23 ± 0.05 ^f
crude Fat	14.25 ± 0.59 ^a	14.12 ± 0.08 ^a	15.15 ± 0.07 ^b	11.93 ± 0.61 ^c	3.15 ± 0.32 ^d	9.99 ± 0.57 ^e
Crude Fiber	5.21 ± 0.32 ^a	7.99 ± 0.11 ^b	4.80 ± 0.28 ^c	4.42 ± 0.16 ^d	4.44 ± 0.11 ^d	4.28 ± 0.26 ^d
Carbohydrate	51.3 ± 1.91 ^a	45.39 ± 1.50 ^b	53.33 ± 0.88 ^c	64.89 ± 0.43 ^d	66.46 ± 0.22 ^d	65.13 ± 0.52 ^d

Results are presented as mean ± standard deviation n = 3

Values with different superscript in the same row are significantly different at

P<0.05

Table 2: Effect of Landrace on the Proximate Contents of Bambaranut.

parameters	Landrace			SE
	Black	Cream	Zebra	
Moisture	9.55 ^a	9.71 ^a	9.45 ^a	0.2
Ash	3.39 ^a	4.06 ^b	3.28 ^a	0.07
Crude Protein	11.04 ^a	11.99 ^b	10.94 ^a	0.12
crude Fat	13.09 ^a	8.64 ^b	12.57 ^c	0.18
Crude Fiber	4.82 ^a	6.22 ^b	4.54 ^c	0.08
Carbohydrate	58.10 ^a	55.93 ^b	59.23 ^a	0.45

4.2. Mineral Elements

4.2.1. Mineral contents

The effect of sprouting on mineral contents of

bambaranut is presented in Table 3. Based on the result, sprouting has effect of increasing some of the minerals while decreasing others.

Table 3: Effect of sprouting on Mineral contents of Bambaranut.

Elements (mg/kg)	sprouted			Unsprouted		
	Black	Cream	Zebra	Black	Cream	Zebra
Na	17.2 ± 0.05 ^a	16.89 ± 0.64 ^a	12.88 ± 0.31 ^b	26.17 ± 0.46 ^c	110.93 ± 0.37 ^d	13.92 ± 0.04 ^e
Fe	2.40 ± 0.31 ^a	2.20 ± 0.18 ^a	4.78 ± 0.25 ^b	7.10 ± 0.009 _c	4.06 ± 0.05 ^d	1.79 ± 0.04 ^e
Ca	45.04 ± 0.03 ^a	44.16 ± 0.02 ^b	37.37 ± 0.05 ^c	39.49 ± 0.025 _d	38.31 ± 0.55 ^e	43.2 ± 0.63 ^f
K	519.97 ± 0.41 ^a	551.30 ± 0.60 ^b	518.98 ± 0.22 ^a	551.9 4 ± 0.21 ^c	464.8 ± 0.40 ^d	615.57 ± 0.05 ^e
Zn	1.17 ± 0.11 ^a	1.09 ± 0.04 ^b	1.12 ± 0.001 ^a	1.08 ± 0.004 _b	1.61 ± 0.02 ^c	1.07 ± 0.005 ^b
Mg	102.77 ± 0.30 ^a	89.86 ± 0.31 ^b	106.9 ± 0.20 ^c	106.0 4 ± 0.54 ^c	87.66 ± 0.09 ^d	114.97 ± 0.35 ^e
Mn	0.51 ± 0.007 ^a	0.75 ± 0.05 ^b	0.51 ± 0.03 ^a	0.50 ± 0.04 ^a	0.58 ± 0.02 ^c	0.51 ± 0.02 ^a
Se	38.93 ± 0.35 ^a	30.31 ± 0.51 ^b	24.62 ± 0.01 ^c	32.32 ± 0.55 ^d	29.00 ± 0.20 ^e	36.51 ± 0.03 ^f
Cu	0.40 ± 0.04 ^a	0.31 ± 0.04 ^b	0.30 ± 0.04 ^b	0.32 ± 0.22 ^b	0.29 ± 0.03 ^b	0.33 ± 0.04 ^b

Results are presented as mean ± standard deviation n = 3

Values with different superscript in the same row are significantly different at P<0.05

Table 4: Effect of Landrace on Mineral contents of Bambaranut.

Elements	Sprouted	Unsprouted	SE
Na	15.66 ^a	50.34 ^b	0.13
Fe	3.12 ^a	4.32 ^b	0.04
Ca	42.19 ^a	40.33 ^b	0.12
K	530.08 ^a	544.10 ^b	0.12
Zn	1.13 ^a	1.25 ^b	0.02
Mg	99.84 ^a	102.89 ^b	0.11
Mn	0.59 ^a	0.53 ^b	0.01
Se	31.29 ^a	32.61 ^b	0.12
Cu	0.34 ^a	0.31 ^a	0.13

5. DISCUSSION

5.1. Proximate Contents

The effects of sprouting on the proximate contents of three landraces of Bambaranut are presented in Table 1. Generally, irrespective of sprouting or not, *Vigna subterranea* landraces did not significantly ($P<0.05$) differ in moisture contents but differ in other proximate parameters (Table 2). Similarly, sprouting leads to significant changes in all the proximate parameters irrespective of the landrace. The moisture and carbohydrate contents tend to decrease significantly after sprouting whereas crude protein, ash, crude fiber and crude fat increased significantly. The decrease in moisture content is in disagreement with (19) that sprouting leads to increase in moisture content. The result of this study also disagrees with Shah *et al.* (2011) that sprouting has no effect on moisture content. The decrease in moisture content is an indication that sprouted Bambaranut will have a better shelf life.

Increase in ash contents observed in this study agrees with (17) when chick pea and soybean were sprouted for 2 - 4 days and (18) when mung bean, pea, and lentil were sprouted. The increased ash contents observed indicates that the sprouted bambaranut could have more mineral contents. The decrease in carbohydrate contents during sprouting may have led to the apparent increase observed in ash (18). The apparent increase in protein observed is attributed to increased synthesis of enzyme proteins such as proteases by sprouted seeds or a compositional change due to degradation of other constituents (19). The decrease in fiber contents observed reverberates the findings of (16), the increase could be attributed to the release of nutrients. Previous studies reported a decrease in crude fat contents following sprouting (16). However, the current study has observed significant increase. The significant reduction in carbohydrate contents is in agreement with (16), sprouting cause biochemical changes in carbohydrate that may lead to change in energy value. Hydrolytic enzymes are activated during sprouting leading to the breakdown of starch and non-starch polysaccharides (20). The actions of α - and β -amylases and α -glucosidase result in starch breakdown. These hydrolytic processes produce products (sugars and short-chain carbohydrates) that are perfect for weaning foods as viscosity and digestibility raise along with nutrient absorption.

The sprouted cream bambaranut landrace has the highest protein content, the value $19.93\pm 0.13\%$ is significantly different ($P<0.05$) from those of unsprouted cream landrace as well as the other two landraces (sprouted and unsprouted) (Table 1). Lowest carbohydrate ($45.39\pm 1.50\%$) content was observed in sprouted cream bambaranut landrace, the value differs significantly ($P<0.05$). The

sprouted cream Bambaranut landrace has the highest crude fiber contents ($7.99\pm 0.11\%$) and is significantly ($P<0.05$) different from other landraces irrespective of sprouting or not. Highest crude fat ($15.15\pm 0.07\%$) content was observed in sprouted zebra landrace, the value differs significantly ($P<0.05$) from other landraces. There is no significant difference ($P<0.05$) between fat contents of sprouted black and sprouted cream landrace. The sprouted Black landrace has the highest ash content.

In view of the aforementioned observations, most especially the apparent decrease in moisture contents, increase in ash contents coupled with increased protein and decreased carbohydrate contents, it could be deduced that the effect of sprouting on the proximate parameters of Bambaranut lead to an increases in the nutritional quality. The decrease in moisture content could translate to an increase in shelf life of bambaranut flour. Similarly, increase in protein and the decreased in carbohydrate implies that sprouted bambaranut could be utilized by diabetic patients.

5.2. Minerals

The results of minerals contents of three sprouted and unsprouted landraces of bambaranut are presented in Table 3. The landraces differs significantly in some of the minerals such as Na, Fe, Ca, K, Zn, Mg, Mn, and Se. However, the amount of some minerals did not significantly differ between some landraces irrespective of sprouting or not. For instance the black and zebra landraces have similar Zn and Mn contents. All the three unsprouted landraces have similar Cu contents. Irrespective of the landrace, significant ($P<0.05$) difference was observed in Na, Fe, Ca, K, Zn, Mg, Mn, and Se after sprouting but there was no significant difference in Cu. Overall, sprouting leads to decrease in Na, Fe, K, Zn, Mg and Se and increase in Ca and Mn (Table 4). There is no significant difference ($P<0.05$) in Na and Fe between sprouted black and cream landraces, Zn and Mn between sprouted black and zebra. However, sprouted landraces differed in Ca, K, Mg, and Se. The results of this study showed that the sprouted cream and black landraces have increased in selenium contents while increased in zinc content is observed in black and zebra landraces.

Regulation of the intracellular-extracellular potassium (K^+) gradient is very important for life, acute changes in K^+ plasma levels may lead to fatal consequences. Potassium is a vasodilator, it increases blood flow and decrease in potassium concentration in blood produces vasoconstriction (21). Dietary supplementation and restriction of potassium influence the resistance to blood flow through vascular beds such as cerebral and renal vascular beds (22).

Calcium (Ca) is needed for normal growth, development and maintenance of skeleton (23). Calcium is required in high amount during all stages of life but the requirement is more during growth period for instance childhood, during pregnancy and breast feeding (24). Appropriate intake of calcium causes reduction in hypertension and hypertension disorders related to pregnancy, lowering cholesterol levels, proper muscular contraction, oocyte activation, aiding blood clotting, regulation of heart beat and fluid balance (25). Deficiency of calcium, especially over a long time, can lead to osteoporosis in which the bone deteriorates and there is an increased risk of fractures. Consumption of a well-balanced diet can provide all the necessary nutrients and help prevent calcium deficiency (26).

Magnesium is required for many metabolic reactions as a cofactor, such reactions include protein synthesis, cellular energy production and storage, reproduction, DNA and RNA synthesis, stabilizing mitochondrial membranes among others (27). Magnesium plays a critical role in nerve transmission, cardiac excitability, activation of the immune system, neuromuscular conduction, muscular contraction, vasomotor tone, blood pressure, and glucose and insulin metabolism. Magnesium has multiple functions within the body, therefore potassium plays a major role in disease prevention and overall health, hence the role of magnesium is essential (27). Deficiency of magnesium is associated with a number of chronic diseases such as migraine headaches (28), Alzheimer's disease (29), stroke and hypertension, cardiovascular disease, and type 2 diabetes mellitus (30). Magnesium is found to influence fetal programming and disease presentation in child and adulthood (27) and it is indispensable for the aggregation of ribosomes into polysomes. To be biologically active and be synthesized from ADP, ATP requires magnesium (31).

Manganese is essential micronutrients in human that is principally obtained from the diet (32). It functions primarily as a coenzyme in many biological processes, such as macronutrient metabolism, bone formation, free radical defense systems, and in the brain ammonia clearance and neurotransmitter synthesis. It is found in all tissues and is a critical component of many proteins and enzymes (33). An association has been reported between dietary Mn and glucose metabolism, insufficient dietary Mn impairs insulin secretion and glucose metabolism. However, supplementation of Mn modifies the enzyme profiles of carbohydrate metabolism and improves high-fat-diet-induced beta cell injury and insulin resistance in animal models of diabetes (34). Manganese is a component of metalloproteins such as arginase, acetyl-CoA carboxylase, phosphoenolpyruvate decarboxylase, and pyruvate carboxylase, Mn superoxide dismutase (a mitochondrial

antioxidant), glutamine synthetase and glycosyltransferases (33). Human milk is generally low in Mn (1.8–27.5 µg/L); but concentrations in infant formulas can vary dramatically (33–300 µg/L) (54).

Adequate provision of Fe is essential for the functioning of many biochemical processes including electron transfer reactions, gene regulation, binding and transport of oxygen, and regulation of cell growth and differentiation, DNA synthesis and healthy function and development of brain (35). In a global scale, Fe deficiency is the most prevalent micro nutrient deficiency and a major public health risk in developing and industrialized countries. The deficiency affects more than a billion people of different age groups around the world, it is the common cause of anemia and a common deficiency among non anemic children, especially among children of developing countries (36). Deficiency of iron causes impaired immune function, impaired mental function, impaired physical performance, complications of pregnancy, increased absorption of lead and cadmium, altered drug metabolism, increased insulin sensitivity and fatigue (35).

The increase in selenium observed in cream and black landrace is of interest, selenium is a micronutrient that is necessary in trace amounts for the proper functioning of organisms (37). It has a key importance for maintaining homeostasis of the human system, especially for the proper functioning of the immune system. As a component of glutathione peroxidase, selenium is essentially involved in the protection of cells against the effect of excess H₂O₂, and also plays role in heavy metal detoxification. Selenium is required for proper functioning of the thyroid gland, it induces the occurrence of the selenoprotein synthesis (a process involved in the antioxidant defense mechanism of the organism) and it possesses anticarcinogenic properties against some cancers as well as anti-diabetic activities and reproductive efficiency (38).

Copper has multiple metabolic functions, severe deficiencies are associated with cardiac, bone, immune, and central nervous system problems and must be acquired through the diet and trafficked to the organs, cells, and proteins requiring copper for health (39). It is an indispensable cofactor used for redox reactions involving copper containing oxidases. Copper enzymes regulate various physiologic pathways such as energy production, iron metabolism, connective tissue maturation, and neurotransmission (40). Dietary copper deficiency or overload leads to dysregulation of lipid metabolism.

Zinc is essentially involved in the regulation of many physiological and biochemical events in the organism such as maintenance of integrity of cell

membrane, metabolism of protein, carbohydrate and lipid, recovery from wound injury and in the regulation of a number of other biological processes associated with normal growth and development (41). Zinc acts as a cofactor of many enzymes, at least one enzyme in every enzyme classification (42). Deficiency of Zn in children causes an increase in infection and diarrhea leading to the death of about 800,000 children worldwide yearly (43). Zinc deficiency was also indicated as a risk factor for immune deficiency and hence susceptibility to infection in the elderly (41). Depletion of zinc stores has been reported to be a risk factor of pneumonia in the elderly. Zinc is being considered as prophylactic or adjunct therapy for COVID-19, with 12 clinical trials underway, highlighting the relevance of this trace element for global pandemics (44). Zinc is a cofactor of at least one enzyme in every enzyme classification (43).

6. CONCLUSION

This study showed that sprouting enhances the nutritional quality of bambaranut irrespective of the landrace and could be used to increase the shelf life of foods. Similarly, sprouting could be used in healthy diet preparations. The increase in protein and decreased in carbohydrate contents is an indication that sprouted bambaranut could be utilized by diabetic patients.




7. REFERENCES

- Baryeh EA. Physical properties of bambara groundnuts. *Journal of Food Engineering*. 2001 Mar;47(4):321-6. Available from: [<URL>](#).
- Massawe F, Mwale S, Azam-Ali S, Roberts J. Breeding in bambara groundnut (*Vigna subterranea* (L.) Verdc.): strategic considerations. *African Journal of Biotechnology*. 2005;4(6):463-71.
- Alhassan A, Dangambo M, Abdulmumin T, others. Evaluation of the proximate contents of bambara groundnut *Vigna subterranea* (L.) Verdc grown in MadobiLGA, Kano State, Nigeria. *Brit J Appl Scie Tech*. 2015;8(4):361-5.
- Ghavidel RA, Prakash J. The impact of germination and dehulling on nutrients, antinutrients, in vitro iron and calcium bioavailability and in vitro starch and protein digestibility of some legume seeds. *LWT - Food Science and Technology*. 2007 Sep;40(7):1292-9. Available from: [<URL>](#).
- Roland WSU, Pouvreau L, Curran J, van de Velde F, de Kok PMT. Flavor Aspects of Pulse Ingredients. *Cereal Chemistry Journal*. 2017 Jan;94(1):58-65. Available from: [<URL>](#).
- Nkhata SG, Ayua E, Kamau EH, Shingiro JB. Fermentation and germination improve nutritional value of cereals and legumes through activation of endogenous enzymes. *Food Sci Nutr*. 2018 Nov;6(8):2446-58. Available from: [<URL>](#).
- Association ESS, others. ESSA hygiene guideline for the production of sprouts and seeds for sprouting. ESSA: Brussels, Belgium. 2016;
- Wanyama AW. Evaluation of Phytoconstituents, Antioxidants Potential, Cytotoxic, Antimicrobial Activities and Mineral Composition of *Vigna subterranea* (L) Verdc. Extracts [Internet] [Master's Thesis]. [Kenya]: Jomo Kenyetta University of Agriculture and Technology; 2018. Available from: [<URL>](#)
- Dhaliwal Y, AGGARWAL RK. Composition of fat in soybeans as affected by duration of germination and drying temperature. *Journal of food science and technology (Mysore)*. 1999;36(3):266-7.
- Falmata F, Modu S, Sanda S, Babagana M, Chamba G. Rheological and microbiological assessment of complementary meal produced from sprouted and fermented sorghum (*S. bicolor*) blended with cowpea (*Vigna unguiculata*) and groundnut (*Arachis hypogea*). *Merit Research Journal of Food Science and Technology*. 2014;2(3):31-7.
- Association of Official Analytical Chemists. food composition, additives, natural contaminants. 17th ed. Horwitz W, editor. Arlington, Va: AOAC International; 2000. (Official methods of analysis of AOAC International). ISBN: 978-0-935584-67-7.
- Egan H, Kirk RS, Sawyer R, Pearson D. Pearson's chemical analysis of foods. 8th ed. Edinburgh; New York: Churchill Livingstone; 1981. 591 p. ISBN: 978-0-443-02149-7.
- Nielsen SS. Introduction to the Chemical Analysis of Foods. West Lafayette, Indiana: Purdue University; 2002.
- Christian GD. ANALYTICAL CHEMISTRY, 6TH ED [Internet]. Wiley India Pvt. Limited; 2007. Available from: [<URL>](#)
- USEPA. Metals (Atomic Absorption methods). General procedure for analysis by atomic absorption. USEP; 1983.
- Steve IO, others. Influence of germination and fermentation on chemical composition, protein quality and physical properties of wheat flour (*Triticum aestivum*). *Journal of Cereals and Oil seeds*. 2012;3(3):35-47.
- Atudorei D, Stroe SG, Codină GG. Impact of Germination on the Microstructural and Physicochemical Properties of Different Legume Types. *Plants*. 2021 Mar 22;10(3):592. Available from: [<URL>](#).
- Ibrahim A, Anwar A, Sani M, Ya'u S, Tasi'u A, Sani M, et al. Assessment of antioxidant activity and mineral elements composition of fenugreek seed extract. *Dutse Journal of Pure Applied Sciences*. 2020;6(2):75-84.
- Bau HM, Villaume C, Nicolas JP, Méjean L. Effect of Germination on Chemical Composition, Biochemical Constituents and Antinutritional Factors of Soya Bean (*Glycine max*) Seeds. *J Sci Food Agric*. 1997 Jan;73(1):1-9. Available from: [<URL>](#).
- Rumiyati, James AP, Jayasena V. Effect of Germination on the Nutritional and Protein Profile of Australian Sweet Lupin (*Lupinus angustifolius* L.). *FNS*. 2012;03(05):621-6. Available from: [<URL>](#).

21. Haddy FJ, Vanhoutte PM, Feletou M. Role of potassium in regulating blood flow and blood pressure. *American Journal of Physiology-Regulatory, Integrative and Comparative Physiology*. 2006 Mar;290(3):R546-52. Available from: [<URL>](#).
22. Manger WM, Simchon S, Stier CTJ, Loscalzo J, Jan KM, Jan R, et al. Protective effects of dietary potassium chloride on hemodynamics of Dahl salt-sensitive rats in response to chronic administration of sodium chloride. *Journal of Hypertension [Internet]*. 2003;21(12). Available from: [<URL>](#).
23. Flynn A. The role of dietary calcium in bone health. *Proc Nutr Soc*. 2003 Nov;62(4):851-8. Available from: [<URL>](#).
24. Heaney RP. Absorbability and utility of calcium in mineral waters. *The American Journal of Clinical Nutrition*. 2006 Aug 1;84(2):371-4. Available from: [<URL>](#).
25. Wang X, Chen H, Ouyang Y, Liu J, Zhao G, Bao W, et al. Dietary calcium intake and mortality risk from cardiovascular disease and all causes: a meta-analysis of prospective cohort studies. *BMC Med*. 2014 Dec;12(1):158. Available from: [<URL>](#).
26. Pine C, Adair P, Burnside G, Robinson L, Edwards RT, Albadri S, et al. A new primary dental care service compared with standard care for child and family to reduce the re-occurrence of childhood dental caries (Dental RECUR): study protocol for a randomised controlled trial. *Trials*. 2015 Dec;16(1):505. Available from: [<URL>](#).
27. Fanni D, Gerosa C, Nurchi VM, Manchia M, Saba L, Coghe F, et al. The Role of Magnesium in Pregnancy and in Fetal Programming of Adult Diseases. *Biol Trace Elem Res*. 2021 Oct;199(10):3647-57. Available from: [<URL>](#).
28. WHO. Headache disorders. Fact Sheet #277 [Internet]. WHO; 2012. Available from: [<URL>](#)
29. Barbagallo M, Belvedere M, Di Bella G, Dominguez LJ. Altered ionized magnesium levels in mild-to-moderate Alzheimer's disease. *Magnesium Research*. 2011 Sep;24(3):115-21. Available from: [<URL>](#).
30. Volpe SL. Magnesium in Disease Prevention and Overall Health. *Advances in Nutrition*. 2013 May;4(3):378S-383S. Available from: [<URL>](#).
31. Holm NG. The significance of Mg in prebiotic geochemistry. *Geobiology*. 2012 Jul;10(4):269-79. Available from: [<URL>](#).
32. Rondanelli M, Faliva MA, Peroni G, Infantino V, Gasparri C, Iannello G, et al. Essentiality of Manganese for Bone Health: An Overview and Update. *Natural Product Communications*. 2021 May;16(5):1934578X2110166. Available from: [<URL>](#).
33. Carver PL, editor. *Essential Metals in Medicine: Therapeutic Use and Toxicity of Metal Ions in the Clinic [Internet]*. De Gruyter; 2019 [cited 2023 Feb 8]. Available from: [<URL>](#)
34. Du S, Wu X, Han T, Duan W, Liu L, Qi J, et al. Dietary manganese and type 2 diabetes mellitus: two prospective cohort studies in China. *Diabetologia*. 2018 Sep;61(9):1985-95. Available from: [<URL>](#).
35. Beard JL. Iron Biology in Immune Function, Muscle Metabolism and Neuronal Functioning. *The Journal of Nutrition*. 2001 Feb 1;131(2):568S-580S. Available from: [<URL>](#).
36. Shill KB, Karmakar P, Kibria MG, Das A, Rahman MA, Hossain MS, et al. Prevalence of iron-deficiency anaemia among university students in Noakhali region, Bangladesh. *J Health Popul Nutr*. 2014 Mar;32(1):103-10. PMID: 24847599, PMCID: PMC4089078
37. Kieliszek M, Błażej S. Current Knowledge on the Importance of Selenium in Food for Living Organisms: A Review. *Molecules*. 2016 May 10;21(5):609. Available from: [<URL>](#).
38. Kang D, Lee J, Wu C, Guo X, Lee BJ, Chun JS, et al. The role of selenium metabolism and selenoproteins in cartilage homeostasis and arthropathies. *Exp Mol Med*. 2020 Aug;52(8):1198-208. Available from: [<URL>](#).
39. Committee on Copper in Drinking Water, National Research Council. *Copper in Drinking Water*. National Academies Press; 2000.
40. Hordyjewska A, Popiołek Ł, Kocot J. The many “faces” of copper in medicine and treatment. *Biometals*. 2014 Aug;27(4):611-21. Available from: [<URL>](#).
41. Baltaci AK, Mogulkoc R, Baltaci SB. The role of zinc in the endocrine system. *Pakistan journal of pharmaceutical sciences*. 2019;32(1).
42. McCall KA, Huang C chin, Fierke CA. Function and Mechanism of Zinc Metalloenzymes. *The Journal of Nutrition*. 2000 May;130(5):S1437-46. Available from: [<URL>](#).
43. Hambidge KM, Krebs NF. Zinc Deficiency: A Special Challenge1. *The Journal of Nutrition*. 2007 Apr;137(4):1101-5. Available from: [<URL>](#).
44. Joachimiak MP. Zinc against COVID-19? Symptom surveillance and deficiency risk groups. Lau SKP, editor. *PLoS Negl Trop Dis*. 2021 Jan 4;15(1):e0008895. Available from: [<URL>](#).



Forecasting the Degradation of Vitamin C in Commonly Consumed Vegetable Cabbage (*Brassica oleracea*) Dipped in Different Pre-treatment Solutions

Awagu Emenike Fidelis^{1*} , Okoroafor Henry Chinedu² , Okike Obinna Odii² ,
Daramola Dare Samson² , Arohunmolase Omolara Mary² 

¹Nigerian Stored Products Research Institute, Perishable Crops Research Department, Ilorin, Nigeria

²Nigerian Stored Products Research Institute Perishable Crops Research Department, Port Harcourt, Nigeria

Abstract: Vitamin C is considered an essential vitamin that is commonly found in most fruits and vegetables. It is susceptible to easy degradation, especially during pre-treatment and storage. This study aimed at forecasting the degradation of vitamin C in commonly consumed vegetable (cabbage) dipped in different pre-treatment solutions at different time intervals. The samples after dipping at different time intervals were prepared for analysis. Evaluation of the ascorbic acid content of the vegetable was determined using High-Performance Liquid Chromatography (HPLC). This consists of an isocratic elution procedure with ultraviolet-visible detection at 245 nm. The half-lives and rate constants were calculated using the integrated law method. Forecasts were determined using time series analysis. Degradation of vitamin C in this study followed a first-order kinetic model, and the average coefficient of determination (R^2 -value) was greater than 0.9413. The rate constants of vitamin C degradation for the vegetable dipped in different pretreatment solutions (sodium chloride, sodium benzoate, sodium metabisulfite and vinegar) at different time intervals were 0.0804, 0.1049, 0.0706 and 0.0553 minutes⁻¹; half-lives were 8.2322, 7.3896, 10.9675, and 12.1086 minutes, respectively. The vegetable dipped in different pretreatments for 90 minutes exhibited $\ln(C)$ forecast of -2.2057, -4.6307, -1.1746, and 0.0789, respectively. The coefficient of correlation for sodium chloride, sodium benzoate, sodium metabisulfite, and vinegar are 0.084, 0.093, 0.063 and 0.059 respectively. The kinetic models were formulated using predicted initial contents, processing time, and measured contents. The vegetable dipped in vinegar pretreatment solution using $\ln(C) = \ln(C_0) - 0.0553t$ gave the best model. From the results, the most appropriate pretreatment solution for enhancing the shelf life of cabbage is synthetic vinegar (prepared from acetic acid) because it has a lower rate constant, lower coefficient of correlation, and the longest half-life.

Keywords: HPLC, Cabbage, Pretreatment Solutions, Ascorbic Acid, Rate Constant, Forecast

Submitted: March 31, 2022. **Accepted:** January 12, 2023.

Cite this: Awagu EF, Okoroafor HC, Okike OO, Daramola DS, Arohunmolase OM. Forecasting the Degradation of Vitamin C in Commonly Consumed Vegetable Cabbage (*Brassica oleracea*) Dipped in Different Pre-treatment Solutions. JOTCSA. 10(1):109-16.

DOI: <https://doi.org/10.18596/jotcsa.1093112>.

***Corresponding author. E-mail:** nykefidel@yahoo.com.

1. INTRODUCTION

Vitamin C is water-soluble and is a very important component of a healthy meal (1, 2). The increasing demand for nutritious food has led to several attempts to maximize the retention of nutrients in both processed and stored foods. Vitamin C serves as a quality indicator for other food nutrients especially during processing and storage of foods

because, if vitamin C is well retained, the other nutrients are also well retained (1). Vitamin C is the most unstable vitamin, which easily deteriorates during processing and storage. This can be because of certain variables such as pH (3, 4), temperature (5, 6), light (7, 8), the presence of enzymes (9, 10), hydrogen peroxide (11), and metallic catalysts (12-14).

Cabbage is a very essential and highly rated leafy vegetable, which contains minerals, vitamins, and alkaline salts. It is medicinal because of its wonderful cleansing properties such as the detoxification of reactive oxygen species (ROS) in the body (15). It contains tartronic acid which inhibits fat formation and other elements which enhance the body's immunity, slows down aging, inhibits cancer formation, and estrogenic activities. Cabbage is a very good source of vitamin C (16). The body cleansing properties of cabbage is because of a high content of ascorbic acid and sulfur-containing glucosinolates, anthocyanins, flavonoids, and other useful plant metabolites (17). Hydrolytic products of glucosinolates are responsible for the prevention of oxidative stress, induction of detoxification enzymes, stimulation of the immune system and the reduction of cancer risk (18).

Sodium chloride solution inhibits polyphenol oxidase (PPO), thereby preventing browning of fruits and vegetable products (19). Benzoic acid and its salts are very common preservatives, which inhibits an enzyme in the citric acid cycle of microorganisms. These pretreatment solutions function effectively under highly acidic conditions. They inhibit the activities of yeasts, mold, and microorganisms producing aflatoxins, but are not too effective against bacteria (20). The chemical preservative such as sodium metabisulfite is effective in the control of pathogenic bacteria causing food poisoning and infection (21). Research revealed that vinegar had the highest effect on the bacterial load of vegetables. This might be due to the acidic pH of vinegar, and some microorganisms cannot withstand acidic conditions (22).

Thermal processing is a traditional method for pretreating fruits and vegetables, and this includes drying, cooking, and blanching. However, ascorbic acid (vitamin C) is one of the key vitamins and it is highly susceptible to degradation and this is influenced by several factors such as high temperature, oxygen, and light (23, 24). Understanding the mechanism through which vitamin C is degraded during food processing is an essential tool in the regulation of the parameters needed to improve vitamin C retention. Additionally, understanding the degradation kinetics and various kinetic models is crucial in forecasting vitamin C loss and change in quality under certain processing conditions. Kinetic modeling enables us to quantify these changes and the rate at which they occur. It also aids us in understanding fundamental reaction mechanisms required for quality control and modeling. Vitamin C degradation kinetics in modeled systems follows first-order kinetics; but is very complex in food systems (25). This complexity as observed in food systems hinders the formulation of suitable mechanistic models. To get a good fit for the experimental data, pseudo-kinetic models, such as zero-order, first-order, or second-order kinetics, are

commonly used. The model that produces the highest coefficient of determination value (R^2) is considered the best fit for the analysis.

A time series analysis comprises of formulating a model that represents a time series and deploying the same in forecasting future values. The present study aimed at determining the rate of degradation of vitamin C in cabbage dipped in different pretreatment solutions, to recommend the best; development of kinetic models for forecasting the degradation of vitamin C in cabbage under the studied conditions; and to forecast future values.

2. MATERIALS AND METHODS

Metaphosphoric acid, L-ascorbic acid, orthophosphoric acid, and acetonitrile (High-Pressure Liquid Chromatography (HPLC)-Grade) were all purchased from Merck (Darmstadt, Germany). De-ionized water of $18 \text{ M}\Omega \text{ cm}^{-1}$ resistivity purified with a milli-Q system (Millipore, Bedford, MA, USA) was used for chromatographic analysis; ascorbic acid stock standard solution kept inside a glass-stoppered bottle (26).

Freshly cut vegetable (cabbage) weighing 4.5 kg, was washed with clean water, and drained using a clean muslin cloth. Stems were removed with a clean, sharp knife. The weighed cabbage leaves of 4.5 kg were divided into 9 lots of 100 g each and dipped differently into 2 liters of water containing 0.6 g each of sodium chloride ($27.3 \pm 0.92 \text{ }^\circ\text{C}$), sodium benzoate ($26.8 \pm 0.64 \text{ }^\circ\text{C}$) and sodium metabisulfite ($27.9 \pm 0.18 \text{ }^\circ\text{C}$) for 5, 10, 15, 20, 25, 30, 35 and 40 minutes, respectively. Also 100 g of the cabbage was dipped into 2 liters of water containing 100 mL of vinegar at various time intervals. The dipped leaves at the completion of time in the pretreatment solutions were immediately ran under running tap water for 30 seconds to stop further effects of the pretreatments. They were then drained differently for 2 minutes using a clean muslin cloth. The initial sample was blended using a Kenwood blender (Philips, HR 1702, Borehamwood, England, UK) and then filtered using cheese cloth. HPLC was used to determine the initial ascorbic acid degradation using the liquid extract, before dipping into pretreatment solutions. The mobile phase employed was a mixture of 0.5% NaH_2PO_4 (pH 2.25 with H_3PO_4)-acetonitrile (93:7). Flow rate of the mobile phase was $1.2 \text{ cm}^3\text{min}^{-1}$ and an injection volume of 20 μL was used in the quantitative analysis. The temperature of analytical column was kept constant at $25 \text{ }^\circ\text{C}$. The remaining samples were spread evenly on labeled trays and kept under a room temperature range of $25 - 29 \text{ }^\circ\text{C}$ and relative humidity range of 50 - 61 % using a thermometer and hygrometer. The sample without any form of treatment was used as the experimental control. At the end of the drying period, the samples were blended, sieved, and the liquid extract (1 g of each sample to 25 mL of extractant containing 5 % metaphosphoric acid

(MPA) at 10 °C and in the dark) was used in determining the final rate of degradation of ascorbic acid. All extractions were carried out in triplicate and obtained solutions were then filtered and stored at 4 °C before analysis. The injection of the extracts into HPLC system was performed twice.

2.1. Kinetic Modeling

Integrated rate law was used in modeling the degradation of vitamin C and various models were formulated using the integral method of analysis. The integral law equation is as follows (27):

$$\frac{dC}{dt} = -K[C]^n \quad (1)$$

This was used to formulate three models based on concentration (order of reaction $n = 0, 1$ and 2) and their half-lives ($t_{1/2}$).

Zero order model ($n = 0$):

$$C = C_0 - kt \quad (2)$$

$$t_{\frac{1}{2}} = \frac{C_0}{2k} \quad (3)$$

First order model ($n = 1$):

$$\ln(C) = \ln(C_0) - kt \quad (4)$$

$$\left(t_{\frac{1}{2}}\right) = \ln\left(\frac{2}{k}\right) \quad (5)$$

Second order model ($n = 2$):

$$\frac{1}{c} = \frac{1}{C_0} + kt \quad (6)$$

$$t_{\frac{1}{2}} = \frac{1}{kC_0} \quad (7)$$

Where, k = rate constant

C_0 = initial concentration of vitamin C in sample

C = concentration of vitamin C in sample at time t

$t_{1/2}$ = half-life of vitamin C in sample

3. RESULTS

Table 1 presents concentrations (mg/100 g) of vitamin C in cabbage dipped in different time intervals in sodium chloride, sodium benzoate, sodium metabisulfite, and vinegar, respectively, indicating a decrease in vitamin C with an increase in time in all the pre-treatment solutions.

Table 2 shows that R^2 and R^2 adjusted increased in value as P -values decreased with increasing time. The p -value continually tends to zero as the R^2 value increases. This implies that vitamin C degradation kinetics for cabbage dipped in different pre-treatment solutions may be best described by first order kinetics.

Table 3 shows pretreatment solutions, temperature of the pre-treatments, rate constants, half-life, and proposed model. The lower the rate constant, the lower the degradation of vitamin C.

Table 1: Vitamin C degradation in cabbage dipped in different pretreatment solutions.

Time (min)	NA Vit.C (mg/100 g)	SB Vit.C (mg/100 g)	SM Vit.C (mg/100 g)	VIN Vit.C (mg/100 g)
5	128.80	37.23	80.01	150.09
10	80.81	31.57	69.77	75.79
15	35.08	28.92	59.78	68.46
20	27.43	14.78	48.69	54.89
25	20.73	11.47	35.97	45.23
30	19.19	6.99	25.77	37.86
35	9.37	2.89	17.25	21.08
40	5.16	1.41	7.33	14.25

$n = 3$ (triplicate), NA: sodium chloride SB; sodium benzoate, SM: sodium metabisulfite, VIN: vinegar

Table 2: Kinetic model regression analysis for cabbage dipped in different pretreatment solutions.

Pretreatment	R^2	R^2 Adjusted	P-value
NA	0.946726	0.936071	0.000227
SB	0.958414	0.950097	0.000122
SM	0.925188	0.910226	0.000534
VIN	0.934826	0.921791	0.000377

Table 3: Rate constant kinetic model regression analysis for cabbage dipped in different pretreatment solutions.

PT	Temp (°C)	k (min ⁻¹)	Half-Life (min)	Proposed model
NaCl	27.3 ± 0.92	0.0804	8.2322	$\ln(C) = \ln(C_0) - 0.0804t$
SB	26.8 ± 0.64	0.1049	7.3896	$\ln(C) = \ln(C_0) - 0.1049t$
SM	27.9 ± 0.18	0.0706	10.9675	$\ln(C) = \ln(C_0) - 0.0706t$
VIN	27.4 ± 0.19	0.0553	12.1086	$\ln(C) = \ln(C_0) - 0.0553t$

Figure 1 presents first-order kinetics for cabbage dipped in different pre-treatment solutions, showing that the rate of degradation at any time is

dependent on the initial concentration of vitamin C in the vegetable.

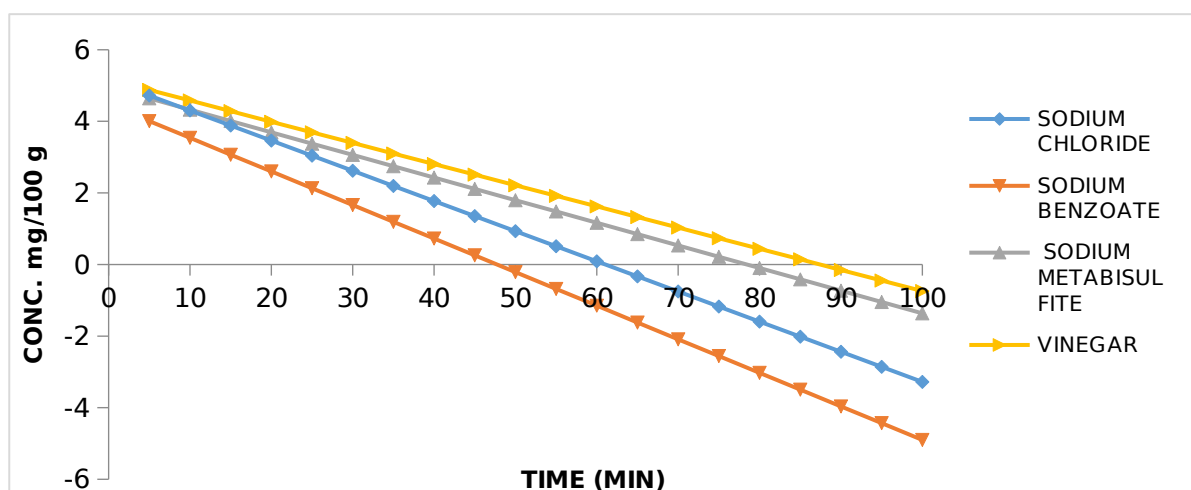


Figure 1: Plot of first-order kinetics for cabbage dipped in different pretreatment solutions.

Table 4: First-order kinetics Trendline equation and R Squared value for cabbage dipped in different pretreatment solutions.

Cabbage Dipped in Solutions	Y intercept	R Square
Sodium Chloride	$-0.084x + 5.143$	0.963
Sodium Benzoate	$-0.093x + 4.474$	0.939
Sodium Metabisulfite	$-0.063x + 4.956$	0.913
Vinegar	$-0.059x + 5.171$	0.953

The coefficient of correlation for sodium chloride, sodium benzoate, sodium metabisulfite and vinegar are 0.084, 0.093, 0.063 and 0.059 respectively (Figure 1). $0.059 < 0.063 < 0.084 < 0.093$. This implies that vitamin C in cabbage dipped in vinegar solution was more stable than vitamin C in cabbage dipped in the other pre-treatments.

Figure 2 presents cabbage dipped in different pre-treatment solutions and the forecasted shelf-life. Cabbage dipped in vinegar was preferred among others. From the time series forecast analysis, it can be deduced that vitamin C is more stable in cabbage dipped in vinegar solution because it has the least coefficient of correlation (0.059).

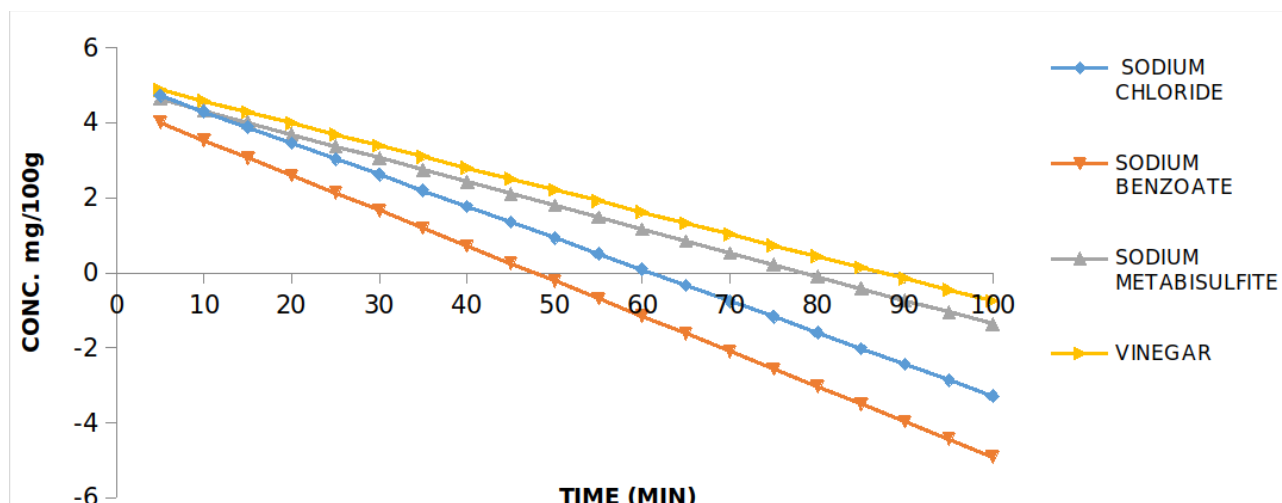


Figure 2: Plot of time series forecast analysis for cabbage dipped in different pre-treatment solutions.

Table 5: First-order kinetics Forecast Trendline equation and R Squared value for cabbage dipped in different pretreatment solutions.

Cabbage Dipped in Solutions	Y intercept	R Square
Sodium Chloride	-0.084x + 5.143	1
Sodium Benzoate	-0.093x + 4.474	1
Sodium Metabisulfite	-0.063x + 4.956	1
Vinegar	-0.059x + 5.171	1

4. DISCUSSION

Table 1 shows the variations in ascorbic acid concentration of cabbage dipped in different pretreatment solutions at different time intervals during processing and storage. Table 2 is a summary of kinetic model regression analysis results, and Table 3 shows vitamin C first-order kinetics degradation of cabbage dipped in the different pretreatment solutions. In Table 1, it was observed that the concentration of vitamin C in cabbage steadily decreased with increasing time. This reveals that vitamin C in the vegetable dipped in different pretreatment solutions degrade with time during processing and storage. Vitamin C concentration of cabbage decreased with time during processing and storage, but in varying degrees, and this was influenced by the different processing and storage methods (25). This concurs with some previously reported research findings on citrus and strawberry fruit juices (28, 29), and it also conforms to the degradation kinetics of vitamin C in model systems (16). The kinetic plots of the model (Eq. 4) in Figure 1 reveal that the first-order model was the best fit at different times. The goodness of fit data in Table 2 confirms this. Their R^2 values were the highest and p -values the lowest with different pretreatments. The first-order kinetic model showed a good fit for vitamin C degradation of most materials dipped in NaCl and has been utilized by several researchers (30-33). This was confirmed for NA from Table 2, R^2 :

0.946726, p -value: 0.000227. Thus, first-order kinetics best describes the vitamin C degradation kinetics in the vegetable dipped in 0.3 g/L of each sodium chloride, sodium benzoate, sodium metabisulfite and 50 mL/L of vinegar pretreatments. The model with maximum R^2 and the minimum p -value is considered the best (34, 35). Furthermore, from Table 3, the rate constant of the vegetable sample dipped in vinegar exhibited the lowest rate constant of 0.0592 minutes⁻¹, indicating less degradation. Since the magnitude of the rate constant reveals the rate of reaction, it therefore shows that degradation of vitamin C occurred faster in those samples dipped at an increased time. In other words, the rate of degradation at any given time depends on the initial concentration of vitamin C in the vegetable. Additionally, the processing pretreatment solutions had an average mild temperature of 27.35 °C as shown in Table 3. An increase in storage temperature is therefore believed to result in an increase in the losses of vitamin C in the stored products (36, 5, 23, 37). The post-harvest losses of vegetables can be greatly reduced by extending their shelf-life (8). This trend as clearly revealed in the half-life of the samples in Table 3 supports these facts. The cabbage vegetable dipped in vinegar had the longest half-life of 12 minutes and 11 seconds. The product shelf life is often determined by the decrease of ascorbic acid concentration to industrially unacceptable levels (38). Again, from Figure 2, the $\ln(C)$ forecast

dipped for 90 minutes and exhibited -2.2057, -4.63069, -1.17463, and 0.078902 showing that vinegar richer in vitamin C. From Table 3, the kinetic models formulated using the predicted initial contents, the processing time, and measured contents, dipped in vinegar pretreatment solution with the model; $\ln(C) = \ln(C_0) - 0.0553t$ gave the best model.

Ascorbic acid is often used as the most common nutrient loss indicator during storage. The retention of ascorbic acid in food products is a reliable representative index during the processing of foods (36, 24). The proposed simulation model monitors the degradation of vitamin C (ascorbic acid) in cabbage and expresses the advantages of the computer simulation technique over the laboratory chemical analysis.

5. CONCLUSION

This work developed models in which the experimental variable can be imputed, and the desired results were computed for a better understanding of the vitamin C values and to make accurate predictions of different outcomes, regarding their shelf-life. Additionally, the models enable appropriate forecasting in agricultural produce. It also produces value-added products by slowing down or inhibiting chemical deterioration and microbial growth. All these absolutely support and authenticate that rate constant is the major determining factor in accessing the degradation of commonly consumed vegetables, which cabbage dipped in vinegar signified lesser degradation. The retention of ascorbic acid in cabbage after dipping in vinegar pre-treatment solution is a suitable indicator for the retention of other nutrients in cabbage.

6. REFERENCES

1. Szczuko M, Migrała R, Drozd A, Banaszczak M, Maciejewska D, Chlubek D, et al. Role of water soluble vitamins in the reduction diet of an amateur sportsman. *Open Life Sciences*. 2018 May 18;13(1):163-73. Available from: [<URL>](#).
2. Devaki SJ, Raveendran RL. Vitamin C: Sources, Functions, Sensing and Analysis. In: Hamza AH, editor. *Vitamin C* [Internet]. InTech; 2017 [cited 2023 Feb 20]. Available from: [<URL>](#)
3. Farah HS, Alhmoud JF, Al-Othman A, Alqaisi KM, Atoom AM, Shadid K, et al. Effect of pH, temperature and metal salts in different storage conditions on the stability of vitamin C content of yellow bell pepper extracted in aqueous media. *Systematic Reviews in Pharmacy*. 2020;11(9):661-7.
4. Doseděl M, Jirkovský E, Macáková K, Krčmová L, Javorská L, Pourová J, et al. Vitamin C—Sources, Physiological Role, Kinetics, Deficiency, Use, Toxicity, and Determination. *Nutrients*. 2021 Feb 13;13(2):615. Available from: [<URL>](#).
5. Essodolom P, Chantal BE, Mamatchi M, Kous'anta A. Effect of temperature on the degradation of ascorbic acid (vitamin c) contained in infant supplement flours during the preparation of porridges. *Int J Adv Res*. 2020;8(3):116-21.
6. Herbig AL, Renard CMGC. Factors that impact the stability of vitamin C at intermediate temperatures in a food matrix. *Food Chemistry*. 2017 Apr;220:444-51. Available from: [<URL>](#).
7. Nakilcioğlu-Taş E, Ötleş S. Kinetic modelling of vitamin C losses in fresh citrus juices under different storage conditions. *An Acad Bras Ciênc*. 2020;92(2):e20190328. Available from: [<URL>](#).
8. Pathy K. Process for preparation of vitamin C and method for determination of vitamin c in tablets. *SF J Chem Res*. 2018;2(1):1-17.
9. Attila Szócs, Vancea S, Kiss I, Donáth-Nagy G. Quantification of Plasma and Leukocyte Vitamin C by High Performance Liquid Chromatography with Mass Spectrometric Detection. *J Anal Chem*. 2020 Sep;75(9):1168-76. Available from: [<URL>](#).
10. Özkan M, Kirca A, Cemeroğlu B. Effects of hydrogen peroxide on the stability of ascorbic acid during storage in various fruit juices. *Food Chemistry*. 2004 Dec;88(4):591-7. Available from: [<URL>](#).
11. Yin X, Chen K, Cheng H, Chen X, Feng S, Song Y, et al. Chemical Stability of Ascorbic Acid Integrated into Commercial Products: A Review on Bioactivity and Delivery Technology. *Antioxidants*. 2022 Jan 13;11(1):153. Available from: [<URL>](#).
12. Miftari H. Effect of drying in the preservation of apple and its vitamin C content. *International Journal of Food Technology and Nutrition*. 2021;4(7-8):44-8. Available from: [<URL>](#).
13. Shen J, Griffiths PT, Campbell SJ, Uttinger B, Kalberer M, Paulson SE. Ascorbate oxidation by iron, copper and reactive oxygen species: review, model development, and derivation of key rate constants. *Sci Rep*. 2021 Apr 1;11(1):7417. Available from: [<URL>](#).
14. Farah HS, Alhmoud JF, Al-Othman A, Alqaisi KM, Atoom AM, Shadid K, Shakya A, AlQaisi T. Effect of pH, Temperature and Metal Salts in Different Storage Conditions on the Stability of Vitamin C Content of Yellow Bell Pepper Extracted in Aqueous Media. *Sys Rev Pharm*. 2020; 11(9):661-7.
15. Morales-López J, Centeno-Álvarez M, Nieto-Camacho A, López MG, Pérez-Hernández E, Pérez-Hernández N, et al. Evaluation of antioxidant and hepatoprotective effects of white cabbage essential oil. *Pharmaceutical Biology*. 2017 Jan 1;55(1):233-41. Available from: [<URL>](#).
16. Hailemariam GA, Wudineh TA. Effect of Cooking Methods on Ascorbic Acid Destruction of Green Leafy Vegetables. *Journal of Food Quality*. 2020 Mar 9;2020:1-5. Available from: [<URL>](#).
17. Kapusta-Duch J, Kopec A, Piatkowska E, Borczak B, Leszczynska T. The beneficial effects of Brassica vegetables on human health. *Roczniki Państwowego Zakładu Higieny*. 2012;63(4):389-95.
18. Sanlier N, Guler S. The benefits of Brassica vegetables on human health. *J Hum Health Res*. 2018;1(1):1-13.
19. Ma Y, Wang H, Yan H, Malik AU, Dong T, Wang Q. Pre-cut NaCl solution treatment effectively inhibited the

- browning of fresh-cut potato by influencing polyphenol oxidase activity and several free amino acids contents. *Postharvest Biology and Technology*. 2021 Aug;178:111543. Available from: [<URL>](#).
20. Oladapo A, Akinyosoye F, Abiodun O. The inhibitory effect of different chemical food preservatives on the growth of selected food borne pathogenic bacteria. *African Journal of Microbiology Research*. 2014;8(14):1510-5.
21. Kim C, Wilkins K, Bowers M, Wynn C, Ndegwa E. Influence of pH and Temperature on Growth Characteristics of Leading Foodborne Pathogens in a Laboratory Medium and Select Food Beverages. *Austin Food Sci*. 2018;3(1):1031. Available from: [<URL>](#).
22. Xiao HW, Bai JW, Sun DW, Gao ZJ. The application of superheated steam impingement blanching (SSIB) in agricultural products processing - A review. *Journal of Food Engineering*. 2014 Jul;132:39-47. Available from: [<URL>](#).
23. Nwakaudu M, Nkwocha A, Madu I, Enwereji C, Ireaja I. Kinetic modeling of vitamin C (ascorbic acid) degradation in tomato and pawpaw under market storage conditions. *International Journal of Current Research*. 2015;7(6):16783-8.
24. Burdurlu HS, Koca N, Karadeniz F. Degradation of vitamin C in citrus juice concentrates during storage. *Journal of Food Engineering*. 2006 May;74(2):211-6. Available from: [<URL>](#).
25. Derossi A, De Pilli T, Fiore AG. Vitamin C kinetic degradation of strawberry juice stored under non-isothermal conditions. *LWT - Food Science and Technology*. 2010 May;43(4):590-5. Available from: [<URL>](#).
26. Awagu EF, Ekanem EO, Kolo AM, Adamu MM. Kinetic Modeling of Vitamin C (Ascorbic Acid) Degradation in Blanched Commonly Consumed Salad Vegetables Using Computer Simulation Analysis. *IOSR JAC*. 2017 Apr;10(04):59-66. Available from: [<URL>](#).
27. Blasco R, Esteve MJ, Frígola A, Rodrigo M. Ascorbic acid degradation kinetics in mushrooms in a high-temperature short-time process controlled by a thermoresistometer. *LWT - Food Science and Technology*. 2004 Mar;37(2):171-5. Available from: [<URL>](#).
28. Frías JM, Oliveira JC. Kinetic models of ascorbic acid thermal degradation during hot air drying of maltodextrin solutions. *Journal of Food Engineering*. 2001 Mar;47(4):255-62. Available from: [<URL>](#).
29. Zheng H, Lu H. Effect of microwave pretreatment on the kinetics of ascorbic acid degradation and peroxidase inactivation in different parts of green asparagus (*Asparagus officinalis* L.) during water blanching. *Food Chemistry*. 2011 Oct;128(4):1087-93. Available from: [<URL>](#).
30. Mitra J, Shrivastava SL, Srinivasa Rao P. Vacuum dehydration kinetics of onion slices. *Food and Bioprocess Processing*. 2011 Jan;89(1):1-9. Available from: [<URL>](#).
31. Silva EM, da Silva JS, Pena RS, Rogez H. A combined approach to optimize the drying process of flavonoid-rich leaves (*Inga edulis*) using experimental design and mathematical modelling. *Food and Bioprocess Processing*. 2011 Jan;89(1):39-46. Available from: [<URL>](#).
32. Leong SY, Oey I. Effect of endogenous ascorbic acid oxidase activity and stability on vitamin C in carrots (*Daucus carota* subsp. *sativus*) during thermal treatment. *Food Chemistry*. 2012 Oct;134(4):2075-85. Available from: [<URL>](#).
33. Wawire M, Oey I, Mathooko F, Njoroge C, Shitanda D, Hendrickx M. Thermal Stability of Ascorbic Acid and Ascorbic Acid Oxidase in African Cowpea Leaves (*Vigna unguiculata*) of Different Maturities. *J Agric Food Chem*. 2011 Mar 9;59(5):1774-83. Available from: [<URL>](#).
34. Talukder S, Khalequzzaman KM, Chowdhury MNA, Khuda SMKE, Masudalam Md. Prepackaging, storage losses and physiological changes of fresh bitter melon as influenced by Post Harvest Treatments. *Journal of Biological Science*. 2004; 4(5):613-5.
35. Giannakourou MC, Taoukis PS. Kinetic modelling of vitamin C loss in frozen green vegetables under variable storage conditions. *Food Chemistry*. 2003 Oct;83(1):33-41. Available from: [<URL>](#).
36. Bhardwaj RL, Pandey S. Juice Blends—A Way of Utilization of Under-Utilized Fruits, Vegetables, and Spices: A Review. *Critical Reviews in Food Science and Nutrition*. 2011 Jul;51(6):563-70. Available from: [<URL>](#).
37. Cvetkovic B, Jokanovic M. Effect of preservation method and storage condition on ascorbic acid loss in beverages. *Acta per tech*. 2009;(40):1-7. Available from: [<URL>](#).



Applications of New Generation Solvents for Extraction of Herbal Products prior to Atomic and Molecular Analysis

Selin IŞIK^{1*} , Abdullahi Garba USMAN¹ 

¹Near East University, Department of Analytical Chemistry, North Cyprus, Mersin-10, 99138, Turkey.

Abstract: In this review, an up to date and current knowledge of some of the green solvents, which includes supercritical fluids extraction (SFE), switchable polarity solvents (SPS), and natural deep eutectic solvents (NADES) are discussed with more emphasis on the extraction of active components of herbal products. Different scientific articles and books have been researched and reviewed to explain the applications of new generation solvents for extraction of herbal products prior to atomic and molecular analysis from the past until now. Currently, the most of techniques used in processing herbal products involve the use of extraction methods. Therefore, trends in extraction methods focuses mainly on finding reasonable solutions that minimizes the use of toxic solvents and allows the usage of renewable and green solvents from natural products, which ensure high quality and safe extracts. In future, SFE is definitely going to be on the industrial scale due to its numerous applications in the large scale especially for herbal, food, cosmetics and pharmaceutical products etc.

Keywords: Extraction; natural deep eutectic solvents (NADES); new generation solvent; supercritical fluids extraction (SFE); switchable polarity solvents (SPS). September 22, 2022 January 19, 2023 Işık S, Usman AG. Applications of New Generation Solvents for Extraction of Herbal Products Prior to Atomic and Molecular Analysis. JOTCSA. 2023;10(1):117-28. <https://doi.org/10.18596/jotcsa.1178753> Phone: +905338253139.

1. INTRODUCTION

The separation between molecular analysis and atomic analysis, which are regarded as two distinct and extremely divergent areas, has existed in analytical chemistry for many years. As a matter of fact, the tools and extraction techniques created for atomic analysis—which inevitably need vaporization, atomization, and occasionally even ionization—are extremely different from those used for molecular analysis, and the spectra seen in both situations show considerable differences (1). However, given the different types of works that connect these two disciplines nowadays, such a division needs to be reevaluated. High-resolution continuum source atomic absorption spectrometers (HR-CS-AAS), which use either flame (F) or graphite furnace atomizers (GF), have considerably revolutionized the science of atomic absorption (2). As the concept of using continuum sources instead of line sources for AAS can be virtually traced back to the invention of the technology, several devices have been developed based on such concepts (3). Molecular analysis is regarded as a laboratory procedure that entails the examination of various sample materials, including food, herbals, cells, tissues, and environmental samples, for the identification of various target analytes at a molecular level using various analytical techniques,

including high performance liquid chromatography (HPLC) and gas chromatography (GC), using different detectors (4).

Generally, major industrial and conventional chemical processes involve the use of flammable, toxic, volatile, hazardous, and environmentally destructive solvents in chemical reactions and separation processes (1). These have a negative impact on the economic and environmental performance of such processes (2). Conventional or classical extraction methods are also time-consuming, laborious, and involve large amounts of energy-consuming solvents such as alcohols, chloroalkanes, and other hydrocarbons (3). Therefore, since most bioactive components are water-insoluble, this can ultimately aggravate the degradation of some target analytes (4). It is worthy of note that, despite the use of high amounts of solvents and high energy consumption, the yield is also lower in comparison to the alternatives (5). Therefore, a few decades ago, safer, effective extraction methods in accordance with a sound compromise of their environmental, economic, and social requirements began to be considered as replacements (6).

Green chemistry as a concept was first introduced in 1991 by PT Anastas when he launched a unique

program in order to implement sustainable development in the area of chemical technology (7).

Green chemistry has 12 principles which serve as guidelines for designing chemical products and methods (8,9) that reduce or occasionally remove the application and generation of harmful and hazardous chemical materials altogether by using solvents and chemicals that are entirely non-toxic to human health as well as the immediate environment in order to design and create effective and non-hazardous methods facilitating the use of renewable solvents known as 'new generation solvents' or 'solvents of the future' (10). Gu and Jerome proposed the first requirements for a solvent and a process to be considered green based on their availability, biodegradability, flammability, grade, performance, price, recyclability, renewability, stability, storage, toxicity, and synthesis (11). There is no doubt that these are reasonable and sound conditions (12).

Nevertheless, it can also cause a dilemma regarding classifying a solvent as a green solvent, because in most cases, a solvent cannot fulfill all these parameters. For example, a solvent can fulfill eleven or ten or nine out of the total twelve conditions of a green solvent (13). Therefore, can this solvent still be regarded as green? It is therefore crucial to be precise regarding the meaning of these green solvents. The term itself can therefore be misleading due to its novelty and relative nature (14). Though Warner and Anastas defined "green chemistry" as a process of reducing the toxicity and hazards of processes or methods, they did not define it as a method that does not cause any damage or harm (15). Therefore, a solvent can be considered green if it is 'greener' when compared with the current classical solvent to be replaced, which can be supported with clear and strong evidence (1). In almost all cases, the choice will be based on a compromise between different conditions, as seen in Figure 1 below (17,18).

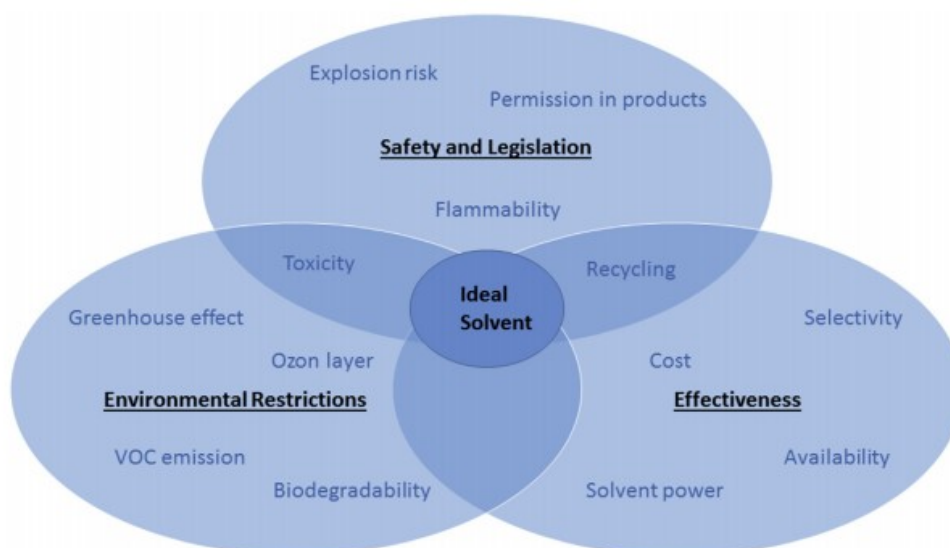


Figure 1: An ideal solvent is a combination and involves a compromise of different and multitude requirements (Adapted from Chemat *et al.* (11)).

These are termed "new generation solvents" owing to their tunable properties, which may prove to be a class of solvents that offer energy and material efficiency greater than existing solvents that need further exploitation to improve their application as a green chemical process (19).

Finally, given their limited context, there is a need to use their applicability in micro-extraction methods, particularly for switchable polarity solvents (SPS) (20).

In conclusion, the aim of this review is to show some applications and wide extraction methods using new generation solvents for herbal products prior to atomic and molecular analysis (21). In this regard, atomic analysis entails the identification and characterization of various sample materials,

particularly environmental, cosmetic, food, and herbal samples, for the identification, isolation, and confirmation of analytes at the elemental state via atomization using various analytical techniques such as FAAS and inductively coupled plasma mass spectrometry (ICP-MS). While molecular analysis is considered a laboratory procedure that involves the study of different sample materials such as food, herbals, cells, tissue, and environmental samples for the identification of various target analytes at a molecular level using different analytical techniques such as HPLC and GC using different detectors.

2. SOLVENT-FREE SYSTEM

Sometimes the best solvent is no solvent at all. A solvent-free system completely satisfies the 5th

condition of green chemistry. Numerous studies have shown that there is an abundance of industrial and chemical processes in which the use of solvents is completely avoided (22). However, this is not always possible. Especially if the absence of the solvent leads to dangerous overheating or results in a higher demand for energy (23). Therefore, these disadvantages would definitely surmount the advantages of using a non-solvent system (solvent-free process). Some decades ago, scientists tried synthesizing polymers using solvent-free conventional reactions (24). It is indeed notable that some industrial polymerizations have succeeded in using solvent free methods in synthesis as well as in separation, such as solid state polymerization and melt polymerization (25). For example, PET is produced commercially through melt polymerization and then followed by the solid state polymerization method (26). It is possible to produce polymers, for example poly (phenylene vinylene), by ensuring that there is close contact among the molecules of the starting materials for about five minutes in the ball milling process (27). This ball milling process is not only used in polymer science, but also has diverse applications in organic synthesis (28). Apart from avoiding the use of organic solvents, it

also has numerous advantages, such as a reduction in reaction time and high energy efficiency (29). As far as the solvent-free process is concerned, mentioning the solvent-free microwave extraction method is significant, which is a well-designed technique introduced by Lucchesi and his group in the year 2004 (30). This sophisticated method can be applied to extracting essential oils from fresh plant material in a microwave-assisted dry distillation process (31). It is a quick, robust, and sensitive method that gives a strong alternative to the time-consuming and long-lasting conventional hydro-distillation method (32).

3. SUPERCRITICAL FLUID EXTRACTIONS

These are substances which exist as a single phase above their critical points of temperature and pressure (33). This critical point can be defined as the point at which liquid and vapor can be distinguished without the need for boundaries (34). For example, the supercritical point of water was discovered to be 374 °C and 22.7 MPa C (Figure 2A), while the supercritical point of CO₂ was discovered to be 31 °C and 7.3 MPa C (Figure 2B) (35).

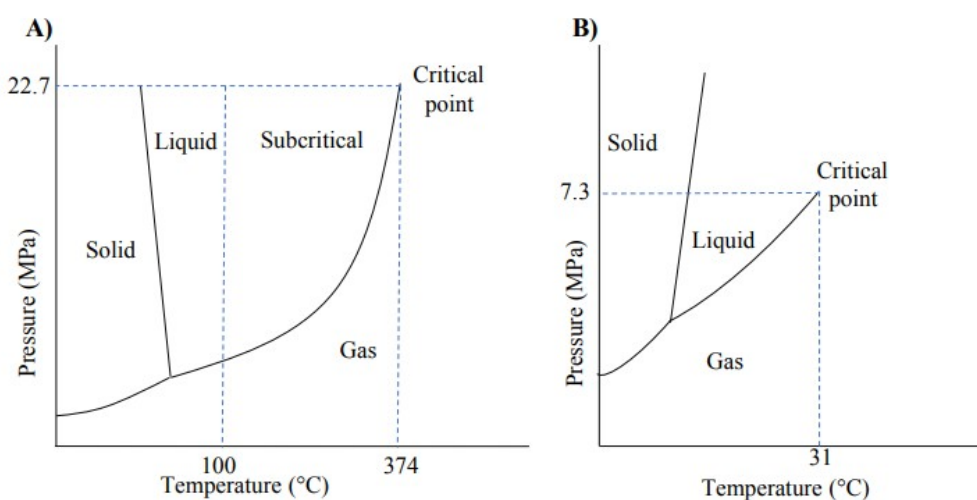


Figure 2: Phase diagram of water and CO₂ (Adapted from Lucchesi et al., 2004 (35)).

Due to their tunable properties of low viscosity (gas-like) and high density (liquid-like), these are considered to be important new generation solvents that improve solubility and mass transfer properties (36). The properties of certain supercritical fluids are mentioned in Table 1. In analytical chemistry, supercritical propane-butane, water, ammonia, and CO₂ have also been used. Because of its low critical temperature and pressure (31 °C and 7.3 MPa), inertness, purity, non-toxicity, and availability, CO₂ is the most widely used supercritical fluid. Furthermore, the strength of **supercritical carbon dioxide** (scCO₂) solvation can be adjusted by changing the temperature and pressure (37).

Another benefit of CO₂ is that it is gaseous at room temperature and pressure, making active product recovery relatively quick and cheap, as well as the ability to produce solvent-free extracts. scCO₂'s ability to operate at low temperatures while using a non-oxidizing medium is also advantageous for sample processing of medicinal, food, biological, and natural products, as it allows for the extraction of thermally labile or readily oxidized compounds with minimal degradation. scCO₂ has solubilizing properties similar to n-hexane and n-heptane due to its low dielectric constant and dipole moment near to zero. Due to charge isolation and its electronic composition, it has a quadrupole moment, allowing it to behave as both a Lewis acid and a Lewis base. Despite having a quadrupole

moment, ScCO₂ acts like a nonpolar solvent, limiting its use in removing hydrophilic analytes. A polar modifier or (co-solvent) is normally applied to tune the polarity and increase the solvating ability to address this constraint. Chemical solvents such

as methanol, ethanol, and ethyl acetate are applied to ScCO₂ in small amounts (1-20 vol percent) to broaden its extraction spectrum to include more polar analytes.

Table 1: Physical properties (density, diffusion and viscosity) of gaseous, supercritical and liquid states. (35).

State	Density (g/cm ³)	Diffusion (cm ² /s)	Viscosity (g/cm•s)
Gas	10 ⁻³	10 ⁻¹	10 ⁻⁴
Supercritical	10 ⁻¹ - 1	10 ⁻⁴ - 10 ⁻³	10 ⁻⁴ - 10 ⁻³
Liquid	1	<10 ⁻⁵	10 ⁻²

Supercritical fluid extraction of herbal and biologically active components is now a growing area of interest. It gives an ability to process plant and herbal products at a very low temperature, in absence of toxic and harmful solvents, in addition to limiting thermal degradation of the analytes (38). Any fluid can be used as a supercritical fluid if it fulfils the characteristics under critical conditions. However, cost, solvation power and toxicity determine the best and suitable solvent to be used in a particular and specific application. It has been reported that propane, dimethyl ether and ethane have been used in extraction of herbal products and biologically active compounds as supercritical solvents (39).

compounds are mainly categorized into two main divisions: (1) undesired or unwanted chemical substances that need to be removed from the plant materials (matrix), for example, removal of caffeine from tea and coffee, defatting of press cakes, as well as removal of various factors such as porosity, particle size, nature of the matrix, and moisture, as well as removal of some parameters from some processes, such as temperature, pressure, and solvent flow rate, which can have an effect on the supercritical fluid result, (2) the extraction of biologically active components from plant material (40). Table 2 shows a selection of common applications of supercritical fluid extraction from herbal and plant origins, along with extraction properties such as pressure, modifiers, and temperature.

For easy understanding, we need to know that the supercritical fluid methods for most of the natural

Table 2: Supercritical-CO₂ extraction of some selected herbal bioactive compounds (selected from plant origin) (6).

Material	Extract	Modifier	T (°C)	P (bar)
Almond	Oil, tocopherols	Methanol	35-50	350-550
Aloe Vera leaves	α -tocopherol	Ethanol	40-70	300-600
Black pepper	Oleoresin, piperine	-	35-55	200-300
Ginger	Oleoresin	Ethanol, isopropanol	25-35	200-250
Thyme	Total extract, thymol,	-	40	80-400
Walnut	Oil	Ethanol	40-60	300-500
Grape skin	Resveratrol	Ethanol	40	150
Ginkgo leaves	Terpenes, flavonoids	Ethanol	60-110	242-312

4. SWITCHABLE POLARITY SOLVENTS (SPS)

Generally, switchable solvents (SS) are mixtures of compounds that have the ability to abruptly change their physical properties, such as polarity (hydrophilicity), conductivity, solubilizing capability

or viscosity (41,42). The switching of polarity is induced through bubbling of CO₂ gas at atmospheric pressure into the reaction vessels (43). The CO₂ will further reacts and associates with a compound in the reaction system forming an ionic liquid (IL) having different properties from the

initial molecular liquid (44). This process can simply be reversed through removal of CO₂ by bubbling inert gasses, N₂ gas, NaOH or sometimes through applying mild heat to the liquid (45).

It has been reported that various materials have the ability to switch some of their characteristics, for example polymers, solutes, and surfactants (46). With the aid of suitable reagents such as organic bases, water also has the ability to switch to higher ionic strength from lower ionic strength (47). SS are very important for processes that need various solvent characteristics in consecutive steps, such as product recovery or extraction (48).

The use and application of switchable solvents reduces the number of solvents required during a chemical process (49,50).

Switchable polarity solvents (SPS) were first introduced by Jessop in the year 2005, which contain either only one component, for example, secondary amines, or are composed of multiple components (51). Usually, two components of switchable polarity solvents are composed of amidine or sometimes guanidine together with a primary amine or an alcohol (52). Other combinations, such as guanidine or diamines/acidic alcohol chemical mixtures, are possible (53).

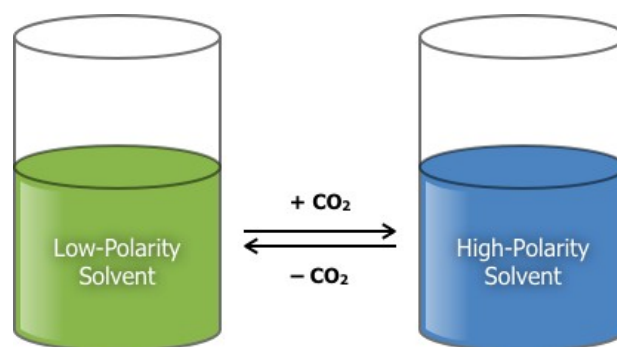


Figure 3: Switchable polarity solvent switching from low-polarity to high polarity by bubbling CO₂ (Adapted from Jessop et al., (56)).

Each SPS has its own properties (54,55). These characteristics have to be taken into consideration when selecting the best SPS for a certain chemical process (56). Systems containing amidine 1,8-diazabicyclo-[5.4.0]-undec-7-ene, for example, are extremely sensitive to moisture, whereas some secondary amines and other amidines SPS are less sensitive (57). One of the advantages of single component SPSs is that they do not need any operator to monitor the mole ratio of these two liquids. Furthermore, secondary amines are cost-effective when compared with amidines (58, 59).

One of the major challenges of industrial processes is solvent removal from hydrophobic materials without the use of distillation processes (60). However, the idea is possible provided that there is a solvent which can reversibly switch from hydrophobic state to a more hydrophilic one (61). Therefore, the discovery of SPS plays a major role in solving this negative inconvenience in industrial processes, because the removal of solvents through distillation is the most common industrial activity that suffers from the main drawbacks that lead to environmental hazards and damage (62). Firstly, because distillation usually employs the usage of a volatile substance, it results in smog formation through great vapor emission. Secondly, it needs a high input of energy (63). Therefore, there is a need to find a new and efficient non-distillative approach for the separation of solvents from their products, in order to avoid the usage of volatile solvents (64,65).

Soylak et al. reported that N,N,N-tributylpentanamide was first used as an SPS that can be applied for extracting low polarity products such as vegetable oils, and then the solvent is removed from the product using carbonated water (66,67). Carbonated water has the ability to extract the solvents from the products due to the fact that the CO₂ can convert the solvent into the polar form. Subsequently, the solvent is then separated from the carbonated water by removing the CO₂, because the removal triggers the conversion of the solvent into its non-polar form. And finally, the removal of the solvent from the herbal product does not require distillation (68,69).

Memon et al., (2017) proposed a green and novel switchable solvent, which was hyphenated with liquid phase micro extraction (SS-LPME) for extraction and preconcentration of the nutritionally and biologically important element Co(II) from tobacco and food samples using flame atomic absorption spectrometry. To improve conversion from the deprotonated form to the protonated form, N, Ndimethyl-n-octylamine bicarbonate was synthesized and used as a switchable solvent in the presence of CO₂ to improve conversion from the deprotonated to the protonated form, and then examined for analyte extraction. A quantitative recovery was achieved (70,71). This study involves the formation of a complex at a pH of 4.0 between Co(II) and 1-nitroso-2-naphthol, which serves as a ligand, and then extraction through conversion of the solvent to a nonpolar N,N-dimethyl-n-octylamine phase. The accuracy and validity of this

method were checked using standard reference material (IC-INCT-OBTL-5) and additional recovery verification. The LOD and LOQ were also found to be $3.2 \mu\text{g L}^{-1}$ and $10.6 \mu\text{g L}^{-1}$ respectively. Finally, this method was efficiently used for the atomic analysis of tobacco, herbal products, and food samples (72).

5. NATURAL DEEP EUTECTIC SOLVENTS (NADES)

In 2003, Abbot and his co-workers introduced deep eutectic solvents (DES) for the first time (73). They reported excellent properties for some eutectic mixtures of a range of quaternary ammonium salts and urea (74). DES are now widely regarded as a novel class of sustainable solvents that serve as green alternatives to ionic liquids (ILs) (75). Because of their similar properties such as starting materials, non-flammability, non-volatility, and high viscosity, DES are considered the 4th generation of ionic liquids (78). However, DES are not entirely made up of ionic species (76,77). DES are created by combining two or more components, such as organic salts (phosphonium salt or quaternary ammonium) and hydrogen bond donors (HBD) or metal salts that can associate with one another via hydrogen bonding (78). The charge delocalization that occurs results in a decrease in the melting point of the final product when compared with the individual melting points of the starting materials (79). Nevertheless, DES has numerous advantages and applications over ILs, such as lower economic and environmental impact (80,81). This is more pronounced for DES that are produced naturally from primary metabolites of living cells, known as natural deep eutectic solvents (NADES), which are mostly found in abundance in our diet, such as amines, sugars, carboxylic acids, polyalcohol and choline (82). These NADES satisfy all the principles of green solvents, which produces many advantages, such as readily available starting materials, reduced toxicity, cost-effectiveness, and simplicity of preparation, among the others. Moreover, they possess excellent physicochemical properties such as adjustable viscosity, wide range of polarity, liquids even at lower temperatures, and high solubilizing capacity for a wide range of compounds that can be fine-tuned for a certain application because of their different structural possibilities (83).

Due to the above properties of NADES, there is a rapid increase in their application for the extraction of biological ingredients of herbal materials such as phenolic acid, saponins, flavonoids, alkaloids, terpenoids and anthocyanin, which clearly indicated the possibility of using NADES in extracting different hydrophobic and hydrophilic naturally occurring chemical compounds (84,85).

In order to select a suitable NADES for extracting active compounds from herbal materials, it is very important to try different combinations having

different physicochemical parameters. For instance, Dai et al., reported that seven NADES were used in the extraction of aromatic pigments having wide range of polarity from *Carthamus tinctorius* L. showing that NADES with low polarity possess the lowest efficiency for polar active compounds but higher extraction ability for non-polar active compounds and vice versa (86). This corresponds to the rule of "like dissolves like". Various researchers draw the same conclusion when extracting phenolic compounds from grape skin. In the study, they used choline-chloride based NADES that contains organic acids, polyalcohol or sugars as the hydrogen bond donors (HBD). However, polyalcohol and sugar based NADES are less polar than organic acid based NADES, having a polarity almost equal to that of methanol (87,88).

Furthermore, to improve the extraction efficiency of NADES, there is a need to optimize the NADES content of water. Increasing the water content decreases its viscosity, thereby increasing the transfer of mass from the herbal matrices to a solution and hence increasing the efficiency of the extraction (89). The main problem with using NADES for extraction is its viscosity, which is generally high at room temperature. For instance, some NADES cannot be utilized directly for extraction without diluting them with water due to their high viscosity. However, increasing the water content decreases the interaction between the solvent and the target analyte. Also, an excess of water in NADES can lead to halide-HBD supramolecular complex breakage and thereby form a single aqueous solution of each of the initial components. In general, a NADES with high water content are more suitable for the extraction of more polar compounds, while those with low water content are more suitable for extracting non-polar compounds. However, water content has a significant effect on the yield for both non-polar and polar-active components. Furthermore, the stability of the target analytes while using NADESs should be taken into consideration as an important factor when selecting a specific solvent. In a study to determine the stability of some phenolic components of safflower extracts, the results showed that using NADES improved compound stability over using conventional solvents (39). The stability in NADES is due to the strong hydrogen bonding that exists between the molecules of the solvent and solute, whereby among the studied NADES, sugar-based NADES showed the highest stability (90). This interaction is responsible for decreasing the mobility of the solute molecules, and this reduces the contact time with oxygen and air, hence minimizes oxidative degradation, which is the major factor that causes degradation of the active compounds (91). There is a need for further research on the reasons behind bioactive ingredients' stability in NADESs for a full understanding of the mechanism (92,93).

Furthermore, before final selection of NADES, its environmental effects should be checked and

examined, because the assumption that NADES are non-toxic is based on toxicity results for individual components used in preparing NADES, which are naturally occurring biomaterials that are pharmaceutically accepted (94). The assumption does not take into account the probability of the existence of combined and synergistic effects of the individual components that make up the NADES (95).

According to the current research trend, there is little or no application of the NADES extraction method on an industrial scale for green extraction of herbal active components on a large scale. Therefore, to achieve such industrial implementation, environmental and economic factors should be considered (96). Though the price of NADES is comparable to that of conventional and classical solvents, their production is regarded as a sustainable process (97). Nevertheless, other factors should be considered, such as the recovery of the target bioactive component as well as the NADES recyclability, before implementing this technique in large scales. Nonetheless, researchers (98-107) reported that NADES is a suitable alternative technique that involves renewability and sustainability for the extraction of value added compounds as well as other precious analytes prior to both atomic and molecular analysis.

CONCLUSION

Currently, most of the techniques used in processing herbal products involve the use of extraction methods. Therefore, trends in extraction methods focus mainly on finding reasonable solutions that minimize the use of toxic solvents and allow the use of renewable and green solvents from natural products that ensure high quality and safe extracts. In the future, SFE is definitely going to be on an industrial scale due to its numerous applications on a large scale, especially for herbal, food, cosmetics, pharmaceutical products etc. Due to its various applications, as mentioned in this research, CO₂ is a vital chemical compound. SFE shows diverse advantages over conventional solvents. Also, switchable polarity solvents (SPS) have shown excellent applications on an industrial scale through switching one of their characteristics from the non-polar form to the polar form simply by bubbling CO₂, which enables complete miscibility and ensures the extraction of the bioactive components. However, there is a need for more development and transference of this technique into the micro extraction method as there is less data and research in that field. Moreover, NADES show unique physicochemical parameters and completely satisfy all the principles of a green solvent that can be used for extracting bioactive compounds from herbal materials, due to their low environmental and economic impacts. However, there is a need for transferring this technique to the industrial scale owing to the meager amount of research

conducted in the published technical literature that is used on a large scale.

Finally, the need for the identification, analysis, and standardization of herbal products is of paramount importance, owing to their significant application in society and to verify fraudulence, fraud, counterfeit, and adulteration.

CONFLICT OF INTEREST

None reported.

ACKNOWLEDGMENTS

The authors will like to thank and acknowledge their appreciations and gratitude to the relevant cited references of this review, which discussed the applications of solvents of the future for herbal products extractions.

REFERENCES

1. Vanhaecke F. A new scope for JAAS! *J Anal At Spectrom.* 2015;30(5):1015-6. Available from: [<URL>](#).
2. Walsh A. The development of atomic absorption methods of elemental analysis 1952-1962. *Anal Chem.* 1991 Oct 1;63(19):933A-941A. Available from: [<URL>](#).
3. Hahn DW, Omenetto N. Laser-induced breakdown spectroscopy (LIBS), part I: review of basic diagnostics and plasma-particle interactions: still-challenging issues within the analytical plasma community. *Applied spectroscopy.* 2010;64(12):335A-336A. Available from: [<URL>](#).
4. Glaus R, Riedel J, Gornushkin I. Insight into the Formation of Molecular Species in Laser-Induced Plasma of Isotopically Labeled Organic Samples. *Anal Chem.* 2015 Oct 6;87(19):10131-7. Available from: [<URL>](#).
5. Chen TL, Kim H, Pan SY, Tseng PC, Lin YP, Chiang PC. Implementation of green chemistry principles in circular economy system towards sustainable development goals: Challenges and perspectives. *Science of The Total Environment.* 2020 May;716:136998. Available from: [<URL>](#).
6. Cvjetko Bubalo M, Vidović S, Radojčić Redovniković I, Jokić S. New perspective in extraction of plant biologically active compounds by green solvents. *Food and Bioproducts Processing.* 2018 May;109:52-73. Available from: [<URL>](#).
7. Mumladze T, Yousef S, Tatariants M, Kriūkienė R, Makarevicius V, Lukošiuūtė SI, et al. Sustainable approach to recycling of multilayer flexible packaging using switchable hydrophilicity solvents. *Green Chem.* 2018;20(15):3604-18. Available from: [<URL>](#).
8. Yardımcı B, Üzer A, Apak R. Spectrophotometric Fluoride Determination Using St. John's Wort Extract as a Green Chromogenic Complexant for Al(III). *ACS Omega.* 2022 Dec 13;7(49):45432-42. Available from: [<URL>](#).
9. Rattanakit P, Maungchang R. Determining Iron(III) Concentration in a Green Chemistry Experiment Using *Phyllanthus emblica* (Indian Gooseberry) Extract and Spectrophotometry. *J Chem Educ.* 2019 Apr 9;96(4):756-60. Available from: [<URL>](#).

10. Cravotto G, Boffa L, Mantegna S, Perego P, Avogadro M, Cintas P. Improved extraction of vegetable oils under high-intensity ultrasound and/or microwaves. *Ultrasonics Sonochemistry*. 2008 Jul;15(5):898-902. Available from: [<URL>](#).
11. Chemat F, Vian MA, Cravotto G. Green Extraction of Natural Products: Concept and Principles. *IJMS*. 2012 Jul 11;13(7):8615-27. [<URL>](#).
12. Bernhoft A. Bioactive compounds in plants: benefits and risks for man and animals: proceedings from a symposium held in Norwegian Academy of Science and Letters, Oslo, 13-14 November 2008. Oslo: Novus Forlag; 2010. ISBN: 978-82-7099-583-7.
13. Anastas P, Eghbali N. Green Chemistry: Principles and Practice. *Chem Soc Rev*. 2010;39(1):301-12. Available from: [<URL>](#).
14. Sadravi S, Honarasa F. Spectrophotometric nanomolar determination of glucose by using C-dots- Fe_3O_4 magnetic nanozyme. *J Chem Sci*. 2019 Jul;131(7):58. Available from: [<URL>](#).
15. Gu Y, Jérôme F. Glycerol as a sustainable solvent for green chemistry. *Green Chem*. 2010;12(7):1127. Available from: [<URL>](#).
16. Ammani HM, Usman AG. Synthesis and characterization of 2-benzoxazolone and its derivatives. *Asian Journal of Natural & Applied Sciences Vol*. 2018;7:2.
17. Li X, Lu H, Liu D, Wang B. Preparation of composite switchable water with hydrophobic tertiary amine for washing oil sands. *Journal of CO2 Utilization*. 2019 Jan;29:254-61. Available from: [<URL>](#).
18. Aher JS, Kardel AV, Gaware MR, Lokhande DD, Bhagare AM. One pot synthesis of pyrimidine-5-carbonitrile and pyrimidine-5-carboxamide using ammonium chloride under solvent free condition. *J Chem Sci*. 2019 Jul;131(7):54. Available from: [<URL>](#).
19. Wang Z. Green Chemistry: Recent Advances in Developing Catalytic Processes in Environmentally-Benign Solvent Systems [Internet]. Powerpoint Presentation presented at: Frontiers of Chemistry Presentation; 2008; Pittsburgh, USA. Available from: [<URL>](#).
20. Verma GK, Raghuvanshi K, Kumar R, Singh MS. An efficient one-pot three-component synthesis of functionalized pyrimido[4,5-b]quinolines and indeno fused pyrido[2,3-d]pyrimidines in water. *Tetrahedron Letters*. 2012 Jan;53(4):399-402. Available from: [<URL>](#).
21. Pompeo N, Torokhtii K, Silva E. Surface impedance measurements in thin conducting films: Substrate and finite-thickness-induced uncertainties. In: 2017 IEEE International Instrumentation and Measurement Technology Conference (I2MTC) [Internet]. Torino, Italy: IEEE; 2017 [cited 2023 Jan 30]. p. 1-5. Available from: [<URL>](#).
22. Wang X, Gao M, Zhang Z, Gu H, Liu T, Yu N, et al. Development of CO₂-Mediated Switchable Hydrophilicity Solvent-Based Microextraction Combined with HPLC-UV for the Determination of Bisphenols in Foods and Drinks. *Food Anal Methods*. 2018 Aug;11(8):2093-104. Available from: [<URL>](#).
23. Yuan X, Richter BE, Jiang K, Boniface KJ, Cormier A, Sanders CA, et al. Carbonated water for the separation of carboxylic compounds: a chromatography approach. *Green Chem*. 2018;20(2):440-8. Available from: [<URL>](#).
24. Asare Bediako BB, Zhou P, Rugabirwa B, Liu Q, Su Y, Wang H, et al. A switchable hydrophilicity solvent mediated process to prepare fine silica aerogel powder as an excellent flattening agent. *Advanced Powder Technology*. 2019 Mar;30(3):565-71. Available from: [<URL>](#).
25. Yilmaz E, Soylak M. Ultrasound assisted-deep eutectic solvent based on emulsification liquid phase microextraction combined with microsample injection flame atomic absorption spectrometry for valence speciation of chromium(III/VI) in environmental samples. *Talanta*. 2016 Nov;160:680-5. Available from: [<URL>](#).
26. Kanberoglu GS, Yilmaz E, Soylak M. Application of deep eutectic solvent in ultrasound-assisted emulsification microextraction of quercetin from some fruits and vegetables. *Journal of Molecular Liquids*. 2019 Apr;279:571-7. Available from: [<URL>](#).
27. Diederich F, Rubin Y. Synthetic Approaches toward Molecular and Polymeric Carbon Allotropes. *Angew Chem Int Ed Engl*. 1992 Sep;31(9):1101-23. Available from: [<URL>](#).
28. Leder C, Rastogi T, Kümmerer K. Putting benign by design into practice-novel concepts for green and sustainable pharmacy: Designing green drug derivatives by non-targeted synthesis and screening for biodegradability. *Sustainable Chemistry and Pharmacy*. 2015 Dec;2:31-6. Available from: [<URL>](#).
29. Tuerhong M, Xu Y, Yin XB. Review on Carbon Dots and Their Applications. *Chinese Journal of Analytical Chemistry*. 2017 Jan;45(1):139-50. Available from: [<URL>](#).
30. Rooney JM. Carbocationic Polymerization: N-Vinylcarbazole. In: *Comprehensive Polymer Science and Supplements* [Internet]. Elsevier; 1989 [cited 2023 Jan 30]. p. 697-704. Available from: [<URL>](#).
31. Madhura TR, Kumar GG, Ramaraj R. Gold nanoparticles decorated silicate sol-gel matrix embedded reduced graphene oxide and manganese ferrite nanocomposite-materials-modified electrode for glucose sensor application. *J Chem Sci*. 2019 May;131(5):35. Available from: [<URL>](#).
32. Zou N, Wei X, Zong Z, Li X, Wang Z, Wang X. A novel enzymatic biosensor for detection of intracellular hydrogen peroxide based on 1-aminopyrene and reduced graphene oxides. *J Chem Sci*. 2019 Apr;131(4):28. Available from: [<URL>](#).
33. Okoh OO, Sadimenko AP, Afolayan AJ. Comparative evaluation of the antibacterial activities of the essential oils of *Rosmarinus officinalis* L. obtained by hydrodistillation and solvent free microwave extraction methods. *Food Chemistry*. 2010 May;120(1):308-12. Available from: [<URL>](#).
34. Fang L, Leng Y, Gao P. Processing of hydroxyapatite reinforced ultrahigh molecular weight polyethylene for biomedical applications. *Biomaterials*. 2005 Jun;26(17):3471-8. Available from: [<URL>](#).
35. Lucchesi ME, Chemat F, Smadja J. An original solvent free microwave extraction of essential oils from spices. *Flavour Fragr J*. 2004 Mar;19(2):134-8. Available from: [<URL>](#).

36. Zou N, Wei X, Zong Z, Li X, Wang Z, Wang X. A novel enzymatic biosensor for detection of intracellular hydrogen peroxide based on 1-aminopyrene and reduced graphene oxides. *J Chem Sci.* 2019 Apr;131(4):28. Available from: [<URL>](#).
37. Lucchesi ME, Chemat F, Smadja J. Solvent-free microwave extraction of essential oil from aromatic herbs: comparison with conventional hydro-distillation. *Journal of Chromatography A.* 2004 Jul;1043(2):323-7. Available from: [<URL>](#).
38. Xu L. Recent advances on supercritical fluid extraction of essential oils. *Afr J Pharm Pharmacol.* 2011 Sep 8;5(9):1196-211. Available from: [<URL>](#).
39. Alhamimi S. Extraction and chromatography of bioactive compounds in complex samples using supercritical CO₂ technology [Internet] [PhD Thesis]. [Sweden]: Lund University; 2018. Available from: [<URL>](#).
40. Gumerov FM, Khairutdinov VF, Akhmetzyanov TR, Gabitov FR, Zaripov ZI, Farakhov MI, et al. Supercritical Fluid Propane-Butane Extraction Treatment of Oil Sludge. *Russ J Phys Chem B.* 2017 Dec;11(7):1103-8. Available from: [<URL>](#).
41. Mothibedi K, Mokgadi J, Torto N. Determination of Flavonoids in Ginkgo Biloba Using Bond Elut Plexa Solid Phase Extraction Sorbent for Cleanup and HPLC-DAD Analysis [Internet]. Agilent Technologies; 2011. Available from: [<URL>](#).
42. Hala EA, Yasser AF, Abeer AEW. Application of numerical modeling for optimization of selective hot water extraction of taxifolin from milk thistle seeds. *Afr J Biotechnol.* 2013 Aug 29;10(48):9804-11. Available from: [<URL>](#).
43. Pourmortazavi SM, Hajimirsadeghi SS. Supercritical fluid extraction in plant essential and volatile oil analysis. *Journal of Chromatography A.* 2007 Sep;1163(1-2):2-24. Available from: [<URL>](#).
44. Cvjetko Bubalo M, Ćurko N, Tomašević M, Kovačević Ganić K, Radojčić Redovniković I. Green extraction of grape skin phenolics by using deep eutectic solvents. *Food Chemistry.* 2016 Jun;200:159-66. Available from: [<URL>](#).
45. Jokić S, Bijuk M, Aladić K, Bilić M, Molnar M. Optimisation of supercritical CO₂ extraction of grape seed oil using response surface methodology. *Int J Food Sci Technol.* 2016 Feb;51(2):403-10. Available from: [<URL>](#).
46. Yılmaz E, Soylak M. Switchable solvent-based liquid phase microextraction of copper(ii): optimization and application to environmental samples. *J Anal At Spectrom.* 2015;30(7):1629-35. Available from: [<URL>](#).
47. Vanderveen JR, Burra S, Geng J, Goyon A, Jardine A, Shin HE, et al. Characterizing the Effects of a "Switchable Water" Additive on the Aqueous Solubility of Small Molecules. *ChemPhysChem.* 2018 Aug 17;19(16):2093-100. Available from: [<URL>](#).
48. Wang S, Zheng C, Zhao J, Li X, Lu H. Extracting and recovering diesel from oil-based drill cuttings using switchable hydrophilic solvents. *Chemical Engineering Research and Design.* 2017 Dec;128:27-36. Available from: [<URL>](#).
49. Soylak M, Khan M, Yılmaz E. Switchable solvent based liquid phase microextraction of uranium in environmental samples: a green approach. *Anal Methods.* 2016;8(5):979-86. Available from: [<URL>](#).
50. Zare F, Ghaedi M, Jannesar R, Tayebi L. Switchable polarity solvents for preconcentration and simultaneous determination of amino acids in human plasma samples. *New J Chem.* 2018;42(12):10007-15. Available from: [<URL>](#).
51. Grabner B. Switchable Solvents and Room-Temperature Solid Phase Ionic Liquids in Biocatalysis [Internet] [Master's Thesis]. [Graz, Austria]: Technische Universität Graz; 2015. Available from: [<URL>](#).
52. Ahmar H, Nejati-Yazdinejad M, Najafi M, Hasheminasab KS. Switchable Hydrophilicity Solvent-Based Homogenous Liquid-Liquid Microextraction (SHS-HLLME) Combined with GC-FID for the Quantification of Methadone and Tramadol. *Chromatographia.* 2018 Jul;81(7):1063-70. Available from: [<URL>](#).
53. Stone ML, Rae C, Stewart FF, Wilson AD. Switchable polarity solvents as draw solutes for forward osmosis. *Desalination.* 2013 Mar;312:124-9. Available from: [<URL>](#).
54. Reimund KK, Coscia BJ, Arena JT, Wilson AD, McCutcheon JR. Characterization and membrane stability study for the switchable polarity solvent N,N-dimethylcyclohexylamine as a draw solute in forward osmosis. *Journal of Membrane Science.* 2016 Mar;501:93-9. Available from: [<URL>](#).
55. Hardy S, de Wispelaere IM, Leitner W, Liauw MA. Comprehensive monitoring of a biphasic switchable solvent synthesis. *Analyst.* 2013;138(3):819-24. Available from: [<URL>](#).
56. Vanderveen JR, Geng J, Zhang S, Jessop PG. Diamines as switchable-hydrophilicity solvents with improved phase behaviour. *RSC Adv.* 2018;8(48):27318-25. Available from: [<URL>](#).
57. Jessop PG. Fundamental properties and practical applications of ionic liquids: concluding remarks. *Faraday Discuss.* 2018;206:587-601. Available from: [<URL>](#).
58. Ezoddin M, Abdi K, Lamei N. Development of air assisted liquid phase microextraction based on switchable-hydrophilicity solvent for the determination of palladium in environmental samples. *Talanta.* 2016 Jun;153:247-52. Available from: [<URL>](#).
59. Jessop PG, Kozycz L, Rahami ZG, Schoenmakers D, Boyd AR, Wechsler D, et al. Tertiary amine solvents having switchable hydrophilicity. *Green Chem.* 2011;13(3):619. Available from: [<URL>](#).
60. Donaldson ME, Mestre VL, Vinci D, Liotta CL, Eckert CA. Switchable Solvents for in-Situ Acid-Catalyzed Hydrolysis of β -Pinene. *Ind Eng Chem Res.* 2009 Mar 4;48(5):2542-7. Available from: [<URL>](#).
61. Jessop PG, Phan L, Carrier A, Robinson S, Dürr CJ, Harjani JR. A solvent having switchable hydrophilicity. *Green Chem.* 2010;12(5):809. Available from: [<URL>](#).
62. Durelle J. Designing Switchable-Hydrophilicity Solvents and Modelling their Behaviour [Internet] [Master's Thesis]. [Canada]: Queen's University; 2014. Available from: [<URL>](#).
63. Fu D, Farag S, Chaouki J, Jessop PG. Extraction of phenols from lignin microwave-pyrolysis oil using a

- switchable hydrophilicity solvent. *Bioresource Technology*. 2014 Feb;154:101-8. Available from: [<URL>](#).
64. Shahvandi SK, Banitaba MH, Ahmar H. Development of a new pH assisted homogeneous liquid-liquid microextraction by a solvent with switchable hydrophilicity: Application for GC-MS determination of methamphetamine. *Talanta*. 2018 Jul;184:103-8. Available from: [<URL>](#).
65. Memon ZM, Yilmaz E, Soylak M. Switchable solvent based green liquid phase microextraction method for cobalt in tobacco and food samples prior to flame atomic absorption spectrometric determination. *Journal of Molecular Liquids*. 2017 Mar;229:459-64. Available from: [<URL>](#).
66. Tetko IV, Gasteiger J, Todeschini R, Mauri A, Livingstone D, Ertl P, et al. Virtual Computational Chemistry Laboratory – Design and Description. *J Comput Aided Mol Des*. 2005 Jun;19(6):453-63. Available from: [<URL>](#).
67. Sendur OF, Turan Y, Bal S, Gurgan A. Toxic Neuropathy Due to N-Hexane: Report of Three Cases. *Inhalation Toxicology*. 2009 Feb;21(3):210-4. Available from: [<URL>](#).
68. Lasarte-Aragonés G, Lucena R, Cárdenas S, Valcárcel M. Use of switchable solvents in the microextraction context. *Talanta*. 2015 Jan;131:645-9. Available from: [<URL>](#).
69. Phan L, Andreatta JR, Horvey LK, Edie CF, Luco AL, Mirchandani A, et al. Switchable-Polarity Solvents Prepared with a Single Liquid Component. *J Org Chem*. 2008 Jan 1;73(1):127-32. Available from: [<URL>](#).
70. Soylak M, Unsal YE. Solid-phase extraction of heavy metal ions on bucky tubes disc in natural water and herbal plant samples. *Environ Monit Assess*. 2011 Oct;181(1-4):577-86. Available from: [<URL>](#).
71. Campbell KN, Sommers AH, Campbell BK. The Preparation of Unsymmetrical Secondary Aliphatic Amines 1. *J Am Chem Soc*. 1944 Jan;66(1):82-4. Available from: [<URL>](#).
72. Soylak M, Şahin U, Elçi L. Spectrophotometric determination of molybdenum in steel samples utilizing selective sorbent extraction on Amberlite XAD-8 resin. *Analytica Chimica Acta*. 1996 Mar;322(1-2):111-5. Available from: [<URL>](#).
73. Vanderveen JR, Durelle J, Jessop PG. Design and evaluation of switchable-hydrophilicity solvents. *Green Chem*. 2014;16(3):1187-97. Available from: [<URL>](#).
74. Hardy S, Liauw MA. Mixing behaviour investigation of a switchable solvent synthesis using ATR-IR spectroscopy. *Chemical Engineering Journal*. 2013 Nov;233:292-6. Available from: [<URL>](#).
75. Caruso R, O'Connor R, Stephens W, Cummings K, Fong G. Toxic Metal Concentrations in Cigarettes Obtained from U.S. Smokers in 2009: Results from the International Tobacco Control (ITC) United States Survey Cohort. *IJERPH*. 2013 Dec 20;11(1):202-17. Available from: [<URL>](#).
76. Oliveira PR, Lamy-Mendes AC, Rezende EIP, Mangrich AS, Marcolino Junior LH, Bergamini MF. Electrochemical determination of copper ions in spirit drinks using carbon paste electrode modified with biochar. *Food Chemistry*. 2015 Mar;171:426-31. Available from: [<URL>](#).
77. Abbott AP, Capper G, Davies DL, Rasheed RK, Tambyrajah V. Novel solvent properties of choline chloride/urea mixtures. Electronic supplementary information (ESI) available: spectroscopic data. See [<URL>](#). *Chem Commun*. 2003 Dec 19;(1):70-1.
78. Abbott AP, Capper G, Davies DL, Munro HL, Rasheed RK, Tambyrajah V. Preparation of novel, moisture-stable, Lewis-acidic ionic liquids containing quaternary ammonium salts with functional side chains. *Chem Commun*. 2001;(19):2010-1. Available from: [<URL>](#).
79. Sitze MS, Schreiter ER, Patterson EV, Freeman RG. Ionic Liquids Based on FeCl₃ and FeCl₂. Raman Scattering and ab Initio Calculations. *Inorg Chem*. 2001 May 1;40(10):2298-304. Available from: [<URL>](#).
80. Miao X, Liu T, Zhang C, Geng X, Meng Y, Li X. Fluorescent aliphatic hyperbranched polyether: chromophore-free and without any N and P atoms. *Phys Chem Chem Phys*. 2016;18(6):4295-9. Available from: [<URL>](#).
81. Zhang Q, De Oliveira Vigier K, Royer S, Jérôme F. Deep eutectic solvents: syntheses, properties and applications. *Chem Soc Rev*. 2012;41(21):7108. Available from: [<URL>](#).
82. Choi YH, van Spronsen J, Dai Y, Verberne M, Hollmann F, Arends IWCE, et al. Are Natural Deep Eutectic Solvents the Missing Link in Understanding Cellular Metabolism and Physiology? *Plant Physiology*. 2011 Aug 5;156(4):1701-5. Available from: [<URL>](#).
83. Faggian M, Sut S, Perissutti B, Baldan V, Grabnar I, Dall'Acqua S. Natural Deep Eutectic Solvents (NADES) as a Tool for Bioavailability Improvement: Pharmacokinetics of Rutin Dissolved in Proline/Glycine after Oral Administration in Rats: Possible Application in Nutraceuticals. *Molecules*. 2016 Nov 14;21(11):1531. Available from: [<URL>](#).
84. Zainal-Abidin MH, Hayyan M, Hayyan A, Jayakumar NS. New horizons in the extraction of bioactive compounds using deep eutectic solvents: A review. *Analytica Chimica Acta*. 2017 Aug;979:1-23. Available from: [<URL>](#).
85. Mbous YP, Hayyan M, Hayyan A, Wong WF, Hashim MA, Looi CY. Applications of deep eutectic solvents in biotechnology and bioengineering—Promises and challenges. *Biotechnology Advances*. 2017 Mar;35(2):105-34. Available from: [<URL>](#).
86. Radošević K, Ćurko N, Gaurina Srček V, Cvjetko Bubalo M, Tomašević M, Kovačević Ganić K, et al. Natural deep eutectic solvents as beneficial extractants for enhancement of plant extracts bioactivity. *LWT*. 2016 Nov;73:45-51. Available from: [<URL>](#).
87. Dai Y, van Spronsen J, Witkamp GJ, Verpoorte R, Choi YH. Natural deep eutectic solvents as new potential media for green technology. *Analytica Chimica Acta*. 2013 Mar;766:61-8. Available from: [<URL>](#).
88. Wang M, Wang J, Zhang Y, Xia Q, Bi W, Yang X, et al. Fast environment-friendly ball mill-assisted deep eutectic solvent-based extraction of natural products. *Journal of Chromatography A*. 2016 Apr;1443:262-6. [<URL>](#).

89. Dai Y, Verpoorte R, Choi YH. Natural deep eutectic solvents providing enhanced stability of natural colorants from safflower (*Carthamus tinctorius*). *Food Chemistry*. 2014 Sep;159:116–21. Available from: [<URL>](#).
90. Dai Y, Rozema E, Verpoorte R, Choi YH. Application of natural deep eutectic solvents to the extraction of anthocyanins from *Catharanthus roseus* with high extractability and stability replacing conventional organic solvents. *Journal of Chromatography A*. 2016 Feb;1434:50–6. Available from: [<URL>](#).
91. Castañeda-Ovando A, Pacheco-Hernández Ma de L, Páez-Hernández MaE, Rodríguez JA, Galán-Vidal CA. Chemical studies of anthocyanins: A review. *Food Chemistry*. 2009 Apr;113(4):859–71. Available from: [<URL>](#).
92. Wei ZF, Wang XQ, Peng X, Wang W, Zhao CJ, Zu YG, et al. Fast and green extraction and separation of main bioactive flavonoids from *Radix Scutellariae*. *Industrial Crops and Products*. 2015 Jan;63:175–81. Available from: [<URL>](#).
93. Biswal MR, Rai S, Prakash MK. Molecular dynamics based antimicrobial activity descriptors for synthetic cationic peptides. *J Chem Sci*. 2019 Feb;131(2):16. Available from: [<URL>](#).
94. Qi XL, Peng X, Huang YY, Li L, Wei ZF, Zu YG, et al. Green and efficient extraction of bioactive flavonoids from *Equisetum palustre* L. by deep eutectic solvents-based negative pressure cavitation method combined with macroporous resin enrichment. *Industrial Crops and Products*. 2015 Aug;70:142–8. Available from: [<URL>](#).
95. Bi W, Tian M, Row KH. Evaluation of alcohol-based deep eutectic solvent in extraction and determination of flavonoids with response surface methodology optimization. *Journal of Chromatography A*. 2013 Apr;1285:22–30. Available from: [<URL>](#).
96. Huang Y, Feng F, Jiang J, Qiao Y, Wu T, Voglmeir J, et al. Green and efficient extraction of rutin from tartary buckwheat hull by using natural deep eutectic solvents. *Food Chemistry*. 2017 Apr;221:1400–5. Available from: [<URL>](#).
97. Bajkacz S, Adamek J. Evaluation of new natural deep eutectic solvents for the extraction of isoflavones from soy products. *Talanta*. 2017 Jun;168:329–35. Available from: [<URL>](#).
98. Cunha SC, Fernandes JO. Extraction techniques with deep eutectic solvents. *TrAC Trends in Analytical Chemistry*. 2018 Aug;105:225–39. Available from: [<URL>](#).
99. Wei Z, Qi X, Li T, Luo M, Wang W, Zu Y, et al. Application of natural deep eutectic solvents for extraction and determination of phenolics in *Cajanus cajan* leaves by ultra performance liquid chromatography. *Separation and Purification Technology*. 2015 Jul;149:237–44. Available from: [<URL>](#).
100. Bajkacz S, Adamek J. Development of a Method Based on Natural Deep Eutectic Solvents for Extraction of Flavonoids from Food Samples. *Food Anal Methods*. 2018 May;11(5):1330–44. Available from: [<URL>](#).
101. Fernández M de los Á, Boiteux J, Espino M, Gomez FJV, Silva MF. Natural deep eutectic solvents-mediated extractions: The way forward for sustainable analytical developments. *Analytica Chimica Acta*. 2018 Dec;1038:1–10. Available from: [<URL>](#).
102. Shishov A, Bulatov A, Locatelli M, Carradori S, Andrich V. Application of deep eutectic solvents in analytical chemistry. A review. *Microchemical Journal*. 2017 Nov;135:33–8. Available from: [<URL>](#).
103. Mehariya S, Fratini F, Lavecchia R, Zuorro A. Green extraction of value-added compounds from microalgae: A short review on natural deep eutectic solvents (NADES) and related pre-treatments. *Journal of Environmental Chemical Engineering*. 2021 Oct;9(5):105989. Available from: [<URL>](#).
104. Popovic BM, Micic N, Potkonjak A, Blagojevic B, Pavlovic K, Milanov D, et al. Novel extraction of polyphenols from sour cherry pomace using natural deep eutectic solvents – Ultrafast microwave-assisted NADES preparation and extraction. *Food Chemistry*. 2022 Jan;366:130562. Available from: [<URL>](#).
105. Hikmawanti NPE, Ramadon D, Jantan I, Mun'im A. Natural Deep Eutectic Solvents (NADES): Phytochemical Extraction Performance Enhancer for Pharmaceutical and Nutraceutical Product Development. *Plants*. 2021 Oct 1;10(10):2091. Available from: [<URL>](#).
106. Nystedt HL, Grønlien KG, Tønnesen HH. Interactions of natural deep eutectic solvents (NADES) with artificial and natural membranes. *Journal of Molecular Liquids*. 2021 Apr;328:115452. Available from: [<URL>](#).
107. Canales R, Espino M, Pasini S, Silva MF. Chemometric and green metric strategies for sustainable analytical methods: phenolic compounds in lettuce-NADES extracts. *Anal Methods*. 2021;13(10):1261–8. Available from: [<URL>](#).



Synthesis, Spectral Characterization, Crystal Structure, and Antioxidant Properties of novel Palladium(II) Complex from ONS Donor 1,5-bis(2-hydroxybenzylidene)thiocarbohydrazone

Yeliz Kaya^{1*} 

¹Istanbul University-Cerrahpaşa, Faculty of Engineering, Department of Chemistry, Istanbul, Türkiye

Abstract: A new Pd(II) complex, [Pd(PPh₃)(L)] (L = 1,5-bis(2-hydroxybenzylidene)thiocarbohydrazone, PPh₃ = triphenylphosphine), was synthesized and characterized by FTIR, ¹H NMR and UV-Vis spectroscopies and elemental analysis. The molecular structure of [Pd(PPh₃)(L)] was confirmed by the single-crystal X-ray diffraction technique. Palladium ion has distorted square planar geometry according to X-ray diffraction studies. The free thiocarbohydrazone (L), potentially a pentadentate ONSNO donor, acted as a tridentate ONS donor. The antioxidant capacity of the free thiocarbohydrazone and Pd(II) complex was determined using the CUPRAC (cupric reducing antioxidant capacity) method. Also, the DPPH method was used to test the free radical scavenging activity of the free thiocarbohydrazone and Pd(II) complex. Antioxidant activity studies showed that free thiocarbohydrazone exhibited better activity than Pd(II) complex.

Keywords: Thiocarbohydrazone; Palladium(II) complex; Triphenylphosphine; Crystal structure; Antioxidant activity.

Submitted: October 25, 2022. **Accepted:** December 19, 2022.

Cite this: Kaya Y. Synthesis, Spectral Characterization, Crystal Structure, and Antioxidant Properties of novel Palladium(II) Complex from ONS Donor 1,5-bis(2-hydroxybenzylidene)thiocarbohydrazone. JOTCSA. 2023;10(1):129-38.

DOI: <https://doi.org/10.18596/jotcsa.1194323>.

***Corresponding author. E-mail:** yeliz.kaya@iuc.edu.tr.

1. INTRODUCTION

Thiocarbohydrazide (NH₂-NH-C(S)-NH-NH₂) and its derivatives are a class of compounds that have applications in many fields and therefore attract great interest (1, 2). One or both of the hydrazine groups of thiocarbohydrazide can form Schiff bases called mono- or bithiocarbohydrazone by reacting with aldehydes or ketones (3, 4). Thiocarbohydrazones are interesting ligand systems as they have a variety of potential donor sites; they can bind many transition metals through both azomethinic nitrogen and sulfur atoms in their structure and donor atoms originating from aldehyde or ketone (5). These compounds and their metal complexes show biological activities such as antimicrobial, antioxidant, anticancer, antiviral, antidiabetic, and hepatoprotective (5-17). In addition, there has been an increase in the use of thiocarbohydrazones as

spectrophotometric reagents in metal determination in recent years (18-20).

Interest in phosphine-based ligands and their metal complexes increased after their roles were discovered in catalysis and stereoselective synthesis (21, 22). These compounds have also been shown to have significant bioactivities such as antitumor, antiviral, antifungal, antibacterial, and antioxidant (13, 23). Among these compounds, especially phosphine-based palladium(II) and nickel(II) complexes have been reported to have important bioactivities (22, 23). In addition, transition metal-phosphine complexes are very important for both industrial and laboratory scale catalytic applications (24).

Cisplatin, carboplatin, and oxaliplatin are effective metal-based anticancer agents (25, 26). Due to

serious side effects, drug resistance and the limited spectrum of tumors, extensive attempts have been made to replace these drugs with more efficient, less toxic and targeted anticancer drugs (e.g. Pd, Ni, Ru and Au complexes) (26-28). Because their coordination geometry and complex forming processes are very similar to platinum(II) complexes, palladium(II) complexes have received special attention as metal-organic antitumor drugs (27-31). Palladium(II) complexes have also antimicrobial and antioxidant properties (32). Carbon-carbon bond formation reactions catalyzed by palladium, such as the Suzuki Miyaura, Heck, and Sonogashira coupling reactions, are significant synthetical transformations. These synthetic transformations are widely used to prepare a wide range of organic molecules and materials, including natural products, fine chemicals, drugs, agrochemicals, and polymers (33). Many catalytic systems have been improved using palladium catalysts such as [Pd(PPh₃)₄] and [PdCl₂(PPh₃)₂] (34-36). However, some palladium(II) complexes containing triphenylphosphine secondary ligand have been found to be inhibitors of enzymes such as alkaline phosphatase (ALP), topoisomerase-II, β -glucuronidase, carbonic anhydrase and acetylcholinesterase (37-41).

There are only very few reports concerning Pd(II) complexes containing both thiocarbohydrazone and triphenylphosphine in the literature (41, 42). Therefore, in this study, a new Pd(II) complex was synthesized using 1,5-bis(2-hydroxybenzylidene)thiocarbohydrazone (L) and [PdCl₂(PPh₃)₂] to test its potential antioxidant activity. The characterization of free thiocarbohydrazone and Pd(II) complex were performed using elemental analysis, FTIR, ¹H NMR and UV-Vis spectroscopic techniques. The antioxidant activities of free thiocarbohydrazone and Pd(II) complex were also examined using DPPH• radical scavenging activity and CUPRAC method.

2. EXPERIMENTAL SECTION

2.1. Materials and Physical Measurements

Thiocarbohydrazide was obtained according to the published procedure (43). All other chemicals were purchased from chemical companies and used as received.

Elemental analyzes, IR and ¹H NMR spectra, UV-Vis data (in 4 x 10⁻⁵ M DMSO) and magnetic susceptibility measurements were performed using a Thermo Finnigan Flash EA 1112 elemental analyzer, an Agilent Cary 630 FTIR, a Varian UNITY INOVA 500 MHz NMR device, a Shimadzu 2600 UV-Vis spectrophotometer and a Sherwood Scientific MK I model device, respectively.

2.2. Synthesis of 1,5-bis(2-hydroxybenzylidene)thiocarbohydrazone (L)

Ligand (L) was prepared according to our reported article (44). Thiocarbohydrazide (0.01 mol, 1.06 g) and 2-hydroxybenzaldehyde (0.02 mol, 2.44 g) was mixed in methanol (25 mL). The mixture was refluxed for 4 h. The light-yellow colored product, which precipitated after a few days, was filtered and washed with methanol. Elemental analysis and spectroscopic data for L confirmed its synthesis (Figure 1).

Yield: 85%. Color: Light-yellow. M.p.: 190-191 °C. Calc. for C₁₅H₁₄N₄O₂S (314.36 g mol⁻¹): C: 57.31, H: 4.49, N: 17.82, S: 10.20%; found: C: 57.50, H: 4.46, N: 17.84, S: 10.28%. ¹H NMR (500 MHz, DMSO-d₆, ppm): 11.70 (s, 2H, -OH), 11.62 (s, 1H, -NH), 10.62 (s, 1H, -NH), 8.67 (s, 2H, -CH=N-), 7.35-6.89 (m, 8H, aromatic H). IR (cm⁻¹): ν (OH) 3195, ν (NH) 3133, ν (C=N) 1613, ν (C=S) 1240. UV-Vis [λ_{max} (nm)]: 251 $\pi \rightarrow \pi^*$, 302 $\pi \rightarrow \pi^*$, 351 $n \rightarrow \pi^*$, 367 $n \rightarrow \pi^*$.

2.3. Synthesis of [Pd(PPh₃)₂](L)

1 mmol of [PdCl₂(PPh₃)₂] (0.71 g) dissolved in ethanol (5 mL) was mixed with 1 mmol of L (0.31 g) dissolved in ethanol (10 mL) and dichloromethane (5 mL). Then, Et₃N (1 drop) was added to the mixture and the mixture was stirred under reflux for 5 h to afford an orange precipitate. The obtained solid was filtered and washed with ethanol (Figure 1).

Yield: 52%. Color: Orange. M.p.: 271-273 °C. Calc. for C₃₃H₂₇N₄O₂PPdS (681.05 g mol⁻¹): C: 58.20, H: 4.00, N: 8.23, S: 4.71%; found: C: 58.03, H: 3.96, N: 8.14, S: 4.57%. ¹H NMR (500 MHz, DMSO-d₆, ppm): 11.65 (s, 1H, -OH), 10.64 (s, 1H, -NH), 8.48 (s, 1H, -CH=N-), 8.11 (s, 1H, -CH=N-), 7.65-5.71 (m, 23H, aromatic H). IR (cm⁻¹): ν (OH) 3190, ν (NH) 3154, ν (C=N) 1618 and 1598, ν (PPh₃) 1432, 1099, 738, 690. UV-Vis [λ_{max} (nm)]: 256 $\pi \rightarrow \pi^*$, 280 $\pi \rightarrow \pi^*$, 313 $\pi \rightarrow \pi^*$, 339 $n \rightarrow \pi^*$, 355 $n \rightarrow \pi^*$, 410 $n \rightarrow \pi^*$, 424 LMCT.

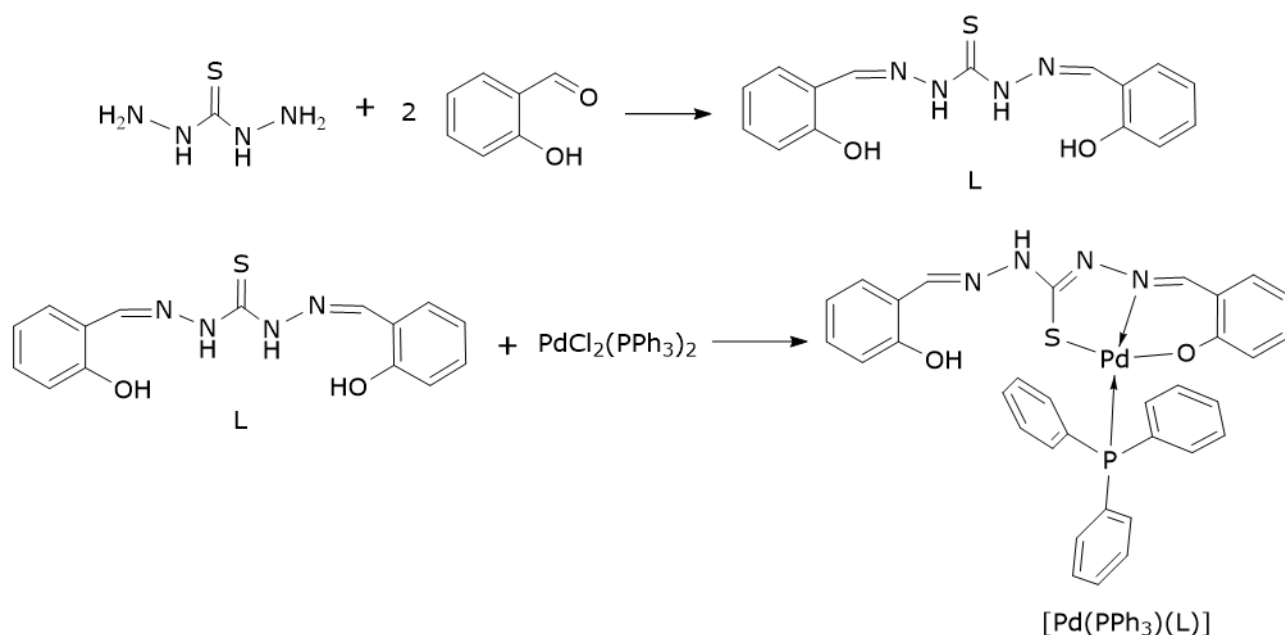


Figure 1: The general synthesis of the free thiocarbohydrazone and Pd(II) complex.

2.4. Determination of Crystal Structure

Slow evaporation of [Pd(PPh₃)(L)] in ethanol + DCM gave single crystals suitable for determining the molecular structure of the complex. A Bruker APEX II CCD three-circle diffractometer was used for X-ray diffraction data collection and unit cell determination at room temperature. Indexing, data reduction and integration were performed using APEX2 (45) and SAINT (46). Structure solution and refinement were performed with the SHELXT (47) and SHELXL (48) programs. The program Mercury was used to represent the molecular structure (49). Hydrogen atoms were positioned geometrically and treated with the riding model. The crystallographic data of [Pd(PPh₃)(L)] are given in Table 1. The selected bond distances and angles are listed in Table 2.

2.5. CUPRAC and DPPH Methods

The radical scavenging activities of free thiocarbohydrazone and Pd(II) complex were measured using the DPPH method according to the formerly declared method with minor changes (50). To a tube; 2 mL of 10⁻⁴ M DPPH in ethanol, 1 mL of 10⁻⁴ M of the sample in ethanol (containing 1% DMSO) and (1 - x) mL of ethanol were added. The mixture (4 mL) was incubated in a dark place at 25 °C. After 30 minutes, the absorbances of the sample and control solutions were measured against ethanol at 515 nm. The control solution was obtained by mixing DPPH solution (2 mL) and ethanol (2 mL). Trolox was used as the reference compound. The radical scavenging activity was computed from Equation (1) below.

$$\% \text{radical scavenging activity} = \left[\frac{A_{\text{control}} - A_{\text{sample}}}{A_{\text{control}}} \right] \times 100 \quad \text{Equation (1)}$$

mol⁻¹ cm⁻¹).

Antioxidant capacities of free thiocarbohydrazone and Pd(II) complex were determined by CUPRAC method (51). To a tube; 1 mL of 10⁻² M CuCl₂·2H₂O in water, 1 mL of 7.5 × 10⁻³ M neocuproine in ethanol, 1 mL of 1 M NH₄Ac in water, x mL of 10⁻⁴ M sample in ethanol (containing 1% DMSO) and (1.1 - x) mL of water were added and the total volume was adjusted to 4.1 mL. The mixture was incubated in a dark place for 30 minutes. Then, the absorbance values were recorded at 450 nm. The results were given as TEAC (trolox equivalent antioxidant capacity) coefficient. TEAC values were calculated by dividing the molar absorptivity (ε) of the compounds by that of Trolox (ε_{trolox} = 1.67 × 10⁴ L

3. RESULTS AND DISCUSSION

3.1. Synthesis and Spectral Characterization

The ligand was prepared by the condensation of thiocarbohydrazide (0.01 mol) with 2-hydroxybenzaldehyde (0.02 mol). The reaction of free thiocarbohydrazone (L) with an equimolar amount of [PdCl₂(PPh₃)₂] afforded the Pd(II) complex [Pd(PPh₃)(L)]. The complex is soluble in DCM, DMF and DMSO solvents. The μ_{eff} measurement showed that the complex is diamagnetic. The elemental analysis and spectroscopic data agreed with the

proposed molecular formula of the free thiocarbohydrazone and Pd(II) complex.

In the IR spectrum of L, the characteristic peaks of OH, NH, C=N and C=S groups were seen at 3195, 3133, 1613 and 1240 cm^{-1} , respectively. The bands of OH and NH groups were observed at 3190 and 3154 cm^{-1} in the spectrum of $[\text{Pd}(\text{PPh}_3)(\text{L})]$. This can be interpreted as one of the OH and NH groups of L did not participate in the formation of the complex. The absence of the band attributed to the $\nu(\text{C}=\text{S})$ in the spectrum of $[\text{Pd}(\text{PPh}_3)(\text{L})]$ can be explained by the tautomerism of the C=S group with one NH group to form the C-SH in the molecule of L. One of the bands belonging to the azomethine groups in L shifted to lower wavenumber (1598 cm^{-1}) in the spectrum of $[\text{Pd}(\text{PPh}_3)(\text{L})]$. This indicates the coordination of one of the azomethine nitrogen atoms of the ligand to the metal atom. $[\text{Pd}(\text{PPh}_3)(\text{L})]$ spectrum also includes the characteristic bands of the coordinated PPh_3 ligand at 1432, 1099, 738, 690 cm^{-1} (10, 41, 52).

^1H NMR spectrum of L exhibits two $\text{OH}_{\text{phenolic}}$ protons at 11.70 ppm whereas the spectrum of $[\text{Pd}(\text{PPh}_3)(\text{L})]$ adopts only one $\text{OH}_{\text{phenolic}}$ signal at 11.65 ppm since other OH proton is involved in bonding with palladium ion. Although the spectrum of L exhibits two NH signals at 11.62 and 10.62 ppm, the spectrum of $[\text{Pd}(\text{PPh}_3)(\text{L})]$ displays only one signal at 10.64 ppm. The disappearance of the proton in the NH group indicates the deprotonation in the NH group through the sulfur atom by tautomerism ($\text{NH}-\text{C}=\text{S} \leftrightarrow \text{N}=\text{C}-\text{SH}$). The spectrum of L shows signals belonging to two azomethine protons at 8.67 ppm, one of which undergoes a downfield shift by complexation (41, 44, 53).

The electronic spectrum of L exhibits two absorptions at 251 and 302 nm assigned to $\pi \rightarrow \pi^*$ transitions of phenyl rings. These bands were seen at 256, 280 and 313 nm in the spectrum of $[\text{Pd}(\text{PPh}_3)(\text{L})]$. The absorption bands at 315 and 367 nm in the spectrum of L are due to $n \rightarrow \pi^*$ transitions of the C=N and C=S groups. The fact that these

bands appear at 339, 355 and 410 nm in the spectrum of $[\text{Pd}(\text{PPh}_3)(\text{L})]$ can be interpreted as the metal atom being coordinated to the ligand via the azomethine nitrogen and sulfur atom. Also, different from the spectrum of L, the band attributed to the charge transfer transition (LMCT) was observed at 424 nm in the spectrum of $[\text{Pd}(\text{PPh}_3)(\text{L})]$ (26, 41, 54).

3.2. Crystal Structure Analysis

According to the results of the crystallographic analysis, $[\text{Pd}(\text{PPh}_3)(\text{L})]$ crystallizes in the $\text{P}2_1/\text{n}$ space group and as a monoclinic crystal system. The molecular structure and atom labeling scheme of $[\text{Pd}(\text{PPh}_3)(\text{L})]$ is shown in Figure 2. There are two crystallographically independent $[\text{Pd}(\text{PPh}_3)(\text{L})]$ molecules with similar parameters in the asymmetric unit. The palladium ion displays a slightly distorted square planar geometry involving oxygen, nitrogen, sulfur and phosphorus atoms. Although free thiocarbohydrazone is a potential pentadentate, it acts as a dibasic tridentate ONS donor in $[\text{Pd}(\text{PPh}_3)(\text{L})]$. In the complex, ligand is coordinated to Pd(II), forming six and five-membered chelate rings with O2-Pd1-N4, O4-Pd2-N8 and N4-Pd1-S1, N8-Pd2-S2 angles of 93.3(3) $^\circ$, 92.9(3) $^\circ$ and 84.0(3) $^\circ$, 85.0(3) $^\circ$ respectively, and these angles are similar to those observed in related Pd(II) complexes (26, 41, 55). The S1-Pd1-O2 [176.7(2) $^\circ$], S2-Pd2-O4 [177.0(2) $^\circ$] and N4-Pd1-P006 [178.4(3) $^\circ$], N8-Pd2-P005 [178.8(3) $^\circ$] bond angles are very close to the ideal angle of 180 $^\circ$. The binding parameters show that there is a slight distortion from ideal geometry around palladium ion. Pd-S [2.245(3) Å], Pd-O [2.013(8) Å and 2.014(8) Å], Pd-N [2.017(9) Å and 2.029(9) Å], and Pd-P [2.265(3) Å and 2.258(3) Å] bond distances are within normal ranges and are in good agreement with those found in four-coordinate Pd(II) complexes containing triphenylphosphine (26, 41, 56). C8-S1 [1.761(12) Å] and C41-S2 [1.764(12) Å] bond distances indicate that L is bound to palladium ion in the thiolate form (41, 42, 57). In addition, the molecular structure of $[\text{Pd}(\text{PPh}_3)(\text{L})]$ is stabilized by weak and moderately bound intermolecular and intramolecular hydrogen bonds (Table 3).

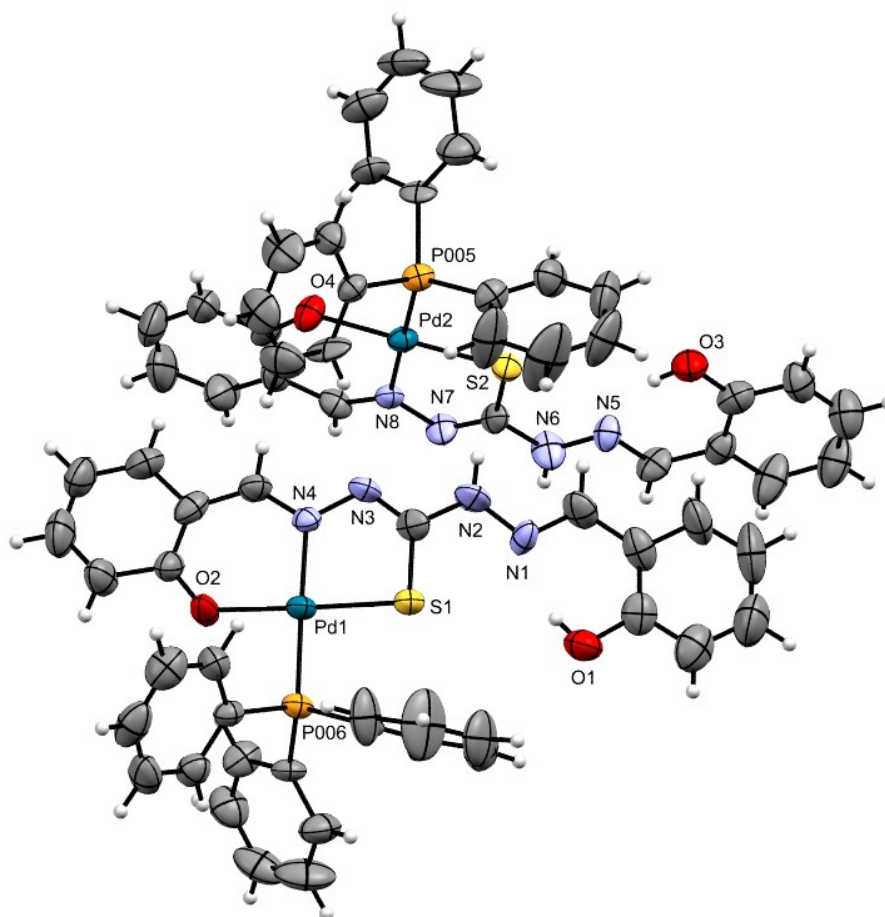


Figure 2: The molecular structure of $[\text{Pd}(\text{PPh}_3)(\text{L})]$ with the atom numbering scheme excluding C and H.

Table 1: Crystal data and structure refinement parameters for $[\text{Pd}(\text{PPh}_3)(\text{L})]$.

Name of the parameter	Value
CCDC	2196022
Empirical formula	$\text{C}_{33}\text{H}_{27}\text{N}_4\text{O}_2\text{PPdS}$
Formula weight	681.01
Temperature (K)	273.15
Crystal system	Monoclinic
Space group	$\text{P2}_1/\text{n}$
a (Å)	27.539(6)
b (Å)	8.765(2)
c (Å)	28.691(7)
α (°)	90
β (°)	110.690(4)
γ (°)	90

Crystal size (mm ³)	0.491 × 0.24 × 0.042
Wavelength (Å)	0.71073
Volume (Å ³)	6479(3)
Z	8
D _{calc.} (g.cm ⁻³)	1.396
μ (mm ⁻¹)	0.721
F(000)	2768.0
θ range for data collection (°)	2.548 to 49.998
Index ranges	-32 ≤ h ≤ 30, 0 ≤ k ≤ 10, 0 ≤ l ≤ 34
Reflections collected	11398
Independent reflections	11398
Data/restraints/parameters	11398/0/760
Goodness-of-fit on F ² (S)	1.115
Final R indexes [I ≥ 2σ(I)]	R ₁ = 0.0991, wR ₂ = 0.2255
Final R indexes [all data]	R ₁ = 0.1328, wR ₂ = 0.2368
Largest diff. peak/hole (e.Å ⁻³)	1.15/-1.80

Table 2: The selected bond lengths (Å) and bond angles (°) for [Pd(PPh₃)(L)].

Bond lengths (Å)		Bond angles (°)	
Pd1—S1	2.245(3)	S1—Pd1—O2	176.7(2)
Pd2—S2	2.245(3)	S2—Pd2—O4	177.0(2)
Pd1—O2	2.013(8)	N4—Pd1—P006	178.4(3)
Pd2—O4	2.014(8)	N8—Pd2—P005	178.8(3)
Pd1—N4	2.017(9)	O2—Pd1—P006	87.9(2)
Pd2—N8	2.029(9)	O4—Pd2—P005	87.5(2)
Pd1—P006	2.265(3)	O2—Pd1—N4	93.3(3)
Pd2—P005	2.258(3)	O4—Pd2—N8	92.9(3)
N4—N3	1.384(12)	S1—Pd1—P006	94.78(11)
N8—N7	1.392(12)	S2—Pd2—P005	94.63(11)
N2—N1	1.359(14)	S1—Pd1—N4	84.0(3)
N6—N5	1.349(13)	S2—Pd2—N8	85.0(3)

Table 3: Geometric values for hydrogen bonds for [Pd(PPh₃)(L)].

D-H...A	D-H [Å]	H...A [Å]	D...A [Å]	D-H...A [°]
O1-H1...N1	0.821(8)	1.968(9)	2.617(12)	135.5(8)
O3-H3A...N5	0.819(10)	1.894(11)	2.617(15)	146.6(7)
N2-H2...S2	0.859(11)	2.709(3)	3.461(11)	146.8(8)
N6-H6A...S1 ⁱ	0.860(12)	2.787(3)	3.513(12)	143.2(7)
C66-H66...N3	0.930(11)	2.487(11)	3.393(15)	164.9(9)
C29-H29...N7 ⁱⁱ	0.931(16)	2.519(12)	3.440(2)	168.4(8)
C54-H54...O4	0.928(16)	2.471(9)	3.283(18)	146.2(8)
C52-H52...O3 ⁱⁱⁱ	0.931(16)	2.518(7)	3.410(17)	160.6(11)

Symmetry codes: (i) +x, 1+y, +z; (ii) +x, -1+y, +z; (iii) 1-x, 3-y, 1-z.

3.3. Antioxidant Properties

The total antioxidant capacity of the free thiocarbohydrazone and Pd(II) complex was determined using the CUPRAC method. The TEAC values of the free thiocarbohydrazone and Pd(II) complex are given in Table 4. When the values are examined, it is seen that the total antioxidant capacity of both free thiocarbohydrazone and Pd(II) complex is better than Trolox (TEAC_{trolox} = 1). It also appears that free thiocarbohydrazone shows higher activity than [Pd(PPh₃)(L)]. Similar to the antioxidant capacity, the antiradical activity of [Pd(PPh₃)(L)] is also lower than that of the free thiocarbo-

hydrazone (Table 5). The degree of conjugation of the whole molecule and the number and position of the OH groups are substantial for electron transfer (58). This impacts the antioxidant activity of the tested compounds. The NH group in the thiocarbohydrazone also contributes to antioxidant activity (59). So, we can say that the decrease in the number of OH and NH groups in the free thiocarbohydrazone by complexation is the reason why the TEAC value and % radical scavenging activity of [Pd(PPh₃)(L)] are lower than that of free thiocarbohydrazone.

Table 4: The TEAC values of the compounds with regard to the CUPRAC assay.

Compounds	Molar absorptivity (L mol ⁻¹ cm ⁻¹)	TEAC	Correlation coeff. (r)
L	5.9089 × 10 ⁴	3.54 ± 0.719	0.9939
[Pd(PPh ₃)(L)]	2.5189 × 10 ⁴	1.51 ± 0.087	0.9995

Table 5: % free radical scavenging activities of the compounds (initial concentration: 10⁻⁴ M, sample volume: 1 mL).

Compounds	Free Radical Scavenging Activity (%)
L	77.84 ± 0.19
[Pd(PPh ₃)(L)]	55.07 ± 1.08
Trolox	82.33 ± 2.95

CONCLUSION

A new Pd(II) complex was synthesized from 1,5-bis(2-hydroxybenzylidene)thiocarbohydrazone (L) and structurally characterized. Crystal data showed that the complex had five- and six-membered chelate rings by the coordination of one oxygen, one nitrogen and one sulfur atom on the thiocarbohydrazone to the palladium ion. In the palladium ion with the distorted square planar geometry, the fourth coordination was completed with a phosphorus atom of triphenylphosphine co-ligand. Antioxidant activities of free thiocarbohydrazone and Pd(II) complex were studied using CUPRAC and DPPH methods. TEAC values determined according to the CUPRAC method showed that both free thiocarbohydrazone and Pd(II) complex had better antioxidant capacity than Trolox. Also, the DPPH radical scavenging ability of free thiocarbohydrazone was higher than that of the Pd(II) complex. In conclusion, free thiocarbohydrazone and Pd(II) complex with good antioxidant activity can be suggested as promising components for the prevention of oxidative stress-induced diseases.

CONFLICT OF INTEREST

The author declares no conflict of interest.

ACKNOWLEDGMENTS

I dedicate this paper to Prof. Dr. Ayşe ERÇAĞ, the mentor of my research career.

REFERENCES

1. El-Mahdy KM, El-Kazak AM, Abdel-Megid M, Seada M, Farouk O. of Some New Heterocyclic Schiff Bases Derived from Thiocarbohydrazone. ACSi. 2016 Mar 15;63(1):18-25. Available from: [<URL>](#).
2. Mamatha GP, Sherigara BS, Mahadevan KM. Electrooxidation of carbo/thiocarbohydrazone and their hydrazone derivatives at a glassy carbon electrode. J Chem Sci. 2007 May;119(3):267-74. Available from: [<URL>](#).
3. Kurzer F, Wilkinson M. Chemistry of carbohydrazone and thiocarbohydrazone. Chemical Reviews. 1970;70(1):111-49.
4. Metwally MA, Khalifa ME, Koketsu M. Thiocarbohydrazides: Synthesis and reactions. American Journal of Chemistry. 2012;2(2):38-51.
5. Bonaccorso C, Marzo T, La Mendola D. Biological Applications of Thiocarbohydrazones and Their Metal Complexes: A Perspective Review. Pharmaceuticals. 2019 Dec 25;13(1):4. Available from: [<URL>](#).
6. Nalawade A, Nalawade R, Londhe B, Tarwal N, Shejwal R. MICROWAVE ASSISTED SYNTHESIS, STRUCTURE, SPECTRAL CHARACTERIZATION AND BIOLOGICAL STUDIES OF (E)-N'-(4-FLUOROBENZYLIDENE)HYDRAZINECARBOTHIOHYDRAZIDE. International Journal of Pharmaceutical Science Invention. 2015;4(5):1-4.
7. Zafarian H, Sedaghat T, Motamedi H, Amiri Rudbari H. A multiprotic ditopic thiocarbohydrazone ligand in the formation of mono- and di-nuclear organotin(IV) complexes: Crystal structure, antibacterial activity and DNA cleavage. Journal of Organometallic Chemistry. 2016 Dec;825-826:25-32. Available from: [<URL>](#).
8. Singh DP, Kumar K, Chopra RM ne'e. Spectroscopic studies and antibacterial activities of some new 16-membered octaazamacrocyclic complexes derived from thiocarbohydrazone and pentane-2,4-dione. Spectrochimica Acta Part A: Molecular and Biomolecular Spectroscopy. 2011 Feb;78(2):629-34. Available from: [<URL>](#).
9. Melha KSA. In-vitro antibacterial, antifungal activity of some transition metal complexes of thiosemicarbazone Schiff base (HL) derived from N⁴-(7'-chloroquinolin-4'-ylamino) thiosemicarbazide. Journal of Enzyme Inhibition and Medicinal Chemistry. 2008 Jan 1;23(4):493-503. Available from: [<URL>](#).
10. Parsekar SU, Paliwal K, Haldar P, Antharjanam PKS, Kumar M. Synthesis, Characterization, Crystal Structure, DNA and HSA Interactions, and Anticancer Activity of a Mononuclear Cu(II) Complex with a Schiff Base Ligand Containing a Thiadiazoline Moiety. ACS Omega. 2022 Jan 25;7(3):2881-96. Available from: [<URL>](#).
11. Ibrahim AA, Kareem MM, Al-Noor TH, Al-Muhimeed T, AlObaid AA, Albukhaty S, et al. Pt(II)-Thiocarbohydrazone Complex as Cytotoxic Agent and Apoptosis Inducer in Caov-3 and HT-29 Cells through the P53 and Caspase-8 Pathways. Pharmaceuticals. 2021 May 26;14(6):509. Available from: [<URL>](#).
12. Muğlu H, Kurt BZ, Sönmez F, Güzel E, Çavuş MS, Yakan H. Preparation, antioxidant activity, and theoretical studies on the relationship between antioxidant and electronic properties of bis(thio/carbohydrazone) derivatives. Journal of Physics and Chemistry of Solids. 2022 May;164:110618. Available from: [<URL>](#).
13. Kaya Y, Erçağ A, Koca A. New square-planar nickel(II)-triphenylphosphine complexes containing ONS donor ligands: Synthesis, characterization, electrochemical and antioxidant properties. Journal of Molecular Structure. 2020 Apr;1206:127653. Available from: [<URL>](#).
14. Kaya Y, Erçağ A, Uğuz Ö, Koca A, Zorlu Y, Hacıoğlu M, et al. New asymmetric bithiocarbohydrazones and their mixed ligand nickel(II) complexes: Synthesis, characterization, crystal structure, electrochemical-spectroelectrochemical property, antimicrobial and antioxidant activity. Polyhedron. 2021 Oct;207:115372. Available from: [<URL>](#).
15. Abbas SY, Farag AA, Ammar YA, Atrees AA, Mohamed AF, El-Henawy AA. Synthesis, characterization, and antiviral activity of novel fluorinated isatin derivatives. Monatsh Chem. 2013 Nov;144(11):1725-33. Available from: [<URL>](#).
16. Srividya L, Reddy A, Rama N. Antidiabetic activity of 1-(4-chlorobenzylidene)-5-(2-oxoindolin-3-ylidene) thiocarbohydrazone in chick model. Asian J Biol Sci. 2017;10:126-30.
17. Tejasree Ch, Kiran G, Rajyalakshmi G, Rama Narsimha Reddy A. Hepatoprotective activity of 1-(4-(Dimethylamino)Benzylidene)-5-(2-Oxoindolin-3-ylidene) Thiocarbohydrazone in rats. Toxicological & Environmental

- Chemistry. 2013 Oct;95(9):1589-94. Available from: [<URL>](#).
18. Sadlapurkar AV, Barache UB, Shaikh AB, Gaikwad SH, Lokhande TN. 2-chlorobenzaldehyde thiosemicarbazone: a novel reagent for liquid-liquid extractive spectrophotometric determination of copper(II) from environmental and real samples. *International Journal of Environmental Analytical Chemistry*. 2021 Apr 13;1-21. Available from: [<URL>](#).
19. Nalawade AM, Nalawade RA, Shejwal RV, Kamble GS, Ling YC, Anuse MA. Development of a reliable analytical method for the precise extractive spectrophotometric determination of cadmium(II) by using of chromogenic reagent: analysis of real samples. *International Journal of Environmental Analytical Chemistry*. 2022 Dec 16;102(16):4158-77. Available from: [<URL>](#).
20. Sadlapurkar AV, Barache UB, Shaikh AB, Dhale PC, Gaikwad SH, Lokhande TN. Statistically designed extractive spectrophotometric determination scheme for bismuth(III) with 2-chlorobenzaldehyde thiosemicarbazone: Analysis of environmental and real resources. *Chemical Data Collections*. 2022 Feb;37:100798. Available from: [<URL>](#).
21. Güveli Ş, Agopcan Çınar S, Karahan Ö, Aviyente V, Ülküseven B. Nickel(II)-PPh₃ Complexes of S, N - Substituted Thiosemicarbazones – Structure, DFT Study, and Catalytic Efficiency. *Eur J Inorg Chem*. 2016 Feb;2016(4):538-44. Available from: [<URL>](#).
22. Priyarega S, Kalaivani P, Prabhakaran R, Hashimoto T, Endo A, Natarajan K. Nickel(II) complexes containing thiosemicarbazone and triphenylphosphine: Synthesis, spectroscopy, crystallography and catalytic activity. *Journal of Molecular Structure*. 2011 Sep;1002(1-3):58-62. Available from: [<URL>](#).
23. Shabbir M, Akhter Z, Ashraf AR, Ismail H, Habib A, Mirza B. Nickel(II) and palladium(II) triphenylphosphine complexes incorporating tridentate Schiff base ligands: Synthesis, characterization and biocidal activities. *Journal of Molecular Structure*. 2017 Dec;1149:720-6. Available from: [<URL>](#).
24. Rohlík Z, Holzhauser P, Kotek J, Rudovský J, Němec I, Hermann P, et al. Synthesis and coordination properties of palladium(II) and platinum(II) complexes with phosphonated triphenylphosphine derivatives. *Journal of Organometallic Chemistry*. 2006 May;691(11):2409-23. Available from: 10.1016/j.jorgchem.2006.01.024. Available from: [<URL>](#).
25. Tan CP, Lu YY, Ji LN, Mao ZW. Metallomics insights into the programmed cell death induced by metal-based anticancer compounds. *Metallomics*. 2014;6(5):978. Available from: [<URL>](#).
26. Elsayed SA, Badr HE, di Biase A, El-Hendawy AM. Synthesis, characterization of ruthenium(II), nickel(II), palladium(II), and platinum(II) triphenylphosphine-based complexes bearing an ONS-donor chelating agent: Interaction with biomolecules, antioxidant, in vitro cytotoxic, apoptotic activity and cell cycle analysis. *Journal of Inorganic Biochemistry*. 2021 Oct;223:111549. Available from: [<URL>](#).
27. Anu D, Naveen P, Devendhiran T, Shyamsivappan S, Kumarasamy K, Lin MC, et al. Synthesis, spectral characterization, X-ray crystallography and biological evaluations of Pd(II) complexes containing 4(N)-substituted thiosemicarbazone. *Journal of Coordination Chemistry*. 2021 Dec 17;74(21-24):3153-69. Available from: [<URL>](#).
28. Nadeem S, Bolte M, Ahmad S, Fazeelat T, Tirmizi SA, Rauf MK, et al. Synthesis, crystal structures and antibacterial and antiproliferative activities in vitro of palladium(II) complexes of triphenylphosphine and thioamides. *Inorganica Chimica Acta*. 2010 Oct;363(13):3261-9. Available from: [<URL>](#).
29. Shanmugapriya A, Jain R, Sabarinathan D, Kalaiarasi G, Dallemer F, Prabhakaran R. Structurally different mono-, bi- and trinuclear Pd(II) complexes and their DNA/protein interaction, DNA cleavage, and anti-oxidant, anti-microbial and cytotoxic studies. *New J Chem*. 2017;41(18):10324-38. Available from: [<URL>](#).
30. Ayyannan G, Mohanraj M, Gopiraman M, Uthayamalar R, Raja G, Bhuvanesh N, et al. New Palladium(II) complexes with ONO chelated hydrazone ligand: Synthesis, characterization, DNA/BSA interaction, antioxidant and cytotoxicity. *Inorganica Chimica Acta*. 2020 Nov;512:119868. Available from: [<URL>](#).
31. Khan H, Badshah A, Said M, Murtaza G, Sirajuddin M, Ahmad J, et al. Synthesis, structural characterization and biological screening of heteroleptic palladium(II) complexes. *Inorganica Chimica Acta*. 2016 Jun;447:176-82. Available from: [<URL>](#).
32. Kavitha P, Laxma Reddy K. Pd(II) complexes bearing chromone based Schiff bases: Synthesis, characterisation and biological activity studies. *Arabian Journal of Chemistry*. 2016 Sep;9(5):640-8. Available from: [<URL>](#).
33. Boubakri L, Mansour L, Harrath AH, Özdemir I, Yaşar S, Hamdi N. N-Heterocyclic carbene-Pd(II)-PPh₃ complexes as a new highly efficient catalyst system for the Sonogashira cross-coupling reaction: Synthesis, characterization and biological activities. *Journal of Coordination Chemistry*. 2018 Jan 17;71(2):183-99. Available from: [<URL>](#).
34. Bahl A, Grahn W, Stadler S, Feiner F, Bourhill G, Bräuchle C, et al. Novel, Blue-Transparent Frequency Doublers Based on 1,8-Di(hetero)arylnaphthalenes. *Angew Chem Int Ed Engl*. 1995 Jul 31;34(1314):1485-8. Available from: [<URL>](#).
35. Goldfinger MB, Crawford KB, Swager TM. Directed Electrophilic Cyclizations: Efficient Methodology for the Synthesis of Fused Polycyclic Aromatics. *J Am Chem Soc*. 1997 May 1;119(20):4578-93. Available from: [<URL>](#).
36. Hartwig JF, Kawatsura M, Hauck SI, Shaughnessy KH, Alcazar-Roman LM. Room-Temperature Palladium-Catalyzed Amination of Aryl Bromides and Chlorides and Extended Scope of Aromatic C–N Bond Formation with a Commercial Ligand. *J Org Chem*. 1999 Jul 1;64(15):5575-80. Available from: [<URL>](#).
37. Asma M, Badshah A, Ali S, Sohail M, Fettouhi M, Ahmad S, et al. Synthesis, Characterization of Mixed Ligand Palladium(II) Complexes of Triphenylphosphine and Anilines and their Enzyme Inhibition Studies against β -glucuronidase. The Crystal Structure of trans-dichloro-(m-chloroaniline)(triphenylphosphine)palladium(II). *Transition Met Chem*. 2006 May;31(4):556-9. Available from: [<URL>](#).
38. Shabbir M, Akhter Z, Ahmad I, Ahmed S, Shafiq M, Mirza B, et al. Schiff base triphenylphosphine palladium (II)

- complexes: Synthesis, structural elucidation, electrochemical and biological evaluation. *Journal of Molecular Structure*. 2016 Aug;1118:250-8. Available from: [<URL>](#).
39. Rocha FV, Barra CV, Garrido SS, Manente FA, Carlos IZ, Ellena J, et al. Cationic Pd(II) complexes acting as topoisomerase II inhibitors: Synthesis, characterization, DNA interaction and cytotoxicity. *Journal of Inorganic Biochemistry*. 2016 Jun;159:165-8. Available from: [<URL>](#).
40. Ahmed M, Khan SZ, Sher N, Rehman ZU, Mushtaq N, Khan RA. Kinetic and toxicological effects of synthesized palladium(II) complex on snake venom (*Bungarus sindanus*) acetylcholinesterase. *J Venom Anim Toxins incl Trop Dis [Internet]*. 2021 [cited 2023 Feb 8]; Available from: [<URL>](#).
41. Kaya Y, Erçağ A, Zorlu Y, Demir Y, Gülçin İ. New Pd(II) complexes of the bithiocarbohydrazones derived from isatin and disubstituted salicylaldehydes: Synthesis, characterization, crystal structures and inhibitory properties against some metabolic enzymes. *J Biol Inorg Chem*. 2022 Mar;27(2):271-81. Available from: [<URL>](#).
42. Ibrahim AA, Khaledi H, Ali HM. A multiprotic indole-based thiocarbohydrazone in the formation of mono-, di- and hexa-nuclear metal complexes. *Polyhedron*. 2014 Oct;81:457-64. Available from: [<URL>](#).
43. Burns GR. Metal complexes of thiocarbohydrazone. *Inorganic Chemistry*. 1968;7(2):277-83.
44. Kaya İ, Temizkan K, Kaya Y, Erçağ A. The monomers and polymers of azomethine-based thiocarbohydrazones: Fluorescent activities, fluorescence quantum yields of polymers in water and DMF solutions. *Materials Science and Engineering: B*. 2022 Aug;282:115782. Available from: [<URL>](#).
45. Bruker. APEX2, version 201411-0, Bruker. Bruker, AXS Inc, Madison, WI; 2014.
46. Bruker. SAINT, version 834 A, Bruker. Bruker AXS Inc, Madison, WI; 2013.
47. Sheldrick GM. *SHELXT* - Integrated space-group and crystal-structure determination. *Acta Crystallogr A Found Adv*. 2015 Jan 1;71(1):3-8. Available from: [<URL>](#).
48. Sheldrick GM. Crystal structure refinement with *SHELXL*. *Acta Crystallogr C Struct Chem*. 2015 Jan 1;71(1):3-8. Available from: [<URL>](#).
49. Macrae CF, Sovago I, Cottrell SJ, Galek PTA, McCabe P, Pidcock E, et al. *Mercury 4.0*: from visualization to analysis, design and prediction. *J Appl Crystallogr*. 2020 Feb 1;53(1):226-35. Available from: [<URL>](#).
50. Sánchez-Moreno C, Larrauri JA, Saura-Calixto F. A procedure to measure the antiradical efficiency of polyphenols. *J Sci Food Agric*. 1998 Feb;76(2):270-6. Available from: [<URL>](#).
51. Apak R, Güçlü K, Özyürek M, Karademir SE. Novel Total Antioxidant Capacity Index for Dietary Polyphenols and Vitamins C and E, Using Their Cupric Ion Reducing Capability in the Presence of Neocuproine: CUPRAC Method. *J Agric Food Chem*. 2004 Dec 1;52(26):7970-81. Available from: [<URL>](#).
52. Yanping R, Rongbin D, Liufang W, Jigui W. Synthesis, Characterization and Crystal Structure of 1,5-Bis(2-Hydroxybenzaldehyde)-Dithiocarbohydrazone. *Synthetic Communications*. 1999 Feb;29(4):613-7. Available from: [<URL>](#).
53. Lugasi SO. New synthetic pathways for thiocarbohydrazone and salicylaldehyde azine compounds. Available from: [<URL>](#).
54. Kaya Y, Erçağ A, Koca A. Synthesis, structures, electrochemical studies and antioxidant activities of cis-dioxomolybdenum(VI) complexes of the new bithiocarbohydrazones. *Journal of Molecular Structure*. 2015 Dec;1102:117-26. Available from: [<URL>](#).
55. Özerkan D, Ertik O, Kaya B, Kuruca SE, Yanardag R, Ülküseven B. Novel palladium (II) complexes with tetradentate thiosemicarbazones. Synthesis, characterization, in vitro cytotoxicity and xanthine oxidase inhibition. *Invest New Drugs*. 2019 Dec;37(6):1187-97. Available from: [<URL>](#).
56. Manna CK, Naskar R, Bera B, Das A, Mondal TK. A new palladium(II) phosphino complex with ONS donor Schiff base ligand: Synthesis, characterization and catalytic activity towards Suzuki-Miyaura cross-coupling reaction. *Journal of Molecular Structure*. 2021 Aug;1237:130322. Available from: [<URL>](#).
57. Takjoo R, Takjoo R, Yazdanbakhsh M, Aghaei kaju A, Chen Y. Mixed Ligand Palladium(II) Complex with NS-Bidentate S -Allyldithiocarbazate Schiff Base: Synthesis, Spectral Characterization, Crystal Structure and Decoding Intermolecular Interactions with Hirshfeld Surface Analysis. *Chin J Chem*. 2010 Feb;28(2):221-8. Available from: [<URL>](#).
58. Apak R, Güçlü K, Özyürek M, Celik SE. Mechanism of antioxidant capacity assays and the CUPRAC (cupric ion reducing antioxidant capacity) assay. *Microchimica Acta*. 2008;160(4).
59. Asha TM, Prathapachandra Kurup MR. An insight into the potent antioxidant activity of a dithiocarbohydrazone appended cis -dioxidomolybdenum (VI) complexes. *Appl Organomet Chem [Internet]*. 2020 Sep [cited 2023 Feb 8];34(9). Available from: [<URL>](#)



Assay of Tretinoin using Safranin-O as a Chromogenic Reagent in Bulk and Dosage Forms

Thuttgartunta Manikya Sastry^{1*} , Venkata Nagalakshmi Kiilana¹ ,
and Rama Krishna Karipeddi² 

¹Gayatri Vidya Parishad College of Engineering (Autonomous), Chemistry, Department of Chemistry, Visakhapatnam-530048, India

²GITAM, Deemed to be University, Department of Chemistry, Rushikonda, Visakhapatnam- 530045, India

Abstract: A new, economical and accurate analytical technique was developed for the assay of tretinoin (TTN) in bulk and formulations. While developing the method, it was found that the reaction was carried out due to the formation of ion-pair association complex involving the carboxyl group in the side chain of the TTN with safranin-O. The colored species formed was stable up to 60 minutes. The optical density of color species was measured at 520 nm. All the variables were optimized. The linearity range lies for the developed method within the concentration ranges of 2-10 $\mu\text{g mL}^{-1}$. The linear correlation coefficient (r) and molar absorptivity (ϵ_{max}) values were found as 0.9999 and $1.66 \times 10^4 \text{ L mol}^{-1}\text{cm}^{-1}$. Percentage recoveries were found from 99.2 ± 1.8 to 100.2 ± 0.7 . The method was validated as per ICH guidelines.

Keywords: Bioactive compounds, tretinoin, safranin-O(SFN-O), Ion-pair association complex, spectrophotometry.

Submitted: September 17, 2022. **Accepted:** January 04, 2023.

Cite this: Manikya Sastry T, Nagalakshmi KV, Ramakrishna K. Assay of Tretinoin using Safranin-O as a Chromogenic Reagent in Bulk and Dosage forms. JOTCSA. 2023;10(1):139-46.

DOI: <https://doi.org/10.18596/jotcsa.1176621>.

***Corresponding author. E-mail:** tmsastry@yahoo.com.

1. INTRODUCTION

Bioactive compounds are found in both plant and animal products and can also be synthetically produced. Drugs are an important class of bioactive compounds. The estimation based on the reactions with suitable chromogenic agents are simple and inexpensive. Over-the-counter (OTC) drugs used for skin care are classified as dry skin products, acne products, sunscreen and suntan products and foot care products. Acne occurs most commonly during adolescence and found in 80-90% of teenagers due to hormonal changes. The acne product namely tretinoin works by replacement of skin cells. Acne vulgaris is considered as common skin related problem that was treated with combination therapy using topical drug clindamycin and tretinoin (TTN)

(1). Literature survey revealed that there is an evidence about the determination TTN by HPLC (2-6), RP-HPLC (7-12), UPLC (13), LC (14), and GC (15). Studies on phototoxicity of tretinoin (16), UV-spectrophotometry (17-22), and UV-derivative spectroscopy (23-25) were also carried out by the previous authors. Most of the analytical methods involve sophisticated instruments which are expensive, and require maintenance and are not within the reach of most of the laboratories. Visible spectrophotometry can be chosen as an alternative technique. It is a highly preferable method for routine analysis because of its simplicity, low time and economical advantages. The novelty of this technique lies in its sensitivity and further depends on the nature of reaction and not on the sophistication of the instrument. No evidence is

found in the literature for the determination of TTN by visible spectrophotometry. Hence the authors made an attempt to develop simple and sensitive visible spectroscopic method for the assay TTN in bulk and formulations using safranin-O (SFN-O) as a chromogenic reagent. Figure 1 shows the structural molecule for tretinoin.

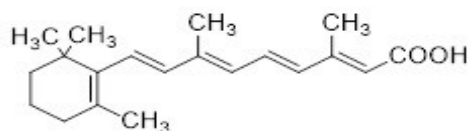


Figure 1: Chemical structure of Tretinoin (2E,4E,6E,8E)-3,7-Dimethyl-9-(2,6,6-trimethylcyclohex-1-enyl) nona-2,4,6,8-all-trans-tetraenoic acid).

2. EXPERIMENTAL SECTION

2.1. Materials and Methods

2.1.1. Instrumentation

Shimadzu UV double beam spectrophotometer has been chosen for obtaining precise and accurate optical density measurements. In addition a digital pH meter (equiptronics, India) was used to measure the pH of the samples. An electrical balance (Dhona 200 D, India) was used to weigh all the materials.

2.1.2. Chemicals and Reagents

TTN (Biophore India), Formulations namely Retino-A (Ethnorjansencilag), Airol (Piramal Health care). Avita, Bertek pharmaceutical Inc.) and Eudyna, (German Remedies.) were procured from the registered pharmacy.

Reagents namely SFN-O (Fluka, Mumbai, India, 98% purity), Sodium hydroxide (Qualigens Mumbai, India, 99% purity) and solvent CHCl_3 (Qualigens

Mumbai, India, 99% purity) were procured for this study are of analytical grade.

Aqueous solutions of SFN-O (Fluka; 0.01%, 2.86×10^{-4} M) was prepared by dissolving 10 mg of safranin-O in 100 mL of distilled water and washed with CHCl_3 to remove chloroform-soluble impurities. Buffer solution was prepared by mixing 50 mL of 0.025 M borax solution with 15 mL of 0.1 M of sodium hydroxide and diluted to 100 mL with distilled water and pH was adjusted to 9.8.

2.1.3. Bulk sample solution

Stock solution (mg mL^{-1}) for bulk drug sample was prepared in 100 mL of chloroform by dissolving 100 mg of tretinoin. Working standard solutions of concentration of $40 \mu\text{g mL}^{-1}$ were prepared from the above stock solution. Further dilution was done using chloroform.

2.1.4. Formulations

Cream equivalent to 50 mg was dissolved in 30 mL of aqueous methanol (3:1). The resulting solution was extracted with solvent CHCl_3 (3 x 25.0 mL portions) followed by filtration. The total chloroform extract was kept for drying with 5 g of anhydrous Na_2SO_4 and then filtered. This filtrate was made up to 200 mL with chloroform to obtain the stock solution of ($250 \mu\text{g mL}^{-1}$). The stock solution was further diluted to a concentration of $40 \mu\text{g mL}^{-1}$.

2.1.5. Calibration curve - UV method (Reference method)

Stock solution (mg mL^{-1}) was prepared by dissolving 100 mg of bulk drug sample in 100 mL isopropanol. From this stock solution, working standard solution of concentration $10 \mu\text{g mL}^{-1}$ was prepared using the same solvent. The absorption spectrum of bulk drug sample was recorded against a reagent blank within the UV region using Shimadzu double beam spectrophotometer (Figure 2).

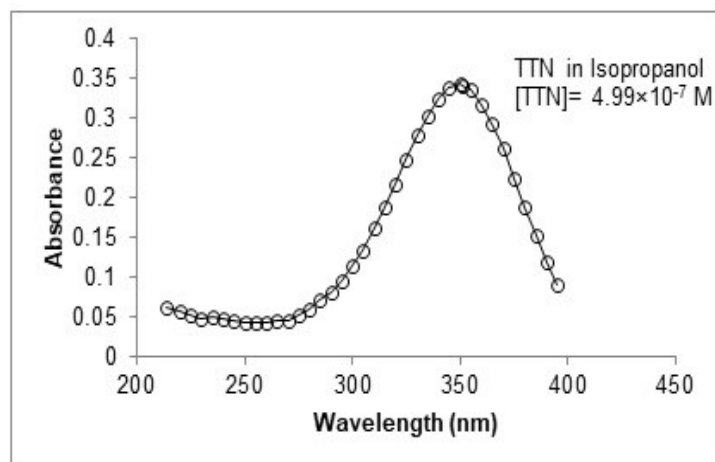


Figure 2: Absorption spectrum of tretinoin ($[\text{TTN}] = 4.99 \times 10^{-7} \text{M}$) against (blank).

A series of solutions were prepared by taking 0.5-2.5 mL standard drug solution ($10 \mu\text{g mL}^{-1}$) into 20.0 mL calibrated tubes. These are diluted to 10.0 mL with double distilled water. The optical densities of all the sample solutions were measured at 352 nm against

reagent blank (isopropanol). The concentration of the drug was deduced from its calibration curve drawn between optical density and concentration of TTN (Figure 3).

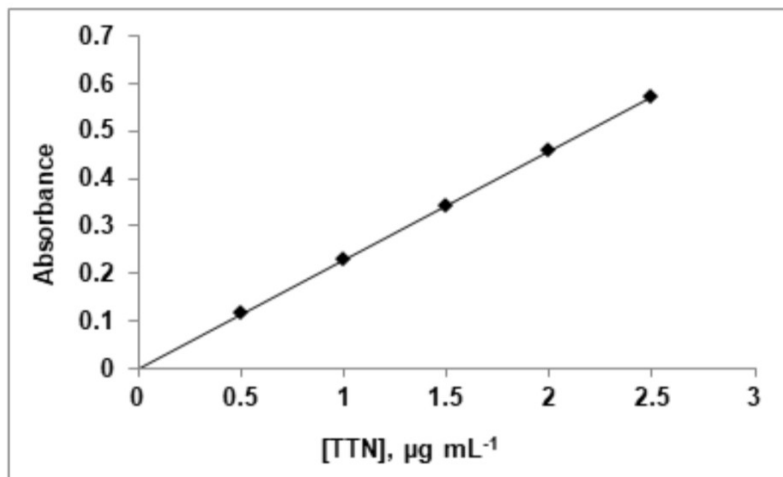


Figure 3: Calibrated curve of tretinoin ($[\text{TTN}] = 4.99 \times 10^{-7} \text{ M}$).

2.1.6. Method development

A series of solutions were prepared by taking aliquots of standard drug solution (0.5 - 2.5 mL, $40 \mu\text{g mL}^{-1}$), 2.0 mL of $2.85 \times 10^{-4} \text{ M}$ safranin solution and 1.0 mL of buffer solution (pH 9.8) into 50.0 mL separating funnels. The volume of each sample was diluted to 15.0 mL with distilled water and 10.0 mL chloroform was added. The contents of the separating funnel were shaken for two minutes. The

two layers were separated and the absorbance of organic layer was measured at 520 nm against blank. The optical density of colored species was observed to decrease after 60 min indicating the decomposition of colored complex. The concentration of the drug was deduced from its calibration curve drawn between optical density and concentration of TTN (Figure 4).

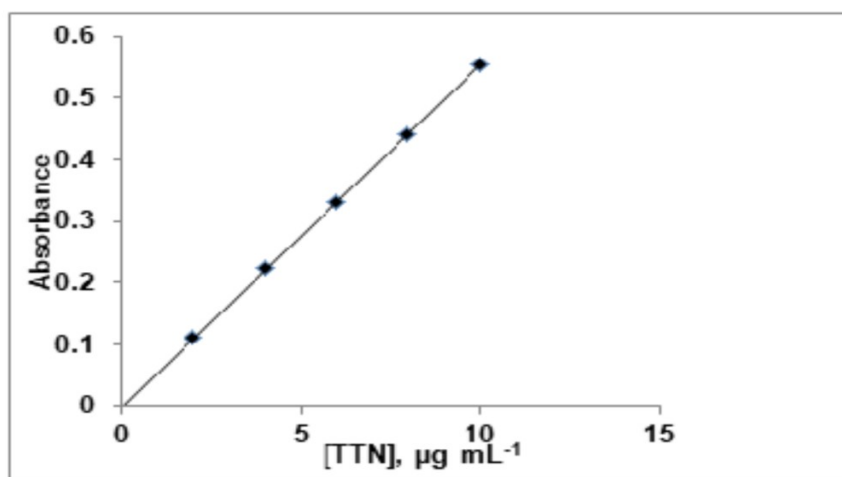


Figure 4: Calibrated curve of TTN - SFN-O method.

3. RESULTS AND DISCUSSION

3.1. Selection of Analytical Wavelength

The sample solution containing fixed amount of TTN, SFN-O (basic dye), buffer and other furnished

variables as mentioned in the procedure has been scanned in the visible region (350 - 750 nm) against the reagent blank. The absorption spectrum of the colored species formed on the basis of ion-pair association complex showed maximum absorbance

at 520 nm and this wavelength has been selected for the analysis. The spectrum of the safranin-O (basic dye) showed maximum absorbance whereas

blank solution against chloroform showed negligible absorbance at this wavelength (Figure 5).

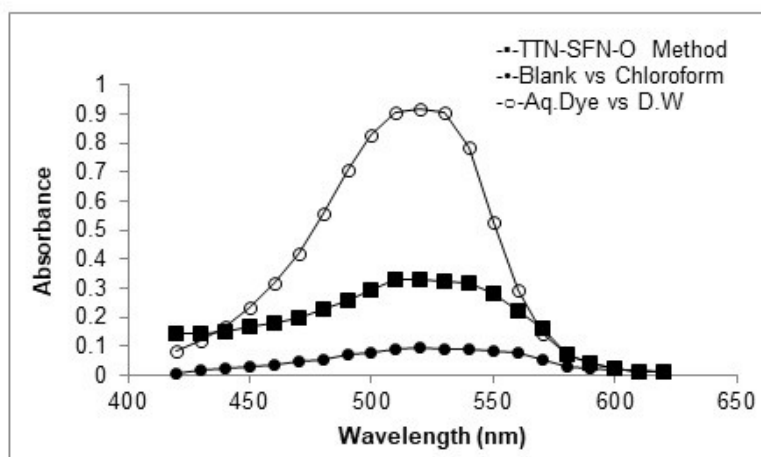


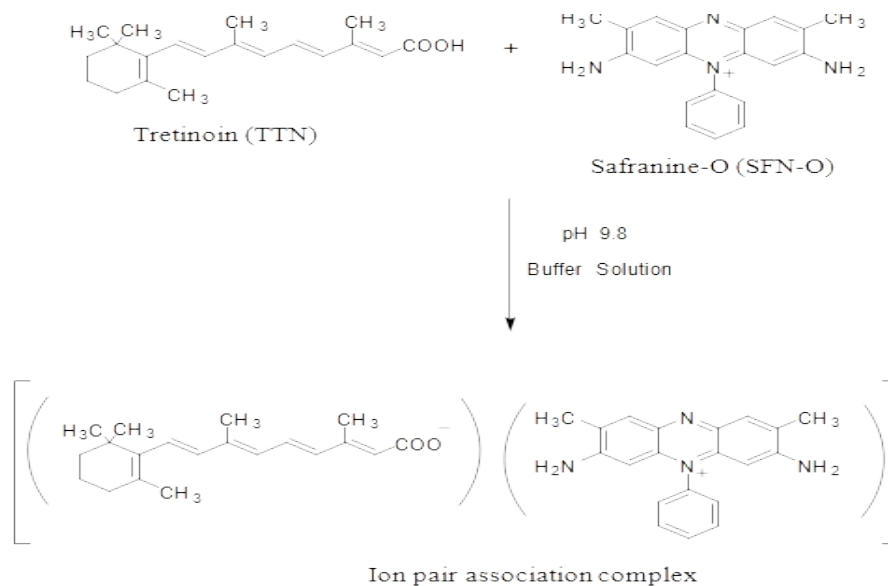
Figure 5: Absorption spectrum of TTN-SFN-O method.

3.2. Optimum Conditions

The responses of several factors like concentration of SFN-O ($0.29 - 0.72 \times 10^{-4} \text{ mol L}^{-1}$) the volume of extracting solvent chosen, time of stability of ion-pair association complex formation (1-60 minutes), intensity of colored species produced, the ratio of aqueous to CHCl_3 were studied (26). The following optimum conditions were fixed for the proposed technique are; 2.0 mL ($0.57 \times 10^{-4} \text{ mol L}^{-1}$) SFN-O, 1.0 mL borax buffer (pH=9.8) with 2 min agitation time at $28 \pm 2^\circ \text{C}$. The ion pair association complex is stable up to 60 minutes afterwards the absorbance slowly decreased indicating the decomposition of the complex.

3.3. Mechanism of Ion-pair Association Complex

In TTN, the carboxyl group in the side chain involved in the formation of the ion pair association complex with SFN-O in alkaline medium. Based on the analogy studies, the ion-pair association complex formation mechanism is explained. The negative charge appeared on the carboxylate anion of the drug (TTN) molecule and the positive charge of SFN-O held together through electrostatic force of attraction. The obtained product behaved as a single molecule. The probable sequence of mechanism of the reaction is given in Scheme 1.



Scheme 1: Ion pair association complex of tretinoin with safranin-O at pH 9.8.

3.4. Validation of Analytical Data

Following (ICH) requirements (27), the TTN-SFN-O system developed was validated statistically. Validation parameters like slope (b), intercept (a), linear correlation coefficient (r), inter and intraday precision (%RSD) were studied. Optical and regression characteristics like ϵ_{\max} ($\text{Lmol}^{-1}\text{cm}^{-1}$) and λ_{\max} (nm) values were found to be 1.66×10^4 and 520, respectively. The limits of linearity range for TTN-SFN-O system was found to have 2 - 10 $\mu\text{g mL}^{-1}$. The calibrated curve drawn at specified

concentration levels consisting of linearity with linear correlation coefficient (r) value 0.9999. Limit of detection (LOD) and Limit of quantification (LOQ) for the developed method were calculated. Sensitivity of developed method is explained on the basis of molar absorptivity values. Precision was explained in terms of relative standard deviation (%RSD) considering from six (n=6) determinations of the sample solution under optimum conditions. The results are given in Tables 1 and 2.

Table 1: Optical conditions for the proposed technique.

Optical condition	TTN-SFN-O method
Wavelength (λ_{\max})	520 nm
Molar absorptivity (ϵ_{\max})	$1.66 \times 10^4 \text{ L mol}^{-1}\text{cm}^{-1}$
Limits of linearity range	2-10 $\mu\text{g mL}^{-1}$
LOD	$7.19 \times 10^{-3} \mu\text{g mL}^{-1}$
LOQ	$2.18 \times 10^{-2} \mu\text{g mL}^{-1}$
Standard error of estimation (S_e)	1.23×10^{-3}
Sandell's Sensitivity	$1.81 \times 10^{-2} \mu\text{g cm}^{-2}$

Table 2: Validation parameters for the proposed technique.

Validation parameter	TTN-SFN-O method
Slope (b)	5.51×10^{-2}
Standard deviation on slope (S_b)	2.00×10^{-4}
Intercept (a)	1.80×10^{-4}
Standard deviation on intercept (S_a)	1.20×10^{-4}
Linear correlation coefficient (r)	0.9999
Intra -day precision (%RSD)*	0.65
Inter- day precision (%RSD)*	0.68
0.01 Level of confidence limits	1.07
0.05 Level of confidence limits	0.68

$y = a + bC$ where C is the concentration of analyte in $\mu\text{g/mL}$ and y is the absorbance unit. Calculated from six determinations.

The accuracy of the analytical procedure was checked in terms of % recovery. Recovery experiments were carried out by introducing a calculated quantity of drug to the pre-analyzed formulations at different levels and determining the accuracy of the techniques proposed. Values of % Recovery were found to be 99.2 - 100.2% (± 0.8 to ± 0.7) for considering three determinations (n=3). The results of proposed method (formulations) and UV reference method were compared through student t- and F- tests. It was observed that no significant difference was noticed in between developed and UV reference methods as the results are found within the acceptable limits (Based on 95% confidence limit values for student "t"- test and "F"-test respectively. The results are given in Table 3. The proposed method was compared with literature method (20) and found to be more sensitive with reference to molar absorptivity, linear correlation coefficient (r), LOD and LOQ values.

Precision and accuracy was calculated in terms of relative standard deviation (%RSD) and %Recovery values. The results are given in Table 4.

4. CONCLUSION

An accurate analytical technique developed for the assay of TTN in bulk and formulations. The developed technique is found to be best among the literature methods in terms of stability, sensitivity and cost. The sensitivity of developed method lies only in the reaction's nature with the reagent chosen but not on the instrument's sophistication. The excipients commonly found in formulations did not intervene in the assay. Hence the developed method is specific and suitable and found as an alternative to instrumental methods such as LC-MS, HPLC, GLC and GC-MS, in quality control laboratories.

Table 3: Assay of TTN in Pharmaceutical Formulations (TTN-SFN-O Method).

Formulation Proprietary name	Labeled Amount (g)	Amount found by proposed method (g)(n=6) ^a	95% Confidence limit values F -Test ^b	95% Confidence limit values t-Test ^c	Quantity found by UV absorption method (g)(n=3)	% Recovery developed method ^d
Cream (Retino-A)	20.0	20.04	0.15	1.55	20.1 ± 0.1	100.2 ± 0.7
Cream (Ainol)	20.0	20.03	3.07	1.19	20.1 ± 0.2	100.1 ± 0.7
Cream (Avita)	20.0	19.84	2.99	0.03	19.9 ± 0.2	99.2 ± 1.8
Cream (Eudyna)	20.0	19.94	1.07	0.90	19.9 ± 0.1	99.7 ± 0.6

^aAverage value of six observations. ^bTabulated value of 5.05 for “F” -Test. ^cTabulated value of 2.57 for student “t” -Test. ^dAverage value of three measurements (n=3).

Table 4: Comparison of proposed method with literature (20) method.

Reagent used	Iodine (I ₂)	SFN-O
Wavelength(λ_{max}) nm	295	520
Molar absorptivity(ϵ_{max}) L mol ⁻¹ cm ⁻¹	1.31×10 ⁴	1.66×10 ⁴
Limits of linearity range(μ g mL ⁻¹)	9.04 - 29.71	2-10
Linear correlation coefficient (r)	0.9974	0.9999
Relative standard deviation (%RSD)	1.95-0.88	Intraday(0.65) Interday(0.68)
% Recovery	97.84 - 102.80	99.7 - 100.2
LOD μ g mL ⁻¹	4.35	0.007
LOQ μ g mL ⁻¹	13.17	0.022
Method	Zayed MA and Abdel-Basset MH (20)	Present method

5. CONFLICT OF INTEREST

None.

6. ACKNOWLEDGMENTS

The authors (Dr. T. Manikyasastry and Dr.K. V. Nagalakshmi) are grateful to the organisation, GVPCOE (A) for their encouragement and support.

7. REFERENCES

1. Fu LW, Vender RB. Newer approach in topical combination therapy for acne. *Skin Therapy let.* 2011;16(9):3-6.
2. Platzer DJ, White BA. Development and validation of a gradient HPLC method for the determination of clindamycin and related compounds in a novel tablet formulation. *J Pharm Biomed Anal.* 2006;41:84-88. DOI: [<URL>](#).
3. Tashtoush BM, Jacobson EL, Jacobson MK. A rapid HPLC method for simultaneous de-termination of tretinoin and isotretinoin in dermatological formulations. *J Pharm Biomed Anal.* 2007;43(3):859-864. DOI: [<URL>](#).
4. Fawzia I, Mohie KSE, El-Deen AK, and Kuniyoshi S. A New HPLC-DAD Method for the Concurrent Determination of Hydroquinone, Hydrocortisone Acetate and Tretinoin in Different Pharmaceuticals for Melasma Treatment. *Journal of Chromatographic Science.* 2019;57(6):495-501. DOI: [<URL>](#).
5. Abdelghani M, Mohamed SB. Simplified HPLC method for simultaneous determination of erythromycin and tretinoin in topical gel form. *Sep Sci plus.* 2020;1-8. DOI: [<URL>](#).
6. Sadaf S, Shahid H, Mohsin J, Ali R, Shahid I, Hamad A, Samar OA, Eslam B, HamoudH. Somaily, Rami AP, EmanA and Abd-E F. Simultaneous HPLC Determination of Clindamycin Phosphate, Tretinoin, and Preservatives in Gel Dosage Form Using a Novel Stability-Indicating Method. *Inorganics.*2022; 10(10):1-15. DOI: [<URL>](#).
7. Yuenong RY, Eden B, Richard B, Robert H, Barry H. Simultaneous determination of tretinoin and clindamycin phosphate and their degradation products in topical formulations by reverse phase HPLC. *J Sep Sci.* 2004;27:71-77. DOI: [<URL>](#).
8. Vaidya V, Baing MM, Joshi SS. Reverse phase high performance liquid chromatographic determination of tretinoin in bulk material, *Indian Drugs.* 2005; 42(1):42-45.
9. Sheliya K, Shah K, Kapupara P. Development and validation of analytical method for simultaneous estimation of mometasonefuroate, hydroquinone and tretinoin in topical formulation by RP-HPLC. *J Chem Pharm Res.* 2014; 6(4):934-940.
10. Vasanthi R, Rajitha N, Raja MA, Shrishva V, Banji D, Kumar DS. Analytical method development and validation

of Isotretinoin in tablet dosage formulation. Asian J Pharm Anal Med Chem. 2015;3(3):145-153.

11. Ashish A, Manoj S, Reverse-phase High-performance Liquid Chromatography Estimation of Methotrexate and Tretinoin in Bulk and Pharmaceutical Dosage Forms. International Journal of Pharmaceutical & Biological Archives 2019; 10(2):146-153.

12. Jamel MKA, Gagy AA. Development and validation of analytical spectrophotometric and RP-HPLC methods for the simultaneous estimation of hydroquinone, hydrocortisone and tretinoin ternary mixture in topical formulation. International journal of pharmacy and pharmaceutical sciences. 2019;11(11):10-16. DOI: [<URL>](#).

13. His SL, Surman P and Al-Kassas R. Development of a stability-indicating UPLC method for determination of isotretinoin in bulk drug. Pharmaceutical Development and Technology, 2018; 24 (2):189-198.

14. Dileusa DO, Diego FDA, Edilene GDO, Ruy CRB. Liquid chromatography method to assay tretinoin in skin layers: validation and application in skin penetration/retention studies. Heliyon. 2020;6:e03098. DOI: [<URL>](#).

15. Martins LE, Danielle G, Almeida DA, Nelson R, Antoniosi F. Development of a gas chromatography method for the determination of isotretinoin and its degradation products in pharmaceuticals. J Pharm Biomed Anal. 2005;38:678-685. DOI: [<URL>](#).

16. Slade HB, Shroot B, Feldman SR, Cargill DI, Stanfield J. Reappraising the phototoxicity of tretinoin: a report of four controlled clinical trials. Photodermatology, Photoimmunology & Photomedicine. 2009;25(3):146-152. DOI: [<URL>](#).

17. Maryam B, Ali YF, Jahanbakhsh G, Mohammad M, Ahari M, Nahid S, Mohammad Taghi B, Simultaneous spectrophotometric determination of minoxidil and tretinoin by the H-point standard addition method and partial least squares. Chem pap. 2009;63(3):336-344. DOI: [<URL>](#).

18. Patel P, Kabra P, Kimbahune R, Urmila GH. Quantitative estimation of isotretinoin (13-cis retinoic acid) in bulk and formulation by UV-visible spectrophotometry. Res J Pharm Biol Chem Sci. 2011;2(1):167-172.

19. Pankti D, Kusum M, Mehul P. Development and validation of UV-visible spectrophotometric method for simultaneous estimation of mometasone furoate, hydroquinone and tretinoin from their pharmaceutical dosage form. Int J Pharm Sci Rev Res. 2013;21(1): 296-300.

20. Zayed MA and Abdel-Basset MH. Spectrophotometric Micro determination of Tretinoin, Isotretinoin using Iodine and Tazarotene Micro determination Via Reaction with Rose-Bengal Reagent. Egypt. J. Chem. 61(1);2018:143 - 153. DOI: [<URL>](#).

21. Suraj D, Lobsang TK, Hauzel L, Laldinchhana, Sabir H. Development and validation of UV-spectrophotometric method for the determination of tretinoin. Journal of Xi'an Shiyou University. 2022;18(9):547-553.

22. Kiran D, Deepak N, Arvind N. Simultaneous UV spectrophotometric valuation of isotretinoin & their promoted drug. Int. J. Pharm. Sci. Rev. Res. 2018;49(1):82-85.

23. Barazandeh TM, Namadchian M, Fadaye VS, Souri E. Derivative spectrophotometric method for simultaneous determination of clindamycin phosphate and tretinoin in pharmaceutical dosage forms. DARU. 2013;21(1): 2-7.

24. Mahrous MS, Abdel-Khalek MM, Beltagy YA. Simultaneous Quantitation of Minoxidil and Tretinoin in Magistral and Pharmaceutical Preparations by First Derivative Spectrophotometry. Anal Lett. 2006;25(9):1673-1686. DOI: [<URL>](#).

25. Nazira S and Abdulkader S. Development and validation of derivative UV spectroscopic method for simultaneous estimation of nicotinamide and tretinoin in their binary mixtures and pharmaceutical preparations. Sarkis and Sawan BMC Chemistry. 2022;16(15):1-11. DOI: [<URL>](#).

26. Massart DL, Vandeginste BGM, Doming S N, Michotte Y, Kaufman L. Chemometrics, A text Book, Amsterdam: Elsevier. 1988;293; 80.

27. ICH Harmonized Tripartite Guideline; International Conference on Harmonization of Technical Requirements for Registration of Pharmaceuticals for Human Use, Text and Methodology on Validation of Analytical Procedures, Q2, (R1); 2005.



Health Risk Assessment of Some Heavy Metals in Lipstick Brands Sold in Local Markets in Iraq

Fatima Mallalah Mohammed^{1*} , Maryam Abdulghafor Ahmed² , Hadeel M. Oraibi³ 

1 Middle Technical University - Technical Institute - Baqubah - Department of Community Health Technique, Baghdad, Iraq.

2 Renewable Energy Sciences Department, College of Energy & Environmental Science, Al-Karkh University of Science, Baghdad, Iraq

3 Department of Biology, Collage of science, University of Diyala, Iraq.

Abstract: Heavy metals found in cosmetics are a safety threat to the health of consumers. Therefore, in this study, we evaluated the levels of heavy metals such as cadmium (Cd), chromium (Cr), copper (Cu), lead (Pb), zinc (Zn), and arsenic (As) in lipstick makeup. The level of heavy metals in lipstick was discovered by using an analytical technique with high selectivity and sensitivity, namely atomic absorption spectrometry. Twenty lipsticks were selected from the same brands, yet differing in price. Ten original (expensive) and ten knockoff (cheap) lipsticks were chosen from shops in Diyala, Iraq. The detection-limit (LOD) was in between 0.01 and 0.1, the quantification-limit (LOQ) was within 0.03 and 0.33, the recovery values (Rec.%) ranged from 100.17% to 101.1%, the RE values were 0.81%, and the RSD values were 1.33%. The results also revealed that the levels of metals are in the order of Pb > Cd > Zn > Cu > As > Cr. However, the levels of heavy metals that were estimated in this study were less than the permissible limit set by the executive authorities, so there seems to be no concern associated with these heavy metals. However, the daily and frequent use of lipstick by women exposes them to low levels of toxic metals as these metals accumulate over time and pose adverse effects on the health of the users. The results of the hazard quotient (HQ) and health risk index (HI) indicate there was no harmful effect on human health related to heavy metals present in lipstick. Whereas the results of the biological activity of the samples indicated that there was no bacterial growth in expensive samples, cheap samples were contaminated with some types of organisms; this indicates poor quality.

Keywords: Cosmetics, heavy metals, toxicity effects, health risk assessment, biological activity.

Submitted: August 03, 2022. **Accepted:** December 19, 2022.

Cite this: Mohammed FM, Ahmed MA, Oraibi HM. Health Risk Assessment of Some Heavy Metals in Lipsticks Sold in Local Markets in Iraq. JOTCSA. 2023;10(1):147-60.

DOI: <https://doi.org/10.18596/jotcsa.1154686>.

***Corresponding author. E-mail:** fm609426@gmail.com.

1. INTRODUCTION

Cosmetics are materials that are used as personal care products with the intention of coming into contact with the various outside parts of the human body like nails, hair system, epidermis, and mucous membranes of the oral cavity for cleaning, perfuming, beautifying, and changing their appearance, correcting bodily odors, and keeping the surface of the body in a good state (1). Many

different products are marketed under the name "cosmetics" like shampoos, bath oils, baby products, perfumes, body lotions, personal hygiene products, and fingernail polish (2,3). To increase the elegance and glamour of ones look lipsticks are used (4). Recently, the use of lipstick has increased, resulting in their mass produce all over the world, and this industry is estimated to be in billions of dollars, with the global lipstick market expected to reach \$13.4 billion by 2024 (5). Lipstick is composed of oils,

waxes, dyes, moisturizers, and antioxidants. Oils make easy the application of lipstick and add glossy properties to its appearance, waxes give thermal stability to the lipstick; and dyes give multiple colors to the final product (6-8) with many other auxiliary components to enhance their desired effects depending on the manufacturers (7). Many lipsticks have been reported to contain many heavy metals such as cadmium (Cd), lead (Pb), arsenic (As), chromium (Cr), and cobalt (Co) (6, 9). Either as basic ingredients or for functional reasons, they are added to cosmetics for functional reason; for example, Al, Au, Cu, and Ag are added for a wonderful metallic finish. As well, Fe, Cd, Ni, Cr, Cu, Zn, Ti, Al, Mn, Ba, and Pb, are used as dyes. However, their presence is limited to certain percentages set by the relevant authorities (10). They are considered to be just impurities in the product (11) as a result of contamination of metallic devices used during the manufacturing process, along with insufficient purification of raw materials (12,13). Thus, frequent daily use of lipstick contaminated with heavy metals is more dangerous due to direct oral ingestion (14). After that, the heavy metal ions get absorbed and form complexes with carboxylic acid (-COOH), amine (-NH₂), and thiol (-SH) of proteins; therefore, this leads to cellular malfunction or death and thus leads to a variety of diseases (15,16). Several previous studies have been conducted to estimate some heavy metals in lipstick cosmetics, Pb is the most common metal among all other metals. Zakaria and Ho (17) found the concentration of lead

in lipstick samples sold in Malaysian markets is 3.21 mg/g. Another study conducted in Saudi Arabia determined the levels of heavy metals in lipstick, the results of this study indicated the presence of high concentrations of Pb in local lipstick compared to other sources. Zainy et al. (18) found high levels of toxic metals in lipstick with dark colors compared to light colors. In addition, there are many other studies carried out to estimate the level of heavy metals in cosmetics (19-24). These studies use different techniques like UV-VIS & microfluidic Paper-based analytical device platform (μPADs) (25), inductively coupled plasma mass spectroscopy (ICP-MS) (26), inductively coupled plasma optical-emission spectroscopy (ICP-OES) (27), laser-induced breakdown spectroscopy (LIBS) (28), X-ray fluorescence (XRD) (29), graphite furnace atomic absorption spectrometry (GFAAS) (21), and including flame atomic absorption spectrometry (FAAS) (30) to evaluate the concentration of toxic metals in cosmetics. Table 1 shows a comparison between the proposed method (AAS) and other methods. Previous studies have successfully assessed the level of heavy metals in the original lipstick, however, no study has been conducted to evaluate and compare the levels of heavy metals in both the original and knockoff lipsticks sold in the local markets in Diyala/Iraq. Therefore, in this study, the level of some heavy metals in original and knockoff lipsticks was determined and compared and their health risk were assessed.

Table 1: The comparison between the proposed method (AAS) with other methods.

Proposed method (AAS)	Other methods (ICP-MS, ICP-OES, LIBS, XRD, UV-Vis, μPADs, etc.)
<ul style="list-style-type: none"> • Techniques based on atomic absorption spectrometry (AAS) are FAAS and GFAAS. It is an analytical technique widely used to determine the level of heavy metals in several types of samples, such as cosmetics, food, water, drugs, soil, and nanomaterials (31). • It has a very high sensitivity, so it can measure very low concentrations of up to 1000 ppm. • High selectivity and detection limit than other techniques, so that a particular element in the sample can be measured out of all the other elements present. • Accuracy in results. • It requires the use of a very small amount of sample, which reduce residue generation • Low spectral interference • Less contamination of samples. • Digestion time is shorter (32,33). • Quick nature. 	<ul style="list-style-type: none"> ▪ These analytical techniques (UV-Vis, μPADs, ICP-MS, ICP-OES, LIBS) are used to determine heavy metals in various samples, including cosmetics. • ICP-MS and ICP-OES: the advantages of these techniques are their wide linear range and low detection limits; the disadvantages of these techniques are the presence of spectral and other non-spectral interferences, and the method of sample digestion is very important in order to obtain samples with low carbon content and the least amount of suspended solids, in order to avoid clogging the nebulizer system and carbon deposition on the interface of the equipments (34). • LIBS and XRD are techniques for direct analysis of heavy metals in cosmetics without the need for a sample preparation step. However, these techniques have some disadvantages represented by spectral overlaps, poor accuracy, and high standard deviation values (35). • The UV-Vis and μPADs techniques need to perform color reactions, which means consuming a quantity of reagents and needing a longer time, and the results are less accurate compared to the atomic absorption technology. Also, the μPADs technique is not widely available in laboratories

- One of the disadvantages of this technique is the overlap of some atomic lines, which can be reduced or overcome.

(36,37).

- Some of these techniques, such as ICP-OES, ICP-MS, and LIBS, require trained people to work on them in addition to being difficult procedures.

1.1 Toxicological Effects of Some Heavy Metals

Cosmetics (such as lipstick) are one of the most significant sources of toxic heavy metal release into the environment and the biological systems of humans compared with other sources (water, air, and food) (1,38). Due to the cumulative properties of these elements in the human body, they are a concern for consumers. Cd, Cr, Cu, Pb, Zn, and Ni are heavy metals that preoccupy the minds of lipstick users because of their negative effects on human health (39).

1.1.1. Cd

Cd is one of the heavy metals that is dangerous, and cadmium compounds are present in lipstick to give different pigments from yellow to deep orange (40,41). Cadmium selenide and cadmium sulfide are used for yellow and green colors, respectively, and can produce a wide range of colors when other metals are added (42). In general, in cosmetics, cadmium should not exceed the permissible limit of 3 ppm, the limit set by regulatory authorities (43). The exposure to cadmium through lipstick ingestion can cause severe stomach irritation, vomiting, low blood pressure, and diarrhea, while long-time exposure to low concentrations can cause bone deformation (the ability of bones to break easily because of calcium metabolism), hepatic damage, and renal damage (44).

1.1.2. Cr

Cr is an essential nutrient and plays a significant role in cholesterol and glucose metabolism (45). In contrast, chromium (VI) is a very toxic metal that spreads easily in the body and is considered a carcinogen for humans according to IARC (International Agency for Research on Cancer) (46, 47). Chromium (VI) is banned in cosmetic products, whereas Cu, Cr(OH)₃, and Cr₂O₃ are allowed as cosmetic colorants (48). According to the EPA the safe level of chromium in cosmetics is 1 ppm (49). When exposed to chromium (VI) by ingestion, it can cause problems with the kidneys, liver, and stomach (50).

1.1.3. Cu

Cu is an essential trace metal in the human body, and it is used in many industries, including the cosmetics industry (51). Copper is used in cosmetics as coloring pigments or to block UV rays (52). The permissible limit for copper in cosmetics when used as a color additive is 50 µg/g (53). However, it may have harmful effects at high levels (54). It may cause nose and throat irritation and even dermatitis. Chronic exposure to Cu can result in numerous physiological and behavioral disturbances, which include acute brain damage, cirrhosis of the liver,

aggressive behavior, and hemolytic anemia, as well as psychiatric disturbances such as depression (11).

1.1.4. Pb

Like cadmium, lead is a heavy metal and one of the most toxic chemical pollutants in human history. It is used in lipstick to give a synthetic pearlescent pigment, which increases the shimmer effect of product (7). Lead in lipstick can be ingested when licking the lips, eating, or drinking. Thus, lead will accumulate in the body over time, even if the permissible limit does not exceed (10 to 20 ppm), the limits set by Health Canada and the US Food and Drug Administration. Pb is an impurity found in cosmetics (55). When excessive Pb accumulates in the human body, it can cause many harmful effects, including acute and chronic poisoning, pathological changes in organs, diseases of the cardiovascular system, kidney, bone, and liver, and even cancer (56).

1.1.5. Zn

Zinc is a metal of great importance to humans and is considered to have no significant toxicological effect. The presence of zinc in cosmetics has several possibilities depending on the type of compound; some zinc salts make it easier to apply cosmetics to the skin (57). However, the presence of an excess of Zn causes neurological diseases and gastrointestinal disorders (58). and can cause other health effects such as stomach cramps, vomiting, nausea, skin irritation, and anemia (55).

1.1.6 As

As is one of the most common heavy metals found in lipstick products, which are added as impurities (12). It can have many negative effects on human health, such as elevated blood pressure, melanosis, and gangrene (59). A combination of heavy metals like Hg, Pb, Cd, and As can generate synergistic effects that lead to dysfunction and cognitive damage (60). Chronic exposure to As can result in macrophage dysfunction due to impairments in the immune system. Ultraviolet light (UV) and arsenic are the major risk factors that contribute to squamous cell carcinoma and basal cell carcinoma (61). As a result of these health effects, the concentration of arsenic in cosmetics should not exceed 3 ppm (47).

This work aimed to determine the concentration of some heavy metals like Cd, Cr, Cu, Pb, Zn, and As in lipstick brands by using flame atomic absorption spectrophotometer (FAAS) technique, and the levels of heavy metals were compared to those of original and copied lipstick brands. Moreover, estimation of bacterial contamination and knowledge of the type of organism present in the lipsticks of original

(expensive) and knockoff (cheap) brands sold in local markets in Diyala, Iraq.

2. METHODOLOGY

2.1. Collection of Samples

Twenty lipstick samples (ten originals and ten fake (knockoff) samples) were purchased from the local markets in Diyala, Iraq. The lipsticks used in this

study have the same brands, characteristics, and colors, but they differ in price. The expensive (original) lipstick was imported from several countries (Ireland, Türkiye, China, France, USA), as written on the labels, while the cheap (knockoff) lipstick is mostly of the same origin. Some of them are of different origins, and some are of unknown origins. Table 2 lists information on expensive and cheap lipsticks.

Table 2. Information on the lipstick samples.

Knockoff lipstick (n = 10)			Original lipstick (n = 10)		
Origin	Color	Samples code	Origin	Color	Samples code
Unknown	Violet -Red	1A	Ireland	Violet -Red	A1
	Maroon	2A		Maroon	A2
Türkiye	Pink	1B	Türkiye	Pink	B1
	Brown	2B		Brown	B2
Unknown	Red	1C	China	Red	C1
	Chocolate	2C		Chocolate	C2
USA	Purple	1D	USA	Purple	D1
China	Orange	1E	China	Orange	E1
France	Pink	1F	France	Pink	F1
China	Red	1G	USA	Red	G1

2.2. Reagents and Chemicals

Samples were prepared by using analytical grade HClO_4 (purity 70%, Sigma Aldrich, USA) and concentrated HNO_3 (purity 69.5%, BDH, England). Also, all samples were diluted with distilled water.

2.3. Optimal Conditions of Digestion Method (hydrogen function, Temperature, Time of Heating, and Order of addition).

To verify the method used, the effects of some variables were studied: the effect of *hydrogen function*, temperature (50-250 °C), time of heating (15, 30, 60, and 120 minutes), and order of addition.

2.3.1. Hydrogen function influence

Acids play a key role in the digestion of cosmetic samples, especially HNO_3 , which is used alone or with other acids. The main function of these acids is as oxidizing agents by which inorganic metal oxides can be dissolved in cosmetic samples (62). The preparation of solutions containing a mixture of concentrated acids $\text{HClO}_4:\text{HNO}_3$ of different proportions (1:1,1:2, 1:3,1:4, 2:1,3:1, and 4:1). The result of this step shows that 1:3 is optimal.

Influence of Heating Time: Heating the reaction components for different times (15, 30, 60, 120, and 150) minutes. 120 minutes were enough to complete the reaction.

2.3.2. Influence of temperature

In general, temperatures help to get rid of steam and organic impurities by converting organic carbon into carbon dioxide gas (CO_2). High temperatures cause the loss of heavy metals to be determined from the samples, while low temperatures cause incomplete oxidation of the materials. The reaction mixture was heated to different temperatures (50, 100, 150, 200, and 250 °C). The results of this step indicated that heating to 100 °C for two hours was good.

2.3.3. Order of addition

The change in reaction components' addition order; the sample (A) first, then the acid mixture (B), and finally distilled water (C) was the most appropriate. Figure 1 shows the results of the optimal conditions for the method used for the determination of heavy metals in lipsticks.

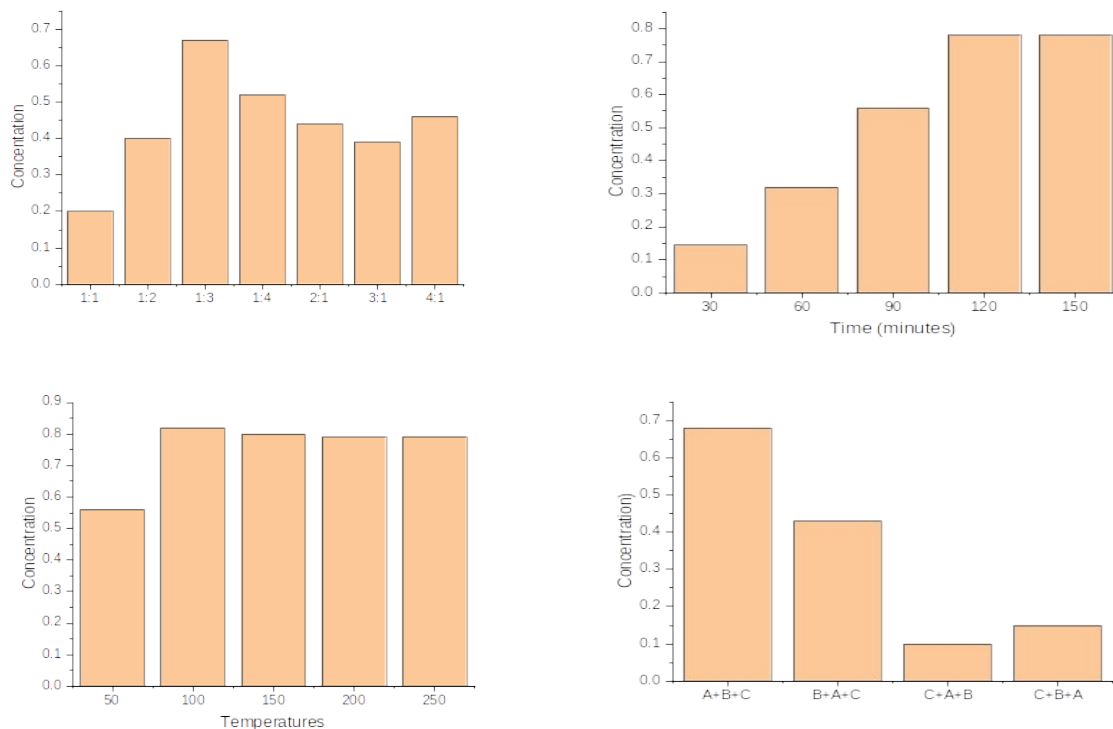


Figure 1. Influence of (a) hydrogen function (1:1,1:2, 1:3,1:4, 2:1,3:1, and 4:1), (b) temperature (50-250) °C, heating time (15, 30, 60, 120, and 150) minutes, and (d) order of addition ((A) lipstick sample, (B) acid mixture, (C) water).

2.4. Optimum Digestion Method of Samples

In this work, wet acidic digestion was used for the determination of a quantity of heavy metals like Cd, Cr, Cu, Pb, Zn, and As by the method adopted by Sani et al. (2016) (3). With some modifications, 0.5 g of each lipstick was weighed using an electronic balance and placed in a conical flask, followed by 5 mL of a concentrated acid mixture HClO₄:HNO₃ (1:3), which was then heated for 2 hours on a hot plate at 100 °C. Then 3 mL of the concentrated mixture was added, and the solution was heated again for two hours to complete the digestion process. The

digested samples were cooled to room temperature and diluted to 25 mL with deionized water. The solution was filtered through filter paper (Whatman No. 41) to remove unwanted components, and the pure solution was used for metal determination.

2.5. Analysis of Heavy Metals by FAAS

The quantities of Cd, Cr, Cu, Pb, Zn, and As in lipstick samples were determined by using flame atomic absorption. Table 3 shows the operating parameters of AAS.

Table 3: Operating parameters of the Atomic Absorption Spectrophotometer(AAS) used in the heavy metal analysis.

Operating parameters	As	Zn	Pb	Cu	Cr	Cd
Wavelength (nm)	193.7	213.9	283.30	324.80	357.90	228.80
Slit width (nm)	0.50	0.70	0.70	0.70	0.70	0.70
Detection limit (mg/L)	0.05	0.03	0.08	0.005	0.04	0.01
Lamp current (mA)	5.00	5.00	5.00	1.50	2.00	2.00
Flame Type (Color)	Air-Acetylene/(lean/Blue)	Air-Acetylene/(lean/Blue)	Air-Acetylene/(lean/Blue)	Air-Acetylene/(lean/Blue)	Air-Acetylene/(rich/Yellow)	Air-Acetylene/(lean/Blue)

2.6. Method Validation

2.6.1. Linearity

To ensure the reliability of the results. The quantification of the concentration of the metals was carried out using a five-point calibration curve for each of the metals used in the study. The calibration was accomplished by adding the standards prepared in concentrations of 1, 5, 10, 25, and 50 ppm from the 1000 ppm standard stock solution. The analytical procedure validation for quantitative analysis of heavy metals in cosmetics products was performed using linear ranges, detection limit, quantification limit, precision, accuracy, and recoveries of spiked standards in the defined calibration ranges were calculated. Analytical method validation for heavy metals analysis was applied in accordance with Eurachem guide.

2.6.2. Limit of detection (LOD) and limit of quantification (LOQ)

The limit of detection was estimated as the mean plus three times the standard deviation (SD) of a blank sample, and it was determined following the equation below:

$$LOD = 3 \frac{SD}{b} \quad (\text{Eq. 1})$$

$$LOQ = 10 \frac{SD}{b} \quad (\text{Eq. 2})$$

where, SD is the standard deviation- of the blank (based on three independent analyses of sample blank). b is the calibration-graph slope (21).

2.6.3. Accuracy

Because of the unavailability of certified material for lipstick, the accuracy of the method was obtained by adding the true values of Cd, Cr, Cu, Pb, Zn, and As to the cosmetics matrix. The same analytical procedure was applied for test samples, and the percentages of relative error (%RE) and analyte percentage relative recovery (%Recovery) were calculated by the following equation:

$$\%RE = \left(\frac{\text{found} - \text{true}}{\text{true}} \right) \times 100 \quad (\text{Eq. 3})$$

$$\%Recovery = \left(\frac{\text{found}}{\text{true}} \right) \times 100 \quad (\text{Eq. 4})$$

found:- result value, true:- real value.

The analytical recovery figures for spiked lipstick are shown in Table 4.

2.6.4. Precision

The precision of method was determined by relative standard deviation (%RSD). It is studied by using

three concentrations of heavy metals, which are calculated using the following equation:

$$\%RSD = \left(\frac{SD}{x} \right) \times 100 \quad (\text{Eq. 5})$$

$$SD = \left[\sum \frac{(x_i - x)^2}{(n-1)} \right]^{0.5}, x = \sum \frac{x_i}{n} \quad (\text{Eq. 6})$$

Where SD: standard deviation, x: the average of the samples.

2.7. Health Risk Assessment

Exposure routes: A lipstick may enter a human body through ingestion; this intake can be calculated using the following equation:

$$ADDing = \frac{C \times IR \times EF \times ED}{BW \times AT \times C} \quad (\text{Eq. 7})$$

ADDing is the average ingested daily dose (mg/kg day); C is the concentration of heavy metals; IR is the intake rate (40 mg/day); EF is the exposure frequency (260 days/years); ED is the exposure duration (35 years); BW is the body weight (57.9 kg); AT is the average time (calculated by ED × 365 days/year); and CF is the conversion factor (10⁻³).

After calculating the average daily dose, the hazard quotient-(HQ) for non-carcinogenic health effects was calculated using the following formula:

$$HQ = \frac{ADDing}{RfD} \quad (\text{Eq. 8})$$

Where, Rf D (Reference Oral Dose) is the specific reference dose (mg/kg/day) that varies for all metals (17), Rf Ds used for the hazard assessment were 0.001 for Cd, 0.003 for Cr, 0.04 for Cu, 0.004 for Pb, 0.3 for Zn, And 0.001 for As (24, 63).

When the ADDing value is less than the Rf D, there will be no health effect, but if the ADDing value is greater than the Rf D, there may be noncarcinogenic health effects.

HQ < 1 indicates no adverse health effects, while HQ ≥ 1 indicates likely adverse health effects. The health risk index (HI) was used to calculate the total risk effect of all the elements studied. This index was calculated using the following formula:

$$HI = \sum HQ \quad (\text{Eq. 9})$$

$$HI = \sum HQ = HQCd + HQCr + HQCu + HQPb + HQZn + HQAs$$

2.8. Study of Biological Activity

To detect the antibacterial activity, two groups of lipstick samples were used, the first group consisted of 10 samples of the original (expensive), and the second group also used 10 samples of knockoff (cheap). In this study, a range of different gram-negative and gram-positive bacteria were selected. The isolates of gram-negative bacteria included (*E.coli*, *Pseudomonas aeruginosa*) while gram-positive bacterial include (*Staphylococcus aureus*, *Staphylococcus epidermidis*) isolate. The microbial activity of different lipsticks was determined by the (agar, well, diffusion) method (64). In this method, growth was cultivated on a Muller-Hinton Agar plate (HiMedia, Mumbai, India). After the plates had dried, one well was drilled into each of the agar plates using a sterile cork borer with a diameter of 5.0 mm. A micropipette was used to dispense 80 µL of lipstick suspension from each sample into each well of a Muller-Hinton agar plate. After standing for at least an hour to allow pre-diffusion to occur, the

plates were incubated for 48 hours at 37 °C. In millimeters, the zone of inhibition was measured. Three duplicates of each experiment were carried out.

2.8.1. Statistical analysis

All results are expressed as the mean±SD, and all data were analyzed by t- test, which was used for general comparison between two groups of lipstick using SPSS software.

3. RESULTS AND DISCUSSION

The analytical producer validation for quantitative analysis of heavy metals in cosmetics products was performed using linear ranges, ranging from 1 to 50 ppm, coefficients of correlation ranged from 0.9983 to 0.9995, LOD ranged from (0.01 to 0.1), and LOQ was set from(0.03 to 0.33), which indicates a selective and sensitive method. Table 4 shows the results obtained in this study.

Table 4: Method validation results of the heavy metals studies.

LOQ (ppm)	LOD (ppm)	R ²	Linear range	Regression Equation	Metals
0.33	0.1	0.9983	1-50	y = 0.0293x + 0.1421	Cd
0.1	0.03	0.9985	1-50	y = 0.0243x + 0.0199	Cr
0.17	0.05	0.9989	1-50	y = 0.0261x + 0.0354	Cu
0.33	0.1	0.9995	1-50	y = 0.0299x + 0.0431	Pb
0.07	0.02	0.9979	1-50	y = 0.0244x + 0.0151	Zn
0.03	0.01	0.9992	1-50	y = 0.0179x + 0.0778	As

For accuracy and precision, spiking was performed using the calibration-standard solution in three fortification levels (1, 5, and 25 ppm) of the linear range as the sample matrix for accuracy and precision calculations, using Equations 3, 4, and 5 to calculate the values of percentage of relative error,

percentage of recovery, and relative standard deviation. The results (Table 5) were presented as mean data, indicating the recovery values (from 100.17% to 101.1%), RE values of 0.81%, and RSD values of ≤ 1.33 %, confirming good accuracy and precision.

Table 5: Accuracy and precision of studied metals.

*(%RSD)	*(%RE)	*(% Recovery)			Metals
		25 ppm	5 ppm	1 ppm	
1.32	0.71	100.23 ±0.67	101.2±1.76	100.7±1.53	Cd
1.21	0.46	100.06±0.38	100.4±2.11	100.9±1.15	Cr
1.1	0.54	100.57±0.70	100.87±2.05	100.17±0.55	Cu
0.78	0.58	100.3±0.36	100.5±0.71	100.43±1.55	Pb
1.33	0.53	99.7±1.11	100.8±1.23	101.1±1.66	Zn
0.65	0.81	101.43±0.76	100.7±0.72	100.3±0.46	As

*Average of three replicates.

3.1. Concentration of Heavy Metals in Lipstick Samples

In this study, twenty samples of different brands of lipstick were investigated. The concentration of each heavy metal in the lipstick samples is given in Table 6.

The acceptable limit of heavy metal content in cosmetics was set by (USFDA) in 2007, in particular 3 ppm for cadmium, 1 ppm for chromium, 50 mg/g for copper, 10 ppm for lead, and 3 ppm for arsenic. Based on Table 3, the concentrations of Cd in the

studied brands of lipstick were from 0.11 to 0.56 ppm in the original brand and 0.21 to 0.88 in knockoff brand; these values did not exceed the legal threshold of 3 ppm set by the US Food and Drug Administration and Health Canada (41).

In a study reported by Saleh et al. to determine the level of cadmium in lipsticks sold at different prices, the results showed that the level of cadmium ranged from 0.03 to 0.07 ppm (41). Previous studies have shown different concentrations of cadmium in lipstick samples. Nourmoradi et al. detected that the

cadmium concentration in some brands of lipstick was within the range of 4.08 to 60.20 mg/g (1). Another study reported by Iwegbue et al. found that the concentration of cadmium ranged between 0.34 and 37.3 (46), 0.01 to 0.06 (65), and 0.77 to 1.19 (66). A study in Jordan found the levels of Cd ranged from 0.12 to 2.72 (67). However, the level of cadmium in the present study was lower than that in other studies conducted by Nourmoradi et al. and Iwegbue et al. (1, 42).

The concentration of Cr in the original and knockoff brands of lipstick samples was not detected. This is consistent with the European Union's prohibition on the presence of chromium in cosmetics (17).

Different studies in many countries have shown different ranges for chromium in lipstick. In Iran, Naalband et al. found the concentration of Cr in lipstick ranged between 0.06 and 0.75 (40). In Malaysia, Zakaria et al. found that the Cr ranged between 0.24 and 2.25 (17). In Portugal and Brazil, Pinto et al. reported that the concentration of Cr ranged between 2.26 and 2.28 (68). In another study conducted by Sani et al., the researchers determined the levels of chromium in lipsticks with varying prices. The results showed the levels of chromium ranged from 0 to 0.05 ppm (3). The concentration values of Cr obtained in this study were lower than the values in the other study mentioned above.

Table 6: Concentrations (ppm) of heavy metals in original (expensive) and knockoff (cheap) lipsticks.

Metals	Original			Knockoff		
	Mean±SD	Min	Max	Mean±SD	Min	Max
Cd	0.34±0.23	0.11	0.56	0.55±0.18	0.26	0.88
Cr	< LOD	< LOD	< LOD	< LOD	< LOD	< LOD
Cu	0.12±0.07	0.014	0.28	0.22±0.13	0.06	0.39
Pb	0.68±0.19	0.5	1.06	0.98±0.17	0.76	1.26
Zn	0.19±0.18	0.026	0.5	0.33± 0.31	0.067	0.77
As	0.04±0.03	0.012	0.098	0.1±0.07	0.034	0.28

*values are expressed as an, average for, three determinations.

The concentration of copper (Cu) in the original and knockoff brands of lipstick ranged from 0.014 to 0.28 and 0.06 to 0.39, respectively. In other studies, the levels of copper in lipstick have been reported. For example, researchers found the level of copper in some brands of lipstick ranged between 0.0 and 75.92 (57). Iwegbue CM et al. conducted a study to estimate several heavy metals, like copper (Cu), in 160 samples of facial cosmetics, including lipstick, sold in southern Nigeria. The results showed that the concentration of copper ranged from 1.1 to 135.4 ppm (42). A study published by Chauhan SB et al. found that the concentration of Cu in lipstick ranged between 0.0498 and 7.0782 (69), as well as 1.86 and 21.72 (24). The results showed that the level of this heavy metal in the current study was comparable to that found in the study conducted by Chandak et al. (2014), while the levels of Cu in this study were less than the values obtained in other studies (24,42,57). However, the results show that the concentration of copper was less than (50 mg/g), the standard allowed by the regulatory authorities for copper in cosmetics (6).

Pb is found naturally in the earth's crust. Lead was detected in all brands of lipstick used in this study; the levels of Pb ranged from 0.5 to 1.06 ppm in the original brand and 0.76 to 1.26 ppm in the knockoff brand. Pb levels in lipstick were measured in ppm in various studies. In a study conducted by Nnorom in 2005, the levels of Pb ranged between 87 and 123 ppm (50); in 2012, they ranged between 5.5 and 47.8 (66); and in 2013, they ranged between 0.58 and 3.36 (70). In 2016, they ranged between 0.18

and 0.8 (40), and in 2020, they ranged between 0.286 and 6.234 (24). The observed levels of Pb in this study are similar to those reported in this study by Nourmoradi et al. (2013), and Kamarehie et al. (2020), but they are lower than those in the previous studies. The lead values used in this study, however, did not exceed the permissible limit for lead as an impurity in cosmetics of 20 ppm and 10 ppm, respectively, as set by the US Food and Drug Administration and Health Canada (71).

Zn was used as a pigment in cosmetics; the average concentration of Zn in the studied brands ranged between 0.0026 and 0.5 ppm, 0.067 and 0.77 ppm, and the means were 0.19 and 0.33, in the original and knockoff brands, respectively. In other countries, different ranges of Zn in lipstick brands have been reported. For example, in a study from Iran, Ghaderpoori, M. et al. reported concentrations ranging between 3.64 and 216.53 ppm (72). In Pakistan, a range between 0.4757 and 6.7694 ppm was reported by Kamarehie et al. 2020 (73). In Khyber, the range was between 0.696 and 1.610 ppm (15). In Nigeria, the level of Zn ranged from 2.23 to 3.01 ppm was reported by Okol et al(6). In Poland, it ranged from 1.73 to 488.13 ppm (57). When the Zn range values in this study were compared to other studies in the aforementioned countries, the level of Zn in this study was found to be similar to those in the Khyber City study reported by Ullah et al., while being lower than the other studies mentioned above. However, the mean concentrations of Zn were higher than the LOD.

The concentration of As in different brands of lipstick used in this study ranged from 0.012 to 0.098 and 0.034 to 0.28 ppm. Different studies conducted in different times reported the levels of As in lipstick. In 2014, Ouremi et al. reported levels of As ranging between 0.8 and 3.0 ppm (47). In 2015, they ranged from 0.11 to 0.43 ppm (74). In 2019, it ranged from 0.990 to 9.235 ppm (21). In 2020, it ranged 0.29 to 4.83 ppm (75). The level of As in the present study was lower than in the above mentioned studies. The level of arsenic in the studied samples was less than (3 ppm), which is the permissible limit for As in cosmetics, according to Health Canada (76).

In this study, the amount of heavy metals was less than the limit allowed by the executive authorities, and in addition, the original brand of lipstick gave a better result than the imitation. When comparing the results of this study with those of previous studies, it was found that the amount of heavy metals in the present study was similar to the values reported in the literature for lipstick products. The concentrations of the heavy metals analyzed are in the following order: Pb > Cd > Zn > Cu > As > Cr. Lead has the highest concentration, while chromium has the least (25). The results in Table 4 confirm the proposed method's accuracy and precision in heavy metals' determination. A t-test was conducted to compare expensive and cheap lipstick products. The results of the test showed that there were no statistically significant differences in the concentrations of heavy metals. Among the expensive and cheap cosmetics.

3.2. Risk Assessment

Heavy metals in cosmetics may seem like a small proportion of the sources that threaten human health in comparison to air, food, and water. Therefore, its harmful effects must be avoided. In this part of the study, to determine the non-carcinogenicity risk of contact with cosmetics products, the hazardous quotient (HQ) and hazardous index (HI) were estimated from Equations

7 and 8. Table 8 shows the results for HQ and HI as calculated. According to Table 8, the amount of HQ in all lipstick brands examined was below 1, indicating there was no significant non-carcinogenic health risk for lipstick users. The highest amount of HQ was found in lead (6.3E-01), which was observed in the sample (1B), but the lowest amount of HQ was found in zinc (4.3E-05), which was detected in the sample (A1). According to HI, the amount of HI for all samples used in our study was lower than 1. This indicates that the consumer was at the safety limit.

3.3. Anti-bacterial Activity

The results indicated that there was no bacterial growth in the original brand of lipstick, and this is in accordance with the laws of the US Food and Drug Administration. While in the case of knockoff brands (1A, 2A, 1B, 2B, E, 1C, 2C, 1D, 1E, 1F, and 1G), these samples showed the most antimicrobial effects on gram-negative and gram-positive bacterial isolates. This contradicts what the US Food and Drug Administration law stipulates that "cosmetics are not required to be sterile, but rather, they must not be contaminated with microorganisms that may cause disease, and cosmetics are required to remain in this state even when used before consumers" (77). Figure 2, shows the anti-bacterial activity in knockoff lipstick samples.

These results are in agreement with many studies. According to a recent study conducted by Siya using thermal sequencing analysis, on 20 lipstick samples, the results indicated that the samples were contaminated with 105 bacterial genera, including *Streptococcus*, *Staphylococcus*, *Pseudomonas*, and *Escherichia* (78). Another study reported by Vassoler, M., et al. analyzed the microbiological quality of 30 lipstick samples sold in Brazil; the results indicated the presence of bacterial contamination with different types of bacteria, including *S. aureus* and *S. epidermidis* (79).

Table 7: Estimated adding of selected metals found in the original and knockoff lipstick brands.

Original Lipstick						
Code	Cd	Cr	Cu	Pb	Zn	As
A1	1.6E-04	0	7.1E-06	4.3E-04	1.3E-05	1.1E-05
A2	2.8E-04	0	5.2E-05	3.8E-04	4.6E-05	1.3E-05
B1	1.1E-04	0	5.5E-05	2.5E-04	4.3E-05	1.5E-05
B2	2.2E-04	0	4.3E-05	2.7E-04	1.5E-05	1.4E-05
C1	1.5E-04	0	5.3E-05	4.1E-04	2.2E-05	4.5E-05
C2	2.2E-04	0	5.7E-05	3.3E-04	1.2E-04	2.4E-05
D1	2.8E-04	0	1.4E-04	3.0E-04	2.2E-04	1.9E-05
E1	2.3E-04	0	6.3E-05	2.5E-04	4.1E-05	0.5E-05
F1	1.5E-04	0	7.3E-05	2.4E-04	1.6E-04	4.9E-05
G1	5.3E-05	0	4.3E-05	5.3E-04	2.5E-04	2.4E-05

Knockoff Lipstick						
Code	Cd	Cr	Cu	Pb	Zn	As
1A	2.3E-04	0	3.1E-05	5.1E-04	3.3E-05	2.1E-05
2A	3.3E-04	0	9.3E-05	4.4E-04	1.6E-04	2.4E-05
1B	1.9E-04	0	1.5E-04	6.3E-04	4.2E-05	2.5E-05
2B	3.4E-04	0	4.6E-05	4.1E-04	6.1E-05	5.4E-05
1C	3.1E-04	0	2.3E-04	4.6E-04	5.2E-05	5.5E-05
2C	1.3E-04	0	1.1E-04	5.3E-04	1.3E-04	5.4E-05
1D	4.4E-04	0	1.9E-04	4.7E-04	2.9E-04	3.1E-05
1E	3.4E-04	0	6.8E-05	3.8E-04	4.8E-05	1.7E-05
1F	2.3E-04	0	8.3E-05	3.2E-04	4.4E-04	1.4E-04
1G	2.2E-04	0	8.4E-05	6.2E-04	3.5E-04	5.4E-05

Table 8:- Health risk assessment of heavy metals (HQ and HI) in original and knockoff lipstick brands.

Original Lipstick							
Code	Cd	Cr	Cu	Pb	Zn	As	Total HQ or HI
A1	0.16	ND	0.0002	0.43	0.000043	0.011	0.601
A2	0.28	ND	0.0013	0.38	0.00015	0.013	0.674
B1	0.11	ND	0.0014	0.25	0.00014	0.015	0.372
B2	0.22	ND	0.0011	0.27	0.00005	0.014	0.505
C1	0.15	ND	0.0013	0.41	0.00007	0.045	0.606
C2	0.09	ND	0.0014	0.33	0.00004	0.024	0.445
D1	0.28	ND	0.0035	0.30	0.00073	0.019	0.603
E1	0.23	ND	0.0015	0.25	0.00014	0.005	0.487
F1	0.15	ND	0.0018	0.24	0.00053	0.049	0.441
G1	0.053	ND	0.0011	0.53	0.00083	0.024	0.609

Knockoff Lipstick							
Code	Cd	Cr	Cu	Pb	Zn	As	Total HQ or HI
1A	0.23	ND	0.0008	0.51	0.00011	0.021	0.762
2A	0.33	ND	0.0023	0.44	0.00053	0.024	0.797
1B	0.19	ND	0.0038	0.63	0.00014	0.025	0.849
2B	0.34	ND	0.0012	0.41	0.00020	0.054	0.805
1C	0.31	ND	0.0058	0.46	0.00017	0.055	0.831
2C	0.13	ND	0.0028	0.53	0.00043	0.054	0.717
1D	0.44	ND	0.0048	0.47	0.00097	0.031	0.947
1E	0.34	ND	0.0017	0.38	0.00016	0.017	0.739
1F	0.23	ND	0.0021	0.32	0.00147	0.14	0.694
1G	0.22	ND	0.0021	0.62	0.00117	0.054	0.897

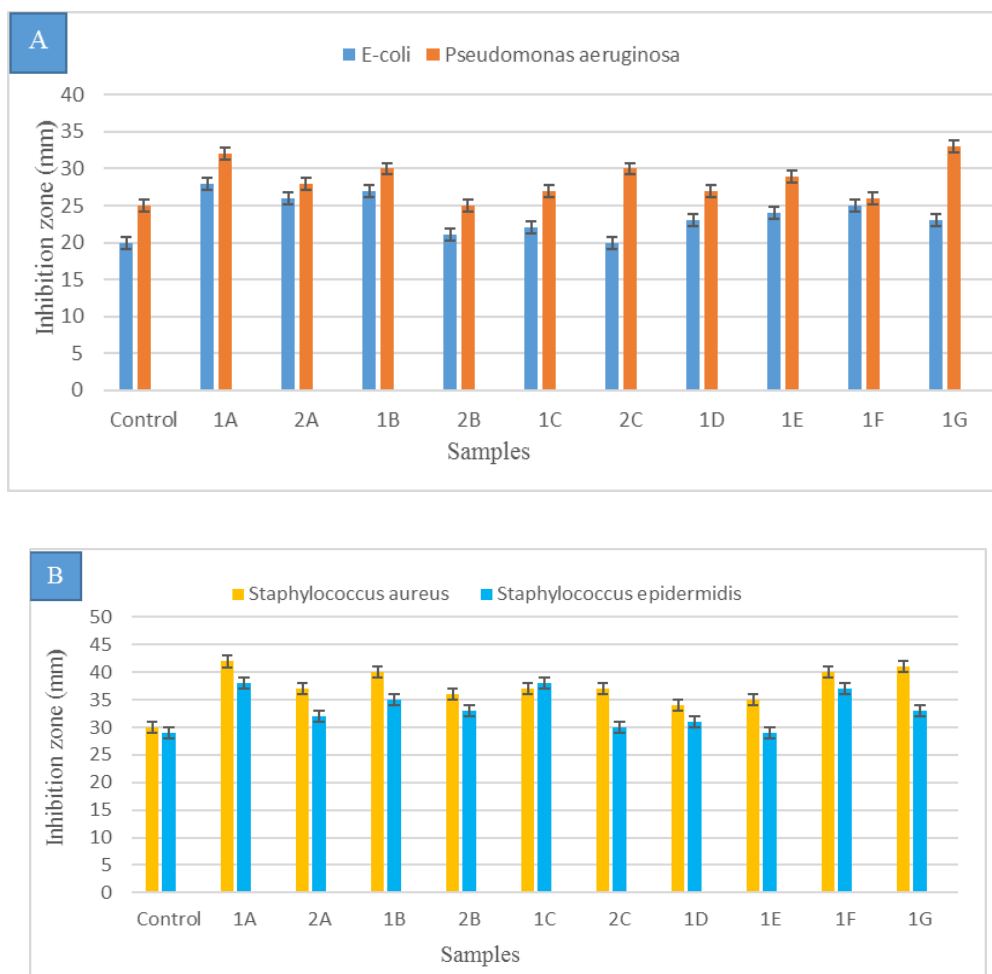


Figure 2: Antimicrobial-activity of knockoff lipstick samples. (A) Inhibition of different gram-negative bacteria isolates by lipsticks samples, (B) Inhibition of different gram-positive bacteria isolates by lipstick samples.

4. CONCLUSION

The primary components present in lipstick are oils, waxes, dyes, and alcohols. Even though heavy metals are not an essential component of lipsticks, they are in cosmetics as impurities. And even with good manufacturing processes, the presence of heavy metals is unavoidable in cosmetics. Therefore, the executive authorities have set values for heavy metals in cosmetics that should not be exceeded. FAAS is a simple and rapid analytical method used to estimate the quantity of cadmium, chromium, copper, lead, zinc, and arsenic in two groups of lipstick samples used in this study. The results showed that the samples used in this study contained all the metals that were analyzed. Except for chromium, which was not detected in all the studied samples, whether expensive or cheap, while the levels of lead were higher than all other metals, they were less than the permissible limit set by the executive authorities. The results of the THQ showed that the values were below 1 for all tested samples, meaning that the detected heavy metals in lipstick did not pose a dangerous health risk to consumers,

and the original brand of lipstick showed better results than knockoff brands. However, there are concerns that daily and repeated use of cosmetics contaminated with toxic heavy metals may lead to biological accumulation in body tissues and cause negative health effects on consumers. The results of the biological activity show that there was no bacterial growth in the original lipstick samples while there was contamination with organisms in the cheap samples.

5. CONFLICT OF INTEREST

The researchers declare that there are no conflicts of interest regarding the current manuscript.

6. ACKNOWLEDGMENTS

The researches acknowledge and thankful to the University of Diyala, and the faculty of Sciences for submitting the entire requirements to do this research.

7. REFERENCES

1. Balarastaghi S, Khashaiarmanesh Z, Makhdoumi P, Alavizadeh SH, Sameie Moghadam Z, Shirani K, et al. Determination of toxic element levels (lead and cadmium) in commonly used cosmetic products in Iran. *Toxin Reviews*. 2018 Apr 3;37(2):117-22. Available from: [<URL>](#).
2. Marinao T, Iovinea A, Casellab P, Martinoc M, Chianese S, Laroccac V, et al. From *Haematococcus pluvialis* microalgae a powerful antioxidant for cosmetic applications. *Chem Eng*. 2020;79:271-6.
3. Sani A, Gaya MB, Abubakar FA. Determination of some heavy metals in selected cosmetic products sold in Kano metropolis, Nigeria. *Toxicology Reports*. 2016;3:866-9. Available from: [<URL>](#).
4. Karanje PS, Doijad RC, Bhosale RR, others. Formulation and evaluation of herbal lipstick containing *Amaranthus cruentus* Linn. *Int J Res Anal Rev*. 2020;7:246-55.
5. Gurrieri L, Drenten J. The feminist politics of choice: lipstick as a marketplace icon. *Consumption Markets & Culture*. 2021 May 4;24(3):225-40. Available from: [<URL>](#).
6. Oklo A, Eneche D, Aondoakaa MAM. Heavy metals in some lipstick products marketed in Makurdi metropolis, Benue state Nigeria. *International Journal of Environment, Agriculture and Biotechnology*. 2020;5(2).
7. Shukri NM, Bashir NAA, Shohaimi NAM, Abdullah WNW, Abdullah NH, Ab Halim AZ, et al. Assessment of permissible limits for heavy metals in various inspired and authentic lipsticks. *Malaysian Journal of Chemistry*. 2020;
8. Batista ÉF, Augusto A dos S, Pereira-Filho ER. Chemometric evaluation of Cd, Co, Cr, Cu, Ni (inductively coupled plasma optical emission spectrometry) and Pb (graphite furnace atomic absorption spectrometry) concentrations in lipstick samples intended to be used by adults and children. *Talanta*. 2016 Apr;150:206-12. Available from: [<URL>](#).
9. Parizi MG, Sedaghat Z, Mazloomi M, Fararouei M. Serum level of lead and cadmium is linked to facial cosmetics use among Iranian young women. *Environ Sci Pollut Res*. 2021 Mar;28(11):13913-8. Available from: [<URL>](#).
10. Chopi R, Sharma S, Sharma S, Singh R. Trends in the forensic analysis of cosmetic evidence. *Forensic Chemistry*. 2019 Jun;14:100165. Available from: [<URL>](#).
11. Ayenimo JG, Yusuf AM, Adekunle AS, Makinde OW. Heavy Metal Exposure from Personal Care Products. *Bull Environ Contam Toxicol*. 2010 Jan;84(1):8-14. Available from: [<URL>](#).
12. Volpe MG, Nazzaro M, Coppola R, Rapuano F, Aquino RP. Determination and assessments of selected heavy metals in eye shadow cosmetics from China, Italy, and USA. *Microchemical Journal*. 2012 Mar;101:65-9. Available from: [<URL>](#).
13. Al-Saleh I, Al-Enazi S, Shinwari N. Assessment of lead in cosmetic products. *Regulatory Toxicology and Pharmacology*. 2009 Jul;54(2):105-13. Available from: [<URL>](#).
14. Sainio EL, Jolanki R, Hakala E, Kanerva L. Metals and arsenic in eye shadows: METALS AND ARSENIC IN EYE SHADOWS. *Contact Dermatitis*. 2000 Jan;42(1):5-10. Available from: [<URL>](#).
15. Ullah H, Noreen S, Fozia, Rehman A, Waseem A, Zubair S, et al. Comparative study of heavy metals content in cosmetic products of different countries marketed in Khyber Pakhtunkhwa, Pakistan. *Arabian Journal of Chemistry*. 2017 Jan;10(1):10-8. Available from: [<URL>](#).
16. Abdulkareem E, Abdulsattar J, Abdulsattar B. Iron (II) Determination in Lipstick Samples using Spectrophotometric and Microfluidic Paper-based Analytical Device (μ PADs) Platform via Complexation Reaction with Iron Chelator 1, 10-phenanthroline: A Comparative Study. *BSJ*. 2022 Apr 1;19(2):355-67. Available from: [<URL>](#).
17. Zakaria A, Ho YB. Heavy metals contamination in lipsticks and their associated health risks to lipstick consumers. *Regulatory Toxicology and Pharmacology*. 2015 Oct;73(1):191-5. Available from: [<URL>](#).
18. Zainy FMA. Heavy Metals in Lipstick Products Marketed in Saudi Arabia. *JCDSA*. 2017;07(04):336-48. Available from: [<URL>](#).
19. Sharafi K, Fatahi N, Yarmohammadi H, Moradi M, Dargahi A. Determination of cadmium and Lead concentrations in cosmetics (lipstick and hair color) in Kermanshah markets. *Journal of Health*. 2017;8(2):143-50. Available from:
20. Copat C, Grasso A, Fiore M, Cristaldi A, Zuccarello P, Signorelli SS, et al. Trace elements in seafood from the Mediterranean sea: An exposure risk assessment. *Food and Chemical Toxicology*. 2018 May;115:13-9. Available from: [<URL>](#).
21. Saadatzaheh A, Afzalan S, Zadehdabagh R, Tishezan L, Najafi N, Seyedtabib M, et al. Determination of heavy metals (lead, cadmium, arsenic, and mercury) in authorized and unauthorized cosmetics. *Cutaneous and Ocular Toxicology*. 2019 Jul 3;38(3):207-11. Available from: [<URL>](#).
22. Arshad H, Mehmood MZ, Shah MH, Abbasi AM. Evaluation of heavy metals in cosmetic products and their health risk assessment. *Saudi Pharmaceutical Journal*. 2020 Jul;28(7):779-90. Available from: [<URL>](#).
23. Świerczek L, Cieřlik B, Matysiak A, Konieczka P. Determination of heavy metals in eyeshadows from China. *Monatsh Chem*. 2019 Sep 1;150(9):1675-80. Available from: [<URL>](#).
24. Ghaderpoori M, Kamarehie B, Jafari A, Alinejad AA, Hashempour Y, Saghi MH, et al. Health risk assessment of heavy metals in cosmetic products sold in Iran: the Monte Carlo simulation. *Environ Sci Pollut Res*. 2020 Mar;27(7):7588-95. Available from: [<URL>](#).
25. Abdulkareem EA, Abdulsattar JO. Determination of Nickel and Cobalt in Cosmetic Products Marketed in Iraq Using Spectrophotometric and Microfluidic Paper-based Analytical Device (μ PADs) Platform. *Baghdad Scij*. 2022 Dec 1;19(6):1286-96. Available from: [<URL>](#).
26. Pawlaczyk A, Gajek M, Balcerek M, Szykowska-Jóźwiak MI. Determination of Metallic Impurities by ICP-MS Technique in Eyeshadows Purchased in Poland. Part I. *Molecules*. 2021 Nov 8;26(21):6753. Available from: [<URL>](#).

27. Mrmošanin J, Pavlović A, Mitić S, Tošić S, Pecev-Marinković E, Krstić J, et al. The Evaluation of ICP OES for the Determination of Potentially Toxic Elements in Lipsticks: Health Risk Assessment. ACSi. 2019 Dec 18;802-13. Available from: [<URL>](#).
28. Rehan I, Gondal MA, Rehan K, Sultana S, Khan S, Rehman MU, et al. Nondestructive Determination of Chromium, Nickel, and Zinc in Neem Leaves and Facial Care Products by Laser Induced Breakdown Spectroscopy (LIBS). Analytical Letters. 2022 Apr 13;55(6):990-1003. Available from: [<URL>](#).
29. Rawat K, Sharma N, Singh VK. X-Ray Fluorescence and Comparison with Other Analytical Methods (AAS, ICP-AES, LA-ICP-MS, IC, LIBS, SEM-EDS, and XRD). In: Singh VK, Kawai J, Tripathi DK, editors. X-Ray Fluorescence in Biological Sciences [Internet]. 1st ed. Wiley; 2022 [cited 2023 Feb 11]. p. 1-20. Available from: [<URL>](#)
30. Kilic S, Kilic M, Soylak M. The Determination of Toxic Metals in some Traditional Cosmetic Products and Health Risk Assessment. Biol Trace Elem Res. 2021 Jun;199(6):2272-7. Available from: [<URL>](#).
31. Zhong WS, Ren T, Zhao LJ. Determination of Pb (Lead), Cd (Cadmium), Cr (Chromium), Cu (Copper), and Ni (Nickel) in Chinese tea with high-resolution continuum source graphite furnace atomic absorption spectrometry. Journal of Food and Drug Analysis. 2016 Jan;24(1):46-55. Available from: [<URL>](#).
32. Fernández-Martínez R, Rucandio I, Gómez-Pinilla I, Borlaf F, García F, Larrea MT. Evaluation of different digestion systems for determination of trace mercury in seaweeds by cold vapour atomic fluorescence spectrometry. Journal of Food Composition and Analysis. 2015 Mar;38:7-12. Available from: [<URL>](#).
33. Khalaf HS, Al-Haidari AMA, Dikran SB, Mohammed AK. Spectrophotometric determination of sulfamethoxazole following simple diazotization and coupling with diphenylamine. Ibn AL-Haitham Journal For Pure and Applied Science. 2017;27(3):365-80.
34. Kántor T, Bartha A, Ballók MI. Studies on chemical removal of excess nitric acid using formic acid in solutions analyzed by inductively coupled plasma optical emission spectrometry. Chemia analityczna. 2009;54(6):1265-83.
35. El Haddad J, Canioni L, Bousquet B. Good practices in LIBS analysis: Review and advices. Spectrochimica Acta Part B: Atomic Spectroscopy. 2014 Nov;101:171-82. Available from: [<URL>](#).
36. Ozer T, McMahon C, Henry CS. Advances in Paper-Based Analytical Devices. Annual Rev Anal Chem. 2020 Jun 12;13(1):85-109. Available from: [<URL>](#).
37. Lisowski P, Zarzycki PK. Microfluidic Paper-Based Analytical Devices (μ PADs) and Micro Total Analysis Systems (μ TAS): Development, Applications and Future Trends. Chromatographia. 2013 Oct;76(19-20):1201-14. Available from: [<URL>](#).
38. Alsaffar N, Hussein H. Determination of heavy metals in some cosmetics available in locally markets. IOSR Journal of Environmental Science, Toxicology and Food Technology. 2014;8(8):9-12.
39. Nkansah MA, Owusu-Afriyie E, Opoku F. Determination of lead and cadmium contents in lipstick and their potential health risks to consumers. J Consum Prot Food Saf. 2018 Dec;13(4):367-73. Available from: [<URL>](#).
40. Naalbandi H, Saeedi M, Moharrami Moghanlou O, Akbari J, Morteza-Semnani K, Alizadeh R, et al. Evaluation of heavy metal content of some lipsticks in Iran market. Pharmaceutical and Biomedical Research. 2016;2(3):31-7.
41. Saleh FAF, Saif RNA, Murshed DMA, Abdulmageed BAM. Determination of Cadmium in Some Cosmetic Products [Internet]. CHEMISTRY; 2020 Sep [cited 2023 Feb 11]. Available from: [<URL>](#)
42. Iwegbue CMA, Bassey FI, Obi G, Tesi GO, Martincigh BS. Concentrations and exposure risks of some metals in facial cosmetics in Nigeria. Toxicology Reports. 2016;3:464-72.
43. Whitehouse L. Germany Reduces Heavy Metal Limits in Cosmetics. 2017 [Internet]. 2017 [cited 2023 Nov 2]. Available from: [<URL>](#)
44. Alam MF, Akhter M, Mazumder B, Ferdous A, Hossain MD, Dafader NC, et al. Assessment of some heavy metals in selected cosmetics commonly used in Bangladesh and human health risk. J Anal Sci Technol. 2019 Dec;10(1):2. Available from: [<URL>](#).
45. Schroeder HA. The poisons around us: toxic metals in food, air, and water. Bloomington: Indiana University Press; 1974. 144 p. ISBN: 978-0-253-16675-3.
46. Franken A, Eloff FC, Du Plessis J, Du Plessis JL. *In Vitro* Permeation of Metals through Human Skin: A Review and Recommendations. Chem Res Toxicol. 2015 Dec 21;28(12):2237-49. Available from: [<URL>](#).
47. Ouremi OI, Ayodele OE. Lipsticks and nail polishes: potential sources of heavy metal in human body. Int J Pharm Res Allied Sci. 2014;3(4):45-51.
48. Brzóška MM, Galażyn-Sidorczuk M, Borowska S. Metals in Cosmetics. In: Chen JK, Thyssen JP, editors. Metal Allergy [Internet]. Cham: Springer International Publishing; 2018 [cited 2023 Feb 11]. p. 177-96. Available from: [<URL>](#)
49. Corazza M, Baldo F, Pagnoni A, Miscioscia R, Virgili A, others. Measurement of nickel, cobalt and chromium in toy make-up by atomic absorption spectroscopy. Acta Derm Venereol. 2009;89(2):130-3.
50. Khalid A, Bukhari IH, Riaz M, Rehman G, Ain Q, Bokhari TH, et al. Determination of lead, cadmium, chromium, and nickel in different brands of lipsticks. International Journal of Biology, Pharmacy and Allied Sciences. 2013;1(2):263-71.
51. Engwa GA, Ferdinand PU, Nwalo FN, Unachukwu MN, others. Mechanism and health effects of heavy metal toxicity in humans. Poisoning in the modern world-new tricks for an old dog. 2019;10:70-90.
52. Cha NR, Lee JK, Lee YR, Jeong HJ, Kim HK, Lee SY. Determination of Iron, Copper, Zinc, Lead, Nickel and Cadmium in Cosmetic Matrices by Flame Atomic Absorption Spectroscopy. Analytical Letters. 2010 Jan 12;43(2):259-68. Available from: [<URL>](#).
53. Wang B, Su Y, Tian L, Peng S, Ji R. Heavy metals in face paints: Assessment of the health risks to Chinese opera actors. Science of The Total Environment. 2020 Jul;724:138163. Available from: [<URL>](#).

54. Wirth JJ, Mijal RS. Adverse Effects of Low Level Heavy Metal Exposure on Male Reproductive Function. *Systems Biology in Reproductive Medicine*. 2010 Jan 1;56(2):147-67. Available from: [<URL>](#).
55. Lim DS, Roh TH, Kim MK, Kwon YC, Choi SM, Kwack SJ, et al. Non-cancer, cancer, and dermal sensitization risk assessment of heavy metals in cosmetics. *Journal of Toxicology and Environmental Health, Part A*. 2018 Jun 3;81(11):432-52. Available from: [<URL>](#).
56. Soares AR, Nascentes CC. Development of a simple method for the determination of lead in lipstick using alkaline solubilization and graphite furnace atomic absorption spectrometry. *Talanta*. 2013 Feb;105:272-7. Available from: [<URL>](#).
57. Łodyga-Chruścińska E, Sykuła A, Więdocha M. Hidden Metals in Several Brands of Lipstick and Face Powder Present on Polish Market. *Cosmetics*. 2018 Oct 1;5(4):57. Available from: [<URL>](#).
58. Bartzatt R. Neurological impact of zinc excess and deficiency in vivo. *European Journal of Nutrition & Food Safety* (ISSN: 2347-5641). 2017;7(3):155-60.
59. Radfard M, Yunesian M, Nabizadeh R, Biglari H, Nazmara S, Hadi M, et al. Drinking water quality and arsenic health risk assessment in Sistan and Baluchestan, Southeastern Province, Iran. *Human and Ecological Risk Assessment: An International Journal*. 2019 May 19;25(4):949-65. Available from: [<URL>](#).
60. Bilal M, Mehmood S, Iqbal HMN. The Beast of Beauty: Environmental and Health Concerns of Toxic Components in Cosmetics. *Cosmetics*. 2020 Feb 28;7(1):13. Available from: [<URL>](#).
61. Yu S, Liao WT, Lee CH, Chai CY, Yu CL, Yu HS. Immunological dysfunction in chronic arsenic exposure: From subclinical condition to skin cancer. *J Dermatol*. 2018 Nov;45(11):1271-7. Available from: [<URL>](#).
62. Papadopoulos A, Assimomytis N, Varvaresou A. Sample Preparation of Cosmetic Products for the Determination of Heavy Metals. *Cosmetics*. 2022 Feb 4;9(1):21. Available from: [<URL>](#).
63. Abd El-Aziz R, Abbassy MM, Hosny G. A comparative study on health risk Assessments of some heavy metals in cosmetics commonly used in Alexandria, Egypt. *Int J Environ Sci Toxic Res*. 2017;5(3):53-62.
64. Parekh J, Chanda S. Antibacterial and phytochemical studies on twelve species of Indian medicinal plants. *African Journal of Biomedical Research*. 2007;10(2):175-81.
65. Mohammadi M, Riyahi Bakhtiari A, Khodabandeh S and. Determination of Cadmium and Lead Concentration in Cosmetics (Sunscreens, Lipstick and Hair Color). *Iranian Journal of Health and Environment*. 2014;6(4):481-90. Available from: [<URL>](#).
66. Ghaderpoori M, Kamarehie B, Jafari A, Alinejad AA, Hashempour Y, Saghi MH, et al. Health risk assessment of heavy metals in cosmetic products sold in Iran: the Monte Carlo simulation. *Environ Sci Pollut Res*. 2020 Mar;27(7):7588-95. Available from: [<URL>](#).
67. Malvandi H, Sancholi F. Assessments of some metals contamination in lipsticks and their associated health risks to lipstick consumers in Iran. *Environ Monit Assess*. 2018 Nov;190(11):680. Available from: [<URL>](#).
68. Pinto E, Paiva K, Carvalhido A, Almeida A. Elemental impurities in lipsticks: Results from a survey of the Portuguese and Brazilian markets. *Regulatory Toxicology and Pharmacology*. 2018 Jun;95:307-13. Available from: [<URL>](#).
69. Chauhan SB, Chandak A, Agrawal S. Evaluation of heavy metals contamination in marketed lipsticks. *International Journal of Advanced Research*. 2014;2(4):257-62.
70. Nourmoradi H, Foroghi M, Farhadkhani M, Vahid Dastjerdi M. Assessment of Lead and Cadmium Levels in Frequently Used Cosmetic Products in Iran. *Journal of Environmental and Public Health*. 2013;2013:1-5. Available from: [<URL>](#).
71. Benabbes M, Chentoufi MA, Mojemmi B, Benzeid H, Toure HA, Shallangwa GA, et al. Determination of Lead and Cadmium in Synthetic and Natural Hair Dyes in Morocco Using Differential Pulse Polarography: Port Electrochim Acta. 2021;39(1):37-44. Available from: [<URL>](#).
72. Ghaderpoori M, Kamarehie B, Jafari A, Alinejad AA, Hashempour Y, Saghi MH, et al. Health risk assessment of heavy metals in cosmetic products sold in Iran: the Monte Carlo simulation. *Environ Sci Pollut Res*. 2020 Mar;27(7):7588-95. Available from: [<URL>](#).
73. Munir A, Hayyat MU, Shahzad L, Sharif F, Farhan M, Ghafoor GZ. Assessment of heavy metals concentrations in commercially available lipsticks in Pakistan. *Environmental Forensics*. 2020 Oct 1;21(3-4):259-66. Available from: [<URL>](#).
74. Nasirudeen M, Amaechi A. Spectrophotometric determination of heavy metals in cosmetics sourced from Kaduna Metropolis, Nigeria. *Science world journal*. 2015;10(3):1-5. Available from: [<URL>](#).
75. Kilic S, Kilic M, Soylak M. The Determination of Toxic Metals in some Traditional Cosmetic Products and Health Risk Assessment. *Biol Trace Elem Res*. 2021 Jun;199(6):2272-7. Available from: [<URL>](#).
76. Lee BM, Kwon S, Cho YM, Kim KB, Seo K, Min CS, et al. Perspectives on trace chemical safety and chemophobia: risk communication and risk management. *Journal of Toxicology and Environmental Health, Part A*. 2019 Feb 1;82(3):186-99. Available from: [<URL>](#).
77. Stewart SE, Parker MD, Amézquita A, Pitt TL. Microbiological risk assessment for personal care products. *Int J Cosmet Sci*. 2016 Dec;38(6):634-45. Available from: [<URL>](#).
78. Siya K, Thomas J, Vinod Kumar R, Saji A, Iype A, Akhil S. Lipsticks: The microbial cellar: An original study. *J Microsc Ultrastruct*. 2019;7(4):194. Available from: [<URL>](#).
79. Vassoler M, Tonial F, Fagundes SC, Fagundes MA, Zortéa NB, Rossato-Grando L, et al. Microbiological Contamination of In-Store Lipstick Testers Available to the Consumer. *Mundo Saúde*. 2020 Jul 27;44:e0442020. Available from: [<URL>](#).



Spectrophotometric and Smartphone-based Dual Monitoring Method for the Determination of Al(III) Ions Using Fermented Black Carrot Juice (Şalgam/Shalgam) as a Green Chromogenic Agent

Batuhan Yardımcı^{1*} 

¹Zonguldak Bülent Ecevit University, Science and Technology Application and Research Center (ARTMER), Zonguldak, 67600, Turkey

Abstract: In this study, anthocyanin-rich fermented black carrot juice (şalgam/shalgam) was used as a chromogenic agent in order to develop eco-friendly, low-cost, simple, fast, and practical both visible spectrophotometric and smartphone-based methods for the determination of Al(III) ions in water samples. Formation of Al(III)-anthocyanin complex results in a color change from red to purple in direct proportion to the increasing Al(III) concentration. For the spectrophotometric analysis, the analytical response of the developed method between absorbance and logarithm of Al(III) concentration exhibits a satisfying wide linear concentration range from 37.0 to 1850.0 μM . The LOD and LOQ values are 6.67 μM and 22.0 μM , respectively. For smartphone-based analysis, the analytical response of the developed method between B values and Al(III) concentration obtained a linear concentration range from 18.5 to 111.0 μM . The LOD and LOQ values are 4.40 μM and 14.5 μM , respectively. LOD values are below the acceptable limit of Al(III) in water according to WHO (7.41 μM) for both methods. The interfering effect of common water ions was investigated, and the observed interferences from Sn^{2+} , Fe^{2+} , and Fe^{3+} were easily eliminated using enough concentration of Na_2EDTA without affecting the blank absorbance/B value of the Al(III)-anthocyanin complex for two monitoring methods. The selectivity of the developed method was investigated in the presence of possible species such as benzoic acid, lactic acid, amino acids, and salt. Developed spectrophotometric and smartphone-based methods applied to real water samples and validated against the reference ICP-OES method at 95% confidence level using Student's *t*- and *F*-tests.

Keywords: Chromogenic agent, aluminum(III) ions, fermented black carrot juice (Shalgam), anthocyanin, spectrophotometry, smartphone

Submitted: November 08, 2022. **Accepted:** January 11, 2023.

Cite this: Yardımcı B. Spectrophotometric and smartphone-based dual monitoring method for the determination of Al(III) ions using fermented black carrot juice (şalgam/shalgam) as a green chromogenic agent. JOTCSA. 2023;10(1):161-76.

DOI: <https://doi.org/10.18596/jotcsa.1201498>.

Corresponding author. E-mail: batuhan.yardimci@beun.edu.tr.

1. INTRODUCTION

Aluminum is not found free in nature. It ranks third among the most abundant metals in the earth's crust and constitutes approximately 8% of the crust's mass (1) and it is mainly found as silicate minerals (2). Due to the widespread presence of aluminum in the environment and industrial developments, its relationship with human health is becoming increasingly important. The amount of free Al(III) increases as the aluminum in the soil leaks into the environment and surface waters due

to acid rain (1). While aluminum is in ionic form; it can react with biological species. When it reacts, it causes harmful effects by suppressing or changing the function of the biological species (3). Aluminum ion is thought to be the reason for neurological disorders and it causes changes in enzymatic reactions by affecting neurofibrillary and neurotransmitters in the central nervous system. As a result; diseases such as Parkinson's disease, Alzheimer's disease, and dialysis encephalopathy occur (4). Aluminum is also thought to have the ability to replace iron and other metals in proteins

found in living things (5). Determination of Al(III) concentration is a critical issue for researchers due to its direct impact on the environment and human health. Different kinds of conventional analytical methods such as AAS (6), ICP-MS (7), ion-selective electrode-based potentiometry (ISE) (8) voltammetry (9), and fluorimetry (10) have been developed to determine the concentration of Al(III). Most of these methods are limited due to the requirements of time-consuming processes, expensive and complicated equipment, and a skilled person. Although fluorescent probes for the determination of Al(III) stand out among these methods due to their selectivity and sensitivity, the disadvantages of this method are that they have time-consuming complicated probe design and synthesis processes, are toxic, have low solubility in water, have low photostability and excess reagent consumption (11, 12).

Spectrophotometry is one of the versatile and good alternative analytical techniques to determine the concentration of many analytes, especially in water samples, and has many advantages such as low cost, easy applicability, fast analysis, reliability, high sensitivity at low concentrations, and wide analytical working range (13).

Recently, smartphone-based colorimetric and fluorometric methods have gained importance over traditional bulky devices due to their many properties such as quick analysis, low-cost and simple production, portability, and ease to use. The smartphone-based methods exhibit a highly comparable performance of analysis according to the traditional methods (14,15). Analysis of different kinds of samples by smartphone is based on the measurement of red (R), green (G), and blue (B) values with help of various software (15-17).

Anthocyanins are water-soluble flavonoid pigments that provide bright colors from light pink to dark blue when found in fruits and vegetables (18). In recent years, anthocyanins have gained great importance among researchers due to their antioxidant capacity, bioavailability properties, food coloring, and food stabilizer properties (19). In fact, according to studies no adverse events have been encountered in the intake of anthocyanins in high doses (20). Anthocyanins also have metal-chelating abilities such as dihydroxy B-ring substituted flavonoids (21). Fermented black carrot (şalgam/shalgam) juice, a dark red-colored and sour soft traditional Turkish beverage, is one of the sources of natural anthocyanin pigments originating from black carrot. It is very popular in the southern part of Türkiye. In addition, recently, fermented black carrot juice has taken its place in the markets of numerous European countries (22). Fermented black carrot juice is defined as a beverage formed as a result of lactic acid fermentation of black carrot, turnip, salt, extract of sourdough, and bulgur flour components (23). Turnip and bulgur are minor components of şalgam and turnip helps to develop the sensory character (24), while bulgur flour is used

as a source of microorganisms in the first fermentation stage. In addition, the reason for using salt is to control the fermentation flora (25). Fermented black carrot juice gets its red color from the main ingredient, black carrots. According to studies, cyanidin glycosides as an aglycone have been found in black carrots as the main anthocyanin compound (26,27), malvidin, and peonidin glycosides in black carrot roots (27,28). Furthermore, fermented black carrot juice has been reported to contain an average of 114.1 mg L⁻¹ anthocyanin as cyanidin-3-glycoside (25). It is stated that commercially fermented black carrot contains the anthocyanins cyanidin-3-galactoside, cyanidin-3-glucoside, and cyanidin-3-arabinoside using LC/MS/MS and also its total phenolic content (517.21 µg GAE/mL) and antioxidant capacity (in µmol Trolox equivalents/mL) were investigated with FRAP (2.26), DPPH (4.44) and ABTS (3.42) assays (29). Different types of metal determinations were studied from various anthocyanin-derived plants by utilizing the metal complexing properties of anthocyanins (30,31). In such studies, anthocyanins were extracted from natural plants, but the negative properties of isolated anthocyanins are time-consuming processes for the extraction stage, low extraction efficiency, instability, and degradation properties in the presence of light, heat, and oxygen (19,32). An important feature of anthocyanins from purple carrots is dominant that the cultivars are in the acyl form. Acylated anthocyanins are more stable compounds than other types of anthocyanins and degrade more slowly during storage (29). Fermented black carrot may also enhance the stability, absorption, and bioactivity of its anthocyanins (32), as well as metal complexes of anthocyanins, which are known to stabilize the structure more (19), and it can be concluded that by forming a complex with the metal, its repeatability will be better in the determination of the relevant metal.

In the light of this information, low-cost, non-toxic, anthocyanin-rich, sugar-free, and gluten-free, commercially fermented black carrot juice with good stability was preferred as a chromogenic agent. This chromogenic agent meets the at least three principles of green analytical chemistry (33) such as removing or replacing toxic reagents, using reagents obtained from a renewable source, and reducing the risk to the operator. In this way, the concentration of Al(III) in water samples can be determined quickly and simply via color changing from red to purple in direct proportion to the amount of Al(III) ions because of the formation of the Al(III)-anthocyanin complex, without any pre-treatment such as time-consuming extraction.

2. MATERIAL AND METHODS

2.1. Chemicals and Instrumentation

All reagents used in this study were of analytical grade except Lactic acid (80%). The fermented black carrot juice was bought from the local market. Aluminum nitrate nonahydrate (Al(NO₃)₃·9H₂O),

lead(II) nitrate ($\text{Pb}(\text{NO}_3)_2$), chromium(III) nitrate nonahydrate ($\text{Cr}(\text{NO}_3)_3 \cdot 9\text{H}_2\text{O}$), cadmium acetate dihydrate ($\text{Cd}(\text{CH}_3\text{COO})_2 \cdot 2\text{H}_2\text{O}$), ethylenediaminetetraacetic acid disodium salt (Na_2EDTA), sodium benzoate ($\text{C}_6\text{H}_5\text{COONa}$), sodium acetate (CH_3COONa), L-glycine ($\text{NH}_2\text{CH}_2\text{COOH}$), L-lysine hydrochloride ($\text{H}_2\text{N}(\text{CH}_2)_4\text{CH}(\text{NH}_2)\text{CO}_2\text{H} \cdot \text{HCl}$), and sodium bicarbonate (NaHCO_3) were purchased from Sigma Aldrich. Iron(III) nitrate nonahydrate ($\text{Fe}(\text{NO}_3)_3 \cdot 9\text{H}_2\text{O}$), iron(II) chloride tetrahydrate ($\text{FeCl}_2 \cdot 4\text{H}_2\text{O}$), manganese (II) nitrate tetrahydrate ($\text{Mn}(\text{NO}_3)_2 \cdot 4\text{H}_2\text{O}$), ammonium chloride (NH_4Cl), potassium nitrate (KNO_3), calcium nitrate tetrahydrate ($\text{Ca}(\text{NO}_3)_2 \cdot 4\text{H}_2\text{O}$), magnesium nitrate hexahydrate ($\text{Mg}(\text{NO}_3)_2 \cdot 6\text{H}_2\text{O}$), copper(II) sulfate pentahydrate ($\text{CuSO}_4 \cdot 5\text{H}_2\text{O}$), Tin(II) chloride dihydrate ($\text{SnCl}_2 \cdot 2\text{H}_2\text{O}$), zinc sulphate heptahydrate ($\text{ZnSO}_4 \cdot 7\text{H}_2\text{O}$), sodium nitrate (NaNO_3), sodium chloride (NaCl), sodium sulfate (Na_2SO_4), and sodium hydroxide (NaOH) were purchased from Merck. Lactic acid was obtained from Bioliv food industry and trade import export limited company. Potassium hydrogen phthalate ($\text{HOOC}_6\text{H}_4\text{COOK}$) was bought from CDH (Central drug house Ltd.). Sodium phosphate monobasic (NaH_2PO_4) was obtained from Riedel-de Haën. L-arginine ($\text{H}_2\text{NC}(=\text{NH})\text{NH}(\text{CH}_2)_3\text{CH}(\text{NH}_2)\text{CO}_2\text{H}$) was purchased from sepenatural. L-cysteine hydrochloride monohydrate ($\text{HSCH}_2\text{CH}(\text{NH}_2)\text{COOH} \cdot \text{HCl} \cdot \text{H}_2\text{O}$) was obtained from Akcan Kimya and L-glutamine ($\text{H}_2\text{NCOCH}_2\text{CH}_2\text{CH}(\text{NH}_2)\text{CO}_2\text{H}$) was bought from Hardline nutrition.

Precisa XB 220A Analytical Balance was used to weigh all the chemicals. Rayleigh VIS-723G visible (vis.) spectrophotometer and its glass cuvettes (optical thickness 5 mm) were used for all absorbance measurements. Only Shimadzu UV-1800 spectrophotometer was used for the characterization of anthocyanin. For RGB measurements, the Samsung Galaxy S10 Plus is used with its convenient black box that allows the phone to fit on it. Wisetherm-fuzzy control, wsd HB-48 dry bath was used to determine the optimum temperature for the proposed method. Both detection systems were validated against the ICP-OES (34) method using PerkinElmer Avio 200 ICP-OES.

2.2. Preparation of Solutions

Fermented black carrot juice bought from the market was stored at +4 °C and diluted with ultrapure water at a ratio of 1/2 (v/v) when necessary for the proposed method.

Working solutions of different initial concentrations of Al(III) were freshly prepared from the stock solutions of Al(III) at 3.7×10^{-2} M in ultrapure water. Potassium hydrogen phthalate (KHP)-NaOH buffer solutions were prepared from the appropriate amount of 0.1 M KHP and 0.1 M NaOH to adjust the pH 4.0, pH 5.0, and pH 6.0 values.

After preparing stock solutions of each common water ion (Cl^- , NO_3^- , HCO_3^- , SO_4^{2-} , PO_4^{3-} , CH_3COO^- , K^+ , NH_4^+ , Ca^{2+} , Mg^{2+} , Mn^{2+} , Cu^{2+} , Ni^{2+} , Zn^{2+} , Cd^{2+} , Pb^{2+} , Sn^{2+} , Fe^{2+} , Fe^{3+} , and Cr^{3+}) at the appropriate concentration, mixtures of each ion solution were prepared as certain fold of the Al(III) ions.

In order to observe the characteristic three absorption bands of anthocyanins, the solution was prepared by dissolving the precipitate in a mixture of MeOH and 2 M HCl (85:15 v/v) after the fermented black carrot juice was kept at 10.000 rpm for 10 min in an ultracentrifuge device.

For investigation of selectivity, stock solutions of 9.15 g L^{-1} of L-cysteine hydrochloride monohydrate, L-arginine, L-glycine, L-lysine hydrochloride, and L-glutamine were prepared. Additively, the stock solution of 40.25 g L^{-1} of lactic acid, 8.5%, w/v NaCl, and 0.1% (w/v) sodium benzoate were prepared.

2.3. Preparation of the Proposed Method for Al(III) Detection

For the spectrophotometric method, after adding 1.0 mL of fermented black carrot juice diluted 1/2 (v/v) with ultrapure water, 1.0 mL of pH 6.0 KHP-NaOH buffer solution (0.1 M), and 0.5 mL of Al(III) solution at different initial concentrations (185.0-9250.0 μM) to the test tubes and waiting for 4.5 minutes at room temperature (RT), absorbance readings were recorded against the blank at a wavelength of 575 nm (Scheme 1). For the blank solution, 0.5 mL of ultrapure water is added instead of Al(III) solution.

Summarized procedure: for sample solutions, add 1.0 mL of fermented black carrot juice diluted 1/2 (v/v) with ultrapure water + 1.0 mL of pH 6.0 KHP-NaOH buffer solution (0.1 M) + 0.5 mL of Al(III) solutions at different initial concentrations (185.0-9250.0 μM); wait 4.5 min. at RT.; record the absorbance at λ_{575} nm against the blank solution ($V_{\text{total}} = 2.5 \text{ mL}$).

For the smartphone-based method, the Samsung Galaxy S10 Plus was used with its smaller black colored box (16.5×8×3 cm) that comes out of the phone box when purchasing the phone and allows the phone to fit on. This box was evaluated by using it for RGB measurements (Figure 1A). A cardboard sample holder (8×3 cm) was designed to fit the square space of the black box (Figure 1B and Figure 1C). The blue (B) values were recorded via PhotoMetrix software obtained from the google play store without any payment for the android system. The region of interest was chosen 96×96 and flash mod was selected "on" to see and take the B values of samples in the box. Also, the 1.5 mL of glass vials were used instead of the cuvette (Figure 1C and Figure 1D).

1.0 mL of fermented black carrot juice diluted 1/2 (v/v) with ultrapure water, 1.0 mL of pH 6.0 KHP-NaOH buffer solution (0.1 M), and 0.5 mL of Al(III) solution at different initial concentrations (92.5-

555.0 μM) were added the test tubes and waiting for 4.5 minutes at RT, the B value measurements of blank and sample solution were recorded using the black box with the smartphone (Scheme 1).

2.4. Investigation of Interference Effect of Common Ions and Selectivity

Dual monitoring methods were applied in the presence of common water ions and the recovery values of Al(III) were calculated. Interference effects were removed easily using Na_2EDTA for Sn^{2+} , Fe^{2+} , and L-ascorbic acid for Fe^{3+} (35). In addition, it was investigated whether possible species other than anthocyanin in fermented black carrot juice affect the proposed method.

First of all, the maximum concentration of Na_2EDTA that will not dissociate the Al(III)-anthocyanin complex in the proposed method was investigated. The reason for optimizing the amount of Na_2EDTA is to prevent the discoloration of the Al(III)-anthocyanin complex due to the excess EDTA in the medium. To this end, mixed Al(III) solutions at an initial concentration of 1850.0 μM and Na_2EDTA at different concentrations (1850.0, 3700.0, 5550.0, and 7400.0 μM) were prepared separately. The

appropriate Na_2EDTA concentration was determined by applying the proposed method to these mentioned mixture solutions and the solution containing only 1850.0 μM initial concentration of Al(III). Then, different mass ratios of Na_2EDTA were investigated along with Fe^{2+} and Sn^{2+} ions in 1:1 metal:Al(III) solutions to remove the interference due to Fe^{2+} and Sn^{2+} ions by masking (without exceeding the optimum amount of Na_2EDTA).

2.5. Application of the Proposed Method to Real Water Samples.

The proposed method was successfully applied to drinking water and tap water samples using vis. spectrophotometer and smartphone. Later, the recovery (%) and RSD (%) values of Al(III) were calculated.

2.6. Method Validation of the Developed Methods Against the ICP-OES Method for Al(III) Detection.

Both the spectrophotometric and smartphone-based proposed methods have been validated with the ICP-OES method (34). The confidence level was calculated using *t*- and *F*- tests via the proposed method and ICP-OES method.

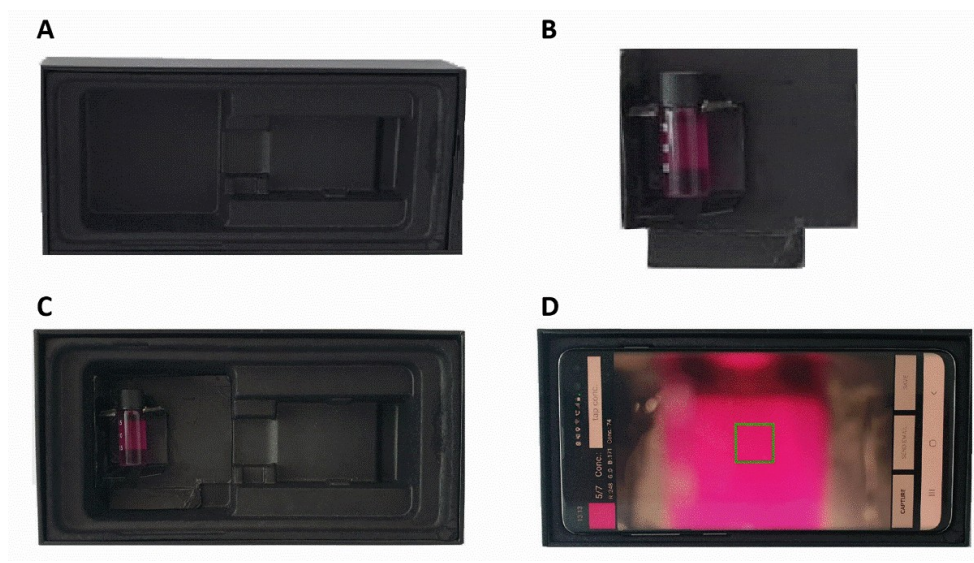
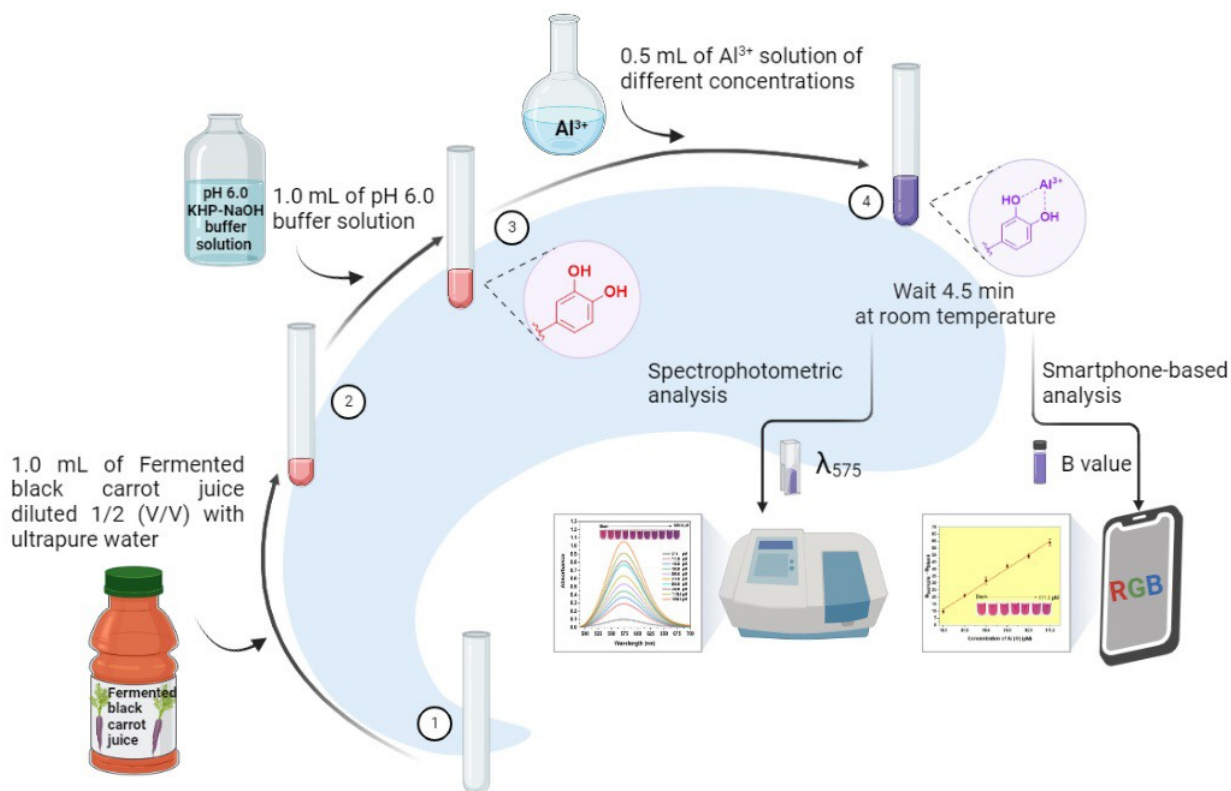


Figure 1: Representation of smartphone-based colorimetric detection of Al(III) ions (A) the original black box in which the phone was kept at the time of purchase and (B) sample holder made of cardboard; (C) sample holder placed in the black box; (D) reading the RGB values with the help of software by placing the phone in the black box designed for itself.



Scheme 1: Preparation of the proposed method for Al(III) detection using spectrophotometric and smartphone-based analysis.

2.7. Statistical Analysis

Excel software (Microsoft Office 2016) was used for performing the statistical analyses and calculating the means and the standard error of the mean. The mean \pm standard deviation (SD) was shown as a result. Validation of the proposed method for determining the Al(III) content against the ICP-OES method was made using the statistical tools of the same software.

3. RESULTS AND DISCUSSION

3.1. Optimization of the Parameters

The figures obtained for the optimization of each parameter were formed as a result of three repetitive analyses ($N = 3$). Aluminum forms an insoluble complex known as the $\text{Al}(\text{OH})_3$ with increasing pH values and shows low solubility between pH 6.0-8.0 (36). It is also reported that cyanidin complexes formed with Al(III) in the pH range of 3.0-6.0 (32). Therefore, pH optimization studies were carried out between the pH range of 4.0-6.0 in order to select the optimal pH value. This experiment was applied for two different initial concentrations of Al(III) one at 555.0 μM and the other at 1850.0 μM for each pH value. For this purpose, after adding 1.0 mL of fermented black carrot juice diluted 1/2 (v/v) with ultrapure water, 1.0 mL of KHP-NaOH (0.1M) buffer solution (pH 4.0 or pH 5.0 or pH 6.0), and 0.5 mL of 555.0 μM or 1850.0 μM initial concentrations of Al(III) to the test tubes, respectively ($V_{\text{total}} = 2.5 \text{ mL}$), solutions in the

test tubes were kept for 4.5 min at RT and the absorbances were recorded against the blank samples at 575 nm wavelength. As shown in Figure 2A, pH 6.0, where the absorbance differences are maximum for both 555.0 μM and 1850.0 μM initial concentration of Al(III), was chosen as the optimal pH value.

In order to select the optimal time, separate experiments were studied for two different initial concentrations of Al(III) one at 555.0 μM and the other at 1850.0 μM for each time interval. For this purpose, after adding 1.0 mL of fermented black carrot juice diluted 1/2 (v/v) with ultrapure water, 1.0 mL of pH 6.0 KHP-NaOH (0.1M) buffer solution, 0.5 mL of 555.0 μM or 1850.0 μM initial concentrations of Al(III) to the test tubes, respectively ($V_{\text{total}} = 2.5 \text{ mL}$), solutions in the test tubes were kept separately for different time intervals starting from 0.5 min to 10 min at RT and the absorbances were recorded against the blank samples at 575 nm wavelength. According to Figure 2B, the optimal time for complex formation to reach equilibrium was determined as 4.5 minutes.

In order to select the optimal temperature, two different Al(III) solutions one at 555.0 μM and the other at 1850.0 μM initial concentrations were studied separately. After adding 1.0 mL of fermented black carrot juice diluted 1/2 (v/v) with ultrapure water, 1.0 mL of pH 6.0 KHP-NaOH (0.1M) buffer solution, 0.5 mL of 555.0 μM or 1850.0 μM

initial concentrations of Al(III) to the test tubes, respectively ($V_{\text{total}} = 2.5 \text{ mL}$), solutions in the test tubes were kept separately 4.5 min at different temperatures (25.0-100.0 °C) and the absorbances were recorded against the blank samples at 575 nm wavelength. As it is understood from Figure 2C, since there is no significant change in absorbance values at different temperatures, 25.0 °C (RT) was selected as the optimal temperature for the proposed method.

For the smartphone-based method, the R and G values were constant, and also it was observed that the calibration equation could be obtained by increasing the B values in direct proportion to the increasing Al(III) concentration between 18.5 and 111.0 μM so that, B value was selected to form calibration plot (Figure 2D).

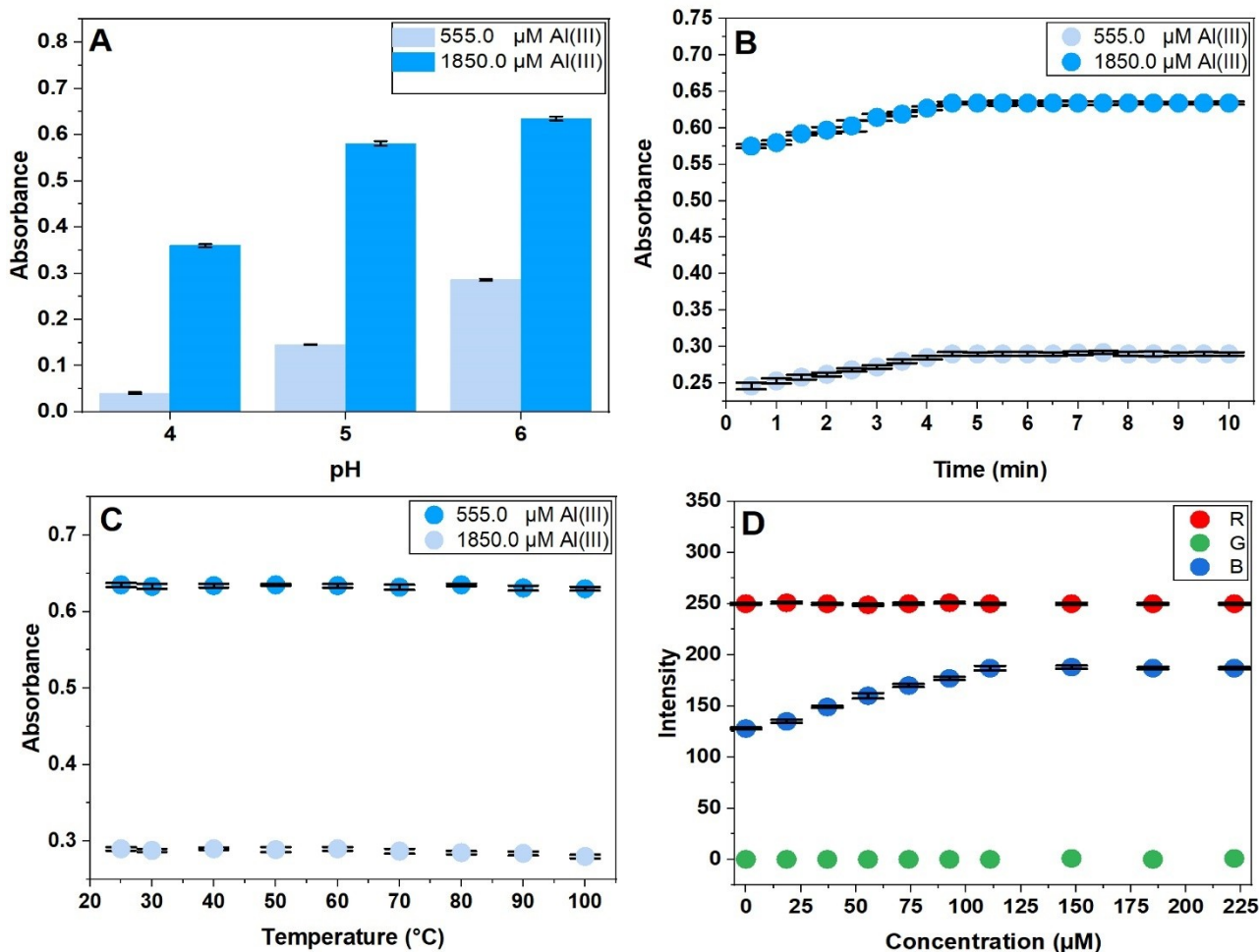


Figure 2: Optimization of the proposed method parameters: (A) optimal pH; (B) optimal time; (C) optimal temperature for spectrophotometric method and (D) selecting optimal RGB value for constructing calibration equation for smartphone-based method.

3.2. Characterization and Working Principle of the Proposed Method

Anthocyanins are known as colorful flavonoids including a flavylium cation (37) and they have a metal binding ability due to their two vicinal or three hydroxyl (-OH) substitutes located at the B ring (catechol or pyrogallol moiety). Polyvalent metal ions cause the loss of hydrogen ions bound to these rings and convert the flavylium cation to a quinoid base as shown in Figure 3A (38). Anthocyanins consist of a completely delocalized π -conjugated system, which gives a maximum absorption band in the wavelength range of 500-550 nm. Metal binding to anthocyanins causes a decrease in the energy

required for light-induced electron transfer in this chromophore system and also both maximum absorption shift towards the larger wavelength (bathochromic shift) and the increasing intensity of maximum absorbance (hyperchromic effect) are observed (21). According to some researchers, a bathochromic shift occurs due to the strong charge transfer from the ligand to the metallic center (LMCT), and according to others, it depends on the decrease in the HOMO-LUMO gap in the flavonoid molecule rather than a LMCT (39).

Furthermore, this phenomenon causes the color changing of the solution and enables the

determination of relevant metal via UV-vis. spectroscopy (21). When the proposed method was applied and absorbances values were recorded against the water, a 20 nm bathochromic shift was (from 536 to 556 nm) observed between blank solution and 1295.0 μM initial concentration of Al(III) due to the formation of Al(III)-anthocyanin complex (Figure 3B). The bathochromic shift proved the presence of the ortho-dihydroxyl group of anthocyanin. The fermented black carrot juice was centrifuged at 10.000 rpm for 10 minutes and the

supernatant phase was decanted, then the precipitant was dissolved in 2 mL of methanol, and its flavonoid properties were controlled by applying the Shinoda's test (40). After a few pieces of magnesium ribbon and 1 mL of concentrated HCl were added to the methanolic solution, pink color was observed a few minutes later. Additionally, the observation of maximum absorption at 280, 330, and 535 nm wavelengths in the MeOH/HCl solution, confirms the phenolic and flavonoid groups in the anthocyanin compound.

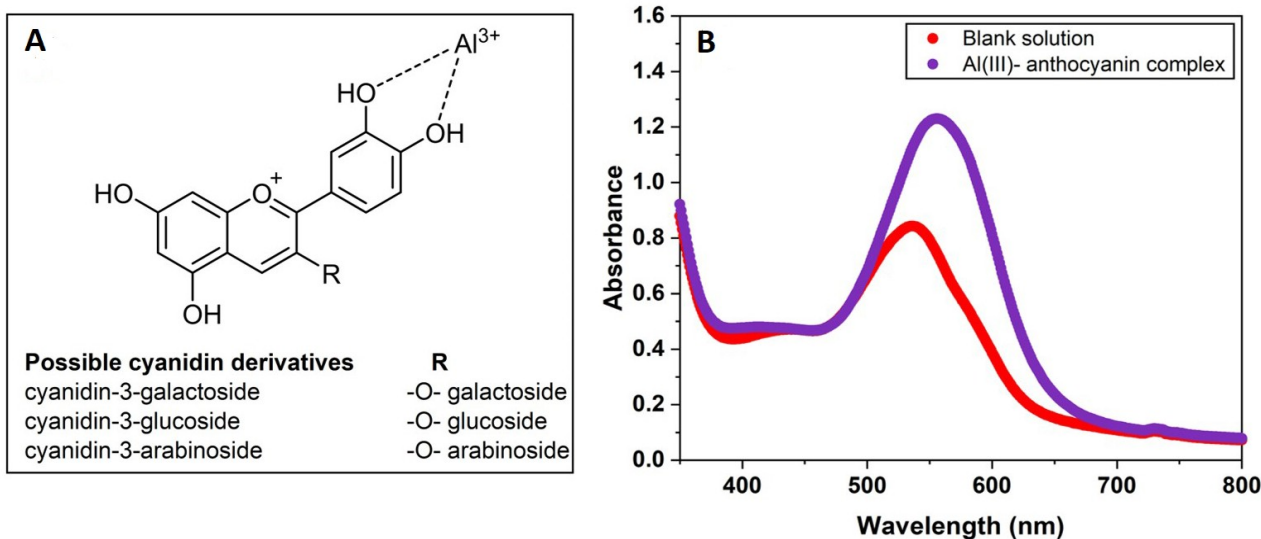


Figure 3: Working principle of the proposed method: (A) Al(III) complexation sites of possible cyanidin derivatives; (B) demonstration of the vis. spectra taken against the water as a result of applying the proposed method to Al(III) at an initial concentration of 1295.0 μM and blank solution.

3.3. Analytical Performance of the Proposed Method for the Determination of Al(III) Using Both Vis. Spectrophotometer and Smartphone

When the proposed method was applied to Al(III) solutions at different initial concentrations, a color change from red to purple was observed in direct proportion to the increasing logarithm of the concentration of Al(III) (Figure 4A and Figure 4B). There are many studies in which the absorbance values vary linearly with the logarithm of the analyte concentration (41, 42). All the absorbance measurements were recorded against the blank solution at 575 nm wavelength. The linear calibration equation was obtained with the absorbance versus the logarithm of the concentration of the Al(III) at the wavelength of 575 nm.

Linear calibration equation for Al(III):

$A_{575 \text{ nm}} = 0.585 \log C_{\text{Al(III)}} - 0.87$ ($N = 10$, $r = 0.9963$)
where $C_{\text{Al(III)}}$ is the final concentration of Al(III) (in micromole L^{-1} (μM)).

The linear final concentration range is from 37.0 to 1850.0 μM . Furthermore, the limit of detection (LOD) and the limit of quantification (LOQ) values are 6.67 μM and 22.0 μM , respectively. The limit of detection was calculated in micromole per liter units according to the literature (43, 44). ($\text{LOD} = 3\sigma_{\text{blank}}/\text{antilog } m$,

$\text{LOQ} = 10\sigma_{\text{blank}}/\text{antilog } m$ where σ_{blank} denotes the standard deviation of a blank and m shows the slope of the calibration line). The coefficients of variation (CVs) of intra- and inter-assay calculations for Al(III) were 0.96 and 1.07%, respectively ($N = 5$).

For the smartphone-based measurements, color changing from red to purple enabled to form calibration plot between B values and different concentrations of Al(III) in the concentration range of 18.5-111.0 μM by applying the proposed method (Figure 4C).

In smartphone-based colorimetric methods, there are studies in which calibration plots are created by subtracting the relevant values (R, G, or B values) of the sample and blank solution (45, 46). The calibration equation was obtained by subtracting the B values of the blank solution (B_{blank}) from the B values of the samples (B_{sample}).

Linear calibration equation for Al(III) using a smartphone:

$y = 0.529 C_{\text{Al(III)}} + 1.35$ ($N = 6$, $r = 0.9972$)
where $C_{\text{Al(III)}}$ is the final concentration of Al(III) (in micromole L^{-1}).

The limit of detection (LOD) and the limit of quantification (LOQ) values are 4.40 μM and 14.50

μM , respectively. The limit of detection was found in micromole per liter units. ($\text{LOD} = 3\sigma_{\text{blank}}/m$, $\text{LOQ} = 10\sigma_{\text{blank}}/m$ where σ_{blank} denotes the standard deviation of a blank and m shows the slope of the calibration line). The coefficients of variation (CVs) of intra- and inter-assay calculations for Al(III) were 1.69 and 2.11%, respectively ($N = 5$). Both spectrophotometric and smartphone-based developed method measurements have good precision according to the CVs results and also the

LOD values are below $7.41 \mu\text{M}$, which is the acceptable limit for Al(III) ions in water by the WHO (47).

When the analytical performance of the proposed sensor method and recent studies were compared (Table 1), the proposed sensor method stands out with its not preparation time, short analysis time, and quite good wide linear response range.

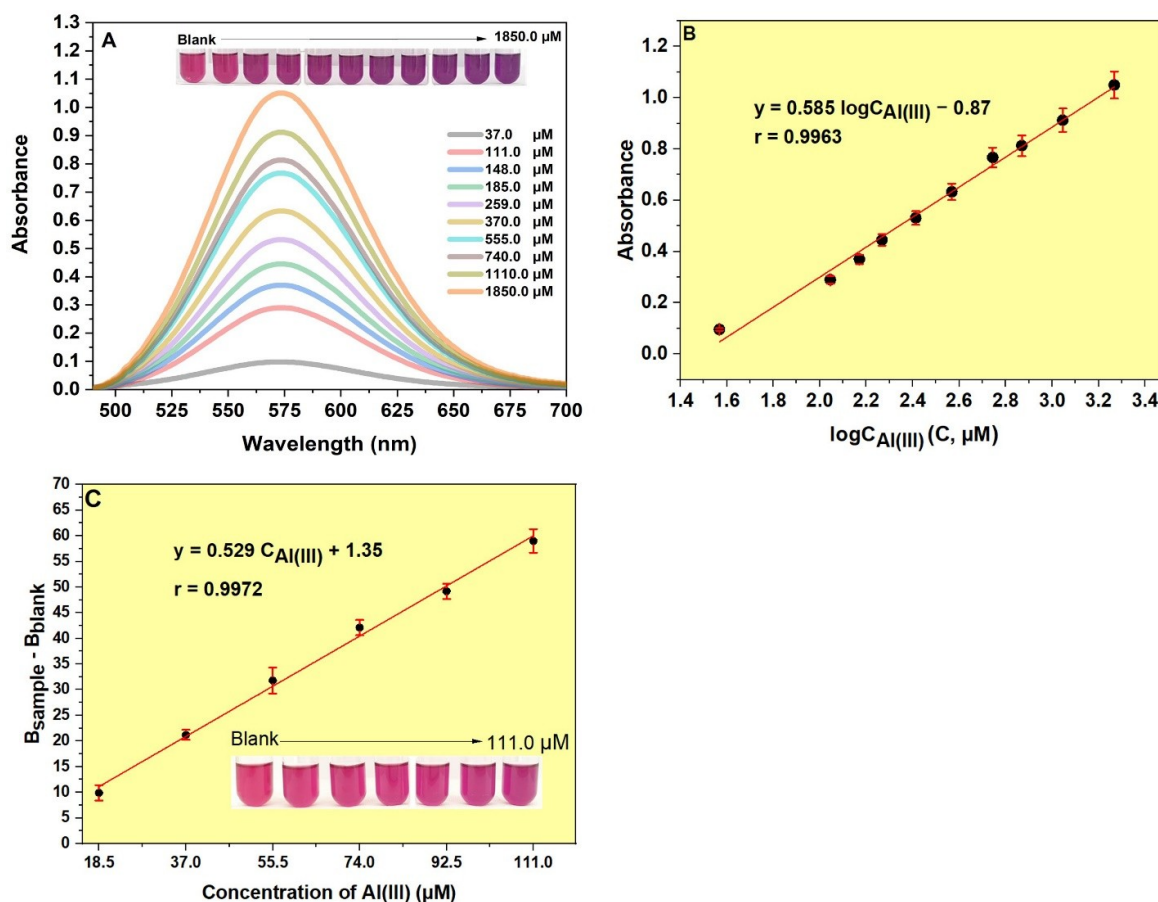


Figure 4: (A) The vis. spectrum of fermented black carrot juice containing different concentrations of Al(III) in an aqueous medium and their photograph (inset); (B) calibration plot of different concentrations of Al(III) solutions mixed with fermented black carrot juice for vis. spectrophotometer; (C) formed calibration plot via Blue (B) values using a smartphone and also the photograph of (inset) different concentrations of Al(III) solutions mixed with fermented black carrot juice.

Table 1: Comparison of the analytical performance of some optical and paper-based methods for the determination of Al(III) ions.

No	Detection method	Probe	Probe Preparation Time	Analysis Time	Linear response range	LOD	Real water application	Ref.
1	Paper-based fluorometric	Rhodamine grafted CDs	84 h (~3.5 days)	10 min	1×10^{-4} - 1×10^{-2} M	3.89×10^{-5} M	x	48
2	Fluorometric	PAA-AuNPs	135 min	10 min	50-150 μ M	2 μ M 8 μ M (with bare eye)	x	49
3	Fluorometric	CDs	140 min	10 min	0.15-38.46 μ M	113.8 nM	✓	50
	Smartphone based-method	CDs	140 min	15 min	15.39-153.85 μ M	5.55 μ M	✓	50
4	Colorimetric	Pectin-rich apple extract-based AuNPs	50 min	1 min	0-100 μ M	20 μ M	✓	51
5	Colorimetric	Cyanidin extracted from red cabbage as a chelating agent	73 h (~3 days)	a few min	n.a	50 μ M	✓	31
6	Colorimetric	Anthocyanin immobilization in CMC/starch films	~ 67 h (~2.8 days)	60 min ($C \leq 3$ mg L^{-1}), 20 min ($C \geq 5$ mg L^{-1})	n.a	1.9×10^{-4} M	x	52
7	Proposed Colorimetric method	Fermented black carrot juice	Direct (0 min.)	4.5 min	37.0-1850.0 μ M	6.67 μ M	✓	This work
	Proposed smartphone-based method	Fermented black carrot juice	Direct (0 min.)	4.5 min	18.5-111.0 μ M	4.40 μ M	✓	This work

n.a: not available, C: concentration, CDs: carbon nanodots, PAA-AuNPs: polyacrylate functionalized gold nanoparticles, CMC: carboxymethylcellulose, Conc.: concentration.

3.4. Investigation of Interference Effect of Common Ions and Selectivity

The interference effect of different common water ions on the proposed method was studied (Table 2), each containing a different mass ratio of Cl^- , NO_3^- , HCO_3^- , SO_4^{2-} , PO_4^{3-} , CH_3COO^- , K^+ , NH_4^+ , Ca^{2+} , Mg^{2+} , Mn^{2+} , Cu^{2+} , Ni^{2+} , Zn^{2+} , Cd^{2+} , Pb^{2+} , Sn^{2+} , Fe^{2+} , Fe^{3+} , and Cr^{3+} with the initial concentration of $1850.0 \mu\text{M}$ of Al(III) (e.g., 1-, 200- fold of Al(III)) for spectrophotometric method and $370.0 \mu\text{M}$ of Al(III) for the smartphone-based method. Additively, the Al(III) recovery (%) values were calculated in the range of 87.29-112.93 and 88.00-111.29% by the spectrophotometric and smartphone-based methods, respectively, as shown in Figure 5. First, the proposed method was applied to mixed solutions including the initial concentration of $1850.0 \mu\text{M}$ of Al(III) mixed with different concentrations of Na_2EDTA solutions to find the maximum concentration of Na_2EDTA that would not interact with Al(III) in the Al(III) -anthocyanin complex. A tolerable maximum initial concentration of Na_2EDTA was determined as $5550.0 \mu\text{M}$ in the mixed solution with the initial concentration of Al(III) at $1850.0 \mu\text{M}$ when the proposed method was applied, and no difference in absorption was observed when compared with the Al(III) -anthocyanin complex solution. Later the interference effects of Fe^{2+} and

Sn^{2+} were easily removed with Na_2EDTA ($\text{Fe}^{2+}:\text{EDTA}$ ratio 1:3 (w/w) and $\text{Sn}^{2+}:\text{EDTA}$ ratio 1:3 (w/w)) as a masking agent without affecting Al(III) -anthocyanin complex before applying the proposed method.

In order to remove the interference effect of Fe^{3+} on the proposed method L-ascorbic acid (35) was used with the 1-fold of Fe^{3+} ($\text{Fe}^{3+}:\text{L-ascorbic acid}$ ratio 1:1 (w/w)).

Fermented black carrot juice contains a maximum amount of 8.05 g L^{-1} lactic acid, 1.97% NaCl (w/v), 1.83 g L^{-1} total amino acids (53), and 0.02% sodium benzoate (54) (w/v) known as the preservative, apart from black carrot, which is the main ingredient. Additionally, it is also stated that it does not contain gluten and sugar. It was tested whether colored complexes were formed with Al(III) at $9250.0 \mu\text{M}$ initial concentration when the proposed method was applied to other species at the specified concentration in the content without using fermented black carrot juice for selectivity. L-cysteine hydrochloride monohydrate, L-arginine, L-glycine, L-lysine hydrochloride, and L-glutamine were used separately as amino acids. As can be seen in Figure 6, no coloration was observed when the proposed method was applied to other ingredients.

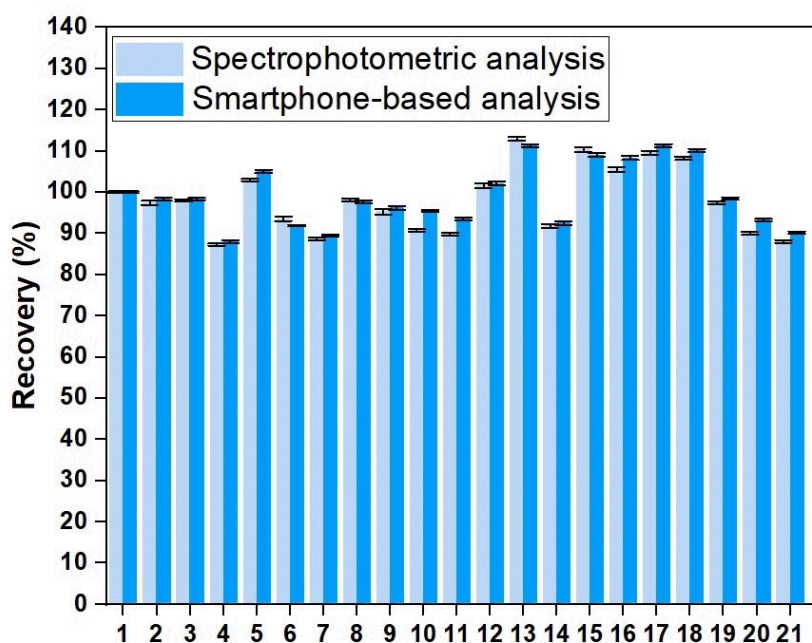


Figure 5: The response of Al(III) ions (1) and possible interference species $\{\text{Cl}^-$ (2), NO_3^- (3), HCO_3^- (4), CH_3COO^- (5), SO_4^{2-} (6), PO_4^{3-} (7), K^+ (8), NH_4^+ (9), Ca^{2+} (10), Mg^{2+} (11), Mn^{2+} (12), Cu^{2+} (13), Ni^{2+} (14), Zn^{2+} (15), Cd^{2+} (16), Pb^{2+} (17), $[\text{Sn}^{2+} + \text{EDTA}]$ (18) $[(\text{Fe}^{2+} + \text{EDTA})]$ (19), $[(\text{Fe}^{3+} + \text{L-ascorbic acid})]$ (20), and Cr^{3+} (21)} in the presence of Al(III) at the initial concentration of $1850.0 \mu\text{M}$ for spectrophotometric method and $370.0 \mu\text{M}$ for smartphone-based method.

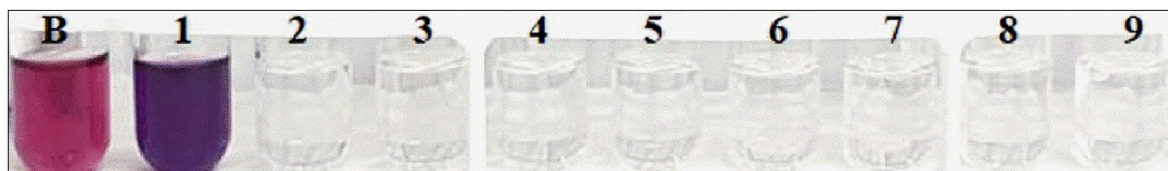


Figure 6: Color states of solutions in the test tubes with the proposed method in the presence of blank solution (B), (1) Al(III) (9250.0 μM), and mixture solutions without using fermented black carrot juice (2) lactic acid (8.05 g L^{-1}), (3) NaCl (1.97%, w/v), (4) sodium benzoate (0.02%, w/v), (5) L-cysteine hydrochloride monohydrate (1.83 g L^{-1}), (6) L-arginine (1.83 g L^{-1}), (7) L-glycine (1.83 g L^{-1}), (8) L-lysine hydrochloride (1.83 g L^{-1}) and (9) L-glutamine (1.83 g L^{-1}).

3.5. Application of the Proposed Method to Real Water Samples

Tap water and drinking water were filtered (CHROMAFIL, PET-20/25) before applying the sensor method. Drinking water and tap water were spiked separately with different concentrations of Al(III) solutions by standard addition method and then the proposed method was applied to real samples using both spectrophotometric and smartphone-based analyses. For the spectrophotometric analysis, Al(III) recoveries (%) and RSD % values for drinking water were found between 97.14-100.99 and 0.77-2.11%, respectively, while these values for tap water were found between 94.16-99.91 and 0.92-2.23% (Table 3). For the smartphone-based analysis, Al(III) recoveries (%) and RSD % values for drinking water were found between 97.43-100.27 and 0.80-2.35%, respectively, while these values for tap water were found between 97.43-94.23 and 1.24-2.65% (Table 3). According to these results, the proposed methods could be used for the determination of Al(III) in real water samples.

3.6. Method Validation of the Proposed Sensor Against the ICP-OES Method for Al(III) Detection

In order to obtain the calibration equation, the concentration range of 18.5-740.0 μM standard

Al(III) solutions were analyzed according to US EPA method 200.7 with ICP-OES (34).

Three repetitive analyses were performed for each standard concentration to generate the calibration equation. The calibration equation between intensity (CPS) and concentration was:

Intensity = 6480 $C_{\text{Al(III)}}$ + 56674 ($r = 0.9999$) for Al(III).

($C_{\text{Al(III)}}$: final concentration of Al(III) in micromole L^{-1} (μM)).

Statistical comparison between the results of the proposed and ICP-OES methods applied to both 370.0 μM and 74.0 μM of Al(III) spiked-drinking water as a real sample was made on $N = 5$ repetitive analyses, substantially showing no important difference in precision and accuracy between the results. The population means and variances were compared using t - and F - tests, respectively. The confidence levels used in the validation of findings were 95% (nominal 0.05 significance level) for both of t - and F - tests. Statistical parameters of the proposed methods and the reference ICP-OES method were shown in Table 4.

Table 2: Al(III) recovery (%) results when the proposed method is applied to ionic species commonly found in the water of different mass ratios with Al(III).

Interferent	Mass ratio (Al ³⁺ :ions (w/w))	Error (%)	
		For spectrophotometer	For smartphone
Cl ⁻	1200	-2.57	-1.70
NO ₃ ⁻	1200	-2.00	-1.60
HCO ₃ ⁻	5	-12.71	-12.00
CH ₃ COO ⁻	300	+2.97	+5.02
SO ₄ ²⁻	1200	-6.44	-8.10
PO ₄ ³⁻	7	-11.31	-10.55
K ⁺	1200	-1.95	-2.31
NH ₄ ⁺	600	-4.75	-3.82
Ca ²⁺	300	-9.29	-4.51
Mg ²⁺	200	-10.14	-6.49
Mn ²⁺	300	+1.53	+2.13
Cu ²⁺	10	+12.93	+11.29
Ni ²⁺	500	-8.20	-7.53
Zn ²⁺	60	+10.39	+9.01
Cd ²⁺	250	+5.52	+ 8.32
Pb ²⁺	50	+9.60	+ 11.27
Sn ²⁺	1	before EDTA masking: +42.90 after EDTA masking: +8.23	before EDTA masking: +31.30 after EDTA masking: + 10.15
Fe ²⁺	1	before EDTA masking: +14.32 after EDTA masking: -2.61	before EDTA masking: +26.40 after EDTA masking: -1.54
Fe ³⁺	1	before using L -ascorbic acid masking: +26.85 after L-ascorbic acid masking: +10.0	before using L-ascorbic acid masking: +38.2 after L-ascorbic acid masking: +6.72
Cr ³⁺	10	-11.89	-9.82

Table 3: Determination of Al(III) in drinking water and tap water samples by applying the proposed method.

Samples	Spectrophotometric Analysis				Smartphone-based Analysis			
	Spiked (µM)	Found (µM)	Recovery %	RSD % (N=3)	Spiked (µM)	Found (µM)	Recovery %	RSD % (N= 3)
Drinking water	37.0	36.9	99.73	1.25	18.5	18.2	98.38	1.54
	111.0	112.1	100.99	2.11	37.0	37.1	100.27	0.96
	185.0	184.7	99.84	0.98	55.5	54.6	98.38	0.80
	370.0	359.4	97.14	0.77	74.0	72.1	97.43	2.35
Tap water	37.0	36.5	98.65	2.23	18.5	18.0	97.30	1.63
	111.0	110.9	99.91	0.92	37.0	35.2	95.13	2.65
	185.0	183.7	99.30	1.12	55.5	52.3	94.23	1.24
	370.0	348.4	94.16	0.99	74.0	72.1	97.43	1.72

Table 4: Statistical comparison of the proposed method with ICP-OES reference method for the determination of Al(III).

Method	Mean Conc. (µM)	SD (σ)	S ^{a,b}	t ^{a,b}	T _{table} ^b	F ^b	F _{table} ^b
Proposed method (For spectroscopy)	372.96	0.108	-	-	-	-	-
ICP-OES reference method (For spectroscopy)	368.15	0.046	0.051	1.80	2.306	5.60	6.39
Proposed method (For smartphone)	75.92	0.051	-	-	-	-	-
ICP-OES reference method (For smartphone)	75.55	0.050	0.056	0.47	2.306	0.78	6.39

^a $S^2 = ((n_1 - 1)s_1^2 + (n_2 - 1)s_2^2) / (n_1 + n_2 - 2)$ and $t = (\bar{a}_1 - \bar{a}_2) / (S(1/n_1 + 1/n_2)^{1/2})$, where S is the pooled standard deviation, s_1 and s_2 are the standard deviations of the two populations with sample sizes of n_1 and n_2 , and sample means of \bar{a}_1 and \bar{a}_2 respectively (t has $(n_1 + n_2 - 2)$ degrees of freedom); here, $n_1 = n_2 = 5$.

^bStatistical comparison made on paired data produced with proposed and reference methods; the results given only on the row of the reference method.

4. CONCLUSION

In this study, in accordance with the principles of green analytical chemistry, anthocyanin-rich fermented black carrot juice was used as a green and chromogenic agent instead of polluting chemicals in order to determine the concentration of Al(III) ions in water samples. The application of this developed method to real water samples is eco-friendly, simple, fast, and practical. In addition, fermented black carrot juice is a healthy beverage rich in antioxidants and anthocyanins, and it is a chromogenic agent that can be used safely in the laboratory and is quite cheap (approx. 0.44 €). As can be seen from Table 1, the preparation of the chromogenic agent by other methods is very time-consuming and complex steps, and furthermore, the

proposed spectrophotometric method allows a very wide linear Al(III) concentration range (37.0 to 1850.0 µM) without any preliminary preparation. Thanks to the closed box system for analysis, the method developed based on a smartphone ensures usability in any field due to its portability and it can be easily applied to samples. Smartphones are more reachable and cheaper than other portable analytical devices. The high recoveries obtained by the application of both detection methods demonstrate their accuracy and applicability to real samples (tap water and drinking water) for the determination of Al(III). Additively, the recorded relative standard deviation values were very low (<5.0%) for spectrophotometric and smartphone-based methods. LOD values of spectrophotometric and smartphone-based methods are 6.67 µM and

4.40 μM , respectively, and both proposed methods obtain the required WHO permissible detection limit for Al(III) in drinking water. This method may open the way to novel low-cost Al(III) quantification methods without any extraction processes utilizing anthocyanin-rich fermented black carrot juice obtained from local markets.

5. CONFLICT OF INTEREST

The author declares no competing financial interest.

6. REFERENCES

- Goswami S, Paul S, Manna A. Selective “naked eye” detection of Al (III) and PPI in aqueous media on a rhodamine-isatin hybrid moiety. *RSC Adv.* 2013;3(27):10639-10643. [<DOI>](#).
- Imadi SR, Waseem S, Kazi AG, Azooz MM, Ahmad P. Aluminum toxicity in plants: an overview. *Plant Metal Interaction.* 2016;1-20. [<DOI>](#).
- Maity D, Govindaraju T. Naphthaldehyde-Urea/Thiourea conjugates as turn-on fluorescent probes for Al³⁺ based on restricted C=N isomerization. *European Journal of Inorganic Chemistry.* 2011;(36):5479-5485. [<DOI>](#).
- Al-Kindy SM, Al-Hinai A, Al-Rasbi NK, Suliman FEO, Al-Lawati HJ. Spectrofluorimetric determination of aluminium in water samples using N-((2-hydroxynaphthalen-1-yl) methylene) acetylhydrazide. *Journal of Taibah University for Science.* 2015;9(4):601-609. [<DOI>](#).
- Michael JK. Powder-Metallurgy Aluminum Alloys. *Aluminum Alloys-Contemporary Research and Applications: Contemporary Research and Applications.* 2012;1:323.
- Frankowski M, Ziola-Frankowska A, Sienkiewicz J. New method for speciation analysis of aluminium fluoride complexes by HPLC-FAAS hyphenated technique. *Talanta.* 2010;80(5): 2120-2126. [<DOI>](#).
- Melnyk LJ, Morgan JN, Fernando R, Pellizzari ED, Akinbo O. Determination of metals in composite diet samples by inductively coupled plasma-mass spectrometry. *Journal of AOAC International.* 2003;86(2):439-448. [<DOI>](#).
- Mahdavi M, Nezamzadeh-Ejhieh A. An aluminum selective electrode via modification of PVC membrane by modified clinoptilolite nanoparticles with hexadecyltrimethyl ammonium bromide (HDTMA-Br) surfactant containing Arsenazo III. *Journal of colloid and interface science.* 2017; 494:317-324. [<DOI>](#).
- Zuziak J, Reczyński W, Baś B, Jakubowska M. Voltammetric determination of aluminum (III) as Al-Alizarin S complex in tea leaves and infusions. *Analytical biochemistry.* 2018;558:69-79. [<DOI>](#).
- Guha S, Lohar S, Sahana A, Banerjee A, Safin DA, Babashkina MG et al. Coumarin-based “turn-on” fluorescent sensor for the determination of Al³⁺: single crystal X-ray structure and cell staining properties. *Dalton Transactions.* 2013;42(28):10198-10207. [<DOI>](#).
- Wang B, Liu X, Duan W, Dai S, Lu H. Visual and ratiometric fluorescent determination of Al³⁺ by a red-emission carbon dot-quercetin system. *Microchemical Journal.* 2020;156: 104807. [<DOI>](#).
- Huang P, Li J, Liu X, Wu F. Colorimetric determination of aluminum (III) based on the aggregation of Schiff base-functionalized gold nanoparticles. *Microchimica Acta.* 2016;183(2): 863-869. [<DOI>](#).
- Zezi-Arruda MA, Poppi RJ. Spectrophotometry / Inorganic Compounds. *Encyclopedia of Analytical Science.* 2005;351-358. [<DOI>](#).
- Alawsi T, Mattia GP, Al-Bawi Z, Beraldi R. Smartphone-based colorimetric sensor application for measuring biochemical material concentration. *Sensing and Bio-Sensing Research.* 2021;32:100404. [<DOI>](#).
- Liu T, Zhang S, Liu W, Zhao S, Lu Z, Wang Y, Wang G, Zou P, Wang X, Zhao Q, Rao H. Smartphone based platform for ratiometric fluorometric and colorimetric determination H₂O₂ and glucose. *Sensors and Actuators B: Chemical.* 2020;305:127524. [<DOI>](#).
- Serhan M, Jackemeyer D, Long M, Sprowls M, Perez ID et al. Total iron measurement in human serum with a novel smartphone-based assay. *IEEE Journal of Translational Engineering in Health and Medicine.* 2020;8:1-9. [<DOI>](#).
- Saranchina NV, Slizhov YG, Vodova YM, Murzakasymova NS, Ilyina AM et al. Smartphone-based colorimetric determination of fluoride anions using polymethacrylate optode. *Talanta.* 2021;226:122103. [<DOI>](#).
- Fang J. Classification of fruits based on anthocyanin types and relevance to their health effects. *Nutrition.* 2015;31(11-12):1301-1306. [<DOI>](#).
- Silva S, Costa EM, Calhau C, Morais RM, Pintado ME. Anthocyanin extraction from plant tissues: A review. *Critical reviews in food science and nutrition.* 2017;57(14):3072-30833. [<DOI>](#).
- Clifford MN. Anthocyanins-nature, occurrence and dietary burden. *Journal of the Science of Food and Agriculture.* 2000;80(7):1063-1072. [<DOI>](#).
- Fedenko VS, Shemet SA, Landi M. UV-vis spectroscopy and colorimetric models for detecting anthocyanin-metal complexes in plants: An overview

of in vitro and in vivo techniques. *Journal of plant physiology*. 2017;212:13-28. [<DOI>](#).

22. Tanguler H, Erten H. Chemical and microbiological characteristics of shalgam (salgam); A traditional Turkish lactic acid fermented beverage. *Journal of Food Quality*. 2012;35(4):298-306. [<DOI>](#).

23. Tanguler H, Selli, S, Sen K, Cabaroglu T, Erten, H. Aroma composition of shalgam: a traditional Turkish lactic acid fermented beverage. *Journal of Food Science and Technology*. 2017;54(7):2011-2019. [<DOI>](#).

24. Canbaş A, Fenercioglu H. Salgam suyu üzerinde bir araştırma. *Gıda*. 1984;9(5):279-286 (in Turkish).

25. Erten H, Tanguler H, Canbaş A, A traditional Turkish lactic acid fermented beverage: Shalgam (Salgam). *Food Reviews International*. 2008;24(3):352-359. [<DOI>](#).

26. Kammerer D, Carle R, Schieber A. Quantification of anthocyanins in black carrot extracts (*Daucus carota* ssp. *sativus* var. *atrorubens* Alef.) and evaluation of their color properties. *European Food Research and Technology*. 2004;219(5):479-486. [<DOI>](#).

27. Narayan MS, Venkataraman LV. Characterisation of anthocyanins derived from carrot (*Daucus carota*) cell culture. *Food Chemistry*. 2000;70:361-363. [<DOI>](#).

28. Canbas A. Siyah havucun renk maddesi üzerine bir araştırma. *Doğa*. 1985;9(3):394-398 (in Turkish).

29. Ekinci FY, Baser GM, Özcan E, Üstündağ ÖG, Korachi M. Characterization of chemical, biological, and antiproliferative properties of fermented black carrot juice, shalgam. *European Food Research and Technology*. 2016;242(8):1355-1368. [<DOI>](#).

30. Porrawatkul P, Pimsen R, Kuyyogsuy A, Nuengmatcha P. Simple and selective naked-eye and visual detection of Cu^{2+} and Al^{3+} ions using Hibiscus Rosa-Sinensis Linn flower Extract. *Oriental Journal of Chemistry*. 2018;34(1):188. [<DOI>](#).

31. Khaodee W, Aeungmaitrepirom W, Tuntulani T. Effectively simultaneous naked-eye detection of Cu (II), Pb (II), Al (III) and Fe (III) using cyanidin extracted from red cabbage as chelating agent. *Spectrochimica Acta Part A: Molecular and Biomolecular Spectroscopy*. 2014;126:98-104. [<DOI>](#).

32. Park S, Kang S, Jeong DY, Jeong SY, Park JJ et al. Cyanidin and malvidin in aqueous extracts of black carrots fermented with *Aspergillus oryzae* prevent the impairment of energy, lipid and glucose metabolism in estrogen-deficient rats by AMPK activation. *Genes & nutrition*. 2015;10(2):1-14. [<DOI>](#).

33. Gałuszka A, Migaszewski Z, Namieśnik J. The 12 principles of green analytical chemistry and the SIGNIFICANCE mnemonic of green analytical practices. *TrAC Trends in Analytical Chemistry*. 2013;50:78-84. [<DOI>](#).

34. U. USEPA, Method 200.7: determination of metals and trace elements in water and wastes by inductively coupled plasma-atomic emission spectrometry. Rev. 4.4, 1994; EPA600/R-94-111.

35. Zolgharnein J, Shahrjerdi A, Azimi G, Ghasemi J. Spectrophotometric determination of trace amounts of fluoride using an Al-xylenol orange complex as a colored reagent. *Analytical Sciences*. 2009;25(10):1249-1253. [<DOI>](#).

36. Krupińska I. Aluminium drinking water treatment residuals and their toxic impact on human health. *Molecules*. 2020;25(3):641. [<DOI>](#).

37. Grotewold, E. The genetics and biochemistry of floral pigments. *Annual review of plant biology*. 2006;57(1):761-780. [<DOI>](#).

38. Schreiber HD, Swink AM, Godsey TD. The chemical mechanism for Al^{3+} complexing with delphinidin: A model for the bluing of hydrangea sepals. *Journal of inorganic biochemistry*. 2010;104(7):732-739. [<DOI>](#).

39. Ren J, Meng S, Lekka CE, Kaxiras E. Complexation of flavonoids with iron: structure and optical signatures. *The Journal of Physical Chemistry B*. 2008;112(6):1845-1850. [<DOI>](#).

40. Ravishankara MN, Shrivastava N, Padh H, Rajani M. Evaluation of antioxidant properties of root bark of *Hemidesmus indicus* R. Br.(Anantmul). *Phytomedicine*. 2002;9(2):153-160. [<DOI>](#).

41. Jiang Y, Miao Y, Ding Z, Lu Y. In situ formed silicon-based nanoparticles enabled highly efficient dual-mode biosensing of chlorpyrifos. *Food Chemistry*. 2023;403:134243. [<DOI>](#).

42. Shang C, Li Y, Zhang Q, Tang S, Tang X, Ren H, Hu P, Lu S, Li P, Zhou, Y. Alkaline phosphatase-triggered dual-signal immunoassay for colorimetric and electrochemical detection of zearalenone in cornmeal. *Sensors and Actuators B: Chemical*. 2022;358:131525. [<DOI>](#).

43. Durmazel S, Üzer A, Apak, R. Naked-Eye Detection of 3-Nitro-1, 2, 4-triazole-5-one at Sub-Femtomolar Levels with Melamine and Unlabeled Au Nanoparticles. *ACS Applied Nano Materials*. 2022;5(4): 5244-5257. [<DOI>](#).

44. Ular N, Uzer A, Durmazel S, Ercag E, Apak R. Diaminocyclohexane-functionalized/thioglycolic acid-modified gold nanoparticle-based colorimetric sensing of trinitrotoluene and tetryl. *ACS sensors*. 2018;3(11): 2335-2342. [<DOI>](#).

45. Shahvar A, Shamsaei D, Saraji M. A portable smartphone-based colorimetric sensor for rapid determination of water content in ethanol. *Measurement*. 2020;150:107068. [<DOI>](#).
46. Bandi R, Alle M, Park CW, Han SY, Kwon GJ, Kim NH, Kim JC, Lee SH. Cellulose nanofibrils/carbon dots composite nanopapers for the smartphone-based colorimetric detection of hydrogen peroxide and glucose. *Sensors and Actuators B: Chemical*. 2021;330:129330. [<DOI>](#).
47. Han T, Feng X, Tong B, Shi J, Chen L et al. A novel "turn-on" fluorescent chemosensor for the selective detection of Al³⁺ based on aggregation-induced emission. *Chemical communications*. 2012;48(3):416-418. [<DOI>](#).
48. Kim Y, Jang G, Lee TS. New fluorescent metal-ion detection using a paper-based sensor strip containing tethered rhodamine carbon nanodots. *ACS applied materials & interfaces*. 2015;7(28):15649-15657. [<DOI>](#).
49. Kumar A, Bhatt M, Vyas G, Bhatt S, Paul P. Sunlight induced preparation of functionalized gold nanoparticles as recyclable colorimetric dual sensor for aluminum and fluoride in water. *ACS applied materials & interfaces*. 2017;9(20):17359-17368. [<DOI>](#).
50. Wei W, Huang J, Gao W, Lu X, Shi X. Carbon dots fluorescence-based colorimetric sensor for sensitive detection of aluminum ions with a smartphone. *Chemosensors*. 2021;9(2):25. [<DOI>](#).
51. Park H, Kim W, Kim M, Lee G, Lee W et al. Eco-friendly and enhanced colorimetric detection of aluminum ions using pectin-rich apple extract-based gold nanoparticles. *Spectrochimica Acta Part A: Molecular and Biomolecular Spectroscopy*. 2021;245:118880. [<DOI>](#).
52. da Silva HM, Mageste AB, e Silva SJB, Ferreira GMD, Ferreira GMD. Anthocyanin immobilization in carboxymethylcellulose/starch films: A sustainable sensor for the detection of Al(III) ions in aqueous matrices. *Carbohydrate Polymers*. 2020;230:115679. [<DOI>](#).
53. Canbas A, Deryaoglu A. Şalgam suyunun üretim tekniği ve bileşimi üzerinde bir araştırma. *Doga-Turkish Journal of Agricultural and Forestry* 1993;17:119-129.
54. Coskun F. A traditional Turkish fermented non-alcoholic beverage, "Shalgam". *Beverages* 2017; 3: 49. [<DOI>](#).



The Preparation and Physicochemical Analysis of Local Black Soap from Coconut Oil and Plantain Peel Biochar

Mary Otuosorochukwu Nnyia¹ , Abiodun Oladipo² , Ebube Victoria Anyaebosim³ , and Onome Ejeromedoghene^{4*} 

¹CAS Key Laboratory of Standardization and Measurement of Nano Technology, Chinese Academy of Sciences Beijing, 100190 People's Republic of China

²Co-Innovation Center for Sustainable Forestry in Southern China, College of Forestry, Nanjing Forestry University, 210037 Nanjing, Jiangsu, China

³Department of Applied Chemistry and Engineering, Taiyuan University of Technology (Yingxi Campus), Wanbailin District, Taiyuan, Shanxi Province 030024, People's Republic of China

⁴School of Chemistry and Chemical Engineering, Southeast University, 211189 Nanjing, Jiangsu Province, People's Republic of China

Abstract: Local black soap, produced from coconut oil and plantain peel biochar (alkaline source) was presented in this study since the agricultural raw materials gain significance in environmentally benign feedstocks for saponification reactions. The physicochemical analysis of the coconut oil and plantain peel biochar shows remarkable free fatty acid (FFA) and alkalinity contents respectively suitable for soap making. The physicochemical properties of the as-prepared local black soap demonstrated a good moisture content (15.1 %) showing that it can be stored for long periods without any water-associated deteriorations. The percentage of matter insoluble in water (4.4 %), matter insoluble in alcohol (12.3 %), FFA content (2.1 %), and pH (9) were found to be higher than the acceptable limit according to the Nigerian Industry Standards (NIS). Also, the total fatty matter (TFM) was higher (67.6 %) than the minimum acceptable level with a good foam height of 2.5 cm. The overall results show good soap properties and are suitable for domestic purposes.

Keywords: Local black soap, plantain peel, coconut oil, Agricultural feedstocks

Submitted: July 06, 2022. **Accepted:** December 01, 2022.

Cite this: Nnyia MO, Oladipo A, Anyaebosim EV, Ejeromedoghene O. The Preparation and Physicochemical Analysis of Local Black Soap from Coconut Oil and Plantain Peel Biochar. JOTCSA. 2023;10(1):177-84.

DOI: <https://doi.org/10.18596/jotcsa.1141351>.

***Corresponding author. E-mail:** oejeromedoghene@seu.edu.cn.

1. INTRODUCTION

The agrarian diversity in human and economic growth is a significant concern. Over the years, raw materials of agrarian origin have been sourced as benign feedstocks for many industrial activities because they are eco-friendly, cheap, and readily available. This has increased the awareness of agricultural production, necessary to meet the demand emanating from population increase and also for servicing commercial industries. Interestingly, large quantities of waste materials which are residues of agrarian practices, contribute

significantly to the degradation of the environment and as such must be carefully handled to prevent any form of negative consequences such as pollution and economic loss (1,2).

Today, several researchers are beginning to focus on the recyclability of bio-waste materials, pollution control, and income generation. However, the conversion of agricultural wastes into new products or their use in the formulation of new products must certainly characterize the chemical composition, surface morphology as well as physicochemical properties of any of these

materials (3). For instance, the shells from peanuts account for about 20% of the peanut with production amounting to 46 metric tons every year. The peanuts are majorly disposed of through burning which contributes to environmental pollution and in some cases could be used in the production of livestock feed which requires proper treatment and processing. Peanut shells contain antioxidants due to the presence of Phyto derivatives used relevantly in cosmetic industries and were reported to function as an absorbent to eliminate heavy metals (4,5). Hence, agro- and non-agro-waste residues have been extensively explored as sustainable unfired earth-building materials for blocks construction (6), waste ginger straw has been examined as a productive heterogeneous catalyst for biodiesel production (7), while Chickpea husk has shown huge prospects for textile coloring and operational finishing (8).

Nevertheless, the production of soap from natural products in place of synthetic chemicals is gaining attention in recent times. Agricultural by-products (wastes) are considered sources of organic materials in soap production because they have been reported to contain phytochemicals for moisturizing the human skin and treatment of skin-related infections (9,10). Organic compounds from

agro-wastes have shown antibacterial activity against *Streptococcus pyogenes* and *Pseudomonas aeruginosa* as presented by Rambabu and colleagues (11). More also, agro-waste materials e.g. plantain peels have been considered a viable source of alkaline for saponification reactions because of the important class of phytochemicals (alkaloids, flavonoids, terpenoids, phenols, etc.) as well as vital minerals components (calcium, copper, potassium, phosphorus, zinc, etc.) (12). Besides, oils derived from agro-materials (e.g. palm oil and coconut oil) contain saponifiable free fatty acids as well as alkaloids, terpenoids, saponins, etc. (13-15). Soaps are typically fatty acid salts that can be firm or soft depending on the components utilized. They are made from fats/oils that have been hydrolyzed with an alkaline to produce fatty acid salts (soap) and glycerol (by-product) (Figure 1) (16). Negative ions comprising long hydrocarbon chains connected to a carboxyl group are common in the soaps that are being produced, giving it a cleansing action when used for bathing, washing, or general cleaning (17). Therefore, this paper examines the production of local black soap using two agro-feedstocks (coconut oil and plantain peel), and the physiochemical properties of the soap produced were also examined.

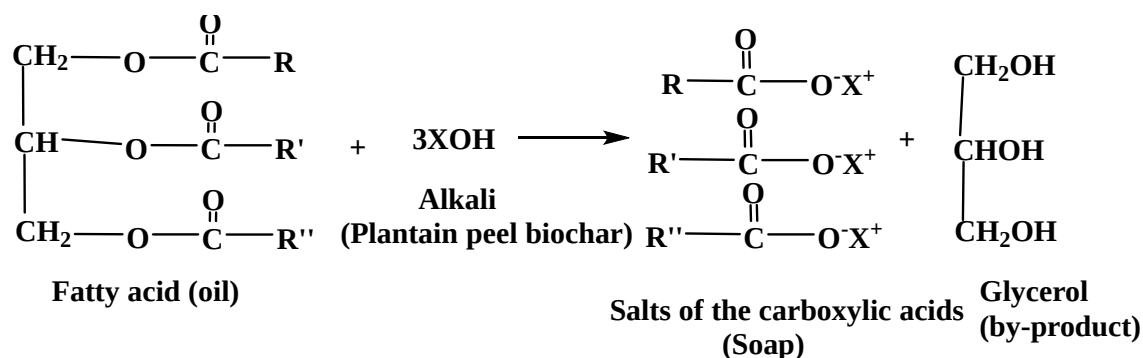


Figure 1: Saponification reaction of a triglyceride and alkaline to produce soap.

2. EXPERIMENTAL SECTION

2.1. Sample Collection and Materials Used

Waste plantain peels were collected from a local eatery. Pure coconut oil was bought from commercial vendors. The other analytical grade reagent used like Hydrochloric acid (HCl), Potassium Hydroxide (KOH), Phenolphthalein indicator, Ethanol (C₂H₅OH), Nitric acid (HNO₃), Neutralized isopropyl alcohol (IPA), Sodium hydroxide (NaOH) Sulfuric acid (H₂SO₄), Acetone, Diethyl ether, Methyl orange indicator, and Barium chloride (BaCl₂) were supplied by Maya Reagent, and Sinopharm Chemical Reagent Co. Ltd. For the production of aqueous solutions, distilled water was employed.

2.2. Preparation of Plantain Peel Biochar

To remove dirt, fresh plantain skins were washed with distilled water and dried in a slightly warmer setting. Plantain peel biochar was made by cutting the peels into little pieces and heated in a furnace for 5 h at 600 °C. The resulting biochar was allowed to cool in a desiccator before being pulverized in a mortar and sieved with a mesh.

2.3. Production Process of Local Black Soap

The native black soap was made by combining 100 g of plantain skin biochar with 500 mL of water in a beaker. The mixture was stirred and allowed to settle for 72 h. The alkaline extract was then filtered with cotton wool and a funnel. The heat was used to condense the alkaline extract, and coconut oil was slowly introduced in a 4:1 ratio. These were further heated on a hot plate and stirred at 60 °C until complete saponification

occurs. The soap was allowed to cure for 24 h to obtain the local black soap (18) (Figure 2).



Figure 2: Schematic route for the preparation of local black soap.

2.4 Physicochemical analysis

The physicochemical analysis of the plantain peels biochar, coconut oil, and local black soap was performed according to established procedures (18,19).

2.4.1 Determination of moisture content

Weighing 2.15 g of black soap on a pre-weighed crucible and keeping it in an oven at 100°C - 105°C for 1 h was used to determine the moisture content of the soap. The soap was allowed to be cooled before being weighed once more. The given equation was used to compute the percentage moisture content (Eq. 1).

$$\text{Percentage Moisture Content} = \frac{w_3 - w_2}{w_1} \times 100\% \quad (\text{Eq. 1})$$

Where W_1 =sample weight; W_2 =weight of crucible; W_3 =weight after drying.

2.4.2 Determination of water-insoluble matter

Weighing 5.06 g of black soap into a 250 mL beaker, yielded the amount of water-insoluble materials in the soap. The soap was then dissolved in 100 mL of distilled water by heating on a hotplate. The soap solution was filtered and rinsed

with distilled water three times. Further, the residue was kept in an oven (100 °C - 105 °C) for 1 h. After cooling in a desiccator, the residual weight was calculated. The following formula was used to compute the proportion of water insoluble-matter (Eq. 2):

$$\text{Percentage Moisture Insoluble Matter} = \frac{w_3 - w_2}{w_1} \times 100\% \quad (\text{Eq. 2})$$

Where W_1 =weight of sample; W_2 =weight of filter paper; W_3 =weight of filter paper residue after drying.

2.4.3 Determination of free fatty acid (FFA)

Firstly, 10 g of the black soap was weighed into a conical flask, followed by the addition of 100 mL of neutralized isopropyl alcohol (IPA) to determine the amount of FFA in the soap. The solution was

allowed to boil on a hot plate until the soap was dissolved. Next, 10 mL of barium chloride was added to the mixture and titrated against NaOH using phenolphthalein as the indicator. The percentage FFA was calculated by Eq.3:

$$\text{Percentage FFA} = \frac{\text{endpoint} \times \text{Normality of base} \times 200 \times 100}{1000 \times \text{weight of sample}} \quad (\text{Eq. 3})$$

2.4.4 Determination of alcohol-insoluble matter

In a beaker, 2 g of the black soap was heated with 100 mL of neutralized IPA to estimate the proportion of the alcohol-insoluble matter. The soap solution was filtered and the insoluble matter was transferred using a hot neutralized IPA until all

the soap entrained within the filter paper has been removed. The residue was baked for 30 min and then cooled in a desiccator. The percentage of the alcohol-insoluble matter was calculated according to Eq. 4.

$$\text{Percentage Moisture Insoluble Matter} = \frac{W_3 - W_2}{W_1} \times 100\% \quad (\text{Eq. 4})$$

Where W_1 =weight of sample; W_2 =weight of filter paper; W_3 =weight of filter paper + residue after drying.

2.4.5 Determination of pH

By dissolving 2 g of local black soap in 200 mL of distilled water, the pH of the soap was calculated. The pH meter's electrode was then dipped into the solution to record the pH.

phase separation. The solution was further separated by shaking until the aqueous layer became clear and allowed to stand. The solution was re-washed with diethyl ether and with water until methyl orange was neutralized. The set-up was allowed to stand for another 5 min and run off any separated water. The solvent was then distilled off by adding 5 mL of acetone to the clean solution and heating it to evaporate the diethyl ether. Also, the acetone was removed under the steam of dry air. The beaker was placed in the oven for 30 min and allowed to cool and the weight was taken. The percentage of the total fatty matter was collected as calculated according to Eq. 5.

2.4.6 Determination of total fatty matter (TFM)

By heating 5 g of the local black soap with 100 mL of distilled water, the total fatty matter was measured. For facile precipitation of the fatty components from the soap, the soap solution was transferred into a separating funnel, followed by the addition of methyl orange indicator and sulfuric acid. Thereafter, the soap solution was cooled, and diethyl ether (100 mL) was introduced to allow

$$\text{Percentage Moisture Insoluble Matter} = \frac{W_3 - W_2}{W_1} \times 100\% \quad (\text{Eq. 5})$$

Where W_1 =weight of sample; W_2 =weight of beaker; W_3 =weight after drying.

2.4.7 Determination of foam height (lathering ability)

By dissolving 2 g of local black soap in distilled water, the foam height of the soap was determined. This was agitated in a clean blender with 200 mL of distilled water for 30 s. Thereafter, the height of the foam formed was measured on a 1000 mL tube.

4.5 which makes it fit for the production of soft soaps.

3. RESULTS AND DISCUSSION

3.1 Physicochemical and Structural Properties of Plantain Peel Biochar

Physicochemical properties of plantain peel biochar show an ash content of 11.3% which indicates the presence of sufficient minerals in the sample collected. In the presence of oxidizing agents, ash is the inorganic residue left after the water and organic matter have been removed by heating (20). The value of pH was 13 which indicates a strong alkaline content and a lye concentration of

Furthermore, the characterization of the plantain peel biochar with Fourier transform infrared (FT-IR) reveals a prominent peak at 3413 cm^{-1} which could be due to OH stretch (alcohol and carboxylic acid) (Figure 3). The weak peak at 2923 cm^{-1} confirms the presence of OH from carboxylic acid which could be due to the presence of phytochemicals like tannins (e.g. gallic acid), cellulose, and hemicelluloses in the plantain peels (21). More also, the peak at 1620 cm^{-1} could be ascribed to C=C vibrational stretch. The Peaks observed at $1387\text{-}1246\text{ cm}^{-1}$ can be attributed to the C-H bending of cellulose, hemicelluloses, or lignin polymer. The peak at 1100 cm^{-1} could be associated with the =C-O-C symmetric and asymmetric stretch in ether linkages of polyphenols (22); while the weak peaks appearing at $841\text{-}624\text{ cm}^{-1}$ might be linked to the presence of amine groups and other mineral elements (23).

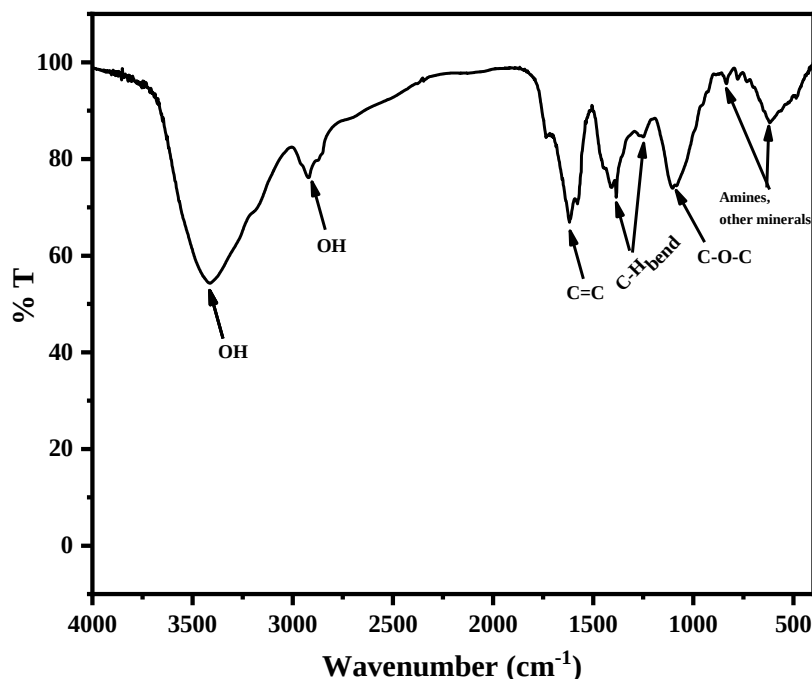


Figure 3: FT-IR spectrum of plantain peel biochar.

In addition, the structural morphology of the plantain peel biochar shows porous and thick fibrous-like nature with a cluster of small particles on the surface (Figure 4). The morphological structure observed usually exhibits a higher surface area, with promising prospects to make a good soap material (24). The porous nature of the material will enable good interaction with the chemical content in the oil to give a good soap formulation.

3.2 Physicochemical Properties of Coconut Oil

The results in Table 1 show the physicochemical features of the coconut oil utilized in the local black soap production. The density of the coconut oil was 0.902 g/mL. The saponification value is the amount of KOH necessary to saponify 1 g of oil in milligrams. It is a measure of the free acid and saponifiable ester groups. This important parameter helps to determine the amount of salt to be formed. Substantial saponification and ester values of 259.00 mgKOH and 228.3 mgKOH

respectively were obtained in the coconut oil revealing promising prospects for soap making. More also, coconut oils contain significant saturated and unsaturated fatty acids which contribute to the hardness, aroma, and cleansing properties of soaps. The coconut oil had a free fatty acid (FFA) concentration of 2.60, with a corresponding FFA composition (Table 2). The titer value provides information on the actual value of the melting point of the soap during saponification. The result obtained shows a titer value of 20.4°C. This implies that the coconut oil possesses a low melting point with good soap-forming properties. The coconut oil demonstrated a low acid value of 1.240 mg KOH and a low moisture content of 0.4%. This indicates that the oil will remain stable for a long time and will effectively preserve the soap against rancidity. The physicochemical parameters obtained for the coconut oil are within acceptable standards and results from other studies (25).

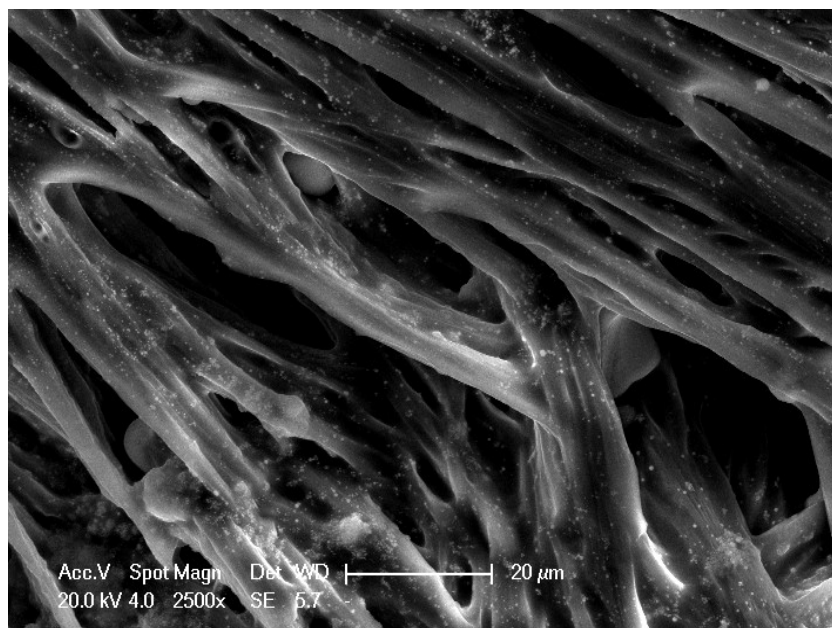


Figure 4: SEM micrograph of plantain peel biochar.

Table 1: Physicochemical properties of the coconut oil for local black soap production.

Property	Value
Density (g/mL)	0.901
Saponification value (mgKOH)	259.00
Ester value (mgKOH)	228.3
FFA (%)	2.60
Titre value (°C)	20.4
Acid value mgKOH	1.240
Moisture content (%)	0.4

Table 2: Coconut oil's approximate fatty acid content.

Type of fatty acid	Composition (%)
Lauric acid	48.00
Myristic acid	18.49
Palmitic acid	8.80
Oleic acid	7.81
Stearic acid	3.00
Caprylic acid	5.55
Caproic acid	0.50
Linoleic acid	1.35
Capric acid	6.50

3.3 Physicochemical Properties of Local Black Soap

The physicochemical parameters of the native black soap obtained were compared with the Nigerian Industrial Standard (NIS) (Table 3). The reaction of unsaponified fat with excess water in the soap to form glycerol and FFA, assisted by soap hydrolysis, represents the FFA levels in soaps. The obtained black soap displayed a moisture level of 15.1%, which was insignificantly higher (0.1%) than the NIS model. The good moisture content of the black soap shows that it can be stored for 12 - 24 months without any water-induced

deterioration. Thus, the black soap can be considered harmless for domestic and commercial applications (26). The percentage of black soap that was insoluble in water was 4.4%, which was more than the allowed standard of 2.5%. The soap's lather will be affected by the excessive amounts of insoluble particles in the water. Similarly, the percentage of matters insoluble in alcohol of the local black soap was 12.3%, higher than the acceptable limit of 5.0%. This reveals that there are plausibly insoluble fats and sodium silicate insoluble in alcohol in the local soap. This

could indicate that the black soap included waxes and lipids that are water-insoluble (27).

Table 3: Comparison of the physicochemical parameters of the native black soap produced (in this study) to the Nigerian Industrial Standard (NIS).

Parameter	Local black soap	NIS
Physical appearance	Blackish brown	-
Moisture content (%)	15.1	15 max.
Matters insoluble in water (%)	4.4	2.5 max.
Matters insoluble in alcohol (%)	12.3	5 max.
Free fatty acid content	2.1	0.2 max.
pH	9	6-10
Total fatty matters (%)	67.6	60 min.
Foam height (cm)	2.5	-

The FFA content of the local black soap was 2.1%. This value was higher than the specified limit and implies poor transparency of the black soap (28). The black soap shows a pH of 9 since soaps are alkaline substances thereby functioning as barriers against dangerous organisms such as bacteria and viruses, this can counteract the body's protective acid mantle. The obtained pH of the soap shows that the saponification process is completely hydrolyzed, and may not impact corrosive action when applied to the skin. On the other hand, the corrosive nature of local black soaps is solvable by increasing oil content (29). Thus, the local black soap may be suitable for domestic use.

The soap's cleansing ability is proportional to its total fatty matter (TFM). The TFM of the local black soap was 67.6%, higher than the minimum of 60 % set by the NIS. This suggests that the local black soap possesses high cleansing properties. The foam height is an attribute associated with oil composition used in black soap production. Lauric acid, the major FFA in coconut oil has a remarkable foaming property. Thus, the foam, high of 2.5 cm shows the good formability of the local black soap (30).

4. CONCLUSION

The production of local black soap from agro-based feedstocks of coconut oil (triglycerides) and plantain peel biochar (alkaline source) is hereby presented in this study. The physicochemical characterization of the plantain peel biochar demonstrated good alkalinity which makes it fit for making soft soaps. The physicochemical characterization of the coconut oil extracts, indicates good fatty acid content and remarkable oil properties within acceptable standards. Thus, the physicochemical parameters of the black soap displayed good formability and harmless properties for domestic and commercial applications. However, the results reveal the presence of some sort of waxes and fat components in the soap reducing the transparency of the black soap. Nevertheless, local black soap manufacturing should be encouraged since it has good quality for

commercial consumption and thereby reduces the waste generated from plantain peels.

5. CONFLICT OF INTEREST STATEMENT

The authors declare no conflict of interest.

6. REFERENCES

1. Oluseun Adejumo I, Adebukola Adebisi O. Agricultural Solid Wastes: Causes, Effects, and Effective Management. In: M. Saleh H, editor. *Strategies of Sustainable Solid Waste Management* [Internet]. IntechOpen; 2021 [cited 2023 Feb 4]. Available from: [<URL>](#).
2. Santolini E, Bovo M, Barbaresi A, Torreggiani D, Tassinari P. Turning Agricultural Wastes into Biomaterials: Assessing the Sustainability of Scenarios of Circular Valorization of Corn Cob in a Life-Cycle Perspective. *Applied Sciences*. 2021 Jul 7;11(14):6281. Available from: [<URL>](#).
3. Durga ML, Gangil S, Bhargav VK. Conversion of agricultural waste to valuable carbonaceous material: Brief review. *Materials Today: Proceedings*. 2022;56:1290-7. Available from: [<URL>](#).
4. Arumugam N, Biely P, Puchart V, Singh S, Pillai S. Structure of peanut shell xylan and its conversion to oligosaccharides. *Process Biochemistry*. 2018 Sep;72:124-9. Available from: [<URL>](#).
5. Adhikari B, Dhungana SK, Waqas Ali M, Adhikari A, Kim ID, Shin DH. Antioxidant activities, polyphenol, flavonoid, and amino acid contents in peanut shell. *Journal of the Saudi Society of Agricultural Sciences*. 2019 Oct;18(4):437-42. Available from: [<URL>](#).
6. Jannat N, Hussien A, Abdullah B, Cotgrave A. Application of agro and non-agro waste materials for unfired earth blocks construction: A review. *Construction and Building Materials*. 2020 Sep;254:119346. Available from: [<URL>](#).
7. Yu H, Cao Y, Li H, Zhao G, Zhang X, Cheng S, et al. An efficient heterogeneous acid catalyst derived from waste ginger straw for biodiesel production. *Renewable Energy*. 2021 Oct;176:533-42. Available from: [<URL>](#).
8. Jose S, Pandit P, Pandey R. Chickpea husk - A potential agro waste for coloration and functional finishing of textiles. *Industrial Crops and Products*. 2019 Dec;142:111833. Available from: [<URL>](#).

9. Alharbi KL, Raman J, Shin HJ. Date Fruit and Seed in Nutricosmetics. *Cosmetics*. 2021 Jun 24;8(3):59. Available from: [<URL>](#).
10. Ogunbiyi A, Enechukwu NA. African black soap: Physicochemical, phytochemical properties, and uses. *Dermatologic Therapy [Internet]*. 2021 May [cited 2023 Feb 4];34(3). Available from: [<URL>](#)
11. Rambabu K, Edathil AA, Nirmala GS, Hasan SW, Yousef AF, Show PL, et al. Date-fruit syrup waste extract as a natural additive for soap production with enhanced antioxidant and antibacterial activity. *Environmental Technology & Innovation*. 2020 Nov;20:101153. Available from: [<URL>](#).
12. Sani MU, Muhammad AK. Assessment of phytochemical and mineral composition of unripe and ripe plantain (*Musa paradisiaca*) peels. *Afr J Food Sci*. 2021 Mar 31;15(3):107-12. Available from: [<URL>](#).
13. Basseyy EE, Gwana MA, Mu'azu AKN, Modu GU. Qualitative phytochemicals screening and antimicrobial susceptibility patterns of coconut oil extract on some selected bacteria and fungi. *World J Adv Res Rev*. 2019 Apr 30;1(3):001-13. Available from: [<URL>](#).
14. Ajongbalo K. Chemical Properties of Local Black Soap Produced from Cocoa Pod Ash and Palm Oil Waste. *IJTSRD*. 2020;4(6):713-5. Available from: [<URL>](#).
15. Tacin MV, Massi FP, Fungaro MHP, Teixeira MFS, de Paula AV, de Carvalho Santos-Ebinuma V. Biotechnological valorization of oils from agro-industrial wastes to produce lipase using *Aspergillus* sp. from Amazon. *Biocatalysis and Agricultural Biotechnology*. 2019 Jan;17:369-78. Available from: [<URL>](#).
16. Adebomi AI, Oladipupo OA, Mary AO. The African black soap from *Elaeis guineensis* (Palm kernel oil) and *Theobroma cacao* (Cocoa) and its transition metal complexes. *Afr J Biotechnol*. 2017 May 3;16(18):1042-7. Available from: [<URL>](#).
17. Adeyinka OM, Olukemi AR, Farombi AG. Physicochemical Properties of African Black Soap, and It's Comparison with Industrial Black Soap. *Am J Chem*. 2014;2014(1):35-7.
18. Edah AO, Nnoli CB, Wetkum DF. Physicochemical Properties and Anti-Microbial Activity of Local Black Soap and its Comparison with Ghana Soap with Respect to Nigerian Industrial Standard. *ARJC*. 2017;1(1):30-6. Available from: [<URL>](#).
19. Idoko O, Emmanuel SA, Salau AA, Obigwa PA. Quality assessment on some soaps sold in Nigeria. *Nig J Tech*. 2018 Nov 15;37(4):1137. Available from: [<URL>](#).
20. Taiwo A, Oluwadare I, Shobo A, Amolegbe S. Extraction and potential application of caustic potash from kolanut husk, uguwu pod husk and plantain peels. *Scientific Research and Essay*. 2008;3(10):515-7.
21. Aderibigbe AD, Ogunlalu OU, Oluwasina OO, Amoo IA. Adsorption Studies of Pb²⁺ From Aqueous Solutions Using Unmodified and Citric Acid - Modified Plantain (*Musa paradisiaca*) Peels. *IOSR JAC*. 2017 Mar;10(2):30-9. Available from: [<URL>](#).
22. Agama-Acevedo E, Sañudo-Barajas JA, Vélez De La Rocha R, González-Aguilar GA, Bello-Peréz LA. Potential of plantain peels flour (*Musa paradisiaca* L.) as a source of dietary fiber and antioxidant compound. *CyTA - Journal of Food*. 2016 Jan 2;14(1):117-23. Available from: [<URL>](#).
23. Zango ZU. Cationic dyes removal using low-cost banana peel biosorbent. *American Journal of Materials Science*. 2018;8(2):32-8.
24. Etim A, Betiku E, Ajala S, Olaniyi P, Ojumu T. Potential of Ripe Plantain Fruit Peels as an Ecofriendly Catalyst for Biodiesel Synthesis: Optimization by Artificial Neural Network Integrated with Genetic Algorithm. *Sustainability*. 2018 Mar 6;10(3):707. Available from: [<URL>](#).
25. Martins J, Santos J, da Conceicao M. Comparative Study of Physico-Chemical Properties of Coconut Oil (*Cocos nucifera* L.) Obtained by Industrial and Artisanal Processes. *Biotechnol Ind J*. 2020;16(3):210.
26. Vivian OP, Nathan O, Osano A, Mesopirr L, Omwoyo WN. Assessment of the physicochemical properties of selected commercial soaps manufactured and sold in Kenya. *Open J Appl Sci*. 2014;4(8):433-40. Available from: [<URL>](#).
27. Oyekunle JAO, Ore OT, Ogunjumelo OH, Akanni MS. Comparative chemical analysis of Indigenous Nigerian soaps with conventional ones. *Heliyon*. 2021 Apr;7(4):e06689. Available from: [<URL>](#).
28. Hayati SN, Rosyida VT, Darsih C, Nisa K, Indriarningsih AW, Apriyana W, et al. Physicochemical properties, antimicrobial and antioxidant activity of ganoderma transparent soap. *IOP Conf Ser: Earth Environ Sci*. 2020 Mar 1;462(1):012047. Available from: [<URL>](#).
29. Warra AA. A report on soap making in Nigeria using indigenous technology and raw materials. *Afr J Pure Appl Chem*. 2013 Apr 30;7(4):139-45. Available from: [<URL>](#).
30. Issa M, Isaac I, Matthew O, Shalangwa B, Sunday M. Physicochemical analysis for quality and safety of some selected animal soaps compared to human soaps in plateau state, Nigeria. *IOSR J Appl Chem*. 2020;13(3):25-8.



Determination of the Anticarcinogenic Activity of 5-Hydroxymethyl-2-furfural Produced from Grape Must Under *in vitro* Conditions

Kubra Kelleci^{1,2*} , Eda Golebatmaz³ 

¹Beykoz University, Vocational School, Department of Medical Services and Techniques, Istanbul, 34805, Turkey

²Yildiz Technical University, Faculty of Chemistry and Metallurgy, Department of Bioengineering, Istanbul, 34210 Turkey

³Eskişehir Osmangazi University, Institute of Science and Technology, Department of Biology, Eskişehir, 26040, Turkey

Abstract: Every year, millions of tons of food and beverage waste are thrown away unused around the world. The carbohydrates found in food waste create a raw material potential for the production of high value-added products that are used in energy, feed and pharmacology. One of these products, 5-Hydroxymethyl-2-furfural (5-HMF), is a by-product of simple dehydration of carbohydrates. It finds wide use in the field of pharmacy due to its anticancer, antifungal and antimicrobial activities. Many studies have stated that the sugar source with the highest conversion rate in 5-HMF production is fructose. For this reason, in this study, it was aimed to realize the production of 5-HMF in autoclave sterilization carried out under high temperature and pressure using grape must waste, which is known to have high fructose content, and determine the anticarcinogenic activity and cytotoxicity of the produced 5-HMF under *in vitro* conditions. In this study, it was determined that the medium containing DMSO increased the sugar conversion percentage, 5-HMF efficiency and selectivity in the waste grape must more than the medium containing only water. In the production of 5-HMF, the conversion of sugar in the medium saturated with salt, and the efficiency and selectivity of 5-HMF were determined as 97.04%, 68.61% and 70.82%, respectively, when DMSO organic solvent was used. In addition, it has been determined that 5-HMF produced from waste grape must has a toxic effect on both healthy cells and cancer cells and has anticancer properties.

Keywords: 5-HMF, anticancer, grape must, fructose, DMSO.

Submitted: July 07, 2022. **Accepted:** January 01, 2023.

Cite this: Kelleci K, Golebatmaz E. Determination of the Anticarcinogenic Activity of 5-Hydroxymethyl-2-furfural Produced from Grape Must Under *in vitro* Conditions. JOTCSA. 2023;10(1):185-92.

DOI: <https://doi.org/10.18596/jotcsa.1142274>.

***Corresponding author. E-mail:** kubrakelleci@beykoz.edu.tr.

1. INTRODUCTION

It is known that approximately 931 million tons of food and drink are thrown away every year (1). Carbohydrates, which are found in large quantities in food waste, are a potential source of raw materials for the production of petrochemical products (2). Due to the fact that petrochemical products are decreasing day by day and the damage these products cause to nature, researchers have turned to the search for renewable energy sources (3) and it has been foreseen that furan derivatives such as 5-Hydroxymethyl -2-furfural (5-HMF) will be

one of the most important renewable energy sources in the future. According to the report prepared by the United States Department of Energy, 5-HMF and its oxidation products are among the 10 promising biomass-based products that are predicted to replace petroleum-derived products (4). In addition to being used as an energy source, it is also widely used in the synthesis of a wide range of products covering the food and pharmaceutical industries.

5-HMF is a by-product of the acid-catalyzed dehydration of simple carbohydrates (glucose,

fructose, xylose, etc.). The conversion of glucose and sucrose to 5-HMF was 60-70%, while the conversion of fructose to 5-HMF was found to be 100% (5,6). Therefore, the current industrial production process is based on the use of fructose (7). Although the market value varies according to the product quality and production process, it is known to be between 2-300 US dollars per kilogram (8). Considering that costs are also related to raw material access, the use of waste fructose instead of pure fructose will reduce costs, thus increasing access to 5-HMF and increasing its economic value (4). Therefore, in this study, 5-HMF production potential from grape must, which is known to have high fructose content, was investigated during autoclave sterilization under high temperature and pressure.

In addition, when literature studies were examined, it was reported that high levels of 5-HMF were detected in dried fruits and juices made from dried fruits (25-2900 mg/kg), as well as in caramel products (up to 9500 mg/kg). Bread (up to 410 mg/kg) and coffee (up to 420 mg/L) are also among the most important sources of human exposure to 5-HMF, although the levels in these foodstuffs are high (9,10). Estimated daily intake of 5-HMF is 30-150 mg per person (11); which is several times higher than the estimated daily intake of other heat-induced food toxicants such as acrylamide and furan (12,13).

In this study, it was aimed to obtain 5-HMF, which causes high human exposure due to food and beverage consumption, from grape must, which is known to have high fructose content, and to determine its anticarcinogenic activity and cytotoxic activity using LNCaP prostate cancer cell line and J774 murine macrophage cell line.

2. EXPERIMENTAL SECTION

2.1. Materials

99% purity DMSO (Dimethylsulfoxide; Sigma-Aldrich 276855) was used as the solvent. After the experimental study, 5-HMF, levulinic acid, formic acid analyzes were performed using Shimadzu LC-20AT HPLC device. Transgenomic Corogel 87H3 column was used for the analysis of 5-HMF, fructose and organic acids. Levulinic acid standard (Sigma-Aldrich 41474), formic acid standard (Sigma-Aldrich F0507), 5-hydroxymethyl-2-furfural (5-HMF) standard (Sigma-Aldrich H40807) were used for HPLC analysis. ISOLAB brand PTFE 0.45µm syringe filters were used for the filtration process applied before the analysis of the samples.

RPMI-1640 (Gibco 21875034), FBS (Fetal Bovine Serum; Sigma-Aldrich F7524), penicillin-streptomycin antibiotics (Sigma-Aldrich P4083), DMEM (Sigma-Aldrich D0822), Trypsin-EDTA solutions (Gibco 25200056) used in MTT analysis and cell culture studies to be used in anticarcinogenic activity and cytotoxicity of 5-HMF were purchased.

2.2. Production of 5-HMF from Grape Must

Grape must was preferred in the study due to its high fructose content. Studies have shown that the salt-saturated medium in 5-HMF production accelerates the transition of sugars to the organic phase after they are converted to 5-HMF in aqueous medium. Therefore, in this study, NaCl was used to prepare a saturated salt solution. Studies in the literature have shown that the use of organic solvents during production significantly increases the conversion rate of fructose from beverage wastes, 5-HMF efficiency and 5-HMF selectivity (14). Therefore, in this study, DMSO organic solvent, which is known to be used frequently in the literature, was used for the production of 5-HMF and the results were compared with the water environment where organic solvent was not used. The pH value of the experimental medium was fixed to 0.6 using HCl.

In the study, the volume of DMSO and grape must was determined as 76% and 24%, respectively. It was aimed to dehydrate the fructose to 5-HMF by exposing the samples taken in glass tubes at different concentrations for 3 hours in autoclave at 120°C. After completion of the reaction, the purity was checked by HPLC. All experiments were repeated 3 times. All chemical and organic solvents used in the study were of analytical purity (>99.5%) and were obtained from SIGMA.

2.3. HPLC Analysis

5-HMF sample and fructose analyzes were performed using SPD Detector SPD M-10A (Phenomenex; 50 x 4.6 mm; 5 µm particle size) HPLC (Shimadzu Liquid Chromatography) instrument with C18 column. It was carried out using acetonitrile and water (30:70 v/v) as mobile phase in isocratic mode with a UV wavelength of 320 nm, a flow rate of 0.6 mL/min. The samples were loaded into the HPLC device after passing through 0.45µm filters before analysis.

2.4. LNCaP and J774 Macrophage Cell Culture

The human prostate cancer (LNCaP; CRL1740™) cell line previously purchased from the American Culture Collection (ATCC) and stored in a cryobank was used in this study. Prostate cancer cells were inoculated in a 25 cm² culture dish containing 10% FBS, 1% penicillin-streptomycin antibiotic solution and 5 mL of DMEM, and incubated at 37°C under ambient conditions with 5% CO₂ and 95% humidity. The cells were refreshed every 2 days and monitored with an inverted light microscope. When the cell density reached 70-80%, they were transferred to a 75 cm² culture dish and the medium of the cells was refreshed every 2 days. Cell density and pollution were monitored using an inverted light microscope, and the continuity of the cell line was ensured by passage of cells until they were taken into the experiment.

LNCaP cells were exposed to 0.25% Trypsin-EDTA solution for 5 minutes. At the end of the time, it was checked under an inverted light microscope and it

was observed whether the cells were separated from the surface of the culture dish. The separated cells were transferred to a centrifuge tube containing 9 mL of medium and centrifuged at +10°C, 1200 rpm for 5 minutes. At the end of the time, the supernatant part in the centrifuge tube was discarded, and the cell pellet, which had settled to the bottom, was homogenized by pipetting with 2 mL of medium. The method of staining dead cells with Trypan Blue Dye (Sigma-Aldrich) was used to determine the cell number and percent viability. After counting the cells, the calculation was made as 1×10^4 live cells in 100 μ L of medium in each well, and inoculated into 96-well culture dishes. Culture dishes with 96 wells inoculated were incubated for 24 hours in a carbon dioxide incubator containing 5% CO₂ and 95% humidity at 37°C.

J774 murine macrophage cell line, T25 in RPMI-1640 broth containing 10% fetal bovine serum (FBS), 80 μ g/mL Gentamicin and 1 M HEPES in a humid atmosphere at 37°C, 95% humidity and 5% CO₂ cultured in culture flasks. After the cells reached the required confluency (80-90%), they were physically collected and centrifuged at 25°C, 1000 rpm for 5 minutes. Then, seeding was carried out in 96-well plates at 1×10^5 cells/ml per well. Cells inoculated into the culture media created were kept under the required incubation conditions for 24 hours. Macrophage cells are used to perform cytotoxicity assays. Cell growth was monitored daily with an inverted microscope.

2.5. Determination of Cytotoxic Concentrations

To determine non-toxic concentrations in J774 macrophage cells, in which LNCaP cells were used as hosts before 5-HMF components were used, 5×10^4 J774 macrophage cells were seeded into each well of a 96-well microplate and incubated at 37°C for 24 hours. After the macrophages adhered, 5 different concentrations of 5-HMF (5 μ g/mL, 10 μ g/mL, 25 μ g/mL, 50 μ g/mL and 100 μ g/mL), which were homogenized with (10%) DMSO/H₂O and sterilized by passing through a 0.20 μ m membrane filter, were diluted and added to the wells for another 24 hours. After 48 hours of incubation, MTT assay was performed on macrophage cells. 10 μ L of MTT solution with a final concentration of 10 mg/mL in PBS was transferred to each well of the microplate and cells were incubated for 4 hours at 37°C to form formazan crystals due to the reaction between MTT salt and viability dehydrogenase enzymes. Then, 100 μ L of DMSO was added to each well to dissolve the formazan crystals. Absorbance values were measured at 570 nm using an ELISA reader. All studies were performed in 3 replicates.

Cell viability analysis data were obtained using equation 1 and data plots were generated.

$$\text{Cell viability (\%)} = \frac{\text{Abs of sample} \times 100}{\text{Abs of control}} \quad (1)$$

2.6. Statistical Analysis

Obtained data were calculated as mean \pm standard deviation. For statistical analysis, parametric tests (Unpaired sample t-test, analysis of variance and Mann-Whitney U test) were used using the "SPSS 16.0 for Windows" program. Significance level was accepted as 5%.

3. RESULTS AND DISCUSSION

3.1. HPLC analysis

In this study, in which 5-HMF production potential from grape must was investigated during autoclave sterilization under high temperature and pressure, it was determined that the reducing sugar content in the grape must waste used in the experiments was 16.4%. In this study, it was determined that the medium containing DMSO increased the sugar conversion percentage, 5-HMF efficiency and selectivity in the waste grape must more than the medium containing only water. In the production of 5-HMF, the conversion of sugar in the medium saturated with salt, and the efficiency and selectivity of 5-HMF were determined as 97.04%, 68.61% and 70.82%, respectively, when DMSO organic solvent was used, while the values obtained in the medium containing only water were 68.13%, 45.04% and it was determined as 63.27%. Chromatogram graphs obtained from HPLC analyzes are given in Appendix 1, and 5-HMF calibration chart is given in Appendix-2. In addition, HPLC chromatogram images of levulinic acid and formic acid standards are given in Appendix- 3 and Appendix -4.

3.2. Toxicity Study

The cytotoxic effects on the J774 macrophage cell line were investigated. No significant cytotoxicity was detected at low concentrations in the study ($p < 0.05$). It has been observed that it has an inhibitory effect in direct proportion with increasing concentrations. To investigate the survival percentages of LNCaP cells, MTT cellular viability assay was performed after 24 hours of incubation. It has been shown that 5-HMF is not very toxic to macrophage cells compared to LNCaP cells. According to the results of cytotoxicity and anti-cancer activity, viable cell ratios are shown in the graphs. When the J774 macrophage cell toxicity results were compared with the control cell, it was observed that 5-HMF did not cause toxicity at concentrations up to 10 μ g.

According to the results of J774 cytotoxicity in Figure 1, it was seen that the most effective concentration increasing cell proliferation was at 5 μ g/mL. It was observed that toxicity occurred in the cells with increasing concentrations from 25 μ g/mL. The anticancer effect due to the increasing concentration of 5-HMF for 24 hours was examined in LNCaP cells and the effect levels are given in Figure 2. The anti-cancer effects of 5-HMF on LNCaP cells, whose toxicity was measured with J774 cells, were compared with control cells. As shown in the graph of the results in Figure 2, an anti-cancer effect was observed from 10 μ g/mL with increasing

concentrations. The most effective anti-cancer activity occurred at 100 $\mu\text{g}/\text{mL}$, and it was seen that it affected more than half of the LNCaP cells.

Toxicity studies were performed on 5-HMF obtained after experimental studies, both on J774 cells and on LNCaP cells, and it was determined to be anticancer.

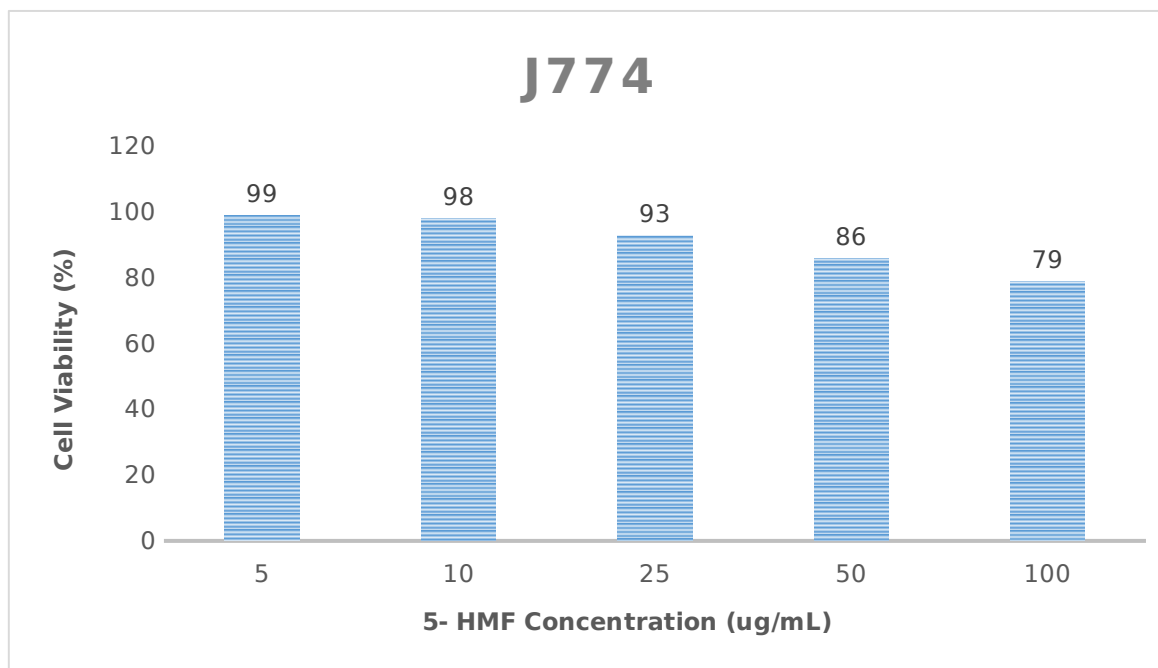


Figure 1: Decreased cell viability with increasing 5-HMF concentration in J774 macrophage cells.

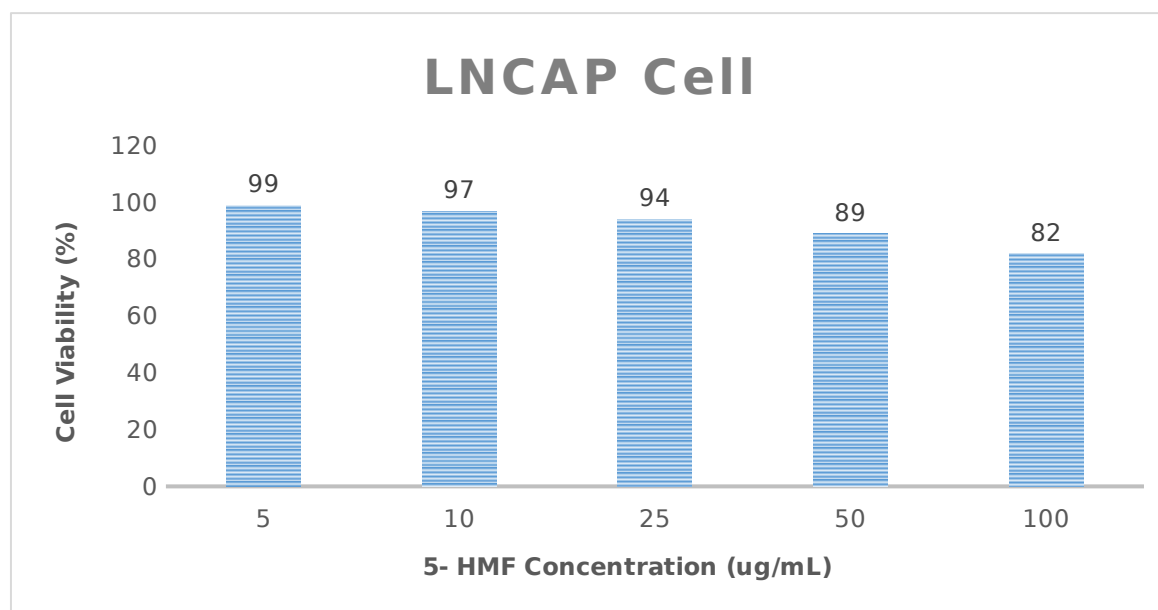


Figure 2: Decreased cell viability with increasing 5-HMF concentration in LNCaP cells.

4. CONCLUSION

In this study, the production potential and anticarcinogenic effect of 5-HMF from grape must waste, which is known to have high fructose content, was investigated under in vitro conditions. In the study, DMSO was used as an organic solvent in order to increase the productivity of the product, since 5-HMF decomposes at high temperatures, in acidic and aqueous environments, and turns into

levulinic acid and formic acid. It is known that DMSO is frequently used in previous studies on 5-HMF production (6). In addition, it has been revealed by the studies that the experimental medium saturated with salt in the production of 5-HMF accelerates the transition of sugars to the organic phase after conversion to 5-HMF in aqueous medium. In our study, it was determined that DMSO organic solvent significantly increased the sugar conversion percentage, 5-HMF efficiency and selectivity in the

waste grape must compared to the medium containing only water. Previous studies in the literature support our results (6).

Toxicity studies of 5-HMF produced during autoclave sterilization with waste grape must were carried out in both healthy cells and cancer cells and its anticancer activity was determined. J774 murine macrophage cell line was used for healthy cells and LNCaP prostate cancer cell line was used for carcinogen cells.

According to the data obtained from the studies, it was found that the highest 5-HMF concentration, 100 µg/mL, caused damage to both cell lines. At this concentration, there was also a moderate but statistically significant reduction in cell viability in all cell lines. It has been determined that 5-HMF also causes significant cell death at lower concentrations. Therefore, it has been found that 5-HMF obtained after experimental studies has a toxic effect and is anticancer in both healthy cells and cancer cells.

This study is one of the limited studies on the production of 5-HMF from food and beverage wastes in our country and the determination of its anticancer activity. It provides important data and is a source for the studies to be done on the production and analysis methods we use in this study and the optimization of 5-HMF production methods. It is important to investigate the effects on yield by using different ionic solvents and different catalysts in 5-HMF production by researchers. It is also recommended to test the anticancer activity under in vivo conditions.

5. CONFLICT OF INTEREST

The authors report no conflicts of interest.

6. REFERENCES

1. Rajendran N, Han J. Integrated polylactic acid and biodiesel production from food waste: Process synthesis and economics. *Bioresource Technology*. 2022 Jan;343:126119. Available from: [<URL>](#).
2. Yu IKM, Ong KL, Tsang DCW, Haque MA, Kwan TH, Chen SS, et al. Chemical transformation of food and beverage waste-derived fructose to hydroxymethylfurfural as a value-added product. *Catalysis Today*. 2018 Sep;314:70-7. Available from: [<URL>](#).
3. Twidell J. *Renewable Energy Resources* [Internet]. 4th ed. London: Routledge; 2021 [cited 2023 Feb 4]. Available from: [<URL>](#)
4. Kazi FK, Patel AD, Serrano-Ruiz JC, Dumesic JA, Anex RP. Techno-economic analysis of dimethylfuran (DMF) and hydroxymethylfurfural (HMF) production from pure fructose in catalytic processes. *Chemical Engineering Journal*. 2011 May;169(1-3):329-38. Available from: [<URL>](#).
5. He Q, Lu Y, Peng Q, Chen W, Fan G, Chai B, et al. Synthesis of 5-hydroxymethylfurfural from fructose catalyzed by sulfonated carbon-based solid acid. *Biomass Conv Bioref* [Internet]. 2021 Sep 4 [cited 2023 Feb 4]; Available from: [<URL>](#)
6. Rosatella AA, Simeonov SP, Frade RFM, Afonso CAM. 5-Hydroxymethylfurfural (HMF) as a building block platform: Biological properties, synthesis and synthetic applications. *Green Chem*. 2011;13(4):754. Available from: [<URL>](#).
7. Kläusli T. AVA Biochem: commercialising renewable platform chemical 5-HMF. *Green Processing and Synthesis*. 2014 Jun 1;3(3):235-6. Available from: [<URL>](#).
8. Yu IKM, Tsang DCW, Yip ACK, Chen SS, Wang L, Ok YS, et al. Catalytic valorization of starch-rich food waste into hydroxymethylfurfural (HMF): Controlling relative kinetics for high productivity. *Bioresource Technology*. 2017 Aug;237:222-30. Available from: [<URL>](#).
9. Husøy T, Haugen M, Murkovic M, Jöbstl D, Stølen LH, Bjellaas T, et al. Dietary exposure to 5-hydroxymethylfurfural from Norwegian food and correlations with urine metabolites of short-term exposure. *Food and Chemical Toxicology*. 2008 Dec;46(12):3697-702. Available from: [<URL>](#).
10. Murkovic M, Pichler N. Analysis of 5-hydroxymethylfurfural in coffee, dried fruits and urine. *Mol Nutr Food Res*. 2006 Sep;50(9):842-6. Available from: [<URL>](#).
11. Janzowski C, Glaab V, Samimi E, Schlatter J, Eisenbrand G. 5-Hydroxymethylfurfural: assessment of mutagenicity, DNA-damaging potential and reactivity towards cellular glutathione. *Food and Chemical Toxicology*. 2000 Sep;38(9):801-9. Available from: [<URL>](#).
12. Svensson K, Abramsson L, Becker W, Glynn A, Hellenäs KE, Lind Y, et al. Dietary intake of acrylamide in Sweden. *Food and Chemical Toxicology*. 2003 Nov;41(11):1581-6. Available from: [<URL>](#).
13. Morehouse KM, Nyman PJ, McNeal TP, DiNovi MJ, Perfetti GA. Survey of furan in heat processed foods by headspace gas chromatography/mass spectrometry and estimated adult exposure. *Food Additives & Contaminants: Part A*. 2008 Mar;25(3):259-64. Available from: [<URL>](#).
14. Román-Leshkov Y, Dumesic JA. Solvent Effects on Fructose Dehydration to 5-Hydroxymethylfurfural in Biphase Systems Saturated with Inorganic Salts. *Top Catal*. 2009 Apr;52(3):297-303. Available from: [<URL>](#).

Supplementary Information

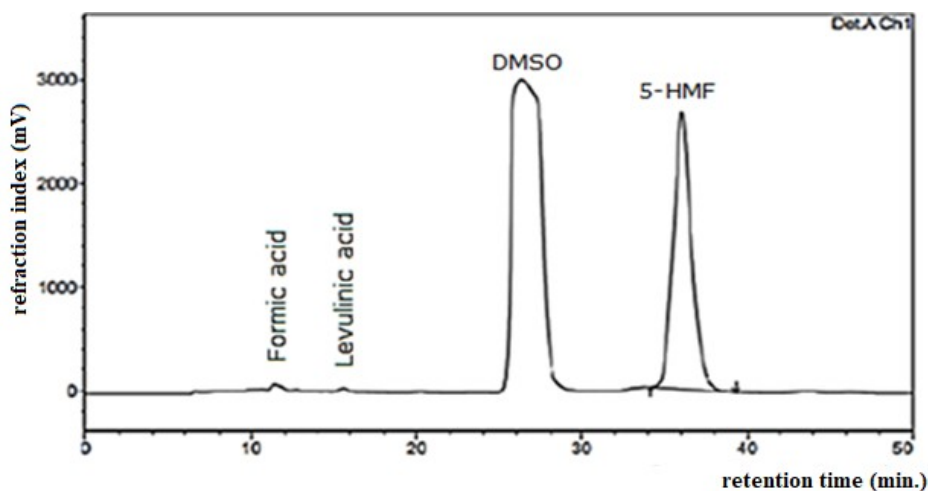
Determination of the Anticarcinogenic Activity of 5-Hydroxymethyl-2-furfural Produced from Grape Must Under *in vitro* ConditionsKubra Kelleci^{1,2*} , Eda Golebatmaz³ ¹ Beykoz University, Vocational School, Department of Medical Services and Techniques, Istanbul, 34805, Turkey² Yıldız Technical University, Faculty of Chemistry and Metallurgy, Department of Bioengineering, Istanbul, 34210 Turkey³ Eskişehir Osmangazi University, Institute of Science and Technology, Department of Biology, Eskişehir, 26040, Turkey

Figure S1: Chromatogram for HPLC Analysis.

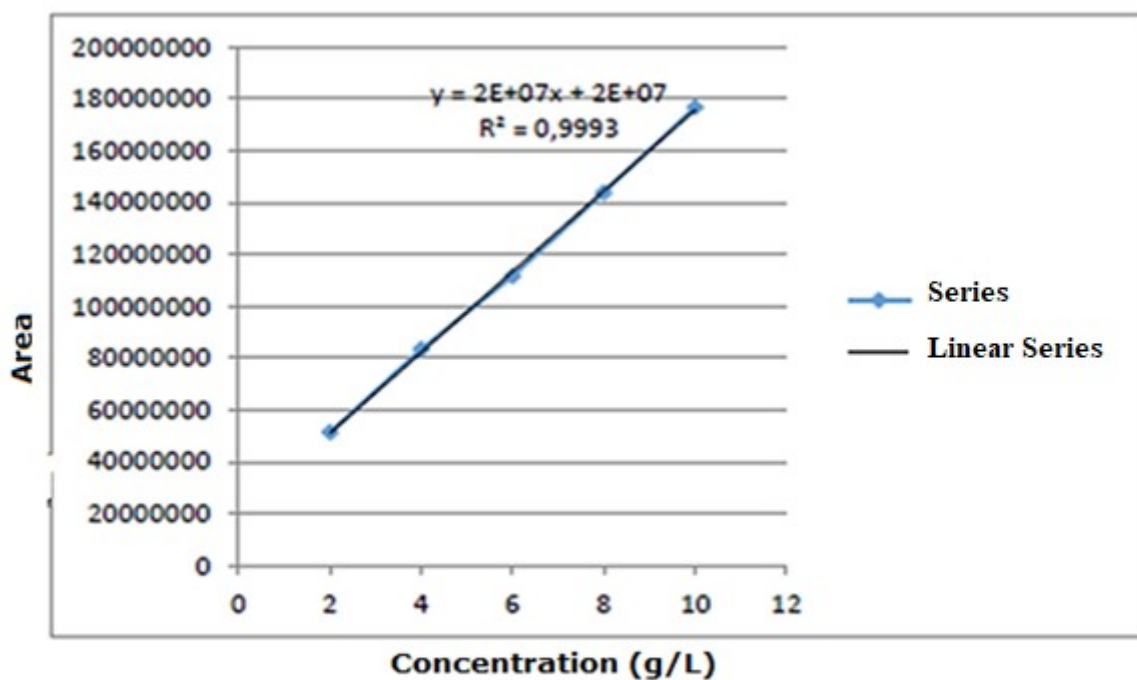


Figure S2: 5-HMF calibration graph.

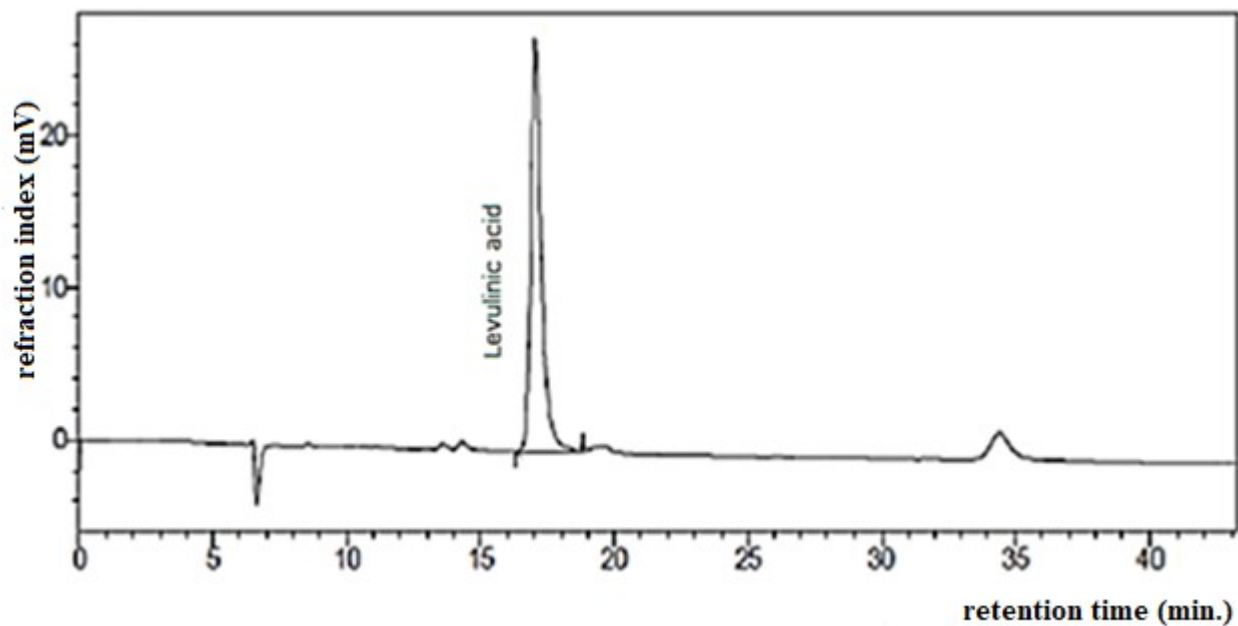


Figure S3: Chromatogram of Levulinic acid

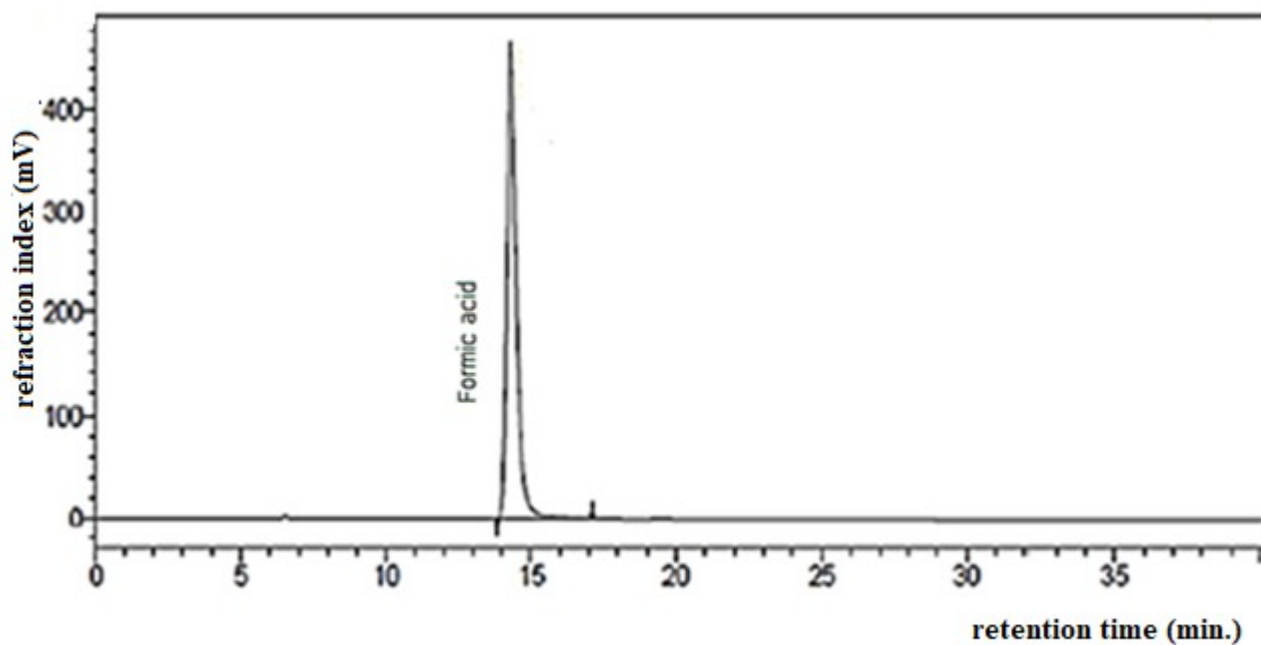


Figure S4: Chromatogram of Formic acid.



Novel Green Method for the Spectrophotometric Determination of Metoclopramide Hydrochloride in Pharmaceutical Formulations

Ghufran A. Alhammadi^{1,2*} , Lamy A. Sarsam² 

¹University of Mosul, Department of Chemistry, College of Science, Mosul, Iraq.

²College of Science, University of Mosul, Department of New and Renewable Energies, Mosul, Iraq.

Abstract: A less environmentally harmful reagent, 2-tert-Butyl-4-methoxyphenol (BHA), is used to evaluate Metoclopramide hydrochloride (MCP.H) by simple, rapid, sensitive, accurate and precise spectrophotometric method, through azo coupling reaction between metoclopramide hydrochloride medicine and its pharmaceutical preparation by utilizing BHA as a reagent, (MCP.H) azo-dye formed shows the higher absorption peak at 504 nm. Absorbance-concentration relation is linear over the range from 20 to 280 $\mu\text{g} / 5 \text{ mL}$, (i.e. 4-56 ppm) with a good sensitivity (molar absorptivity $0.26 \times 10^4 \text{ L} \cdot \text{mol}^{-1} \cdot \text{cm}^{-1}$); good precision (RSD better than 0.844 %) and high accuracy (relative error less than + 0.4%), Sandell's sensitivity index is $-0.1293 \mu\text{g} \cdot \text{cm}^{-2}$, the calculated limit of detection (LOD) is $0.0658 \mu\text{g/mL}$ and the evaluated limit of quantitation (LOQ) is $0.2193 \mu\text{g/mL}$. The application has had successful results for the assay of metoclopramide hydrochloride in dosage forms of tablets and injection.

Keywords: Butylated hydroxyanisole, metoclopramide hydrochloride, spectrophotometry friendly environment.

Submitted: August 05, 2022. **Accepted:** January 04, 2023.

Cite this: Alhammadi GA, Sarsam LA. Novel Green Method for the Spectrophotometric Determination of Metoclopramide Hydrochloride in Pharmaceutical Formulations. JOTCSA. 2023;10(1):193-204.

DOI: <https://doi.org/10.18596/jotcsa.1158403>.

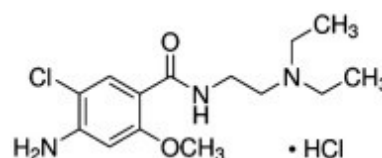
***Corresponding author. E-mail:** lamyasarsam@uomosul.edu.iq.

1. INTRODUCTION

Metoclopramide hydrochloride (MCP.H), [4-amino-5-chloro-N-[2-diethylaminoethyl]-2-methoxybenzamide hydrochloride], (Sketch 1), is used as an anti-vomiting agent in the treatment of certain types of queasiness and emetic as well as to increase gastrointestinal motility (1). Oral forms of the drug are rapidly absorbed in the gastrointestinal tract, therefore they are not suitable for administration to children or elderly patients after surgery, as vomiting is often performed before absorption in the gastrointestinal tract (2). Taking the medicine causes some side effects, including dry mouth, insomnia, and changes in arterial blood pressure (3).

A survey of the literature reported that metoclopramide hydrochloride was estimated under optimal conditions by different spectrophotometric methods and using various chemical reagents, such as: azo-dye coupling (3-11), oxidative coupling (12-14), Schiff base Reaction (15), and charge transfer complex (16). A number

of researchers were able to estimate (MCP.H) by using other spectrophotometric methods such as UV, colored ion-pair complex, oxidation, reduction reaction and nucleophilic substitution reaction, in the presence of chemical reagents and under various optimal condition (17-20), diverse HPLC methods (21-25), Fluorescent analysis (26), and Glassy carbon electrode (GCE) were also used (27).



Sketch 1: $\text{C}_{14}\text{H}_{23}\text{Cl}_2\text{N}_3\text{O}_2 \cdot \text{HCl}$ M.wt. = 336.26 g/mol.

Currently, the recent methodological development in analytical chemistry gave rise to a plethora of improved and durable versions of an environmentally friendly approach (28), some of these concepts are safe compounds (29). As a result, this study describes a simple, sensitive and environ-

mentally friendly spectrophotometric method for assay of (MCP.H), using 2-tert-Butyl-4-methoxyphenol (BHA), a synthetic antioxidant as a safer reagent. (30).

2. EXPERIMENTAL

2.1 Apparatus

A JASCOV-630 UV-VIS (Tokyo, Japan) double beam spectrophotometer was used for all spectral and absorbance measurements with matched of 1.0 cm path length glass cells. ABS 120-4 Kern & Sohn GmbH used for weighing the samples.

2.2. The reagents

All the reagents used were of analytical-reagent grade. MCP.H stock standard solution 500 $\mu\text{g/mL}$: prepared by dissolving 0.05 g of pure MCP.H (NDI-Iraq) in distilled water and diluting to the marked in 100 mL volumetric flask using the same solvent. The stock solution was properly diluted to create the working solution 200 $\mu\text{g/mL}$. The prepared solutions were transferred to a dark bottle and kept in a cooled place which are stable for one month at least.

Sodium nitrite stock solution 1×10^{-2} M: was prepared by dissolving 0.0690 g of sodium nitrite in distilled water and diluting to the mark into a 100 mL volumetric flask. The stock solution was properly diluted to create 5.94×10^{-4} M working solution.

Butylated hydroxyanisole (BHA) reagent solution 5.54×10^{-4} M : was prepared by dissolving 0.0101 g of reagent (Miavit / Germany) in distilled water and

diluting to the marked in 100 mL volumetric flask. The produced solutions, which can be used for at least two weeks, were transferred to a dark bottle and kept in a cool location.

2.2.1. MCP.H Tablet solution (200 $\mu\text{g} / \text{mL}$)

The average weight of 10 Metoclopramide tablets Bp 10 mg (Flamingo Pharma, UK), was ground and mixed well. A portion of this powder, equivalent to 0.0200 g, accurately weighed. then was dissolved in warm distilled water and filtered it, the residue was washed and the same of solvent completed to the mark 100 mL in volumetric flask.

2.2.2. Injection solution (200 $\mu\text{g} / \text{mL}$)

Using a 100 mL volumetric flask, 4 mL of METOCOL Injection 10 mg/ 2 mL (Pioneer, Iraq) were taken, and the volume was then increased to the proper amount with distilled water.

2.2.3. General procedure for calibration

In a series of 5 mL calibrated flasks, an aliquot of a standard solution (200 $\mu\text{g/mL} = 5.94 \times 10^{-4}$ M) containing 0.1-1.4 mL of MCP.H was added. Equimolar sodium nitrite solution (5.94×10^{-4} M) was added to this solution, and 0.2 mL of a 1 M hydrochloric acid solution was used to correct the pH. The mixture was vigorously shaken, wait for 5 minutes to complete the diazotization step. Then, 1 mL of BHA (5.54×10^{-4} M) and 0.25 mL of 0.5 M sodium carbonate solutions were added. The mixture was thoroughly mixed and waited for between 2- 5 minutes before being diluted to the proper concentration with distilled water. The colored azo dye's absorbance at 504 nm against the equivalent reagent.

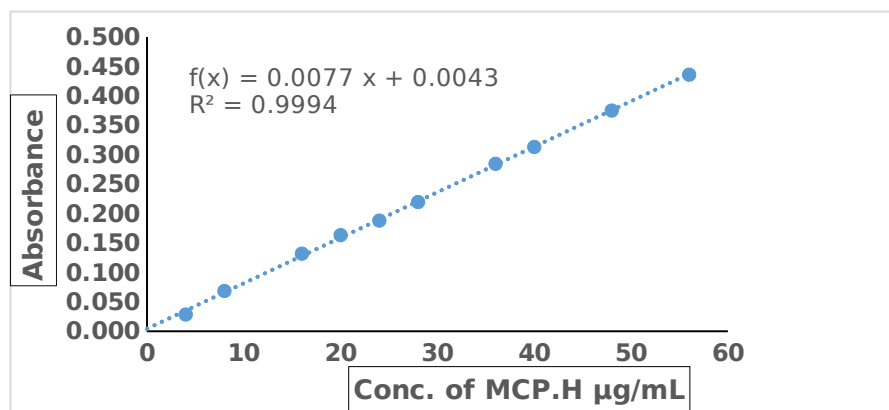


Figure 1: Standard curve for estimating MCP.H.

Figure 1 shows a good linearity over the range of the concentration between 4 to 56 $\mu\text{g/mL}$ with good sensitivity in which that the molar absorptivity is 0.26×10^4 L / mol.cm and sensitivity index of Sandell is $0.1293 \mu\text{g/cm}^2$.

3. RESULTS AND DISCUSSION

3.1. Study of the optimum conditions

3.1.1. Choosing of the acid

A number of different acids with the concentration of 1.0 M and an amount of 0.25 mL was used in this study. The results are shown in Table 1. As shown in Table 1. the maximum intensity of the colored product's absorptions occurs when 1 M hydrochloric acid is fixed in the following experiments.

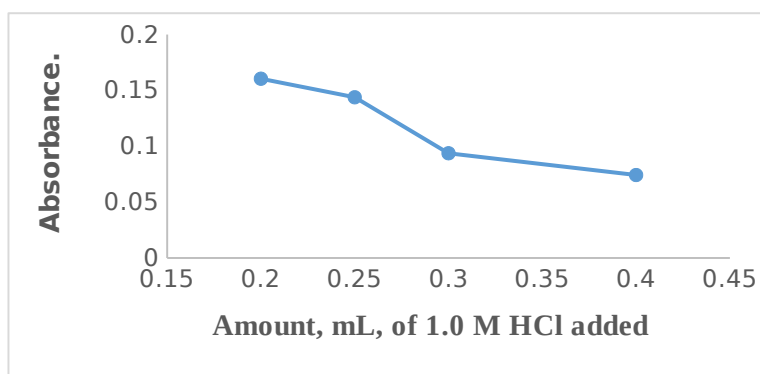
Table 1: Choosing the appropriate acid type.

Type of acid	λ_{\max}	Absorbance
H ₃ PO ₄	509	0.1304
HCl	504	0.1502
H ₂ SO ₄	508	0.0989
HNO ₃	Turbid	Turbid
CH ₃ COOH	510	0.0723

3.2. Effect of Different Volumes of 1 M Hydrochloric Acid Solution

Different volumes (0.1-0.4 mL) of 1.0 M hydrochloric acid were added to the reaction medium 5 mL volumetric flask. Figure 2 found that

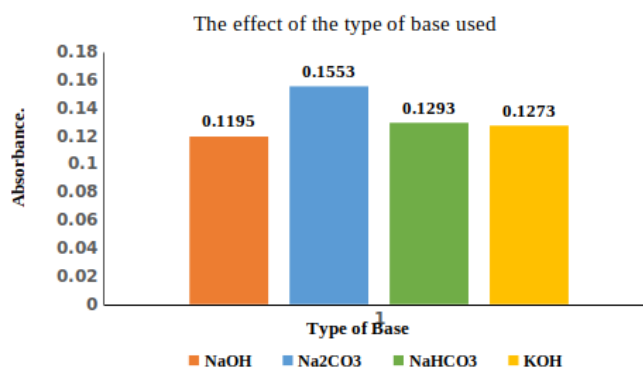
0.1 mL was turbid, and after 0.2 mL of hydrochloric acid the absorbance of the colored azo dye product decreases with the increase of acid amount added. So 0.2 mL of 1 M hydrochloric acid was chosen.

**Figure 2:** Effect of different volumes of 1 M hydrochloric acid solution.

3.3. Choosing the Base

Several alkaline solutions (potassium hydroxide, sodium bicarbonate, sodium carbonate and sodium hydroxide) with a concentration of 0.5 M were

investigated. Sodium carbonate was choice which considered as a best alkaline medium for producing maximal absorbance of the red azo dye and was chosen. Figure 3 illustrates the results.

**Figure 3:** Choosing the appropriate of base type.

3.4. Effect of Different Amount of 0.5 M Sodium Carbonate

Different volumes (0.1 - 0.5 mL) of 0.5 M sodium carbonate solution were added to the reaction

medium, Figure 4 found that 0.5 mL was turbid and 0.3 mL was enough to obtain the maximum absorbance, which was utilized in all future studies.

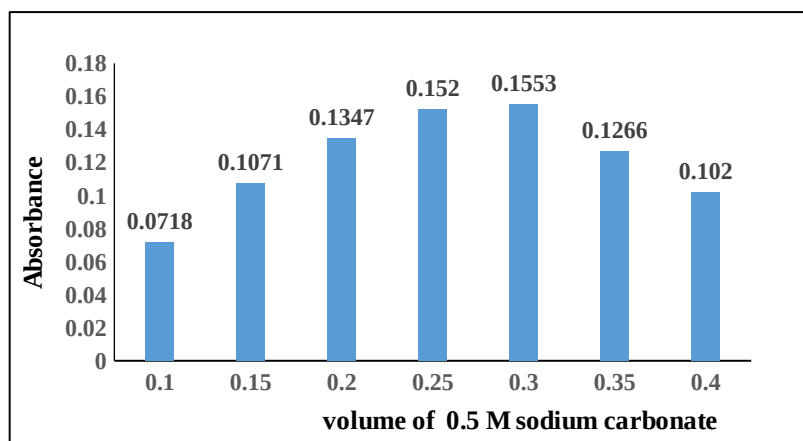


Figure 4: Effect of different amount of 0.5M sodium carbonate.

3.5. Effect of BHA Reagent Amount

The effect of changing volumes 0.5-1.5 mL of 5.54×10^{-4} M BHA coupling agent, studied against different concentrations of MCP.H, which was evident that the absorbance increases with

increasing BHA concentration, the determination coefficient of measured absorbances has been evaluated. Table 2 shows that 1 mL of 5.54×10^{-4} M of the coupling agent solution gives the best results.

Table 2: Effect of BHA reagent amount.

mL of 5.54×10^{-4} M reagent	Absorbance / μg of MCP.H						R^2
	36	32	28	24	20	12	
0.5	0.237	0.236	0.212	0.176	0.148	0.093	0.9702
0.75	0.266	0.249	0.215	0.176	0.147	0.097	0.9915
1.0	0.287	0.251	0.224	0.189	0.155	0.094	0.9991
1.25	0.286	0.243	0.221	0.188	0.159	0.099	0.9961
1.5	0.286	0.246	0.221	0.181	0.152	0.094	0.9964

3.6. Study of the Effect of Surfactants

1 mL of anionic sodium dodecyl sulfate (SDS), cationic cetylpyridinium chloride (CPC), cetyl trimethyl ammonium bromide (CTAB), and neutral iso-octylphenoxy-poly ethoxy ethanol (Triton X-100) were used to examine the impact of surfactants on absorption intensity. The use of surfactant was disregarded because the inclusion of SDS resulted in turbid solution and the addition of CPC reduces absorption intensity, while the addition of CTAB and Triton X-100 had no effect on absorption intensity.

3.7. Study of the Effect of Temperature

The effect of different temperature between 0°C to 40°C was studied, on the diazotization and coupling reaction show that the absorbance of the azo dye remains constant in the 25°C but decrease at lower than room temperature and higher than 30°C . Therefore, it has been recommended to carry out reaction at room temperature (25°C).

3.8. Stability of the Azo Dye Product

Following the mixing of the chemicals, the stability of the colored dye was investigated for 1 hour using 20 and 40 g/mL shows that the colored product maintains its stability for at least 55 minutes. See Table 3.

3.9. Final Absorption Spectrum

The BHA-MCP.H product's absorption spectra were plotted under the optimum reaction conditions obtained in Fig. 5 that a reddish orange colored compound had a maximum absorption at 504 nm versus blank.

Table 3: Stability of the azo dye product.

Time, min	Absorbance / μg of DMCPH per mL	
	20	40
0	0.1638	0.3113
5	0.1644	0.3077
10	0.1646	0.3053
15	0.1632	0.3085
20	0.1615	0.3062
25	0.1628	0.3056
30	0.1604	0.3057
35	0.1593	0.3059
40	0.1586	0.3046
45	0.1588	0.3019
50	0.1575	0.2998
55	0.1560	0.2965
60	0.1553	0.2967

3.10. Accuracy and Precision of the Suggested Method

The accuracy and precision of the suggested method were tested by analyzing of three different concentration (20, 36, 48) $\mu\text{g/mL}$ with four

replicates. The low relative error and low percentage relative standard deviation were summarized in Table 4. These values indicate the high accuracy and precision of the proposed method.

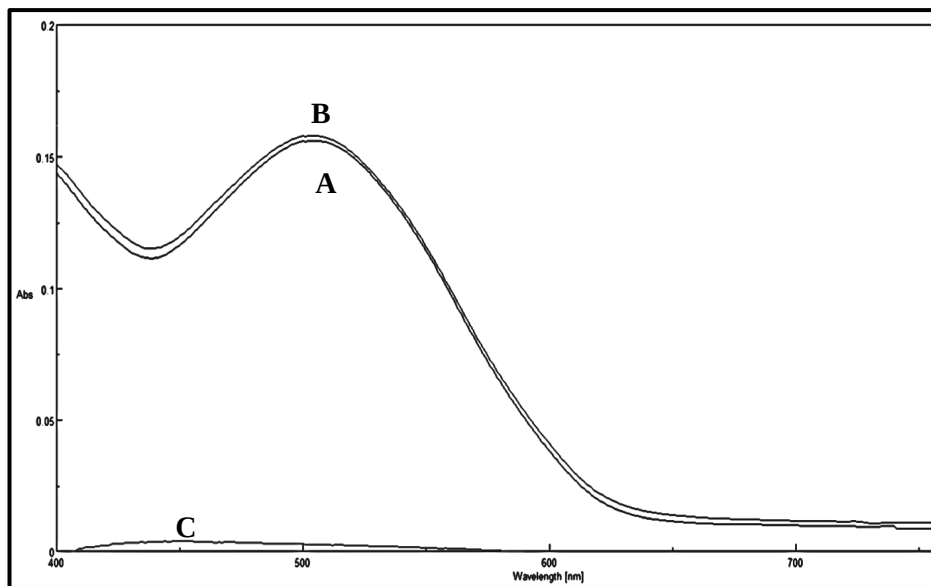


Figure 5: Final Absorption of spectra of (A) MCP.H (20 $\mu\text{g/mL}$) with BHA versus blank and (B) MCP.H with BHA versus distilled water (C) Blank versus distilled water.

Table 4: Accuracy and precision of the suggested method.

Amount of MCP.H $\mu\text{g/mL}$	Recovery, %*	Relative error, %*	Relative standard deviation, %*
20	100.12	+0.12	0.902
36	99.09	- 0.90	1.08
48	99.63	- 0.36	0.551

*Average of four determinations.

3.11. The Nature of the Dye

The stoichiometry of the product was studied applying the continuous variation method (Job's method). The results obtained in Figure 6 shows

that a 2:1 azo dye was formed between diazotized MPC.H and BHA. The scheme below shows the proposed mechanism for the azo dye structure.

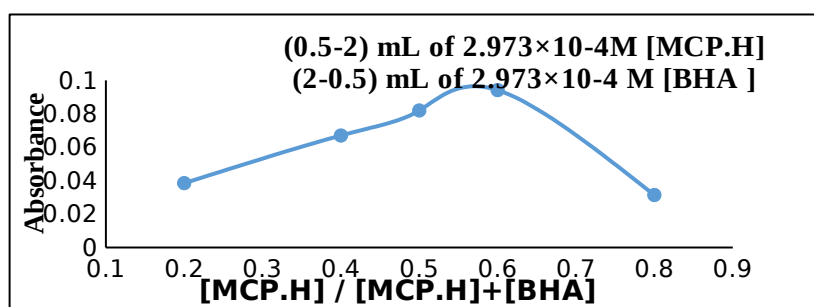
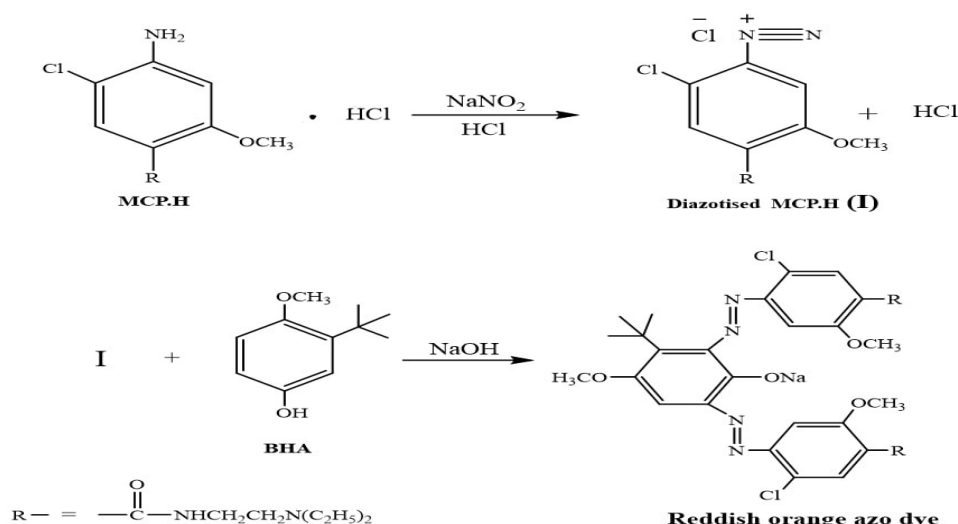


Figure 6: Continuous variation method.



Scheme 2: The suggested mechanism for MCP.H and BHA azo dye.

The azo dye's stability constant in aqueous solution was calculated and found to be 3.0379×10^{12} (31).

Table 5: Summary of optical characteristics and statistical data for the proposed method.

Parameter	Optimum conditions
Reagent	BHA
Linearity range, ($\mu\text{g mL}^{-1}$)	4-56
Molar absorptivity, ($\text{L}\cdot\text{mol}^{-1}\cdot\text{cm}^{-1}$)	0.26×10^4
Sandel's Index, ($\mu\text{g}\cdot\text{cm}^2$)	0.1293
λ_{max} , (nm)	504
Acid	HCl
Base	Sodium carbonate
LOD, ($\mu\text{g}\cdot\text{mL}^{-1}$)*	0.0658
LOQ, ($\mu\text{g}\cdot\text{mL}^{-1}$)*	0.2193
Average recovery, (%)**	99.6
RSD**	0.844
Correlation coefficient	0.9994
Medium	Aqueous
Solvent	Water

* Average of ten determinations.

**Average of four determinations of blank.

3.12. Effect of Interferences

Table 6 visions the effects of a few typical excipients associated with MCP.H in pharmaceutical preparations. The study shows that these additives has no negative effects on the efficiency of the suggested procedure.

3.13. Application Part

In order of demonstrate the applicability of the suggested method to the determination of MCP.H, on the form of tablets and injections, with three different concentrations, the results are summarized in Table 7. The assay results were indicating a good applicability of the of proposed method.

Table 6: Effect of excipients for MCP.H assay.

Excipients (1000 $\mu\text{g/mL}$)	Recovery (%) of 20 $\mu\text{g/ mL}$ MCP.H per $\mu\text{g/ mL}$ of excipient added		
	50	100	300
Lactose	98.59	100.51	101.3
Glucose	99.23	99.62	100.64
Starch	100.26	101.73	100.06

Table 7: Assay of MCP.H in pharmaceutical preparations using the proposed method.

$\mu\text{g MCP.H / mL}$	SDZ Present (μg)	SDZ Found (μg)	Relative Error (%) *	Recovery (%) *	RSD (%) *
Metoclopramide tablets Bp 10 mg (Flamingo pharma, UK)	20	20.16	0.826	100.82	1.40
	36	35.97	-0.052	99.94	0.80
	48	48.09	+0.219	100.2	1.06
METOCOL Injection 10 mg / 2 mL (Pioneer, Iraq)	20	20.04	+0.244	100.24	1.29
	36	36.12	+0.360	100.36	0.22
	48	47.83	-0.339	99.66	0.74

*Average of four determinations.

3.14. Evaluation of the proposed method's results

To elucidate that there is no interference with the additives employed in the pharmaceutical manufactures, the drug content of tablet and injection preparations was also estimated using the standard addition method, for 20 and 32 ppm of

the two MCP.H pharmaceutical preparations solution separately and adding various concentrations of the standard MCP.H solution under the condition that the maximum extent of the estimate in the calibration curve is not override. Figure 7A,B and Table 8 shows the results (32).

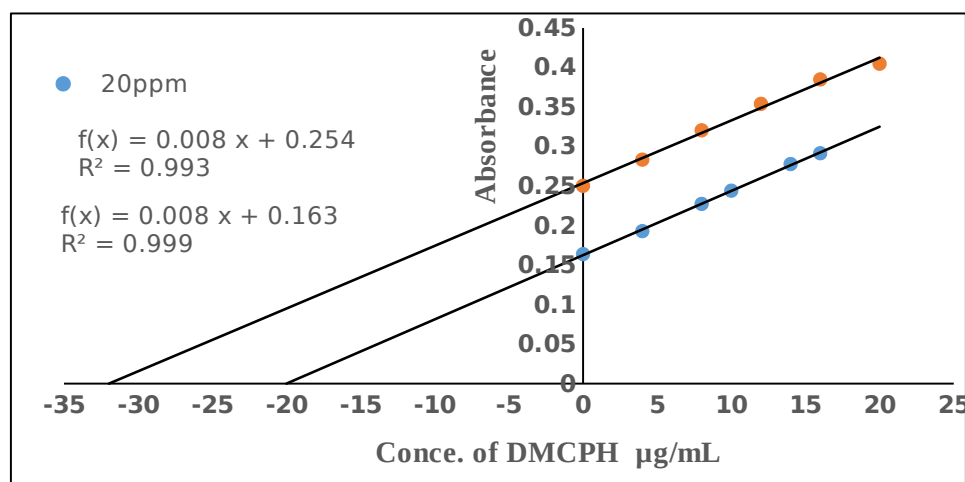


Figure 7A: Plot of standard addition method to estimate MCP.H in tablet.

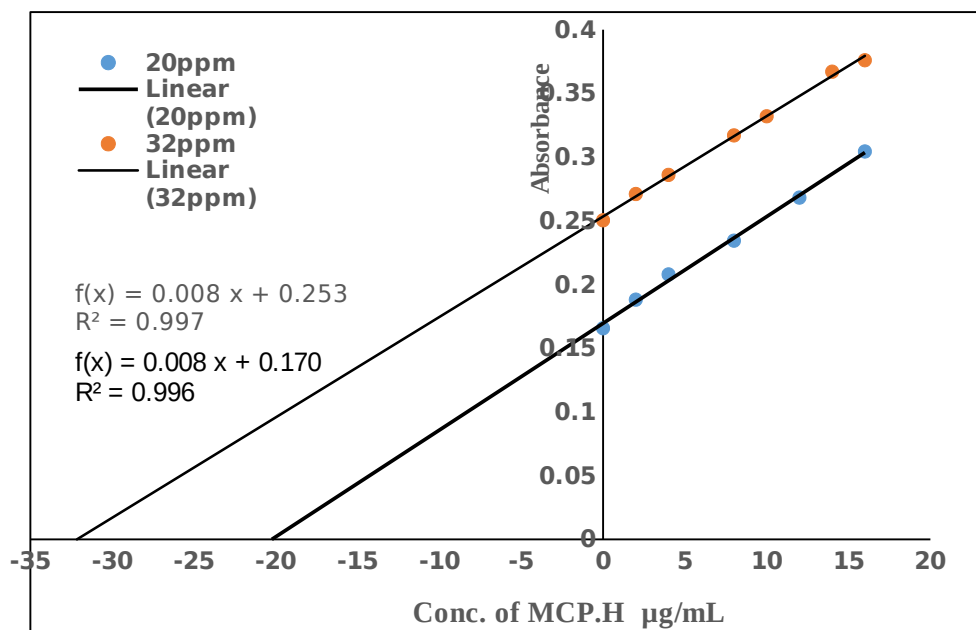


Figure 7B: Plot of standard addition method to estimate MCP.H in injection.

Table 8: Standard addition method to estimate MCP.H.

Pharmaceutical preparation	MCP.H Present (µg)	MCP.H measured (µg)	Recovery (%)*	Relative error, %*
METOCOL Injection 10 mg / 2 mL (Pioneer, Iraq)	20	20.17	100.85	+ 0.85
	32	32.07	100.22	+ 0.22
Metoclopramide tablets Bp 10 mg (Flamingo pharma, UK)	20	20.06	100.30	+ 0.30
	32	32.17	100.35	+ 0.35

*Average of four determinations.

3.15. Statistical Agreement t-test

The present method and the British Pharmacopeia one (based on potentiometric titration of pure medication with 0.1 M sodium hydroxide) at the 95 percent confidence level with 4 degrees of freedom were applied simultaneously for the t-test calculation (33). The value was compared with statistical Tables for four degrees of freedom at 95

percent validation level. The estimated t-test value (1.1255) was below the threshold of $t_{2.776} = (n_1 + n_2 - 2 = 2)$. These are confirming that, in terms of precision and accuracy in the determination of MCP.H in tablets, there are no appreciable discrepancies between the suggested approach and British Pharmacopeia's method.

Table 9: Comparison of the suggested method with the literature's method.

Parameters	Present method	Literature method Ref. #34
Reagent	BHA	p-Nitroaniline
λ_{max} , (nm)	504	513
Temperature °C	Room Temp.	Room Temp.
Medium	Aqueous	Aqueous
Linearity range, ($\mu\text{g mL}^{-1}$)	4-56	0.2-25
Molar absorptivity, L / mol.cm)	0.26×10^4	0.23×10^4
Sandell's Index, ($\mu\text{g.cm}^2$)	0.1293	0.1462
Nature of dye product Drug: Reagent	2:1	1:1
Average recovery,(%)	99.6	----
LOD, ($\mu\text{g.mL}^{-1}$)	0.0658	0.182
LOQ, ($\mu\text{g.mL}^{-1}$)	0.2193	0.553
Color of azo dye	Reddish-orange	Red
Application of the method	Tablet & Injection	Tablet & Injection

The results are shown in Table 9. The proposed method is not less important, of higher quality, and more sensitive than methods found in the literature. It does not require organic solvents; it can also be used to prepare pharmaceuticals with satisfactory results.

4. CONCLUSION

For the determination of metoclopramide hydrochloride in pharmaceutical preparations (administered as tablets or injections), an environmentally friendly method was used, in addition of being easy, sensitive and highly accurate, through its reaction with non toxic reagent (BHA), and free of organic solvents. In addition the method did not need any separation steps.

5. ACKNOWLEDGMENTS

The authors express their honest thanks to Department of Chemistry and New and Renewable Energies, College of Science, University of Mosul, Mosul, Iraq to benefit the research facilities.

6. REFERENCES

- Martindale W. The Extra Pharmacopoeia [Internet]. Creative Media Partners, LLC; 2018. Available from: [<URL>](#).
- El-Sonbaty MM, Ismail HR, Kassem AA, Samy AM, Akl MA. Mucoadhesive thermoreversible formulation of metoclopramide for rectal administration: a promising strategy for potential management of chemotherapy-induced nausea and vomiting. *Pharm Devel Technol*. 2020 May 27;25(5):535-46. Available from: [<URL>](#).
- Thanoon E, Saeed A. Development of Green Spectrophotometric Method for Determination of

Metoclopramide Hydrochloride. *Egypt J Chem*. 2021 Mar 9;64(7):3451-6. Available from: [<URL>](#).

4. Devi OZ, Basavaiah K, Vinay KB. Application of potassium permanganate to spectrophotometric assay of metoclopramide hydrochloride in pharmaceuticals. *J Appl Spectrosc*. 2012 Jan;78(6):873-83. Available from: [<URL>](#).

5. Wasan Abdulameer Al-Uzri LD, Hadi H, Fadhel L. Spectrophotometric Determination of Metoclopramide in its Pharmaceutical Preparations using Diazotization Coupling Reaction. *Iraqi Nat J Chem*. 2015;15(2):175-90.

6. Begum M, Koki IB, Rizwan M, Syed AA. Sensitive and Selective Spectrophotometric Methods for the Determination of Cisaprid, Metoclopramide Hydrochloride, Sulphadoxine and Sulphamethoxazole. *Int J Chem Mater Environ Res*. 2016;3(4):84-90.

7. Abd-Alrassol KS, Qasim QA, AL-Rikabi MA, AL-Salman HNK. The development of analytical methods to determine metoclopramide hydrochloric acid in the standard raw and it compared with pharmaceuticals. *Int J Res Pharm Sci*. 2019;10(4):1-14.

8. Abdulkareem HM, Al-Tameemi M, Ibraheem IH, Hadi MS. Surfactant cloud point extraction as a procedure of preconcentrating for metoclopramide determination using spectro analytical technique. *Baghdad Sci J*. 2020;17(1):57-65.

9. Ganduh SH, Aljeboree AM, Mahdi MA, Jasim LS. Spectrophotometric Determination of Metoclopramide-HCl in the standard raw and it compared with pharmaceuticals. *J Pharm Neg Res*. 2021 Jan 2;21(2):44-8. Available from: [<URL>](#).





10. Mubder NS, Kadhim EA, Ibraheem IH, Mahmood H, Dhahir SA, Al-Neshmi H. Micro Spectrophotometric Determination and Cloud Point Extraction of Metoclopramide with 4-Nitro Phenol in Pure Form and Pharmaceutical Drugs. *Ann Roman Soc Cell Biol*. 2021;25(4):12088-103.

11. Abbas SM, Jamur JMS, Nasif AM. Spectrophotometric Method for the Determination of Metoclopramide in Pharmaceutical Forms. *J Appl Spectrosc.* 2021 May;88(2):433-40. Available from: [<URL>](#).
12. Salih E, Mohamad I, Al-Najafi S. Spectrophotometric Assay of Metoclopramide Hydrochloride in pharmaceutical preparations via oxidative coupling Reaction with proma zine Hydrochloride and N-Bromosuccinimide. *J Edu Sci.* 2006 Sep 1;18(3):10-9. Available from: [<URL>](#).
13. Khaleel AI, Amine ST, Salih SH. Comparative study for determination of metoclopramide hydrochloride drug by selective electrodes and spectrophotometric methods. *Tikrit J Pure Sci.* 2013;18(1):149-61. Available from: [<URL>](#).
14. Al-Shirifi AN, Dikran SB, Halboos MH. Application of central composite design method to oxidative coupling spectrophotometric determination of metoclopramide hydrochloride in pure form and pharmaceutical preparations. *J Global Pharma Technol.* 2018;10(5):143-52.
15. Ali R, Othman N. Spectrophotometric Determination of Metoclopramide Hydrochloride in Pharmaceutical Preparations Via Schiff's Base Reaction: In Mosul, Ninevah, Iraq; 2021 [cited 2023 Feb 5]. Available from: [<URL>](#)
16. Liu J, Li H, Wang Y. Spectrophotometric determination of metoclopramide based on the charge transfer reaction between metoclopramide and purpurin. *Fenxi Kexue Xuebao.* 2010;26(3):361-3.
17. Ahmed NR, Essa MJ, Hamdoon AK. Ultraviolet assay of metoclopramide HCl in pharmaceutical formulations application to content uniformity testing. *Eur J Biomed Pharm Sci.* 2020;7(1):191-5.
18. Okram Zenita Devi, Kanakapura Basavaiah, Kanakapura Basavaiah Vinay, Hosakere Doddarevanna Revanasiddappa. Determination of Metoclopramide Hydrochloride in Pharmaceuticals and Spiked Human Urine through Diazotization Reaction. *J Food Drug Anal.* 2012 Jan 1;20(2):454-63. Available from: [<URL>](#).
19. Saleem BA. Spectrophotometric determination of some drugs using oxidation reduction reactions. *Ibn Al-Haitham J Pure Appl Sci.* 2019;32(3):43-55.
20. Mashkour MS, Kahlol MK, AL-Hasnawi SW. Colorimetric Determination of Metoclopramide Hydrochloride and Glutathione by using 1,2 Naphthaquinolinc-4-Sulphonate Sodium Reagents. *Res J Pharm Technol.* 2018;11(8):3290-4. Available from: [<URL>](#).
21. Valavala Sr SN, Tondepu S, Kandagatla S. LC-MS characterization of acid degradation products of metoclopramide: Development and validation of a stability-indicating RP-HPLC method. *Int J Res Pharm Sci.* 2020;11(1):781-9.
22. Karaiskou SG, Kouskoura MG, Markopoulou CK. Modern pediatric formulations of the soft candies in the form of a jelly: determination of metoclopramide content and dissolution. *Pharm Devel Technol.* 2020 Jan 2;25(1):20-7. Available from: [<URL>](#).
23. Khan A, Iqbal Z, Khan MI, Javed K, Khan A, Ahmad L, et al. Simultaneous determination of cefdinir and cefixime in human plasma by RP-HPLC/UV detection method: Method development, optimization, validation, and its application to a pharmacokinetic study. *J Chrom B.* 2011 Aug;879(24):2423-9. Available from: [<URL>](#).
24. Vamshikrishna G, Neelima M, Bhavani M, Sreekanth G, Shobha S. A Simple Rp-Hplc method for simultaneous estimation of paracetamol and metoclopramide. HCl in tablet dosage form. *IOSR J Pharm Biol Sci.* 2014;9:69-78.
25. Othman NS, Mahmood H, Khaleel N. Spectrophotometric and high performance liquid chromatographic methods for determination of metoclopramide in pharmaceutical preparations, Rafidain J. *Sci.* 2011;22:39-56.
26. Al-Awadie NST, Al-banaa MAK. Determination of metoclopramide hydrochloride via quenched continuous fluorescence of fluorescein sodium salt molecule. *J Pharm Sci Res.* 2019;11(6):2312-21.
27. Mazloun-Ardakani M, Kalantari AA, Alizadeh Z, Mohamadian-Sarcheshmeh H, Banitaba H. Electrochemical Investigation for Sensitive Determination of Metoclopramide Based on Ytterbium Oxide Nanoparticles Supported on Graphene. *Anal Bioanal Chem Res.* 2022;9(3):299-307.
28. Guardia M de la, Garrigues S. Handbook of green analytical chemistry. Chichester, West Sussex Hoboken: John Wiley & Sons; 2012. ISBN: 978-1-119-94072-2.
29. Casas Ferreira AM, Fernández Laespada ME, Pérez Pavón JL, Moreno Cordero B. Development of an environmentally friendly methodological approach to determine chlorinated hydrocarbons and chlorobenzenes in soils. *Green Chem Lett Rev.* 2014 Jan 2;7(1):50-9. Available from: [<URL>](#).
30. Özgür M, Kalaycıoğlu Z, Dülger Ö. Simultaneous spectrophotometric determination of phenolic antioxidant (BHA and BHT) concentrations in pharmaceutical preparations and chewing gums using the H-point standard addition method. *Macedon J Chem Chem Eng.* 2017 Dec 21;36(2):211. Available from: [<URL>](#).

31. Hargis LG. Analytical chemistry: Principles and techniques. 1988 Jan; Available from: [<URL>](#)
32. British Pharmacopoeia Commission. British pharmacopoeia. 2016. London: The Stationery Office; 2015.
33. Christian GD, Dasgupta PK, Schug K. Analytical chemistry. Seventh edition. Hoboken, NJ: John Wiley and Sons, Inc.; 2014. ISBN: 978-1-118-80527-5.
34. Abd Alrada WA, Sulaiman ID. Determination of Metochloropramide Hydrochloride by spectrophotometric method by using diazotized p-nitroaniline reagent. International J Drug Del Technol. 2020;10:68-73.



Eco-friendly Approach for Silver Nanoparticles Synthesis from Lemon Extract and their Anti-oxidant, Anti-bacterial, and Anti-cancer Activities

Nisreen Jassam Alaallah^{1*} , Ekhlas A. AbdulKareem² , Aseel Faeq Ghaidan³ ,
and Nuha A. Imran⁴ 

¹Anbar Education Directorate, Ministry of Education, Iraq.

^{2,4}Department of Chemistry, Collage of science, University of Diyala, Iraq

³Iraqi Center for Cancer and Medical Genetic Research.

Abstract: To create silver nanoparticles, researchers use bionanotechnology techniques because they are economical and environmentally friendly. The current study shows that lemon juice (*Citrus-limon*) can be used to biosynthesize silver nanoparticles (Ag NPs). The synthesized silver nanoparticles have been characterized by the surface plasmon resonance (SPR) measured at $\lambda_{max} = 430$ nm, confirming the formation of AgNPs. Moreover, Fourier Transform Infrared (FTIR) analysis was carried out to identify possible bio-molecules responsible for the bio-reduction of silver ions. The x-ray diffraction (XRD) peaks at (111, 200, 220, 222, and 311) confirm the found face-centered cubic (FCC) crystal structure of AgNPs in solution. Transmission-Electron-Microscopy (TEM) images showed that AgNPs have spherical morphology with sizes ranging from 10-50 nm. Furthermore, the Particles Size Analyzer (PSA) confirmed these sizes and ranges. Synthesized AgNPs have high anti-oxidant activity according to the (scavenging of DPPH radicals, total anti-oxidant, and reducing power) assays. Also, the anti-bacterial activity of AgNPs was evaluated by a well diffusion method, and the results suggest that they are more sensitive to gram-positive bacteria than gram-negative ones, with the average diameter of the inhibition zones for AgNPs ranging from 4.11 to 25.87 mm and 1.38 to 22.3 mm against *S. aureus* and *E. coli* bacteria, respectively. *In vitro* studies of AgNPs against MCF-7 breast cancer cell lines showed a good cytotoxic effect $p < 0.05$ with an IC_{50} value of 47 $\mu\text{g/mL}$; this study could be beneficial for nanotechnology-based pharmaceutical and biomedical applications.

Keywords: Silver nanoparticles, citrus limon juice, anti-oxidant activity, anti-bacterial activity, anti-cancer activity.

Submitted: August 09, 2022. **Accepted:** January 20, 2023.

Cite this: Alaallah NJ, AbdulKareem EA, Ghaidan AF, Imran NA. Eco-friendly Approach for Silver Nanoparticles Synthesis from Lemon Extract and their Anti-oxidant, Anti-bacterial, and Anti-cancer Activities. JOTCSA. 2023;10(1):205-16.

DOI: <https://doi.org/10.18596/jotcsa.1159851>.

*Corresponding author. E-mail: nisreenjassamalaallah@gmail.com.

1. INTRODUCTION

Metal nanoparticles that appear in size ranging from 1 - 100 nm have received increasing interest due to their optical and optoelectronic properties that are unique compared to their bulk counterparts; this has made them enter into different fields such as catalysis, optics, environmental, electronics, and biotechnology, which is an area of constant interest (1,2). Among these, silver nanoparticles (AgNPs) are widely used in a variety of applications because they have a small size, large surface area, and high

dispersive capacity and exhibit anti-microbial, anti-cancer, anti-diabetic, anti-oxidant, anti-inflammatory properties and also used in food preservation, water purifications ointment fabrication, and cosmetics (3, 4). Physical and chemical processes are still used today to create nanoparticles, but they result in many dangerous by-products that harm the environment. Therefore, there is a constant need for developing new methodologies and approaches for simple, rapid, consuming less energy, performing under moderate operation conditions, and eco-friendly nanoparticle synthesis methods. Many

scientists focus on the green synthesis of nanoparticles from plant extracts (5). It has been reported that nanoparticles synthesized by plant parts (such as seeds, roots, leaves, stems, flowers, and fruits) have more biological activities than

nanoparticle synthesis by chemical methods (6-8). Figure 1 represents an illustrative scheme for forming silver nanoparticles from different plant parts.

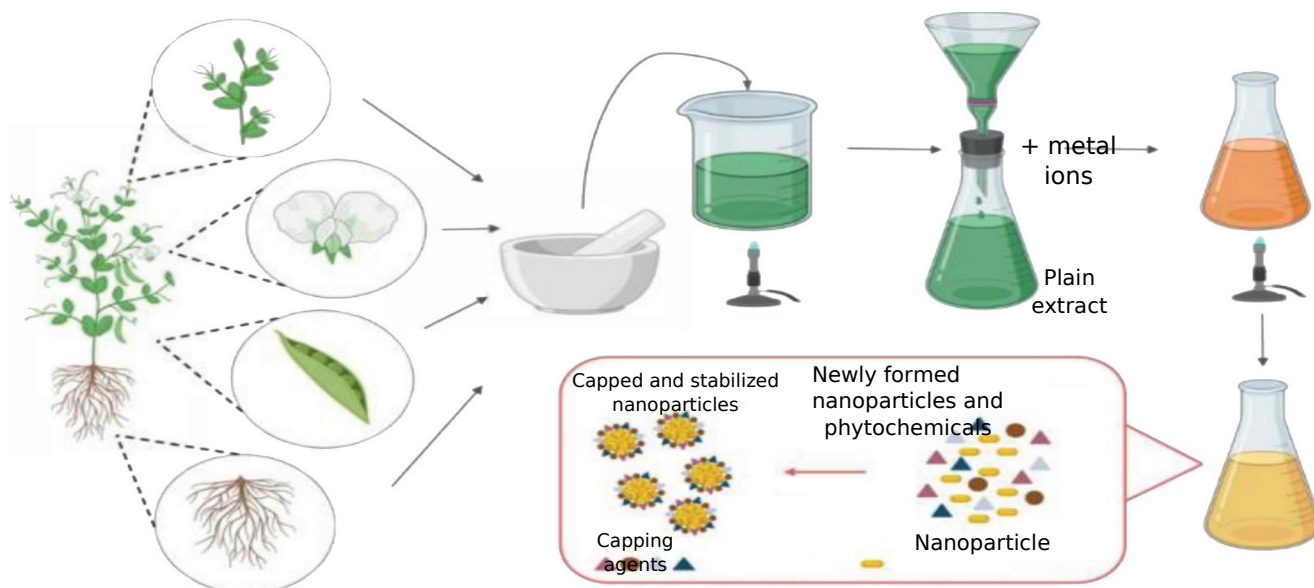


Figure 1: Green synthesis of metal nanoparticles by plant parts (9).

In recent times, nanoparticles using plant extracts have received attention as it is an economical and straightforward method (10). The main idea in the synthesis of AgNPs is by reducing agents that reduce silver ions (Ag^{+1}) to neutral silver (Ag^0) (22). Fruits, including lemon, are considered a rich source of flavanones, polys-methoxylated flavones, and carboxylic acids such as ascorbic acid and citric acid, which are very rare in other plants, and these materials could be used as reducing agents (5,11).

In this work, silver nanoparticles were synthesis through environmentally friendly synthesis techniques by using the extract from *Citrus limon* (lemon), the reason behind selecting this particular plant is that (i) lemon is a cheap, commercially available, and environmentally safe fruit and (ii) anti-microbial properties of the synthesized nanoparticles might be enhanced (12,13). In this regard, numerous studies on the synthesis of nanomaterials using plant parts such as *Citrus sinensis*, *Citrus tangerina*, and *Citrus limon* peel extract(5), *Citrus sinensis* peel extract (14), Lemons leaves extract (10,15), *Lemon Citrus Latifolia* extract (16), and *Citrus limon* (lemon) juice aqueous extract (13,17-19), Although there have been studies conducted with lemon, they have been limited to studying anti-bacterial activities. This study is the first to study the effectiveness of silver nanoparticles manufactured from lemon juice on cancer cell lines (MCF-7) and follow up on their anti-oxidant and anti-bacterial activities.

This work also provides more information on the chemical structure of silver nanoparticles

synthesized from aqueous lemon juice by UV, FTIR, XRD, TEM, AFM, and PSA.

2. METHODOLOGY

2.1. Materials

Silver nitrate (AgNO_3) was purchased from BDH, Sigma Aldrich. Fresh lemon was taken from local markets in Baquba / Diyala. Other chemical compounds required for anti-oxidant, anti-bacterial, and anti-cancer studies were of the highest purity. In this study, all glass tool was washed using distilled water and dried in the oven till used in the experiments, and all solutions were prepared using distilled water.

2.2. Preparation of Lemon Juice

Fresh lemon (*C. Limon*) fruit samples were sliced and strained through a nylon mesh with fine holes to obtain the juice. Then, the juice obtained was put into a centrifuge at 10,000 rpm for 10 minutes to remove any unwanted impurities. This extract was collected in a dark volumetric flask (25 mL) and stored at 4 °C for further experiments (17).

2.3. Synthesis of Silver Nanoparticles (AgNPs) from Lemon Juice

For the green synthesis of AgNPs, 1 mL of the lemon juice was added to 4 mL of 1 mM silver nitrate (AgNO_3) solution in a suitable test tube. The solution was heated in a water bath at 100°C for 30 minutes until AgNPs were formed, and reduction was confirmed by changing color from colorless to brownish-yellow (18).

2.4. Characterization of Synthesized Silver Nanoparticles

2.4.1. UV-vis spectroscopy

The optical properties of silver nanoparticles were calculated using ultraviolet-Visible spectrophotometer model Shimadzu UV-1700 (Shimadzu Corp, Kyoto, Japan). UV-Vis spectroscopic analysis was performed by continuous scanning in the range of 300-900 nm, an effective and widely applied technique for determining the formulation stability of metal nanoparticles (20) with some modification.

2.4.2. Fourier transform infrared (FTIR) analysis

FTIR is an analytical chemical method used to measure the intensity of infrared radiation against its wave number or wavelength light. It was performed to determine the functional groups involved in reducing Ag⁺ to AgNPs. The infrared spectra of the dried AgNPs and lemon powder were measured with the KBr disc in the range of 400-4000 cm⁻¹ using (S-8400, Shimadzu, Japan) FTIR spectrometer (21).

2.4.3. X-Ray diffraction (XRD) analysis

To confirm and determine the crystal structure of AgNPs. The powder X-Ray diffraction (XRD) of the AgNPs was recorded using X-ray diffractometer model (Philips X'Pert-MPD diffractometer, the Netherlands) ranging from 10 to 80°, and monochromatic CuK α radiation having wavelength ($\lambda = 1.5406\text{\AA}$) was used for XRD analysis (22).

2.5. Microscopy

2.5.1. Transmission electron microscopy (TEM) analysis

A thin film of the aqueous suspension of AgNPs was prepared by placing 10 μL of suspension on a small copper grid and letting the grid dry before starting the measurement. The morphology of the AgNPs was investigated by TEM using a (JEOL JEM-2100) with an acceleration voltage of 200kV which gives a high-resolution image (19).

2.5.2. Atomic force microscopy (AFM) analysis

AFM was used to assess the size and form of AgNPs produced through biological synthesis. The AFM usually measures the height of AgNPs. AFM is a measurement by taking a few drops of aqueous suspension and placing it on a glass slide, leaving 24 hours at room temperature to dry completely. Images obtained from the AFM were collected using Pico-Scan software (17).

2.5.3. Particle size analyzer (PSA) analysis

Particle size analyzer equipment (Horiba LA-3000Light Scattering Particle Size Distribution Analyzer, Horiba Ltd, Kyoto, Japan) was used to determine the particle size of the produced AgNPs. The normal log distribution of the nanoparticles based on intensity and size was studied comparatively. Measurements were taken between 5.0 and 500.0 nm(23).

2.6. Anti-Oxidant Assays

The synthesized AgNPs were estimated for anti-oxidant activity using three methods as follows: L-Ascorbic acid (AA) was used as a reference.

2.6.1. Scavenging of DPPH radical assay

The anti-oxidant activity of the lemon juices and AgNPs was measured by using (2,2-diphenyl-1-picryl-hydroxyl)(DPPH) assay, as described by Chang et al.(24). 1 mL of serial dilutions of lemon juice and synthesized AgNPs were prepared in different concentrations (100, 200, 300, and 400 $\mu\text{g}/\text{mL}$). To each dilution, 1 mL of DPPH (0.135 mM in ethanol) was added, incubated, and left in the dark at room temperature for (30 minutes). The absorbance of the control and samples were determined at $\lambda_{\text{max}} = 517$ nm, and ascorbic acid was used as a positive control.

The capability of AgNPs to scavenge the DPPH radical was recorded as a percentage inhibition in Equation 1:

$$\% \text{Inhibition} = \left(\frac{OD_{\text{Control}} - OD_{\text{Sample}}}{OD_{\text{Control}}} \times 100 \right) \quad (\text{Eq. 1})$$

where OD_{control} is the optical density of the control samples (DPPH solution without samples) and OD_{samples} is the optical density of the sample (DPPH solution and samples).

2.6.2. Total anti-oxidant assay

The total anti-oxidant activity of lemon juice and AgNPs was estimated according to the method conducted by Prieto et al. (25). An aliquot of 0.3 mL of each diluted juice prepared as described above was mixed with (3 mL) of reagent solution (4 mM ammonium-molybdate ((NH₄)₂MoO₄), 28 mM sodium phosphate (Na₃PO₄), and 0.6 M sulfuric acid (H₂SO₄), incubated at 95 °C for 90 minutes. After cooling the tubes, the samples' absorbance was measured at $\lambda_{\text{max}} = 695$ nm, and the anti-oxidant activity was determined as (%) using this formula:

$$\text{Total Anti-Oxidant} = \left(\frac{OD_{\text{Control}} - OD_{\text{Sample}}}{OD_{\text{Control}}} \times 100 \right) \quad (\text{Eq. 2})$$

2.6.3. Reducing power assay

The ferric (Fe³⁺) reducing the power of lemon juice and AgNPs was evaluated according to methods described by Oyaizu (26). Various concentrations of 1ml lemon juice and AgNPs were mixed with equal volumes of sodium phosphate buffers (0.2 M, pH=6.6) and 1 mL of potassium hexacyanoferrate (K₃Fe(CN)₆) (1%, w/v), and the resultant mixtures were incubated at 50 °C for 20 minutes. The reaction was stopped by adding 1 mL of trichloroacetic acid (TCA) (10%, w/v) and then centrifuging at 10,000 rpm for 10 minutes. A resultant supernatant solution (1.5 mL) was mixed for 10 minutes with distilled water (1.5 mL) and 0.1 mL of ferric chloride (FeCl₃)

solution (0.1%, w/v). Then, the absorbance of the mixture was measured at $\lambda_{\max} = 700$ nm against a blank solution. Higher absorbance values of the reaction mixture determined increased reducing power. Three replicates of each sample were made, and the average was recorded.

2.7. Antimicrobial Activity

A standard well diffusion procedure depends on investigating the inhibition effect of lemon juice and AgNPs of bacterial growth for two human pathogenic bacteria, *Staphylococcus aureus* as Gram-positive and *Escherichia coli* as Gram-negative (27). About 25 mL of nutrient agars were poured on Petri dishes and left to solidify. Inoculation of bacteria was performed by streaking on the agar surface of each plate hole 5 mm wide was on agar by punched with a sterile cork borer (10, 25, 50, and 100) μ L of lemon juice, and a solution containing AgNPs was transported and placed in these holes. The plates were permissible to stand by for (30 minutes) to (1 hour). The incubation of inoculated agar was done for 24 hours at an optimum temperature for bacteria growth equal to 37 °C. Then, the inhibition zone of bacteria growth was determined in millimeters. All experiments were conducted in triplicate.

2.8. Cytotoxicity Assay

The cytotoxicity assay of lemon juice and AgNPs was estimated by the MTT assay using a human breast cancer cell line MCF-7. In this method, MCF-7 cells were seeded onto 96-well plates $\sim 1 \times 10^5$ cells/wells at (37 °C) for 24 hours, and then cells were treated with different concentrations ranging from 10 to 100 μ g/mL of AgNPs along with cell control and lemon juice. Cells that had been treated with MTT (0.5 mg/L) were added, and they were then incubated at 37°C in a CO₂ incubator for 4 hours. Cells were washed with 100 μ l of phosphate-buffered saline

(PBS) after the MTT-containing medium was discarded. After incubation, the MTT formazan crystals were dissolved in (100 μ l) of dimethyl sulfoxide (DMSO, 10%), and purple-blue formazone dye was measured at 620 nm in a multiwell ELISA plate reader (Thermo-Multiskan EX)(28). The optical density (OD) value was used to compute the percentage of cell viability by using the following formula.

$$\text{Percentage of cell viability} = \frac{OD_{\text{cells with AgNPs}}}{OD_{\text{cells without AgNPs}}} \times 100$$

(Eq. 3)

Also, the cytotoxicity assay was estimated by finding the IC₅₀ value, which was the concentration showing 50% inhibition activity.

2.9. Statistical Analysis

A statistical comparison was carried out using a one-way analysis of variance (ANOVA), followed by Tukey's test. Each experiment was performed in triplicate, and the results were expressed as the mean \pm standard deviation; statistical significance was accepted at a level of (p < 0.05).

3. RESULTS AND DISCUSSION

3.1. Biosynthesis of AgNPs

In this study, the biosynthesis of AgNPs was carried out by reducing the aqueous silver solution of AgNO₃ with lemon juice. The results indicated an apparent change in the color of the solution from colorless to yellowish-brown; this occurred in a period of (30 minutes), and this change indicates the formation of AgNPs. Figure 2 shows the color change obtained, which agrees with a number of other studies (16,17,19).



Figure 2: The change in color indicating the synthesis of AgNPs.

3.2. Characterization of AgNPs

3.2.1. UV-Visible analysis

Ultraviolet-Visible (UV-Vis) spectroscopy was used to characterize the synthesis of AgNPs. Figure 3 shows UV-Visible spectra of the synthesis of AgNPs. Lemon juice and AgNO₃ were involved as controls. The peak at $\lambda_{\max} = 430$ nm in UV absorption refers to the conformation of AgNPs; the peaks' broadness exhibits the particle size variability. The result of this

study was similar to the results observed by Patil et al. (29).

3.2.2. FTIR analysis

FT-IR absorption spectra of lemon juice before and after bio-reduction, as shown in Figure 4, shows various bending and stretching bands viz, 3429, 1730, 1630, 1400, 1225, 1106, 899, 596, and 520 cm⁻¹. The broad peak at 3429 cm⁻¹ corresponded to (-N-H) stretching of amides (II). The peak at 1730 cm⁻¹ is sharp and related to (-C=O) stretching in (-

COOH) carboxylic acid. The peak at 1630 cm^{-1} (weaker), related to amide I, arisen due to carbonyl stretch in the protein. The peak at 1400 cm^{-1} corresponded to -O-H and -C-H bending. The peak at 1200 cm^{-1} corresponds to -C-O stretching in the carboxylic acid group (COOH). The peak at 1021 cm^{-1} is related to C-N stretching vibrations of amine. The peak at 1106 cm^{-1} appeared as a significant peak, which might be attributed to the C-O groups of the polyols such as polysaccharides, flavones, and terpenoids excessively found in plant extract used as reducing agents during the synthesis of AgNPs (30). The peak at 899 cm^{-1} is related to C-H aromatic in benzene groups. The peaks between 596 and 520 cm^{-1} represent to silver nanoparticle's connection with oxygen from the hydroxyl group. From the measurement of FT-IR, it can be concluded that some of the bio-organic compounds present in lemon juice, such as flavonoids, alkaloids, and phenols, can play an essential role in reducing silver salt to metallic silver (Ag^0). Moreover, these composites act as capping and stabilizing agents, which helps prevent the silver nanoparticles from accumulating. This suggests that the biological components included in lemon juice perform dual functions of conformation and stabilization of AgNPs in an aqueous medium. Additionally, this study's results agree with those of other studies (10).

3.2.3. XRD analysis

The XRD spectra of the synthesized AgNPs are shown in (Figure 5). Bragg's diffraction peaks for AgNPs are observed at 38.4° , 44.53° , 64.45° , 79.77° , and 82.96° , equivalent to 111, 200, 220, 311, and 222, representative face centered cubic (FCC) structure of silver, respectively. The average crystallite size of AgNPs were calculated to be about 17.8 nm, using Scherer formula $D=0.94 \lambda/\beta \cos \theta$, D represents the size of particles (nm), λ is the wavelength of the X-ray ($\text{Cu K}\alpha = 1.5406\text{ \AA}$), β is the full width of the (XRD) peak at half height, and θ is the Bragg angle, that is (111), and θ is the position of that line in the pattern. The X-ray diffraction pattern demonstrated the lack of contaminants and the effective synthesis of pure AgNPs (31). The results of XRD analysis agree with the previously published research demonstrating the cubic structure of silver (32).

3.2.4. TEM analysis

TEM analysis of silver nanoparticles shows that AgNPs were mainly spherical with average sizes of 19 nm (Figure 6). AgNPs are usually present and readily aggregate during the manufacturing process. However, the fact that they were present and homogenous in our approach suggests that the AgNPs were stabilized using a capping agent,

possibly the bio-organic chemicals found in lemon juice (33). Compared with the previous studies, the silver nanoparticles in this work were similar in shape and size to those obtained in studies (16,34). In comparison, it was smaller than AgNPs obtained in studies (35-37).

3.2.5. AFM analysis

Atomic force microscopy (AFM) is used to evaluate the surface topography and size of AgNPs. Figures (7 - A) and (7 - B) showed the three-dimensional (3D) and two-dimensional (2D) images of AgNPs showing spherical or mostly spherical shapes of nanoparticles with an average size was $<100\text{ nm}$. AgNPs have been shown as a topographic image.

3.2.6. PSA analysis

The AgNPs size and distribution profile are depicted in Figure 8 using particle sizes analysis (PSA). The result showed that most particle distributions (90%) have modest nanoscale sizes, with a mean particle size of 35 nm.

3.3. Antioxidant Activity

Oxidation is an important biological process that contributes to energy production in many living organisms; however, the out-of-control production of oxygen-derived free radicals. Reactive oxygen species (ROS) cause damage to complex life molecules such as proteins, carbohydrates, nucleic acid, and lipids (38). This causes the emergence of several health problems, such as cancer, hepatic diseases, cardiovascular diseases, and renal failure (39). Anti-oxidants are agents that restrict the harmful effects of these oxidant reactions. These restrictions can include preventing the formation of free radicals or permanently removing free radicals, thus enhancing the immune defense and reducing the incidence of diseases (40). In this work, the anti-oxidant activity of lemon juice and synthesized AgNPs was examined using three different methods because a single, universal technique cannot accurately assess anti-oxidant capacity. The (DPPH) free radical scavenging activity is the better test for measuring anti-oxidant activity due to its simplicity, stability, and testing speed. In DPPH assay of lemon juice and AgNPs compared with ascorbic acid as standard. The results in (Figure 9) indicate that AgNPs have higher DPPH activity by 86% compared with lemon juice at $400\text{ }\mu\text{g/mL}$ concentration, and their activity increased with increased concentration. Therefore, we can say that AgNPs could be used as treatment agents for several diseases caused by oxidative stress. The result obtained in this study is in agreement with previous studies (41-43).

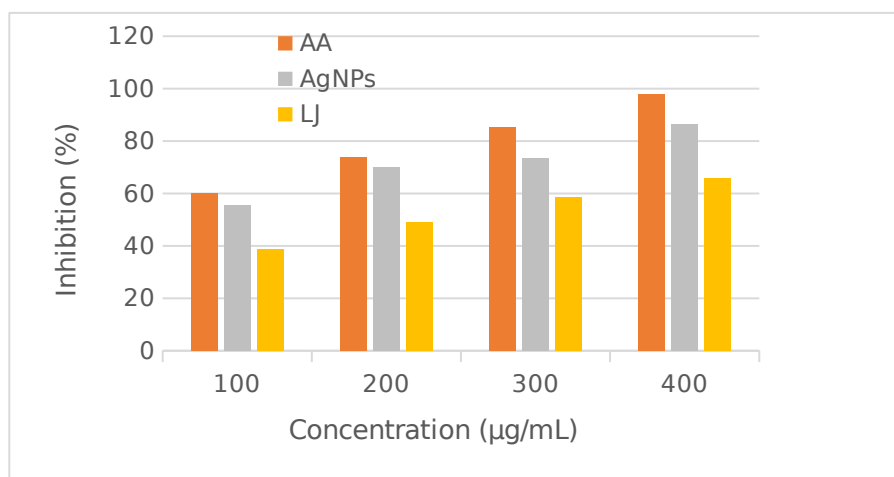


Figure 9: %Inhibition of DPPH free radical scavenging activity of Lemon juice (LJ), bio-synthesized AgNPs, and Ascorbic Acid (AA) at different concentrations.

In the total anti-oxidant method (phosphomolybdate), the basis of this method is the reduction of Mo(VI) to Mo(V) by the anti-oxidant compound and conformation of green phosphate,

Mo(V) complex. The results presented in Figure 10 showed that AgNPs have more anti-oxidant activity than ascorbic acid or lemon juice.

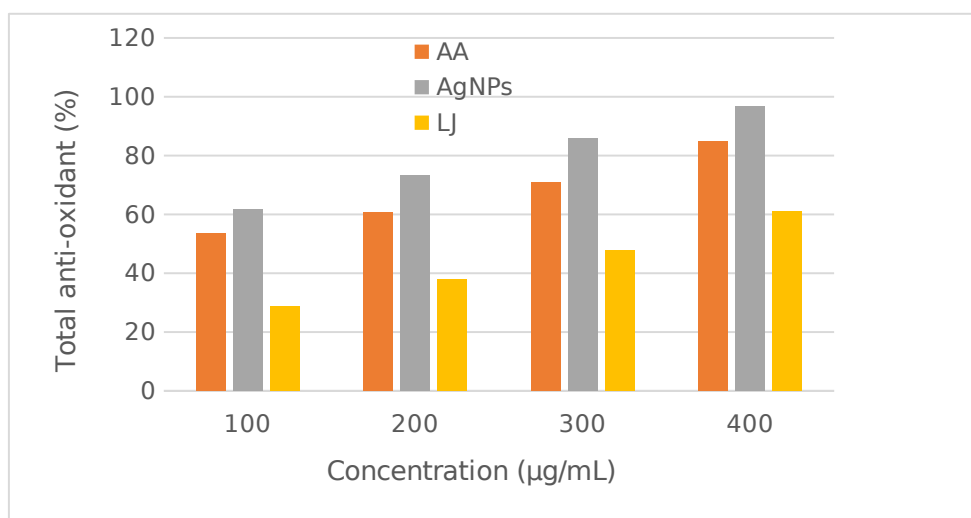


Figure 10: Total anti-oxidant capacity of Lemon Juice (LJ), biosynthesized AgNPs, and Ascorbic Acid (AA), at different concentrations.

In the reducing power assay, the ability of an anti-oxidant to donate an electron is measured when a reaction occurs between samples and potassium ferricyanide (Fe^{3+}) to generate potassium ferrocyanide (Fe^{2+}), followed by a reaction with ferric

chloride ($FeCl_3$) to form a ferric-ferrous complex (44). As shown in Figure 11, AgNPs have more anti-oxidant activity than lemon juice. The maximum and minimum optical densities were detected for AgNPs and lemon juice at 2.11 and 0.99 at 400 µg/mL.

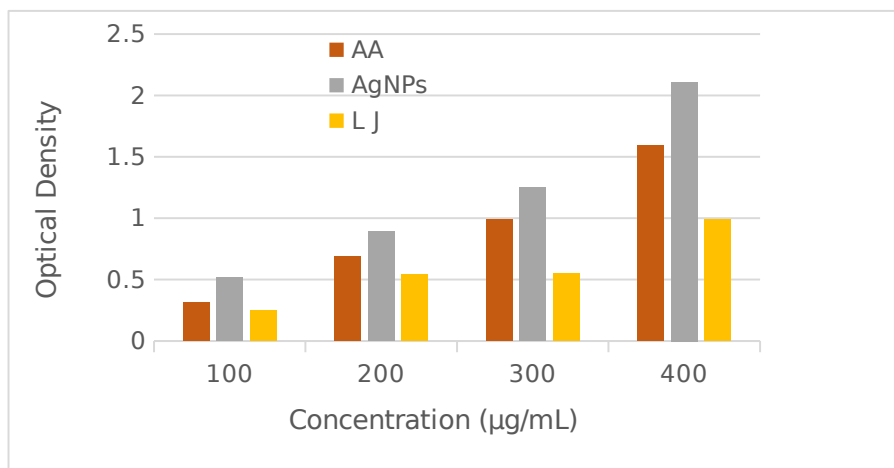


Figure 11: Reducing power activity of Lemon Juice (LJ), biosynthesized AgNPs, and Ascorbic Acid (AA) at different concentrations.

The analysis of variance (ANOVA) test findings showed statistically significant differences between lemon juice and the AgNPs when compared to ascorbic acid as a reference.

We conclude from this study that AgNPs synthesized from lemon juice have a stronger anti-oxidant capacity than the juice. This work highlights the importance of the therapeutic value of AgNPs synthesized from lemon juice as a source for developing anti-oxidant drugs.

3.4. Anti-Bacterial Effectiveness of Silver Nanoparticles

The anti-bacterial activity of lemon juice and synthesized AgNPs is shown in Figure 12 and Figure 13 against *Escherichia coli* (*E. coli*) and *Staphylococcus aureus* (*S. aureus*), respectively. Also, the values of zone of inhibition observed round the wells of synthesized AgNPs are given in Table 1 as (Mean±SD). and lemon juice and silver nitrate (control) are given in Table 2. The results in Table 2 showed that the effect of AgNO₃ for the dose of 60 µL against *E. coli* and *S. aureus* was low, and the reason for this may be due to its very low concentration (1 mM). Similarly, when comparing the effect of lemon juice and AgNPs as anti-bacterial, the results indicated a slight effect of lemon juice compared with the activity of AgNPs as an anti-bacterial for all doses (Tables 1 and 2). Although silver has anti-bacterial properties, lemon juice is rich in biologically active compounds such as flavonoids, carotenoids, and phenolic compounds, which act as natural antibiotics against pathogens in the body, such as bacteria (10,43). AgNPs differed significantly at $p < 0.05$ from lemon juice and AgNO₃ (45). AgNPs have activity of silver NP derived from lemon juice showed enhancement in activity due to the synergistic effect of silver and biologically active compounds of lemon juice. As shown in the data in Tables 1 and 2. This is in agreement with many studies; Samreen, Muzaffar, et al. (2018) conducted a study on different bacterial strains, and the results indicated a significant inhibition of AgNPs compared to the absence of any inhibition for lemon extract

(45). Furthermore, Mosae Selvakumar, Antonyraj, et al. (2016), and Niluxsshun, Masilamani, et al. (2021) discovered that lemon extract has slight activity while the zone of inhibition around AgNPs was significantly higher than the extract and controls and nearer to the inhibition of standard antibiotics (5,19). Also, it has been observed that AgNPs were more sensitive to, Gram-positive bacteria (*S. aureus*) than Gram-negative bacteria (*E. coli*). However, the mean inhibition zone diameter against *E. coli* for this study at a dose of 100 µL was higher compared to other studies such as *lemon* extract 3.0 mm (46), *Nicotiana tobaccum* leaf 4.0 mm (47), and *Neem* leaves 6.0 mm (48). Moreover, the anti-bacterial activity of AgNPs was found to increase with increasing doses (Table 1). This may be because of the different sizes and shapes of nanoparticles, especially AgNPs, which are spherical and have a high surface to volume ratio to interact with the cell walls of pathogens giving the best anti-microbial activity (49). This result agrees with several works of literature revealing that nanoparticles are more active against Gram-positive bacteria than Gram-negative bacteria (50, 51). And that the bactericidal property of nanoparticles depends entirely on the dose and particle size (52). The mechanism underlying the anti-bacterial activity of AgNPs is very complex. This can be explained as silver ions (Ag⁺) acting as an anti-bacterial by interacting with the peptidoglycan cell wall and that the thickness of the peptidoglycan layer differs in species of bacteria (Gram-negative bacteria and Gram-positive bacteria). This is the main reason why bacteria are differently affected by the attack by AgNPs (29). Other investigations have reported that the positive charge of AgNPs interacts with the negative charge on the cell wall of bacteria, which leads to changes in the morphology of the cell wall and increases the permeability of the membrane by making pores and thereby causing the death of bacteria (53,54). Also, it is said that Ag⁺ interaction with amino (-NH₂) and thiol (-SH) groups of protein on cell membrane, which results may be responsible for the induction of ROS, which leads to the inhibition of respiratory enzymes and, consequently death (5). Ag⁺ affects

bacterial cells through several mechanisms, including cell wall leakage, interaction with bacterial enzymes and DNA, ribosomal destabilization, and

interruption in the electron transport chain, resulting in cell death (55).

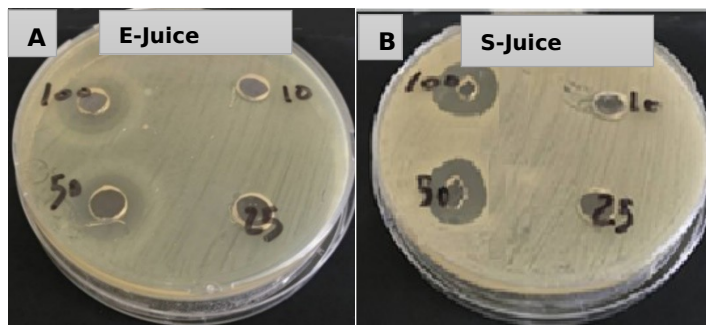


Figure 12: Anti-bacterial activity of lemon juice against (A) E= *Escherichia coli*, (B) S= *Staphylococcus aureus*.

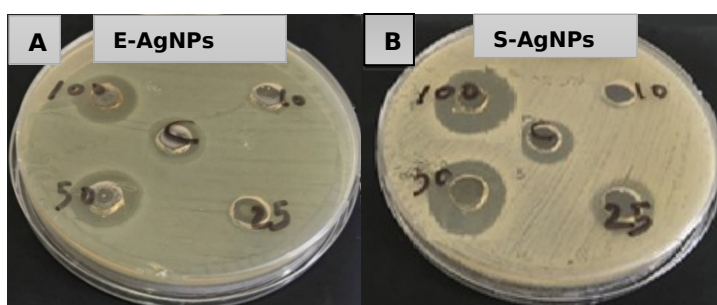


Figure 13: Anti-bacterial activity of AgNPs against (A) E= *Escherichia coli*, (B) S= *Staphylococcus aureus*.

Table 1: Effect of AgNPs on the growth of bacterial species.

Dose of lemon juice (µL)	<i>E. coli</i> (Mean±SD)	<i>S. aureus</i> (Mean±SD)	Dose of AgNPs (µL)	<i>E. coli</i> (Mean±SD)	<i>S. aureus</i> (Mean±SD)
10	0.00±0.00	0.00±0.00	10	1.38±0.41	4.11±0.39
25	0.00±0.00	5.17±0.29	25	3.93±0.83	13.13±0.32
50	10.2±0.62	11.4±0.40	50	17.5±0.5	20.47±0.45
100	13.03±0.35	14.5±0.45	100	22.3±0.57	25.87±0.96

Table 2: Effect of AgNPs, lemon juice (control), and AgNO₃ on the growth of bacterial species.

Dose of solution (µL)	AgNPs		Zone of inhibition (mm) Lemon juice		AgNO ₃	
	<i>E. coli</i> (Mean±SD)	<i>S. aureus</i> (Mean±SD)	<i>E. coli</i> (Mean±SD)	<i>S. aureus</i> (Mean±SD)	<i>E. coli</i> (Mean±SD)	<i>S. aureus</i> (Mean±SD)
60	19.0±0.26	22.67±0.32	11.4±0.62	13.2±0.40	5.53±0.50	6.06±0.60

3.5. Anti-cancer activity

In our study, the anti-cancer activity of the green synthesis AgNPs at different concentrations levels 10, 25, 50, 75, and 100 µg mL⁻¹ was studied against a human breast cancer cell line MCF-7. The result showed that AgNPs had positive anti-cancer effects on MCF-7 cancer cells. In figure 14, the nanoparticles showed dose-dependent anti-cancer activity. The required concentrations for 50% inhibition of the cell viability (IC₅₀) were calculated graphically; it was about 47 µg/mL for AgNPs, while

IC₅₀ was recorded at 215 µg/mL for lemon juice. AgNPs showed significant inhibition of cell growth of about 80%, while the lemon juice showed very low cytotoxicity of 29%. According to the optical microscopic analysis of cancer cells, exposure to an aqueous suspension of AgNPs caused significant morphological changes in the cells, including aggregation, cellular shrinkage, and rounding, compared to untreated cells. The result obtained in this study was in agreement with another study (56).

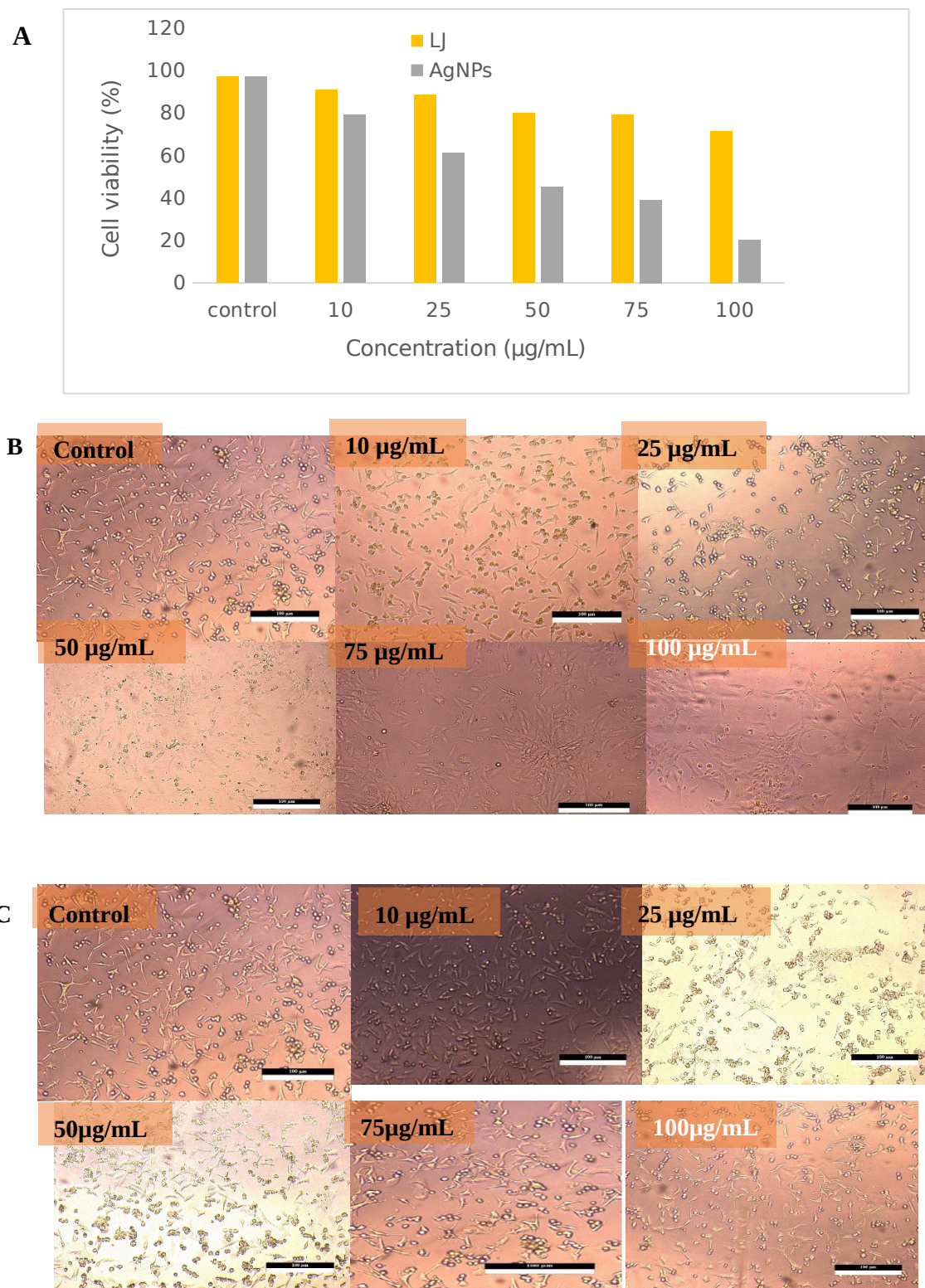


Figure 14:- Cytotoxic activity of AgNPs and lemon juice (LJ) MCF-7 cell line **(A)** Histogram demonstrating the cell viability percentage of MCF-7 cells at different concentrations 10, 25, 50, 75, and 100 µg/mL of AgNPs and lemon juice. **(B)** Photomicrographs showing changes in MCF-7 cell line after being treated with different concentrations 10, 25, 50, 75, and 100 µg/mL of AgNPs, and **(C)** Photomicrographs showing MCF-7 cell line after being treated with different concentrations 10, 25, 50, 75 and 100 µg/mL of lemon juice.

One of the potential mechanisms for inducing apoptosis in cancer cells involves the synthesis of AgNPs, which trigger reactive oxygen species (ROS)

and, in turn, the production of toxic free radicals and the disruption of mitochondria, both of which result in cellular apoptosis (57). Many researchers have

reported the cellular internalization of AgNPs, according to the surface properties of AgNPs. AgNPs carry a positive charge, while normal-cancer cell membranes contain substances such as lipids (especially PO₄³⁻ groups) with a negative charge; Having an opposite charge is responsible for cellular internalization and thus causes cancer cell death (55). In another study conducted by one of the researchers on the breast cancer cell line, the study reported that silver nanoparticles (GSNPs) manufactured from *Mentha-arvensis* induce cytotoxicity by mediating caspase 9-dependent apoptosis in breast cancer cell lines (58). In a study conducted by one of the researchers on silver nanoparticles, it was found that these AgNPs nanoparticles can contribute to cellular degradation by autophagy and thus cause cancer cell death (59). Three methods have been proposed. To take advantage of the biosynthesis of nanoparticles that cause apoptosis in cancer cells, that is mitochondrial damage, activation of death transmembrane receptors, and injury of the endoplasmic reticulum (60-62).

4. CONCLUSION

In this study, the Ag-NPs were successfully synthesized by green synthesis using lemon (*Citrus limon*) juice with different groups of phytochemicals such as phenols, terpenes, and flavonoids. The characteristics of the biosynthesized AgNPs were measured by different equipments (UV-visible spectrophotometer, FT-IR spectrometer, TEM, AFM, and PSA). Moreover, several medicinal aspects of these NPs, including anti-oxidant, anti-bacterial, and anti-cancer activity, were evaluated, and the AgNPs showed potential anti-microbial activity against Gram-positive and Gram-negative bacteria. The anti-oxidant activity of AgNPs showed the highest effect. In addition, the results indicate that AgNPs had anti-cancer activities against human breast (MCF-7) cancer cell lines in a dose-dependent manner. These green methods of AgNP formation open a new window for treating many infectious diseases and cancers.

5. CONFLICT OF INTEREST

Regarding the current manuscript, the researchers affirm that there are no conflicts of interest

6. ACKNOWLEDGMENTS

The researchers are grateful to the University of Diyala and the Faculty of Sciences for supplying the resources necessary for this study.

7. REFERENCES

1. Kumar B, Smita K, Cumbal L, Debut A, Pathak RN. Sonochemical Synthesis of Silver Nanoparticles Using Starch: A Comparison. *Bioinorganic Chemistry and Applications*. 2014;2014:1-8. Available from: [<URL>](#).
2. Mohammed RS, Aadim KA, Ahmed KA. Synthesis of CuO/ZnO and MgO/ZnO Core/Shell Nanoparticles with

Plasma Gets and Study of their Structural and Optical Properties. *Journal of Modern Science*. 2022;8(2):9.

3. Jakinala P, Lingampally N, Hameeda B, Sayyed RZ, Khan M. Y, Elsayed EA, et al. Silver nanoparticles from insect wing extract: Biosynthesis and evaluation for antioxidant and antimicrobial potential. Kumar P, editor. *PLoS ONE*. 2021 Mar 18;16(3):e0241729. Available from: [<URL>](#).

4. Ahmed RH, Mustafa DE. Green synthesis of silver nanoparticles mediated by traditionally used medicinal plants in Sudan. *Int Nano Lett*. 2020 Mar;10(1):1-14. Available from: [<URL>](#).

5. Niluxshun MCD, Masilamani K, Mathiventhan U. Green Synthesis of Silver Nanoparticles from the Extracts of Fruit Peel of Citrus tangerina, Citrus sinensis, and Citrus limon for Antibacterial Activities. Ciccarella G, editor. *Bioinorganic Chemistry and Applications*. 2021 Feb 2;2021:1-8. Available from: [<URL>](#).

6. Choudhury R, Majumder M, Roy DN, Basumallick S, Misra TK. Phytotoxicity of Ag nanoparticles prepared by biogenic and chemical methods. *Int Nano Lett*. 2016 Sep;6(3):153-9. Available from: [<URL>](#).

7. Pirtarighat S, Ghannadnia M, Baghshahi S. Green synthesis of silver nanoparticles using the plant extract of *Salvia spinosa* grown in vitro and their antibacterial activity assessment. *J Nanostruct Chem*. 2019 Mar;9(1):1-9. Available from: [<URL>](#).

8. Vasylyev G, Vorobyova V, Skiba M, Khrokalo L. Green Synthesis of Silver Nanoparticles Using Waste Products (Apricot and Black Currant Pomace) Aqueous Extracts and Their Characterization. *Advances in Materials Science and Engineering*. 2020 Jul 13;2020:1-11. Available from: [<URL>](#).

9. Yazdani M, Rostamzadeh P, Rahbar M, Alam M, Abbasi K, Tahmasebi E, et al. The Potential Application of Green-Synthesized Metal Nanoparticles in Dentistry: A Comprehensive Review. De Matteis V, editor. *Bioinorganic Chemistry and Applications*. 2022 Mar 3;2022:1-27. Available from: [<URL>](#).

10. Vankar PS, Shukla D. Biosynthesis of silver nanoparticles using lemon leaves extract and its application for antimicrobial finish on fabric. *Appl Nanosci*. 2012 Jun;2(2):163-8. Available from: [<URL>](#).

11. Vinson JA, Su X, Zubik L, Bose P. Phenol Antioxidant Quantity and Quality in Foods: Fruits. *J Agric Food Chem*. 2001 Nov 1;49(11):5315-21. Available from: [<URL>](#).

12. Selvam SI, Joicesky SMB, Dashli AA, Vinothini A, Premkumar K. Assessment of anti bacterial, anti inflammation and wound healing activity in Wistar albino rats using green silver nanoparticles synthesized from *Tagetes erecta* leaves. *JANS*. 2021 Mar 14;13(1):343-51. Available from: [<URL>](#).

13. Pandey S, Oza G, Vishwanathan M, Sharon M. Biosynthesis of highly stable gold nanoparticles using Citrus limone. *Ann Biol Res*. 2012;3(5):2378-82.

14. Kaviya S, Santhanalakshmi J, Viswanathan B, Muthumary J, Srinivasan K. Biosynthesis of silver nanoparticles using citrus sinensis peel extract and its antibacterial activity. *Spectrochimica Acta Part A: Molecular and Biomolecular Spectroscopy*. 2011 Aug;79(3):594-8. Available from: [<URL>](#).

15. Rai A, Chaudhary M, Ahmad A, Bhargava S, Sastry M. Synthesis of triangular Au core-Ag shell nanoparticles. *Materials Research Bulletin*. 2007 Jul;42(7):1212-20. Available from: [<URL>](#).
16. Linh DHT, Anh NP, Mi TTA, Tinh NT, Cuong HT, Quynh TL, et al. Biosynthesis, Characteristics and Antibacterial Activity of Silver Nanoparticles Using *Lemon Citrus Latifolia* Extract. *Mater Trans*. 2018 Sep 1;59(9):1501-5. Available from: [<URL>](#).
17. Prathna TC, Chandrasekaran N, Raichur AM, Mukherjee A. Biomimetic synthesis of silver nanoparticles by Citrus limon (lemon) aqueous extract and theoretical prediction of particle size. *Colloids and Surfaces B: Biointerfaces*. 2011 Jan;82(1):152-9. Available from: [<URL>](#).
18. Biv K, Nolan R. Green Synthesis of Silver Nanoparticles using Lemon Extract, Characterization, and Antimicrobial Properties [Internet]. Poster presentation presented at: Undergraduate Posters; 2021 May; Salem, Massachusetts. Available from: [<URL>](#)
19. Mosae Selvakumar P, Antonyraj CA, Babu R, Dakhsinamurthy A, Manikandan N, Palanivel A. Green Synthesis and Antimicrobial Activity of Monodispersed Silver Nanoparticles Synthesized Using Lemon Extract. *Synthesis and Reactivity in Inorganic, Metal-Organic, and Nano-Metal Chemistry*. 2016 Feb 1;46(2):291-4. Available from: [<URL>](#).
20. Niraimathi KL, Sudha V, Lavanya R, Brindha P. Biosynthesis of silver nanoparticles using *Alternanthera sessilis* (Linn.) extract and their antimicrobial, antioxidant activities. *Colloids and Surfaces B: Biointerfaces*. 2013 Feb;102:288-91. Available from: [<URL>](#).
21. Hawar SN, Al-Shmgani HS, Al-Kubaisi ZA, Sulaiman GM, Dewir YH, Rikisahedew JJ. Green Synthesis of Silver Nanoparticles from *Alhagi graecorum* Leaf Extract and Evaluation of Their Cytotoxicity and Antifungal Activity. Omri A, editor. *Journal of Nanomaterials*. 2022 Jan 5;2022:1-8. Available from: [<URL>](#).
22. Gondwal M, Joshi nee Pant G. Synthesis and Catalytic and Biological Activities of Silver and Copper Nanoparticles Using *Cassia occidentalis*. *International Journal of Biomaterials*. 2018;2018:1-10. Available from: [<URL>](#).
23. Mohamed NH, Ismail MA, Abdel-Mageed WM, Mohamed Shoreit AA. Antimicrobial activity of latex silver nanoparticles using *Calotropis procera*. *Asian Pacific Journal of Tropical Biomedicine*. 2014 Nov;4(11):876-83. Available from: [<URL>](#).
24. Villaño D, Fernández-Pachón MS, Moyá ML, Troncoso AM, García-Parrilla MC. Radical scavenging ability of polyphenolic compounds towards DPPH free radical. *Talanta*. 2007 Jan 15;71(1):230-5. Available from: [<URL>](#).
25. Prieto P, Pineda M, Aguilar M. Spectrophotometric Quantitation of Antioxidant Capacity through the Formation of a Phosphomolybdenum Complex: Specific Application to the Determination of Vitamin E. *Analytical Biochemistry*. 1999 May;269(2):337-41. Available from: [<URL>](#).
26. Singh R, Singh S, Kumar S, Arora S. Evaluation of antioxidant potential of ethyl acetate extract/fractions of *Acacia auriculiformis* A. Cunn. *Food and Chemical Toxicology*. 2007 Jul;45(7):1216-23. Available from: [<URL>](#).
27. Mulvaney P. Surface Plasmon Spectroscopy of Nanosized Metal Particles. *Langmuir*. 1996 Jan 1;12(3):788-800. Available from: [<URL>](#).
28. Jinu U, Gomathi M, Saiqa I, Geetha N, Benelli G, Venkatachalam P. Green engineered biomolecule-capped silver and copper nanohybrids using *Prosopis cineraria* leaf extract: Enhanced antibacterial activity against microbial pathogens of public health relevance and cytotoxicity on human breast cancer cells (MCF-7). *Microbial Pathogenesis*. 2017 Apr;105:86-95. Available from: [<URL>](#).
29. Wanjari AK, Patil MP, Chaudhari UE, Gulhane VN, Kim GD, Kiddane AT. Bactericidal and photocatalytic degradation of methyl orange of silver-silver chloride nanoparticles synthesized using aqueous phyto-extract. *Particulate Science and Technology*. 2022 Nov 17;40(8):1033-40. Available from: [<URL>](#).
30. Pourmortazavi SM, Taghdiri M, Makari V, Rahimi-Nasrabadi M. Procedure optimization for green synthesis of silver nanoparticles by aqueous extract of *Eucalyptus oleosa*. *Spectrochimica Acta Part A: Molecular and Biomolecular Spectroscopy*. 2015 Feb;136:1249-54. Available from: [<URL>](#).
31. Iftikhar M, Zahoor M, Naz S, Nazir N, Batiha GES, Ullah R, et al. Green Synthesis of Silver Nanoparticles Using *Grewia optiva* Leaf Aqueous Extract and Isolated Compounds as Reducing Agent and Their Biological Activities. Yin J, editor. *Journal of Nanomaterials*. 2020 Oct 24;2020:1-10. Available from: [<URL>](#).
32. Tyagi PK, Tyagi S, Gola D, Arya A, Ayatollahi SA, Alshehri MM, et al. Ascorbic Acid and Polyphenols Mediated Green Synthesis of Silver Nanoparticles from *Tagetes erecta* L. Aqueous Leaf Extract and Studied Their Antioxidant Properties. Tapia Hernández JA, editor. *Journal of Nanomaterials*. 2021 Aug 2;2021:1-9. Available from: [<URL>](#).
33. Udayasoorian C, Kumar KV, Jayabalakrishnan M. Extracellular synthesis of silver nanoparticles using leaf extract of *Cassia auriculata*. *Dig J Nanomater Biostruct*. 2011;6(1):279-83.
34. Göl F, Aygün A, Seyrankaya A, Gür T, Yenikaya C, Şen F. Green synthesis and characterization of *Camellia sinensis* mediated silver nanoparticles for antibacterial ceramic applications. *Materials Chemistry and Physics*. 2020 Aug;250:123037. Available from: [<URL>](#).
35. Kharabi Masooleh A, Ahmadikhah A, Saidi A. Green synthesis of stable silver nanoparticles by the main reduction component of green tea (*Camellia sinensis* L.). *IET nanobiotechnol*. 2019 Apr;13(2):183-8. Available from: [<URL>](#).
36. Ali S, Jalal M, Ahmad H, Sharma D, Ahmad A, Umar K, et al. Green Synthesis of Silver Nanoparticles from *Camellia sinensis* and Its Antimicrobial and Antibiofilm Effect against Clinical Isolates. *Materials*. 2022 Oct 8;15(19):6978. Available from: [<URL>](#).
37. Chandra A, Bhattarai A, Yadav AK, Adhikari J, Singh M, Giri B. Green Synthesis of Silver Nanoparticles Using Tea Leaves from Three Different Elevations. *ChemistrySelect*. 2020 Apr 16;5(14):4239-46. Available from: [<URL>](#).
38. Gomaa EZ. Antimicrobial, antioxidant and antitumor activities of silver nanoparticles synthesized by *Allium cepa* extract: A green approach. *Journal of Genetic Engineering and Biotechnology*. 2017 Jun;15(1):49-57. Available from: [<URL>](#).

39. Es-haghi A, Javadi F, Taghavizadeh Yazdi ME, Amiri MS. The Expression of Antioxidant Genes and Cytotoxicity of Biosynthesized Cerium Oxide Nanoparticles Against Hepatic Carcinoma Cell Line. *Avicenna J Med Biochem.* 2019 Jun 25;7(1):16-20. Available from: [<URL>](#).

40. Pham-Huy LA, He H, Pham-Huy C. Free radicals, antioxidants in disease and health. *Int J Biomed Sci.* 2008 Jun;4(2):89-96.

41. M G, Dj M, Vinaykiya V, V B, Dutta S, Pawar R, et al. Screening of Antibacterial and Antioxidant Activity of Biogenically Synthesized Silver Nanoparticles from *Alternaria alternata*, Endophytic Fungus of *Dendrophthoe falcata*-a Parasitic Plant. *BioNanoSci.* 2022 Mar;12(1):128-41. Available from: [<URL>](#).

42. Taha ZK, Hawar SN, Sulaiman GM. Extracellular biosynthesis of silver nanoparticles from *Penicillium italicum* and its antioxidant, antimicrobial and cytotoxicity activities. *Biotechnol Lett.* 2019 Sep;41(8-9):899-914. Available from: [<URL>](#).

43. Khane Y, Benouis K, Albukhaty S, Sulaiman GM, Abomughaid MM, Al Ali A, et al. Green Synthesis of Silver Nanoparticles Using Aqueous Citrus limon Zest Extract: Characterization and Evaluation of Their Antioxidant and Antimicrobial Properties. *Nanomaterials.* 2022 Jun 10;12(12):2013. Available from: [<URL>](#).

44. Alavi M, Karimi N. Characterization, antibacterial, total antioxidant, scavenging, reducing power and ion chelating activities of green synthesized silver, copper and titanium dioxide nanoparticles using *Artemisia haussknechtii* leaf extract. *Artificial Cells, Nanomedicine, and Biotechnology.* 2017 Dec 12;1-16. Available from: [<URL>](#).

45. Samreen FG, Muzaffar R, Nawaz M, Gul S, Basra MAR. Synthesis, Characterization and Anti-Microbial Activity of Citrus limon Mediated Nanoparticles [Internet]. *LIFE SCIENCES*; 2018 Nov [cited 2023 Feb 5]. Available from: [<URL>](#)

46. Link MP, Goorin AM, Miser AW, Green AA, Pratt CB, Belasco JB, et al. The Effect of Adjuvant Chemotherapy on Relapse-Free Survival in Patients with Osteosarcoma of the Extremity. *N Engl J Med.* 1986 Jun 19;314(25):1600-6. Available from: [<URL>](#).

47. Prasad KS, Pathak D, Patel A, Dalwadi P, Prasad R, Patel P, et al. Biogenic synthesis of silver nanoparticles using *Nicotiana tobaccum* leaf extract and study of their antibacterial effect. *African Journal of Biotechnology.* 2011;10(41):8122.

48. Verma A, Mehata MS. Controllable synthesis of silver nanoparticles using Neem leaves and their antimicrobial activity. *Journal of Radiation Research and Applied Sciences.* 2016 Jan;9(1):109-15. Available from: [<URL>](#).

49. Babu RH, Yugandhar P, Savithamma N. Synthesis, characterization and antimicrobial studies of bio silica nanoparticles prepared from *Cynodon dactylon* L.: a green approach. *Bull Mater Sci.* 2018 Jun;41(3):65. Available from: [<URL>](#).

50. Patil MP, Rokade AA, Ngabire D, Kim GD. Green Synthesis of Silver Nanoparticles Using Water Extract from Galls of *Rhus Chinensis* and Its Antibacterial Activity. *J Clust Sci.* 2016 Sep;27(5):1737-50. Available from: [<URL>](#).

51. Paul B, Bhuyan B, Purkayastha DD, Dhar SS. Photocatalytic and antibacterial activities of gold and silver

nanoparticles synthesized using biomass of *Parkia roxburghii* leaf. *Journal of Photochemistry and Photobiology B: Biology.* 2016 Jan;154:1-7. Available from: [<URL>](#).

52. Khan SS, Mukherjee A, Chandrasekaran N. Studies on interaction of colloidal silver nanoparticles (SNPs) with five different bacterial species. *Colloids and Surfaces B: Biointerfaces.* 2011 Oct;87(1):129-38. Available from: [<URL>](#).

53. Sondi I, Salopek-Sondi B. Silver nanoparticles as antimicrobial agent: a case study on *E. coli* as a model for Gram-negative bacteria. *Journal of Colloid and Interface Science.* 2004 Jul;275(1):177-82. Available from: [<URL>](#).

54. Patil SV, Borase HP, Patil CD, Salunke BK. Biosynthesis of Silver Nanoparticles Using Latex from Few Euphorbian Plants and Their Antimicrobial Potential. *Appl Biochem Biotechnol.* 2012 Jun;167(4):776-90. Available from: [<URL>](#).

55. Patil MP, Kim GD. Eco-friendly approach for nanoparticles synthesis and mechanism behind antibacterial activity of silver and anticancer activity of gold nanoparticles. *Appl Microbiol Biotechnol.* 2017 Jan;101(1):79-92. Available from: [<URL>](#).

56. Majeed S, Danish M, Zakariya NA, Hashim R, Ansari MT, Alkahtani S, et al. In Vitro Evaluation of Antibacterial, Antioxidant, and Antidiabetic Activities and Glucose Uptake through 2-NBDG by Hep-2 Liver Cancer Cells Treated with Green Synthesized Silver Nanoparticles. *Srivastava S, editor. Oxidative Medicine and Cellular Longevity.* 2022 May 17;2022:1-14. Available from: [<URL>](#).

57. Ovais M, Khalil AT, Raza A, Khan MA, Ahmad I, Islam NU, et al. Green synthesis of silver nanoparticles via plant extracts: beginning a new era in cancer theranostics. *Nanomedicine.* 2016 Dec;11(23):3157-77. Available from: [<URL>](#).

58. Banerjee PP, Bandyopadhyay A, Nagesh H, Policegoudra R, Bhattacharya S, Karak N, et al. *Mentha arvensis* (Linn.)-mediated green silver nanoparticles trigger caspase 9-dependent cell death in MCF7 and MDA-MB-231 cells. *BCTT.* 2017 Apr;Volume 9:265-78. Available from: [<URL>](#).

59. Soshnikova V, Kim YJ, Singh P, Huo Y, Markus J, Ahn S, et al. Cardamom fruits as a green resource for facile synthesis of gold and silver nanoparticles and their biological applications. *Artificial Cells, Nanomedicine, and Biotechnology.* 2018 Jan 2;46(1):108-17. Available from: [<URL>](#).

60. Mohammadinejad R, Moosavi MA, Tavakol S, Vardar DÖ, Hosseini A, Rahmati M, et al. Necrotic, apoptotic and autophagic cell fates triggered by nanoparticles. *Autophagy.* 2019 Jan 2;15(1):4-33. Available from: [<URL>](#).

61. Barabadi H, Vahidi H, Damavandi Kamali K, Rashedi M, Saravanan M. Antineoplastic Biogenic Silver Nanomaterials to Combat Cervical Cancer: A Novel Approach in Cancer Therapeutics. *J Clust Sci.* 2020 Jul;31(4):659-72. Available from: [<URL>](#).

62. Hembram KC, Kumar R, Kandha L, Parhi PK, Kundu CN, Bindhani BK. Therapeutic prospective of plant-induced silver nanoparticles: application as antimicrobial and anticancer agent. *Artificial Cells, Nanomedicine, and Biotechnology.* 2018 Nov 12;46(sup3):38-51. Available from: [<URL>](#).



Production of Biodiesel from Waste Cooking Oil Using KOH/Al₂O₃ as a Heterogeneous Catalyst

Asmo Abdillahi Hassan¹ , Ibrahim Yaagoub Erwa^{1*} , Razan Ali Salim¹ ,
Omer A. Omer Ishag , and Maysoun Ali Ahmed¹ 

¹International University of Africa, Department of Applied and Industrial Chemistry, Khartoum, 12223, Sudan.

Abstract: The catalytic performance of potassium hydroxide supported on alumina (KOH/Al₂O₃) for transesterification of waste cooking oil (WCO) was investigated. XRD, FTIR, and SEM techniques were used to characterize the catalyst after it had been synthesized using the wet impregnation method. The properties of the WCO and the produced biodiesel were evaluated. The main fatty acids of WCO were linoleic (45.61%), elaidic (33.86%), palmitic (10.32%), and stearic acid (4.80%), the acid value (2.29 mg KOH/g), FFA (1.15%), density at 25 °C (0.91 g/cm³), viscosity at 40 °C (34.09 mm²/s), water content (0.0017%), and flash point (206 °C). The XRD pattern of the catalyst showed diffraction peaks of KAlO₂ attributed to the orthorhombic crystal system having a 12.46% degree of crystallinity. The SEM micrographs confirmed the amorphous nature of the catalyst. The presence of K-O and Al-O bonds in the catalyst was confirmed by the FTIR. A biodiesel yield of 86.6% was achieved with the following variables: oil to methanol ratio of 1:4, catalyst loading of 1.5% (w/v%), reaction temperature of 55 °C, and a reaction time of 1 h. The results appeared to show a decreasing pattern of yield after 4 cycles of reaction from 86.60 to 51.50%. The fuel properties were density (0.8919 g/cm³), viscosity (7.428 cSt), flash point (65 °C), acid number (0.54 mg KOH/g) and water content (0.0196%). Furthermore, the properties of the prepared biodiesel have been found to comply with the ASTM and EN standard specifications. This catalyst showed promising results for manufacturing biodiesel from low-cost feedstock.

Keywords: Biodiesel, waste cooking oil, catalytic performance, Heterogeneous catalyst, wet impregnation.

Submitted: August 19, 2022. **Accepted:** January 10, 2023.

Cite this: Hassan AA, Erwa IY, Salim RA, Ishag O, Ahmed MA. Production of Biodiesel from Waste Cooking Oil Using KOH/Al₂O₃ as a Heterogeneous Catalyst. JOTCSA. 2023;10:217-26.

DOI: <https://doi.org/10.18596/jotcsa.1163670>.

***Corresponding author. E-mail:** ibrachem9@gmail.com.

1. INTRODUCTION

The majority of the world's energy demands are met by petroleum-based fuels, but they are finite and unsustainable. New alternative sources for petroleum-based fuel have been extensively researched as a result of depletion of petroleum reserves and rising environmental concerns (1). Biodiesel is a renewable energy source that can replace fossil-based diesel and can reduce the drawbacks of diesel emission (2).

The use of biodiesel as a fuel source has several advantages, in addition to being a renewable, sustainable, biodegradable source, generally non-toxic and environmental friendliness, as it reduces CO₂ emissions and hazardous compounds such as

arithmetic, sulphur, particulate matter and NO_x, biodiesel shares a variety of similar physical and chemical properties with petroleum diesel (3-5). Biodiesel is superior to diesel fuel due to its higher oxygen composition, high cetane content, higher flash point, cleaner combustion, and appropriate lubrication characteristics. Therefore, typical compression-ignition engines may use pure biodiesel or biodiesel blends without the need for substantial modifications (6,7). Biodiesel is a clear liquid with a light- to dark-yellow color. It has a boiling point of more than 200 °C, a flash point of 100 to 170 °C, a cloud point of -3 to 12 °C, a pour point of -15 to 16 °C, a kinematic viscosity at 40 °C of 1.9-6.0 mm²/s, a distillation range of 195-325 °C, a vapour pressure (mm Hg at 22 °C) less than 5, a freezing point (-3 °C), Cetane number of 48-60,

lower calorific value of 37300–38500 kJ/kg, and upper calorific value of 39300–39600 kJ/kg; oxygen content of 10–11% (wt%); sulfur content of 0.05% (wt%) (5,7,8). The oxygen content of biodiesel enhances the engine's combustion process and contributes to reducing exhaust emissions. Diesel fuels with high cetane values have a variety of benefits, including improved cylinder combustion, easier engine running in cold weather, and longer engine life (9). Dilution, micro-emulsion, pyrolysis, and transesterification methods were proposed as solutions to lower the viscosity of vegetable and animal oils, reduce the molecular weight, improve the volatility of the fuel, and decrease emissions such as HC and CO. The most widely utilized among these processes is the transesterification method (7, 10).

Biodiesel is made from natural oils or animal fats and alcohol via a transesterification reaction, which converts triglycerides into esters known as fatty acid methyl esters (FAME) (11). Commercial production of biodiesel is possible from a wide range of renewable biomass feedstocks, including edible oils. (e.g. peanut, rapeseed/canola, soybean, sunflower, palm, corn, cottonseed, coconut, mustard, olive, and sesame oils) and non-edible oils (e.g. jatropha, castor, neem, jojoba, passion seed, and moringa oils), animal fats (e.g. pork lard, beef tallow, poultry fat, fish oil, chicken fat), and waste cooking oils (12, 13). Competition with food is brought on by the production of biodiesel from conventionally grown oilseed crops. Due to the increasing demand for edible oils for food and their current high cost for use as fuel, the use of non-edible vegetable oils and waste oils is essential in developing countries (12). WCO refers to cooking oils that have been used in food preparation but might no longer suitable to use in food production. WCO may come from domestic, commercial or industrial sources. A waste stream such as WCO requires proper management, and irresponsible disposal can result in problems (14).

Biodiesel is defined as fatty acid methyl esters (FAME) derived from the transesterification of triglycerides (vegetable oils or animal fats) with alcohol and a suitable catalyst (15). The main catalysts utilized can be classed as homogeneous or heterogeneous. Homogeneous catalysts (base/acid) react with the reaction mixture in the same liquid phase are commonly used for biodiesel production from different feedstocks under mild reaction conditions. However, these traditional catalysts cause several technical problems i.e. reaction corrosion, large amounts of waste water production, separation problems, thereby increase the cost of biodiesel production, whereas heterogeneous catalysts react with the reaction mixture in a separate phase, usually as a solid. Heterogeneous catalysts are non-corrosive, environmentally beneficial, and a green process. They may be recycled and reused multiple times, making biodiesel production more cost-effective; thereby resolve many of problems associated with

homogeneous catalyzed biodiesel technology (16). The aim of this research was to investigate different transesterification process conditions; oil to methanol molar ratio, temperature, catalyst loading and reaction time on biodiesel production from WCO using potassium hydroxide supported on alumina as a heterogeneous catalyst. The reusability of the catalyst was also investigated over several consecutive runs and properties of the produced biodiesel were evaluated based on standards set of ASTM D6751 (17) and EN 14214 (18).

2. EXPERIMENTAL SECTION

2.1. Materials

Refined waste peanut oil was collected from Royal Broast fast food restaurant in Khartoum, Sudan. The oil was used once for frying. The solid particles and other impurities were filtered through normal sieves and then heated to 120 °C for 2 h to eliminate water traces. Then, the pre-treated WCO was stored in a clean glass air tight container. All chemicals used in this study were of analytical grade and used without any purification include: methanol (99%); ethanol (99%); potassium hydroxide (KOH) with purity 99%; aluminium oxide (Al₂O₃); were purchased from Merck Co. (Dannstadt, Germany)

2.2. Characterization of the WCO

The density, acid value, kinematic viscosity, flash point, water content and color the samples were assessed using the methods described by ASTM International (19-24). The fatty acids composition of the WCO sample was determined using (GC/MS-QP2010SE, Shimadzu, Japan) equipped with capillary column (Rtx-5MS- 30 m × 0.25 mm I.D × 0.25 μm) with the following analytical conditions: injector temperature was 300 °C; the injector was operated in the split mode; oven temperature was programmed from 60 °C to 300 °C at 10 °C/min; the carrier gas was helium at flow rate of 1.6 mL/min; volume of injection was 1 μL. The MS conditions were ion source temperature 200 °C, the interface temperature was 250 °C, the mass scan range was 40 – 500 m/z, and the total run time was 34 min. The spectra of the components were compared with the database of spectrum of known components stored in the GC-MS library (NIST).

2.3. Preparation of the Catalyst

Alkaline modified alumina was prepared via wet impregnation of aqueous solution of potassium hydroxide and alumina as a support. About 25 g of KOH was dissolved in 100 mL of distilled water. Then, the required amount of alumina powder was added to the solution (1:4 weight ration of Al₂O₃ to KOH). The slurry was vigorously stirred for 24 h, on magnetic stirrer at room temperature. The obtained precipitate was aged in mother liquid overnight (~24 h) at 40 °C. The solid product was separated by filtration using a vacuum filter system. It later dried in a 110 °C oven for 12 h. The dried solid obtained was calcined at 400 °C for 4 h in a muffle furnace (25).

2.4. Characterization of the Catalyst

The bulk structure, composition and crystalline structure of the synthesized catalyst were determined using X-ray diffractometer (XRD) (GNR, Italy), equipped with Cu K α radiation (40 kV 40 mA) with a wavelength (λ) of 1.54 Å. The sample was scanned from 4 to 90° (2 θ) and the phases were identified using X, Pert Highscore plus software by searching and matching the obtained patterns with the JCPDS (Joint committee of powder diffraction standards) database file. The morphology of the catalyst was studied by scanning electron microscopy (SEM), the micrographs were obtained by using a (TESCAN VEGA3) microscope; the elemental analysis was performed by energy dispersive spectroscopy (OXFORD EDS) detector. FTIR analysis of the catalyst was carried out using potassium bromide (KBr) powder method on a FTIR spectrophotometer (IRT racer-100, Shimadzu, Japan) with a resolution of 2 cm⁻¹ at 500 – 4000 cm⁻¹ range

2.5. Transesterification Reaction

The transesterification reaction of WCO was carried out with various catalyst loading, different methanol / oil molar ratios, various reaction temperatures and reaction time. Before starting the transesterification reaction, the oil was heated to 70 °C then cooled to the reaction temperature between 50 – 60 °C. The specified amount of oil, methanol and catalyst were carefully measured and poured in a 250 mL three-neck round-bottom flask equipped with a magnetic stirrer at 400 rpm and a water-cooled condenser. The reaction was allowed to proceed for a specified reaction time (1 – 2 h). Then reaction mixture was cooled to 25 °C. After cooling, the mixture was centrifuged at 3000 rpm for 10 min and the catalyst was filtered using a vacuum filter. The liquid was left in a separating funnel for 3 h for separation. The glycerol layer was discharged, and the excess methanol was washed from the biodiesel layer five times using warm distilled water (80 – 100 °C) in a separatory funnel (The amount of water was about 30% of fuel volume). Finally, the produced fatty acid methyl esters (FAME_s) were collected and the biodiesel yield was calculated using Equation 1.

$$\text{Biodiesel yield (\%)} = \frac{\text{Weight of FAMEs}}{\text{Weight of oil}} \times 100 \quad (\text{Eq.1})$$

The catalyst was isolated from the reaction product in the first reaction, washed with methanol three times and dried at 60 °C in an oven for 2 h (25) and reused in the transesterification reaction in optimal conditions, the procedures were repeated three times.

2.6. Product Analysis

The resulting biodiesel from the transesterification reaction was analysed using appropriate ASTM standard methods. The following fuel properties were determined: density was determined using a 25 cm³ pycnometer at 15 °C temperatures,

according to Standard ASTM D-4052, viscosity, HK-1005A kinematic viscosity apparatus was used at a temperature of 40 °C according to Standard ASTM D-445, acid number was determined by dissolved the sample in a 50 cm³ of ethanol and the acid presented in the sample was titrated with 0.1 N potassium hydroxide solution. Flash point was determined using a method ASTM-D93, closed cup, at which application of an ignition source causes the vapours of a specimen to ignite under specified conditions of test. Water content of the sample was determined by aquamax Karl Fischer coulometric titration, pre-titration is performed automatically (19-24). The characteristics of the produced biodiesel were compared with ASTM D6751 (17) biodiesel standard and EN14214 (18) fossil diesel standards to confirm their acceptability as a fuel in diesel engines.

3. RESULTS AND DISCUSSION

3.1. Characterization of the WCO

In this study, the WCO used as a feedstock was characterized based on its physicochemical properties. The properties were summarized in Table 1. Free fatty acid (FFA) was measured to determine the availability of WCO for using in transesterification directly. Previous studies have suggested feedstock FFA content of less than 2% for transesterification process (26), and if the acid value is very high, WCO requires a pre-treatment to decrease its fatty acid content before the conversion to biodiesel to prevent saponification reaction. The obtained results of showed an acid number of 2.29 mg KOH/g of oil and FFA of 1.15%, this implies that the WCO could be directly converted into biodiesel via transesterification process. Regarding the density, it was determined at 25 °C to be 0.911 g/cm³, this value was in an agreement with those recorded by Mahesh et al. (1) and Yusuff et al. (27). The kinematic viscosity of WCO at 40°C was determined to be 34.09 mm²/s, and this value was in the range from 39.07 to 28.8 mm²/s, reported in previous studies (26,28,29). The flash point in this study was lower than that reported in the study done by Anisah et al. (26) as 247.7 °C. The value of the water content of the oil was much lower than the value determined in the previous study (30), the oil feedstock should be anhydrous (water content <0.3%). These data show that this feedstock is appropriate to obtain high ester yields.

Ten fatty acids were identified in WCO as shown in Table 2, the main fatty acids present in the WCO were linoleic acid (45.61%) followed by elaidic acid (33.86%), palmitic acid (10.32%) and stearic acid (4.80%). Approximately 45.61% of the fatty acids were found to be poly-unsaturated, 34.55% mono-unsaturated and 16.47% saturated fatty acids. The four main components were found in WCO: linoleic, elaidic, palmitic and stearic acids, were higher than that obtained in a previous study (31).

Table 1: Physicochemical properties of WCO.

Property	Experimental Values*
Acid value (mg KOH/g)	2.29
FFA (%)	1.15
Density at 25 °C (g/cm ³)	0.911
Viscosity at 40 °C (mm ² /s)	34.09
Flash point (°C)	206
Color	<4.0
Water count (%)	0.0017

* Values recorded as mean value.

Table 2: Chemical composition of WCO.

Fatty acid	IUPAC name	Formula	Structure	wt%
Linoleic	9,12-Octadecadienoic acid	C ₁₈ H ₃₂ O ₂	C18:2	45.61
Elaidic	9-Octadecenoic acid	C ₁₈ H ₃₄ O ₂	C18:1	33.86
Palmitic	Hexadecanoic acid	C ₁₆ H ₃₂ O ₂	C16:0	10.32
Stearic	Methyl stearate	C ₁₈ H ₃₆ O ₂	C18:0	4.80
Behenic	Docosanoic acid	C ₂₂ H ₄₄ O ₂	C22:0	0.80
Palmitoleic	9-Hexadecenoic acid	C ₁₆ H ₃₀ O ₂	C16:1	0.45
Myristic	Methyl tetradecanoate	C ₁₄ H ₂₈ O ₂	C14:0	0.19
Lignocerc	Tetracosanoic acid	C ₂₄ H ₄₈ O ₂	C24:0	0.19
Lauric	Dodecanoic acid	C ₁₂ H ₂₄ O ₂	C12:0	0.06
Phthalic	1,2-Benzenedicarboxylic acid, bis(2-methylpropyl)	C ₁₆ H ₂₂ O ₄	C16:0	0.05

* The obtained results in terms of fatty acid methyl esters from GC-MS library data system reviewed and the results listed out in the form of fatty acid chains.

3.2. Characterization of the Catalyst

The XRD analysis was conducted to determine the variation of the structure, amorphous content and degree crystallinity of the catalyst depicted in Figure 2. The XRD pattern of the catalyst show a diffraction peaks of KAlO₂ appears at 2θ of 17.06°, 22.89°, 32.86°, 33.71°, 34.11°, 37.24°, 37.66°, 39.52°, 42.67°, 68.16° and 89.83° which were attributed to orthorhombic type of AlKO₂ formed on the catalyst surface with lattice parameter (in Å) of 5.456, 10.9617 and 15.4893 for a, b and c respectively (Table 3). The AlKO₂ levels were observed to be consistent with the data obtained by the authors in

(32), whereby some diffraction were similar and the other rapprochement to that found in this study. The similar peaks were 17° and 34°. Meanwhile, the characteristic peaks of alumina at angles of 2θ = 37° and 67.21° were almost unchanged on the XRD pattern, indicating that Al₂O₃ still retained its amorphous structure. A similar pattern was obtained by Santos et al. (32). As in a previous studies (33, 34) the formation of K₂O₂ is clearly observed at 2θ = 31°, 33°, 34° and 42° (JCPDS file (50-05241). In this study the catalyst was successfully converted to desired species (K₂O₂) for the reaction.

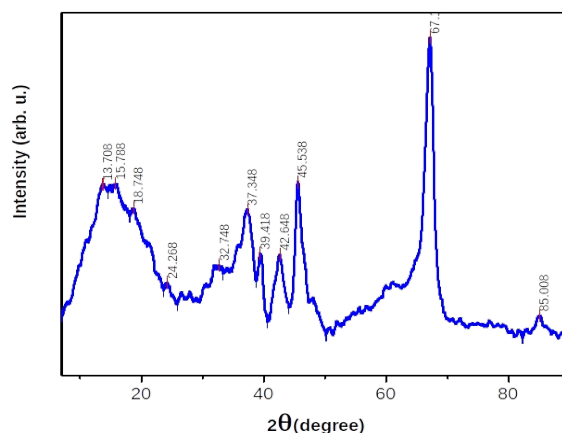
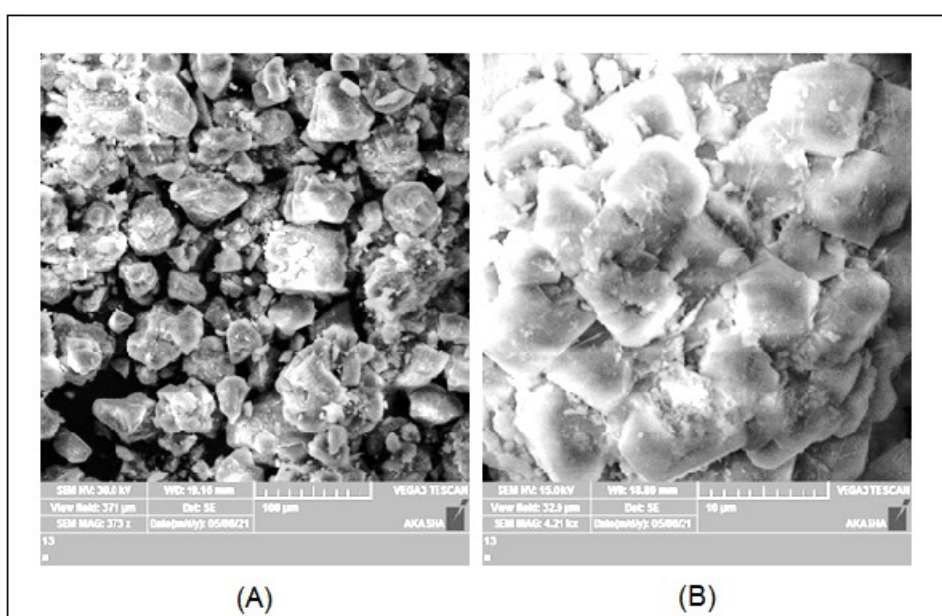
**Figure 1:** XRD pattern of the of KOH/Al₂O₃ catalyst.

Table 3: XRD matched peak analysis report.

Property	Amount
Formula sum	Al K O ₂
Peaks matched	17
Crystal system	Orthorhombic
Unit cell (Å)	a = 5.4560, b = 10.9617 and c = 15.4893
Calc. density (g/cm ³)	2.813
Degree of crystallinity (wt%)	12.46
Amorphous content (wt %)	87.54

The particle morphology of the catalyst was captured via SEM, and the micrograph of KOH/Al₂O₃ presented in Figure 2 shows the particles of aluminium oxide impregnated by potassium hydroxide. The catalyst has irregular crystallinity

and small sized crystals. Figure 2 clearly shows that there are no definite morphologies in the sample. It looks that the particles were agglomerated and form a cluster.

**Figure 2:** SEM image of KOH/Al₂O₃ catalyst.

The FTIR spectrum of the prepared KOH/Al₂O₃ in the range 400 – 4000 cm⁻¹ was shown in Figure 3. The spectrum shows an intensive band at 3500 cm⁻¹ belongs to the ν_s(Al)O-H stretching vibrations, three moderate bands observed at the frequencies of 1149, 1083 and 1026 cm⁻¹ can be attributed to the K-O bond and the four weak bands at 1732, 871, 813 and 617 cm⁻¹ are the combination bands. The absorption edge of the hydroxyl bands on the

surface was found at 1732 cm⁻¹. The bands appearing in the region of 600 – 870 cm⁻¹ include the tension of Al-O bonds, whereby aluminium exhibits vibrations extended in the region from 750 to 850 cm⁻¹. These absorption bands agree precisely with the ones previously reported in the literature (35) that introduced FTIR spectrum closed to that obtained in this study.

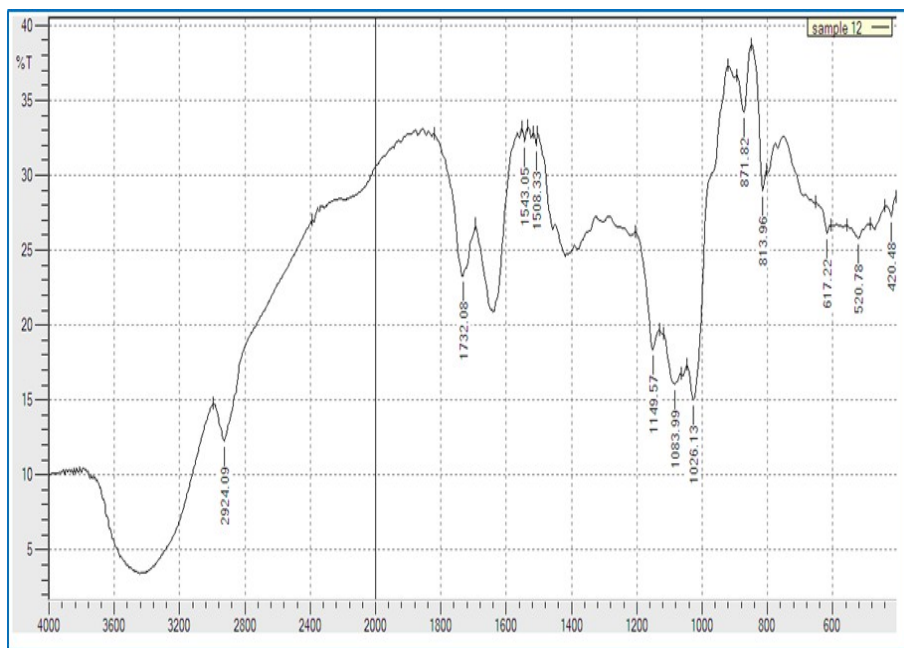


Figure 3: FTIR spectrum of KOH impregnated into Al₂O₃.

3.3. Transesterification Reaction

3.3.1. Effect of WCO/methanol molar ratio

The study of the influence of the WCO/methanol molar ratio (1:4; 1:5 and 1:6) was carried out at temperature of 50 °C for 1 h of reaction with 1% catalyst loading. Results in Figure 4 shows that the highest conversion was achieved with 1:4 WCO/methanol molar ratios, but afterwards shows a decline in conversion rate with the WCO/methanol

molar ratio going from 1:5 to 1:6. An excess methanol increases the solubility of the by-product (glycerol) which then may initiate the reversible reaction to reduce the conversion. The optimum methanol/oil molar ratio was observed at 1:4. This result is in line with the work of Gim bun et al. (36); they produced biodiesel from rubber seed oil and found that the 1:4 ratio was the best ratio for generating good biodiesel quality.

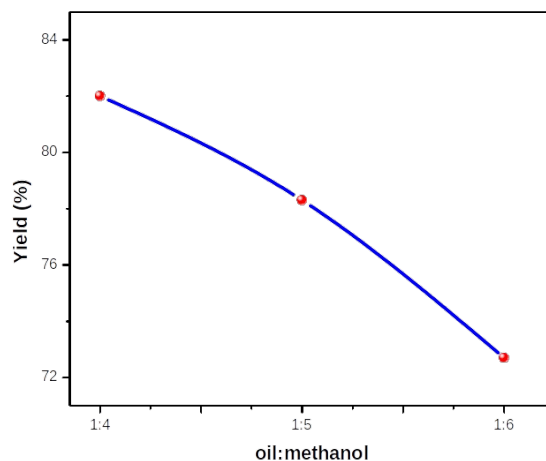


Figure 4: Effect of WCO /methanol molar ratio on biodiesel production.

3.3.2. Effect of the catalyst loading

The effect of KOH/Al₂O₃ catalyst loading (1 to 2 w/v %) on biodiesel yield was evaluated at oil to methanol ratio of 1:4, temperature of 55 °C with 1 h reaction time. It was shown in Figure 5 that the biodiesel yield increases from 84.5% to 86.6% as the catalyst loading increases from 1 to 1.5% and

decreased to 81.1 % afterwards. This might be due to the formation of more triglycerides in the saponification side reaction as a result of the excessive addition of catalyst (37). It was found that the optimum catalyst loading in this study was 1.5% with biodiesel conversion of 86.6%.

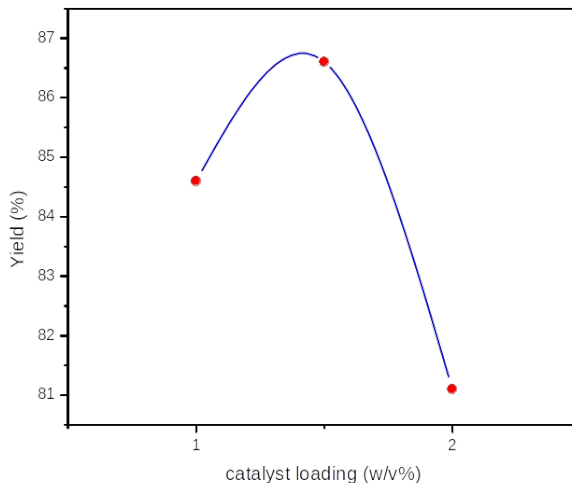


Figure 5: Effect of catalyst loading in biodiesel yield.

3.3.3. Effect of temperature

The effect of temperature on the transesterification of WCO was investigated by carrying out the experiments at a fixed WCO/methanol ratio of 1:4 and amount of catalyst of 1% (w/v %) with a reaction time of 1 h. The experimental temperature was in the range from 50 °C to 60 °C, as shown in Figure 6. It was observed that increasing the reaction temperature had a favourable influence on

the degree of transesterification. With a rise in temperature, the conversion rose at a faster rate. At higher reaction temperatures, however, there was an opportunity of methanol loss and product darkness increased. High reaction temperatures also increased the assembly cost of biodiesel. The optimum temperature for this reaction was found to be 55 °C due to the lower boiling point (64.5 °C) at which methanol evaporates (38).

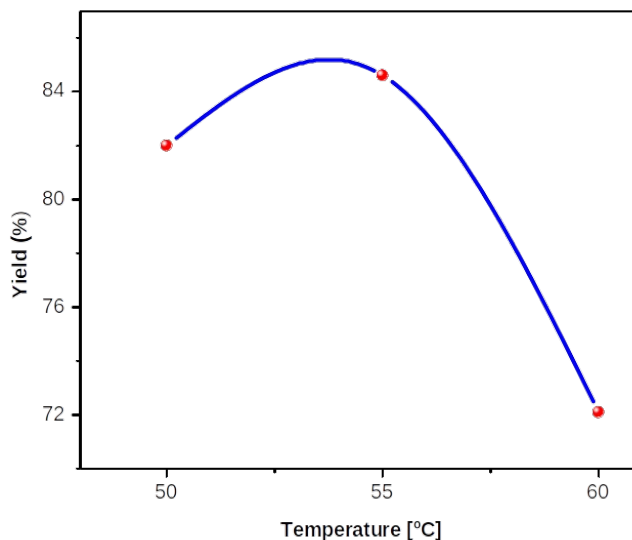


Figure 6: Effect of temperature in transesterification of WCO.

3.3.4. Effect of reaction time

The effect of reaction time was studied as it had a significant impact on the transesterification of waste cooking oil. The reaction time varied from 1 to 2 h in oil to methanol ratio of 1:4 with 1.5% catalyst loading at temperature of 55 °C. The transesterification reaction produces the maximum biodiesel yield of 86.6 % after 1 h of reaction. Almost all the oil has been transformed into methyl esters leading to a maximum conversion. However,

the yield decreased after 2 hours of the reaction. This may be due to the longer reaction time led to a reversible process that led to an increase in glycerides (37).

3.3.5. Reusability test

Catalyst reusability is an important aspect in the development of biodiesel. The reusability of the catalyst was determined at the optimum conditions for four cycles as shown in Figure 7 it was noticed

that after cycle 1 with yield of 86.6%, the cycle demonstrated a declining pattern of yield of biodiesel which was 68.7%, 60.6% and 51.5% for cycle 2, 3 and 4 respectively where the yield of biodiesel decreased due to a decrease in catalytic

activity. The reduction in catalytic activity was caused by the loss of catalyst during the filtration process, activation, and morphology change of the catalyst used (2).

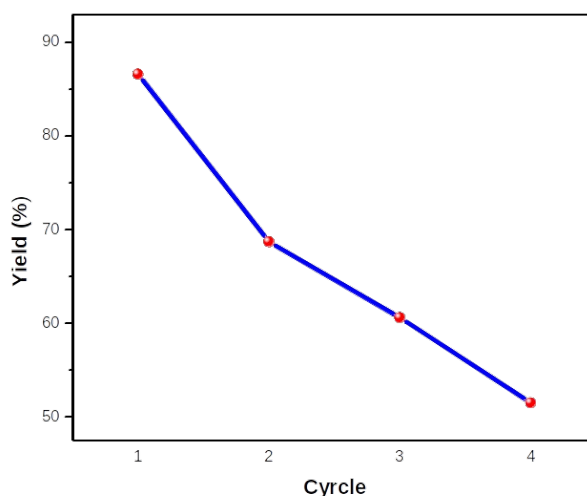


Figure 7: Reusability test for KOH/Al₂O₃ catalyst.

3.3.6. Characterization of produced biodiesel from WCO

By applying the aforementioned optimum conditions, the obtained biodiesel yield was ~ 86.6%. At molar ratio of 1:4, temperature 55 °C, catalyst loading 1.5% in 1 h. The produced biodiesel was evaluated on the basis of its fuel properties compared to ASTM 6751 (17) & EN 14214 (18) standards. Density, viscosity, acid number, flash point, and water content are the most important properties of biodiesel to measure the quality of the product.

Based on the data shown in Table 4 there isn't very much different from the ASTM 6751 (17) & EN 14214 (18) standards, except the viscosity still doesn't meet with the standards. This viscosity value is lower than that generated by Fathallah & Pinto, (39) and higher than Ashok et al. (40) and Ahmed et al. (41). However, because biodiesel is always combined with petroleum diesel in engine applications, the biodiesel in this study can be used as fuel (42).

Table 4: WCO biodiesel properties compared with ASTM & EN14214 Standards.

Property	WCO biodiesel	ASTM D6751	EN 14214
Density at 15 °C (g/mL)	0.8919	0.82-0.9	0.86-0.9
Viscosity at 40 °C (cSt)	7.428	1.9-6.0	3.5-5.0
Acid value (mg KOH/g)	0.54	0.50 max	0.50 max
Flash point (°C)	65	130 min	120 min
Color	<1.5	-	-
Water count (%)	0.0196	0.03 (v/v%)	500 (mg/kg)

4. CONCLUSION

The potential of potassium hydroxide supported on alumina (KOH/Al₂O₃) as heterogeneous catalyst for biodiesel production from peanut waste cooking oil (WCO) has been evaluated. The determined physicochemical properties of WCO make it an attractive alternative feedstock for biodiesel production. The optimal reaction conditions were: oil to methanol ratio 1:4 catalyst loading of 1.5%, reaction temperature of 55 °C, reaction time 1 h, with a yield of 86.6%. The fuel characteristics of the synthesized methyl ester from the WCO at the

optimal process conditions were found to be in accordance with the ASTM 6751 & EN 14214 standard specifications. Reusability test shows that the synthesized catalyst is reusable up to 4 times. The catalyst employed gave a good performance and easily separates from the product mixture. Thus, WCO is a promising feedstock for biodiesel and (KOH/Al₂O₃) is a promising catalyst for methyl ester synthesis via heterogeneous catalytic transesterification under milder reaction conditions.

5. CONFLICT OF INTEREST

The authors declare no conflict of interest.

6. ACKNOWLEDGMENTS

The authors are grateful to the International University of Africa, the Sudanese Thermal Generation Company, and General Directorate Petroleum Laboratories Research Studies- Ministry of Petroleum - Sudan for providing the laboratory facilities necessary to conduct this research work.

7. REFERENCES

1. Mahesh SE, Ramanathan A, Begum KMS, Narayanan A. Biodiesel production from waste cooking oil using KBr impregnated CaO as catalyst. *En Conv Manag.* 2015;91:442-50. [<DOI>](#).
2. Fitriana N, Husin H, Yanti D, Pontas K, Alam PN, Ridho M, et al. Synthesis of K₂O/zeolite catalysts by KOH impregnation for biodiesel production from waste frying oil. *IOP Conf Ser: Mater Sci Eng.* 2018;334:012011. [<DOI>](#).
3. Yan S, DiMaggio C, Mohan S, Kim M, Salley SO, Ng KYS. Advancements in heterogeneous catalysis for biodiesel synthesis. *Top Catal.* 2010;53:721-36. [<DOI>](#).
4. Abdullah SH, Hanapi NH, Azid A, Umar R, Juahir H, Khatoon H, Endut A. A review of biomass-derived heterogeneous catalyst for a sustainable biodiesel production. *Renew Sust En Rev.* 2017 Apr 1;70:1040-51. [<DOI>](#).
5. Simsek S. Effects of biodiesel obtained from Canola, sefflower oils and waste oils on the engine performance and exhaust emissions. *Fuel.* 2020;265:117026. [<DOI>](#).
6. Simsek S, Özdalyan B. Improvements to the composition of fusel oil and analysis of the effects of fusel oil-gasoline blends on a spark-ignited (SI) engine's performance and emissions. *Energies* 2018;11(3):625.
7. Simsek S, Uslu S. Comparative evaluation of the influence of waste vegetable oil and waste animal oil-based biodiesel on diesel engine performance and emissions. *Fuel.* 2020;280:118613. [<DOI>](#).
8. Barnwal BK, Sharma MP. Prospects of biodiesel production from vegetable oils in India. *Renewable and Sustainable Energy Reviews.* 2005;9(4):363-78. [<DOI>](#).
9. Şimşek S, Uslu S. Analysis of the effects of cetane improver addition to diesel on engine performance and emissions. *Int J Auto Eng Technol.* 2021:26-32. [<DOI>](#).
10. Demirbaş A. Chemical and fuel properties of seventeen vegetable oils. *En Sour.* 2003;25(7):721-8. [<DOI>](#).
11. Wicaksono A, Saptadi S, editors. Waste cooking oil into biodiesel transformation and its economical potency through circular economic model in Semarang Barat Area Indonesia. *E3S Web of Conf;* 2019: EDP Sci. [<DOI>](#).
12. Kayode B, Hart A. An overview of transesterification methods for producing biodiesel from waste vegetable oils. *Biofuels* 2019;10(3):419-37. [<DOI>](#).
13. Osorio-González CS, Gómez-Falcon N, Sandoval-Salas F, Saini R, Brar SK, Ramírez AA. Production of biodiesel from castor oil: A review. *Energies.* 2020;13(10):2467. [<DOI>](#).
14. Saini RD. Conversion of waste cooking oil to biodiesel. *International J Petrol Sci Technol.* 2017;11(1):9-21. [<URL>](#).
15. Raqeeb MA, Bhargavi R. Biodiesel production from waste cooking oil. *J Chem Pharm Res.* 2015;7(12):670-81. [<URL>](#).
16. Said N, Ani F, Said M. Review of the production of biodiesel from waste cooking oil using solid catalysts. *J Mech Eng Sci.* 2015;8:1302-11. [<DOI>](#).
17. ASTM. D 6751-20a: Standard specification for biodiesel fuel blend stock (B100) for middle distillate fuels. ASTM Int, West Conshohocken, PA, USA; 2020. [<URL>](#).
18. CEN. EN 14214:2008. Automotive fuels - Fatty acid methyl esters (FAME) for diesel engines - Requirements and test methods. CEN, European Committee for Standardization; 2008. [<URL>](#).
19. ASTM. D4052-18a. Standard test method for density, relative density, and API gravity of liquids by digital density meter ASTM Int, West Conshohocken, PA, USA; 2018. [<DOI>](#).
20. ASTM. D664-18. Standard test method for acid number of petroleum products by potentiometric titration. ASTM Int, West Conshohocken, PA, USA; 2018. [<URL>](#).
21. ASTM D445-21e1: standard test method for kinematic viscosity of transparent and opaque liquids (and calculation of dynamic viscosity). ASTM Int, West Conshohocken; 2021. [<URL>](#).
22. ASTM D93-20. Standard test methods for flash point by Pensky-Martens closed cup tester. ASTM Int, West Conshohocken, PA, USA; 2020. [<URL>](#).
23. ASTM D2709-16. Standard test method for water and sediment in middle distillate fuels by centrifuge. ASTM Int, West Conshohocken, PA, USA; 2016. [<URL>](#).
24. ASTM D1500-12. Standard test method for ASTM color of petroleum products (ASTM color scale). ASTM Int, West Conshohocken, PA, USA; 2012. [<URL>](#).
25. Helmi M, Hemmati A, Tahvildari K. Biodiesel production from *Amygdalus scoparia* using KOH/Al₂O₃ catalyst: optimization by response surface methodology. *Iran J En Environ.* 2021;12(1):34-44. [<DOI>](#).
26. Anisah PM, Suwandi, Agustian E. Effect of transesterification on the result of waste cooking oil conversion to biodiesel. *J Phys: Conf Ser.* 2019;1170:012067. [<DOI>](#).
27. Yusuff AS, Adeniyi OD, Azeez SO, Olutoye MA, Akpan UG. Synthesis and characterization of anthill-eggshell-Ni-Co mixed oxides composite catalyst for biodiesel production from waste frying oil. *Biofuels, Bioprod Bioref.* 2019;13(1):37-47. [<DOI>](#).
28. Hajy HT, Tahvildari K. Efficient Synthesis of biodiesel from waste cooking oil catalysed by Al₂O₃ impregnated with NaOH. *J Chem Petrol Eng (J Fac Eng).* 2015;49(2):143-51. [<URL>](#).

29. Patil PD, Gude VG, Reddy HK, Muppaneni T, Deng S. Biodiesel production from waste cooking oil using sulfuric acid and microwave irradiation processes. *J Environ Prot.* 2012;03(01):107-13. [<DOI>](#).
30. Priambodo R, Chen TC, Lu MC, Gedanken A, Liao JD, Huang YH. Novel technology for bio-diesel production from cooking and waste cooking oil by microwave irradiation. *En Proc.* 2015 Aug 1;75:84-91. [<DOI>](#).
31. Samuel O., Waheed M., Bolaji B., Dairo O. Production of biodiesel from Nigerian restaurant waste cooking oil using blender. *International J Renew En Res.* 2013; 3(4): 976-979. [<URL>](#).
32. Santoso A, Sumari, Urfa Zakiyya U, Tiara Nur A. Methyl ester synthesis of crude palm oil off grade using the K_2O/Al_2O_3 catalyst and its potential as biodiesel. *IOP Conf Ser: Mater Sci Eng.* 2019;515:012042. DOI: [<DOI>](#).
33. NollHakim L, Shohaimi NA, Ibrahim ML, Mokhtar WN, Ab Halim AZ. Transesterification of Waste Cooking Oil Utilizing Heterogeneous K_2CO_3/Al_2O_3 and KOH/Al_2O_3 Catalysts. *Malay Inst Chem.* 2021;23(2):74-83. [<DOI>](#).
34. Lokman NollHakim MAH, Shohaimi NAM, Mokhtar WNAW, Ibrahim ML, Abdullah RF. Immobilization of potassium-based heterogeneous catalyst over alumina beads and powder support in the transesterification of waste cooking oil. *Catalysts.* 2021;11(8):976. [<DOI>](#).
35. Haghazari N, Abdollahifar M, Jahani F. The effect of NaOH and KOH on the characterization of mesoporous AIOOH nanostructures in the hydrothermal route. *J Mex Chem Soc.* 2014 Jun;58(2):95-8. [<URL>](#).
36. Gim bun J, Ali S, Kanwal CC, Shah LA, Ghazali NH, Cheng CK, Nurdin S. Biodiesel production from rubber seed oil using a limestone based catalyst. *Adv Mater Phys Chem.* 2012 Oct 26;2(04):138-41. [<DOI>](#).
37. Kusumo F, Shamsuddin AH, Ahmad AR, Dharma S, Milano J, Silitonga AS, et al. Production of biodiesel from *Jatropha curcas* mixed with waste cooking oil assisted by ultrasound. *IOP Conf Ser: Earth Environ Sci.* 2020 Apr 1;476(1):012082. [<DOI>](#).
38. Ding J, Xia Z, Lu J. Esterification and deacidification of a waste cooking oil (TAN 68.81 mg KOH/g) for biodiesel production. *Energies.* 2012 Jul 25;5(8):2683-91. [<DOI>](#).
39. Fathallah AZM, Pinto F. The Influence of NaCl dissolved on biodiesel of used cooking oil on performance and its degradation of main components of diesel engine. *IOP Conf Ser: Earth Environ Sci.* 2022;972(1):012030. [<DOI>](#).
40. Ashok A, Kennedy LJ, Vijaya JJ, Aruldoss U. Optimization of biodiesel production from waste cooking oil by magnesium oxide nanocatalyst synthesized using coprecipitation method. *Clean Technol Environ Pol.* 2018 Aug;20(6):1219-31. [<DOI>](#).
41. Ahmed, H. M., Abdeldaim, S. O., & Erwa, I. Y. (2021). Production of biodiesel from heat-treated edible oil. *J Phys: Conf Ser*, 2063(1), 012027. [<DOI>](#).
42. Abdullah, Rahmawati Sianipar RN, Ariyani D, Nata IF. Conversion of palm oil sludge to biodiesel using alum and KOH as catalysts. *Sus Environ Res.* 2017;27(6):291-5. [<DOI>](#).



A Highly Sensitive Non-Enzymatic Sensor for the Determination of Glucose Based on Aniline-2-sulfonic acid-Modified Cu Electrode

Melih Besir Arvas^{1*} 

¹Istanbul University Department of Chemistry, Istanbul, 34134, Turkey

Abstract: Herein, the copper-based electrodes were successfully synthesized with galvanostatic electrodeposition method. The effect of materials obtained at different concentrations of ASA and anodization times on glucose sensing ability was investigated. During the anodization of copper foil in the presence of ASA molecules, it formed a tree branch-like structure connected to each other while decorating the electrode surface. The Cu(30)/ASA(0.02) electrode exhibited a relatively wide linear range (0.2 – 10.0 mM) and a low detection limit (0.826 μ M). These excellent activities were mainly attributed to the surface morphology, which functions as highly active sites and enhanced electronic conductive pathways with the addition of ASA. In addition, the stability obtained together with the excellent sensing ability in beverages makes the electrodes useful for practical applications.

Keywords: Copper foil, anodization method, glucose, non-enzymatic sensor, aniline 2-sulfonic acid.

Submitted: October 01, 2022. **Accepted:** December 26, 2022.

Cite this: Arvas MB. A Highly Sensitive Non-Enzymatic Sensor for the Determination of Glucose Based on Aniline-2-sulfonic acid-Modified Cu Electrode. JOTCSA. 2023;10(1):227-40.

DOI: <https://doi.org/10.18596/jotcsa.1182942>.

***Corresponding author. E-mail:** mbesirarvas@gmail.com.

1. INTRODUCTION

In various industries, such as clinical diagnosis, medicine, and the food business, it is critical to create fast, practical, and reliable methods for determining glucose. Because most diabetics are unaware of the early indicators of the condition, regular blood sugar monitoring and exact detection are essential for diagnosing and controlling this life-threatening disease. Because of their excellent sensitivity and selectivity, most electrochemical glucose biosensors on the market today are made primarily with the glucose oxidase enzyme for blood glucose detection in various body fluids (1-3). However, enzymatic glucose sensors have some drawbacks, such as enzyme denaturation, high cost, low chemical stability, and expensive manufacturing methods, hence enzyme-free glucose sensors are being developed to replace enzymatic glucose sensors. Enzyme-free glucose sensors appear to be a promising alternative to enzyme-based glucose sensors, although existing non-enzymatic glucose sensors still require significant sensitivity and selectivity improvements. Researchers are

particularly interested in studies that focus on developing stable, simple, repeatable, low-cost non-enzymatic glucose sensors and synthesizing more sensitive materials.

Non-enzymatic electrodes, such as electrodes modified with noble metals, metal alloys, and metal nanoparticles, have been developed with a lot of effort (4-9). Copper and copper oxide-based materials, for example, are low-cost, non-toxic semiconductors with good electrochemical and catalytic characteristics (10). By adjusting the process conditions, different morphologies of copper and copper oxide-based materials can be synthesized using simple procedures (11). Furthermore, their nanostructures have distinct characteristics, such as a large surface area, low density, and the existence of active sites even on the interior surfaces (12,13). Previous research has looked into copper and copper oxide-based materials' high catalytic activity in alkaline solutions for glucose detection. Jiang et al. described a non-enzymatic glucose sensor electrode made of Cu NPs with nitrogen-doped graphene as the sensing

component (14). Zhang et al. used a simple substrate-assisted electroless deposition (SAED) process to create a flexible enzyme-free glucose amperometric biosensor on free-standing reduced graphene oxide (rGO) membranes using a laser-induced graphene (Cu NPs-LIG) composite (15). Anand et al. reported a sensitive nonenzymatic glucose sensor based on copper nanowires (CuNWs)/polyaniline (PANI)/reduced graphene oxide (rGO) nanocomposite ink by solvothermal mixing of CuNWs, PANI, rGO and binders (16). Phetsang et al. developed a non-enzymatic glucose sensor based on a screen-printed carbon electrode modified with copper(II) and reduced graphene oxide (17). Controllable morphology investigations are carried out with the doped form formed by adding a dopant in order to improve the sensitivity of the copper-based glucose sensor. Aniline 2-sulfonic acid (ASA) may be promising as a dopant with sulfo groups because the sulfonic acid group is defined by the maximum degree of dissociation (18,19). Because of the sulfo groups and nitrogen atoms in the monomer chain structure, aniline 2-sulfonic acid (ASA) has not yet been explored as a doping at copper electrode material (20).

We used a simple one-step anodization procedure to make tree branch-shaped CuO-Cu₂O/copper/aniline 2-sulfonic acid directly on copper foil. The synthesis technique, which uses copper foil as both a current collector and a copper source, simplifies electrode fabrication while simultaneously increasing charge efficiency with additives for increased sensor sensitivity. Scanning electron microscopy (SEM), energy distribution spectrum (EDS), X-ray diffraction (XRD), Fourier-transform infrared spectroscopy (FT-IR), and electrochemical tests were used to characterize the aniline 2-sulfonic acid modified copper foil electrode. Compared to Cu(30) electrodes and many other non-enzymatic glucose sensors, the Cu(30)/ASA/(0.03) electrode for glucose sensors has good electrocatalytic capabilities for glucose oxidation and detection. This new electrode material, which takes advantage of ASA's functional groups, promises to be an outstanding non-enzymatic glucose sensor with high sensitivity, excellent selectivity, a wide detection range, and excellent surface properties.

2. EXPERIMENTAL

2.1. Chemicals and Reagents

Acetone (C₃H₆O, ≥99.9%), ethanol absolute (C₂H₅OH, ≥97.9%), sodium hydroxide (NaOH, ≥97.0%), copper(II) sulfate pentahydrate (CuSO₄·5H₂O, ≥98.0%), were purchased from Sigma Aldrich. Copper foil (99.9%) was provided by Alfa Aesar. All beverage samples were obtained from the local market for real samples analysis. Distilled water

(Milli-Q, 18 MΩ.cm resistivity) was used to prepare all the aqueous solutions.

2.2. Synthesis of Tree Branch-Shaped CuO-Cu₂O/copper/aniline-2-sulfonic acid Electrode

The electrodes were prepared by controlled galvanostatic electrodeposition method. Copper electrodes were cleaned with ethanol, acetone, deionized water in the ultrasonic bath for 15 min to remove contaminants on the electrode surface and dried at the room temperature overnight, respectively. In a typical synthesis procedure, a constant current of 0.5 A cm⁻² is applied for 30 s in a two-electrode cell. Cu foil (1×3 cm²) was used as a cathode electrode for the electrochemical deposition and another piece of Cu foil used as an anode electrode. The effect of electrochemical deposition time on the growth of the copper oxides was investigated at anodization times of 10, 20, 30, 40 and 50 second in 0.4 M CuSO₄ and 1.5 M H₂SO₄ electrolyte solution. Then, CuO-Cu₂O/copper/aniline 2-sulfonic acid electrodes were prepared under similar electrochemical conditions by adding in the presence of between 0.005, 0.01, 0.02, 0.03, 0.04, 0.05 M ASA concentration (see Table 1). The prepared electrodes were thoroughly rinsed with distilled water and ethanol several times, and dried in an oven at 60 °C for 3 hours. The obtained electrodes were used as the sensing material for sensitive glucose detection.

2.3. Characterization

Scanning electron microscopy (SEM) and energy distribution spectrum (EDS) were used to examine the surface morphologies and elemental analyses of the electrodes prepared using Zeiss EVO® LS 10 SEM, USA. Fourier-transform infrared spectroscopy (FT-IR) for the analysis of chemical structure was recorded Perkin Elmer Spectrum 100 spectrophotometer. X-RAY diffractometer (XRD, PANalytical X'Pert PRO Cu) at 45 kV and 2θ range of 10-80° was used to determine the phase and crystallinity of the structures coated on the electrode surface.

2.4. Electrochemical Measurements

All electrodes were tested using Ivium Vertex Instruments Potentiostat/Galvanostat (Ivium Technologies B.V, Netherlands) and recorded with the IviumSoft Potentiostat/Galvanostat software. The electrochemical sensor was carried out based on four methods in applications, cyclic voltammetry (CV), differential pulse voltammetry (DPV), chronoamperometry (CA) and electrochemical impedance spectroscopy (EIS). In the presence of probable interfering substances such as ascorbic acid, lactic acid, uric acid, maltose, lactose, and urea, the selectivity of the sensor electrode was studied.

Table 1: The ratio of raw materials used in sensor electrode samples.

Sample	Anodization Time (s)	ASA (M)
Cu	-	-
Cu(10)	10.0	-
Cu(20)	20.0	-
Cu(30)	30.0	-
Cu(40)	40.0	-
Cu(50)	50.0	-
Cu(30)/ASA/(0.005)	30.0	0.005
Cu(30)/ASA/(0.01)	30.0	0.01
Cu(30)/ASA/(0.02)	30.0	0.02
Cu(30)/ASA/(0.03)	30.0	0.03
Cu(30)/ASA/(0.04)	30.0	0.04
Cu(30)/ASA/(0.05)	30.0	0.05

2.5. Preparation of Real Samples

All beverage samples were obtained from local shops for real sample analysis. In order to detect glucose in real samples by electrochemical methods, beverage samples such as cola, fruit juice and ice tea were placed directly into the test cell. To perform the sensor sensitivity of electrode, 10 mL of NaOH (0.1 M) electrolyte was added so that the real sample concentrations were 5.0 mM.

3. RESULTS AND DISCUSSION

As the material has highly porous interfaces, it is a promising material for sensor electrodes. The sensor properties of this material produced at different anodization times were systematically tested using cyclic voltammetry measurement. The electrochemical properties of copper samples were investigated with a cyclic voltammetry (CV) method in 1.0 M NaOH solution within presence of 5 mM glucose in a potential window of -0.2 V to 1.0 V with

scan rate of 50 mV s^{-1} . Figure 1a shows that all electrodes had an oxidation peak in the region of 0.3–0.6 V, which can be attributed to Cu(II) to Cu(III) conversion. Kuwana et al. reported the most widely accepted method of glucose oxidation at the CuO electrode in an alkaline media (21). Cu(III) oxidation could catalyse glucose oxidation to gluconolactone, which could then be further oxidized to glucose acid (22). Among all the electrodes, Cu(30) showed the highest anodic current peak indicating the highest electrocatalytic performance. As shown in Figure 1a the cyclic voltammograms of anodized copper in various times, 30 seconds was obtained as the optimum time as Cu oxidized at that time and it improved the surface properties of the sensor. In order to improve the electrochemical performance of Cu(30) electrodes, the electrodes were anodized in the presence of ASA concentration and cyclic voltammetry (CV) and electrochemical impedance spectroscopy (EIS) measurements were used to investigate the effect of ASA in Figure 1b and 1c.

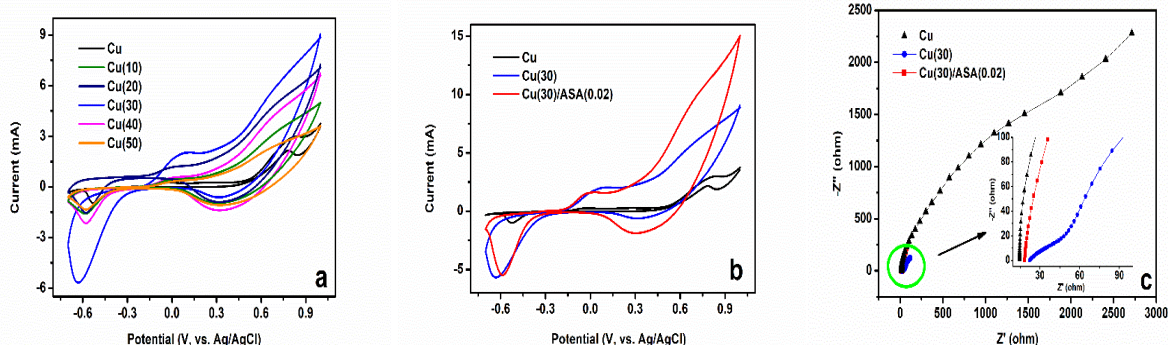


Figure 1: (a) Cyclic voltammograms of the copper electrodes in 1.0 M NaOH in presence of 5 mM glucose with scan rate of 50 mV s^{-1} ; (b) Cyclic voltammograms of the Cu, Cu(30) and Cu(30)/ASA(0.02) electrodes in 1.0 M NaOH in presence of 5 mM glucose with scan rate of 50 mV s^{-1} ; (c) Electrochemical impedance spectra of the Cu, Cu(30) and Cu(30)/ASA(0.02) electrodes in 1.0 M NaOH in presence of 5 mM glucose the inset is the enlarged with region of the high frequency.

With the synthesized Cu(30)/ASA(0.02) electrode, ASA improved the electrochemical activity and surface area, and the corresponding cyclic

voltammograms were shown in Figure 1b. The sensor Cu(30)/ASA(0.02) electrode with higher electrochemical properties has more activity than

anodized Cu(30) and bare copper (Cu) electrode sensors. The ASA modified electrode acted as electron mediators, enhancing the synergistic effect. Thus, the selectivity of the electrode against the glucose was improved. This result can also be related to the porous structure of the Cu(30)/ASA(0.02) electrode's wide surface area following anodization with the addition of ASA to the medium.

Figure 1c showed the electrochemical impedance spectra (EIS) of Cu, Cu(30) and Cu(30)/ASA(0.02) electrodes in 0.1 M NaOH solution from 0.01 Hz to 10000 Hz. The resulting Nyquist curves were fitted according to the equivalent simple circuit model. Solution resistance, charge transfer resistance, double layer capacitance, and Warburg impedance are represented by the impedances R_s , R_{ct} , C_{dl} , and W , respectively. R_s is the ohmic resistance and is the resistivity of the electrolyte and corrosion products on the surface. R_{ct} , on the other hand, was linked to the velocity resistance that governs the corrosion reaction. W is connected to the diffusion rate of mobile ions to the electrode surface, whereas C_{dl} is related to the capacitive behaviour of the electrodes. The R_s values of Cu, Cu(30) and Cu(30)/ASA(0.02) electrodes were 15.73 Ω , 22.76 Ω and 17.83 Ω , respectively. After anodization of copper for 30 seconds, the R_s value of the Cu(30)/ASA(0.02) electrode synthesized by adding ASA to the anodization medium was lower. The R_{ct} values of Cu, Cu(30) and Cu(30)/ASA(0.02) electrodes were 1338 Ω , 47.68 Ω and 23.49 Ω , respectively. The R_{ct} value of the Cu(30)/ASA(0.02) electrode obtained after the anodization process with the addition of ASA decreased by almost half compared to the Cu(30) electrode. The C_{dl} values of Cu, Cu(30) and Cu(30)/ASA(0.02) electrodes were 34.89e-6, 110.4e-6 and 124.7e-6, respectively. When the electrode was anodized with ASA for 30 seconds, the capacitive behaviour of the electrode improved. Cu, Cu(30), and Cu(30)/ASA(0.02) electrodes had W impedance values of 17.31e-3, 4.33e-3, and 14.39e-3, respectively. The sulfonyl groups in ASA had a favourable effect on electrode surface, lowering charge transfer resistance and accelerating ion diffusion rates. As a result, electron transfer on the electrode surface was accelerated, and the electrode's selectivity against the analyte was enhanced. The influence of the ASA concentration on the anodization of copper electrode for sensor applications was investigated using cyclic voltammetry and electrochemical impedance spectroscopy. Figure 2a shows a comparison of electrochemical tests utilizing a three-electrode system in 0.1 M NaOH electrolyte from a -0.7 V to 1.0 V potential window with a scan rate of 50 mV s⁻¹ in the presence of ASA concentrations ranging from 0.005 to 0.05 M. At the cyclic voltammogram, the Cu(30)/ASA(0.02) containing 0.02 M ASA showed the maximum current density rise.

To consider the electrocatalytic activity between the electrodes due to the concentration difference, the

higher catalytic activity of Cu(30)/ASA(0.02) could be attributed to two reasons. First, it could be that the Cu(30)/ASA(0.02) electrode has high electrode surface area due to the well-dispersed negative charge of ASA during its synthesis. Because ASA contains sulfonic acids with a high protonation degree and electrical conductivity characteristics in its molecular structure (23-25). Therefore, it may have raised the deposition efficiency of copper oxide on the electrode surface, which was directly related to its catalytic activity on glucose oxidation. The addition of less or more 0.02 M ASA, on the other hand, may have resulted in decreased copper oxide electrocatalytic activity for glucose oxidation. As a result, the ASA content in the Cu(30) electrodes was optimized to 0.02 M.

Figure 2b shows the Nyquist curves of EIS analyses of Cu(30)/ASA electrodes made with various ASA concentrations. The equivalent simple circuit model was used to fit the Nyquist curves. The impedance values of R_s , R_{ct} , C_{dl} , and W were investigated in the electrode impedance analyses. The Cu(30)/ASA(0.005) electrode had the lowest R_s value, which was 16.69. Cu(30)/ASA(0.01), Cu(30)/ASA(0.02), Cu(30)/ASA(0.03), Cu(30)/ASA(0.04), and Cu(30)/ASA(0.05) electrodes had R_s values of 21.89, 18.55, 22.76, 27.14, and 31.08 respectively. Because they were performed under the same experimental conditions, the R_s values were close to one other, but there were minor differences. In the anodization process of the electrodes, an increase in R_s values occurred at increasing concentrations after 0.02 M ASA concentration. The R_{ct} values of Cu(30)/ASA(0.005), Cu(30)/ASA(0.01), Cu(30)/ASA(0.02), Cu(30)/ASA(0.03), Cu(30)/ASA(0.04) and Cu(30)/ASA(0.05) electrodes were 17.74 Ω , 21.68 Ω , 23.49 Ω , 31.25 Ω , 33.46 Ω , and 38.89 Ω , respectively. While R_{ct} values changed more in increasing concentrations after 0.02 M ASA concentration, semi-circle formation related to R_{ct} formed in Nyquist curves was also observed clearly. The results showed that when the concentration of ASA added to the medium during the anodization process increases, charge transfer to the surface becomes more difficult. The C_{dl} values of Cu(30)/ASA(0.005), Cu(30)/ASA(0.01), Cu(30)/ASA(0.02), Cu(30)/ASA(0.03), Cu(30)/ASA(0.04), and Cu(30)/ASA(0.05) electrodes were 68.96e-6, 89.34e-6, 124.7e-6, 45.81e-6, 30.49e-6 and 23.35e-6, respectively. The W impedance values of Cu(30)/ASA(0.005), Cu(30)/ASA(0.01), Cu(30)/ASA(0.02), Cu(30)/ASA(0.03), Cu(30)/ASA(0.04) and Cu(30)/ASA(0.05) electrodes were 10.06e-3, 11.89e-3, 14.39e-3, 6.61e-3, 4.43e-3 and 2.96e-3, respectively. The highest diffusion rate ratio was obtained in Cu(30)/ASA(0.02) electrode. Similar to the downward trend in R_{ct} values, W impedance values also decreased after 0.02 M ASA concentration. Excessive amount of ASA added to the medium affected the anodization negatively and slowed down the ion transfer and ion transfer rate.

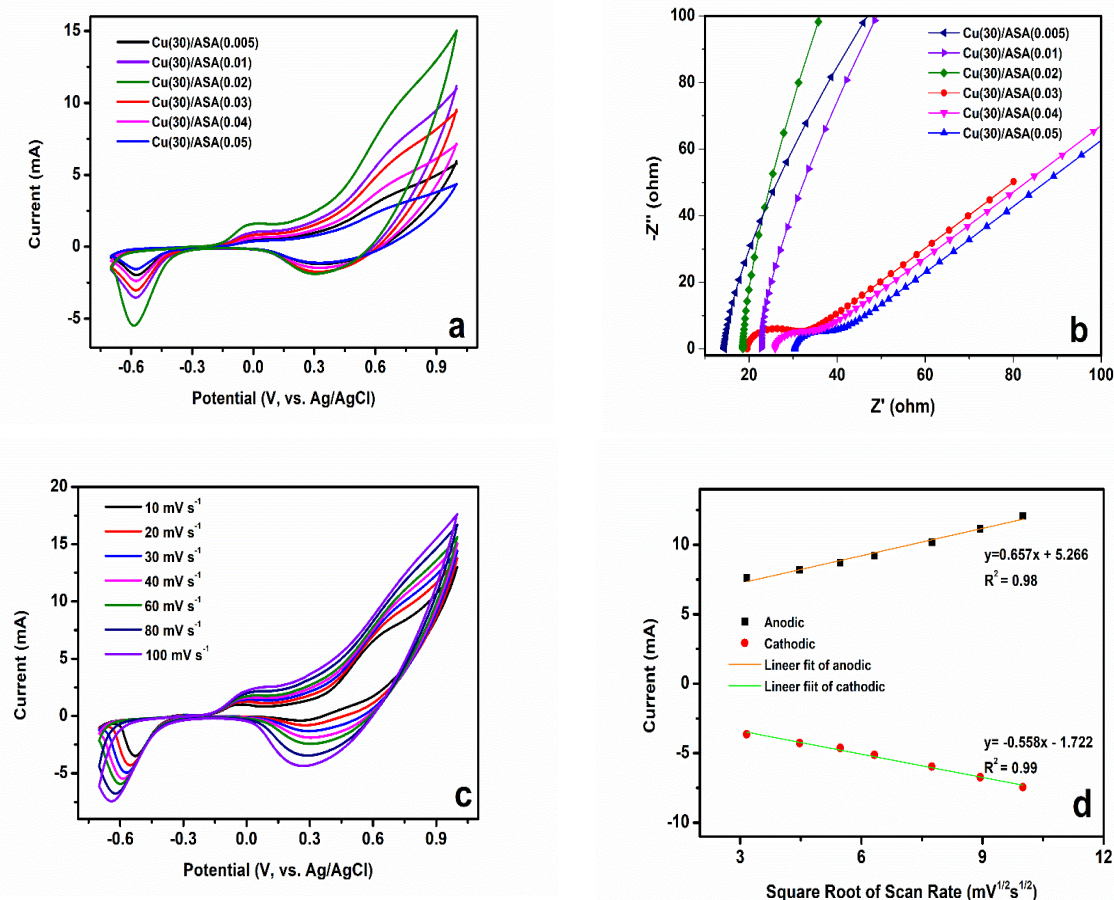
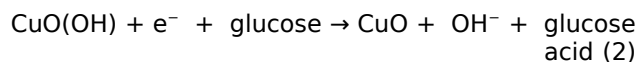


Figure 2: (a) CV of synthesized Cu(30) electrodes in the presence of various ASA concentration, (b) EIS spectra of synthesized Cu(30) electrodes in the presence of various ASA concentration, (c) Effect of scan rate on the CV of Cu(30)/ASA(0.02) in 5 mM of glucose at varying the scan rate from 10, 20, 30, 40, 60, 80 and 100 mV s^{-1} , (d) corresponding plot of peak current versus square root of scan rate for Cu(30)/ASA(0.02) electrode.

Figure 2c shows the rate performance of cyclic voltammetry in a three-electrode system with a platinum counter electrode and an Ag/AgCl reference electrode in 0.1 M NaOH electrolyte solution in the presence of 5 mM glucose solution at scan rates of 10 to 100 mV s^{-1} with a voltage ranging from 0.7 V to 1.0 V. Peak currents gradually rose when scan rates were raised up to 100 mV s^{-1} . Redox current peaks were clearly visible in Figure 2d, and glucose oxidation at the anodic peak current (I_{pa}) altered proportionally with the scan rate. When the current linearity curves were plotted against the scanning speed, the findings revealed that two straight lines with good linearity were achieved, anodic and cathodic (R^2 a: 0.983, R^2 c: 0.998). It's clear that Cu(30)/ASA(0.02) has good electrochemical activity

for glucose detection. The possible reaction mechanism was given below (26)(27):



The major processes occurring in CuO-based sensors are presented in equations (1) and (2) to allow electro-oxidation of glucose. The electro-oxidation of glucose by redox active ions ($\text{Cu}^{2+}/\text{Cu}^{3+}$) in the form of CuO/CuO(OH) complexes is a generally established non-enzymatic process. Furthermore, glucose sensing with a non-enzymatic CuO-based glucose sensor necessitates a medium with a high pH (13) (28).

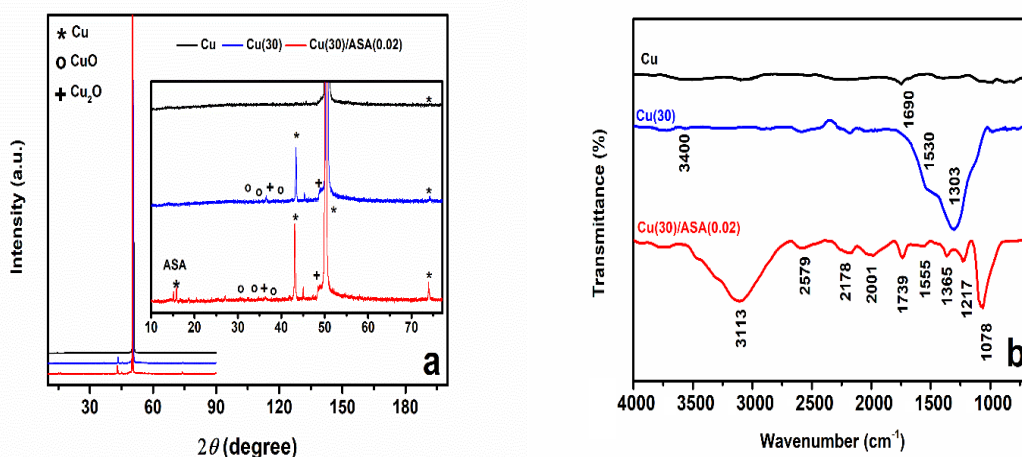


Figure 3: a) XRD patterns and b) FTIR spectra of the Cu, Cu(30) and Cu(30)/ASA(0.02) electrodes.

Cu, Cu(30), and Cu(30)/ASA(0.02) electrodes were examined using XRD analysis to investigate the crystal structure and phase composition, as shown in Figure 3a. At $2\theta = 43.35$, 50.47 , and 74.16° , three prominent reflection peaks were found, indicating the (1 1 1), (2 0 0), and (2 2 0) crystal planes of the copper metal structure, respectively (JCPDS No. 02-1225) (29). An unknown peak was also observed at all three electrodes at $2\theta = 45.34^\circ$. Since the copper used in the experiments was not a high purity research grade product, it was possible for the material to contain unknown impurities. The different peaks were observed and defined in the XRD spectrum of Cu(30) grown on copper plate. The crystal structure and phase composition of the Cu(30) electrode can be linked to the cubic Cu substrate's (111), (200), and (220) planes. The copper metal corresponding peak observed in the sample may originate from copper under-layer or voids in the Cu(30) and Cu(30)/ASA(0.02) electrodes. The structure of monoclinic CuO (JCPDS no. 45-0937) and the structure of cubic Cu_2O could be the additional diffraction peaks besides Cu indicated with symbols (JCPDS no. 05-0667) (30,31).

The stretching vibrations of the O-H bond in air, molecular water adsorbed on the surface of Cu plate were characterized in the FTIR spectrum of Cu plate displayed in Figure 3b at 3407 cm^{-1} (32).

Furthermore, a vibration of O-H bond was also observed around 1690 cm^{-1} , indicating that the associated hydroxyl groups were chemically poorly absorbed due to atmospheric molecular water (33). The formation of O_2 adsorption on CuO was confirmed by the formation of the intense $\nu(\text{O-O})$ band around 1530 cm^{-1} (34). The variation of the intensity of the peaks with the anodization of copper can be attributed to the change in crystallinity. The C=O bond was attributed to the band at 1303 cm^{-1} , indicating that components from the electrolyte media were included into the formed oxide (26). A various peak forms were observed in the FTIR spectrum, which shows the structural change of the Cu(30)/ASA(0.02) electrode with the addition of aniline 2-sulfonic acid to the medium. The peak at 3113 cm^{-1} may be attributed to the interaction between the copper oxide and the N-H group of ASA, hydrogen bond formation between the copper oxide and the N-H group of ASA at the electrode surface (35).

For Cu(30)/ASA(002), the bands at 2579 cm^{-1} , 2178 cm^{-1} , and 2001 cm^{-1} were caused by aromatic C-H stretching C=O group was given to the band at 1739 cm^{-1} . The C=C stretching quinonoid and benzenoid rings of ASA were responsible for the bands at 1555 cm^{-1} and 1365 cm^{-1} , while the C-N stretching of the benzenoid units of ASA was relevant for the bands at 1217 cm^{-1} and 1078 cm^{-1} (18,19,35).

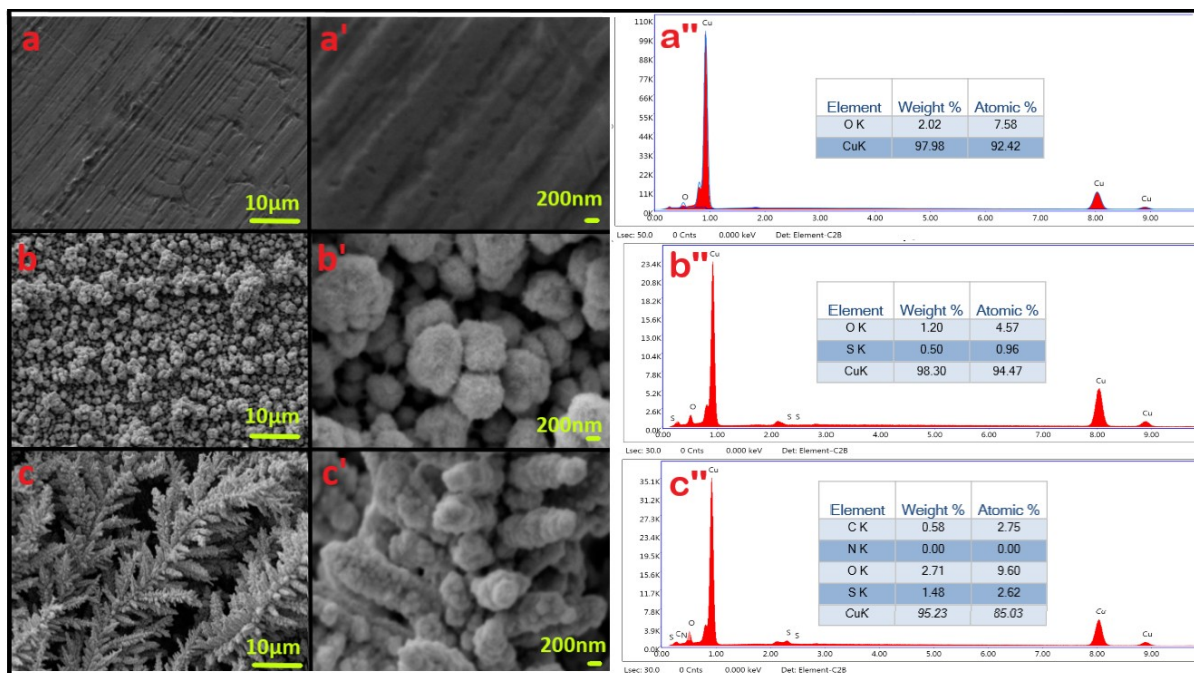


Figure 4: Comparison of the SEM images, EDS spectra for (a, a', a'')cCu electrode, (b, b',b'') Cu(30) electrode and (c, c',c'') Cu(30)/ASA(0.02) electrode.

The SEM images and EDS analysis of the surface of the copper-based electrodes were shown in Figure 4. Numerous CuO/Cu₂O microstructures coated uniformly agglomerates are shown in Figure 4 (b,b''). The homogeneous clusters were formed on the entire surface of the electrode and grain sizes are about ~0.1 µm. When the SEM image was examined at a higher magnification, it was seen that there were two different morphologies. The structures of needle with a diameter and length of about 200 nm and the other one was flower-like aggregates about a few microns in diameter in shown in the surface of Cu(30) electrode. As shown in Figure 4 (c,c''), interestingly, tree branch-shaped copper oxide structure observed in the presence of 0.02 M ASA concentration. When the SEM image was examined with a higher magnification, it was observed that there were nanoparticles 200 nm below the Cu(30)/ASA(0.02) electrode surface. When the SEM photographs are examined, the synthesized material exhibits an active rough structure at extremely nanoscale. The Cu(30)/ASA(0.02) electrode was much more porous, allowing electrooxidation to occur for the glucose sensor due to the availability of free interspace and increased surface area. It was in agreement with the

electrochemical results that the Cu(30)/ASA(0.02) sensor showed a higher sensitivity than others.

The elemental distributions of the electrodes were determined by EDS measurement and the EDS spectrum of Cu, Cu(30) and Cu(30)/ASA(0.02) was presented in Figure 4 (a'',b''c'') and the percentage of elements was tabulated in the figures. EDS is an important technique for determining the atomic composition of elements in materials. EDS analysis also confirms that ASA interacts with the electrode surface during copper anodization process. The fundamental peaks of Cu and O are observed in all the EDS spectrums. The element S in the EDS spectrum of copper, which was also anodized in sulfuric acid electrolyte solution, originated from the electrolyte in the medium (36). Atomic percentage of Cu(30)/ASA(0.02) compared to atomic percentage of Cu(30), it was observed that the percentage of element S increased significantly with the addition of ASA. The atomic percentage of S increased from 0.96% to 2.62% as shown in Figure 4b'' and 4c''. Furthermore, EDS analysis showed Cu(30)/ASA (0.02) composition consisting of C, N, O, S and Cu elements included in the ASA added to the synthesis medium without other impurities.

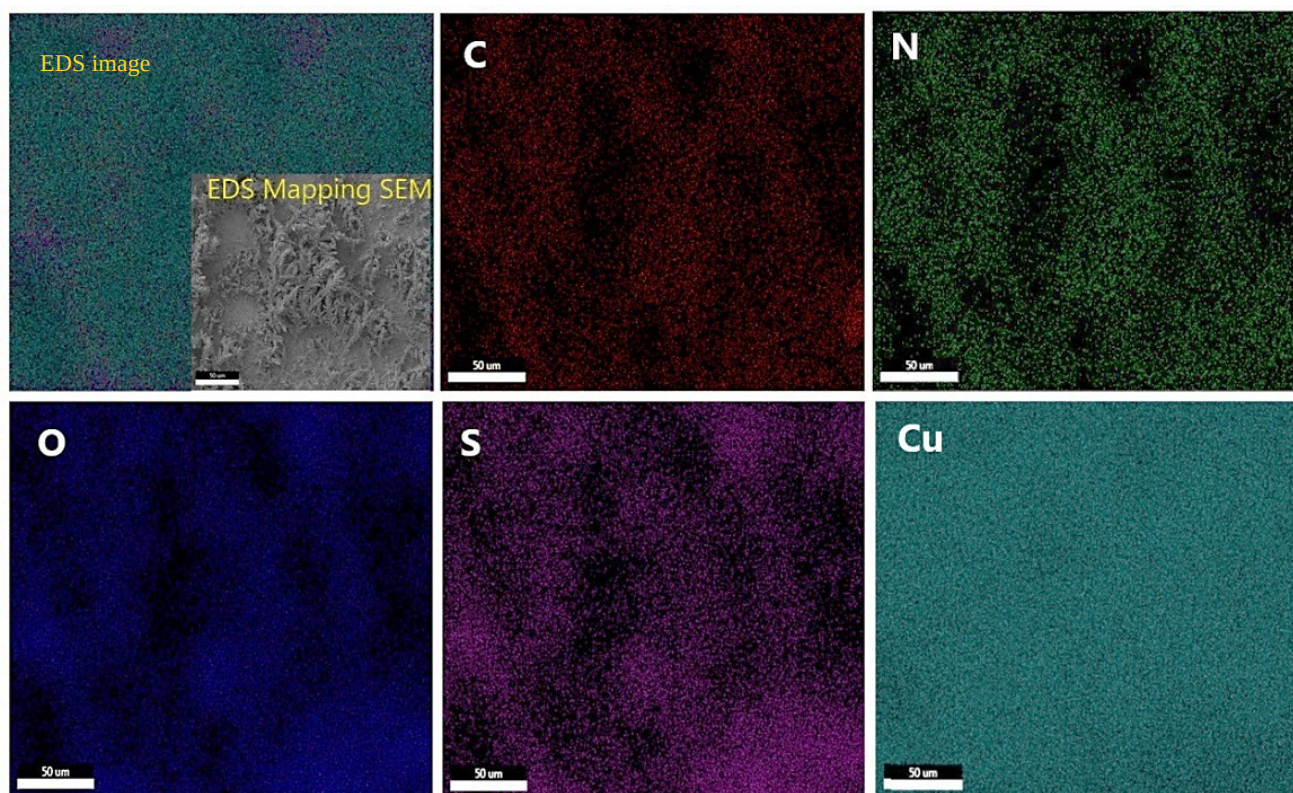


Figure 5: Elemental mapping of Cu(30)/ASA(0.02) electrode.

EDS mapping analyses of Cu(30)/ASA(0.02) are shown in Figure 5. In EDS mappings where the elements appear to be completely homogeneously distributed, it was observed that copper oxide and ASA showed good chemical interaction. The growth of copper oxides on certain active surfaces with the addition of ASA in the SEM morphology also proved this analysis.

Figure 6a demonstrated the electrocatalytic response of Cu(30)/ASA(0.02) electrode for the detection of the different concentrations of glucose (0.2, 0.5, 1.0, 2.0, 3.0, 5.0, 7.0 and 10.0 mM) in DPV technique (DPV parameters; step potential = 0.0050 V; modulation amplitude = 0.0250 V; modulation time = 0.20 s and interval time-0.5 s). Cu(30)/ASA(0.02) clearly exhibits a high degree of electrocatalytic activity for glucose detection. The size of the wave around 0.35 V to 0.65 V gradually increased as the glucose concentration raised for the Cu(30)/ASA(0.02) electrode. A good correlation was exhibited between glucose concentrations and peak currents (Figure 6b).

Typically, glucose oxidation peak current risen linearly with glucose concentration for values between 0.2 and 10 mM with correlation coefficient (R^2) as 0.998. The lowest detection limits for glucose (LOD) were found to be 0.826 μM ($S/N=3$) (Figure 6) ($\text{LOD} = 3\sigma/S$; the standard deviation and S is the sensitivity). Similarly, Cu(30)/ASA(0.02) was tested by cyclic voltammetry to examine glucose sensitivity. The glucose oxidation peak was seen at

0.35-0.65 V, and the oxidation current increased as the glucose concentration increased from 0.2 to 10.0 mM, as shown in Figure 6c. Table 2 shows the electrochemical sensor parameters for the glucose sensor, as well as prior publications using copper electrodes. It's worth noting that the Cu(30)/ASA(0.02) sensor's performance is comparable to that of prior investigations.

Some biological samples in the biological sample can be quickly oxidized at a positive potential, causing glucose detection to be interfered. As shown in Figure 7, the selectivity of the Cu(30)/ASA(0.02) electrode over glucose was investigated using various interfering species such as maltose, lactose, ascorbic acid, uric acid, lactic acid, and urea. Amperometric tests were used to analyse the electrolyte solution of 0.1 M NaOH. By adding 0.1 mM interfering agents and 2 mM glucose solution to a constantly stirred 0.1 M NaOH solution, the interaction of these electroactive biological samples was examined. As a result, in the presence of other biological species, the Cu(30)/ASA(0.02) electrode was better suited for glucose determination. This supports the idea that the Cu(30)/ASA(0.02) electrode's high surface area will give more sensitive selectivity for glucose detection under physiological settings, as it enhances selective glucose oxidation. Several factors are likely to have influenced this remarkable selectivity behaviour. First, because ASA reduces copper oxide agglomeration, the electrode material lasts longer. Second, tree branch-shaped copper oxide allows for

quick ion/electron transfer between the electrode and the electrolyte contact, resulting in improved sensing performance.

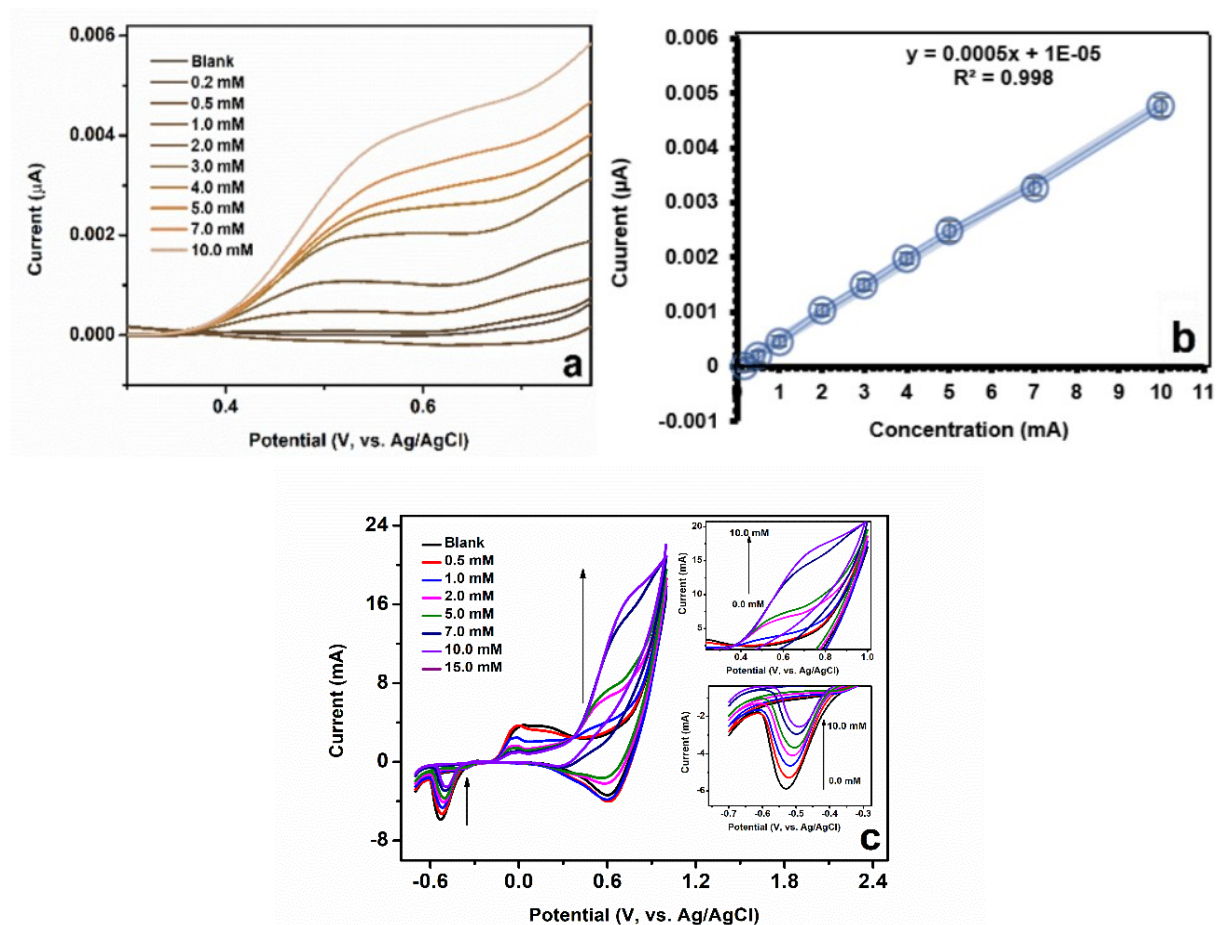


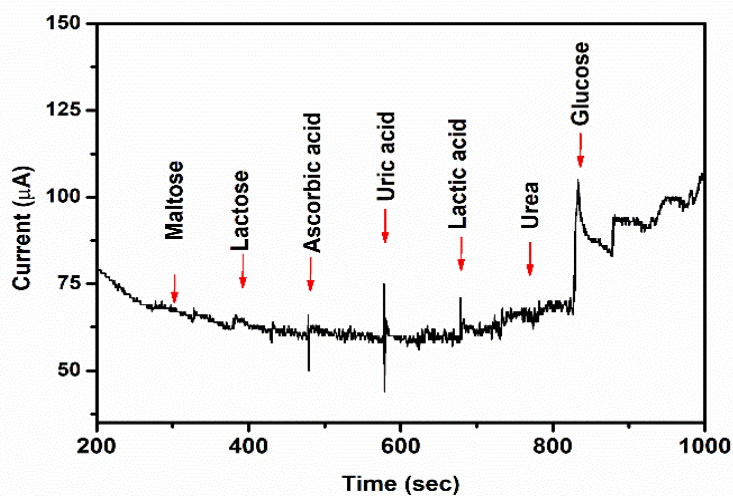
Figure 6: (a) Differential pulse voltammogram of Cu(30)/ASA(0.02) electrode in 1.0 M NaOH for values between 0.2 and 10 mM of glucose, (b) a plot of current density with respect to the concentration, (c) CV of Cu(30)/ASA(0.02) electrode in 1.0 M NaOH for values between 0.2 and 10 mM of glucose.

The sensor electrode's repeatability and stability were further tested using five separate electrodes and the addition of a 5.0 mM glucose solution in 0.1 M NaOH. The results demonstrate that the relative standard deviation value (RSD) was 2.41%, indicating that the sensor was reliable and repeatable. The sensor's stability was assessed over a 28-day period by assessing its sensitivity to 5.0 mM glucose. The sensitivity was tested every seven days after the same procedures were repeated and stored at room temperature. The electrode recovered 94 percent of the time, according to the results. The results show that it can be used in practical uses for most common analyses.

Glucose detection in real samples such as cherry juice, cola, and iced tea drinks was performed to assess the practical use of the Cu(30)/ASA(0.02) electrode. Drinks diluted with multiple applications of glucose standards were introduced to 0.1 M NaOH to determine glucose concentration in real samples. Figure 8 shows the result of the measurements (DPV parameters: step potential 0.0050 V, modulation amplitude 0.0250 V, modulation duration 0.20 s, and interval time 0.5 s.). Cherry juice, cola, and iced tea had average glucose concentrations of 4.3 ± 0.19 , 5.2 ± 0.24 , and 4.8 ± 0.21 mM, with RSDs of 3.31%, 3.89%, and 3.49% respectively. The electrode was found to be capable of sensing glucose in both real samples and in different types of beverages.

Table 2: List of copper-based non-enzymatic glucose sensors.

Electrode materials	Analyte	Linear range	Limit of detection	Ref.
CuO/GCE	0.1 M PBS	5 μ M-15 mM	1.42 μ M	(26)
Copper-salen	0.5 M KCl	4.0-69 μ M	1.2 μ M	(37)
CuCo-CFs/Nafion/GC electrode	0.1 M NaOH	0.02-11 mM	1.0 μ M	(38)
CuO/PANI-NF/FTO	0.1 M NaOH	0.25 μ M to 4.6 mM	0.24 μ M	(39)
CuO/NiO/PANI/GCE	0.1 M NaOH	0.02-2.5 mM	2.0 μ M	(40)
CuO-U	0.1 M NaOH	1.0 μ M to 10.0 mM	1.74 μ M	(41)
CuS nanosheets/Cu ₂ O/CuO NWAs/Cu foil	0.1 M NaOH	0.002-4.1 mM	0.89 μ M	(42)
CuO-C-dots	0.1 M NaOH	0.5-2.0 and 2.0-5.0 mM	200 μ M	(43)
CuO-flower	0.1 M NaOH	0.001-1 mM	0.25 μ M	(44)
CuO micro-/nanostructures	0.1 M NaOH	0.9-16 mM	20.0 μ M	(45)
Cu(30)/ASA(0.02)	0.1 M NaOH	0.2-10.0 mM	0.83 μ M	(This work)

**Figure 7:** Amperometric response of the interference study of different samples in 0.1 M NaOH at potential 0.5 V.

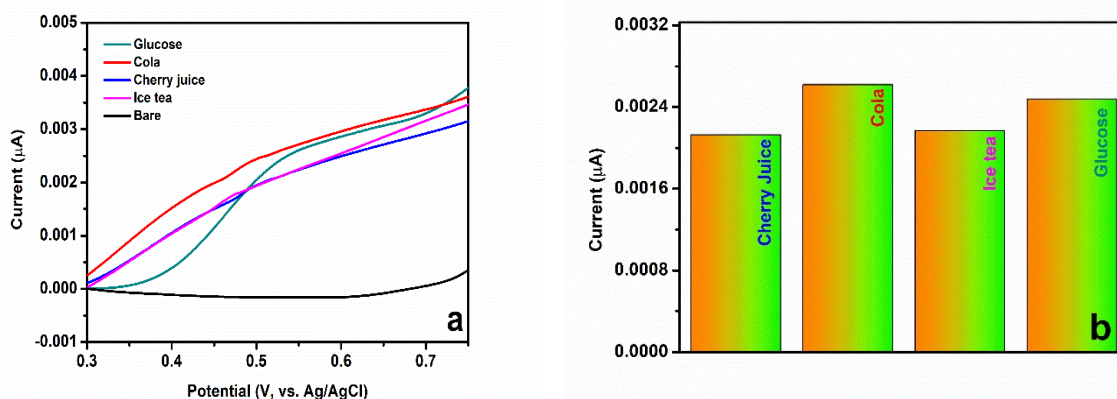


Figure 8: (a) DPV voltammogram, (b) the current density obtained DPV of different types of beverages in the real sample.

4. CONCLUSION

In this work, a new electrode material of Cu(30)/ASA(0.02) was synthesized and characterized for the non-enzymatic glucose sensor applications. In order to obtain a new electrochemical sensor for the prepared electrode, the effect of ASA added in the medium during the anodization of the copper foil was investigated for glucose. The electrode material was explored structurally and morphologically, as it provides a conductive path for quick electron/ion transfer to copper and facilitates harsh redox conditions by effectively increasing the active surface area. The electrode demonstrated an outstanding glucose sensing performance with acceptable sensitivity and a linear range analytical response, 0.2 to 10.0 mM, with a 0.826 μM limit of detection in DPV analysis for sensor application. Furthermore, the developed electrode has the potential to detect glucose in biological and food samples due to appropriate selectivity, stability, and great sensing performance in real beverages.

5. ACKNOWLEDGMENTS

M.B. Arvas especially thanks Prof. Dr. Yuçel Şahin for his valuable contributions to this study.

6. REFERENCES

1. Yoo E-H, Lee S-Y. Glucose Biosensors: An Overview of Use in Clinical Practice. *Sensors* [Internet]. 2010 May 4;10(5):4558-76. Available from: [<URL>](#).
2. Khor SM, Choi J, Won P, Ko SH. Challenges and Strategies in Developing an Enzymatic Wearable Sweat Glucose Biosensor as a Practical Point-Of-Care Monitoring Tool for Type II Diabetes. *Nanomaterials* [Internet]. 2022 Jan 10;12(2):221. Available from: [<URL>](#).
3. Osuna V, Vega-Rios A, Zaragoza-Contreras EA, Estrada-Moreno IA, Dominguez RB. Progress of Polyaniline Glucose Sensors for Diabetes Mellitus Management Utilizing Enzymatic and Non-Enzymatic Detection. *Biosensors* [Internet]. 2022 Feb 22;12(3):137. Available from: [<URL>](#).
4. Hassan MH, Vyas C, Grieve B, Bartolo P. Recent Advances in Enzymatic and Non-Enzymatic Electrochemical Glucose Sensing. *Sensors* [Internet]. 2021 Jul 8;21(14):4672. Available from: [<URL>](#).
5. Malekzad H, Sahandi Zangabad P, Mirshekari H, Karimi M, Hamblin MR. Noble metal nanoparticles in biosensors: recent studies and applications. *Nanotechnol Rev* [Internet]. 2017 Jun 27;6(3):301-29. Available from: [<URL>](#).
6. Barbee B, Muchharla B, Adedeji A, Karoui A, Kumar Sadasivuni K, Sha MS, et al. Cu and Ni Co-sputtered heteroatomic thin film for enhanced nonenzymatic glucose detection. *Sci Rep* [Internet]. 2022 May 7;12(1):7507. Available from: [<URL>](#).
7. Pourbeyram S, Mehdizadeh K. Nonenzymatic glucose sensor based on disposable pencil graphite electrode modified by copper nanoparticles. *J Food Drug Anal* [Internet]. 2016 Oct 1;24(4):894-902. Available from: [<URL>](#).
8. Yazar S, Kurtulbaş E, Ortaboy S, Atun G, Şahin S. Screening of the antioxidant properties of olive (*Olea europaea*) leaf extract by titanium based reduced graphene oxide electrode. *Korean J Chem Eng* [Internet]. 2019 Jul 25;36(7):1184-92. Available from: [<URL>](#).
9. Kurtulbaş E, Yazar S, Ortaboy S, Atun G, Şahin S. Evaluation of the phenolic antioxidants of olive (*Olea europaea*) leaf extract obtained by a green approach: Use of reduced graphene oxide for electrochemical analysis. *Chem Eng Commun* [Internet]. 2020 Jul 2;207(7):920-32. Available from: [<URL>](#).
10. Białaś K, Moschou D, Marken F, Estrela P. Electrochemical sensors based on metal nanoparticles with biocatalytic activity. *Microchim Acta* [Internet]. 2022 Apr 2;189(4):172. Available from: [<URL>](#).
11. Liu X, Cui S, Sun Z, Du P. Copper oxide nanomaterials synthesized from simple copper salts as active catalysts for electrocatalytic water oxidation. *Electrochim Acta* [Internet]. 2015 Apr 1;160:202-8. Available from: [<URL>](#).

12. Arvas MB, Gencten M, Sahin Y. One-step synthesized N-doped graphene-based electrode materials for supercapacitor applications. *Ionics (Kiel)* [Internet]. 2021 May 5;27(5):2241-56. Available from: [<URL>](#).
13. Mansuroglu A, Arvas MB, Kiraz C, Sayhan B, Akgumus A, Gencten M, et al. N-Doped Graphene Oxide as Additive for Fumed Silica Based Gel Electrolyte of Valve Regulated Lead Acid Batteries. *J Electrochem Soc* [Internet]. 2021 Jun 1;168(6):060512. Available from: [<URL>](#).
14. Jiang D, Liu Q, Wang K, Qian J, Dong X, Yang Z, et al. Enhanced non-enzymatic glucose sensing based on copper nanoparticles decorated nitrogen-doped graphene. *Biosens Bioelectron* [Internet]. 2014 Apr 15;54:273-8. Available from: [<URL>](#).
15. Zhang Y, Li N, Xiang Y, Wang D, Zhang P, Wang Y, et al. A flexible non-enzymatic glucose sensor based on copper nanoparticles anchored on laser-induced graphene. *Carbon N Y* [Internet]. 2020 Jan 1;156:506-13. Available from: [<URL>](#).
16. Anand VK, Bhatt K, Kumar S, Archana B, Sharma S, Singh K, et al. Sensitive and Enzyme-Free Glucose Sensor Based on Copper Nanowires/Polyaniline/Reduced Graphene Oxide Nanocomposite Ink. *Int J Nanosci* [Internet]. 2021 Apr 10 [cited 2023 Feb 26];20(02):2150020. Available from: [<URL>](#).
17. Phetsang S, Kidkhunthod P, Chanlek N, Jakmune J, Mungkornasawakul P, Ounnunkad K. Copper/reduced graphene oxide film modified electrode for non-enzymatic glucose sensing application. *Sci Rep* [Internet]. 2021 Apr 29;11(1):9302. Available from: [<URL>](#).
18. Yazar S, Arvas MB, Sahin Y. An ultrahigh-energy density and wide potential window aqueous electrolyte supercapacitor built by polypyrrole/aniline 2-sulfonic acid modified carbon felt electrode. *Int J Energy Res* [Internet]. 2022 May 9;46(6):8042-60. Available from: [<URL>](#).
19. Arvas MB, Yazar S, Sahin Y. Electrochemical synthesis and characterization of self-doped aniline 2-sulfonic acid-modified flexible electrode with high areal capacitance and rate capability for supercapacitors. *Synth Met* [Internet]. 2022 Apr 1;285:117017. Available from: [<URL>](#).
20. Sokolova MP, Bobrova N V., Dmitriev IY, Vlasov P V., Smirnov NN, Elyashevich GK, et al. Anticorrosion activity of aniline-aniline-2-sulfonic acid copolymers on the steel surface. *Russ J Appl Chem* [Internet]. 2016 Mar 15;89(3):432-8. Available from: [<URL>](#).
21. Marioli JM, Kuwana T. Electrochemical characterization of carbohydrate oxidation at copper electrodes. *Electrochim Acta* [Internet]. 1992 Jun;37(7):1187-97. Available from: [<URL>](#).
22. Li Z, Chen Y, Xin Y, Zhang Z. Sensitive electrochemical nonenzymatic glucose sensing based on anodized CuO nanowires on three-dimensional porous copper foam. *Sci Rep* [Internet]. 2015 Nov 2;5(1):16115. Available from: [<URL>](#).
23. Wang G, Ding Y, Wang F, Li X, Li C. Poly(aniline-2-sulfonic acid) modified multiwalled carbon nanotubes with good aqueous dispersibility. *J Colloid Interface Sci* [Internet]. 2008 Jan 1;317(1):199-205. Available from: [<URL>](#).
24. Şahin Y, Pekmez K, Yıldız A. Electropolymerization and in situ sulfonation of aniline in water-acetonitrile mixture containing FSO₃H. *Synth Met* [Internet]. 2002 Nov;131(1-3):7-14. Available from: [<URL>](#).
25. Şahin Y, Pekmez K, Yıldız A. Electrochemical preparation of soluble sulfonated polymers and aniline copolymers of aniline sulfonic acids in dimethylsulfoxide. *J Appl Polym Sci* [Internet]. 2003 Nov 21;90(8):2163-9. Available from: [<URL>](#).
26. Sudha V, Murugadoss G, Thangamuthu R. Structural and morphological tuning of Cu-based metal oxide nanoparticles by a facile chemical method and highly electrochemical sensing of sulphite. *Sci Rep* [Internet]. 2021 Feb 9;11(1):3413. Available from: [<URL>](#).
27. Abunahla H, Mohammad B, Alazzam A, Jaoude MA, Al-Qutayri M, Abdul Hadi S, et al. MOMSense: Metal-Oxide-Metal Elementary Glucose Sensor. *Sci Rep* [Internet]. 2019 Apr 2;9(1):5524. Available from: [<URL>](#).
28. Strakosas X, Selberg J, Pansodtee P, Yonas N, Manapongpun P, Teodorescu M, et al. A non-enzymatic glucose sensor enabled by bioelectronic pH control. *Sci Rep* [Internet]. 2019 Jul 26;9(1):10844. Available from: [<URL>](#).
29. Jayarathne RMHH, Pitigala PKDDP, Perera VP. Electronic and structural properties of Cu₂O polycrystalline thin films grown on adhesive copper tape. *Proc Tech Sess* [Internet]. 2019 [cited 2023 Feb 26];35:31-8. Available from: [<URL>](#).
30. He D, Wang G, Liu G, Suo H, Zhao C. Construction of leaf-like CuO-Cu₂O nanocomposites on copper foam for high-performance supercapacitors. *Dalt Trans* [Internet]. 2017;46(10):3318-24. Available from: [<URL>](#).
31. Volanti DP, Keyson D, Cavalcante LS, Simões AZ, Joya MR, Longo E, et al. Synthesis and characterization of CuO flower-nanostructure processing by a domestic hydrothermal microwave. *J Alloys Compd* [Internet]. 2008 Jul 14;459(1-2):537-42. Available from: [<URL>](#).
32. Petrov T, Markova-Deneva I, Chauvet O, Nikolov R, Denev I. SEM and FT-IR spectroscopy study of Cu, Sn and Cu-Sn nanoparticles. *J Univ Chem Technol Metall* [Internet]. 2012;47(2):197-206. Available from: [<URL>](#).
33. Diraz Uribe CE, Vallejo Lozada WA, Martinez Ortega F. Synthesis and characterization of TiO₂ thin films doped with copper to be used in photocatalysis. *Iteckne*. 2013;10(1):16-20.
34. Abd-Elnaiem AM, Abdel-Rahim MA, Abdel-Latief AY, Mohamed AA-R, Mojsilović K, Stepniowski WJ. Fabrication, Characterization and Photocatalytic Activity of Copper Oxide Nanowires Formed by Anodization of Copper Foams. *Materials (Basel)* [Internet]. 2021 Sep 2;14(17):5030. Available from: [<URL>](#).
35. Hesari Z, Shirkavand Hadavand B. Synthesis and Study on Conductivity of Urethane Acrylate/Polyaniline/CuO Nanocomposites. *J Appl Chem Res* [Internet]. 2018;12(4):66-77. Available from: [<URL>](#).
36. Yazar S, Atun G. Electrochemical synthesis of tunable polypyrrole-based composites on carbon fabric for wide potential window aqueous supercapacitor. *Int J Energy Res* [Internet]. 2022 Aug 27;46(10):14408-23. Available from: [<URL>](#).

37. Dadamos TRL, Teixeira MFS. Electrochemical sensor for sulfite determination based on a nanostructured copper-salen film modified electrode. *Electrochim Acta* [Internet]. 2009 Jul 30;54(19):4552-8. Available from: [<URL>](#).
38. Li M, Liu L, Xiong Y, Liu X, Nsabimana A, Bo X, et al. Bimetallic MCo (M=Cu, Fe, Ni, and Mn) nanoparticles doped-carbon nanofibers synthesized by electrospinning for nonenzymatic glucose detection. *Sensors Actuators B Chem* [Internet]. 2015 Feb 1;207:614-22. Available from: [<URL>](#).
39. Esmaeeli A, Ghaffarinejad A, Zahedi A, Vahidi O. Copper oxide-polyaniline nanofiber modified fluorine doped tin oxide (FTO) electrode as non-enzymatic glucose sensor. *Sensors Actuators B Chem* [Internet]. 2018 Aug 1;266:294-301. Available from: [<URL>](#).
40. Ghanbari K, Babaei Z. Fabrication and characterization of non-enzymatic glucose sensor based on ternary NiO/CuO/polyaniline nanocomposite. *Anal Biochem* [Internet]. 2016 Apr 1;498:37-46. Available from: [<URL>](#).
41. Mamleyev ER, Weidler PG, Nefedov A, Szabó DV, Islam M, Mager D, et al. Nano- and Microstructured Copper/Copper Oxide Composites on Laser-Induced Carbon for Enzyme-Free Glucose Sensors. *ACS Appl Nano Mater* [Internet]. 2021 Dec 24;4(12):13747-60. Available from: [<URL>](#).
42. Wei C, Zou X, Liu Q, Li S, Kang C, Xiang W. A highly sensitive non-enzymatic glucose sensor based on CuS nanosheets modified Cu₂O/CuO nanowire arrays. *Electrochim Acta* [Internet]. 2020 Feb 20;334:135630. Available from: [<URL>](#).
43. Sridara T, Upan J, Saianand G, Tuantranont A, Karuwan C, Jakmunee J. Non-Enzymatic Amperometric Glucose Sensor Based on Carbon Nanodots and Copper Oxide Nanocomposites Electrode. *Sensors* [Internet]. 2020 Feb 2;20(3):808. Available from: [<URL>](#).
44. Ashok A, Kumar A, Tarlochan F. Highly efficient nonenzymatic glucose sensors based on CuO nanoparticles. *Appl Surf Sci* [Internet]. 2019 Jul 1;481:712-22. Available from: [<URL>](#).
45. Anu Prathap MU, Kaur B, Srivastava R. Hydrothermal synthesis of CuO micro-/nanostructures and their applications in the oxidative degradation of methylene blue and non-enzymatic sensing of glucose/H₂O₂. *J Colloid Interface Sci* [Internet]. 2012 Mar 15;370(1):144-54. Available from: [<URL>](#).



Novel Well-defined Polystyrene-*block*-Poly(lactide-co-glycolide) Block Copolymers

Ozcan Altintas* 

Department of Chemistry, University of Minnesota, Minneapolis, Minnesota 55455, United States

Abstract: A facile preparation of polystyrene-*block*-poly(lactide-co-glycolide) PS-*b*-PLGA block copolymers was reported in detail. Well-defined PS-*b*-PLGA block copolymers were successfully obtained via living anionic polymerization and ring-opening polymerization. First, hydroxyl-terminated linear polystyrenes were prepared by living anionic polymerization. The resulting polymers were used as macroinitiators for ring-opening copolymerization of lactide and glycolide in the presence of the 1,8-diazabicyclo[5.4.0]undec-7-ene (DBU) as a catalyst in dichloromethane at ambient temperature. Transesterification and formation of DBU-initiated polymers were minimized by optimizing the catalyst concentration. Three block copolymers were synthesized in various molecular weights from 5000 g/mol to 33600 g/mol with low polydispersity. The formation of well-defined PS-*b*-PLGA block copolymers was followed by nuclear magnetic resonance spectroscopy and size-exclusion chromatography. Thermal properties of the block copolymers were investigated by thermal gravimetric analysis and differential scanning calorimetry. The morphology of the block copolymers was investigated using small-angle X-ray scattering in the bulk and via grazing incidence small-angle X-ray scattering as well as atomic force microscopy in thin film demonstrating organized nanostructures with uniform domain sizes. Overall, this manuscript describes an expanded polymer toolbox for PLGA-based polymers for next-generation lithography applications.

Keywords: Block copolymers, polystyrene, polyester, morphology, and phase separation.

Submitted: October 12, 2022. **Accepted:** January 09, 2023.

Cite this: Altintas O. Novel Well-defined Polystyrene-*block*-Poly(lactide-co-glycolide) Block Copolymers. JOTCSA. 2023;10(1):241-52.

DOI: <https://doi.org/10.18596/jotcsa.1184492>.

***Corresponding author. E-mail:** ozcanaltintas@gmail.com.

1. INTRODUCTION

Block polymers consist of chemically different sub-chains which are covalently attached at junction points (1). Block polymers have gained significant interest in many fields of nanotechnology applications such as fabrication of nanomaterials (2), nanoporous films (3), storage media (4), sensors (5) and nanolithography (6). Block polymers in the bulk or thin film have demonstrated remarkable ability to form well-defined nanostructures because of their microphase separation on the nanoscale (7,8). Block polymer thin films spontaneously produce various well-defined equilibrium morphologies in bulk and solution ranging from spheres, cylinders, lamellae, and more complex structures. The resulting morphologies depend on the following parameters: the number of monomeric units in a block copolymer and the volume fraction

of domains as well as the Flory-Huggins parameter (9-11). Lamellae and cylindrical phases are of particular interest in industry (12).

Reversible deactivation radical polymerization (RDRP) techniques (13) such as atom transfer radical polymerization (ATRP) (14,15), reversible addition-fragmentation chain transfer (RAFT) polymerization (16,17) and nitroxide-mediated polymerization (NMP) (18) are the most versatile methods to design and control polymer structure. However, the RDRP methods have their own limitations, including the use of transition metals and sulfur-containing final products as well as slow polymerization rates (19). Among all the living polymerization techniques, anionic polymerization is a unique method for the preparation of polymers with uniform structures (20,21). Well-defined telechelic linear polymers consisting of one or more

functional groups at chain-ends can readily be prepared via living anionic polymerization (21). These functional polymers can be utilized as building blocks such as macroinitiators and cross-linkers for the synthesis of various polymer architectures (22).

Recent years, aliphatic polyesters of lactones and lactides were achieved by ring opening polymerization (ROP) (23-25) have attracted substantial interest due to bacterial decomposition process and forming natural byproducts (26). They have been practiced in various applications ranging from biomedical industries (25) to ordered nanostructured morphologies (19). For example, nanoporous materials can be readily generated from microphase separation of block copolymers having aliphatic polyester and subsequently selective removing of the polyester domains (27,28).

Because of the poor solubility of glycolide and its polymers in common solvents, controlled polymerization of glycolide has been challenging task (29). The copolymerization of lactide and glycolide represents an efficient method to synthesize soluble poly(glycolide) (PGA) derivatives. Hoyer and coworkers developed a strategy for PLGA-based block copolymers and commercially available hydroxyl functional poly(ethylene glycol) as an initiator using DBU as the catalyst (30). More recently, Long and coworkers synthesized and characterized functional PEG-*b*-PLGA copolymers and studied their subsequent performance in vat photopolymerization for tissue scaffolding applications (31).

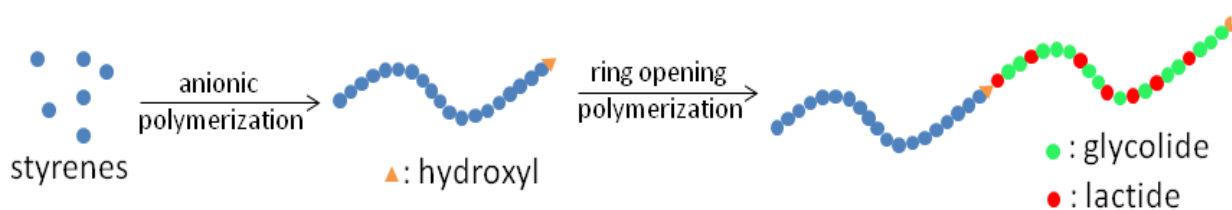
To the best of our knowledge, well-defined PS-*b*-PLGA block copolymers via a combination of living anionic polymerization and ROP of lactide and

glycolide have not been reported yet. In the current contribution, the goal is to fill this synthetic gap and study the effects of molecular architecture on the resultant thermal and morphological properties. First of all, the macroinitiators were prepared by living anionic polymerization using a *sec*-butyl lithium as an initiator. Subsequently, novel PS-*b*-PLGA block copolymers were prepared via ROP of cyclic esters. The resulting block copolymers were characterized via ¹H nuclear magnetic resonance (NMR), size exclusion chromatography (SEC), Fourier-transform infrared spectroscopy (FTIR), thermal gravimetric analysis (TGA) and differential scanning calorimetry (DSC). The morphologies of the block copolymers were identified small-angle X-ray scattering (SAXS), atomic force microscopy (AFM) as well as grazing-incidence small-angle scattering (GISAXS).

2. EXPERIMENTAL SECTION

2.1. Materials

Glycolide (99%) and D,L-lactide (99%) were received from Ortec and purified by recrystallization from ethyl acetate and toluene three times, respectively. The monomers were dried in vacuum and brought into the glove box prior to use. DBU (98%), styrene (99%), calcium hydride (CaH₂, 95%), *sec*-butyllithium solution (1.4 M in cyclohexane), di-*n*-butyl magnesium solution (1.0 M in heptane), and ethylene oxide (99.5%) were purchased from Sigma-Aldrich and used as received. Hexafluoro isopropanol (HFIP, 99%) was purchased from Oakwood Chemical and used as received. Methanol, acetone, ethyl acetate, and tetrahydrofuran (THF) were purchased from Sigma-Aldrich as analytical grade and used as received. Solvents for the polymerizations were retrieved from solvent purification columns.



Scheme 1: The preparation of well-defined PS-*b*-PLGA block copolymers.

2.2. Characterization Methods

2.2.1. Nuclear magnetic resonance (NMR) spectroscopy

¹H and ¹³C NMR spectra were obtained using either a 400 or 500 MHz Bruker Avance III HD spectrometer. Chemical shifts were referenced to tetramethylsilane (TMS) as an internal standard at 0.00 ppm for ¹H spectra taken in CDCl₃ containing 5% w/v TMS.

2.2.2. Size exclusion chromatography (SEC)

SEC (CHCl₃ system) data was calibrated to polystyrene standards (polymer laboratories) and acquired on a hp 1100 series liquid chromatography with three successive varian plgel mixed-c columns using chloroform as the mobile phase (35 °C, flow rate = 1 mL/min) and an hp 1047a ri detector. SEC (THF System) analysis was performed at 25 °C on an Agilent 1260 Infinity liquid chromatography system equipped with three Waters Styragel columns in series, a Wyatt DAWN Heleos II 18-angle light

scattering detector, and a Wyatt OPTILAB T-rEX refractive index detector and using THF as the eluent with a flow rate of 1 mL/min. Polydispersity (\bar{D}) was calculated from the light scattering data using Astra software.

2.2.3. Fourier-transform infrared (FT-IR) spectroscopy

Solid-state FT-IR spectra were recorded on a Bruker Alpha Platinum attenuated total reflectance unit (Bruker) coupled to a Bruker Vertex 80 Fourier-transform spectrometer. A series of spectra were collected between 400 and 4000 cm^{-1} in single beam mode using OMNIC software. The measurements were obtained using 164 scans/sample at a resolution of 4 cm^{-1} .

2.2.4. Thermal gravimetric analysis (TGA)

The thermal stability of the polymers was determined using TGA, a TA Instruments Q500. Approximately 5 mg of the polymer was heated at 10 $^{\circ}\text{C}/\text{min}$ from ambient temperature to 550 $^{\circ}\text{C}$ in a nitrogen atmosphere.

2.2.5. Differential scanning calorimetry (DSC)

DSC measurements were conducted using a Discovery DSC (TA Instruments Inc.). Approximately 5 mg samples were subjected to a heating and cooling rate of 10 $^{\circ}\text{C}/\text{min}$ under nitrogen atmosphere. DSC data analysis was performed using TRIOS software package. The thermal transitions were obtained from the second heating curve. The glass transition temperature (T_g) was determined from the mid-point of the step change in the heat flow signal.

2.2.6. Ellipsometry

The film thicknesses of the freshly spin-coated thin films on the Si wafers were measured by Ellipsometry on a J. A. Woollam Co., Inc. V-VASE.

2.2.7. Atomic force microscopy (AFM)

Tapping mode AFM was performed on a Bruker Nanoscope V Multimode 8 scanning probe microscope under ambient conditions with silicon cantilever tips.

2.2.8. X-ray scattering (SAXS/GISAX)

SAXS experiments at ambient temperature were conducted at the Advanced Photon Source in Argonne National Laboratory (Argonne, IL) using beamline 5-ID-D. SAXS data were collected with an energy 17 keV radiation and a sample-to-detector distance of 6 m. GISAXS measurements were performed at beam line 8-ID-E at the Advanced Photon Source of Argonne National Laboratory. Samples were placed in a vacuum chamber and illuminated with an energy 7.35 keV radiation at incident angles in the range of 0.2-0.24 $^{\circ}$; the scattering data were recorded with a Pilatus 1MF pixel array detector positioned 2175 mm from the sample. Acquisition times were approximately 10 s per frame.

2.3. Synthesis

2.3.1. Synthesis of ω -(hydroxy)polystyrene homopolymer via anionic polymerization

Following a modified literature procedure (32), hydroxyl functional polystyrenes were synthesized by living anionic polymerization in cyclohexane using *sec*-butyl lithium as the initiator at 40 $^{\circ}\text{C}$ overnight. Styrene was first freeze-pump-thawed three times and distilled twice over CaH_2 and then once over di-*n*-butylmagnesium and subsequently transferred to a flame-dried air-free burette. Cyclohexane (600 mL) was transferred from the solvent purification columns to a flame-dried air-free flask, then an argon/vacuum manifold, a manometer through Teflon valves, a septum, and the flask of purified styrene (50 g, 0.48 mol) were all connected to a 1-L flask equipped with five internal glass connectors and a Teflon-coated stir bar. The reactor was evacuated with high vacuum of 27 mTorr, flamed-dried and backfilled with argon five times. Finally, the cyclohexane was added to the reactor followed by the addition of *sec*-butyllithium (7.2 mL of 1.40 M *sec*-butyllithium in cyclohexane) with an airtight syringe through the septum. The reaction solution was heated to 40 $^{\circ}\text{C}$ in an oil bath. The styrene was added and the reaction mixture was stirred overnight, observing an orange-red color indicating the presence of poly(styryllithium) chain ends. Ethylene oxide (EO, 5 equivalents to *sec*-butyllithium initiator) was purified over di-*n*-butylmagnesium and transferred to a flame-dried air-free burette. The polymerization solution was cooled to the room temperature and the purified ethylene oxide was added by warming small doses from an externally chilled burette connected to the reactor with Ultra-Torr (Swagelok) Cajon tubing. The reaction was allowed to stir overnight under positive pressure. The reaction mixture turned colorless and subsequently was terminated by the addition of degassed methanol. The polymer was isolated by precipitation in cold methanol and the precipitate was filtered off and dried under high vacuum at 70 $^{\circ}\text{C}$ to afford the polymer as a white powder. ^1H NMR in CDCl_3 $\{\delta, \text{ppm}\}$: 7.40-6.30 (5H, aromatic protons of PS), 3.50-3.20 (2H, $\text{CH}_2\text{-OH}$), 1.78-1.18 (aliphatic protons of PS), $M_{n,\text{NMR}} = 4800$ g/mol. $M_{n,\text{SEC}} = 4900$ g/mol, $\bar{D} = 1.03$.

2.3.2. Synthesis of poly(styrene)-*b*-poly(glycolide-co-lactide) copolymer via ring opening polymerization

Solutions of the hydroxyl-terminated polystyrene (1 g, 0.208 mmol in 10 mL of DCM), lactide (0.59 g, 4.1 mmol in 18 mL of DCM), 1,8-diazabicyclo[5.4.0]undec-7-ene (DBU, 15 μL in 2 mL of DCM) and glycolide (0.965 g, 8.32 mmol in 20 mL of THF) were first prepared in a controlled atmosphere (nitrogen) glove box. A flame-dried Schlenk flask was then equipped with a septum and a stir bar. The solutions of the macroinitiator and lactide were added to the reaction flask under argon atmosphere, followed by addition of the DBU solution. The solution of glycolide was then added via a syringe pump at a rate of 200 $\mu\text{L}/\text{min}$. At the end of the addition (100 min), solid benzoic acid (25 mg) was added to

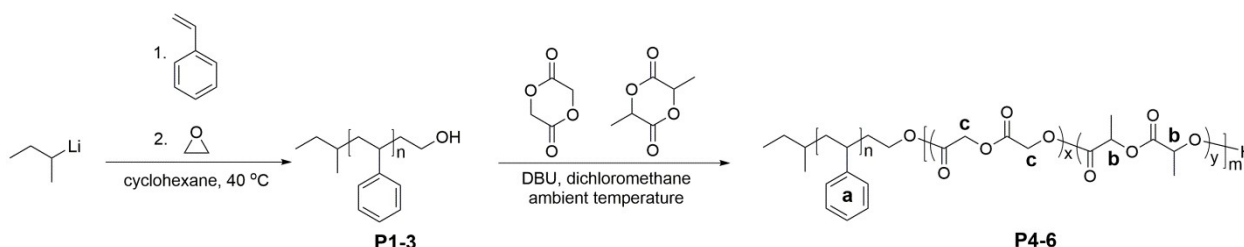
terminate the polymerization. The PS-*b*-PLGA block copolymer was purified by precipitation into methanol from the reaction mixture and dried at 60 °C under vacuum overnight. ¹H NMR in CDCl₃ { δ , ppm}: 7.40-6.30 (5H, aromatic protons of PS), 5.21 (CH of PLA), 4.86 (CH₂ of PGA), 1.61 (CH₃ of PLA), 1.78-1.18 (aliphatic protons of PS), $M_{n,NMR}$ = 10800 g/mol, $M_{n,SEC}$ = 9100 g/mol, \bar{D} = 1.15.

3. RESULTS AND DISCUSSIONS

Herein, novel well-defined PS-*b*-PLGA block copolymers were achieved using living anionic polymerization and ROP methods and subsequently morphology of the polymers was investigated in bulk as well as in thin film studies.

Styrene was polymerized using *sec*-BuLi in cyclohexane at 40 °C for 16 hours subsequently ethylene oxide was added to achieve the hydroxyl-

terminated polystyrenes. Molecular weight of the homopolymers were determined by ¹H NMR and SEC. The SEC traces of the homopolymers demonstrate unimodal molecular weight distributions (refer to Figure S1 in the Supporting Information (SI) section). ¹H NMR spectrum (Figure S2 in the SI section) was utilized to estimate the number-average molecular weight, $M_{n,NMR}$, of the homopolymer comparing the integrated areas aromatic protons of the polystyrene at 6.3-7.3 ppm and the nine protons of the initiator at 0.9-1.1 ppm. It was found that molecular weights obtained from both techniques are in excellent agreement. The percentage of the hydroxyl group at chain-end of the homopolymers was estimated by the integral areas of the methylene protons adjacent the hydroxyl group as well as the initiator protons indicating quantitative hydroxyl end-group incorporation (see Table 1).



Scheme 2: The chemical structures of the PS-*b*-PLGA block copolymers.

Table 1: Molecular Properties of the PS-OH Macroinitiators.

Polymer	$M_{n,NMR}^a$ (g/mol)	$M_{n,SEC}^b$ (g/mol)	\bar{D}^b	EGF ^c
P1	2400	2300	1.03	0.98
P2	4800	4900	1.03	0.99
P3	13700	13400	1.03	0.96

^aDetermined using ¹H NMR spectroscopy; ^bdetermined from SEC in THF using MALLS-SEC; ^cend group fidelity (EGF) or percentage of the hydroxyl group at chain-end.

The ROP of glycolide by Beuermann (29) and lactide by Waymouth (33) has been reported in the absence of any initiator, DBU can act as an initiator to form macrocyclics and linear chains. Thus, the ROP of the cyclic esters was applied both in the presence and absence of a macroinitiator using DBU and observing the formation of oligomeric species in the SEC traces when [initiator]₀/ [DBU]₀ = 1 (refer to Figure S3). Subsequently the concentration of DBU was optimized for the ROP of the cyclic esters using the hydroxyl functional polystyrene. After performing the polymerization at various concentration of DBU, it was found that 2 mM concentration of DBU is sufficient to achieve well-defined linear polymers. Next, the block copolymers were accomplished by the ROP of lactide and glycolide using DBU as the catalyst and the hydroxyl-terminated polystyrene as the

macroinitiator. The purified block copolymers were characterized by SEC comparing to PS standards using CHCl₃ as elution solvent. For example, the SEC trace of P5 in Figure 1 shows a shift towards higher molecular mass, compared with its corresponding polymer precursor (P2). Additionally, no significant increase in the dispersity was observed for the formed block copolymer (PS-*b*-PLGA, P5). Additional details for the macroinitiator and block copolymer are given in Tables 1 and 2. The ¹H NMR spectrum of P5 shows corresponding CH peak of the PLA and CH₂ of the PGA repeat units at 5.21 ppm and 4.86 ppm, respectively, confirming successful block copolymer incorporation (refer to Figure 2). The $M_{n,NMR}$ of the block copolymers was obtained by using the aromatic protons of PS, the CH of the PLA and the two protons of PGA. Volume fractions of PLA and PGA segments in the block copolymer were

calculated using ^1H NMR spectrum based on homopolymer densities. In addition, the lactide/glycolide weight fractions of the block copolymers were obtained from integral area of the peaks at 5.21 ppm and 4.86 ppm, respectively and

reported in Table 2. Further evidence for the block copolymer formation was obtained from FT-IR (refer to Figure S4) as the carbonyl stretching band of the PLGA chains were appeared at 1754 cm^{-1} .

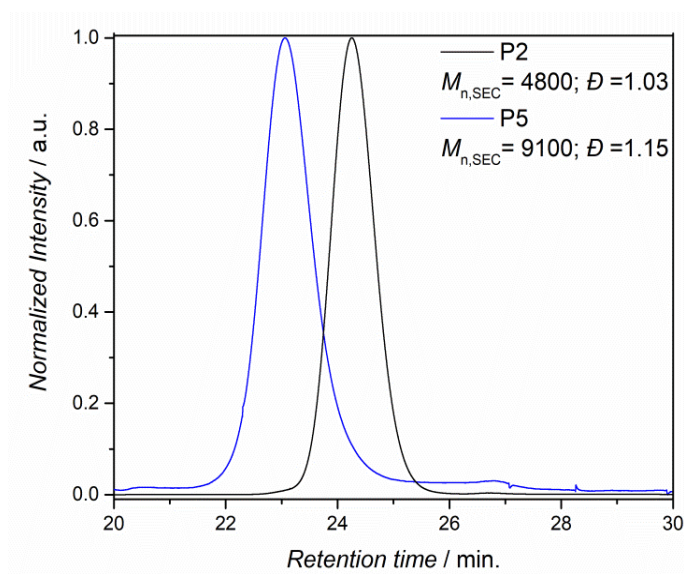


Figure 1: SEC traces of the hydroxyl-terminated polystyrene (P2) and the corresponding block copolymer (PS-*b*-PLGA, P5). Additional details for the macroinitiator and block copolymers are given in Tables 1 and 2 as well as Figure S1 and S2.

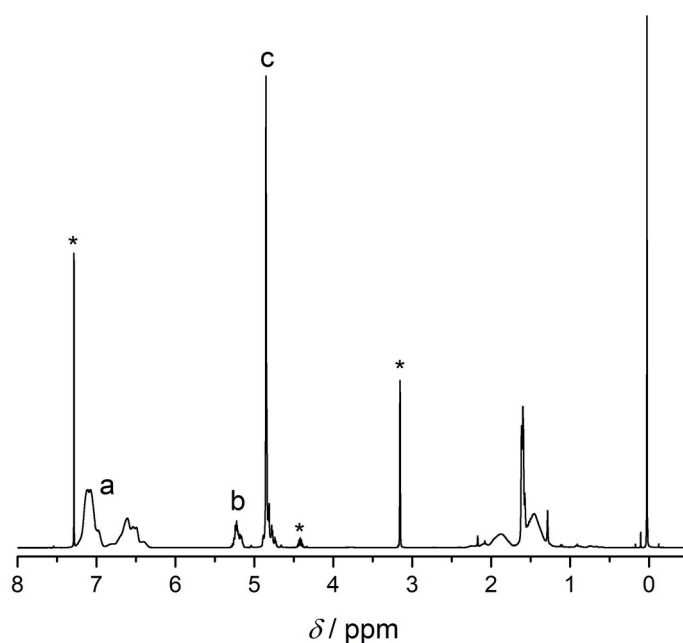


Figure 2: ^1H NMR spectra of PS-*b*-PLGA (P5) in CDCl_3 /hexafluoro-2-propanol (HFIP) (v/v: 9/1) at ambient temperature. The peaks marked with an asterisk are due to solvent (HFIP). The chemical structures can be found in Scheme 2.

The thermal behavior of the PS-*b*-PLGA block copolymers was examined via TGA heating from room temperature to 550 °C at a rate of 10 °C/min under nitrogen which are depicted in Figure 3. The PS-*b*-PLGA block copolymers demonstrated a two-

step weight loss. Initially the block copolymers lost ~60% weight at 350 °C corresponding to the PLGA thermal degradation temperature and subsequently complete degradation occurred at 420 °C referring to the decomposition of PS.

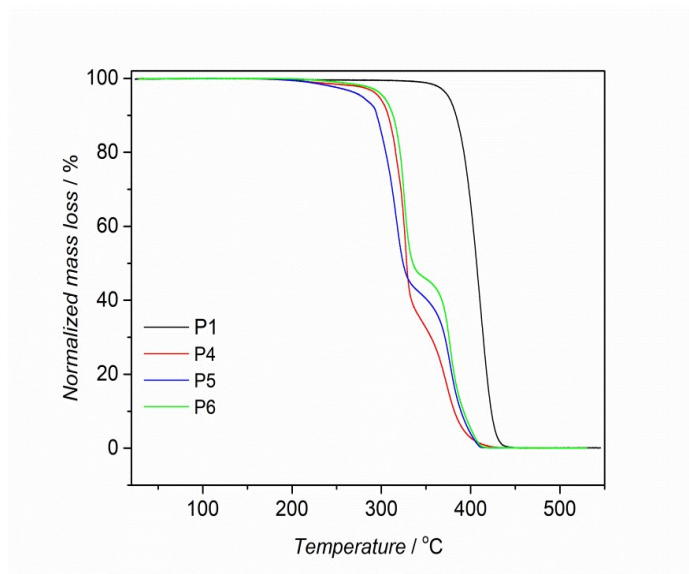


Figure 3: TGA traces of block copolymers and precursor polymer.

The thermal transitions of the block copolymer were investigated using DSC in order to observe the glass transition temperatures (T_g) and the peak melting temperature (T_m). The second heating traces of the block copolymers are shown in Figure 4. The DSC trace of the PS-*b*-PLGA block copolymer (P6) shows a T_g at 43 °C corresponding to the PLGA chains, then a second glass transition at about 96 °C referring to

the T_g of the PS chains, which are in excellent agreement with reported values (29). Upon further heating, melting of the semi-crystalline domains of PLGA is detected by observing the T_m at ~150 °C. The degree of crystallinity (X_c) of PS-*b*-PLGA block copolymers was calculated by the following literature (32).

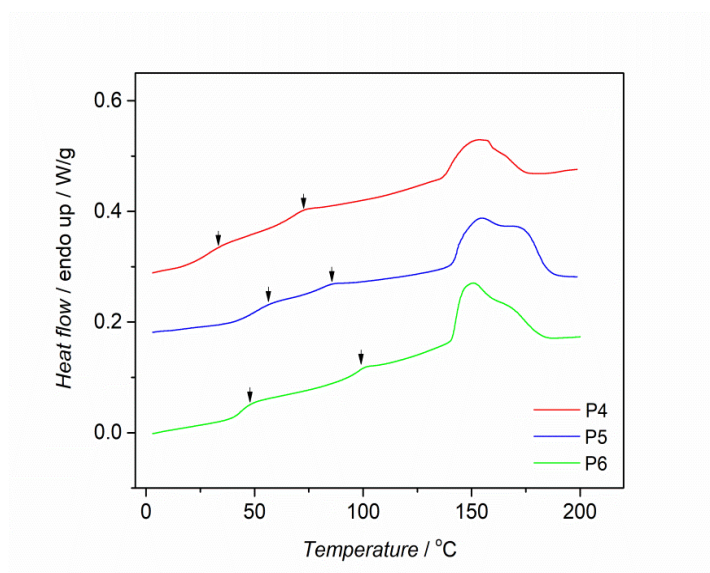


Figure 4: DSC traces for PS-*b*-PLGA block copolymers.

Table 2: Molecular and Thermal Characteristics of Block Copolymers.

Polymer	$M_{n,NMR}^a$ (g/mol)	$M_{n,SEC}^b$ (g/mol)	\mathcal{D}^b	f_{PLGA}^c	w_{PGA}^d	$T_{g,PS}^e$ (°C)	$T_{g,PLGA}^f$ (°C)	$T_{m,PGA}^g$ (°C)	X_c^h (%)	T_d^i (°C)	D_{SAXS}^k (nm)
P4	5000	5500	1.16	0.45	0.33	68	26	166	30	298	15
P5	10800	9100	1.15	0.48	0.38	83	49	169	25	285	16
P6	33600	19500	1.17	0.52	0.31	98	43	147	29	308	27

^aCalculated using ¹H NMR spectra. ^bDetermined via SEC. ^cVolume fraction of PLGA. ^dWeight fraction of PLGA. ^e $T_{g,PS}$ is the glass transition temperature of the PS and ^f $T_{g,PLGA}$ is for the PLGA. ^g $T_{m,PGA}$ is PLGA melting temperature. ^hDegree of crystallinity. ⁱ5% mass loss was determined by TGA. ^kDomain spacing was obtained from SAXS data.

The morphology of the block copolymers was investigated via SAXS. The block copolymers were annealed at 110 °C under inert atmosphere for 16 h. Subsequently the block copolymers were slowly cooled to the room temperature before examining the bulk microphase separation via SAXS. Domain spacings ($D = 2\pi/q^*$) were obtained by using the principal scattering peak position (q^*) and summarized in Table 2. The SAXS scattering profiles

of the block copolymers at 25 °C show a main scattering peak with domain spacing of 15-27 nm, which indicates microphase separation. Because of the lack of well-defined second order reflections, the morphology of the block copolymers could not be determined via SAXS (Figure 5). It is possible that the polymer chains were not able to move in bulk below the melting temperature due to their semi-crystalline nature.

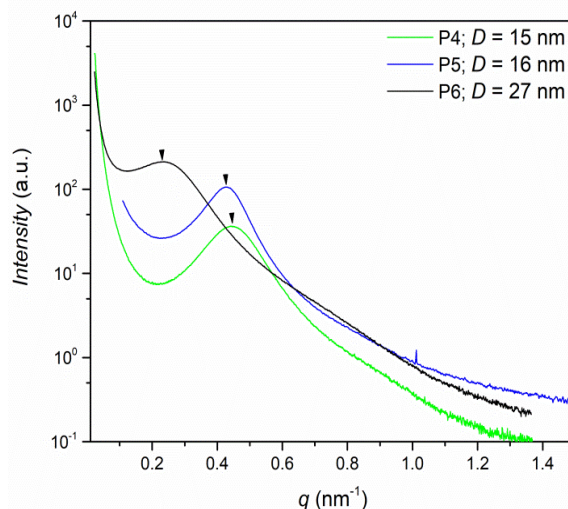


Figure 5: The SAXS data obtained at ambient temperature for the corresponding block copolymers.

Subsequently the surface phase structures of polymer films were analyzed by AFM (35). Block copolymer solutions (10 mg/mL) in $\text{CHCl}_3/\text{HFIP}$ (v/v: 9/1) were spin-coated onto HMDS-modified silicon wafers. The thickness of the polymer film, measured by ellipsometer, was around 54 nm. Solvent vapor annealed (SVA) was applied in $\text{CHCl}_3/\text{HFIP}$ (v/v: 9/1) for five minutes (36). After SVA, the thin film was

analyzed by AFM in the tapping mode showing the image in Figure 6. The AFM characterization of P5 demonstrated well-segregated microdomains with uniform domain size throughout the $1 \times 1 \mu\text{m}$ sample suggesting possible perpendicular lamellar orientation in the PS-*b*-PLGA thin films (Figure 5). The domain spacing from the AFM image (20 nm) and SAXS (16 nm) is comparable.

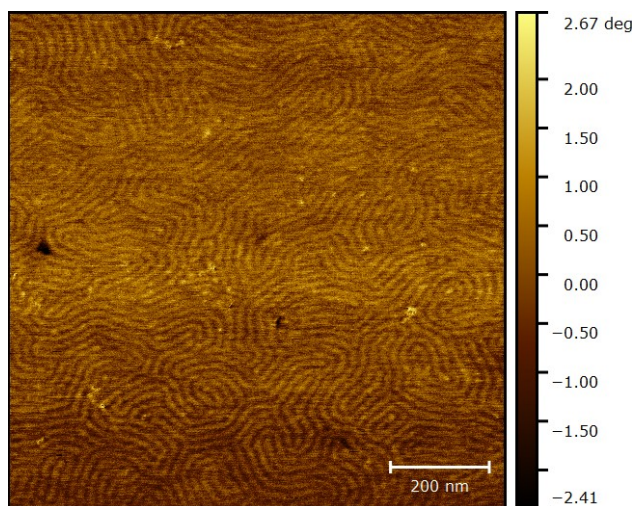


Figure 6: AFM phase image of PS-*b*-PLGA (P5).

The morphological characterization in block polymer thin films can be obtained through the small-angle

X-ray scattering (GISAXS) technique (37). In addition to SAXS and AFM characterizations, the one-

dimensional GISAX data for P5 was shown in Figure 7. The fundamental domain spacing was estimated to be 15.8 nm from the principle scattering peak maxima at $q_y^* = 0.396/\text{nm}$. Because of the symmetric volume fractions of each segment ($f_{\text{PLGA}} = 0.48$), it might be indicative of a lamellar morphology (38). Moreover, the spacing of the

features from the GISAXS (15.8 nm) is in excellent agreement with the bulk spacing obtained by SAXS (16 nm). Based on the DSC, AFM and GISAXS analysis, the symmetric PS-*b*-PLGA block copolymer could be microphase-separated with a perpendicular lamellar morphology.

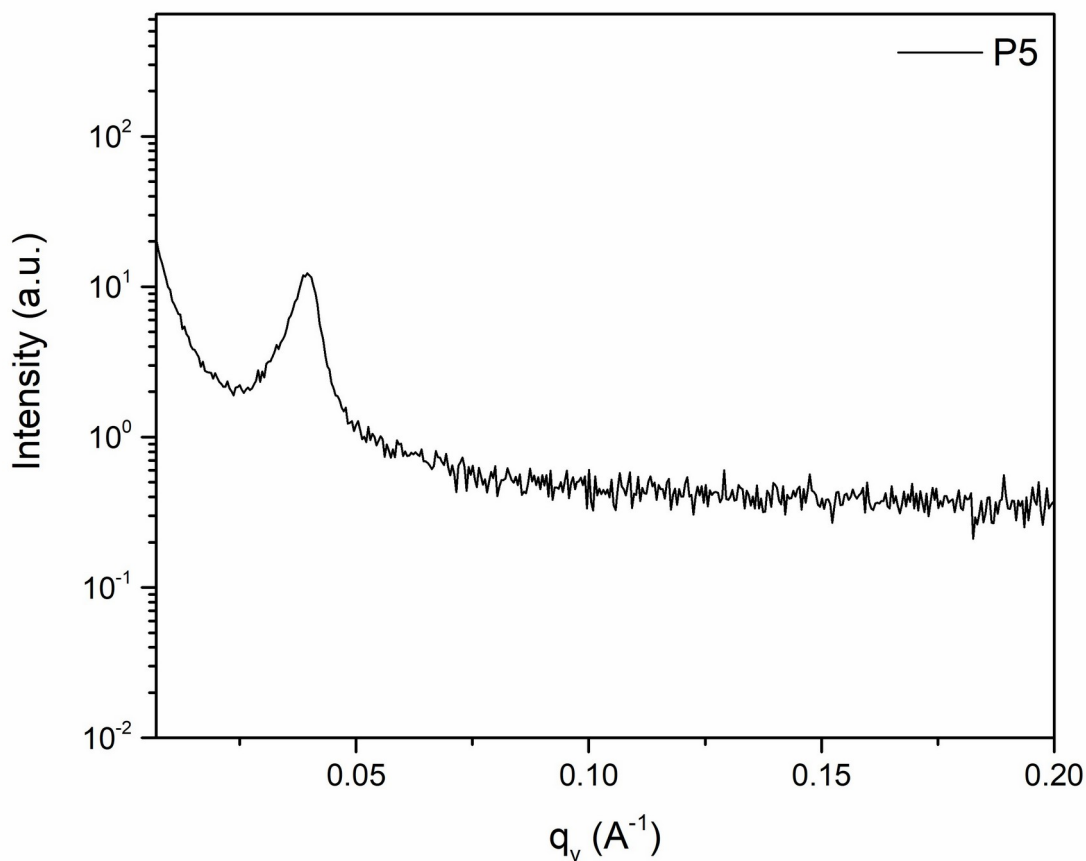


Figure 7: 1D synchrotron GISAXS profile for the block copolymer (P5, $M_{n,\text{NMR}} = 10800$ g/mol, $f_{\text{PLGA}} = 0.48$) at room temperature.

4. CONCLUSION

A versatile synthetic approach for the synthesis of PS-*b*-PLGA block copolymers was -for the first time- demonstrated. Well-defined PS-*b*-PLGA polymers were successfully obtained via advanced polymerization methods. Initially hydroxyl-terminated linear polystyrenes were prepared and then copolymerization of lactide and glycolide was achieved using the macroinitiator and DBU at ambient temperature leading to PS-*b*-PLGA block copolymers. Transesterification and formation of DBU-initiated polymers were minimized by optimizing the catalyst concentration to 2 mM. Number-average molar mass of the block copolymers as well as the block volume fraction were calculated based on ^1H NMR spectra. Furthermore, the block copolymer formation was followed by SEC traces. The stability of the block copolymer was analyzed by TGA demonstrating less than 5% weight loss up to 270 °C. Thermal properties of the block copolymer were obtained by

DSC indicating two clear glass transition and melting temperatures suggesting well-defined microphase separation. The formation of the organized nanostructures was observed by SAXS, GISAXS and AFM. Although no higher order reflections were observed in the SAXS characterization, these polymers have a fundamental spacing ranging of 15-27 nm. The results from DSC, AFM and GISAXS demonstrate that the morphology of the block copolymer is presumably perpendicular lamellar as each segment ($f_{\text{PLGA}} = 0.48$) has the symmetric volume fractions. The present results unambiguously prove that the formation of PS-*b*-PLGA block copolymers on a very well-defined level is indeed possible employing high precision macromolecular design strategies. This manuscript have demonstrated the synthesis, characterization, and morphology of PLGA-based block copolymers as well as potential use in nanopatterning and advanced multilayer applications.

5. ACKNOWLEDGMENTS

The author graciously thanks Prof. Marc Hillmyer (UMN), Prof. Frank Bates (UMN), and Dr. Joshua Speros (BASF) for helpful discussion as well as for their financial support. SAXS and GISAXS data were obtained at the Advanced Photon Source, a U.S. Department of Energy (DOE) Office of Science User Facility operated for the DOE Office of Science by Argonne National Laboratory. Parts of this work were carried out in the Characterization Facility, University of Minnesota.

6. REFERENCES

- Bates CM, Bates FS. 50th Anniversary Perspective : Block Polymers—Pure Potential. *Macromolecules*. 2017 Jan 10;50(1):3-22. Available from: [<URL>](#).
- Lazzari M, López-Quintela MA. Block Copolymers as a Tool for Nanomaterial Fabrication. *Adv Mater*. 2003 Oct 2;15(19):1583-94. Available from: [<URL>](#).
- Jackson EA, Hillmyer MA. Nanoporous Membranes Derived from Block Copolymers: From Drug Delivery to Water Filtration. *ACS Nano*. 2010 Jul 27;4(7):3548-53. Available from: [<URL>](#).
- Kim HC, Park SM, Hinsberg WD. Block Copolymer Based Nanostructures: Materials, Processes, and Applications to Electronics. *Chem Rev*. 2010 Jan 13;110(1):146-77. Available from: [<URL>](#).
- Jung YS, Jung W, Tuller HL, Ross CA. Nanowire Conductive Polymer Gas Sensor Patterned Using Self-Assembled Block Copolymer Lithography. *Nano Lett*. 2008 Nov 12;8(11):3776-80. Available from: [<URL>](#).
- Park M, Harrison C, Chaikin P, others. Block Copolymer Lithography: Periodic Arrays of 10. Holes in. 1:1401-4.
- Bates FS, Hillmyer MA, Lodge TP, Bates CM, Delaney KT, Fredrickson GH. Multiblock Polymers: Panacea or Pandora's Box? *Science*. 2012 Apr 27;336(6080):434-40. Available from: [<URL>](#).
- Darling SB. Directing the self-assembly of block copolymers. *Progress in Polymer Science*. 2007 Oct;32(10):1152-204. Available from: [<URL>](#).
- Leibler L. Theory of microphase separation in block copolymers. *Macromolecules*. 1980;13(6):1602-17.
- Bates FS. Polymer-Polymer Phase Behavior. *Science*. 1991 Feb 22;251(4996):898-905. Available from: [<URL>](#).
- Bates FS, Fredrickson GH. Block copolymers-designer soft materials. *Physics today*. 2000;52.
- Luo M, Epps TH. Directed Block Copolymer Thin Film Self-Assembly: Emerging Trends in Nanopattern Fabrication. *Macromolecules*. 2013 Oct 8;46(19):7567-79. Available from: [<URL>](#).
- Klumperman B. Reversible Deactivation Radical Polymerization. In: John Wiley & Sons, Inc., editor. *Encyclopedia of Polymer Science and Technology* [Internet]. 1st ed. Wiley; 2015 [cited 2023 Feb 8]. p. 1-27. Available from: [<URL>](#).
- Matyjaszewski K. Atom Transfer Radical Polymerization (ATRP): Current Status and Future Perspectives. *Macromolecules*. 2012 May 22;45(10):4015-39. Available from: [<URL>](#).
- Ouchi M, Sawamoto M. 50th Anniversary Perspective : Metal-Catalyzed Living Radical Polymerization: Discovery and Perspective. *Macromolecules*. 2017 Apr 11;50(7):2603-14. Available from: [<URL>](#).
- Perrier S. 50th Anniversary Perspective: RAFT Polymerization—A User Guide. *Macromolecules*. 2017 Oct 10;50(19):7433-47. Available from: [<URL>](#).
- Moad G. RAFT polymerization to form stimuli-responsive polymers. *Polym Chem*. 2017;8(1):177-219. Available from: [<URL>](#).
- Nicolas J, Guillaneuf Y, Lefay C, Bertin D, Gigmes D, Charleux B. Nitroxide-mediated polymerization. *Progress in Polymer Science*. 2013 Jan;38(1):63-235. Available from: [<URL>](#).
- Vanderlaan ME, Hillmyer MA. "Uncontrolled" Preparation of Disperse Poly(lactide)- block -poly(styrene)-block -poly(lactide) for Nanopatterning Applications. *Macromolecules*. 2016 Nov 8;49(21):8031-40. Available from: [<URL>](#).
- Szwarc M. 'Living' polymers. *Nature*. 1956;178:1168-9.
- Hirao A, Loykulant S, Ishizone T. Recent advance in living anionic polymerization of functionalized styrene derivatives. *Progress in Polymer Science*. 2002 Oct;27(8):1399-471. Available from: [<URL>](#).
- Hadjichristidis N, Pitsikalis M, Pispas S, Iatrou H. Polymers with Complex Architecture by Living Anionic Polymerization. *Chem Rev*. 2001 Dec 1;101(12):3747-92. Available from: [<URL>](#).
- Dechy-Cabaret O, Martin-Vaca B, Bourissou D. Controlled Ring-Opening Polymerization of Lactide and Glycolide. *Chem Rev*. 2004 Dec 1;104(12):6147-76. Available from: [<URL>](#).
- Meduri A, Fuoco T, Lamberti M, Pellicchia C, Pappalardo D. Versatile Copolymerization of Glycolide and rac -Lactide by Dimethyl(salicylaldiminato)aluminum Compounds. *Macromolecules*. 2014 Jan 28;47(2):534-43. Available from: [<URL>](#).
- Albertsson AC, Varma IK. Recent Developments in Ring Opening Polymerization of Lactones for Biomedical Applications. *Biomacromolecules*. 2003 Nov 1;4(6):1466-86. Available from: [<URL>](#).
- Chiellini E, Solaro R. Biodegradable Polymeric Materials. *Adv Mater*. 1996 Apr;8(4):305-13. Available from: [<URL>](#).
- Saba SA, Mousavi MPS, Bühlmann P, Hillmyer MA. Hierarchically Porous Polymer Monoliths by Combining Controlled Macro- and Microphase Separation. *J Am Chem Soc*. 2015 Jul 22;137(28):8896-9. Available from: [<URL>](#).
- Altay E, Jang YJ, Kua XQ, Hillmyer MA. Synthesis, Microstructure, and Properties of High-Molar-Mass Polyglycolide Copolymers with Isolated Methyl Defects. *Biomacromolecules*. 2021 Jun 14;22(6):2532-43. Available from: [<URL>](#).

29. Kemo VM, Schmidt C, Zhang Y, Beuermann S. Low Temperature Ring-Opening Polymerization of Diglycolide Using Organocatalysts with PEG as Macroinitiator. *Macromol Chem Phys*. 2016 Apr;217(7):842-9. Available from: [<URL>](#).
30. Qian H, Wohl AR, Crow JT, Macosko CW, Hoyer TR. A Strategy for Control of "Random" Copolymerization of Lactide and Glycolide: Application to Synthesis of PEG- b - PLGA Block Polymers Having Narrow Dispersity. *Macromolecules*. 2011 Sep 27;44(18):7132-40. Available from: [<URL>](#).
31. Wilts EM, Gula A, Davis C, Chartrain N, Williams CB, Long TE. Vat photopolymerization of liquid, biodegradable PLGA-based oligomers as tissue scaffolds. *European Polymer Journal*. 2020 May;130:109693. Available from: [<URL>](#).
32. Zalusky AS, Olayo-Valles R, Wolf JH, Hillmyer MA. Ordered Nanoporous Polymers from Polystyrene-Polylactide Block Copolymers. *J Am Chem Soc*. 2002 Oct 1;124(43):12761-73. Available from: [<URL>](#).
33. Brown HA, De Crisci AG, Hedrick JL, Waymouth RM. Amidine-Mediated Zwitterionic Polymerization of Lactide. *ACS Macro Lett*. 2012 Sep 18;1(9):1113-5. Available from: [<URL>](#).
34. Chu CC. Differential scanning calorimetric study of the crystallization kinetics of polyglycolic acid at high undercooling. *Polymer*. 1980 Dec;21(12):1480-2. Available from: [<URL>](#).
35. Wang D, Russell TP. Advances in Atomic Force Microscopy for Probing Polymer Structure and Properties. *Macromolecules*. 2018 Jan 9;51(1):3-24. Available from: [<URL>](#).
36. Yao L, Oquendo LE, Schulze MW, Lewis RM, Gladfelter WL, Hillmyer MA. Poly(cyclohexylethylene)- block - Poly(lactide) Oligomers for Ultrasmall Nanopatterning Using Atomic Layer Deposition. *ACS Appl Mater Interfaces*. 2016 Mar 23;8(11):7431-9. Available from: [<URL>](#).
37. Posselt D, Zhang J, Smilgies DM, Berezkin AV, Potemkin II, Papadakis CM. Restructuring in block copolymer thin films: In situ GISAXS investigations during solvent vapor annealing. *Progress in Polymer Science*. 2017 Mar;66:80-115. Available from: [<URL>](#).
38. Vora A, Wojtecki RJ, Schmidt K, Chunder A, Cheng JY, Nelson A, et al. Development of polycarbonate-containing block copolymers for thin film self-assembly applications. *Polym Chem*. 2016;7(4):940-50. Available from: [<URL>](#).



Comparison of Four Different Polymeric Adsorbents as Clean-up Agents for Pesticide Analysis in Tea with LC MS/MS

Nihat Özcan¹ 

¹TUBITAK Marmara Research Center, Kocaeli, TÜRKİYE

Abstract: Previously published studies indicate that tea (*Camellia sinensis*) contains essential oils, flavonoids, phenolics, lipids, natural pigments, sugars, and oligosaccharides. These essential biomolecules in *Camellia sinensis* cause serious problems in the determination of pesticide residues. High amount of co-extractives can exhibit chromatographic characteristics similar to some pesticides, which may cause serious matrix effects and significant interference in mass spectrometry analysis. In this study, we compared four polymeric resins as clean-up sorbents for the determination of 216 pesticide residues in tea by a high performance liquid chromatography triple quadrupole mass spectrometry. styrene-divinylbenzene (Diaion HP20), Polyamide 6, Polyvinylpyrrolidone (PPVP), and Amberlite XAD 7 were used as clean-up sorbents instead of PSA. However, to evaluate the effectiveness of the adsorbents, recovery studies were carried out using these adsorbents. In addition, GC-MS analysis was also performed to see the ability of these adsorbents to remove co-extracts. According to the recovery results, when the acceptable limit was accepted as 60-140%, it was determined that the resin that gave the best results with 170 pesticides was polyamide. Diaion was the second resin with 166 pesticides, while XAD, PSA which was used as control group and PPVP were determined as the third, fourth, and fifth resins with very close values of 159, 155, and 152 pesticides, respectively. According to GC-MS total ion analysis, it was observed that PSA gave the chromatogram with the least co-extract, while it was observed that PSA was the worst adsorbent in removing caffeine, one of the main bioactive compounds in tea. XAD-7 and Polyamide were found to be the best adsorbents in removing caffeine.

Keywords: Pesticide, LC-MS/MS, Tea, Adsorption, QuEChERS, clean-up.

Submitted: July 05, 2022. **Accepted:** February 09, 2023.

Cite this: Özcan N. Comparison of Four Different Polymeric Adsorbents as Clean-up Agents for Pesticide Analysis in Tea with LC MS/MS. JOTCSA. 2023;10(1):253-66.

DOI: <https://doi.org/10.18596/jotcsa.1140922>.

***Corresponding author. E-mail:** nihat.ozcan@tubitak.gov.tr.

1. INTRODUCTION

Pesticides are widely used in agriculture to protect the products from harmful pests and diseases. Besides its positive effects, pesticide residue can be hazardous to human health. For this reason, many countries have applied monitoring programs to control pesticide residues in edible products. Pesticide residues can easily be found in tea due to their widespread usage in order to kill pests and to eliminate weeds and diseases during the tea cultivation (1). Tea is one of the most widely consumed beverages for centuries. Tea contains essential oils, flavonoids, phenolics, lipids, natural pigments, sugars, and oligosaccharides (2). Therefore, tea is an important source of antioxidants

and its health-promoting effects have been widely investigated. Antioxidant effect of tea mainly comes from polyphenols such as flavonols (quercetin, kaempferol, myricetin), flavan-3-ols (catechins and theaflavins), and alkaloids (caffeine and theaflavins), gallic acid derivatives, hydroxycinnamate quinic esters (caffeoylquinic acids) (3, 4). On the other hand, these essential characteristic compounds of tea cause serious problems for determination of pesticide residues in tea. A high amount of co-extractives can exhibit chromatographic characteristics similar to some pesticides, which may cause serious matrix effects and significant interference in mass spectrometric analysis (2). In the mass spectrometer, these polyphenols compete with the target analytes for access to the droplet

surface prior to gas phase emission which may suppress or enhance the ionization of target compounds, and affect the detection results (5). Since the target analytes occur at low concentrations and belong to a wide range of chemical classes, it is critical that isolation of pesticide residues in acceptable recovery range while minimizing co extractives and matrix effects.

In the literature, there are previously published methods for determination of pesticide residues in tea. These methods usually include solid phase extraction (6-8) and dispersive solid phase extraction (QuEChERS) (9, 10). In time, the QuEChERS methods has been most widely used method for determination of pesticide residues in food samples. Furthermore, this method has become a standard test method of AOAC 2007.01. Despite the fact that this method has been developed in the determination of pesticide residues in fruits and vegetables, with slight modifications it can be used for other food matrices. The method includes extraction of pesticide with acetonitrile, and the raw extract is cleaned up with dispersive solid phase extraction (SPE) by mixing with magnesium sulfate and primary secondary amine (PSA) to remove water and undesired co-extractives. PSA is the most commonly used sorbents in QuEChERS methods and its main function is to remove co-extracted constituents such as fatty acids, sugars, and ionic lipids. Another sorbent option is known as C18. The C18 has a nonpolar nature which is useful in removing fat and wax content of the matrix. Although PSA and C18 are widely used as dispersive solid phase extraction sorbents, some novel sorbents have been used as alternatives to cope with complex matrixes. Li et al (2013), developed a novel magnetic SPE method based on magnetic cobalt ferrite-filled carbon nanotubes to determine organochlorine pesticides in tea and honey samples (1). Liu et al (2014), have used graphene with PSA and graphitized carbon black as dispersive solid phase extraction sorbent for the clean-up of tea samples (11). Hou et al (2013), have developed a modified QuEChERS method using multi-walled carbon nanotubes as a dispersive solid phase extraction sorbent for the analysis of 78 pesticides in tea (12). Rejczak and Tuzimski (2017) have used zirconium(IV) oxide (ZrO₂)-based sorbents and PSA as dispersive solid phase extraction clean up material for determination of pesticide in milk (13). Li et al. (2013) have used PPVP, PSA and GCB as clean-up sorbents to remove co-eluting matrix components for the determination of 16 pesticide residues in tea (14). Sun et al. (2022) used a combined sorbent package consisting of MWNTs-OH and PSA for the extraction and purification of 57 pesticides to remove the interferences of pigment in *Lonicerae japonicae* flower buds and improve the quantitative accuracy in pesticide residues analysis (15). Zhao and Shi used non-porous boron nitride nanorods (p-BNNRs) as clean-up sorbents to eliminate matrix interference in QuEChERS analysis

method for the detection of five neonicotinoid pesticide residues in goji berries (16).

Polyamide is well suited for the separation of natural substances with phenolic and polyphenolic groups. Because of its swelling properties, polyamide has a higher adsorption capacities than most sorbents currently on the market. This swelling property makes it suited for preparative chromatography as well as for the analysis of biological material (separation of undesirable accompanying compounds). Polyamide is commonly used as an adsorbent for the isolation and identification of natural substances with phenolic and polyphenolic functional groups, e.g. anthocyanins, anthoxanthines, anthraquinone derivatives, and flavones.

Diaion (synthetic adsorbent resin) is a macroporous styrenic polymeric bead type resin designed for adsorption/desorption process scale applications. Its matrix provides an aromatic non-polar surface with excellent selectivity for hydrophobic areas of molecules, including biomolecules like antibiotics via low-energy van der Waals interactions. It is remarkable for its wide pore polymeric structure which provides excellent broad spectrum adsorption characteristics.

Polyvinylpolypyrrolidone (PVPP) is a resinous polymer that acts similarly to proteinaceous fining agents. It is particularly useful in the selective removal of flavans and mono- and dimeric phenolics. As such, PVPP has particular value in diminishing undesirable bitter taste. For this reason, it is usually added relatively early in maturation. It is also efficient in preventing oxidative browning and removing its brown by-products from white wines. It functions well at cool temperatures and precipitates spontaneously. Meng et al. (2021), used a d-SPE purification method for the determination of 134 pesticide in tea using a multi-functional filter which consisted of two layers, an upper layer of porous PVPP to absorb polyphenols and a lower layer containing a mixture of PSA, GCB and anhydrous magnesium sulfate, to remove substances such as pigments (17). Guo et al. (2018), develop a method for determination of 20 pesticide residues from polyphenol-rich agricultural samples (tea, apple, broccoli, and shallot) by using PVPP to precipitate polyphenols. They used clean-up combination of PVPP (150 mg), PSA (50 mg) and GCB (10 mg) in the clean-up step to remove co-extracts (18). XAD adsorbents are very porous spherical polymers based on highly crosslinked, macro-reticular polystyrene, aliphatic, or phenol-formaldehyde condensate polymers. Amberlite XAD-7 is a non-ionic aliphatic acrylic polymer, which derives its adsorptive properties from its macro-reticular structure (containing both a continuous polymer phase and a continuous pore phase), high surface area, and the aliphatic nature of its surface. It is characterized as a hydrophobic adsorbent having a somewhat more hydrophilic structure comparing to

XAD-4. Its macro-reticular structure also gives it excellent physical and thermal stability and it is also stable at all pH range in an aqueous solution. Due to its aliphatic nature amberlite XAD-7 can adsorb non-polar compounds from aqueous systems and can also adsorb polar compounds from non-polar solvents (19,20).

In this study, it was aimed to modify the QuEChERS method by using polymeric adsorbents as a clean-up agent in pesticide analysis in tea. The adsorbents used in this study were used for the first time in the QuEChERS method as a clean up agent in pesticide analysis in tea. In addition, these adsorbents were tested for the first time for the analysis of a high number of pesticides (216) in the analysis of pesticides in tea samples. In this study, we compared four polymeric resins as clean-up sorbents for the determination of 216 pesticide residues in tea by high performance liquid chromatography triple quadrupole mass spectrometry. We used Diaion, Polyamide, PPVP, and XAD 7 as clean-up sorbents instead of PSA. Since tea includes a high amount of phenolic compounds which can cause interference in determination of pesticide residue, these polymeric resins may more effectively remove co-extracts from tea sample. In addition, to evaluate the effectiveness of adsorbents, recovery studies were carried out using these adsorbents and GC-MS analysis was carried out to evaluate the ability of these adsorbents to remove co-extracts.

2. EXPERIMENTAL SECTION

2.1. Chemicals

Acetonitrile, magnesium sulfate, sodium acetate, Dianon, PPVP, XAD7 and Polyamide were used (Sigma Aldrich, and Dr. Erhenstorfer, Germany). Pesticide standards used in this study were given in Table 2. Individual standard solutions 1000 mg/L were prepared in acetonitrile and further dilutions were made with acetonitrile. Black tea samples were purchased from a local market and were checked for existence of pesticides.

2.2. Extraction and Clean-up

The extraction was carried out according to BS EN 15662 "Foods of plant origin". Multimethod was used for the determination of pesticide residues using GC- and LC-based analysis followed by acetonitrile extraction/partitioning and clean-up by dispersive SPE called "Modular QuEChERS-method". A 2 g tea sample was weighed into 50 mL polypropylene centrifuge tube and 10 mL deionized water was added. After mixing and allowed to soak for 10 mins, 10 mL of acetonitrile was added and shaken vigorously for 15 mins using a shaker. Buffer salt mixtures (4 g of anhydrous magnesium sulfate, 1 g of sodium chloride, 1 g of trisodium citrate

dihydrate, and 0.5 g of disodium hydrogen citrate sesquihydrate) was added and immediately shaken vigorously for 1 min by hand and centrifuged for 5 min at 4000 rpm. After centrifugation, 6 mL of the supernatant was taken into a 15-mL polypropylene tube, 450 mg sorbent and 900 mg magnesium sulfate were added and agitated for 1 minute.

In the clean-up step four polymeric resins namely, Dianon, Polyamide, PPVP and XAD-7 were used. PSA was used for comparison with the standard method. To avoid possible deviation which may come from the extraction process, spiking of standard pesticide solution to the samples were made after the extraction step and just before the clean-up process. After spiking of pesticide standard solutions, Dianon, Polyamide, PPVP, XAD-7 and PSA were added with magnesium sulfate as clean up reagent as described BS EN 15662 method. For each resin, two different concentrations and 6 replicates were performed. After centrifuging at 4000 rpm for 5 mins 1 mL supernatant were taken for LC-MS/MS analysis (API 4000 Q-TRAP).

2.3. LC-MS/MS analysis

For the liquid chromatographic analysis Shimadzu HPLC (UFLC LC-20AD) system was used. The chromatographic separation was achieved with inertsil 100 mm x 2,1 mm column with 3 µm particle size. The mobile phase A contained methanol/water (2+8, v/v) with 5 mmol/L ammonium formate and mobile phase B contained methanol/water (9+1, v/v) with 5 mmol/L ammonium formate. The gradient program was given at Table 1. A 10 µL of the sample was injected at a flow rate of 0.3 mL at 40 °C.

Table 1: LC flow program.

Time	%B
0 min	0
11 min	100
23 min	100
25 min	0
36 min	0

Determination of pesticides was achieved by Applied bio-system triple quadrupole mass spectrometer was operated in multiple reactions monitoring (MRM). The mass spectrometer ion source parameters were: curtain gas, ion source gas, temperature, and ion spray voltage were set to 20 mL/min, 50 mL/min, 550 °C, and 5500 V, respectively. Pesticide and their transitions ions used for the quantification, collision energy (CE), and de-clustering voltage (DP) are listed in Table 2.

Table 2: LC-MS/MS parameters of the pesticides.

Pesticide	Polarity	Q1 mass	Q3 mass	DP (v)	CE (v)
2 4 D	ESI -	219.0	160.9	20	15
2.4.5-T	ESI -	253.0	195	40	10
Acephate	ESI +	184.1	124.9	10	25
Acetamiprid	ESI +	223.0	126	61	27
Aclonifen	ESI +	265.0	182.1	55	40
Alachlor	ESI +	270.1	238.1	30	15
Atrazine	ESI +	216.1	174.0	71	25
Azoxystrobin	ESI +	404.1	371.9	36	20
Benalaxyl	ESI +	326.2	148.2	26	25
Benfluralin	ESI +	336.0	57	30	10
Bentazone	ESI -	239.1	132	51	30
Bifenazate	ESI +	299.0	253	40	10
Bitertanol	ESI +	338.2	70	5	25
Boscalid	ESI +	343.0	307	71	25
Bromacil	ESI +	261.0	205	21	20
Bromophos Ethyl	ESI +	394.9	338.7	51	25
Bromoxynil	ESI -	273.9	79	46	35
Bromuconazole	ESI +	378.0	159	46	35
Bupirimate	ESI +	317.1	166.1	31	33
Buprofezin	ESI +	306.2	201.2	6	15
Butacarboxim Sulfoxide	ESI +	207.1	131.9	41	10
Cadusafos	ESI +	271.1	159	66	20
Carbaryl	ESI +	202.1	144.9	66	15
Carbendazim	ESI +	192.1	160	56	25
Carbofuran	ESI +	222.1	165.1	46	10
Carbosulfan	ESI +	381.2	118.1	36	25
Carboxin	ESI +	236.1	142.9	26	21
Chlorfenvinphos	ESI +	358.9	155	36	20
Chlorfluazuron	ESI +	539.9	158	70	25
Chloridazon	ESI +	222	92.2	91	35
Chloroxuron	ESI +	291.1	72	51	40
Chlorpropham	ESI +	214	172	25	10
Chlorpyrifos	ESI +	349.9	96.9	21	41
Chlorpyrifos-Methyl	ESI +	321.9	125.1	25	27
Chlorsulfuron	ESI +	358	141	50	25
Chlorthamid	ESI +	205.9	118.9	35	55
Cinidon-Ethyl	ESI +	411.1	348	40	30
Clofentezine	ESI +	303.1	102.1	55	45
Cyazofamid	ESI +	325	108	36	20
Cyclanilide	ESI -	272	159.9	55	30
Cycloate	ESI +	216.1	154.3	56	10
Cymoxanil	ESI +	199.1	128	61	10
Cyproconazole	ESI +	292.1	70.2	15	35
Cyprodinil	ESI +	226.1	76.9	81	65
Deltamethrin	ESI +	522.9	280.7	16	25
Demeton S Methyl	ESI +	248	89.1	6	17
Demeton S Methyl Sulfoxide	ESI +	247	169	10	15
Desmedipham	ESI +	318.1	182.2	31	20
Di-Allate	ESI +	270	86.1	41	23
Diazinon	ESI +	305.1	169.1	20	30
Dichlofluanid	ESI +	350	223.9	20	40
Dichlorprop-P	ESI -	233.0	161	20	15
Dichlorvos	ESI +	220.9	127.1	71	27
Difenoconazole	ESI +	406.1	250.9	41	35
Dimethenamide	ESI +	276.1	244.1	11	20
Dimethoate	ESI +	230	125	31	10
Dimethomorph	ESI +	388.1	301.1	45	30

Pesticide	Polarity	Q1 mass	Q3 mass	DP (v)	CE (v)
Dimoxytrobin	ESI +	327	116	30	10
Diniconazole	ESI +	326	70	55	45
Dinobutan	ESI +	327	215	45	10
Dinoterb	ESI -	239.1	176	30	50
Diphenylamine	ESI +	170.1	93.1	66	35
Disulfoton	ESI +	275	89.2	10	10
Disulfoton Sulfone	ESI +	307	153	50	10
Disulfoton Sulfoxide	ESI +	291	213	30	10
Ditalimfos	ESI +	300	130	35	10
Dithianion	ESI +	296	264	50	25
Diuron	ESI +	233	72	65	30
Epoxiconazole	ESI +	330.1	121	36	25
Eptc	ESI +	190.1	128.1	46	15
Esfenvalerat	ESI +	437.1	125	25	50
Ethiofencarb	ESI +	226.1	107.2	41	20
Ethion	ESI +	385	199.1	15	20
Ethirimol	ESI +	210.2	98.1	86	35
Ethofumesate	ESI +	304.1	121.1	35	25
Ethoprophos	ESI +	243	131	20	30
Ethoxyquin	ESI +	218.2	160.2	66	45
Etozole	ESI +	360.2	141	65	40
Etrimfos	ESI +	293.1	125	25	35
Famoxodane	ESI +	392.2	238	16	25
Fenamidone	ESI +	312.1	92.2	40	35
Fenamiphos	ESI +	304.1	217.1	40	30
Fenarimol	ESI +	331	81	45	45
Fenazaquin	ESI +	307.2	161.2	51	30
Fenbuconazole	ESI +	337.1	125.1	41	40
Fenhexamid	ESI +	302.1	97.2	90	35
Fenitrothion	ESI +	278.1	125	41	30
Fenoxaprop-Ethyl	ESI +	362.1	288.1	45	23
Fenoxycarb	ESI +	302.1	88	66	30
Fenpropatrin	ESI +	350.2	125.1	41	20
Fenpropimorph	ESI +	304.3	147.1	45	40
Fenthion	ESI +	279.1	169.1	20	25
Fenvalerate	ESI +	437.1	125	35	55
Flazasulfuron	ESI +	408.1	182.1	40	25
Fluazifop-P-Butyl	ESI +	384.1	282.1	50	27
Fludioxinil	ESI -	247	125.9	56	40
Flufenacet	ESI +	364.1	194.2	10	17
Flufenoxuron	ESI +	489	158.1	85	30
Fluopicolide	ESI +	383	109	35	10
Flurochloridone	ESI +	312	291.9	60	30
Flurtamone	ESI +	334.1	247.1	50	30
Flusilazole	ESI +	316.1	247.1	36	25
Flutolanil	ESI +	324.1	262.1	86	25
Foramsulfuron	ESI +	453.1	182.2	50	25
Fosthiasate	ESI +	284	104.1	61	27
Furathiocarb	ESI +	383.2	195	50	23
Heptenophos	ESI +	251	127	35	20
Hexaconazole	ESI +	314.1	70.1	35	40
Hexythiazox	ESI +	353.1	227.9	65	20
Imazalil	ESI +	297	158.9	25	30
Imazamox	ESI +	306	246	30	10
Indoxacarb	ESI +	528.1	203	75	50
Iprodione	ESI -	328	141.1	5	10
Iprovalicarb	ESI +	321.2	119	46	23
Isoproturon	ESI +	207.1	165.2	46	20
imazaquin	ESI +	312.1	199.1	45	35

Pesticide	Polarity	Q1 mass	Q3 mass	DP (v)	CE (v)
Imidachloprid	ESI +	256.1	175	45	25
İoxynil	ESI -	369.8	126.8	45	35
İsoxaben	ESI +	333	150	40	30
Lambda Cyhalothrin	ESI +	467.1	225	16	23
Malathion	ESI +	331	99	17	30
Mcpa	ESI -	199	140.8	45	20
Mecarbam	ESI +	330	227	25	15
Mecoprop-P	ESI -	213	140.7	50	15
Mepanipyrim	ESI +	224.1	77	41	10
Mesosulfuron Methyl	ESI +	504.1	182.1	60	33
Metalaxyl-M	ESI +	280.1	220	45	19
Metazachlor	ESI +	278.1	210.1	5	15
Methacrifos	ESI +	241	209.1	31	15
Methamidophos	ESI +	142	124.9	25	20
Metolachlor	ESI +	284	252	25	30
Metosulam	ESI +	418	175.1	26	25
Metribuzin	ESI +	215.1	187.2	61	25
Mevinphos	ESI +	225	193.1	30	10
Molinate	ESI +	188.1	83.2	20	25
Monocroptos	ESI +	224.1	127	46	21
Monolinuron	ESI +	215.1	125.9	51	25
Monuron	ESI +	199.1	72	51	29
Myclobutanil	ESI +	289.1	70.1	35	30
Nuarimol	ESI +	315	81.1	40	40
Omethoate	ESI +	214.1	109	46	35
Oxadiazyl	ESI +	341	223	25	10
Oxadiazon	ESI +	362.1	220	40	30
Oxadixyl	ESI +	279.1	219.2	45	25
Oxamyl	ESI +	237.1	90	20	15
Oxasulfuron	ESI +	407.1	150.1	55	25
Oxycarboxin	ESI +	268	175.1	35	20
Oxyflourfen	ESI +	379	316	20	25
Penconazole	ESI +	284.1	158.9	41	40
Pendimethalin	ESI +	282.1	212.2	5	15
Permethrin	ESI +	408.1	153.1	30	25
Pethoxamid	ESI +	296	250	15	10
Phenmedipham	ESI +	301.1	136.1	56	25
Phenthoate	ESI +	321	163.1	36	17
Phorate	ESI +	278.1	74.9	5	23
Phosalon	ESI +	367.9	182	50	20
Phosmet	ESI +	317.9	160.1	30	20
Phosphamidon	ESI +	300	127.1	35	25
Picloram	ESI -	240.9	196.9	66	15
Picolinafen	ESI +	377.1	145	56	70
Primicarb	ESI +	239.1	72.1	15	30
Primiphos-Methyl	ESI +	306.1	164.1	25	30
Prochloraz	ESI +	376	308	15	15
Profenofos	ESI +	372.9	302.9	55	25
Prometyrn	ESI +	242.1	158.1	30	30
Propamocarb Hydrochloride	ESI +	189.2	102	51	10
Propanil	ESI +	218	162	56	10
Propargite	ESI +	368.1	175.1	5	20
Propham	ESI +	180.1	138.1	31	10
Propiconazole	ESI +	342.1	69.1	45	33
Propyzamide	ESI +	256	173.1	35	30
Prothiophos	ESI +	344.9	240.9	40	27
Pymetrozine	ESI +	218.1	105	76	10
Pyraclostrobin-	ESI +	388.1	194	5	20
Pyrazophos	ESI +	374.1	222.1	60	30

Pesticide	Polarity	Q1 mass	Q3 mass	DP (v)	CE (v)
Pyridaben	ESI +	365.1	309.1	26	20
Pyridaphention	ESI +	341	189	45	30
Pyridate	ESI +	379.1	207.1	5	20
Pyrimethanil	ESI +	200.1	106.9	50	30
Pyriproxyfen	ESI +	322.1	96.2	15	20
Quinalphos	ESI +	299	163	20	30
Quinoxifen	ESI +	307.9	162	20	60
Quizalofop Ethyl	ESI +	373.1	298.9	70	25
Resmethrin	ESI +	356.2	171.2	20	20
Rimsulfuron	ESI +	432.1	182	46	30
Simazine	ESI +	202.1	132.2	66	10
Spiroxamine	ESI +	298.3	144.2	40	30
Sulfosulfuron	ESI +	471.1	261	10	25
Tauflualinate	ESI +	520.1	208.1	30	23
Tebuconazole	ESI +	308.1	70	20	40
Tepp	ESI +	291.1	179	45	25
Terbufos	ESI +	289	57.1	30	35
Terbumeton	ESI +	226.1	170.2	25	25
Terbuthylazine	ESI +	230.1	174.1	40	20
Terbutryn	ESI +	242.1	186.1	20	25
Tetrachlorvinphos	ESI +	366.9	127.1	46	21
Thiacloprid	ESI +	253	126	81	30
Thiamethoxam	ESI +	292	211	50	15
Thiamethoxam	ESI +	292	211	40	25
Thifensulfuron Methyl	ESI +	388	167	35	20
Thiodicarb	ESI +	355	88	26	20
Thiophanate Methyl	ESI +	343	151	26	25
Tolclophos-Methyl	ESI +	301	175	46	35
Tolyfluanid	ESI +	364	237.9	6	20
Triadimefon	ESI +	294	197.2	36	20
Triadimenol	ESI +	296.1	70.1	10	20
Tri-Allate	ESI +	304	142.9	40	35
Triasulfuron	ESI +	402.1	167.1	46	25
Triazophos	ESI +	314	119.1	36	50
Tribenuron Methyl	ESI +	396.1	155	50	20
Trichlorfon	ESI +	274	108.9	10	30
Tridemorph	ESI +	298.3	116.1	55	30
Trifloxystrobin	ESI +	409.1	186.1	10	25
Triflumizole	ESI +	346	278	10	15
Triticonazole	ESI +	318.1	70.2	35	35
Zoxamide	ESI +	336	159	40	15

2.4. Recovery

To evaluate the effectiveness of the sorbent, pesticide standard solutions tea samples were spiked at two different concentration levels, viz. 10 and 100 µg/kg and analyzed with the method which was described in sample preparation above. Standard solutions were added just before the clean-up step to eliminate possible deviation coming from extraction step. Four different sorbents, namely Dianon, Polyamide, PPVP, and XAD, were used as clean-up sorbents and PSA was used as the control group. Pesticide standard solutions were added to the samples at 10 and 100 µg/kg levels. After analyzing samples with LC-MS/MS, recovery% values were calculated according to Equation 1.

$$Recovery(\%) = \left(\frac{C_1}{C_2} \right) \times 100 \quad (\text{Eq. 1})$$

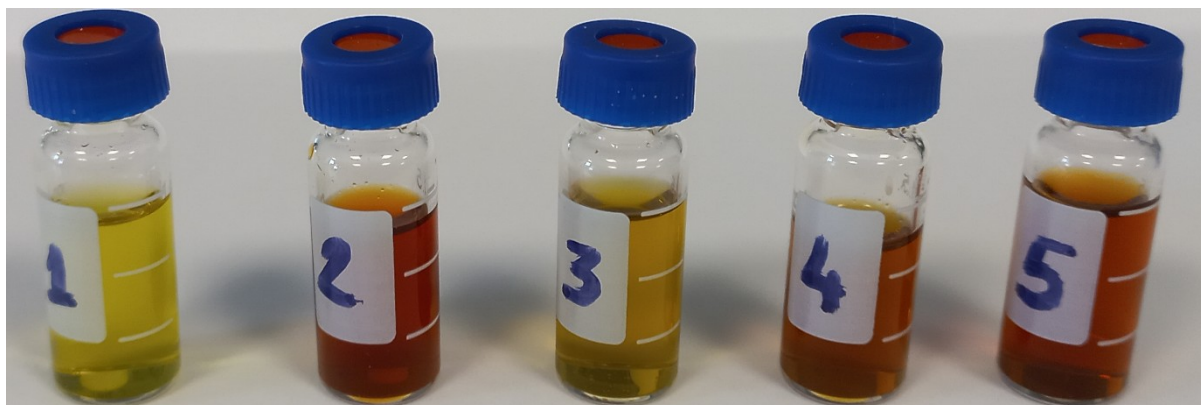
2.5. Matrix Effect

In order to see the effectiveness of these 4 different adsorbents in eliminating the co-extracts, the blank tea extracts, which were clean-up with these adsorbents, were analyzed by GC-MS. GC-MS analyses were carried out in total ion mode to see the composition of co-extracts. GC/MS analyses were carried out using a capillary HP-50 column (50% phenyl-methyl polysiloxane, with 30 m length, 0.25 ID and 0.25 µm film thickness). Oven program of gas chromatography are given in Table 3.

Table 3: Gas Chromatography Oven Program.

Initial Temp.(°C)	Rate (°C/Min)	Last Temp.(°C)	Hold (min)
50	-	50	4
50	5	260	4

3. RESULTS AND DISCUSSION

**Figure 1:** Appearance of the extracts after clean-up 1: PSA, 2: Diaion, 3: Polyamide, 4: PPVP, 5: XAD 7.

After clean-up process, samples were analyzed with LC-MS/MS. In the spiking solution, 216 pesticides were included. After clean up process appearance of the tea extracts were shown in Figure 1. It was observed that both PSA and polyamide could better in removing the color of the tea extract than the rest of the sorbents. For the determination of these 216 pesticides matrix, matched calibrations were used.

Matrix matched calibrations were prepared for each resin with using the same resin. Recovery studies were performed with each resin in six replicates at 10 and 100 µg/kg. The recovery values for each pesticide were given in Table 4. Also, the recovery ratios for each resins were summarized in Table 5 and Figure 2. For both concentration levels, similar recovery results were obtained.

Table 4: Recovery ratios for each resins.

Recovery%	PSA	Diaion	Polyamide	PPVP	XAD
<60	41	12	23	17	22
60 - 80	9	9	9	4	4
80 - 120	135	130	84	86	99
120 - 140	11	27	77	62	56
>140	20	38	23	47	35
Total	216	216	216	216	216

According to the recovery results, it was observed that the PSA was the best with 135 pesticides in the generally accepted range of 80-120%. After PSA, Diaion was determined as the second with 130 pesticides in the range of 80-120%. Polyamide and PPVP were at the bottom with 84 and 86 pesticides, respectively, in the range of 80 - 120%, while XAD differentiated with 99 pesticides both from PSA and Diaion, and from Polyamide and PPVP. On the other hand, if we select the acceptable limit as 60-140%, polyamide was determined as the resin that gave the best results with 170 pesticides. While Diaion was the second resin with 166 pesticides, XAD, PSA and PPVP were determined as the third, fourth and fifth resins with very close values 159, 155 and 152 pesticides, respectively. It is noteworthy that PSA is determined as the third resin when the acceptable

range is referred to as 60-140%. Another remarkable point is that 41 pesticides give a recovery value of less than 60% when PSA was used as clean-up resin. These results are compatible with previously published reports indicative of recoveries of some pesticides were adversely affected by PSA (21). Especially pesticides those containing the P=O group tend to be adsorbed to PSA. On the other hand, 12 pesticides gave a recovery value of less than 60% when Diaion was used as clean-up resin. Although polymeric adsorbents are widely used in the purification of bioactive compounds from tea, they have not been used as a stand-alone cleaning agent in pesticide analysis before. However, some studies have been conducted in which PVPP is used as a clean-up agent in combination with different adsorbents. Jiao and et al. (2016) have developed a

method for the determination of eight pesticide residues with LC-MS/MS, combining a QuEChERS method using PVPP and GCB clean-up with a dilution factor of 400 method in order to diminish the complex and varied matrix interference due to co-extracted from tea. They found average recoveries of eight neonicotinoid insecticides ranged from 66.3 to 108.0% (22). Cao et al. (2015) have developed a method based on matrix solid phase dispersion for the determination and the quantification of 16 pesticides in various tea samples by using PVPP (750 mg), PSA (1 g) and GCB (50 mg) as clean-up sorbent. The recoveries of this method at three spiked concentration levels ranged from 87.7 to 99.6% (14). Hou et al. (2022) developed a method to scan for 134 pesticide residues in tea was developed that employs a novel Multi-Functional Filter (MFF) contained a mixture of 50 mg of PSA, 10 mg of GCB, 150 mg of porous PVPP, and 150 mg of anhydrous MgSO₄. They calculated recoveries at two spiked levels (50, 100 µg/kg) ranged between 66.83–118.33%. They reported that purification through the multi-function filter (MFF-3-Layered) reduced the matrix effect more than purification via the modified QuEChERS method (17). Although polymeric

adsorbents were used in combination with other adsorbents in these studies, similar results were obtained in our study when they were used alone.

In order to evaluate the clean up efficiency of the adsorbent, gas chromatography mass spectrometry analyses were carried out. Blank tea extracts were analyzed with GC-MS after clean up with these adsorbents. Total ion chromatograms of each extracts were taken to evaluate removal efficiency of co-extracts. Chromatograms were given in Figure 3. As a result of GC MS analysis, it was observed that PSA gave the chromatogram with the least amount of co-extracts. On the other hand, it was observed that PSA was the worst adsorbent in removing caffeine, which is one of the main bioactive compound in tea. XAD-7 and polyamide were found to be the best adsorbents in removing caffeine. PSA was, as expected, very effective in removing the fatty acids. While no fatty acids were found in the extracts cleaned with PSA, fatty acids were detected in the extracts cleaned with other adsorbents. PPVP was found to be insufficient in removing both caffeine and fatty acids.

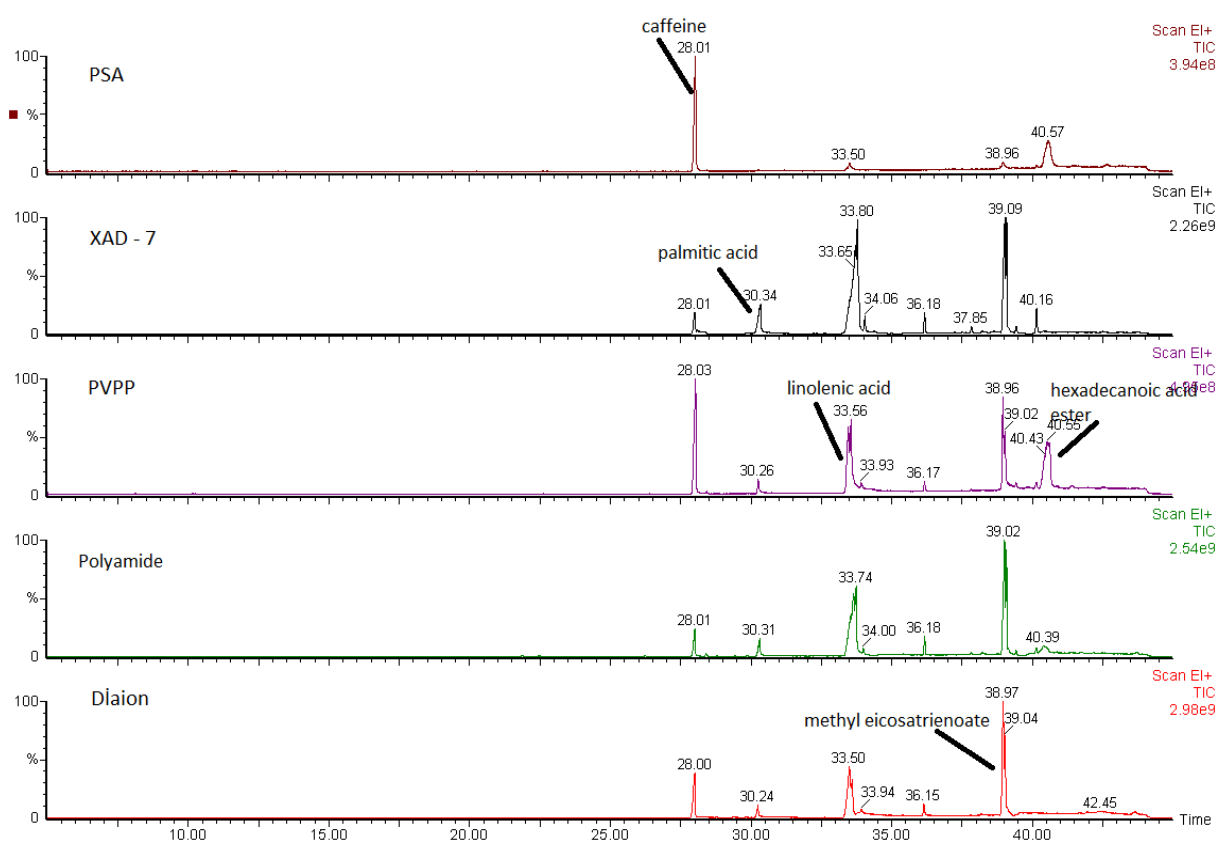


Figure 2: GC-MS chromatogram of tea extracts after clean up.

Table 5: Recovery values of the pesticides.

Pesticide	Recovery %				
	Dianon	PPVP	PSA	PA	XAD
2,4-D	<0.01	289	40.85	308	<0.01
2,4,5-T	117	68	<0.01	64	105

Pesticide	Recovery %				
	Dianon	PPVP	PSA	PA	XAD
Acephate	204.5	114.5	76.5	102	103.5
Acetamiprid	62	157.5	367.5	114	129.5
Aclonifen	95.5	186.5	<0.01	128	40.95
Alachlor	110.5	125.5	100	119.5	124.5
Atrazine	112.5	107.5	99.5	103.5	124
Azoxystrobin	319.5	171	391	415	426.5
Benalaxyl	107.5	117.5	97	128	117
Benfluralin	510	458	<0.01	<0.01	<0.01
Bentazon	113.5	54.5	83.5	100.5	108.5
Bifenazate	130.5	132.5	113	70	114.5
Bitertanol	98	106	92.5	132	115
Boscalid	93.5	134	96	117.5	139.5
Bromacil Pztf	94	119	122.5	98	78
Bromophos Ethyl	151.5	100	90	123.5	116
Bromoxynil	99.5	48.05	40.55	90	106.5
Bromuconazole	43.85	107.5	105	<0.01	111
Bupirimate	103.5	133	100.5	128.5	113
Buprofezin	89	112	92.5	112.5	115.5
Butacarboxim Sulfoxide	112.5	129	90.5	116.5	129.5
Cadusafos	119	125.5	101	138.5	146.5
Carbaryl	130	102.5	117	117.5	110
Carbendazim	131	118	208.5	186.5	89
Carbofuran	112	129	116	123	130.5
Carbosulfan	<0.01	105	101.5	88.5	187
Carboxin	101	110.5	99	113.5	109.5
Chlorfenvinphos	99.5	120.5	108	121.5	116
Chlorfluazuron	54.5	129	101	117.5	102
Chloridazon	89.5	91	71	185.5	140
Chloroxuron	106	119.5	102	120.5	104
Chlorpropham	126	139.5	131	<0.01	156
Chlorpyrifos	103	123.5	<0.01	145	119.5
Chlorpyrifos-Methyl	123	123	116	137.5	130
Chlorsulfuron	119	<0.01	22.3	126	123.5
Chlorthamid	286.5	<0.01	70.5	41.8	122.5
Cinidon-Ethyl	110.5	114	103	115.5	124.5
Clofentezine	48.25	128	89.5	117	112.5
Cyazofamid	127.5	130	108	120	127.5
Cyclanilide	113.5	42.9	19.75	63.5	95.5
Cycloate	100.5	119	102.5	127	130.5
Cymoxanil	119.5	66.5	108.5	138.5	84.5
Cyproconazole	128	114	111	108.5	141
Cyprodinil	90	117	99.5	142.5	127.5
Deltamethrin	75.5	90.5	110	137.5	123.5
Demeton S Methyl	228.5	1725	<0.01	148	237
Demeton S Methyl Sulfoxide	105	<0.01	<0.01	140	153.5
Desmedipham	106.5	110.5	106.5	113.5	110
Di-Allate	100	112.5	103	124	107.5
Diazinon	106.5	123.5	102	125	115
Dichlofluanid	404.5	405.5	128	<0.01	415
Dichlorprop-P	115	85.5	10.75	86	94.5
Dichlorvos	203.5	161	<0.01	75.5	207
Difenoconazole	94	115	92	124	118.5
Dimethenamide	113.5	116	100	115.5	116.5
Dimethoate	65.5	132	96	113.5	58
Dimethomorph	112	120.5	102	116.5	110
Dimoxytrobin	277	350	415	160	302.5
Diniconazole	105.5	102.5	89	119.5	114
Dinobutan	433	500	<0.01	<0.01	<0.01

Pesticide	Recovery %				
	Dianon	PPVP	PSA	PA	XAD
Dinoterb	106	97.5	75	112.5	107
Diphenylamine	106	113.5	127	122.5	113.5
Disulfoton	465.5	494.5	<0.01	<0.01	431.5
Disulfoton Sulfone	150.5	158.5	115.5	129.5	144.5
Disulfoton Sulfoxide	<0.01	<0.01	<0.01	153.5	<0.01
Ditalimfos	111.5	127	93.5	122.5	122.5
Dithianion	95.5	1155	104	72	35.35
Diuron	113	115	107	103.5	113
Epoxiconazole	181	190	124.5	<0.01	193
Eptc	110.5	121.5	152.5	139	115.5
Esfenvalerat	137	170.5	<0.01	104	105.5
Ethiofencarb	126.5	120.5	102	119.5	123.5
Ethion	<0.01	<0.01	300.5	<0.01	61
Ethirimol	91.5	131	106	112.5	136.5
Ethofumesate	137.5	144	<0.01	117.5	152.5
Ethoprophos	166.5	720	94	91	<0.01
Ethoxyquin	100.5	114	97.5	110.5	100
Etoxzole	87.5	130.5	93	126.5	116
Etrimfos	108	146.5	105.5	126.5	129.5
Famoxodane	138	178	474.5	325	389.5
Fenamidone	111.5	127	101.5	116.5	121
Fenamiphos	118	114.5	101.5	119.5	117.5
Fenarimol	113.5	107	116	104	116
Fenazaquin	315	321.5	<0.01	<0.01	446
Fenbuconazole	104	129.5	106.5	118.5	121
Fenhexamid	119.5	111.5	94.5	115.5	128.5
Fenitrothion	226	319	100	<0.01	435
Fenoxaprop-Ethyl	98	117.5	99	119	118
Fenoxycarb	115.5	135.5	109.5	122.5	149.5
Fenpropatrin	109.5	145	112.5	127	131.5
Fenpropimorph	110	119	99	115.5	113
Fenthion	111	181	<0.01	133	<0.01
Fenvalerate	137	170.5	145.5	104	105.5
Flazasulfuron	119.5	103.5	37.5	106	109
Fluazifop-P-Butyl	122.5	118.5	97.5	123	117.5
Fludioxinil	118	111.5	107	110.5	108.5
Flufenacet	113	123	103.5	122	128.5
Flufenoxuron	112.5	129	104	120	105.5
Fluopicolide	116	121	112	119	118
Flurochloridone	117.5	113.5	114.5	128.5	120
Flurtamone	389.5	<0.01	349	<0.01	89.5
Flusilazole	113.5	113	103.5	120.5	119.5
Flutolanil	119.5	111	108	118.5	127.5
Foramsulfuron	144.5	94	<0.01	<0.01	57.5
Fosthiasate	114.5	127	111.5	110	112
Furathiocarb	101.5	118.5	98	126	116
Heptenophos	116	185.5	158.5	96.5	133.5
Hexaconazole	116.5	103.5	105.5	108.5	122.5
Hexythiazox	74	131	95.5	126	113.5
Imazalil	106	103.5	80.5	140	117
Imazamox	<0.01	98	2.79	61	4.74
Indoxacarb	117	103.5	109.5	154.5	180
Iprodione	134.5	233	102	113.5	74
Iprovalicarb	117.5	123.5	100.5	117.5	115.5
Isoproturon	113.5	113.5	109.5	116	127.5
İmazaquin	296	<0.01	123	<0.01	965
İmidachloprid	133.5	115	96	126.5	79.5
İoxynil	109	36.45	53	78.5	110

Pesticide	Recovery %				
	Dianon	PPVP	PSA	PA	XAD
Isoxaben	111	130.5	102.5	113	103
Lambda Cyhalothrin	89	111.5	121.5	126	159.5
Malathion	162.5	144	100.5	<0.01	121.5
Mcpa	120.5	74.5	9.45	76	90.5
Mecarbam	119.5	123	100	124	127
Mecoprop-P	110	102	9.35	91	95
Mepanipyrim	118	128	92.5	111	105
Mesosulfuron Methyl	141.5	126	71	133.5	80.5
Metalaxyl-M	114.5	123.5	109	122.5	114.5
Metazachlor	112.5	116.5	105.5	115	124
Methacrifos	148.5	173	164	137	166
Methamidophos	158.5	221	78.5	176.5	107.5
Metolachlor	<0.01	<0.01	41.75	245	<0.01
Metosulam	106	126	36.5	128	117.5
Metribuzin	70	177.5	109	75.5	101.5
Mevinphos	91.5	63.5	645	116.5	<0.01
Molinate	97.5	121.5	101.5	120.5	117.5
Monocroptos	125	123.5	102.5	119	118
Monolinuron	106.5	125	115.5	119.5	115.5
Monuron	110	107.5	107.5	126	120.5
Myclobutanil	472	468	114	1445	122.5
Nuarimol	79.5	103	104	119.5	115.5
Omethoate	107.5	155.5	84	120.5	97.5
Oxadiazyl	239	163.5	141.5	197	99
Oxadiazon	96.5	107.5	103.5	129.5	124.5
Oxadixyl	119	108.5	106.5	128.5	112.5
Oxamyl	92	117.5	125	107	108.5
Oxasulfuron	114.5	109	54.5	117.5	103
Oxycarboxin	135.5	84.5	101	131	147.5
Oxyflourfen	99	<0.01	116.5	525	164.5
Penconazole	104	126.5	113	123.5	116
Pendimethalin	87	115	0.04105	112	0.112
Permethrin	82	106	42.35	142.5	0.635
Pethoxamid	31.7	400	163	<0.01	27.6
Phenmedipham	104.5	110.5	105.5	116	110.5
Phenthoate	159	117.5	113	144	125
Phorate	104	127	98	122.5	117
Phosalon	116	116	115.5	113.5	130.5
Phosmet	106.5	116	99.5	128	115.5
Phosphamidon	95.5	117.5	105.5	132	58
Picloram	145.5	153	82.5	165	132
Picolinafen	99	117	104	123	114.5
Primicarb	109	125	102	124.5	128.5
Primiphos-Methyl	99.5	131.5	99	123.5	120
Prochloraz	107.5	116.5	94.5	122.5	108.5
Profenofos	83	126.5	101.5	116	137
Prometyrn	109	125.5	98	125	117
Propamocarb Hydrochloride	113	124.5	63	138	99.5
Propanil	88.5	145.5	92	113.5	124.5
Propargite	103	127	<0.01	114.5	124.5
Propham	118	125	129	120	145.5
Propiconazole	112.5	109.5	102.5	102.5	133.5
Propyzamide	129	107.5	101.5	107	154
Prothiophos	455.5	570	<0.01	138.5	111
Pymetrozine	6.3	181.5	<0.01	7800	126
Pyraclostrobin-	198	183	145.5	133.5	224
Pyrazophos	107	113.5	105	129.5	130.5
Pyridaben	87	104.5	124.5	115.5	101.5

Pesticide	Recovery %				
	Diaion	PPVP	PSA	PA	XAD
Pyridaphention	107	120	113.5	115.5	119.5
Pyridate	81.5	96	57	116	97.5
Pyrimethanil	107.5	120.5	104	124	112.5
Pyriproxyfen	80	118.5	101.5	122	113.5
Quinalphos	103.5	121.5	104.5	129	110
Quinoxifen	64	107	113.5	145	<0.01
Quizalofop Ethyl	89.5	119.5	98	126.5	129.5
Resmethrin	84	98	74	90	98.5
Rimsulfuron	123	119	30.8	131.5	112.5
Simazine	440	321	359	427	360
Spiroxamine	109	98	92	115.5	114
Sulfosulfuron	385	<0.01	53.5	<0.01	417
Tauflualinate	75	117	<0.01	133	123
Tebuconazole	98.5	120.5	107.5	124.5	105.5
Tepp	355	<0.01	430	<0.01	625
Terbufos	108.5	131.5	100	139.5	130.5
Terbumeton	110.5	119.5	105	119	121
Terbuthylazine	113	129.5	101	134	112
Terbutryn	98	124.5	94	123.5	113
Tetrachlorvinphos	125	130	104.5	131	101
Thiacloprid	188	200	77.5	95	166
Thiamethoxam	<0.01	<0.01	<0.01	<0.01	131.5
Thifensulfuron Methyl	132.5	142	43.75	124	<0.01
Thiodicarb	128	129.5	111.5	110	128
Thiomethoxam	309	580	330	<0.01	477.5
Thiophanate Methyl	98.5	423.5	102.5	<0.01	133.5
Tolclophos-Methyl	129.5	119.5	120.5	137	<0.01
Tolyfluanid	122	135.5	105.5	135	123.5
Triadimefon	132	120.5	98.5	119	<0.01
Triadimenol	141.5	122.5	112	124	<0.01
Tri-Allate	78.5	153	106.5	98.5	138
Triasulfuron	119.5	130	58.5	125	124.5
Triazophos	282	261.5	<0.01	<0.01	320
Tribenuron Methyl	111	107	80	98.5	93
Trichlorfon	357.5	462	436.5	615	399.5
Tridemorph	117.5	109	99.5	119.5	115
Trifloxystrobin	114	119	96	119	109.5
Triflumizole	107	121	98.5	127	131.5
Triticonazole	133	111.5	106.5	119.5	128.5
Zoxamide	237	<0.01	333.5	<0.01	350

4. CONCLUSION

In this study, the suitability of 4 polymeric resins, namely; Diaion, Polyamide, PPVP and XAD 7 as a clean-up reagent for determination of pesticide residues in tea. In addition, a clean-up process was performed using PSA to compare with the standard method. In order to evaluate the effectiveness of the sorbents, recovery studies were carried out and compared with the recovery study carried out with PSA. According to the recovery results, it was observed that the PSA was the best with 135 pesticides in the generally accepted range of 80-120%. After PSA, Diaion was determined as the second with 130 pesticides in the range of 80-120%. On the other hand, when the acceptable limit was accepted as 60-140%, it was determined that the resin that gave the best results with 170 pesticides

was polyamide. Diaion was the second resin with 166 pesticides, while XAD, PSA and PPVP were determined as the third, fourth and fifth resins with very close values of 159, 155 and 152 pesticides, respectively. According to GC-MS total ion analysis of blank tea extracts cleaned with these adsorbents, it was observed that PSA gave the chromatogram with the least co- extract, while it was observed that PSA was the worst adsorbent in removing caffeine, one of the main bioactive compounds in tea. XAD-7 and polyamide were found to be the best adsorbents in removing caffeine. According to result of this study, it was evaluated that the use of polyamide together with PSA as a clean-up reagent for pesticide analysis in tea would be the most effective method for removing both fatty acids and bioactive components in tea.

5. CONFLICT OF INTEREST

Author have no conflict of interest.

6. REFERENCES

- Li X, Zhang Z, Li P, Zhang Q, Zhang W, Ding X. Determination for major chemical contaminants in tea (*Camellia sinensis*) matrices: A review. *Food Research International*. 2013 Oct;53(2):649-58. Available from: [<URL>](#).
- Rutkowska E, Łozowicka B, Kaczyński P. Modification of Multiresidue QuEChERS Protocol to Minimize Matrix Effect and Improve Recoveries for Determination of Pesticide Residues in Dried Herbs Followed by GC-MS/MS. *Food Anal Methods*. 2018 Mar;11(3):709-24. Available from: [<URL>](#).
- Zhang C, Suen CLC, Yang C, Quek SY. Antioxidant capacity and major polyphenol composition of teas as affected by geographical location, plantation elevation and leaf grade. *Food Chemistry*. 2018 Apr;244:109-19. Available from: [<URL>](#).
- Pang GF, Fan CL, Cao YZ, Yan F, Li Y, Kang J, et al. High Throughput Analytical Techniques for the Determination and Confirmation of Residues of 653 Multiclass Pesticides and Chemical Pollutants in Tea by GC/MS, GC/MS/MS, and LC/MS/MS: Collaborative Study, First Action 2014.09. *Journal of AOAC INTERNATIONAL*. 2015 Sep 1;98(5):1428-54. Available from: [<URL>](#).
- Guan Y, Tang H, Chen D, Xu T, Li L. Modified QuEChERS method for the analysis of 11 pesticide residues in tea by liquid chromatography-tandem mass spectrometry. *Anal Methods*. 2013;5(12):3056. Available from: [<URL>](#).
- Hayward DG, Wong JW, Park HY. Determinations for Pesticides on Black, Green, Oolong, and White Teas by Gas Chromatography Triple-Quadrupole Mass Spectrometry. *J Agric Food Chem*. 2015 Sep 23;63(37):8116-24. Available from: [<URL>](#).
- Hou X, Lei S, Guo L, Qiu S. Optimization of a multi-residue method for 101 pesticides in green tea leaves using gas chromatography-tandem mass spectrometry. *Revista Brasileira de Farmacognosia*. 2016 Jul;26(4):401-7. Available from: [<URL>](#).
- Zhao HX, Zhao SC, Deng LG, Mao JS, Guo CY, Yang GS, et al. Rapid Determination of Organonitrogen, Organophosphorus and Carbamate Pesticides in Tea by Ultrahigh-Performance Liquid Chromatography-Tandem Mass Spectrometry (UPLC-MS/MS). *Food Anal Methods*. 2013 Apr;6(2):497-505. Available from: [<URL>](#).
- Wu CC. Multiresidue method for the determination of pesticides in Oolong tea using QuEChERS by gas chromatography-triple quadrupole tandem mass spectrometry. *Food Chemistry*. 2017 Aug;229:580-7. Available from: [<URL>](#).
- Saito-Shida S, Nemoto S, Teshima R. Multiresidue determination of pesticides in tea by gas chromatography-tandem mass spectrometry. *Journal of Environmental Science and Health, Part B*. 2015 Nov 2;50(11):760-76. Available from: [<URL>](#).
- Liu X, Guan W, Hao X, Wu X, Ma Y, Pan C. Pesticide Multi-Residue Analysis in Tea Using d-SPE Sample Cleanup with Graphene Mixed with Primary Secondary Amine and Graphitized Carbon Black Prior to LC-MS/MS. *Chromatographia*. 2014 Jan;77(1-2):31-7. Available from: [<URL>](#).
- Hou X, Lei S, Qiu S, Guo L, Yi S, Liu W. A multi-residue method for the determination of pesticides in tea using multi-walled carbon nanotubes as a dispersive solid phase extraction adsorbent. *Food Chemistry*. 2014 Jun;153:121-9. Available from: [<URL>](#).
- Rejczak T, Tuzimski T. QuEChERS-based extraction with dispersive solid phase extraction clean-up using PSA and ZrO₂-based sorbents for determination of pesticides in bovine milk samples by HPLC-DAD. *Food Chemistry*. 2017 Feb;217:225-33. Available from: [<URL>](#).
- Cao Y, Tang H, Chen D, Li L. A novel method based on MSPD for simultaneous determination of 16 pesticide residues in tea by LC-MS/MS. *Journal of Chromatography B*. 2015 Aug;998-999:72-9. Available from: [<URL>](#).
- Sun X, Luo J, Lu Q, Li C, Zhao Z, An F, et al. Application of hydroxylated multi-walled carbon nanotubes as depigmentation agent in the determination of multiple pesticide residues in *Lonicerae japonicae* flower buds. *Microchemical Journal*. 2022 Jun;177:107280. Available from: [<URL>](#).
- Zhao WH, Shi YP. A porous boron nitride nanorods-based QuEChERS analysis method for detection of five neonicotinoid pesticide residues in goji berries. *Journal of Chromatography A*. 2022 May;1670:462968. Available from: [<URL>](#).
- Meng X, Song W, Xiao Y, Zheng P, Cui C, Gao W, et al. Rapid determination of 134 pesticides in tea through multi-functional filter cleanup followed by UPLC-QTOF-MS. *Food Chemistry*. 2022 Feb;370:130846. Available from: [<URL>](#).
- Guo J, Tong M, Tang J, Bian H, Wan X, He L, et al. Analysis of multiple pesticide residues in polyphenol-rich agricultural products by UPLC-MS/MS using a modified QuEChERS extraction and dilution method. *Food Chemistry*. 2019 Feb;274:452-9. Available from: [<URL>](#).
- Ahmad A, Siddique JA, Laskar MA, Kumar R, Mohd-Setapar SH, Khatoun A, et al. New generation Amberlite XAD resin for the removal of metal ions: A review. *Journal of Environmental Sciences*. 2015 May;31:104-23. Available from: [<URL>](#).
- Kyriakopoulos GG, Hourdakakis AA, Doulia DD. Adsorption of Pesticides on Resins. *Journal of Environmental Science and Health, Part B*. 2003 Mar;38(2):157-68. Available from: [<URL>](#).
- Rajski Ł, Lozano A, Belmonte-Valles N, Uclés A, Uclés S, Mezcuá M, et al. Comparison of three multiresidue methods to analyse pesticides in green tea with liquid and gas chromatography/tandem mass spectrometry. *Analyst*. 2013;138(3):921-31. Available from: [<URL>](#).
- Jiao W, Xiao Y, Qian X, Tong M, Hu Y, Hou R, et al. Optimized combination of dilution and refined QuEChERS to overcome matrix effects of six types of tea for determination eight neonicotinoid insecticides by ultra performance liquid chromatography-electrospray tandem mass spectrometry. *Food Chemistry*. 2016 Nov;210:26-34. Available from: [<URL>](#).



A Simultaneous Determination Method for the Analysis of Chloride and Nitrate Ions in Air Samples by PLS1

Çiğdem Kuş¹ , Havva Bekiroğlu Ataş^{1,2} , Adnan Kenar¹ , Mustafa Taştekin^{1*} 

¹Department of Chemistry, Faculty of Science, Ankara University, 06100, Ankara, Turkey

²General Directorate of Public Health /Department of Consumer Safety and Public Health Laboratories, National Public Health Reference Laboratory, 06100, Ankara, Turkey

Abstract: This study describes a multi-ion-selective electrode system for the simultaneous determination of nitrate and chloride ions in air samples by using multivariate calibration methods. The measurement system was constituted of two ion-selective electrodes, an Ag/AgCl double-junction reference electrode and a multi-potentiometer. The measurements were performed at pH 5.0 acetic acid/sodium acetate buffer. The obtained data were evaluated by using Partial Least Squares (PLS1). The system was used to analyze the synthetic samples and fume-hood samples in terms of the amount of chloride and nitrate. The percentage recovery values obtained from fume-hood samples were $93.8\% \pm 3.8$ and $102.4\% \pm 2.5$ for chloride and nitrate, respectively. The presented system could be an easy-to-use approach for monitoring the amount of chloride and nitrate species in the scope of occupational health and safety analysis.

Keywords: Multiple ion-selective electrode array, nitrate analysis, chloride analysis, multivariate calibration techniques, chemometrics, air samples.

Submitted: June 01, 2022. **Accepted:** January 04, 2023.

Cite this: Kuş Ç, Bekiroğlu Ataş H, Kenar A, Taştekin M. A Simultaneous Determination Method for the Analysis of Chloride and Nitrate Ions in Air Samples by PLS1. JOTCSA. 2023;10(1):89-96.

DOI: <https://doi.org/10.18596/jotcsa.1124772>.

***Corresponding author. E-mail:** mustafa.tastekin@science.ankara.edu.tr.

INTRODUCTION

Chloride and nitrate ions are frequently encountered in environmental samples such as water, soil and air, and these components affect human health. These ions are also found in the structure of strong acids such as hydrochloric acid and nitric acid.

Nitric acid is used in explosives and ammonium nitrate production for fertilization. In addition, it is used in organic synthesis, metallurgy, ore flotation (separation of free ore grains in liquid by flotation method, etc.), and reprocessing of spent nuclear fuels. Nitric acid is highly corrosive to most metals. Reactions between nitric acid and various organic metals are often highly exothermic and explosive. In addition, toxic gases are released when nitric acid reacts with metals.

The chloride ion is often used to purify drinking water and wastewater treatment. On the other

hand, hydrochloric acid is used as an industrial acidifier. It is also used for refining tantalum and tin ores, converting corn starch to syrup, removing stones formed in heat exchangers and boilers in the industry.

The analysis of these and similar ions has always attracted attention. For example, ion chromatography is one of the most used methods (1). In addition, there are other studies conducted by capillary electrophoresis (2) and voltammetric (3) or potentiometric ion-selective electrodes (4, 5) in order to do anion analysis.

Nowadays, special attention is paid to occupational health and safety issues, and some sanctions are applied when necessary. For example, in the industry, the employer has to make some analyses done in the work environment to save the employees' health. According to the Occupational Safety and Health Administration (OSHA), about 32 million workers work with and are potentially

exposed to one or more chemical hazards (6). It is also known that chemical exposure may cause or contribute to many serious health effects such as heart ailments, kidney and lung damage, cancer, burns, and rashes.

Chemicals have exposure limits in the scope of occupational health and safety. For example, the legal airborne permissible exposure limit (PEL) for hydrochloric acid is 5 ppm and can not be exceeded at any time (7). On the other hand, the PEL value is lower for nitric acid, and it is 2 ppm averaged over an 8-hour work shift (8). In such cases, the sampling for air should be done from the environment near the employee's breathing zone, where the ions are most intense.

Analyses can be conducted when a lot of types of components are together in the matrix. The analyses may result in errors due to the species that cause interference. To prevent this, the species that have an interfering effect should be removed from the matrix or masked. After these sample preparations, analysis is carried out by single-variate calibration techniques. However, this situation leads to loss of time and extra cost, and as the number of processes increases, systematic error possibility rises. In order to prevent these adverse effects, multivariate calibration methods can be an alternative (9).

Multivariate calibration methods have been preferred several times by the researchers that carry out spectroscopic studies (10-13). In addition, the use of these techniques with electrochemical studies such as anodic or cathodic differential pulse voltammetry have been reported before (14, 15). Many of these methods, especially spectroscopic ones, have advantages such as repeatability and sensitivity. On the other hand, the main handicaps of spectroscopic techniques are being overpriced, having complex procedures, and being more suitable for benchtop analysis. Potentiometry has become a good alternative for multivariate calibration studies since it has a small and uncomplicated design that allows field measurements. Moreover, compared to the other methods, it is relatively cheap and can be applied easily (16).

The technology, which is created by using multi-ion selective electrode arrays and multivariate calibration methods together, calls "electronic tongue" (17). Electronic tongues benefit the cross sensitivities of different ion-selective electrodes involving a sensor array and evaluate the results by a chemometric database. Although the use of multi-ISE arrays and chemometrics for the qualitative and quantitative analysis of different cations have been reported frequently (18-25), there are limited studies about the anion analyses by using the multi-ISE arrays (26-31). Some of these reported studies are only for anion analysis, while others are based on the analysis of both anions and cations. Also, in some cases, while the

study was designed for the simultaneous determination of more than one anion, researchers could not get that point by virtue of the interfering effect of analytes on each other (32).

Different multivariate calibration methods can be used during the electronic tongue studies, such as Classical Least Squares (CLS), Principal Component Regression (PCR) and Partial Least Squares (PLS1). Among all these methods, PLS1 is one of the most preferred multivariate calibration methods for the simultaneous determination of interfering species. It has also been previously reported that, in many different respects, PLS can be considered as a first-stop convenience method because it is well known and used (33).

In the study described here, a multi-ion-selective electrode array (multi-ISE array) was designed for the simultaneous determination of chloride and nitrate anions in the air samples. The system was used for analyzing the fume-hood samples, and the obtained results were evaluated by PLS1. While there are previously reported studies with the application in various samples such as water, beverages, honey, etc., to the best of our knowledge, this is the first study in which simultaneous determination of chloride and nitrate ions has been conducted in air samples by using a multi-ISE array and multi-variable calibration methods.

EXPERIMENTAL SECTION

Reagents and Solutions

Acetic acid, ammonium acetate, disodium hydrogen phosphate (Na_2HPO_4), potassium dihydrogen phosphate (KH_2PO_4), hydrochloric acid, nitric acid, sodium acetate, sodium chloride, sodium hydroxide, and sodium nitrate were purchased from Merck. Deionized water (Mes Mp Minupure Basic pure) was used to prepare stock solutions, buffer solutions, and synthetic samples.

Equipment

The potential measurements were conducted by a Lawson EMF-16 multiplexer, and the obtained data was recorded in a computer via EMF program. During the measurements, a double junction Ag/AgCl electrode (Thermo Orion) was used as a reference electrode. A Sentek P11 pH electrode was used for pH measurements. The chloride-selective electrode (Sentek) and the nitrate-selective electrode (Sentek) used in the study were commercially available. The fume-hood samples were prepared by using an air sampling pump (GirlAir-PLUS).

Preparation of the training set solutions

Chloride and nitrate stock solutions were prepared from sodium salts. A two-factor/five-level experimental design was used to prepare the training set solutions, and the five-level experimental design was simplified to 25 calibration solutions as described in the literature

(34). The level and concentration values of training set solutions are given in Table 1. 5 mL of chloride and nitrate stock solutions (ten times concentrated according to the concentrations stated in Table 1)

and 5 mL of pH=5.0 acetic acid/sodium acetate buffer were placed into a volumetric flask, and the final volume was completed to 50 mL with deionized water.

Table 1: Level and concentration values for the calibration solutions.

Level Values	Cl ⁻ (mol/L)	NO ₃ ⁻ (mol/L)
-2	0.0001	0.0001
-1	0.0003	0.0003
0	0.0010	0.0010
1	0.0030	0.0030
2	0.0100	0.0100

Preparation of synthetic samples

Both synthetic chloride and nitrate samples were prepared with a concentration of 0.002 mol/L. 5 mL synthetic sample stock solution (ten times concentrated stock solutions) and 5 mL pH=5.0 acetic acid/sodium acetate buffer were mixed in a volumetric flask, and the final volume was completed to 50 mL with deionized water.

Preparation of fume-hood samples

The air sample collection mechanism used during the study is shown in Figure 1. 0.001 mol/L 200 mL NaOH solution was put into the washing flask of the mechanism. The mechanism was placed in a fume-

hood and kept at the specified time. Hydrochloric acid and nitric acid solutions were placed in a glass beaker and heated by a heater to evaporate more quickly. The air sampling pump, which was adjusted to 3000 mL per minute, was attached to the washing flask. The air sample was collected in the washing flask for three hours and thirty minutes.

5 mL of air sample collected in NaOH solution and 5 mL of buffer solution were mixed in a volumetric flask, and the final volume was adjusted to 50 mL with deionized water.



Figure 1: The air sample collection mechanism.

Potentiometric measurements

The multi-ISE array consists of a chloride-selective commercial electrode, a nitrate-selective commercial electrode and a double junction

Ag/AgCl reference electrode. Potentiometric measurements were conducted in the presence of acetic acid/ sodium acetate buffer solution (pH=5.0). The EMF measurement of the multi-ISE

array was compared against the reference electrode. The changes in the EMF were measured twice consecutively with the Lawson L-EMF DAQ 3.0 software of the multiplexer, and these changes were recorded on a computer.

Data Processing

The acquired data were evaluated by using PLS1. A training set and a potential matrix with basic codes written in the laboratory in Octave 5.1.0 free licensed software compatible MATLAB were used in order to perform the multivariate calibration techniques (9, 34). The EMF values of the training set, synthetic samples, and the fume-hood samples were recorded in the computer. The predicted values were calculated, and the differences between the known and the predicted concentrations were used to evaluate the EMF values.

First, a cross-validation process was performed with the results of training set solutions. After that, the number of principal components was found by plotting the predicted residual error of sum of squares (PRESS) values against the factor numbers. Chloride and nitrate concentrations were estimated in the training, synthetic and fume-hood sample sets with PLS1 by applying a cross-validation process again with the number of principal components obtained by the graphical results.

Analysis of the synthetic and fume-hood samples

The synthetic samples and the fume-hood samples were analyzed with the prepared multi-electrode array. In order to calculate the recovery values, the standard addition method was used. Chloride and nitrate standard solutions (1 mol/L) were spiked to both synthetic and fume-hood samples after the calibration with the training set. Standard additions were conducted by using 50 µL, 100 µL, 100 µL, 100 µL volumes respectively. Percentage recoveries of both chloride and nitrate anions were obtained using the difference between the anion concentrations calculated at the end of the standard addition and the initially calculated anion concentrations.

RESULTS AND DISCUSSION

Performance characteristics of the ion-selective electrodes

In nitrate and chloride calibration solutions, the slopes, correlation coefficients (R^2), and linear working ranges of each ion-selective electrode composing a multi-ISE array were determined separately. Calibration solutions were prepared in the range of $1,0 \times 10^{-1}$ mol/L - $1,0 \times 10^{-6}$ mol/L. Also, the selectivity coefficients of electrodes against other analyte ions were determined by using the IUPAC recommended separate solution method (35). The selectivity coefficients and the performance characteristics calculated from calibrations are given in Table 2.

Table 2: Performance characteristics of the ion-selective electrodes.

Ion-selective electrode	Slope (mV per decade)	R^2	Working Range (mol/L)	$\log K_{A,B}^*$
Chloride	51.48	0.9999	1×10^{-1} - 1×10^{-3}	0.205
Nitrate	51.15	0.9964	1×10^{-1} - 1×10^{-4}	1.054

$$*E_2 - E_1 / \pm s = \log K_{A,B}$$

The effect of pH on the performance of ion-selective electrodes

To determine the effect of pH on the performance of the ion-selective electrodes, the measurements were carried out in the solutions that contained no buffer, pH=7.0 buffer (ammonium acetate),

pH=6.8 ($\text{KH}_2\text{PO}_4/\text{Na}_2\text{HPO}_4$) buffer and pH=5.0 (acetic acid/sodium acetate) buffer. When the obtained data were evaluated, it was observed that the best slope, intercept and R^2 values were gained at pH=5.0. The results are detailed in Table 3.

Table 3: The effect of pH on the performance of the multi-ISE array.

Buffer Solution	Ion	Slope	R^2	Intercept
No Buffer	NO_3^-	0.9929	0.9862	0.0003
	Cl^-	0.9847	0.9725	0.0005
pH=7.0 Buffer	NO_3^-	0.9829	0.9973	0.0002
	Cl^-	0.7864	0.8647	0.0004
pH=6.8 Buffer	NO_3^-	0.9903	0.9942	0.0003
	Cl^-	0.9739	0.9741	0.0008
pH=5.0 Buffer	NO_3^-	0.9962	0.9987	0.00008
	Cl^-	0.9972	0.9938	0.00007

Data Processing

Cross-Validation: To perform the cross-validation of the method "leave-one-out" technique was used. In accordance with this purpose, one of the 25 training set solutions was accepted as a sample, and the remaining 24 training set solutions were used in calibration. In the calibration made with 24 training solutions, the content of the 25th solution was determined. The same procedure was repeated for each solution.

PRESS values and the factor numbers were plotted by using distinctions between known and predicted concentrations in each solution. The principal

component numbers were appointed from the minimum points of these graphs. The obtained graphs are given in Figure 2. The principal component numbers were six for both chloride and nitrate by PLS1.

The concentrations of the analytes in synthetic samples were estimated via PLS1 by applying a cross-validation process with the principal component numbers. The percentage recovery values calculated according to described in Experimental Section were found $103.8\% \pm 3.5$ and $103.1\% \pm 1.6$ for chloride and nitrate, respectively.

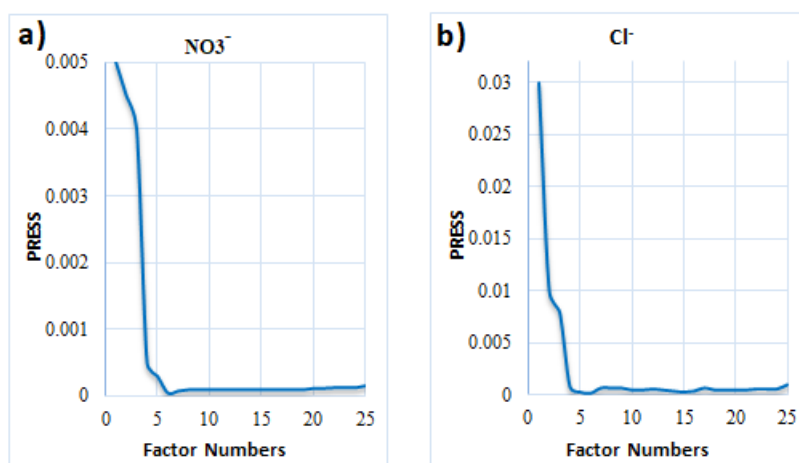


Figure 2: The number of factors according to PRESS values for PLS1 method.

Analytical application of the multi-ISE array to the fume-hood samples

The $C_{\text{known}} - C_{\text{predicted}}$ graphs obtained by PLS1 are given in Figure 3. Measurements were taken with multi-ISE in six different fume cupboard samples prepared according to described in Experimental

Section. The chloride and nitrate concentrations were calculated by PLS1, and according to these calculations, 0.63 m^3 of air was drawn from the fume-hood and 41.87 mg chloride ions and 77.46 mg nitrate ions were found in 1 m^3 air.

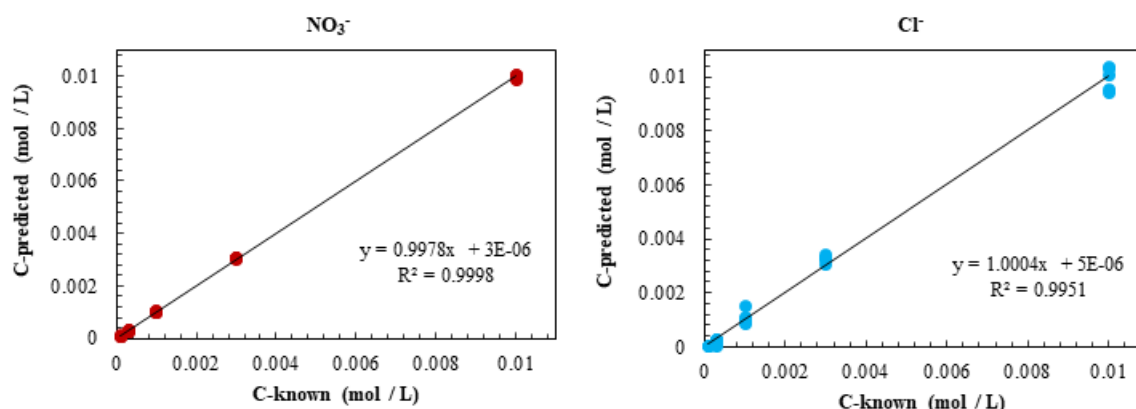


Figure 3: The concentration values calculated by PLS1 against the known concentrations.

When the percentage recovery values calculated from the standard addition were evaluated, it was observed that these values were $93.8\% \pm 3.8$ and $102.4\% \pm 2.5$ for chloride and nitrate, respectively. In addition, the percentage recovery results were

checked for systematic errors using the *t*-test and it was determined that there was no systematic error at 99% confidence level (degree of freedom (DF):3) in the results obtained from the multi-ISE array (Table 4). According to these results, it can

be concluded that the use of multi-variable calibration methods with the multi-ISE array is could be a good alternative for the anion analysis

because it is not only easy and cheap but also gives good recovery values.

Table 4: Statistical comparison of the nitrate and chloride concentrations in fume-hood samples.

	Analyte	Recovery%	t_e	t_c	$t_c > t_e$
$t_e = \frac{\mu - \bar{x}}{\frac{s}{\sqrt{n}}}$	NO ₃ ⁻	102.4 ± 2.5	1.92	5.84	5.84 > 1.92
	Cl ⁻	93.8 ± 3.8	3.26	5.84	5.84 > 3.26

There are many commercially available anion and cation-selective electrodes on the market. The costs of these electrodes are quite affordable compared to more complex analytical devices, which are suitable for benchtop analysis. In fact, the proposed system can be used in different sample matrices for different anions/cations with the help of a chemometric approach and different ion-selective electrodes. On the other hand, in the light of this study, laboratories can also develop similar systems with ion-selective electrodes, which they designed.

Results obtained from single ion-selective electrodes

Both nitrate and chloride concentrations in the fume-hood samples were determined using single ion-selective electrodes. To that end, potential readings were acquired in the calibration solutions of the analytes to each ion-selective electrode sensitive, and concentration values were obtained by using the created calibration curves and the Nernst equation. As indicated in Table 5, there is a significant difference between the results obtained from single ion-selective electrodes and multi-ISE array, especially for nitrate concentrations.

Table 5: The percentage recoveries of Cl⁻ and NO₃⁻ in fume hood samples by using single ISEs.

	ISE	Analyte	Recovery%	t_e	t_c	$t_c > t_e$
$t_e = \frac{\mu - \bar{x}}{s/\sqrt{n}}$	Nitrate ISE	NO ₃ ⁻	60.3 ± 3.1	25.61	5.84	5.84 < 25.61
	DF : 3	Chloride ISE	Cl ⁻	104.1 ± 5.3	1.55	5.84

According to these results, it can be concluded that the use of a multi-ISE array in the analysis could be more advantageous. Also, more accurate results can be gained compared to a single electrode.

CONCLUSION

In this study, we proposed a multi-ISE array for the simultaneous determination of chloride and nitrate anions in air samples. The system was used to analyze the synthetic samples and fume-hood samples in terms of the amount of chloride and nitrate anions. The measurement system was consisted of two ion-selective electrodes, an Ag/AgCl double-junction reference electrode, and a multi-potentiometer. The obtained data were evaluated by using PLS1. The application of the multi-ISE array was demonstrated by the simultaneous determination of nitrate and chloride ions in air samples obtained from a fume-hood with good recoveries. The presented sensor could be an easy to use approach for monitoring the amount of chloride and nitrate in the scope of occupational health and safety analysis.

While it is possible to analyze samples taken from air samples by chromatography systems combined with thermal desorption, it is possible to conduct the analysis more straightforward and cheaper

with the system proposed in the study. To the best of our knowledge, this is the first study in which simultaneous determination of chloride and nitrate ions has been carried out in air samples by a multi-ISE array and multi-variable calibration methods. Considering the benefits of the proposed system, such as reducing costs and minimizing the need for extensive facilities and number of personnel, we believe that this study will elucidate future studies and will be of interest to most laboratories that carry out similar analyses.

CONFLICT OF INTEREST

The authors declare that they have no conflict of interest.

ACKNOWLEDGMENTS

The authors gratefully acknowledge the financial support of Ankara University Research Fund (BAP No. 12B4240008).

REFERENCES









- Gómez-Ordóñez E, Alonso E, Rupérez P. A simple ion chromatography method for inorganic anion analysis in edible seaweeds. *Talanta*. 2010;82(4):1313-1317. <DOI>.

2. Baryla NE, Lucy C. A. Semi-permanent surfactant coatings for inorganic anion analysis in capillary electrophoresis. *J. Chromatogr. A.* 2002;956(1-2):271-277. [<DOI>](#).
3. Zhang J, Harris A R, Cattrall RW, Bond AM. Voltammetric ion-selective electrodes for the selective determination of cations and anions. *Anal. Chem.* 2010;82(5):1624-1633. [<DOI>](#).
4. Dalkıran B, Ertürün HEK, Özel AD, Canel E, Özkınalı S, Kılıç E. Chromate-selective electrodes prepared by using calix [4] arenes for the speciation of Cr (VI) and Cr (III). *Ionics.* 2017;23(9):2509-2519. [<DOI>](#).
5. Suman S, Singh R. Anion selective electrodes: A brief compilation. *Microchem. J.* 2019;(149):104045. [<DOI>](#).
6. OSHA 3084, (1998). Chemical Hazard Communication U.S. Department of Labor Occupational Safety and Health Administration. June 01, 2022 [<URL>](#).
7. Hazardous Substance Fact Sheet, Hydrogen Chloride (2016). June 01, 2022. [<URL>](#).
8. Hazardous Substance Fact Sheet, Nitric Acid (2016). June 01, 2022. [<URL>](#).
9. Gemperline P. Practical Guide to Chemometrics. 2nd ed. Boca Raton: CRC Press; 2006. [<DOI>](#).
10. Moreno-Martin G, León-González ME, Madrid Y. Simultaneous determination of the size and concentration of AgNPs in water samples by UV-vis spectrophotometry and chemometrics tools. *Talanta.* 2018;(188):393-403. [<DOI>](#).
11. Altunay N, Katin KP, Gürsoy N, Elik A, Şimşek S, Kaya S. Spectrophotometric determination of aflatoxin B1 in food sample: Chemometric optimization and theoretical supports for reaction mechanisms and binding regions. *J. Food Compos. Anal.* 2020;(94):103646. [<DOI>](#).
12. Elmas ŞNK, Arslan FN, Akin G, Kenar A, Janssen HG, Yılmaz I. Synchronous fluorescence spectroscopy combined with chemometrics for rapid assessment of cold-pressed grape seed oil adulteration: Qualitative and quantitative study. *Talanta.* 2019;(196):22-31. [<DOI>](#).
13. Ata Ş, Akyüz M, Dinç E. Chemometric approach to the optimisation of LC-FL and GC-MS methods for the determination of nitrite and nitrate in some biological, food and environmental samples. *Int. J. Environ. Anal. Chem.* 2016;96(7):636-652. [<DOI>](#).
14. Gardiner J, Stiff MJ. The determination of cadmium, lead, copper and zinc in ground water, estuarine water, sewage and sewage effluent by anodic stripping voltammetry. *Water Res.* 1975;9(5-6):517-523. [<DOI>](#).
15. Locatelli C, Torsi G. Determination of Se, As, Cu, Pb, Cd, Zn and Mn by anodic and cathodic stripping voltammetry in marine environmental matrices in the presence of reciprocal interference. Proposal of a new analytical procedure. *Microchem. J.* 2000;65(3):293-303. [<DOI>](#).
16. Ergün EGC, Kenar A. Simultaneous determination of copper (II) and zinc (II) via simple acid-base titrimetry using glass pH electrode. *Turk. J. Chem.* 2018;42(2):257-263. [<DOI>](#).
17. Del Valle M. Sensor arrays and electronic tongue systems. *Int. J. Electrochem.* 2012;212:986025. [<DOI>](#).
18. Ataş HB, Kenar A, Taştekin M. An electronic tongue for simultaneous determination of Ca²⁺, Mg²⁺, K⁺ and NH₄⁺ in water samples by multivariate calibration methods. *Talanta.* 2020;(217):121110. [<DOI>](#).
19. Eylem CC, Taştekin M, Kenar A. Simultaneous determination of copper and zinc in brass samples by PCR and PLS1 methods using a multiple ion-selective electrode array. *Talanta.* 2018;(183):184-191. [<DOI>](#).
20. Saurina J, López-Aviles E, Moal A, Hernández-Cassou S. Determination of calcium and total hardness in natural waters using a potentiometric sensor array. *Anal. Chim. Acta.* 2002;464(1):89-98. [<DOI>](#).
21. Gallardo J, Alegret S, Muñoz R, De-Román M, Leija L, Hernandez PR, Del Valle M. An electronic tongue using potentiometric all-solid-state PVC-membrane sensors for the simultaneous quantification of ammonium and potassium ions in water. *Anal. Bioanal. Chem.* 2003;377(2):248-256. [<DOI>](#).
22. Calvo D, Bartrolí J, Del Valle M. Multicomponent Titration of Calcium+ Magnesium Mixtures Employing a Potentiometric Electronic-Tongue. *Anal. Lett.* 2007;40(8):1579-1595. [<DOI>](#).
23. Wilson D, Del Valle M, Alegret S, Valderrama C, Florido A. Potentiometric electronic tongue-flow injection analysis system for the monitoring of heavy metal biosorption processes. *Talanta.* 2012;93:285-292. [<DOI>](#).
24. Calvo D, del Valle M. Simultaneous titration of ternary alkaline-earth mixtures employing a potentiometric electronic tongue. *Microchem. J.* 2007;87(1):27-34. [<DOI>](#).
25. Nery EW, Kubota LT. Integrated, paper-based potentiometric electronic tongue for the analysis of beer and wine. *Anal. Chim. Acta.* 2016;918:60-68. [<DOI>](#).
26. Cortina M, Duran A, Alegret S, Del Valle M. A sequential injection electronic tongue employing the transient response from potentiometric sensors for anion multidetermination. *Anal. Bioanal. Chem.* 2006;385(7):1186-1194. [<DOI>](#).
27. Cuartero M, García MS, Ortuño JA. Differential dynamic potentiometric responses obtained with ion-selective electrodes for perchlorate, thiocyanate, iodide, nitrate, sulfate, picrate and bis (trifluoromethylsulfonyl) imide. *Electrochim. Acta.* 2013;(93):272-278. [<DOI>](#).
28. Wilson D, Abbas MN, Radwan ALA, Del Valle M. Potentiometric electronic tongue to resolve mixtures of sulfide and perchlorate anions. *Sensors.* 2011;11(3):3214-3226. [<DOI>](#).
29. Gil L, García-Breijo E, Ibañez J, Labrador RH, Llobet E, Martínez-Máñez R, Soto J. Electronic tongue for qualitative analysis of aqueous solutions of salts using thick-film technology and metal electrodes. *Sensors.* 2006;6(9):1128-1138. [<DOI>](#).
30. Shirmardi A, Shamsipur M, Akhond M, Monjezi J. Electronic tongue for simultaneous determination of cyanide, thiocyanate and iodide. *Measurement.* 2016;88:27-33. [<DOI>](#).
31. Nuñez L, Cetó X, Pividori MI, Zanon MVB, Del Valle M. Development and application of an electronic tongue for detection and monitoring of nitrate, nitrite and ammonium levels in waters. *Microchem. J.* 2013;110:273-279. [<DOI>](#).

32. Gutiérrez M, Alegret S, Caceres R, Casadesús J, Marfa O, Del Valle M. Application of a potentiometric electronic tongue to fertigation strategy in greenhouse cultivation. *Comput. Electron. Agr.* 2007;57(1):12-22. [<DOI>](#).
33. Ni Y, Kokot S. Does chemometrics enhance the performance of electroanalysis?. *Anal. Chim. Acta.* 2008;626(2):130-146. [<DOI>](#)
34. Brereton RG. Multilevel Multifactor Designs for Multivariate Calibration. *Analyst.* 1997;122(12):1521-1529. [<DOI>](#).
35. Brereton RG. *Chemometrics*. Chichester, UK: John Wiley & Sons; 2003. ISBN: 978-0-470-84574-5.
36. Umezawa Y, Umezawa K, Sato H. Selectivity coefficients for ion-selective electrodes: recommended methods for reporting K_A , B_{pot} values (Technical Report). *Pure Appl. Chem.* 1995;67(3):507-518. [<DOI>](#).



Comparative Studies of some Chemical and Micronutrient Contents in three Sprouted Samples of Bambaranut (*Vigna subterranean* [I] verdc.) Landraces

Tasiu Mikail^{1,2} , Muhammad Sani Sule² , Adamu Jubril Alhassan² ,
Abdullahi Abdulkadir Imam² , Yusuf Yunusa Muhammad² , Sagir Ismail¹ ,
Kamaluddeen Babagana² , Abdulmumin Yunusa¹ 

¹Kano University of Science and Technology, Department of Biochemistry, Wudil, Nigeria

²Bayero University, Department of Biochemistry, Kano, Nigeria

³Bayero University, Department of Animal Science, Kano, Nigeria

Abstract: The research was carried out to evaluate the effect of sprouting on chemical and micronutrient contents of Bambaranut (*Vigna subterranea* [I] verdc.) grown in Kano, Nigeria. Three landraces of Bambaranut (cream, black and zebra) were used for the study. The proximate and mineral contents were analyzed in accordance with the standard methods of analysis. The result of the proximate analysis showed that the moisture and carbohydrate contents reduced significantly ($P < 0.05$) after sprouting while ash, crude protein, crude fat, and crude fiber significantly increased, there was no significant ($P < 0.05$) difference in moisture, crude fiber, and carbohydrate contents between the landraces. The landraces differ in crude protein and fat contents. The results of minerals analysis shows that the landraces differ significantly in Na, Fe, Ca, K, Mg, and Se. However, the amount of Zn, Mn did not significantly differ between the landraces irrespective of sprouting or not. All the three landraces did not differ ($P < 0.05$) in Cu contents. Sprouting leads to decrease in Na, Fe, K, Zn, Mg and Se and increase in Ca and Mn. This study showed that sprouting improves the nutritional quality of Bambaranut irrespective of the landrace.

Keywords: Sprouting, Chemical, Micronutrients, Bambaranut

Submitted: August 27, 2022. **Accepted:** January 14, 2023.

Cite this: Mikail T, Sule MS, Alhassan AJ, Imam AA, Muhammad YY, Sagir I, et al. Comparative Studies of some Chemical and Micronutrient Contents in three Sprouted Samples of Bambaranut (*Vigna subterranea* [I] verdc.). JOTCSA. 2023;10(1):97-108.

DOI: <https://doi.org/10.18596/jotcsa.1167021>.

***Corresponding author. E-mail:** tasiuikail@kustwudil.edu.ng.

1. INTRODUCTION

Bambaranut (*Vigna subterranea* (L.) Verdc) is the third most important grain legume in semi-arid Africa. Resistant to high temperature, drought, insect and weevil attack, bambaranut is suitable for poor soils and has high nutritive value (1). Bambaranut (*Vigna subterranea* (L.) Verdc) has a large number of landraces throughout Africa where small-scale farmers have preserved its genetic diversity on-farm (2). Bambara groundnut is an excellent source macro and micronutrients and has

nutritional potentials that can mitigate malnutrition when properly explored. Therefore, Bambaranut is very important food for poor people especially in Africa who cannot have access to the expensive animal protein. The seed of Bambaranut (Figure 1) is rich in essential amino acids including isoleucine, leucine, lysine, methionine, phenylalanine, threonine, and valine but has not been considered as stable food as cereals such as wheat, maize, and rice (3). Bambara groundnut oil could have medicinal and nutritional benefits, it contains saturated fatty acids that help in lowering the

levels of LDL cholesterol in while increasing HDL cholesterol in blood, this can in turn lower the risk of developing cardiovascular diseases, while providing nutrients, such as vitamin E.

Sprouting is a period characterized by intense metabolic activity in the plant and represents a re-emerging trend in healthy foods and has positive impact on the enhancement of the nutritional properties (4) and taste (5). Germination was reported to increase the nutritional value of cereals and legumes through activation of endogenous enzymes (6). According to the European Sprouted Seeds Association (ESSA) (7) sprouts are the product that results from the germination of seeds and their growth in water or another medium, harvested prior to the development of true leaves and which is set to be eaten whole, including the seed. Consumption of sprouted grains is said to be useful for human health. Positive consumer perceptions about sprouted cereals have resulted in new food and beverage product launches (8). Under ambient conditions, when grains and seeds are soaked and sprouted, endogenous and newly synthesized enzymes begin to alter the seed constituents. Thus, complex macromolecules are broken down into lower molecular weight molecules which are more digestible and more readily absorbed by the body (9). In this work, we determine the effect of sprouting on proximate and mineral composition of three landraces of bambaranut grown in Kano, Nigeria.



Figure 1: Bambaranut seeds.

2. MATERIALS AND METHODS

2.1. Sample Collection and Preparation

Three Bambaranut landraces samples (cream, black, and zebra) were obtained from four areas of Kano state. The sample was sorted, cleaned, washed, and soaked in water overnight. The water was changed at intervals of 3 hours to avoid fermentation (10). The cream and zebra colored samples were soaked for 15 hours overnight whereas the black colored was soaked for 24 hours. The soaked samples were placed in petri dishes for germination period of 5 days. The dishes were covered with cotton to create enabling environment for sprouting to occur. After a period of 5 days, the samples developed shoots (sprouts)

(see Figure 3A, B and C). After sprouting, the sprouted samples were dried and milled. The resulting powdered samples were used for proximate and mineral analysis. The graphical sketch of sprouting are presented in Figure 2.

3. METHODS

3.1. Determination of the Proximate Composition

The proximate composition (moisture, ash, crude protein, crude fat, fiber, and carbohydrate) of Bambaranut was determined in accordance with standard methods of AOAC (11) as follows.

3.2. Determination of Moisture Content

A clean petri dish was weighed (W_1) and 5 g of the powdered sample was placed in the dish and then weighed (W_2). The content was placed in an oven at 120 °C for 3 hours. The dish was removed and cooled in desiccators for 30 minutes and finally weighed (W_3) (14). The moisture content was calculated using the equation below.

$$\%Moisture = \frac{W_2 - W_3}{W_2 - W_1} \times 100$$

3.3. Determination of Ash Content

A clean crucible was weighed (W_1) and 5 g of dried powdered sample was measured in to the crucible and weighed (W_2). The crucible was transferred in to muffle furnace at 550 °C for ashing. After ashing, the furnace was turned off and allowed to cool. The samples were carefully removed from the furnace to avoid losing ash that may be fluffy. The crucibles were transferred to desiccator and allowed to cool for 30 minutes and then weighed (W_3) (13). The ash content was calculated using the following equation

$$\%Ash = \frac{W_3 - W_1}{W_2 - W_1} \times 100$$

3.4. Determination of Crude Protein Content

The crude protein was determined by Kjeldahl distillation as described by (13). Based on the Kjeldahl procedure, proteins and other organic food constituents in a sample are digested using sulfuric acid and with catalysts. The total organic nitrogen is transformed to ammonium sulfate and the digest is neutralized using alkali and distilled into a boric acid solution. The resulting borate anions are titrated using standardized acid, which is converted to nitrogen in the sample. The result of the analysis represents the crude protein content of the food because nitrogen also comes from non-protein components.

3.5. General Procedures and Reactions

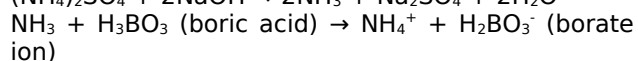
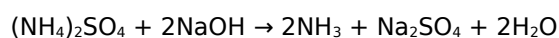
3.5.1. Digestion

The samples were placed in Kjeldahl flask. Acid and catalyst were added to the flask, the mixtures were

allowed to digest formation of clear mixture indicates a complete breakdown of all organic matter in the samples. Non volatile ammonium sulfate was formed in the reaction of nitrogen and sulfuric acid. in the course of digestion, protein nitrogen was liberated leading to the formation of ammonium ions, sulfuric acid oxidizes organic matter and reacts with ammonium that was formed, carbon and hydrogen are converted to carbon dioxide and water.

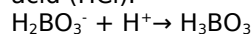
3.5.2. Neutralization and distillation

The digest was diluted using water. Alkali containing sodium thiosulfate was added so that the sulfuric acid is neutralized. The resulting ammonia was distilled into a boric acid solution containing the indicators methylene blue and methyl red.



3.5.3. Titration

Borate ion (proportional to the amount of nitrogen) is titrated with standardized 0.02 M Hydrochloric acid (HCl).



The amount of nitrogen was calculated using the following formula

Moles of HCl = Moles of NH_3 = Moles of N in the sample

A reagent blank is run and reagent nitrogen was subtracted from the sample nitrogen.

$$\%N = \frac{NH_4Cl \times \text{corrected acid volume}}{\text{weight of sample in g}} \times \frac{14 \text{ g of N}}{1 \text{ mole of N}} \times 100$$

Where NH_4Cl = Normality of HCl in moles/1000 mL
Corrected acid volume = (mL of std. acid for sample) - (mL of std. acid for blank)

14 = atomic weight of nitrogen

A factor is used to convert percent N to percent crude protein. Most proteins contain 16 percent N, so the conversion factor is 6.25 (100/16 = 6.25).

$\% N \times 6.25 = \% \text{ protein}$

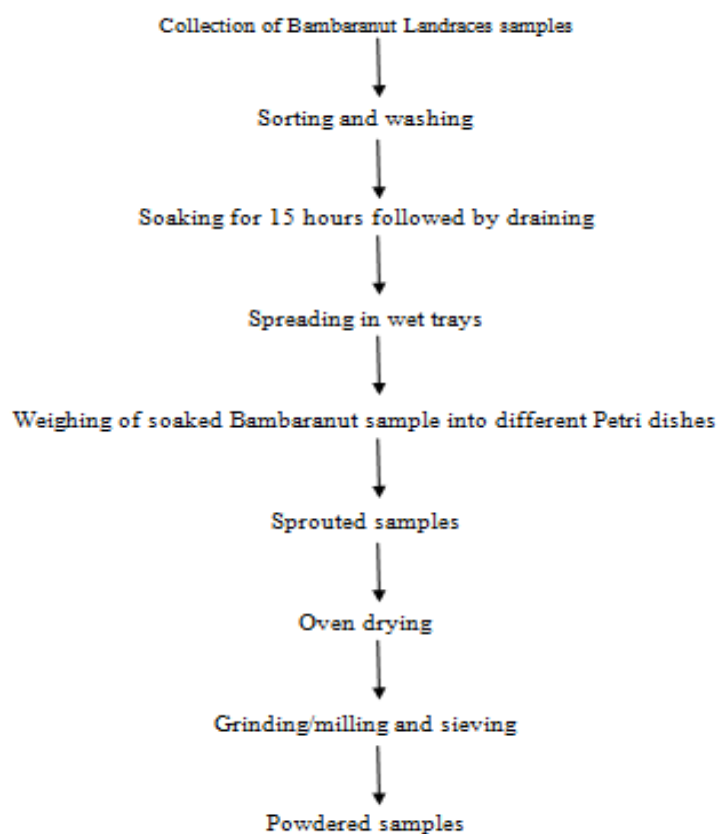


Figure 2: Schematic presentation of sprouting.

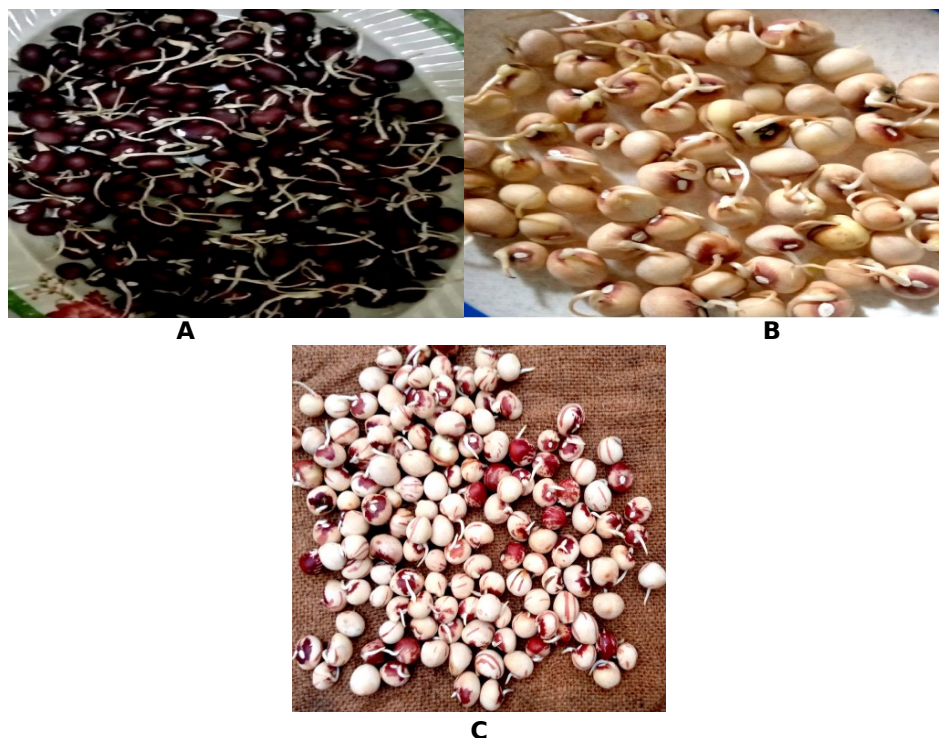


Figure 3: Sprouted Bambaranut (A) Black landrace, (B) Cream landrace (C) Zebra landrace.

3.6. Determination of Crude Fat

3.6.1. Principle

Organic solvents, such as petroleum ether, have the ability to dissolve fat in a given sample. It has a low boiling point (40-80 °C). Therefore when in Soxhlet assembly connected to a reflux condenser, it dissolves the fat in the sample and washes it down in to the flask, and the ether can easily be evaporated and recollected afterwards. The difference in weight between the empty flask before extraction and the weight of flask after extraction gives the weight of lipid being extracted (13).

3.6.2. Procedure

A quantity (3 g) of the sample was carefully weighed (W_1) in to a folded filter paper and small cotton wool placed on top. The content was accurately tied by a thread at both ends of the filter paper and weighed. The content was positioned in the extraction thimble and little cotton wool positioned on top. The whole apparatus was subsequently connected following the addition of 300 milliliters of petroleum ether in to the extraction flask and weighed (W_2). The extraction was maintained for 3 hours by means of the heating mantle and making sure of the incessant flow of water in the condenser. The sample was then removed, air-dried and then positioned in an oven at 80 °C until a constant weight was determined. The extraction flask was transferred to an oven so that the solvent (petroleum ether) can easily be evaporated leaving behind the extract. After evaporation the flask was weighed (W_3). The crude fat in the sample was

calculated using the following equation;

$$\% \text{ crude fat in the sample} = \frac{W_3 - W_2}{W_1} \times 100$$

3.7. Determination of Crude Fiber

Crude fiber is the insoluble and combustible organic residue which remains after the sample has been treated under prescribed conditions of consecutive treatments with light petroleum ether, boiling in dilute sulfuric acid and sodium hydroxide, and washing with boiling water, alcohol and petroleum ether (13).

3.7.1. Procedure

In to the extraction apparatus, 3 g of the sample was weighed and extracted three times using light petroleum ether by stirring, settling followed by decantation. The extracted air dried sample was placed in to a dried 100-milliliter conical flask, 200 mL of 0.127 sulfuric acid was added in to the flask, the sample was dispersed by some of the solution. The content was boiled for 30 minutes, at the same time a stable volume was maintained. The flask was made to rotate every few minutes so as to mix up the contents and get rid of particles from the side. The Buchner funnel was prepared while waiting for the mixture to boil. The Buchner funnel was preset to a perforated plate and linked with the funnel, the filter paper was as well preset to envelop the openings in the plate. The boiled water was added in to the funnel and was allowed to wait until the funnel was hot and afterwards drained by suction. At the end of 30 minutes of the boiling

period, the mixture was allowed to stand for a minute and then poured immediately into a shallow layer of hot water under gentle suction into the funnel. The insoluble matter was washed with boiled water for several times until the washing was free from acid, then it was washed back into the original flask by means of a wash bottle containing 200 mL of 0.313 M sodium hydroxide solution. The mixture was boiled for 30 minutes with the same precautions as those used in the earlier boiling with acid. After 30 minutes of boiling, it was made to stand for a minute and subsequently filtered without delay. The insoluble material was placed in the filter paper using boiling water, after that it was washed using 1% hydrochloric acid, it was finally washed with boiling water making it free from acid. This was subsequently washed two times using alcohol and three times using petroleum ether. The insoluble material was then placed in a dried weighed crucible and dried at 100 °C to constant weight. The crucible with its contents was transferred to a heating mantle in a fume cupboard to remove the organic matter. Subsequently, the crucible was transferred to a muffle furnace at 550°C for 3 hours. The ash content was then obtained by weighing. The crude fiber was calculated using the following equation;

$$\% \text{Crude Fiber} = \frac{\text{weight of ash}}{\text{weight of sample}} \times 100$$

3.8. Determination of Carbohydrate by Difference

Carbohydrate content was determined by difference as follows;

$$\% \text{Carbohydrate} = 100 - (\text{Moisture} + \text{Ash}) \\ (+ \text{Protein} + \text{Lipid} + \text{Crude Fiber})$$

3.9. Determination of Mineral Elements Atomic Absorption Spectroscopy (AAS)

Principle

Atomic Absorption Spectrophotometer is an analytical instrument that is based on the principle of atomic absorption spectroscopy. This involves the aspiration of sample solution into the flame and the sample element is changed to atomic vapor. The flame therefore contains atoms of that

element. Some are thermally energized by the flame, but the majority stayed in the ground state. These ground state atoms subsequently absorb radiation of particular wavelengths that is formed by a special source prepared from that element. The absorption follows Beer's Law, that the absorbance is directly proportional to the concentration of the atomic vapor in the flame. That is the concentration of atomic vapor is directly proportional to the concentration of the element in solution being aspirated (16).

3.9.1. Procedure for AAS

The minerals (Ca, Cu, Fe, K, Mg, Mn, Na, Zn, and Se) were determined by Atomic Absorption Spectrophotometer as described by (15). A hollow cathode lamp was selected for the analysis, the lamp was made to warm up for 15 minutes. For the duration of the 15 minutes period, the instrument was aligned by positioning the monochromator at the right wavelength. The monochromator slit width was chosen. The hollow cathode current was as well adjusted in line with the manufacturer's reference. Afterward, the flame was lit and the flow of fuel and oxidant were regulated. The burner and nebulizer flow rate for maximum percent absorption and stability were adjusted after which the photometer was balanced. The samples were aspirated and the concentrations were obtained using calibration curve. A series of standards of the elements in question were run and a calibration curve was constructed by plotting the concentrations of the standards against the absorbance.

3.10. Statistical analysis

Results were analyzed by two-way analysis of variance (Post hoc) using SPSS software. Difference of mean were determined at P<0.05 level of significance.

4. RESULTS

4.1. Proximate Composition

Table 1 presents the effect of sprouting on the proximate contents of three landraces of Bambaranut grown in Kano. The result indicates significant increase in ash, crude protein, crude fat, and crude fiber and decrease in moisture and carbohydrate contents after sprouting.

Table 1: Effect of sprouting on the proximate contents of three landraces of Bambaranut.

Parameter (%)	Sprouted			Unsprouted		
	Black	Cream	Zebra	Black	Cream	Zebra
Moisture	7.10 ± 0.50 ^a	7.42 ± 0.06 ^a	6.81 ± 0.16 ^a	11.99 ± 1.03 ^b	12.01 ± 0.22 ^b	12.09 ± 0.04 ^b
Ash	4.68 ± 0.29 ^a	4.28 ± 0.05 ^b	4.30 ± 0.02 ^a	2.09 ± 0.05 ^c	3.84 ± 0.25 ^d	2.25 ± 0.08 ^c
Crude Protein	17.45 ± 0.56 ^a	19.93 ± 0.13 ^b	15.65 ± 0.37 ^c	4.63 ± 0.07 ^d	10.05 ± 0.08 ^e	6.23 ± 0.05 ^f
crude Fat	14.25 ± 0.59 ^a	14.12 ± 0.08 ^a	15.15 ± 0.07 ^b	11.93 ± 0.61 ^c	3.15 ± 0.32 ^d	9.99 ± 0.57 ^e
Crude Fiber	5.21 ± 0.32 ^a	7.99 ± 0.11 ^b	4.80 ± 0.28 ^c	4.42 ± 0.16 ^d	4.44 ± 0.11 ^d	4.28 ± 0.26 ^d
Carbohydrate	51.3 ± 1.91 ^a	45.39 ± 1.50 ^b	53.33 ± 0.88 ^c	64.89 ± 0.43 ^d	66.46 ± 0.22 ^d	65.13 ± 0.52 ^d

Results are presented as mean ± standard deviation n = 3

Values with different superscript in the same row are significantly different at

P<0.05

Table 2: Effect of Landrace on the Proximate Contents of Bambaranut.

parameters	Landrace			SE
	Black	Cream	Zebra	
Moisture	9.55 ^a	9.71 ^a	9.45 ^a	0.2
Ash	3.39 ^a	4.06 ^b	3.28 ^a	0.07
Crude Protein	11.04 ^a	11.99 ^b	10.94 ^a	0.12
crude Fat	13.09 ^a	8.64 ^b	12.57 ^c	0.18
Crude Fiber	4.82 ^a	6.22 ^b	4.54 ^c	0.08
Carbohydrate	58.10 ^a	55.93 ^b	59.23 ^a	0.45

4.2. Mineral Elements

4.2.1. Mineral contents

The effect of sprouting on mineral contents of

bambaranut is presented in Table 3. Based on the result, sprouting has effect of increasing some of the minerals while decreasing others.

Table 3: Effect of sprouting on Mineral contents of Bambaranut.

Elements (mg/kg)	sprouted			Unsprouted		
	Black	Cream	Zebra	Black	Cream	Zebra
Na	17.2 ± 0.05 ^a	16.89 ± 0.64 ^a	12.88 ± 0.31 ^b	26.17 ± 0.46 ^c	110.93 ± 0.37 ^d	13.92 ± 0.04 ^e
Fe	2.40 ± 0.31 ^a	2.20 ± 0.18 ^a	4.78 ± 0.25 ^b	7.10 ± 0.009 ^c	4.06 ± 0.05 ^d	1.79 ± 0.04 ^e
Ca	45.04 ± 0.03 ^a	44.16 ± 0.02 ^b	37.37 ± 0.05 ^c	39.49 ± 0.025 ^d	38.31 ± 0.55 ^e	43.2 ± 0.63 ^f
K	519.97 ± 0.41 ^a	551.30 ± 0.60 ^b	518.98 ± 0.22 ^a	551.9 4 ± 0.21 ^c	464.8 ± 0.40 ^d	615.57 ± 0.05 ^e
Zn	1.17 ± 0.11 ^a	1.09 ± 0.04 ^b	1.12 ± 0.001 ^a	1.08 ± 0.004 ^b	1.61 ± 0.02 ^c	1.07 ± 0.005 ^b
Mg	102.77 ± 0.30 ^a	89.86 ± 0.31 ^b	106.9 ± 0.20 ^c	106.0 4 ± 0.54 ^c	87.66 ± 0.09 ^d	114.97 ± 0.35 ^e
Mn	0.51 ± 0.007 ^a	0.75 ± 0.05 ^b	0.51 ± 0.03 ^a	0.50 ± 0.04 ^a	0.58 ± 0.02 ^c	0.51 ± 0.02 ^a
Se	38.93 ± 0.35 ^a	30.31 ± 0.51 ^b	24.62 ± 0.01 ^c	32.32 ± 0.55 ^d	29.00 ± 0.20 ^e	36.51 ± 0.03 ^f
Cu	0.40 ± 0.04 ^a	0.31 ± 0.04 ^b	0.30 ± 0.04 ^b	0.32 ± 0.22 ^b	0.29 ± 0.03 ^b	0.33 ± 0.04 ^b

Results are presented as mean ± standard deviation n = 3

Values with different superscript in the same row are significantly different at P<0.05

Table 4: Effect of Landrace on Mineral contents of Bambaranut.

Elements	Sprouted	Unsprouted	SE
Na	15.66 ^a	50.34 ^b	0.13
Fe	3.12 ^a	4.32 ^b	0.04
Ca	42.19 ^a	40.33 ^b	0.12
K	530.08 ^a	544.10 ^b	0.12
Zn	1.13 ^a	1.25 ^b	0.02
Mg	99.84 ^a	102.89 ^b	0.11
Mn	0.59 ^a	0.53 ^b	0.01
Se	31.29 ^a	32.61 ^b	0.12
Cu	0.34 ^a	0.31 ^a	0.13

5. DISCUSSION

5.1. Proximate Contents

The effects of sprouting on the proximate contents of three landraces of Bambaranut are presented in Table 1. Generally, irrespective of sprouting or not, *Vigna subterranea* landraces did not significantly ($P<0.05$) differ in moisture contents but differ in other proximate parameters (Table 2). Similarly, sprouting leads to significant changes in all the proximate parameters irrespective of the landrace. The moisture and carbohydrate contents tend to decrease significantly after sprouting whereas crude protein, ash, crude fiber and crude fat increased significantly. The decrease in moisture content is in disagreement with (19) that sprouting leads to increase in moisture content. The result of this study also disagrees with Shah *et al.* (2011) that sprouting has no effect on moisture content. The decrease in moisture content is an indication that sprouted Bambaranut will have a better shelf life.

Increase in ash contents observed in this study agrees with (17) when chick pea and soybean were sprouted for 2 - 4 days and (18) when mung bean, pea, and lentil were sprouted. The increased ash contents observed indicates that the sprouted bambaranut could have more mineral contents. The decrease in carbohydrate contents during sprouting may have led to the apparent increase observed in ash (18). The apparent increase in protein observed is attributed to increased synthesis of enzyme proteins such as proteases by sprouted seeds or a compositional change due to degradation of other constituents (19). The decrease in fiber contents observed reverberates the findings of (16), the increase could be attributed to the release of nutrients. Previous studies reported a decrease in crude fat contents following sprouting (16). However, the current study has observed significant increase. The significant reduction in carbohydrate contents is in agreement with (16), sprouting cause biochemical changes in carbohydrate that may lead to change in energy value. Hydrolytic enzymes are activated during sprouting leading to the breakdown of starch and non-starch polysaccharides (20). The actions of α - and β -amylases and α -glucosidase result in starch breakdown. These hydrolytic processes produce products (sugars and short-chain carbohydrates) that are perfect for weaning foods as viscosity and digestibility raise along with nutrient absorption.

The sprouted cream bambaranut landrace has the highest protein content, the value $19.93\pm 0.13\%$ is significantly different ($P<0.05$) from those of unsprouted cream landrace as well as the other two landraces (sprouted and unsprouted) (Table 1). Lowest carbohydrate ($45.39\pm 1.50\%$) content was observed in sprouted cream bambaranut landrace, the value differs significantly ($P<0.05$). The

sprouted cream Bambaranut landrace has the highest crude fiber contents ($7.99\pm 0.11\%$) and is significantly ($P<0.05$) different from other landraces irrespective of sprouting or not. Highest crude fat ($15.15\pm 0.07\%$) content was observed in sprouted zebra landrace, the value differs significantly ($P<0.05$) from other landraces. There is no significant difference ($P<0.05$) between fat contents of sprouted black and sprouted cream landrace. The sprouted Black landrace has the highest ash content.

In view of the aforementioned observations, most especially the apparent decrease in moisture contents, increase in ash contents coupled with increased protein and decreased carbohydrate contents, it could be deduced that the effect of sprouting on the proximate parameters of Bambaranut lead to an increases in the nutritional quality. The decrease in moisture content could translate to an increase in shelf life of bambaranut flour. Similarly, increase in protein and the decreased in carbohydrate implies that sprouted bambaranut could be utilized by diabetic patients.

5.2. Minerals

The results of minerals contents of three sprouted and unsprouted landraces of bambaranut are presented in Table 3. The landraces differs significantly in some of the minerals such as Na, Fe, Ca, K, Zn, Mg, Mn, and Se. However, the amount of some minerals did not significantly differ between some landraces irrespective of sprouting or not. For instance the black and zebra landraces have similar Zn and Mn contents. All the three unsprouted landraces have similar Cu contents. Irrespective of the landrace, significant ($P<0.05$) difference was observed in Na, Fe, Ca, K, Zn, Mg, Mn, and Se after sprouting but there was no significant difference in Cu. Overall, sprouting leads to decrease in Na, Fe, K, Zn, Mg and Se and increase in Ca and Mn (Table 4). There is no significant difference ($P<0.05$) in Na and Fe between sprouted black and cream landraces, Zn and Mn between sprouted black and zebra. However, sprouted landraces differed in Ca, K, Mg, and Se. The results of this study showed that the sprouted cream and black landraces have increased in selenium contents while increased in zinc content is observed in black and zebra landraces.

Regulation of the intracellular-extracellular potassium (K^+) gradient is very important for life, acute changes in K^+ plasma levels may lead to fatal consequences. Potassium is a vasodilator, it increases blood flow and decrease in potassium concentration in blood produces vasoconstriction (21). Dietary supplementation and restriction of potassium influence the resistance to blood flow through vascular beds such as cerebral and renal vascular beds (22).

Calcium (Ca) is needed for normal growth, development and maintenance of skeleton (23). Calcium is required in high amount during all stages of life but the requirement is more during growth period for instance childhood, during pregnancy and breast feeding (24). Appropriate intake of calcium causes reduction in hypertension and hypertension disorders related to pregnancy, lowering cholesterol levels, proper muscular contraction, oocyte activation, aiding blood clotting, regulation of heart beat and fluid balance (25). Deficiency of calcium, especially over a long time, can lead to osteoporosis in which the bone deteriorates and there is an increased risk of fractures. Consumption of a well-balanced diet can provide all the necessary nutrients and help prevent calcium deficiency (26).

Magnesium is required for many metabolic reactions as a cofactor, such reactions include protein synthesis, cellular energy production and storage, reproduction, DNA and RNA synthesis, stabilizing mitochondrial membranes among others (27). Magnesium plays a critical role in nerve transmission, cardiac excitability, activation of the immune system, neuromuscular conduction, muscular contraction, vasomotor tone, blood pressure, and glucose and insulin metabolism. Magnesium has multiple functions within the body, therefore potassium plays a major role in disease prevention and overall health, hence the role of magnesium is essential (27). Deficiency of magnesium is associated with a number of chronic diseases such as migraine headaches (28), Alzheimer's disease (29), stroke and hypertension, cardiovascular disease, and type 2 diabetes mellitus (30). Magnesium is found to influence fetal programming and disease presentation in child and adulthood (27) and it is indispensable for the aggregation of ribosomes into polysomes. To be biologically active and be synthesized from ADP, ATP requires magnesium (31).

Manganese is essential micronutrients in human that is principally obtained from the diet (32). It functions primarily as a coenzyme in many biological processes, such as macronutrient metabolism, bone formation, free radical defense systems, and in the brain ammonia clearance and neurotransmitter synthesis. It is found in all tissues and is a critical component of many proteins and enzymes (33). An association has been reported between dietary Mn and glucose metabolism, insufficient dietary Mn impairs insulin secretion and glucose metabolism. However, supplementation of Mn modifies the enzyme profiles of carbohydrate metabolism and improves high-fat-diet-induced beta cell injury and insulin resistance in animal models of diabetes (34). Manganese is a component of metalloproteins such as arginase, acetyl-CoA carboxylase, phosphoenolpyruvate decarboxylase, and pyruvate carboxylase, Mn superoxide dismutase (a mitochondrial

antioxidant), glutamine synthetase and glycosyltransferases (33). Human milk is generally low in Mn (1.8–27.5 µg/L); but concentrations in infant formulas can vary dramatically (33–300 µg/L) (54).

Adequate provision of Fe is essential for the functioning of many biochemical processes including electron transfer reactions, gene regulation, binding and transport of oxygen, and regulation of cell growth and differentiation, DNA synthesis and healthy function and development of brain (35). In a global scale, Fe deficiency is the most prevalent micro nutrient deficiency and a major public health risk in developing and industrialized countries. The deficiency affects more than a billion people of different age groups around the world, it is the common cause of anemia and a common deficiency among non anemic children, especially among children of developing countries (36). Deficiency of iron causes impaired immune function, impaired mental function, impaired physical performance, complications of pregnancy, increased absorption of lead and cadmium, altered drug metabolism, increased insulin sensitivity and fatigue (35).

The increase in selenium observed in cream and black landrace is of interest, selenium is a micronutrient that is necessary in trace amounts for the proper functioning of organisms (37). It has a key importance for maintaining homeostasis of the human system, especially for the proper functioning of the immune system. As a component of glutathione peroxidase, selenium is essentially involved in the protection of cells against the effect of excess H₂O₂, and also plays role in heavy metal detoxification. Selenium is required for proper functioning of the thyroid gland, it induces the occurrence of the selenoprotein synthesis (a process involved in the antioxidant defense mechanism of the organism) and it possesses anticarcinogenic properties against some cancers as well as anti-diabetic activities and reproductive efficiency (38).

Copper has multiple metabolic functions, severe deficiencies are associated with cardiac, bone, immune, and central nervous system problems and must be acquired through the diet and trafficked to the organs, cells, and proteins requiring copper for health (39). It is an indispensable cofactor used for redox reactions involving copper containing oxidases. Copper enzymes regulate various physiologic pathways such as energy production, iron metabolism, connective tissue maturation, and neurotransmission (40). Dietary copper deficiency or overload leads to dysregulation of lipid metabolism.

Zinc is essentially involved in the regulation of many physiological and biochemical events in the organism such as maintenance of integrity of cell

membrane, metabolism of protein, carbohydrate and lipid, recovery from wound injury and in the regulation of a number of other biological processes associated with normal growth and development (41). Zinc acts as a cofactor of many enzymes, at least one enzyme in every enzyme classification (42). Deficiency of Zn in children causes an increase in infection and diarrhea leading to the death of about 800,000 children worldwide yearly (43). Zinc deficiency was also indicated as a risk factor for immune deficiency and hence susceptibility to infection in the elderly (41). Depletion of zinc stores has been reported to be a risk factor of pneumonia in the elderly. Zinc is being considered as prophylactic or adjunct therapy for COVID-19, with 12 clinical trials underway, highlighting the relevance of this trace element for global pandemics (44). Zinc is a cofactor of at least one enzyme in every enzyme classification (43).

6. CONCLUSION

This study showed that sprouting enhances the nutritional quality of bambaranut irrespective of the landrace and could be used to increase the shelf life of foods. Similarly, sprouting could be used in healthy diet preparations. The increase in protein and decreased in carbohydrate contents is an indication that sprouted bambaranut could be utilized by diabetic patients.






7. REFERENCES

- Baryeh EA. Physical properties of bambara groundnuts. *Journal of Food Engineering*. 2001 Mar;47(4):321-6. Available from: [<URL>](#).
- Massawe F, Mwale S, Azam-Ali S, Roberts J. Breeding in bambara groundnut (*Vigna subterranea* (L.) Verdc.): strategic considerations. *African Journal of Biotechnology*. 2005;4(6):463-71.
- Alhassan A, Dangambo M, Abdulmumin T, others. Evaluation of the proximate contents of bambara groundnut *Vigna subterranea* (L.) Verdc grown in MadobiLGA, Kano State, Nigeria. *Brit J Appl Scie Tech*. 2015;8(4):361-5.
- Ghavidel RA, Prakash J. The impact of germination and dehulling on nutrients, antinutrients, in vitro iron and calcium bioavailability and in vitro starch and protein digestibility of some legume seeds. *LWT - Food Science and Technology*. 2007 Sep;40(7):1292-9. Available from: [<URL>](#).
- Roland WSU, Pouvreau L, Curran J, van de Velde F, de Kok PMT. Flavor Aspects of Pulse Ingredients. *Cereal Chemistry Journal*. 2017 Jan;94(1):58-65. Available from: [<URL>](#).
- Nkhata SG, Ayua E, Kamau EH, Shingiro JB. Fermentation and germination improve nutritional value of cereals and legumes through activation of endogenous enzymes. *Food Sci Nutr*. 2018 Nov;6(8):2446-58. Available from: [<URL>](#).
- Association ESS, others. ESSA hygiene guideline for the production of sprouts and seeds for sprouting. ESSA: Brussels, Belgium. 2016;
- Wanyama AW. Evaluation of Phytoconstituents, Antioxidants Potential, Cytotoxic, Antimicrobial Activities and Mineral Composition of *Vigna subterranea* (L) Verdc. Extracts [Internet] [Master's Thesis]. [Kenya]: Jomo Kenyetta University of Agriculture and Technology; 2018. Available from: [<URL>](#)
- Dhaliwal Y, AGGARWAL RK. Composition of fat in soybeans as affected by duration of germination and drying temperature. *Journal of food science and technology (Mysore)*. 1999;36(3):266-7.
- Falmata F, Modu S, Sanda S, Babagana M, Chamba G. Rheological and microbiological assessment of complementary meal produced from sprouted and fermented sorghum (*S. bicolor*) blended with cowpea (*Vigna unguiculata*) and groundnut (*Arachis hypogea*). *Merit Research Journal of Food Science and Technology*. 2014;2(3):31-7.
- Association of Official Analytical Chemists. food composition, additives, natural contaminants. 17th ed. Horwitz W, editor. Arlington, Va: AOAC International; 2000. (Official methods of analysis of AOAC International). ISBN: 978-0-935584-67-7.
- Egan H, Kirk RS, Sawyer R, Pearson D. Pearson's chemical analysis of foods. 8th ed. Edinburgh; New York: Churchill Livingstone; 1981. 591 p. ISBN: 978-0-443-02149-7.
- Nielsen SS. Introduction to the Chemical Analysis of Foods. West Lafayette, Indiana: Purdue University; 2002.
- Christian GD. ANALYTICAL CHEMISTRY, 6TH ED [Internet]. Wiley India Pvt. Limited; 2007. Available from: [<URL>](#)
- USEPA. Metals (Atomic Absorption methods). General procedure for analysis by atomic absorption. USEP; 1983.
- Steve IO, others. Influence of germination and fermentation on chemical composition, protein quality and physical properties of wheat flour (*Triticum aestivum*). *Journal of Cereals and Oil seeds*. 2012;3(3):35-47.
- Atudorei D, Stroe SG, Codină GG. Impact of Germination on the Microstructural and Physicochemical Properties of Different Legume Types. *Plants*. 2021 Mar 22;10(3):592. Available from: [<URL>](#).
- Ibrahim A, Anwar A, Sani M, Ya'u S, Tasi'u A, Sani M, et al. Assessment of antioxidant activity and mineral elements composition of fenugreek seed extract. *Dutse Journal of Pure Applied Sciences*. 2020;6(2):75-84.
- Bau HM, Villaume C, Nicolas JP, Méjean L. Effect of Germination on Chemical Composition, Biochemical Constituents and Antinutritional Factors of Soya Bean (*Glycine max*) Seeds. *J Sci Food Agric*. 1997 Jan;73(1):1-9. Available from: [<URL>](#).
- Rumiyati, James AP, Jayasena V. Effect of Germination on the Nutritional and Protein Profile of Australian Sweet Lupin (*Lupinus angustifolius* L.). *FNS*. 2012;03(05):621-6. Available from: [<URL>](#).

21. Haddy FJ, Vanhoutte PM, Feletou M. Role of potassium in regulating blood flow and blood pressure. *American Journal of Physiology-Regulatory, Integrative and Comparative Physiology*. 2006 Mar;290(3):R546-52. Available from: [<URL>](#).
22. Manger WM, Simchon S, Stier CTJ, Loscalzo J, Jan KM, Jan R, et al. Protective effects of dietary potassium chloride on hemodynamics of Dahl salt-sensitive rats in response to chronic administration of sodium chloride. *Journal of Hypertension [Internet]*. 2003;21(12). Available from: [<URL>](#).
23. Flynn A. The role of dietary calcium in bone health. *Proc Nutr Soc*. 2003 Nov;62(4):851-8. Available from: [<URL>](#).
24. Heaney RP. Absorbability and utility of calcium in mineral waters. *The American Journal of Clinical Nutrition*. 2006 Aug 1;84(2):371-4. Available from: [<URL>](#).
25. Wang X, Chen H, Ouyang Y, Liu J, Zhao G, Bao W, et al. Dietary calcium intake and mortality risk from cardiovascular disease and all causes: a meta-analysis of prospective cohort studies. *BMC Med*. 2014 Dec;12(1):158. Available from: [<URL>](#).
26. Pine C, Adair P, Burnside G, Robinson L, Edwards RT, Albadri S, et al. A new primary dental care service compared with standard care for child and family to reduce the re-occurrence of childhood dental caries (Dental RECUR): study protocol for a randomised controlled trial. *Trials*. 2015 Dec;16(1):505. Available from: [<URL>](#).
27. Fanni D, Gerosa C, Nurchi VM, Manchia M, Saba L, Coghe F, et al. The Role of Magnesium in Pregnancy and in Fetal Programming of Adult Diseases. *Biol Trace Elem Res*. 2021 Oct;199(10):3647-57. Available from: [<URL>](#).
28. WHO. Headache disorders. Fact Sheet #277 [Internet]. WHO; 2012. Available from: [<URL>](#)
29. Barbagallo M, Belvedere M, Di Bella G, Dominguez LJ. Altered ionized magnesium levels in mild-to-moderate Alzheimer's disease. *Magnesium Research*. 2011 Sep;24(3):115-21. Available from: [<URL>](#).
30. Volpe SL. Magnesium in Disease Prevention and Overall Health. *Advances in Nutrition*. 2013 May;4(3):378S-383S. Available from: [<URL>](#).
31. Holm NG. The significance of Mg in prebiotic geochemistry. *Geobiology*. 2012 Jul;10(4):269-79. Available from: [<URL>](#).
32. Rondanelli M, Faliva MA, Peroni G, Infantino V, Gasparri C, Iannello G, et al. Essentiality of Manganese for Bone Health: An Overview and Update. *Natural Product Communications*. 2021 May;16(5):1934578X2110166. Available from: [<URL>](#).
33. Carver PL, editor. *Essential Metals in Medicine: Therapeutic Use and Toxicity of Metal Ions in the Clinic* [Internet]. De Gruyter; 2019 [cited 2023 Feb 8]. Available from: [<URL>](#)
34. Du S, Wu X, Han T, Duan W, Liu L, Qi J, et al. Dietary manganese and type 2 diabetes mellitus: two prospective cohort studies in China. *Diabetologia*. 2018 Sep;61(9):1985-95. Available from: [<URL>](#).
35. Beard JL. Iron Biology in Immune Function, Muscle Metabolism and Neuronal Functioning. *The Journal of Nutrition*. 2001 Feb 1;131(2):568S-580S. Available from: [<URL>](#).
36. Shill KB, Karmakar P, Kibria MG, Das A, Rahman MA, Hossain MS, et al. Prevalence of iron-deficiency anaemia among university students in Noakhali region, Bangladesh. *J Health Popul Nutr*. 2014 Mar;32(1):103-10. PMID: 24847599, PMCID: PMC4089078
37. Kieliszek M, Błażej S. Current Knowledge on the Importance of Selenium in Food for Living Organisms: A Review. *Molecules*. 2016 May 10;21(5):609. Available from: [<URL>](#).
38. Kang D, Lee J, Wu C, Guo X, Lee BJ, Chun JS, et al. The role of selenium metabolism and selenoproteins in cartilage homeostasis and arthropathies. *Exp Mol Med*. 2020 Aug;52(8):1198-208. Available from: [<URL>](#).
39. Committee on Copper in Drinking Water, National Research Council. *Copper in Drinking Water*. National Academies Press; 2000.
40. Hordyjewska A, Popiołek Ł, Kocot J. The many "faces" of copper in medicine and treatment. *Biometals*. 2014 Aug;27(4):611-21. Available from: [<URL>](#).
41. Baltaci AK, Mogulkoc R, Baltaci SB. The role of zinc in the endocrine system. *Pakistan journal of pharmaceutical sciences*. 2019;32(1).
42. McCall KA, Huang C chin, Fierke CA. Function and Mechanism of Zinc Metalloenzymes. *The Journal of Nutrition*. 2000 May;130(5):S1437-46. Available from: [<URL>](#).
43. Hambidge KM, Krebs NF. Zinc Deficiency: A Special Challenge1. *The Journal of Nutrition*. 2007 Apr;137(4):1101-5. Available from: [<URL>](#).
44. Joachimiak MP. Zinc against COVID-19? Symptom surveillance and deficiency risk groups. Lau SKP, editor. *PLoS Negl Trop Dis*. 2021 Jan 4;15(1):e0008895. Available from: [<URL>](#).



Forecasting the Degradation of Vitamin C in Commonly Consumed Vegetable Cabbage (*Brassica oleracea*) Dipped in Different Pre-treatment Solutions

Awagu Emenike Fidelis^{1*} , Okoroafor Henry Chinedu² , Okike Obinna Odii² ,
Daramola Dare Samson² , Arohunmolase Omolara Mary² 

¹Nigerian Stored Products Research Institute, Perishable Crops Research Department, Ilorin, Nigeria

²Nigerian Stored Products Research Institute Perishable Crops Research Department, Port Harcourt, Nigeria

Abstract: Vitamin C is considered an essential vitamin that is commonly found in most fruits and vegetables. It is susceptible to easy degradation, especially during pre-treatment and storage. This study aimed at forecasting the degradation of vitamin C in commonly consumed vegetable (cabbage) dipped in different pre-treatment solutions at different time intervals. The samples after dipping at different time intervals were prepared for analysis. Evaluation of the ascorbic acid content of the vegetable was determined using High-Performance Liquid Chromatography (HPLC). This consists of an isocratic elution procedure with ultraviolet-visible detection at 245 nm. The half-lives and rate constants were calculated using the integrated law method. Forecasts were determined using time series analysis. Degradation of vitamin C in this study followed a first-order kinetic model, and the average coefficient of determination (R^2 -value) was greater than 0.9413. The rate constants of vitamin C degradation for the vegetable dipped in different pretreatment solutions (sodium chloride, sodium benzoate, sodium metabisulfite and vinegar) at different time intervals were 0.0804, 0.1049, 0.0706 and 0.0553 minutes⁻¹; half-lives were 8.2322, 7.3896, 10.9675, and 12.1086 minutes, respectively. The vegetable dipped in different pretreatments for 90 minutes exhibited $\ln(C)$ forecast of -2.2057, -4.6307, -1.1746, and 0.0789, respectively. The coefficient of correlation for sodium chloride, sodium benzoate, sodium metabisulfite, and vinegar are 0.084, 0.093, 0.063 and 0.059 respectively. The kinetic models were formulated using predicted initial contents, processing time, and measured contents. The vegetable dipped in vinegar pretreatment solution using $\ln(C) = \ln(C_0) - 0.0553t$ gave the best model. From the results, the most appropriate pretreatment solution for enhancing the shelf life of cabbage is synthetic vinegar (prepared from acetic acid) because it has a lower rate constant, lower coefficient of correlation, and the longest half-life.

Keywords: HPLC, Cabbage, Pretreatment Solutions, Ascorbic Acid, Rate Constant, Forecast

Submitted: March 31, 2022. **Accepted:** January 12, 2023.

Cite this: Awagu EF, Okoroafor HC, Okike OO, Daramola DS, Arohunmolase OM. Forecasting the Degradation of Vitamin C in Commonly Consumed Vegetable Cabbage (*Brassica oleracea*) Dipped in Different Pre-treatment Solutions. JOTCSA. 10(1):109-16.

DOI: <https://doi.org/10.18596/jotcsa.1093112>.

***Corresponding author. E-mail:** nykefidel@yahoo.com.

1. INTRODUCTION

Vitamin C is water-soluble and is a very important component of a healthy meal (1, 2). The increasing demand for nutritious food has led to several attempts to maximize the retention of nutrients in both processed and stored foods. Vitamin C serves as a quality indicator for other food nutrients especially during processing and storage of foods

because, if vitamin C is well retained, the other nutrients are also well retained (1). Vitamin C is the most unstable vitamin, which easily deteriorates during processing and storage. This can be because of certain variables such as pH (3, 4), temperature (5, 6), light (7, 8), the presence of enzymes (9, 10), hydrogen peroxide (11), and metallic catalysts (12-14).

Cabbage is a very essential and highly rated leafy vegetable, which contains minerals, vitamins, and alkaline salts. It is medicinal because of its wonderful cleansing properties such as the detoxification of reactive oxygen species (ROS) in the body (15). It contains tartronic acid which inhibits fat formation and other elements which enhance the body's immunity, slows down aging, inhibits cancer formation, and estrogenic activities. Cabbage is a very good source of vitamin C (16). The body cleansing properties of cabbage is because of a high content of ascorbic acid and sulfur-containing glucosinolates, anthocyanins, flavonoids, and other useful plant metabolites (17). Hydrolytic products of glucosinolates are responsible for the prevention of oxidative stress, induction of detoxification enzymes, stimulation of the immune system and the reduction of cancer risk (18).

Sodium chloride solution inhibits polyphenol oxidase (PPO), thereby preventing browning of fruits and vegetable products (19). Benzoic acid and its salts are very common preservatives, which inhibits an enzyme in the citric acid cycle of microorganisms. These pretreatment solutions function effectively under highly acidic conditions. They inhibit the activities of yeasts, mold, and microorganisms producing aflatoxins, but are not too effective against bacteria (20). The chemical preservative such as sodium metabisulfite is effective in the control of pathogenic bacteria causing food poisoning and infection (21). Research revealed that vinegar had the highest effect on the bacterial load of vegetables. This might be due to the acidic pH of vinegar, and some microorganisms cannot withstand acidic conditions (22).

Thermal processing is a traditional method for pretreating fruits and vegetables, and this includes drying, cooking, and blanching. However, ascorbic acid (vitamin C) is one of the key vitamins and it is highly susceptible to degradation and this is influenced by several factors such as high temperature, oxygen, and light (23, 24). Understanding the mechanism through which vitamin C is degraded during food processing is an essential tool in the regulation of the parameters needed to improve vitamin C retention. Additionally, understanding the degradation kinetics and various kinetic models is crucial in forecasting vitamin C loss and change in quality under certain processing conditions. Kinetic modeling enables us to quantify these changes and the rate at which they occur. It also aids us in understanding fundamental reaction mechanisms required for quality control and modeling. Vitamin C degradation kinetics in modeled systems follows first-order kinetics; but is very complex in food systems (25). This complexity as observed in food systems hinders the formulation of suitable mechanistic models. To get a good fit for the experimental data, pseudo-kinetic models, such as zero-order, first-order, or second-order kinetics, are

commonly used. The model that produces the highest coefficient of determination value (R^2) is considered the best fit for the analysis.

A time series analysis comprises of formulating a model that represents a time series and deploying the same in forecasting future values. The present study aimed at determining the rate of degradation of vitamin C in cabbage dipped in different pretreatment solutions, to recommend the best; development of kinetic models for forecasting the degradation of vitamin C in cabbage under the studied conditions; and to forecast future values.

2. MATERIALS AND METHODS

Metaphosphoric acid, L-ascorbic acid, orthophosphoric acid, and acetonitrile (High-Pressure Liquid Chromatography (HPLC)-Grade) were all purchased from Merck (Darmstadt, Germany). De-ionized water of 18 M Ω cm⁻¹ resistivity purified with a milli-Q system (Millipore, Bedford, MA, USA) was used for chromatographic analysis; ascorbic acid stock standard solution kept inside a glass-stoppered bottle (26).

Freshly cut vegetable (cabbage) weighing 4.5 kg, was washed with clean water, and drained using a clean muslin cloth. Stems were removed with a clean, sharp knife. The weighed cabbage leaves of 4.5 kg were divided into 9 lots of 100 g each and dipped differently into 2 liters of water containing 0.6 g each of sodium chloride (27.3 \pm 0.92 °C), sodium benzoate (26.8 \pm 0.64 °C) and sodium metabisulfite (27.9 \pm 0.18 °C) for 5, 10, 15, 20, 25, 30, 35 and 40 minutes, respectively. Also 100 g of the cabbage was dipped into 2 liters of water containing 100 mL of vinegar at various time intervals. The dipped leaves at the completion of time in the pretreatment solutions were immediately ran under running tap water for 30 seconds to stop further effects of the pretreatments. They were then drained differently for 2 minutes using a clean muslin cloth. The initial sample was blended using a Kenwood blender (Philips, HR 1702, Borehamwood, England, UK) and then filtered using cheese cloth. HPLC was used to determine the initial ascorbic acid degradation using the liquid extract, before dipping into pretreatment solutions. The mobile phase employed was a mixture of 0.5% NaH₂PO₄ (pH 2.25 with H₃PO₄)-acetonitrile (93:7). Flow rate of the mobile phase was 1.2 cm³min⁻¹ and an injection volume of 20 μ L was used in the quantitative analysis. The temperature of analytical column was kept constant at 25 °C. The remaining samples were spread evenly on labeled trays and kept under a room temperature range of 25 - 29 °C and relative humidity range of 50 - 61 % using a thermometer and hygrometer. The sample without any form of treatment was used as the experimental control. At the end of the drying period, the samples were blended, sieved, and the liquid extract (1 g of each sample to 25 mL of extractant containing 5 % metaphosphoric acid

(MPA) at 10 °C and in the dark) was used in determining the final rate of degradation of ascorbic acid. All extractions were carried out in triplicate and obtained solutions were then filtered and stored at 4 °C before analysis. The injection of the extracts into HPLC system was performed twice.

2.1. Kinetic Modeling

Integrated rate law was used in modeling the degradation of vitamin C and various models were formulated using the integral method of analysis. The integral law equation is as follows (27):

$$\frac{dC}{dt} = -K[C]^n \quad (1)$$

This was used to formulate three models based on concentration (order of reaction $n = 0, 1$ and 2) and their half-lives ($t_{1/2}$).

Zero order model ($n = 0$):

$$C = C_0 - kt \quad (2)$$

$$t_{\frac{1}{2}} = \frac{C_0}{2k} \quad (3)$$

First order model ($n = 1$):

$$\ln(C) = \ln(C_0) - kt \quad (4)$$

$$\left(t_{\frac{1}{2}}\right) = \ln\left(\frac{2}{k}\right) \quad (5)$$

Second order model ($n = 2$):

$$\frac{1}{c} = \frac{1}{C_0} + kt \quad (6)$$

$$t_{\frac{1}{2}} = \frac{1}{kC_0} \quad (7)$$

Where, k = rate constant

C_0 = initial concentration of vitamin C in sample

C = concentration of vitamin C in sample at time t

$t_{1/2}$ = half-life of vitamin C in sample

3. RESULTS

Table 1 presents concentrations (mg/100 g) of vitamin C in cabbage dipped in different time intervals in sodium chloride, sodium benzoate, sodium metabisulfite, and vinegar, respectively, indicating a decrease in vitamin C with an increase in time in all the pre-treatment solutions.

Table 2 shows that R^2 and R^2 adjusted increased in value as P-values decreased with increasing time. The p-value continually tends to zero as the R^2 value increases. This implies that vitamin C degradation kinetics for cabbage dipped in different pre-treatment solutions may be best described by first order kinetics.

Table 3 shows pretreatment solutions, temperature of the pre-treatments, rate constants, half-life, and proposed model. The lower the rate constant, the lower the degradation of vitamin C.

Table 1: Vitamin C degradation in cabbage dipped in different pretreatment solutions.

Time (min)	NA Vit.C (mg/100 g)	SB Vit.C (mg/100 g)	SM Vit.C (mg/100 g)	VIN Vit.C (mg/100 g)
5	128.80	37.23	80.01	150.09
10	80.81	31.57	69.77	75.79
15	35.08	28.92	59.78	68.46
20	27.43	14.78	48.69	54.89
25	20.73	11.47	35.97	45.23
30	19.19	6.99	25.77	37.86
35	9.37	2.89	17.25	21.08
40	5.16	1.41	7.33	14.25

$n = 3$ (triplicate), NA: sodium chloride SB; sodium benzoate, SM: sodium metabisulfite, VIN: vinegar

Table 2: Kinetic model regression analysis for cabbage dipped in different pretreatment solutions.

Pretreatment	R^2	R^2 Adjusted	P-value
NA	0.946726	0.936071	0.000227
SB	0.958414	0.950097	0.000122
SM	0.925188	0.910226	0.000534
VIN	0.934826	0.921791	0.000377

Table 3: Rate constant kinetic model regression analysis for cabbage dipped in different pretreatment solutions.

PT	Temp (°C)	k (min ⁻¹)	Half-Life (min)	Proposed model
NaCl	27.3 ± 0.92	0.0804	8.2322	$\ln(C) = \ln(C_0) - 0.0804t$
SB	26.8 ± 0.64	0.1049	7.3896	$\ln(C) = \ln(C_0) - 0.1049t$
SM	27.9 ± 0.18	0.0706	10.9675	$\ln(C) = \ln(C_0) - 0.0706t$
VIN	27.4 ± 0.19	0.0553	12.1086	$\ln(C) = \ln(C_0) - 0.0553t$

Figure 1 presents first-order kinetics for cabbage dipped in different pre-treatment solutions, showing that the rate of degradation at any time is

dependent on the initial concentration of vitamin C in the vegetable.

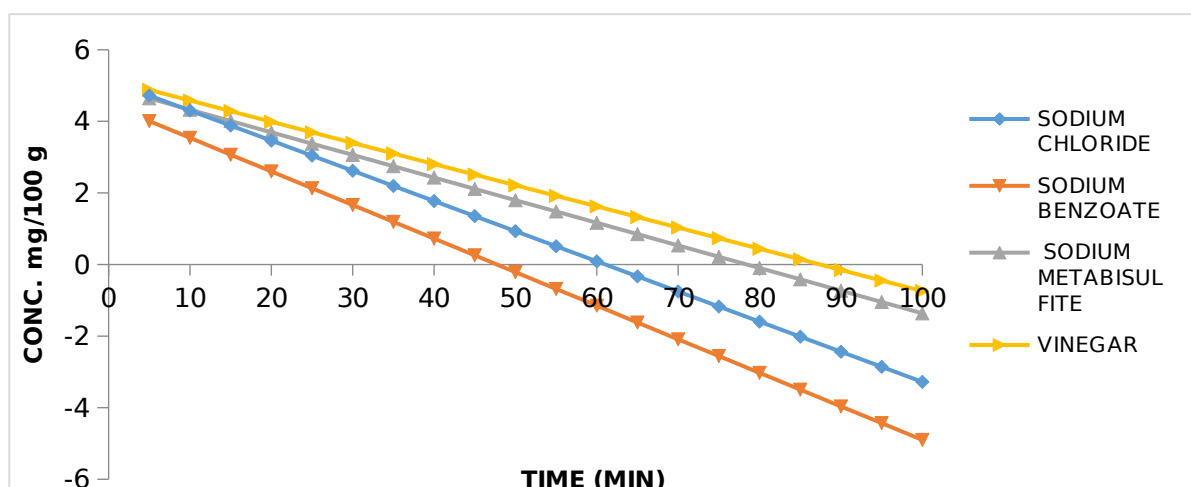


Figure 1: Plot of first-order kinetics for cabbage dipped in different pretreatment solutions.

Table 4: First-order kinetics Trendline equation and R Squared value for cabbage dipped in different pretreatment solutions.

Cabbage Dipped in Solutions	Y intercept	R Square
Sodium Chloride	$-0.084x + 5.143$	0.963
Sodium Benzoate	$-0.093x + 4.474$	0.939
Sodium Metabisulfite	$-0.063x + 4.956$	0.913
Vinegar	$-0.059x + 5.171$	0.953

The coefficient of correlation for sodium chloride, sodium benzoate, sodium metabisulfite and vinegar are 0.084, 0.093, 0.063 and 0.059 respectively (Figure 1). $0.059 < 0.063 < 0.084 < 0.093$. This implies that vitamin C in cabbage dipped in vinegar solution was more stable than vitamin C in cabbage dipped in the other pre-treatments.

Figure 2 presents cabbage dipped in different pre-treatment solutions and the forecasted shelf-life. Cabbage dipped in vinegar was preferred among others. From the time series forecast analysis, it can be deduced that vitamin C is more stable in cabbage dipped in vinegar solution because it has the least coefficient of correlation (0.059).

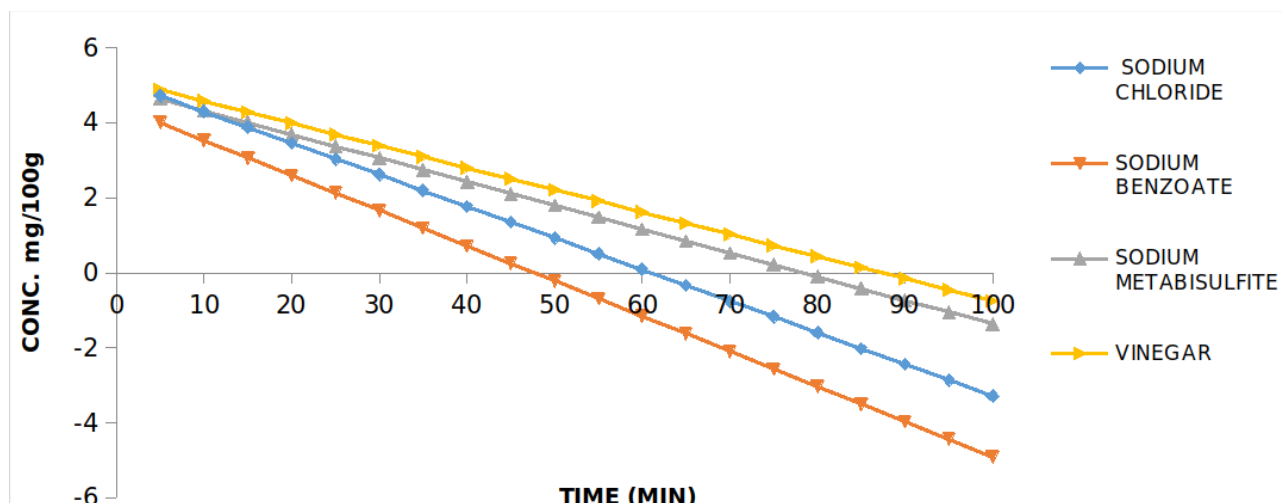


Figure 2: Plot of time series forecast analysis for cabbage dipped in different pre-treatment solutions.

Table 5: First-order kinetics Forecast Trendline equation and R Squared value for cabbage dipped in different pretreatment solutions.

Cabbage Dipped in Solutions	Y intercept	R Square
Sodium Chloride	-0.084x + 5.143	1
Sodium Benzoate	-0.093x + 4.474	1
Sodium Metabisulfite	-0.063x + 4.956	1
Vinegar	-0.059x + 5.171	1

4. DISCUSSION

Table 1 shows the variations in ascorbic acid concentration of cabbage dipped in different pretreatment solutions at different time intervals during processing and storage. Table 2 is a summary of kinetic model regression analysis results, and Table 3 shows vitamin C first-order kinetics degradation of cabbage dipped in the different pretreatment solutions. In Table 1, it was observed that the concentration of vitamin C in cabbage steadily decreased with increasing time. This reveals that vitamin C in the vegetable dipped in different pretreatment solutions degrade with time during processing and storage. Vitamin C concentration of cabbage decreased with time during processing and storage, but in varying degrees, and this was influenced by the different processing and storage methods (25). This concurs with some previously reported research findings on citrus and strawberry fruit juices (28, 29), and it also conforms to the degradation kinetics of vitamin C in model systems (16). The kinetic plots of the model (Eq. 4) in Figure 1 reveal that the first-order model was the best fit at different times. The goodness of fit data in Table 2 confirms this. Their R^2 values were the highest and p -values the lowest with different pretreatments. The first-order kinetic model showed a good fit for vitamin C degradation of most materials dipped in NaCl and has been utilized by several researchers (30-33). This was confirmed for NA from Table 2, R^2 :

0.946726, p -value: 0.000227. Thus, first-order kinetics best describes the vitamin C degradation kinetics in the vegetable dipped in 0.3 g/L of each sodium chloride, sodium benzoate, sodium metabisulfite and 50 mL/L of vinegar pretreatments. The model with maximum R^2 and the minimum p -value is considered the best (34, 35). Furthermore, from Table 3, the rate constant of the vegetable sample dipped in vinegar exhibited the lowest rate constant of 0.0592 minutes⁻¹, indicating less degradation. Since the magnitude of the rate constant reveals the rate of reaction, it therefore shows that degradation of vitamin C occurred faster in those samples dipped at an increased time. In other words, the rate of degradation at any given time depends on the initial concentration of vitamin C in the vegetable. Additionally, the processing pretreatment solutions had an average mild temperature of 27.35 °C as shown in Table 3. An increase in storage temperature is therefore believed to result in an increase in the losses of vitamin C in the stored products (36, 5, 23, 37). The post-harvest losses of vegetables can be greatly reduced by extending their shelf-life (8). This trend as clearly revealed in the half-life of the samples in Table 3 supports these facts. The cabbage vegetable dipped in vinegar had the longest half-life of 12 minutes and 11 seconds. The product shelf life is often determined by the decrease of ascorbic acid concentration to industrially unacceptable levels (38). Again, from Figure 2, the $\ln(C)$ forecast

dipped for 90 minutes and exhibited -2.2057, -4.63069, -1.17463, and 0.078902 showing that vinegar richer in vitamin C. From Table 3, the kinetic models formulated using the predicted initial contents, the processing time, and measured contents, dipped in vinegar pretreatment solution with the model; $\ln(C) = \ln(C_0) - 0.0553t$ gave the best model.

Ascorbic acid is often used as the most common nutrient loss indicator during storage. The retention of ascorbic acid in food products is a reliable representative index during the processing of foods (36, 24). The proposed simulation model monitors the degradation of vitamin C (ascorbic acid) in cabbage and expresses the advantages of the computer simulation technique over the laboratory chemical analysis.

5. CONCLUSION

This work developed models in which the experimental variable can be imputed, and the desired results were computed for a better understanding of the vitamin C values and to make accurate predictions of different outcomes, regarding their shelf-life. Additionally, the models enable appropriate forecasting in agricultural produce. It also produces value-added products by slowing down or inhibiting chemical deterioration and microbial growth. All these absolutely support and authenticate that rate constant is the major determining factor in accessing the degradation of commonly consumed vegetables, which cabbage dipped in vinegar signified lesser degradation. The retention of ascorbic acid in cabbage after dipping in vinegar pre-treatment solution is a suitable indicator for the retention of other nutrients in cabbage.

6. REFERENCES

- Szczuko M, Migrała R, Drozd A, Banaszczak M, Maciejewska D, Chlubek D, et al. Role of water soluble vitamins in the reduction diet of an amateur sportsman. *Open Life Sciences*. 2018 May 18;13(1):163-73. Available from: [<URL>](#).
- Devaki SJ, Raveendran RL. Vitamin C: Sources, Functions, Sensing and Analysis. In: Hamza AH, editor. *Vitamin C* [Internet]. InTech; 2017 [cited 2023 Feb 20]. Available from: [<URL>](#)
- Farah HS, Alhmoud JF, Al-Othman A, Alqaisi KM, Atoom AM, Shadid K, et al. Effect of pH, temperature and metal salts in different storage conditions on the stability of vitamin C content of yellow bell pepper extracted in aqueous media. *Systematic Reviews in Pharmacy*. 2020;11(9):661-7.
- Doseděl M, Jirkovský E, Macáková K, Krčmová L, Javorská L, Pourová J, et al. Vitamin C—Sources, Physiological Role, Kinetics, Deficiency, Use, Toxicity, and Determination. *Nutrients*. 2021 Feb 13;13(2):615. Available from: [<URL>](#).
- Essodolom P, Chantal BE, Mamatchi M, Kous'anta A. Effect of temperature on the degradation of ascorbic acid (vitamin c) contained in infant supplement flours during the preparation of porridges. *Int J Adv Res*. 2020;8(3):116-21.
- Herbig AL, Renard CMGC. Factors that impact the stability of vitamin C at intermediate temperatures in a food matrix. *Food Chemistry*. 2017 Apr;220:444-51. Available from: [<URL>](#).
- Nakilcioğlu-Taş E, Ötleş S. Kinetic modelling of vitamin C losses in fresh citrus juices under different storage conditions. *An Acad Bras Ciênc*. 2020;92(2):e20190328. Available from: [<URL>](#).
- Pathy K. Process for preparation of vitamin C and method for determination of vitamin c in tablets. *SF J Chem Res*. 2018;2(1):1-17.
- Attila Szócs, Vancea S, Kiss I, Donáth-Nagy G. Quantification of Plasma and Leukocyte Vitamin C by High Performance Liquid Chromatography with Mass Spectrometric Detection. *J Anal Chem*. 2020 Sep;75(9):1168-76. Available from: [<URL>](#).
- Özkan M, Kirca A, Cemeroğlu B. Effects of hydrogen peroxide on the stability of ascorbic acid during storage in various fruit juices. *Food Chemistry*. 2004 Dec;88(4):591-7. Available from: [<URL>](#).
- Yin X, Chen K, Cheng H, Chen X, Feng S, Song Y, et al. Chemical Stability of Ascorbic Acid Integrated into Commercial Products: A Review on Bioactivity and Delivery Technology. *Antioxidants*. 2022 Jan 13;11(1):153. Available from: [<URL>](#).
- Miftari H. Effect of drying in the preservation of apple and its vitamin C content. *International Journal of Food Technology and Nutrition*. 2021;4(7-8):44-8. Available from: [<URL>](#).
- Shen J, Griffiths PT, Campbell SJ, Uttinger B, Kalberer M, Paulson SE. Ascorbate oxidation by iron, copper and reactive oxygen species: review, model development, and derivation of key rate constants. *Sci Rep*. 2021 Apr 1;11(1):7417. Available from: [<URL>](#).
- Farah HS, Alhmoud JF, Al-Othman A, Alqaisi KM, Atoom AM, Shadid K, Shakya A, AlQaisi T. Effect of pH, Temperature and Metal Salts in Different Storage Conditions on the Stability of Vitamin C Content of Yellow Bell Pepper Extracted in Aqueous Media. *Sys Rev Pharm*. 2020; 11(9):661-7.
- Morales-López J, Centeno-Álvarez M, Nieto-Camacho A, López MG, Pérez-Hernández E, Pérez-Hernández N, et al. Evaluation of antioxidant and hepatoprotective effects of white cabbage essential oil. *Pharmaceutical Biology*. 2017 Jan 1;55(1):233-41. Available from: [<URL>](#).
- Hailemariam GA, Wudineh TA. Effect of Cooking Methods on Ascorbic Acid Destruction of Green Leafy Vegetables. *Journal of Food Quality*. 2020 Mar 9;2020:1-5. Available from: [<URL>](#).
- Kapusta-Duch J, Kopec A, Piatkowska E, Borczak B, Leszczynska T. The beneficial effects of Brassica vegetables on human health. *Roczniki Państwowego Zakładu Higieny*. 2012;63(4):389-95.
- Sanlier N, Guler S. The benefits of Brassica vegetables on human health. *J Hum Health Res*. 2018;1(1):1-13.
- Ma Y, Wang H, Yan H, Malik AU, Dong T, Wang Q. Pre-cut NaCl solution treatment effectively inhibited the

- browning of fresh-cut potato by influencing polyphenol oxidase activity and several free amino acids contents. *Postharvest Biology and Technology*. 2021 Aug;178:111543. Available from: [<URL>](#).
20. Oladapo A, Akinyosoye F, Abiodun O. The inhibitory effect of different chemical food preservatives on the growth of selected food borne pathogenic bacteria. *African Journal of Microbiology Research*. 2014;8(14):1510-5.
21. Kim C, Wilkins K, Bowers M, Wynn C, Ndegwa E. Influence of Ph and Temperature on Growth Characteristics of Leading Foodborne Pathogens in a Laboratory Medium and Select Food Beverages. *Austin Food Sci*. 2018;3(1):1031. Available from: [<URL>](#).
22. Xiao HW, Bai JW, Sun DW, Gao ZJ. The application of superheated steam impingement blanching (SSIB) in agricultural products processing - A review. *Journal of Food Engineering*. 2014 Jul;132:39-47. Available from: [<URL>](#).
23. Nwakaudu M, Nkwocha A, Madu I, Enwereji C, Ireaja I. Kinetic modeling of vitamin C (ascorbic acid) degradation in tomato and pawpaw under market storage conditions. *International Journal of Current Research*. 2015;7(6):16783-8.
24. Burdurlu HS, Koca N, Karadeniz F. Degradation of vitamin C in citrus juice concentrates during storage. *Journal of Food Engineering*. 2006 May;74(2):211-6. Available from: [<URL>](#).
25. Derossi A, De Pilli T, Fiore AG. Vitamin C kinetic degradation of strawberry juice stored under non-isothermal conditions. *LWT - Food Science and Technology*. 2010 May;43(4):590-5. Available from: [<URL>](#).
26. Awagu EF, Ekanem EO, Kolo AM, Adamu MM. Kinetic Modeling of Vitamin C (Ascorbic Acid) Degradation in Blanched Commonly Consumed Salad Vegetables Using Computer Simulation Analysis. *IOSR JAC*. 2017 Apr;10(04):59-66. Available from: [<URL>](#).
27. Blasco R, Esteve MJ, Frígola A, Rodrigo M. Ascorbic acid degradation kinetics in mushrooms in a high-temperature short-time process controlled by a thermoresistometer. *LWT - Food Science and Technology*. 2004 Mar;37(2):171-5. Available from: [<URL>](#).
28. Frías JM, Oliveira JC. Kinetic models of ascorbic acid thermal degradation during hot air drying of maltodextrin solutions. *Journal of Food Engineering*. 2001 Mar;47(4):255-62. Available from: [<URL>](#).
29. Zheng H, Lu H. Effect of microwave pretreatment on the kinetics of ascorbic acid degradation and peroxidase inactivation in different parts of green asparagus (*Asparagus officinalis* L.) during water blanching. *Food Chemistry*. 2011 Oct;128(4):1087-93. Available from: [<URL>](#).
30. Mitra J, Shrivastava SL, Srinivasa Rao P. Vacuum dehydration kinetics of onion slices. *Food and Bioprocess Processing*. 2011 Jan;89(1):1-9. Available from: [<URL>](#).
31. Silva EM, da Silva JS, Pena RS, Rogez H. A combined approach to optimize the drying process of flavonoid-rich leaves (*Inga edulis*) using experimental design and mathematical modelling. *Food and Bioprocess Processing*. 2011 Jan;89(1):39-46. Available from: [<URL>](#).
32. Leong SY, Oey I. Effect of endogenous ascorbic acid oxidase activity and stability on vitamin C in carrots (*Daucus carota* subsp. *sativus*) during thermal treatment. *Food Chemistry*. 2012 Oct;134(4):2075-85. Available from: [<URL>](#).
33. Wawire M, Oey I, Mathooko F, Njoroge C, Shitanda D, Hendrickx M. Thermal Stability of Ascorbic Acid and Ascorbic Acid Oxidase in African Cowpea Leaves (*Vigna unguiculata*) of Different Maturities. *J Agric Food Chem*. 2011 Mar 9;59(5):1774-83. Available from: [<URL>](#).
34. Talukder S, Khalequzzaman KM, Chowdhury MNA, Khuda SMKE, Masudalam Md. Prepackaging, storage losses and physiological changes of fresh bitter melon as influenced by Post Harvest Treatments. *Journal of Biological Science*. 2004; 4(5):613-5.
35. Giannakourou MC, Taoukis PS. Kinetic modelling of vitamin C loss in frozen green vegetables under variable storage conditions. *Food Chemistry*. 2003 Oct;83(1):33-41. Available from: [<URL>](#).
36. Bhardwaj RL, Pandey S. Juice Blends—A Way of Utilization of Under-Utilized Fruits, Vegetables, and Spices: A Review. *Critical Reviews in Food Science and Nutrition*. 2011 Jul;51(6):563-70. Available from: [<URL>](#).
37. Cvetkovic B, Jokanovic M. Effect of preservation method and storage condition on ascorbic acid loss in beverages. *Acta per tech*. 2009;(40):1-7. Available from: [<URL>](#).



Applications of New Generation Solvents for Extraction of Herbal Products prior to Atomic and Molecular Analysis

Selin IŞIK^{1*} , Abdullahi Garba USMAN¹ 

¹Near East University, Department of Analytical Chemistry, North Cyprus, Mersin-10, 99138, Turkey.

Abstract: In this review, an up to date and current knowledge of some of the green solvents, which includes supercritical fluids extraction (SFE), switchable polarity solvents (SPS), and natural deep eutectic solvents (NADES) are discussed with more emphasis on the extraction of active components of herbal products. Different scientific articles and books have been researched and reviewed to explain the applications of new generation solvents for extraction of herbal products prior to atomic and molecular analysis from the past until now. Currently, the most of techniques used in processing herbal products involve the use of extraction methods. Therefore, trends in extraction methods focuses mainly on finding reasonable solutions that minimizes the use of toxic solvents and allows the usage of renewable and green solvents from natural products, which ensure high quality and safe extracts. In future, SFE is definitely going to be on the industrial scale due to its numerous applications in the large scale especially for herbal, food, cosmetics and pharmaceutical products etc.

Keywords: Extraction; natural deep eutectic solvents (NADES); new generation solvent; supercritical fluids extraction (SFE); switchable polarity solvents (SPS). September 22, 2022 January 19, 2023 Işık S, Usman AG. Applications of New Generation Solvents for Extraction of Herbal Products Prior to Atomic and Molecular Analysis. JOTCSA. 2023;10(1):117-28. <https://doi.org/10.18596/jotcsa.1178753> Phone: +905338253139.

1. INTRODUCTION

The separation between molecular analysis and atomic analysis, which are regarded as two distinct and extremely divergent areas, has existed in analytical chemistry for many years. As a matter of fact, the tools and extraction techniques created for atomic analysis—which inevitably need vaporization, atomization, and occasionally even ionization—are extremely different from those used for molecular analysis, and the spectra seen in both situations show considerable differences (1). However, given the different types of works that connect these two disciplines nowadays, such a division needs to be reevaluated. High-resolution continuum source atomic absorption spectrometers (HR-CS-AAS), which use either flame (F) or graphite furnace atomizers (GF), have considerably revolutionized the science of atomic absorption (2). As the concept of using continuum sources instead of line sources for AAS can be virtually traced back to the invention of the technology, several devices have been developed based on such concepts (3). Molecular analysis is regarded as a laboratory procedure that entails the examination of various sample materials, including food, herbals, cells, tissues, and environmental samples, for the identification of various target analytes at a molecular level using various analytical techniques,

including high performance liquid chromatography (HPLC) and gas chromatography (GC), using different detectors (4).

Generally, major industrial and conventional chemical processes involve the use of flammable, toxic, volatile, hazardous, and environmentally destructive solvents in chemical reactions and separation processes (1). These have a negative impact on the economic and environmental performance of such processes (2). Conventional or classical extraction methods are also time-consuming, laborious, and involve large amounts of energy-consuming solvents such as alcohols, chloroalkanes, and other hydrocarbons (3). Therefore, since most bioactive components are water-insoluble, this can ultimately aggravate the degradation of some target analytes (4). It is worthy of note that, despite the use of high amounts of solvents and high energy consumption, the yield is also lower in comparison to the alternatives (5). Therefore, a few decades ago, safer, effective extraction methods in accordance with a sound compromise of their environmental, economic, and social requirements began to be considered as replacements (6).

Green chemistry as a concept was first introduced in 1991 by PT Anastas when he launched a unique

program in order to implement sustainable development in the area of chemical technology (7).

Green chemistry has 12 principles which serve as guidelines for designing chemical products and methods (8,9) that reduce or occasionally remove the application and generation of harmful and hazardous chemical materials altogether by using solvents and chemicals that are entirely non-toxic to human health as well as the immediate environment in order to design and create effective and non-hazardous methods facilitating the use of renewable solvents known as 'new generation solvents' or 'solvents of the future' (10). Gu and Jerome proposed the first requirements for a solvent and a process to be considered green based on their availability, biodegradability, flammability, grade, performance, price, recyclability, renewability, stability, storage, toxicity, and synthesis (11). There is no doubt that these are reasonable and sound conditions (12).

Nevertheless, it can also cause a dilemma regarding classifying a solvent as a green solvent, because in most cases, a solvent cannot fulfill all these parameters. For example, a solvent can fulfill eleven or ten or nine out of the total twelve conditions of a green solvent (13). Therefore, can this solvent still be regarded as green? It is therefore crucial to be precise regarding the meaning of these green solvents. The term itself can therefore be misleading due to its novelty and relative nature (14). Though Warner and Anastas defined "green chemistry" as a process of reducing the toxicity and hazards of processes or methods, they did not define it as a method that does not cause any damage or harm (15). Therefore, a solvent can be considered green if it is 'greener' when compared with the current classical solvent to be replaced, which can be supported with clear and strong evidence (1). In almost all cases, the choice will be based on a compromise between different conditions, as seen in Figure 1 below (17,18).

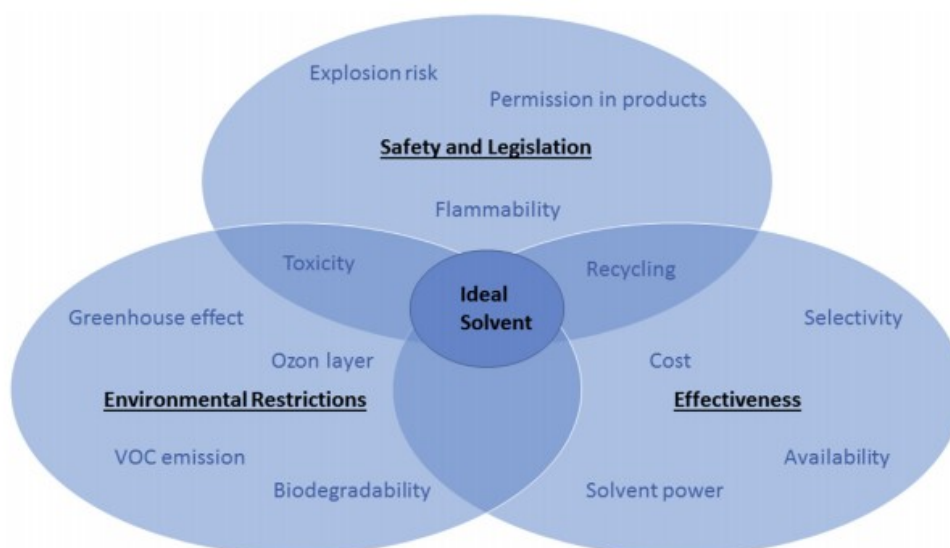


Figure 1: An ideal solvent is a combination and involves a compromise of different and multitude requirements (Adapted from Chemat *et al.* (11)).

These are termed "new generation solvents" owing to their tunable properties, which may prove to be a class of solvents that offer energy and material efficiency greater than existing solvents that need further exploitation to improve their application as a green chemical process (19).

Finally, given their limited context, there is a need to use their applicability in micro-extraction methods, particularly for switchable polarity solvents (SPS) (20).

In conclusion, the aim of this review is to show some applications and wide extraction methods using new generation solvents for herbal products prior to atomic and molecular analysis (21). In this regard, atomic analysis entails the identification and characterization of various sample materials,

particularly environmental, cosmetic, food, and herbal samples, for the identification, isolation, and confirmation of analytes at the elemental state via atomization using various analytical techniques such as FAAS and inductively coupled plasma mass spectrometry (ICP-MS). While molecular analysis is considered a laboratory procedure that involves the study of different sample materials such as food, herbals, cells, tissue, and environmental samples for the identification of various target analytes at a molecular level using different analytical techniques such as HPLC and GC using different detectors.

2. SOLVENT-FREE SYSTEM

Sometimes the best solvent is no solvent at all. A solvent-free system completely satisfies the 5th

condition of green chemistry. Numerous studies have shown that there is an abundance of industrial and chemical processes in which the use of solvents is completely avoided (22). However, this is not always possible. Especially if the absence of the solvent leads to dangerous overheating or results in a higher demand for energy (23). Therefore, these disadvantages would definitely surmount the advantages of using a non-solvent system (solvent-free process). Some decades ago, scientists tried synthesizing polymers using solvent-free conventional reactions (24). It is indeed notable that some industrial polymerizations have succeeded in using solvent free methods in synthesis as well as in separation, such as solid state polymerization and melt polymerization (25). For example, PET is produced commercially through melt polymerization and then followed by the solid state polymerization method (26). It is possible to produce polymers, for example poly (phenylene vinylene), by ensuring that there is close contact among the molecules of the starting materials for about five minutes in the ball milling process (27). This ball milling process is not only used in polymer science, but also has diverse applications in organic synthesis (28). Apart from avoiding the use of organic solvents, it

also has numerous advantages, such as a reduction in reaction time and high energy efficiency (29). As far as the solvent-free process is concerned, mentioning the solvent-free microwave extraction method is significant, which is a well-designed technique introduced by Lucchesi and his group in the year 2004 (30). This sophisticated method can be applied to extracting essential oils from fresh plant material in a microwave-assisted dry distillation process (31). It is a quick, robust, and sensitive method that gives a strong alternative to the time-consuming and long-lasting conventional hydro-distillation method (32).

3. SUPERCRITICAL FLUID EXTRACTIONS

These are substances which exist as a single phase above their critical points of temperature and pressure (33). This critical point can be defined as the point at which liquid and vapor can be distinguished without the need for boundaries (34). For example, the supercritical point of water was discovered to be 374 °C and 22.7 MPa C (Figure 2A), while the supercritical point of CO₂ was discovered to be 31 °C and 7.3 MPa C (Figure 2B) (35).

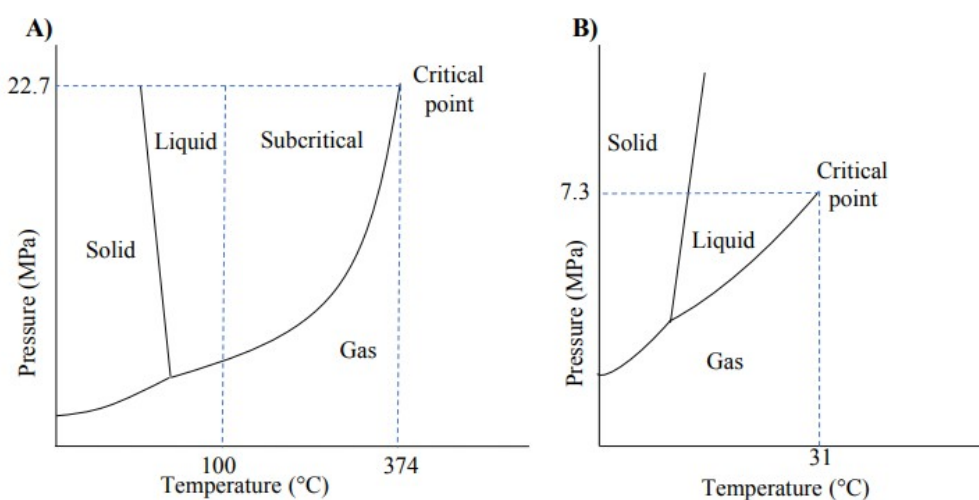


Figure 2: Phase diagram of water and CO₂ (Adapted from Lucchesi et al., 2004 (35)).

Due to their tunable properties of low viscosity (gas-like) and high density (liquid-like), these are considered to be important new generation solvents that improve solubility and mass transfer properties (36). The properties of certain supercritical fluids are mentioned in Table 1. In analytical chemistry, supercritical propane-butane, water, ammonia, and CO₂ have also been used. Because of its low critical temperature and pressure (31 °C and 7.3 MPa), inertness, purity, non-toxicity, and availability, CO₂ is the most widely used supercritical fluid. Furthermore, the strength of **supercritical carbon dioxide** (scCO₂) solvation can be adjusted by changing the temperature and pressure (37).

Another benefit of CO₂ is that it is gaseous at room temperature and pressure, making active product recovery relatively quick and cheap, as well as the ability to produce solvent-free extracts. scCO₂'s ability to operate at low temperatures while using a non-oxidizing medium is also advantageous for sample processing of medicinal, food, biological, and natural products, as it allows for the extraction of thermally labile or readily oxidized compounds with minimal degradation. scCO₂ has solubilizing properties similar to n-hexane and n-heptane due to its low dielectric constant and dipole moment near to zero. Due to charge isolation and its electronic composition, it has a quadrupole moment, allowing it to behave as both a Lewis acid and a Lewis base. Despite having a quadrupole

moment, ScCO₂ acts like a nonpolar solvent, limiting its use in removing hydrophilic analytes. A polar modifier or (co-solvent) is normally applied to tune the polarity and increase the solvating ability to address this constraint. Chemical solvents such

as methanol, ethanol, and ethyl acetate are applied to ScCO₂ in small amounts (1-20 vol percent) to broaden its extraction spectrum to include more polar analytes.

Table 1: Physical properties (density, diffusion and viscosity) of gaseous, supercritical and liquid states. (35).

State	Density (g/cm ³)	Diffusion (cm ² /s)	Viscosity (g/cm•s)
Gas	10 ⁻³	10 ⁻¹	10 ⁻⁴
Supercritical	10 ⁻¹ - 1	10 ⁻⁴ - 10 ⁻³	10 ⁻⁴ - 10 ⁻³
Liquid	1	<10 ⁻⁵	10 ⁻²

Supercritical fluid extraction of herbal and biologically active components is now a growing area of interest. It gives an ability to process plant and herbal products at a very low temperature, in absence of toxic and harmful solvents, in addition to limiting thermal degradation of the analytes (38). Any fluid can be used as a supercritical fluid if it fulfils the characteristics under critical conditions. However, cost, solvation power and toxicity determine the best and suitable solvent to be used in a particular and specific application. It has been reported that propane, dimethyl ether and ethane have been used in extraction of herbal products and biologically active compounds as supercritical solvents (39).

compounds are mainly categorized into two main divisions: (1) undesired or unwanted chemical substances that need to be removed from the plant materials (matrix), for example, removal of caffeine from tea and coffee, defatting of press cakes, as well as removal of various factors such as porosity, particle size, nature of the matrix, and moisture, as well as removal of some parameters from some processes, such as temperature, pressure, and solvent flow rate, which can have an effect on the supercritical fluid result, (2) the extraction of biologically active components from plant material (40). Table 2 shows a selection of common applications of supercritical fluid extraction from herbal and plant origins, along with extraction properties such as pressure, modifiers, and temperature.

For easy understanding, we need to know that the supercritical fluid methods for most of the natural

Table 2: Supercritical-CO₂ extraction of some selected herbal bioactive compounds (selected from plant origin) (6).

Material	Extract	Modifier	T (°C)	P (bar)
Almond	Oil, tocopherols	Methanol	35-50	350-550
Aloe Vera leaves	α -tocopherol	Ethanol	40-70	300-600
Black pepper	Oleoresin, piperine	-	35-55	200-300
Ginger	Oleoresin	Ethanol, isopropanol	25-35	200-250
Thyme	Total extract, thymol,	-	40	80-400
Walnut	Oil	Ethanol	40-60	300-500
Grape skin	Resveratrol	Ethanol	40	150
Ginkgo leaves	Terpenes, flavonoids	Ethanol	60-110	242-312

4. SWITCHABLE POLARITY SOLVENTS (SPS)

Generally, switchable solvents (SS) are mixtures of compounds that have the ability to abruptly change their physical properties, such as polarity (hydrophilicity), conductivity, solubilizing capability

or viscosity (41,42). The switching of polarity is induced through bubbling of CO₂ gas at atmospheric pressure into the reaction vessels (43). The CO₂ will further reacts and associates with a compound in the reaction system forming an ionic liquid (IL) having different properties from the

initial molecular liquid (44). This process can simply be reversed through removal of CO₂ by bubbling inert gasses, N₂ gas, NaOH or sometimes through applying mild heat to the liquid (45).

It has been reported that various materials have the ability to switch some of their characteristics, for example polymers, solutes, and surfactants (46). With the aid of suitable reagents such as organic bases, water also has the ability to switch to higher ionic strength from lower ionic strength (47). SS are very important for processes that need various solvent characteristics in consecutive steps, such as product recovery or extraction (48).

The use and application of switchable solvents reduces the number of solvents required during a chemical process (49,50).

Switchable polarity solvents (SPS) were first introduced by Jessop in the year 2005, which contain either only one component, for example, secondary amines, or are composed of multiple components (51). Usually, two components of switchable polarity solvents are composed of amidine or sometimes guanidine together with a primary amine or an alcohol (52). Other combinations, such as guanidine or diamines/acidic alcohol chemical mixtures, are possible (53).

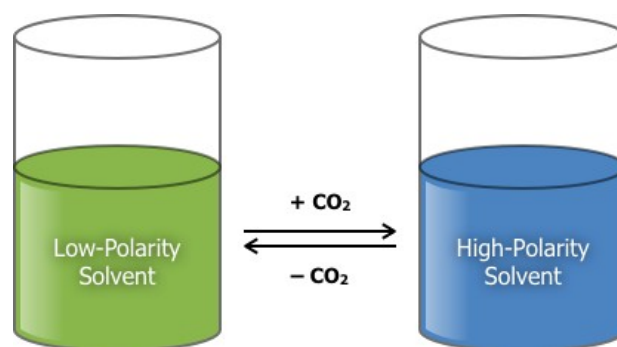


Figure 3: Switchable polarity solvent switching from low-polarity to high polarity by bubbling CO₂ (Adapted from Jessop et al., (56)).

Each SPS has its own properties (54,55). These characteristics have to be taken into consideration when selecting the best SPS for a certain chemical process (56). Systems containing amidine 1,8-diazabicyclo-[5.4.0]-undec-7-ene, for example, are extremely sensitive to moisture, whereas some secondary amines and other amidines SPS are less sensitive (57). One of the advantages of single component SPSs is that they do not need any operator to monitor the mole ratio of these two liquids. Furthermore, secondary amines are cost-effective when compared with amidines (58, 59).

One of the major challenges of industrial processes is solvent removal from hydrophobic materials without the use of distillation processes (60). However, the idea is possible provided that there is a solvent which can reversibly switch from hydrophobic state to a more hydrophilic one (61). Therefore, the discovery of SPS plays a major role in solving this negative inconvenience in industrial processes, because the removal of solvents through distillation is the most common industrial activity that suffers from the main drawbacks that lead to environmental hazards and damage (62). Firstly, because distillation usually employs the usage of a volatile substance, it results in smog formation through great vapor emission. Secondly, it needs a high input of energy (63). Therefore, there is a need to find a new and efficient non-distillative approach for the separation of solvents from their products, in order to avoid the usage of volatile solvents (64,65).

Soylak et al. reported that N,N,N-tributylpentanamide was first used as an SPS that can be applied for extracting low polarity products such as vegetable oils, and then the solvent is removed from the product using carbonated water (66,67). Carbonated water has the ability to extract the solvents from the products due to the fact that the CO₂ can convert the solvent into the polar form. Subsequently, the solvent is then separated from the carbonated water by removing the CO₂, because the removal triggers the conversion of the solvent into its non-polar form. And finally, the removal of the solvent from the herbal product does not require distillation (68,69).

Memon et al., (2017) proposed a green and novel switchable solvent, which was hyphenated with liquid phase micro extraction (SS-LPME) for extraction and preconcentration of the nutritionally and biologically important element Co(II) from tobacco and food samples using flame atomic absorption spectrometry. To improve conversion from the deprotonated form to the protonated form, N, Ndimethyl-n-octylamine bicarbonate was synthesized and used as a switchable solvent in the presence of CO₂ to improve conversion from the deprotonated to the protonated form, and then examined for analyte extraction. A quantitative recovery was achieved (70,71). This study involves the formation of a complex at a pH of 4.0 between Co(II) and 1-nitroso-2-naphthol, which serves as a ligand, and then extraction through conversion of the solvent to a nonpolar N,N-dimethyl-n-octylamine phase. The accuracy and validity of this

method were checked using standard reference material (IC-INCT-OBTL-5) and additional recovery verification. The LOD and LOQ were also found to be $3.2 \mu\text{g L}^{-1}$ and $10.6 \mu\text{g L}^{-1}$ respectively. Finally, this method was efficiently used for the atomic analysis of tobacco, herbal products, and food samples (72).

5. NATURAL DEEP EUTECTIC SOLVENTS (NADES)

In 2003, Abbot and his co-workers introduced deep eutectic solvents (DES) for the first time (73). They reported excellent properties for some eutectic mixtures of a range of quaternary ammonium salts and urea (74). DES are now widely regarded as a novel class of sustainable solvents that serve as green alternatives to ionic liquids (ILs) (75). Because of their similar properties such as starting materials, non-flammability, non-volatility, and high viscosity, DES are considered the 4th generation of ionic liquids (78). However, DES are not entirely made up of ionic species (76,77). DES are created by combining two or more components, such as organic salts (phosphonium salt or quaternary ammonium) and hydrogen bond donors (HBD) or metal salts that can associate with one another via hydrogen bonding (78). The charge delocalization that occurs results in a decrease in the melting point of the final product when compared with the individual melting points of the starting materials (79). Nevertheless, DES has numerous advantages and applications over ILs, such as lower economic and environmental impact (80,81). This is more pronounced for DES that are produced naturally from primary metabolites of living cells, known as natural deep eutectic solvents (NADES), which are mostly found in abundance in our diet, such as amines, sugars, carboxylic acids, polyalcohol and choline (82). These NADES satisfy all the principles of green solvents, which produces many advantages, such as readily available starting materials, reduced toxicity, cost-effectiveness, and simplicity of preparation, among the others. Moreover, they possess excellent physicochemical properties such as adjustable viscosity, wide range of polarity, liquids even at lower temperatures, and high solubilizing capacity for a wide range of compounds that can be fine-tuned for a certain application because of their different structural possibilities (83).

Due to the above properties of NADES, there is a rapid increase in their application for the extraction of biological ingredients of herbal materials such as phenolic acid, saponins, flavonoids, alkaloids, terpenoids and anthocyanin, which clearly indicated the possibility of using NADES in extracting different hydrophobic and hydrophilic naturally occurring chemical compounds (84,85).

In order to select a suitable NADES for extracting active compounds from herbal materials, it is very important to try different combinations having

different physicochemical parameters. For instance, Dai et al., reported that seven NADES were used in the extraction of aromatic pigments having wide range of polarity from *Carthamus tinctorius* L. showing that NADES with low polarity possess the lowest efficiency for polar active compounds but higher extraction ability for non-polar active compounds and vice versa (86). This corresponds to the rule of "like dissolves like". Various researchers draw the same conclusion when extracting phenolic compounds from grape skin. In the study, they used choline-chloride based NADES that contains organic acids, polyalcohol or sugars as the hydrogen bond donors (HBD). However, polyalcohol and sugar based NADES are less polar than organic acid based NADES, having a polarity almost equal to that of methanol (87,88).

Furthermore, to improve the extraction efficiency of NADES, there is a need to optimize the NADES content of water. Increasing the water content decreases its viscosity, thereby increasing the transfer of mass from the herbal matrices to a solution and hence increasing the efficiency of the extraction (89). The main problem with using NADES for extraction is its viscosity, which is generally high at room temperature. For instance, some NADES cannot be utilized directly for extraction without diluting them with water due to their high viscosity. However, increasing the water content decreases the interaction between the solvent and the target analyte. Also, an excess of water in NADES can lead to halide-HBD supramolecular complex breakage and thereby form a single aqueous solution of each of the initial components. In general, a NADES with high water content are more suitable for the extraction of more polar compounds, while those with low water content are more suitable for extracting non-polar compounds. However, water content has a significant effect on the yield for both non-polar and polar-active components. Furthermore, the stability of the target analytes while using NADESs should be taken into consideration as an important factor when selecting a specific solvent. In a study to determine the stability of some phenolic components of safflower extracts, the results showed that using NADES improved compound stability over using conventional solvents (39). The stability in NADES is due to the strong hydrogen bonding that exists between the molecules of the solvent and solute, whereby among the studied NADES, sugar-based NADES showed the highest stability (90). This interaction is responsible for decreasing the mobility of the solute molecules, and this reduces the contact time with oxygen and air, hence minimizes oxidative degradation, which is the major factor that causes degradation of the active compounds (91). There is a need for further research on the reasons behind bioactive ingredients' stability in NADESs for a full understanding of the mechanism (92,93).

Furthermore, before final selection of NADES, its environmental effects should be checked and

examined, because the assumption that NADES are non-toxic is based on toxicity results for individual components used in preparing NADES, which are naturally occurring biomaterials that are pharmaceutically accepted (94). The assumption does not take into account the probability of the existence of combined and synergistic effects of the individual components that make up the NADES (95).

According to the current research trend, there is little or no application of the NADES extraction method on an industrial scale for green extraction of herbal active components on a large scale. Therefore, to achieve such industrial implementation, environmental and economic factors should be considered (96). Though the price of NADES is comparable to that of conventional and classical solvents, their production is regarded as a sustainable process (97). Nevertheless, other factors should be considered, such as the recovery of the target bioactive component as well as the NADES recyclability, before implementing this technique in large scales. Nonetheless, researchers (98-107) reported that NADES is a suitable alternative technique that involves renewability and sustainability for the extraction of value added compounds as well as other precious analytes prior to both atomic and molecular analysis.

CONCLUSION

Currently, most of the techniques used in processing herbal products involve the use of extraction methods. Therefore, trends in extraction methods focus mainly on finding reasonable solutions that minimize the use of toxic solvents and allow the use of renewable and green solvents from natural products that ensure high quality and safe extracts. In the future, SFE is definitely going to be on an industrial scale due to its numerous applications on a large scale, especially for herbal, food, cosmetics, pharmaceutical products etc. Due to its various applications, as mentioned in this research, CO₂ is a vital chemical compound. SFE shows diverse advantages over conventional solvents. Also, switchable polarity solvents (SPS) have shown excellent applications on an industrial scale through switching one of their characteristics from the non-polar form to the polar form simply by bubbling CO₂, which enables complete miscibility and ensures the extraction of the bioactive components. However, there is a need for more development and transference of this technique into the micro extraction method as there is less data and research in that field. Moreover, NADES show unique physicochemical parameters and completely satisfy all the principles of a green solvent that can be used for extracting bioactive compounds from herbal materials, due to their low environmental and economic impacts. However, there is a need for transferring this technique to the industrial scale owing to the meager amount of research

conducted in the published technical literature that is used on a large scale.

Finally, the need for the identification, analysis, and standardization of herbal products is of paramount importance, owing to their significant application in society and to verify fraudulence, fraud, counterfeit, and adulteration.

CONFLICT OF INTEREST

None reported.

ACKNOWLEDGMENTS

The authors will like to thank and acknowledge their appreciations and gratitude to the relevant cited references of this review, which discussed the applications of solvents of the future for herbal products extractions.

REFERENCES

1. Vanhaecke F. A new scope for JAAS! J Anal At Spectrom. 2015;30(5):1015-6. Available from: <URL>.
2. Walsh A. The development of atomic absorption methods of elemental analysis 1952-1962. Anal Chem. 1991 Oct 1;63(19):933A-941A. Available from: <URL>.
3. Hahn DW, Omenetto N. Laser-induced breakdown spectroscopy (LIBS), part I: review of basic diagnostics and plasma-particle interactions: still-challenging issues within the analytical plasma community. Applied spectroscopy. 2010;64(12):335A-336A. Available from: <URL>.
4. Glaus R, Riedel J, Gornushkin I. Insight into the Formation of Molecular Species in Laser-Induced Plasma of Isotopically Labeled Organic Samples. Anal Chem. 2015 Oct 6;87(19):10131-7. Available from: <URL>.
5. Chen TL, Kim H, Pan SY, Tseng PC, Lin YP, Chiang PC. Implementation of green chemistry principles in circular economy system towards sustainable development goals: Challenges and perspectives. Science of The Total Environment. 2020 May;716:136998. Available from: <URL>.
6. Cvjetko Bubalo M, Vidović S, Radojčić Redovniković I, Jokić S. New perspective in extraction of plant biologically active compounds by green solvents. Food and Bioproducts Processing. 2018 May;109:52-73. Available from: <URL>.
7. Mumladze T, Yousef S, Tatariants M, Kriūkienė R, Makarevicius V, Lukošiušė S, et al. Sustainable approach to recycling of multilayer flexible packaging using switchable hydrophilicity solvents. Green Chem. 2018;20(15):3604-18. Available from: <URL>.
8. Yardımcı B, Üzer A, Apak R. Spectrophotometric Fluoride Determination Using St. John's Wort Extract as a Green Chromogenic Complexant for Al(III). ACS Omega. 2022 Dec 13;7(49):45432-42. Available from: <URL>.
9. Rattanakit P, Maungchang R. Determining Iron(III) Concentration in a Green Chemistry Experiment Using Phyllanthus emblica (Indian Gooseberry) Extract and Spectrophotometry. J Chem Educ. 2019 Apr 9;96(4):756-60. Available from: <URL>.

10. Cravotto G, Boffa L, Mantegna S, Perego P, Avogadro M, Cintas P. Improved extraction of vegetable oils under high-intensity ultrasound and/or microwaves. *Ultrasonics Sonochemistry*. 2008 Jul;15(5):898-902. Available from: [<URL>](#).
11. Chemat F, Vian MA, Cravotto G. Green Extraction of Natural Products: Concept and Principles. *IJMS*. 2012 Jul 11;13(7):8615-27. [<URL>](#).
12. Bernhoft A. Bioactive compounds in plants: benefits and risks for man and animals: proceedings from a symposium held in Norwegian Academy of Science and Letters, Oslo, 13-14 November 2008. Oslo: Novus Forlag; 2010. ISBN: 978-82-7099-583-7.
13. Anastas P, Eghbali N. Green Chemistry: Principles and Practice. *Chem Soc Rev*. 2010;39(1):301-12. Available from: [<URL>](#).
14. Sadravi S, Honarasa F. Spectrophotometric nanomolar determination of glucose by using C-dots- Fe_3O_4 magnetic nanozyme. *J Chem Sci*. 2019 Jul;131(7):58. Available from: [<URL>](#).
15. Gu Y, Jérôme F. Glycerol as a sustainable solvent for green chemistry. *Green Chem*. 2010;12(7):1127. Available from: [<URL>](#).
16. Ammani HM, Usman AG. Synthesis and characterization of 2-benzoxazolone and its derivatives. *Asian Journal of Natural & Applied Sciences Vol*. 2018;7:2.
17. Li X, Lu H, Liu D, Wang B. Preparation of composite switchable water with hydrophobic tertiary amine for washing oil sands. *Journal of CO2 Utilization*. 2019 Jan;29:254-61. Available from: [<URL>](#).
18. Aher JS, Kardel AV, Gaware MR, Lokhande DD, Bhagare AM. One pot synthesis of pyrimidine-5-carbonitrile and pyrimidine-5-carboxamide using ammonium chloride under solvent free condition. *J Chem Sci*. 2019 Jul;131(7):54. Available from: [<URL>](#).
19. Wang Z. Green Chemistry: Recent Advances in Developing Catalytic Processes in Environmentally-Benign Solvent Systems [Internet]. Powerpoint Presentation presented at: Frontiers of Chemistry Presentation; 2008; Pittsburgh, USA. Available from: [<URL>](#).
20. Verma GK, Raghuvanshi K, Kumar R, Singh MS. An efficient one-pot three-component synthesis of functionalized pyrimido[4,5-b]quinolines and indeno fused pyrido[2,3-d]pyrimidines in water. *Tetrahedron Letters*. 2012 Jan;53(4):399-402. Available from: [<URL>](#).
21. Pompeo N, Torokhtii K, Silva E. Surface impedance measurements in thin conducting films: Substrate and finite-thickness-induced uncertainties. In: 2017 IEEE International Instrumentation and Measurement Technology Conference (I2MTC) [Internet]. Torino, Italy: IEEE; 2017 [cited 2023 Jan 30]. p. 1-5. Available from: [<URL>](#).
22. Wang X, Gao M, Zhang Z, Gu H, Liu T, Yu N, et al. Development of CO₂-Mediated Switchable Hydrophilicity Solvent-Based Microextraction Combined with HPLC-UV for the Determination of Bisphenols in Foods and Drinks. *Food Anal Methods*. 2018 Aug;11(8):2093-104. Available from: [<URL>](#).
23. Yuan X, Richter BE, Jiang K, Boniface KJ, Cormier A, Sanders CA, et al. Carbonated water for the separation of carboxylic compounds: a chromatography approach. *Green Chem*. 2018;20(2):440-8. Available from: [<URL>](#).
24. Asare Bediako BB, Zhou P, Rugabirwa B, Liu Q, Su Y, Wang H, et al. A switchable hydrophilicity solvent mediated process to prepare fine silica aerogel powder as an excellent flattening agent. *Advanced Powder Technology*. 2019 Mar;30(3):565-71. Available from: [<URL>](#).
25. Yilmaz E, Soylak M. Ultrasound assisted-deep eutectic solvent based on emulsification liquid phase microextraction combined with microsample injection flame atomic absorption spectrometry for valence speciation of chromium(III/VI) in environmental samples. *Talanta*. 2016 Nov;160:680-5. Available from: [<URL>](#).
26. Kanberoglu GS, Yilmaz E, Soylak M. Application of deep eutectic solvent in ultrasound-assisted emulsification microextraction of quercetin from some fruits and vegetables. *Journal of Molecular Liquids*. 2019 Apr;279:571-7. Available from: [<URL>](#).
27. Diederich F, Rubin Y. Synthetic Approaches toward Molecular and Polymeric Carbon Allotropes. *Angew Chem Int Ed Engl*. 1992 Sep;31(9):1101-23. Available from: [<URL>](#).
28. Leder C, Rastogi T, Kümmerer K. Putting benign by design into practice-novel concepts for green and sustainable pharmacy: Designing green drug derivatives by non-targeted synthesis and screening for biodegradability. *Sustainable Chemistry and Pharmacy*. 2015 Dec;2:31-6. Available from: [<URL>](#).
29. Tuerhong M, Xu Y, Yin XB. Review on Carbon Dots and Their Applications. *Chinese Journal of Analytical Chemistry*. 2017 Jan;45(1):139-50. Available from: [<URL>](#).
30. Rooney JM. Carbocationic Polymerization: N-Vinylcarbazole. In: *Comprehensive Polymer Science and Supplements* [Internet]. Elsevier; 1989 [cited 2023 Jan 30]. p. 697-704. Available from: [<URL>](#).
31. Madhura TR, Kumar GG, Ramaraj R. Gold nanoparticles decorated silicate sol-gel matrix embedded reduced graphene oxide and manganese ferrite nanocomposite-materials-modified electrode for glucose sensor application. *J Chem Sci*. 2019 May;131(5):35. Available from: [<URL>](#).
32. Zou N, Wei X, Zong Z, Li X, Wang Z, Wang X. A novel enzymatic biosensor for detection of intracellular hydrogen peroxide based on 1-aminopyrene and reduced graphene oxides. *J Chem Sci*. 2019 Apr;131(4):28. Available from: [<URL>](#).
33. Okoh OO, Sadimenko AP, Afolayan AJ. Comparative evaluation of the antibacterial activities of the essential oils of *Rosmarinus officinalis* L. obtained by hydrodistillation and solvent free microwave extraction methods. *Food Chemistry*. 2010 May;120(1):308-12. Available from: [<URL>](#).
34. Fang L, Leng Y, Gao P. Processing of hydroxyapatite reinforced ultrahigh molecular weight polyethylene for biomedical applications. *Biomaterials*. 2005 Jun;26(17):3471-8. Available from: [<URL>](#).
35. Lucchesi ME, Chemat F, Smadja J. An original solvent free microwave extraction of essential oils from spices. *Flavour Fragr J*. 2004 Mar;19(2):134-8. Available from: [<URL>](#).

36. Zou N, Wei X, Zong Z, Li X, Wang Z, Wang X. A novel enzymatic biosensor for detection of intracellular hydrogen peroxide based on 1-aminopyrene and reduced graphene oxides. *J Chem Sci.* 2019 Apr;131(4):28. Available from: [<URL>](#).
37. Lucchesi ME, Chemat F, Smadja J. Solvent-free microwave extraction of essential oil from aromatic herbs: comparison with conventional hydro-distillation. *Journal of Chromatography A.* 2004 Jul;1043(2):323-7. Available from: [<URL>](#).
38. Xu L. Recent advances on supercritical fluid extraction of essential oils. *Afr J Pharm Pharmacol.* 2011 Sep 8;5(9):1196-211. Available from: [<URL>](#).
39. Alhamimi S. Extraction and chromatography of bioactive compounds in complex samples using supercritical CO₂ technology [Internet] [PhD Thesis]. [Sweden]: Lund University; 2018. Available from: [<URL>](#).
40. Gumerov FM, Khairutdinov VF, Akhmetzyanov TR, Gabitov FR, Zaripov ZI, Farakhov MI, et al. Supercritical Fluid Propane-Butane Extraction Treatment of Oil Sludge. *Russ J Phys Chem B.* 2017 Dec;11(7):1103-8. Available from: [<URL>](#).
41. Mothibedi K, Mokgadi J, Torto N. Determination of Flavonoids in Ginkgo Biloba Using Bond Elut Plexa Solid Phase Extraction Sorbent for Cleanup and HPLC-DAD Analysis [Internet]. Agilent Technologies; 2011. Available from: [<URL>](#).
42. Hala EA, Yasser AF, Abeer AEW. Application of numerical modeling for optimization of selective hot water extraction of taxifolin from milk thistle seeds. *Afr J Biotechnol.* 2013 Aug 29;10(48):9804-11. Available from: [<URL>](#).
43. Pourmortazavi SM, Hajimirsadeghi SS. Supercritical fluid extraction in plant essential and volatile oil analysis. *Journal of Chromatography A.* 2007 Sep;1163(1-2):2-24. Available from: [<URL>](#).
44. Cvjetko Bubalo M, Ćurko N, Tomašević M, Kovačević Ganić K, Radojčić Redovniković I. Green extraction of grape skin phenolics by using deep eutectic solvents. *Food Chemistry.* 2016 Jun;200:159-66. Available from: [<URL>](#).
45. Jokić S, Bijuk M, Aladić K, Bilić M, Molnar M. Optimisation of supercritical CO₂ extraction of grape seed oil using response surface methodology. *Int J Food Sci Technol.* 2016 Feb;51(2):403-10. Available from: [<URL>](#).
46. Yılmaz E, Soylak M. Switchable solvent-based liquid phase microextraction of copper(ii): optimization and application to environmental samples. *J Anal At Spectrom.* 2015;30(7):1629-35. Available from: [<URL>](#).
47. Vanderveen JR, Burra S, Geng J, Goyon A, Jardine A, Shin HE, et al. Characterizing the Effects of a "Switchable Water" Additive on the Aqueous Solubility of Small Molecules. *ChemPhysChem.* 2018 Aug 17;19(16):2093-100. Available from: [<URL>](#).
48. Wang S, Zheng C, Zhao J, Li X, Lu H. Extracting and recovering diesel from oil-based drill cuttings using switchable hydrophilic solvents. *Chemical Engineering Research and Design.* 2017 Dec;128:27-36. Available from: [<URL>](#).
49. Soylak M, Khan M, Yılmaz E. Switchable solvent based liquid phase microextraction of uranium in environmental samples: a green approach. *Anal Methods.* 2016;8(5):979-86. Available from: [<URL>](#).
50. Zare F, Ghaedi M, Jannesar R, Tayebi L. Switchable polarity solvents for preconcentration and simultaneous determination of amino acids in human plasma samples. *New J Chem.* 2018;42(12):10007-15. Available from: [<URL>](#).
51. Grabner B. Switchable Solvents and Room-Temperature Solid Phase Ionic Liquids in Biocatalysis [Internet] [Master's Thesis]. [Graz, Austria]: Technische Universität Graz; 2015. Available from: [<URL>](#).
52. Ahmar H, Nejati-Yazdinejad M, Najafi M, Hasheminasab KS. Switchable Hydrophilicity Solvent-Based Homogenous Liquid-Liquid Microextraction (SHS-HLLME) Combined with GC-FID for the Quantification of Methadone and Tramadol. *Chromatographia.* 2018 Jul;81(7):1063-70. Available from: [<URL>](#).
53. Stone ML, Rae C, Stewart FF, Wilson AD. Switchable polarity solvents as draw solutes for forward osmosis. *Desalination.* 2013 Mar;312:124-9. Available from: [<URL>](#).
54. Reimund KK, Coscia BJ, Arena JT, Wilson AD, McCutcheon JR. Characterization and membrane stability study for the switchable polarity solvent N,N-dimethylcyclohexylamine as a draw solute in forward osmosis. *Journal of Membrane Science.* 2016 Mar;501:93-9. Available from: [<URL>](#).
55. Hardy S, de Wispelaere IM, Leitner W, Liauw MA. Comprehensive monitoring of a biphasic switchable solvent synthesis. *Analyst.* 2013;138(3):819-24. Available from: [<URL>](#).
56. Vanderveen JR, Geng J, Zhang S, Jessop PG. Diamines as switchable-hydrophilicity solvents with improved phase behaviour. *RSC Adv.* 2018;8(48):27318-25. Available from: [<URL>](#).
57. Jessop PG. Fundamental properties and practical applications of ionic liquids: concluding remarks. *Faraday Discuss.* 2018;206:587-601. Available from: [<URL>](#).
58. Ezoddin M, Abdi K, Lamei N. Development of air assisted liquid phase microextraction based on switchable-hydrophilicity solvent for the determination of palladium in environmental samples. *Talanta.* 2016 Jun;153:247-52. Available from: [<URL>](#).
59. Jessop PG, Kozycz L, Rahami ZG, Schoenmakers D, Boyd AR, Wechsler D, et al. Tertiary amine solvents having switchable hydrophilicity. *Green Chem.* 2011;13(3):619. Available from: [<URL>](#).
60. Donaldson ME, Mestre VL, Vinci D, Liotta CL, Eckert CA. Switchable Solvents for in-Situ Acid-Catalyzed Hydrolysis of β -Pinene. *Ind Eng Chem Res.* 2009 Mar 4;48(5):2542-7. Available from: [<URL>](#).
61. Jessop PG, Phan L, Carrier A, Robinson S, Dürr CJ, Harjani JR. A solvent having switchable hydrophilicity. *Green Chem.* 2010;12(5):809. Available from: [<URL>](#).
62. Durelle J. Designing Switchable-Hydrophilicity Solvents and Modelling their Behaviour [Internet] [Master's Thesis]. [Canada]: Queen's University; 2014. Available from: [<URL>](#).
63. Fu D, Farag S, Chaouki J, Jessop PG. Extraction of phenols from lignin microwave-pyrolysis oil using a

- switchable hydrophilicity solvent. *Bioresource Technology*. 2014 Feb;154:101-8. Available from: [<URL>](#).
64. Shahvandi SK, Banitaba MH, Ahmar H. Development of a new pH assisted homogeneous liquid-liquid microextraction by a solvent with switchable hydrophilicity: Application for GC-MS determination of methamphetamine. *Talanta*. 2018 Jul;184:103-8. Available from: [<URL>](#).
65. Memon ZM, Yilmaz E, Soylak M. Switchable solvent based green liquid phase microextraction method for cobalt in tobacco and food samples prior to flame atomic absorption spectrometric determination. *Journal of Molecular Liquids*. 2017 Mar;229:459-64. Available from: [<URL>](#).
66. Tetko IV, Gasteiger J, Todeschini R, Mauri A, Livingstone D, Ertl P, et al. Virtual Computational Chemistry Laboratory – Design and Description. *J Comput Aided Mol Des*. 2005 Jun;19(6):453-63. Available from: [<URL>](#).
67. Sendur OF, Turan Y, Bal S, Gurgan A. Toxic Neuropathy Due to N-Hexane: Report of Three Cases. *Inhalation Toxicology*. 2009 Feb;21(3):210-4. Available from: [<URL>](#).
68. Lasarte-Aragonés G, Lucena R, Cárdenas S, Valcárcel M. Use of switchable solvents in the microextraction context. *Talanta*. 2015 Jan;131:645-9. Available from: [<URL>](#).
69. Phan L, Andreatta JR, Horvey LK, Edie CF, Luco AL, Mirchandani A, et al. Switchable-Polarity Solvents Prepared with a Single Liquid Component. *J Org Chem*. 2008 Jan 1;73(1):127-32. Available from: [<URL>](#).
70. Soylak M, Unsal YE. Solid-phase extraction of heavy metal ions on bucky tubes disc in natural water and herbal plant samples. *Environ Monit Assess*. 2011 Oct;181(1-4):577-86. Available from: [<URL>](#).
71. Campbell KN, Sommers AH, Campbell BK. The Preparation of Unsymmetrical Secondary Aliphatic Amines 1. *J Am Chem Soc*. 1944 Jan;66(1):82-4. Available from: [<URL>](#).
72. Soylak M, Şahin U, Elçi L. Spectrophotometric determination of molybdenum in steel samples utilizing selective sorbent extraction on Amberlite XAD-8 resin. *Analytica Chimica Acta*. 1996 Mar;322(1-2):111-5. Available from: [<URL>](#).
73. Vanderveen JR, Durelle J, Jessop PG. Design and evaluation of switchable-hydrophilicity solvents. *Green Chem*. 2014;16(3):1187-97. Available from: [<URL>](#).
74. Hardy S, Liauw MA. Mixing behaviour investigation of a switchable solvent synthesis using ATR-IR spectroscopy. *Chemical Engineering Journal*. 2013 Nov;233:292-6. Available from: [<URL>](#).
75. Caruso R, O'Connor R, Stephens W, Cummings K, Fong G. Toxic Metal Concentrations in Cigarettes Obtained from U.S. Smokers in 2009: Results from the International Tobacco Control (ITC) United States Survey Cohort. *IJERPH*. 2013 Dec 20;11(1):202-17. Available from: [<URL>](#).
76. Oliveira PR, Lamy-Mendes AC, Rezende EIP, Mangrich AS, Marcolino Junior LH, Bergamini MF. Electrochemical determination of copper ions in spirit drinks using carbon paste electrode modified with biochar. *Food Chemistry*. 2015 Mar;171:426-31. Available from: [<URL>](#).
77. Abbott AP, Capper G, Davies DL, Rasheed RK, Tambyrajah V. Novel solvent properties of choline chloride/urea mixtures. Electronic supplementary information (ESI) available: spectroscopic data. See [<URL>](#). *Chem Commun*. 2003 Dec 19;(1):70-1.
78. Abbott AP, Capper G, Davies DL, Munro HL, Rasheed RK, Tambyrajah V. Preparation of novel, moisture-stable, Lewis-acidic ionic liquids containing quaternary ammonium salts with functional side chains. *Chem Commun*. 2001;(19):2010-1. Available from: [<URL>](#).
79. Sitze MS, Schreiter ER, Patterson EV, Freeman RG. Ionic Liquids Based on FeCl₃ and FeCl₂. Raman Scattering and ab Initio Calculations. *Inorg Chem*. 2001 May 1;40(10):2298-304. Available from: [<URL>](#).
80. Miao X, Liu T, Zhang C, Geng X, Meng Y, Li X. Fluorescent aliphatic hyperbranched polyether: chromophore-free and without any N and P atoms. *Phys Chem Chem Phys*. 2016;18(6):4295-9. Available from: [<URL>](#).
81. Zhang Q, De Oliveira Vigier K, Royer S, Jérôme F. Deep eutectic solvents: syntheses, properties and applications. *Chem Soc Rev*. 2012;41(21):7108. Available from: [<URL>](#).
82. Choi YH, van Spronsen J, Dai Y, Verberne M, Hollmann F, Arends IWCE, et al. Are Natural Deep Eutectic Solvents the Missing Link in Understanding Cellular Metabolism and Physiology? *Plant Physiology*. 2011 Aug 5;156(4):1701-5. Available from: [<URL>](#).
83. Faggian M, Sut S, Perissutti B, Baldan V, Grabnar I, Dall'Acqua S. Natural Deep Eutectic Solvents (NADES) as a Tool for Bioavailability Improvement: Pharmacokinetics of Rutin Dissolved in Proline/Glycine after Oral Administration in Rats: Possible Application in Nutraceuticals. *Molecules*. 2016 Nov 14;21(11):1531. Available from: [<URL>](#).
84. Zainal-Abidin MH, Hayyan M, Hayyan A, Jayakumar NS. New horizons in the extraction of bioactive compounds using deep eutectic solvents: A review. *Analytica Chimica Acta*. 2017 Aug;979:1-23. Available from: [<URL>](#).
85. Mbous YP, Hayyan M, Hayyan A, Wong WF, Hashim MA, Looi CY. Applications of deep eutectic solvents in biotechnology and bioengineering—Promises and challenges. *Biotechnology Advances*. 2017 Mar;35(2):105-34. Available from: [<URL>](#).
86. Radošević K, Ćurko N, Gaurina Srček V, Cvjetko Bubalo M, Tomašević M, Kovačević Ganić K, et al. Natural deep eutectic solvents as beneficial extractants for enhancement of plant extracts bioactivity. *LWT*. 2016 Nov;73:45-51. Available from: [<URL>](#).
87. Dai Y, van Spronsen J, Witkamp GJ, Verpoorte R, Choi YH. Natural deep eutectic solvents as new potential media for green technology. *Analytica Chimica Acta*. 2013 Mar;766:61-8. Available from: [<URL>](#).
88. Wang M, Wang J, Zhang Y, Xia Q, Bi W, Yang X, et al. Fast environment-friendly ball mill-assisted deep eutectic solvent-based extraction of natural products. *Journal of Chromatography A*. 2016 Apr;1443:262-6. [<URL>](#).

89. Dai Y, Verpoorte R, Choi YH. Natural deep eutectic solvents providing enhanced stability of natural colorants from safflower (*Carthamus tinctorius*). *Food Chemistry*. 2014 Sep;159:116–21. Available from: [<URL>](#).
90. Dai Y, Rozema E, Verpoorte R, Choi YH. Application of natural deep eutectic solvents to the extraction of anthocyanins from *Catharanthus roseus* with high extractability and stability replacing conventional organic solvents. *Journal of Chromatography A*. 2016 Feb;1434:50–6. Available from: [<URL>](#).
91. Castañeda-Ovando A, Pacheco-Hernández Ma de L, Páez-Hernández MaE, Rodríguez JA, Galán-Vidal CA. Chemical studies of anthocyanins: A review. *Food Chemistry*. 2009 Apr;113(4):859–71. Available from: [<URL>](#).
92. Wei ZF, Wang XQ, Peng X, Wang W, Zhao CJ, Zu YG, et al. Fast and green extraction and separation of main bioactive flavonoids from *Radix Scutellariae*. *Industrial Crops and Products*. 2015 Jan;63:175–81. Available from: [<URL>](#).
93. Biswal MR, Rai S, Prakash MK. Molecular dynamics based antimicrobial activity descriptors for synthetic cationic peptides. *J Chem Sci*. 2019 Feb;131(2):16. Available from: [<URL>](#).
94. Qi XL, Peng X, Huang YY, Li L, Wei ZF, Zu YG, et al. Green and efficient extraction of bioactive flavonoids from *Equisetum palustre* L. by deep eutectic solvents-based negative pressure cavitation method combined with macroporous resin enrichment. *Industrial Crops and Products*. 2015 Aug;70:142–8. Available from: [<URL>](#).
95. Bi W, Tian M, Row KH. Evaluation of alcohol-based deep eutectic solvent in extraction and determination of flavonoids with response surface methodology optimization. *Journal of Chromatography A*. 2013 Apr;1285:22–30. Available from: [<URL>](#).
96. Huang Y, Feng F, Jiang J, Qiao Y, Wu T, Voglmeir J, et al. Green and efficient extraction of rutin from tartary buckwheat hull by using natural deep eutectic solvents. *Food Chemistry*. 2017 Apr;221:1400–5. Available from: [<URL>](#).
97. Bajkacz S, Adamek J. Evaluation of new natural deep eutectic solvents for the extraction of isoflavones from soy products. *Talanta*. 2017 Jun;168:329–35. Available from: [<URL>](#).
98. Cunha SC, Fernandes JO. Extraction techniques with deep eutectic solvents. *TrAC Trends in Analytical Chemistry*. 2018 Aug;105:225–39. Available from: [<URL>](#).
99. Wei Z, Qi X, Li T, Luo M, Wang W, Zu Y, et al. Application of natural deep eutectic solvents for extraction and determination of phenolics in *Cajanus cajan* leaves by ultra performance liquid chromatography. *Separation and Purification Technology*. 2015 Jul;149:237–44. Available from: [<URL>](#).
100. Bajkacz S, Adamek J. Development of a Method Based on Natural Deep Eutectic Solvents for Extraction of Flavonoids from Food Samples. *Food Anal Methods*. 2018 May;11(5):1330–44. Available from: [<URL>](#).
101. Fernández M de los Á, Boiteux J, Espino M, Gomez FJV, Silva MF. Natural deep eutectic solvents-mediated extractions: The way forward for sustainable analytical developments. *Analytica Chimica Acta*. 2018 Dec;1038:1–10. Available from: [<URL>](#).
102. Shishov A, Bulatov A, Locatelli M, Carradori S, Andrush V. Application of deep eutectic solvents in analytical chemistry. A review. *Microchemical Journal*. 2017 Nov;135:33–8. Available from: [<URL>](#).
103. Mehariya S, Fratini F, Lavecchia R, Zuorro A. Green extraction of value-added compounds from microalgae: A short review on natural deep eutectic solvents (NADES) and related pre-treatments. *Journal of Environmental Chemical Engineering*. 2021 Oct;9(5):105989. Available from: [<URL>](#).
104. Popovic BM, Micic N, Potkonjak A, Blagojevic B, Pavlovic K, Milanov D, et al. Novel extraction of polyphenols from sour cherry pomace using natural deep eutectic solvents – Ultrafast microwave-assisted NADES preparation and extraction. *Food Chemistry*. 2022 Jan;366:130562. Available from: [<URL>](#).
105. Hikmawanti NPE, Ramadon D, Jantan I, Mun'im A. Natural Deep Eutectic Solvents (NADES): Phytochemical Extraction Performance Enhancer for Pharmaceutical and Nutraceutical Product Development. *Plants*. 2021 Oct 1;10(10):2091. Available from: [<URL>](#).
106. Nystedt HL, Grønlien KG, Tønnesen HH. Interactions of natural deep eutectic solvents (NADES) with artificial and natural membranes. *Journal of Molecular Liquids*. 2021 Apr;328:115452. Available from: [<URL>](#).
107. Canales R, Espino M, Pasini S, Silva MF. Chemometric and green metric strategies for sustainable analytical methods: phenolic compounds in lettuce-NADES extracts. *Anal Methods*. 2021;13(10):1261–8. Available from: [<URL>](#).



Synthesis, Spectral Characterization, Crystal Structure, and Antioxidant Properties of novel Palladium(II) Complex from ONS Donor 1,5-bis(2-hydroxybenzylidene)thiocarbohydrazone

Yeliz Kaya^{1*} 

¹Istanbul University-Cerrahpaşa, Faculty of Engineering, Department of Chemistry, Istanbul, Türkiye

Abstract: A new Pd(II) complex, [Pd(PPh₃)(L)] (L = 1,5-bis(2-hydroxybenzylidene)thiocarbohydrazone, PPh₃ = triphenylphosphine), was synthesized and characterized by FTIR, ¹H NMR and UV-Vis spectroscopies and elemental analysis. The molecular structure of [Pd(PPh₃)(L)] was confirmed by the single-crystal X-ray diffraction technique. Palladium ion has distorted square planar geometry according to X-ray diffraction studies. The free thiocarbohydrazone (L), potentially a pentadentate ONSNO donor, acted as a tridentate ONS donor. The antioxidant capacity of the free thiocarbohydrazone and Pd(II) complex was determined using the CUPRAC (cupric reducing antioxidant capacity) method. Also, the DPPH method was used to test the free radical scavenging activity of the free thiocarbohydrazone and Pd(II) complex. Antioxidant activity studies showed that free thiocarbohydrazone exhibited better activity than Pd(II) complex.

Keywords: Thiocarbohydrazone; Palladium(II) complex; Triphenylphosphine; Crystal structure; Antioxidant activity.

Submitted: October 25, 2022. **Accepted:** December 19, 2022.

Cite this: Kaya Y. Synthesis, Spectral Characterization, Crystal Structure, and Antioxidant Properties of novel Palladium(II) Complex from ONS Donor 1,5-bis(2-hydroxybenzylidene)thiocarbohydrazone. JOTCSA. 2023;10(1):129-38.

DOI: <https://doi.org/10.18596/jotcsa.1194323>.

***Corresponding author. E-mail:** yeliz.kaya@iuc.edu.tr.

1. INTRODUCTION

Thiocarbohydrazone (NH₂-NH-C(S)-NH-NH₂) and its derivatives are a class of compounds that have applications in many fields and therefore attract great interest (1, 2). One or both of the hydrazine groups of thiocarbohydrazone can form Schiff bases called mono- or bithiocarbohydrazone by reacting with aldehydes or ketones (3, 4). Thiocarbohydrazones are interesting ligand systems as they have a variety of potential donor sites; they can bind many transition metals through both azomethinic nitrogen and sulfur atoms in their structure and donor atoms originating from aldehyde or ketone (5). These compounds and their metal complexes show biological activities such as antimicrobial, antioxidant, anticancer, antiviral, antidiabetic, and hepatoprotective (5-17). In addition, there has been an increase in the use of thiocarbohydrazones as

spectrophotometric reagents in metal determination in recent years (18-20).

Interest in phosphine-based ligands and their metal complexes increased after their roles were discovered in catalysis and stereoselective synthesis (21, 22). These compounds have also been shown to have significant bioactivities such as antitumor, antiviral, antifungal, antibacterial, and antioxidant (13, 23). Among these compounds, especially phosphine-based palladium(II) and nickel(II) complexes have been reported to have important bioactivities (22, 23). In addition, transition metal-phosphine complexes are very important for both industrial and laboratory scale catalytic applications (24).

Cisplatin, carboplatin, and oxaliplatin are effective metal-based anticancer agents (25, 26). Due to

serious side effects, drug resistance and the limited spectrum of tumors, extensive attempts have been made to replace these drugs with more efficient, less toxic and targeted anticancer drugs (e.g. Pd, Ni, Ru and Au complexes) (26-28). Because their coordination geometry and complex forming processes are very similar to platinum(II) complexes, palladium(II) complexes have received special attention as metal-organic antitumor drugs (27-31). Palladium(II) complexes have also antimicrobial and antioxidant properties (32). Carbon-carbon bond formation reactions catalyzed by palladium, such as the Suzuki Miyaura, Heck, and Sonogashira coupling reactions, are significant synthetical transformations. These synthetic transformations are widely used to prepare a wide range of organic molecules and materials, including natural products, fine chemicals, drugs, agrochemicals, and polymers (33). Many catalytic systems have been improved using palladium catalysts such as [Pd(PPh₃)₄] and [PdCl₂(PPh₃)₂] (34-36). However, some palladium(II) complexes containing triphenylphosphine secondary ligand have been found to be inhibitors of enzymes such as alkaline phosphatase (ALP), topoisomerase-II, β -glucuronidase, carbonic anhydrase and acetylcholinesterase (37-41).

There are only very few reports concerning Pd(II) complexes containing both thiocarbohydrazone and triphenylphosphine in the literature (41, 42). Therefore, in this study, a new Pd(II) complex was synthesized using 1,5-bis(2-hydroxybenzylidene)thiocarbohydrazone (L) and [PdCl₂(PPh₃)₂] to test its potential antioxidant activity. The characterization of free thiocarbohydrazone and Pd(II) complex were performed using elemental analysis, FTIR, ¹H NMR and UV-Vis spectroscopic techniques. The antioxidant activities of free thiocarbohydrazone and Pd(II) complex were also examined using DPPH• radical scavenging activity and CUPRAC method.

2. EXPERIMENTAL SECTION

2.1. Materials and Physical Measurements

Thiocarbohydrazide was obtained according to the published procedure (43). All other chemicals were purchased from chemical companies and used as received.

Elemental analyzes, IR and ¹H NMR spectra, UV-Vis data (in 4 x 10⁻⁵ M DMSO) and magnetic susceptibility measurements were performed using a Thermo Finnigan Flash EA 1112 elemental analyzer, an Agilent Cary 630 FTIR, a Varian UNITY INOVA 500 MHz NMR device, a Shimadzu 2600 UV-Vis spectrophotometer and a Sherwood Scientific MK I model device, respectively.

2.2. Synthesis of 1,5-bis(2-hydroxybenzylidene)thiocarbohydrazone (L)

Ligand (L) was prepared according to our reported article (44). Thiocarbohydrazide (0.01 mol, 1.06 g) and 2-hydroxybenzaldehyde (0.02 mol, 2.44 g) was mixed in methanol (25 mL). The mixture was refluxed for 4 h. The light-yellow colored product, which precipitated after a few days, was filtered and washed with methanol. Elemental analysis and spectroscopic data for L confirmed its synthesis (Figure 1).

Yield: 85%. Color: Light-yellow. M.p.: 190-191 °C. Calc. for C₁₅H₁₄N₄O₂S (314.36 g mol⁻¹): C: 57.31, H: 4.49, N: 17.82, S: 10.20%; found: C: 57.50, H: 4.46, N: 17.84, S: 10.28%. ¹H NMR (500 MHz, DMSO-d₆, ppm): 11.70 (s, 2H, -OH), 11.62 (s, 1H, -NH), 10.62 (s, 1H, -NH), 8.67 (s, 2H, -CH=N-), 7.35-6.89 (m, 8H, aromatic H). IR (cm⁻¹): ν (OH) 3195, ν (NH) 3133, ν (C=N) 1613, ν (C=S) 1240. UV-Vis [λ_{max} (nm)]: 251 $\pi \rightarrow \pi^*$, 302 $\pi \rightarrow \pi^*$, 351 $n \rightarrow \pi^*$, 367 $n \rightarrow \pi^*$.

2.3. Synthesis of [Pd(PPh₃)₂](L)

1 mmol of [PdCl₂(PPh₃)₂] (0.71 g) dissolved in ethanol (5 mL) was mixed with 1 mmol of L (0.31 g) dissolved in ethanol (10 mL) and dichloromethane (5 mL). Then, Et₃N (1 drop) was added to the mixture and the mixture was stirred under reflux for 5 h to afford an orange precipitate. The obtained solid was filtered and washed with ethanol (Figure 1).

Yield: 52%. Color: Orange. M.p.: 271-273 °C. Calc. for C₃₃H₂₇N₄O₂PPdS (681.05 g mol⁻¹): C: 58.20, H: 4.00, N: 8.23, S: 4.71%; found: C: 58.03, H: 3.96, N: 8.14, S: 4.57%. ¹H NMR (500 MHz, DMSO-d₆, ppm): 11.65 (s, 1H, -OH), 10.64 (s, 1H, -NH), 8.48 (s, 1H, -CH=N-), 8.11 (s, 1H, -CH=N-), 7.65-5.71 (m, 23H, aromatic H). IR (cm⁻¹): ν (OH) 3190, ν (NH) 3154, ν (C=N) 1618 and 1598, ν (PPh₃) 1432, 1099, 738, 690. UV-Vis [λ_{max} (nm)]: 256 $\pi \rightarrow \pi^*$, 280 $\pi \rightarrow \pi^*$, 313 $\pi \rightarrow \pi^*$, 339 $n \rightarrow \pi^*$, 355 $n \rightarrow \pi^*$, 410 $n \rightarrow \pi^*$, 424 LMCT.

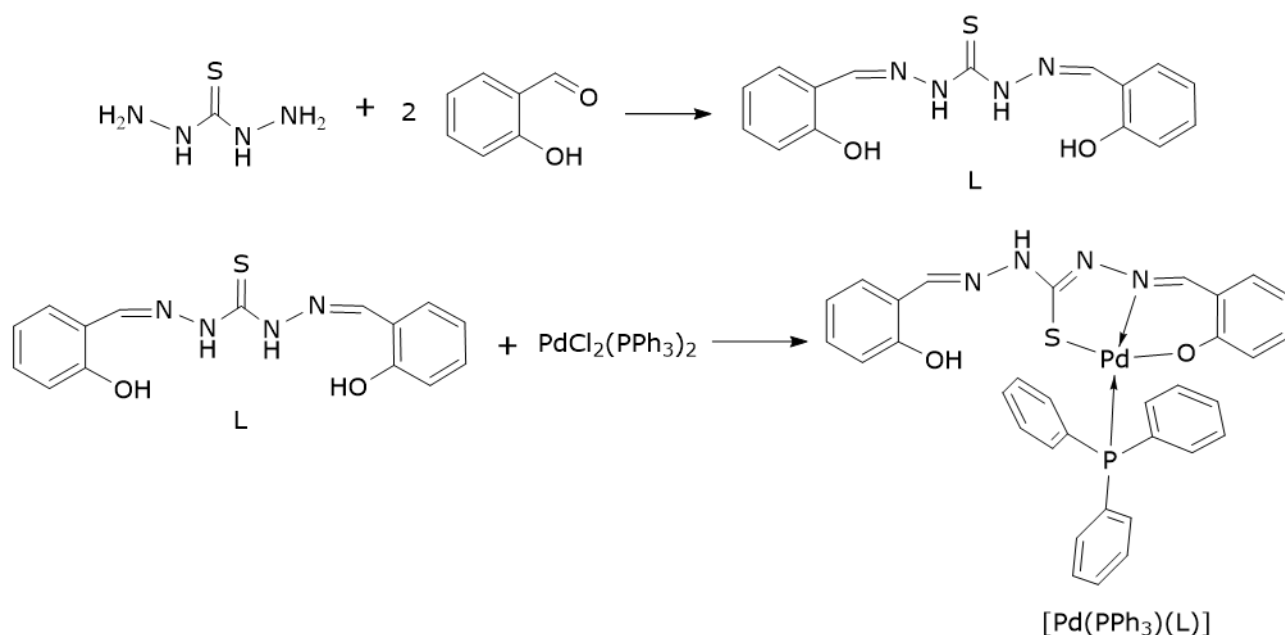


Figure 1: The general synthesis of the free thiocarbohydrazone and Pd(II) complex.

2.4. Determination of Crystal Structure

Slow evaporation of [Pd(PPh₃)(L)] in ethanol + DCM gave single crystals suitable for determining the molecular structure of the complex. A Bruker APEX II CCD three-circle diffractometer was used for X-ray diffraction data collection and unit cell determination at room temperature. Indexing, data reduction and integration were performed using APEX2 (45) and SAINT (46). Structure solution and refinement were performed with the SHELXT (47) and SHELXL (48) programs. The program Mercury was used to represent the molecular structure (49). Hydrogen atoms were positioned geometrically and treated with the riding model. The crystallographic data of [Pd(PPh₃)(L)] are given in Table 1. The selected bond distances and angles are listed in Table 2.

2.5. CUPRAC and DPPH Methods

The radical scavenging activities of free thiocarbohydrazone and Pd(II) complex were measured using the DPPH method according to the formerly declared method with minor changes (50). To a tube; 2 mL of 10⁻⁴ M DPPH in ethanol, 1 mL of 10⁻⁴ M of the sample in ethanol (containing 1% DMSO) and (1 - x) mL of ethanol were added. The mixture (4 mL) was incubated in a dark place at 25 °C. After 30 minutes, the absorbances of the sample and control solutions were measured against ethanol at 515 nm. The control solution was obtained by mixing DPPH solution (2 mL) and ethanol (2 mL). Trolox was used as the reference compound. The radical scavenging activity was computed from Equation (1) below.

$$\% \text{radical scavenging activity} = \left[\frac{A_{\text{control}} - A_{\text{sample}}}{A_{\text{control}}} \right] \times 100 \quad \text{Equation (1)}$$

mol⁻¹ cm⁻¹).

3. RESULTS AND DISCUSSION

3.1. Synthesis and Spectral Characterization

Antioxidant capacities of free thiocarbohydrazone and Pd(II) complex were determined by CUPRAC method (51). To a tube; 1 mL of 10⁻² M CuCl₂·2H₂O in water, 1 mL of 7.5 × 10⁻³ M neocuproine in ethanol, 1 mL of 1 M NH₄Ac in water, x mL of 10⁻⁴ M sample in ethanol (containing 1% DMSO) and (1.1 - x) mL of water were added and the total volume was adjusted to 4.1 mL. The mixture was incubated in a dark place for 30 minutes. Then, the absorbance values were recorded at 450 nm. The results were given as TEAC (trolox equivalent antioxidant capacity) coefficient. TEAC values were calculated by dividing the molar absorptivity (ε) of the compounds by that of Trolox (ε_{trolox} = 1.67 × 10⁴ L

The ligand was prepared by the condensation of thiocarbohydrazide (0.01 mol) with 2-hydroxybenzaldehyde (0.02 mol). The reaction of free thiocarbohydrazone (L) with an equimolar amount of [PdCl₂(PPh₃)₂] afforded the Pd(II) complex [Pd(PPh₃)(L)]. The complex is soluble in DCM, DMF and DMSO solvents. The μ_{eff} measurement showed that the complex is diamagnetic. The elemental analysis and spectroscopic data agreed with the

proposed molecular formula of the free thiocarbohydrazone and Pd(II) complex.

In the IR spectrum of L, the characteristic peaks of OH, NH, C=N and C=S groups were seen at 3195, 3133, 1613 and 1240 cm^{-1} , respectively. The bands of OH and NH groups were observed at 3190 and 3154 cm^{-1} in the spectrum of $[\text{Pd}(\text{PPh}_3)(\text{L})]$. This can be interpreted as one of the OH and NH groups of L did not participate in the formation of the complex. The absence of the band attributed to the $\nu(\text{C}=\text{S})$ in the spectrum of $[\text{Pd}(\text{PPh}_3)(\text{L})]$ can be explained by the tautomerism of the C=S group with one NH group to form the C-SH in the molecule of L. One of the bands belonging to the azomethine groups in L shifted to lower wavenumber (1598 cm^{-1}) in the spectrum of $[\text{Pd}(\text{PPh}_3)(\text{L})]$. This indicates the coordination of one of the azomethine nitrogen atoms of the ligand to the metal atom. $[\text{Pd}(\text{PPh}_3)(\text{L})]$ spectrum also includes the characteristic bands of the coordinated PPh_3 ligand at 1432, 1099, 738, 690 cm^{-1} (10, 41, 52).

^1H NMR spectrum of L exhibits two $\text{OH}_{\text{phenolic}}$ protons at 11.70 ppm whereas the spectrum of $[\text{Pd}(\text{PPh}_3)(\text{L})]$ adopts only one $\text{OH}_{\text{phenolic}}$ signal at 11.65 ppm since other OH proton is involved in bonding with palladium ion. Although the spectrum of L exhibits two NH signals at 11.62 and 10.62 ppm, the spectrum of $[\text{Pd}(\text{PPh}_3)(\text{L})]$ displays only one signal at 10.64 ppm. The disappearance of the proton in the NH group indicates the deprotonation in the NH group through the sulfur atom by tautomerism ($\text{NH}-\text{C}=\text{S} \leftrightarrow \text{N}=\text{C}-\text{SH}$). The spectrum of L shows signals belonging to two azomethine protons at 8.67 ppm, one of which undergoes a downfield shift by complexation (41, 44, 53).

The electronic spectrum of L exhibits two absorptions at 251 and 302 nm assigned to $\pi \rightarrow \pi^*$ transitions of phenyl rings. These bands were seen at 256, 280 and 313 nm in the spectrum of $[\text{Pd}(\text{PPh}_3)(\text{L})]$. The absorption bands at 315 and 367 nm in the spectrum of L are due to $n \rightarrow \pi^*$ transitions of the C=N and C=S groups. The fact that these

bands appear at 339, 355 and 410 nm in the spectrum of $[\text{Pd}(\text{PPh}_3)(\text{L})]$ can be interpreted as the metal atom being coordinated to the ligand via the azomethine nitrogen and sulfur atom. Also, different from the spectrum of L, the band attributed to the charge transfer transition (LMCT) was observed at 424 nm in the spectrum of $[\text{Pd}(\text{PPh}_3)(\text{L})]$ (26, 41, 54).

3.2. Crystal Structure Analysis

According to the results of the crystallographic analysis, $[\text{Pd}(\text{PPh}_3)(\text{L})]$ crystallizes in the $\text{P2}_1/\text{n}$ space group and as a monoclinic crystal system. The molecular structure and atom labeling scheme of $[\text{Pd}(\text{PPh}_3)(\text{L})]$ is shown in Figure 2. There are two crystallographically independent $[\text{Pd}(\text{PPh}_3)(\text{L})]$ molecules with similar parameters in the asymmetric unit. The palladium ion displays a slightly distorted square planar geometry involving oxygen, nitrogen, sulfur and phosphorus atoms. Although free thiocarbohydrazone is a potential pentadentate, it acts as a dibasic tridentate ONS donor in $[\text{Pd}(\text{PPh}_3)(\text{L})]$. In the complex, ligand is coordinated to Pd(II), forming six and five-membered chelate rings with O2-Pd1-N4, O4-Pd2-N8 and N4-Pd1-S1, N8-Pd2-S2 angles of 93.3(3) $^\circ$, 92.9(3) $^\circ$ and 84.0(3) $^\circ$, 85.0(3) $^\circ$ respectively, and these angles are similar to those observed in related Pd(II) complexes (26, 41, 55). The S1-Pd1-O2 [176.7(2) $^\circ$], S2-Pd2-O4 [177.0(2) $^\circ$] and N4-Pd1-P006 [178.4(3) $^\circ$], N8-Pd2-P005 [178.8(3) $^\circ$] bond angles are very close to the ideal angle of 180 $^\circ$. The binding parameters show that there is a slight distortion from ideal geometry around palladium ion. Pd-S [2.245(3) Å], Pd-O [2.013(8) Å and 2.014(8) Å], Pd-N [2.017(9) Å and 2.029(9) Å], and Pd-P [2.265(3) Å and 2.258(3) Å] bond distances are within normal ranges and are in good agreement with those found in four-coordinate Pd(II) complexes containing triphenylphosphine (26, 41, 56). C8-S1 [1.761(12) Å] and C41-S2 [1.764(12) Å] bond distances indicate that L is bound to palladium ion in the thiolate form (41, 42, 57). In addition, the molecular structure of $[\text{Pd}(\text{PPh}_3)(\text{L})]$ is stabilized by weak and moderately bound intermolecular and intramolecular hydrogen bonds (Table 3).

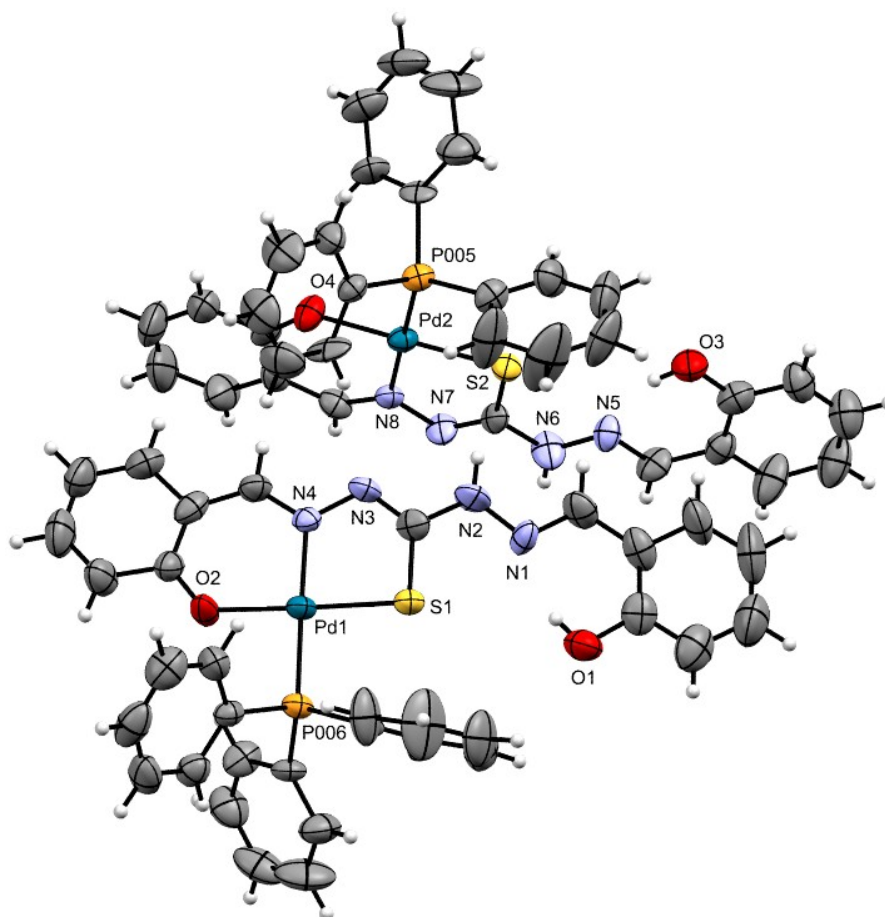


Figure 2: The molecular structure of $[\text{Pd}(\text{PPh}_3)(\text{L})]$ with the atom numbering scheme excluding C and H.

Table 1: Crystal data and structure refinement parameters for $[\text{Pd}(\text{PPh}_3)(\text{L})]$.

Name of the parameter	Value
CCDC	2196022
Empirical formula	$\text{C}_{33}\text{H}_{27}\text{N}_4\text{O}_2\text{PPdS}$
Formula weight	681.01
Temperature (K)	273.15
Crystal system	Monoclinic
Space group	$\text{P}2_1/\text{n}$
a (Å)	27.539(6)
b (Å)	8.765(2)
c (Å)	28.691(7)
α (°)	90
β (°)	110.690(4)
γ (°)	90

Crystal size (mm ³)	0.491 × 0.24 × 0.042
Wavelength (Å)	0.71073
Volume (Å ³)	6479(3)
Z	8
D _{calc.} (g.cm ⁻³)	1.396
μ (mm ⁻¹)	0.721
F(000)	2768.0
θ range for data collection (°)	2.548 to 49.998
Index ranges	-32 ≤ h ≤ 30, 0 ≤ k ≤ 10, 0 ≤ l ≤ 34
Reflections collected	11398
Independent reflections	11398
Data/restraints/parameters	11398/0/760
Goodness-of-fit on F ² (S)	1.115
Final R indexes [I ≥ 2σ(I)]	R ₁ = 0.0991, wR ₂ = 0.2255
Final R indexes [all data]	R ₁ = 0.1328, wR ₂ = 0.2368
Largest diff. peak/hole (e.Å ⁻³)	1.15/-1.80

Table 2: The selected bond lengths (Å) and bond angles (°) for [Pd(PPh₃)(L)].

Bond lengths (Å)		Bond angles (°)	
Pd1—S1	2.245(3)	S1—Pd1—O2	176.7(2)
Pd2—S2	2.245(3)	S2—Pd2—O4	177.0(2)
Pd1—O2	2.013(8)	N4—Pd1—P006	178.4(3)
Pd2—O4	2.014(8)	N8—Pd2—P005	178.8(3)
Pd1—N4	2.017(9)	O2—Pd1—P006	87.9(2)
Pd2—N8	2.029(9)	O4—Pd2—P005	87.5(2)
Pd1—P006	2.265(3)	O2—Pd1—N4	93.3(3)
Pd2—P005	2.258(3)	O4—Pd2—N8	92.9(3)
N4—N3	1.384(12)	S1—Pd1—P006	94.78(11)
N8—N7	1.392(12)	S2—Pd2—P005	94.63(11)
N2—N1	1.359(14)	S1—Pd1—N4	84.0(3)
N6—N5	1.349(13)	S2—Pd2—N8	85.0(3)

Table 3: Geometric values for hydrogen bonds for [Pd(PPh₃)(L)].

D-H...A	D-H [Å]	H...A [Å]	D...A [Å]	D-H...A [°]
O1-H1...N1	0.821(8)	1.968(9)	2.617(12)	135.5(8)
O3-H3A...N5	0.819(10)	1.894(11)	2.617(15)	146.6(7)
N2-H2...S2	0.859(11)	2.709(3)	3.461(11)	146.8(8)
N6-H6A...S1 ⁱ	0.860(12)	2.787(3)	3.513(12)	143.2(7)
C66-H66...N3	0.930(11)	2.487(11)	3.393(15)	164.9(9)
C29-H29...N7 ⁱⁱ	0.931(16)	2.519(12)	3.440(2)	168.4(8)
C54-H54...O4	0.928(16)	2.471(9)	3.283(18)	146.2(8)
C52-H52...O3 ⁱⁱⁱ	0.931(16)	2.518(7)	3.410(17)	160.6(11)

Symmetry codes: (i) +x, 1+y, +z; (ii) +x, -1+y, +z; (iii) 1-x, 3-y, 1-z.

3.3. Antioxidant Properties

The total antioxidant capacity of the free thiocarbohydrazone and Pd(II) complex was determined using the CUPRAC method. The TEAC values of the free thiocarbohydrazone and Pd(II) complex are given in Table 4. When the values are examined, it is seen that the total antioxidant capacity of both free thiocarbohydrazone and Pd(II) complex is better than Trolox (TEAC_{trolox} = 1). It also appears that free thiocarbohydrazone shows higher activity than [Pd(PPh₃)(L)]. Similar to the antioxidant capacity, the antiradical activity of [Pd(PPh₃)(L)] is also lower than that of the free thiocarbo-

hydrazone (Table 5). The degree of conjugation of the whole molecule and the number and position of the OH groups are substantial for electron transfer (58). This impacts the antioxidant activity of the tested compounds. The NH group in the thiocarbohydrazone also contributes to antioxidant activity (59). So, we can say that the decrease in the number of OH and NH groups in the free thiocarbohydrazone by complexation is the reason why the TEAC value and % radical scavenging activity of [Pd(PPh₃)(L)] are lower than that of free thiocarbohydrazone.

Table 4: The TEAC values of the compounds with regard to the CUPRAC assay.

Compounds	Molar absorptivity (L mol ⁻¹ cm ⁻¹)	TEAC	Correlation coeff. (r)
L	5.9089 × 10 ⁴	3.54 ± 0.719	0.9939
[Pd(PPh ₃)(L)]	2.5189 × 10 ⁴	1.51 ± 0.087	0.9995

Table 5: % free radical scavenging activities of the compounds (initial concentration: 10⁻⁴ M, sample volume: 1 mL).

Compounds	Free Radical Scavenging Activity (%)
L	77.84 ± 0.19
[Pd(PPh ₃)(L)]	55.07 ± 1.08
Trolox	82.33 ± 2.95

CONCLUSION

A new Pd(II) complex was synthesized from 1,5-bis(2-hydroxybenzylidene)thiocarbohydrazone (L) and structurally characterized. Crystal data showed that the complex had five- and six-membered chelate rings by the coordination of one oxygen, one nitrogen and one sulfur atom on the thiocarbohydrazone to the palladium ion. In the palladium ion with the distorted square planar geometry, the fourth coordination was completed with a phosphorus atom of triphenylphosphine co-ligand. Antioxidant activities of free thiocarbohydrazone and Pd(II) complex were studied using CUPRAC and DPPH methods. TEAC values determined according to the CUPRAC method showed that both free thiocarbohydrazone and Pd(II) complex had better antioxidant capacity than Trolox. Also, the DPPH radical scavenging ability of free thiocarbohydrazone was higher than that of the Pd(II) complex. In conclusion, free thiocarbohydrazone and Pd(II) complex with good antioxidant activity can be suggested as promising components for the prevention of oxidative stress-induced diseases.

CONFLICT OF INTEREST

The author declares no conflict of interest.

ACKNOWLEDGMENTS

I dedicate this paper to Prof. Dr. Ayşe ERÇAĞ, the mentor of my research career.

REFERENCES

1. El-Mahdy KM, El-Kazak AM, Abdel-Megid M, Seada M, Farouk O. of Some New Heterocyclic Schiff Bases Derived from Thiocarbohydrazone. ACSi. 2016 Mar 15;63(1):18-25. Available from: [<URL>](#).
2. Mamatha GP, Sherigara BS, Mahadevan KM. Electrooxidation of carbo/thiocarbohydrazone and their hydrazone derivatives at a glassy carbon electrode. J Chem Sci. 2007 May;119(3):267-74. Available from: [<URL>](#).
3. Kurzer F, Wilkinson M. Chemistry of carbohydrazone and thiocarbohydrazone. Chemical Reviews. 1970;70(1):111-49.
4. Metwally MA, Khalifa ME, Koketsu M. Thiocarbohydrazides: Synthesis and reactions. American Journal of Chemistry. 2012;2(2):38-51.
5. Bonaccorso C, Marzo T, La Mendola D. Biological Applications of Thiocarbohydrazones and Their Metal Complexes: A Perspective Review. Pharmaceuticals. 2019 Dec 25;13(1):4. Available from: [<URL>](#).
6. Nalawade A, Nalawade R, Londhe B, Tarwal N, Shejwal R. MICROWAVE ASSISTED SYNTHESIS, STRUCTURE, SPECTRAL CHARACTERIZATION AND BIOLOGICAL STUDIES OF (E)-N'-(4-FLUOROBENZYLIDENE)HYDRAZINECARBOTHIOHYDRAZIDE. International Journal of Pharmaceutical Science Invention. 2015;4(5):1-4.
7. Zafarian H, Sedaghat T, Motamedi H, Amiri Rudbari H. A multiprotic ditopic thiocarbohydrazone ligand in the formation of mono- and di-nuclear organotin(IV) complexes: Crystal structure, antibacterial activity and DNA cleavage. Journal of Organometallic Chemistry. 2016 Dec;825-826:25-32. Available from: [<URL>](#).
8. Singh DP, Kumar K, Chopra RM ne'e. Spectroscopic studies and antibacterial activities of some new 16-membered octaazamacrocyclic complexes derived from thiocarbohydrazone and pentane-2,4-dione. Spectrochimica Acta Part A: Molecular and Biomolecular Spectroscopy. 2011 Feb;78(2):629-34. Available from: [<URL>](#).
9. Melha KSA. In-vitro antibacterial, antifungal activity of some transition metal complexes of thiosemicarbazone Schiff base (HL) derived from N⁴-(7'-chloroquinolin-4'-ylamino) thiosemicarbazide. Journal of Enzyme Inhibition and Medicinal Chemistry. 2008 Jan 1;23(4):493-503. Available from: [<URL>](#).
10. Parsekar SU, Paliwal K, Haldar P, Antharjanam PKS, Kumar M. Synthesis, Characterization, Crystal Structure, DNA and HSA Interactions, and Anticancer Activity of a Mononuclear Cu(II) Complex with a Schiff Base Ligand Containing a Thiadiazoline Moiety. ACS Omega. 2022 Jan 25;7(3):2881-96. Available from: [<URL>](#).
11. Ibrahim AA, Kareem MM, Al-Noor TH, Al-Muhimeed T, AlObaid AA, Albukhaty S, et al. Pt(II)-Thiocarbohydrazone Complex as Cytotoxic Agent and Apoptosis Inducer in Caov-3 and HT-29 Cells through the P53 and Caspase-8 Pathways. Pharmaceuticals. 2021 May 26;14(6):509. Available from: [<URL>](#).
12. Muğlu H, Kurt BZ, Sönmez F, Güzel E, Çavuş MS, Yakan H. Preparation, antioxidant activity, and theoretical studies on the relationship between antioxidant and electronic properties of bis(thio/carbohydrazone) derivatives. Journal of Physics and Chemistry of Solids. 2022 May;164:110618. Available from: [<URL>](#).
13. Kaya Y, Erçağ A, Koca A. New square-planar nickel(II)-triphenylphosphine complexes containing ONS donor ligands: Synthesis, characterization, electrochemical and antioxidant properties. Journal of Molecular Structure. 2020 Apr;1206:127653. Available from: [<URL>](#).
14. Kaya Y, Erçağ A, Uğuz Ö, Koca A, Zorlu Y, Hacıoğlu M, et al. New asymmetric bithiocarbohydrazones and their mixed ligand nickel(II) complexes: Synthesis, characterization, crystal structure, electrochemical-spectroelectrochemical property, antimicrobial and antioxidant activity. Polyhedron. 2021 Oct;207:115372. Available from: [<URL>](#).
15. Abbas SY, Farag AA, Ammar YA, Atrees AA, Mohamed AF, El-Henawy AA. Synthesis, characterization, and antiviral activity of novel fluorinated isatin derivatives. Monatsh Chem. 2013 Nov;144(11):1725-33. Available from: [<URL>](#).
16. Srividya L, Reddy A, Rama N. Antidiabetic activity of 1-(4-chlorobenzylidene)-5-(2-oxoindolin-3-ylidene) thiocarbohydrazone in chick model. Asian J Biol Sci. 2017;10:126-30.
17. Tejasree Ch, Kiran G, Rajyalakshmi G, Rama Narsimha Reddy A. Hepatoprotective activity of 1-(4-(Dimethylamino)Benzylidene)-5-(2-Oxoindolin-3-ylidene) Thiocarbohydrazone in rats. Toxicological & Environmental

- Chemistry. 2013 Oct;95(9):1589-94. Available from: [<URL>](#).
18. Sadlapurkar AV, Barache UB, Shaikh AB, Gaikwad SH, Lokhande TN. 2-chlorobenzaldehyde thiosemicarbazone: a novel reagent for liquid-liquid extractive spectrophotometric determination of copper(II) from environmental and real samples. *International Journal of Environmental Analytical Chemistry*. 2021 Apr 13;1-21. Available from: [<URL>](#).
19. Nalawade AM, Nalawade RA, Shejwal RV, Kamble GS, Ling YC, Anuse MA. Development of a reliable analytical method for the precise extractive spectrophotometric determination of cadmium(II) by using of chromogenic reagent: analysis of real samples. *International Journal of Environmental Analytical Chemistry*. 2022 Dec 16;102(16):4158-77. Available from: [<URL>](#).
20. Sadlapurkar AV, Barache UB, Shaikh AB, Dhale PC, Gaikwad SH, Lokhande TN. Statistically designed extractive spectrophotometric determination scheme for bismuth(III) with 2-chlorobenzaldehyde thiosemicarbazone: Analysis of environmental and real resources. *Chemical Data Collections*. 2022 Feb;37:100798. Available from: [<URL>](#).
21. Güveli Ş, Agopcan Çınar S, Karahan Ö, Aviyente V, Ülküseven B. Nickel(II)-PPh₃ Complexes of S, N - Substituted Thiosemicarbazones – Structure, DFT Study, and Catalytic Efficiency. *Eur J Inorg Chem*. 2016 Feb;2016(4):538-44. Available from: [<URL>](#).
22. Priyarega S, Kalaivani P, Prabhakaran R, Hashimoto T, Endo A, Natarajan K. Nickel(II) complexes containing thiosemicarbazone and triphenylphosphine: Synthesis, spectroscopy, crystallography and catalytic activity. *Journal of Molecular Structure*. 2011 Sep;1002(1-3):58-62. Available from: [<URL>](#).
23. Shabbir M, Akhter Z, Ashraf AR, Ismail H, Habib A, Mirza B. Nickel(II) and palladium(II) triphenylphosphine complexes incorporating tridentate Schiff base ligands: Synthesis, characterization and biocidal activities. *Journal of Molecular Structure*. 2017 Dec;1149:720-6. Available from: [<URL>](#).
24. Rohlík Z, Holzhauser P, Kotek J, Rudovský J, Němec I, Hermann P, et al. Synthesis and coordination properties of palladium(II) and platinum(II) complexes with phosphonated triphenylphosphine derivatives. *Journal of Organometallic Chemistry*. 2006 May;691(11):2409-23. Available from: [10.1016/j.jorgchem.2006.01.024](#). Available from: [<URL>](#).
25. Tan CP, Lu YY, Ji LN, Mao ZW. Metallomics insights into the programmed cell death induced by metal-based anticancer compounds. *Metallomics*. 2014;6(5):978. Available from: [<URL>](#).
26. Elsayed SA, Badr HE, di Biase A, El-Hendawy AM. Synthesis, characterization of ruthenium(II), nickel(II), palladium(II), and platinum(II) triphenylphosphine-based complexes bearing an ONS-donor chelating agent: Interaction with biomolecules, antioxidant, in vitro cytotoxic, apoptotic activity and cell cycle analysis. *Journal of Inorganic Biochemistry*. 2021 Oct;223:111549. Available from: [<URL>](#).
27. Anu D, Naveen P, Devendhiran T, Shyamsivappan S, Kumarasamy K, Lin MC, et al. Synthesis, spectral characterization, X-ray crystallography and biological evaluations of Pd(II) complexes containing 4(N)-substituted thiosemicarbazone. *Journal of Coordination Chemistry*. 2021 Dec 17;74(21-24):3153-69. Available from: [<URL>](#).
28. Nadeem S, Bolte M, Ahmad S, Fazeelat T, Tirmizi SA, Rauf MK, et al. Synthesis, crystal structures and antibacterial and antiproliferative activities in vitro of palladium(II) complexes of triphenylphosphine and thioamides. *Inorganica Chimica Acta*. 2010 Oct;363(13):3261-9. Available from: [<URL>](#).
29. Shanmugapriya A, Jain R, Sabarinathan D, Kalaiarasi G, Dallemer F, Prabhakaran R. Structurally different mono-, bi- and trinuclear Pd(II) complexes and their DNA/protein interaction, DNA cleavage, and anti-oxidant, anti-microbial and cytotoxic studies. *New J Chem*. 2017;41(18):10324-38. Available from: [<URL>](#).
30. Ayyannan G, Mohanraj M, Gopiraman M, Uthayamalar R, Raja G, Bhuvanesh N, et al. New Palladium(II) complexes with ONO chelated hydrazone ligand: Synthesis, characterization, DNA/BSA interaction, antioxidant and cytotoxicity. *Inorganica Chimica Acta*. 2020 Nov;512:119868. Available from: [<URL>](#).
31. Khan H, Badshah A, Said M, Murtaza G, Sirajuddin M, Ahmad J, et al. Synthesis, structural characterization and biological screening of heteroleptic palladium(II) complexes. *Inorganica Chimica Acta*. 2016 Jun;447:176-82. Available from: [<URL>](#).
32. Kavitha P, Laxma Reddy K. Pd(II) complexes bearing chromone based Schiff bases: Synthesis, characterisation and biological activity studies. *Arabian Journal of Chemistry*. 2016 Sep;9(5):640-8. Available from: [<URL>](#).
33. Boubakri L, Mansour L, Harrath AH, Özdemir I, Yaşar S, Hamdi N. N-Heterocyclic carbene-Pd(II)-PPh₃ complexes as a new highly efficient catalyst system for the Sonogashira cross-coupling reaction: Synthesis, characterization and biological activities. *Journal of Coordination Chemistry*. 2018 Jan 17;71(2):183-99. Available from: [<URL>](#).
34. Bahl A, Grahn W, Stadler S, Feiner F, Bourhill G, Bräuchle C, et al. Novel, Blue-Transparent Frequency Doublers Based on 1,8-Di(hetero)arylnaphthalenes. *Angew Chem Int Ed Engl*. 1995 Jul 31;34(1314):1485-8. Available from: [<URL>](#).
35. Goldfinger MB, Crawford KB, Swager TM. Directed Electrophilic Cyclizations: Efficient Methodology for the Synthesis of Fused Polycyclic Aromatics. *J Am Chem Soc*. 1997 May 1;119(20):4578-93. Available from: [<URL>](#).
36. Hartwig JF, Kawatsura M, Hauck SI, Shaughnessy KH, Alcazar-Roman LM. Room-Temperature Palladium-Catalyzed Amination of Aryl Bromides and Chlorides and Extended Scope of Aromatic C–N Bond Formation with a Commercial Ligand. *J Org Chem*. 1999 Jul 1;64(15):5575-80. Available from: [<URL>](#).
37. Asma M, Badshah A, Ali S, Sohail M, Fettouhi M, Ahmad S, et al. Synthesis, Characterization of Mixed Ligand Palladium(II) Complexes of Triphenylphosphine and Anilines and their Enzyme Inhibition Studies against β -glucuronidase. The Crystal Structure of trans-dichloro-(m-chloroaniline)(triphenylphosphine)palladium(II). *Transition Met Chem*. 2006 May;31(4):556-9. Available from: [<URL>](#).
38. Shabbir M, Akhter Z, Ahmad I, Ahmed S, Shafiq M, Mirza B, et al. Schiff base triphenylphosphine palladium (II)

- complexes: Synthesis, structural elucidation, electrochemical and biological evaluation. *Journal of Molecular Structure*. 2016 Aug;1118:250-8. Available from: [<URL>](#).
39. Rocha FV, Barra CV, Garrido SS, Manente FA, Carlos IZ, Ellena J, et al. Cationic Pd(II) complexes acting as topoisomerase II inhibitors: Synthesis, characterization, DNA interaction and cytotoxicity. *Journal of Inorganic Biochemistry*. 2016 Jun;159:165-8. Available from: [<URL>](#).
40. Ahmed M, Khan SZ, Sher N, Rehman ZU, Mushtaq N, Khan RA. Kinetic and toxicological effects of synthesized palladium(II) complex on snake venom (*Bungarus sindanus*) acetylcholinesterase. *J Venom Anim Toxins incl Trop Dis [Internet]*. 2021 [cited 2023 Feb 8]; Available from: [<URL>](#)
41. Kaya Y, Erçağ A, Zorlu Y, Demir Y, Gülçin İ. New Pd(II) complexes of the bithiocarbohydrazones derived from isatin and disubstituted salicylaldehydes: Synthesis, characterization, crystal structures and inhibitory properties against some metabolic enzymes. *J Biol Inorg Chem*. 2022 Mar;27(2):271-81. Available from: [<URL>](#).
42. Ibrahim AA, Khaledi H, Ali HM. A multiprotic indole-based thiocarbohydrazone in the formation of mono-, di- and hexa-nuclear metal complexes. *Polyhedron*. 2014 Oct;81:457-64. Available from: [<URL>](#).
43. Burns GR. Metal complexes of thiocarbohydrazone. *Inorganic Chemistry*. 1968;7(2):277-83.
44. Kaya İ, Temizkan K, Kaya Y, Erçağ A. The monomers and polymers of azomethine-based thiocarbohydrazones: Fluorescent activities, fluorescence quantum yields of polymers in water and DMF solutions. *Materials Science and Engineering: B*. 2022 Aug;282:115782. Available from: [<URL>](#).
45. Bruker. APEX2, version 201411-0, Bruker. Bruker, AXS Inc, Madison, WI; 2014.
46. Bruker. SAINT, version 834 A, Bruker. Bruker AXS Inc, Madison, WI; 2013.
47. Sheldrick GM. *SHELXT* - Integrated space-group and crystal-structure determination. *Acta Crystallogr A Found Adv*. 2015 Jan 1;71(1):3-8. Available from: [<URL>](#).
48. Sheldrick GM. Crystal structure refinement with *SHELXL*. *Acta Crystallogr C Struct Chem*. 2015 Jan 1;71(1):3-8. Available from: [<URL>](#).
49. Macrae CF, Sovago I, Cottrell SJ, Galek PTA, McCabe P, Pidcock E, et al. *Mercury 4.0*: from visualization to analysis, design and prediction. *J Appl Crystallogr*. 2020 Feb 1;53(1):226-35. Available from: [<URL>](#).
50. Sánchez-Moreno C, Larrauri JA, Saura-Calixto F. A procedure to measure the antiradical efficiency of polyphenols. *J Sci Food Agric*. 1998 Feb;76(2):270-6. Available from: [<URL>](#)
51. Apak R, Güçlü K, Özyürek M, Karademir SE. Novel Total Antioxidant Capacity Index for Dietary Polyphenols and Vitamins C and E, Using Their Cupric Ion Reducing Capability in the Presence of Neocuproine: CUPRAC Method. *J Agric Food Chem*. 2004 Dec 1;52(26):7970-81. Available from: [<URL>](#).
52. Yanping R, Rongbin D, Liufang W, Jigui W. Synthesis, Characterization and Crystal Structure of 1,5-Bis(2-Hydroxybenzaldehyde)-Dithiocarbohydrazone. *Synthetic Communications*. 1999 Feb;29(4):613-7. Available from: [<URL>](#).
53. Lugasi SO. New synthetic pathways for thiocarbohydrazone and salicylaldehyde azine compounds. Available from: [<URL>](#).
54. Kaya Y, Erçağ A, Koca A. Synthesis, structures, electrochemical studies and antioxidant activities of cis-dioxomolybdenum(VI) complexes of the new bithiocarbohydrazones. *Journal of Molecular Structure*. 2015 Dec;1102:117-26. Available from: [<URL>](#).
55. Özerkan D, Ertik O, Kaya B, Kuruca SE, Yanardag R, Ülküseven B. Novel palladium (II) complexes with tetradentate thiosemicarbazones. Synthesis, characterization, in vitro cytotoxicity and xanthine oxidase inhibition. *Invest New Drugs*. 2019 Dec;37(6):1187-97. Available from: [<URL>](#).
56. Manna CK, Naskar R, Bera B, Das A, Mondal TK. A new palladium(II) phosphino complex with ONS donor Schiff base ligand: Synthesis, characterization and catalytic activity towards Suzuki-Miyaura cross-coupling reaction. *Journal of Molecular Structure*. 2021 Aug;1237:130322. Available from: [<URL>](#).
57. Takjoo R, Takjoo R, Yazdanbakhsh M, Aghaei kaju A, Chen Y. Mixed Ligand Palladium(II) Complex with NS-Bidentate S -Allyldithiocarbazate Schiff Base: Synthesis, Spectral Characterization, Crystal Structure and Decoding Intermolecular Interactions with Hirshfeld Surface Analysis. *Chin J Chem*. 2010 Feb;28(2):221-8. Available from: [<URL>](#).
58. Apak R, Güçlü K, Özyürek M, Celik SE. Mechanism of antioxidant capacity assays and the CUPRAC (cupric ion reducing antioxidant capacity) assay. *Microchimica Acta*. 2008;160(4).
59. Asha TM, Prathapachandra Kurup MR. An insight into the potent antioxidant activity of a dithiocarbohydrazone appended cis -dioxidomolybdenum (VI) complexes. *Appl Organomet Chem [Internet]*. 2020 Sep [cited 2023 Feb 8];34(9). Available from: [<URL>](#)



Assay of Tretinoin using Safranin-O as a Chromogenic Reagent in Bulk and Dosage Forms

Thuttgartunta Manikya Sastry^{1*} , Venkata Nagalakshmi Kiilana¹ ,
and Rama Krishna Karipeddi² 

¹Gayatri Vidya Parishad College of Engineering (Autonomous), Chemistry, Department of Chemistry, Visakhapatnam-530048, India

²GITAM, Deemed to be University, Department of Chemistry, Rushikonda, Visakhapatnam- 530045, India

Abstract: A new, economical and accurate analytical technique was developed for the assay of tretinoin (TTN) in bulk and formulations. While developing the method, it was found that the reaction was carried out due to the formation of ion-pair association complex involving the carboxyl group in the side chain of the TTN with safranin-O. The colored species formed was stable up to 60 minutes. The optical density of color species was measured at 520 nm. All the variables were optimized. The linearity range lies for the developed method within the concentration ranges of 2-10 $\mu\text{g mL}^{-1}$. The linear correlation coefficient (r) and molar absorptivity (ϵ_{max}) values were found as 0.9999 and $1.66 \times 10^4 \text{ L mol}^{-1}\text{cm}^{-1}$. Percentage recoveries were found from 99.2 ± 1.8 to 100.2 ± 0.7 . The method was validated as per ICH guidelines.

Keywords: Bioactive compounds, tretinoin, safranin-O(SFN-O), Ion-pair association complex, spectrophotometry.

Submitted: September 17, 2022. **Accepted:** January 04, 2023.

Cite this: Manikya Sastry T, Nagalakshmi KV, Ramakrishna K. Assay of Tretinoin using Safranin-O as a Chromogenic Reagent in Bulk and Dosage forms. JOTCSA. 2023;10(1):139-46.

DOI: <https://doi.org/10.18596/jotcsa.1176621>.

***Corresponding author. E-mail:** tmsastry@yahoo.com.

1. INTRODUCTION

Bioactive compounds are found in both plant and animal products and can also be synthetically produced. Drugs are an important class of bioactive compounds. The estimation based on the reactions with suitable chromogenic agents are simple and inexpensive. Over-the-counter (OTC) drugs used for skin care are classified as dry skin products, acne products, sunscreen and suntan products and foot care products. Acne occurs most commonly during adolescence and found in 80-90% of teenagers due to hormonal changes. The acne product namely tretinoin works by replacement of skin cells. Acne vulgaris is considered as common skin related problem that was treated with combination therapy using topical drug clindamycin and tretinoin (TTN)

(1). Literature survey revealed that there is an evidence about the determination TTN by HPLC (2-6), RP-HPLC (7-12), UPLC (13), LC (14), and GC (15). Studies on phototoxicity of tretinoin (16), UV-spectrophotometry (17-22), and UV-derivative spectroscopy (23-25) were also carried out by the previous authors. Most of the analytical methods involve sophisticated instruments which are expensive, and require maintenance and are not within the reach of most of the laboratories. Visible spectrophotometry can be chosen as an alternative technique. It is a highly preferable method for routine analysis because of its simplicity, low time and economical advantages. The novelty of this technique lies in its sensitivity and further depends on the nature of reaction and not on the sophistication of the instrument. No evidence is

found in the literature for the determination of TTN by visible spectrophotometry. Hence the authors made an attempt to develop simple and sensitive visible spectroscopic method for the assay TTN in bulk and formulations using safranin-O (SFN-O) as a chromogenic reagent. Figure 1 shows the structural molecule for tretinoin.

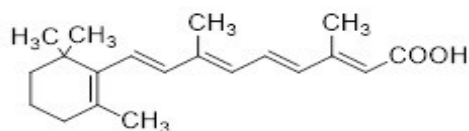


Figure 1: Chemical structure of Tretinoin (2E,4E,6E,8E)-3,7-Dimethyl-9-(2,6,6-trimethylcyclohex-1-enyl) nona-2,4,6,8-all-trans-tetraenoic acid).

2. EXPERIMENTAL SECTION

2.1. Materials and Methods

2.1.1. Instrumentation

Shimadzu UV double beam spectrophotometer has been chosen for obtaining precise and accurate optical density measurements. In addition a digital pH meter (equiptronics, India) was used to measure the pH of the samples. An electrical balance (Dhona 200 D, India) was used to weigh all the materials.

2.1.2. Chemicals and Reagents

TTN (Biophore India), Formulations namely Retino-A (Ethnorjansencilag), Airol (Piramal Health care). Avita, Bertek pharmaceutical Inc.) and Eudyna, (German Remedies.) were procured from the registered pharmacy.

Reagents namely SFN-O (Fluka, Mumbai, India, 98% purity), Sodium hydroxide (Qualigens Mumbai, India, 99% purity) and solvent CHCl_3 (Qualigens

Mumbai, India, 99% purity) were procured for this study are of analytical grade.

Aqueous solutions of SFN-O (Fluka; 0.01%, 2.86×10^{-4} M) was prepared by dissolving 10 mg of safranin-O in 100 mL of distilled water and washed with CHCl_3 to remove chloroform-soluble impurities. Buffer solution was prepared by mixing 50 mL of 0.025 M borax solution with 15 mL of 0.1 M of sodium hydroxide and diluted to 100 mL with distilled water and pH was adjusted to 9.8.

2.1.3. Bulk sample solution

Stock solution (mg mL^{-1}) for bulk drug sample was prepared in 100 mL of chloroform by dissolving 100 mg of tretinoin. Working standard solutions of concentration of $40 \mu\text{g mL}^{-1}$ were prepared from the above stock solution. Further dilution was done using chloroform.

2.1.4. Formulations

Cream equivalent to 50 mg was dissolved in 30 mL of aqueous methanol (3:1). The resulting solution was extracted with solvent CHCl_3 (3 x 25.0 mL portions) followed by filtration. The total chloroform extract was kept for drying with 5 g of anhydrous Na_2SO_4 and then filtered. This filtrate was made up to 200 mL with chloroform to obtain the stock solution of ($250 \mu\text{g mL}^{-1}$). The stock solution was further diluted to a concentration of $40 \mu\text{g mL}^{-1}$.

2.1.5. Calibration curve - UV method (Reference method)

Stock solution (mg mL^{-1}) was prepared by dissolving 100 mg of bulk drug sample in 100 mL isopropanol. From this stock solution, working standard solution of concentration $10 \mu\text{g mL}^{-1}$ was prepared using the same solvent. The absorption spectrum of bulk drug sample was recorded against a reagent blank within the UV region using Shimadzu double beam spectrophotometer (Figure 2).

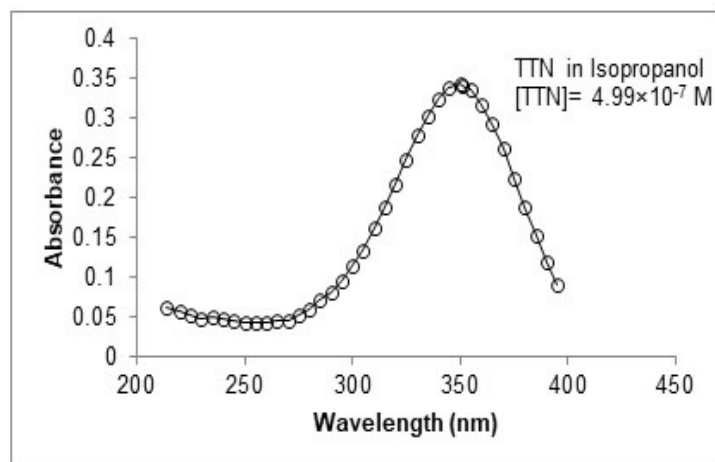


Figure 2: Absorption spectrum of tretinoin ($[\text{TTN}] = 4.99 \times 10^{-7} \text{M}$) against (blank).

A series of solutions were prepared by taking 0.5-2.5 mL standard drug solution ($10 \mu\text{g mL}^{-1}$) into 20.0 mL calibrated tubes. These are diluted to 10.0 mL with double distilled water. The optical densities of all the sample solutions were measured at 352 nm against

reagent blank (isopropanol). The concentration of the drug was deduced from its calibration curve drawn between optical density and concentration of TTN (Figure 3).

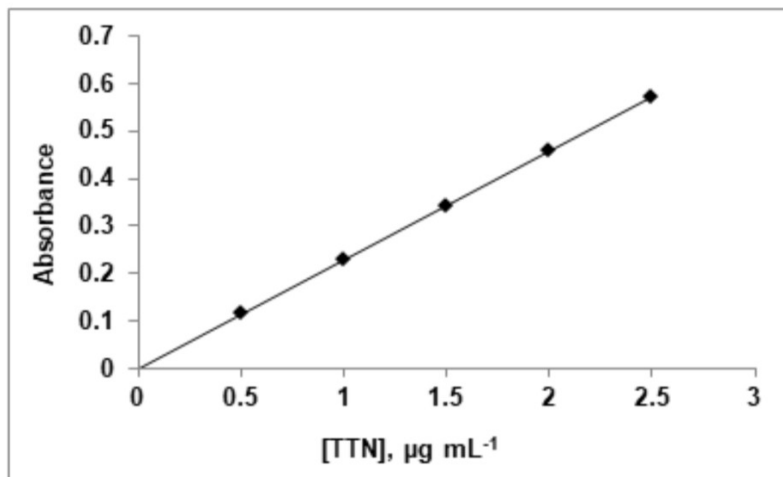


Figure 3: Calibrated curve of tretinoin ($[\text{TTN}] = 4.99 \times 10^{-7} \text{ M}$).

2.1.6. Method development

A series of solutions were prepared by taking aliquots of standard drug solution (0.5 - 2.5 mL, $40 \mu\text{g mL}^{-1}$), 2.0 mL of $2.85 \times 10^{-4} \text{ M}$ safranin solution and 1.0 mL of buffer solution (pH 9.8) into 50.0 mL separating funnels. The volume of each sample was diluted to 15.0 mL with distilled water and 10.0 mL chloroform was added. The contents of the separating funnel were shaken for two minutes. The

two layers were separated and the absorbance of organic layer was measured at 520 nm against blank. The optical density of colored species was observed to decrease after 60 min indicating the decomposition of colored complex. The concentration of the drug was deduced from its calibration curve drawn between optical density and concentration of TTN (Figure 4).

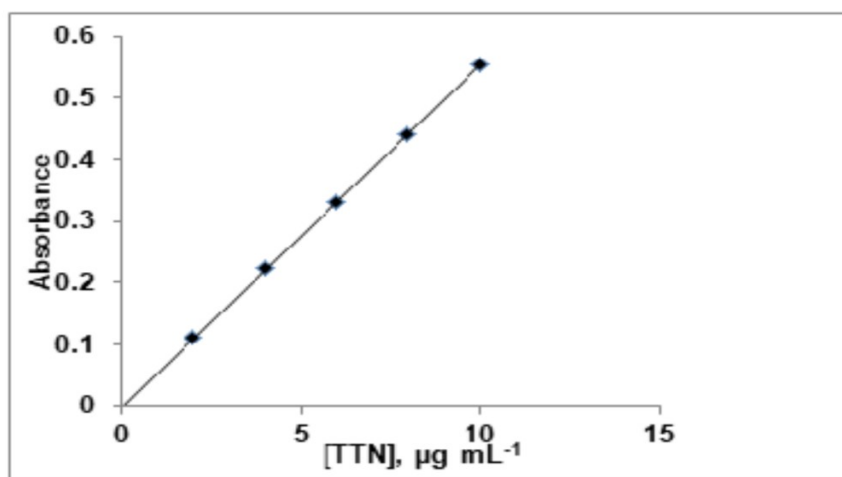


Figure 4: Calibrated curve of TTN - SFN-O method.

3. RESULTS AND DISCUSSION

3.1. Selection of Analytical Wavelength

The sample solution containing fixed amount of TTN, SFN-O (basic dye), buffer and other furnished

variables as mentioned in the procedure has been scanned in the visible region (350 - 750 nm) against the reagent blank. The absorption spectrum of the colored species formed on the basis of ion-pair association complex showed maximum absorbance

at 520 nm and this wavelength has been selected for the analysis. The spectrum of the safranin-O (basic dye) showed maximum absorbance whereas

blank solution against chloroform showed negligible absorbance at this wavelength (Figure 5).

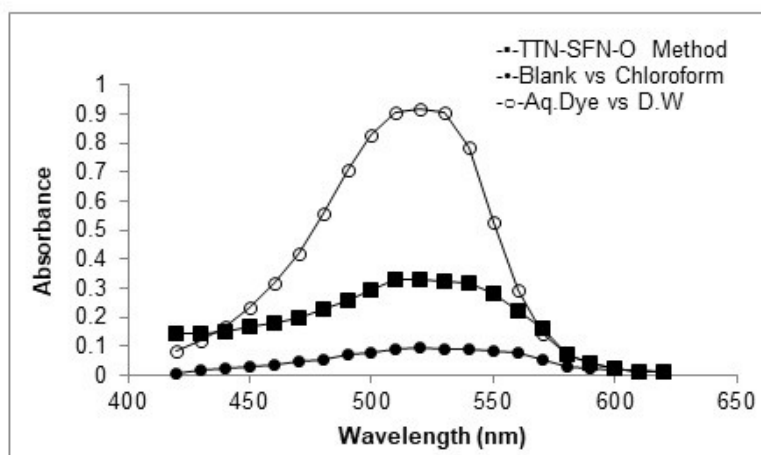


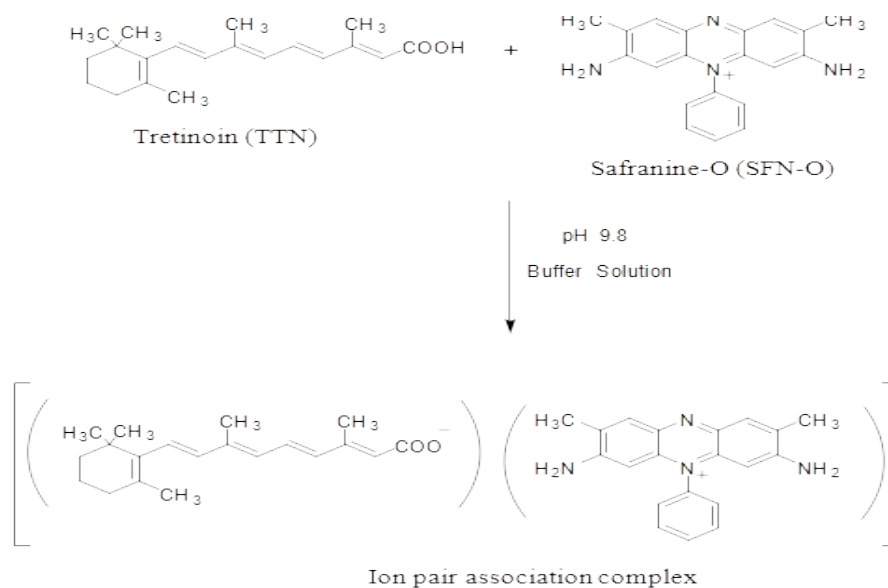
Figure 5: Absorption spectrum of TTN-SFN-O method.

3.2. Optimum Conditions

The responses of several factors like concentration of SFN-O ($0.29 - 0.72 \times 10^{-4} \text{ mol L}^{-1}$) the volume of extracting solvent chosen, time of stability of ion-pair association complex formation (1-60 minutes), intensity of colored species produced, the ratio of aqueous to CHCl_3 were studied (26). The following optimum conditions were fixed for the proposed technique are; 2.0 mL ($0.57 \times 10^{-4} \text{ mol L}^{-1}$) SFN-O, 1.0 mL borax buffer (pH=9.8) with 2 min agitation time at $28 \pm 2^\circ \text{C}$. The ion pair association complex is stable up to 60 minutes afterwards the absorbance slowly decreased indicating the decomposition of the complex.

3.3. Mechanism of Ion-pair Association Complex

In TTN, the carboxyl group in the side chain involved in the formation of the ion pair association complex with SFN-O in alkaline medium. Based on the analogy studies, the ion-pair association complex formation mechanism is explained. The negative charge appeared on the carboxylate anion of the drug (TTN) molecule and the positive charge of SFN-O held together through electrostatic force of attraction. The obtained product behaved as a single molecule. The probable sequence of mechanism of the reaction is given in Scheme 1.



Scheme 1: Ion pair association complex of tretinoin with safranin-O at pH 9.8.

3.4. Validation of Analytical Data

Following (ICH) requirements (27), the TTN-SFN-O system developed was validated statistically. Validation parameters like slope (b), intercept (a), linear correlation coefficient (r), inter and intraday precision (%RSD) were studied. Optical and regression characteristics like ϵ_{\max} ($\text{Lmol}^{-1}\text{cm}^{-1}$) and λ_{\max} (nm) values were found to be 1.66×10^4 and 520, respectively. The limits of linearity range for TTN-SFN-O system was found to have 2 - 10 $\mu\text{g mL}^{-1}$. The calibrated curve drawn at specified

concentration levels consisting of linearity with linear correlation coefficient (r) value 0.9999. Limit of detection (LOD) and Limit of quantification (LOQ) for the developed method were calculated. Sensitivity of developed method is explained on the basis of molar absorptivity values. Precision was explained in terms of relative standard deviation (%RSD) considering from six (n=6) determinations of the sample solution under optimum conditions. The results are given in Tables 1 and 2.

Table 1: Optical conditions for the proposed technique.

Optical condition	TTN-SFN-O method
Wavelength (λ_{\max})	520 nm
Molar absorptivity (ϵ_{\max})	$1.66 \times 10^4 \text{ L mol}^{-1}\text{cm}^{-1}$
Limits of linearity range	2-10 $\mu\text{g mL}^{-1}$
LOD	$7.19 \times 10^{-3} \mu\text{g mL}^{-1}$
LOQ	$2.18 \times 10^{-2} \mu\text{g mL}^{-1}$
Standard error of estimation (S_e)	1.23×10^{-3}
Sandell's Sensitivity	$1.81 \times 10^{-2} \mu\text{g cm}^{-2}$

Table 2: Validation parameters for the proposed technique.

Validation parameter	TTN-SFN-O method
Slope (b)	5.51×10^{-2}
Standard deviation on slope (S_b)	2.00×10^{-4}
Intercept (a)	1.80×10^{-4}
Standard deviation on intercept (S_a)	1.20×10^{-4}
Linear correlation coefficient (r)	0.9999
Intra -day precision (%RSD)*	0.65
Inter- day precision (%RSD)*	0.68
0.01 Level of confidence limits	1.07
0.05 Level of confidence limits	0.68

$y = a + bC$ where C is the concentration of analyte in $\mu\text{g/mL}$ and y is the absorbance unit. Calculated from six determinations.

The accuracy of the analytical procedure was checked in terms of % recovery. Recovery experiments were carried out by introducing a calculated quantity of drug to the pre-analyzed formulations at different levels and determining the accuracy of the techniques proposed. Values of % Recovery were found to be 99.2 - 100.2% (± 0.8 to ± 0.7) for considering three determinations (n=3). The results of proposed method (formulations) and UV reference method were compared through student t- and F- tests. It was observed that no significant difference was noticed in between developed and UV reference methods as the results are found within the acceptable limits (Based on 95% confidence limit values for student "t"- test and "F"-test respectively. The results are given in Table 3. The proposed method was compared with literature method (20) and found to be more sensitive with reference to molar absorptivity, linear correlation coefficient (r), LOD and LOQ values.

Precision and accuracy was calculated in terms of relative standard deviation (%RSD) and %Recovery values. The results are given in Table 4.

4. CONCLUSION

An accurate analytical technique developed for the assay of TTN in bulk and formulations. The developed technique is found to be best among the literature methods in terms of stability, sensitivity and cost. The sensitivity of developed method lies only in the reaction's nature with the reagent chosen but not on the instrument's sophistication. The excipients commonly found in formulations did not intervene in the assay. Hence the developed method is specific and suitable and found as an alternative to instrumental methods such as LC-MS, HPLC, GLC and GC-MS, in quality control laboratories.

Table 3: Assay of TTN in Pharmaceutical Formulations (TTN-SFN-O Method).

Formulation Proprietary name	Labeled Amount (g)	Amount found by proposed method (g)(n=6) ^a	95% Confidence limit values F -Test ^b	95% Confidence limit values t-Test ^c	Quantity found by UV absorption method (g)(n=3)	% Recovery developed method ^d
Cream (Retino-A)	20.0	20.04	0.15	1.55	20.1 ± 0.1	100.2 ± 0.7
Cream (Ainol)	20.0	20.03	3.07	1.19	20.1 ± 0.2	100.1 ± 0.7
Cream (Avita)	20.0	19.84	2.99	0.03	19.9 ± 0.2	99.2 ± 1.8
Cream (Eudyna)	20.0	19.94	1.07	0.90	19.9 ± 0.1	99.7 ± 0.6

^aAverage value of six observations. ^bTabulated value of 5.05 for “F” -Test. ^cTabulated value of 2.57 for student “t” -Test. ^dAverage value of three measurements (n=3).

Table 4: Comparison of proposed method with literature (20) method.

Reagent used	Iodine (I ₂)	SFN-O
Wavelength(λ_{max}) nm	295	520
Molar absorptivity(ϵ_{max}) L mol ⁻¹ cm ⁻¹	1.31×10 ⁴	1.66×10 ⁴
Limits of linearity range(μ g mL ⁻¹)	9.04 - 29.71	2-10
Linear correlation coefficient (r)	0.9974	0.9999
Relative standard deviation (%RSD)	1.95-0.88	Intraday(0.65) Interday(0.68)
% Recovery	97.84 - 102.80	99.7 - 100.2
LOD μ g mL ⁻¹	4.35	0.007
LOQ μ g mL ⁻¹	13.17	0.022
Method	Zayed MA and Abdel-Basset MH (20)	Present method

5. CONFLICT OF INTEREST

None.

6. ACKNOWLEDGMENTS

The authors (Dr. T. Manikyasastry and Dr.K. V. Nagalakshmi) are grateful to the organisation, GVPCOE (A) for their encouragement and support.

7. REFERENCES

1. Fu LW, Vender RB. Newer approach in topical combination therapy for acne. *Skin Therapy let.* 2011;16(9):3-6.
2. Platzer DJ, White BA. Development and validation of a gradient HPLC method for the determination of clindamycin and related compounds in a novel tablet formulation. *J Pharm Biomed Anal.* 2006;41:84-88. DOI: [<URL>](#).
3. Tashtoush BM, Jacobson EL, Jacobson MK. A rapid HPLC method for simultaneous de-termination of tretinoin and isotretinoin in dermatological formulations. *J Pharm Biomed Anal.* 2007;43(3):859-864. DOI: [<URL>](#).
4. Fawzia I, Mohie KSE, El-Deen AK, and Kuniyoshi S. A New HPLC-DAD Method for the Concurrent Determination of Hydroquinone, Hydrocortisone Acetate and Tretinoin in Different Pharmaceuticals for Melasma Treatment. *Journal of Chromatographic Science.* 2019;57(6):495-501. DOI: [<URL>](#).
5. Abdelghani M, Mohamed SB. Simplified HPLC method for simultaneous determination of erythromycin and tretinoin in topical gel form. *Sep Sci plus.* 2020;1-8. DOI: [<URL>](#).
6. Sadaf S, Shahid H, Mohsin J, Ali R, Shahid I, Hamad A, Samar OA, Eslam B, HamoudH. Somaily, Rami AP, EmanA and Abd-E F. Simultaneous HPLC Determination of Clindamycin Phosphate, Tretinoin, and Preservatives in Gel Dosage Form Using a Novel Stability-Indicating Method. *Inorganics.*2022; 10(10):1-15. DOI: [<URL>](#).
7. Yuenong RY, Eden B, Richard B, Robert H, Barry H. Simultaneous determination of tretinoin and clindamycin phosphate and their degradation products in topical formulations by reverse phase HPLC. *J Sep Sci.* 2004;27:71-77. DOI: [<URL>](#).
8. Vaidya V, Baing MM, Joshi SS. Reverse phase high performance liquid chromatographic determination of tretinoin in bulk material, *Indian Drugs.* 2005; 42(1):42-45.
9. Sheliya K, Shah K, Kapupara P. Development and validation of analytical method for simultaneous estimation of mometasonefuroate, hydroquinone and tretinoin in topical formulation by RP-HPLC. *J Chem Pharm Res.* 2014; 6(4):934-940.
10. Vasanthi R, Rajitha N, Raja MA, Shrishva V, Banji D, Kumar DS. Analytical method development and validation

of Isotretinoin in tablet dosage formulation. Asian J Pharm Anal Med Chem. 2015;3(3):145-153.

11. Ashish A, Manoj S, Reverse-phase High-performance Liquid Chromatography Estimation of Methotrexate and Tretinoin in Bulk and Pharmaceutical Dosage Forms. International Journal of Pharmaceutical & Biological Archives 2019; 10(2):146-153.

12. Jamel MKA, Gagy AA. Development and validation of analytical spectrophotometric and RP-HPLC methods for the simultaneous estimation of hydroquinone, hydrocortisone and tretinoin ternary mixture in topical formulation. International journal of pharmacy and pharmaceutical sciences. 2019;11(11):10-16. DOI: [<URL>](#).

13. His SL, Surman P and Al-Kassas R. Development of a stability-indicating UPLC method for determination of isotretinoin in bulk drug. Pharmaceutical Development and Technology, 2018; 24 (2):189-198.

14. Dileusa DO, Diego FDA, Edilene GDO, Ruy CRB. Liquid chromatography method to assay tretinoin in skin layers: validation and application in skin penetration/retention studies. Heliyon. 2020;6:e03098. DOI: [<URL>](#).

15. Martins LE, Danielle G, Almeida DA, Nelson R, Antoniosi F. Development of a gas chromatography method for the determination of isotretinoin and its degradation products in pharmaceuticals. J Pharm Biomed Anal. 2005;38:678-685. DOI: [<URL>](#).

16. Slade HB, Shroot B, Feldman SR, Cargill DI, Stanfield J. Reappraising the phototoxicity of tretinoin: a report of four controlled clinical trials. Photodermatology, Photoimmunology & Photomedicine. 2009;25(3):146-152. DOI: [<URL>](#).

17. Maryam B, Ali YF, Jahanbakhsh G, Mohammad M, Ahari M, Nahid S, Mohammad Taghi B, Simultaneous spectrophotometric determination of minoxidil and tretinoin by the H-point standard addition method and partial least squares. Chem pap. 2009;63(3):336-344. DOI: [<URL>](#).

18. Patel P, Kabra P, Kimbahune R, Urmila GH. Quantitative estimation of isotretinoin (13-cis retinoic acid) in bulk and formulation by UV-visible spectrophotometry. Res J Pharm Biol Chem Sci. 2011;2(1):167-172.

19. Pankti D, Kusum M, Mehul P. Development and validation of UV-visible spectrophotometric method for simultaneous estimation of mometasone furoate, hydroquinone and tretinoin from their pharmaceutical dosage form. Int J Pharm Sci Rev Res. 2013;21(1): 296-300.

20. Zayed MA and Abdel-Basset MH. Spectrophotometric Micro determination of Tretinoin, Isotretinoin using Iodine and Tazarotene Micro determination Via Reaction with Rose-Bengal Reagent. Egypt. J. Chem. 61(1);2018:143 - 153. DOI: [<URL>](#).

21. Suraj D, Lobsang TK, Hauzel L, Laldinchhana, Sabir H. Development and validation of UV-spectrophotometric method for the determination of tretinoin. Journal of Xi'an Shiyou University. 2022;18(9):547-553.

22. Kiran D, Deepak N, Arvind N. Simultaneous UV spectrophotometric valuation of isotretinoin & their promoted drug. Int. J. Pharm. Sci. Rev. Res. 2018;49(1):82-85.

23. Barazandeh TM, Namadchian M, Fadaye VS, Souri E. Derivative spectrophotometric method for simultaneous determination of clindamycin phosphate and tretinoin in pharmaceutical dosage forms. DARU. 2013;21(1): 2-7.

24. Mahrous MS, Abdel-Khalek MM, Beltagy YA. Simultaneous Quantitation of Minoxidil and Tretinoin in Magistral and Pharmaceutical Preparations by First Derivative Spectrophotometry. Anal Lett. 2006;25(9):1673-1686. DOI: [<URL>](#).

25. Nazira S and Abdulkader S. Development and validation of derivative UV spectroscopic method for simultaneous estimation of nicotinamide and tretinoin in their binary mixtures and pharmaceutical preparations. Sarkis and Sawan BMC Chemistry. 2022;16(15):1-11. DOI: [<URL>](#).

26. Massart DL, Vandeginste BGM, Doming S N, Michotte Y, Kaufman L. Chemometrics, A text Book, Amsterdam: Elsevier. 1988;293; 80.

27. ICH Harmonized Tripartite Guideline; International Conference on Harmonization of Technical Requirements for Registration of Pharmaceuticals for Human Use, Text and Methodology on Validation of Analytical Procedures, Q2, (R1); 2005.



Health Risk Assessment of Some Heavy Metals in Lipstick Brands Sold in Local Markets in Iraq

Fatima Mallalah Mohammed^{1*} , Maryam Abdulghafor Ahmed² , Hadeel M. Oraibi³ 

1 Middle Technical University - Technical Institute - Baqubah - Department of Community Health Technique, Baghdad, Iraq.

2 Renewable Energy Sciences Department, College of Energy & Environmental Science, Al-Karkh University of Science, Baghdad, Iraq

3 Department of Biology, Collage of science, University of Diyala, Iraq.

Abstract: Heavy metals found in cosmetics are a safety threat to the health of consumers. Therefore, in this study, we evaluated the levels of heavy metals such as cadmium (Cd), chromium (Cr), copper (Cu), lead (Pb), zinc (Zn), and arsenic (As) in lipstick makeup. The level of heavy metals in lipstick was discovered by using an analytical technique with high selectivity and sensitivity, namely atomic absorption spectrometry. Twenty lipsticks were selected from the same brands, yet differing in price. Ten original (expensive) and ten knockoff (cheap) lipsticks were chosen from shops in Diyala, Iraq. The detection-limit (LOD) was in between 0.01 and 0.1, the quantification-limit (LOQ) was within 0.03 and 0.33, the recovery values (Rec.%) ranged from 100.17% to 101.1%, the RE values were 0.81%, and the RSD values were 1.33%. The results also revealed that the levels of metals are in the order of Pb > Cd > Zn > Cu > As > Cr. However, the levels of heavy metals that were estimated in this study were less than the permissible limit set by the executive authorities, so there seems to be no concern associated with these heavy metals. However, the daily and frequent use of lipstick by women exposes them to low levels of toxic metals as these metals accumulate over time and pose adverse effects on the health of the users. The results of the hazard quotient (HQ) and health risk index (HI) indicate there was no harmful effect on human health related to heavy metals present in lipstick. Whereas the results of the biological activity of the samples indicated that there was no bacterial growth in expensive samples, cheap samples were contaminated with some types of organisms; this indicates poor quality.

Keywords: Cosmetics, heavy metals, toxicity effects, health risk assessment, biological activity.

Submitted: August 03, 2022. **Accepted:** December 19, 2022.

Cite this: Mohammed FM, Ahmed MA, Oraibi HM. Health Risk Assessment of Some Heavy Metals in Lipsticks Sold in Local Markets in Iraq. JOTCSA. 2023;10(1):147-60.

DOI: <https://doi.org/10.18596/jotcsa.1154686>.

***Corresponding author. E-mail:** fm609426@gmail.com.

1. INTRODUCTION

Cosmetics are materials that are used as personal care products with the intention of coming into contact with the various outside parts of the human body like nails, hair system, epidermis, and mucous membranes of the oral cavity for cleaning, perfuming, beautifying, and changing their appearance, correcting bodily odors, and keeping the surface of the body in a good state (1). Many

different products are marketed under the name "cosmetics" like shampoos, bath oils, baby products, perfumes, body lotions, personal hygiene products, and fingernail polish (2,3). To increase the elegance and glamour of ones look lipsticks are used (4). Recently, the use of lipstick has increased, resulting in their mass produce all over the world, and this industry is estimated to be in billions of dollars, with the global lipstick market expected to reach \$13.4 billion by 2024 (5). Lipstick is composed of oils,

waxes, dyes, moisturizers, and antioxidants. Oils make easy the application of lipstick and add glossy properties to its appearance, waxes give thermal stability to the lipstick; and dyes give multiple colors to the final product (6-8) with many other auxiliary components to enhance their desired effects depending on the manufacturers (7). Many lipsticks have been reported to contain many heavy metals such as cadmium (Cd), lead (Pb), arsenic (As), chromium (Cr), and cobalt (Co) (6, 9). Either as basic ingredients or for functional reasons, they are added to cosmetics for functional reason; for example, Al, Au, Cu, and Ag are added for a wonderful metallic finish. As well, Fe, Cd, Ni, Cr, Cu, Zn, Ti, Al, Mn, Ba, and Pb, are used as dyes. However, their presence is limited to certain percentages set by the relevant authorities (10). They are considered to be just impurities in the product (11) as a result of contamination of metallic devices used during the manufacturing process, along with insufficient purification of raw materials (12,13). Thus, frequent daily use of lipstick contaminated with heavy metals is more dangerous due to direct oral ingestion (14). After that, the heavy metal ions get absorbed and form complexes with carboxylic acid (-COOH), amine (-NH₂), and thiol (-SH) of proteins; therefore, this leads to cellular malfunction or death and thus leads to a variety of diseases (15,16). Several previous studies have been conducted to estimate some heavy metals in lipstick cosmetics, Pb is the most common metal among all other metals. Zakaria and Ho (17) found the concentration of lead

in lipstick samples sold in Malaysian markets is 3.21 mg/g. Another study conducted in Saudi Arabia determined the levels of heavy metals in lipstick, the results of this study indicated the presence of high concentrations of Pb in local lipstick compared to other sources. Zainy et al. (18) found high levels of toxic metals in lipstick with dark colors compared to light colors. In addition, there are many other studies carried out to estimate the level of heavy metals in cosmetics (19-24). These studies use different techniques like UV-VIS & microfluidic Paper-based analytical device platform (μPADs) (25), inductively coupled plasma mass spectroscopy (ICP-MS) (26), inductively coupled plasma optical-emission spectroscopy (ICP-OES) (27), laser-induced breakdown spectroscopy (LIBS) (28), X-ray fluorescence (XRD) (29), graphite furnace atomic absorption spectrometry (GFAAS) (21), and including flame atomic absorption spectrometry (FAAS) (30) to evaluate the concentration of toxic metals in cosmetics. Table 1 shows a comparison between the proposed method (AAS) and other methods. Previous studies have successfully assessed the level of heavy metals in the original lipstick, however, no study has been conducted to evaluate and compare the levels of heavy metals in both the original and knockoff lipsticks sold in the local markets in Diyala/Iraq. Therefore, in this study, the level of some heavy metals in original and knockoff lipsticks was determined and compared and their health risk were assessed.

Table 1: The comparison between the proposed method (AAS) with other methods.

Proposed method (AAS)	Other methods (ICP-MS, ICP-OES, LIBS, XRD, UV-Vis, μPADs, etc.)
<ul style="list-style-type: none"> • Techniques based on atomic absorption spectrometry (AAS) are FAAS and GFAAS. It is an analytical technique widely used to determine the level of heavy metals in several types of samples, such as cosmetics, food, water, drugs, soil, and nanomaterials (31). • It has a very high sensitivity, so it can measure very low concentrations of up to 1000 ppm. • High selectivity and detection limit than other techniques, so that a particular element in the sample can be measured out of all the other elements present. • Accuracy in results. • It requires the use of a very small amount of sample, which reduce residue generation • Low spectral interference • Less contamination of samples. • Digestion time is shorter (32,33). • Quick nature. 	<ul style="list-style-type: none"> ▪ These analytical techniques (UV-Vis, μPADs, ICP-MS, ICP-OES, LIBS) are used to determine heavy metals in various samples, including cosmetics. • ICP-MS and ICP-OES: the advantages of these techniques are their wide linear range and low detection limits; the disadvantages of these techniques are the presence of spectral and other non-spectral interferences, and the method of sample digestion is very important in order to obtain samples with low carbon content and the least amount of suspended solids, in order to avoid clogging the nebulizer system and carbon deposition on the interface of the equipments (34). • LIBS and XRD are techniques for direct analysis of heavy metals in cosmetics without the need for a sample preparation step. However, these techniques have some disadvantages represented by spectral overlaps, poor accuracy, and high standard deviation values (35). • The UV-Vis and μPADs techniques need to perform color reactions, which means consuming a quantity of reagents and needing a longer time, and the results are less accurate compared to the atomic absorption technology. Also, the μPADs technique is not widely available in laboratories

- One of the disadvantages of this technique is the overlap of some atomic lines, which can be reduced or overcome.

(36,37).

- Some of these techniques, such as ICP-OES, ICP-MS, and LIBS, require trained people to work on them in addition to being difficult procedures.

1.1 Toxicological Effects of Some Heavy Metals

Cosmetics (such as lipstick) are one of the most significant sources of toxic heavy metal release into the environment and the biological systems of humans compared with other sources (water, air, and food) (1,38). Due to the cumulative properties of these elements in the human body, they are a concern for consumers. Cd, Cr, Cu, Pb, Zn, and Ni are heavy metals that preoccupy the minds of lipstick users because of their negative effects on human health (39).

1.1.1. Cd

Cd is one of the heavy metals that is dangerous, and cadmium compounds are present in lipstick to give different pigments from yellow to deep orange (40,41). Cadmium selenide and cadmium sulfide are used for yellow and green colors, respectively, and can produce a wide range of colors when other metals are added (42). In general, in cosmetics, cadmium should not exceed the permissible limit of 3 ppm, the limit set by regulatory authorities (43). The exposure to cadmium through lipstick ingestion can cause severe stomach irritation, vomiting, low blood pressure, and diarrhea, while long-time exposure to low concentrations can cause bone deformation (the ability of bones to break easily because of calcium metabolism), hepatic damage, and renal damage (44).

1.1.2. Cr

Cr is an essential nutrient and plays a significant role in cholesterol and glucose metabolism (45). In contrast, chromium (VI) is a very toxic metal that spreads easily in the body and is considered a carcinogen for humans according to IARC (International Agency for Research on Cancer) (46, 47). Chromium (VI) is banned in cosmetic products, whereas Cu, Cr(OH)₃, and Cr₂O₃ are allowed as cosmetic colorants (48). According to the EPA the safe level of chromium in cosmetics is 1 ppm (49). When exposed to chromium (VI) by ingestion, it can cause problems with the kidneys, liver, and stomach (50).

1.1.3. Cu

Cu is an essential trace metal in the human body, and it is used in many industries, including the cosmetics industry (51). Copper is used in cosmetics as coloring pigments or to block UV rays (52). The permissible limit for copper in cosmetics when used as a color additive is 50 µg/g (53). However, it may have harmful effects at high levels (54). It may cause nose and throat irritation and even dermatitis. Chronic exposure to Cu can result in numerous physiological and behavioral disturbances, which include acute brain damage, cirrhosis of the liver,

aggressive behavior, and hemolytic anemia, as well as psychiatric disturbances such as depression (11).

1.1.4. Pb

Like cadmium, lead is a heavy metal and one of the most toxic chemical pollutants in human history. It is used in lipstick to give a synthetic pearlescent pigment, which increases the shimmer effect of product (7). Lead in lipstick can be ingested when licking the lips, eating, or drinking. Thus, lead will accumulate in the body over time, even if the permissible limit does not exceed (10 to 20 ppm), the limits set by Health Canada and the US Food and Drug Administration. Pb is an impurity found in cosmetics (55). When excessive Pb accumulates in the human body, it can cause many harmful effects, including acute and chronic poisoning, pathological changes in organs, diseases of the cardiovascular system, kidney, bone, and liver, and even cancer (56).

1.1.5. Zn

Zinc is a metal of great importance to humans and is considered to have no significant toxicological effect. The presence of zinc in cosmetics has several possibilities depending on the type of compound; some zinc salts make it easier to apply cosmetics to the skin (57). However, the presence of an excess of Zn causes neurological diseases and gastrointestinal disorders (58). and can cause other health effects such as stomach cramps, vomiting, nausea, skin irritation, and anemia (55).

1.1.6 As

As is one of the most common heavy metals found in lipstick products, which are added as impurities (12). It can have many negative effects on human health, such as elevated blood pressure, melanosis, and gangrene (59). A combination of heavy metals like Hg, Pb, Cd, and As can generate synergistic effects that lead to dysfunction and cognitive damage (60). Chronic exposure to As can result in macrophage dysfunction due to impairments in the immune system. Ultraviolet light (UV) and arsenic are the major risk factors that contribute to squamous cell carcinoma and basal cell carcinoma (61). As a result of these health effects, the concentration of arsenic in cosmetics should not exceed 3 ppm (47).

This work aimed to determine the concentration of some heavy metals like Cd, Cr, Cu, Pb, Zn, and As in lipstick brands by using flame atomic absorption spectrophotometer (FAAS) technique, and the levels of heavy metals were compared to those of original and copied lipstick brands. Moreover, estimation of bacterial contamination and knowledge of the type of organism present in the lipsticks of original

(expensive) and knockoff (cheap) brands sold in local markets in Diyala, Iraq.

2. METHODOLOGY

2.1. Collection of Samples

Twenty lipstick samples (ten originals and ten fake (knockoff) samples) were purchased from the local markets in Diyala, Iraq. The lipsticks used in this

study have the same brands, characteristics, and colors, but they differ in price. The expensive (original) lipstick was imported from several countries (Ireland, Türkiye, China, France, USA), as written on the labels, while the cheap (knockoff) lipstick is mostly of the same origin. Some of them are of different origins, and some are of unknown origins. Table 2 lists information on expensive and cheap lipsticks.

Table 2. Information on the lipstick samples.

Knockoff lipstick (n = 10)			Original lipstick (n = 10)		
Origin	Color	Samples code	Origin	Color	Samples code
Unknown	Violet -Red	1A	Ireland	Violet -Red	A1
	Maroon	2A		Maroon	A2
Türkiye	Pink	1B	Türkiye	Pink	B1
	Brown	2B		Brown	B2
Unknown	Red	1C	China	Red	C1
	Chocolate	2C		Chocolate	C2
USA	Purple	1D	USA	Purple	D1
China	Orange	1E	China	Orange	E1
France	Pink	1F	France	Pink	F1
China	Red	1G	USA	Red	G1

2.2. Reagents and Chemicals

Samples were prepared by using analytical grade HClO_4 (purity 70%, Sigma Aldrich, USA) and concentrated HNO_3 (purity 69.5%, BDH, England). Also, all samples were diluted with distilled water.

2.3. Optimal Conditions of Digestion Method (hydrogen function, Temperature, Time of Heating, and Order of addition).

To verify the method used, the effects of some variables were studied: the effect of *hydrogen function*, temperature (50-250 °C), time of heating (15, 30, 60, and 120 minutes), and order of addition.

2.3.1. Hydrogen function influence

Acids play a key role in the digestion of cosmetic samples, especially HNO_3 , which is used alone or with other acids. The main function of these acids is as oxidizing agents by which inorganic metal oxides can be dissolved in cosmetic samples (62). The preparation of solutions containing a mixture of concentrated acids $\text{HClO}_4:\text{HNO}_3$ of different proportions (1:1,1:2, 1:3,1:4, 2:1,3:1, and 4:1). The result of this step shows that 1:3 is optimal.

Influence of Heating Time: Heating the reaction components for different times (15, 30, 60, 120, and 150) minutes. 120 minutes were enough to complete the reaction.

2.3.2. Influence of temperature

In general, temperatures help to get rid of steam and organic impurities by converting organic carbon into carbon dioxide gas (CO_2). High temperatures cause the loss of heavy metals to be determined from the samples, while low temperatures cause incomplete oxidation of the materials. The reaction mixture was heated to different temperatures (50, 100, 150, 200, and 250 °C). The results of this step indicated that heating to 100 °C for two hours was good.

2.3.3. Order of addition

The change in reaction components' addition order; the sample (A) first, then the acid mixture (B), and finally distilled water (C) was the most appropriate. Figure 1 shows the results of the optimal conditions for the method used for the determination of heavy metals in lipsticks.

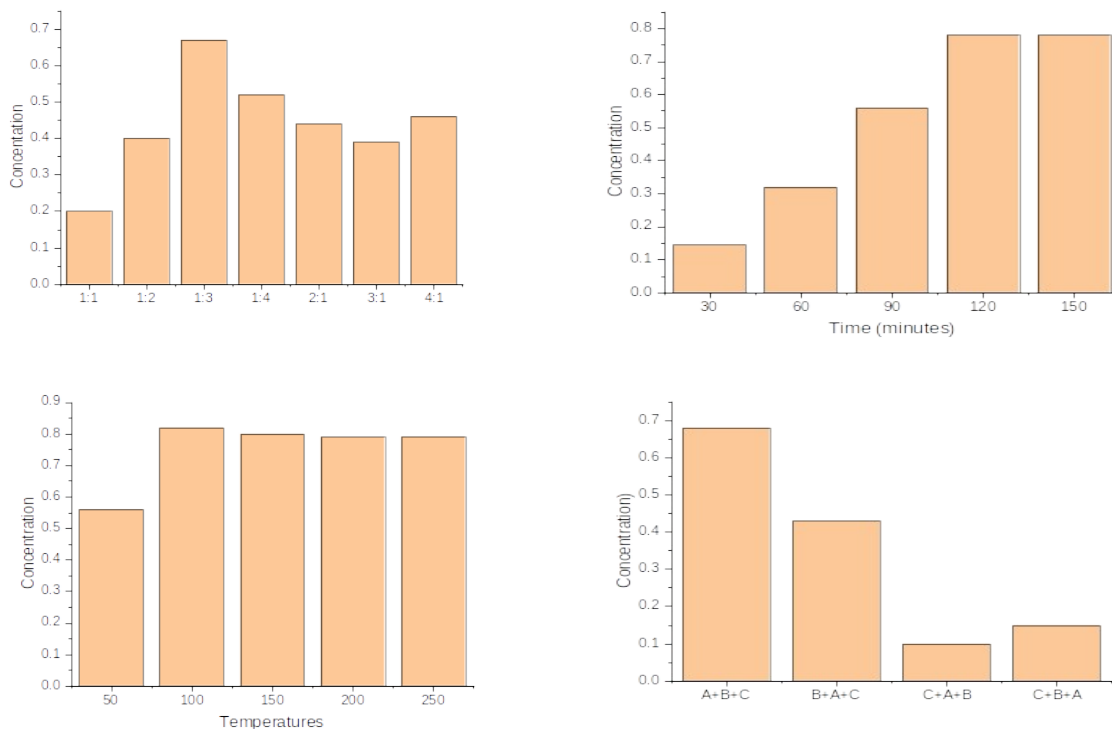


Figure 1. Influence of (a) hydrogen function (1:1,1:2, 1:3,1:4, 2:1,3:1, and 4:1), (b) temperature (50-250) °C, heating time (15, 30, 60, 120, and 150) minutes, and (d) order of addition ((A) lipstick sample, (B) acid mixture, (C) water).

2.4. Optimum Digestion Method of Samples

In this work, wet acidic digestion was used for the determination of a quantity of heavy metals like Cd, Cr, Cu, Pb, Zn, and As by the method adopted by Sani et al. (2016) (3). With some modifications, 0.5 g of each lipstick was weighed using an electronic balance and placed in a conical flask, followed by 5 mL of a concentrated acid mixture HClO₄:HNO₃ (1:3), which was then heated for 2 hours on a hot plate at 100 °C. Then 3 mL of the concentrated mixture was added, and the solution was heated again for two hours to complete the digestion process. The

digested samples were cooled to room temperature and diluted to 25 mL with deionized water. The solution was filtered through filter paper (Whatman No. 41) to remove unwanted components, and the pure solution was used for metal determination.

2.5. Analysis of Heavy Metals by FAAS

The quantities of Cd, Cr, Cu, Pb, Zn, and As in lipstick samples were determined by using flame atomic absorption. Table 3 shows the operating parameters of AAS.

Table 3: Operating parameters of the Atomic Absorption Spectrophotometer(AAS) used in the heavy metal analysis.

Operating parameters	As	Zn	Pb	Cu	Cr	Cd
Wavelength (nm)	193.7	213.9	283.30	324.80	357.90	228.80
Slit width (nm)	0.50	0.70	0.70	0.70	0.70	0.70
Detection limit (mg/L)	0.05	0.03	0.08	0.005	0.04	0.01
Lamp current (mA)	5.00	5.00	5.00	1.50	2.00	2.00
Flame Type (Color)	Air-Acetylene/(lean/Blue)	Air-Acetylene/(lean/Blue)	Air-Acetylene/(lean/Blue)	Air-Acetylene/(lean/Blue)	Air-Acetylene/(rich/Yellow)	Air-Acetylene/(lean/Blue)

2.6. Method Validation

2.6.1. Linearity

To ensure the reliability of the results. The quantification of the concentration of the metals was carried out using a five-point calibration curve for each of the metals used in the study. The calibration was accomplished by adding the standards prepared in concentrations of 1, 5, 10, 25, and 50 ppm from the 1000 ppm standard stock solution. The analytical procedure validation for quantitative analysis of heavy metals in cosmetics products was performed using linear ranges, detection limit, quantification limit, precision, accuracy, and recoveries of spiked standards in the defined calibration ranges were calculated. Analytical method validation for heavy metals analysis was applied in accordance with Eurachem guide.

2.6.2. Limit of detection (LOD) and limit of quantification (LOQ)

The limit of detection was estimated as the mean plus three times the standard deviation (SD) of a blank sample, and it was determined following the equation below:

$$LOD = 3 \frac{SD}{b} \quad (\text{Eq. 1})$$

$$LOQ = 10 \frac{SD}{b} \quad (\text{Eq. 2})$$

where, SD is the standard deviation- of the blank (based on three independent analyses of sample blank). b is the calibration-graph slope (21).

2.6.3. Accuracy

Because of the unavailability of certified material for lipstick, the accuracy of the method was obtained by adding the true values of Cd, Cr, Cu, Pb, Zn, and As to the cosmetics matrix. The same analytical procedure was applied for test samples, and the percentages of relative error (%RE) and analyte percentage relative recovery (%Recovery) were calculated by the following equation:

$$\%RE = \left(\frac{\text{found} - \text{true}}{\text{true}} \right) \times 100 \quad (\text{Eq. 3})$$

$$\%Recovery = \left(\frac{\text{found}}{\text{true}} \right) \times 100 \quad (\text{Eq. 4})$$

found:- result value, true:- real value.

The analytical recovery figures for spiked lipstick are shown in Table 4.

2.6.4. Precision

The precision of method was determined by relative standard deviation (%RSD). It is studied by using

three concentrations of heavy metals, which are calculated using the following equation:

$$\%RSD = \left(\frac{SD}{x} \right) \times 100 \quad (\text{Eq. 5})$$

$$SD = \left[\sum \frac{(x_i - x)^2}{(n-1)} \right]^{0.5}, x = \sum \frac{x_i}{n} \quad (\text{Eq. 6})$$

Where SD: standard deviation, x: the average of the samples.

2.7. Health Risk Assessment

Exposure routes: A lipstick may enter a human body through ingestion; this intake can be calculated using the following equation:

$$ADDing = \frac{C \times IR \times EF \times ED}{BW \times AT \times C} \quad (\text{Eq. 7})$$

ADDing is the average ingested daily dose (mg/kg day); C is the concentration of heavy metals; IR is the intake rate (40 mg/day); EF is the exposure frequency (260 days/years); ED is the exposure duration (35 years); BW is the body weight (57.9 kg); AT is the average time (calculated by ED × 365 days/year); and CF is the conversion factor (10⁻³).

After calculating the average daily dose, the hazard quotient-(HQ) for non-carcinogenic health effects was calculated using the following formula:

$$HQ = \frac{ADDing}{RfD} \quad (\text{Eq. 8})$$

Where, Rf D (Reference Oral Dose) is the specific reference dose (mg/kg/day) that varies for all metals (17), Rf Ds used for the hazard assessment were 0.001 for Cd, 0.003 for Cr, 0.04 for Cu, 0.004 for Pb, 0.3 for Zn, And 0.001 for As (24, 63).

When the ADDing value is less than the Rf D, there will be no health effect, but if the ADDing value is greater than the Rf D, there may be noncarcinogenic health effects.

HQ < 1 indicates no adverse health effects, while HQ ≥ 1 indicates likely adverse health effects. The health risk index (HI) was used to calculate the total risk effect of all the elements studied. This index was calculated using the following formula:

$$HI = \sum HQ \quad (\text{Eq. 9})$$

$$HI = \sum HQ = HQCd + HQCr + HQCu + HQPb + HQZn + HQAs$$

2.8. Study of Biological Activity

To detect the antibacterial activity, two groups of lipstick samples were used, the first group consisted of 10 samples of the original (expensive), and the second group also used 10 samples of knockoff (cheap). In this study, a range of different gram-negative and gram-positive bacteria were selected. The isolates of gram-negative bacteria included (*E.coli*, *Pseudomonas aeruginosa*) while gram-positive bacterial include (*Staphylococcus aureus*, *Staphylococcus epidermidis*) isolate. The microbial activity of different lipsticks was determined by the (agar, well, diffusion) method (64). In this method, growth was cultivated on a Muller-Hinton Agar plate (HiMedia, Mumbai, India). After the plates had dried, one well was drilled into each of the agar plates using a sterile cork borer with a diameter of 5.0 mm. A micropipette was used to dispense 80 µL of lipstick suspension from each sample into each well of a Muller-Hinton agar plate. After standing for at least an hour to allow pre-diffusion to occur, the

plates were incubated for 48 hours at 37 °C. In millimeters, the zone of inhibition was measured. Three duplicates of each experiment were carried out.

2.8.1. Statistical analysis

All results are expressed as the mean±SD, and all data were analyzed by t- test, which was used for general comparison between two groups of lipstick using SPSS software.

3. RESULTS AND DISCUSSION

The analytical producer validation for quantitative analysis of heavy metals in cosmetics products was performed using linear ranges, ranging from 1 to 50 ppm, coefficients of correlation ranged from 0.9983 to 0.9995, LOD ranged from (0.01 to 0.1), and LOQ was set from(0.03 to 0.33), which indicates a selective and sensitive method. Table 4 shows the results obtained in this study.

Table 4: Method validation results of the heavy metals studies.

LOQ (ppm)	LOD (ppm)	R ²	Linear range	Regression Equation	Metals
0.33	0.1	0.9983	1-50	y = 0.0293x + 0.1421	Cd
0.1	0.03	0.9985	1-50	y = 0.0243x + 0.0199	Cr
0.17	0.05	0.9989	1-50	y = 0.0261x + 0.0354	Cu
0.33	0.1	0.9995	1-50	y = 0.0299x + 0.0431	Pb
0.07	0.02	0.9979	1-50	y = 0.0244x + 0.0151	Zn
0.03	0.01	0.9992	1-50	y = 0.0179x + 0.0778	As

For accuracy and precision, spiking was performed using the calibration-standard solution in three fortification levels (1, 5, and 25 ppm) of the linear range as the sample matrix for accuracy and precision calculations, using Equations 3, 4, and 5 to calculate the values of percentage of relative error,

percentage of recovery, and relative standard deviation. The results (Table 5) were presented as mean data, indicating the recovery values (from 100.17% to 101.1%), RE values of 0.81%, and RSD values of ≤ 1.33 %, confirming good accuracy and precision.

Table 5: Accuracy and precision of studied metals.

*(%RSD)	*(%RE)	*(% Recovery)			Metals
		25 ppm	5 ppm	1 ppm	
1.32	0.71	100.23 ±0.67	101.2±1.76	100.7±1.53	Cd
1.21	0.46	100.06±0.38	100.4±2.11	100.9±1.15	Cr
1.1	0.54	100.57±0.70	100.87±2.05	100.17±0.55	Cu
0.78	0.58	100.3±0.36	100.5±0.71	100.43±1.55	Pb
1.33	0.53	99.7±1.11	100.8±1.23	101.1±1.66	Zn
0.65	0.81	101.43±0.76	100.7±0.72	100.3±0.46	As

*Average of three replicates.

3.1. Concentration of Heavy Metals in Lipstick Samples

In this study, twenty samples of different brands of lipstick were investigated. The concentration of each heavy metal in the lipstick samples is given in Table 6.

The acceptable limit of heavy metal content in cosmetics was set by (USFDA) in 2007, in particular 3 ppm for cadmium, 1 ppm for chromium, 50 mg/g for copper, 10 ppm for lead, and 3 ppm for arsenic. Based on Table 3, the concentrations of Cd in the

studied brands of lipstick were from 0.11 to 0.56 ppm in the original brand and 0.21 to 0.88 in knockoff brand; these values did not exceed the legal threshold of 3 ppm set by the US Food and Drug Administration and Health Canada (41).

In a study reported by Saleh et al. to determine the level of cadmium in lipsticks sold at different prices, the results showed that the level of cadmium ranged from 0.03 to 0.07 ppm (41). Previous studies have shown different concentrations of cadmium in lipstick samples. Nourmoradi et al. detected that the

cadmium concentration in some brands of lipstick was within the range of 4.08 to 60.20 mg/g (1). Another study reported by Iwegbue et al. found that the concentration of cadmium ranged between 0.34 and 37.3 (46), 0.01 to 0.06 (65), and 0.77 to 1.19 (66). A study in Jordan found the levels of Cd ranged from 0.12 to 2.72 (67). However, the level of cadmium in the present study was lower than that in other studies conducted by Nourmoradi et al. and Iwegbue et al. (1, 42).

The concentration of Cr in the original and knockoff brands of lipstick samples was not detected. This is consistent with the European Union's prohibition on the presence of chromium in cosmetics (17).

Different studies in many countries have shown different ranges for chromium in lipstick. In Iran, Naalband et al. found the concentration of Cr in lipstick ranged between 0.06 and 0.75 (40). In Malaysia, Zakaria et al. found that the Cr ranged between 0.24 and 2.25 (17). In Portugal and Brazil, Pinto et al. reported that the concentration of Cr ranged between 2.26 and 2.28 (68). In another study conducted by Sani et al., the researchers determined the levels of chromium in lipsticks with varying prices. The results showed the levels of chromium ranged from 0 to 0.05 ppm (3). The concentration values of Cr obtained in this study were lower than the values in the other study mentioned above.

Table 6: Concentrations (ppm) of heavy metals in original (expensive) and knockoff (cheap) lipsticks.

Metals	Original			Knockoff		
	Mean±SD	Min	Max	Mean±SD	Min	Max
Cd	0.34±0.23	0.11	0.56	0.55±0.18	0.26	0.88
Cr	< LOD	< LOD	< LOD	< LOD	< LOD	< LOD
Cu	0.12±0.07	0.014	0.28	0.22±0.13	0.06	0.39
Pb	0.68±0.19	0.5	1.06	0.98±0.17	0.76	1.26
Zn	0.19±0.18	0.026	0.5	0.33± 0.31	0.067	0.77
As	0.04±0.03	0.012	0.098	0.1±0.07	0.034	0.28

*values are expressed as an, average for, three determinations.

The concentration of copper (Cu) in the original and knockoff brands of lipstick ranged from 0.014 to 0.28 and 0.06 to 0.39, respectively. In other studies, the levels of copper in lipstick have been reported. For example, researchers found the level of copper in some brands of lipstick ranged between 0.0 and 75.92 (57). Iwegbue CM et al. conducted a study to estimate several heavy metals, like copper (Cu), in 160 samples of facial cosmetics, including lipstick, sold in southern Nigeria. The results showed that the concentration of copper ranged from 1.1 to 135.4 ppm (42). A study published by Chauhan SB et al. found that the concentration of Cu in lipstick ranged between 0.0498 and 7.0782 (69), as well as 1.86 and 21.72 (24). The results showed that the level of this heavy metal in the current study was comparable to that found in the study conducted by Chandak et al. (2014), while the levels of Cu in this study were less than the values obtained in other studies (24,42,57). However, the results show that the concentration of copper was less than (50 mg/g), the standard allowed by the regulatory authorities for copper in cosmetics (6).

Pb is found naturally in the earth's crust. Lead was detected in all brands of lipstick used in this study; the levels of Pb ranged from 0.5 to 1.06 ppm in the original brand and 0.76 to 1.26 ppm in the knockoff brand. Pb levels in lipstick were measured in ppm in various studies. In a study conducted by Nnorom in 2005, the levels of Pb ranged between 87 and 123 ppm (50); in 2012, they ranged between 5.5 and 47.8 (66); and in 2013, they ranged between 0.58 and 3.36 (70). In 2016, they ranged between 0.18

and 0.8 (40), and in 2020, they ranged between 0.286 and 6.234 (24). The observed levels of Pb in this study are similar to those reported in this study by Nourmoradi et al. (2013), and Kamarehie et al. (2020), but they are lower than those in the previous studies. The lead values used in this study, however, did not exceed the permissible limit for lead as an impurity in cosmetics of 20 ppm and 10 ppm, respectively, as set by the US Food and Drug Administration and Health Canada (71).

Zn was used as a pigment in cosmetics; the average concentration of Zn in the studied brands ranged between 0.0026 and 0.5 ppm, 0.067 and 0.77 ppm, and the means were 0.19 and 0.33, in the original and knockoff brands, respectively. In other countries, different ranges of Zn in lipstick brands have been reported. For example, in a study from Iran, Ghaderpoori, M. et al. reported concentrations ranging between 3.64 and 216.53 ppm (72). In Pakistan, a range between 0.4757 and 6.7694 ppm was reported by Kamarehie et al. 2020 (73). In Khyber, the range was between 0.696 and 1.610 ppm (15). In Nigeria, the level of Zn ranged from 2.23 to 3.01 ppm was reported by Okol et al(6). In Poland, it ranged from 1.73 to 488.13 ppm (57). When the Zn range values in this study were compared to other studies in the aforementioned countries, the level of Zn in this study was found to be similar to those in the Khyber City study reported by Ullah et al., while being lower than the other studies mentioned above. However, the mean concentrations of Zn were higher than the LOD.

The concentration of As in different brands of lipstick used in this study ranged from 0.012 to 0.098 and 0.034 to 0.28 ppm. Different studies conducted in different times reported the levels of As in lipstick. In 2014, Ouremi et al. reported levels of As ranging between 0.8 and 3.0 ppm (47). In 2015, they ranged from 0.11 to 0.43 ppm (74). In 2019, it ranged from 0.990 to 9.235 ppm (21). In 2020, it ranged 0.29 to 4.83 ppm (75). The level of As in the present study was lower than in the above mentioned studies. The level of arsenic in the studied samples was less than (3 ppm), which is the permissible limit for As in cosmetics, according to Health Canada (76).

In this study, the amount of heavy metals was less than the limit allowed by the executive authorities, and in addition, the original brand of lipstick gave a better result than the imitation. When comparing the results of this study with those of previous studies, it was found that the amount of heavy metals in the present study was similar to the values reported in the literature for lipstick products. The concentrations of the heavy metals analyzed are in the following order: Pb > Cd > Zn > Cu > As > Cr. Lead has the highest concentration, while chromium has the least (25). The results in Table 4 confirm the proposed method's accuracy and precision in heavy metals' determination. A t-test was conducted to compare expensive and cheap lipstick products. The results of the test showed that there were no statistically significant differences in the concentrations of heavy metals. Among the expensive and cheap cosmetics.

3.2. Risk Assessment

Heavy metals in cosmetics may seem like a small proportion of the sources that threaten human health in comparison to air, food, and water. Therefore, its harmful effects must be avoided. In this part of the study, to determine the non-carcinogenicity risk of contact with cosmetics products, the hazardous quotient (HQ) and hazardous index (HI) were estimated from Equations

7 and 8. Table 8 shows the results for HQ and HI as calculated. According to Table 8, the amount of HQ in all lipstick brands examined was below 1, indicating there was no significant non-carcinogenic health risk for lipstick users. The highest amount of HQ was found in lead (6.3E-01), which was observed in the sample (1B), but the lowest amount of HQ was found in zinc (4.3E-05), which was detected in the sample (A1). According to HI, the amount of HI for all samples used in our study was lower than 1. This indicates that the consumer was at the safety limit.

3.3. Anti-bacterial Activity

The results indicated that there was no bacterial growth in the original brand of lipstick, and this is in accordance with the laws of the US Food and Drug Administration. While in the case of knockoff brands (1A, 2A, 1B, 2B, E, 1C, 2C, 1D, 1E, 1F, and 1G), these samples showed the most antimicrobial effects on gram-negative and gram-positive bacterial isolates. This contradicts what the US Food and Drug Administration law stipulates that "cosmetics are not required to be sterile, but rather, they must not be contaminated with microorganisms that may cause disease, and cosmetics are required to remain in this state even when used before consumers" (77). Figure 2, shows the anti-bacterial activity in knockoff lipstick samples.

These results are in agreement with many studies. According to a recent study conducted by Siya using thermal sequencing analysis, on 20 lipstick samples, the results indicated that the samples were contaminated with 105 bacterial genera, including *Streptococcus*, *Staphylococcus*, *Pseudomonas*, and *Escherichia* (78). Another study reported by Vassoler, M., et al. analyzed the microbiological quality of 30 lipstick samples sold in Brazil; the results indicated the presence of bacterial contamination with different types of bacteria, including *S. aureus* and *S. epidermidis* (79).

Table 7: Estimated adding of selected metals found in the original and knockoff lipstick brands.

Original Lipstick						
Code	Cd	Cr	Cu	Pb	Zn	As
A1	1.6E-04	0	7.1E-06	4.3E-04	1.3E-05	1.1E-05
A2	2.8E-04	0	5.2E-05	3.8E-04	4.6E-05	1.3E-05
B1	1.1E-04	0	5.5E-05	2.5E-04	4.3E-05	1.5E-05
B2	2.2E-04	0	4.3E-05	2.7E-04	1.5E-05	1.4E-05
C1	1.5E-04	0	5.3E-05	4.1E-04	2.2E-05	4.5E-05
C2	2.2E-04	0	5.7E-05	3.3E-04	1.2E-04	2.4E-05
D1	2.8E-04	0	1.4E-04	3.0E-04	2.2E-04	1.9E-05
E1	2.3E-04	0	6.3E-05	2.5E-04	4.1E-05	0.5E-05
F1	1.5E-04	0	7.3E-05	2.4E-04	1.6E-04	4.9E-05
G1	5.3E-05	0	4.3E-05	5.3E-04	2.5E-04	2.4E-05

Knockoff Lipstick						
Code	Cd	Cr	Cu	Pb	Zn	As
1A	2.3E-04	0	3.1E-05	5.1E-04	3.3E-05	2.1E-05
2A	3.3E-04	0	9.3E-05	4.4E-04	1.6E-04	2.4E-05
1B	1.9E-04	0	1.5E-04	6.3E-04	4.2E-05	2.5E-05
2B	3.4E-04	0	4.6E-05	4.1E-04	6.1E-05	5.4E-05
1C	3.1E-04	0	2.3E-04	4.6E-04	5.2E-05	5.5E-05
2C	1.3E-04	0	1.1E-04	5.3E-04	1.3E-04	5.4E-05
1D	4.4E-04	0	1.9E-04	4.7E-04	2.9E-04	3.1E-05
1E	3.4E-04	0	6.8E-05	3.8E-04	4.8E-05	1.7E-05
1F	2.3E-04	0	8.3E-05	3.2E-04	4.4E-04	1.4E-04
1G	2.2E-04	0	8.4E-05	6.2E-04	3.5E-04	5.4E-05

Table 8:- Health risk assessment of heavy metals (HQ and HI) in original and knockoff lipstick brands.

Original Lipstick							
Code	Cd	Cr	Cu	Pb	Zn	As	Total HQ or HI
A1	0.16	ND	0.0002	0.43	0.000043	0.011	0.601
A2	0.28	ND	0.0013	0.38	0.00015	0.013	0.674
B1	0.11	ND	0.0014	0.25	0.00014	0.015	0.372
B2	0.22	ND	0.0011	0.27	0.00005	0.014	0.505
C1	0.15	ND	0.0013	0.41	0.00007	0.045	0.606
C2	0.09	ND	0.0014	0.33	0.00004	0.024	0.445
D1	0.28	ND	0.0035	0.30	0.00073	0.019	0.603
E1	0.23	ND	0.0015	0.25	0.00014	0.005	0.487
F1	0.15	ND	0.0018	0.24	0.00053	0.049	0.441
G1	0.053	ND	0.0011	0.53	0.00083	0.024	0.609

Knockoff Lipstick							
Code	Cd	Cr	Cu	Pb	Zn	As	Total HQ or HI
1A	0.23	ND	0.0008	0.51	0.00011	0.021	0.762
2A	0.33	ND	0.0023	0.44	0.00053	0.024	0.797
1B	0.19	ND	0.0038	0.63	0.00014	0.025	0.849
2B	0.34	ND	0.0012	0.41	0.00020	0.054	0.805
1C	0.31	ND	0.0058	0.46	0.00017	0.055	0.831
2C	0.13	ND	0.0028	0.53	0.00043	0.054	0.717
1D	0.44	ND	0.0048	0.47	0.00097	0.031	0.947
1E	0.34	ND	0.0017	0.38	0.00016	0.017	0.739
1F	0.23	ND	0.0021	0.32	0.00147	0.14	0.694
1G	0.22	ND	0.0021	0.62	0.00117	0.054	0.897

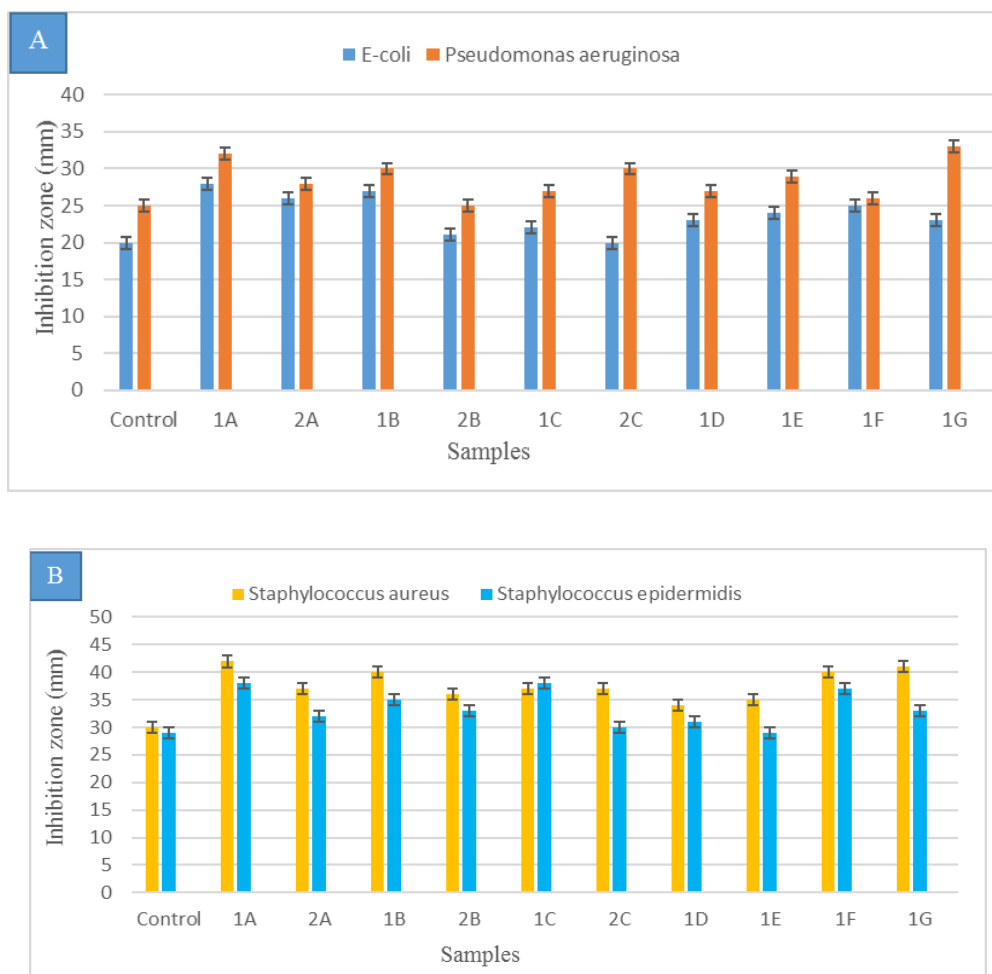


Figure 2: Antimicrobial-activity of knockoff lipstick samples. (A) Inhibition of different gram-negative bacteria isolates by lipsticks samples, (B) Inhibition of different gram-positive bacteria isolates by lipstick samples.

4. CONCLUSION

The primary components present in lipstick are oils, waxes, dyes, and alcohols. Even though heavy metals are not an essential component of lipsticks, they are in cosmetics as impurities. And even with good manufacturing processes, the presence of heavy metals is unavoidable in cosmetics. Therefore, the executive authorities have set values for heavy metals in cosmetics that should not be exceeded. FAAS is a simple and rapid analytical method used to estimate the quantity of cadmium, chromium, copper, lead, zinc, and arsenic in two groups of lipstick samples used in this study. The results showed that the samples used in this study contained all the metals that were analyzed. Except for chromium, which was not detected in all the studied samples, whether expensive or cheap, while the levels of lead were higher than all other metals, they were less than the permissible limit set by the executive authorities. The results of the THQ showed that the values were below 1 for all tested samples, meaning that the detected heavy metals in lipstick did not pose a dangerous health risk to consumers,

and the original brand of lipstick showed better results than knockoff brands. However, there are concerns that daily and repeated use of cosmetics contaminated with toxic heavy metals may lead to biological accumulation in body tissues and cause negative health effects on consumers. The results of the biological activity show that there was no bacterial growth in the original lipstick samples while there was contamination with organisms in the cheap samples.

5. CONFLICT OF INTEREST

The researchers declare that there are no conflicts of interest regarding the current manuscript.

6. ACKNOWLEDGMENTS

The researches acknowledge and thankful to the University of Diyala, and the faculty of Sciences for submitting the entire requirements to do this research.

7. REFERENCES

1. Balarastaghi S, Khashaiarmanesh Z, Makhdomi P, Alavizadeh SH, Sameie Moghadam Z, Shirani K, et al. Determination of toxic element levels (lead and cadmium) in commonly used cosmetic products in Iran. *Toxin Reviews*. 2018 Apr 3;37(2):117-22. Available from: [<URL>](#).
2. Marinao T, Iovinea A, Casellab P, Martinoc M, Chianese S, Laroccac V, et al. From *Haematococcus pluvialis* microalgae a powerful antioxidant for cosmetic applications. *Chem Eng*. 2020;79:271-6.
3. Sani A, Gaya MB, Abubakar FA. Determination of some heavy metals in selected cosmetic products sold in Kano metropolis, Nigeria. *Toxicology Reports*. 2016;3:866-9. Available from: [<URL>](#).
4. Karanje PS, Doijad RC, Bhosale RR, others. Formulation and evaluation of herbal lipstick containing *Amaranthus cruentus* Linn. *Int J Res Anal Rev*. 2020;7:246-55.
5. Gurrieri L, Drenten J. The feminist politics of choice: lipstick as a marketplace icon. *Consumption Markets & Culture*. 2021 May 4;24(3):225-40. Available from: [<URL>](#).
6. Oklo A, Eneche D, Aondoakaa MAM. Heavy metals in some lipstick products marketed in Makurdi metropolis, Benue state Nigeria. *International Journal of Environment, Agriculture and Biotechnology*. 2020;5(2).
7. Shukri NM, Bashir NAA, Shohaimi NAM, Abdullah WNW, Abdullah NH, Ab Halim AZ, et al. Assessment of permissible limits for heavy metals in various inspired and authentic lipsticks. *Malaysian Journal of Chemistry*. 2020;
8. Batista EF, Augusto A dos S, Pereira-Filho ER. Chemometric evaluation of Cd, Co, Cr, Cu, Ni (inductively coupled plasma optical emission spectrometry) and Pb (graphite furnace atomic absorption spectrometry) concentrations in lipstick samples intended to be used by adults and children. *Talanta*. 2016 Apr;150:206-12. Available from: [<URL>](#).
9. Parizi MG, Sedaghat Z, Mazloomi M, Fararouei M. Serum level of lead and cadmium is linked to facial cosmetics use among Iranian young women. *Environ Sci Pollut Res*. 2021 Mar;28(11):13913-8. Available from: [<URL>](#).
10. Chopi R, Sharma S, Sharma S, Singh R. Trends in the forensic analysis of cosmetic evidence. *Forensic Chemistry*. 2019 Jun;14:100165. Available from: [<URL>](#).
11. Ayenimo JG, Yusuf AM, Adekunle AS, Makinde OW. Heavy Metal Exposure from Personal Care Products. *Bull Environ Contam Toxicol*. 2010 Jan;84(1):8-14. Available from: [<URL>](#).
12. Volpe MG, Nazzaro M, Coppola R, Rapuano F, Aquino RP. Determination and assessments of selected heavy metals in eye shadow cosmetics from China, Italy, and USA. *Microchemical Journal*. 2012 Mar;101:65-9. Available from: [<URL>](#).
13. Al-Saleh I, Al-Enazi S, Shinwari N. Assessment of lead in cosmetic products. *Regulatory Toxicology and Pharmacology*. 2009 Jul;54(2):105-13. Available from: [<URL>](#).
14. Sainio EL, Jolanki R, Hakala E, Kanerva L. Metals and arsenic in eye shadows: METALS AND ARSENIC IN EYE SHADOWS. *Contact Dermatitis*. 2000 Jan;42(1):5-10. Available from: [<URL>](#).
15. Ullah H, Noreen S, Fozia, Rehman A, Waseem A, Zubair S, et al. Comparative study of heavy metals content in cosmetic products of different countries marketed in Khyber Pakhtunkhwa, Pakistan. *Arabian Journal of Chemistry*. 2017 Jan;10(1):10-8. Available from: [<URL>](#).
16. Abdulkareem E, Abdulsattar J, Abdulsattar B. Iron (II) Determination in Lipstick Samples using Spectrophotometric and Microfluidic Paper-based Analytical Device (μ PADs) Platform via Complexation Reaction with Iron Chelator 1, 10-phenanthroline: A Comparative Study. *BSJ*. 2022 Apr 1;19(2):355-67. Available from: [<URL>](#).
17. Zakaria A, Ho YB. Heavy metals contamination in lipsticks and their associated health risks to lipstick consumers. *Regulatory Toxicology and Pharmacology*. 2015 Oct;73(1):191-5. Available from: [<URL>](#).
18. Zainy FMA. Heavy Metals in Lipstick Products Marketed in Saudi Arabia. *JCDSA*. 2017;07(04):336-48. Available from: [<URL>](#).
19. Sharafi K, Fatahi N, Yarmohammadi H, Moradi M, Dargahi A. Determination of cadmium and Lead concentrations in cosmetics (lipstick and hair color) in Kermanshah markets. *Journal of Health*. 2017;8(2):143-50. Available from:
20. Copat C, Grasso A, Fiore M, Cristaldi A, Zuccarello P, Signorelli SS, et al. Trace elements in seafood from the Mediterranean sea: An exposure risk assessment. *Food and Chemical Toxicology*. 2018 May;115:13-9. Available from: [<URL>](#).
21. Saadatzaheh A, Afzalan S, Zadehdabagh R, Tishezan L, Najafi N, Seyedtabib M, et al. Determination of heavy metals (lead, cadmium, arsenic, and mercury) in authorized and unauthorized cosmetics. *Cutaneous and Ocular Toxicology*. 2019 Jul 3;38(3):207-11. Available from: [<URL>](#).
22. Arshad H, Mehmood MZ, Shah MH, Abbasi AM. Evaluation of heavy metals in cosmetic products and their health risk assessment. *Saudi Pharmaceutical Journal*. 2020 Jul;28(7):779-90. Available from: [<URL>](#).
23. Świerczek L, Cieřlik B, Matysiak A, Konieczka P. Determination of heavy metals in eyeshadows from China. *Monatsh Chem*. 2019 Sep 1;150(9):1675-80. Available from: [<URL>](#).
24. Ghaderpoori M, Kamarehie B, Jafari A, Alinejad AA, Hashempour Y, Saghi MH, et al. Health risk assessment of heavy metals in cosmetic products sold in Iran: the Monte Carlo simulation. *Environ Sci Pollut Res*. 2020 Mar;27(7):7588-95. Available from: [<URL>](#).
25. Abdulkareem EA, Abdulsattar JO. Determination of Nickel and Cobalt in Cosmetic Products Marketed in Iraq Using Spectrophotometric and Microfluidic Paper-based Analytical Device (μ PADs) Platform. *Baghdad Scij*. 2022 Dec 1;19(6):1286-96. Available from: [<URL>](#).
26. Pawlaczyk A, Gajek M, Balcerek M, Szykowska-Jóźwik MI. Determination of Metallic Impurities by ICP-MS Technique in Eyeshadows Purchased in Poland. Part I. *Molecules*. 2021 Nov 8;26(21):6753. Available from: [<URL>](#).

27. Mrmošanin J, Pavlović A, Mitić S, Tošić S, Pecev-Marinković E, Krstić J, et al. The Evaluation of ICP OES for the Determination of Potentially Toxic Elements in Lipsticks: Health Risk Assessment. ACSi. 2019 Dec 18;802-13. Available from: [<URL>](#).
28. Rehan I, Gondal MA, Rehan K, Sultana S, Khan S, Rehman MU, et al. Nondestructive Determination of Chromium, Nickel, and Zinc in Neem Leaves and Facial Care Products by Laser Induced Breakdown Spectroscopy (LIBS). Analytical Letters. 2022 Apr 13;55(6):990-1003. Available from: [<URL>](#).
29. Rawat K, Sharma N, Singh VK. X-Ray Fluorescence and Comparison with Other Analytical Methods (AAS, ICP-AES, LA-ICP-MS, IC, LIBS, SEM-EDS, and XRD). In: Singh VK, Kawai J, Tripathi DK, editors. X-Ray Fluorescence in Biological Sciences [Internet]. 1st ed. Wiley; 2022 [cited 2023 Feb 11]. p. 1-20. Available from: [<URL>](#)
30. Kilic S, Kilic M, Soylak M. The Determination of Toxic Metals in some Traditional Cosmetic Products and Health Risk Assessment. Biol Trace Elem Res. 2021 Jun;199(6):2272-7. Available from: [<URL>](#).
31. Zhong WS, Ren T, Zhao LJ. Determination of Pb (Lead), Cd (Cadmium), Cr (Chromium), Cu (Copper), and Ni (Nickel) in Chinese tea with high-resolution continuum source graphite furnace atomic absorption spectrometry. Journal of Food and Drug Analysis. 2016 Jan;24(1):46-55. Available from: [<URL>](#).
32. Fernández-Martínez R, Rucandio I, Gómez-Pinilla I, Borlaf F, García F, Larrea MT. Evaluation of different digestion systems for determination of trace mercury in seaweeds by cold vapour atomic fluorescence spectrometry. Journal of Food Composition and Analysis. 2015 Mar;38:7-12. Available from: [<URL>](#).
33. Khalaf HS, Al-Haidari AMA, Dikran SB, Mohammed AK. Spectrophotometric determination of sulfamethoxazole following simple diazotization and coupling with diphenylamine. Ibn AL-Haitham Journal For Pure and Applied Science. 2017;27(3):365-80.
34. Kántor T, Bartha A, Ballók MI. Studies on chemical removal of excess nitric acid using formic acid in solutions analyzed by inductively coupled plasma optical emission spectrometry. Chemia analityczna. 2009;54(6):1265-83.
35. El Haddad J, Canioni L, Bousquet B. Good practices in LIBS analysis: Review and advices. Spectrochimica Acta Part B: Atomic Spectroscopy. 2014 Nov;101:171-82. Available from: [<URL>](#).
36. Ozer T, McMahon C, Henry CS. Advances in Paper-Based Analytical Devices. Annual Rev Anal Chem. 2020 Jun 12;13(1):85-109. Available from: [<URL>](#).
37. Lisowski P, Zarzycki PK. Microfluidic Paper-Based Analytical Devices (μ PADs) and Micro Total Analysis Systems (μ TAS): Development, Applications and Future Trends. Chromatographia. 2013 Oct;76(19-20):1201-14. Available from: [<URL>](#).
38. Alsaffar N, Hussein H. Determination of heavy metals in some cosmetics available in locally markets. IOSR Journal of Environmental Science, Toxicology and Food Technology. 2014;8(8):9-12.
39. Nkansah MA, Owusu-Afriyie E, Opoku F. Determination of lead and cadmium contents in lipstick and their potential health risks to consumers. J Consum Prot Food Saf. 2018 Dec;13(4):367-73. Available from: [<URL>](#).
40. Naalbandi H, Saeedi M, Moharrami Moghanlou O, Akbari J, Morteza-Semnani K, Alizadeh R, et al. Evaluation of heavy metal content of some lipsticks in Iran market. Pharmaceutical and Biomedical Research. 2016;2(3):31-7.
41. Saleh FAF, Saif RNA, Murshed DMA, Abdulmageed BAM. Determination of Cadmium in Some Cosmetic Products [Internet]. CHEMISTRY; 2020 Sep [cited 2023 Feb 11]. Available from: [<URL>](#)
42. Iwegbue CMA, Bassey FI, Obi G, Tesi GO, Martincigh BS. Concentrations and exposure risks of some metals in facial cosmetics in Nigeria. Toxicology Reports. 2016;3:464-72.
43. Whitehouse L. Germany Reduces Heavy Metal Limits in Cosmetics. 2017 [Internet]. 2017 [cited 2023 Nov 2]. Available from: [<URL>](#)
44. Alam MF, Akhter M, Mazumder B, Ferdous A, Hossain MD, Dafader NC, et al. Assessment of some heavy metals in selected cosmetics commonly used in Bangladesh and human health risk. J Anal Sci Technol. 2019 Dec;10(1):2. Available from: [<URL>](#).
45. Schroeder HA. The poisons around us: toxic metals in food, air, and water. Bloomington: Indiana University Press; 1974. 144 p. ISBN: 978-0-253-16675-3.
46. Franken A, Eloff FC, Du Plessis J, Du Plessis JL. *In Vitro* Permeation of Metals through Human Skin: A Review and Recommendations. Chem Res Toxicol. 2015 Dec 21;28(12):2237-49. Available from: [<URL>](#).
47. Ouremi OI, Ayodele OE. Lipsticks and nail polishes: potential sources of heavy metal in human body. Int J Pharm Res Allied Sci. 2014;3(4):45-51.
48. Brzóška MM, Galażyn-Sidorczuk M, Borowska S. Metals in Cosmetics. In: Chen JK, Thyssen JP, editors. Metal Allergy [Internet]. Cham: Springer International Publishing; 2018 [cited 2023 Feb 11]. p. 177-96. Available from: [<URL>](#)
49. Corazza M, Baldo F, Pagnoni A, Miscioscia R, Virgili A, others. Measurement of nickel, cobalt and chromium in toy make-up by atomic absorption spectroscopy. Acta Derm Venereol. 2009;89(2):130-3.
50. Khalid A, Bukhari IH, Riaz M, Rehman G, Ain Q, Bokhari TH, et al. Determination of lead, cadmium, chromium, and nickel in different brands of lipsticks. International Journal of Biology, Pharmacy and Allied Sciences. 2013;1(2):263-71.
51. Engwa GA, Ferdinand PU, Nwalo FN, Unachukwu MN, others. Mechanism and health effects of heavy metal toxicity in humans. Poisoning in the modern world-new tricks for an old dog. 2019;10:70-90.
52. Cha NR, Lee JK, Lee YR, Jeong HJ, Kim HK, Lee SY. Determination of Iron, Copper, Zinc, Lead, Nickel and Cadmium in Cosmetic Matrices by Flame Atomic Absorption Spectroscopy. Analytical Letters. 2010 Jan 12;43(2):259-68. Available from: [<URL>](#).
53. Wang B, Su Y, Tian L, Peng S, Ji R. Heavy metals in face paints: Assessment of the health risks to Chinese opera actors. Science of The Total Environment. 2020 Jul;724:138163. Available from: [<URL>](#).

54. Wirth JJ, Mijal RS. Adverse Effects of Low Level Heavy Metal Exposure on Male Reproductive Function. *Systems Biology in Reproductive Medicine*. 2010 Jan 1;56(2):147-67. Available from: [<URL>](#).
55. Lim DS, Roh TH, Kim MK, Kwon YC, Choi SM, Kwack SJ, et al. Non-cancer, cancer, and dermal sensitization risk assessment of heavy metals in cosmetics. *Journal of Toxicology and Environmental Health, Part A*. 2018 Jun 3;81(11):432-52. Available from: [<URL>](#).
56. Soares AR, Nascentes CC. Development of a simple method for the determination of lead in lipstick using alkaline solubilization and graphite furnace atomic absorption spectrometry. *Talanta*. 2013 Feb;105:272-7. Available from: [<URL>](#).
57. Łodyga-Chruścińska E, Sykuła A, Więdocha M. Hidden Metals in Several Brands of Lipstick and Face Powder Present on Polish Market. *Cosmetics*. 2018 Oct 1;5(4):57. Available from: [<URL>](#).
58. Bartzatt R. Neurological impact of zinc excess and deficiency in vivo. *European Journal of Nutrition & Food Safety* (ISSN: 2347-5641). 2017;7(3):155-60.
59. Radfard M, Yunesian M, Nabizadeh R, Biglari H, Nazmara S, Hadi M, et al. Drinking water quality and arsenic health risk assessment in Sistan and Baluchestan, Southeastern Province, Iran. *Human and Ecological Risk Assessment: An International Journal*. 2019 May 19;25(4):949-65. Available from: [<URL>](#).
60. Bilal M, Mehmood S, Iqbal HMN. The Beast of Beauty: Environmental and Health Concerns of Toxic Components in Cosmetics. *Cosmetics*. 2020 Feb 28;7(1):13. Available from: [<URL>](#).
61. Yu S, Liao WT, Lee CH, Chai CY, Yu CL, Yu HS. Immunological dysfunction in chronic arsenic exposure: From subclinical condition to skin cancer. *J Dermatol*. 2018 Nov;45(11):1271-7. Available from: [<URL>](#).
62. Papadopoulos A, Assimomytis N, Varvaresou A. Sample Preparation of Cosmetic Products for the Determination of Heavy Metals. *Cosmetics*. 2022 Feb 4;9(1):21. Available from: [<URL>](#).
63. Abd El-Aziz R, Abbassy MM, Hosny G. A comparative study on health risk Assessments of some heavy metals in cosmetics commonly used in Alexandria, Egypt. *Int J Environ Sci Toxic Res*. 2017;5(3):53-62.
64. Parekh J, Chanda S. Antibacterial and phytochemical studies on twelve species of Indian medicinal plants. *African Journal of Biomedical Research*. 2007;10(2):175-81.
65. Mohammadi M, Riyahi Bakhtiari A, Khodabandeh S and. Determination of Cadmium and Lead Concentration in Cosmetics (Sunscreens, Lipstick and Hair Color). *Iranian Journal of Health and Environment*. 2014;6(4):481-90. Available from: [<URL>](#).
66. Ghaderpoori M, Kamarehie B, Jafari A, Alinejad AA, Hashempour Y, Saghi MH, et al. Health risk assessment of heavy metals in cosmetic products sold in Iran: the Monte Carlo simulation. *Environ Sci Pollut Res*. 2020 Mar;27(7):7588-95. Available from: [<URL>](#).
67. Malvandi H, Sancholi F. Assessments of some metals contamination in lipsticks and their associated health risks to lipstick consumers in Iran. *Environ Monit Assess*. 2018 Nov;190(11):680. Available from: [<URL>](#).
68. Pinto E, Paiva K, Carvalhido A, Almeida A. Elemental impurities in lipsticks: Results from a survey of the Portuguese and Brazilian markets. *Regulatory Toxicology and Pharmacology*. 2018 Jun;95:307-13. Available from: [<URL>](#).
69. Chauhan SB, Chandak A, Agrawal S. Evaluation of heavy metals contamination in marketed lipsticks. *International Journal of Advanced Research*. 2014;2(4):257-62.
70. Nourmoradi H, Foroghi M, Farhadkhani M, Vahid Dastjerdi M. Assessment of Lead and Cadmium Levels in Frequently Used Cosmetic Products in Iran. *Journal of Environmental and Public Health*. 2013;2013:1-5. Available from: [<URL>](#).
71. Benabbes M, Chentoufi MA, Mojemmi B, Benzeid H, Toure HA, Shallangwa GA, et al. Determination of Lead and Cadmium in Synthetic and Natural Hair Dyes in Morocco Using Differential Pulse Polarography: Port Electrochim Acta. 2021;39(1):37-44. Available from: [<URL>](#).
72. Ghaderpoori M, Kamarehie B, Jafari A, Alinejad AA, Hashempour Y, Saghi MH, et al. Health risk assessment of heavy metals in cosmetic products sold in Iran: the Monte Carlo simulation. *Environ Sci Pollut Res*. 2020 Mar;27(7):7588-95. Available from: [<URL>](#).
73. Munir A, Hayyat MU, Shahzad L, Sharif F, Farhan M, Ghafoor GZ. Assessment of heavy metals concentrations in commercially available lipsticks in Pakistan. *Environmental Forensics*. 2020 Oct 1;21(3-4):259-66. Available from: [<URL>](#).
74. Nasirudeen M, Amaechi A. Spectrophotometric determination of heavy metals in cosmetics sourced from Kaduna Metropolis, Nigeria. *Science world journal*. 2015;10(3):1-5. Available from: [<URL>](#).
75. Kilic S, Kilic M, Soylak M. The Determination of Toxic Metals in some Traditional Cosmetic Products and Health Risk Assessment. *Biol Trace Elem Res*. 2021 Jun;199(6):2272-7. Available from: [<URL>](#).
76. Lee BM, Kwon S, Cho YM, Kim KB, Seo K, Min CS, et al. Perspectives on trace chemical safety and chemophobia: risk communication and risk management. *Journal of Toxicology and Environmental Health, Part A*. 2019 Feb 1;82(3):186-99. Available from: [<URL>](#).
77. Stewart SE, Parker MD, Amézquita A, Pitt TL. Microbiological risk assessment for personal care products. *Int J Cosmet Sci*. 2016 Dec;38(6):634-45. Available from: [<URL>](#).
78. Siya K, Thomas J, Vinod Kumar R, Saji A, Iype A, Akhil S. Lipsticks: The microbial cellar: An original study. *J Microsc Ultrastruct*. 2019;7(4):194. Available from: [<URL>](#).
79. Vassoler M, Tonial F, Fagundes SC, Fagundes MA, Zortéa NB, Rossato-Grando L, et al. Microbiological Contamination of In-Store Lipstick Testers Available to the Consumer. *Mundo Saúde*. 2020 Jul 27;44:e0442020. Available from: [<URL>](#).



Spectrophotometric and Smartphone-based Dual Monitoring Method for the Determination of Al(III) Ions Using Fermented Black Carrot Juice (Şalgam/Shalgam) as a Green Chromogenic Agent

Batuhan Yardımcı^{1*} 

¹Zonguldak Bülent Ecevit University, Science and Technology Application and Research Center (ARTMER), Zonguldak, 67600, Turkey

Abstract: In this study, anthocyanin-rich fermented black carrot juice (şalgam/shalgam) was used as a chromogenic agent in order to develop eco-friendly, low-cost, simple, fast, and practical both visible spectrophotometric and smartphone-based methods for the determination of Al(III) ions in water samples. Formation of Al(III)-anthocyanin complex results in a color change from red to purple in direct proportion to the increasing Al(III) concentration. For the spectrophotometric analysis, the analytical response of the developed method between absorbance and logarithm of Al(III) concentration exhibits a satisfying wide linear concentration range from 37.0 to 1850.0 μM . The LOD and LOQ values are 6.67 μM and 22.0 μM , respectively. For smartphone-based analysis, the analytical response of the developed method between B values and Al(III) concentration obtained a linear concentration range from 18.5 to 111.0 μM . The LOD and LOQ values are 4.40 μM and 14.5 μM , respectively. LOD values are below the acceptable limit of Al(III) in water according to WHO (7.41 μM) for both methods. The interfering effect of common water ions was investigated, and the observed interferences from Sn^{2+} , Fe^{2+} , and Fe^{3+} were easily eliminated using enough concentration of Na_2EDTA without affecting the blank absorbance/B value of the Al(III)-anthocyanin complex for two monitoring methods. The selectivity of the developed method was investigated in the presence of possible species such as benzoic acid, lactic acid, amino acids, and salt. Developed spectrophotometric and smartphone-based methods applied to real water samples and validated against the reference ICP-OES method at 95% confidence level using Student's *t*- and *F*-tests.

Keywords: Chromogenic agent, aluminum(III) ions, fermented black carrot juice (Shalgam), anthocyanin, spectrophotometry, smartphone

Submitted: November 08, 2022. **Accepted:** January 11, 2023.

Cite this: Yardımcı B. Spectrophotometric and smartphone-based dual monitoring method for the determination of Al(III) ions using fermented black carrot juice (şalgam/shalgam) as a green chromogenic agent. JOTCSA. 2023;10(1):161-76.

DOI: <https://doi.org/10.18596/jotcsa.1201498>.

Corresponding author. E-mail: batuhan.yardimci@beun.edu.tr.

1. INTRODUCTION

Aluminum is not found free in nature. It ranks third among the most abundant metals in the earth's crust and constitutes approximately 8% of the crust's mass (1) and it is mainly found as silicate minerals (2). Due to the widespread presence of aluminum in the environment and industrial developments, its relationship with human health is becoming increasingly important. The amount of free Al(III) increases as the aluminum in the soil leaks into the environment and surface waters due

to acid rain (1). While aluminum is in ionic form; it can react with biological species. When it reacts, it causes harmful effects by suppressing or changing the function of the biological species (3). Aluminum ion is thought to be the reason for neurological disorders and it causes changes in enzymatic reactions by affecting neurofibrillary and neurotransmitters in the central nervous system. As a result; diseases such as Parkinson's disease, Alzheimer's disease, and dialysis encephalopathy occur (4). Aluminum is also thought to have the ability to replace iron and other metals in proteins

found in living things (5). Determination of Al(III) concentration is a critical issue for researchers due to its direct impact on the environment and human health. Different kinds of conventional analytical methods such as AAS (6), ICP-MS (7), ion-selective electrode-based potentiometry (ISE) (8) voltammetry (9), and fluorimetry (10) have been developed to determine the concentration of Al(III). Most of these methods are limited due to the requirements of time-consuming processes, expensive and complicated equipment, and a skilled person. Although fluorescent probes for the determination of Al(III) stand out among these methods due to their selectivity and sensitivity, the disadvantages of this method are that they have time-consuming complicated probe design and synthesis processes, are toxic, have low solubility in water, have low photostability and excess reagent consumption (11, 12).

Spectrophotometry is one of the versatile and good alternative analytical techniques to determine the concentration of many analytes, especially in water samples, and has many advantages such as low cost, easy applicability, fast analysis, reliability, high sensitivity at low concentrations, and wide analytical working range (13).

Recently, smartphone-based colorimetric and fluorometric methods have gained importance over traditional bulky devices due to their many properties such as quick analysis, low-cost and simple production, portability, and ease to use. The smartphone-based methods exhibit a highly comparable performance of analysis according to the traditional methods (14,15). Analysis of different kinds of samples by smartphone is based on the measurement of red (R), green (G), and blue (B) values with help of various software (15-17).

Anthocyanins are water-soluble flavonoid pigments that provide bright colors from light pink to dark blue when found in fruits and vegetables (18). In recent years, anthocyanins have gained great importance among researchers due to their antioxidant capacity, bioavailability properties, food coloring, and food stabilizer properties (19). In fact, according to studies no adverse events have been encountered in the intake of anthocyanins in high doses (20). Anthocyanins also have metal-chelating abilities such as dihydroxy B-ring substituted flavonoids (21). Fermented black carrot (şalgam/shalgam) juice, a dark red-colored and sour soft traditional Turkish beverage, is one of the sources of natural anthocyanin pigments originating from black carrot. It is very popular in the southern part of Türkiye. In addition, recently, fermented black carrot juice has taken its place in the markets of numerous European countries (22). Fermented black carrot juice is defined as a beverage formed as a result of lactic acid fermentation of black carrot, turnip, salt, extract of sourdough, and bulgur flour components (23). Turnip and bulgur are minor components of şalgam and turnip helps to develop the sensory character (24), while bulgur flour is used

as a source of microorganisms in the first fermentation stage. In addition, the reason for using salt is to control the fermentation flora (25). Fermented black carrot juice gets its red color from the main ingredient, black carrots. According to studies, cyanidin glycosides as an aglycone have been found in black carrots as the main anthocyanin compound (26,27), malvidin, and peonidin glycosides in black carrot roots (27,28). Furthermore, fermented black carrot juice has been reported to contain an average of 114.1 mg L⁻¹ anthocyanin as cyanidin-3-glycoside (25). It is stated that commercially fermented black carrot contains the anthocyanins cyanidin-3-galactoside, cyanidin-3-glucoside, and cyanidin-3-arabinoside using LC/MS/MS and also its total phenolic content (517.21 µg GAE/mL) and antioxidant capacity (in µmol Trolox equivalents/mL) were investigated with FRAP (2.26), DPPH (4.44) and ABTS (3.42) assays (29). Different types of metal determinations were studied from various anthocyanin-derived plants by utilizing the metal complexing properties of anthocyanins (30,31). In such studies, anthocyanins were extracted from natural plants, but the negative properties of isolated anthocyanins are time-consuming processes for the extraction stage, low extraction efficiency, instability, and degradation properties in the presence of light, heat, and oxygen (19,32). An important feature of anthocyanins from purple carrots is dominant that the cultivars are in the acyl form. Acylated anthocyanins are more stable compounds than other types of anthocyanins and degrade more slowly during storage (29). Fermented black carrot may also enhance the stability, absorption, and bioactivity of its anthocyanins (32), as well as metal complexes of anthocyanins, which are known to stabilize the structure more (19), and it can be concluded that by forming a complex with the metal, its repeatability will be better in the determination of the relevant metal.

In the light of this information, low-cost, non-toxic, anthocyanin-rich, sugar-free, and gluten-free, commercially fermented black carrot juice with good stability was preferred as a chromogenic agent. This chromogenic agent meets the at least three principles of green analytical chemistry (33) such as removing or replacing toxic reagents, using reagents obtained from a renewable source, and reducing the risk to the operator. In this way, the concentration of Al(III) in water samples can be determined quickly and simply via color changing from red to purple in direct proportion to the amount of Al(III) ions because of the formation of the Al(III)-anthocyanin complex, without any pre-treatment such as time-consuming extraction.

2. MATERIAL AND METHODS

2.1. Chemicals and Instrumentation

All reagents used in this study were of analytical grade except Lactic acid (80%). The fermented black carrot juice was bought from the local market. Aluminum nitrate nonahydrate (Al(NO₃)₃·9H₂O),

lead(II) nitrate ($\text{Pb}(\text{NO}_3)_2$), chromium(III) nitrate nonahydrate ($\text{Cr}(\text{NO}_3)_3 \cdot 9\text{H}_2\text{O}$), cadmium acetate dihydrate ($\text{Cd}(\text{CH}_3\text{COO})_2 \cdot 2\text{H}_2\text{O}$), ethylenediaminetetraacetic acid disodium salt (Na_2EDTA), sodium benzoate ($\text{C}_6\text{H}_5\text{COONa}$), sodium acetate (CH_3COONa), L-glycine ($\text{NH}_2\text{CH}_2\text{COOH}$), L-lysine hydrochloride ($\text{H}_2\text{N}(\text{CH}_2)_4\text{CH}(\text{NH}_2)\text{CO}_2\text{H} \cdot \text{HCl}$), and sodium bicarbonate (NaHCO_3) were purchased from Sigma Aldrich. Iron(III) nitrate nonahydrate ($\text{Fe}(\text{NO}_3)_3 \cdot 9\text{H}_2\text{O}$), iron(II) chloride tetrahydrate ($\text{FeCl}_2 \cdot 4\text{H}_2\text{O}$), manganese (II) nitrate tetrahydrate ($\text{Mn}(\text{NO}_3)_2 \cdot 4\text{H}_2\text{O}$), ammonium chloride (NH_4Cl), potassium nitrate (KNO_3), calcium nitrate tetrahydrate ($\text{Ca}(\text{NO}_3)_2 \cdot 4\text{H}_2\text{O}$), magnesium nitrate hexahydrate ($\text{Mg}(\text{NO}_3)_2 \cdot 6\text{H}_2\text{O}$), copper(II) sulfate pentahydrate ($\text{CuSO}_4 \cdot 5\text{H}_2\text{O}$), Tin(II) chloride dihydrate ($\text{SnCl}_2 \cdot 2\text{H}_2\text{O}$), zinc sulphate heptahydrate ($\text{ZnSO}_4 \cdot 7\text{H}_2\text{O}$), sodium nitrate (NaNO_3), sodium chloride (NaCl), sodium sulfate (Na_2SO_4), and sodium hydroxide (NaOH) were purchased from Merck. Lactic acid was obtained from Bioliv food industry and trade import export limited company. Potassium hydrogen phthalate ($\text{HOOC}_6\text{H}_4\text{COOK}$) was bought from CDH (Central drug house Ltd.). Sodium phosphate monobasic (NaH_2PO_4) was obtained from Riedel-de Haën. L-arginine ($\text{H}_2\text{NC}(=\text{NH})\text{NH}(\text{CH}_2)_3\text{CH}(\text{NH}_2)\text{CO}_2\text{H}$) was purchased from sepenatural. L-cysteine hydrochloride monohydrate ($\text{HSCH}_2\text{CH}(\text{NH}_2)\text{COOH} \cdot \text{HCl} \cdot \text{H}_2\text{O}$) was obtained from Akcan Kimya and L-glutamine ($\text{H}_2\text{NCOCH}_2\text{CH}_2\text{CH}(\text{NH}_2)\text{CO}_2\text{H}$) was bought from Hardline nutrition.

Precisa XB 220A Analytical Balance was used to weigh all the chemicals. Rayleigh VIS-723G visible (vis.) spectrophotometer and its glass cuvettes (optical thickness 5 mm) were used for all absorbance measurements. Only Shimadzu UV-1800 spectrophotometer was used for the characterization of anthocyanin. For RGB measurements, the Samsung Galaxy S10 Plus is used with its convenient black box that allows the phone to fit on it. Wisetherm-fuzzy control, wsd HB-48 dry bath was used to determine the optimum temperature for the proposed method. Both detection systems were validated against the ICP-OES (34) method using PerkinElmer Avio 200 ICP-OES.

2.2. Preparation of Solutions

Fermented black carrot juice bought from the market was stored at +4 °C and diluted with ultrapure water at a ratio of 1/2 (v/v) when necessary for the proposed method.

Working solutions of different initial concentrations of Al(III) were freshly prepared from the stock solutions of Al(III) at 3.7×10^{-2} M in ultrapure water. Potassium hydrogen phthalate (KHP)-NaOH buffer solutions were prepared from the appropriate amount of 0.1 M KHP and 0.1 M NaOH to adjust the pH 4.0, pH 5.0, and pH 6.0 values.

After preparing stock solutions of each common water ion (Cl^- , NO_3^- , HCO_3^- , SO_4^{2-} , PO_4^{3-} , CH_3COO^- , K^+ , NH_4^+ , Ca^{2+} , Mg^{2+} , Mn^{2+} , Cu^{2+} , Ni^{2+} , Zn^{2+} , Cd^{2+} , Pb^{2+} , Sn^{2+} , Fe^{2+} , Fe^{3+} , and Cr^{3+}) at the appropriate concentration, mixtures of each ion solution were prepared as certain fold of the Al(III) ions.

In order to observe the characteristic three absorption bands of anthocyanins, the solution was prepared by dissolving the precipitate in a mixture of MeOH and 2 M HCl (85:15 v/v) after the fermented black carrot juice was kept at 10.000 rpm for 10 min in an ultracentrifuge device.

For investigation of selectivity, stock solutions of 9.15 g L^{-1} of L-cysteine hydrochloride monohydrate, L-arginine, L-glycine, L-lysine hydrochloride, and L-glutamine were prepared. Additively, the stock solution of 40.25 g L^{-1} of lactic acid, 8.5%, w/v NaCl, and 0.1% (w/v) sodium benzoate were prepared.

2.3. Preparation of the Proposed Method for Al(III) Detection

For the spectrophotometric method, after adding 1.0 mL of fermented black carrot juice diluted 1/2 (v/v) with ultrapure water, 1.0 mL of pH 6.0 KHP-NaOH buffer solution (0.1 M), and 0.5 mL of Al(III) solution at different initial concentrations (185.0-9250.0 μM) to the test tubes and waiting for 4.5 minutes at room temperature (RT), absorbance readings were recorded against the blank at a wavelength of 575 nm (Scheme 1). For the blank solution, 0.5 mL of ultrapure water is added instead of Al(III) solution.

Summarized procedure: for sample solutions, add 1.0 mL of fermented black carrot juice diluted 1/2 (v/v) with ultrapure water + 1.0 mL of pH 6.0 KHP-NaOH buffer solution (0.1 M) + 0.5 mL of Al(III) solutions at different initial concentrations (185.0-9250.0 μM); wait 4.5 min. at RT.; record the absorbance at λ_{575} nm against the blank solution ($V_{\text{total}} = 2.5 \text{ mL}$).

For the smartphone-based method, the Samsung Galaxy S10 Plus was used with its smaller black colored box (16.5×8×3 cm) that comes out of the phone box when purchasing the phone and allows the phone to fit on. This box was evaluated by using it for RGB measurements (Figure 1A). A cardboard sample holder (8×3 cm) was designed to fit the square space of the black box (Figure 1B and Figure 1C). The blue (B) values were recorded via PhotoMetrix software obtained from the google play store without any payment for the android system. The region of interest was chosen 96×96 and flash mod was selected "on" to see and take the B values of samples in the box. Also, the 1.5 mL of glass vials were used instead of the cuvette (Figure 1C and Figure 1D).

1.0 mL of fermented black carrot juice diluted 1/2 (v/v) with ultrapure water, 1.0 mL of pH 6.0 KHP-NaOH buffer solution (0.1 M), and 0.5 mL of Al(III) solution at different initial concentrations (92.5-

555.0 μM) were added the test tubes and waiting for 4.5 minutes at RT, the B value measurements of blank and sample solution were recorded using the black box with the smartphone (Scheme 1).

2.4. Investigation of Interference Effect of Common Ions and Selectivity

Dual monitoring methods were applied in the presence of common water ions and the recovery values of Al(III) were calculated. Interference effects were removed easily using Na_2EDTA for Sn^{2+} , Fe^{2+} , and L-ascorbic acid for Fe^{3+} (35). In addition, it was investigated whether possible species other than anthocyanin in fermented black carrot juice affect the proposed method.

First of all, the maximum concentration of Na_2EDTA that will not dissociate the Al(III)-anthocyanin complex in the proposed method was investigated. The reason for optimizing the amount of Na_2EDTA is to prevent the discoloration of the Al(III)-anthocyanin complex due to the excess EDTA in the medium. To this end, mixed Al(III) solutions at an initial concentration of 1850.0 μM and Na_2EDTA at different concentrations (1850.0, 3700.0, 5550.0, and 7400.0 μM) were prepared separately. The

appropriate Na_2EDTA concentration was determined by applying the proposed method to these mentioned mixture solutions and the solution containing only 1850.0 μM initial concentration of Al(III). Then, different mass ratios of Na_2EDTA were investigated along with Fe^{2+} and Sn^{2+} ions in 1:1 metal:Al(III) solutions to remove the interference due to Fe^{2+} and Sn^{2+} ions by masking (without exceeding the optimum amount of Na_2EDTA).

2.5. Application of the Proposed Method to Real Water Samples.

The proposed method was successfully applied to drinking water and tap water samples using vis. spectrophotometer and smartphone. Later, the recovery (%) and RSD (%) values of Al(III) were calculated.

2.6. Method Validation of the Developed Methods Against the ICP-OES Method for Al(III) Detection.

Both the spectrophotometric and smartphone-based proposed methods have been validated with the ICP-OES method (34). The confidence level was calculated using *t*- and *F*- tests via the proposed method and ICP-OES method.

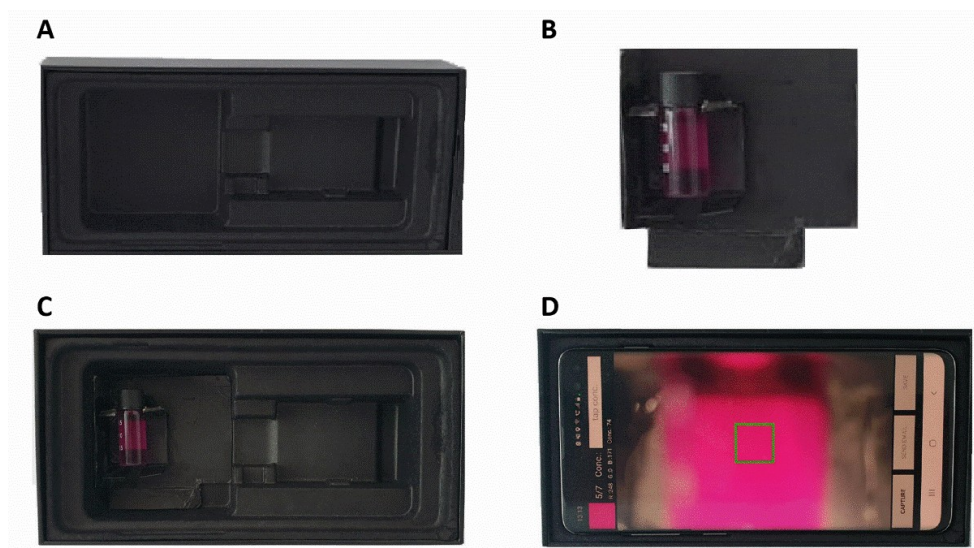
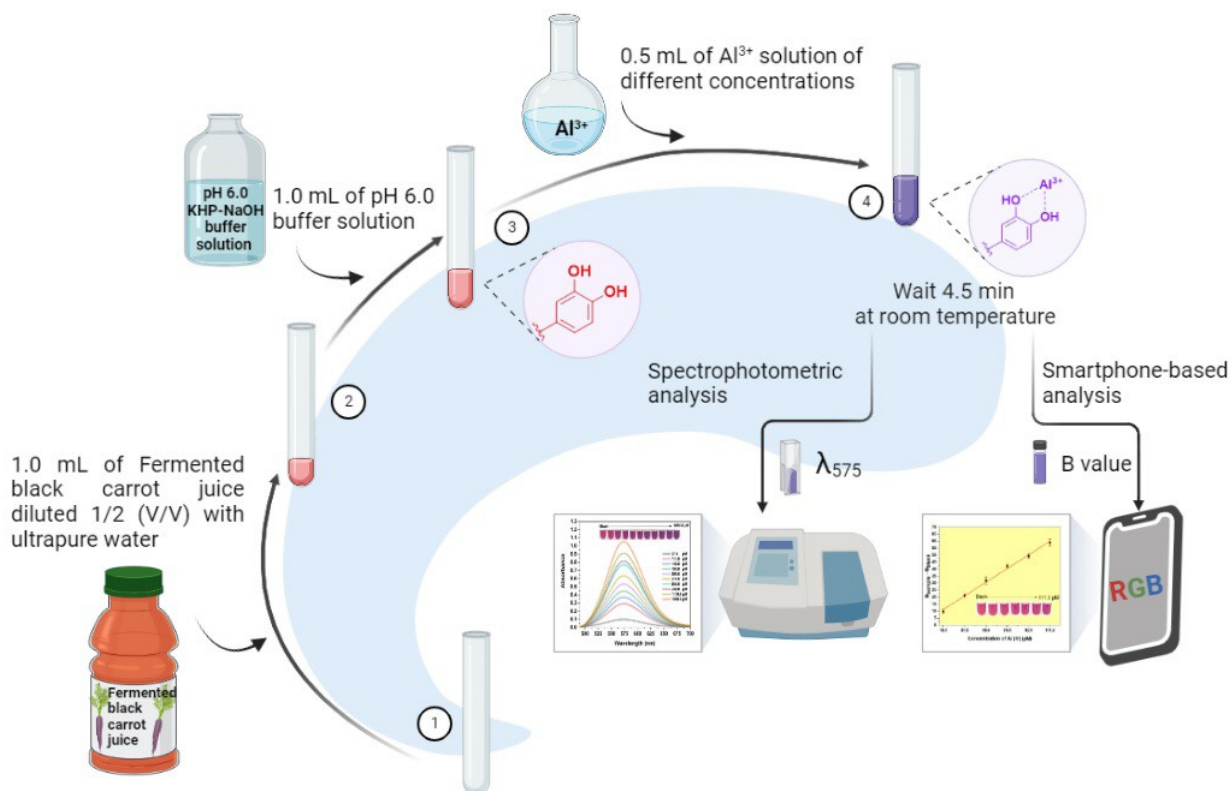


Figure 1: Representation of smartphone-based colorimetric detection of Al(III) ions (A) the original black box in which the phone was kept at the time of purchase and (B) sample holder made of cardboard; (C) sample holder placed in the black box; (D) reading the RGB values with the help of software by placing the phone in the black box designed for itself.



Scheme 1: Preparation of the proposed method for Al(III) detection using spectrophotometric and smartphone-based analysis.

2.7. Statistical Analysis

Excel software (Microsoft Office 2016) was used for performing the statistical analyses and calculating the means and the standard error of the mean. The mean \pm standard deviation (SD) was shown as a result. Validation of the proposed method for determining the Al(III) content against the ICP-OES method was made using the statistical tools of the same software.

3. RESULTS AND DISCUSSION

3.1. Optimization of the Parameters

The figures obtained for the optimization of each parameter were formed as a result of three repetitive analyses ($N = 3$). Aluminum forms an insoluble complex known as the $\text{Al}(\text{OH})_3$ with increasing pH values and shows low solubility between pH 6.0-8.0 (36). It is also reported that cyanidin complexes formed with Al(III) in the pH range of 3.0-6.0 (32). Therefore, pH optimization studies were carried out between the pH range of 4.0-6.0 in order to select the optimal pH value. This experiment was applied for two different initial concentrations of Al(III) one at 555.0 μM and the other at 1850.0 μM for each pH value. For this purpose, after adding 1.0 mL of fermented black carrot juice diluted 1/2 (v/v) with ultrapure water, 1.0 mL of KHP-NaOH (0.1M) buffer solution (pH 4.0 or pH 5.0 or pH 6.0), and 0.5 mL of 555.0 μM or 1850.0 μM initial concentrations of Al(III) to the test tubes, respectively ($V_{\text{total}} = 2.5 \text{ mL}$), solutions in the

test tubes were kept for 4.5 min at RT and the absorbances were recorded against the blank samples at 575 nm wavelength. As shown in Figure 2A, pH 6.0, where the absorbance differences are maximum for both 555.0 μM and 1850.0 μM initial concentration of Al(III), was chosen as the optimal pH value.

In order to select the optimal time, separate experiments were studied for two different initial concentrations of Al(III) one at 555.0 μM and the other at 1850.0 μM for each time interval. For this purpose, after adding 1.0 mL of fermented black carrot juice diluted 1/2 (v/v) with ultrapure water, 1.0 mL of pH 6.0 KHP-NaOH (0.1M) buffer solution, 0.5 mL of 555.0 μM or 1850.0 μM initial concentrations of Al(III) to the test tubes, respectively ($V_{\text{total}} = 2.5 \text{ mL}$), solutions in the test tubes were kept separately for different time intervals starting from 0.5 min to 10 min at RT and the absorbances were recorded against the blank samples at 575 nm wavelength. According to Figure 2B, the optimal time for complex formation to reach equilibrium was determined as 4.5 minutes.

In order to select the optimal temperature, two different Al(III) solutions one at 555.0 μM and the other at 1850.0 μM initial concentrations were studied separately. After adding 1.0 mL of fermented black carrot juice diluted 1/2 (v/v) with ultrapure water, 1.0 mL of pH 6.0 KHP-NaOH (0.1M) buffer solution, 0.5 mL of 555.0 μM or 1850.0 μM

initial concentrations of Al(III) to the test tubes, respectively ($V_{\text{total}} = 2.5 \text{ mL}$), solutions in the test tubes were kept separately 4.5 min at different temperatures (25.0-100.0 °C) and the absorbances were recorded against the blank samples at 575 nm wavelength. As it is understood from Figure 2C, since there is no significant change in absorbance values at different temperatures, 25.0 °C (RT) was selected as the optimal temperature for the proposed method.

For the smartphone-based method, the R and G values were constant, and also it was observed that the calibration equation could be obtained by increasing the B values in direct proportion to the increasing Al(III) concentration between 18.5 and 111.0 μM so that, B value was selected to form calibration plot (Figure 2D).

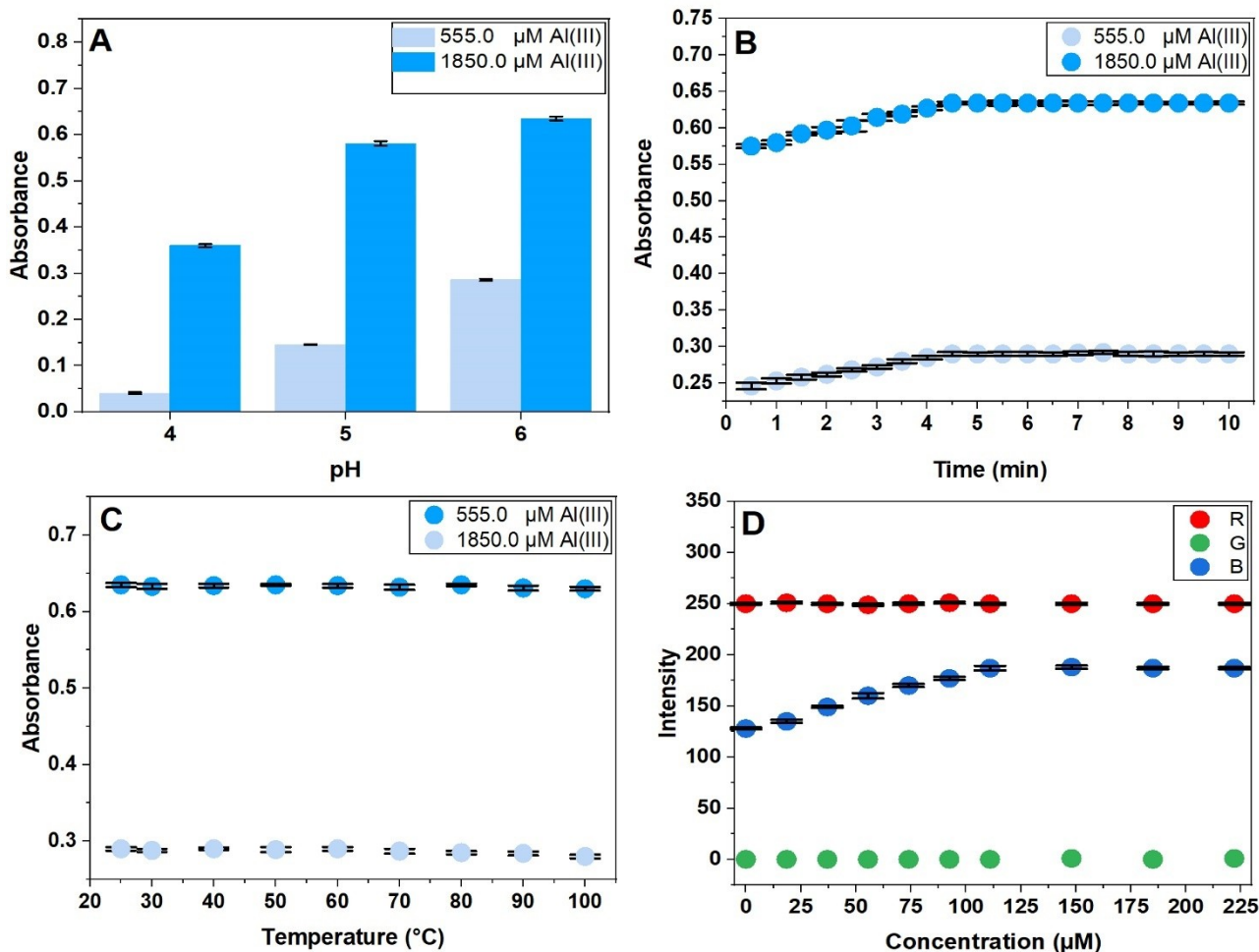


Figure 2: Optimization of the proposed method parameters: (A) optimal pH; (B) optimal time; (C) optimal temperature for spectrophotometric method and (D) selecting optimal RGB value for constructing calibration equation for smartphone-based method.

3.2. Characterization and Working Principle of the Proposed Method

Anthocyanins are known as colorful flavonoids including a flavylium cation (37) and they have a metal binding ability due to their two vicinal or three hydroxyl (-OH) substitutes located at the B ring (catechol or pyrogallol moiety). Polyvalent metal ions cause the loss of hydrogen ions bound to these rings and convert the flavylium cation to a quinoid base as shown in Figure 3A (38). Anthocyanins consist of a completely delocalized π -conjugated system, which gives a maximum absorption band in the wavelength range of 500-550 nm. Metal binding to anthocyanins causes a decrease in the energy

required for light-induced electron transfer in this chromophore system and also both maximum absorption shift towards the larger wavelength (bathochromic shift) and the increasing intensity of maximum absorbance (hyperchromic effect) are observed (21). According to some researchers, a bathochromic shift occurs due to the strong charge transfer from the ligand to the metallic center (LMCT), and according to others, it depends on the decrease in the HOMO-LUMO gap in the flavonoid molecule rather than a LMCT (39).

Furthermore, this phenomenon causes the color changing of the solution and enables the

determination of relevant metal via UV-vis. spectroscopy (21). When the proposed method was applied and absorbances values were recorded against the water, a 20 nm bathochromic shift was (from 536 to 556 nm) observed between blank solution and 1295.0 μM initial concentration of Al(III) due to the formation of Al(III)-anthocyanin complex (Figure 3B). The bathochromic shift proved the presence of the ortho-dihydroxyl group of anthocyanin. The fermented black carrot juice was centrifuged at 10.000 rpm for 10 minutes and the

supernatant phase was decanted, then the precipitant was dissolved in 2 mL of methanol, and its flavonoid properties were controlled by applying the Shinoda's test (40). After a few pieces of magnesium ribbon and 1 mL of concentrated HCl were added to the methanolic solution, pink color was observed a few minutes later. Additionally, the observation of maximum absorption at 280, 330, and 535 nm wavelengths in the MeOH/HCl solution, confirms the phenolic and flavonoid groups in the anthocyanin compound.

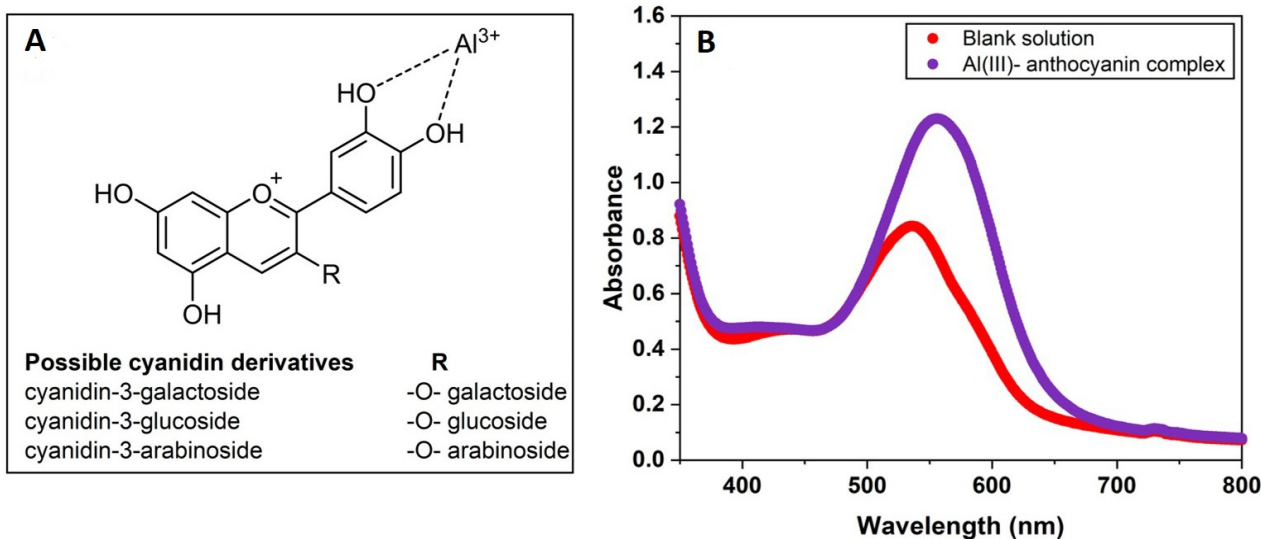


Figure 3: Working principle of the proposed method: (A) Al(III) complexation sites of possible cyanidin derivatives; (B) demonstration of the vis. spectra taken against the water as a result of applying the proposed method to Al(III) at an initial concentration of 1295.0 μM and blank solution.

3.3. Analytical Performance of the Proposed Method for the Determination of Al(III) Using Both Vis. Spectrophotometer and Smartphone

When the proposed method was applied to Al(III) solutions at different initial concentrations, a color change from red to purple was observed in direct proportion to the increasing logarithm of the concentration of Al(III) (Figure 4A and Figure 4B). There are many studies in which the absorbance values vary linearly with the logarithm of the analyte concentration (41, 42). All the absorbance measurements were recorded against the blank solution at 575 nm wavelength. The linear calibration equation was obtained with the absorbance versus the logarithm of the concentration of the Al(III) at the wavelength of 575 nm.

Linear calibration equation for Al(III):

$A_{575\text{ nm}} = 0.585 \log C_{\text{Al(III)}} - 0.87$ ($N = 10$, $r = 0.9963$)
where $C_{\text{Al(III)}}$ is the final concentration of Al(III) (in micromole L^{-1} (μM)).

The linear final concentration range is from 37.0 to 1850.0 μM . Furthermore, the limit of detection (LOD) and the limit of quantification (LOQ) values are 6.67 μM and 22.0 μM , respectively. The limit of detection was calculated in micromole per liter units according to the literature (43, 44). ($\text{LOD} = 3\sigma_{\text{blank}}/\text{antilog } m$,

$\text{LOQ} = 10\sigma_{\text{blank}}/\text{antilog } m$ where σ_{blank} denotes the standard deviation of a blank and m shows the slope of the calibration line). The coefficients of variation (CVs) of intra- and inter-assay calculations for Al(III) were 0.96 and 1.07%, respectively ($N = 5$).

For the smartphone-based measurements, color changing from red to purple enabled to form calibration plot between B values and different concentrations of Al(III) in the concentration range of 18.5-111.0 μM by applying the proposed method (Figure 4C).

In smartphone-based colorimetric methods, there are studies in which calibration plots are created by subtracting the relevant values (R, G, or B values) of the sample and blank solution (45, 46). The calibration equation was obtained by subtracting the B values of the blank solution (B_{blank}) from the B values of the samples (B_{sample}).

Linear calibration equation for Al(III) using a smartphone:

$y = 0.529 C_{\text{Al(III)}} + 1.35$ ($N = 6$, $r = 0.9972$)
where $C_{\text{Al(III)}}$ is the final concentration of Al(III) (in micromole L^{-1}).

The limit of detection (LOD) and the limit of quantification (LOQ) values are 4.40 μM and 14.50

μM , respectively. The limit of detection was found in micromole per liter units. ($\text{LOD} = 3\sigma_{\text{blank}}/m$, $\text{LOQ} = 10\sigma_{\text{blank}}/m$ where σ_{blank} denotes the standard deviation of a blank and m shows the slope of the calibration line). The coefficients of variation (CVs) of intra- and inter-assay calculations for Al(III) were 1.69 and 2.11%, respectively ($N = 5$). Both spectrophotometric and smartphone-based developed method measurements have good precision according to the CVs results and also the

LOD values are below $7.41 \mu\text{M}$, which is the acceptable limit for Al(III) ions in water by the WHO (47).

When the analytical performance of the proposed sensor method and recent studies were compared (Table 1), the proposed sensor method stands out with its not preparation time, short analysis time, and quite good wide linear response range.

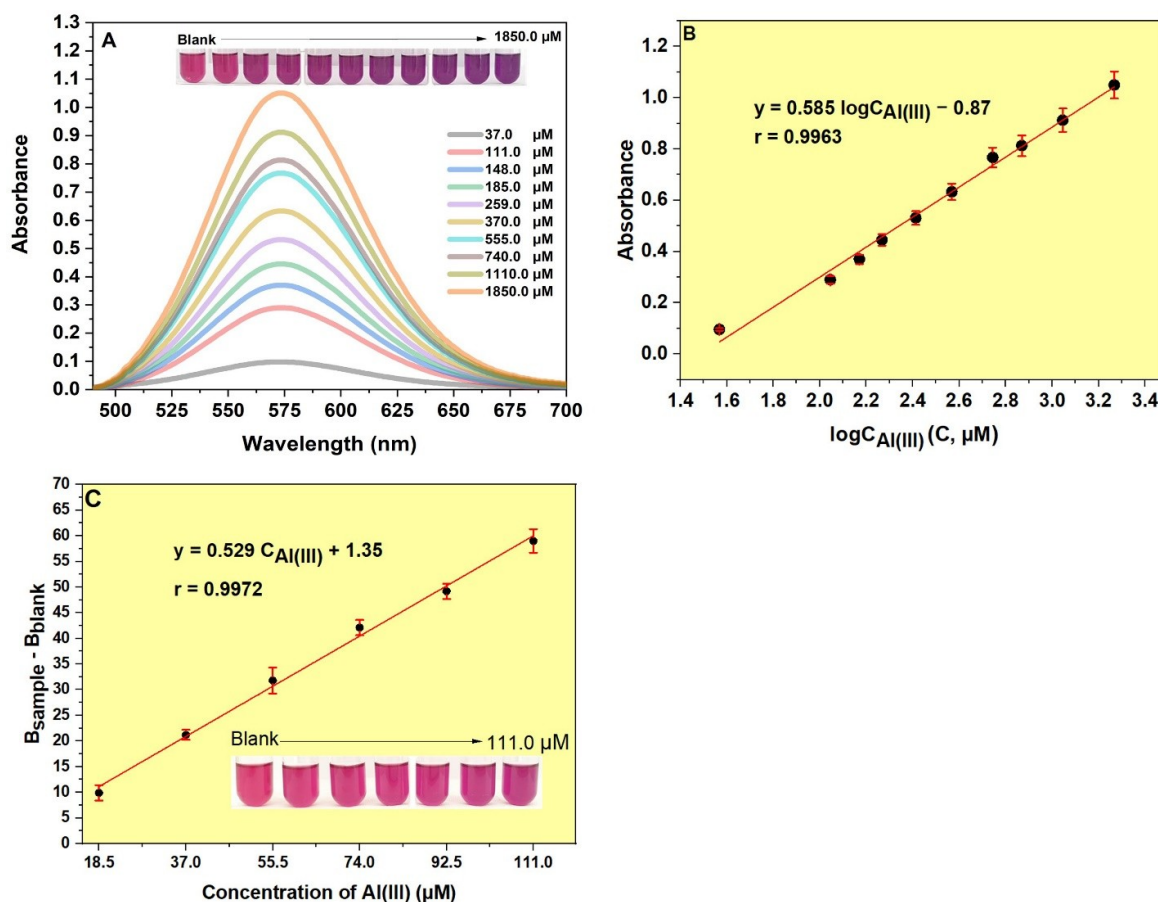


Figure 4: (A) The vis. spectrum of fermented black carrot juice containing different concentrations of Al(III) in an aqueous medium and their photograph (inset); (B) calibration plot of different concentrations of Al(III) solutions mixed with fermented black carrot juice for vis. spectrophotometer; (C) formed calibration plot via Blue (B) values using a smartphone and also the photograph of (inset) different concentrations of Al(III) solutions mixed with fermented black carrot juice.

Table 1: Comparison of the analytical performance of some optical and paper-based methods for the determination of Al(III) ions.

No	Detection method	Probe	Probe Preparation Time	Analysis Time	Linear response range	LOD	Real water application	Ref.
1	Paper-based fluorometric	Rhodamine grafted CDs	84 h (~3.5 days)	10 min	1×10^{-4} - 1×10^{-2} M	3.89×10^{-5} M	x	48
2	Fluorometric	PAA-AuNPs	135 min	10 min	50-150 μ M	2 μ M 8 μ M (with bare eye)	x	49
3	Fluorometric	CDs	140 min	10 min	0.15-38.46 μ M	113.8 nM	✓	50
	Smartphone based-method	CDs	140 min	15 min	15.39-153.85 μ M	5.55 μ M	✓	50
4	Colorimetric	Pectin-rich apple extract-based AuNPs	50 min	1 min	0-100 μ M	20 μ M	✓	51
5	Colorimetric	Cyanidin extracted from red cabbage as a chelating agent	73 h (~3 days)	a few min	n.a	50 μ M	✓	31
6	Colorimetric	Anthocyanin immobilization in CMC/starch films	~ 67 h (~2.8 days)	60 min ($C \leq 3$ mg L^{-1}), 20 min ($C \geq 5$ mg L^{-1})	n.a	1.9×10^{-4} M	x	52
7	Proposed Colorimetric method	Fermented black carrot juice	Direct (0 min.)	4.5 min	37.0-1850.0 μ M	6.67 μ M	✓	This work
	Proposed smartphone-based method	Fermented black carrot juice	Direct (0 min.)	4.5 min	18.5-111.0 μ M	4.40 μ M	✓	This work

n.a: not available, C: concentration, CDs: carbon nanodots, PAA-AuNPs: polyacrylate functionalized gold nanoparticles, CMC: carboxymethylcellulose, Conc.: concentration.

3.4. Investigation of Interference Effect of Common Ions and Selectivity

The interference effect of different common water ions on the proposed method was studied (Table 2), each containing a different mass ratio of Cl^- , NO_3^- , HCO_3^- , SO_4^{2-} , PO_4^{3-} , CH_3COO^- , K^+ , NH_4^+ , Ca^{2+} , Mg^{2+} , Mn^{2+} , Cu^{2+} , Ni^{2+} , Zn^{2+} , Cd^{2+} , Pb^{2+} , Sn^{2+} , Fe^{2+} , Fe^{3+} , and Cr^{3+} with the initial concentration of $1850.0 \mu\text{M}$ of Al(III) (e.g., 1-, 200- fold of Al(III)) for spectrophotometric method and $370.0 \mu\text{M}$ of Al(III) for the smartphone-based method. Additively, the Al(III) recovery (%) values were calculated in the range of 87.29-112.93 and 88.00-111.29% by the spectrophotometric and smartphone-based methods, respectively, as shown in Figure 5. First, the proposed method was applied to mixed solutions including the initial concentration of $1850.0 \mu\text{M}$ of Al(III) mixed with different concentrations of Na_2EDTA solutions to find the maximum concentration of Na_2EDTA that would not interact with Al(III) in the Al(III) -anthocyanin complex. A tolerable maximum initial concentration of Na_2EDTA was determined as $5550.0 \mu\text{M}$ in the mixed solution with the initial concentration of Al(III) at $1850.0 \mu\text{M}$ when the proposed method was applied, and no difference in absorption was observed when compared with the Al(III) -anthocyanin complex solution. Later the interference effects of Fe^{2+} and

Sn^{2+} were easily removed with Na_2EDTA ($\text{Fe}^{2+}:\text{EDTA}$ ratio 1:3 (w/w) and $\text{Sn}^{2+}:\text{EDTA}$ ratio 1:3 (w/w)) as a masking agent without affecting Al(III) -anthocyanin complex before applying the proposed method.

In order to remove the interference effect of Fe^{3+} on the proposed method L-ascorbic acid (35) was used with the 1-fold of Fe^{3+} ($\text{Fe}^{3+}:\text{L-ascorbic acid}$ ratio 1:1 (w/w)).

Fermented black carrot juice contains a maximum amount of 8.05 g L^{-1} lactic acid, 1.97% NaCl (w/v), 1.83 g L^{-1} total amino acids (53), and 0.02% sodium benzoate (54) (w/v) known as the preservative, apart from black carrot, which is the main ingredient. Additionally, it is also stated that it does not contain gluten and sugar. It was tested whether colored complexes were formed with Al(III) at $9250.0 \mu\text{M}$ initial concentration when the proposed method was applied to other species at the specified concentration in the content without using fermented black carrot juice for selectivity. L-cysteine hydrochloride monohydrate, L-arginine, L-glycine, L-lysine hydrochloride, and L-glutamine were used separately as amino acids. As can be seen in Figure 6, no coloration was observed when the proposed method was applied to other ingredients.

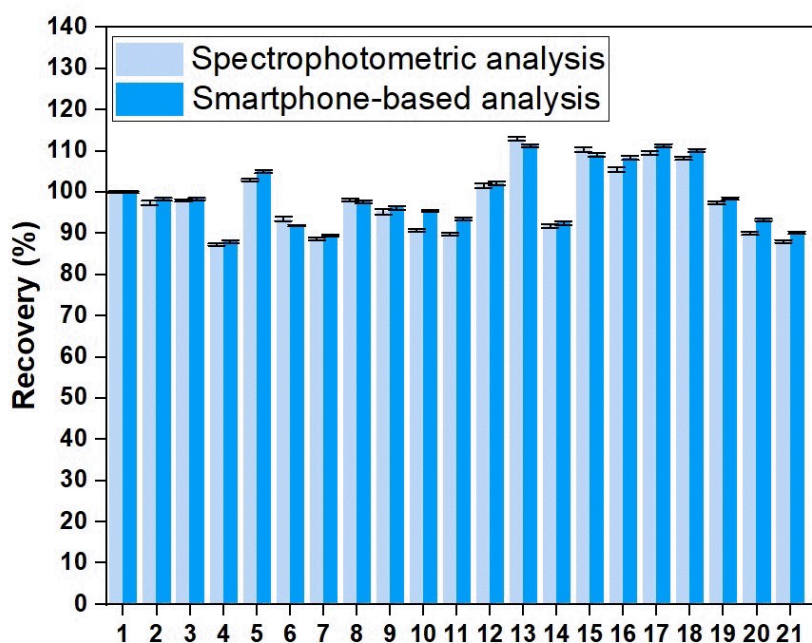


Figure 5: The response of Al(III) ions (1) and possible interference species $\{\text{Cl}^-$ (2), NO_3^- (3), HCO_3^- (4), CH_3COO^- (5), SO_4^{2-} (6), PO_4^{3-} (7), K^+ (8), NH_4^+ (9), Ca^{2+} (10), Mg^{2+} (11), Mn^{2+} (12), Cu^{2+} (13), Ni^{2+} (14), Zn^{2+} (15), Cd^{2+} (16), Pb^{2+} (17), $[\text{Sn}^{2+} + \text{EDTA}]$ (18) $[(\text{Fe}^{2+} + \text{EDTA})]$ (19), $[(\text{Fe}^{3+} + \text{L-ascorbic acid})]$ (20), and Cr^{3+} (21)} in the presence of Al(III) at the initial concentration of $1850.0 \mu\text{M}$ for spectrophotometric method and $370.0 \mu\text{M}$ for smartphone-based method.

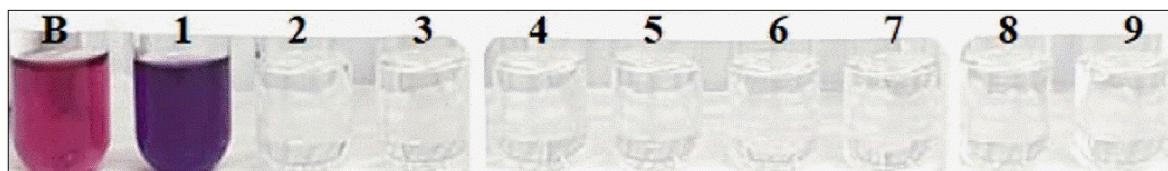


Figure 6: Color states of solutions in the test tubes with the proposed method in the presence of blank solution (B), (1) Al(III) (9250.0 μM), and mixture solutions without using fermented black carrot juice (2) lactic acid (8.05 g L^{-1}), (3) NaCl (1.97%, w/v), (4) sodium benzoate (0.02%, w/v), (5) L-cysteine hydrochloride monohydrate (1.83 g L^{-1}), (6) L-arginine (1.83 g L^{-1}), (7) L-glycine (1.83 g L^{-1}), (8) L-lysine hydrochloride (1.83 g L^{-1}) and (9) L-glutamine (1.83 g L^{-1}).

3.5. Application of the Proposed Method to Real Water Samples

Tap water and drinking water were filtered (CHROMAFIL, PET-20/25) before applying the sensor method. Drinking water and tap water were spiked separately with different concentrations of Al(III) solutions by standard addition method and then the proposed method was applied to real samples using both spectrophotometric and smartphone-based analyses. For the spectrophotometric analysis, Al(III) recoveries (%) and RSD % values for drinking water were found between 97.14-100.99 and 0.77-2.11%, respectively, while these values for tap water were found between 94.16-99.91 and 0.92-2.23% (Table 3). For the smartphone-based analysis, Al(III) recoveries (%) and RSD % values for drinking water were found between 97.43-100.27 and 0.80-2.35%, respectively, while these values for tap water were found between 97.43-94.23 and 1.24-2.65% (Table 3). According to these results, the proposed methods could be used for the determination of Al(III) in real water samples.

3.6. Method Validation of the Proposed Sensor Against the ICP-OES Method for Al(III) Detection

In order to obtain the calibration equation, the concentration range of 18.5-740.0 μM standard

Al(III) solutions were analyzed according to US EPA method 200.7 with ICP-OES (34).

Three repetitive analyses were performed for each standard concentration to generate the calibration equation. The calibration equation between intensity (CPS) and concentration was:

Intensity = 6480 $C_{\text{Al(III)}}$ + 56674 ($r = 0.9999$) for Al(III).

($C_{\text{Al(III)}}$: final concentration of Al(III) in micromole L^{-1} (μM)).

Statistical comparison between the results of the proposed and ICP-OES methods applied to both 370.0 μM and 74.0 μM of Al(III) spiked-drinking water as a real sample was made on $N = 5$ repetitive analyses, substantially showing no important difference in precision and accuracy between the results. The population means and variances were compared using t - and F - tests, respectively. The confidence levels used in the validation of findings were 95% (nominal 0.05 significance level) for both of t - and F - tests. Statistical parameters of the proposed methods and the reference ICP-OES method were shown in Table 4.

Table 2: Al(III) recovery (%) results when the proposed method is applied to ionic species commonly found in the water of different mass ratios with Al(III).

Interferent	Mass ratio (Al ³⁺ :ions (w/w))	Error (%)	
		For spectrophotometer	For smartphone
Cl ⁻	1200	-2.57	-1.70
NO ₃ ⁻	1200	-2.00	-1.60
HCO ₃ ⁻	5	-12.71	-12.00
CH ₃ COO ⁻	300	+2.97	+5.02
SO ₄ ²⁻	1200	-6.44	-8.10
PO ₄ ³⁻	7	-11.31	-10.55
K ⁺	1200	-1.95	-2.31
NH ₄ ⁺	600	-4.75	-3.82
Ca ²⁺	300	-9.29	-4.51
Mg ²⁺	200	-10.14	-6.49
Mn ²⁺	300	+1.53	+2.13
Cu ²⁺	10	+12.93	+11.29
Ni ²⁺	500	-8.20	-7.53
Zn ²⁺	60	+10.39	+9.01
Cd ²⁺	250	+5.52	+ 8.32
Pb ²⁺	50	+9.60	+ 11.27
Sn ²⁺	1	before EDTA masking: +42.90	before EDTA masking: +31.30
		after EDTA masking: +8.23	after EDTA masking: + 10.15
Fe ²⁺	1	before EDTA masking: +14.32	before EDTA masking: +26.40
		after EDTA masking: -2.61	after EDTA masking: -1.54
Fe ³⁺	1	before using L -ascorbic acid masking: +26.85	before using L-ascorbic acid masking: +38.2
		after L-ascorbic acid masking: +10.0	after L-ascorbic acid masking: +6.72
Cr ³⁺	10	-11.89	-9.82

Table 3: Determination of Al(III) in drinking water and tap water samples by applying the proposed method.

Samples	Spectrophotometric Analysis				Smartphone-based Analysis			
	Spiked (µM)	Found (µM)	Recovery %	RSD % (N=3)	Spiked (µM)	Found (µM)	Recovery %	RSD % (N= 3)
Drinking water	37.0	36.9	99.73	1.25	18.5	18.2	98.38	1.54
	111.0	112.1	100.99	2.11	37.0	37.1	100.27	0.96
	185.0	184.7	99.84	0.98	55.5	54.6	98.38	0.80
	370.0	359.4	97.14	0.77	74.0	72.1	97.43	2.35
Tap water	37.0	36.5	98.65	2.23	18.5	18.0	97.30	1.63
	111.0	110.9	99.91	0.92	37.0	35.2	95.13	2.65
	185.0	183.7	99.30	1.12	55.5	52.3	94.23	1.24
	370.0	348.4	94.16	0.99	74.0	72.1	97.43	1.72

Table 4: Statistical comparison of the proposed method with ICP-OES reference method for the determination of Al(III).

Method	Mean Conc. (µM)	SD (σ)	S ^{a,b}	t ^{a,b}	T _{table} ^b	F ^b	F _{table} ^b
Proposed method (For spectroscopy)	372.96	0.108	-	-	-	-	-
ICP-OES reference method (For spectroscopy)	368.15	0.046	0.051	1.80	2.306	5.60	6.39
Proposed method (For smartphone)	75.92	0.051	-	-	-	-	-
ICP-OES reference method (For smartphone)	75.55	0.050	0.056	0.47	2.306	0.78	6.39

^a $S^2 = ((n_1 - 1)s_1^2 + (n_2 - 1)s_2^2) / (n_1 + n_2 - 2)$ and $t = (\bar{a}_1 - \bar{a}_2) / (S(1/n_1 + 1/n_2)^{1/2})$, where S is the pooled standard deviation, s_1 and s_2 are the standard deviations of the two populations with sample sizes of n_1 and n_2 , and sample means of \bar{a}_1 and \bar{a}_2 respectively (t has $(n_1 + n_2 - 2)$ degrees of freedom); here, $n_1 = n_2 = 5$.

^bStatistical comparison made on paired data produced with proposed and reference methods; the results given only on the row of the reference method.

4. CONCLUSION

In this study, in accordance with the principles of green analytical chemistry, anthocyanin-rich fermented black carrot juice was used as a green and chromogenic agent instead of polluting chemicals in order to determine the concentration of Al(III) ions in water samples. The application of this developed method to real water samples is eco-friendly, simple, fast, and practical. In addition, fermented black carrot juice is a healthy beverage rich in antioxidants and anthocyanins, and it is a chromogenic agent that can be used safely in the laboratory and is quite cheap (approx. 0.44 €). As can be seen from Table 1, the preparation of the chromogenic agent by other methods is very time-consuming and complex steps, and furthermore, the

proposed spectrophotometric method allows a very wide linear Al(III) concentration range (37.0 to 1850.0 µM) without any preliminary preparation. Thanks to the closed box system for analysis, the method developed based on a smartphone ensures usability in any field due to its portability and it can be easily applied to samples. Smartphones are more reachable and cheaper than other portable analytical devices. The high recoveries obtained by the application of both detection methods demonstrate their accuracy and applicability to real samples (tap water and drinking water) for the determination of Al(III). Additively, the recorded relative standard deviation values were very low (<5.0%) for spectrophotometric and smartphone-based methods. LOD values of spectrophotometric and smartphone-based methods are 6.67 µM and

4.40 μM , respectively, and both proposed methods obtain the required WHO permissible detection limit for Al(III) in drinking water. This method may open the way to novel low-cost Al(III) quantification methods without any extraction processes utilizing anthocyanin-rich fermented black carrot juice obtained from local markets.

5. CONFLICT OF INTEREST

The author declares no competing financial interest.

6. REFERENCES

- Goswami S, Paul S, Manna A. Selective “naked eye” detection of Al (III) and PPI in aqueous media on a rhodamine-isatin hybrid moiety. *RSC Adv.* 2013;3(27):10639-10643. [<DOI>](#).
- Imadi SR, Waseem S, Kazi AG, Azooz MM, Ahmad P. Aluminum toxicity in plants: an overview. *Plant Metal Interaction.* 2016;1-20. [<DOI>](#).
- Maity D, Govindaraju T. Naphthaldehyde-Urea/Thiourea conjugates as turn-on fluorescent probes for Al^{3+} based on restricted C=N isomerization. *European Journal of Inorganic Chemistry.* 2011;(36):5479-5485. [<DOI>](#).
- Al-Kindy SM, Al-Hinai A, Al-Rasbi NK, Suliman FEO, Al-Lawati HJ. Spectrofluorimetric determination of aluminium in water samples using N-((2-hydroxynaphthalen-1-yl) methylene) acetylhydrazide. *Journal of Taibah University for Science.* 2015;9(4):601-609. [<DOI>](#).
- Michael JK. Powder-Metallurgy Aluminum Alloys. *Aluminum Alloys-Contemporary Research and Applications: Contemporary Research and Applications.* 2012;1:323.
- Frankowski M, Ziola-Frankowska A, Sienkiewicz J. New method for speciation analysis of aluminium fluoride complexes by HPLC-FAAS hyphenated technique. *Talanta.* 2010;80(5): 2120-2126. [<DOI>](#).
- Melnyk LJ, Morgan JN, Fernando R, Pellizzari ED, Akinbo O. Determination of metals in composite diet samples by inductively coupled plasma-mass spectrometry. *Journal of AOAC International.* 2003;86(2):439-448. [<DOI>](#).
- Mahdavi M, Nezamzadeh-Ejhieh A. An aluminum selective electrode via modification of PVC membrane by modified clinoptilolite nanoparticles with hexadecyltrimethyl ammonium bromide (HDTMA-Br) surfactant containing Arsenazo III. *Journal of colloid and interface science.* 2017; 494:317-324. [<DOI>](#).
- Zuziak J, Reczyński W, Baś B, Jakubowska M. Voltammetric determination of aluminum (III) as Al-Alizarin S complex in tea leaves and infusions. *Analytical biochemistry.* 2018;558:69-79. [<DOI>](#).
- Guha S, Lohar S, Sahana A, Banerjee A, Safin DA, Babashkina MG et al. Coumarin-based “turn-on” fluorescent sensor for the determination of Al^{3+} : single crystal X-ray structure and cell staining properties. *Dalton Transactions.* 2013;42(28):10198-10207. [<DOI>](#).
- Wang B, Liu X, Duan W, Dai S, Lu H. Visual and ratiometric fluorescent determination of Al^{3+} by a red-emission carbon dot-quercetin system. *Microchemical Journal.* 2020;156: 104807. [<DOI>](#).
- Huang P, Li J, Liu X, Wu F. Colorimetric determination of aluminum (III) based on the aggregation of Schiff base-functionalized gold nanoparticles. *Microchimica Acta.* 2016;183(2): 863-869. [<DOI>](#).
- Zezi-Arruda MA, Poppi RJ. Spectrophotometry / Inorganic Compounds. *Encyclopedia of Analytical Science.* 2005;351-358. [<DOI>](#).
- Alawsi T, Mattia GP, Al-Bawi Z, Beraldi R. Smartphone-based colorimetric sensor application for measuring biochemical material concentration. *Sensing and Bio-Sensing Research.* 2021;32:100404. [<DOI>](#).
- Liu T, Zhang S, Liu W, Zhao S, Lu Z, Wang Y, Wang G, Zou P, Wang X, Zhao Q, Rao H. Smartphone based platform for ratiometric fluorometric and colorimetric determination H_2O_2 and glucose. *Sensors and Actuators B: Chemical.* 2020;305:127524. [<DOI>](#).
- Serhan M, Jackemeyer D, Long M, Sprowls M, Perez ID et al. Total iron measurement in human serum with a novel smartphone-based assay. *IEEE Journal of Translational Engineering in Health and Medicine.* 2020;8:1-9. [<DOI>](#).
- Saranchina NV, Slizhov YG, Vodova YM, Murzakasymova NS, Ilyina AM et al. Smartphone-based colorimetric determination of fluoride anions using polymethacrylate optode. *Talanta.* 2021;226:122103. [<DOI>](#).
- Fang J. Classification of fruits based on anthocyanin types and relevance to their health effects. *Nutrition.* 2015;31(11-12):1301-1306. [<DOI>](#).
- Silva S, Costa EM, Calhau C, Morais RM, Pintado ME. Anthocyanin extraction from plant tissues: A review. *Critical reviews in food science and nutrition.* 2017;57(14):3072-30833. [<DOI>](#).
- Clifford MN. Anthocyanins-nature, occurrence and dietary burden. *Journal of the Science of Food and Agriculture.* 2000;80(7):1063-1072. [<DOI>](#).
- Fedenko VS, Shemet SA, Landi M. UV-vis spectroscopy and colorimetric models for detecting anthocyanin-metal complexes in plants: An overview

of in vitro and in vivo techniques. *Journal of plant physiology*. 2017;212:13-28. [<DOI>](#).

22. Tanguler H, Erten H. Chemical and microbiological characteristics of shalgam (salgam); A traditional Turkish lactic acid fermented beverage. *Journal of Food Quality*. 2012;35(4):298-306. [<DOI>](#).

23. Tanguler H, Selli, S, Sen K, Cabaroglu T, Erten, H. Aroma composition of shalgam: a traditional Turkish lactic acid fermented beverage. *Journal of Food Science and Technology*. 2017;54(7):2011-2019. [<DOI>](#).

24. Canbaş A, Fenercioglu H. Salgam suyu üzerinde bir araştırma. *Gıda*. 1984;9(5):279-286 (in Turkish).

25. Erten H, Tanguler H, Canbaş A, A traditional Turkish lactic acid fermented beverage: Shalgam (Salgam). *Food Reviews International*. 2008;24(3):352-359. [<DOI>](#).

26. Kammerer D, Carle R, Schieber A. Quantification of anthocyanins in black carrot extracts (*Daucus carota* ssp. *sativus* var. *atorrubens* Alef.) and evaluation of their color properties. *European Food Research and Technology*. 2004;219(5):479-486. [<DOI>](#).

27. Narayan MS, Venkataraman LV. Characterisation of anthocyanins derived from carrot (*Daucus carota*) cell culture. *Food Chemistry*. 2000;70:361-363. [<DOI>](#).

28. Canbas A. Siyah havucun renk maddesi üzerine bir araştırma. *Doğa*. 1985;9(3):394-398 (in Turkish).

29. Ekinci FY, Baser GM, Özcan E, Üstündağ ÖG, Korachi M. Characterization of chemical, biological, and antiproliferative properties of fermented black carrot juice, shalgam. *European Food Research and Technology*. 2016;242(8):1355-1368. [<DOI>](#).

30. Porrawatkul P, Pimsen R, Kuyyogsuy A, Nuengmatcha P. Simple and selective naked-eye and visual detection of Cu^{2+} and Al^{3+} ions using Hibiscus Rosa-Sinensis Linn flower Extract. *Oriental Journal of Chemistry*. 2018;34(1):188. [<DOI>](#).

31. Khaodee W, Aeungmaitrepirom W, Tuntulani T. Effectively simultaneous naked-eye detection of Cu (II), Pb (II), Al (III) and Fe (III) using cyanidin extracted from red cabbage as chelating agent. *Spectrochimica Acta Part A: Molecular and Biomolecular Spectroscopy*. 2014;126:98-104. [<DOI>](#).

32. Park S, Kang S, Jeong DY, Jeong SY, Park JJ et al. Cyanidin and malvidin in aqueous extracts of black carrots fermented with *Aspergillus oryzae* prevent the impairment of energy, lipid and glucose metabolism in estrogen-deficient rats by AMPK activation. *Genes & nutrition*. 2015;10(2):1-14. [<DOI>](#).

33. Gałuszka A, Migaszewski Z, Namieśnik J. The 12 principles of green analytical chemistry and the SIGNIFICANCE mnemonic of green analytical practices. *TrAC Trends in Analytical Chemistry*. 2013;50:78-84. [<DOI>](#).

34. U. USEPA, Method 200.7: determination of metals and trace elements in water and wastes by inductively coupled plasma-atomic emission spectrometry. Rev. 4.4, 1994; EPA600/R-94-111.

35. Zolgharnein J, Shahrjerdi A, Azimi G, Ghasemi J. Spectrophotometric determination of trace amounts of fluoride using an Al-xylenol orange complex as a colored reagent. *Analytical Sciences*. 2009;25(10):1249-1253. [<DOI>](#).

36. Krupińska I. Aluminium drinking water treatment residuals and their toxic impact on human health. *Molecules*. 2020;25(3):641. [<DOI>](#).

37. Grotewold, E. The genetics and biochemistry of floral pigments. *Annual review of plant biology*. 2006;57(1):761-780. [<DOI>](#).

38. Schreiber HD, Swink AM, Godsey TD. The chemical mechanism for Al^{3+} complexing with delphinidin: A model for the bluing of hydrangea sepals. *Journal of inorganic biochemistry*. 2010;104(7):732-739. [<DOI>](#).

39. Ren J, Meng S, Lekka CE, Kaxiras E. Complexation of flavonoids with iron: structure and optical signatures. *The Journal of Physical Chemistry B*. 2008;112(6):1845-1850. [<DOI>](#).

40. Ravishankara MN, Shrivastava N, Padh H, Rajani M. Evaluation of antioxidant properties of root bark of *Hemidesmus indicus* R. Br.(Anantmul). *Phytomedicine*. 2002;9(2):153-160. [<DOI>](#).

41. Jiang Y, Miao Y, Ding Z, Lu Y. In situ formed silicon-based nanoparticles enabled highly efficient dual-mode biosensing of chlorpyrifos. *Food Chemistry*. 2023;403:134243. [<DOI>](#).

42. Shang C, Li Y, Zhang Q, Tang S, Tang X, Ren H, Hu P, Lu S, Li P, Zhou, Y. Alkaline phosphatase-triggered dual-signal immunoassay for colorimetric and electrochemical detection of zearalenone in cornmeal. *Sensors and Actuators B: Chemical*. 2022;358:131525. [<DOI>](#).

43. Durmazel S, Üzer A, Apak, R. Naked-Eye Detection of 3-Nitro-1, 2, 4-triazole-5-one at Sub-Femtomolar Levels with Melamine and Unlabeled Au Nanoparticles. *ACS Applied Nano Materials*. 2022;5(4): 5244-5257. [<DOI>](#).

44. Ular N, Uzer A, Durmazel S, Ercag E, Apak R. Diaminocyclohexane-functionalized/thioglycolic acid-modified gold nanoparticle-based colorimetric sensing of trinitrotoluene and tetryl. *ACS sensors*. 2018;3(11): 2335-2342. [<DOI>](#).

45. Shahvar A, Shamsaei D, Saraji M. A portable smartphone-based colorimetric sensor for rapid determination of water content in ethanol. *Measurement*. 2020;150:107068. [<DOI>](#).
46. Bandi R, Alle M, Park CW, Han SY, Kwon GJ, Kim NH, Kim JC, Lee SH. Cellulose nanofibrils/carbon dots composite nanopapers for the smartphone-based colorimetric detection of hydrogen peroxide and glucose. *Sensors and Actuators B: Chemical*. 2021;330:129330. [<DOI>](#).
47. Han T, Feng X, Tong B, Shi J, Chen L et al. A novel "turn-on" fluorescent chemosensor for the selective detection of Al³⁺ based on aggregation-induced emission. *Chemical communications*. 2012;48(3):416-418. [<DOI>](#).
48. Kim Y, Jang G, Lee TS. New fluorescent metal-ion detection using a paper-based sensor strip containing tethered rhodamine carbon nanodots. *ACS applied materials & interfaces*. 2015;7(28):15649-15657. [<DOI>](#).
49. Kumar A, Bhatt M, Vyas G, Bhatt S, Paul P. Sunlight induced preparation of functionalized gold nanoparticles as recyclable colorimetric dual sensor for aluminum and fluoride in water. *ACS applied materials & interfaces*. 2017;9(20):17359-17368. [<DOI>](#).
50. Wei W, Huang J, Gao W, Lu X, Shi X. Carbon dots fluorescence-based colorimetric sensor for sensitive detection of aluminum ions with a smartphone. *Chemosensors*. 2021;9(2):25. [<DOI>](#).
51. Park H, Kim W, Kim M, Lee G, Lee W et al. Eco-friendly and enhanced colorimetric detection of aluminum ions using pectin-rich apple extract-based gold nanoparticles. *Spectrochimica Acta Part A: Molecular and Biomolecular Spectroscopy*. 2021;245:118880. [<DOI>](#).
52. da Silva HM, Mageste AB, e Silva SJB, Ferreira GMD, Ferreira GMD. Anthocyanin immobilization in carboxymethylcellulose/starch films: A sustainable sensor for the detection of Al(III) ions in aqueous matrices. *Carbohydrate Polymers*. 2020;230:115679. [<DOI>](#).
53. Canbas A, Deryaoglu A. Şalgam suyunun üretim tekniği ve bileşimi üzerinde bir araştırma. *Doga-Turkish Journal of Agricultural and Forestry* 1993;17:119-129.
54. Coskun F. A traditional Turkish fermented non-alcoholic beverage, "Shalgam". *Beverages* 2017; 3: 49. [<DOI>](#).



The Preparation and Physicochemical Analysis of Local Black Soap from Coconut Oil and Plantain Peel Biochar

Mary Otuosorochukwu Nnyia¹ , Abiodun Oladipo² , Ebube Victoria Anyaebosim³ , and Onome Ejeromedoghene^{4*} 

¹CAS Key Laboratory of Standardization and Measurement of Nano Technology, Chinese Academy of Sciences Beijing, 100190 People's Republic of China

²Co-Innovation Center for Sustainable Forestry in Southern China, College of Forestry, Nanjing Forestry University, 210037 Nanjing, Jiangsu, China

³Department of Applied Chemistry and Engineering, Taiyuan University of Technology (Yingxi Campus), Wanbailin District, Taiyuan, Shanxi Province 030024, People's Republic of China

⁴School of Chemistry and Chemical Engineering, Southeast University, 211189 Nanjing, Jiangsu Province, People's Republic of China

Abstract: Local black soap, produced from coconut oil and plantain peel biochar (alkaline source) was presented in this study since the agricultural raw materials gain significance in environmentally benign feedstocks for saponification reactions. The physicochemical analysis of the coconut oil and plantain peel biochar shows remarkable free fatty acid (FFA) and alkalinity contents respectively suitable for soap making. The physicochemical properties of the as-prepared local black soap demonstrated a good moisture content (15.1 %) showing that it can be stored for long periods without any water-associated deteriorations. The percentage of matter insoluble in water (4.4 %), matter insoluble in alcohol (12.3 %), FFA content (2.1 %), and pH (9) were found to be higher than the acceptable limit according to the Nigerian Industry Standards (NIS). Also, the total fatty matter (TFM) was higher (67.6 %) than the minimum acceptable level with a good foam height of 2.5 cm. The overall results show good soap properties and are suitable for domestic purposes.

Keywords: Local black soap, plantain peel, coconut oil, Agricultural feedstocks

Submitted: July 06, 2022. **Accepted:** December 01, 2022.

Cite this: Nnyia MO, Oladipo A, Anyaebosim EV, Ejeromedoghene O. The Preparation and Physicochemical Analysis of Local Black Soap from Coconut Oil and Plantain Peel Biochar. JOTCSA. 2023;10(1):177-84.

DOI: <https://doi.org/10.18596/jotcsa.1141351>.

***Corresponding author. E-mail:** oejeromedoghene@seu.edu.cn.

1. INTRODUCTION

The agrarian diversity in human and economic growth is a significant concern. Over the years, raw materials of agrarian origin have been sourced as benign feedstocks for many industrial activities because they are eco-friendly, cheap, and readily available. This has increased the awareness of agricultural production, necessary to meet the demand emanating from population increase and also for servicing commercial industries. Interestingly, large quantities of waste materials which are residues of agrarian practices, contribute

significantly to the degradation of the environment and as such must be carefully handled to prevent any form of negative consequences such as pollution and economic loss (1,2).

Today, several researchers are beginning to focus on the recyclability of bio-waste materials, pollution control, and income generation. However, the conversion of agricultural wastes into new products or their use in the formulation of new products must certainly characterize the chemical composition, surface morphology as well as physicochemical properties of any of these

materials (3). For instance, the shells from peanuts account for about 20% of the peanut with production amounting to 46 metric tons every year. The peanuts are majorly disposed of through burning which contributes to environmental pollution and in some cases could be used in the production of livestock feed which requires proper treatment and processing. Peanut shells contain antioxidants due to the presence of Phyto derivatives used relevantly in cosmetic industries and were reported to function as an absorbent to eliminate heavy metals (4,5). Hence, agro- and non-agro-waste residues have been extensively explored as sustainable unfired earth-building materials for blocks construction (6), waste ginger straw has been examined as a productive heterogeneous catalyst for biodiesel production (7), while Chickpea husk has shown huge prospects for textile coloring and operational finishing (8).

Nevertheless, the production of soap from natural products in place of synthetic chemicals is gaining attention in recent times. Agricultural by-products (wastes) are considered sources of organic materials in soap production because they have been reported to contain phytochemicals for moisturizing the human skin and treatment of skin-related infections (9,10). Organic compounds from

agro-wastes have shown antibacterial activity against *Streptococcus pyogenes* and *Pseudomonas aeruginosa* as presented by Rambabu and colleagues (11). More also, agro-waste materials e.g. plantain peels have been considered a viable source of alkaline for saponification reactions because of the important class of phytochemicals (alkaloids, flavonoids, terpenoids, phenols, etc.) as well as vital minerals components (calcium, copper, potassium, phosphorus, zinc, etc.) (12). Besides, oils derived from agro-materials (e.g. palm oil and coconut oil) contain saponifiable free fatty acids as well as alkaloids, terpenoids, saponins, etc. (13-15). Soaps are typically fatty acid salts that can be firm or soft depending on the components utilized. They are made from fats/oils that have been hydrolyzed with an alkaline to produce fatty acid salts (soap) and glycerol (by-product) (Figure 1) (16). Negative ions comprising long hydrocarbon chains connected to a carboxyl group are common in the soaps that are being produced, giving it a cleansing action when used for bathing, washing, or general cleaning (17). Therefore, this paper examines the production of local black soap using two agro-feedstocks (coconut oil and plantain peel), and the physiochemical properties of the soap produced were also examined.

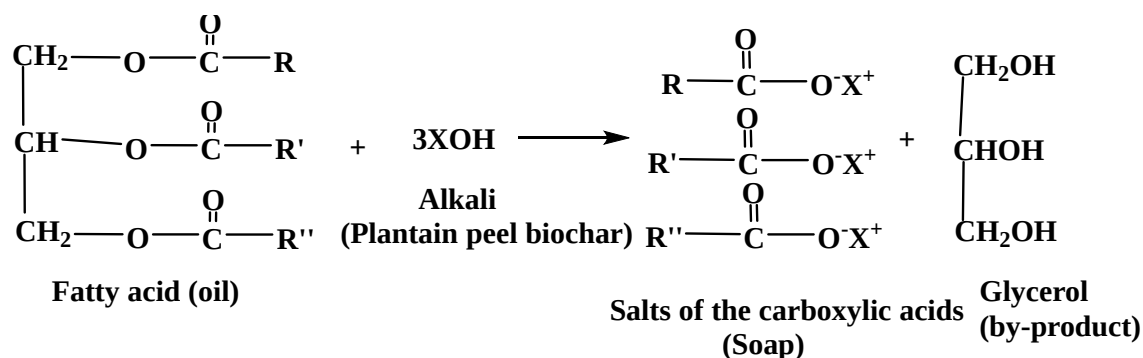


Figure 1: Saponification reaction of a triglyceride and alkaline to produce soap.

2. EXPERIMENTAL SECTION

2.1. Sample Collection and Materials Used

Waste plantain peels were collected from a local eatery. Pure coconut oil was bought from commercial vendors. The other analytical grade reagent used like Hydrochloric acid (HCl), Potassium Hydroxide (KOH), Phenolphthalein indicator, Ethanol (C₂H₅OH), Nitric acid (HNO₃), Neutralized isopropyl alcohol (IPA), Sodium hydroxide (NaOH) Sulfuric acid (H₂SO₄), Acetone, Diethyl ether, Methyl orange indicator, and Barium chloride (BaCl₂) were supplied by Maya Reagent, and Sinopharm Chemical Reagent Co. Ltd. For the production of aqueous solutions, distilled water was employed.

2.2. Preparation of Plantain Peel Biochar

To remove dirt, fresh plantain skins were washed with distilled water and dried in a slightly warmer setting. Plantain peel biochar was made by cutting the peels into little pieces and heated in a furnace for 5 h at 600 °C. The resulting biochar was allowed to cool in a desiccator before being pulverized in a mortar and sieved with a mesh.

2.3. Production Process of Local Black Soap

The native black soap was made by combining 100 g of plantain skin biochar with 500 mL of water in a beaker. The mixture was stirred and allowed to settle for 72 h. The alkaline extract was then filtered with cotton wool and a funnel. The heat was used to condense the alkaline extract, and coconut oil was slowly introduced in a 4:1 ratio. These were further heated on a hot plate and stirred at 60 °C until complete saponification

occurs. The soap was allowed to cure for 24 h to obtain the local black soap (18) (Figure 2).

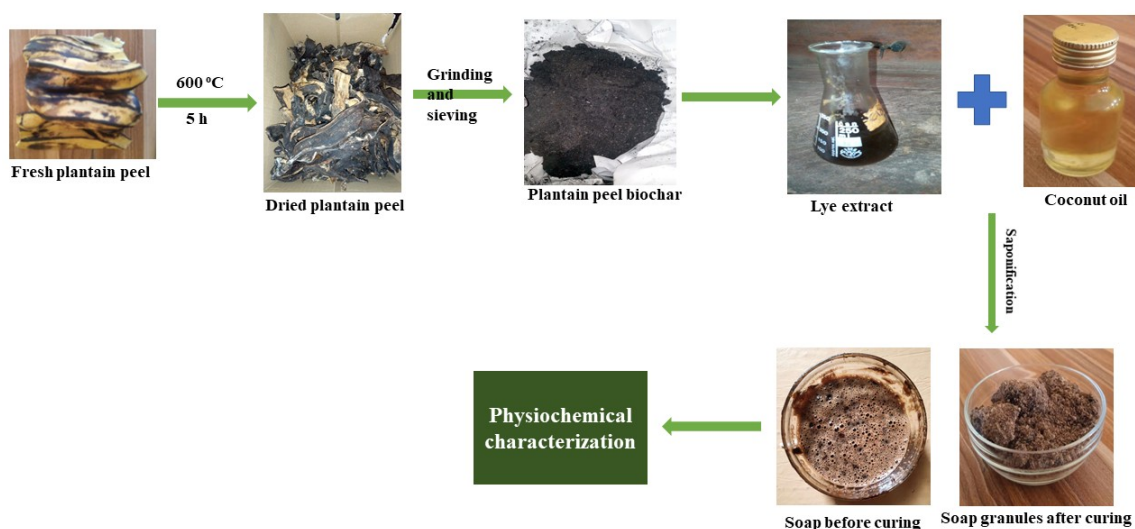


Figure 2: Schematic route for the preparation of local black soap.

2.4 Physicochemical analysis

The physicochemical analysis of the plantain peels biochar, coconut oil, and local black soap was performed according to established procedures (18,19).

2.4.1 Determination of moisture content

Weighing 2.15 g of black soap on a pre-weighed crucible and keeping it in an oven at 100°C - 105°C for 1 h was used to determine the moisture content of the soap. The soap was allowed to be cooled before being weighed once more. The given equation was used to compute the percentage moisture content (Eq. 1).

$$\text{Percentage Moisture Content} = \frac{w_3 - w_2}{w_1} \times 100\% \quad (\text{Eq. 1})$$

Where W_1 =sample weight; W_2 =weight of crucible; W_3 =weight after drying.

2.4.2 Determination of water-insoluble matter

Weighing 5.06 g of black soap into a 250 mL beaker, yielded the amount of water-insoluble materials in the soap. The soap was then dissolved in 100 mL of distilled water by heating on a hotplate. The soap solution was filtered and rinsed

with distilled water three times. Further, the residue was kept in an oven (100 °C - 105 °C) for 1 h. After cooling in a desiccator, the residual weight was calculated. The following formula was used to compute the proportion of water insoluble-matter (Eq. 2):

$$\text{Percentage Moisture Insoluble Matter} = \frac{w_3 - w_2}{w_1} \times 100\% \quad (\text{Eq. 2})$$

Where W_1 =weight of sample; W_2 =weight of filter paper; W_3 =weight of filter paper residue after drying.

2.4.3 Determination of free fatty acid (FFA)

Firstly, 10 g of the black soap was weighed into a conical flask, followed by the addition of 100 mL of neutralized isopropyl alcohol (IPA) to determine the amount of FFA in the soap. The solution was

allowed to boil on a hot plate until the soap was dissolved. Next, 10 mL of barium chloride was added to the mixture and titrated against NaOH using phenolphthalein as the indicator. The percentage FFA was calculated by Eq.3:

$$\text{Percentage FFA} = \frac{\text{endpoint} \times \text{Normality of base} \times 200 \times 100}{1000 \times \text{weight of sample}} \quad (\text{Eq. 3})$$

2.4.4 Determination of alcohol-insoluble matter

In a beaker, 2 g of the black soap was heated with 100 mL of neutralized IPA to estimate the proportion of the alcohol-insoluble matter. The soap solution was filtered and the insoluble matter was transferred using a hot neutralized IPA until all

the soap entrained within the filter paper has been removed. The residue was baked for 30 min and then cooled in a desiccator. The percentage of the alcohol-insoluble matter was calculated according to Eq. 4.

$$\text{Percentage Moisture Insoluble Matter} = \frac{W_3 - W_2}{W_1} \times 100\% \quad (\text{Eq. 4})$$

Where W_1 =weight of sample; W_2 =weight of filter paper; W_3 =weight of filter paper + residue after drying.

2.4.5 Determination of pH

By dissolving 2 g of local black soap in 200 mL of distilled water, the pH of the soap was calculated. The pH meter's electrode was then dipped into the solution to record the pH.

phase separation. The solution was further separated by shaking until the aqueous layer became clear and allowed to stand. The solution was re-washed with diethyl ether and with water until methyl orange was neutralized. The set-up was allowed to stand for another 5 min and run off any separated water. The solvent was then distilled off by adding 5 mL of acetone to the clean solution and heating it to evaporate the diethyl ether. Also, the acetone was removed under the steam of dry air. The beaker was placed in the oven for 30 min and allowed to cool and the weight was taken. The percentage of the total fatty matter was collected as calculated according to Eq. 5.

2.4.6 Determination of total fatty matter (TFM)

By heating 5 g of the local black soap with 100 mL of distilled water, the total fatty matter was measured. For facile precipitation of the fatty components from the soap, the soap solution was transferred into a separating funnel, followed by the addition of methyl orange indicator and sulfuric acid. Thereafter, the soap solution was cooled, and diethyl ether (100 mL) was introduced to allow

$$\text{Percentage Moisture Insoluble Matter} = \frac{W_3 - W_2}{W_1} \times 100\% \quad (\text{Eq. 5})$$

Where W_1 =weight of sample; W_2 =weight of beaker; W_3 =weight after drying.

2.4.7 Determination of foam height (lathering ability)

By dissolving 2 g of local black soap in distilled water, the foam height of the soap was determined. This was agitated in a clean blender with 200 mL of distilled water for 30 s. Thereafter, the height of the foam formed was measured on a 1000 mL tube.

4.5 which makes it fit for the production of soft soaps.

3. RESULTS AND DISCUSSION

3.1 Physicochemical and Structural Properties of Plantain Peel Biochar

Physicochemical properties of plantain peel biochar show an ash content of 11.3% which indicates the presence of sufficient minerals in the sample collected. In the presence of oxidizing agents, ash is the inorganic residue left after the water and organic matter have been removed by heating (20). The value of pH was 13 which indicates a strong alkaline content and a lye concentration of

Furthermore, the characterization of the plantain peel biochar with Fourier transform infrared (FT-IR) reveals a prominent peak at 3413 cm^{-1} which could be due to OH stretch (alcohol and carboxylic acid) (Figure 3). The weak peak at 2923 cm^{-1} confirms the presence of OH from carboxylic acid which could be due to the presence of phytochemicals like tannins (e.g. gallic acid), cellulose, and hemicelluloses in the plantain peels (21). More also, the peak at 1620 cm^{-1} could be ascribed to C=C vibrational stretch. The Peaks observed at $1387\text{-}1246 \text{ cm}^{-1}$ can be attributed to the C-H bending of cellulose, hemicelluloses, or lignin polymer. The peak at 1100 cm^{-1} could be associated with the =C-O-C symmetric and asymmetric stretch in ether linkages of polyphenols (22); while the weak peaks appearing at $841\text{-}624 \text{ cm}^{-1}$ might be linked to the presence of amine groups and other mineral elements (23).

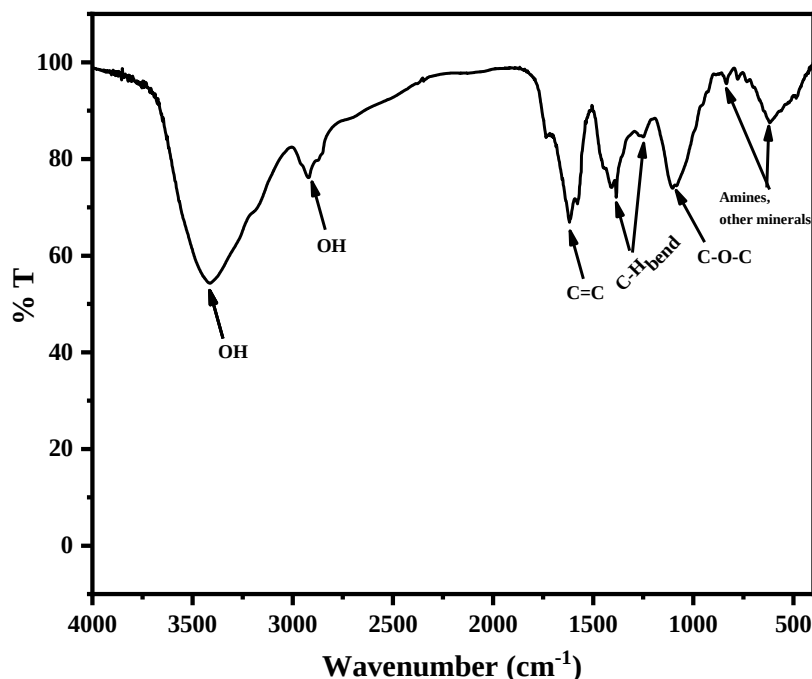


Figure 3: FT-IR spectrum of plantain peel biochar.

In addition, the structural morphology of the plantain peel biochar shows porous and thick fibrous-like nature with a cluster of small particles on the surface (Figure 4). The morphological structure observed usually exhibits a higher surface area, with promising prospects to make a good soap material (24). The porous nature of the material will enable good interaction with the chemical content in the oil to give a good soap formulation.

3.2 Physicochemical Properties of Coconut Oil

The results in Table 1 show the physicochemical features of the coconut oil utilized in the local black soap production. The density of the coconut oil was 0.902 g/mL. The saponification value is the amount of KOH necessary to saponify 1 g of oil in milligrams. It is a measure of the free acid and saponifiable ester groups. This important parameter helps to determine the amount of salt to be formed. Substantial saponification and ester values of 259.00 mgKOH and 228.3 mgKOH

respectively were obtained in the coconut oil revealing promising prospects for soap making. More also, coconut oils contain significant saturated and unsaturated fatty acids which contribute to the hardness, aroma, and cleansing properties of soaps. The coconut oil had a free fatty acid (FFA) concentration of 2.60, with a corresponding FFA composition (Table 2). The titer value provides information on the actual value of the melting point of the soap during saponification. The result obtained shows a titer value of 20.4°C. This implies that the coconut oil possesses a low melting point with good soap-forming properties. The coconut oil demonstrated a low acid value of 1.240 mg KOH and a low moisture content of 0.4%. This indicates that the oil will remain stable for a long time and will effectively preserve the soap against rancidity. The physicochemical parameters obtained for the coconut oil are within acceptable standards and results from other studies (25).

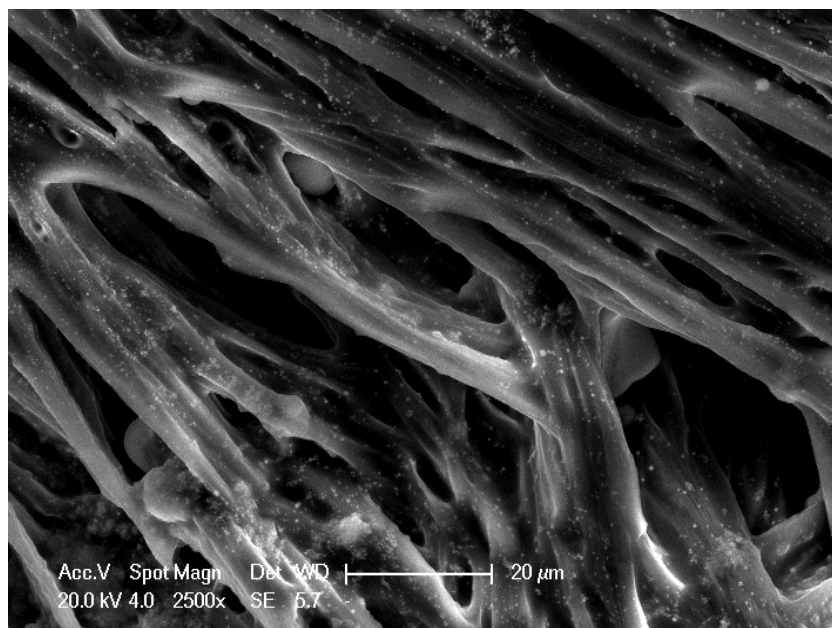


Figure 4: SEM micrograph of plantain peel biochar.

Table 1: Physicochemical properties of the coconut oil for local black soap production.

Property	Value
Density (g/mL)	0.901
Saponification value (mgKOH)	259.00
Ester value (mgKOH)	228.3
FFA (%)	2.60
Titre value (°C)	20.4
Acid value mgKOH	1.240
Moisture content (%)	0.4

Table 2: Coconut oil's approximate fatty acid content.

Type of fatty acid	Composition (%)
Lauric acid	48.00
Myristic acid	18.49
Palmitic acid	8.80
Oleic acid	7.81
Stearic acid	3.00
Caprylic acid	5.55
Caproic acid	0.50
Linoleic acid	1.35
Capric acid	6.50

3.3 Physicochemical Properties of Local Black Soap

The physicochemical parameters of the native black soap obtained were compared with the Nigerian Industrial Standard (NIS) (Table 3). The reaction of unsaponified fat with excess water in the soap to form glycerol and FFA, assisted by soap hydrolysis, represents the FFA levels in soaps. The obtained black soap displayed a moisture level of 15.1%, which was insignificantly higher (0.1%) than the NIS model. The good moisture content of the black soap shows that it can be stored for 12 - 24 months without any water-induced

deterioration. Thus, the black soap can be considered harmless for domestic and commercial applications (26). The percentage of black soap that was insoluble in water was 4.4%, which was more than the allowed standard of 2.5%. The soap's lather will be affected by the excessive amounts of insoluble particles in the water. Similarly, the percentage of matters insoluble in alcohol of the local black soap was 12.3%, higher than the acceptable limit of 5.0%. This reveals that there are plausibly insoluble fats and sodium silicate insoluble in alcohol in the local soap. This

could indicate that the black soap included waxes and lipids that are water-insoluble (27).

Table 3: Comparison of the physicochemical parameters of the native black soap produced (in this study) to the Nigerian Industrial Standard (NIS).

Parameter	Local black soap	NIS
Physical appearance	Blackish brown	-
Moisture content (%)	15.1	15 max.
Matters insoluble in water (%)	4.4	2.5 max.
Matters insoluble in alcohol (%)	12.3	5 max.
Free fatty acid content	2.1	0.2 max.
pH	9	6-10
Total fatty matters (%)	67.6	60 min.
Foam height (cm)	2.5	-

The FFA content of the local black soap was 2.1%. This value was higher than the specified limit and implies poor transparency of the black soap (28). The black soap shows a pH of 9 since soaps are alkaline substances thereby functioning as barriers against dangerous organisms such as bacteria and viruses, this can counteract the body's protective acid mantle. The obtained pH of the soap shows that the saponification process is completely hydrolyzed, and may not impact corrosive action when applied to the skin. On the other hand, the corrosive nature of local black soaps is solvable by increasing oil content (29). Thus, the local black soap may be suitable for domestic use.

The soap's cleansing ability is proportional to its total fatty matter (TFM). The TFM of the local black soap was 67.6%, higher than the minimum of 60 % set by the NIS. This suggests that the local black soap possesses high cleansing properties. The foam height is an attribute associated with oil composition used in black soap production. Lauric acid, the major FFA in coconut oil has a remarkable foaming property. Thus, the foam, high of 2.5 cm shows the good formability of the local black soap (30).

4. CONCLUSION

The production of local black soap from agro-based feedstocks of coconut oil (triglycerides) and plantain peel biochar (alkaline source) is hereby presented in this study. The physicochemical characterization of the plantain peel biochar demonstrated good alkalinity which makes it fit for making soft soaps. The physicochemical characterization of the coconut oil extracts, indicates good fatty acid content and remarkable oil properties within acceptable standards. Thus, the physicochemical parameters of the black soap displayed good formability and harmless properties for domestic and commercial applications. However, the results reveal the presence of some sort of waxes and fat components in the soap reducing the transparency of the black soap. Nevertheless, local black soap manufacturing should be encouraged since it has good quality for

commercial consumption and thereby reduces the waste generated from plantain peels.

5. CONFLICT OF INTEREST STATEMENT

The authors declare no conflict of interest.

6. REFERENCES

1. Oluseun Adejumo I, Adebukola Adebisi O. Agricultural Solid Wastes: Causes, Effects, and Effective Management. In: M. Saleh H, editor. *Strategies of Sustainable Solid Waste Management* [Internet]. IntechOpen; 2021 [cited 2023 Feb 4]. Available from: [<URL>](#).
2. Santolini E, Bovo M, Barbaresi A, Torreggiani D, Tassinari P. Turning Agricultural Wastes into Biomaterials: Assessing the Sustainability of Scenarios of Circular Valorization of Corn Cob in a Life-Cycle Perspective. *Applied Sciences*. 2021 Jul 7;11(14):6281. Available from: [<URL>](#).
3. Durga ML, Gangil S, Bhargav VK. Conversion of agricultural waste to valuable carbonaceous material: Brief review. *Materials Today: Proceedings*. 2022;56:1290-7. Available from: [<URL>](#).
4. Arumugam N, Biely P, Puchart V, Singh S, Pillai S. Structure of peanut shell xylan and its conversion to oligosaccharides. *Process Biochemistry*. 2018 Sep;72:124-9. Available from: [<URL>](#).
5. Adhikari B, Dhungana SK, Waqas Ali M, Adhikari A, Kim ID, Shin DH. Antioxidant activities, polyphenol, flavonoid, and amino acid contents in peanut shell. *Journal of the Saudi Society of Agricultural Sciences*. 2019 Oct;18(4):437-42. Available from: [<URL>](#).
6. Jannat N, Hussien A, Abdullah B, Cotgrave A. Application of agro and non-agro waste materials for unfired earth blocks construction: A review. *Construction and Building Materials*. 2020 Sep;254:119346. Available from: [<URL>](#).
7. Yu H, Cao Y, Li H, Zhao G, Zhang X, Cheng S, et al. An efficient heterogeneous acid catalyst derived from waste ginger straw for biodiesel production. *Renewable Energy*. 2021 Oct;176:533-42. Available from: [<URL>](#).
8. Jose S, Pandit P, Pandey R. Chickpea husk - A potential agro waste for coloration and functional finishing of textiles. *Industrial Crops and Products*. 2019 Dec;142:111833. Available from: [<URL>](#).

9. Alharbi KL, Raman J, Shin HJ. Date Fruit and Seed in Nutricosmetics. *Cosmetics*. 2021 Jun 24;8(3):59. Available from: [<URL>](#).
10. Ogunbiyi A, Enechukwu NA. African black soap: Physicochemical, phytochemical properties, and uses. *Dermatologic Therapy [Internet]*. 2021 May [cited 2023 Feb 4];34(3). Available from: [<URL>](#)
11. Rambabu K, Edathil AA, Nirmala GS, Hasan SW, Yousef AF, Show PL, et al. Date-fruit syrup waste extract as a natural additive for soap production with enhanced antioxidant and antibacterial activity. *Environmental Technology & Innovation*. 2020 Nov;20:101153. Available from: [<URL>](#).
12. Sani MU, Muhammad AK. Assessment of phytochemical and mineral composition of unripe and ripe plantain (*Musa paradisiaca*) peels. *Afr J Food Sci*. 2021 Mar 31;15(3):107-12. Available from: [<URL>](#).
13. Basseyy EE, Gwana MA, Mu'azu AKN, Modu GU. Qualitative phytochemicals screening and antimicrobial susceptibility patterns of coconut oil extract on some selected bacteria and fungi. *World J Adv Res Rev*. 2019 Apr 30;1(3):001-13. Available from: [<URL>](#).
14. Ajongbolo K. Chemical Properties of Local Black Soap Produced from Cocoa Pod Ash and Palm Oil Waste. *IJTSRD*. 2020;4(6):713-5. Available from: [<URL>](#).
15. Tacin MV, Massi FP, Fungaro MHP, Teixeira MFS, de Paula AV, de Carvalho Santos-Ebinuma V. Biotechnological valorization of oils from agro-industrial wastes to produce lipase using *Aspergillus* sp. from Amazon. *Biocatalysis and Agricultural Biotechnology*. 2019 Jan;17:369-78. Available from: [<URL>](#).
16. Adebomi AI, Oladipupo OA, Mary AO. The African black soap from *Elaeis guineensis* (Palm kernel oil) and *Theobroma cacao* (Cocoa) and its transition metal complexes. *Afr J Biotechnol*. 2017 May 3;16(18):1042-7. Available from: [<URL>](#).
17. Adeyinka OM, Olukemi AR, Farombi AG. Physicochemical Properties of African Black Soap, and It's Comparison with Industrial Black Soap. *Am J Chem*. 2014;2014(1):35-7.
18. Edah AO, Nnoli CB, Wetkum DF. Physicochemical Properties and Anti-Microbial Activity of Local Black Soap and its Comparison with Ghana Soap with Respect to Nigerian Industrial Standard. *ARJC*. 2017;1(1):30-6. Available from: [<URL>](#).
19. Idoko O, Emmanuel SA, Salau AA, Obigwa PA. Quality assessment on some soaps sold in Nigeria. *Nig J Tech*. 2018 Nov 15;37(4):1137. Available from: [<URL>](#).
20. Taiwo A, Oluwadare I, Shobo A, Amolegbe S. Extraction and potential application of caustic potash from kolanut husk, uguwu pod husk and plantain peels. *Scientific Research and Essay*. 2008;3(10):515-7.
21. Aderibigbe AD, Ogunlalu OU, Oluwasina OO, Amoo IA. Adsorption Studies of Pb²⁺ From Aqueous Solutions Using Unmodified and Citric Acid - Modified Plantain (*Musa paradisiaca*) Peels. *IOSR JAC*. 2017 Mar;10(2):30-9. Available from: [<URL>](#).
22. Agama-Acevedo E, Sañudo-Barajas JA, Vélez De La Rocha R, González-Aguilar GA, Bello-Peréz LA. Potential of plantain peels flour (*Musa paradisiaca* L.) as a source of dietary fiber and antioxidant compound. *CyTA - Journal of Food*. 2016 Jan 2;14(1):117-23. Available from: [<URL>](#).
23. Zango ZU. Cationic dyes removal using low-cost banana peel biosorbent. *American Journal of Materials Science*. 2018;8(2):32-8.
24. Etim A, Betiku E, Ajala S, Olaniyi P, Ojumu T. Potential of Ripe Plantain Fruit Peels as an Ecofriendly Catalyst for Biodiesel Synthesis: Optimization by Artificial Neural Network Integrated with Genetic Algorithm. *Sustainability*. 2018 Mar 6;10(3):707. Available from: [<URL>](#).
25. Martins J, Santos J, da Conceicao M. Comparative Study of Physico-Chemical Properties of Coconut Oil (*Cocos nucifera* L.) Obtained by Industrial and Artisanal Processes. *Biotechnol Ind J*. 2020;16(3):210.
26. Vivian OP, Nathan O, Osano A, Mesopirr L, Omwoyo WN. Assessment of the physicochemical properties of selected commercial soaps manufactured and sold in Kenya. *Open J Appl Sci*. 2014;4(8):433-40. Available from: [<URL>](#).
27. Oyekunle JAO, Ore OT, Ogunjumelo OH, Akanni MS. Comparative chemical analysis of Indigenous Nigerian soaps with conventional ones. *Heliyon*. 2021 Apr;7(4):e06689. Available from: [<URL>](#).
28. Hayati SN, Rosyida VT, Darsih C, Nisa K, Indriarningsih AW, Apriyana W, et al. Physicochemical properties, antimicrobial and antioxidant activity of ganoderma transparent soap. *IOP Conf Ser: Earth Environ Sci*. 2020 Mar 1;462(1):012047. Available from: [<URL>](#).
29. Warra AA. A report on soap making in Nigeria using indigenous technology and raw materials. *Afr J Pure Appl Chem*. 2013 Apr 30;7(4):139-45. Available from: [<URL>](#).
30. Issa M, Isaac I, Matthew O, Shalangwa B, Sunday M. Physicochemical analysis for quality and safety of some selected animal soaps compared to human soaps in plateau state, Nigeria. *IOSR J Appl Chem*. 2020;13(3):25-8.



Determination of the Anticarcinogenic Activity of 5-Hydroxymethyl-2-furfural Produced from Grape Must Under *in vitro* Conditions

Kubra Kelleci^{1,2*} , Eda Golebatmaz³ 

¹Beykoz University, Vocational School, Department of Medical Services and Techniques, Istanbul, 34805, Turkey

²Yildiz Technical University, Faculty of Chemistry and Metallurgy, Department of Bioengineering, Istanbul, 34210 Turkey

³Eskişehir Osmangazi University, Institute of Science and Technology, Department of Biology, Eskişehir, 26040, Turkey

Abstract: Every year, millions of tons of food and beverage waste are thrown away unused around the world. The carbohydrates found in food waste create a raw material potential for the production of high value-added products that are used in energy, feed and pharmacology. One of these products, 5-Hydroxymethyl-2-furfural (5-HMF), is a by-product of simple dehydration of carbohydrates. It finds wide use in the field of pharmacy due to its anticancer, antifungal and antimicrobial activities. Many studies have stated that the sugar source with the highest conversion rate in 5-HMF production is fructose. For this reason, in this study, it was aimed to realize the production of 5-HMF in autoclave sterilization carried out under high temperature and pressure using grape must waste, which is known to have high fructose content, and determine the anticarcinogenic activity and cytotoxicity of the produced 5-HMF under *in vitro* conditions. In this study, it was determined that the medium containing DMSO increased the sugar conversion percentage, 5-HMF efficiency and selectivity in the waste grape must more than the medium containing only water. In the production of 5-HMF, the conversion of sugar in the medium saturated with salt, and the efficiency and selectivity of 5-HMF were determined as 97.04%, 68.61% and 70.82%, respectively, when DMSO organic solvent was used. In addition, it has been determined that 5-HMF produced from waste grape must has a toxic effect on both healthy cells and cancer cells and has anticancer properties.

Keywords: 5-HMF, anticancer, grape must, fructose, DMSO.

Submitted: July 07, 2022. **Accepted:** January 01, 2023.

Cite this: Kelleci K, Golebatmaz E. Determination of the Anticarcinogenic Activity of 5-Hydroxymethyl-2-furfural Produced from Grape Must Under *in vitro* Conditions. JOTCSA. 2023;10(1):185-92.

DOI: <https://doi.org/10.18596/jotcsa.1142274>.

***Corresponding author. E-mail:** kubrakelleci@beykoz.edu.tr.

1. INTRODUCTION

It is known that approximately 931 million tons of food and drink are thrown away every year (1). Carbohydrates, which are found in large quantities in food waste, are a potential source of raw materials for the production of petrochemical products (2). Due to the fact that petrochemical products are decreasing day by day and the damage these products cause to nature, researchers have turned to the search for renewable energy sources (3) and it has been foreseen that furan derivatives such as 5-Hydroxymethyl -2-furfural (5-HMF) will be

one of the most important renewable energy sources in the future. According to the report prepared by the United States Department of Energy, 5-HMF and its oxidation products are among the 10 promising biomass-based products that are predicted to replace petroleum-derived products (4). In addition to being used as an energy source, it is also widely used in the synthesis of a wide range of products covering the food and pharmaceutical industries.

5-HMF is a by-product of the acid-catalyzed dehydration of simple carbohydrates (glucose,

fructose, xylose, etc.). The conversion of glucose and sucrose to 5-HMF was 60-70%, while the conversion of fructose to 5-HMF was found to be 100% (5,6). Therefore, the current industrial production process is based on the use of fructose (7). Although the market value varies according to the product quality and production process, it is known to be between 2-300 US dollars per kilogram (8). Considering that costs are also related to raw material access, the use of waste fructose instead of pure fructose will reduce costs, thus increasing access to 5-HMF and increasing its economic value (4). Therefore, in this study, 5-HMF production potential from grape must, which is known to have high fructose content, was investigated during autoclave sterilization under high temperature and pressure.

In addition, when literature studies were examined, it was reported that high levels of 5-HMF were detected in dried fruits and juices made from dried fruits (25-2900 mg/kg), as well as in caramel products (up to 9500 mg/kg). Bread (up to 410 mg/kg) and coffee (up to 420 mg/L) are also among the most important sources of human exposure to 5-HMF, although the levels in these foodstuffs are high (9,10). Estimated daily intake of 5-HMF is 30-150 mg per person (11); which is several times higher than the estimated daily intake of other heat-induced food toxicants such as acrylamide and furan (12,13).

In this study, it was aimed to obtain 5-HMF, which causes high human exposure due to food and beverage consumption, from grape must, which is known to have high fructose content, and to determine its anticarcinogenic activity and cytotoxic activity using LNCaP prostate cancer cell line and J774 murine macrophage cell line.

2. EXPERIMENTAL SECTION

2.1. Materials

99% purity DMSO (Dimethylsulfoxide; Sigma-Aldrich 276855) was used as the solvent. After the experimental study, 5-HMF, levulinic acid, formic acid analyzes were performed using Shimadzu LC-20AT HPLC device. Transgenomic Corogel 87H3 column was used for the analysis of 5-HMF, fructose and organic acids. Levulinic acid standard (Sigma-Aldrich 41474), formic acid standard (Sigma-Aldrich F0507), 5-hydroxymethyl-2-furfural (5-HMF) standard (Sigma-Aldrich H40807) were used for HPLC analysis. ISOLAB brand PTFE 0.45µm syringe filters were used for the filtration process applied before the analysis of the samples.

RPMI-1640 (Gibco 21875034), FBS (Fetal Bovine Serum; Sigma-Aldrich F7524), penicillin-streptomycin antibiotics (Sigma-Aldrich P4083), DMEM (Sigma-Aldrich D0822), Trypsin-EDTA solutions (Gibco 25200056) used in MTT analysis and cell culture studies to be used in anticarcinogenic activity and cytotoxicity of 5-HMF were purchased.

2.2. Production of 5-HMF from Grape Must

Grape must was preferred in the study due to its high fructose content. Studies have shown that the salt-saturated medium in 5-HMF production accelerates the transition of sugars to the organic phase after they are converted to 5-HMF in aqueous medium. Therefore, in this study, NaCl was used to prepare a saturated salt solution. Studies in the literature have shown that the use of organic solvents during production significantly increases the conversion rate of fructose from beverage wastes, 5-HMF efficiency and 5-HMF selectivity (14). Therefore, in this study, DMSO organic solvent, which is known to be used frequently in the literature, was used for the production of 5-HMF and the results were compared with the water environment where organic solvent was not used. The pH value of the experimental medium was fixed to 0.6 using HCl.

In the study, the volume of DMSO and grape must was determined as 76% and 24%, respectively. It was aimed to dehydrate the fructose to 5-HMF by exposing the samples taken in glass tubes at different concentrations for 3 hours in autoclave at 120°C. After completion of the reaction, the purity was checked by HPLC. All experiments were repeated 3 times. All chemical and organic solvents used in the study were of analytical purity (>99.5%) and were obtained from SIGMA.

2.3. HPLC Analysis

5-HMF sample and fructose analyzes were performed using SPD Detector SPD M-10A (Phenomenex; 50 x 4.6 mm; 5 µm particle size) HPLC (Shimadzu Liquid Chromatography) instrument with C18 column. It was carried out using acetonitrile and water (30:70 v/v) as mobile phase in isocratic mode with a UV wavelength of 320 nm, a flow rate of 0.6 mL/min. The samples were loaded into the HPLC device after passing through 0.45µm filters before analysis.

2.4. LNCaP and J774 Macrophage Cell Culture

The human prostate cancer (LNCaP; CRL1740™) cell line previously purchased from the American Culture Collection (ATCC) and stored in a cryobank was used in this study. Prostate cancer cells were inoculated in a 25 cm² culture dish containing 10% FBS, 1% penicillin-streptomycin antibiotic solution and 5 mL of DMEM, and incubated at 37°C under ambient conditions with 5% CO₂ and 95% humidity. The cells were refreshed every 2 days and monitored with an inverted light microscope. When the cell density reached 70-80%, they were transferred to a 75 cm² culture dish and the medium of the cells was refreshed every 2 days. Cell density and pollution were monitored using an inverted light microscope, and the continuity of the cell line was ensured by passage of cells until they were taken into the experiment.

LNCaP cells were exposed to 0.25% Trypsin-EDTA solution for 5 minutes. At the end of the time, it was checked under an inverted light microscope and it

was observed whether the cells were separated from the surface of the culture dish. The separated cells were transferred to a centrifuge tube containing 9 mL of medium and centrifuged at +10°C, 1200 rpm for 5 minutes. At the end of the time, the supernatant part in the centrifuge tube was discarded, and the cell pellet, which had settled to the bottom, was homogenized by pipetting with 2 mL of medium. The method of staining dead cells with Trypan Blue Dye (Sigma-Aldrich) was used to determine the cell number and percent viability. After counting the cells, the calculation was made as 1×10^4 live cells in 100 μ L of medium in each well, and inoculated into 96-well culture dishes. Culture dishes with 96 wells inoculated were incubated for 24 hours in a carbon dioxide incubator containing 5% CO₂ and 95% humidity at 37°C.

J774 murine macrophage cell line, T25 in RPMI-1640 broth containing 10% fetal bovine serum (FBS), 80 μ g/mL Gentamicin and 1 M HEPES in a humid atmosphere at 37°C, 95% humidity and 5% CO₂ cultured in culture flasks. After the cells reached the required confluency (80-90%), they were physically collected and centrifuged at 25°C, 1000 rpm for 5 minutes. Then, seeding was carried out in 96-well plates at 1×10^5 cells/ml per well. Cells inoculated into the culture media created were kept under the required incubation conditions for 24 hours. Macrophage cells are used to perform cytotoxicity assays. Cell growth was monitored daily with an inverted microscope.

2.5. Determination of Cytotoxic Concentrations

To determine non-toxic concentrations in J774 macrophage cells, in which LNCaP cells were used as hosts before 5-HMF components were used, 5×10^4 J774 macrophage cells were seeded into each well of a 96-well microplate and incubated at 37°C for 24 hours. After the macrophages adhered, 5 different concentrations of 5-HMF (5 μ g/mL, 10 μ g/mL, 25 μ g/mL, 50 μ g/mL and 100 μ g/mL), which were homogenized with (10%) DMSO/H₂O and sterilized by passing through a 0.20 μ m membrane filter, were diluted and added to the wells for another 24 hours. After 48 hours of incubation, MTT assay was performed on macrophage cells. 10 μ L of MTT solution with a final concentration of 10 mg/mL in PBS was transferred to each well of the microplate and cells were incubated for 4 hours at 37°C to form formazan crystals due to the reaction between MTT salt and viability dehydrogenase enzymes. Then, 100 μ L of DMSO was added to each well to dissolve the formazan crystals. Absorbance values were measured at 570 nm using an ELISA reader. All studies were performed in 3 replicates.

Cell viability analysis data were obtained using equation 1 and data plots were generated.

$$\text{Cell viability (\%)} = \frac{\text{Abs of sample} \times 100}{\text{Abs of control}} \quad (1)$$

2.6. Statistical Analysis

Obtained data were calculated as mean \pm standard deviation. For statistical analysis, parametric tests (Unpaired sample t-test, analysis of variance and Mann-Whitney U test) were used using the "SPSS 16.0 for Windows" program. Significance level was accepted as 5%.

3. RESULTS AND DISCUSSION

3.1. HPLC analysis

In this study, in which 5-HMF production potential from grape must was investigated during autoclave sterilization under high temperature and pressure, it was determined that the reducing sugar content in the grape must waste used in the experiments was 16.4%. In this study, it was determined that the medium containing DMSO increased the sugar conversion percentage, 5-HMF efficiency and selectivity in the waste grape must more than the medium containing only water. In the production of 5-HMF, the conversion of sugar in the medium saturated with salt, and the efficiency and selectivity of 5-HMF were determined as 97.04%, 68.61% and 70.82%, respectively, when DMSO organic solvent was used, while the values obtained in the medium containing only water were 68.13%, 45.04% and it was determined as 63.27%. Chromatogram graphs obtained from HPLC analyzes are given in Appendix 1, and 5-HMF calibration chart is given in Appendix-2. In addition, HPLC chromatogram images of levulinic acid and formic acid standards are given in Appendix- 3 and Appendix -4.

3.2. Toxicity Study

The cytotoxic effects on the J774 macrophage cell line were investigated. No significant cytotoxicity was detected at low concentrations in the study ($p < 0.05$). It has been observed that it has an inhibitory effect in direct proportion with increasing concentrations. To investigate the survival percentages of LNCaP cells, MTT cellular viability assay was performed after 24 hours of incubation. It has been shown that 5-HMF is not very toxic to macrophage cells compared to LNCaP cells. According to the results of cytotoxicity and anti-cancer activity, viable cell ratios are shown in the graphs. When the J774 macrophage cell toxicity results were compared with the control cell, it was observed that 5-HMF did not cause toxicity at concentrations up to 10 μ g.

According to the results of J774 cytotoxicity in Figure 1, it was seen that the most effective concentration increasing cell proliferation was at 5 μ g/mL. It was observed that toxicity occurred in the cells with increasing concentrations from 25 μ g/mL. The anticancer effect due to the increasing concentration of 5-HMF for 24 hours was examined in LNCaP cells and the effect levels are given in Figure 2. The anti-cancer effects of 5-HMF on LNCaP cells, whose toxicity was measured with J774 cells, were compared with control cells. As shown in the graph of the results in Figure 2, an anti-cancer effect was observed from 10 μ g/mL with increasing

concentrations. The most effective anti-cancer activity occurred at 100 $\mu\text{g}/\text{mL}$, and it was seen that it affected more than half of the LNCaP cells.

Toxicity studies were performed on 5-HMF obtained after experimental studies, both on J774 cells and on LNCaP cells, and it was determined to be anticancer.

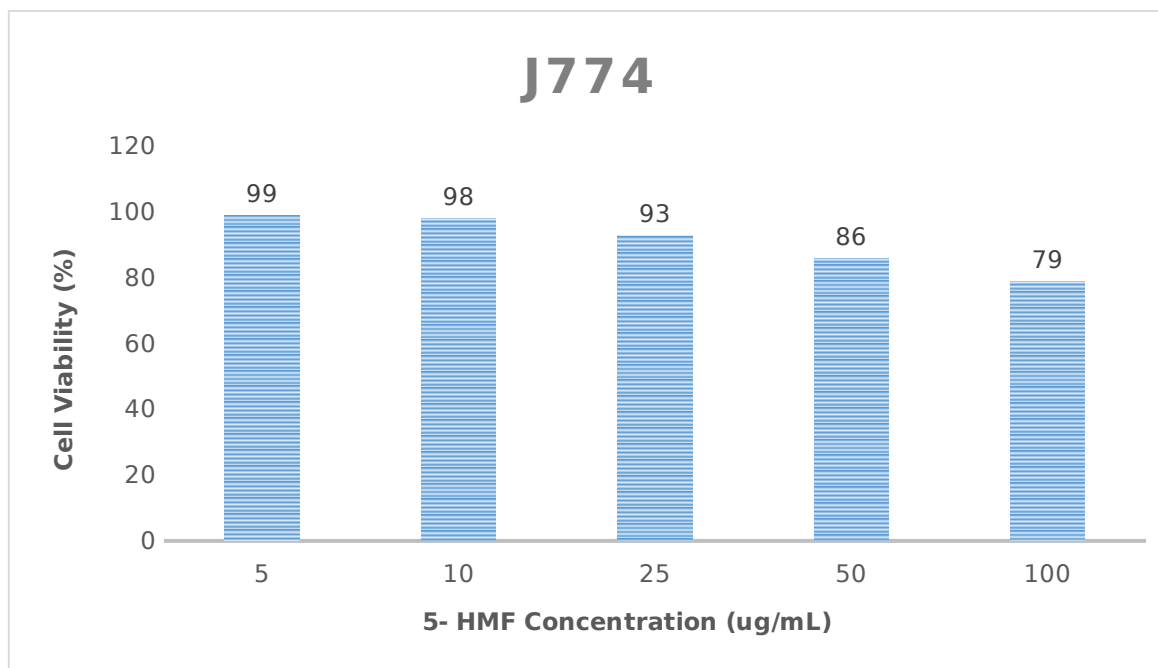


Figure 1: Decreased cell viability with increasing 5-HMF concentration in J774 macrophage cells.

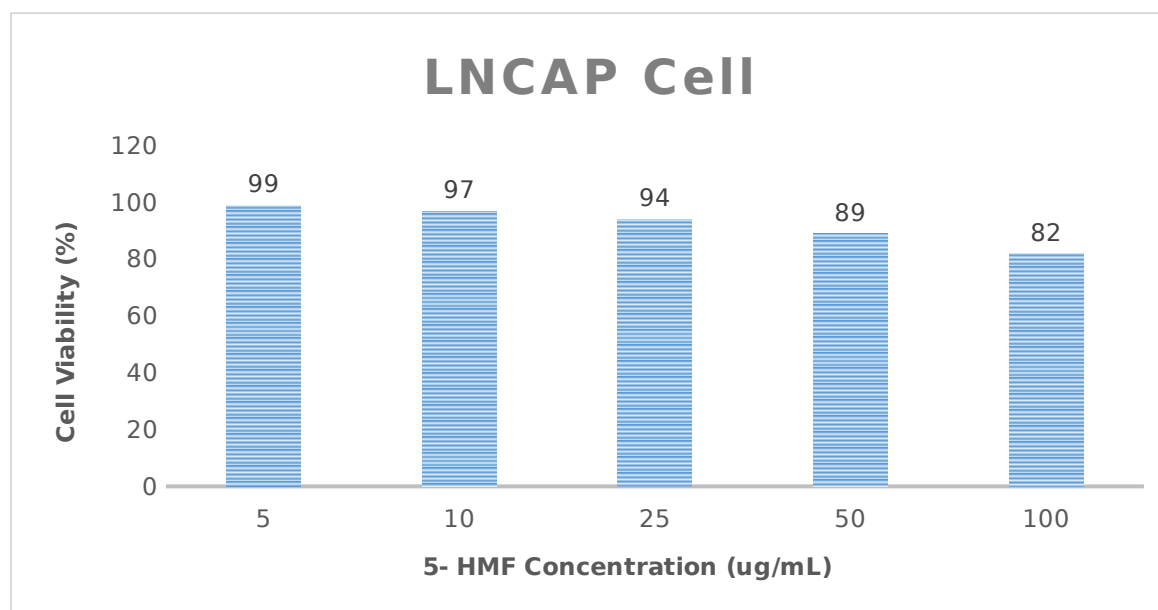


Figure 2: Decreased cell viability with increasing 5-HMF concentration in LNCaP cells.

4. CONCLUSION

In this study, the production potential and anticarcinogenic effect of 5-HMF from grape must waste, which is known to have high fructose content, was investigated under in vitro conditions. In the study, DMSO was used as an organic solvent in order to increase the productivity of the product, since 5-HMF decomposes at high temperatures, in acidic and aqueous environments, and turns into

levulinic acid and formic acid. It is known that DMSO is frequently used in previous studies on 5-HMF production (6). In addition, it has been revealed by the studies that the experimental medium saturated with salt in the production of 5-HMF accelerates the transition of sugars to the organic phase after conversion to 5-HMF in aqueous medium. In our study, it was determined that DMSO organic solvent significantly increased the sugar conversion percentage, 5-HMF efficiency and selectivity in the

waste grape must compared to the medium containing only water. Previous studies in the literature support our results (6).

Toxicity studies of 5-HMF produced during autoclave sterilization with waste grape must were carried out in both healthy cells and cancer cells and its anticancer activity was determined. J774 murine macrophage cell line was used for healthy cells and LNCaP prostate cancer cell line was used for carcinogen cells.

According to the data obtained from the studies, it was found that the highest 5-HMF concentration, 100 µg/mL, caused damage to both cell lines. At this concentration, there was also a moderate but statistically significant reduction in cell viability in all cell lines. It has been determined that 5-HMF also causes significant cell death at lower concentrations. Therefore, it has been found that 5-HMF obtained after experimental studies has a toxic effect and is anticancer in both healthy cells and cancer cells.

This study is one of the limited studies on the production of 5-HMF from food and beverage wastes in our country and the determination of its anticancer activity. It provides important data and is a source for the studies to be done on the production and analysis methods we use in this study and the optimization of 5-HMF production methods. It is important to investigate the effects on yield by using different ionic solvents and different catalysts in 5-HMF production by researchers. It is also recommended to test the anticancer activity under in vivo conditions.

5. CONFLICT OF INTEREST

The authors report no conflicts of interest.

6. REFERENCES

- Rajendran N, Han J. Integrated polylactic acid and biodiesel production from food waste: Process synthesis and economics. *Bioresource Technology*. 2022 Jan;343:126119. Available from: [<URL>](#).
- Yu IKM, Ong KL, Tsang DCW, Haque MA, Kwan TH, Chen SS, et al. Chemical transformation of food and beverage waste-derived fructose to hydroxymethylfurfural as a value-added product. *Catalysis Today*. 2018 Sep;314:70-7. Available from: [<URL>](#).
- Twidell J. *Renewable Energy Resources* [Internet]. 4th ed. London: Routledge; 2021 [cited 2023 Feb 4]. Available from: [<URL>](#)
- Kazi FK, Patel AD, Serrano-Ruiz JC, Dumesic JA, Anex RP. Techno-economic analysis of dimethylfuran (DMF) and hydroxymethylfurfural (HMF) production from pure fructose in catalytic processes. *Chemical Engineering Journal*. 2011 May;169(1-3):329-38. Available from: [<URL>](#).
- He Q, Lu Y, Peng Q, Chen W, Fan G, Chai B, et al. Synthesis of 5-hydroxymethylfurfural from fructose catalyzed by sulfonated carbon-based solid acid. *Biomass Conv Bioref* [Internet]. 2021 Sep 4 [cited 2023 Feb 4]; Available from: [<URL>](#)
- Rosatella AA, Simeonov SP, Frade RFM, Afonso CAM. 5-Hydroxymethylfurfural (HMF) as a building block platform: Biological properties, synthesis and synthetic applications. *Green Chem*. 2011;13(4):754. Available from: [<URL>](#).
- Kläusli T. AVA Biochem: commercialising renewable platform chemical 5-HMF. *Green Processing and Synthesis*. 2014 Jun 1;3(3):235-6. Available from: [<URL>](#).
- Yu IKM, Tsang DCW, Yip ACK, Chen SS, Wang L, Ok YS, et al. Catalytic valorization of starch-rich food waste into hydroxymethylfurfural (HMF): Controlling relative kinetics for high productivity. *Bioresource Technology*. 2017 Aug;237:222-30. Available from: [<URL>](#).
- Husøy T, Haugen M, Murkovic M, Jöbstl D, Stølen LH, Bjellaas T, et al. Dietary exposure to 5-hydroxymethylfurfural from Norwegian food and correlations with urine metabolites of short-term exposure. *Food and Chemical Toxicology*. 2008 Dec;46(12):3697-702. Available from: [<URL>](#).
- Murkovic M, Pichler N. Analysis of 5-hydroxymethylfurfural in coffee, dried fruits and urine. *Mol Nutr Food Res*. 2006 Sep;50(9):842-6. Available from: [<URL>](#).
- Janzowski C, Glaab V, Samimi E, Schlatter J, Eisenbrand G. 5-Hydroxymethylfurfural: assessment of mutagenicity, DNA-damaging potential and reactivity towards cellular glutathione. *Food and Chemical Toxicology*. 2000 Sep;38(9):801-9. Available from: [<URL>](#).
- Svensson K, Abramsson L, Becker W, Glynn A, Hellenäs KE, Lind Y, et al. Dietary intake of acrylamide in Sweden. *Food and Chemical Toxicology*. 2003 Nov;41(11):1581-6. Available from: [<URL>](#).
- Morehouse KM, Nyman PJ, McNeal TP, DiNovi MJ, Perfetti GA. Survey of furan in heat processed foods by headspace gas chromatography/mass spectrometry and estimated adult exposure. *Food Additives & Contaminants: Part A*. 2008 Mar;25(3):259-64. Available from: [<URL>](#).
- Román-Leshkov Y, Dumesic JA. Solvent Effects on Fructose Dehydration to 5-Hydroxymethylfurfural in Biphase Systems Saturated with Inorganic Salts. *Top Catal*. 2009 Apr;52(3):297-303. Available from: [<URL>](#).

Supplementary Information

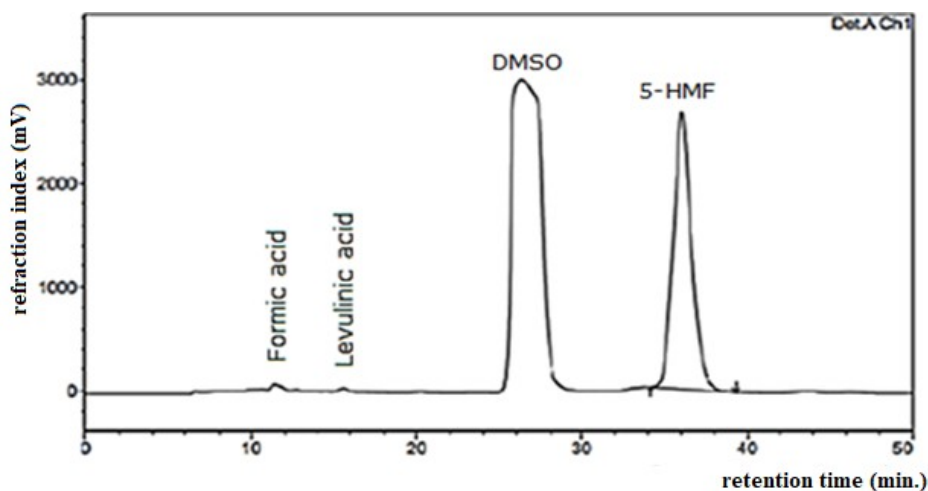
Determination of the Anticarcinogenic Activity of 5-Hydroxymethyl-2-furfural Produced from Grape Must Under *in vitro* ConditionsKubra Kelleci^{1,2*} , Eda Golebatmaz³ ¹ Beykoz University, Vocational School, Department of Medical Services and Techniques, Istanbul, 34805, Turkey² Yıldız Technical University, Faculty of Chemistry and Metallurgy, Department of Bioengineering, Istanbul, 34210 Turkey³ Eskişehir Osmangazi University, Institute of Science and Technology, Department of Biology, Eskişehir, 26040, Turkey

Figure S1: Chromatogram for HPLC Analysis.

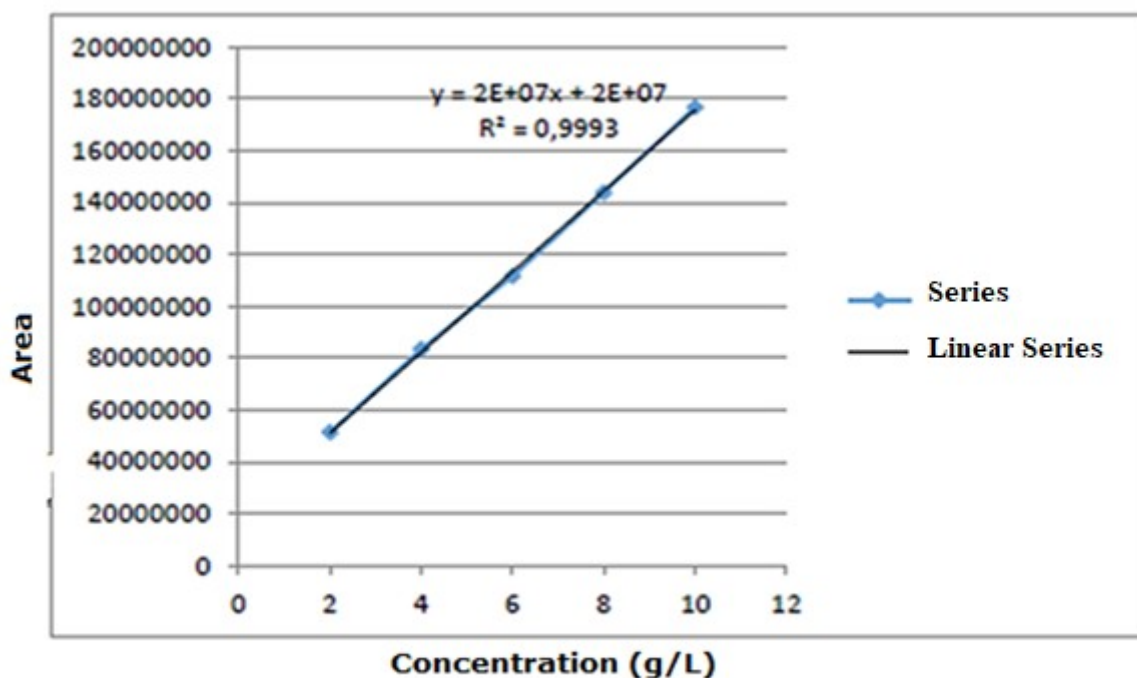


Figure S2: 5-HMF calibration graph.

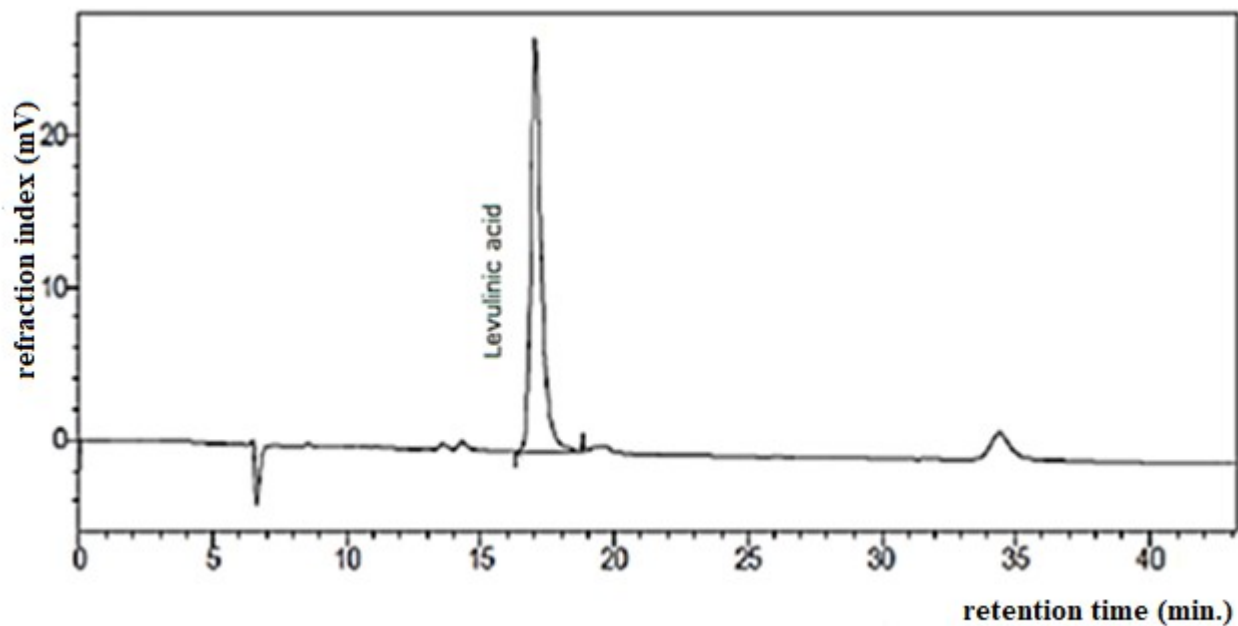


Figure S3: Chromatogram of Levulinic acid

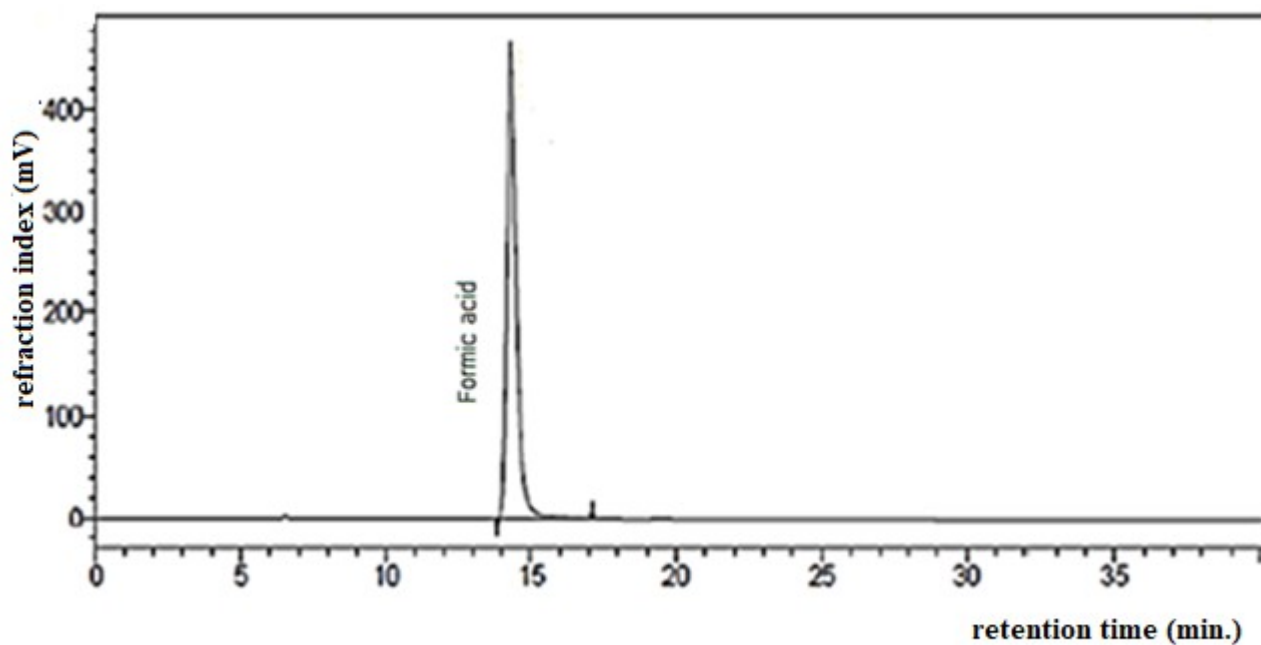


Figure S4: Chromatogram of Formic acid.



Novel Green Method for the Spectrophotometric Determination of Metoclopramide Hydrochloride in Pharmaceutical Formulations

Ghufran A. Alhammadi^{1,2*} , Lamy A. Sarsam² 

¹University of Mosul, Department of Chemistry, College of Science, Mosul, Iraq.

²College of Science, University of Mosul, Department of New and Renewable Energies, Mosul, Iraq.

Abstract: A less environmentally harmful reagent, 2-tert-Butyl-4-methoxyphenol (BHA), is used to evaluate Metoclopramide hydrochloride (MCP.H) by simple, rapid, sensitive, accurate and precise spectrophotometric method, through azo coupling reaction between metoclopramide hydrochloride medicine and its pharmaceutical preparation by utilizing BHA as a reagent, (MCP.H) azo-dye formed shows the higher absorption peak at 504 nm. Absorbance-concentration relation is linear over the range from 20 to 280 $\mu\text{g} / 5 \text{ mL}$, (i.e. 4-56 ppm) with a good sensitivity (molar absorptivity $0.26 \times 10^4 \text{ L} \cdot \text{mol}^{-1} \cdot \text{cm}^{-1}$); good precision (RSD better than 0.844 %) and high accuracy (relative error less than + 0.4%), Sandell's sensitivity index is $-0.1293 \mu\text{g} \cdot \text{cm}^{-2}$, the calculated limit of detection (LOD) is $0.0658 \mu\text{g/mL}$ and the evaluated limit of quantitation (LOQ) is $0.2193 \mu\text{g/mL}$. The application has had successful results for the assay of metoclopramide hydrochloride in dosage forms of tablets and injection.

Keywords: Butylated hydroxyanisole, metoclopramide hydrochloride, spectrophotometry friendly environment.

Submitted: August 05, 2022. **Accepted:** January 04, 2023.

Cite this: Alhammadi GA, Sarsam LA. Novel Green Method for the Spectrophotometric Determination of Metoclopramide Hydrochloride in Pharmaceutical Formulations. JOTCSA. 2023;10(1):193-204.

DOI: <https://doi.org/10.18596/jotcsa.1158403>.

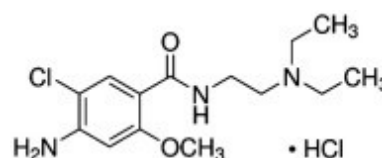
***Corresponding author. E-mail:** lamyasarsam@uomosul.edu.iq.

1. INTRODUCTION

Metoclopramide hydrochloride (MCP.H), [4-amino-5-chloro-N-[2-diethylaminoethyl]-2-methoxybenzamide hydrochloride], (Sketch 1), is used as an anti-vomiting agent in the treatment of certain types of queasiness and emetic as well as to increase gastrointestinal motility (1). Oral forms of the drug are rapidly absorbed in the gastrointestinal tract, therefore they are not suitable for administration to children or elderly patients after surgery, as vomiting is often performed before absorption in the gastrointestinal tract (2). Taking the medicine causes some side effects, including dry mouth, insomnia, and changes in arterial blood pressure (3).

A survey of the literature reported that metoclopramide hydrochloride was estimated under optimal conditions by different spectrophotometric methods and using various chemical reagents, such as: azo-dye coupling (3-11), oxidative coupling (12-14), Schiff base Reaction (15), and charge transfer complex (16). A number

of researchers were able to estimate (MCP.H) by using other spectrophotometric methods such as UV, colored ion-pair complex, oxidation, reduction reaction and nucleophilic substitution reaction, in the presence of chemical reagents and under various optimal condition (17-20), diverse HPLC methods (21-25), Fluorescent analysis (26), and Glassy carbon electrode (GCE) were also used (27).



Sketch 1: $\text{C}_{14}\text{H}_{23}\text{Cl}_2\text{N}_3\text{O}_2 \cdot \text{HCl}$ M.wt. = 336.26 g/mol.

Currently, the recent methodological development in analytical chemistry gave rise to a plethora of improved and durable versions of an environmentally friendly approach (28), some of these concepts are safe compounds (29). As a result, this study describes a simple, sensitive and environ-

mentally friendly spectrophotometric method for assay of (MCP.H), using 2-tert-Butyl-4-methoxyphenol (BHA), a synthetic antioxidant as a safer reagent. (30).

2. EXPERIMENTAL

2.1 Apparatus

A JASCOV-630 UV-VIS (Tokyo, Japan) double beam spectrophotometer was used for all spectral and absorbance measurements with matched of 1.0 cm path length glass cells. ABS 120-4 Kern & Sohn GmbH used for weighing the samples.

2.2. The reagents

All the reagents used were of analytical-reagent grade. MCP.H stock standard solution 500 $\mu\text{g/mL}$: prepared by dissolving 0.05 g of pure MCP.H (NDI-Iraq) in distilled water and diluting to the marked in 100 mL volumetric flask using the same solvent. The stock solution was properly diluted to create the working solution 200 $\mu\text{g/mL}$. The prepared solutions were transferred to a dark bottle and kept in a cooled place which are stable for one month at least.

Sodium nitrite stock solution 1×10^{-2} M: was prepared by dissolving 0.0690 g of sodium nitrite in distilled water and diluting to the mark into a 100 mL volumetric flask. The stock solution was properly diluted to create 5.94×10^{-4} M working solution.

Butylated hydroxyanisole (BHA) reagent solution 5.54×10^{-4} M : was prepared by dissolving 0.0101 g of reagent (Miavit / Germany) in distilled water and

diluting to the marked in 100 mL volumetric flask. The produced solutions, which can be used for at least two weeks, were transferred to a dark bottle and kept in a cool location.

2.2.1. MCP.H Tablet solution (200 $\mu\text{g} / \text{mL}$)

The average weight of 10 Metoclopramide tablets Bp 10 mg (Flamingo Pharma, UK), was ground and mixed well. A portion of this powder, equivalent to 0.0200 g, accurately weighed. then was dissolved in warm distilled water and filtered it, the residue was washed and the same of solvent completed to the mark 100 mL in volumetric flask.

2.2.2. Injection solution (200 $\mu\text{g} / \text{mL}$)

Using a 100 mL volumetric flask, 4 mL of METOCOL Injection 10 mg/ 2 mL (Pioneer, Iraq) were taken, and the volume was then increased to the proper amount with distilled water.

2.2.3. General procedure for calibration

In a series of 5 mL calibrated flasks, an aliquot of a standard solution (200 $\mu\text{g/mL} = 5.94 \times 10^{-4}$ M) containing 0.1-1.4 mL of MCP.H was added. Equimolar sodium nitrite solution (5.94×10^{-4} M) was added to this solution, and 0.2 mL of a 1 M hydrochloric acid solution was used to correct the pH. The mixture was vigorously shaken, wait for 5 minutes to complete the diazotization step. Then, 1 mL of BHA (5.54×10^{-4} M) and 0.25 mL of 0.5 M sodium carbonate solutions were added. The mixture was thoroughly mixed and waited for between 2- 5 minutes before being diluted to the proper concentration with distilled water. The colored azo dye's absorbance at 504 nm against the equivalent reagent.

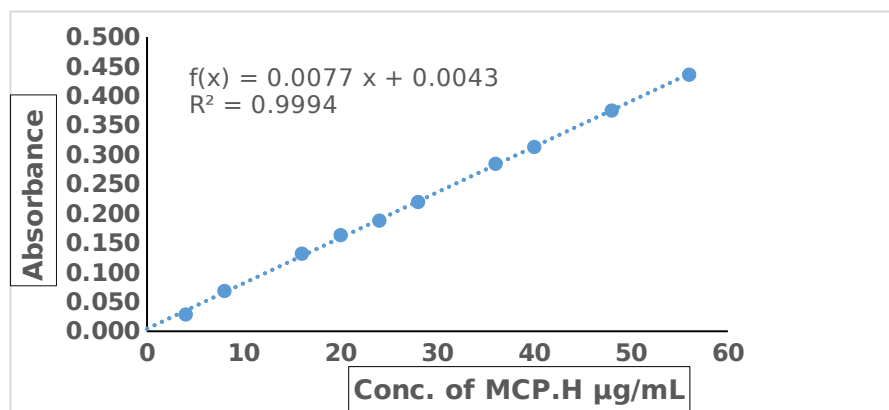


Figure 1: Standard curve for estimating MCP.H.

Figure 1 shows a good linearity over the range of the concentration between 4 to 56 $\mu\text{g/mL}$ with good sensitivity in which that the molar absorptivity is 0.26×10^4 L / mol.cm and sensitivity index of Sandell is $0.1293 \mu\text{g/cm}^2$.

3. RESULTS AND DISCUSSION

3.1. Study of the optimum conditions

3.1.1. Choosing of the acid

A number of different acids with the concentration of 1.0 M and an amount of 0.25 mL was used in this study. The results are shown in Table 1. As shown in Table 1. the maximum intensity of the colored product's absorptions occurs when 1 M hydrochloric acid is fixed in the following experiments.

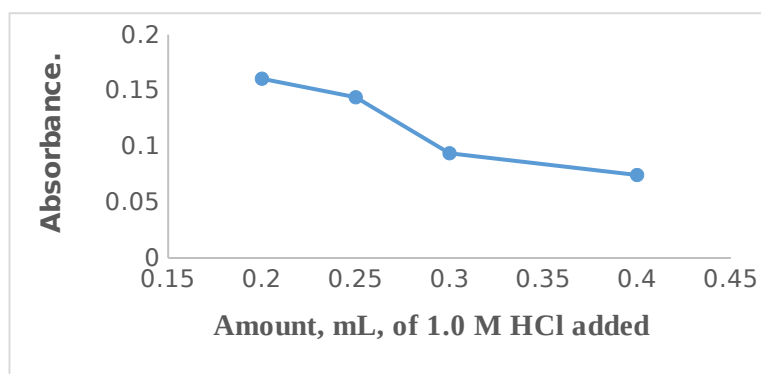
Table 1: Choosing the appropriate acid type.

Type of acid	λ_{\max}	Absorbance
H ₃ PO ₄	509	0.1304
HCl	504	0.1502
H ₂ SO ₄	508	0.0989
HNO ₃	Turbid	Turbid
CH ₃ COOH	510	0.0723

3.2. Effect of Different Volumes of 1 M Hydrochloric Acid Solution

Different volumes (0.1-0.4 mL) of 1.0 M hydrochloric acid were added to the reaction medium 5 mL volumetric flask. Figure 2 found that

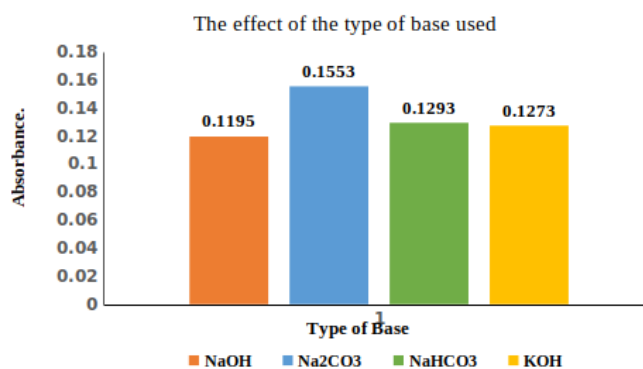
0.1 mL was turbid, and after 0.2 mL of hydrochloric acid the absorbance of the colored azo dye product decreases with the increase of acid amount added. So 0.2 mL of 1 M hydrochloric acid was chosen.

**Figure 2:** Effect of different volumes of 1 M hydrochloric acid solution.

3.3. Choosing the Base

Several alkaline solutions (potassium hydroxide, sodium bicarbonate, sodium carbonate and sodium hydroxide) with a concentration of 0.5 M were

investigated. Sodium carbonate was choice which considered as a best alkaline medium for producing maximal absorbance of the red azo dye and was chosen. Figure 3 illustrates the results.

**Figure 3:** Choosing the appropriate of base type.

3.4. Effect of Different Amount of 0.5 M Sodium Carbonate

Different volumes (0.1 - 0.5 mL) of 0.5 M sodium carbonate solution were added to the reaction

medium, Figure 4 found that 0.5 mL was turbid and 0.3 mL was enough to obtain the maximum absorbance, which was utilized in all future studies.

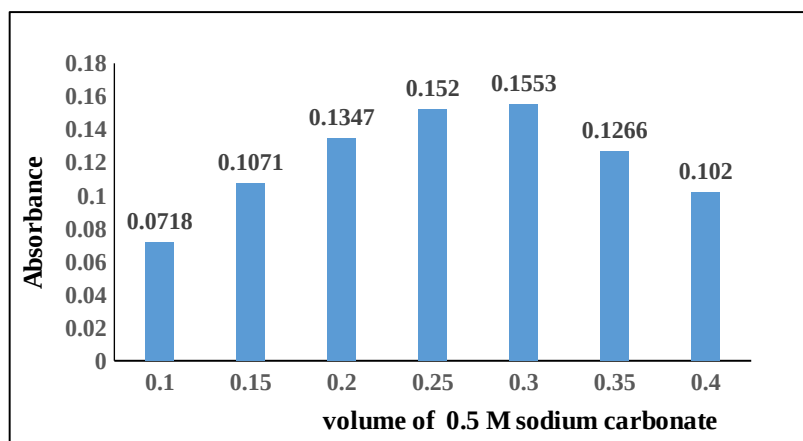


Figure 4: Effect of different amount of 0.5M sodium carbonate.

3.5. Effect of BHA Reagent Amount

The effect of changing volumes 0.5-1.5 mL of 5.54×10^{-4} M BHA coupling agent, studied against different concentrations of MCP.H, which was evident that the absorbance increases with

increasing BHA concentration, the determination coefficient of measured absorbances has been evaluated. Table 2 shows that 1 mL of 5.54×10^{-4} M of the coupling agent solution gives the best results.

Table 2: Effect of BHA reagent amount.

mL of 5.54×10^{-4} M reagent	Absorbance / μg of MCP.H						R^2
	36	32	28	24	20	12	
0.5	0.237	0.236	0.212	0.176	0.148	0.093	0.9702
0.75	0.266	0.249	0.215	0.176	0.147	0.097	0.9915
1.0	0.287	0.251	0.224	0.189	0.155	0.094	0.9991
1.25	0.286	0.243	0.221	0.188	0.159	0.099	0.9961
1.5	0.286	0.246	0.221	0.181	0.152	0.094	0.9964

3.6. Study of the Effect of Surfactants

1 mL of anionic sodium dodecyl sulfate (SDS), cationic cetylpyridinium chloride (CPC), cetyl trimethyl ammonium bromide (CTAB), and neutral iso-octylphenoxy-poly ethoxy ethanol (Triton X-100) were used to examine the impact of surfactants on absorption intensity. The use of surfactant was disregarded because the inclusion of SDS resulted in turbid solution and the addition of CPC reduces absorption intensity, while the addition of CTAB and Triton X-100 had no effect on absorption intensity.

3.7. Study of the Effect of Temperature

The effect of different temperature between 0°C to 40°C was studied, on the diazotization and coupling reaction show that the absorbance of the azo dye remains constant in the 25°C but decrease at lower than room temperature and higher than 30°C . Therefore, it has been recommended to carry out reaction at room temperature (25°C).

3.8. Stability of the Azo Dye Product

Following the mixing of the chemicals, the stability of the colored dye was investigated for 1 hour using 20 and 40 g/mL shows that the colored product maintains its stability for at least 55 minutes. See Table 3.

3.9. Final Absorption Spectrum

The BHA-MCP.H product's absorption spectra were plotted under the optimum reaction conditions obtained in Fig. 5 that a reddish orange colored compound had a maximum absorption at 504 nm versus blank.

Table 3: Stability of the azo dye product.

Time, min	Absorbance / μg of DMCPH per mL	
	20	40
0	0.1638	0.3113
5	0.1644	0.3077
10	0.1646	0.3053
15	0.1632	0.3085
20	0.1615	0.3062
25	0.1628	0.3056
30	0.1604	0.3057
35	0.1593	0.3059
40	0.1586	0.3046
45	0.1588	0.3019
50	0.1575	0.2998
55	0.1560	0.2965
60	0.1553	0.2967

3.10. Accuracy and Precision of the Suggested Method

The accuracy and precision of the suggested method were tested by analyzing of three different concentration (20, 36, 48) $\mu\text{g/mL}$ with four

replicates. The low relative error and low percentage relative standard deviation were summarized in Table 4. These values indicate the high accuracy and precision of the proposed method.

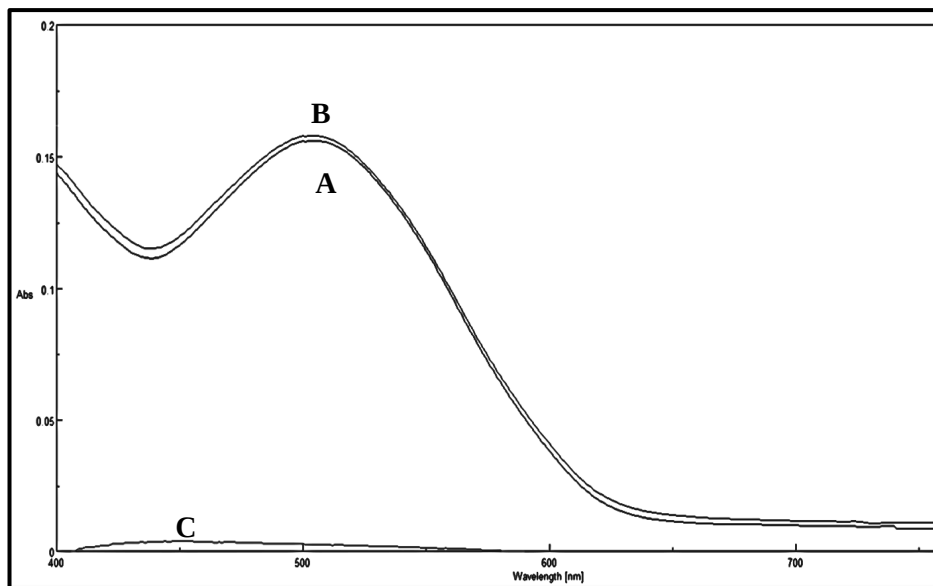


Figure 5: Final Absorption of spectra of (A) MCP.H (20 $\mu\text{g/mL}$) with BHA versus blank and (B) MCP.H with BHA versus distilled water (C) Blank versus distilled water.

Table 4: Accuracy and precision of the suggested method.

Amount of MCP.H $\mu\text{g/mL}$	Recovery, %*	Relative error, %*	Relative standard deviation, %*
20	100.12	+0.12	0.902
36	99.09	- 0.90	1.08
48	99.63	- 0.36	0.551

*Average of four determinations.

3.11. The Nature of the Dye

The stoichiometry of the product was studied applying the continuous variation method (Job's method). The results obtained in Figure 6 shows

that a 2:1 azo dye was formed between diazotized MPC.H and BHA. The scheme below shows the proposed mechanism for the azo dye structure.

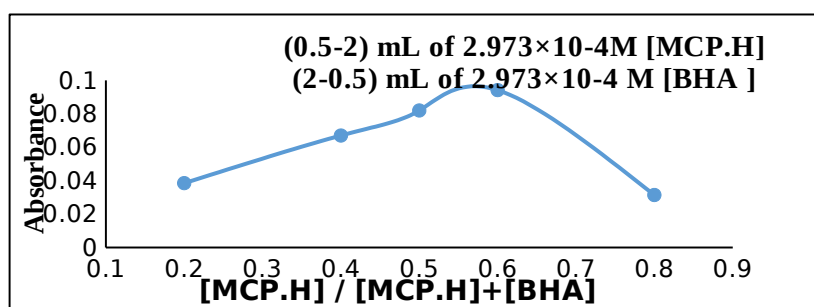
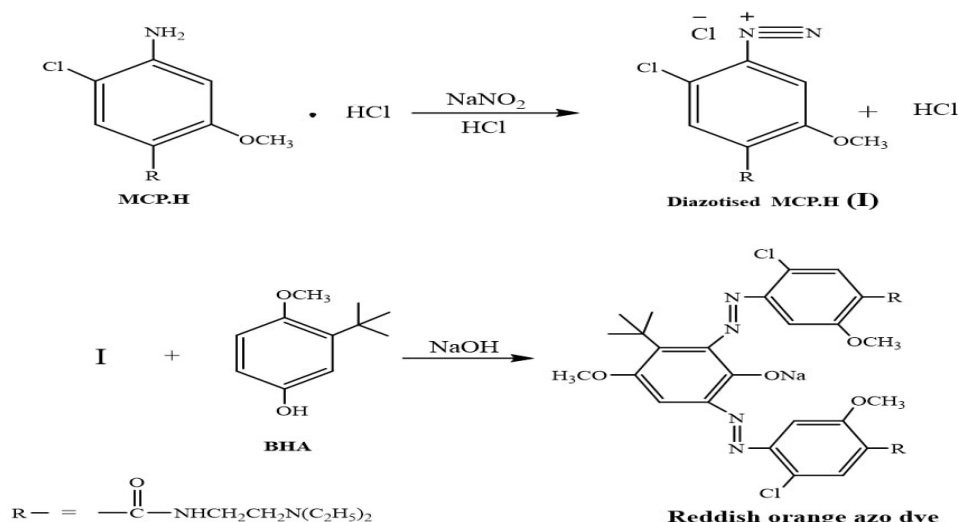


Figure 6: Continuous variation method.



Scheme 2: The suggested mechanism for MCP.H and BHA azo dye.

The azo dye's stability constant in aqueous solution was calculated and found to be 3.0379×10^{12} (31).

Table 5: Summary of optical characteristics and statistical data for the proposed method.

Parameter	Optimum conditions
Reagent	BHA
Linearity range, ($\mu\text{g mL}^{-1}$)	4-56
Molar absorptivity, ($\text{L}\cdot\text{mol}^{-1}\cdot\text{cm}^{-1}$)	0.26×10^4
Sandel's Index, ($\mu\text{g}\cdot\text{cm}^2$)	0.1293
λ_{max} , (nm)	504
Acid	HCl
Base	Sodium carbonate
LOD, ($\mu\text{g}\cdot\text{mL}^{-1}$)*	0.0658
LOQ, ($\mu\text{g}\cdot\text{mL}^{-1}$)*	0.2193
Average recovery, (%)**	99.6
RSD**	0.844
Correlation coefficient	0.9994
Medium	Aqueous
Solvent	Water

* Average of ten determinations.

**Average of four determinations of blank.

3.12. Effect of Interferences

Table 6 visions the effects of a few typical excipients associated with MCP.H in pharmaceutical preparations. The study shows that these additives has no negative effects on the efficiency of the suggested procedure.

3.13. Application Part

In order of demonstrate the applicability of the suggested method to the determination of MCP.H, on the form of tablets and injections, with three different concentrations, the results are summarized in Table 7. The assay results were indicating a good applicability of the of proposed method.

Table 6: Effect of excipients for MCP.H assay.

Excipients (1000 $\mu\text{g/mL}$)	Recovery (%) of 20 $\mu\text{g/ mL}$ MCP.H per $\mu\text{g/ mL}$ of excipient added		
	50	100	300
Lactose	98.59	100.51	101.3
Glucose	99.23	99.62	100.64
Starch	100.26	101.73	100.06

Table 7: Assay of MCP.H in pharmaceutical preparations using the proposed method.

$\mu\text{g MCP.H / mL}$	SDZ Present (μg)	SDZ Found (μg)	Relative Error (%) *	Recovery (%) *	RSD (%) *
Metoclopramide tablets Bp 10 mg (Flamingo pharma, UK)	20	20.16	0.826	100.82	1.40
	36	35.97	-0.052	99.94	0.80
	48	48.09	+0.219	100.2	1.06
METOCOL Injection 10 mg / 2 mL (Pioneer, Iraq)	20	20.04	+0.244	100.24	1.29
	36	36.12	+0.360	100.36	0.22
	48	47.83	-0.339	99.66	0.74

*Average of four determinations.

3.14. Evaluation of the proposed method's results

To elucidate that there is no interference with the additives employed in the pharmaceutical manufactures, the drug content of tablet and injection preparations was also estimated using the standard addition method, for 20 and 32 ppm of

the two MCP.H pharmaceutical preparations solution separately and adding various concentrations of the standard MCP.H solution under the condition that the maximum extent of the estimate in the calibration curve is not override. Figure 7A,B and Table 8 shows the results (32).

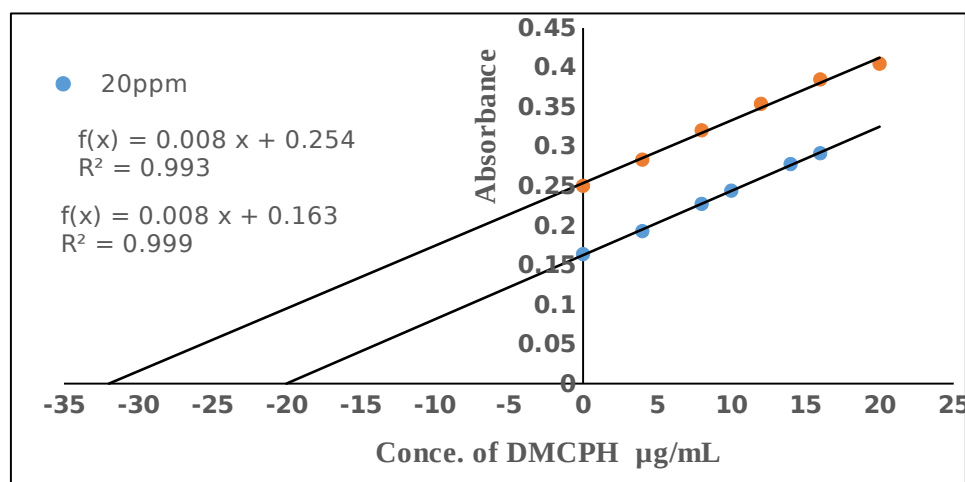


Figure 7A: Plot of standard addition method to estimate MCP.H in tablet.

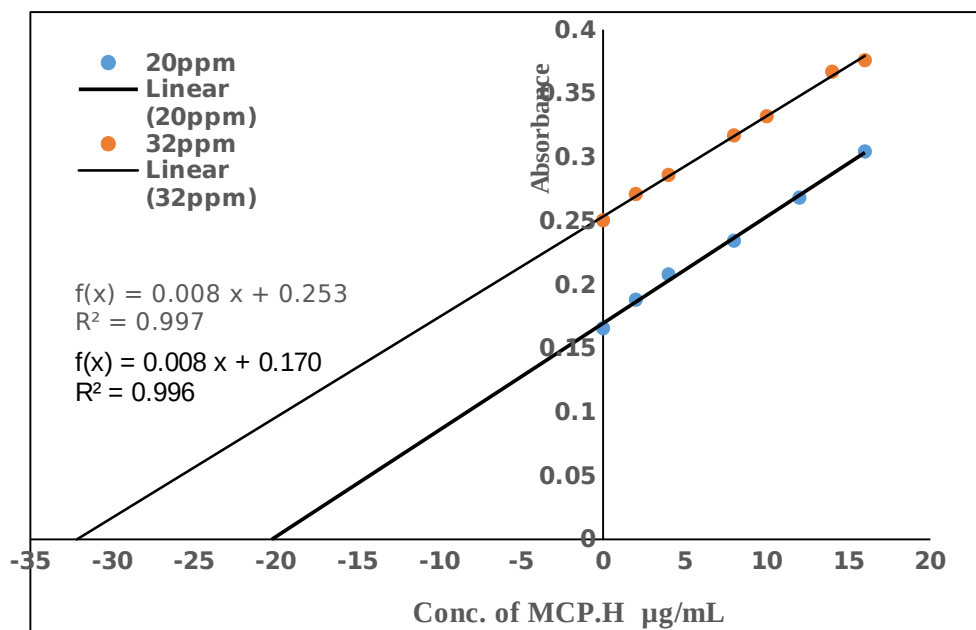


Figure 7B: Plot of standard addition method to estimate MCP.H in injection.

Table 8: Standard addition method to estimate MCP.H.

Pharmaceutical preparation	MCP.H Present (µg)	MCP.H measured (µg)	Recovery (%)*	Relative error, %*
METOCOL Injection 10 mg / 2 mL (Pioneer, Iraq)	20	20.17	100.85	+ 0.85
	32	32.07	100.22	+ 0.22
Metoclopramide tablets Bp 10 mg (Flamingo pharma, UK)	20	20.06	100.30	+ 0.30
	32	32.17	100.35	+ 0.35

*Average of four determinations.

3.15. Statistical Agreement t-test

The present method and the British Pharmacopeia one (based on potentiometric titration of pure medication with 0.1 M sodium hydroxide) at the 95 percent confidence level with 4 degrees of freedom were applied simultaneously for the t-test calculation (33). The value was compared with statistical Tables for four degrees of freedom at 95

percent validation level. The estimated t-test value (1.1255) was below the threshold of $t_{2.776} = (n_1 + n_2 - 2 = 2)$. These are confirming that, in terms of precision and accuracy in the determination of MCP.H in tablets, there are no appreciable discrepancies between the suggested approach and British Pharmacopeia's method.

Table 9: Comparison of the suggested method with the literature's method.

Parameters	Present method	Literature method Ref. #34
Reagent	BHA	p-Nitroaniline
λ_{max} , (nm)	504	513
Temperature °C	Room Temp.	Room Temp.
Medium	Aqueous	Aqueous
Linearity range, ($\mu\text{g mL}^{-1}$)	4-56	0.2-25
Molar absorptivity, L / mol.cm)	0.26×10^4	0.23×10^4
Sandell's Index, ($\mu\text{g.cm}^2$)	0.1293	0.1462
Nature of dye product Drug: Reagent	2:1	1:1
Average recovery,(%)	99.6	----
LOD, ($\mu\text{g.mL}^{-1}$)	0.0658	0.182
LOQ, ($\mu\text{g.mL}^{-1}$)	0.2193	0.553
Color of azo dye	Reddish-orange	Red
Application of the method	Tablet & Injection	Tablet & Injection

The results are shown in Table 9. The proposed method is not less important, of higher quality, and more sensitive than methods found in the literature. It does not require organic solvents; it can also be used to prepare pharmaceuticals with satisfactory results.

4. CONCLUSION

For the determination of metoclopramide hydrochloride in pharmaceutical preparations (administered as tablets or injections), an environmentally friendly method was used, in addition of being easy, sensitive and highly accurate, through its reaction with non toxic reagent (BHA), and free of organic solvents. In addition the method did not need any separation steps.

5. ACKNOWLEDGMENTS

The authors express their honest thanks to Department of Chemistry and New and Renewable Energies, College of Science, University of Mosul, Mosul, Iraq to benefit the research facilities.

6. REFERENCES

- Martindale W. The Extra Pharmacopoeia [Internet]. Creative Media Partners, LLC; 2018. Available from: [<URL>](#).
- El-Sonbaty MM, Ismail HR, Kassem AA, Samy AM, Akl MA. Mucoadhesive thermoreversible formulation of metoclopramide for rectal administration: a promising strategy for potential management of chemotherapy-induced nausea and vomiting. *Pharm Devel Technol*. 2020 May 27;25(5):535-46. Available from: [<URL>](#).
- Thanoon E, Saeed A. Development of Green Spectrophotometric Method for Determination of

Metoclopramide Hydrochloride. *Egypt J Chem*. 2021 Mar 9;64(7):3451-6. Available from: [<URL>](#).

4. Devi OZ, Basavaiah K, Vinay KB. Application of potassium permanganate to spectrophotometric assay of metoclopramide hydrochloride in pharmaceuticals. *J Appl Spectrosc*. 2012 Jan;78(6):873-83. Available from: [<URL>](#).

5. Wasan Abdulameer Al-Uzri LD, Hadi H, Fadhel L. Spectrophotometric Determination of Metoclopramide in its Pharmaceutical Preparations using Diazotization Coupling Reaction. *Iraqi Nat J Chem*. 2015;15(2):175-90.

6. Begum M, Koki IB, Rizwan M, Syed AA. Sensitive and Selective Spectrophotometric Methods for the Determination of Cisaprid, Metoclopramide Hydrochloride, Sulphadoxine and Sulphamethoxazole. *Int J Chem Mater Environ Res*. 2016;3(4):84-90.

7. Abd-Alrassol KS, Qasim QA, AL-Rikabi MA, AL-Salman HNK. The development of analytical methods to determine metoclopramide hydrochloric acid in the standard raw and it compared with pharmaceuticals. *Int J Res Pharm Sci*. 2019;10(4):1-14.

8. Abdulkareem HM, Al-Tameemi M, Ibraheem IH, Hadi MS. Surfactant cloud point extraction as a procedure of preconcentrating for metoclopramide determination using spectro analytical technique. *Baghdad Sci J*. 2020;17(1):57-65.

9. Ganduh SH, Aljeboree AM, Mahdi MA, Jasim LS. Spectrophotometric Determination of Metoclopramide-HCl in the standard raw and it compared with pharmaceuticals. *J Pharm Neg Res*. 2021 Jan 2;21(2):44-8. Available from: [<URL>](#).





10. Mubder NS, Kadhim EA, Ibraheem IH, Mahmood H, Dhahir SA, Al-Neshmi H. Micro Spectrophotometric Determination and Cloud Point Extraction of Metoclopramide with 4-Nitro Phenol in Pure Form and Pharmaceutical Drugs. *Ann Roman Soc Cell Biol*. 2021;25(4):12088-103.

11. Abbas SM, Jamur JMS, Nasif AM. Spectrophotometric Method for the Determination of Metoclopramide in Pharmaceutical Forms. *J Appl Spectrosc.* 2021 May;88(2):433-40. Available from: [<URL>](#).
12. Salih E, Mohamad I, Al-Najafi S. Spectrophotometric Assay of Metoclopramide Hydrochloride in pharmaceutical preparations via oxidative coupling Reaction with proma zine Hydrochloride and N-Bromosuccinimide. *J Edu Sci.* 2006 Sep 1;18(3):10-9. Available from: [<URL>](#).
13. Khaleel AI, Amine ST, Salih SH. Comparative study for determination of metoclopramide hydrochloride drug by selective electrodes and spectrophotometric methods. *Tikrit J Pure Sci.* 2013;18(1):149-61. Available from: [<URL>](#).
14. Al-Shirifi AN, Dikran SB, Halboos MH. Application of central composite design method to oxidative coupling spectrophotometric determination of metoclopramide hydrochloride in pure form and pharmaceutical preparations. *J Global Pharma Technol.* 2018;10(5):143-52.
15. Ali R, Othman N. Spectrophotometric Determination of Metoclopramide Hydrochloride in Pharmaceutical Preparations Via Schiff's Base Reaction: In Mosul, Ninevah, Iraq; 2021 [cited 2023 Feb 5]. Available from: [<URL>](#)
16. Liu J, Li H, Wang Y. Spectrophotometric determination of metoclopramide based on the charge transfer reaction between metoclopramide and purpurin. *Fenxi Kexue Xuebao.* 2010;26(3):361-3.
17. Ahmed NR, Essa MJ, Hamdoon AK. Ultraviolet assay of metoclopramide HCl in pharmaceutical formulations application to content uniformity testing. *Eur J Biomed Pharm Sci.* 2020;7(1):191-5.
18. Okram Zenita Devi, Kanakapura Basavaiah, Kanakapura Basavaiah Vinay, Hosakere Doddarevanna Revanasiddappa. Determination of Metoclopramide Hydrochloride in Pharmaceuticals and Spiked Human Urine through Diazotization Reaction. *J Food Drug Anal.* 2012 Jan 1;20(2):454-63. Available from: [<URL>](#).
19. Saleem BA. Spectrophotometric determination of some drugs using oxidation reduction reactions. *Ibn Al-Haitham J Pure Appl Sci.* 2019;32(3):43-55.
20. Mashkour MS, Kahlol MK, AL-Hasnawi SW. Colorimetric Determination of Metoclopramide Hydrochloride and Glutathione by using 1,2 Naphthaquinolinc-4-Sulphonate Sodium Reagents. *Res J Pharm Technol.* 2018;11(8):3290-4. Available from: [<URL>](#).
21. Valavala Sr SN, Tondepu S, Kandagatla S. LC-MS characterization of acid degradation products of metoclopramide: Development and validation of a stability-indicating RP-HPLC method. *Int J Res Pharm Sci.* 2020;11(1):781-9.
22. Karaiskou SG, Kouskoura MG, Markopoulou CK. Modern pediatric formulations of the soft candies in the form of a jelly: determination of metoclopramide content and dissolution. *Pharm Devel Technol.* 2020 Jan 2;25(1):20-7. Available from: [<URL>](#).
23. Khan A, Iqbal Z, Khan MI, Javed K, Khan A, Ahmad L, et al. Simultaneous determination of cefdinir and cefixime in human plasma by RP-HPLC/UV detection method: Method development, optimization, validation, and its application to a pharmacokinetic study. *J Chrom B.* 2011 Aug;879(24):2423-9. Available from: [<URL>](#).
24. Vamshikrishna G, Neelima M, Bhavani M, Sreekanth G, Shobha S. A Simple Rp-Hplc method for simultaneous estimation of paracetamol and metoclopramide. HCl in tablet dosage form. *IOSR J Pharm Biol Sci.* 2014;9:69-78.
25. Othman NS, Mahmood H, Khaleel N. Spectrophotometric and high performance liquid chromatographic methods for determination of metoclopramide in pharmaceutical preparations, Rafidain J. *Sci.* 2011;22:39-56.
26. Al-Awadie NST, Al-banaa MAK. Determination of metoclopramide hydrochloride via quenched continuous fluorescence of fluorescein sodium salt molecule. *J Pharm Sci Res.* 2019;11(6):2312-21.
27. Mazloum-Ardakani M, Kalantari AA, Alizadeh Z, Mohamadian-Sarcheshmeh H, Banitaba H. Electrochemical Investigation for Sensitive Determination of Metoclopramide Based on Ytterbium Oxide Nanoparticles Supported on Graphene. *Anal Bioanal Chem Res.* 2022;9(3):299-307.
28. Guardia M de la, Garrigues S. Handbook of green analytical chemistry. Chichester, West Sussex Hoboken: John Wiley & Sons; 2012. ISBN: 978-1-119-94072-2.
29. Casas Ferreira AM, Fernández Laespada ME, Pérez Pavón JL, Moreno Cordero B. Development of an environmentally friendly methodological approach to determine chlorinated hydrocarbons and chlorobenzenes in soils. *Green Chem Lett Rev.* 2014 Jan 2;7(1):50-9. Available from: [<URL>](#).
30. Özgür M, Kalaycıoğlu Z, Dülger Ö. Simultaneous spectrophotometric determination of phenolic antioxidant (BHA and BHT) concentrations in pharmaceutical preparations and chewing gums using the H-point standard addition method. *Macedon J Chem Chem Eng.* 2017 Dec 21;36(2):211. Available from: [<URL>](#).

31. Hargis LG. Analytical chemistry: Principles and techniques. 1988 Jan; Available from: [<URL>](#)
32. British Pharmacopoeia Commission. British pharmacopoeia. 2016. London: The Stationery Office; 2015.
33. Christian GD, Dasgupta PK, Schug K. Analytical chemistry. Seventh edition. Hoboken, NJ: John Wiley and Sons, Inc.; 2014. ISBN: 978-1-118-80527-5.
34. Abd Alrada WA, Sulaiman ID. Determination of Metochloropramide Hydrochloride by spectrophotometric method by using diazotized p-nitroaniline reagent. International J Drug Del Technol. 2020;10:68-73.



Eco-friendly Approach for Silver Nanoparticles Synthesis from Lemon Extract and their Anti-oxidant, Anti-bacterial, and Anti-cancer Activities

Nisreen Jassam Alaallah^{1*} , Ekhlas A. AbdulKareem² , Aseel Faeq Ghaidan³ ,
and Nuha A. Imran⁴ 

¹Anbar Education Directorate, Ministry of Education, Iraq.

^{2,4}Department of Chemistry, Collage of science, University of Diyala, Iraq

³Iraqi Center for Cancer and Medical Genetic Research.

Abstract: To create silver nanoparticles, researchers use bionanotechnology techniques because they are economical and environmentally friendly. The current study shows that lemon juice (*Citrus-limon*) can be used to biosynthesize silver nanoparticles (Ag NPs). The synthesized silver nanoparticles have been characterized by the surface plasmon resonance (SPR) measured at $\lambda_{max} = 430$ nm, confirming the formation of AgNPs. Moreover, Fourier Transform Infrared (FTIR) analysis was carried out to identify possible bio-molecules responsible for the bio-reduction of silver ions. The x-ray diffraction (XRD) peaks at (111, 200, 220, 222, and 311) confirm the found face-centered cubic (FCC) crystal structure of AgNPs in solution. Transmission-Electron-Microscopy (TEM) images showed that AgNPs have spherical morphology with sizes ranging from 10-50 nm. Furthermore, the Particles Size Analyzer (PSA) confirmed these sizes and ranges. Synthesized AgNPs have high anti-oxidant activity according to the (scavenging of DPPH radicals, total anti-oxidant, and reducing power) assays. Also, the anti-bacterial activity of AgNPs was evaluated by a well diffusion method, and the results suggest that they are more sensitive to gram-positive bacteria than gram-negative ones, with the average diameter of the inhibition zones for AgNPs ranging from 4.11 to 25.87 mm and 1.38 to 22.3 mm against *S. aureus* and *E. coli* bacteria, respectively. *In vitro* studies of AgNPs against MCF-7 breast cancer cell lines showed a good cytotoxic effect $p < 0.05$ with an IC_{50} value of 47 $\mu\text{g/mL}$; this study could be beneficial for nanotechnology-based pharmaceutical and biomedical applications.

Keywords: Silver nanoparticles, citrus limon juice, anti-oxidant activity, anti-bacterial activity, anti-cancer activity.

Submitted: August 09, 2022. **Accepted:** January 20, 2023.

Cite this: Alaallah NJ, AbdulKareem EA, Ghaidan AF, Imran NA. Eco-friendly Approach for Silver Nanoparticles Synthesis from Lemon Extract and their Anti-oxidant, Anti-bacterial, and Anti-cancer Activities. JOTCSA. 2023;10(1):205-16.

DOI: <https://doi.org/10.18596/jotcsa.1159851>.

*Corresponding author. E-mail: nisreenjassamalaallah@gmail.com.

1. INTRODUCTION

Metal nanoparticles that appear in size ranging from 1 - 100 nm have received increasing interest due to their optical and optoelectronic properties that are unique compared to their bulk counterparts; this has made them enter into different fields such as catalysis, optics, environmental, electronics, and biotechnology, which is an area of constant interest (1,2). Among these, silver nanoparticles (AgNPs) are widely used in a variety of applications because they have a small size, large surface area, and high

dispersive capacity and exhibit anti-microbial, anti-cancer, anti-diabetic, anti-oxidant, anti-inflammatory properties and also used in food preservation, water purifications ointment fabrication, and cosmetics (3, 4). Physical and chemical processes are still used today to create nanoparticles, but they result in many dangerous by-products that harm the environment. Therefore, there is a constant need for developing new methodologies and approaches for simple, rapid, consuming less energy, performing under moderate operation conditions, and eco-friendly nanoparticle synthesis methods. Many

scientists focus on the green synthesis of nanoparticles from plant extracts (5). It has been reported that nanoparticles synthesized by plant parts (such as seeds, roots, leaves, stems, flowers, and fruits) have more biological activities than

nanoparticle synthesis by chemical methods (6-8). Figure 1 represents an illustrative scheme for forming silver nanoparticles from different plant parts.

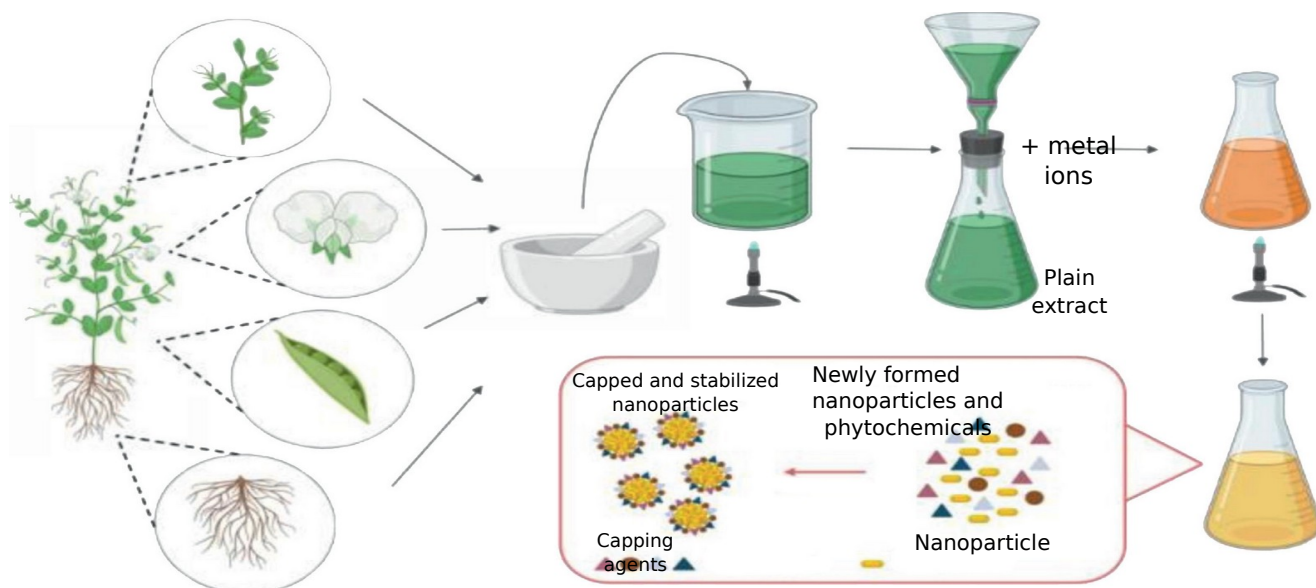


Figure 1: Green synthesis of metal nanoparticles by plant parts (9).

In recent times, nanoparticles using plant extracts have received attention as it is an economical and straightforward method (10). The main idea in the synthesis of AgNPs is by reducing agents that reduce silver ions (Ag^{+1}) to neutral silver (Ag^0) (22). Fruits, including lemon, are considered a rich source of flavanones, polys-methoxylated flavones, and carboxylic acids such as ascorbic acid and citric acid, which are very rare in other plants, and these materials could be used as reducing agents (5,11).

In this work, silver nanoparticles were synthesis through environmentally friendly synthesis techniques by using the extract from *Citrus limon* (lemon), the reason behind selecting this particular plant is that (i) lemon is a cheap, commercially available, and environmentally safe fruit and (ii) anti-microbial properties of the synthesized nanoparticles might be enhanced (12,13). In this regard, numerous studies on the synthesis of nanomaterials using plant parts such as *Citrus sinensis*, *Citrus tangerina*, and *Citrus limon* peel extract(5), *Citrus sinensis* peel extract (14), Lemons leaves extract (10,15), *Lemon Citrus Latifolia* extract (16), and *Citrus limon* (lemon) juice aqueous extract (13,17-19), Although there have been studies conducted with lemon, they have been limited to studying anti-bacterial activities. This study is the first to study the effectiveness of silver nanoparticles manufactured from lemon juice on cancer cell lines (MCF-7) and follow up on their anti-oxidant and anti-bacterial activities.

This work also provides more information on the chemical structure of silver nanoparticles

synthesized from aqueous lemon juice by UV, FTIR, XRD, TEM, AFM, and PSA.

2. METHODOLOGY

2.1. Materials

Silver nitrate (AgNO_3) was purchased from BDH, Sigma Aldrich. Fresh lemon was taken from local markets in Baquba / Diyala. Other chemical compounds required for anti-oxidant, anti-bacterial, and anti-cancer studies were of the highest purity. In this study, all glass tool was washed using distilled water and dried in the oven till used in the experiments, and all solutions were prepared using distilled water.

2.2. Preparation of Lemon Juice

Fresh lemon (*C. Limon*) fruit samples were sliced and strained through a nylon mesh with fine holes to obtain the juice. Then, the juice obtained was put into a centrifuge at 10,000 rpm for 10 minutes to remove any unwanted impurities. This extract was collected in a dark volumetric flask (25 mL) and stored at 4 °C for further experiments (17).

2.3. Synthesis of Silver Nanoparticles (AgNPs) from Lemon Juice

For the green synthesis of AgNPs, 1 mL of the lemon juice was added to 4 mL of 1 mM silver nitrate (AgNO_3) solution in a suitable test tube. The solution was heated in a water bath at 100°C for 30 minutes until AgNPs were formed, and reduction was confirmed by changing color from colorless to brownish-yellow (18).

2.4. Characterization of Synthesized Silver Nanoparticles

2.4.1. UV-vis spectroscopy

The optical properties of silver nanoparticles were calculated using ultraviolet-Visible spectrophotometer model Shimadzu UV-1700 (Shimadzu Corp, Kyoto, Japan). UV-Vis spectroscopic analysis was performed by continuous scanning in the range of 300-900 nm, an effective and widely applied technique for determining the formulation stability of metal nanoparticles (20) with some modification.

2.4.2. Fourier transform infrared (FTIR) analysis

FTIR is an analytical chemical method used to measure the intensity of infrared radiation against its wave number or wavelength light. It was performed to determine the functional groups involved in reducing Ag⁺ to AgNPs. The infrared spectra of the dried AgNPs and lemon powder were measured with the KBr disc in the range of 400-4000 cm⁻¹ using (S-8400, Shimadzu, Japan) FTIR spectrometer (21).

2.4.3. X-Ray diffraction (XRD) analysis

To confirm and determine the crystal structure of AgNPs. The powder X-Ray diffraction (XRD) of the AgNPs was recorded using X-ray diffractometer model (Philips X'Pert-MPD diffractometer, the Netherlands) ranging from 10 to 80°, and monochromatic CuK α radiation having wavelength ($\lambda = 1.5406\text{\AA}$) was used for XRD analysis (22).

2.5. Microscopy

2.5.1. Transmission electron microscopy (TEM) analysis

A thin film of the aqueous suspension of AgNPs was prepared by placing 10 μL of suspension on a small copper grid and letting the grid dry before starting the measurement. The morphology of the AgNPs was investigated by TEM using a (JEOL JEM-2100) with an acceleration voltage of 200kV which gives a high-resolution image (19).

2.5.2. Atomic force microscopy (AFM) analysis

AFM was used to assess the size and form of AgNPs produced through biological synthesis. The AFM usually measures the height of AgNPs. AFM is a measurement by taking a few drops of aqueous suspension and placing it on a glass slide, leaving 24 hours at room temperature to dry completely. Images obtained from the AFM were collected using Pico-Scan software (17).

2.5.3. Particle size analyzer (PSA) analysis

Particle size analyzer equipment (Horiba LA-3000Light Scattering Particle Size Distribution Analyzer, Horiba Ltd, Kyoto, Japan) was used to determine the particle size of the produced AgNPs. The normal log distribution of the nanoparticles based on intensity and size was studied comparatively. Measurements were taken between 5.0 and 500.0 nm(23).

2.6. Anti-Oxidant Assays

The synthesized AgNPs were estimated for anti-oxidant activity using three methods as follows: L-Ascorbic acid (AA) was used as a reference.

2.6.1. Scavenging of DPPH radical assay

The anti-oxidant activity of the lemon juices and AgNPs was measured by using (2,2-diphenyl-1-picryl-hydroxyl)(DPPH) assay, as described by Chang et al.(24). 1 mL of serial dilutions of lemon juice and synthesized AgNPs were prepared in different concentrations (100, 200, 300, and 400 $\mu\text{g}/\text{mL}$). To each dilution, 1 mL of DPPH (0.135 mM in ethanol) was added, incubated, and left in the dark at room temperature for (30 minutes). The absorbance of the control and samples were determined at $\lambda_{\text{max}} = 517$ nm, and ascorbic acid was used as a positive control.

The capability of AgNPs to scavenge the DPPH radical was recorded as a percentage inhibition in Equation 1:

$$\% \text{Inhibition} = \left(\frac{OD_{\text{Control}} - OD_{\text{Sample}}}{OD_{\text{Control}}} \times 100 \right) \quad (\text{Eq. 1})$$

where OD_{control} is the optical density of the control samples (DPPH solution without samples) and OD_{samples} is the optical density of the sample (DPPH solution and samples).

2.6.2. Total anti-oxidant assay

The total anti-oxidant activity of lemon juice and AgNPs was estimated according to the method conducted by Prieto et al. (25). An aliquot of 0.3 mL of each diluted juice prepared as described above was mixed with (3 mL) of reagent solution (4 mM ammonium-molybdate ((NH₄)₂MoO₄), 28 mM sodium phosphate (Na₃PO₄), and 0.6 M sulfuric acid (H₂SO₄), incubated at 95 °C for 90 minutes. After cooling the tubes, the samples' absorbance was measured at $\lambda_{\text{max}} = 695$ nm, and the anti-oxidant activity was determined as (%) using this formula:

$$\text{Total Anti-Oxidant} = \left(\frac{OD_{\text{Control}} - OD_{\text{Sample}}}{OD_{\text{Control}}} \times 100 \right) \quad (\text{Eq. 2})$$

2.6.3. Reducing power assay

The ferric (Fe³⁺) reducing the power of lemon juice and AgNPs was evaluated according to methods described by Oyaizu (26). Various concentrations of 1ml lemon juice and AgNPs were mixed with equal volumes of sodium phosphate buffers (0.2 M, pH=6.6) and 1 mL of potassium hexacyanoferrate (K₃Fe(CN)₆) (1%, w/v), and the resultant mixtures were incubated at 50 °C for 20 minutes. The reaction was stopped by adding 1 mL of trichloroacetic acid (TCA) (10%, w/v) and then centrifuging at 10,000 rpm for 10 minutes. A resultant supernatant solution (1.5 mL) was mixed for 10 minutes with distilled water (1.5 mL) and 0.1 mL of ferric chloride (FeCl₃)

solution (0.1%, w/v). Then, the absorbance of the mixture was measured at $\lambda_{\max} = 700$ nm against a blank solution. Higher absorbance values of the reaction mixture determined increased reducing power. Three replicates of each sample were made, and the average was recorded.

2.7. Antimicrobial Activity

A standard well diffusion procedure depends on investigating the inhibition effect of lemon juice and AgNPs of bacterial growth for two human pathogenic bacteria, *Staphylococcus aureus* as Gram-positive and *Escherichia coli* as Gram-negative (27). About 25 mL of nutrient agars were poured on Petri dishes and left to solidify. Inoculation of bacteria was performed by streaking on the agar surface of each plate hole 5 mm wide was on agar by punched with a sterile cork borer (10, 25, 50, and 100) μ L of lemon juice, and a solution containing AgNPs was transported and placed in these holes. The plates were permissible to stand by for (30 minutes) to (1 hour). The incubation of inoculated agar was done for 24 hours at an optimum temperature for bacteria growth equal to 37 °C. Then, the inhibition zone of bacteria growth was determined in millimeters. All experiments were conducted in triplicate.

2.8. Cytotoxicity Assay

The cytotoxicity assay of lemon juice and AgNPs was estimated by the MTT assay using a human breast cancer cell line MCF-7. In this method, MCF-7 cells were seeded onto 96-well plates $\sim 1 \times 10^5$ cells/wells at (37 °C) for 24 hours, and then cells were treated with different concentrations ranging from 10 to 100 μ g/mL of AgNPs along with cell control and lemon juice. Cells that had been treated with MTT (0.5 mg/L) were added, and they were then incubated at 37°C in a CO₂ incubator for 4 hours. Cells were washed with 100 μ l of phosphate-buffered saline

(PBS) after the MTT-containing medium was discarded. After incubation, the MTT formazan crystals were dissolved in (100 μ l) of dimethyl sulfoxide (DMSO, 10%), and purple-blue formazone dye was measured at 620 nm in a multiwell ELISA plate reader (Thermo-Multiskan EX)(28). The optical density (OD) value was used to compute the percentage of cell viability by using the following formula.

$$\text{Percentage of cell viability} = \frac{OD_{\text{cells with AgNPs}}}{OD_{\text{cells without AgNPs}}} \times 100$$

(Eq. 3)

Also, the cytotoxicity assay was estimated by finding the IC₅₀ value, which was the concentration showing 50% inhibition activity.

2.9. Statistical Analysis

A statistical comparison was carried out using a one-way analysis of variance (ANOVA), followed by Tukey's test. Each experiment was performed in triplicate, and the results were expressed as the mean \pm standard deviation; statistical significance was accepted at a level of ($p < 0.05$).

3. RESULTS AND DISCUSSION

3.1. Biosynthesis of AgNPs

In this study, the biosynthesis of AgNPs was carried out by reducing the aqueous silver solution of AgNO₃ with lemon juice. The results indicated an apparent change in the color of the solution from colorless to yellowish-brown; this occurred in a period of (30 minutes), and this change indicates the formation of AgNPs. Figure 2 shows the color change obtained, which agrees with a number of other studies (16,17,19).



Figure 2: The change in color indicating the synthesis of AgNPs.

3.2. Characterization of AgNPs

3.2.1. UV-Visible analysis

Ultraviolet-Visible (UV-Vis) spectroscopy was used to characterize the synthesis of AgNPs. Figure 3 shows UV-Visible spectra of the synthesis of AgNPs. Lemon juice and AgNO₃ were involved as controls. The peak at $\lambda_{\max} = 430$ nm in UV absorption refers to the conformation of AgNPs; the peaks' broadness exhibits the particle size variability. The result of this

study was similar to the results observed by Patil et al. (29).

3.2.2. FTIR analysis

FT-IR absorption spectra of lemon juice before and after bio-reduction, as shown in Figure 4, shows various bending and stretching bands viz, 3429, 1730, 1630, 1400, 1225, 1106, 899, 596, and 520 cm^{-1} . The broad peak at 3429 cm^{-1} corresponded to (-N-H) stretching of amides (II). The peak at 1730 cm^{-1} is sharp and related to (-C=O) stretching in (-

COOH) carboxylic acid. The peak at 1630 cm^{-1} (weaker), related to amide I, arisen due to carbonyl stretch in the protein. The peak at 1400 cm^{-1} corresponded to -O-H and -C-H bending. The peak at 1200 cm^{-1} corresponds to -C-O stretching in the carboxylic acid group (COOH). The peak at 1021 cm^{-1} is related to C-N stretching vibrations of amine. The peak at 1106 cm^{-1} appeared as a significant peak, which might be attributed to the C-O groups of the polyols such as polysaccharides, flavones, and terpenoids excessively found in plant extract used as reducing agents during the synthesis of AgNPs (30). The peak at 899 cm^{-1} is related to C-H aromatic in benzene groups. The peaks between 596 and 520 cm^{-1} represent to silver nanoparticle's connection with oxygen from the hydroxyl group. From the measurement of FT-IR, it can be concluded that some of the bio-organic compounds present in lemon juice, such as flavonoids, alkaloids, and phenols, can play an essential role in reducing silver salt to metallic silver (Ag^0). Moreover, these composites act as capping and stabilizing agents, which helps prevent the silver nanoparticles from accumulating. This suggests that the biological components included in lemon juice perform dual functions of conformation and stabilization of AgNPs in an aqueous medium. Additionally, this study's results agree with those of other studies (10).

3.2.3. XRD analysis

The XRD spectra of the synthesized AgNPs are shown in (Figure 5). Bragg's diffraction peaks for AgNPs are observed at 38.4° , 44.53° , 64.45° , 79.77° , and 82.96° , equivalent to 111, 200, 220, 311, and 222, representative face centered cubic (FCC) structure of silver, respectively. The average crystallite size of AgNPs were calculated to be about 17.8 nm, using Scherer formula $D=0.94 \lambda/\beta \cos \theta$, D represents the size of particles (nm), λ is the wavelength of the X-ray ($\text{Cu K}\alpha = 1.5406\text{ \AA}$), β is the full width of the (XRD) peak at half height, and θ is the Bragg angle, that is (111), and θ is the position of that line in the pattern. The X-ray diffraction pattern demonstrated the lack of contaminants and the effective synthesis of pure AgNPs (31). The results of XRD analysis agree with the previously published research demonstrating the cubic structure of silver (32).

3.2.4. TEM analysis

TEM analysis of silver nanoparticles shows that AgNPs were mainly spherical with average sizes of 19 nm (Figure 6). AgNPs are usually present and readily aggregate during the manufacturing process. However, the fact that they were present and homogenous in our approach suggests that the AgNPs were stabilized using a capping agent,

possibly the bio-organic chemicals found in lemon juice (33). Compared with the previous studies, the silver nanoparticles in this work were similar in shape and size to those obtained in studies (16,34). In comparison, it was smaller than AgNPs obtained in studies (35-37).

3.2.5. AFM analysis

Atomic force microscopy (AFM) is used to evaluate the surface topography and size of AgNPs. Figures (7 - A) and (7 - B) showed the three-dimensional (3D) and two-dimensional (2D) images of AgNPs showing spherical or mostly spherical shapes of nanoparticles with an average size was $<100\text{ nm}$. AgNPs have been shown as a topographic image.

3.2.6. PSA analysis

The AgNPs size and distribution profile are depicted in Figure 8 using particle sizes analysis (PSA). The result showed that most particle distributions (90%) have modest nanoscale sizes, with a mean particle size of 35 nm.

3.3. Antioxidant Activity

Oxidation is an important biological process that contributes to energy production in many living organisms; however, the out-of-control production of oxygen-derived free radicals. Reactive oxygen species (ROS) cause damage to complex life molecules such as proteins, carbohydrates, nucleic acid, and lipids (38). This causes the emergence of several health problems, such as cancer, hepatic diseases, cardiovascular diseases, and renal failure (39). Anti-oxidants are agents that restrict the harmful effects of these oxidant reactions. These restrictions can include preventing the formation of free radicals or permanently removing free radicals, thus enhancing the immune defense and reducing the incidence of diseases (40). In this work, the anti-oxidant activity of lemon juice and synthesized AgNPs was examined using three different methods because a single, universal technique cannot accurately assess anti-oxidant capacity. The (DPPH) free radical scavenging activity is the better test for measuring anti-oxidant activity due to its simplicity, stability, and testing speed. In DPPH assay of lemon juice and AgNPs compared with ascorbic acid as standard. The results in (Figure 9) indicate that AgNPs have higher DPPH activity by 86% compared with lemon juice at $400\text{ }\mu\text{g/mL}$ concentration, and their activity increased with increased concentration. Therefore, we can say that AgNPs could be used as treatment agents for several diseases caused by oxidative stress. The result obtained in this study is in agreement with previous studies (41-43).

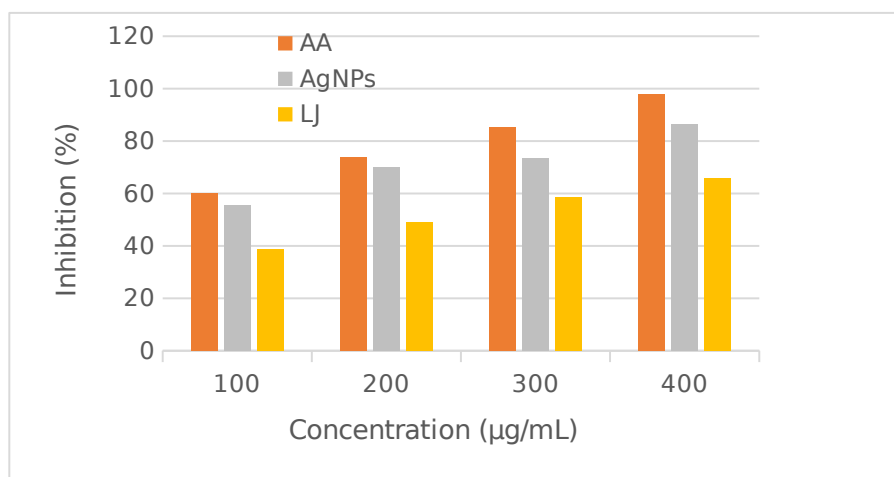


Figure 9: %Inhibition of DPPH free radical scavenging activity of Lemon juice (LJ), bio-synthesized AgNPs, and Ascorbic Acid (AA) at different concentrations.

In the total anti-oxidant method (phosphomolybdate), the basis of this method is the reduction of Mo(VI) to Mo(V) by the anti-oxidant compound and conformation of green phosphate,

Mo(V) complex. The results presented in Figure 10 showed that AgNPs have more anti-oxidant activity than ascorbic acid or lemon juice.

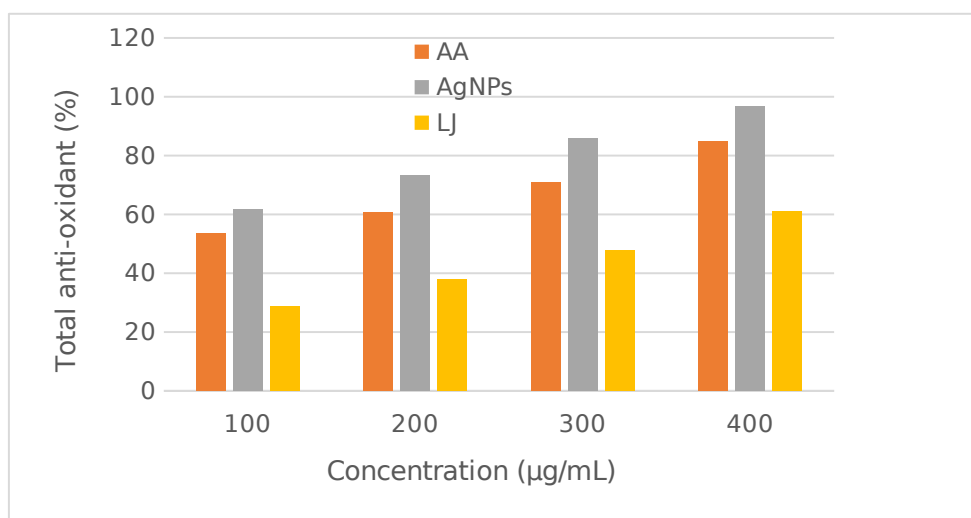


Figure 10: Total anti-oxidant capacity of Lemon Juice (LJ), biosynthesized AgNPs, and Ascorbic Acid (AA), at different concentrations.

In the reducing power assay, the ability of an anti-oxidant to donate an electron is measured when a reaction occurs between samples and potassium ferricyanide (Fe^{3+}) to generate potassium ferrocyanide (Fe^{2+}), followed by a reaction with ferric

chloride ($FeCl_3$) to form a ferric-ferrous complex (44). As shown in Figure 11, AgNPs have more anti-oxidant activity than lemon juice. The maximum and minimum optical densities were detected for AgNPs and lemon juice at 2.11 and 0.99 at 400 µg/mL.

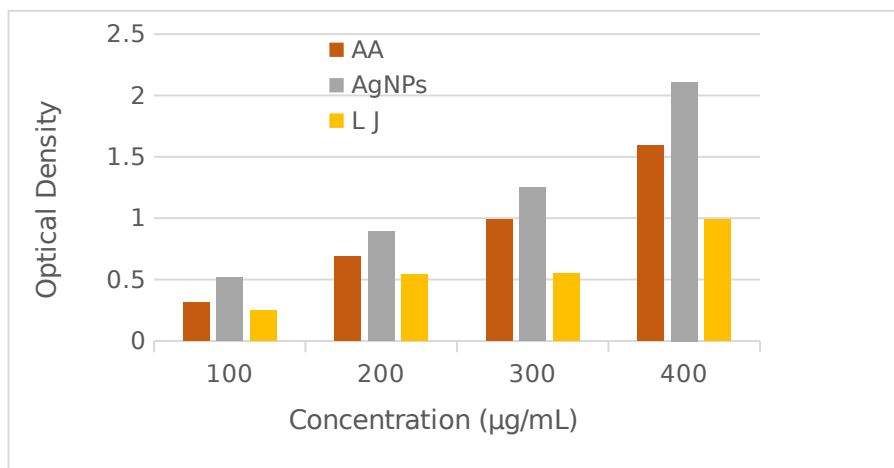


Figure 11: Reducing power activity of Lemon Juice (LJ), biosynthesized AgNPs, and Ascorbic Acid (AA) at different concentrations.

The analysis of variance (ANOVA) test findings showed statistically significant differences between lemon juice and the AgNPs when compared to ascorbic acid as a reference.

We conclude from this study that AgNPs synthesized from lemon juice have a stronger anti-oxidant capacity than the juice. This work highlights the importance of the therapeutic value of AgNPs synthesized from lemon juice as a source for developing anti-oxidant drugs.

3.4. Anti-Bacterial Effectiveness of Silver Nanoparticles

The anti-bacterial activity of lemon juice and synthesized AgNPs is shown in Figure 12 and Figure 13 against *Escherichia coli* (*E. coli*) and *Staphylococcus aureus* (*S. aureus*), respectively. Also, the values of zone of inhibition observed round the wells of synthesized AgNPs are given in Table 1 as (Mean±SD). and lemon juice and silver nitrate (control) are given in Table 2. The results in Table 2 showed that the effect of AgNO₃ for the dose of 60 µL against *E. coli* and *S. aureus* was low, and the reason for this may be due to its very low concentration (1 mM). Similarly, when comparing the effect of lemon juice and AgNPs as anti-bacterial, the results indicated a slight effect of lemon juice compared with the activity of AgNPs as an anti-bacterial for all doses (Tables 1 and 2). Although silver has anti-bacterial properties, lemon juice is rich in biologically active compounds such as flavonoids, carotenoids, and phenolic compounds, which act as natural antibiotics against pathogens in the body, such as bacteria (10,43). AgNPs differed significantly at $p < 0.05$ from lemon juice and AgNO₃ (45). AgNPs have activity of silver NP derived from lemon juice showed enhancement in activity due to the synergistic effect of silver and biologically active compounds of lemon juice. As shown in the data in Tables 1 and 2. This is in agreement with many studies; Samreen, Muzaffar, et al. (2018) conducted a study on different bacterial strains, and the results indicated a significant inhibition of AgNPs compared to the absence of any inhibition for lemon extract

(45). Furthermore, Mosae Selvakumar, Antonyraj, et al. (2016), and Niluxsshun, Masilamani, et al. (2021) discovered that lemon extract has slight activity while the zone of inhibition around AgNPs was significantly higher than the extract and controls and nearer to the inhibition of standard antibiotics (5,19). Also, it has been observed that AgNPs were more sensitive to, Gram-positive bacteria (*S. aureus*) than Gram-negative bacteria (*E. coli*). However, the mean inhibition zone diameter against *E. coli* for this study at a dose of 100 µL was higher compared to other studies such as *lemon* extract 3.0 mm (46), *Nicotiana tobaccum* leaf 4.0 mm (47), and *Neem* leaves 6.0 mm (48). Moreover, the anti-bacterial activity of AgNPs was found to increase with increasing doses (Table 1). This may be because of the different sizes and shapes of nanoparticles, especially AgNPs, which are spherical and have a high surface to volume ratio to interact with the cell walls of pathogens giving the best anti-microbial activity (49). This result agrees with several works of literature revealing that nanoparticles are more active against Gram-positive bacteria than Gram-negative bacteria (50, 51). And that the bactericidal property of nanoparticles depends entirely on the dose and particle size (52). The mechanism underlying the anti-bacterial activity of AgNPs is very complex. This can be explained as silver ions (Ag⁺) acting as an anti-bacterial by interacting with the peptidoglycan cell wall and that the thickness of the peptidoglycan layer differs in species of bacteria (Gram-negative bacteria and Gram-positive bacteria). This is the main reason why bacteria are differently affected by the attack by AgNPs (29). Other investigations have reported that the positive charge of AgNPs interacts with the negative charge on the cell wall of bacteria, which leads to changes in the morphology of the cell wall and increases the permeability of the membrane by making pores and thereby causing the death of bacteria (53,54). Also, it is said that Ag⁺ interaction with amino (-NH₂) and thiol (-SH) groups of protein on cell membrane, which results may be responsible for the induction of ROS, which leads to the inhibition of respiratory enzymes and, consequently death (5). Ag⁺ affects

bacterial cells through several mechanisms, including cell wall leakage, interaction with bacterial enzymes and DNA, ribosomal destabilization, and

interruption in the electron transport chain, resulting in cell death (55).

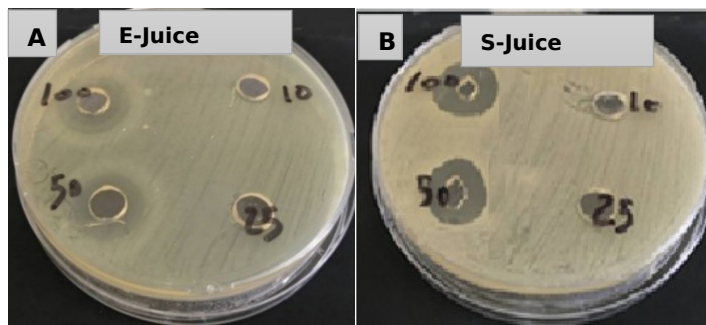


Figure 12: Anti-bacterial activity of lemon juice against (A) E= *Escherichia coli*, (B) S= *Staphylococcus aureus*.

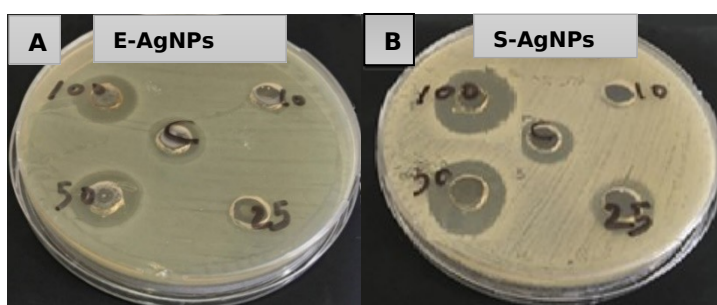


Figure 13: Anti-bacterial activity of AgNPs against (A) E= *Escherichia coli*, (B) S= *Staphylococcus aureus*.

Table 1: Effect of AgNPs on the growth of bacterial species.

Dose of lemon juice (µL)	<i>E. coli</i> (Mean±SD)	<i>S. aureus</i> (Mean±SD)	Dose of AgNPs (µL)	<i>E. coli</i> (Mean±SD)	<i>S. aureus</i> (Mean±SD)
10	0.00±0.00	0.00±0.00	10	1.38±0.41	4.11±0.39
25	0.00±0.00	5.17±0.29	25	3.93±0.83	13.13±0.32
50	10.2±0.62	11.4±0.40	50	17.5±0.5	20.47±0.45
100	13.03±0.35	14.5±0.45	100	22.3±0.57	25.87±0.96

Table 2: Effect of AgNPs, lemon juice (control), and AgNO₃ on the growth of bacterial species.

Dose of solution (µL)	AgNPs		Zone of inhibition (mm) Lemon juice		AgNO ₃	
	<i>E. coli</i> (Mean±SD)	<i>S. aureus</i> (Mean±SD)	<i>E. coli</i> (Mean±SD)	<i>S. aureus</i> (Mean±SD)	<i>E. coli</i> (Mean±SD)	<i>S. aureus</i> (Mean±SD)
60	19.0±0.26	22.67±0.32	11.4±0.62	13.2±0.40	5.53±0.50	6.06±0.60

3.5. Anti-cancer activity

In our study, the anti-cancer activity of the green synthesis AgNPs at different concentrations levels 10, 25, 50, 75, and 100 µg mL⁻¹ was studied against a human breast cancer cell line MCF-7. The result showed that AgNPs had positive anti-cancer effects on MCF-7 cancer cells. In figure 14, the nanoparticles showed dose-dependent anti-cancer activity. The required concentrations for 50% inhibition of the cell viability (IC₅₀) were calculated graphically; it was about 47 µg/mL for AgNPs, while

IC₅₀ was recorded at 215 µg/mL for lemon juice. AgNPs showed significant inhibition of cell growth of about 80%, while the lemon juice showed very low cytotoxicity of 29%. According to the optical microscopic analysis of cancer cells, exposure to an aqueous suspension of AgNPs caused significant morphological changes in the cells, including aggregation, cellular shrinkage, and rounding, compared to untreated cells. The result obtained in this study was in agreement with another study (56).

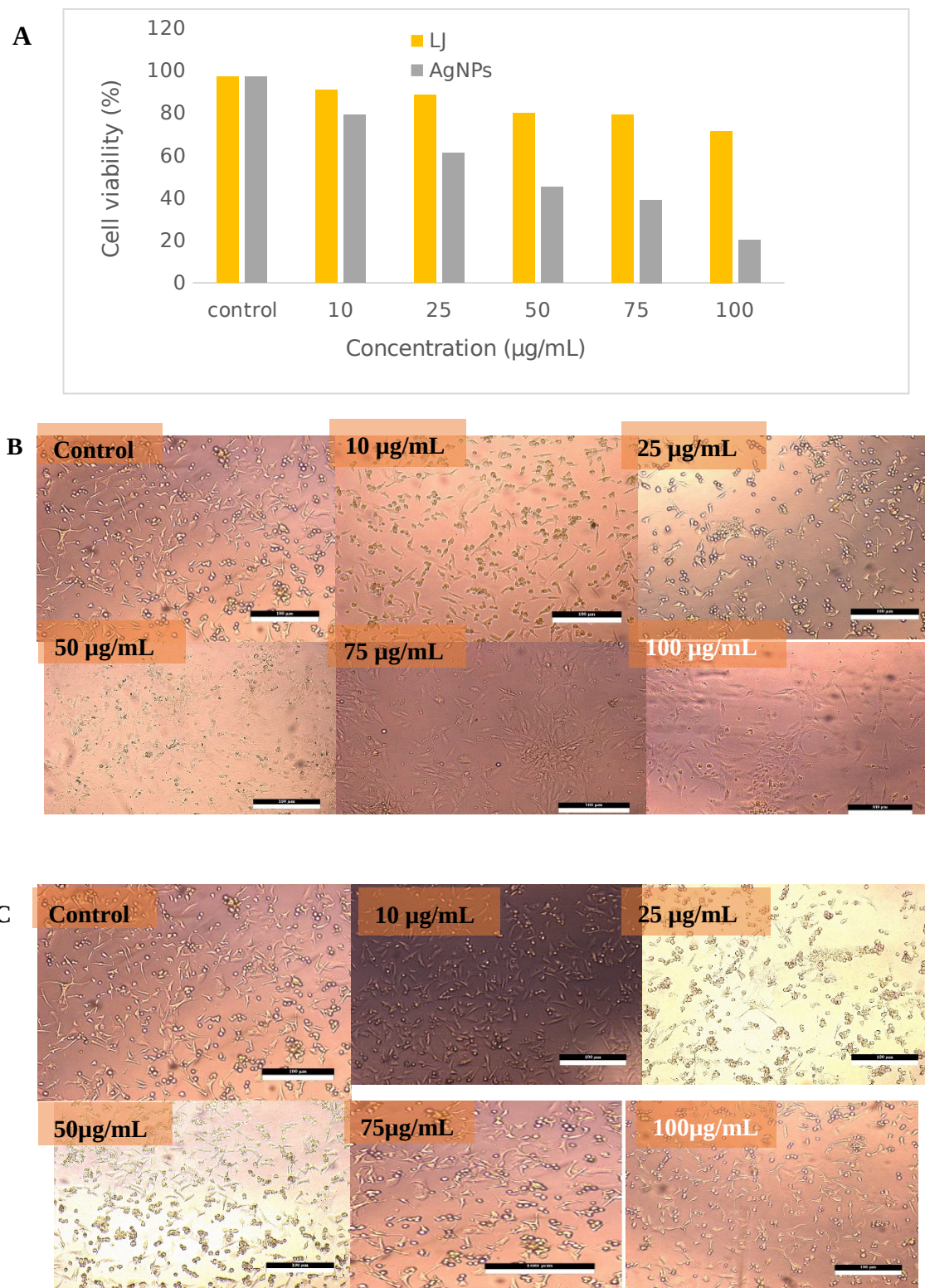


Figure 14:- Cytotoxic activity of AgNPs and lemon juice (LJ) MCF-7 cell line **(A)** Histogram demonstrating the cell viability percentage of MCF-7 cells at different concentrations 10, 25, 50, 75, and 100 µg/mL of AgNPs and lemon juice. **(B)** Photomicrographs showing changes in MCF-7 cell line after being treated with different concentrations 10, 25, 50, 75, and 100 µg/mL of AgNPs, and **(C)** Photomicrographs showing MCF-7 cell line after being treated with different concentrations 10, 25, 50, 75 and 100 µg/mL of lemon juice.

One of the potential mechanisms for inducing apoptosis in cancer cells involves the synthesis of AgNPs, which trigger reactive oxygen species (ROS)

and, in turn, the production of toxic free radicals and the disruption of mitochondria, both of which result in cellular apoptosis (57). Many researchers have

reported the cellular internalization of AgNPs, according to the surface properties of AgNPs. AgNPs carry a positive charge, while normal-cancer cell membranes contain substances such as lipids (especially PO₄³⁻ groups) with a negative charge; Having an opposite charge is responsible for cellular internalization and thus causes cancer cell death (55). In another study conducted by one of the researchers on the breast cancer cell line, the study reported that silver nanoparticles (GSNPs) manufactured from *Mentha-arvensis* induce cytotoxicity by mediating caspase 9-dependent apoptosis in breast cancer cell lines (58). In a study conducted by one of the researchers on silver nanoparticles, it was found that these AgNPs nanoparticles can contribute to cellular degradation by autophagy and thus cause cancer cell death (59). Three methods have been proposed. To take advantage of the biosynthesis of nanoparticles that cause apoptosis in cancer cells, that is mitochondrial damage, activation of death transmembrane receptors, and injury of the endoplasmic reticulum (60-62).

4. CONCLUSION

In this study, the Ag-NPs were successfully synthesized by green synthesis using lemon (*Citrus limon*) juice with different groups of phytochemicals such as phenols, terpenes, and flavonoids. The characteristics of the biosynthesized AgNPs were measured by different equipments (UV-visible spectrophotometer, FT-IR spectrometer, TEM, AFM, and PSA). Moreover, several medicinal aspects of these NPs, including anti-oxidant, anti-bacterial, and anti-cancer activity, were evaluated, and the AgNPs showed potential anti-microbial activity against Gram-positive and Gram-negative bacteria. The anti-oxidant activity of AgNPs showed the highest effect. In addition, the results indicate that AgNPs had anti-cancer activities against human breast (MCF-7) cancer cell lines in a dose-dependent manner. These green methods of AgNP formation open a new window for treating many infectious diseases and cancers.

5. CONFLICT OF INTEREST

Regarding the current manuscript, the researchers affirm that there are no conflicts of interest

6. ACKNOWLEDGMENTS

The researchers are grateful to the University of Diyala and the Faculty of Sciences for supplying the resources necessary for this study.

7. REFERENCES

1. Kumar B, Smita K, Cumbal L, Debut A, Pathak RN. Sonochemical Synthesis of Silver Nanoparticles Using Starch: A Comparison. *Bioinorganic Chemistry and Applications*. 2014;2014:1-8. Available from: [<URL>](#).
2. Mohammed RS, Aadim KA, Ahmed KA. Synthesis of CuO/ZnO and MgO/ZnO Core/Shell Nanoparticles with

Plasma Gets and Study of their Structural and Optical Properties. *Journal of Modern Science*. 2022;8(2):9.

3. Jakinala P, Lingampally N, Hameeda B, Sayyed RZ, Khan M. Y, Elsayed EA, et al. Silver nanoparticles from insect wing extract: Biosynthesis and evaluation for antioxidant and antimicrobial potential. Kumar P, editor. *PLoS ONE*. 2021 Mar 18;16(3):e0241729. Available from: [<URL>](#).

4. Ahmed RH, Mustafa DE. Green synthesis of silver nanoparticles mediated by traditionally used medicinal plants in Sudan. *Int Nano Lett*. 2020 Mar;10(1):1-14. Available from: [<URL>](#).

5. Niluxsshun MCD, Masilamani K, Mathiventhan U. Green Synthesis of Silver Nanoparticles from the Extracts of Fruit Peel of Citrus tangerina, Citrus sinensis, and Citrus limon for Antibacterial Activities. Ciccarella G, editor. *Bioinorganic Chemistry and Applications*. 2021 Feb 2;2021:1-8. Available from: [<URL>](#).

6. Choudhury R, Majumder M, Roy DN, Basumallick S, Misra TK. Phytotoxicity of Ag nanoparticles prepared by biogenic and chemical methods. *Int Nano Lett*. 2016 Sep;6(3):153-9. Available from: [<URL>](#).

7. Pirtarighat S, Ghannadnia M, Baghshahi S. Green synthesis of silver nanoparticles using the plant extract of *Salvia spinosa* grown in vitro and their antibacterial activity assessment. *J Nanostruct Chem*. 2019 Mar;9(1):1-9. Available from: [<URL>](#).

8. Vasylyev G, Vorobyova V, Skiba M, Khrokalo L. Green Synthesis of Silver Nanoparticles Using Waste Products (Apricot and Black Currant Pomace) Aqueous Extracts and Their Characterization. *Advances in Materials Science and Engineering*. 2020 Jul 13;2020:1-11. Available from: [<URL>](#).

9. Yazdani M, Rostamzadeh P, Rahbar M, Alam M, Abbasi K, Tahmasebi E, et al. The Potential Application of Green-Synthesized Metal Nanoparticles in Dentistry: A Comprehensive Review. De Matteis V, editor. *Bioinorganic Chemistry and Applications*. 2022 Mar 3;2022:1-27. Available from: [<URL>](#).

10. Vankar PS, Shukla D. Biosynthesis of silver nanoparticles using lemon leaves extract and its application for antimicrobial finish on fabric. *Appl Nanosci*. 2012 Jun;2(2):163-8. Available from: [<URL>](#).

11. Vinson JA, Su X, Zubik L, Bose P. Phenol Antioxidant Quantity and Quality in Foods: Fruits. *J Agric Food Chem*. 2001 Nov 1;49(11):5315-21. Available from: [<URL>](#).

12. Selvam SI, Joicesky SMB, Dashli AA, Vinothini A, Premkumar K. Assessment of anti bacterial, anti inflammation and wound healing activity in Wistar albino rats using green silver nanoparticles synthesized from *Tagetes erecta* leaves. *JANS*. 2021 Mar 14;13(1):343-51. Available from: [<URL>](#).

13. Pandey S, Oza G, Vishwanathan M, Sharon M. Biosynthesis of highly stable gold nanoparticles using Citrus limone. *Ann Biol Res*. 2012;3(5):2378-82.

14. Kaviya S, Santhanalakshmi J, Viswanathan B, Muthumary J, Srinivasan K. Biosynthesis of silver nanoparticles using citrus sinensis peel extract and its antibacterial activity. *Spectrochimica Acta Part A: Molecular and Biomolecular Spectroscopy*. 2011 Aug;79(3):594-8. Available from: [<URL>](#).

15. Rai A, Chaudhary M, Ahmad A, Bhargava S, Sastry M. Synthesis of triangular Au core-Ag shell nanoparticles. *Materials Research Bulletin*. 2007 Jul;42(7):1212-20. Available from: [<URL>](#).
16. Linh DHT, Anh NP, Mi TTA, Tinh NT, Cuong HT, Quynh TL, et al. Biosynthesis, Characteristics and Antibacterial Activity of Silver Nanoparticles Using *Lemon Citrus Latifolia* Extract. *Mater Trans*. 2018 Sep 1;59(9):1501-5. Available from: [<URL>](#).
17. Prathna TC, Chandrasekaran N, Raichur AM, Mukherjee A. Biomimetic synthesis of silver nanoparticles by Citrus limon (lemon) aqueous extract and theoretical prediction of particle size. *Colloids and Surfaces B: Biointerfaces*. 2011 Jan;82(1):152-9. Available from: [<URL>](#).
18. Biv K, Nolan R. Green Synthesis of Silver Nanoparticles using Lemon Extract, Characterization, and Antimicrobial Properties [Internet]. Poster presentation presented at: Undergraduate Posters; 2021 May; Salem, Massachusetts. Available from: [<URL>](#)
19. Mosae Selvakumar P, Antonyraj CA, Babu R, Dakhsinamurthy A, Manikandan N, Palanivel A. Green Synthesis and Antimicrobial Activity of Monodispersed Silver Nanoparticles Synthesized Using Lemon Extract. *Synthesis and Reactivity in Inorganic, Metal-Organic, and Nano-Metal Chemistry*. 2016 Feb 1;46(2):291-4. Available from: [<URL>](#).
20. Niraimathi KL, Sudha V, Lavanya R, Brindha P. Biosynthesis of silver nanoparticles using *Alternanthera sessilis* (Linn.) extract and their antimicrobial, antioxidant activities. *Colloids and Surfaces B: Biointerfaces*. 2013 Feb;102:288-91. Available from: [<URL>](#).
21. Hawar SN, Al-Shmgani HS, Al-Kubaisi ZA, Sulaiman GM, Dewir YH, Rikisahedew JJ. Green Synthesis of Silver Nanoparticles from *Alhagi graecorum* Leaf Extract and Evaluation of Their Cytotoxicity and Antifungal Activity. Omri A, editor. *Journal of Nanomaterials*. 2022 Jan 5;2022:1-8. Available from: [<URL>](#).
22. Gondwal M, Joshi nee Pant G. Synthesis and Catalytic and Biological Activities of Silver and Copper Nanoparticles Using *Cassia occidentalis*. *International Journal of Biomaterials*. 2018;2018:1-10. Available from: [<URL>](#).
23. Mohamed NH, Ismail MA, Abdel-Mageed WM, Mohamed Shoreit AA. Antimicrobial activity of latex silver nanoparticles using *Calotropis procera*. *Asian Pacific Journal of Tropical Biomedicine*. 2014 Nov;4(11):876-83. Available from: [<URL>](#).
24. Villaño D, Fernández-Pachón MS, Moyá ML, Troncoso AM, García-Parrilla MC. Radical scavenging ability of polyphenolic compounds towards DPPH free radical. *Talanta*. 2007 Jan 15;71(1):230-5. Available from: [<URL>](#).
25. Prieto P, Pineda M, Aguilar M. Spectrophotometric Quantitation of Antioxidant Capacity through the Formation of a Phosphomolybdenum Complex: Specific Application to the Determination of Vitamin E. *Analytical Biochemistry*. 1999 May;269(2):337-41. Available from: [<URL>](#).
26. Singh R, Singh S, Kumar S, Arora S. Evaluation of antioxidant potential of ethyl acetate extract/fractions of *Acacia auriculiformis* A. Cunn. *Food and Chemical Toxicology*. 2007 Jul;45(7):1216-23. Available from: [<URL>](#).
27. Mulvaney P. Surface Plasmon Spectroscopy of Nanosized Metal Particles. *Langmuir*. 1996 Jan 1;12(3):788-800. Available from: [<URL>](#).
28. Jinu U, Gomathi M, Saiqa I, Geetha N, Benelli G, Venkatachalam P. Green engineered biomolecule-capped silver and copper nanohybrids using *Prosopis cineraria* leaf extract: Enhanced antibacterial activity against microbial pathogens of public health relevance and cytotoxicity on human breast cancer cells (MCF-7). *Microbial Pathogenesis*. 2017 Apr;105:86-95. Available from: [<URL>](#).
29. Wanjari AK, Patil MP, Chaudhari UE, Gulhane VN, Kim GD, Kiddane AT. Bactericidal and photocatalytic degradation of methyl orange of silver-silver chloride nanoparticles synthesized using aqueous phyto-extract. *Particulate Science and Technology*. 2022 Nov 17;40(8):1033-40. Available from: [<URL>](#).
30. Pourmortazavi SM, Taghdiri M, Makari V, Rahimi-Nasrabadi M. Procedure optimization for green synthesis of silver nanoparticles by aqueous extract of *Eucalyptus oleosa*. *Spectrochimica Acta Part A: Molecular and Biomolecular Spectroscopy*. 2015 Feb;136:1249-54. Available from: [<URL>](#).
31. Iftikhar M, Zahoor M, Naz S, Nazir N, Batiha GES, Ullah R, et al. Green Synthesis of Silver Nanoparticles Using *Grewia optiva* Leaf Aqueous Extract and Isolated Compounds as Reducing Agent and Their Biological Activities. Yin J, editor. *Journal of Nanomaterials*. 2020 Oct 24;2020:1-10. Available from: [<URL>](#).
32. Tyagi PK, Tyagi S, Gola D, Arya A, Ayatollahi SA, Alshehri MM, et al. Ascorbic Acid and Polyphenols Mediated Green Synthesis of Silver Nanoparticles from *Tagetes erecta* L. Aqueous Leaf Extract and Studied Their Antioxidant Properties. Tapia Hernández JA, editor. *Journal of Nanomaterials*. 2021 Aug 2;2021:1-9. Available from: [<URL>](#).
33. Udayasoorian C, Kumar KV, Jayabalakrishnan M. Extracellular synthesis of silver nanoparticles using leaf extract of *Cassia auriculata*. *Dig J Nanomater Biostruct*. 2011;6(1):279-83.
34. Göl F, Aygün A, Seyrankaya A, Gür T, Yenikaya C, Şen F. Green synthesis and characterization of *Camellia sinensis* mediated silver nanoparticles for antibacterial ceramic applications. *Materials Chemistry and Physics*. 2020 Aug;250:123037. Available from: [<URL>](#).
35. Kharabi Masooleh A, Ahmadikhah A, Saidi A. Green synthesis of stable silver nanoparticles by the main reduction component of green tea (*Camellia sinensis* L.). *IET nanobiotechnol*. 2019 Apr;13(2):183-8. Available from: [<URL>](#).
36. Ali S, Jalal M, Ahmad H, Sharma D, Ahmad A, Umar K, et al. Green Synthesis of Silver Nanoparticles from *Camellia sinensis* and Its Antimicrobial and Antibiofilm Effect against Clinical Isolates. *Materials*. 2022 Oct 8;15(19):6978. Available from: [<URL>](#).
37. Chandra A, Bhattarai A, Yadav AK, Adhikari J, Singh M, Giri B. Green Synthesis of Silver Nanoparticles Using Tea Leaves from Three Different Elevations. *ChemistrySelect*. 2020 Apr 16;5(14):4239-46. Available from: [<URL>](#).
38. Gomaa EZ. Antimicrobial, antioxidant and antitumor activities of silver nanoparticles synthesized by *Allium cepa* extract: A green approach. *Journal of Genetic Engineering and Biotechnology*. 2017 Jun;15(1):49-57. Available from: [<URL>](#).

39. Es-haghi A, Javadi F, Taghavizadeh Yazdi ME, Amiri MS. The Expression of Antioxidant Genes and Cytotoxicity of Biosynthesized Cerium Oxide Nanoparticles Against Hepatic Carcinoma Cell Line. *Avicenna J Med Biochem.* 2019 Jun 25;7(1):16-20. Available from: [<URL>](#).

40. Pham-Huy LA, He H, Pham-Huy C. Free radicals, antioxidants in disease and health. *Int J Biomed Sci.* 2008 Jun;4(2):89-96.

41. M G, Dj M, Vinaykiya V, V B, Dutta S, Pawar R, et al. Screening of Antibacterial and Antioxidant Activity of Biogenically Synthesized Silver Nanoparticles from *Alternaria alternata*, Endophytic Fungus of *Dendrophthoe falcata*-a Parasitic Plant. *BioNanoSci.* 2022 Mar;12(1):128-41. Available from: [<URL>](#).

42. Taha ZK, Hawar SN, Sulaiman GM. Extracellular biosynthesis of silver nanoparticles from *Penicillium italicum* and its antioxidant, antimicrobial and cytotoxicity activities. *Biotechnol Lett.* 2019 Sep;41(8-9):899-914. Available from: [<URL>](#).

43. Khane Y, Benouis K, Albukhaty S, Sulaiman GM, Abomughaid MM, Al Ali A, et al. Green Synthesis of Silver Nanoparticles Using Aqueous Citrus limon Zest Extract: Characterization and Evaluation of Their Antioxidant and Antimicrobial Properties. *Nanomaterials.* 2022 Jun 10;12(12):2013. Available from: [<URL>](#).

44. Alavi M, Karimi N. Characterization, antibacterial, total antioxidant, scavenging, reducing power and ion chelating activities of green synthesized silver, copper and titanium dioxide nanoparticles using *Artemisia haussknechtii* leaf extract. *Artificial Cells, Nanomedicine, and Biotechnology.* 2017 Dec 12;1-16. Available from: [<URL>](#).

45. Samreen FG, Muzaffar R, Nawaz M, Gul S, Basra MAR. Synthesis, Characterization and Anti-Microbial Activity of Citrus limon Mediated Nanoparticles [Internet]. *LIFE SCIENCES*; 2018 Nov [cited 2023 Feb 5]. Available from: [<URL>](#)

46. Link MP, Goorin AM, Miser AW, Green AA, Pratt CB, Belasco JB, et al. The Effect of Adjuvant Chemotherapy on Relapse-Free Survival in Patients with Osteosarcoma of the Extremity. *N Engl J Med.* 1986 Jun 19;314(25):1600-6. Available from: [<URL>](#).

47. Prasad KS, Pathak D, Patel A, Dalwadi P, Prasad R, Patel P, et al. Biogenic synthesis of silver nanoparticles using *Nicotiana tobaccum* leaf extract and study of their antibacterial effect. *African Journal of Biotechnology.* 2011;10(41):8122.

48. Verma A, Mehata MS. Controllable synthesis of silver nanoparticles using Neem leaves and their antimicrobial activity. *Journal of Radiation Research and Applied Sciences.* 2016 Jan;9(1):109-15. Available from: [<URL>](#).

49. Babu RH, Yugandhar P, Savithamma N. Synthesis, characterization and antimicrobial studies of bio silica nanoparticles prepared from *Cynodon dactylon* L.: a green approach. *Bull Mater Sci.* 2018 Jun;41(3):65. Available from: [<URL>](#).

50. Patil MP, Rokade AA, Ngabire D, Kim GD. Green Synthesis of Silver Nanoparticles Using Water Extract from Galls of *Rhus Chinensis* and Its Antibacterial Activity. *J Clust Sci.* 2016 Sep;27(5):1737-50. Available from: [<URL>](#).

51. Paul B, Bhuyan B, Purkayastha DD, Dhar SS. Photocatalytic and antibacterial activities of gold and silver

nanoparticles synthesized using biomass of *Parkia roxburghii* leaf. *Journal of Photochemistry and Photobiology B: Biology.* 2016 Jan;154:1-7. Available from: [<URL>](#).

52. Khan SS, Mukherjee A, Chandrasekaran N. Studies on interaction of colloidal silver nanoparticles (SNPs) with five different bacterial species. *Colloids and Surfaces B: Biointerfaces.* 2011 Oct;87(1):129-38. Available from: [<URL>](#).

53. Sondi I, Salopek-Sondi B. Silver nanoparticles as antimicrobial agent: a case study on *E. coli* as a model for Gram-negative bacteria. *Journal of Colloid and Interface Science.* 2004 Jul;275(1):177-82. Available from: [<URL>](#).

54. Patil SV, Borase HP, Patil CD, Salunke BK. Biosynthesis of Silver Nanoparticles Using Latex from Few Euphorbian Plants and Their Antimicrobial Potential. *Appl Biochem Biotechnol.* 2012 Jun;167(4):776-90. Available from: [<URL>](#).

55. Patil MP, Kim GD. Eco-friendly approach for nanoparticles synthesis and mechanism behind antibacterial activity of silver and anticancer activity of gold nanoparticles. *Appl Microbiol Biotechnol.* 2017 Jan;101(1):79-92. Available from: [<URL>](#).

56. Majeed S, Danish M, Zakariya NA, Hashim R, Ansari MT, Alkahtani S, et al. In Vitro Evaluation of Antibacterial, Antioxidant, and Antidiabetic Activities and Glucose Uptake through 2-NBDG by Hep-2 Liver Cancer Cells Treated with Green Synthesized Silver Nanoparticles. *Srivastava S, editor. Oxidative Medicine and Cellular Longevity.* 2022 May 17;2022:1-14. Available from: [<URL>](#).

57. Ovais M, Khalil AT, Raza A, Khan MA, Ahmad I, Islam NU, et al. Green synthesis of silver nanoparticles via plant extracts: beginning a new era in cancer theranostics. *Nanomedicine.* 2016 Dec;11(23):3157-77. Available from: [<URL>](#).

58. Banerjee PP, Bandyopadhyay A, Nagesh H, Policegoudra R, Bhattacharya S, Karak N, et al. *Mentha arvensis* (Linn.)-mediated green silver nanoparticles trigger caspase 9-dependent cell death in MCF7 and MDA-MB-231 cells. *BCTT.* 2017 Apr;Volume 9:265-78. Available from: [<URL>](#).

59. Soshnikova V, Kim YJ, Singh P, Huo Y, Markus J, Ahn S, et al. Cardamom fruits as a green resource for facile synthesis of gold and silver nanoparticles and their biological applications. *Artificial Cells, Nanomedicine, and Biotechnology.* 2018 Jan 2;46(1):108-17. Available from: [<URL>](#).

60. Mohammadinejad R, Moosavi MA, Tavakol S, Vardar DÖ, Hosseini A, Rahmati M, et al. Necrotic, apoptotic and autophagic cell fates triggered by nanoparticles. *Autophagy.* 2019 Jan 2;15(1):4-33. Available from: [<URL>](#).

61. Barabadi H, Vahidi H, Damavandi Kamali K, Rashedi M, Saravanan M. Antineoplastic Biogenic Silver Nanomaterials to Combat Cervical Cancer: A Novel Approach in Cancer Therapeutics. *J Clust Sci.* 2020 Jul;31(4):659-72. Available from: [<URL>](#).

62. Hembram KC, Kumar R, Kandha L, Parhi PK, Kundu CN, Bindhani BK. Therapeutic prospective of plant-induced silver nanoparticles: application as antimicrobial and anticancer agent. *Artificial Cells, Nanomedicine, and Biotechnology.* 2018 Nov 12;46(sup3):38-51. Available from: [<URL>](#).



Production of Biodiesel from Waste Cooking Oil Using KOH/Al₂O₃ as a Heterogeneous Catalyst

Asmo Abdillahi Hassan¹ , Ibrahim Yaagoub Erwa^{1*} , Razan Ali Salim¹ ,
Omer A. Omer Ishag , and Maysoun Ali Ahmed¹ 

¹International University of Africa, Department of Applied and Industrial Chemistry, Khartoum, 12223, Sudan.

Abstract: The catalytic performance of potassium hydroxide supported on alumina (KOH/Al₂O₃) for transesterification of waste cooking oil (WCO) was investigated. XRD, FTIR, and SEM techniques were used to characterize the catalyst after it had been synthesized using the wet impregnation method. The properties of the WCO and the produced biodiesel were evaluated. The main fatty acids of WCO were linoleic (45.61%), elaidic (33.86%), palmitic (10.32%), and stearic acid (4.80%), the acid value (2.29 mg KOH/g), FFA (1.15%), density at 25 °C (0.91 g/cm³), viscosity at 40 °C (34.09 mm²/s), water content (0.0017%), and flash point (206 °C). The XRD pattern of the catalyst showed diffraction peaks of KAlO₂ attributed to the orthorhombic crystal system having a 12.46% degree of crystallinity. The SEM micrographs confirmed the amorphous nature of the catalyst. The presence of K-O and Al-O bonds in the catalyst was confirmed by the FTIR. A biodiesel yield of 86.6% was achieved with the following variables: oil to methanol ratio of 1:4, catalyst loading of 1.5% (w/v%), reaction temperature of 55 °C, and a reaction time of 1 h. The results appeared to show a decreasing pattern of yield after 4 cycles of reaction from 86.60 to 51.50%. The fuel properties were density (0.8919 g/cm³), viscosity (7.428 cSt), flash point (65 °C), acid number (0.54 mg KOH/g) and water content (0.0196%). Furthermore, the properties of the prepared biodiesel have been found to comply with the ASTM and EN standard specifications. This catalyst showed promising results for manufacturing biodiesel from low-cost feedstock.

Keywords: Biodiesel, waste cooking oil, catalytic performance, Heterogeneous catalyst, wet impregnation.

Submitted: August 19, 2022. **Accepted:** January 10, 2023.

Cite this: Hassan AA, Erwa IY, Salim RA, Ishag O, Ahmed MA. Production of Biodiesel from Waste Cooking Oil Using KOH/Al₂O₃ as a Heterogeneous Catalyst. JOTCSA. 2023;10:217-26.

DOI: <https://doi.org/10.18596/jotcsa.1163670>.

***Corresponding author. E-mail:** ibrachem9@gmail.com.

1. INTRODUCTION

The majority of the world's energy demands are met by petroleum-based fuels, but they are finite and unsustainable. New alternative sources for petroleum-based fuel have been extensively researched as a result of depletion of petroleum reserves and rising environmental concerns (1). Biodiesel is a renewable energy source that can replace fossil-based diesel and can reduce the drawbacks of diesel emission (2).

The use of biodiesel as a fuel source has several advantages, in addition to being a renewable, sustainable, biodegradable source, generally non-toxic and environmental friendliness, as it reduces CO₂ emissions and hazardous compounds such as

arithmetic, sulphur, particulate matter and NO_x, biodiesel shares a variety of similar physical and chemical properties with petroleum diesel (3-5). Biodiesel is superior to diesel fuel due to its higher oxygen composition, high cetane content, higher flash point, cleaner combustion, and appropriate lubrication characteristics. Therefore, typical compression-ignition engines may use pure biodiesel or biodiesel blends without the need for substantial modifications (6,7). Biodiesel is a clear liquid with a light- to dark-yellow color. It has a boiling point of more than 200 °C, a flash point of 100 to 170 °C, a cloud point of -3 to 12 °C, a pour point of -15 to 16 °C, a kinematic viscosity at 40 °C of 1.9-6.0 mm²/s, a distillation range of 195-325 °C, a vapour pressure (mm Hg at 22 °C) less than 5, a freezing point (-3 °C), Cetane number of 48-60,

lower calorific value of 37300–38500 kJ/kg, and upper calorific value of 39300–39600 kJ/kg; oxygen content of 10–11% (wt%); sulfur content of 0.05% (wt%) (5,7,8). The oxygen content of biodiesel enhances the engine's combustion process and contributes to reducing exhaust emissions. Diesel fuels with high cetane values have a variety of benefits, including improved cylinder combustion, easier engine running in cold weather, and longer engine life (9). Dilution, micro-emulsion, pyrolysis, and transesterification methods were proposed as solutions to lower the viscosity of vegetable and animal oils, reduce the molecular weight, improve the volatility of the fuel, and decrease emissions such as HC and CO. The most widely utilized among these processes is the transesterification method (7, 10).

Biodiesel is made from natural oils or animal fats and alcohol via a transesterification reaction, which converts triglycerides into esters known as fatty acid methyl esters (FAME) (11). Commercial production of biodiesel is possible from a wide range of renewable biomass feedstocks, including edible oils. (e.g. peanut, rapeseed/canola, soybean, sunflower, palm, corn, cottonseed, coconut, mustard, olive, and sesame oils) and non-edible oils (e.g. jatropha, castor, neem, jojoba, passion seed, and moringa oils), animal fats (e.g. pork lard, beef tallow, poultry fat, fish oil, chicken fat), and waste cooking oils (12, 13). Competition with food is brought on by the production of biodiesel from conventionally grown oilseed crops. Due to the increasing demand for edible oils for food and their current high cost for use as fuel, the use of non-edible vegetable oils and waste oils is essential in developing countries (12). WCO refers to cooking oils that have been used in food preparation but might no longer suitable to use in food production. WCO may come from domestic, commercial or industrial sources. A waste stream such as WCO requires proper management, and irresponsible disposal can result in problems (14).

Biodiesel is defined as fatty acid methyl esters (FAME) derived from the transesterification of triglycerides (vegetable oils or animal fats) with alcohol and a suitable catalyst (15). The main catalysts utilized can be classed as homogeneous or heterogeneous. Homogeneous catalysts (base/acid) react with the reaction mixture in the same liquid phase are commonly used for biodiesel production from different feedstocks under mild reaction conditions. However, these traditional catalysts cause several technical problems i.e. reaction corrosion, large amounts of waste water production, separation problems, thereby increase the cost of biodiesel production, whereas heterogeneous catalysts react with the reaction mixture in a separate phase, usually as a solid. Heterogeneous catalysts are non-corrosive, environmentally beneficial, and a green process. They may be recycled and reused multiple times, making biodiesel production more cost-effective; thereby resolve many of problems associated with

homogeneous catalyzed biodiesel technology (16). The aim of this research was to investigate different transesterification process conditions; oil to methanol molar ratio, temperature, catalyst loading and reaction time on biodiesel production from WCO using potassium hydroxide supported on alumina as a heterogeneous catalyst. The reusability of the catalyst was also investigated over several consecutive runs and properties of the produced biodiesel were evaluated based on standards set of ASTM D6751 (17) and EN 14214 (18).

2. EXPERIMENTAL SECTION

2.1. Materials

Refined waste peanut oil was collected from Royal Broast fast food restaurant in Khartoum, Sudan. The oil was used once for frying. The solid particles and other impurities were filtered through normal sieves and then heated to 120 °C for 2 h to eliminate water traces. Then, the pre-treated WCO was stored in a clean glass air tight container. All chemicals used in this study were of analytical grade and used without any purification include: methanol (99%); ethanol (99%); potassium hydroxide (KOH) with purity 99%; aluminium oxide (Al₂O₃); were purchased from Merck Co. (Dannstadt, Germany)

2.2. Characterization of the WCO

The density, acid value, kinematic viscosity, flash point, water content and color the samples were assessed using the methods described by ASTM International (19-24). The fatty acids composition of the WCO sample was determined using (GC/MS-QP2010SE, Shimadzu, Japan) equipped with capillary column (Rtx-5MS- 30 m × 0.25 mm I.D × 0.25 μm) with the following analytical conditions: injector temperature was 300 °C; the injector was operated in the split mode; oven temperature was programmed from 60 °C to 300 °C at 10 °C/min; the carrier gas was helium at flow rate of 1.6 mL/min; volume of injection was 1 μL. The MS conditions were ion source temperature 200 °C, the interface temperature was 250 °C, the mass scan range was 40 – 500 m/z, and the total run time was 34 min. The spectra of the components were compared with the database of spectrum of known components stored in the GC-MS library (NIST).

2.3. Preparation of the Catalyst

Alkaline modified alumina was prepared via wet impregnation of aqueous solution of potassium hydroxide and alumina as a support. About 25 g of KOH was dissolved in 100 mL of distilled water. Then, the required amount of alumina powder was added to the solution (1:4 weight ration of Al₂O₃ to KOH). The slurry was vigorously stirred for 24 h, on magnetic stirrer at room temperature. The obtained precipitate was aged in mother liquid overnight (~24 h) at 40 °C. The solid product was separated by filtration using a vacuum filter system. It later dried in a 110 °C oven for 12 h. The dried solid obtained was calcined at 400 °C for 4 h in a muffle furnace (25).

2.4. Characterization of the Catalyst

The bulk structure, composition and crystalline structure of the synthesized catalyst were determined using X-ray diffractometer (XRD) (GNR, Italy), equipped with Cu K α radiation (40 kV 40 mA) with a wavelength (λ) of 1.54 Å. The sample was scanned from 4 to 90° (2 θ) and the phases were identified using X, Pert Highscore plus software by searching and matching the obtained patterns with the JCPDS (Joint committee of powder diffraction standards) database file. The morphology of the catalyst was studied by scanning electron microscopy (SEM), the micrographs were obtained by using a (TESCAN VEGA3) microscope; the elemental analysis was performed by energy dispersive spectroscopy (OXFORD EDS) detector. FTIR analysis of the catalyst was carried out using potassium bromide (KBr) powder method on a FTIR spectrophotometer (IRT racer-100, Shimadzu, Japan) with a resolution of 2 cm⁻¹ at 500 – 4000 cm⁻¹ range

2.5. Transesterification Reaction

The transesterification reaction of WCO was carried out with various catalyst loading, different methanol / oil molar ratios, various reaction temperatures and reaction time. Before starting the transesterification reaction, the oil was heated to 70 °C then cooled to the reaction temperature between 50 – 60 °C. The specified amount of oil, methanol and catalyst were carefully measured and poured in a 250 mL three-neck round-bottom flask equipped with a magnetic stirrer at 400 rpm and a water-cooled condenser. The reaction was allowed to proceed for a specified reaction time (1 – 2 h). Then reaction mixture was cooled to 25 °C. After cooling, the mixture was centrifuged at 3000 rpm for 10 min and the catalyst was filtered using a vacuum filter. The liquid was left in a separating funnel for 3 h for separation. The glycerol layer was discharged, and the excess methanol was washed from the biodiesel layer five times using warm distilled water (80 – 100 °C) in a separatory funnel (The amount of water was about 30% of fuel volume). Finally, the produced fatty acid methyl esters (FAME_s) were collected and the biodiesel yield was calculated using Equation 1.

$$\text{Biodiesel yield (\%)} = \frac{\text{Weight of FAMEs}}{\text{Weight of oil}} \times 100 \quad (\text{Eq.1})$$

The catalyst was isolated from the reaction product in the first reaction, washed with methanol three times and dried at 60 °C in an oven for 2 h (25) and reused in the transesterification reaction in optimal conditions, the procedures were repeated three times.

2.6. Product Analysis

The resulting biodiesel from the transesterification reaction was analysed using appropriate ASTM standard methods. The following fuel properties were determined: density was determined using a 25 cm³ pycnometer at 15 °C temperatures,

according to Standard ASTM D-4052, viscosity, HK-1005A kinematic viscosity apparatus was used at a temperature of 40 °C according to Standard ASTM D-445, acid number was determined by dissolved the sample in a 50 cm³ of ethanol and the acid presented in the sample was titrated with 0.1 N potassium hydroxide solution. Flash point was determined using a method ASTM-D93, closed cup, at which application of an ignition source causes the vapours of a specimen to ignite under specified conditions of test. Water content of the sample was determined by aquamax Karl Fischer coulometric titration, pre-titration is performed automatically (19-24). The characteristics of the produced biodiesel were compared with ASTM D6751 (17) biodiesel standard and EN14214 (18) fossil diesel standards to confirm their acceptability as a fuel in diesel engines.

3. RESULTS AND DISCUSSION

3.1. Characterization of the WCO

In this study, the WCO used as a feedstock was characterized based on its physicochemical properties. The properties were summarized in Table 1. Free fatty acid (FFA) was measured to determine the availability of WCO for using in transesterification directly. Previous studies have suggested feedstock FFA content of less than 2% for transesterification process (26), and if the acid value is very high, WCO requires a pre-treatment to decrease its fatty acid content before the conversion to biodiesel to prevent saponification reaction. The obtained results of showed an acid number of 2.29 mg KOH/g of oil and FFA of 1.15%, this implies that the WCO could be directly converted into biodiesel via transesterification process. Regarding the density, it was determined at 25 °C to be 0.911 g/cm³, this value was in an agreement with those recorded by Mahesh et al. (1) and Yusuff et al. (27). The kinematic viscosity of WCO at 40°C was determined to be 34.09 mm²/s, and this value was in the range from 39.07 to 28.8 mm²/s, reported in previous studies (26,28,29). The flash point in this study was lower than that reported in the study done by Anisah et al. (26) as 247.7 °C. The value of the water content of the oil was much lower than the value determined in the previous study (30), the oil feedstock should be anhydrous (water content <0.3%). These data show that this feedstock is appropriate to obtain high ester yields.

Ten fatty acids were identified in WCO as shown in Table 2, the main fatty acids present in the WCO were linoleic acid (45.61%) followed by elaidic acid (33.86%), palmitic acid (10.32%) and stearic acid (4.80%). Approximately 45.61% of the fatty acids were found to be poly-unsaturated, 34.55% mono-unsaturated and 16.47% saturated fatty acids. The four main components were found in WCO: linoleic, elaidic, palmitic and stearic acids, were higher than that obtained in a previous study (31).

Table 1: Physicochemical properties of WCO.

Property	Experimental Values*
Acid value (mg KOH/g)	2.29
FFA (%)	1.15
Density at 25 °C (g/cm ³)	0.911
Viscosity at 40 °C (mm ² /s)	34.09
Flash point (°C)	206
Color	<4.0
Water count (%)	0.0017

* Values recorded as mean value.

Table 2: Chemical composition of WCO.

Fatty acid	IUPAC name	Formula	Structure	wt%
Linoleic	9,12-Octadecadienoic acid	C ₁₈ H ₃₂ O ₂	C18:2	45.61
Elaidic	9-Octadecenoic acid	C ₁₈ H ₃₄ O ₂	C18:1	33.86
Palmitic	Hexadecanoic acid	C ₁₆ H ₃₂ O ₂	C16:0	10.32
Stearic	Methyl stearate	C ₁₈ H ₃₆ O ₂	C18:0	4.80
Behenic	Docosanoic acid	C ₂₂ H ₄₄ O ₂	C22:0	0.80
Palmitoleic	9-Hexadecenoic acid	C ₁₆ H ₃₀ O ₂	C16:1	0.45
Myristic	Methyl tetradecanoate	C ₁₄ H ₂₈ O ₂	C14:0	0.19
Lignocerc	Tetracosanoic acid	C ₂₄ H ₄₈ O ₂	C24:0	0.19
Lauric	Dodecanoic acid	C ₁₂ H ₂₄ O ₂	C12:0	0.06
Phthalic	1,2-Benzenedicarboxylic acid, bis(2-methylpropyl)	C ₁₆ H ₂₂ O ₄	C16:0	0.05

* The obtained results in terms of fatty acid methyl esters from GC-MS library data system reviewed and the results listed out in the form of fatty acid chains.

3.2. Characterization of the Catalyst

The XRD analysis was conducted to determine the variation of the structure, amorphous content and degree crystallinity of the catalyst depicted in Figure 2. The XRD pattern of the catalyst show a diffraction peaks of KAlO₂ appears at 2θ of 17.06°, 22.89°, 32.86°, 33.71°, 34.11°, 37.24°, 37.66°, 39.52°, 42.67°, 68.16° and 89.83° which were attributed to orthorhombic type of AlKO₂ formed on the catalyst surface with lattice parameter (in Å) of 5.456, 10.9617 and 15.4893 for a, b and c respectively (Table 3). The AlKO₂ levels were observed to be consistent with the data obtained by the authors in

(32), whereby some diffraction were similar and the other rapprochement to that found in this study. The similar peaks were 17° and 34°. Meanwhile, the characteristic peaks of alumina at angles of 2θ = 37° and 67.21° were almost unchanged on the XRD pattern, indicating that Al₂O₃ still retained its amorphous structure. A similar pattern was obtained by Santos et al. (32). As in a previous studies (33, 34) the formation of K₂O₂ is clearly observed at 2θ = 31°, 33°, 34° and 42° (JCPDS file (50-05241). In this study the catalyst was successfully converted to desired species (K₂O₂) for the reaction.

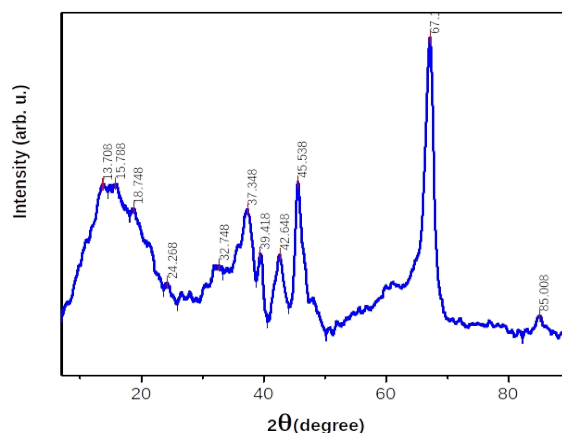
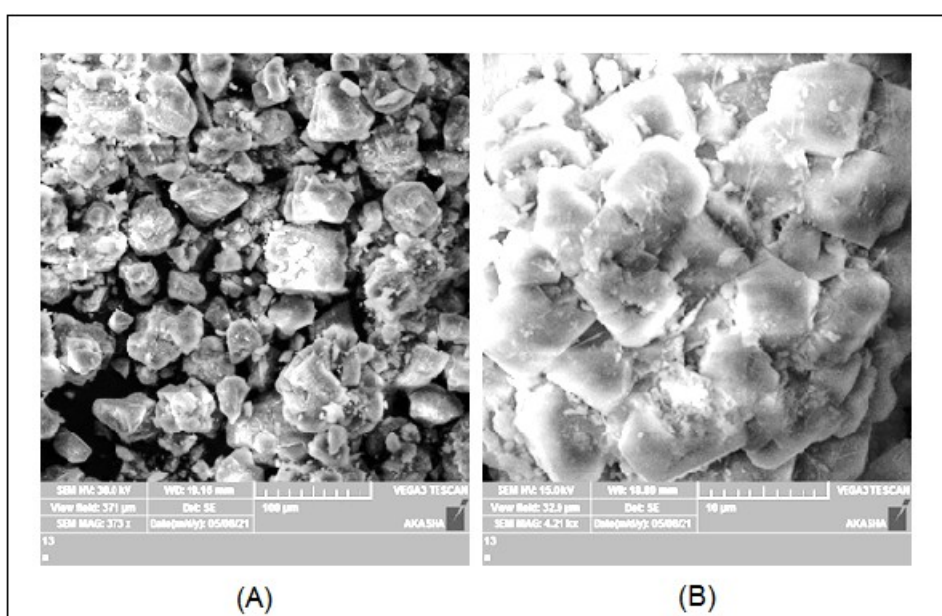
**Figure 1:** XRD pattern of the of KOH/Al₂O₃ catalyst.

Table 3: XRD matched peak analysis report.

Property	Amount
Formula sum	Al K O ₂
Peaks matched	17
Crystal system	Orthorhombic
Unit cell (Å)	a = 5.4560, b = 10.9617 and c = 15.4893
Calc. density (g/cm ³)	2.813
Degree of crystallinity (wt%)	12.46
Amorphous content (wt %)	87.54

The particle morphology of the catalyst was captured via SEM, and the micrograph of KOH/Al₂O₃ presented in Figure 2 shows the particles of aluminium oxide impregnated by potassium hydroxide. The catalyst has irregular crystallinity

and small sized crystals. Figure 2 clearly shows that there are no definite morphologies in the sample. It looks that the particles were agglomerated and form a cluster.

**Figure 2:** SEM image of KOH/Al₂O₃ catalyst.

The FTIR spectrum of the prepared KOH/Al₂O₃ in the range 400 – 4000 cm⁻¹ was shown in Figure 3. The spectrum shows an intensive band at 3500 cm⁻¹ belongs to the ν_s(Al)O-H stretching vibrations, three moderate bands observed at the frequencies of 1149, 1083 and 1026 cm⁻¹ can be attributed to the K-O bond and the four weak bands at 1732, 871, 813 and 617 cm⁻¹ are the combination bands. The absorption edge of the hydroxyl bands on the

surface was found at 1732 cm⁻¹. The bands appearing in the region of 600 – 870 cm⁻¹ include the tension of Al-O bonds, whereby aluminium exhibits vibrations extended in the region from 750 to 850 cm⁻¹. These absorption bands agree precisely with the ones previously reported in the literature (35) that introduced FTIR spectrum closed to that obtained in this study.

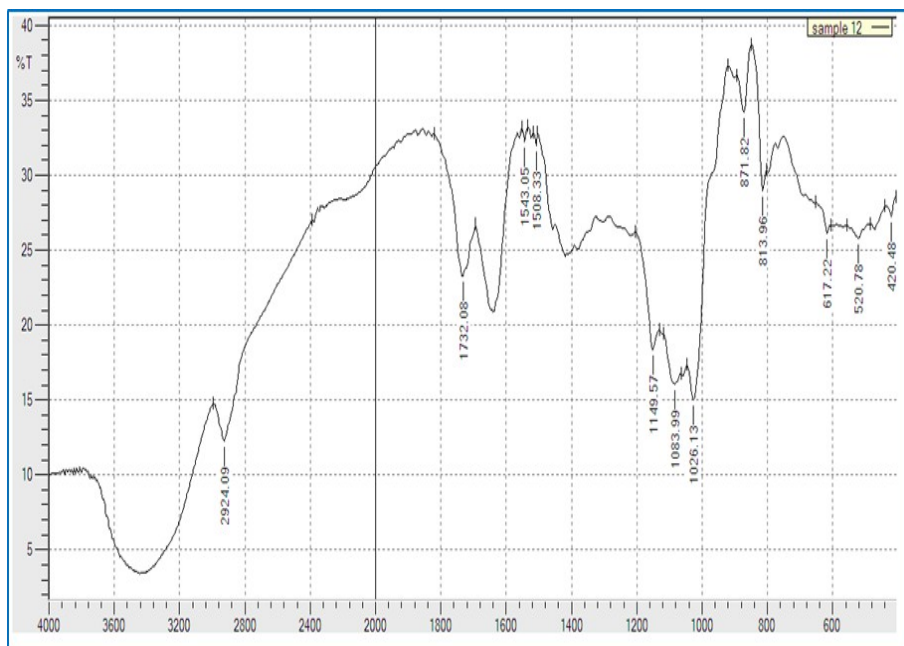


Figure 3: FTIR spectrum of KOH impregnated into Al₂O₃.

3.3. Transesterification Reaction

3.3.1. Effect of WCO/methanol molar ratio

The study of the influence of the WCO/methanol molar ratio (1:4; 1:5 and 1:6) was carried out at temperature of 50 °C for 1 h of reaction with 1% catalyst loading. Results in Figure 4 shows that the highest conversion was achieved with 1:4 WCO/methanol molar ratios, but afterwards shows a decline in conversion rate with the WCO/methanol

molar ratio going from 1:5 to 1:6. An excess methanol increases the solubility of the by-product (glycerol) which then may initiate the reversible reaction to reduce the conversion. The optimum methanol/oil molar ratio was observed at 1:4. This result is in line with the work of Gim bun et al. (36); they produced biodiesel from rubber seed oil and found that the 1:4 ratio was the best ratio for generating good biodiesel quality.

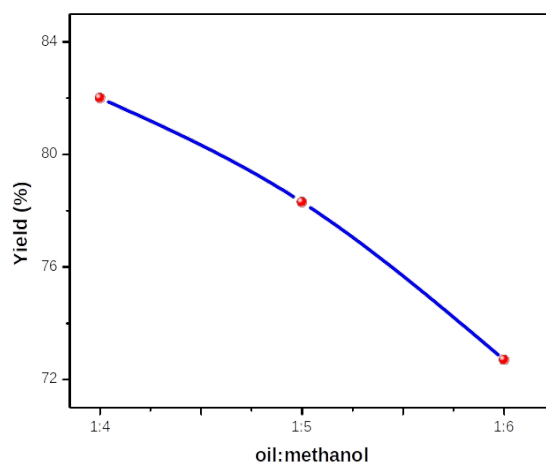


Figure 4: Effect of WCO /methanol molar ratio on biodiesel production.

3.3.2. Effect of the catalyst loading

The effect of KOH/Al₂O₃ catalyst loading (1 to 2 w/v %) on biodiesel yield was evaluated at oil to methanol ratio of 1:4, temperature of 55 °C with 1 h reaction time. It was shown in Figure 5 that the biodiesel yield increases from 84.5% to 86.6% as the catalyst loading increases from 1 to 1.5% and

decreased to 81.1 % afterwards. This might be due to the formation of more triglycerides in the saponification side reaction as a result of the excessive addition of catalyst (37). It was found that the optimum catalyst loading in this study was 1.5% with biodiesel conversion of 86.6%.

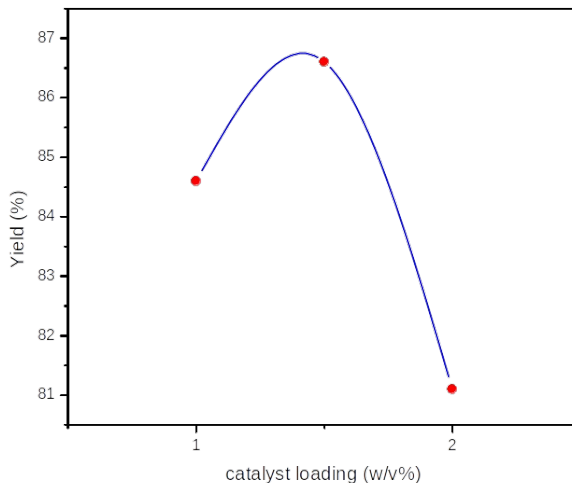


Figure 5: Effect of catalyst loading in biodiesel yield.

3.3.3. Effect of temperature

The effect of temperature on the transesterification of WCO was investigated by carrying out the experiments at a fixed WCO/methanol ratio of 1:4 and amount of catalyst of 1% (w/v %) with a reaction time of 1 h. The experimental temperature was in the range from 50 °C to 60 °C, as shown in Figure 6. It was observed that increasing the reaction temperature had a favourable influence on

the degree of transesterification. With a rise in temperature, the conversion rose at a faster rate. At higher reaction temperatures, however, there was an opportunity of methanol loss and product darkness increased. High reaction temperatures also increased the assembly cost of biodiesel. The optimum temperature for this reaction was found to be 55 °C due to the lower boiling point (64.5 °C) at which methanol evaporates (38).

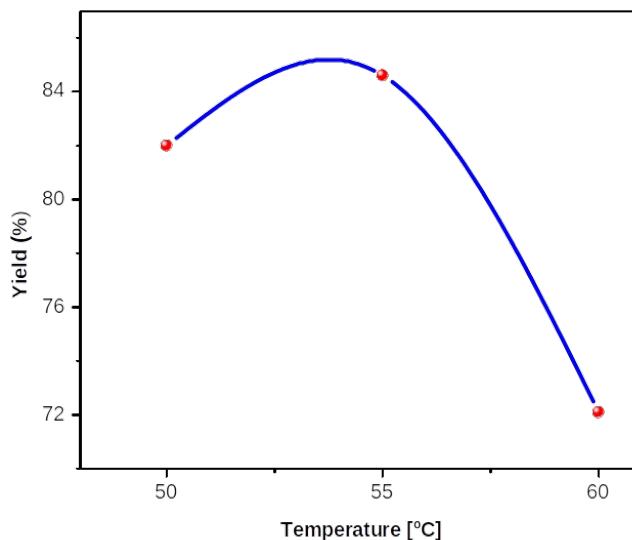


Figure 6: Effect of temperature in transesterification of WCO.

3.3.4. Effect of reaction time

The effect of reaction time was studied as it had a significant impact on the transesterification of waste cooking oil. The reaction time varied from 1 to 2 h in oil to methanol ratio of 1:4 with 1.5% catalyst loading at temperature of 55 °C. The transesterification reaction produces the maximum biodiesel yield of 86.6 % after 1 h of reaction. Almost all the oil has been transformed into methyl esters leading to a maximum conversion. However,

the yield decreased after 2 hours of the reaction. This may be due to the longer reaction time led to a reversible process that led to an increase in glycerides (37).

3.3.5. Reusability test

Catalyst reusability is an important aspect in the development of biodiesel. The reusability of the catalyst was determined at the optimum conditions for four cycles as shown in Figure 7 it was noticed

that after cycle 1 with yield of 86.6%, the cycle demonstrated a declining pattern of yield of biodiesel which was 68.7%, 60.6% and 51.5% for cycle 2, 3 and 4 respectively where the yield of biodiesel decreased due to a decrease in catalytic

activity. The reduction in catalytic activity was caused by the loss of catalyst during the filtration process, activation, and morphology change of the catalyst used (2).

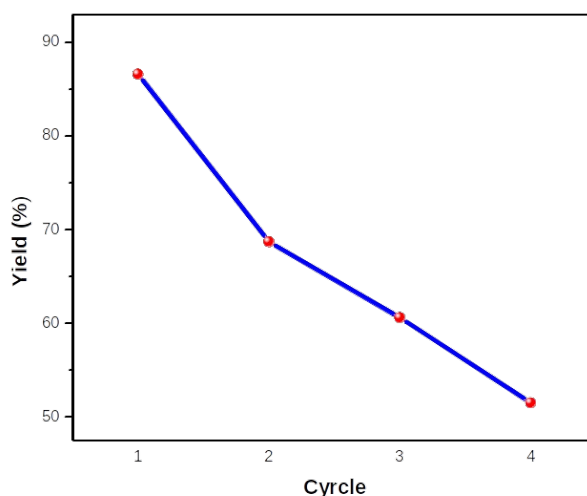


Figure 7: Reusability test for KOH/Al₂O₃ catalyst.

3.3.6. Characterization of produced biodiesel from WCO

By applying the aforementioned optimum conditions, the obtained biodiesel yield was ~ 86.6%. At molar ratio of 1:4, temperature 55 °C, catalyst loading 1.5% in 1 h. The produced biodiesel was evaluated on the basis of its fuel properties compared to ASTM 6751 (17) & EN 14214 (18) standards. Density, viscosity, acid number, flash point, and water content are the most important properties of biodiesel to measure the quality of the product.

Based on the data shown in Table 4 there isn't very much different from the ASTM 6751 (17) & EN 14214 (18) standards, except the viscosity still doesn't meet with the standards. This viscosity value is lower than that generated by Fathallah & Pinto, (39) and higher than Ashok et al. (40) and Ahmed et al. (41). However, because biodiesel is always combined with petroleum diesel in engine applications, the biodiesel in this study can be used as fuel (42).

Table 4: WCO biodiesel properties compared with ASTM & EN14214 Standards.

Property	WCO biodiesel	ASTM D6751	EN 14214
Density at 15 °C (g/mL)	0.8919	0.82-0.9	0.86-0.9
Viscosity at 40 °C (cSt)	7.428	1.9-6.0	3.5-5.0
Acid value (mg KOH/g)	0.54	0.50 max	0.50 max
Flash point (°C)	65	130 min	120 min
Color	<1.5	-	-
Water count (%)	0.0196	0.03 (v/v%)	500 (mg/kg)

4. CONCLUSION

The potential of potassium hydroxide supported on alumina (KOH/Al₂O₃) as heterogeneous catalyst for biodiesel production from peanut waste cooking oil (WCO) has been evaluated. The determined physicochemical properties of WCO make it an attractive alternative feedstock for biodiesel production. The optimal reaction conditions were: oil to methanol ratio 1:4 catalyst loading of 1.5%, reaction temperature of 55 °C, reaction time 1 h, with a yield of 86.6%. The fuel characteristics of the synthesized methyl ester from the WCO at the

optimal process conditions were found to be in accordance with the ASTM 6751 & EN 14214 standard specifications. Reusability test shows that the synthesized catalyst is reusable up to 4 times. The catalyst employed gave a good performance and easily separates from the product mixture. Thus, WCO is a promising feedstock for biodiesel and (KOH/Al₂O₃) is a promising catalyst for methyl ester synthesis via heterogeneous catalytic transesterification under milder reaction conditions.

5. CONFLICT OF INTEREST

The authors declare no conflict of interest.

6. ACKNOWLEDGMENTS

The authors are grateful to the International University of Africa, the Sudanese Thermal Generation Company, and General Directorate Petroleum Laboratories Research Studies- Ministry of Petroleum - Sudan for providing the laboratory facilities necessary to conduct this research work.

7. REFERENCES

1. Mahesh SE, Ramanathan A, Begum KMS, Narayanan A. Biodiesel production from waste cooking oil using KBr impregnated CaO as catalyst. *En Conv Manag.* 2015;91:442-50. [<DOI>](#).
2. Fitriana N, Husin H, Yanti D, Pontas K, Alam PN, Ridho M, et al. Synthesis of K₂O/zeolite catalysts by KOH impregnation for biodiesel production from waste frying oil. *IOP Conf Ser: Mater Sci Eng.* 2018;334:012011. [<DOI>](#).
3. Yan S, DiMaggio C, Mohan S, Kim M, Salley SO, Ng KYS. Advancements in heterogeneous catalysis for biodiesel synthesis. *Top Catal.* 2010;53:721-36. [<DOI>](#).
4. Abdullah SH, Hanapi NH, Azid A, Umar R, Juahir H, Khatoon H, Endut A. A review of biomass-derived heterogeneous catalyst for a sustainable biodiesel production. *Renew Sust En Rev.* 2017 Apr 1;70:1040-51. [<DOI>](#).
5. Simsek S. Effects of biodiesel obtained from Canola, sefflower oils and waste oils on the engine performance and exhaust emissions. *Fuel.* 2020;265:117026. [<DOI>](#).
6. Simsek S, Özdalyan B. Improvements to the composition of fusel oil and analysis of the effects of fusel oil-gasoline blends on a spark-ignited (SI) engine's performance and emissions. *Energies* 2018;11(3):625.
7. Simsek S, Uslu S. Comparative evaluation of the influence of waste vegetable oil and waste animal oil-based biodiesel on diesel engine performance and emissions. *Fuel.* 2020;280:118613. [<DOI>](#).
8. Barnwal BK, Sharma MP. Prospects of biodiesel production from vegetable oils in India. *Renewable and Sustainable Energy Reviews.* 2005;9(4):363-78. [<DOI>](#).
9. Şimşek S, Uslu S. Analysis of the effects of cetane improver addition to diesel on engine performance and emissions. *Int J Auto Eng Technol.* 2021:26-32. [<DOI>](#).
10. Demirbaş A. Chemical and fuel properties of seventeen vegetable oils. *En Sour.* 2003;25(7):721-8. [<DOI>](#).
11. Wicaksono A, Saptadi S, editors. Waste cooking oil into biodiesel transformation and its economical potency through circular economic model in Semarang Barat Area Indonesia. *E3S Web of Conf;* 2019: EDP Sci. [<DOI>](#).
12. Kayode B, Hart A. An overview of transesterification methods for producing biodiesel from waste vegetable oils. *Biofuels* 2019;10(3):419-37. [<DOI>](#).
13. Osorio-González CS, Gómez-Falcon N, Sandoval-Salas F, Saini R, Brar SK, Ramírez AA. Production of biodiesel from castor oil: A review. *Energies.* 2020;13(10):2467. [<DOI>](#).
14. Saini RD. Conversion of waste cooking oil to biodiesel. *International J Petrol Sci Technol.* 2017;11(1):9-21. [<URL>](#).
15. Raqeeb MA, Bhargavi R. Biodiesel production from waste cooking oil. *J Chem Pharm Res.* 2015;7(12):670-81. [<URL>](#).
16. Said N, Ani F, Said M. Review of the production of biodiesel from waste cooking oil using solid catalysts. *J Mech Eng Sci.* 2015;8:1302-11. [<DOI>](#).
17. ASTM. D 6751-20a: Standard specification for biodiesel fuel blend stock (B100) for middle distillate fuels. ASTM Int, West Conshohocken, PA, USA; 2020. [<URL>](#).
18. CEN. EN 14214:2008. Automotive fuels - Fatty acid methyl esters (FAME) for diesel engines - Requirements and test methods. CEN, European Committee for Standardization; 2008. [<URL>](#).
19. ASTM. D4052-18a. Standard test method for density, relative density, and API gravity of liquids by digital density meter ASTM Int, West Conshohocken, PA, USA; 2018. [<DOI>](#).
20. ASTM. D664-18. Standard test method for acid number of petroleum products by potentiometric titration. ASTM Int, West Conshohocken, PA, USA; 2018. [<URL>](#).
21. ASTM D445-21e1: standard test method for kinematic viscosity of transparent and opaque liquids (and calculation of dynamic viscosity). ASTM Int, West Conshohocken; 2021. [<URL>](#).
22. ASTM D93-20. Standard test methods for flash point by Pensky-Martens closed cup tester. ASTM Int, West Conshohocken, PA, USA; 2020. [<URL>](#).
23. ASTM D2709-16. Standard test method for water and sediment in middle distillate fuels by centrifuge. ASTM Int, West Conshohocken, PA, USA; 2016. [<URL>](#).
24. ASTM D1500-12. Standard test method for ASTM color of petroleum products (ASTM color scale). ASTM Int, West Conshohocken, PA, USA; 2012. [<URL>](#).
25. Helmi M, Hemmati A, Tahvildari K. Biodiesel production from *Amygdalus scoparia* using KOH/Al₂O₃ catalyst: optimization by response surface methodology. *Iran J En Environ.* 2021;12(1):34-44. [<DOI>](#).
26. Anisah PM, Suwandi, Agustian E. Effect of transesterification on the result of waste cooking oil conversion to biodiesel. *J Phys: Conf Ser.* 2019;1170:012067. [<DOI>](#).
27. Yusuff AS, Adeniyi OD, Azeez SO, Olutoye MA, Akpan UG. Synthesis and characterization of anthill-eggshell-Ni-Co mixed oxides composite catalyst for biodiesel production from waste frying oil. *Biofuels, Bioprod Bioref.* 2019;13(1):37-47. [<DOI>](#).
28. Hajy HT, Tahvildari K. Efficient Synthesis of biodiesel from waste cooking oil catalysed by Al₂O₃ impregnated with NaOH. *J Chem Petrol Eng (J Fac Eng).* 2015;49(2):143-51. [<URL>](#).

29. Patil PD, Gude VG, Reddy HK, Muppaneni T, Deng S. Biodiesel production from waste cooking oil using sulfuric acid and microwave irradiation processes. *J Environ Prot.* 2012;03(01):107-13. [<DOI>](#).
30. Priambodo R, Chen TC, Lu MC, Gedanken A, Liao JD, Huang YH. Novel technology for bio-diesel production from cooking and waste cooking oil by microwave irradiation. *En Proc.* 2015 Aug 1;75:84-91. [<DOI>](#).
31. Samuel O., Waheed M., Bolaji B., Dairo O. Production of biodiesel from Nigerian restaurant waste cooking oil using blender. *International J Renew En Res.* 2013; 3(4): 976-979. [<URL>](#).
32. Santoso A, Sumari, Urfa Zakiyya U, Tiara Nur A. Methyl ester synthesis of crude palm oil off grade using the K_2O/Al_2O_3 catalyst and its potential as biodiesel. *IOP Conf Ser: Mater Sci Eng.* 2019;515:012042. DOI: [<DOI>](#).
33. NollHakim L, Shohaimi NA, Ibrahim ML, Mokhtar WN, Ab Halim AZ. Transesterification of Waste Cooking Oil Utilizing Heterogeneous K_2CO_3/Al_2O_3 and KOH/Al_2O_3 Catalysts. *Malay Inst Chem.* 2021;23(2):74-83. [<DOI>](#).
34. Lokman NollHakim MAH, Shohaimi NAM, Mokhtar WNAW, Ibrahim ML, Abdullah RF. Immobilization of potassium-based heterogeneous catalyst over alumina beads and powder support in the transesterification of waste cooking oil. *Catalysts.* 2021;11(8):976. [<DOI>](#).
35. Haghazari N, Abdollahifar M, Jahani F. The effect of NaOH and KOH on the characterization of mesoporous AIOOH nanostructures in the hydrothermal route. *J Mex Chem Soc.* 2014 Jun;58(2):95-8. [<URL>](#).
36. Gim bun J, Ali S, Kanwal CC, Shah LA, Ghazali NH, Cheng CK, Nurdin S. Biodiesel production from rubber seed oil using a limestone based catalyst. *Adv Mater Phys Chem.* 2012 Oct 26;2(04):138-41. [<DOI>](#).
37. Kusumo F, Shamsuddin AH, Ahmad AR, Dharma S, Milano J, Silitonga AS, et al. Production of biodiesel from *Jatropha curcas* mixed with waste cooking oil assisted by ultrasound. *IOP Conf Ser: Earth Environ Sci.* 2020 Apr 1;476(1):012082. [<DOI>](#).
38. Ding J, Xia Z, Lu J. Esterification and deacidification of a waste cooking oil (TAN 68.81 mg KOH/g) for biodiesel production. *Energies.* 2012 Jul 25;5(8):2683-91. [<DOI>](#).
39. Fathallah AZM, Pinto F. The Influence of NaCl dissolved on biodiesel of used cooking oil on performance and its degradation of main components of diesel engine. *IOP Conf Ser: Earth Environ Sci.* 2022;972(1):012030. [<DOI>](#).
40. Ashok A, Kennedy LJ, Vijaya JJ, Aruldoss U. Optimization of biodiesel production from waste cooking oil by magnesium oxide nanocatalyst synthesized using coprecipitation method. *Clean Technol Environ Pol.* 2018 Aug;20(6):1219-31. [<DOI>](#).
41. Ahmed, H. M., Abdeldaim, S. O., & Erwa, I. Y. (2021). Production of biodiesel from heat-treated edible oil. *J Phys: Conf Ser*, 2063(1), 012027. [<DOI>](#).
42. Abdullah, Rahmawati Sianipar RN, Ariyani D, Nata IF. Conversion of palm oil sludge to biodiesel using alum and KOH as catalysts. *Sus Environ Res.* 2017;27(6):291-5. [<DOI>](#).



A Highly Sensitive Non-Enzymatic Sensor for the Determination of Glucose Based on Aniline-2-sulfonic acid-Modified Cu Electrode

Melih Besir Arvas^{1*} 

¹Istanbul University Department of Chemistry, Istanbul, 34134, Turkey

Abstract: Herein, the copper-based electrodes were successfully synthesized with galvanostatic electrodeposition method. The effect of materials obtained at different concentrations of ASA and anodization times on glucose sensing ability was investigated. During the anodization of copper foil in the presence of ASA molecules, it formed a tree branch-like structure connected to each other while decorating the electrode surface. The Cu(30)/ASA(0.02) electrode exhibited a relatively wide linear range (0.2 – 10.0 mM) and a low detection limit (0.826 μ M). These excellent activities were mainly attributed to the surface morphology, which functions as highly active sites and enhanced electronic conductive pathways with the addition of ASA. In addition, the stability obtained together with the excellent sensing ability in beverages makes the electrodes useful for practical applications.

Keywords: Copper foil, anodization method, glucose, non-enzymatic sensor, aniline 2-sulfonic acid.

Submitted: October 01, 2022. **Accepted:** December 26, 2022.

Cite this: Arvas MB. A Highly Sensitive Non-Enzymatic Sensor for the Determination of Glucose Based on Aniline-2-sulfonic acid-Modified Cu Electrode. JOTCSA. 2023;10(1):227-40.

DOI: <https://doi.org/10.18596/jotcsa.1182942>.

***Corresponding author. E-mail:** mbesirarvas@gmail.com.

1. INTRODUCTION

In various industries, such as clinical diagnosis, medicine, and the food business, it is critical to create fast, practical, and reliable methods for determining glucose. Because most diabetics are unaware of the early indicators of the condition, regular blood sugar monitoring and exact detection are essential for diagnosing and controlling this life-threatening disease. Because of their excellent sensitivity and selectivity, most electrochemical glucose biosensors on the market today are made primarily with the glucose oxidase enzyme for blood glucose detection in various body fluids (1-3). However, enzymatic glucose sensors have some drawbacks, such as enzyme denaturation, high cost, low chemical stability, and expensive manufacturing methods, hence enzyme-free glucose sensors are being developed to replace enzymatic glucose sensors. Enzyme-free glucose sensors appear to be a promising alternative to enzyme-based glucose sensors, although existing non-enzymatic glucose sensors still require significant sensitivity and selectivity improvements. Researchers are

particularly interested in studies that focus on developing stable, simple, repeatable, low-cost non-enzymatic glucose sensors and synthesizing more sensitive materials.

Non-enzymatic electrodes, such as electrodes modified with noble metals, metal alloys, and metal nanoparticles, have been developed with a lot of effort (4-9). Copper and copper oxide-based materials, for example, are low-cost, non-toxic semiconductors with good electrochemical and catalytic characteristics (10). By adjusting the process conditions, different morphologies of copper and copper oxide-based materials can be synthesized using simple procedures (11). Furthermore, their nanostructures have distinct characteristics, such as a large surface area, low density, and the existence of active sites even on the interior surfaces (12,13). Previous research has looked into copper and copper oxide-based materials' high catalytic activity in alkaline solutions for glucose detection. Jiang et al. described a non-enzymatic glucose sensor electrode made of Cu NPs with nitrogen-doped graphene as the sensing

component (14). Zhang et al. used a simple substrate-assisted electroless deposition (SAED) process to create a flexible enzyme-free glucose amperometric biosensor on free-standing reduced graphene oxide (rGO) membranes using a laser-induced graphene (Cu NPs-LIG) composite (15). Anand et al. reported a sensitive nonenzymatic glucose sensor based on copper nanowires (CuNWs)/polyaniline (PANI)/reduced graphene oxide (rGO) nanocomposite ink by solvothermal mixing of CuNWs, PANI, rGO and binders (16). Phetsang et al. developed a non-enzymatic glucose sensor based on a screen-printed carbon electrode modified with copper(II) and reduced graphene oxide (17). Controllable morphology investigations are carried out with the doped form formed by adding a dopant in order to improve the sensitivity of the copper-based glucose sensor. Aniline 2-sulfonic acid (ASA) may be promising as a dopant with sulfo groups because the sulfonic acid group is defined by the maximum degree of dissociation (18,19). Because of the sulfo groups and nitrogen atoms in the monomer chain structure, aniline 2-sulfonic acid (ASA) has not yet been explored as a doping at copper electrode material (20).

We used a simple one-step anodization procedure to make tree branch-shaped CuO-Cu₂O/copper/aniline 2-sulfonic acid directly on copper foil. The synthesis technique, which uses copper foil as both a current collector and a copper source, simplifies electrode fabrication while simultaneously increasing charge efficiency with additives for increased sensor sensitivity. Scanning electron microscopy (SEM), energy distribution spectrum (EDS), X-ray diffraction (XRD), Fourier-transform infrared spectroscopy (FT-IR), and electrochemical tests were used to characterize the aniline 2-sulfonic acid modified copper foil electrode. Compared to Cu(30) electrodes and many other non-enzymatic glucose sensors, the Cu(30)/ASA/(0.03) electrode for glucose sensors has good electrocatalytic capabilities for glucose oxidation and detection. This new electrode material, which takes advantage of ASA's functional groups, promises to be an outstanding non-enzymatic glucose sensor with high sensitivity, excellent selectivity, a wide detection range, and excellent surface properties.

2. EXPERIMENTAL

2.1. Chemicals and Reagents

Acetone (C₃H₆O, ≥99.9%), ethanol absolute (C₂H₅OH, ≥97.9%), sodium hydroxide (NaOH, ≥97.0%), copper(II) sulfate pentahydrate (CuSO₄·5H₂O, ≥98.0%), were purchased from Sigma Aldrich. Copper foil (99.9%) was provided by Alfa Aesar. All beverage samples were obtained from the local market for real samples analysis. Distilled water

(Milli-Q, 18 MΩ.cm resistivity) was used to prepare all the aqueous solutions.

2.2. Synthesis of Tree Branch-Shaped CuO-Cu₂O/copper/aniline-2-sulfonic acid Electrode

The electrodes were prepared by controlled galvanostatic electrodeposition method. Copper electrodes were cleaned with ethanol, acetone, deionized water in the ultrasonic bath for 15 min to remove contaminants on the electrode surface and dried at the room temperature overnight, respectively. In a typical synthesis procedure, a constant current of 0.5 A cm⁻² is applied for 30 s in a two-electrode cell. Cu foil (1×3 cm²) was used as a cathode electrode for the electrochemical deposition and another piece of Cu foil used as an anode electrode. The effect of electrochemical deposition time on the growth of the copper oxides was investigated at anodization times of 10, 20, 30, 40 and 50 second in 0.4 M CuSO₄ and 1.5 M H₂SO₄ electrolyte solution. Then, CuO-Cu₂O/copper/aniline 2-sulfonic acid electrodes were prepared under similar electrochemical conditions by adding in the presence of between 0.005, 0.01, 0.02, 0.03, 0.04, 0.05 M ASA concentration (see Table 1). The prepared electrodes were thoroughly rinsed with distilled water and ethanol several times, and dried in an oven at 60 °C for 3 hours. The obtained electrodes were used as the sensing material for sensitive glucose detection.

2.3. Characterization

Scanning electron microscopy (SEM) and energy distribution spectrum (EDS) were used to examine the surface morphologies and elemental analyses of the electrodes prepared using Zeiss EVO® LS 10 SEM, USA. Fourier-transform infrared spectroscopy (FT-IR) for the analysis of chemical structure was recorded Perkin Elmer Spectrum 100 spectrophotometer. X-RAY diffractometer (XRD, PANalytical X'Pert PRO Cu) at 45 kV and 2θ range of 10-80° was used to determine the phase and crystallinity of the structures coated on the electrode surface.

2.4. Electrochemical Measurements

All electrodes were tested using Ivium Vertex Instruments Potentiostat/Galvanostat (Ivium Technologies B.V, Netherlands) and recorded with the IviumSoft Potentiostat/Galvanostat software. The electrochemical sensor was carried out based on four methods in applications, cyclic voltammetry (CV), differential pulse voltammetry (DPV), chronoamperometry (CA) and electrochemical impedance spectroscopy (EIS). In the presence of probable interfering substances such as ascorbic acid, lactic acid, uric acid, maltose, lactose, and urea, the selectivity of the sensor electrode was studied.

Table 1: The ratio of raw materials used in sensor electrode samples.

Sample	Anodization Time (s)	ASA (M)
Cu	-	-
Cu(10)	10.0	-
Cu(20)	20.0	-
Cu(30)	30.0	-
Cu(40)	40.0	-
Cu(50)	50.0	-
Cu(30)/ASA/(0.005)	30.0	0.005
Cu(30)/ASA/(0.01)	30.0	0.01
Cu(30)/ASA/(0.02)	30.0	0.02
Cu(30)/ASA/(0.03)	30.0	0.03
Cu(30)/ASA/(0.04)	30.0	0.04
Cu(30)/ASA/(0.05)	30.0	0.05

2.5. Preparation of Real Samples

All beverage samples were obtained from local shops for real sample analysis. In order to detect glucose in real samples by electrochemical methods, beverage samples such as cola, fruit juice and ice tea were placed directly into the test cell. To perform the sensor sensitivity of electrode, 10 mL of NaOH (0.1 M) electrolyte was added so that the real sample concentrations were 5.0 mM.

3. RESULTS AND DISCUSSION

As the material has highly porous interfaces, it is a promising material for sensor electrodes. The sensor properties of this material produced at different anodization times were systematically tested using cyclic voltammetry measurement. The electrochemical properties of copper samples were investigated with a cyclic voltammetry (CV) method in 1.0 M NaOH solution within presence of 5 mM glucose in a potential window of -0.2 V to 1.0 V with

scan rate of 50 mV s^{-1} . Figure 1a shows that all electrodes had an oxidation peak in the region of 0.3–0.6 V, which can be attributed to Cu(II) to Cu(III) conversion. Kuwana et al. reported the most widely accepted method of glucose oxidation at the CuO electrode in an alkaline media (21). Cu(III) oxidation could catalyse glucose oxidation to gluconolactone, which could then be further oxidized to glucose acid (22). Among all the electrodes, Cu(30) showed the highest anodic current peak indicating the highest electrocatalytic performance. As shown in Figure 1a the cyclic voltammograms of anodized copper in various times, 30 seconds was obtained as the optimum time as Cu oxidized at that time and it improved the surface properties of the sensor. In order to improve the electrochemical performance of Cu(30) electrodes, the electrodes were anodized in the presence of ASA concentration and cyclic voltammetry (CV) and electrochemical impedance spectroscopy (EIS) measurements were used to investigate the effect of ASA in Figure 1b and 1c.

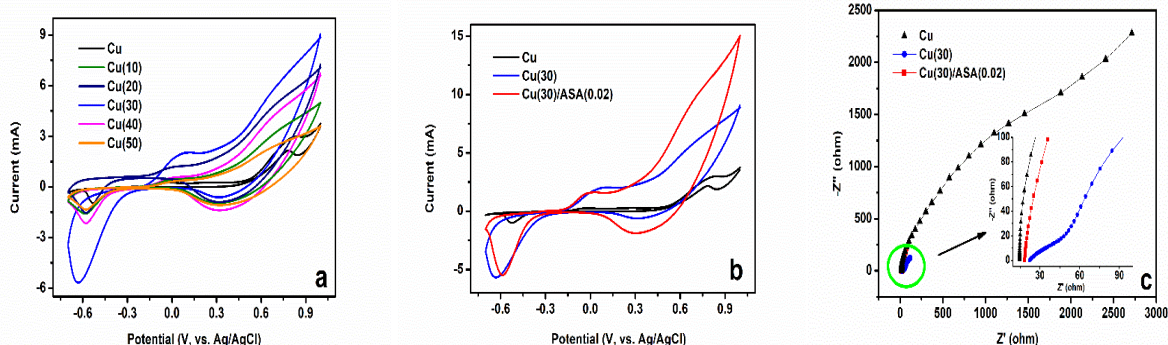


Figure 1: (a) Cyclic voltammograms of the copper electrodes in 1.0 M NaOH in presence of 5 mM glucose with scan rate of 50 mV s^{-1} ; (b) Cyclic voltammograms of the Cu, Cu(30) and Cu(30)/ASA(0.02) electrodes in 1.0 M NaOH in presence of 5 mM glucose with scan rate of 50 mV s^{-1} ; (c) Electrochemical impedance spectra of the Cu, Cu(30) and Cu(30)/ASA(0.02) electrodes in 1.0 M NaOH in presence of 5 mM glucose the inset is the enlarged with region of the high frequency.

With the synthesized Cu(30)/ASA(0.02) electrode, ASA improved the electrochemical activity and surface area, and the corresponding cyclic

voltammograms were shown in Figure 1b. The sensor Cu(30)/ASA(0.02) electrode with higher electrochemical properties has more activity than

anodized Cu(30) and bare copper (Cu) electrode sensors. The ASA modified electrode acted as electron mediators, enhancing the synergistic effect. Thus, the selectivity of the electrode against the glucose was improved. This result can also be related to the porous structure of the Cu(30)/ASA(0.02) electrode's wide surface area following anodization with the addition of ASA to the medium.

Figure 1c showed the electrochemical impedance spectra (EIS) of Cu, Cu(30) and Cu(30)/ASA(0.02) electrodes in 0.1 M NaOH solution from 0.01 Hz to 10000 Hz. The resulting Nyquist curves were fitted according to the equivalent simple circuit model. Solution resistance, charge transfer resistance, double layer capacitance, and Warburg impedance are represented by the impedances R_s , R_{ct} , C_{dl} , and W , respectively. R_s is the ohmic resistance and is the resistivity of the electrolyte and corrosion products on the surface. R_{ct} , on the other hand, was linked to the velocity resistance that governs the corrosion reaction. W is connected to the diffusion rate of mobile ions to the electrode surface, whereas C_{dl} is related to the capacitive behaviour of the electrodes. The R_s values of Cu, Cu(30) and Cu(30)/ASA(0.02) electrodes were 15.73 Ω , 22.76 Ω and 17.83 Ω , respectively. After anodization of copper for 30 seconds, the R_s value of the Cu(30)/ASA(0.02) electrode synthesized by adding ASA to the anodization medium was lower. The R_{ct} values of Cu, Cu(30) and Cu(30)/ASA(0.02) electrodes were 1338 Ω , 47.68 Ω and 23.49 Ω , respectively. The R_{ct} value of the Cu(30)/ASA(0.02) electrode obtained after the anodization process with the addition of ASA decreased by almost half compared to the Cu(30) electrode. The C_{dl} values of Cu, Cu(30) and Cu(30)/ASA(0.02) electrodes were 34.89e-6, 110.4e-6 and 124.7e-6, respectively. When the electrode was anodized with ASA for 30 seconds, the capacitive behaviour of the electrode improved. Cu, Cu(30), and Cu(30)/ASA(0.02) electrodes had W impedance values of 17.31e-3, 4.33e-3, and 14.39e-3, respectively. The sulfonyl groups in ASA had a favourable effect on electrode surface, lowering charge transfer resistance and accelerating ion diffusion rates. As a result, electron transfer on the electrode surface was accelerated, and the electrode's selectivity against the analyte was enhanced. The influence of the ASA concentration on the anodization of copper electrode for sensor applications was investigated using cyclic voltammetry and electrochemical impedance spectroscopy. Figure 2a shows a comparison of electrochemical tests utilizing a three-electrode system in 0.1 M NaOH electrolyte from a -0.7 V to 1.0 V potential window with a scan rate of 50 mV s⁻¹ in the presence of ASA concentrations ranging from 0.005 to 0.05 M. At the cyclic voltammogram, the Cu(30)/ASA(0.02) containing 0.02 M ASA showed the maximum current density rise. To consider the electrocatalytic activity between the electrodes due to the concentration difference, the

higher catalytic activity of Cu(30)/ASA(0.02) could be attributed to two reasons. First, it could be that the Cu(30)/ASA(0.02) electrode has high electrode surface area due to the well-dispersed negative charge of ASA during its synthesis. Because ASA contains sulfonic acids with a high protonation degree and electrical conductivity characteristics in its molecular structure (23-25). Therefore, it may have raised the deposition efficiency of copper oxide on the electrode surface, which was directly related to its catalytic activity on glucose oxidation. The addition of less or more 0.02 M ASA, on the other hand, may have resulted in decreased copper oxide electrocatalytic activity for glucose oxidation. As a result, the ASA content in the Cu(30) electrodes was optimized to 0.02 M.

Figure 2b shows the Nyquist curves of EIS analyses of Cu(30)/ASA electrodes made with various ASA concentrations. The equivalent simple circuit model was used to fit the Nyquist curves. The impedance values of R_s , R_{ct} , C_{dl} , and W were investigated in the electrode impedance analyses. The Cu(30)/ASA(0.005) electrode had the lowest R_s value, which was 16.69. Cu(30)/ASA(0.01), Cu(30)/ASA(0.02), Cu(30)/ASA(0.03), Cu(30)/ASA(0.04), and Cu(30)/ASA(0.05) electrodes had R_s values of 21.89, 18.55, 22.76, 27.14, and 31.08 respectively. Because they were performed under the same experimental conditions, the R_s values were close to one other, but there were minor differences. In the anodization process of the electrodes, an increase in R_s values occurred at increasing concentrations after 0.02 M ASA concentration. The R_{ct} values of Cu(30)/ASA(0.005), Cu(30)/ASA(0.01), Cu(30)/ASA(0.02), Cu(30)/ASA(0.03), Cu(30)/ASA(0.04) and Cu(30)/ASA(0.05) electrodes were 17.74 Ω , 21.68 Ω , 23.49 Ω , 31.25 Ω , 33.46 Ω , and 38.89 Ω , respectively. While R_{ct} values changed more in increasing concentrations after 0.02 M ASA concentration, semi-circle formation related to R_{ct} formed in Nyquist curves was also observed clearly. The results showed that when the concentration of ASA added to the medium during the anodization process increases, charge transfer to the surface becomes more difficult. The C_{dl} values of Cu(30)/ASA(0.005), Cu(30)/ASA(0.01), Cu(30)/ASA(0.02), Cu(30)/ASA(0.03), Cu(30)/ASA(0.04), and Cu(30)/ASA(0.05) electrodes were 68.96e-6, 89.34e-6, 124.7e-6, 45.81e-6, 30.49e-6 and 23.35e-6, respectively. The W impedance values of Cu(30)/ASA(0.005), Cu(30)/ASA(0.01), Cu(30)/ASA(0.02), Cu(30)/ASA(0.03), Cu(30)/ASA(0.04) and Cu(30)/ASA(0.05) electrodes were 10.06e-3, 11.89e-3, 14.39e-3, 6.61e-3, 4.43e-3 and 2.96e-3, respectively. The highest diffusion rate ratio was obtained in Cu(30)/ASA(0.02) electrode. Similar to the downward trend in R_{ct} values, W impedance values also decreased after 0.02 M ASA concentration. Excessive amount of ASA added to the medium affected the anodization negatively and slowed down the ion transfer and ion transfer rate.

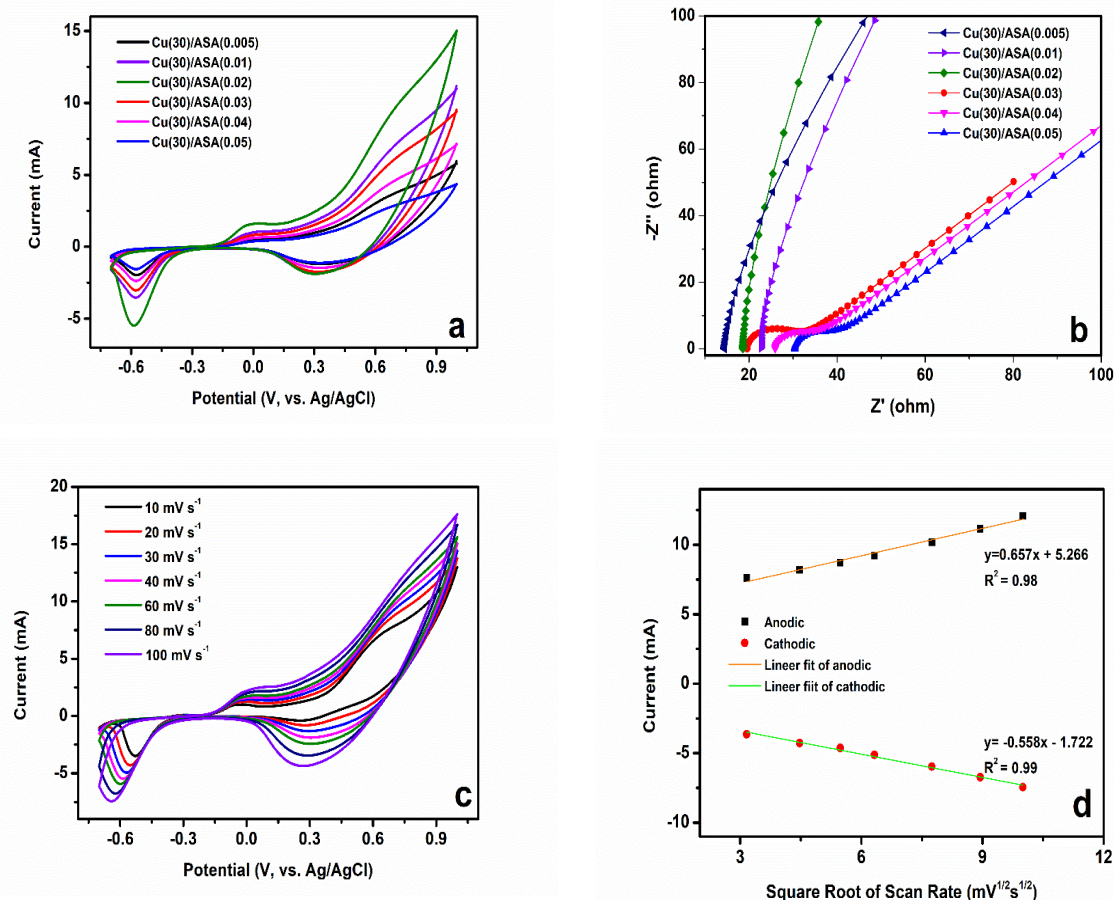
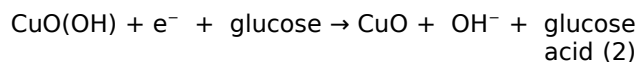


Figure 2: (a) CV of synthesized Cu(30) electrodes in the presence of various ASA concentration, (b) EIS spectra of synthesized Cu(30) electrodes in the presence of various ASA concentration, (c) Effect of scan rate on the CV of Cu(30)/ASA(0.02) in 5 mM of glucose at varying the scan rate from 10, 20, 30, 40, 60, 80 and 100 mV s⁻¹, (d) corresponding plot of peak current versus square root of scan rate for Cu(30)/ASA(0.02) electrode.

Figure 2c shows the rate performance of cyclic voltammetry in a three-electrode system with a platinum counter electrode and an Ag/AgCl reference electrode in 0.1 M NaOH electrolyte solution in the presence of 5 mM glucose solution at scan rates of 10 to 100 mV s⁻¹ with a voltage ranging from 0.7 V to 1.0 V. Peak currents gradually rose when scan rates were raised up to 100 mV s⁻¹. Redox current peaks were clearly visible in Figure 2d, and glucose oxidation at the anodic peak current (I_{pa}) altered proportionally with the scan rate. When the current linearity curves were plotted against the scanning speed, the findings revealed that two straight lines with good linearity were achieved, anodic and cathodic (R^2 a: 0.983, R^2 c: 0.998). It's clear that Cu(30)/ASA(0.02) has good electrochemical activity

for glucose detection. The possible reaction mechanism was given below (26)(27):



The major processes occurring in CuO-based sensors are presented in equations (1) and (2) to allow electro-oxidation of glucose. The electro-oxidation of glucose by redox active ions ($\text{Cu}^{2+}/\text{Cu}^{3+}$) in the form of CuO/CuO(OH) complexes is a generally established non-enzymatic process. Furthermore, glucose sensing with a non-enzymatic CuO-based glucose sensor necessitates a medium with a high pH (13) (28).

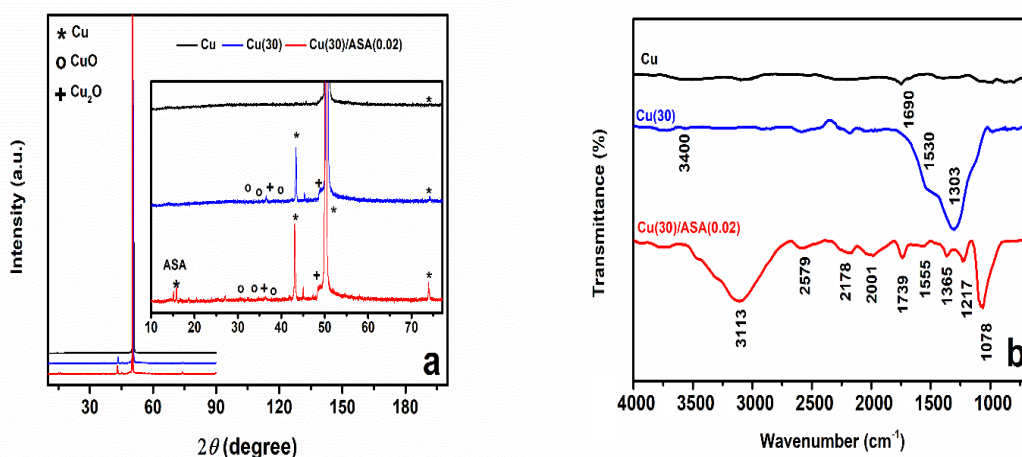


Figure 3: a) XRD patterns and b) FTIR spectra of the Cu, Cu(30) and Cu(30)/ASA(0.02) electrodes.

Cu, Cu(30), and Cu(30)/ASA(0.02) electrodes were examined using XRD analysis to investigate the crystal structure and phase composition, as shown in Figure 3a. At $2\theta = 43.35, 50.47,$ and 74.16° , three prominent reflection peaks were found, indicating the (1 1 1), (2 0 0), and (2 2 0) crystal planes of the copper metal structure, respectively (JCPDS No. 02-1225) (29). An unknown peak was also observed at all three electrodes at $2\theta = 45.34^\circ$. Since the copper used in the experiments was not a high purity research grade product, it was possible for the material to contain unknown impurities. The different peaks were observed and defined in the XRD spectrum of Cu(30) grown on copper plate. The crystal structure and phase composition of the Cu(30) electrode can be linked to the cubic Cu substrate's (111), (200), and (220) planes. The copper metal corresponding peak observed in the sample may originate from copper under-layer or voids in the Cu(30) and Cu(30)/ASA(0.02) electrodes. The structure of monoclinic CuO (JCPDS no. 45-0937) and the structure of cubic Cu₂O could be the additional diffraction peaks besides Cu indicated with symbols (JCPDS no. 05-0667) (30,31).

The stretching vibrations of the O-H bond in air, molecular water adsorbed on the surface of Cu plate were characterized in the FTIR spectrum of Cu plate displayed in Figure 3b at 3407 cm^{-1} (32).

Furthermore, a vibration of O-H bond was also observed around 1690 cm^{-1} , indicating that the associated hydroxyl groups were chemically poorly absorbed due to atmospheric molecular water (33). The formation of O₂ adsorption on CuO was confirmed by the formation of the intense $\nu(\text{O-O})$ band around 1530 cm^{-1} (34). The variation of the intensity of the peaks with the anodization of copper can be attributed to the change in crystallinity. The C=O bond was attributed to the band at 1303 cm^{-1} , indicating that components from the electrolyte media were included into the formed oxide (26). A various peak forms were observed in the FTIR spectrum, which shows the structural change of the Cu(30)/ASA(0.02) electrode with the addition of aniline 2-sulfonic acid to the medium. The peak at 3113 cm^{-1} may be attributed to the interaction between the copper oxide and the N-H group of ASA, hydrogen bond formation between the copper oxide and the N-H group of ASA at the electrode surface (35).

For Cu(30)/ASA(002), the bands at $2579\text{ cm}^{-1}, 2178\text{ cm}^{-1},$ and 2001 cm^{-1} were caused by aromatic C-H stretching C=O group was given to the band at 1739 cm^{-1} . The C=C stretching quinonoid and benzenoid rings of ASA were responsible for the bands at 1555 cm^{-1} and 1365 cm^{-1} , while the C-N stretching of the benzenoid units of ASA was relevant for the bands at 1217 cm^{-1} and 1078 cm^{-1} (18,19,35).

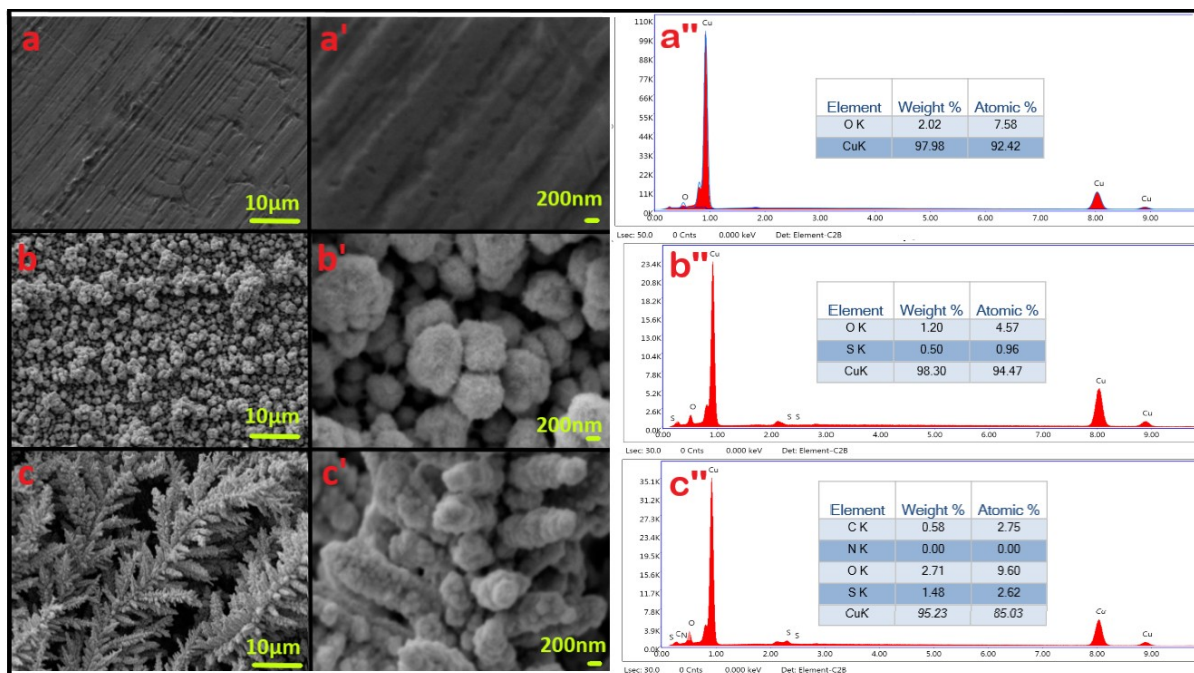


Figure 4: Comparison of the SEM images, EDS spectra for (a, a', a'')cCu electrode, (b, b',b'') Cu(30) electrode and (c, c',c'') Cu(30)/ASA(0.02) electrode.

The SEM images and EDS analysis of the surface of the copper-based electrodes were shown in Figure 4. Numerous CuO/Cu₂O microstructures coated uniformly agglomerates are shown in Figure 4 (b,b''). The homogeneous clusters were formed on the entire surface of the electrode and grain sizes are about ~0.1 µm. When the SEM image was examined at a higher magnification, it was seen that there were two different morphologies. The structures of needle with a diameter and length of about 200 nm and the other one was flower-like aggregates about a few microns in diameter in shown in the surface of Cu(30) electrode. As shown in Figure 4 (c,c''), interestingly, tree branch-shaped copper oxide structure observed in the presence of 0.02 M ASA concentration. When the SEM image was examined with a higher magnification, it was observed that there were nanoparticles 200 nm below the Cu(30)/ASA(0.02) electrode surface. When the SEM photographs are examined, the synthesized material exhibits an active rough structure at extremely nanoscale. The Cu(30)/ASA(0.02) electrode was much more porous, allowing electrooxidation to occur for the glucose sensor due to the availability of free interspace and increased surface area. It was in agreement with the

electrochemical results that the Cu(30)/ASA(0.02) sensor showed a higher sensitivity than others.

The elemental distributions of the electrodes were determined by EDS measurement and the EDS spectrum of Cu, Cu(30) and Cu(30)/ASA(0.02) was presented in Figure 4 (a'',b''c'') and the percentage of elements was tabulated in the figures. EDS is an important technique for determining the atomic composition of elements in materials. EDS analysis also confirms that ASA interacts with the electrode surface during copper anodization process. The fundamental peaks of Cu and O are observed in all the EDS spectrums. The element S in the EDS spectrum of copper, which was also anodized in sulfuric acid electrolyte solution, originated from the electrolyte in the medium (36). Atomic percentage of Cu(30)/ASA(0.02) compared to atomic percentage of Cu(30), it was observed that the percentage of element S increased significantly with the addition of ASA. The atomic percentage of S increased from 0.96% to 2.62% as shown in Figure 4b'' and 4c''. Furthermore, EDS analysis showed Cu(30)/ASA (0.02) composition consisting of C, N, O, S and Cu elements included in the ASA added to the synthesis medium without other impurities.

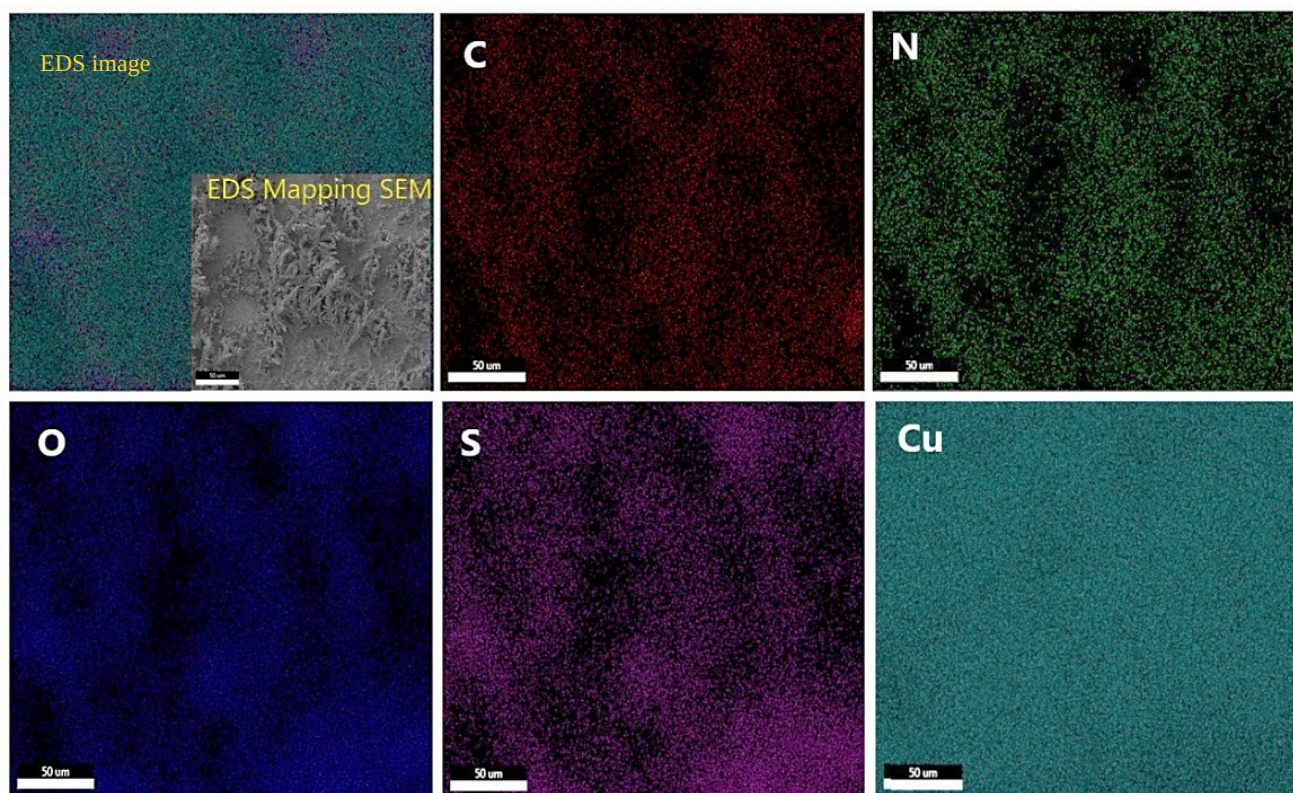


Figure 5: Elemental mapping of Cu(30)/ASA(0.02) electrode.

EDS mapping analyses of Cu(30)/ASA(0.02) are shown in Figure 5. In EDS mappings where the elements appear to be completely homogeneously distributed, it was observed that copper oxide and ASA showed good chemical interaction. The growth of copper oxides on certain active surfaces with the addition of ASA in the SEM morphology also proved this analysis.

Figure 6a demonstrated the electrocatalytic response of Cu(30)/ASA(0.02) electrode for the detection of the different concentrations of glucose (0.2, 0.5, 1.0, 2.0, 3.0, 5.0, 7.0 and 10.0 mM) in DPV technique (DPV parameters; step potential = 0.0050 V; modulation amplitude = 0.0250 V; modulation time = 0.20 s and interval time-0.5 s). Cu(30)/ASA(0.02) clearly exhibits a high degree of electrocatalytic activity for glucose detection. The size of the wave around 0.35 V to 0.65 V gradually increased as the glucose concentration raised for the Cu(30)/ASA(0.02) electrode. A good correlation was exhibited between glucose concentrations and peak currents (Figure 6b).

Typically, glucose oxidation peak current risen linearly with glucose concentration for values between 0.2 and 10 mM with correlation coefficient (R^2) as 0.998. The lowest detection limits for glucose (LOD) were found to be 0.826 μM ($S/N=3$) (Figure 6) ($\text{LOD} = 3\sigma/S$; the standard deviation and S is the sensitivity). Similarly, Cu(30)/ASA(0.02) was tested by cyclic voltammetry to examine glucose sensitivity. The glucose oxidation peak was seen at

0.35-0.65 V, and the oxidation current increased as the glucose concentration increased from 0.2 to 10.0 mM, as shown in Figure 6c. Table 2 shows the electrochemical sensor parameters for the glucose sensor, as well as prior publications using copper electrodes. It's worth noting that the Cu(30)/ASA(0.02) sensor's performance is comparable to that of prior investigations.

Some biological samples in the biological sample can be quickly oxidized at a positive potential, causing glucose detection to be interfered. As shown in Figure 7, the selectivity of the Cu(30)/ASA(0.02) electrode over glucose was investigated using various interfering species such as maltose, lactose, ascorbic acid, uric acid, lactic acid, and urea. Amperometric tests were used to analyse the electrolyte solution of 0.1 M NaOH. By adding 0.1 mM interfering agents and 2 mM glucose solution to a constantly stirred 0.1 M NaOH solution, the interaction of these electroactive biological samples was examined. As a result, in the presence of other biological species, the Cu(30)/ASA(0.02) electrode was better suited for glucose determination. This supports the idea that the Cu(30)/ASA(0.02) electrode's high surface area will give more sensitive selectivity for glucose detection under physiological settings, as it enhances selective glucose oxidation. Several factors are likely to have influenced this remarkable selectivity behaviour. First, because ASA reduces copper oxide agglomeration, the electrode material lasts longer. Second, tree branch-shaped copper oxide allows for

quick ion/electron transfer between the electrode and the electrolyte contact, resulting in improved sensing performance.

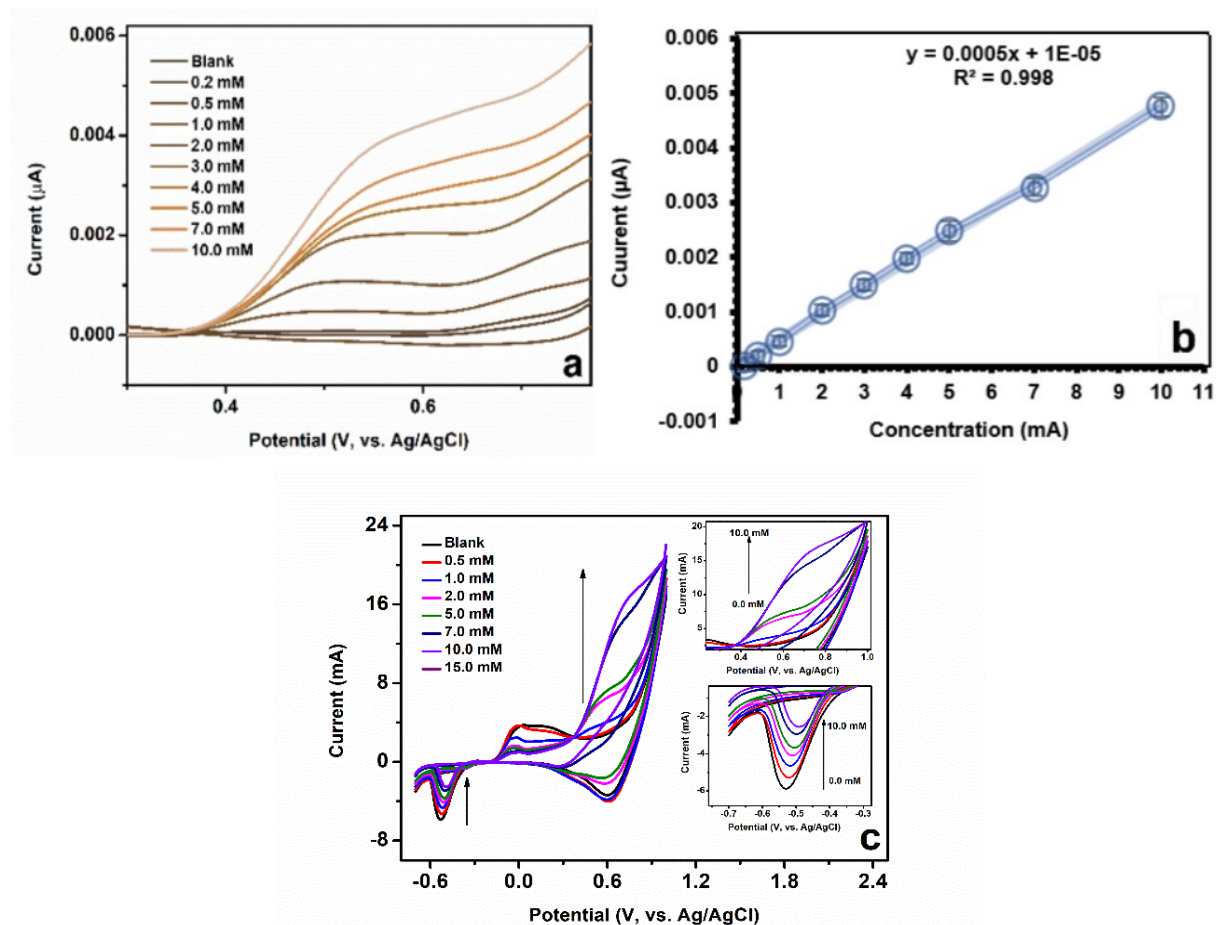


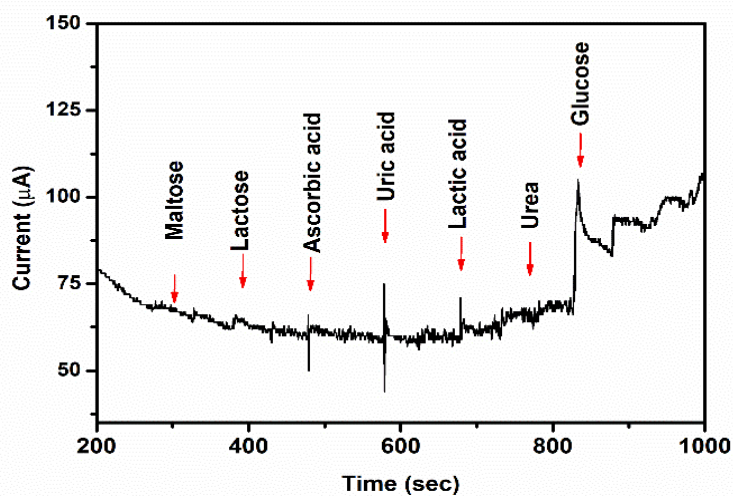
Figure 6: (a) Differential pulse voltammogram of Cu(30)/ASA(0.02) electrode in 1.0 M NaOH for values between 0.2 and 10 mM of glucose, (b) a plot of current density with respect to the concentration, (c) CV of Cu(30)/ASA(0.02) electrode in 1.0 M NaOH for values between 0.2 and 10 mM of glucose.

The sensor electrode's repeatability and stability were further tested using five separate electrodes and the addition of a 5.0 mM glucose solution in 0.1 M NaOH. The results demonstrate that the relative standard deviation value (RSD) was 2.41%, indicating that the sensor was reliable and repeatable. The sensor's stability was assessed over a 28-day period by assessing its sensitivity to 5.0 mM glucose. The sensitivity was tested every seven days after the same procedures were repeated and stored at room temperature. The electrode recovered 94 percent of the time, according to the results. The results show that it can be used in practical uses for most common analyses.

Glucose detection in real samples such as cherry juice, cola, and iced tea drinks was performed to assess the practical use of the Cu(30)/ASA(0.02) electrode. Drinks diluted with multiple applications of glucose standards were introduced to 0.1 M NaOH to determine glucose concentration in real samples. Figure 8 shows the result of the measurements (DPV parameters: step potential 0.0050 V, modulation amplitude 0.0250 V, modulation duration 0.20 s, and interval time 0.5 s.). Cherry juice, cola, and iced tea had average glucose concentrations of 4.3 ± 0.19 , 5.2 ± 0.24 , and 4.8 ± 0.21 mM, with RSDs of 3.31%, 3.89%, and 3.49% respectively. The electrode was found to be capable of sensing glucose in both real samples and in different types of beverages.

Table 2: List of copper-based non-enzymatic glucose sensors.

Electrode materials	Analyte	Linear range	Limit of detection	Ref.
CuO/GCE	0.1 M PBS	5 μ M-15 mM	1.42 μ M	(26)
Copper-salen	0.5 M KCl	4.0-69 μ M	1.2 μ M	(37)
CuCo-CFs/Nafion/GC electrode	0.1 M NaOH	0.02-11 mM	1.0 μ M	(38)
CuO/PANI-NF/FTO	0.1 M NaOH	0.25 μ M to 4.6 mM	0.24 μ M	(39)
CuO/NiO/PANI/GCE	0.1 M NaOH	0.02-2.5 mM	2.0 μ M	(40)
CuO-U	0.1 M NaOH	1.0 μ M to 10.0 mM	1.74 μ M	(41)
CuS nanosheets/Cu ₂ O/CuO NWAs/Cu foil	0.1 M NaOH	0.002-4.1 mM	0.89 μ M	(42)
CuO-C-dots	0.1 M NaOH	0.5-2.0 and 2.0-5.0 mM	200 μ M	(43)
CuO-flower	0.1 M NaOH	0.001-1 mM	0.25 μ M	(44)
CuO micro-/nanostructures	0.1 M NaOH	0.9-16 mM	20.0 μ M	(45)
Cu(30)/ASA(0.02)	0.1 M NaOH	0.2-10.0 mM	0.83 μ M	(This work)

**Figure 7:** Amperometric response of the interference study of different samples in 0.1 M NaOH at potential 0.5 V.

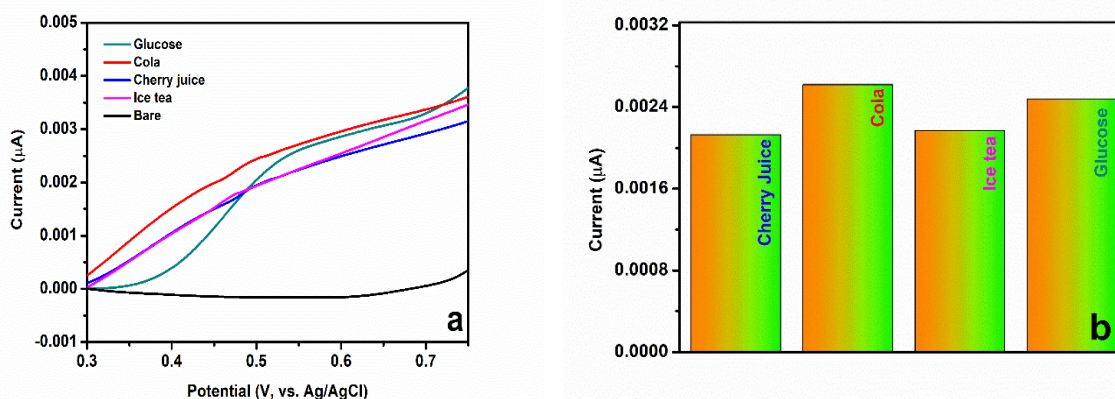


Figure 8: (a) DPV voltammogram, (b) the current density obtained DPV of different types of beverages in the real sample.

4. CONCLUSION

In this work, a new electrode material of Cu(30)/ASA(0.02) was synthesized and characterized for the non-enzymatic glucose sensor applications. In order to obtain a new electrochemical sensor for the prepared electrode, the effect of ASA added in the medium during the anodization of the copper foil was investigated for glucose. The electrode material was explored structurally and morphologically, as it provides a conductive path for quick electron/ion transfer to copper and facilitates harsh redox conditions by effectively increasing the active surface area. The electrode demonstrated an outstanding glucose sensing performance with acceptable sensitivity and a linear range analytical response, 0.2 to 10.0 mM, with a 0.826 μM limit of detection in DPV analysis for sensor application. Furthermore, the developed electrode has the potential to detect glucose in biological and food samples due to appropriate selectivity, stability, and great sensing performance in real beverages.

5. ACKNOWLEDGMENTS

M.B. Arvas especially thanks Prof. Dr. Yuçel Şahin for his valuable contributions to this study.

6. REFERENCES

1. Yoo E-H, Lee S-Y. Glucose Biosensors: An Overview of Use in Clinical Practice. *Sensors* [Internet]. 2010 May 4;10(5):4558-76. Available from: [<URL>](#).
2. Khor SM, Choi J, Won P, Ko SH. Challenges and Strategies in Developing an Enzymatic Wearable Sweat Glucose Biosensor as a Practical Point-Of-Care Monitoring Tool for Type II Diabetes. *Nanomaterials* [Internet]. 2022 Jan 10;12(2):221. Available from: [<URL>](#).
3. Osuna V, Vega-Rios A, Zaragoza-Contreras EA, Estrada-Moreno IA, Dominguez RB. Progress of Polyaniline Glucose Sensors for Diabetes Mellitus Management Utilizing Enzymatic and Non-Enzymatic Detection. *Biosensors* [Internet]. 2022 Feb 22;12(3):137. Available from: [<URL>](#).
4. Hassan MH, Vyas C, Grieve B, Bartolo P. Recent Advances in Enzymatic and Non-Enzymatic Electrochemical Glucose Sensing. *Sensors* [Internet]. 2021 Jul 8;21(14):4672. Available from: [<URL>](#).
5. Malekzad H, Sahandi Zangabad P, Mirshekari H, Karimi M, Hamblin MR. Noble metal nanoparticles in biosensors: recent studies and applications. *Nanotechnol Rev* [Internet]. 2017 Jun 27;6(3):301-29. Available from: [<URL>](#).
6. Barbee B, Muchharla B, Adedeji A, Karoui A, Kumar Sadasivuni K, Sha MS, et al. Cu and Ni Co-sputtered heteroatomic thin film for enhanced nonenzymatic glucose detection. *Sci Rep* [Internet]. 2022 May 7;12(1):7507. Available from: [<URL>](#).
7. Pourbeyram S, Mehdizadeh K. Nonenzymatic glucose sensor based on disposable pencil graphite electrode modified by copper nanoparticles. *J Food Drug Anal* [Internet]. 2016 Oct 1;24(4):894-902. Available from: [<URL>](#).
8. Yazar S, Kurtulbaş E, Ortaboy S, Atun G, Şahin S. Screening of the antioxidant properties of olive (*Olea europaea*) leaf extract by titanium based reduced graphene oxide electrode. *Korean J Chem Eng* [Internet]. 2019 Jul 25;36(7):1184-92. Available from: [<URL>](#).
9. Kurtulbaş E, Yazar S, Ortaboy S, Atun G, Şahin S. Evaluation of the phenolic antioxidants of olive (*Olea europaea*) leaf extract obtained by a green approach: Use of reduced graphene oxide for electrochemical analysis. *Chem Eng Commun* [Internet]. 2020 Jul 2;207(7):920-32. Available from: [<URL>](#).
10. Białaś K, Moschou D, Marken F, Estrela P. Electrochemical sensors based on metal nanoparticles with biocatalytic activity. *Microchim Acta* [Internet]. 2022 Apr 2;189(4):172. Available from: [<URL>](#).
11. Liu X, Cui S, Sun Z, Du P. Copper oxide nanomaterials synthesized from simple copper salts as active catalysts for electrocatalytic water oxidation. *Electrochim Acta* [Internet]. 2015 Apr 1;160:202-8. Available from: [<URL>](#).

12. Arvas MB, Gencten M, Sahin Y. One-step synthesized N-doped graphene-based electrode materials for supercapacitor applications. *Ionics (Kiel)* [Internet]. 2021 May 5;27(5):2241-56. Available from: [<URL>](#).
13. Mansuroglu A, Arvas MB, Kiraz C, Sayhan B, Akgumus A, Gencten M, et al. N-Doped Graphene Oxide as Additive for Fumed Silica Based Gel Electrolyte of Valve Regulated Lead Acid Batteries. *J Electrochem Soc* [Internet]. 2021 Jun 1;168(6):060512. Available from: [<URL>](#).
14. Jiang D, Liu Q, Wang K, Qian J, Dong X, Yang Z, et al. Enhanced non-enzymatic glucose sensing based on copper nanoparticles decorated nitrogen-doped graphene. *Biosens Bioelectron* [Internet]. 2014 Apr 15;54:273-8. Available from: [<URL>](#).
15. Zhang Y, Li N, Xiang Y, Wang D, Zhang P, Wang Y, et al. A flexible non-enzymatic glucose sensor based on copper nanoparticles anchored on laser-induced graphene. *Carbon N Y* [Internet]. 2020 Jan 1;156:506-13. Available from: [<URL>](#).
16. Anand VK, Bhatt K, Kumar S, Archana B, Sharma S, Singh K, et al. Sensitive and Enzyme-Free Glucose Sensor Based on Copper Nanowires/Polyaniline/Reduced Graphene Oxide Nanocomposite Ink. *Int J Nanosci* [Internet]. 2021 Apr 10 [cited 2023 Feb 26];20(02):2150020. Available from: [<URL>](#).
17. Phetsang S, Kidkhunthod P, Chanlek N, Jakmune J, Mungkornasawakul P, Ounnunkad K. Copper/reduced graphene oxide film modified electrode for non-enzymatic glucose sensing application. *Sci Rep* [Internet]. 2021 Apr 29;11(1):9302. Available from: [<URL>](#).
18. Yazar S, Arvas MB, Sahin Y. An ultrahigh-energy density and wide potential window aqueous electrolyte supercapacitor built by polypyrrole/aniline 2-sulfonic acid modified carbon felt electrode. *Int J Energy Res* [Internet]. 2022 May 9;46(6):8042-60. Available from: [<URL>](#).
19. Arvas MB, Yazar S, Sahin Y. Electrochemical synthesis and characterization of self-doped aniline 2-sulfonic acid-modified flexible electrode with high areal capacitance and rate capability for supercapacitors. *Synth Met* [Internet]. 2022 Apr 1;285:117017. Available from: [<URL>](#).
20. Sokolova MP, Bobrova N V., Dmitriev IY, Vlasov P V., Smirnov NN, Elyashevich GK, et al. Anticorrosion activity of aniline-aniline-2-sulfonic acid copolymers on the steel surface. *Russ J Appl Chem* [Internet]. 2016 Mar 15;89(3):432-8. Available from: [<URL>](#).
21. Marioli JM, Kuwana T. Electrochemical characterization of carbohydrate oxidation at copper electrodes. *Electrochim Acta* [Internet]. 1992 Jun;37(7):1187-97. Available from: [<URL>](#).
22. Li Z, Chen Y, Xin Y, Zhang Z. Sensitive electrochemical nonenzymatic glucose sensing based on anodized CuO nanowires on three-dimensional porous copper foam. *Sci Rep* [Internet]. 2015 Nov 2;5(1):16115. Available from: [<URL>](#).
23. Wang G, Ding Y, Wang F, Li X, Li C. Poly(aniline-2-sulfonic acid) modified multiwalled carbon nanotubes with good aqueous dispersibility. *J Colloid Interface Sci* [Internet]. 2008 Jan 1;317(1):199-205. Available from: [<URL>](#).
24. Şahin Y, Pekmez K, Yıldız A. Electropolymerization and in situ sulfonation of aniline in water-acetonitrile mixture containing FSO₃H. *Synth Met* [Internet]. 2002 Nov;131(1-3):7-14. Available from: [<URL>](#).
25. Şahin Y, Pekmez K, Yıldız A. Electrochemical preparation of soluble sulfonated polymers and aniline copolymers of aniline sulfonic acids in dimethylsulfoxide. *J Appl Polym Sci* [Internet]. 2003 Nov 21;90(8):2163-9. Available from: [<URL>](#).
26. Sudha V, Murugadoss G, Thangamuthu R. Structural and morphological tuning of Cu-based metal oxide nanoparticles by a facile chemical method and highly electrochemical sensing of sulphite. *Sci Rep* [Internet]. 2021 Feb 9;11(1):3413. Available from: [<URL>](#).
27. Abunahla H, Mohammad B, Alazzam A, Jaoude MA, Al-Qutayri M, Abdul Hadi S, et al. MOMSense: Metal-Oxide-Metal Elementary Glucose Sensor. *Sci Rep* [Internet]. 2019 Apr 2;9(1):5524. Available from: [<URL>](#).
28. Strakosas X, Selberg J, Pansodtee P, Yonas N, Manapongpun P, Teodorescu M, et al. A non-enzymatic glucose sensor enabled by bioelectronic pH control. *Sci Rep* [Internet]. 2019 Jul 26;9(1):10844. Available from: [<URL>](#).
29. Jayarathne RMHH, Pitigala PKDDP, Perera VP. Electronic and structural properties of Cu₂O polycrystalline thin films grown on adhesive copper tape. *Proc Tech Sess* [Internet]. 2019 [cited 2023 Feb 26];35:31-8. Available from: [<URL>](#).
30. He D, Wang G, Liu G, Suo H, Zhao C. Construction of leaf-like CuO-Cu₂O nanocomposites on copper foam for high-performance supercapacitors. *Dalt Trans* [Internet]. 2017;46(10):3318-24. Available from: [<URL>](#).
31. Volanti DP, Keyson D, Cavalcante LS, Simões AZ, Joya MR, Longo E, et al. Synthesis and characterization of CuO flower-nanostructure processing by a domestic hydrothermal microwave. *J Alloys Compd* [Internet]. 2008 Jul 14;459(1-2):537-42. Available from: [<URL>](#).
32. Petrov T, Markova-Deneva I, Chauvet O, Nikolov R, Denev I. SEM and FT-IR spectroscopy study of Cu, Sn and Cu-Sn nanoparticles. *J Univ Chem Technol Metall* [Internet]. 2012;47(2):197-206. Available from: [<URL>](#).
33. Diraz Uribe CE, Vallejo Lozada WA, Martinez Ortega F. Synthesis and characterization of TiO₂ thin films doped with copper to be used in photocatalysis. *Iteckne*. 2013;10(1):16-20.
34. Abd-Elnaiem AM, Abdel-Rahim MA, Abdel-Latief AY, Mohamed AA-R, Mojsilović K, Stepniowski WJ. Fabrication, Characterization and Photocatalytic Activity of Copper Oxide Nanowires Formed by Anodization of Copper Foams. *Materials (Basel)* [Internet]. 2021 Sep 2;14(17):5030. Available from: [<URL>](#).
35. Hesari Z, Shirkavand Hadavand B. Synthesis and Study on Conductivity of Urethane Acrylate/Polyaniline/CuO Nanocomposites. *J Appl Chem Res* [Internet]. 2018;12(4):66-77. Available from: [<URL>](#).
36. Yazar S, Atun G. Electrochemical synthesis of tunable polypyrrole-based composites on carbon fabric for wide potential window aqueous supercapacitor. *Int J Energy Res* [Internet]. 2022 Aug 27;46(10):14408-23. Available from: [<URL>](#).

37. Dadamos TRL, Teixeira MFS. Electrochemical sensor for sulfite determination based on a nanostructured copper-salen film modified electrode. *Electrochim Acta* [Internet]. 2009 Jul 30;54(19):4552-8. Available from: [<URL>](#).
38. Li M, Liu L, Xiong Y, Liu X, Nsabimana A, Bo X, et al. Bimetallic MCo (M=Cu, Fe, Ni, and Mn) nanoparticles doped-carbon nanofibers synthesized by electrospinning for nonenzymatic glucose detection. *Sensors Actuators B Chem* [Internet]. 2015 Feb 1;207:614-22. Available from: [<URL>](#).
39. Esmaeeli A, Ghaffarinejad A, Zahedi A, Vahidi O. Copper oxide-polyaniline nanofiber modified fluorine doped tin oxide (FTO) electrode as non-enzymatic glucose sensor. *Sensors Actuators B Chem* [Internet]. 2018 Aug 1;266:294-301. Available from: [<URL>](#).
40. Ghanbari K, Babaei Z. Fabrication and characterization of non-enzymatic glucose sensor based on ternary NiO/CuO/polyaniline nanocomposite. *Anal Biochem* [Internet]. 2016 Apr 1;498:37-46. Available from: [<URL>](#).
41. Mamleyev ER, Weidler PG, Nefedov A, Szabó DV, Islam M, Mager D, et al. Nano- and Microstructured Copper/Copper Oxide Composites on Laser-Induced Carbon for Enzyme-Free Glucose Sensors. *ACS Appl Nano Mater* [Internet]. 2021 Dec 24;4(12):13747-60. Available from: [<URL>](#).
42. Wei C, Zou X, Liu Q, Li S, Kang C, Xiang W. A highly sensitive non-enzymatic glucose sensor based on CuS nanosheets modified Cu₂O/CuO nanowire arrays. *Electrochim Acta* [Internet]. 2020 Feb 20;334:135630. Available from: [<URL>](#).
43. Sridara T, Upan J, Saianand G, Tuantranont A, Karuwan C, Jakmunee J. Non-Enzymatic Amperometric Glucose Sensor Based on Carbon Nanodots and Copper Oxide Nanocomposites Electrode. *Sensors* [Internet]. 2020 Feb 2;20(3):808. Available from: [<URL>](#).
44. Ashok A, Kumar A, Tarlochan F. Highly efficient nonenzymatic glucose sensors based on CuO nanoparticles. *Appl Surf Sci* [Internet]. 2019 Jul 1;481:712-22. Available from: [<URL>](#).
45. Anu Prathap MU, Kaur B, Srivastava R. Hydrothermal synthesis of CuO micro-/nanostructures and their applications in the oxidative degradation of methylene blue and non-enzymatic sensing of glucose/H₂O₂. *J Colloid Interface Sci* [Internet]. 2012 Mar 15;370(1):144-54. Available from: [<URL>](#).



Novel Well-defined Polystyrene-*block*-Poly(lactide-co-glycolide) Block Copolymers

Ozcan Altintas* 

Department of Chemistry, University of Minnesota, Minneapolis, Minnesota 55455, United States

Abstract: A facile preparation of polystyrene-*block*-poly(lactide-co-glycolide) PS-*b*-PLGA block copolymers was reported in detail. Well-defined PS-*b*-PLGA block copolymers were successfully obtained via living anionic polymerization and ring-opening polymerization. First, hydroxyl-terminated linear polystyrenes were prepared by living anionic polymerization. The resulting polymers were used as macroinitiators for ring-opening copolymerization of lactide and glycolide in the presence of the 1,8-diazabicyclo[5.4.0]undec-7-ene (DBU) as a catalyst in dichloromethane at ambient temperature. Transesterification and formation of DBU-initiated polymers were minimized by optimizing the catalyst concentration. Three block copolymers were synthesized in various molecular weights from 5000 g/mol to 33600 g/mol with low polydispersity. The formation of well-defined PS-*b*-PLGA block copolymers was followed by nuclear magnetic resonance spectroscopy and size-exclusion chromatography. Thermal properties of the block copolymers were investigated by thermal gravimetric analysis and differential scanning calorimetry. The morphology of the block copolymers was investigated using small-angle X-ray scattering in the bulk and via grazing incidence small-angle X-ray scattering as well as atomic force microscopy in thin film demonstrating organized nanostructures with uniform domain sizes. Overall, this manuscript describes an expanded polymer toolbox for PLGA-based polymers for next-generation lithography applications.

Keywords: Block copolymers, polystyrene, polyester, morphology, and phase separation.

Submitted: October 12, 2022. **Accepted:** January 09, 2023.

Cite this: Altintas O. Novel Well-defined Polystyrene-*block*-Poly(lactide-co-glycolide) Block Copolymers. JOTCSA. 2023;10(1):241-52.

DOI: <https://doi.org/10.18596/jotcsa.1184492>.

***Corresponding author. E-mail:** ozcanaltintas@gmail.com.

1. INTRODUCTION

Block polymers consist of chemically different sub-chains which are covalently attached at junction points (1). Block polymers have gained significant interest in many fields of nanotechnology applications such as fabrication of nanomaterials (2), nanoporous films (3), storage media (4), sensors (5) and nanolithography (6). Block polymers in the bulk or thin film have demonstrated remarkable ability to form well-defined nanostructures because of their microphase separation on the nanoscale (7,8). Block polymer thin films spontaneously produce various well-defined equilibrium morphologies in bulk and solution ranging from spheres, cylinders, lamellae, and more complex structures. The resulting morphologies depend on the following parameters: the number of monomeric units in a block copolymer and the volume fraction

of domains as well as the Flory-Huggins parameter (9-11). Lamellae and cylindrical phases are of particular interest in industry (12).

Reversible deactivation radical polymerization (RDRP) techniques (13) such as atom transfer radical polymerization (ATRP) (14,15), reversible addition-fragmentation chain transfer (RAFT) polymerization (16,17) and nitroxide-mediated polymerization (NMP) (18) are the most versatile methods to design and control polymer structure. However, the RDRP methods have their own limitations, including the use of transition metals and sulfur-containing final products as well as slow polymerization rates (19). Among all the living polymerization techniques, anionic polymerization is a unique method for the preparation of polymers with uniform structures (20,21). Well-defined telechelic linear polymers consisting of one or more

functional groups at chain-ends can readily be prepared via living anionic polymerization (21). These functional polymers can be utilized as building blocks such as macroinitiators and cross-linkers for the synthesis of various polymer architectures (22).

Recent years, aliphatic polyesters of lactones and lactides were achieved by ring opening polymerization (ROP) (23-25) have attracted substantial interest due to bacterial decomposition process and forming natural byproducts (26). They have been practiced in various applications ranging from biomedical industries (25) to ordered nanostructured morphologies (19). For example, nanoporous materials can be readily generated from microphase separation of block copolymers having aliphatic polyester and subsequently selective removing of the polyester domains (27,28).

Because of the poor solubility of glycolide and its polymers in common solvents, controlled polymerization of glycolide has been challenging task (29). The copolymerization of lactide and glycolide represents an efficient method to synthesize soluble poly(glycolide) (PGA) derivatives. Hoyer and coworkers developed a strategy for PLGA-based block copolymers and commercially available hydroxyl functional poly(ethylene glycol) as an initiator using DBU as the catalyst (30). More recently, Long and coworkers synthesized and characterized functional PEG-*b*-PLGA copolymers and studied their subsequent performance in vat photopolymerization for tissue scaffolding applications (31).

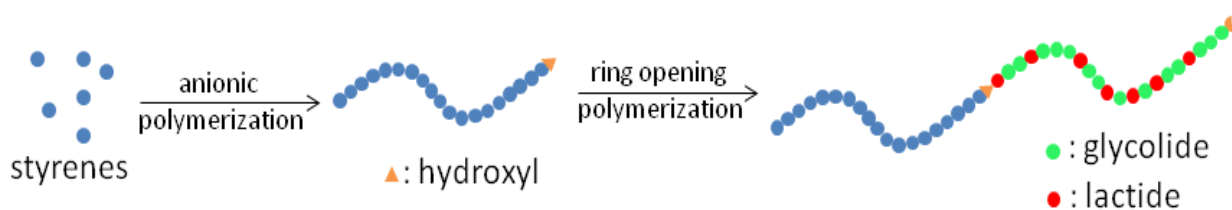
To the best of our knowledge, well-defined PS-*b*-PLGA block copolymers via a combination of living anionic polymerization and ROP of lactide and

glycolide have not been reported yet. In the current contribution, the goal is to fill this synthetic gap and study the effects of molecular architecture on the resultant thermal and morphological properties. First of all, the macroinitiators were prepared by living anionic polymerization using a *sec*-butyl lithium as an initiator. Subsequently, novel PS-*b*-PLGA block copolymers were prepared via ROP of cyclic esters. The resulting block copolymers were characterized via ¹H nuclear magnetic resonance (NMR), size exclusion chromatography (SEC), Fourier-transform infrared spectroscopy (FTIR), thermal gravimetric analysis (TGA) and differential scanning calorimetry (DSC). The morphologies of the block copolymers were identified small-angle X-ray scattering (SAXS), atomic force microscopy (AFM) as well as grazing-incidence small-angle scattering (GISAXS).

2. EXPERIMENTAL SECTION

2.1. Materials

Glycolide (99%) and D,L-lactide (99%) were received from Ortec and purified by recrystallization from ethyl acetate and toluene three times, respectively. The monomers were dried in vacuum and brought into the glove box prior to use. DBU (98%), styrene (99%), calcium hydride (CaH₂, 95%), *sec*-butyllithium solution (1.4 M in cyclohexane), di-*n*-butyl magnesium solution (1.0 M in heptane), and ethylene oxide (99.5%) were purchased from Sigma-Aldrich and used as received. Hexafluoro isopropanol (HFIP, 99%) was purchased from Oakwood Chemical and used as received. Methanol, acetone, ethyl acetate, and tetrahydrofuran (THF) were purchased from Sigma-Aldrich as analytical grade and used as received. Solvents for the polymerizations were retrieved from solvent purification columns.



Scheme 1: The preparation of well-defined PS-*b*-PLGA block copolymers.

2.2. Characterization Methods

2.2.1. Nuclear magnetic resonance (NMR) spectroscopy

¹H and ¹³C NMR spectra were obtained using either a 400 or 500 MHz Bruker Avance III HD spectrometer. Chemical shifts were referenced to tetramethylsilane (TMS) as an internal standard at 0.00 ppm for ¹H spectra taken in CDCl₃ containing 5% w/v TMS.

2.2.2. Size exclusion chromatography (SEC)

SEC (CHCl₃ system) data was calibrated to polystyrene standards (polymer laboratories) and acquired on a hp 1100 series liquid chromatography with three successive varian plgel mixed-c columns using chloroform as the mobile phase (35 °C, flow rate = 1 mL/min) and an hp 1047a ri detector. SEC (THF System) analysis was performed at 25 °C on an Agilent 1260 Infinity liquid chromatography system equipped with three Waters Styragel columns in series, a Wyatt DAWN Heleos II 18-angle light

scattering detector, and a Wyatt OPTILAB T-rEX refractive index detector and using THF as the eluent with a flow rate of 1 mL/min. Polydispersity (\bar{D}) was calculated from the light scattering data using Astra software.

2.2.3. Fourier-transform infrared (FT-IR) spectroscopy

Solid-state FT-IR spectra were recorded on a Bruker Alpha Platinum attenuated total reflectance unit (Bruker) coupled to a Bruker Vertex 80 Fourier-transform spectrometer. A series of spectra were collected between 400 and 4000 cm^{-1} in single beam mode using OMNIC software. The measurements were obtained using 164 scans/sample at a resolution of 4 cm^{-1} .

2.2.4. Thermal gravimetric analysis (TGA)

The thermal stability of the polymers was determined using TGA, a TA Instruments Q500. Approximately 5 mg of the polymer was heated at 10 $^{\circ}\text{C}/\text{min}$ from ambient temperature to 550 $^{\circ}\text{C}$ in a nitrogen atmosphere.

2.2.5. Differential scanning calorimetry (DSC)

DSC measurements were conducted using a Discovery DSC (TA Instruments Inc.). Approximately 5 mg samples were subjected to a heating and cooling rate of 10 $^{\circ}\text{C}/\text{min}$ under nitrogen atmosphere. DSC data analysis was performed using TRIOS software package. The thermal transitions were obtained from the second heating curve. The glass transition temperature (T_g) was determined from the mid-point of the step change in the heat flow signal.

2.2.6. Ellipsometry

The film thicknesses of the freshly spin-coated thin films on the Si wafers were measured by Ellipsometry on a J. A. Wollam Co., Inc. V-VASE.

2.2.7. Atomic force microscopy (AFM)

Tapping mode AFM was performed on a Bruker Nanoscope V Multimode 8 scanning probe microscope under ambient conditions with silicon cantilever tips.

2.2.8. X-ray scattering (SAXS/GISAX)

SAXS experiments at ambient temperature were conducted at the Advanced Photon Source in Argonne National Laboratory (Argonne, IL) using beamline 5-ID-D. SAXS data were collected with an energy 17 keV radiation and a sample-to-detector distance of 6 m. GISAXS measurements were performed at beam line 8-ID-E at the Advanced Photon Source of Argonne National Laboratory. Samples were placed in a vacuum chamber and illuminated with an energy 7.35 keV radiation at incident angles in the range of 0.2-0.24 $^{\circ}$; the scattering data were recorded with a Pilatus 1MF pixel array detector positioned 2175 mm from the sample. Acquisition times were approximately 10 s per frame.

2.3. Synthesis

2.3.1. Synthesis of ω -(hydroxy)polystyrene homopolymer via anionic polymerization

Following a modified literature procedure (32), hydroxyl functional polystyrenes were synthesized by living anionic polymerization in cyclohexane using *sec*-butyl lithium as the initiator at 40 $^{\circ}\text{C}$ overnight. Styrene was first freeze-pump-thawed three times and distilled twice over CaH_2 and then once over di-*n*-butylmagnesium and subsequently transferred to a flame-dried air-free burette. Cyclohexane (600 mL) was transferred from the solvent purification columns to a flame-dried air-free flask, then an argon/vacuum manifold, a manometer through Teflon valves, a septum, and the flask of purified styrene (50 g, 0.48 mol) were all connected to a 1-L flask equipped with five internal glass connectors and a Teflon-coated stir bar. The reactor was evacuated with high vacuum of 27 mTorr, flamed-dried and backfilled with argon five times. Finally, the cyclohexane was added to the reactor followed by the addition of *sec*-butyllithium (7.2 mL of 1.40 M *sec*-butyllithium in cyclohexane) with an airtight syringe through the septum. The reaction solution was heated to 40 $^{\circ}\text{C}$ in an oil bath. The styrene was added and the reaction mixture was stirred overnight, observing an orange-red color indicating the presence of poly(styryllithium) chain ends. Ethylene oxide (EO, 5 equivalents to *sec*-butyllithium initiator) was purified over di-*n*-butylmagnesium and transferred to a flame-dried air-free burette. The polymerization solution was cooled to the room temperature and the purified ethylene oxide was added by warming small doses from an externally chilled burette connected to the reactor with Ultra-Torr (Swagelok) Cajon tubing. The reaction was allowed to stir overnight under positive pressure. The reaction mixture turned colorless and subsequently was terminated by the addition of degassed methanol. The polymer was isolated by precipitation in cold methanol and the precipitate was filtered off and dried under high vacuum at 70 $^{\circ}\text{C}$ to afford the polymer as a white powder. ^1H NMR in CDCl_3 $\{\delta, \text{ppm}\}$: 7.40-6.30 (5H, aromatic protons of PS), 3.50-3.20 (2H, $\text{CH}_2\text{-OH}$), 1.78-1.18 (aliphatic protons of PS), $M_{n,\text{NMR}} = 4800$ g/mol. $M_{n,\text{SEC}} = 4900$ g/mol, $\bar{D} = 1.03$.

2.3.2. Synthesis of poly(styrene)-*b*-poly(glycolide-co-lactide) copolymer via ring opening polymerization

Solutions of the hydroxyl-terminated polystyrene (1 g, 0.208 mmol in 10 mL of DCM), lactide (0.59 g, 4.1 mmol in 18 mL of DCM), 1,8-diazabicyclo[5.4.0]undec-7-ene (DBU, 15 μL in 2 mL of DCM) and glycolide (0.965 g, 8.32 mmol in 20 mL of THF) were first prepared in a controlled atmosphere (nitrogen) glove box. A flame-dried Schlenk flask was then equipped with a septum and a stir bar. The solutions of the macroinitiator and lactide were added to the reaction flask under argon atmosphere, followed by addition of the DBU solution. The solution of glycolide was then added via a syringe pump at a rate of 200 $\mu\text{L}/\text{min}$. At the end of the addition (100 min), solid benzoic acid (25 mg) was added to

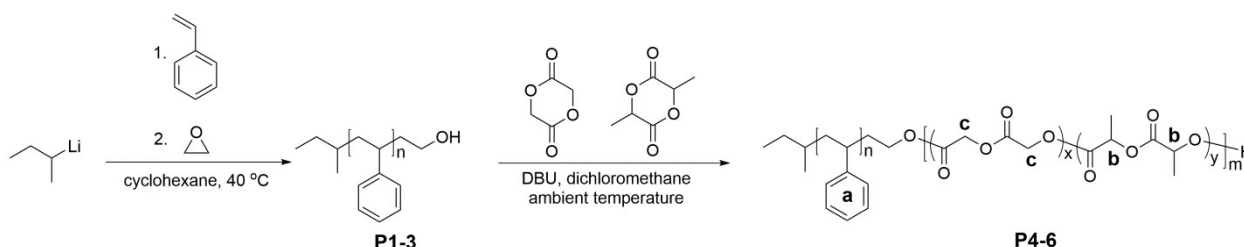
terminate the polymerization. The PS-*b*-PLGA block copolymer was purified by precipitation into methanol from the reaction mixture and dried at 60 °C under vacuum overnight. ¹H NMR in CDCl₃ { δ , ppm}: 7.40-6.30 (5H, aromatic protons of PS), 5.21 (CH of PLA), 4.86 (CH₂ of PGA), 1.61 (CH₃ of PLA), 1.78-1.18 (aliphatic protons of PS), $M_{n,NMR}$ = 10800 g/mol, $M_{n,SEC}$ = 9100 g/mol, \bar{D} = 1.15.

3. RESULTS AND DISCUSSIONS

Herein, novel well-defined PS-*b*-PLGA block copolymers were achieved using living anionic polymerization and ROP methods and subsequently morphology of the polymers was investigated in bulk as well as in thin film studies.

Styrene was polymerized using *sec*-BuLi in cyclohexane at 40 °C for 16 hours subsequently ethylene oxide was added to achieve the hydroxyl-

terminated polystyrenes. Molecular weight of the homopolymers were determined by ¹H NMR and SEC. The SEC traces of the homopolymers demonstrate unimodal molecular weight distributions (refer to Figure S1 in the Supporting Information (SI) section). ¹H NMR spectrum (Figure S2 in the SI section) was utilized to estimate the number-average molecular weight, $M_{n,NMR}$, of the homopolymer comparing the integrated areas aromatic protons of the polystyrene at 6.3-7.3 ppm and the nine protons of the initiator at 0.9-1.1 ppm. It was found that molecular weights obtained from both techniques are in excellent agreement. The percentage of the hydroxyl group at chain-end of the homopolymers was estimated by the integral areas of the methylene protons adjacent the hydroxyl group as well as the initiator protons indicating quantitative hydroxyl end-group incorporation (see Table 1).



Scheme 2: The chemical structures of the PS-*b*-PLGA block copolymers.

Table 1: Molecular Properties of the PS-OH Macroinitiators.

Polymer	$M_{n,NMR}^a$ (g/mol)	$M_{n,SEC}^b$ (g/mol)	\bar{D}^b	EGF ^c
P1	2400	2300	1.03	0.98
P2	4800	4900	1.03	0.99
P3	13700	13400	1.03	0.96

^aDetermined using ¹H NMR spectroscopy; ^bdetermined from SEC in THF using MALLS-SEC; ^cend group fidelity (EGF) or percentage of the hydroxyl group at chain-end.

The ROP of glycolide by Beuermann (29) and lactide by Waymouth (33) has been reported in the absence of any initiator, DBU can act as an initiator to form macrocyclics and linear chains. Thus, the ROP of the cyclic esters was applied both in the presence and absence of a macroinitiator using DBU and observing the formation of oligomeric species in the SEC traces when [initiator]₀/ [DBU]₀ = 1 (refer to Figure S3). Subsequently the concentration of DBU was optimized for the ROP of the cyclic esters using the hydroxyl functional polystyrene. After performing the polymerization at various concentration of DBU, it was found that 2 mM concentration of DBU is sufficient to achieve well-defined linear polymers. Next, the block copolymers were accomplished by the ROP of lactide and glycolide using DBU as the catalyst and the hydroxyl-terminated polystyrene as the

macroinitiator. The purified block copolymers were characterized by SEC comparing to PS standards using CHCl₃ as elution solvent. For example, the SEC trace of P5 in Figure 1 shows a shift towards higher molecular mass, compared with its corresponding polymer precursor (P2). Additionally, no significant increase in the dispersity was observed for the formed block copolymer (PS-*b*-PLGA, P5). Additional details for the macroinitiator and block copolymer are given in Tables 1 and 2. The ¹H NMR spectrum of P5 shows corresponding CH peak of the PLA and CH₂ of the PGA repeat units at 5.21 ppm and 4.86 ppm, respectively, confirming successful block copolymer incorporation (refer to Figure 2). The $M_{n,NMR}$ of the block copolymers was obtained by using the aromatic protons of PS, the CH of the PLA and the two protons of PGA. Volume fractions of PLA and PGA segments in the block copolymer were

calculated using ^1H NMR spectrum based on homopolymer densities. In addition, the lactide/glycolide weight fractions of the block copolymers were obtained from integral area of the peaks at 5.21 ppm and 4.86 ppm, respectively and

reported in Table 2. Further evidence for the block copolymer formation was obtained from FT-IR (refer to Figure S4) as the carbonyl stretching band of the PLGA chains were appeared at 1754 cm^{-1} .

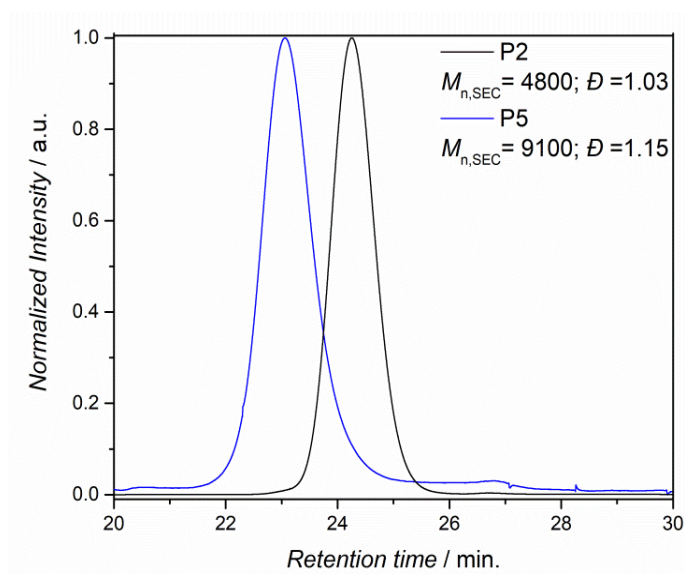


Figure 1: SEC traces of the hydroxyl-terminated polystyrene (P2) and the corresponding block copolymer (PS-*b*-PLGA, P5). Additional details for the macroinitiator and block copolymers are given in Tables 1 and 2 as well as Figure S1 and S2.

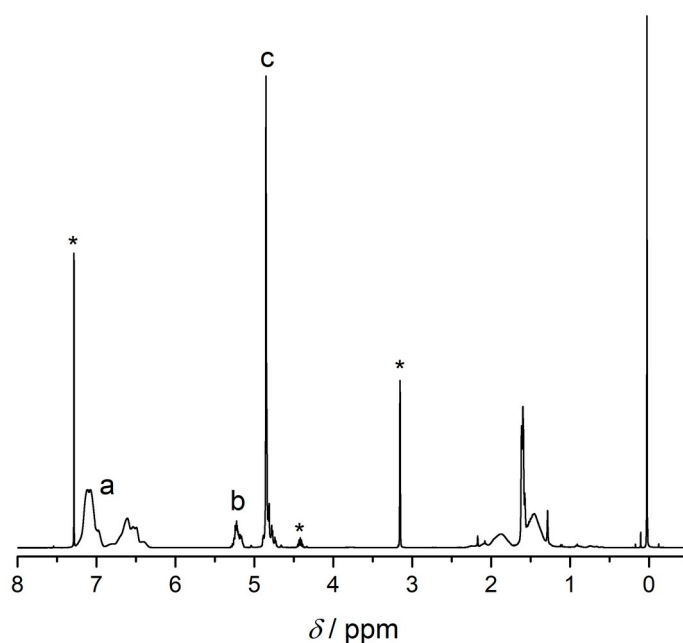


Figure 2: ^1H NMR spectra of PS-*b*-PLGA (P5) in CDCl_3 /hexafluoro-2-propanol (HFIP) (v/v: 9/1) at ambient temperature. The peaks marked with an asterisk are due to solvent (HFIP). The chemical structures can be found in Scheme 2.

The thermal behavior of the PS-*b*-PLGA block copolymers was examined via TGA heating from room temperature to 550 °C at a rate of 10 °C/min under nitrogen which are depicted in Figure 3. The PS-*b*-PLGA block copolymers demonstrated a two-

step weight loss. Initially the block copolymers lost ~60% weight at 350 °C corresponding to the PLGA thermal degradation temperature and subsequently complete degradation occurred at 420 °C referring to the decomposition of PS.

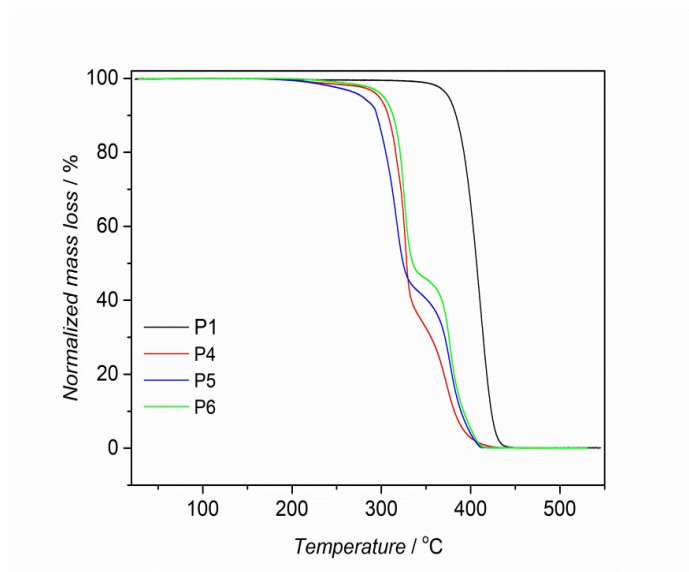


Figure 3: TGA traces of block copolymers and precursor polymer.

The thermal transitions of the block copolymer were investigated using DSC in order to observe the glass transition temperatures (T_g) and the peak melting temperature (T_m). The second heating traces of the block copolymers are shown in Figure 4. The DSC trace of the PS-*b*-PLGA block copolymer (P6) shows a T_g at 43 °C corresponding to the PLGA chains, then a second glass transition at about 96 °C referring to

the T_g of the PS chains, which are in excellent agreement with reported values (29). Upon further heating, melting of the semi-crystalline domains of PLGA is detected by observing the T_m at ~150 °C. The degree of crystallinity (X_c) of PS-*b*-PLGA block copolymers was calculated by the following literature (32).

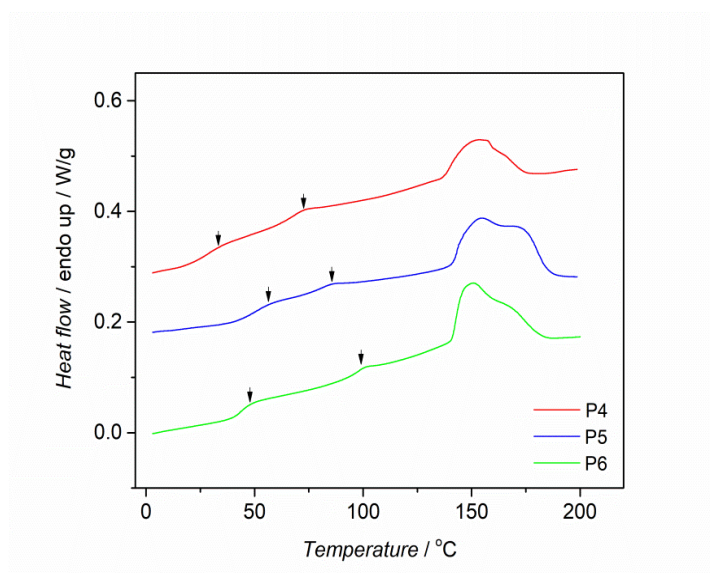


Figure 4: DSC traces for PS-*b*-PLGA block copolymers.

Table 2: Molecular and Thermal Characteristics of Block Copolymers.

Polymer	$M_{n,NMR}^a$ (g/mol)	$M_{n,SEC}^b$ (g/mol)	\mathcal{D}^b	f_{PLGA}^c	w_{PGA}^d	$T_{g,PS}^e$ (°C)	$T_{g,PLGA}^f$ (°C)	$T_{m,PGA}^g$ (°C)	X_c^h (%)	T_d^i (°C)	D_{SAXS}^k (nm)
P4	5000	5500	1.16	0.45	0.33	68	26	166	30	298	15
P5	10800	9100	1.15	0.48	0.38	83	49	169	25	285	16
P6	33600	19500	1.17	0.52	0.31	98	43	147	29	308	27

^aCalculated using ¹H NMR spectra. ^bDetermined via SEC. ^cVolume fraction of PLGA. ^dWeight fraction of PLGA. ^e $T_{g,PS}$ is the glass transition temperature of the PS and ^f $T_{g,PLGA}$ is for the PLGA. ^g $T_{m,PGA}$ is PLGA melting temperature. ^hDegree of crystallinity. ⁱ5% mass loss was determined by TGA. ^kDomain spacing was obtained from SAXS data.

The morphology of the block copolymers was investigated via SAXS. The block copolymers were annealed at 110 °C under inert atmosphere for 16 h. Subsequently the block copolymers were slowly cooled to the room temperature before examining the bulk microphase separation via SAXS. Domain spacings ($D = 2\pi/q^*$) were obtained by using the principal scattering peak position (q^*) and summarized in Table 2. The SAXS scattering profiles

of the block copolymers at 25 °C show a main scattering peak with domain spacing of 15-27 nm, which indicates microphase separation. Because of the lack of well-defined second order reflections, the morphology of the block copolymers could not be determined via SAXS (Figure 5). It is possible that the polymer chains were not able to move in bulk below the melting temperature due to their semi-crystalline nature.

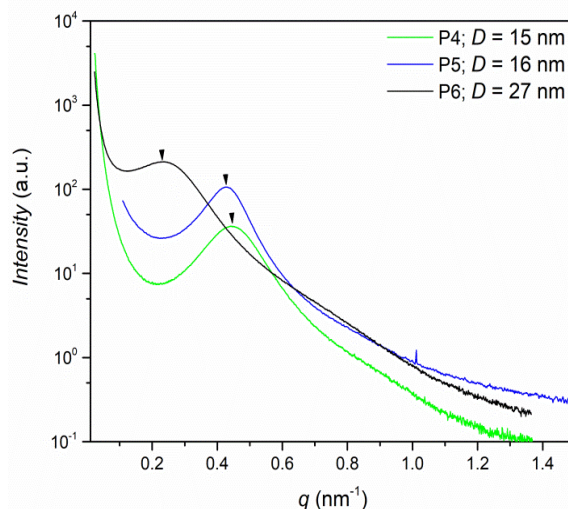


Figure 5: The SAXS data obtained at ambient temperature for the corresponding block copolymers.

Subsequently the surface phase structures of polymer films were analyzed by AFM (35). Block copolymer solutions (10 mg/mL) in $\text{CHCl}_3/\text{HFIP}$ (v/v: 9/1) were spin-coated onto HMDS-modified silicon wafers. The thickness of the polymer film, measured by ellipsometer, was around 54 nm. Solvent vapor annealed (SVA) was applied in $\text{CHCl}_3/\text{HFIP}$ (v/v: 9/1) for five minutes (36). After SVA, the thin film was

analyzed by AFM in the tapping mode showing the image in Figure 6. The AFM characterization of P5 demonstrated well-segregated microdomains with uniform domain size throughout the $1 \times 1 \mu\text{m}$ sample suggesting possible perpendicular lamellar orientation in the PS-*b*-PLGA thin films (Figure 5). The domain spacing from the AFM image (20 nm) and SAXS (16 nm) is comparable.

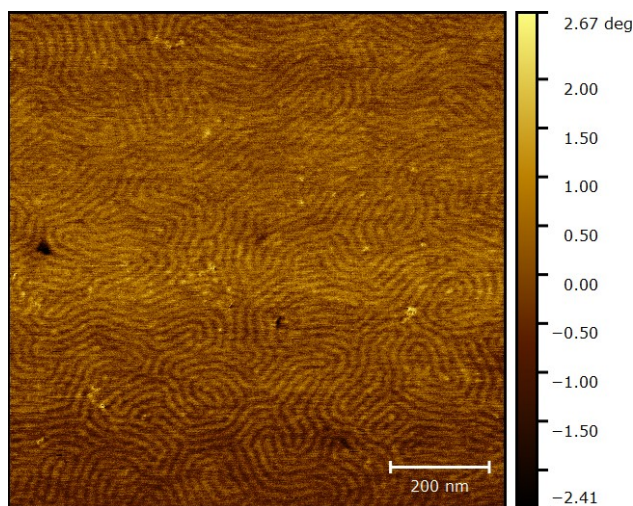


Figure 6: AFM phase image of PS-*b*-PLGA (P5).

The morphological characterization in block polymer thin films can be obtained through the small-angle

X-ray scattering (GISAXS) technique (37). In addition to SAXS and AFM characterizations, the one-

dimensional GISAX data for P5 was shown in Figure 7. The fundamental domain spacing was estimated to be 15.8 nm from the principle scattering peak maxima at $q_y^* = 0.396/\text{nm}$. Because of the symmetric volume fractions of each segment ($f_{\text{PLGA}} = 0.48$), it might be indicative of a lamellar morphology (38). Moreover, the spacing of the

features from the GISAXS (15.8 nm) is in excellent agreement with the bulk spacing obtained by SAXS (16 nm). Based on the DSC, AFM and GISAXS analysis, the symmetric PS-*b*-PLGA block copolymer could be microphase-separated with a perpendicular lamellar morphology.

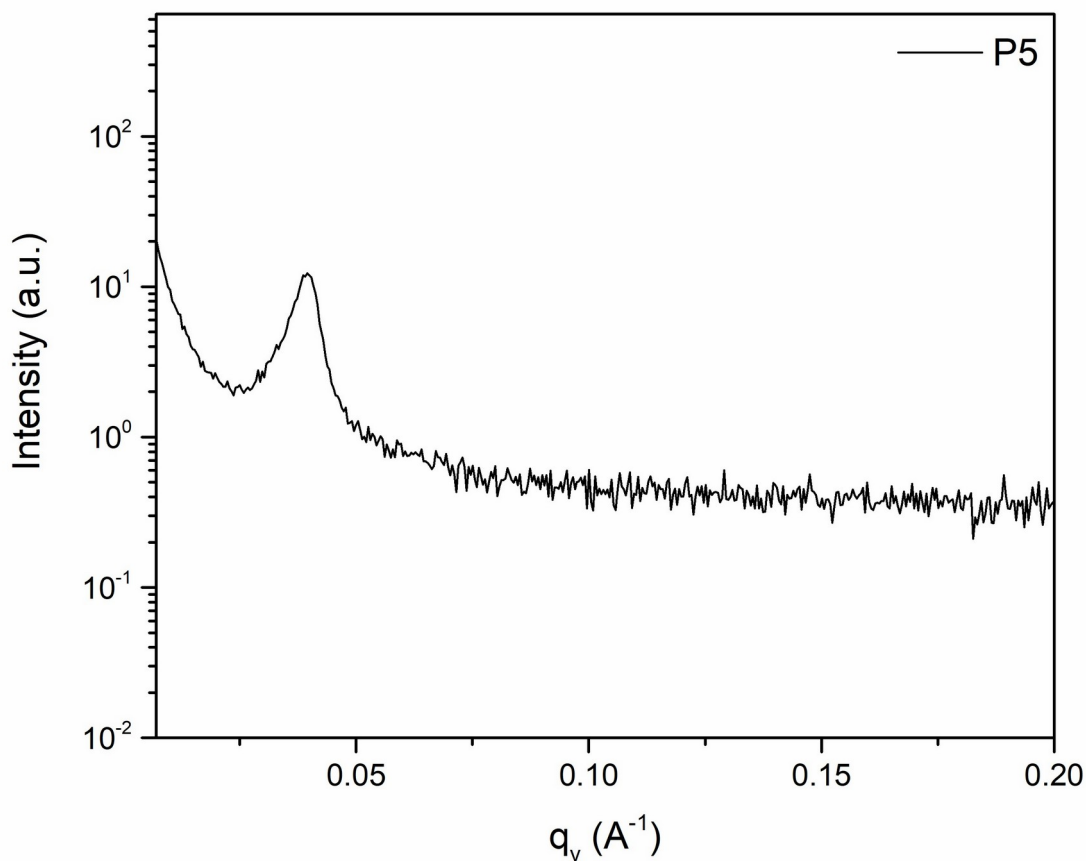


Figure 7: 1D synchrotron GISAXS profile for the block copolymer (P5, $M_{n,\text{NMR}} = 10800 \text{ g/mol}$, $f_{\text{PLGA}} = 0.48$) at room temperature.

4. CONCLUSION

A versatile synthetic approach for the synthesis of PS-*b*-PLGA block copolymers was -for the first time- demonstrated. Well-defined PS-*b*-PLGA polymers were successfully obtained via advanced polymerization methods. Initially hydroxyl-terminated linear polystyrenes were prepared and then copolymerization of lactide and glycolide was achieved using the macroinitiator and DBU at ambient temperature leading to PS-*b*-PLGA block copolymers. Transesterification and formation of DBU-initiated polymers were minimized by optimizing the catalyst concentration to 2 mM. Number-average molar mass of the block copolymers as well as the block volume fraction were calculated based on ^1H NMR spectra. Furthermore, the block copolymer formation was followed by SEC traces. The stability of the block copolymer was analyzed by TGA demonstrating less than 5% weight loss up to 270 °C. Thermal properties of the block copolymer were obtained by

DSC indicating two clear glass transition and melting temperatures suggesting well-defined microphase separation. The formation of the organized nanostructures was observed by SAXS, GISAXS and AFM. Although no higher order reflections were observed in the SAXS characterization, these polymers have a fundamental spacing ranging of 15-27 nm. The results from DSC, AFM and GISAXS demonstrate that the morphology of the block copolymer is presumably perpendicular lamellar as each segment ($f_{\text{PLGA}} = 0.48$) has the symmetric volume fractions. The present results unambiguously prove that the formation of PS-*b*-PLGA block copolymers on a very well-defined level is indeed possible employing high precision macromolecular design strategies. This manuscript have demonstrated the synthesis, characterization, and morphology of PLGA-based block copolymers as well as potential use in nanopatterning and advanced multilayer applications.

5. ACKNOWLEDGMENTS

The author graciously thanks Prof. Marc Hillmyer (UMN), Prof. Frank Bates (UMN), and Dr. Joshua Speros (BASF) for helpful discussion as well as for their financial support. SAXS and GISAXS data were obtained at the Advanced Photon Source, a U.S. Department of Energy (DOE) Office of Science User Facility operated for the DOE Office of Science by Argonne National Laboratory. Parts of this work were carried out in the Characterization Facility, University of Minnesota.

6. REFERENCES

- Bates CM, Bates FS. 50th Anniversary Perspective : Block Polymers—Pure Potential. *Macromolecules*. 2017 Jan 10;50(1):3-22. Available from: [<URL>](#).
- Lazzari M, López-Quintela MA. Block Copolymers as a Tool for Nanomaterial Fabrication. *Adv Mater*. 2003 Oct 2;15(19):1583-94. Available from: [<URL>](#).
- Jackson EA, Hillmyer MA. Nanoporous Membranes Derived from Block Copolymers: From Drug Delivery to Water Filtration. *ACS Nano*. 2010 Jul 27;4(7):3548-53. Available from: [<URL>](#).
- Kim HC, Park SM, Hinsberg WD. Block Copolymer Based Nanostructures: Materials, Processes, and Applications to Electronics. *Chem Rev*. 2010 Jan 13;110(1):146-77. Available from: [<URL>](#).
- Jung YS, Jung W, Tuller HL, Ross CA. Nanowire Conductive Polymer Gas Sensor Patterned Using Self-Assembled Block Copolymer Lithography. *Nano Lett*. 2008 Nov 12;8(11):3776-80. Available from: [<URL>](#).
- Park M, Harrison C, Chaikin P, others. Block Copolymer Lithography: Periodic Arrays of 10. Holes in. 1:1401-4.
- Bates FS, Hillmyer MA, Lodge TP, Bates CM, Delaney KT, Fredrickson GH. Multiblock Polymers: Panacea or Pandora's Box? *Science*. 2012 Apr 27;336(6080):434-40. Available from: [<URL>](#).
- Darling SB. Directing the self-assembly of block copolymers. *Progress in Polymer Science*. 2007 Oct;32(10):1152-204. Available from: [<URL>](#).
- Leibler L. Theory of microphase separation in block copolymers. *Macromolecules*. 1980;13(6):1602-17.
- Bates FS. Polymer-Polymer Phase Behavior. *Science*. 1991 Feb 22;251(4996):898-905. Available from: [<URL>](#).
- Bates FS, Fredrickson GH. Block copolymers-designer soft materials. *Physics today*. 2000;52.
- Luo M, Epps TH. Directed Block Copolymer Thin Film Self-Assembly: Emerging Trends in Nanopattern Fabrication. *Macromolecules*. 2013 Oct 8;46(19):7567-79. Available from: [<URL>](#).
- Klumperman B. Reversible Deactivation Radical Polymerization. In: John Wiley & Sons, Inc., editor. *Encyclopedia of Polymer Science and Technology* [Internet]. 1st ed. Wiley; 2015 [cited 2023 Feb 8]. p. 1-27. Available from: [<URL>](#).
- Matyjaszewski K. Atom Transfer Radical Polymerization (ATRP): Current Status and Future Perspectives. *Macromolecules*. 2012 May 22;45(10):4015-39. Available from: [<URL>](#).
- Ouchi M, Sawamoto M. 50th Anniversary Perspective : Metal-Catalyzed Living Radical Polymerization: Discovery and Perspective. *Macromolecules*. 2017 Apr 11;50(7):2603-14. Available from: [<URL>](#).
- Perrier S. 50th Anniversary Perspective: RAFT Polymerization—A User Guide. *Macromolecules*. 2017 Oct 10;50(19):7433-47. Available from: [<URL>](#).
- Moad G. RAFT polymerization to form stimuli-responsive polymers. *Polym Chem*. 2017;8(1):177-219. Available from: [<URL>](#).
- Nicolas J, Guillaneuf Y, Lefay C, Bertin D, Gigmes D, Charleux B. Nitroxide-mediated polymerization. *Progress in Polymer Science*. 2013 Jan;38(1):63-235. Available from: [<URL>](#).
- Vanderlaan ME, Hillmyer MA. "Uncontrolled" Preparation of Disperse Poly(lactide)- block -poly(styrene)-block -poly(lactide) for Nanopatterning Applications. *Macromolecules*. 2016 Nov 8;49(21):8031-40. Available from: [<URL>](#).
- Szwarc M. 'Living' polymers. *Nature*. 1956;178:1168-9.
- Hirao A, Loykulant S, Ishizone T. Recent advance in living anionic polymerization of functionalized styrene derivatives. *Progress in Polymer Science*. 2002 Oct;27(8):1399-471. Available from: [<URL>](#).
- Hadjichristidis N, Pitsikalis M, Pispas S, Iatrou H. Polymers with Complex Architecture by Living Anionic Polymerization. *Chem Rev*. 2001 Dec 1;101(12):3747-92. Available from: [<URL>](#).
- Dechy-Cabaret O, Martin-Vaca B, Bourissou D. Controlled Ring-Opening Polymerization of Lactide and Glycolide. *Chem Rev*. 2004 Dec 1;104(12):6147-76. Available from: [<URL>](#).
- Meduri A, Fuoco T, Lamberti M, Pellicchia C, Pappalardo D. Versatile Copolymerization of Glycolide and rac -Lactide by Dimethyl(salicylaldiminato)aluminum Compounds. *Macromolecules*. 2014 Jan 28;47(2):534-43. Available from: [<URL>](#).
- Albertsson AC, Varma IK. Recent Developments in Ring Opening Polymerization of Lactones for Biomedical Applications. *Biomacromolecules*. 2003 Nov 1;4(6):1466-86. Available from: [<URL>](#).
- Chiellini E, Solaro R. Biodegradable Polymeric Materials. *Adv Mater*. 1996 Apr;8(4):305-13. Available from: [<URL>](#).
- Saba SA, Mousavi MPS, Bühlmann P, Hillmyer MA. Hierarchically Porous Polymer Monoliths by Combining Controlled Macro- and Microphase Separation. *J Am Chem Soc*. 2015 Jul 22;137(28):8896-9. Available from: [<URL>](#).
- Altay E, Jang YJ, Kua XQ, Hillmyer MA. Synthesis, Microstructure, and Properties of High-Molar-Mass Polyglycolide Copolymers with Isolated Methyl Defects. *Biomacromolecules*. 2021 Jun 14;22(6):2532-43. Available from: [<URL>](#).

29. Kemo VM, Schmidt C, Zhang Y, Beuermann S. Low Temperature Ring-Opening Polymerization of Diglycolide Using Organocatalysts with PEG as Macroinitiator. *Macromol Chem Phys*. 2016 Apr;217(7):842-9. Available from: [<URL>](#).
30. Qian H, Wohl AR, Crow JT, Macosko CW, Hoyer TR. A Strategy for Control of "Random" Copolymerization of Lactide and Glycolide: Application to Synthesis of PEG- b - PLGA Block Polymers Having Narrow Dispersity. *Macromolecules*. 2011 Sep 27;44(18):7132-40. Available from: [<URL>](#).
31. Wilts EM, Gula A, Davis C, Chartrain N, Williams CB, Long TE. Vat photopolymerization of liquid, biodegradable PLGA-based oligomers as tissue scaffolds. *European Polymer Journal*. 2020 May;130:109693. Available from: [<URL>](#).
32. Zalusky AS, Olayo-Valles R, Wolf JH, Hillmyer MA. Ordered Nanoporous Polymers from Polystyrene-Polylactide Block Copolymers. *J Am Chem Soc*. 2002 Oct 1;124(43):12761-73. Available from: [<URL>](#).
33. Brown HA, De Crisci AG, Hedrick JL, Waymouth RM. Amidine-Mediated Zwitterionic Polymerization of Lactide. *ACS Macro Lett*. 2012 Sep 18;1(9):1113-5. Available from: [<URL>](#).
34. Chu CC. Differential scanning calorimetric study of the crystallization kinetics of polyglycolic acid at high undercooling. *Polymer*. 1980 Dec;21(12):1480-2. Available from: [<URL>](#).
35. Wang D, Russell TP. Advances in Atomic Force Microscopy for Probing Polymer Structure and Properties. *Macromolecules*. 2018 Jan 9;51(1):3-24. Available from: [<URL>](#).
36. Yao L, Oquendo LE, Schulze MW, Lewis RM, Gladfelter WL, Hillmyer MA. Poly(cyclohexylethylene)- block - Poly(lactide) Oligomers for Ultrasmall Nanopatterning Using Atomic Layer Deposition. *ACS Appl Mater Interfaces*. 2016 Mar 23;8(11):7431-9. Available from: [<URL>](#).
37. Posselt D, Zhang J, Smilgies DM, Berezkin AV, Potemkin II, Papadakis CM. Restructuring in block copolymer thin films: In situ GISAXS investigations during solvent vapor annealing. *Progress in Polymer Science*. 2017 Mar;66:80-115. Available from: [<URL>](#).
38. Vora A, Wojtecki RJ, Schmidt K, Chunder A, Cheng JY, Nelson A, et al. Development of polycarbonate-containing block copolymers for thin film self-assembly applications. *Polym Chem*. 2016;7(4):940-50. Available from: [<URL>](#).



Comparison of Four Different Polymeric Adsorbents as Clean-up Agents for Pesticide Analysis in Tea with LC MS/MS

Nihat Özcan¹ 

¹TUBITAK Marmara Research Center, Kocaeli, TÜRKİYE

Abstract: Previously published studies indicate that tea (*Camellia sinensis*) contains essential oils, flavonoids, phenolics, lipids, natural pigments, sugars, and oligosaccharides. These essential biomolecules in *Camellia sinensis* cause serious problems in the determination of pesticide residues. High amount of co-extractives can exhibit chromatographic characteristics similar to some pesticides, which may cause serious matrix effects and significant interference in mass spectrometry analysis. In this study, we compared four polymeric resins as clean-up sorbents for the determination of 216 pesticide residues in tea by a high performance liquid chromatography triple quadrupole mass spectrometry. styrene-divinylbenzene (Diaion HP20), Polyamide 6, Polyvinylpyrrolidone (PPVP), and Amberlite XAD 7 were used as clean-up sorbents instead of PSA. However, to evaluate the effectiveness of the adsorbents, recovery studies were carried out using these adsorbents. In addition, GC-MS analysis was also performed to see the ability of these adsorbents to remove co-extracts. According to the recovery results, when the acceptable limit was accepted as 60-140%, it was determined that the resin that gave the best results with 170 pesticides was polyamide. Diaion was the second resin with 166 pesticides, while XAD, PSA which was used as control group and PPVP were determined as the third, fourth, and fifth resins with very close values of 159, 155, and 152 pesticides, respectively. According to GC-MS total ion analysis, it was observed that PSA gave the chromatogram with the least co-extract, while it was observed that PSA was the worst adsorbent in removing caffeine, one of the main bioactive compounds in tea. XAD-7 and Polyamide were found to be the best adsorbents in removing caffeine.

Keywords: Pesticide, LC-MS/MS, Tea, Adsorption, QuEChERS, clean-up.

Submitted: July 05, 2022. **Accepted:** February 09, 2023.

Cite this: Özcan N. Comparison of Four Different Polymeric Adsorbents as Clean-up Agents for Pesticide Analysis in Tea with LC MS/MS. JOTCSA. 2023;10(1):253-66.

DOI: <https://doi.org/10.18596/jotcsa.1140922>.

***Corresponding author. E-mail:** nihat.ozcan@tubitak.gov.tr.

1. INTRODUCTION

Pesticides are widely used in agriculture to protect the products from harmful pests and diseases. Besides its positive effects, pesticide residue can be hazardous to human health. For this reason, many countries have applied monitoring programs to control pesticide residues in edible products. Pesticide residues can easily be found in tea due to their widespread usage in order to kill pests and to eliminate weeds and diseases during the tea cultivation (1). Tea is one of the most widely consumed beverages for centuries. Tea contains essential oils, flavonoids, phenolics, lipids, natural pigments, sugars, and oligosaccharides (2). Therefore, tea is an important source of antioxidants

and its health-promoting effects have been widely investigated. Antioxidant effect of tea mainly comes from polyphenols such as flavonols (quercetin, kaempferol, myricetin), flavan-3-ols (catechins and theaflavins), and alkaloids (caffeine and theaflavins), gallic acid derivatives, hydroxycinnamate quinic esters (caffeoylquinic acids) (3, 4). On the other hand, these essential characteristic compounds of tea cause serious problems for determination of pesticide residues in tea. A high amount of co-extractives can exhibit chromatographic characteristics similar to some pesticides, which may cause serious matrix effects and significant interference in mass spectrometric analysis (2). In the mass spectrometer, these polyphenols compete with the target analytes for access to the droplet

surface prior to gas phase emission which may suppress or enhance the ionization of target compounds, and affect the detection results (5). Since the target analytes occur at low concentrations and belong to a wide range of chemical classes, it is critical that isolation of pesticide residues in acceptable recovery range while minimizing co-extractives and matrix effects.

In the literature, there are previously published methods for determination of pesticide residues in tea. These methods usually include solid phase extraction (6-8) and dispersive solid phase extraction (QuEChERS) (9, 10). In time, the QuEChERS methods has been most widely used method for determination of pesticide residues in food samples. Furthermore, this method has become a standard test method of AOAC 2007.01. Despite the fact that this method has been developed in the determination of pesticide residues in fruits and vegetables, with slight modifications it can be used for other food matrices. The method includes extraction of pesticide with acetonitrile, and the raw extract is cleaned up with dispersive solid phase extraction (SPE) by mixing with magnesium sulfate and primary secondary amine (PSA) to remove water and undesired co-extractives. PSA is the most commonly used sorbents in QuEChERS methods and its main function is to remove co-extracted constituents such as fatty acids, sugars, and ionic lipids. Another sorbent option is known as C18. The C18 has a nonpolar nature which is useful in removing fat and wax content of the matrix. Although PSA and C18 are widely used as dispersive solid phase extraction sorbents, some novel sorbents have been used as alternatives to cope with complex matrixes. Li et al (2013), developed a novel magnetic SPE method based on magnetic cobalt ferrite-filled carbon nanotubes to determine organochlorine pesticides in tea and honey samples (1). Liu et al (2014), have used graphene with PSA and graphitized carbon black as dispersive solid phase extraction sorbent for the clean-up of tea samples (11). Hou et al (2013), have developed a modified QuEChERS method using multi-walled carbon nanotubes as a dispersive solid phase extraction sorbent for the analysis of 78 pesticides in tea (12). Rejczak and Tuzimski (2017) have used zirconium(IV) oxide (ZrO₂)-based sorbents and PSA as dispersive solid phase extraction clean up material for determination of pesticide in milk (13). Li et al. (2013) have used PPVP, PSA and GCB as clean-up sorbents to remove co-eluting matrix components for the determination of 16 pesticide residues in tea (14). Sun et al. (2022) used a combined sorbent package consisting of MWNTs-OH and PSA for the extraction and purification of 57 pesticides to remove the interferences of pigment in *Lonicerae japonicae* flower buds and improve the quantitative accuracy in pesticide residues analysis (15). Zhao and Shi used non-porous boron nitride nanorods (p-BNNRs) as clean-up sorbents to eliminate matrix interference in QuEChERS analysis

method for the detection of five neonicotinoid pesticide residues in goji berries (16).

Polyamide is well suited for the separation of natural substances with phenolic and polyphenolic groups. Because of its swelling properties, polyamide has a higher adsorption capacities than most sorbents currently on the market. This swelling property makes it suited for preparative chromatography as well as for the analysis of biological material (separation of undesirable accompanying compounds). Polyamide is commonly used as an adsorbent for the isolation and identification of natural substances with phenolic and polyphenolic functional groups, e.g. anthocyanins, anthoxanthines, anthraquinone derivatives, and flavones.

Diaion (synthetic adsorbent resin) is a macroporous styrenic polymeric bead type resin designed for adsorption/desorption process scale applications. Its matrix provides an aromatic non-polar surface with excellent selectivity for hydrophobic areas of molecules, including biomolecules like antibiotics via low-energy van der Waals interactions. It is remarkable for its wide pore polymeric structure which provides excellent broad spectrum adsorption characteristics.

Polyvinylpolypyrrolidone (PVPP) is a resinous polymer that acts similarly to proteinaceous fining agents. It is particularly useful in the selective removal of flavans and mono- and dimeric phenolics. As such, PVPP has particular value in diminishing undesirable bitter taste. For this reason, it is usually added relatively early in maturation. It is also efficient in preventing oxidative browning and removing its brown by-products from white wines. It functions well at cool temperatures and precipitates spontaneously. Meng et al. (2021), used a d-SPE purification method for the determination of 134 pesticide in tea using a multi-functional filter which consisted of two layers, an upper layer of porous PVPP to absorb polyphenols and a lower layer containing a mixture of PSA, GCB and anhydrous magnesium sulfate, to remove substances such as pigments (17). Guo et al. (2018), develop a method for determination of 20 pesticide residues from polyphenol-rich agricultural samples (tea, apple, broccoli, and shallot) by using PVPP to precipitate polyphenols. They used clean-up combination of PVPP (150 mg), PSA (50 mg) and GCB (10 mg) in the clean-up step to remove co-extracts (18). XAD adsorbents are very porous spherical polymers based on highly crosslinked, macro-reticular polystyrene, aliphatic, or phenol-formaldehyde condensate polymers. Amberlite XAD-7 is a non-ionic aliphatic acrylic polymer, which derives its adsorptive properties from its macro-reticular structure (containing both a continuous polymer phase and a continuous pore phase), high surface area, and the aliphatic nature of its surface. It is characterized as a hydrophobic adsorbent having a somewhat more hydrophilic structure comparing to

XAD-4. Its macro-reticular structure also gives it excellent physical and thermal stability and it is also stable at all pH range in an aqueous solution. Due to its aliphatic nature amberlite XAD-7 can adsorb non-polar compounds from aqueous systems and can also adsorb polar compounds from non-polar solvents (19,20).

In this study, it was aimed to modify the QuEChERS method by using polymeric adsorbents as a clean-up agent in pesticide analysis in tea. The adsorbents used in this study were used for the first time in the QuEChERS method as a clean up agent in pesticide analysis in tea. In addition, these adsorbents were tested for the first time for the analysis of a high number of pesticides (216) in the analysis of pesticides in tea samples. In this study, we compared four polymeric resins as clean-up sorbents for the determination of 216 pesticide residues in tea by high performance liquid chromatography triple quadrupole mass spectrometry. We used Diaion, Polyamide, PPVP, and XAD 7 as clean-up sorbents instead of PSA. Since tea includes a high amount of phenolic compounds which can cause interference in determination of pesticide residue, these polymeric resins may more effectively remove co-extracts from tea sample. In addition, to evaluate the effectiveness of adsorbents, recovery studies were carried out using these adsorbents and GC-MS analysis was carried out to evaluate the ability of these adsorbents to remove co-extracts.

2. EXPERIMENTAL SECTION

2.1. Chemicals

Acetonitrile, magnesium sulfate, sodium acetate, Dianon, PPVP, XAD7 and Polyamide were used (Sigma Aldrich, and Dr. Erhenstorfer, Germany). Pesticide standards used in this study were given in Table 2. Individual standard solutions 1000 mg/L were prepared in acetonitrile and further dilutions were made with acetonitrile. Black tea samples were purchased from a local market and were checked for existence of pesticides.

2.2. Extraction and Clean-up

The extraction was carried out according to BS EN 15662 "Foods of plant origin". Multimethod was used for the determination of pesticide residues using GC- and LC-based analysis followed by acetonitrile extraction/partitioning and clean-up by dispersive SPE called "Modular QuEChERS-method". A 2 g tea sample was weighed into 50 mL polypropylene centrifuge tube and 10 mL deionized water was added. After mixing and allowed to soak for 10 mins, 10 mL of acetonitrile was added and shaken vigorously for 15 mins using a shaker. Buffer salt mixtures (4 g of anhydrous magnesium sulfate, 1 g of sodium chloride, 1 g of trisodium citrate

dihydrate, and 0.5 g of disodium hydrogen citrate sesquihydrate) was added and immediately shaken vigorously for 1 min by hand and centrifuged for 5 min at 4000 rpm. After centrifugation, 6 mL of the supernatant was taken into a 15-mL polypropylene tube, 450 mg sorbent and 900 mg magnesium sulfate were added and agitated for 1 minute.

In the clean-up step four polymeric resins namely, Dianon, Polyamide, PPVP and XAD-7 were used. PSA was used for comparison with the standard method. To avoid possible deviation which may come from the extraction process, spiking of standard pesticide solution to the samples were made after the extraction step and just before the clean-up process. After spiking of pesticide standard solutions, Dianon, Polyamide, PPVP, XAD-7 and PSA were added with magnesium sulfate as clean up reagent as described BS EN 15662 method. For each resin, two different concentrations and 6 replicates were performed. After centrifuging at 4000 rpm for 5 mins 1 mL supernatant were taken for LC-MS/MS analysis (API 4000 Q-TRAP).

2.3. LC-MS/MS analysis

For the liquid chromatographic analysis Shimadzu HPLC (UFLC LC-20AD) system was used. The chromatographic separation was achieved with inertsil 100 mm x 2,1 mm column with 3 µm particle size. The mobile phase A contained methanol/water (2+8, v/v) with 5 mmol/L ammonium formate and mobile phase B contained methanol/water (9+1, v/v) with 5 mmol/L ammonium formate. The gradient program was given at Table 1. A 10 µL of the sample was injected at a flow rate of 0.3 mL at 40 °C.

Table 1: LC flow program.

Time	%B
0 min	0
11 min	100
23 min	100
25 min	0
36 min	0

Determination of pesticides was achieved by Applied bio-system triple quadrupole mass spectrometer was operated in multiple reactions monitoring (MRM). The mass spectrometer ion source parameters were: curtain gas, ion source gas, temperature, and ion spray voltage were set to 20 mL/min, 50 mL/min, 550 °C, and 5500 V, respectively. Pesticide and their transitions ions used for the quantification, collision energy (CE), and de-clustering voltage (DP) are listed in Table 2.

Table 2: LC-MS/MS parameters of the pesticides.

Pesticide	Polarity	Q1 mass	Q3 mass	DP (v)	CE (v)
2 4 D	ESI -	219.0	160.9	20	15
2.4.5-T	ESI -	253.0	195	40	10
Acephate	ESI +	184.1	124.9	10	25
Acetamiprid	ESI +	223.0	126	61	27
Aclonifen	ESI +	265.0	182.1	55	40
Alachlor	ESI +	270.1	238.1	30	15
Atrazine	ESI +	216.1	174.0	71	25
Azoxystrobin	ESI +	404.1	371.9	36	20
Benalaxyl	ESI +	326.2	148.2	26	25
Benfluralin	ESI +	336.0	57	30	10
Bentazone	ESI -	239.1	132	51	30
Bifenazate	ESI +	299.0	253	40	10
Bitertanol	ESI +	338.2	70	5	25
Boscalid	ESI +	343.0	307	71	25
Bromacil	ESI +	261.0	205	21	20
Bromophos Ethyl	ESI +	394.9	338.7	51	25
Bromoxynil	ESI -	273.9	79	46	35
Bromuconazole	ESI +	378.0	159	46	35
Bupirimate	ESI +	317.1	166.1	31	33
Buprofezin	ESI +	306.2	201.2	6	15
Butacarboxim Sulfoxide	ESI +	207.1	131.9	41	10
Cadusafos	ESI +	271.1	159	66	20
Carbaryl	ESI +	202.1	144.9	66	15
Carbendazim	ESI +	192.1	160	56	25
Carbofuran	ESI +	222.1	165.1	46	10
Carbosulfan	ESI +	381.2	118.1	36	25
Carboxin	ESI +	236.1	142.9	26	21
Chlorfenvinphos	ESI +	358.9	155	36	20
Chlorfluazuron	ESI +	539.9	158	70	25
Chloridazon	ESI +	222	92.2	91	35
Chloroxuron	ESI +	291.1	72	51	40
Chlorpropham	ESI +	214	172	25	10
Chlorpyrifos	ESI +	349.9	96.9	21	41
Chlorpyrifos-Methyl	ESI +	321.9	125.1	25	27
Chlorsulfuron	ESI +	358	141	50	25
Chlorthamid	ESI +	205.9	118.9	35	55
Cinidon-Ethyl	ESI +	411.1	348	40	30
Clofentezine	ESI +	303.1	102.1	55	45
Cyazofamid	ESI +	325	108	36	20
Cyclanilide	ESI -	272	159.9	55	30
Cycloate	ESI +	216.1	154.3	56	10
Cymoxanil	ESI +	199.1	128	61	10
Cyproconazole	ESI +	292.1	70.2	15	35
Cyprodinil	ESI +	226.1	76.9	81	65
Deltamethrin	ESI +	522.9	280.7	16	25
Demeton S Methyl	ESI +	248	89.1	6	17
Demeton S Methyl Sulfoxide	ESI +	247	169	10	15
Desmedipham	ESI +	318.1	182.2	31	20
Di-Allate	ESI +	270	86.1	41	23
Diazinon	ESI +	305.1	169.1	20	30
Dichlofluanid	ESI +	350	223.9	20	40
Dichlorprop-P	ESI -	233.0	161	20	15
Dichlorvos	ESI +	220.9	127.1	71	27
Difenoconazole	ESI +	406.1	250.9	41	35
Dimethenamide	ESI +	276.1	244.1	11	20
Dimethoate	ESI +	230	125	31	10
Dimethomorph	ESI +	388.1	301.1	45	30

Pesticide	Polarity	Q1 mass	Q3 mass	DP (v)	CE (v)
Dimoxytrobin	ESI +	327	116	30	10
Diniconazole	ESI +	326	70	55	45
Dinobutan	ESI +	327	215	45	10
Dinoterb	ESI -	239.1	176	30	50
Diphenylamine	ESI +	170.1	93.1	66	35
Disulfoton	ESI +	275	89.2	10	10
Disulfoton Sulfone	ESI +	307	153	50	10
Disulfoton Sulfoxide	ESI +	291	213	30	10
Ditalimfos	ESI +	300	130	35	10
Dithianion	ESI +	296	264	50	25
Diuron	ESI +	233	72	65	30
Epoxiconazole	ESI +	330.1	121	36	25
Eptc	ESI +	190.1	128.1	46	15
Esfenvalerat	ESI +	437.1	125	25	50
Ethiofencarb	ESI +	226.1	107.2	41	20
Ethion	ESI +	385	199.1	15	20
Ethirimol	ESI +	210.2	98.1	86	35
Ethofumesate	ESI +	304.1	121.1	35	25
Ethoprophos	ESI +	243	131	20	30
Ethoxyquin	ESI +	218.2	160.2	66	45
Etozole	ESI +	360.2	141	65	40
Etrimfos	ESI +	293.1	125	25	35
Famoxodane	ESI +	392.2	238	16	25
Fenamidone	ESI +	312.1	92.2	40	35
Fenamiphos	ESI +	304.1	217.1	40	30
Fenarimol	ESI +	331	81	45	45
Fenazaquin	ESI +	307.2	161.2	51	30
Fenbuconazole	ESI +	337.1	125.1	41	40
Fenhexamid	ESI +	302.1	97.2	90	35
Fenitrothion	ESI +	278.1	125	41	30
Fenoxaprop-Ethyl	ESI +	362.1	288.1	45	23
Fenoxycarb	ESI +	302.1	88	66	30
Fenpropatrin	ESI +	350.2	125.1	41	20
Fenpropimorph	ESI +	304.3	147.1	45	40
Fenthion	ESI +	279.1	169.1	20	25
Fenvalerate	ESI +	437.1	125	35	55
Flazasulfuron	ESI +	408.1	182.1	40	25
Fluazifop-P-Butyl	ESI +	384.1	282.1	50	27
Fludioxinil	ESI -	247	125.9	56	40
Flufenacet	ESI +	364.1	194.2	10	17
Flufenoxuron	ESI +	489	158.1	85	30
Fluopicolide	ESI +	383	109	35	10
Flurochloridone	ESI +	312	291.9	60	30
Flurtamone	ESI +	334.1	247.1	50	30
Flusilazole	ESI +	316.1	247.1	36	25
Flutolanil	ESI +	324.1	262.1	86	25
Foramsulfuron	ESI +	453.1	182.2	50	25
Fosthiasate	ESI +	284	104.1	61	27
Furathiocarb	ESI +	383.2	195	50	23
Heptenophos	ESI +	251	127	35	20
Hexaconazole	ESI +	314.1	70.1	35	40
Hexythiazox	ESI +	353.1	227.9	65	20
Imazalil	ESI +	297	158.9	25	30
Imazamox	ESI +	306	246	30	10
Indoxacarb	ESI +	528.1	203	75	50
Iprodione	ESI -	328	141.1	5	10
Iprovalicarb	ESI +	321.2	119	46	23
Isoproturon	ESI +	207.1	165.2	46	20
imazaquin	ESI +	312.1	199.1	45	35

Pesticide	Polarity	Q1 mass	Q3 mass	DP (v)	CE (v)
Imidachloprid	ESI +	256.1	175	45	25
İoxynil	ESI -	369.8	126.8	45	35
İsoxaben	ESI +	333	150	40	30
Lambda Cyhalothrin	ESI +	467.1	225	16	23
Malathion	ESI +	331	99	17	30
Mcpa	ESI -	199	140.8	45	20
Mecarbam	ESI +	330	227	25	15
Mecoprop-P	ESI -	213	140.7	50	15
Mepanipyrim	ESI +	224.1	77	41	10
Mesosulfuron Methyl	ESI +	504.1	182.1	60	33
Metalaxyl-M	ESI +	280.1	220	45	19
Metazachlor	ESI +	278.1	210.1	5	15
Methacrifos	ESI +	241	209.1	31	15
Methamidophos	ESI +	142	124.9	25	20
Metolachlor	ESI +	284	252	25	30
Metosulam	ESI +	418	175.1	26	25
Metribuzin	ESI +	215.1	187.2	61	25
Mevinphos	ESI +	225	193.1	30	10
Molinate	ESI +	188.1	83.2	20	25
Monocroptos	ESI +	224.1	127	46	21
Monolinuron	ESI +	215.1	125.9	51	25
Monuron	ESI +	199.1	72	51	29
Myclobutanil	ESI +	289.1	70.1	35	30
Nuarimol	ESI +	315	81.1	40	40
Omethoate	ESI +	214.1	109	46	35
Oxadiargyl	ESI +	341	223	25	10
Oxadiazon	ESI +	362.1	220	40	30
Oxadixyl	ESI +	279.1	219.2	45	25
Oxamyl	ESI +	237.1	90	20	15
Oxasulfuron	ESI +	407.1	150.1	55	25
Oxycarboxin	ESI +	268	175.1	35	20
Oxyflourfen	ESI +	379	316	20	25
Penconazole	ESI +	284.1	158.9	41	40
Pendimethalin	ESI +	282.1	212.2	5	15
Permethrin	ESI +	408.1	153.1	30	25
Pethoxamid	ESI +	296	250	15	10
Phenmedipham	ESI +	301.1	136.1	56	25
Phenthoate	ESI +	321	163.1	36	17
Phorate	ESI +	278.1	74.9	5	23
Phosalon	ESI +	367.9	182	50	20
Phosmet	ESI +	317.9	160.1	30	20
Phosphamidon	ESI +	300	127.1	35	25
Picloram	ESI -	240.9	196.9	66	15
Picolinafen	ESI +	377.1	145	56	70
Primicarb	ESI +	239.1	72.1	15	30
Primiphos-Methyl	ESI +	306.1	164.1	25	30
Prochloraz	ESI +	376	308	15	15
Profenofos	ESI +	372.9	302.9	55	25
Prometyrn	ESI +	242.1	158.1	30	30
Propamocarb Hydrochloride	ESI +	189.2	102	51	10
Propanil	ESI +	218	162	56	10
Propargite	ESI +	368.1	175.1	5	20
Propham	ESI +	180.1	138.1	31	10
Propiconazole	ESI +	342.1	69.1	45	33
Propyzamide	ESI +	256	173.1	35	30
Prothiophos	ESI +	344.9	240.9	40	27
Pymetrozine	ESI +	218.1	105	76	10
Pyraclostrobin-	ESI +	388.1	194	5	20
Pyrazophos	ESI +	374.1	222.1	60	30

Pesticide	Polarity	Q1 mass	Q3 mass	DP (v)	CE (v)
Pyridaben	ESI +	365.1	309.1	26	20
Pyridaphention	ESI +	341	189	45	30
Pyridate	ESI +	379.1	207.1	5	20
Pyrimethanil	ESI +	200.1	106.9	50	30
Pyriproxyfen	ESI +	322.1	96.2	15	20
Quinalphos	ESI +	299	163	20	30
Quinoxifen	ESI +	307.9	162	20	60
Quizalofop Ethyl	ESI +	373.1	298.9	70	25
Resmethrin	ESI +	356.2	171.2	20	20
Rimsulfuron	ESI +	432.1	182	46	30
Simazine	ESI +	202.1	132.2	66	10
Spiroxamine	ESI +	298.3	144.2	40	30
Sulfosulfuron	ESI +	471.1	261	10	25
Tauflualinate	ESI +	520.1	208.1	30	23
Tebuconazole	ESI +	308.1	70	20	40
Tepp	ESI +	291.1	179	45	25
Terbufos	ESI +	289	57.1	30	35
Terbumeton	ESI +	226.1	170.2	25	25
Terbuthylazine	ESI +	230.1	174.1	40	20
Terbutryn	ESI +	242.1	186.1	20	25
Tetrachlorvinphos	ESI +	366.9	127.1	46	21
Thiacloprid	ESI +	253	126	81	30
Thiamethoxam	ESI +	292	211	50	15
Thiamethoxam	ESI +	292	211	40	25
Thifensulfuron Methyl	ESI +	388	167	35	20
Thiodicarb	ESI +	355	88	26	20
Thiophanate Methyl	ESI +	343	151	26	25
Tolclophos-Methyl	ESI +	301	175	46	35
Tolyfluanid	ESI +	364	237.9	6	20
Triadimefon	ESI +	294	197.2	36	20
Triadimenol	ESI +	296.1	70.1	10	20
Tri-Allate	ESI +	304	142.9	40	35
Triasulfuron	ESI +	402.1	167.1	46	25
Triazophos	ESI +	314	119.1	36	50
Tribenuron Methyl	ESI +	396.1	155	50	20
Trichlorfon	ESI +	274	108.9	10	30
Tridemorph	ESI +	298.3	116.1	55	30
Trifloxystrobin	ESI +	409.1	186.1	10	25
Triflumizole	ESI +	346	278	10	15
Triticonazole	ESI +	318.1	70.2	35	35
Zoxamide	ESI +	336	159	40	15

2.4. Recovery

To evaluate the effectiveness of the sorbent, pesticide standard solutions tea samples were spiked at two different concentration levels, viz. 10 and 100 µg/kg and analyzed with the method which was described in sample preparation above. Standard solutions were added just before the clean-up step to eliminate possible deviation coming from extraction step. Four different sorbents, namely Dianon, Polyamide, PPVP, and XAD, were used as clean-up sorbents and PSA was used as the control group. Pesticide standard solutions were added to the samples at 10 and 100 µg/kg levels. After analyzing samples with LC-MS/MS, recovery% values were calculated according to Equation 1.

$$Recovery(\%) = \left(\frac{C_1}{C_2} \right) \times 100 \quad (\text{Eq. 1})$$

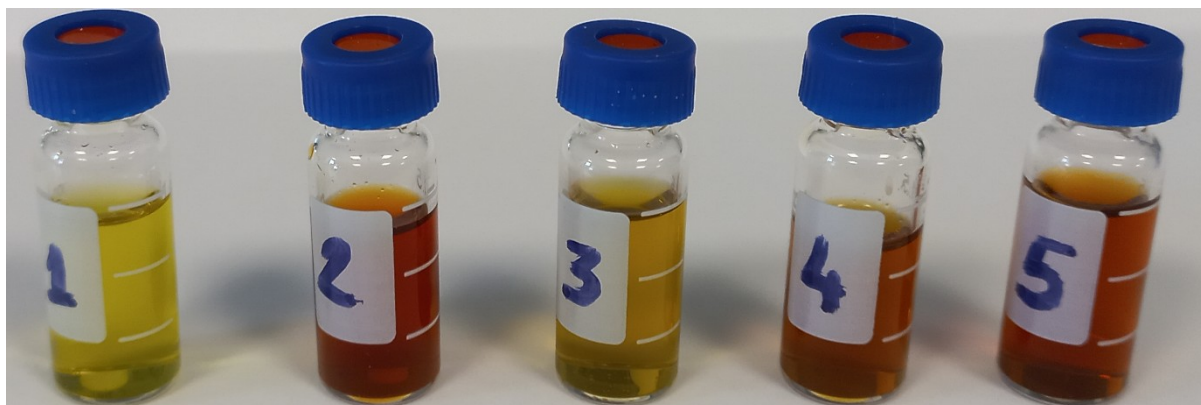
2.5. Matrix Effect

In order to see the effectiveness of these 4 different adsorbents in eliminating the co-extracts, the blank tea extracts, which were clean-up with these adsorbents, were analyzed by GC-MS. GC-MS analyses were carried out in total ion mode to see the composition of co-extracts. GC/MS analyses were carried out using a capillary HP-50 column (50% phenyl-methyl polysiloxane, with 30 m length, 0.25 ID and 0.25 µm film thickness). Oven program of gas chromatography are given in Table 3.

Table 3: Gas Chromatography Oven Program.

Initial Temp.(°C)	Rate (°C/Min)	Last Temp.(°C)	Hold (min)
50	-	50	4
50	5	260	4

3. RESULTS AND DISCUSSION

**Figure 1:** Appearance of the extracts after clean-up 1: PSA, 2: Diaion, 3: Polyamide, 4: PPVP, 5: XAD 7.

After clean-up process, samples were analyzed with LC-MS/MS. In the spiking solution, 216 pesticides were included. After clean up process appearance of the tea extracts were shown in Figure 1. It was observed that both PSA and polyamide could better in removing the color of the tea extract than the rest of the sorbents. For the determination of these 216 pesticides matrix, matched calibrations were used.

Matrix matched calibrations were prepared for each resin with using the same resin. Recovery studies were performed with each resin in six replicates at 10 and 100 µg/kg. The recovery values for each pesticide were given in Table 4. Also, the recovery ratios for each resins were summarized in Table 5 and Figure 2. For both concentration levels, similar recovery results were obtained.

Table 4: Recovery ratios for each resins.

Recovery%	PSA	Diaion	Polyamide	PPVP	XAD
<60	41	12	23	17	22
60 - 80	9	9	9	4	4
80 - 120	135	130	84	86	99
120 - 140	11	27	77	62	56
>140	20	38	23	47	35
Total	216	216	216	216	216

According to the recovery results, it was observed that the PSA was the best with 135 pesticides in the generally accepted range of 80-120%. After PSA, Diaion was determined as the second with 130 pesticides in the range of 80-120%. Polyamide and PPVP were at the bottom with 84 and 86 pesticides, respectively, in the range of 80 - 120%, while XAD differentiated with 99 pesticides both from PSA and Diaion, and from Polyamide and PPVP. On the other hand, if we select the acceptable limit as 60-140%, polyamide was determined as the resin that gave the best results with 170 pesticides. While Diaion was the second resin with 166 pesticides, XAD, PSA and PPVP were determined as the third, fourth and fifth resins with very close values 159, 155 and 152 pesticides, respectively. It is noteworthy that PSA is determined as the third resin when the acceptable

range is referred to as 60-140%. Another remarkable point is that 41 pesticides give a recovery value of less than 60% when PSA was used as clean-up resin. These results are compatible with previously published reports indicative of recoveries of some pesticides were adversely affected by PSA (21). Especially pesticides those containing the P=O group tend to be adsorbed to PSA. On the other hand, 12 pesticides gave a recovery value of less than 60% when Diaion was used as clean-up resin. Although polymeric adsorbents are widely used in the purification of bioactive compounds from tea, they have not been used as a stand-alone cleaning agent in pesticide analysis before. However, some studies have been conducted in which PVPP is used as a clean-up agent in combination with different adsorbents. Jiao and et al. (2016) have developed a

method for the determination of eight pesticide residues with LC-MS/MS, combining a QuEChERS method using PVPP and GCB clean-up with a dilution factor of 400 method in order to diminish the complex and varied matrix interference due to co-extracted from tea. They found average recoveries of eight neonicotinoid insecticides ranged from 66.3 to 108.0% (22). Cao et al. (2015) have developed a method based on matrix solid phase dispersion for the determination and the quantification of 16 pesticides in various tea samples by using PVPP (750 mg), PSA (1 g) and GCB (50 mg) as clean-up sorbent. The recoveries of this method at three spiked concentration levels ranged from 87.7 to 99.6% (14). Hou et al. (2022) developed a method to scan for 134 pesticide residues in tea was developed that employs a novel Multi-Functional Filter (MFF) contained a mixture of 50 mg of PSA, 10 mg of GCB, 150 mg of porous PVPP, and 150 mg of anhydrous MgSO₄. They calculated recoveries at two spiked levels (50, 100 µg/kg) ranged between 66.83–118.33%. They reported that purification through the multi-function filter (MFF-3-Layered) reduced the matrix effect more than purification via the modified QuEChERS method (17). Although polymeric

adsorbents were used in combination with other adsorbents in these studies, similar results were obtained in our study when they were used alone.

In order to evaluate the clean up efficiency of the adsorbent, gas chromatography mass spectrometry analyses were carried out. Blank tea extracts were analyzed with GC-MS after clean up with these adsorbents. Total ion chromatograms of each extracts were taken to evaluate removal efficiency of co-extracts. Chromatograms were given in Figure 3. As a result of GC MS analysis, it was observed that PSA gave the chromatogram with the least amount of co-extracts. On the other hand, it was observed that PSA was the worst adsorbent in removing caffeine, which is one of the main bioactive compound in tea. XAD-7 and polyamide were found to be the best adsorbents in removing caffeine. PSA was, as expected, very effective in removing the fatty acids. While no fatty acids were found in the extracts cleaned with PSA, fatty acids were detected in the extracts cleaned with other adsorbents. PPVP was found to be insufficient in removing both caffeine and fatty acids.

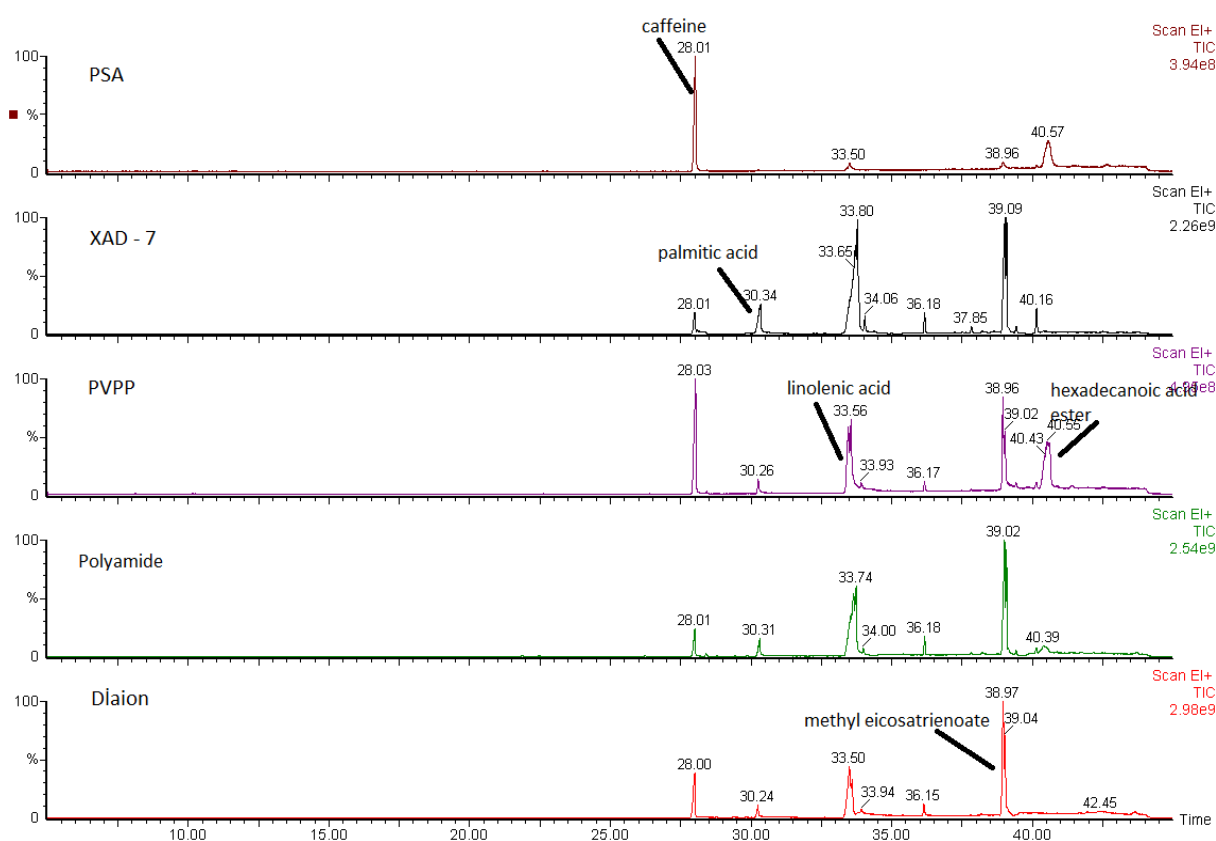


Figure 2: GC-MS chromatogram of tea extracts after clean up.

Table 5: Recovery values of the pesticides.

Pesticide	Recovery %				
	Dianon	PPVP	PSA	PA	XAD
2,4-D	<0.01	289	40.85	308	<0.01
2,4,5-T	117	68	<0.01	64	105

Pesticide	Recovery %				
	Dianon	PPVP	PSA	PA	XAD
Acephate	204.5	114.5	76.5	102	103.5
Acetamiprid	62	157.5	367.5	114	129.5
Aclonifen	95.5	186.5	<0.01	128	40.95
Alachlor	110.5	125.5	100	119.5	124.5
Atrazine	112.5	107.5	99.5	103.5	124
Azoxystrobin	319.5	171	391	415	426.5
Benalaxyl	107.5	117.5	97	128	117
Benfluralin	510	458	<0.01	<0.01	<0.01
Bentazon	113.5	54.5	83.5	100.5	108.5
Bifenazate	130.5	132.5	113	70	114.5
Bitertanol	98	106	92.5	132	115
Boscalid	93.5	134	96	117.5	139.5
Bromacil Pztf	94	119	122.5	98	78
Bromophos Ethyl	151.5	100	90	123.5	116
Bromoxynil	99.5	48.05	40.55	90	106.5
Bromuconazole	43.85	107.5	105	<0.01	111
Bupirimate	103.5	133	100.5	128.5	113
Buprofezin	89	112	92.5	112.5	115.5
Butacarboxim Sulfoxide	112.5	129	90.5	116.5	129.5
Cadusafos	119	125.5	101	138.5	146.5
Carbaryl	130	102.5	117	117.5	110
Carbendazim	131	118	208.5	186.5	89
Carbofuran	112	129	116	123	130.5
Carbosulfan	<0.01	105	101.5	88.5	187
Carboxin	101	110.5	99	113.5	109.5
Chlorfenvinphos	99.5	120.5	108	121.5	116
Chlorfluazuron	54.5	129	101	117.5	102
Chloridazon	89.5	91	71	185.5	140
Chloroxuron	106	119.5	102	120.5	104
Chlorpropham	126	139.5	131	<0.01	156
Chlorpyrifos	103	123.5	<0.01	145	119.5
Chlorpyrifos-Methyl	123	123	116	137.5	130
Chlorsulfuron	119	<0.01	22.3	126	123.5
Chlorthamid	286.5	<0.01	70.5	41.8	122.5
Cinidon-Ethyl	110.5	114	103	115.5	124.5
Clofentezine	48.25	128	89.5	117	112.5
Cyazofamid	127.5	130	108	120	127.5
Cyclanilide	113.5	42.9	19.75	63.5	95.5
Cycloate	100.5	119	102.5	127	130.5
Cymoxanil	119.5	66.5	108.5	138.5	84.5
Cyproconazole	128	114	111	108.5	141
Cyprodinil	90	117	99.5	142.5	127.5
Deltamethrin	75.5	90.5	110	137.5	123.5
Demeton S Methyl	228.5	1725	<0.01	148	237
Demeton S Methyl Sulfoxide	105	<0.01	<0.01	140	153.5
Desmedipham	106.5	110.5	106.5	113.5	110
Di-Allate	100	112.5	103	124	107.5
Diazinon	106.5	123.5	102	125	115
Dichlofluanid	404.5	405.5	128	<0.01	415
Dichlorprop-P	115	85.5	10.75	86	94.5
Dichlorvos	203.5	161	<0.01	75.5	207
Difenoconazole	94	115	92	124	118.5
Dimethenamide	113.5	116	100	115.5	116.5
Dimethoate	65.5	132	96	113.5	58
Dimethomorph	112	120.5	102	116.5	110
Dimoxytrobin	277	350	415	160	302.5
Diniconazole	105.5	102.5	89	119.5	114
Dinobutan	433	500	<0.01	<0.01	<0.01

Pesticide	Recovery %				
	Dianon	PPVP	PSA	PA	XAD
Dinoterb	106	97.5	75	112.5	107
Diphenylamine	106	113.5	127	122.5	113.5
Disulfoton	465.5	494.5	<0.01	<0.01	431.5
Disulfoton Sulfone	150.5	158.5	115.5	129.5	144.5
Disulfoton Sulfoxide	<0.01	<0.01	<0.01	153.5	<0.01
Ditalimfos	111.5	127	93.5	122.5	122.5
Dithianion	95.5	1155	104	72	35.35
Diuron	113	115	107	103.5	113
Epoxiconazole	181	190	124.5	<0.01	193
Eptc	110.5	121.5	152.5	139	115.5
Esfenvalerat	137	170.5	<0.01	104	105.5
Ethiofencarb	126.5	120.5	102	119.5	123.5
Ethion	<0.01	<0.01	300.5	<0.01	61
Ethirimol	91.5	131	106	112.5	136.5
Ethofumesate	137.5	144	<0.01	117.5	152.5
Ethoprophos	166.5	720	94	91	<0.01
Ethoxyquin	100.5	114	97.5	110.5	100
Etoxzole	87.5	130.5	93	126.5	116
Etrimfos	108	146.5	105.5	126.5	129.5
Famoxodane	138	178	474.5	325	389.5
Fenamidone	111.5	127	101.5	116.5	121
Fenamiphos	118	114.5	101.5	119.5	117.5
Fenarimol	113.5	107	116	104	116
Fenazaquin	315	321.5	<0.01	<0.01	446
Fenbuconazole	104	129.5	106.5	118.5	121
Fenhexamid	119.5	111.5	94.5	115.5	128.5
Fenitrothion	226	319	100	<0.01	435
Fenoxaprop-Ethyl	98	117.5	99	119	118
Fenoxycarb	115.5	135.5	109.5	122.5	149.5
Fenpropatrin	109.5	145	112.5	127	131.5
Fenpropimorph	110	119	99	115.5	113
Fenthion	111	181	<0.01	133	<0.01
Fenvalerate	137	170.5	145.5	104	105.5
Flazasulfuron	119.5	103.5	37.5	106	109
Fluazifop-P-Butyl	122.5	118.5	97.5	123	117.5
Fludioxinil	118	111.5	107	110.5	108.5
Flufenacet	113	123	103.5	122	128.5
Flufenoxuron	112.5	129	104	120	105.5
Fluopicolide	116	121	112	119	118
Flurochloridone	117.5	113.5	114.5	128.5	120
Flurtamone	389.5	<0.01	349	<0.01	89.5
Flusilazole	113.5	113	103.5	120.5	119.5
Flutolanil	119.5	111	108	118.5	127.5
Foramsulfuron	144.5	94	<0.01	<0.01	57.5
Fosthiasate	114.5	127	111.5	110	112
Furathiocarb	101.5	118.5	98	126	116
Heptenophos	116	185.5	158.5	96.5	133.5
Hexaconazole	116.5	103.5	105.5	108.5	122.5
Hexythiazox	74	131	95.5	126	113.5
Imazalil	106	103.5	80.5	140	117
Imazamox	<0.01	98	2.79	61	4.74
Indoxacarb	117	103.5	109.5	154.5	180
Iprodione	134.5	233	102	113.5	74
Iprovalicarb	117.5	123.5	100.5	117.5	115.5
Isoproturon	113.5	113.5	109.5	116	127.5
İmazaquin	296	<0.01	123	<0.01	965
İmidachloprid	133.5	115	96	126.5	79.5
İoxynil	109	36.45	53	78.5	110

Pesticide	Recovery %				
	Dianon	PPVP	PSA	PA	XAD
Isoxaben	111	130.5	102.5	113	103
Lambda Cyhalothrin	89	111.5	121.5	126	159.5
Malathion	162.5	144	100.5	<0.01	121.5
Mcpa	120.5	74.5	9.45	76	90.5
Mecarbam	119.5	123	100	124	127
Mecoprop-P	110	102	9.35	91	95
Mepanipyrim	118	128	92.5	111	105
Mesosulfuron Methyl	141.5	126	71	133.5	80.5
Metalaxyl-M	114.5	123.5	109	122.5	114.5
Metazachlor	112.5	116.5	105.5	115	124
Methacrifos	148.5	173	164	137	166
Methamidophos	158.5	221	78.5	176.5	107.5
Metolachlor	<0.01	<0.01	41.75	245	<0.01
Metosulam	106	126	36.5	128	117.5
Metribuzin	70	177.5	109	75.5	101.5
Mevinphos	91.5	63.5	645	116.5	<0.01
Molinate	97.5	121.5	101.5	120.5	117.5
Monocroptos	125	123.5	102.5	119	118
Monolinuron	106.5	125	115.5	119.5	115.5
Monuron	110	107.5	107.5	126	120.5
Myclobutanil	472	468	114	1445	122.5
Nuarimol	79.5	103	104	119.5	115.5
Omethoate	107.5	155.5	84	120.5	97.5
Oxadiargyl	239	163.5	141.5	197	99
Oxadiazon	96.5	107.5	103.5	129.5	124.5
Oxadixyl	119	108.5	106.5	128.5	112.5
Oxamyl	92	117.5	125	107	108.5
Oxasulfuron	114.5	109	54.5	117.5	103
Oxycarboxin	135.5	84.5	101	131	147.5
Oxyflourfen	99	<0.01	116.5	525	164.5
Penconazole	104	126.5	113	123.5	116
Pendimethalin	87	115	0.04105	112	0.112
Permethrin	82	106	42.35	142.5	0.635
Pethoxamid	31.7	400	163	<0.01	27.6
Phenmedipham	104.5	110.5	105.5	116	110.5
Phenthoate	159	117.5	113	144	125
Phorate	104	127	98	122.5	117
Phosalon	116	116	115.5	113.5	130.5
Phosmet	106.5	116	99.5	128	115.5
Phosphamidon	95.5	117.5	105.5	132	58
Picloram	145.5	153	82.5	165	132
Picolinafen	99	117	104	123	114.5
Primicarb	109	125	102	124.5	128.5
Primiphos-Methyl	99.5	131.5	99	123.5	120
Prochloraz	107.5	116.5	94.5	122.5	108.5
Profenofos	83	126.5	101.5	116	137
Prometyrn	109	125.5	98	125	117
Propamocarb Hydrochloride	113	124.5	63	138	99.5
Propanil	88.5	145.5	92	113.5	124.5
Propargite	103	127	<0.01	114.5	124.5
Propham	118	125	129	120	145.5
Propiconazole	112.5	109.5	102.5	102.5	133.5
Propyzamide	129	107.5	101.5	107	154
Prothiophos	455.5	570	<0.01	138.5	111
Pymetrozine	6.3	181.5	<0.01	7800	126
Pyraclostrobin-	198	183	145.5	133.5	224
Pyrazophos	107	113.5	105	129.5	130.5
Pyridaben	87	104.5	124.5	115.5	101.5

Pesticide	Recovery %				
	Diaion	PPVP	PSA	PA	XAD
Pyridaphention	107	120	113.5	115.5	119.5
Pyridate	81.5	96	57	116	97.5
Pyrimethanil	107.5	120.5	104	124	112.5
Pyriproxyfen	80	118.5	101.5	122	113.5
Quinalphos	103.5	121.5	104.5	129	110
Quinoxifen	64	107	113.5	145	<0.01
Quizalofop Ethyl	89.5	119.5	98	126.5	129.5
Resmethrin	84	98	74	90	98.5
Rimsulfuron	123	119	30.8	131.5	112.5
Simazine	440	321	359	427	360
Spiroxamine	109	98	92	115.5	114
Sulfosulfuron	385	<0.01	53.5	<0.01	417
Taufluvalinate	75	117	<0.01	133	123
Tebuconazole	98.5	120.5	107.5	124.5	105.5
Tepp	355	<0.01	430	<0.01	625
Terbufos	108.5	131.5	100	139.5	130.5
Terbumeton	110.5	119.5	105	119	121
Terbuthylazine	113	129.5	101	134	112
Terbutryn	98	124.5	94	123.5	113
Tetrachlorvinphos	125	130	104.5	131	101
Thiacloprid	188	200	77.5	95	166
Thiamethoxam	<0.01	<0.01	<0.01	<0.01	131.5
Thifensulfuron Methyl	132.5	142	43.75	124	<0.01
Thiodicarb	128	129.5	111.5	110	128
Thiomethoxam	309	580	330	<0.01	477.5
Thiophanate Methyl	98.5	423.5	102.5	<0.01	133.5
Tolclophos-Methyl	129.5	119.5	120.5	137	<0.01
Tolyfluanid	122	135.5	105.5	135	123.5
Triadimefon	132	120.5	98.5	119	<0.01
Triadimenol	141.5	122.5	112	124	<0.01
Tri-Allate	78.5	153	106.5	98.5	138
Triasulfuron	119.5	130	58.5	125	124.5
Triazophos	282	261.5	<0.01	<0.01	320
Tribenuron Methyl	111	107	80	98.5	93
Trichlorfon	357.5	462	436.5	615	399.5
Tridemorph	117.5	109	99.5	119.5	115
Trifloxystrobin	114	119	96	119	109.5
Triflumizole	107	121	98.5	127	131.5
Triticonazole	133	111.5	106.5	119.5	128.5
Zoxamide	237	<0.01	333.5	<0.01	350

4. CONCLUSION

In this study, the suitability of 4 polymeric resins, namely; Diaion, Polyamide, PPVP and XAD 7 as a clean-up reagent for determination of pesticide residues in tea. In addition, a clean-up process was performed using PSA to compare with the standard method. In order to evaluate the effectiveness of the sorbents, recovery studies were carried out and compared with the recovery study carried out with PSA. According to the recovery results, it was observed that the PSA was the best with 135 pesticides in the generally accepted range of 80-120%. After PSA, Diaion was determined as the second with 130 pesticides in the range of 80-120%. On the other hand, when the acceptable limit was accepted as 60-140%, it was determined that the resin that gave the best results with 170 pesticides

was polyamide. Diaion was the second resin with 166 pesticides, while XAD, PSA and PPVP were determined as the third, fourth and fifth resins with very close values of 159, 155 and 152 pesticides, respectively. According to GC-MS total ion analysis of blank tea extracts cleaned with these adsorbents, it was observed that PSA gave the chromatogram with the least co- extract, while it was observed that PSA was the worst adsorbent in removing caffeine, one of the main bioactive compounds in tea. XAD-7 and polyamide were found to be the best adsorbents in removing caffeine. According to result of this study, it was evaluated that the use of polyamide together with PSA as a clean-up reagent for pesticide analysis in tea would be the most effective method for removing both fatty acids and bioactive components in tea.

5. CONFLICT OF INTEREST

Author have no conflict of interest.

6. REFERENCES

- Li X, Zhang Z, Li P, Zhang Q, Zhang W, Ding X. Determination for major chemical contaminants in tea (*Camellia sinensis*) matrices: A review. *Food Research International*. 2013 Oct;53(2):649-58. Available from: [<URL>](#).
- Rutkowska E, Łozowicka B, Kaczyński P. Modification of Multiresidue QuEChERS Protocol to Minimize Matrix Effect and Improve Recoveries for Determination of Pesticide Residues in Dried Herbs Followed by GC-MS/MS. *Food Anal Methods*. 2018 Mar;11(3):709-24. Available from: [. <URL>](#).
- Zhang C, Suen CLC, Yang C, Quek SY. Antioxidant capacity and major polyphenol composition of teas as affected by geographical location, plantation elevation and leaf grade. *Food Chemistry*. 2018 Apr;244:109-19. Available from: [. <URL>](#).
- Pang GF, Fan CL, Cao YZ, Yan F, Li Y, Kang J, et al. High Throughput Analytical Techniques for the Determination and Confirmation of Residues of 653 Multiclass Pesticides and Chemical Pollutants in Tea by GC/MS, GC/MS/MS, and LC/MS/MS: Collaborative Study, First Action 2014.09. *Journal of AOAC INTERNATIONAL*. 2015 Sep 1;98(5):1428-54. Available from: [<URL>](#).
- Guan Y, Tang H, Chen D, Xu T, Li L. Modified QuEChERS method for the analysis of 11 pesticide residues in tea by liquid chromatography-tandem mass spectrometry. *Anal Methods*. 2013;5(12):3056. Available from: [<URL>](#).
- Hayward DG, Wong JW, Park HY. Determinations for Pesticides on Black, Green, Oolong, and White Teas by Gas Chromatography Triple-Quadrupole Mass Spectrometry. *J Agric Food Chem*. 2015 Sep 23;63(37):8116-24. Available from: [<URL>](#).
- Hou X, Lei S, Guo L, Qiu S. Optimization of a multi-residue method for 101 pesticides in green tea leaves using gas chromatography-tandem mass spectrometry. *Revista Brasileira de Farmacognosia*. 2016 Jul;26(4):401-7. Available from: [<URL>](#).
- Zhao HX, Zhao SC, Deng LG, Mao JS, Guo CY, Yang GS, et al. Rapid Determination of Organonitrogen, Organophosphorus and Carbamate Pesticides in Tea by Ultrahigh-Performance Liquid Chromatography-Tandem Mass Spectrometry (UPLC-MS/MS). *Food Anal Methods*. 2013 Apr;6(2):497-505. Available from: [<URL>](#).
- Wu CC. Multiresidue method for the determination of pesticides in Oolong tea using QuEChERS by gas chromatography-triple quadrupole tandem mass spectrometry. *Food Chemistry*. 2017 Aug;229:580-7. Available from: [<URL>](#).
- Saito-Shida S, Nemoto S, Teshima R. Multiresidue determination of pesticides in tea by gas chromatography-tandem mass spectrometry. *Journal of Environmental Science and Health, Part B*. 2015 Nov 2;50(11):760-76. Available from: [<URL>](#).
- Liu X, Guan W, Hao X, Wu X, Ma Y, Pan C. Pesticide Multi-Residue Analysis in Tea Using d-SPE Sample Cleanup with Graphene Mixed with Primary Secondary Amine and Graphitized Carbon Black Prior to LC-MS/MS. *Chromatographia*. 2014 Jan;77(1-2):31-7. Available from: [<URL>](#).
- Hou X, Lei S, Qiu S, Guo L, Yi S, Liu W. A multi-residue method for the determination of pesticides in tea using multi-walled carbon nanotubes as a dispersive solid phase extraction adsorbent. *Food Chemistry*. 2014 Jun;153:121-9. Available from: [<URL>](#).
- Rejczak T, Tuzimski T. QuEChERS-based extraction with dispersive solid phase extraction clean-up using PSA and ZrO₂-based sorbents for determination of pesticides in bovine milk samples by HPLC-DAD. *Food Chemistry*. 2017 Feb;217:225-33. Available from: [<URL>](#).
- Cao Y, Tang H, Chen D, Li L. A novel method based on MSPD for simultaneous determination of 16 pesticide residues in tea by LC-MS/MS. *Journal of Chromatography B*. 2015 Aug;998-999:72-9. Available from: [<URL>](#).
- Sun X, Luo J, Lu Q, Li C, Zhao Z, An F, et al. Application of hydroxylated multi-walled carbon nanotubes as depigmentation agent in the determination of multiple pesticide residues in *Lonicerae japonicae* flower buds. *Microchemical Journal*. 2022 Jun;177:107280. Available from: [<URL>](#).
- Zhao WH, Shi YP. A porous boron nitride nanorods-based QuEChERS analysis method for detection of five neonicotinoid pesticide residues in goji berries. *Journal of Chromatography A*. 2022 May;1670:462968. Available from: [.<URL>](#)
- Meng X, Song W, Xiao Y, Zheng P, Cui C, Gao W, et al. Rapid determination of 134 pesticides in tea through multi-functional filter cleanup followed by UPLC-QTOF-MS. *Food Chemistry*. 2022 Feb;370:130846. Available from: [<URL>](#).
- Guo J, Tong M, Tang J, Bian H, Wan X, He L, et al. Analysis of multiple pesticide residues in polyphenol-rich agricultural products by UPLC-MS/MS using a modified QuEChERS extraction and dilution method. *Food Chemistry*. 2019 Feb;274:452-9. Available from: [<URL>](#).
- Ahmad A, Siddique JA, Laskar MA, Kumar R, Mohd-Setapar SH, Khatoun A, et al. New generation Amberlite XAD resin for the removal of metal ions: A review. *Journal of Environmental Sciences*. 2015 May;31:104-23. Available from: [<URL>](#).
- Kyriakopoulos GG, Hourdakakis AA, Doulia DD. Adsorption of Pesticides on Resins. *Journal of Environmental Science and Health, Part B*. 2003 Mar;38(2):157-68. Available from: [<URL>](#).
- Rajski Ł, Lozano A, Belmonte-Valles N, Uclés A, Uclés S, Mezcuá M, et al. Comparison of three multiresidue methods to analyse pesticides in green tea with liquid and gas chromatography/tandem mass spectrometry. *Analyst*. 2013;138(3):921-31. Available from: [<URL>](#).
- Jiao W, Xiao Y, Qian X, Tong M, Hu Y, Hou R, et al. Optimized combination of dilution and refined QuEChERS to overcome matrix effects of six types of tea for determination eight neonicotinoid insecticides by ultra performance liquid chromatography-electrospray tandem mass spectrometry. *Food Chemistry*. 2016 Nov;210:26-34. Available from: [<URL>](#).